2 Magnetic properties of rare earth elements, alloys and compounds

2.1 Rare earth elements

2.2 Rare earth hydrides

2.3 Alloys between rare earth elements

2.4 Compounds of rare earth elements and 3d elements

2.5 Compounds of rare earth elements and 4d or 5d elements
See Subvolume III/19d

2.6 Compounds based on rare earth elements and Cu, Ag or Au
See Subvolume III/19e1

2.7 Compounds of rare earth elements and Be, Mg, Zn, Cd or Hg

2.7.1 Introduction

More than a thousand binary metallic compounds of rare earths (R) exist. Among them, compounds with Be, Mg and group 2B elements constitute a family of about 340 members. One of their main features is the fact that the alloyed metal (X) is nonmagnetic; a deep knowledge of the fundamental aspects of 4f magnetism in a metallic surrounding may then be gained. In the past, studies on polycrystalline samples were mainly based on magnetic susceptibility and spectroscopic measurements. For the last 15 years, magnetic studies have been extensively diversified using monocrystalline materials: the various interactions of the well-localized 4f shell with its surrounding (crystalline electric field – CEF) as well as with its neighbours (pair interactions, not restricted to the Heisenberg exchange) are now rather well determined. This shows in particular how progress in magnetism is strongly dependent on the crystallographic and metallurgical characteristics of the samples.

As a consequence, this review is organized as follows: the first part of the introduction defines the metallurgical conditions for the preparation of single-phase samples in the mono- or polycrystalline state; the crystallographic characteristics are also presented which determine, through the symmetry and the number of the rare-earth sites, the difficulty for the analysis of the magnetic properties. The introduction then gives the salient features of the 4f magnetism observed in these compounds. Finally, review articles are given. Abbreviations, symbols and necessary conversions between magnetic units are listed in the introduction of this volume. In the following subsections, compounds are presented according to their crystallographic structure in order to facilitate comparison in relation with the alloyed metal. Subsect. 2.7.2 is devoted to RX compounds within the CsCl-type structure, subsects. 2.7.3 and 2.7.4 to RX_2 and RX_3 compounds, respectively; subsect. 2.7.5. collects X-rich compounds together, except for the RBe_{13}-series discussed in subsect. 2.7.6. Subsect. 2.7.7. presents the ternary compounds first studied.

2.7.1.1 Crystallography and metallurgy

Table 1. Composition, structure type, space group, symmetry of the rare earth sites, nature of the melting (C: congruent; P: peritectic) and references for binary rare earth compounds with Be, Mg, Zn, Cd, Hg elements.

▶

	Be	Mg	Zn	Cd	Hg	Structure	
R_2X					Yb	orth	$PbCl_2$
RX		La–Lu, Y, Sc	La–Lu, Y, Sc	La–Tm, Lu, Y, Sc	La–Lu, Y, Sc	cub	CsCl
RX_2		La–Sm, Gd Eu, Y, Tb–Lu				cub	$MgCu_2$
				Yb		hex	$MgZn_2$
			La–Lu, Y	Eu		orth	$CeCu_2$
				La–Sm, Gd–Tm, Lu, Y, Sc	La–Er, Yb, Y	hex	$CeCd_2$
RX_3		La–Sm, Gd–Dy		Ce–Nd		cub	BiF_3
				Sc, Gd–Tb	La–Lu, Y, Sc	hex	Ni_3Sn
			Y, Pr–Sm, Gd–Tm, Lu			orth	YZn_3
			Ce			orth	$CeZn_3$
				Tb–Tm, Lu, Y		orth	$ErCd_3$
$R_{14}X_{51}$				Eu, Yb	Eu, Yb	hex	$Gd_{14}Ag_{51}$
R_3X_{11}			Ce–Sm, Gd–Dy, Y, Yb			orth	La_3Al_{11}
$R_{11}X_{45}$				Pr–Sm, Gd–Tm, Lu, Y	La–Sm, Gd	cub	$Sm_{11}Cd_{45}$
			La			orth	$LaZn_4$
$R_{13}X_{58}$			Ce–Sm, Gd–Lu, Y	La–Gd, Y	La	hex	$Pu_{13}Zn_{58}$
R_5X_{24}		Tb–Tm, Lu, Y, Sc				cub	α-Mn
RX_5			La, Ce, Eu			hex	$CaCu_5$
		Eu	Ho–Tm, Lu, Y			rh	$EuMg_5$
R_3X_{17}			Yb			cub	Ru_3Be_{17}
RX_6				Ce–Lu, Y		cub	YCd_6
R_3X_{22}			La–Sm, Gd			tetr	Pu_3Zn_{22}
R_5X_{41}		Ce				tetr	Ce_5Mg_{41}
R_2X_{17}		La, Ce, Eu	Ce–Sm, Gd–Tm, Lu, Y			hex	Th_2Ni_{17}
			La–Sm, Gd–Lu, Y	La		rh	Th_2Zn_{17}
RX_{11}			La–Nd, Eu, Yb	Eu		tetr	$BaCd_{11}$
			Sm			hex	$SmZn_{11}$
				La–Sm		cub	$BaHg_{11}$
RX_{12}		Ce, Pr	Sm, Gd–Tm, Lu, Sc, Y			tetr	$ThMn_{12}$
RX_{13}	La–Lu, Y, Sc		La, Eu, Yb			cub	$NaZn_{13}$

Space group	Rare earth site symmetry	Nature of the melting	Remarks	Ref.
Pnma	m			79 i
Pm3m	m3m	C	RMg: P (close to congruence)	79 i, 65 I 1, 64 M 1, 72 P 1
Fd3m	$\bar{4}3m$	P	close to congruence	72 P 1
$P6_3/mmc$	3m	P	EuMg: C	68 I 1, 72 P 1, 71 P 1
Imma	mm	C		66 L 1, 68 I 1
P6/mmm	6/mmm	C	congruence only for light rare earths	68 I 1
Fm3m	m3m	P	La–$NdMg_3$: C	76 B 2, 73 B 2
$P6_3/mmc$	$\bar{6}m2$	P		69 R 1, 71 B 1, 51 I 1, 76 B 1
Pnma	m	P		68 M 1, 70 B 1
Cmcm	mm	P		66 L 1, 70 B 1
Cmcm	mm	P		72 F 1, 73 B 2
P6/m	6 m		3 magnetically different R sites	79 M 1, 71 P 1
Immm	mmm mm	P		63 C 1, 70 B 1
$F\bar{4}3m$	$\bar{4}3m$ 3m m	~C	5 magnetically different R sites	78 F 1, 79 M 1
		~C	probable orth distortion of $BaAl_4$-type	70 B 1
$P6_3mc$	3m m	~C	5 magnetically different R sites	67 W 1, 73 B 2, 76 B 1
$I\bar{4}3m$	$\bar{4}3m$ 3m	P	close to congruence at the end of the series	65 S 1, 78 D 1
P6/mmm	6/mmm	P		74 M 1, 74 B 1
$P6_3/mmc$	mm	P		74 B 1, 70 M 2, 71 F 1
Im3	m	P		70 B 1
Im3	m	P		71 L 1, 71 P 1
$I4_1/amd$	$\bar{4}2m$ mm	P		70 B 1
I4/m	4/m m	P	close to congruence	70 J 1
$P6_3/mmc$	$\bar{6}m2$	C	existence of both phases for R_2Zn_{17}	67 J 1, 67 V 1, 70 M 1
$R\bar{3}m$	3m	C		67 I 1, 73 B 1
$I4_1/amd$	$\bar{4}2m$	P		67 I 1, 67 V 1, 73 B 2
P6/mmm	6/mmm $\bar{6}m2$	P	4 magnetically different R sites	70 M 3
Pm3m	4/mmm	P		73 B 1, 71 B, 73 B 2
I4/mmm	4/mmm	P	2 phases for $CeMg_{12}$ [70 J 1]	67 V 1, 67 I 1, 70 J 1
Fm3c	43	C	RZn_{13}: P	61 G 1, 67 I 1

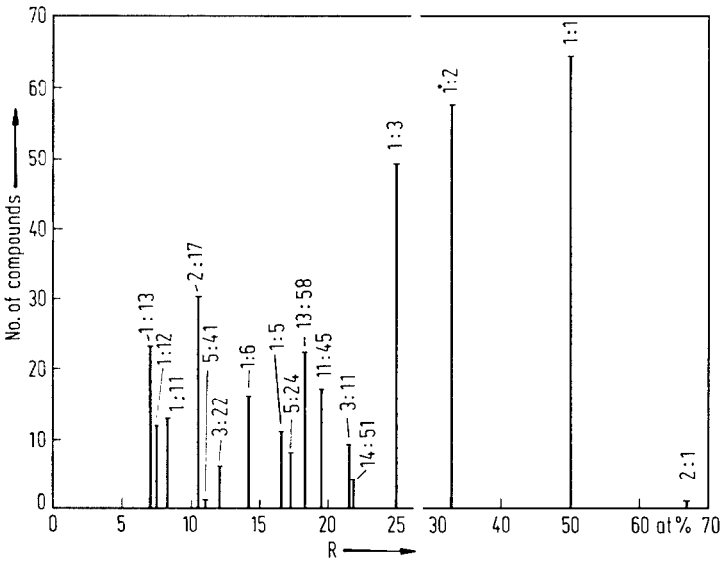

Fig. 1. R-group 2. Histogram of rare earth compounds with Be, Mg, Zn, Cd, Hg as a function of the rare earth concentration. The numerator of ratios corresponds to the rare earth.

All the compounds are characterized by rather difficult metallurgical conditions. This is due to (i) the hazards involved in handling Be or heavy elements like Cd and Hg and (ii) the high vapour pressure of Mg, Zn, Cd, and Hg. This latter difficulty enforces the physicist to use closed refractory metallic crucibles and limits the crystal-growing to the Bridgman method. This in particular explains the weak number of studies for Hg compounds.

The low electronegativity of rare earths in comparison with other elements was shown to be the driving reason for the large number of defined compounds occurring for a given alloyed metal [76 M 4]. Thus 9 different structures have been observed with Mg, 18 with Zn, 14 with Cd and 7 with Hg. On the contrary, only one structure is obtained with Be, the rare earth electronegativity difference with Be being weak. As the stability of a structure also depends on the metallic radii of the components, series for a given metal are often incomplete due to the lanthanide contraction. In some cases only one compound is observed, for which the rare earths Ce, Eu, Yb, exhibit exotic properties.

Figure 1 gives the histogram of about 340 compounds here considered as a function of the rare earth concentration. It also includes Y and Sc compounds. About 180 compounds are distributed in only 3 compositions RX, RX_2, RX_3. Table 1 gives the details of compounds existing in every structure. It thus appears that from a crystallographic point of view Y behaves like a true rare earth while Sc is more different and will not be considered in the following. The RX compounds constitute complete series within the CsCl-type structure for Mg, Zn, Cd, and Hg, allowing systematic magnetic studies and comparisons. RX_2 and RX_3 series are in general very large, if not complete. Compounds defined by more complicated stoichiometric ratios may be often deduced from a simple structure: the $NaZn_{13}$-type structure of RBe_{13} can be considered as a CsCl-type arrangement of polyhedrons of 24 Be at the corners and 1 R at the centre. Table 1 also gives the symmetry of the R site. This in particular defines the number of unknown parameters occurring in the magnetic Hamiltonian: the high symmetry of RX will then facilitate a deep insight in the 4f magnetism. More detailed information on the symmetry may be found in specialized handbooks [67 p, 72 p, 85 v].

Also indicated in Table 1 is the nature of the melting, deduced from phase diagrams gathered in handbooks like "Constitution of binary alloys" [58 h, 65 e, 69 s] or the General Electric "Handbook of binary phase diagrams". Indeed, it is of fundamental importance for magnetic studies to be performed on single-phase materials. This is easily realized for congruently melting compounds, but necessitates more or less complicate annealing in the case of peritectic meltings. In addition a congruent melting greatly facilitates the preparation of large single crystals well-suited for magnetic studies. However, one has to keep in mind that phase diagrams are not fully established and may depend on the purity of the rare earth.

As a consequence of these crystallographic and metallurgical conditions, complete series of binary compounds with congruent melting have motivated the large majority of magnetic studies, particularly when the symmetry of the rare earth is high: thus the main part of the literature is devoted to the RX compounds.

In relation with the large difference in electronegativity between the two components, pseudobinary compounds can usually be obtained by partial substitution of a rare earth for another: this process has been used with nonmagnetic La, Y and, to a smaller extend, Lu for decreasing the magnetic interactions. Substitution of the alloyed metal for another is sometimes found in particular with regard to the nature of the magnetic interactions.

The metallurgical difficulties previously discussed explain that synthesis of ternary or quaternary defined compounds based on Be, Mg or group 2B elements is only starting (subsect. 2.7.7).

2.7.1.2 Magnetism

The origin of the coupling between magnetic ions is of fundamental importance. The high ordering temperatures often observed cannot be accounted for by magnetic dipole forces. Indeed, in metallic systems, conduction electrons play the driving role by propagating their local interaction with the inner 4f shell from one site to the others. This indirect exchange mechanism has been described in the RKKY model of Ruderman and Kittel [54 R 1], Kasuya [56 K 1] and Yosida [57 Y 1] assuming that the conduction electrons behave as free electrons. The Curie temperature Θ is then given by the De Gennes law [62 D 1]. An analogous description may be carried out for the antiferromagnetic ordering temperature. Other properties associated with the magnetic coupling, such as the spin disorder resistivity [62 R 1] or nuclear (NMR and Mössbauer spectroscopy) and electronic (EPR) resonances [57 Y 1], can also be analysed within this simple theory. From an experimental point of view, it met some success, but its shortcomings are now obvious: the rigid-band assumption is unable to explain for instance

(i) the slower decrease of magnetic interactions in $Gd_xY_{1-x}Zn$ than in $Gd_xLa_{1-x}Zn$ with increasing the dilution (Fig. 47),

(ii) the fact that keeping the electron number constant leads to different behaviours in $GdCd_xZn_{1-x}$ and in $Gd(Ag_{0.5}In_{0.5})_xZn_{1-x}$ (Fig. 48),

(iii) the sign reversal for Θ in RMg and RZn series (Table 3), and

(iv) the magnetism of heavy RMg compounds, for which the spin structure is either canted or hesitating between ferro- and antiferromagnetism (subsect. 2.7.2).

De Haas-van Alphen experiments have shown that the Fermi surface is far from being spherical [73 J 1] and evidence has been obtained in NMR experiments for a large 5d character of the conduction band [77 G 1, 77 D 1]. This orbital character of the conduction band gives rise to additional contributions to the magnetic interactions [70 L 1]. This alters the De Gennes law, as was quantitatively shown for the RCd compounds [84 A 1]. The d-character of electrons close to the 4f shell has been confirmed by numerous band calculations [77 H 1] (Fig. 2). A recent thorough study of the complete k–f Coulomb interaction has shown the great difficulty to define precise variation laws within a rare earth series, as well as from one series to another (Figs. 3, 4) [85 S 1]. This may be experimentally underlined by Table 7 which gives exchange forces between successive neighbours deduced from spin wave excitation spectra in heavy RZn compounds.

Another consequence of the d-character of the conduction band is the existence of quadrupolar pair interactions as observed for instance in CsCl-type compounds (subsect. 2.7.2). These high-order pair interactions may be sometimes larger than the bilinear ones as in TmZn and TmCd (Figs. 67, 106). As for these latter terms, again no simple variation law across a series is observed.

With regard to the crystalline electric field (CEF), the failure of the point charge model has been extensively evidenced by systematic and unambiguous determinations based on neutron spectroscopy. Here again, considering the complete k–f local interaction has shown that the large d-character of the conduction band mainly determines the CEF in cubic compounds. The dependence of the CEF parameters on the rare earth is complex and included in the Slater integrals [79 S 1, 86 G 1]. As for the pair interactions, no variation law across an R series or an X series can be easily obtained, in particular for high symmetry.

The CEF is of similar strength as pair interactions. Thus the overall CEF splitting of energy levels in the paramagnetic phase is often of the same order of magnitude as the magnetic ordering temperature. The CEF mixing of the 4f wave functions, particularly strong in high symmetry, enforces a quantum treatment for analysing all the magnetic features. Realized in particular in cubic compounds, this has explained coherently a large number of various anisotropic physical properties (see subsect. 2.7.2).

Table 2. General reviews.

Crystallography and metallurgy	Magnetism
Iandelli and Palenzona [79 i]	Buschow [79 b, 80 b]
Pearson [67 p, 72 p, 85 v]	Kirchmayr and Poldy [79 k]
Hansen, Elliott and Shunk [58 h, 65 e, 69 s] for phase diagrams	Fulde [79 f] for crystal fields
	Lüthi [80 l] for magnetoelastic effects
	Rögl [84 r] for ternary compounds

The metallurgical difficulties previously discussed explain that synthesis of ternary or quaternary defined compounds based on Be, Mg or group 2B elements is only starting (subsect. 2.7.7).

2.7.1.2 Magnetism

The origin of the coupling between magnetic ions is of fundamental importance. The high ordering temperatures often observed cannot be accounted for by magnetic dipole forces. Indeed, in metallic systems, conduction electrons play the driving role by propagating their local interaction with the inner 4f shell from one site to the others. This indirect exchange mechanism has been described in the RKKY model of Ruderman and Kittel [54 R 1], Kasuya [56 K 1] and Yosida [57 Y 1] assuming that the conduction electrons behave as free electrons. The Curie temperature Θ is then given by the De Gennes law [62 D 1]. An analogous description may be carried out for the antiferromagnetic ordering temperature. Other properties associated with the magnetic coupling, such as the spin disorder resistivity [62 R 1] or nuclear (NMR and Mössbauer spectroscopy) and electronic (EPR) resonances [57 Y 1], can also be analysed within this simple theory. From an experimental point of view, it met some success, but its shortcomings are now obvious: the rigid-band assumption is unable to explain for instance

(i) the slower decrease of magnetic interactions in $Gd_xY_{1-x}Zn$ than in $Gd_xLa_{1-x}Zn$ with increasing the dilution (Fig. 47),

(ii) the fact that keeping the electron number constant leads to different behaviours in $GdCd_xZn_{1-x}$ and in $Gd(Ag_{0.5}In_{0.5})_xZn_{1-x}$ (Fig. 48),

(iii) the sign reversal for Θ in RMg and RZn series (Table 3), and

(iv) the magnetism of heavy RMg compounds, for which the spin structure is either canted or hesitating between ferro- and antiferromagnetism (subsect. 2.7.2).

De Haas-van Alphen experiments have shown that the Fermi surface is far from being spherical [73 J 1] and evidence has been obtained in NMR experiments for a large 5d character of the conduction band [77 G 1, 77 D 1]. This orbital character of the conduction band gives rise to additional contributions to the magnetic interactions [70 L 1]. This alters the De Gennes law, as was quantitatively shown for the RCd compounds [84 A 1]. The d-character of electrons close to the 4f shell has been confirmed by numerous band calculations [77 H 1] (Fig. 2). A recent thorough study of the complete k–f Coulomb interaction has shown the great difficulty to define precise variation laws within a rare earth series, as well as from one series to another (Figs. 3, 4) [85 S 1]. This may be experimentally underlined by Table 7 which gives exchange forces between successive neighbours deduced from spin wave excitation spectra in heavy RZn compounds.

Another consequence of the d-character of the conduction band is the existence of quadrupolar pair interactions as observed for instance in CsCl-type compounds (subsect. 2.7.2). These high-order pair interactions may be sometimes larger than the bilinear ones as in TmZn and TmCd (Figs. 67, 106). As for these latter terms, again no simple variation law across a series is observed.

With regard to the crystalline electric field (CEF), the failure of the point charge model has been extensively evidenced by systematic and unambiguous determinations based on neutron spectroscopy. Here again, considering the complete k–f local interaction has shown that the large d-character of the conduction band mainly determines the CEF in cubic compounds. The dependence of the CEF parameters on the rare earth is complex and included in the Slater integrals [79 S 1, 86 G 1]. As for the pair interactions, no variation law across an R series or an X series can be easily obtained, in particular for high symmetry.

The CEF is of similar strength as pair interactions. Thus the overall CEF splitting of energy levels in the paramagnetic phase is often of the same order of magnitude as the magnetic ordering temperature. The CEF mixing of the 4f wave functions, particularly strong in high symmetry, enforces a quantum treatment for analysing all the magnetic features. Realized in particular in cubic compounds, this has explained coherently a large number of various anisotropic physical properties (see subsect. 2.7.2).

Table 2. General reviews.

Crystallography and metallurgy	Magnetism
Iandelli and Palenzona [79 i]	Buschow [79 b, 80 b]
Pearson [67 p, 72 p, 85 v]	Kirchmayr and Poldy [79 k]
Hansen, Elliott and Shunk [58 h, 65 e, 69 s] for phase diagrams	Fulde [79 f] for crystal fields
	Lüthi [80 l] for magnetoelastic effects
	Rögl [84 r] for ternary compounds

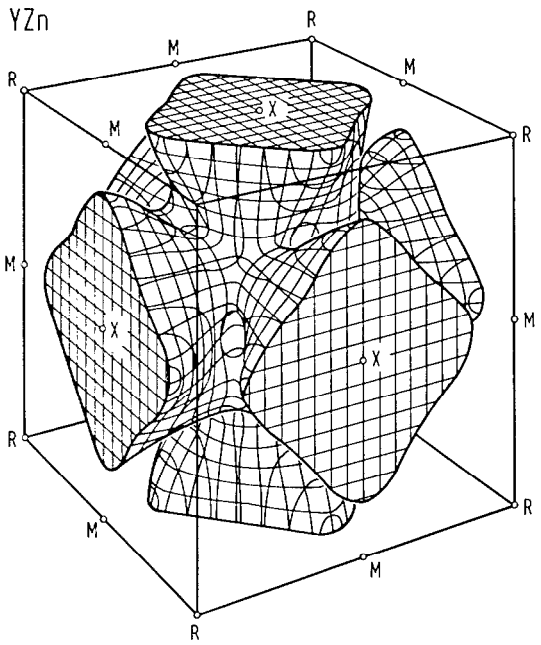

Fig. 2. YZn. Perspective of the third-band Fermi surface in the first Brillouin zone from APW band calculations [77 H 1].

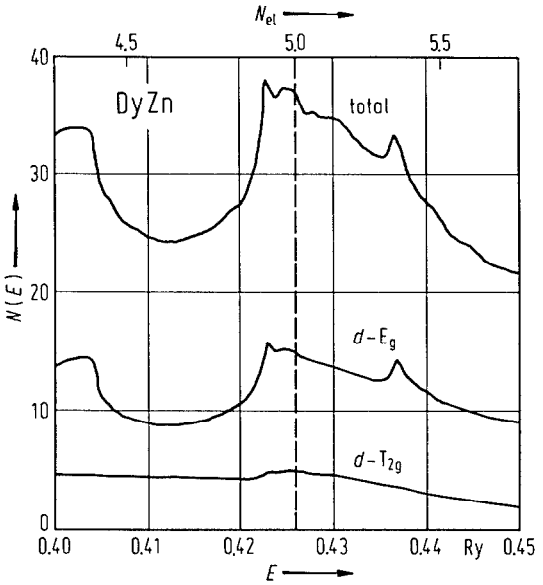

Fig. 4. DyZn. Details of the partial and total densities of states about E_F per Ry and unit cell. The broken line at $E_F = 0.426$ Ry corresponds to 5 conduction electrons per unit cell (upper scale) [85 S 1].

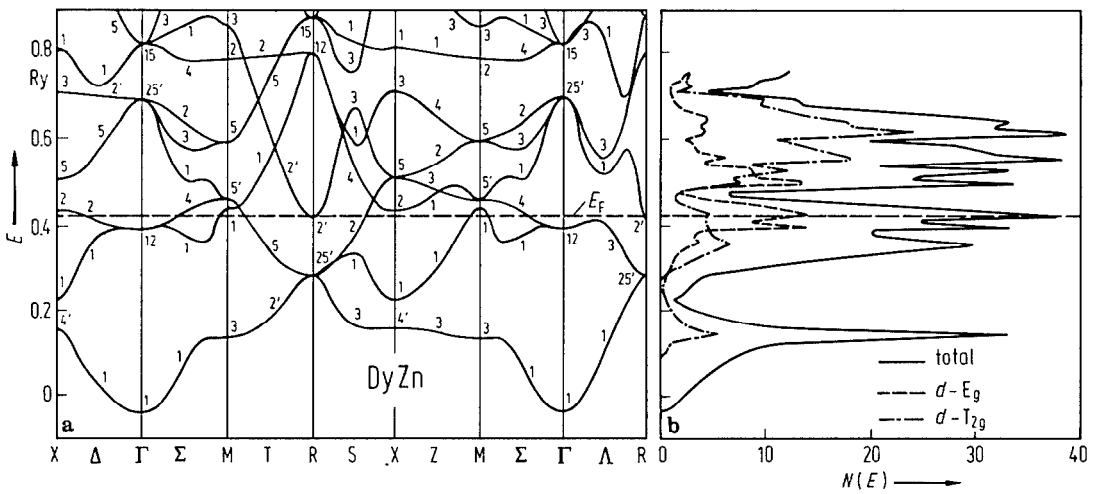

Fig. 3. DyZn. (a) Self consistent APW energy band structure. The broken line shows the Fermi energy $E_F = 0.426$ Ry. (b) Total density and E_g, T_{2g} partial densities of conduction electrons about the Dy nucleus per Ry and unit cell [85 S 1].

2.7.2 RX compounds

The complete series of CsCl-type compounds have been extensively studied, except for the Hg series due to unfavourable metallurgical conditions. They have historically furnished the best support for defining the limits of the RKKY model and revealing the large d-character of the conduction band. The effects of the polarization of the conduction band is here emphasized by the examples of the SmZn and SmCd ferromagnets: conduction electrons are polarized parallel to the 4f spin moment, i.e. antiparallel to the total angular momentum $J=L-S$, and their magnetization exceeds the 4f one [79 G 1]. Because of the weakness of the resulting magnetization these ferromagnets have been considered as antiferromagnets for a long time.

Another peculiar feature of the magnetic coupling is encountered in RMg compounds: a canted structure is found in GdMg, i.e. for an S-state. This cannot be explained in cubic symmetry by isotropic or anisotropic bilinear interactions. The coupling responsible of this canting is not yet known. It seems rather large, but weakly anisotropic. It may also occur in other heavy RMg compounds, where the magnetic structure hesitates between ferro- and antiferromagnetism (Table 3).

As a function of temperature, the spontaneous magnetization does not follow a Brillouin function, but exhibits spin wave contributions (Figs. 14, 97). These latter ones have to be analysed in a CEF model [80 M 2]. However, magnetic dispersion spectra cannot be described coherently across a series (cf. Table 7) although the long-range nature is obvious for bilinear interactions.

RZn and RCd single crystals have revealed a lot of characteristic CEF features: changes of easy magnetization direction are often observed from a twofold axis stable at low temperature to a fourfold or threefold one stable up to the ordering temperature. This first-order phase transition is explained by entropy effects driven by the anisotropic splitting of the level scheme under the exchange field (Figs. 38, 39). The necessity of a quantum treatment is required by the existence of a large anisotropy for both the energy and the magnetization (Table 9). CEF parameters do not vary according to a simple law across a series (Table 5).

The most original feature of these compounds is to exhibit large quadrupolar interactions. They are composed of both magnetoelastic and pair interactions. The magnetoelastic coupling consists of the reappearance of a second-order CEF term by lowering the cubic symmetry; it leads to record strains reaching 1.4%. The existence of such spontaneous deformations facilitates the determination of the actual antiferromagnetic structure from powder neutron diffraction (Figs. 35, 36). This magnetoelasticity constitutes the privileged probe for determining quadrupolar pair interactions: the pair coefficients can be deduced from the softening of elastic constants or from the change of length measured parallel ($\Lambda_{\parallel}$) and perpendicular ($\Lambda_{\perp}$) to an applied magnetic field in the paramagnetic temperature range (parastriction process [80 M 1].) Within the same susceptibility formalism for the disordered temperature range, quadrupolar interactions may be determined through the third-order magnetic susceptibility, i.e., the initial curvature of the magnetization curve [81 M 1].

TmZn and TmCd, which exhibit a quadrupolar ordering, appear as the archetypes of compounds dominated by quadrupolar interactions. However, magnetization processes are also strongly influenced (Figs. 65, 111); in DyZn and DyCd the quadrupolar coupling determines the easy axis in competition with the CEF [85 G 1]. As for the cubic CEF and the bilinear terms, both magnetoelasticity and pair interactions mainly originate from the conduction band [85 S 1].

RCd sets a complex problem, not yet solved, about structural transformations (Figs. 117, 118). Below 210 K, the cubic CsCl-type structure transforms into a structure of lower symmetry for LaCd, CeCd, PrCd and NdCd. Two mechanisms have been proposed, either a splitting of e_g states of the rare earth 5d electrons [73 I 1] or a softening of zone boundary phonons [80 K 3]. The situation is complicated by a second transformation at lower temperature. For heavy RCd compounds, a unique very weak transformation does not significantly modify the magnetic properties.

Table 3. RX compounds. Magnetic properties in the paramagnetic phase (effective magnetic moment per rare earth ion, p_{eff}, paramagnetic Curie temperature Θ) and in the ordered phase (magnetic ordering temperature, T_C or T_N, spin structure, easy magnetization direction, low-temperature spontaneous magnetic moment per rare earth ion, p_s, low-temperature spontaneous tetragonal strain, $c/a-1$).

	p_{eff}	p_{eff}(LT)	Θ	T_C	T_N	Spin structure	Easy axis	p_s	$c/a-1$	Remarks	Figures
	μ_B		K	K				μ_B	%		
LaMg										Pauli paramagnetism [80 P 1]	5, 7
CeMg	2.54	2.50	− 3 [85 P 1]		19.5 [84 P 1]	AF (1/2 0 0) collinear	[001]	1.85	1.3 [78 S 1]	$\Theta = -3$ K: low-temperature value	5–8
PrMg	3.59		− 11		45 [76 A 1]	AF (1/2 0 0) collinear	[001]	2.7	1.4 [78 M 1]		
NdMg	3.66		− 14		48 [73 B 3]	AF (1/2 0 0)		2.1 [75 B 1]			
GdMg	8.36		108	119 [75 A 1]		$C^{(0\,0\,0)}_{(1/2\,0\,0)}$	[111] [01$\bar{1}$]	$p_F = 4.9$ $p_{AF} = 5.1$		$p_{AF} = 0$ for $T > 85$ K [78 M 2]	9–16
TbMg	9.94		83	81 [75 A 1]		$C^{(0\,0\,0)}_{(1/2\,0\,0)}$	[011]	$p_F = 5.16$ $p_{AF} = 5.18$ [75 A 1]		canted structure in all the ordered range [77 S 1]	9, 17–20
DyMg	10.54		25		22 [76 A 1]	AF (1/2 0 0)		6.0		[76 S 1]	21, 22
HoMg	10.77		24	21		F	[111]	5.0		tendency to (1/2 0 0) short-range ordering [76 A 1]	21, 23, 24
ErMg	9.6		9	5.5		F	[111]	2.0		antiferromagnetism increasing at low temperature [76 A 1]	21, 25, 26
TmMg	7.5		2			P				[86 G 1]	27, 29
LaZn										Pauli paramagnetism [85 A 1]	30
CeZn	2.45	2.20	11		30 [81 P 2]	AF (1/2 0 0) collinear	[001]	1.95	1.7 [78 S 1]	$\Theta = 11$ K: low-temperature value	31–34
PrZn	3.68	3.39	− 28		52	AF (1/2 0 0) collinear	[001]	2.35	1.4	[75 M 1]	31, 35, 36

NdZn	3.98	3.40	− 70		70 [75 M 1]	AF (1/2 0 0) multiaxial	[110]	2.55 [75 M 2, 75 M 1]		[111] easy axis for $T > 18$ K [75 M 2]	31, 37–39
SmZn				127		F	[111]	0.055		Van-Vleck-type paramagnetism [79 G 1]	31, 40, 41
EuZn	7.82		14							divalent Eu [65 I 1]	
GdZn	7.54		269	269		F		7.3 [81 R 1]	−0.055 [77 M 1]	easy axis: [111] from NMR spectra [84 K 1] [001] from the spontaneous strain [81 R 1]	42–48
TbZn	9.4		200 [75 M 3]	199.6 [80 S 1]		F	[110]	8.85 [73 M 1]		[001] easy axis for $T > 61.9$ K [80 S 3]	42, 49–55
DyZn	10.3		139	139 [75 M 3]		F	[001]	9.05 [74 A 1]	+0.8 [77 M 1]	strong quadrupolar interactions [85 G 1]	42, 55–59
HoZn	10.6		76	75 [75 M 3]		F	[110]	8.67 [73 M 1]		[111] easy axis for $T > 23$ K [74 M 2]	42, 60–64
ErZn	9.69		25	20 [75 M 3]		F	[001]	6.81 [73 M 2]	−0.38 [77 M 1]		65, 66
TmZn	7.67		0 [76 M 2]	8.12		F	[001]	2	−0.9 [78 M 3]	quadrupolar ordering at $T_0 = 8.55$ K [83 M 3]	67–74
YbZn										divalent Yb [65 I 1]	
YZn										Pauli paramagnetism [85 P 1]	75–78
LaCd										Pauli paramagnetism [84 A 1]	79–82
CeCd	2.50		10 [74 B 2]	16.5		F	[111]	0.8 [85 F 1]		found AF in [84 A 1]	83–85
PrCd	3.44		35		41 [84 A 1]	AF	[111]	2.6 [84 A 1]		phase transition at 18 K in the ordered range [84 K 2]	86–90
NdCd	3.82		70 [74 B 2]	121 [84 A 1]		F	[110]	2.45 [85 A 1]		[111] easy axis for $T > 62.7$ K [84 A 1]	86, 91, 92
SmCd				194		F		0.05		Van-Vleck-type paramagnetism [74 S 1]	93–95

continued

Table 3 (continued).

	p_{eff}	p_{eff}(LT)	Θ	T_C	T_N	Spin structure	Easy axis	p_s	$c/a-1$	Remarks	Figures
	μ_B		K	K				μ_B	%		
EuCd	7.85		− 3							divalent Eu [65 I 1]	
GdCd	7.98		260	258 [84 A 1]		F		7.20		[85 A 1]	96–98
TbCd	9.70		160	158 [84 A 1]		F	[110]	8.9		[001] easy axis for $T > T_R = 67.5$ K [85 A 1]	96, 99–100
DyCd	10.65		80	80 [84 A 1]		F	[001]	8.9		phase transition at 41 K in the ordered range [85 A 1]	96, 101–103
HoCd	10.77		22.5	17 [84 A 1]		F	[111]	7.1		[85 A 1]	96, 104
ErCd	9.71		5	3.3 [84 A 1]		F	[001]	5.0		[85 A 1]	96, 105
TmCd	7.69		0			P [84 A 1]				quadrupolar ordering at $T_Q = 3.2$ K [73 L 1]	70, 106–113
YbCd										divalent Yb [65 I 1]	
YCd										Pauli paramagnetism [84 A 1]	80, 114
CeHg	2.73		− 32							[63 O 1]	
EuHg	7.63		11							divalent Eu [65 I 1]	
TbHg				80						[64 C 1]	
YbHg										divalent Yb [65 I 1]	

Table 4. RX compounds. Room-temperature lattice parameter a, room-temperature electrical resistivity ϱ, magnetic molar susceptibility χ_m or Pauli molar susceptibility χ_P, and electronic specific heat coefficient γ.

	a nm	ϱ (300 K) $\mu\Omega$ cm	χ_m or χ_P 10^{-4} cm^3 mol^{-1}	γ mJ mol^{-1} K^{-2}
LaMg	0.3962 [73 B 3]	0.2 (140 K) [80 P 1]	χ_P: 0.27 [80 P 1]	6.8 [85 P 1]
CeMg	0.3901 [73 B 3]	0.25 (80 K) [80 P 2]		40 [85 P 1]
PrMg	0.3877 [73 B 3]			
NdMg	0.3860 [73 B 3]			
SmMg	0.3832 [73 B 3]			
EuMg	0.4102 [79 i]			
GdMg	0.3808 [73 B 3]	1.56 [83 A 1]		
TbMg	0.3778 [73 B 3]			
DyMg	0.3759 [73 B 3]			
HoMg	0.3755 [73 B 3]			
ErMg	0.3737 [73 B 3]			
TmMg	0.3749 [73 B 3]			
YbMg				
YMg	0.3796 [73 B 3]		χ_P: 1.92 [80 P 1]	7.8 [79 P 1]
LaZn	0.3760 [60 I 1]	0.45 [81 P 1]	χ_P: 0.24 [85 P 1]	9 [85 P 1]
CeZn	0.3713 [63 O 1]	0.58 (200 K) [81 P 2]		19 [85 P 1]
PrZn	0.3678 [60 I 1]			
NdZn	0.3667 [65 I 1]			
SmZn	0.3625 [64 M 2]			
EuZn	0.3812 [65 I 1]		χ (300 K): 0.27 [65 I 1]	
GdZn	0.3601 [60 I 1]			
TbZn	0.3576 [65 I 1]			
DyZn	0.3562 [65 I 1]			
HoZn	0.3546 [65 I 1]			
ErZn	0.3533 [65 I 1]			
TmZn	0.3515 [65 I 1]			
YbZn	0.3629 [65 I 1]		χ (200 K): 0.037 [76 D 1]	
LuZn	0.3491 [65 I 1]	0.24 [86 M 1]		
YZn	0.3577 [71 S 1]		χ_P: 1.9 [85 P 1]	7.3 [85 P 1]
LaCd	0.3905 [60 I 1]	0.75 [84 A 1]	χ_P: 1.3 [84 A 1]	
CeCd	0.3865 [60 I 1]	0.89 [83 K 1]		
PrCd	0.3830 [60 I 1]	0.70 [83 S 1]		
NdCd	0.3811 [60 I 1]	0.90 [84 A 1]		
SmCd	0.3771 [60 I 1]	0.25 [74 S 1]		
EuCd	0.3960 [65 I 1]		χ (300 K): 0.26 [65 I 1]	
GdCd	0.3748 [60 I 1]	1.26 [80 S 2]		
TbCd	0.3734 [65 I 1]			
DyCd	0.3716 [65 I 1]	0.74 [84 A 1]		
HoCd	0.3695 [65 I 1]	0.47 [84 A 1]		
ErCd	0.3677 [65 I 1]	0.39 [84 A 1]		
TmCd	0.3665 [65 I 1]	0.25 [84 A 1]		
YbCd	0.3808 [65 I 1]		χ (300 K): 2.8 [65 I 1]	
LuCd	0.3640 [65 I 1]			
YCd	0.3712 [63 L 1]	0.31 [84 A 1]	χ_P: 1.2 [84 A 1]	
LaHg	0.3864 [76 B 1]			
CeHg	0.3816 [60 I 1]			
PrHg	0.3799 [60 I 1]			
NdHg	0.3780 [60 I 1]			
SmHg	0.3744 [60 I 1]			

continued

Table 4 (continued).

	a nm	ϱ (300 K) $\mu\Omega$ cm	χ_m or χ_P 10^{-4} cm^3 mol^{-1}	γ mJ mol^{-1} K^{-2}
EuHg	0.3880 [65 I 1]		χ (300 K): 0.25 [65 I 1]	
GdHg	0.3719 [60 I 1]			
TbHg	0.3690 [65 I 1]			
DyHg	0.3676 [65 I 1]			
HoHg	0.3660 [65 I 1]			
ErHg	0.3645 [65 I 1]			
TmHg	0.3632 [65 I 1]			
YbHg	0.3731 [65 I 1]		χ (300 K): 3.3 [65 I 1]	
LuHg	0.3607 [65 I 1]			
YHg	0.3670 [63 L 1]			

Table 5. RX compounds. Cubic crystalline electric field parameters of 4th and 6th order, $A_4\langle r^4\rangle$ and $A_6\langle r^6\rangle$, Lea Leask and Wolf parameters [62 L 1], W and x, and the experimental method for their determinations.

	W	x	$A_4\langle r^4\rangle$	$A_6\langle r^6\rangle$	Experimental method	Ref.
	K		K			
CeMg	−32	1	− 83.5	0	neutron spectr.	80 P 2
TbMg	0.5	~0.5	> 0	< 0	magnetic meas.	76 A 1
DyMg	− 0.4	>0.25	> 0	< 0	magnetic meas.	76 A 1
HoMg	0.32	−0.26	42	−13	neutron spectr.	77 S 2
ErMg	− 0.32	−0.03	3.6	−10.8	neutron spectr.	76 M 1
TmMg	0.61	−0.11	− 6.5	−12.9	neutron spectr.	86 G 1
CeZn	−11	1	− 28	0	neutron spectr.	81 P 2
PrZn	− 3.6	−0.57	− 47	−20	neutron spectr.	78 M 1
NdZn	3.4	0.52	−101	−17	neutron spectr.	78 M 1
TbZn	1	−0.3	− 41	−83	magnetic meas.	74 M 2
HoZn	0.36	0.08	− 14	−18	neutron spectr.	77 S 2
ErZn	− 0.61	0.16	− 36	−17.9	neutron spectr.	74 M 3
TmZn	1.2	−0.31	− 38	−19.6	neutron spectr.	78 M 3
NdCd	6.2	0.18	− 32	−15	magnetic meas.	85 A 1
DyCd	− 0.45	−0.32	− 32	−15	magnetic meas.	85 A 1
HoCd	0.33	0.19	− 32	−15	magnetic meas.	85 A 1
ErCd	− 0.5	0.16	− 32	−15	magnetic meas.	85 A 1
TmCd	0.95	−0.34	− 32	−15	magnetic meas.	79 A 1

Table 6. RZn compounds. Elastic constants c_{44}, $\frac{1}{2}(c_{11}-c_{12})$, $c_B=\frac{1}{3}(c_{11}+2c_{12})$ and linear thermal expansion coefficient α at room temperature (if not indicated otherwise), tetragonal and trigonal symmetry magnetoelastic coefficients, B_1 and B_2, respectively.

	c_{44}	$\frac{1}{2}(c_{11}-c_{12})$	c_B	α	B_1	B_2	
	GPa			$10^{-6}K^{-1}$	K		
CeZn					120		[81 P 2]
PrZn					33		[86 M 1]
GdZn	37.6	16.1	59.9 [86 M 1]				
TbZn	38.4	16.4	59.5 [86 M 1]	9.2 [77 M 1]	11	12	[80 M 1]
DyZn	43.2	18.0	61.1 [86 M 1]	10.7 [77 M 1]	10.4	− 1	[80 M 1]
HoZn	47.3	21.8	56.7 [86 M 1]	11 [77 M 1]	3.6	− 6	[80 M 1]
ErZn	51.8	27.3	71.6 [76 M 3]	9.7 [77 M 1]	−11	0	[80 M 1]
TmZn	52.1	23.9	67.7 [76 M 2]	7 (40 K) [84 M 1]	−28	14···34	[80 M 1]
LuZn	54.0	26.3	75.1 [86 M 1]	5 (40 K) [84 M 1]			
YZn	47.3	24.2	62.1 [71 S 1]				

For Tables 7–9, see next page.

Table 10. TmX compounds. Lattice parameter a and elastic constants c_{44}, $\frac{1}{2}(c_{11}-c_{12})$, $c_B=\frac{1}{3}(c_{11}+2c_{12})$ at room temperature, magnetoelastic coefficients B_1, B_2 and quadrupolar pair interaction coefficients K_1, K_2 for tetragonal and trigonal symmetry, respectively, CEF parameters $A_4\langle r^4\rangle$, $A_6\langle r^6\rangle$ and bilinear interaction coefficient Θ^*.

	a	c_{44}	$\frac{1}{2}(c_{11}-c_{12})$	c_B	B_1	B_2
	nm	GPa			K	
TmRh	0.3349 [74 C 1]					
TmCu	0.3415 [65 I 1]	39.4	37.0	75.8 [80 J 1]	−28	26
TmAg	0.3562 [65 I 1]	39.0	24.8	77.1 [86 G 2]	−20.5	31
TmMg	0.3749 [73 B 3]	51.8	36.9	55.1 [86 G 1]	− 5.4	20···30
TmZn	0.3515 [65 I 1]	52.1	23.9	67.7 [76 M 2]	−28	14···34
TmCd	0.3665 [65 I 1]	43.8	15.8	56.4 [73 L 1]	−14	

	K_1	K_2	$A_4\langle r^4\rangle$	$A_6\langle r^6\rangle$	Θ^*
	mK		K		K
TmRh			−105	−15.5	[74 C 1]
TmCu	7	− 60 [80 J 1]	− 60	−19.2	−3.0 [80 J 1]
TmAg	2	− 75 [86 G 2]	− 50.9	−11.8	−3.9 [86 G 2]
TmMg	≦ 2	−200···−100 [86 G 1]	− 6.5	−12.9	2.2 [86 G 1]
TmZn	20	− 90 [80 M 1, 81 M 1]	− 38	−19.6	2.8 [78 M 3, 81 M 1]
TmCd	11	− 50 [78 M 4, 81 M 1]	− 32	−15	0.0 [79 A 1]

Table 7. RZn compounds. Isotropic bilinear exchange parameters J_n between origin site and n^{th} neighbours in (xyz) coordinates (positive values correspond to a ferromagnetic coupling).

n	1	2	3	4	5	6	7	8	9	10	
xyz	100	110	111	200	210	211	220	221 300	310	311	
	J_n [mK]										Ref.
TbZn	700	8	35	−12	−35	− 3.5	93	23	151	−9	80 H 1
HoZn	87	− 2.3	21	− 9	6.4	11.5					78 H 1
TmZn	15.7	−10.1	6.3	− 3.2	2.1	7.6	− 0.6				80 M 2
$Tm_{0.9}Lu_{0.1}Zn$	23.1	− 5.4	3.2	− 7.6	0.1	5.8	− 0.1				81 M 2

Table 8. RCd compounds. Structural instability temperatures.

	T_s [K]		Ref.
LaCd	61	210	84 A 1, 85 A 2
CeCd	107	216	84 A 1
PrCd	125	210	83 S 1, 85 A 2
NdCd	180	210	85 A 2
GdCd		210	85 A 2
DyCd		210	85 A 2
TmCd		210	85 A 2
YCd		210	85 A 2

Table 9. RCd compounds. Magnetic moment at 4.2 K in μ_B per rare earth ion measured along the three main crystallographic directions in a 140 kOe magnetic field (if not indicated otherwise).

	CeCd	PrCd	NdCd	GdCd	TbCd	DyCd	HoCd	ErCd	TmCd
[001]	0.7 [1])	1.56	1.47	7.46	8 (100 kOe)	9.36	7.80	7.64	5.9 [2])
[101]	0.85 [1])		2.57	7.44	8.96	7.80	9.04	6.90	
[111]	1.0 [1])	2.64	2.20	7.44	8.86	7.08	8.36	6.94	
Ref.	85 F 1	84 A 1	85 A 1	85 A 1	85 A 1	85 A 1	85 A 1	85 A 1	79 A 1

[1]) 60 kOe.
[2]) 100 kOe.

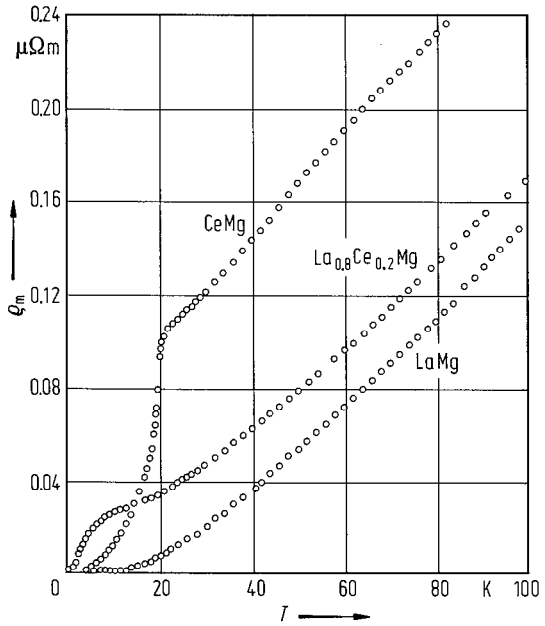

Fig. 5. CeMg, $La_{0.8}Ce_{0.2}Mg$, LaMg. Electrical resistivity less low-temperature residual resistivity, ϱ_m, vs. temperature, for polycrystalline samples [80 P 2].

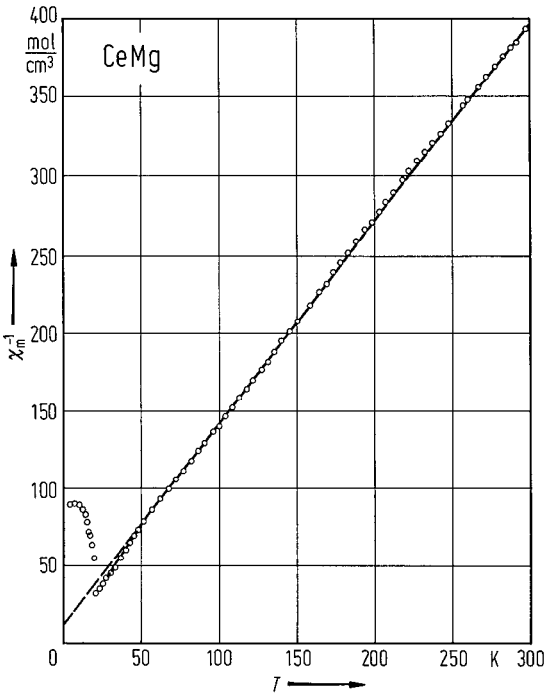

Fig. 6. CeMg. Reciprocal magnetic molar susceptibility χ_m^{-1} vs. temperature for a polycrystalline sample [80 P 2].

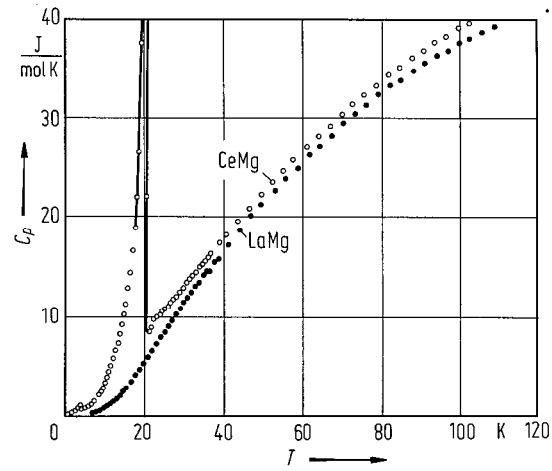

Fig. 7. LaMg, CeMg. Specific heat C_p vs. temperature measured on polycrystalline samples for increasing temperature [80 P 2].

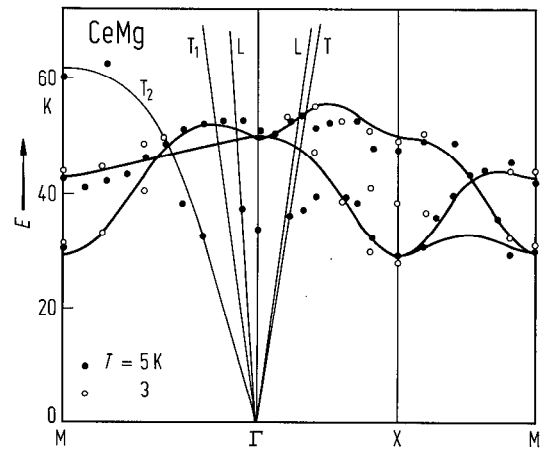

Fig. 8. CeMg. Magnetic excitation curves in the ordered phase at 5 K and 3 K. Phonon branches are indicated by thin lines (L, T correspond to longitudinal and transverse modes, respectively) [84 P 1].

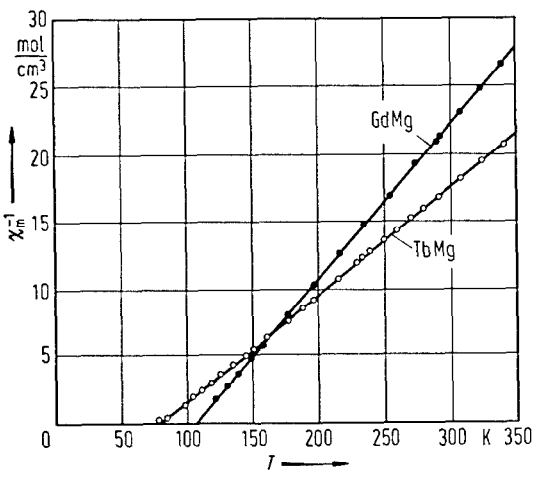

Fig. 9. GdMg, TbMg. Reciprocal magnetic molar susceptibility χ_m^{-1} vs. temperature for monocrystalline samples [75 A 1].

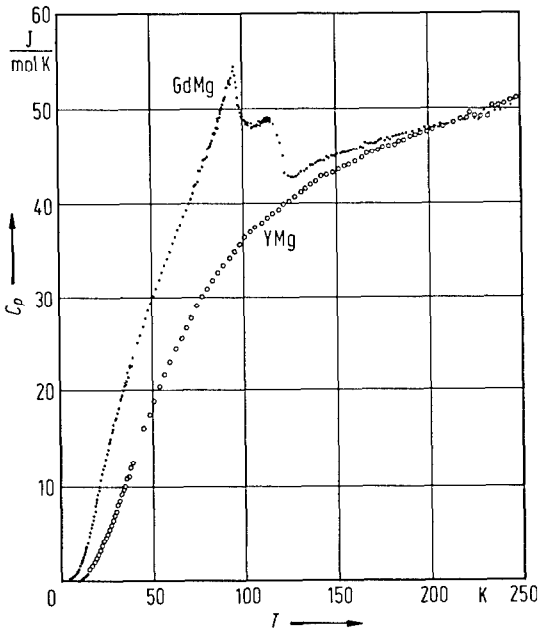

Fig. 10. GdMg, YMg. Specific heat C_p vs. temperature measured on annealed polycrystalline samples for increasing temperature [79 P 1].

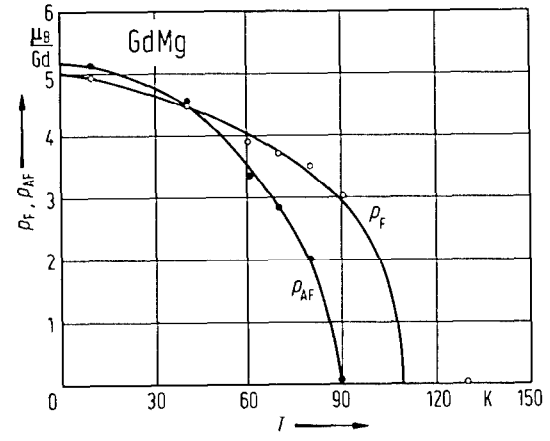

Fig. 11. GdMg. Temperature dependence of ferromagnetic (p_F) and antiferromagnetic (p_{AF}) moments per Gd atom (powder neutron diffraction measurements) [78 M 2].

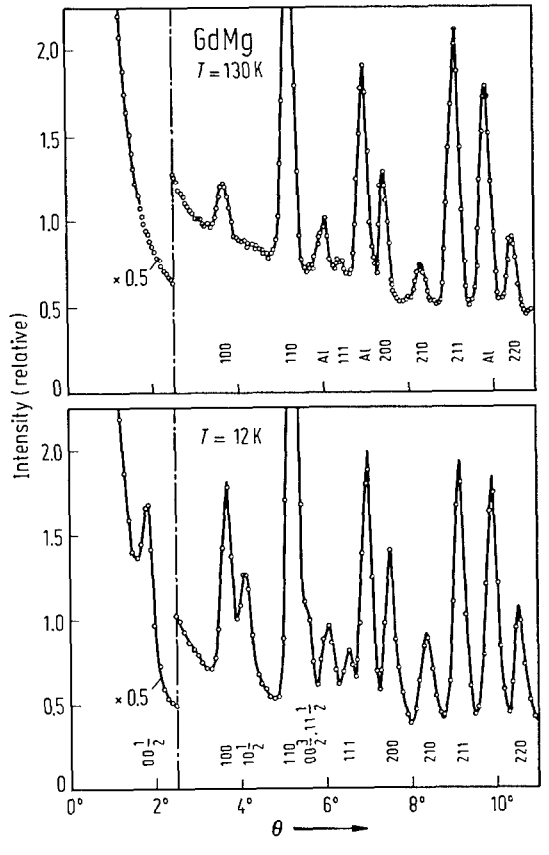

Fig. 12. GdMg. Powder neutron diffraction spectra at 12 and 130 K with $\lambda = 0.5$ Å for an annealed polycrystalline sample [78 M 2]. Peaks labelled Al originate from the container.

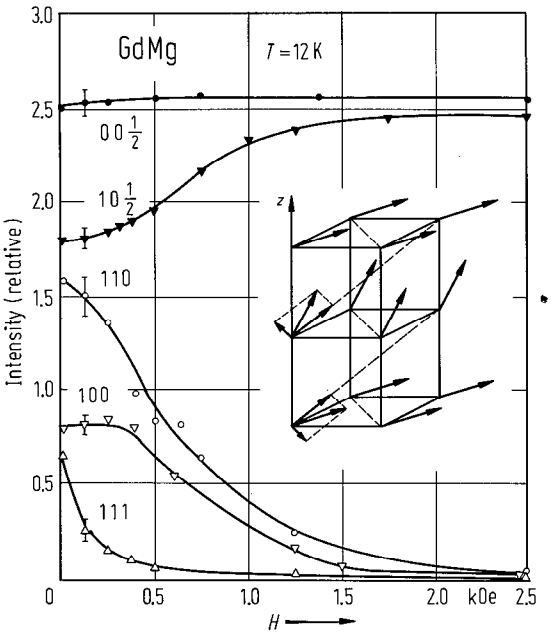

Fig. 13. GdMg. Field dependence of different magnetic intensities of the powder neutron diffraction at 12 K; a different scale was chosen for each line. The inset gives the canted magnetic structure in zero magnetic field [78 M 2].

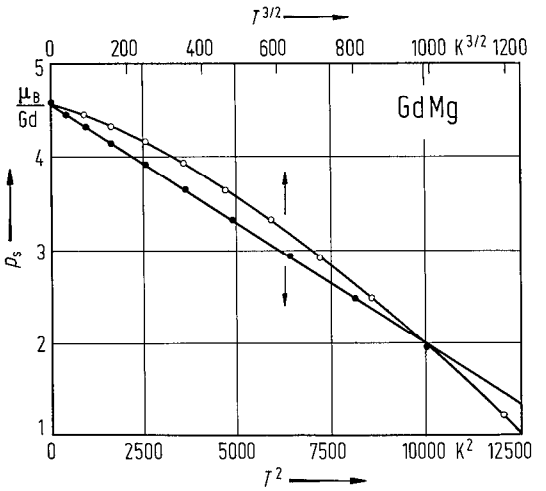

Fig. 14. GdMg. Spontaneous magnetic moment per Gd atom p_s vs. T^2 (lower scale) and vs. $T^{3/2}$ (upper scale) measured on a single crystal [75 A 1].

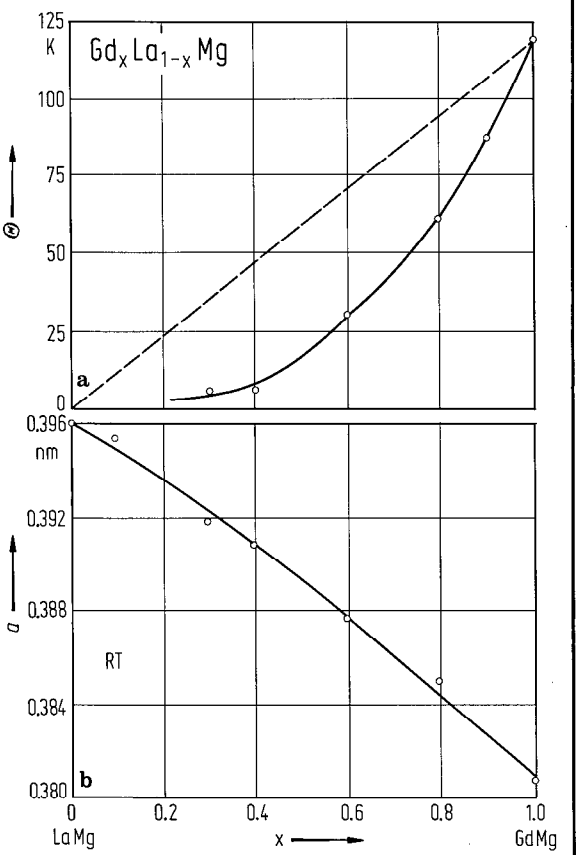

Fig. 15. $Gd_xLa_{1-x}Mg$. (a) Variation with composition of the paramagnetic Curie temperature Θ. (b) shows the composition dependence of the room-temperature lattice constant a [76 B 3].

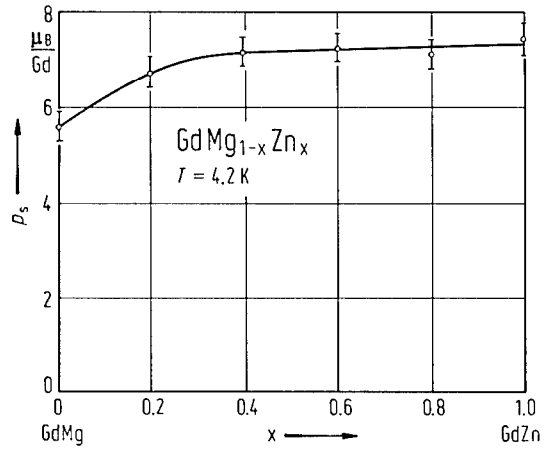

Fig. 16. $GdMg_{1-x}Zn_x$. Variation of the spontaneous magnetic moment per Gd atom, p_s, with composition at 4.2 K [74 B 3].

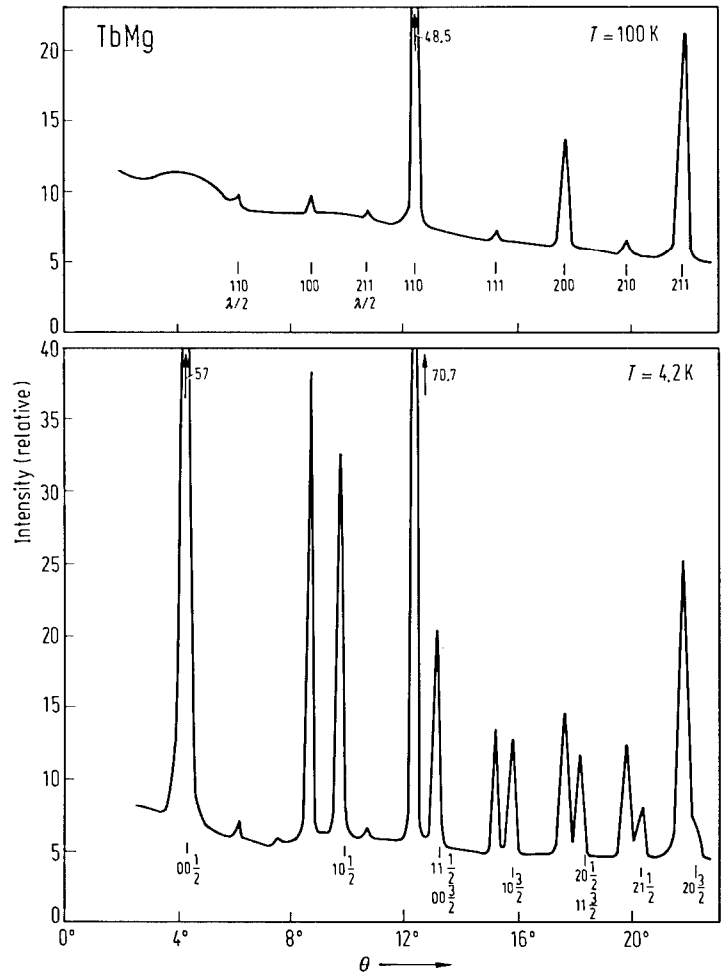

Fig. 17. TbMg. Powder neutron diffraction spectra at 100 and 4.2 K [75 A 1].

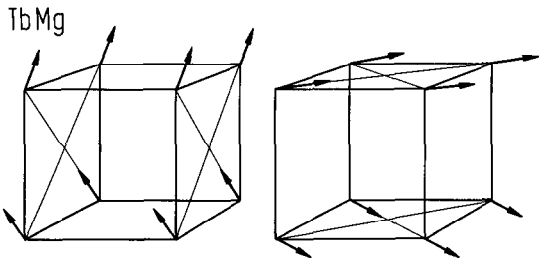

Fig. 18. TbMg. Allowed magnetic structures at 4.2 K [75 A 1].

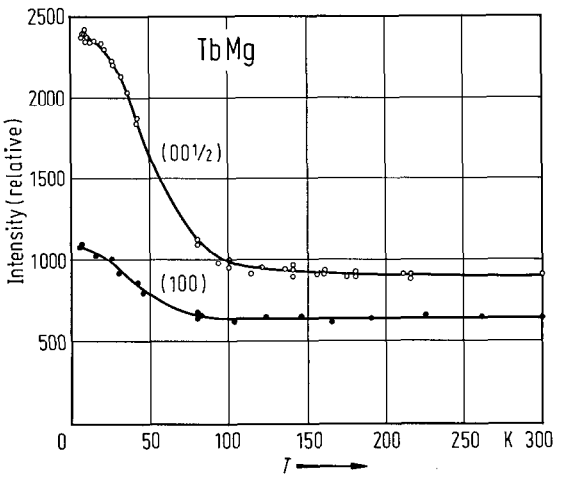

Fig. 19. TbMg. Intensity of the powder neutron diffraction reflections $(00\frac{1}{2})$ and (100) vs. temperature [77 S 1].

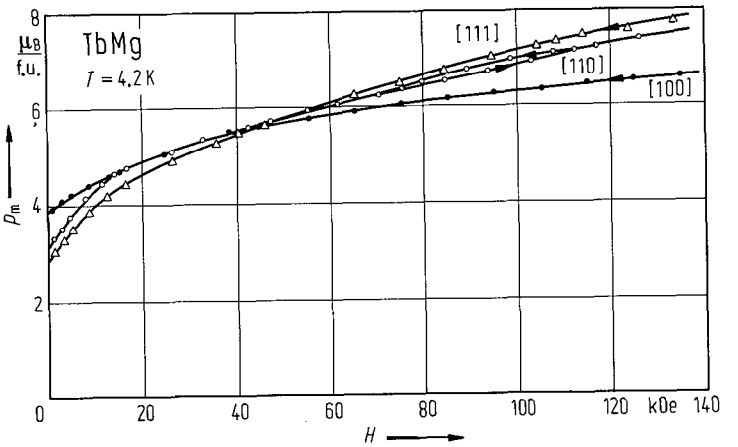

Fig. 20. TbMg. Magnetization curves corrected for demagnetization of a single crystal at 4.2 K. Field directions are indicated; arrows give the field variation [76 A 1].

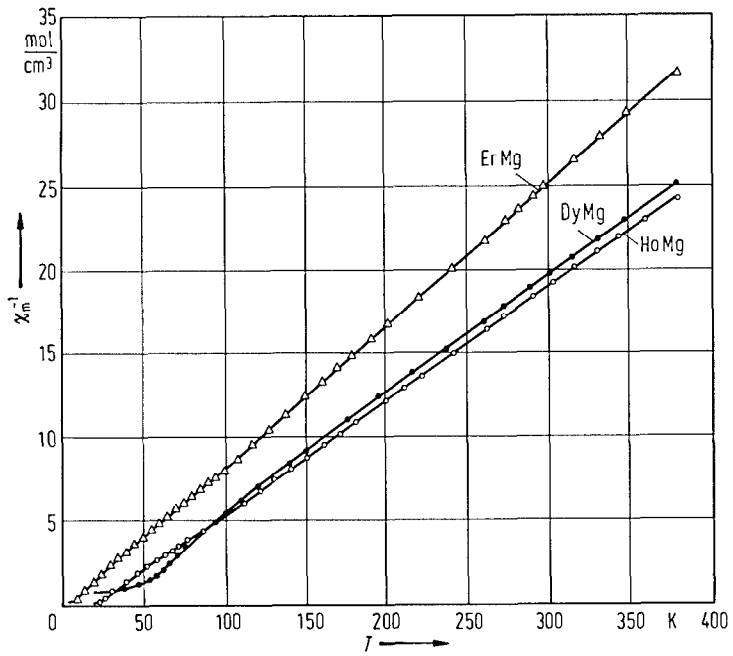

Fig. 21. RMg, R = Dy, Ho, Er. Reciprocal magnetic molar susceptibility χ_m^{-1} vs. temperature for monocrystalline samples [76 A 1].

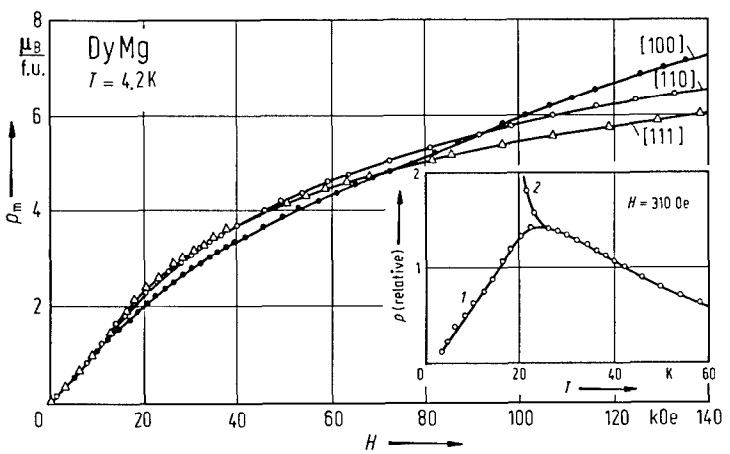

Fig. 22. DyMg. Magnetization curves corrected for demagnetization at 4.2 K. Field directions are indicated. The inset shows the temperature variation in $H = 310$ Oe of the initial magnetization (curve *1*) and of the remanent magnetization after saturation (curve *2*) [76 A 1].

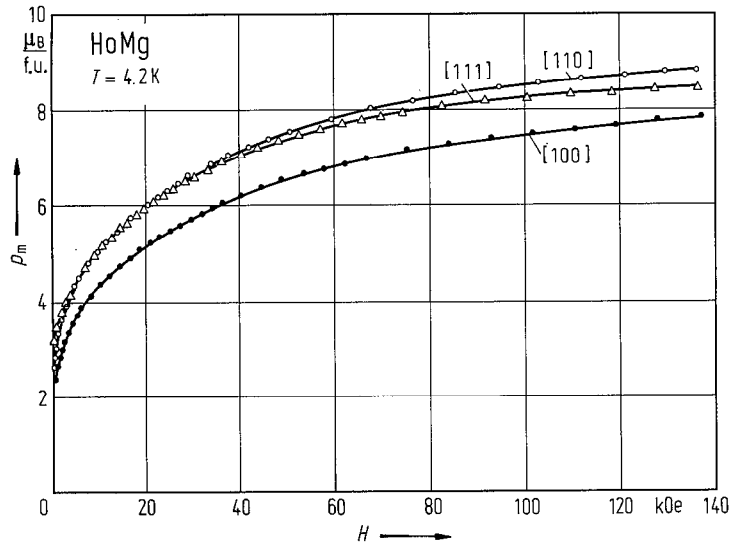

Fig. 23. HoMg. Magnetization curves corrected for demagnetization for a single crystal at 4.2 K. Field directions are indicated [76 A 1].

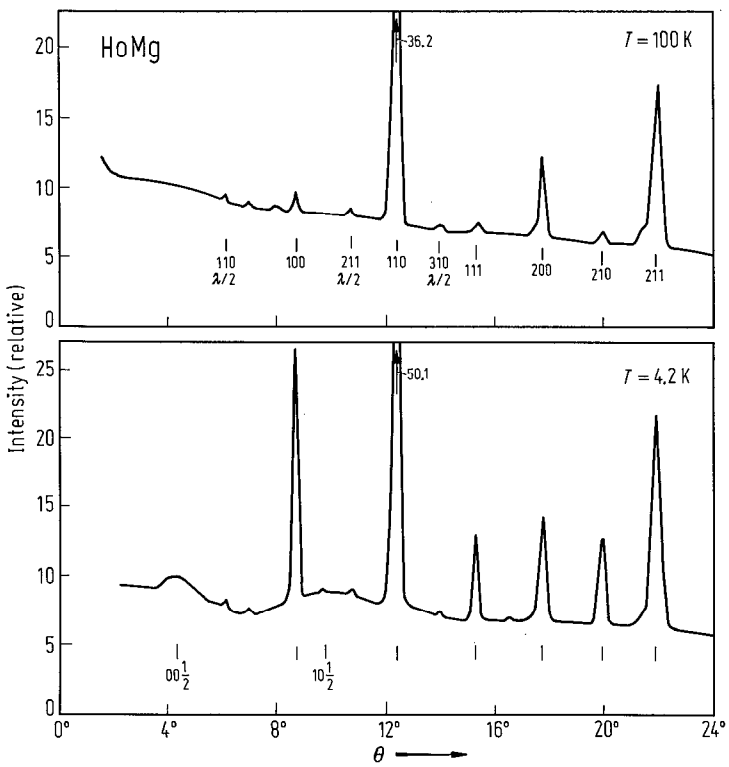

Fig. 24. HoMg. Powder neutron diffraction spectra at 100 K (upper part) and 4.2 K (lower part). Note the intensity bump corresponding to the (0 0 1/2) reflection [76 A 1].

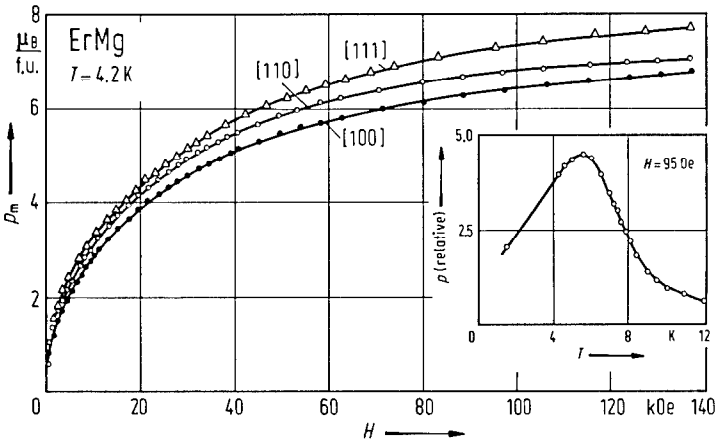

Fig. 25. ErMg. Magnetization curves corrected for demagnetization for a single crystal at 4.2 K. Field directions are indicated. The inset shows the temperature variation of the initial magnetization in $H = 95$ Oe [76 A 1].

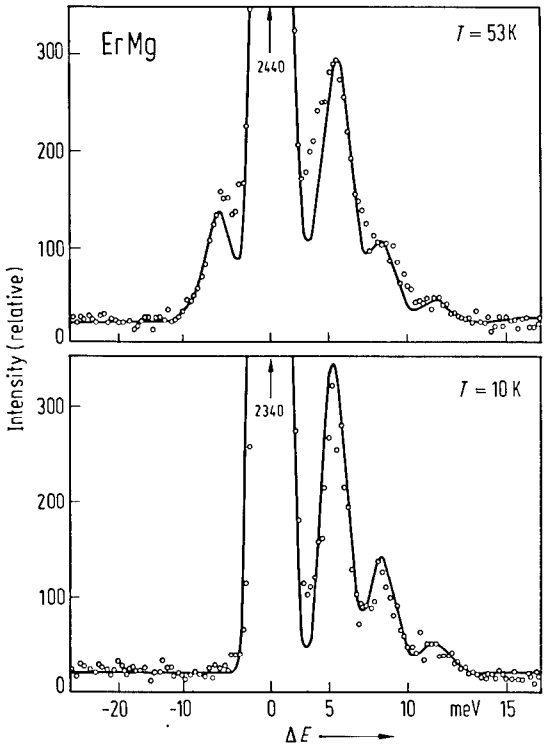

Fig. 26. ErMg. Inelastic neutron scattering spectra in the paramagnetic phase, at 10 K (lower part) and 53 K (upper part) for an incident neutron energy of 36.24 meV. ΔE is the energy transfer from the incident neutron energy. The full lines are calculated in the CEF model [76 M 1].

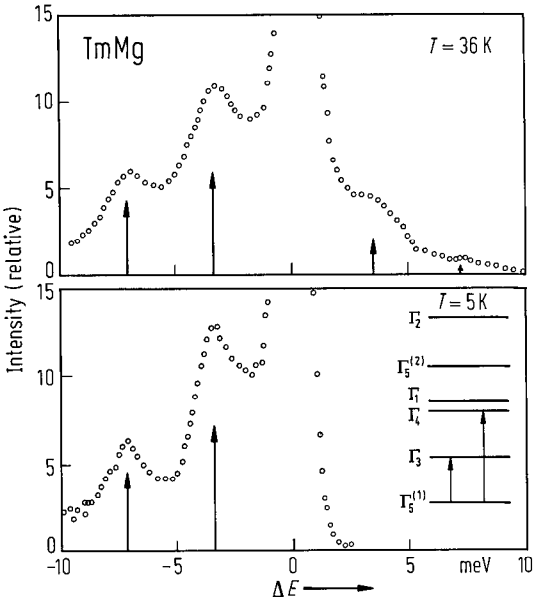

Fig. 27. TmMg. Inelastic neutron scattering spectra in the paramagnetic phase at 5 K and 36 K. The incident neutron energy is 12.6 meV. ΔE is the energy transfer from the incident neutron energy. Arrows correspond to transitions indicated on the level scheme [86 G 1].

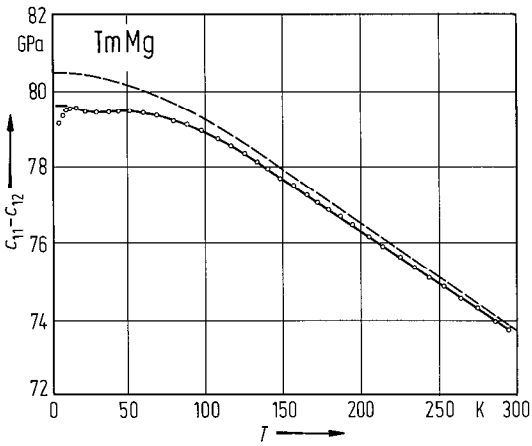

Fig. 29. TmMg. Temperature variation of the shear elastic mode, $c_{11}-c_{12}$. The hatched line is the lattice background without magnetic contributions, the full one is calculated in the quadrupolar interaction model [86 G 1].

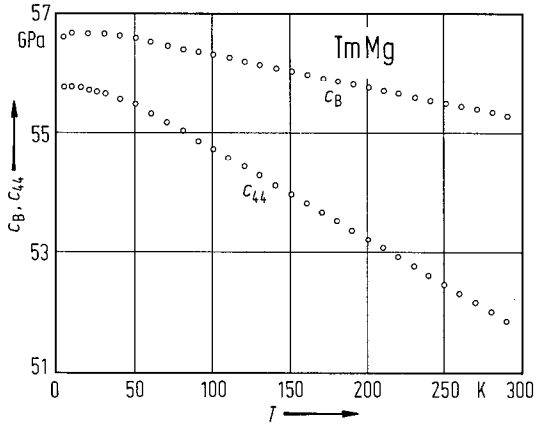

Fig. 28. TmMg. Temperature variation of the shear elastic mode, c_{44}, and of the bulk modulus, c_B [86 G 1].

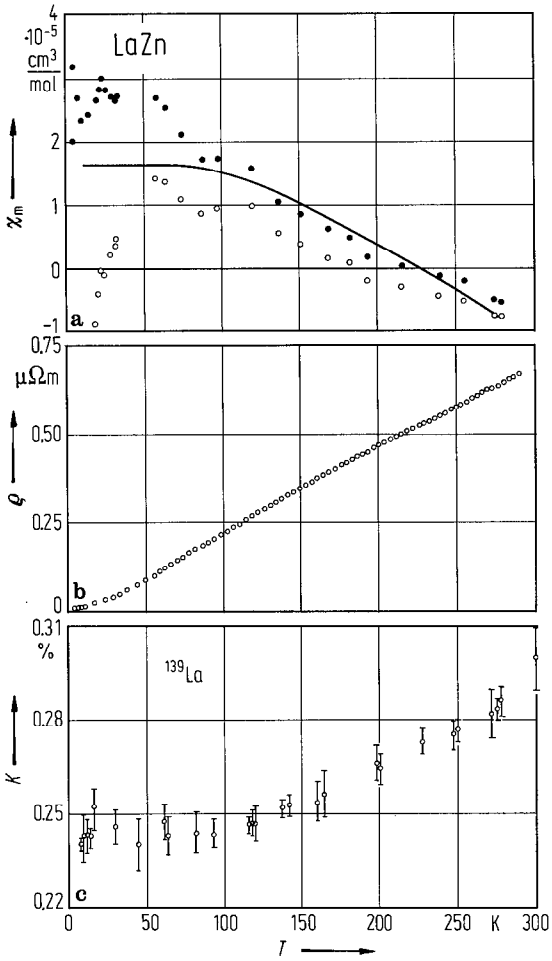

Fig. 30. LaZn. Temperature dependence of (a) the magnetic molar susceptibility χ_m, (b) electrical resistivity ϱ and (c) ^{139}La Knight shift K. Open circles: measured values; solid circles: corrected for impurity contribution. The full line in (a) is a guide for the eye [75 G 1].

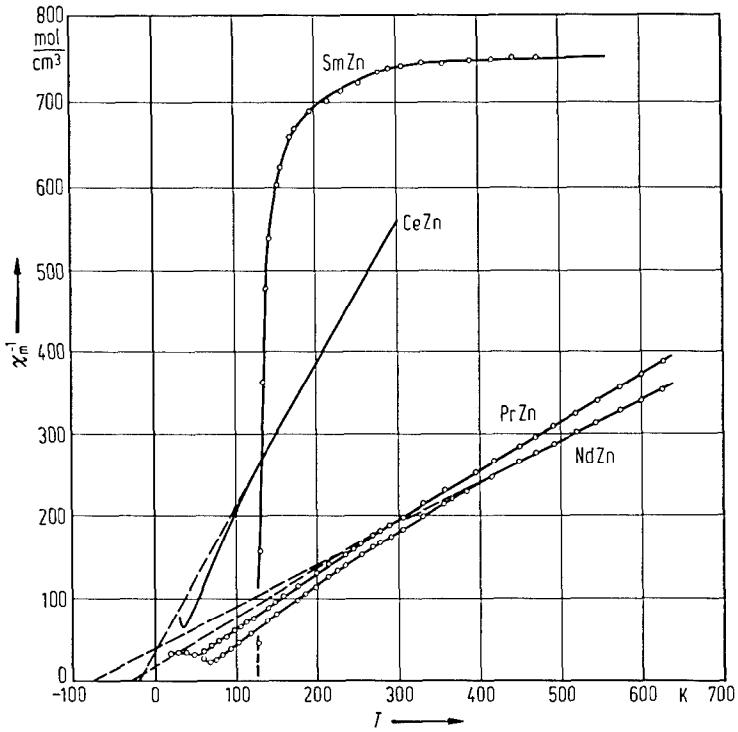

Fig. 31. RZn, R = Ce, Pr, Nd, Sm. Reciprocal magnetic molar susceptibility χ_m^{-1} vs. temperature for annealed polycrystalline samples [75 M 1, 75 M 3].

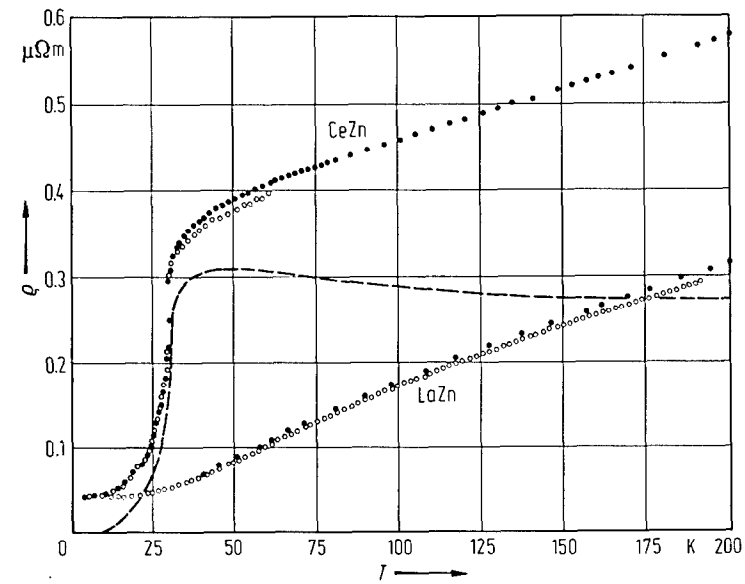

Fig. 32. CeZn, LaZn. Electrical resistivity ϱ vs. temperature (two CeZn and two LaZn samples). The residual resistivities are matched to that of CeZn at low temperature. The broken curve represents the difference between CeZn and LaZn resistivities [81 P 2].

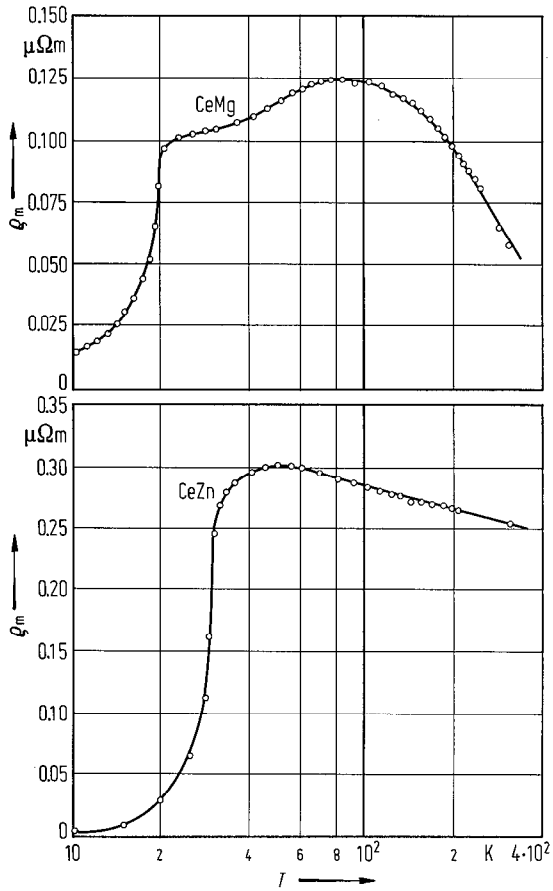

Fig. 33. CeZn, CeMg. Electrical resistivities after correction of lattice contribution and impurity resistivity, ϱ_m, vs. temperature. Note the logarithmic scale for T [81 P 2].

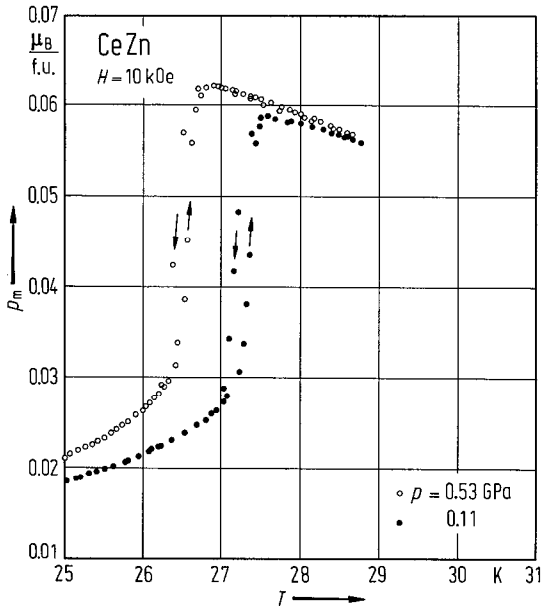

Fig. 34. CeZn. Magnetic moment p_m vs. temperature in a magnetic field of $H = 10$ kOe for hydrostatic pressures $p = 0.53$ GPa (open circles) and $p = 0.11$ GPa (full circles). The curves show a temperature hysteresis of about 0.2 K [83 G 1].

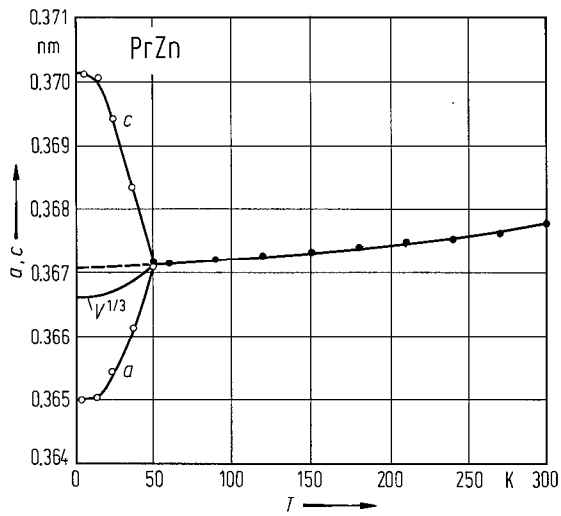

Fig. 35. PrZn. Thermal variation of lattice parameters measured by X-rays on a quenched polycrystalline sample. The hatched line corresponds to the extrapolation in the antiferromagnetic phase of the Grüneisen behaviour from the cubic phase. V corresponds to the volume of the elementary cell [75 M 1].

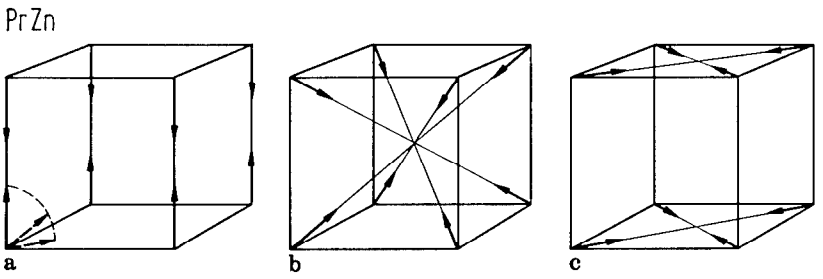

Fig. 36. PrZn. Magnetic structures associated with the (1/2 0 0) magnetic propagation vectors, indistinguishable from a powder neutron diffraction pattern. The spontaneous tetragonal strain (Fig. 35) indicates structure (a) to be the actual one [75 M 1].

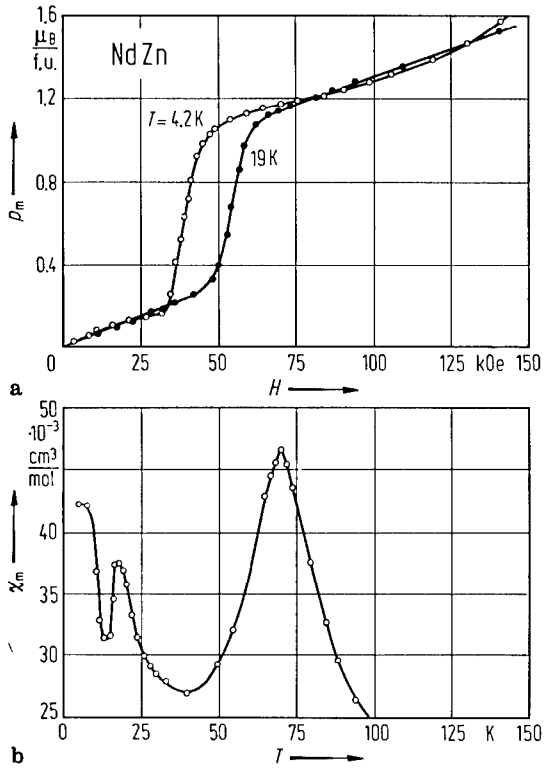

Fig. 37. NdZn. (a) Isothermal magnetization curves below and above the spin reorientation temperature at $T = 4.2$ and 19 K for a polycrystalline sample. (b) Temperature variation of the magnetic molar susceptibility, χ_m [75 M 1].

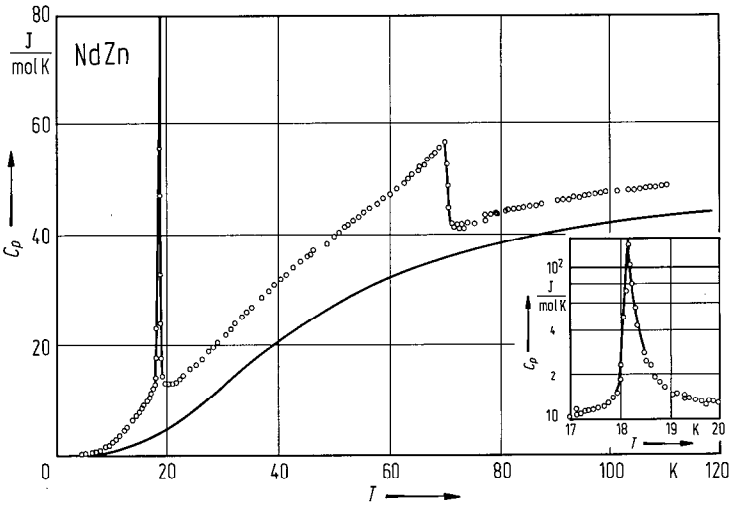

Fig. 38. NdZn. Specific heat C_p measured for increasing temperature. The thin solid line represents the lattice contribution. The inset gives the temperature variation of the specific heat with a logarithmic scale in the low-temperature transition range [75 M 2].

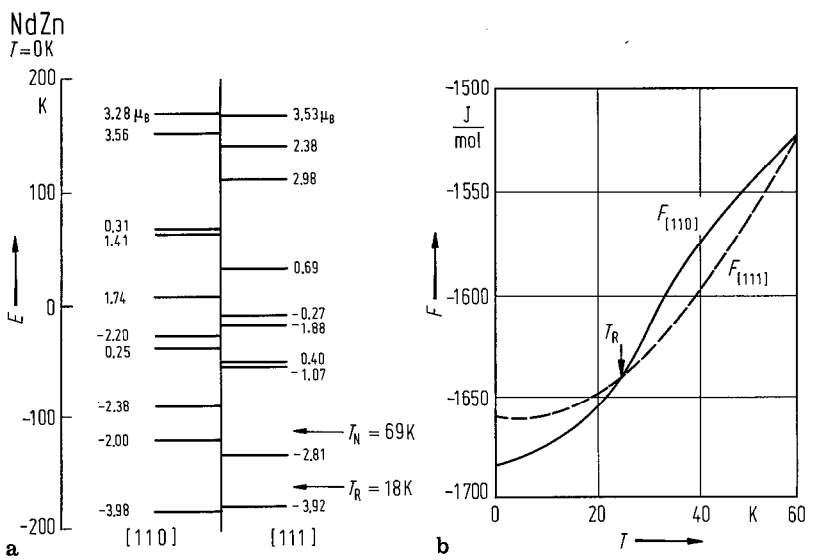

Fig. 39. NdZn. (a) Energy splitting of the Nd multiplet $J=9/2$ for magnetization along the [110] and [111] directions at 0 K. The magnetic moment corresponding to each energy level is indicated. (b) Temperature variation of the [110] (full line) and [111] (hatched line) free energy calculated for the same cubic CEF level scheme. T_R is the temperature for the change of easy magnetization direction, where $T_R = 18$ K is the experimental value [75 M 2].

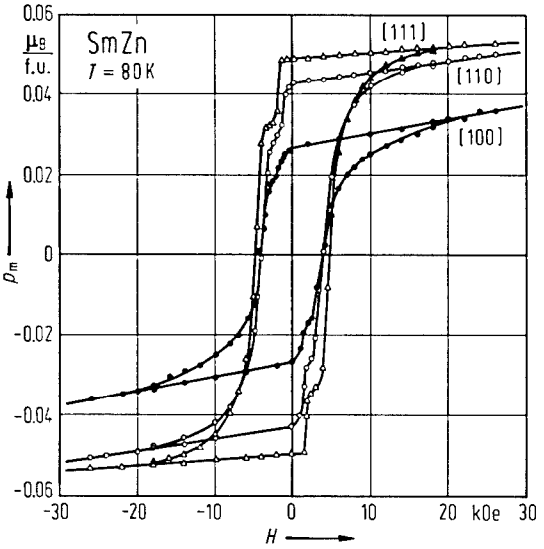

Fig. 40. SmZn. Magnetization processes of a single crystal at 80 K, driven by narrow domain walls. Field directions are indicated [75 M 3].

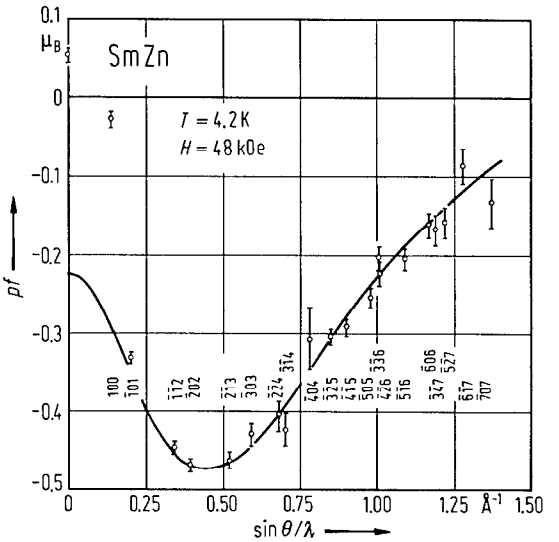

Fig. 41. SmZn. Angular dependence of the magnetic form factor pf at 4.2 K in a magnetic field of 48 kOe for a single crystal. θ is the Bragg angle and the neutron wavelength is $\lambda = 0.42$ Å. The full line gives the calculated dependence of the 4f magnetization; for small θ values, the shift from the pf data corresponds to the band polarization, opposite to the 4f magnetization and larger in modulus at $\theta = 0°$ [79 G 1].

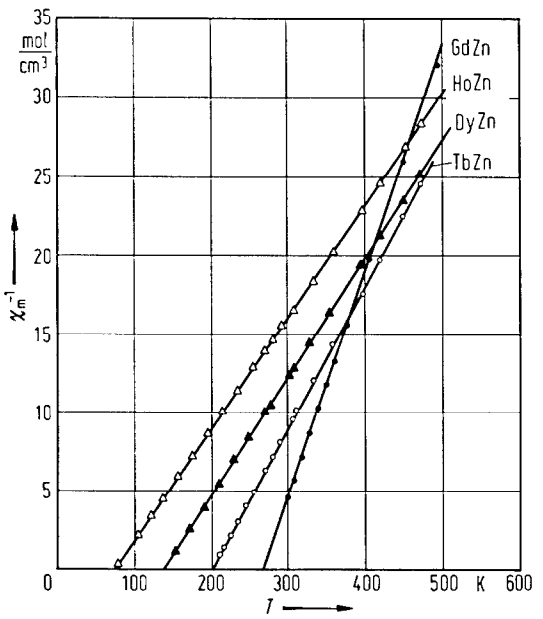

Fig. 42. RZn, R = Gd, Tb, Dy, Ho. Reciprocal magnetic molar susceptibility χ_m^{-1} vs. temperature for monocrystalline samples [75 M 3].

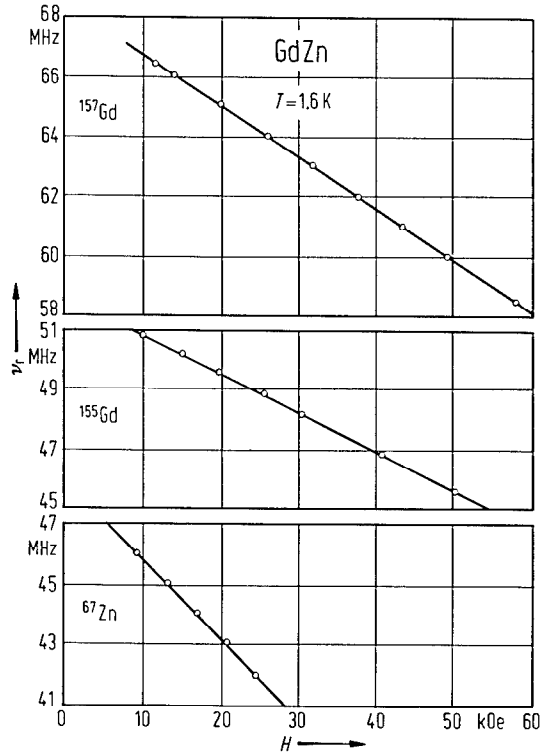

Fig. 43. GdZn. Nuclear magnetic resonance line frequencies ν_r of the ^{157}Gd, ^{155}Gd, and ^{67}Zn isotopes vs. magnetic field H in a monocrystalline sample at 1.6 K [84 K 1].

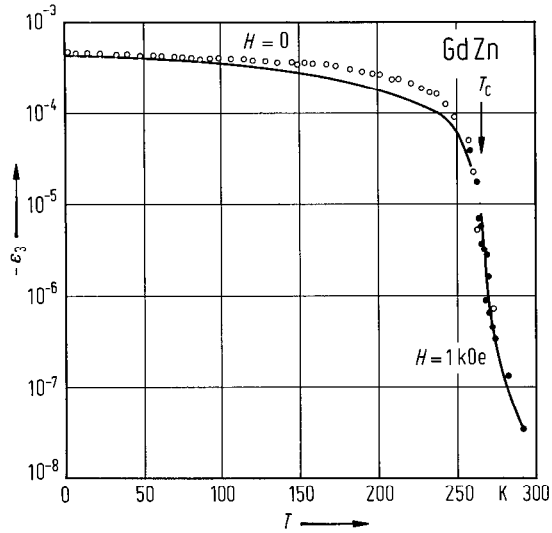

Fig. 44. GdZn. Temperature variation of the spontaneous tetragonal strain $\varepsilon_3 = \sqrt{2/3}\,(c/a-1)$ in the ordered state and of the ε_3 strain induced by a 1-kOe-field in the paramagnetic state (open circles: strain-gauge data; solid circles: dilatometric data; full lines are calculated variations) [77 M 1].

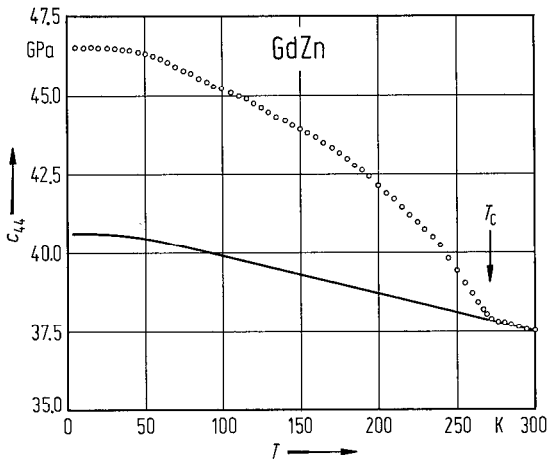

Fig. 46. GdZn. Temperature dependence of the c_{44} elastic mode in both the para- and ferromagnetic phases. The full curve is the extrapolation of the paramagnetic behaviour [81 R 1].

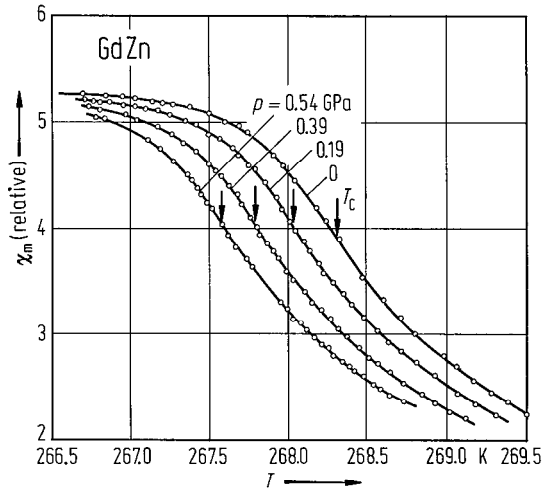

Fig. 45. GdZn. Isobaric magnetic molar susceptibility χ_m vs. temperature. The pressure values are indicated. Arrows give the Curie temperature value [74 H 1].

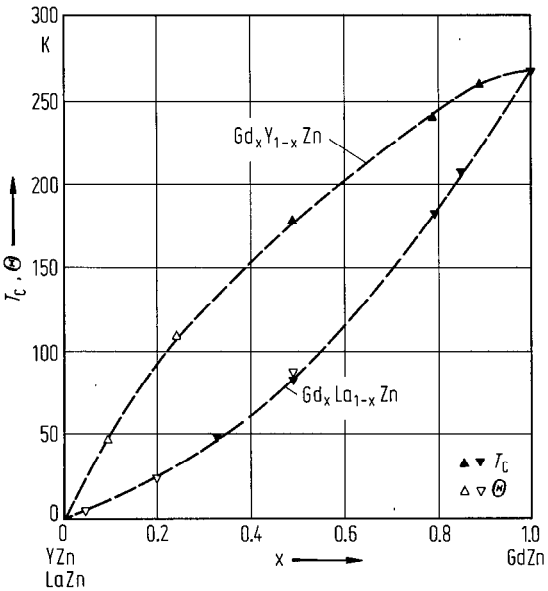

Fig. 47. $Gd_xY_{1-x}Zn$, $Gd_xLa_{1-x}Zn$. Curie temperature T_C and paramagnetic Curie temperature Θ vs. the Gd concentration [76 E 1].

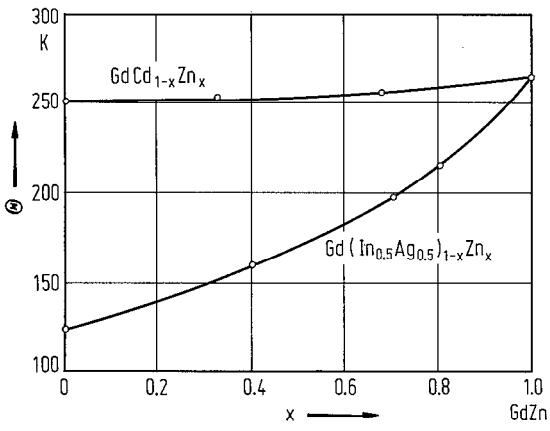

Fig. 48. $GdCd_{1-x}Zn_x$, $Gd(In_{0.5}Ag_{0.5})_{1-x}Zn_x$. Paramagnetic Curie temperature Θ vs. the Zn concentration, the conduction electron number being kept constant [72 B 1].

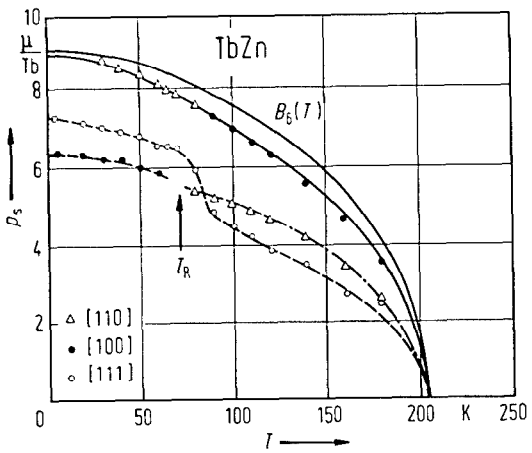

Fig. 49. TbZn. Temperature variation of the spontaneous magnetic moment per Tb atom (full curve) in comparison with the Brillouin function $B_J(T)$ for $J=6$. The initial magnetizations along hard axes (dashed (curves) are also given below and above the spin reorientation temperature, $T_R = 61.9$ K [73 M 1].

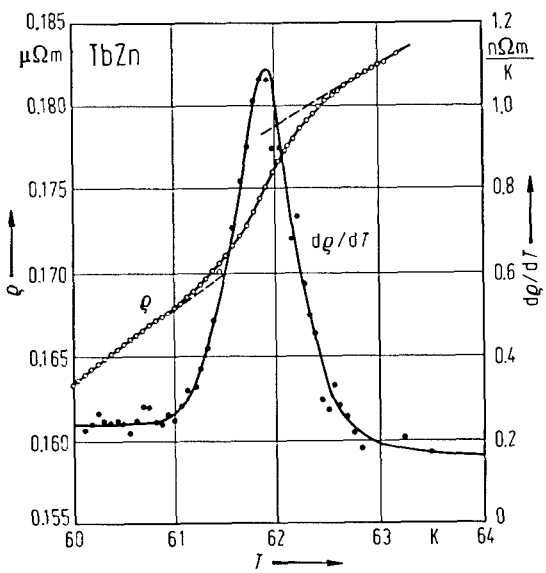

Fig. 51. TbZn. Temperature dependence of the electrical resistivity ϱ and its derivative $d\varrho/dT$ near the spin reorientation temperature T_R [80 S 3].

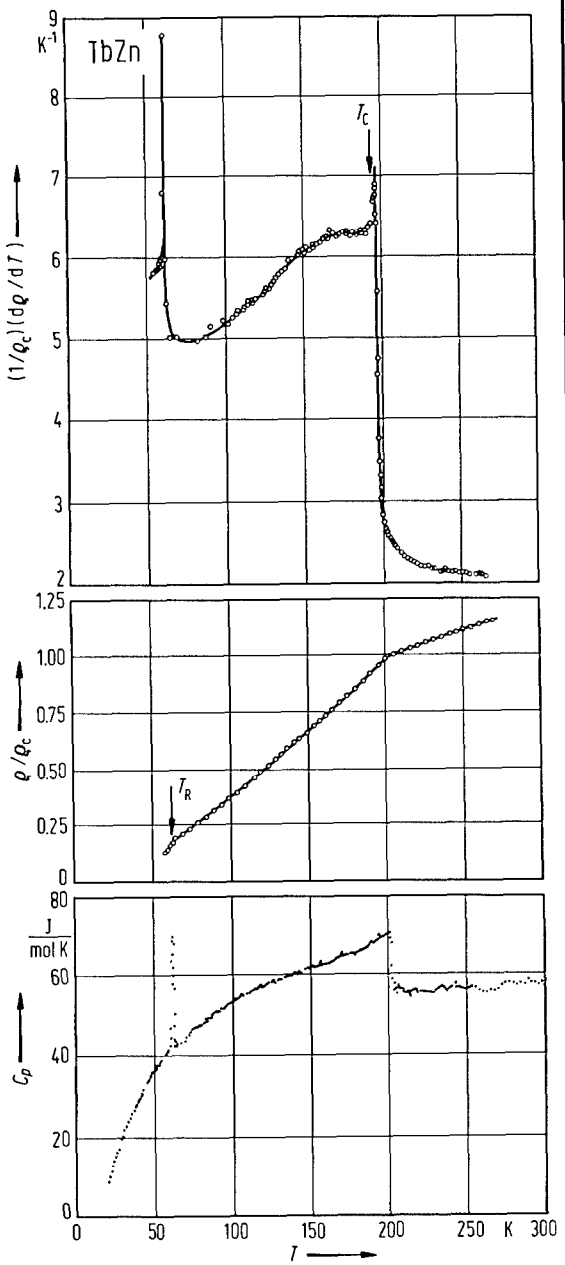

Fig. 50. TbZn. Temperature dependence of the electrical resistivity ϱ and its temperature derivative, normalised with respect to electrical resistivity ϱ_c at the Curie temperature. Sharp peaks occur at the Curie temperature T_C, and the spin reorientation temperature T_R. Lower figure: temperature dependence of the specific heat C_p [80 S 3].

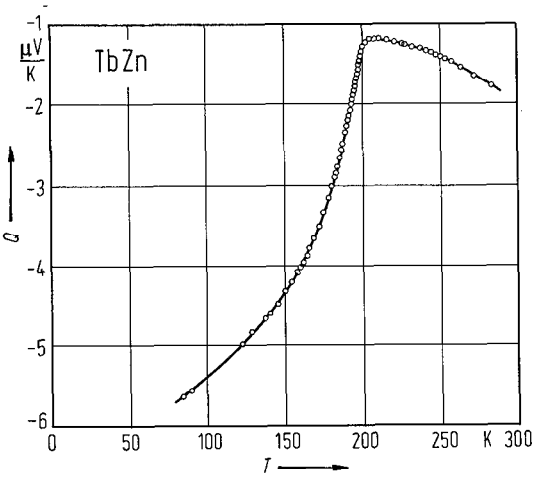

Fig. 52. TbZn. Temperature dependence of the thermoelectric power Q (measurements on a single crystal) [80 S 1].

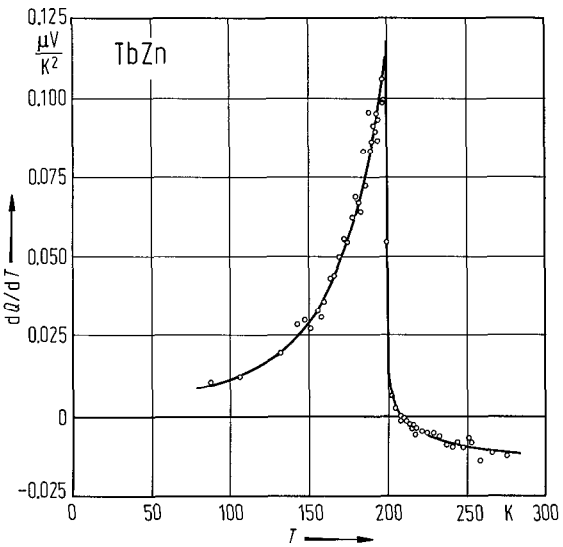

Fig. 53. TbZn. Temperature dependence of the derivative of the thermoelectric power dQ/dT near T_c [80 S 1].

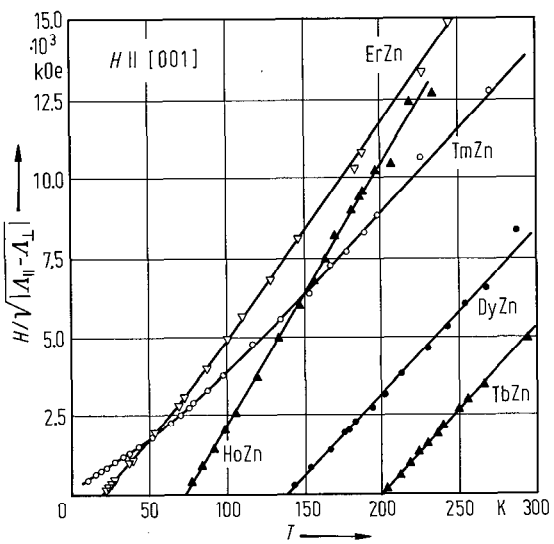

Fig. 54. RZn, R = Tb, Dy, Ho, Er, Tm. Reciprocal parastriction susceptibility, $H/\sqrt{|\Lambda_{\parallel} - \Lambda_{\perp}|}$ vs. temperature for a magnetic field H applied along the [001] axis. The changes of length, $\Lambda_{\parallel}$ and $\Lambda_{\perp}$, are measured parallel and perpendicular to H. Full curves are calculated [80 M 1].

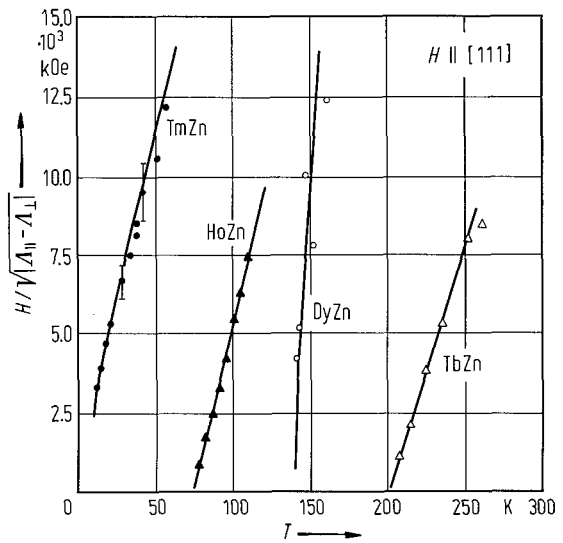

Fig. 55. RZn, R = Tb, Dy, Ho, Tm. Reciprocal parastriction susceptibility $H/\sqrt{|\Lambda_{\parallel} - \Lambda_{\perp}|}$ vs. temperature for a magnetic field H applied along the [111] axis. The changes of length, $\Lambda_{\parallel}$ and $\Lambda_{\perp}$, are measured parallel and perpendicular to H. Full curves are calculated [80 M 1].

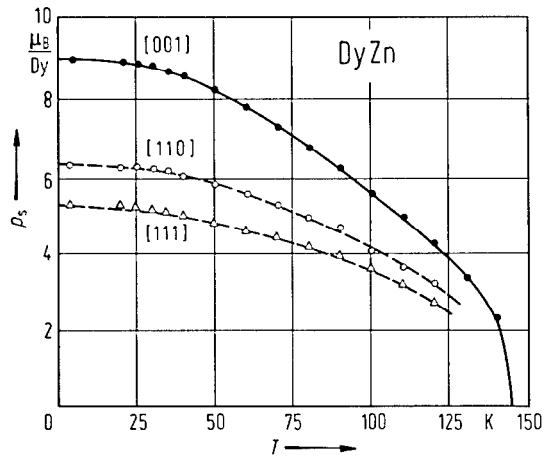

Fig. 56. DyZn. Temperature variations of the spontaneous magnetic moment per Dy site, p_s, along the easy magnetization axis [001] and of its projections on [110] and [111] axes [73 M 2].

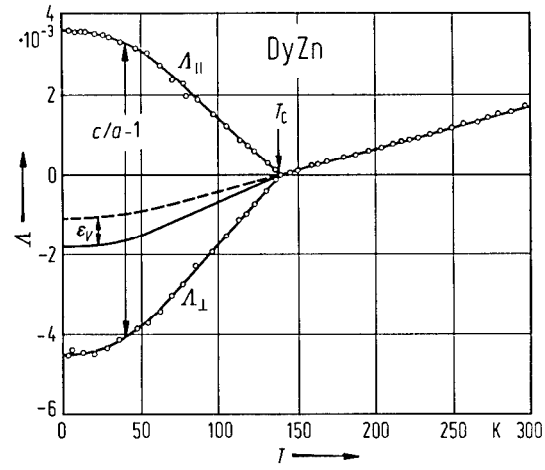

Fig. 57. DyZn. Thermal variations of the change of length, $\Lambda_{\parallel}$ and $\Lambda_{\perp}$, parallel and perpendicular to the magnetic moment lying along a fourfold easy axis of a single-domain sample. The paramagnetic curve is extrapolated down to 0 K (dotted line) according to a Grüneisen law. The bulk strain ε_V corresponds to the shift from the Grüneisen law of the $(\bar{V})^{1/3}$ average lattice parameter. The difference $\Lambda_{\parallel}-\Lambda_{\perp}=c/a-1$ gives the spontaneous tetragonal strain, $\varepsilon_3=\sqrt{2/3}(c/a-1)$ [77 M 1].

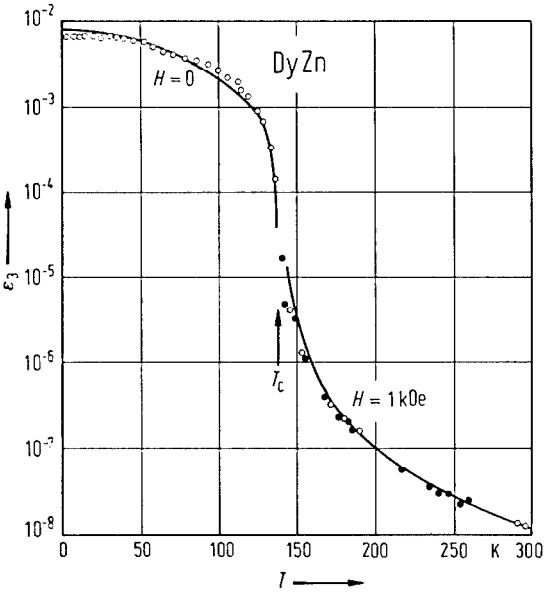

Fig. 58. DyZn. Thermal variation of the spontaneous tetragonal strain $\varepsilon_3=\sqrt{2/3}\,(c/a-1)$ in the ordered state and of the ε_3 strain induced by an 1-kOe-field in the paramagnetic state (open circles: strain-gauge data; solid circles: dilatometric data; full lines are calculated) [77 M 1].

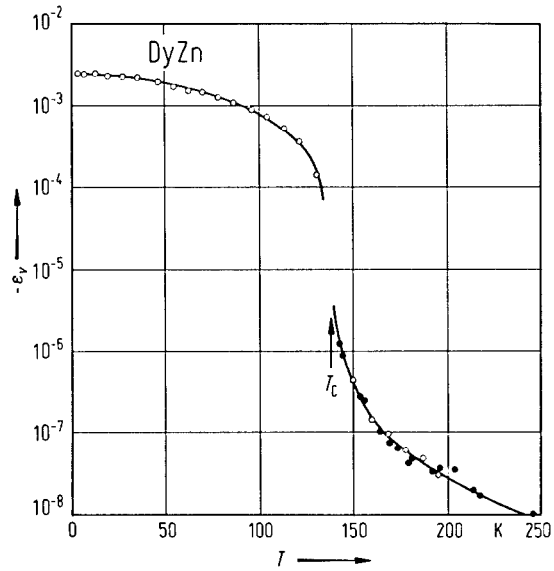

Fig. 59. DyZn. Thermal variations of the spontaneous volume strain ε_V in the ordered state and of the ε_V strain induced by an 1-kOe-field in the paramagnetic state (open circles: strain-gauge data; solid circles: dilatometric data; full lines are calculated variations) [77 M 1].

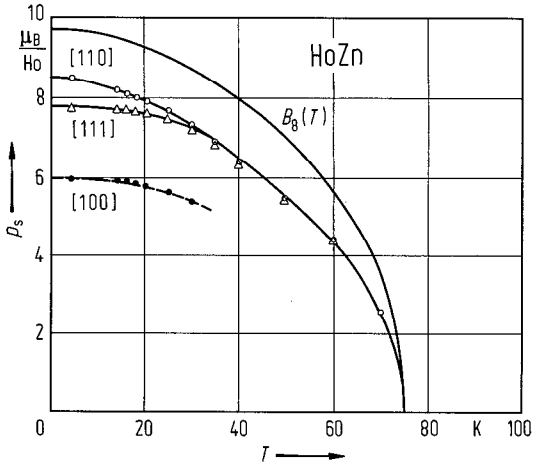

Fig. 60. HoZn. Temperature variation of the spontaneous magnetic moment per Ho site, p_s, extrapolated to zero magnetic field, for the [110] and [111] axes and of its projection along [100]. $B_8(T)$ is the Brillouin function for $J=8$ [73 M 1].

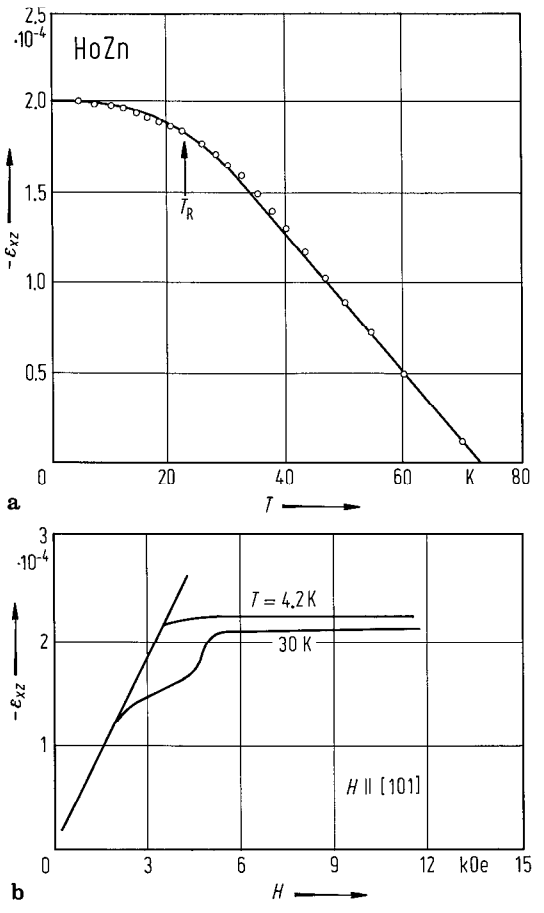

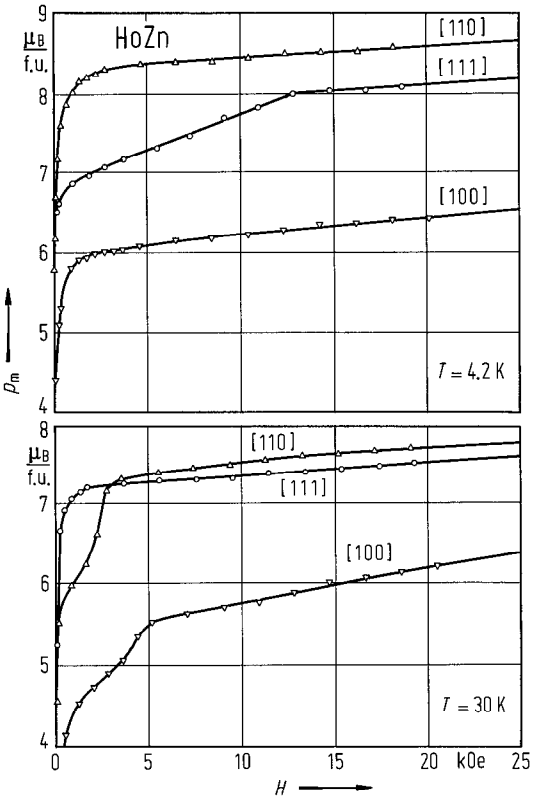

Fig. 61. HoZn. Magnetization processes corrected for demagnetization along the three main axes as indicated at 4.2 K (upper part) and 30 K (lower part) on both sides of the spin reorientation temperature, $T_R=23$ K [73 M 1].

◀

Fig. 62. HoZn. (a) Temperature variation of the saturated shear strain ε_{xz} measured on both sides of the temperature for the change of easy magnetization direction, $T_R=23$ K. In (b) the ε_{xz} field dependence is measured for an applied magnetic field along [101] at 4.2 K (twofold easy direction) and at 30 K (threefold easy direction) [77 M 1].

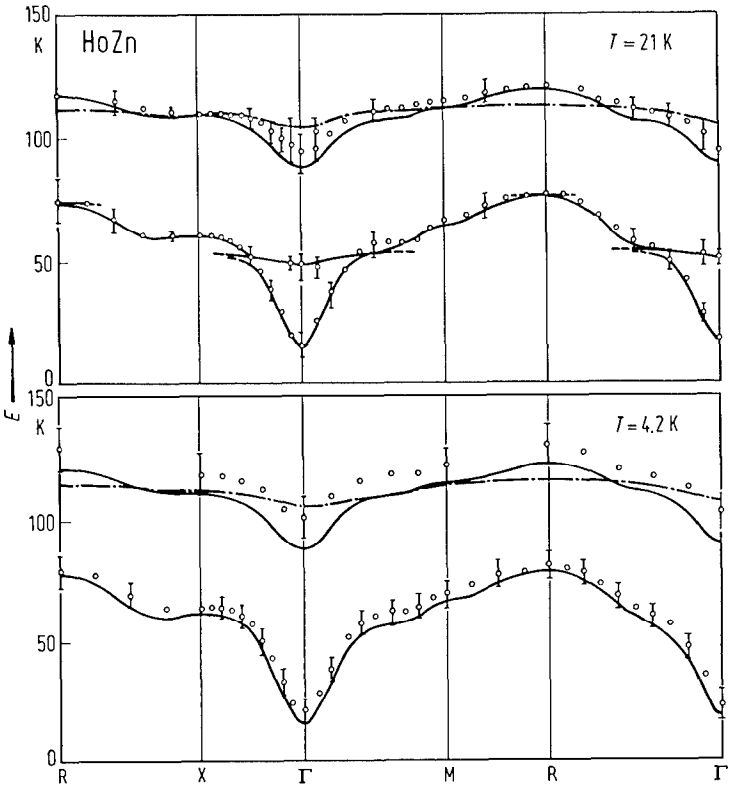

Fig. 63. HoZn. Magnetic dispersion curves in the ordered range at 21 K (upper part) and 4.2 K (lower part). Lines are calculated variations: the chain curves represent a longitudinal excitation. Other branches are transversal ones [78 H 1].

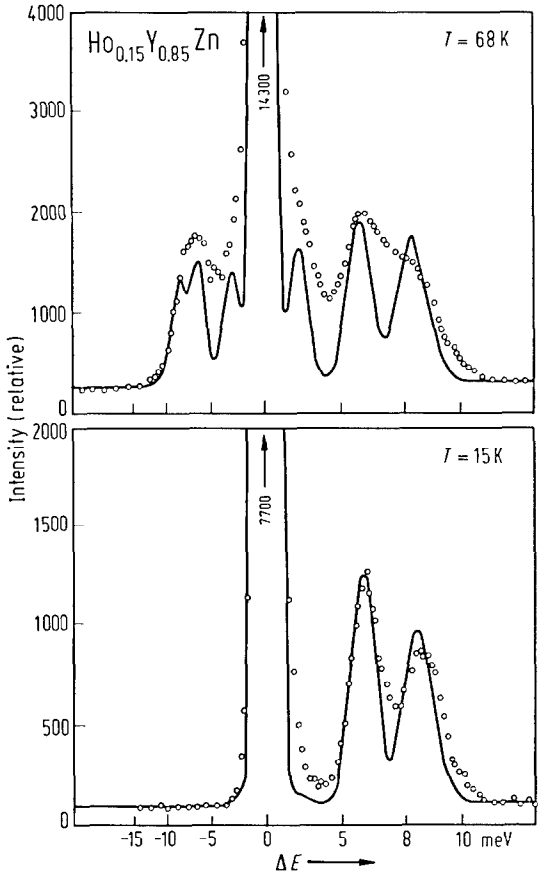

Fig. 64. $Ho_{0.15}Y_{0.85}Zn$. Inelastic neutron scattering intensity in the paramagnetic phase vs. the energy transfer ΔE from the incident neutron energy of 22.69 meV. Solid lines are calculated variations [77 S 2].

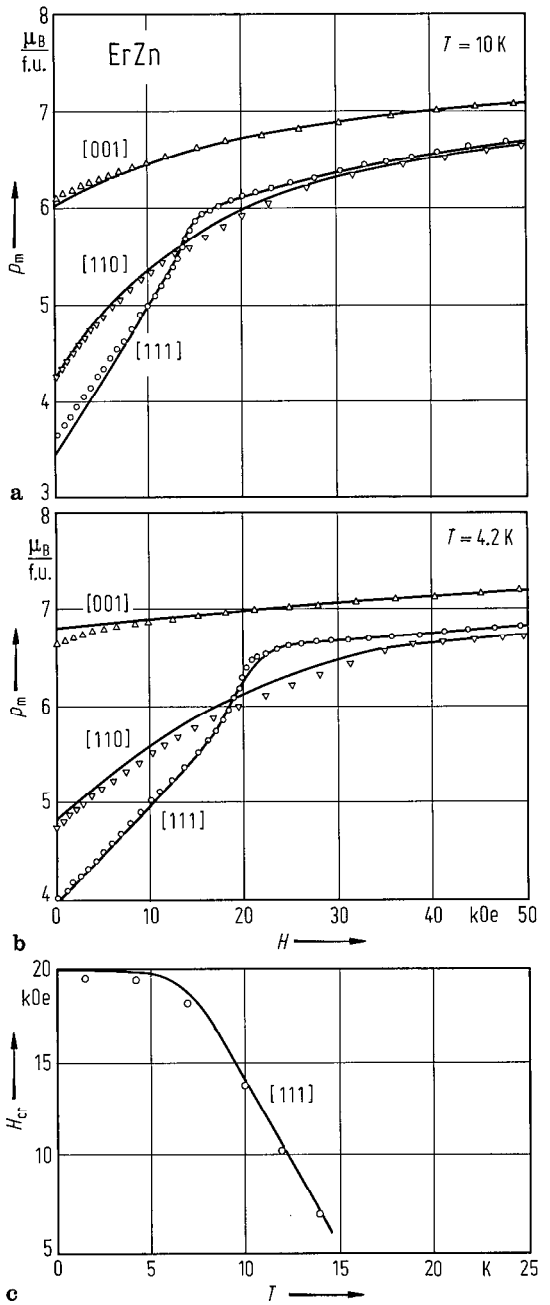

Fig. 65. ErZn. Magnetization curves corrected for demagnetization along the three principal cubic directions at 10 K (a) and 4.2 K (b). The lines are theoretical fits including quadrupolar contributions. (c) shows the temperature dependence of the critical field H_{cr} along [111], for which the magnetization changes suddenly [78 M 5].

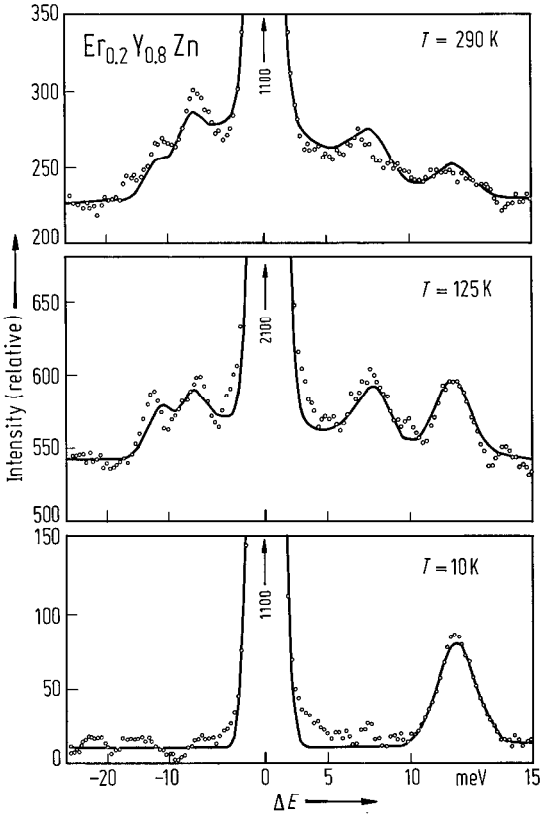

Fig. 66. $Er_{0.2}Y_{0.8}Zn$. Inelastic neutron scattering intensity vs. the energy transfer ΔE from the incident neutron energy of 33.41 meV at different temperatures. The full lines are calculated in the CEF model [74 M 3].

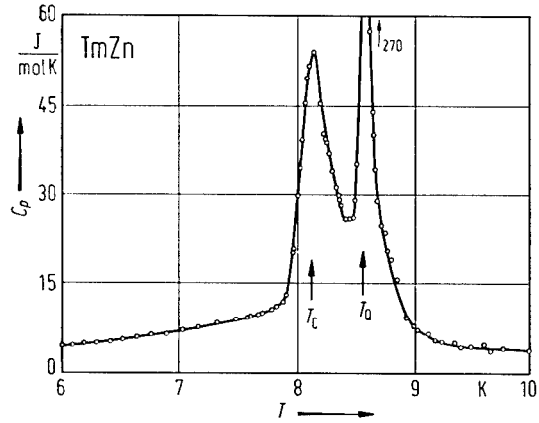

Fig. 67. TmZn. Specific heat, C_p for increasing temperature. At $T_Q = 8.55$ K the quadrupolar ordering is occuring in the paramagnetic phase, at $T_C = 8.12$ K the ferromagnetic ordering (measurements on a single crystal) [78 M 3].

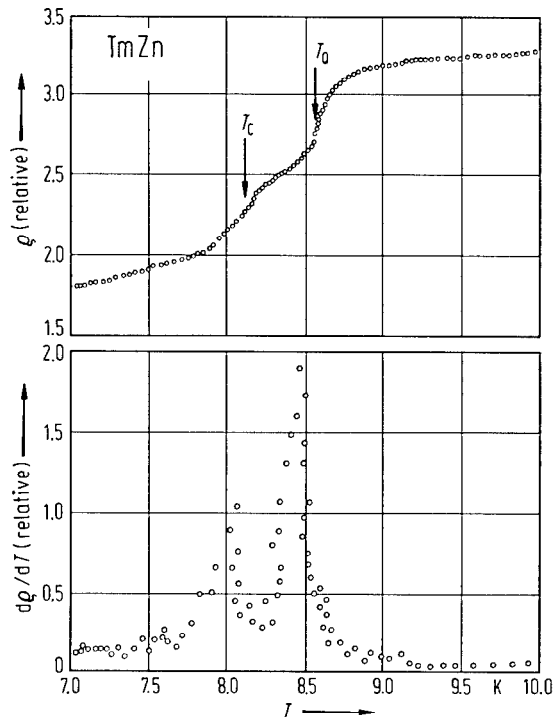

Fig. 68. TmZn. Thermal variation of the electrical resistivity ϱ and its temperature derivative in the phase transition range measured on a single crystal. The two discontinuities correspond to the electronic scattering by spins and quadrupoles, respectively [78 M 3].

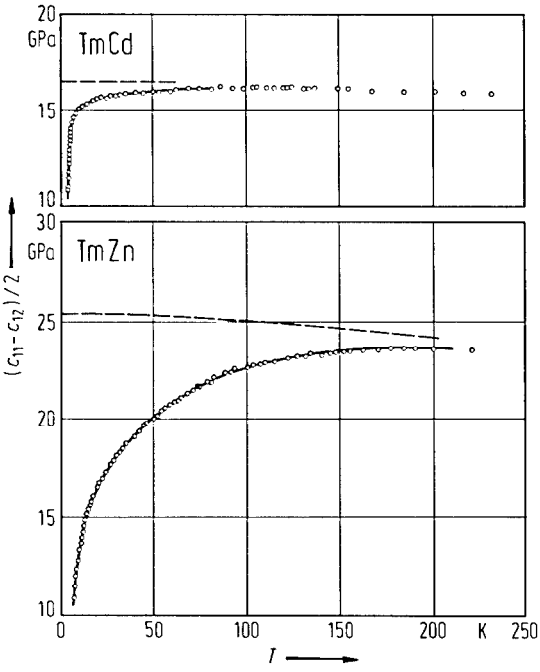

Fig. 70. TmCd, TmZn. Shear elastic mode, $\frac{1}{2}(c_{11}-c_{12})$, vs. temperature. Full lines are calculated behaviours in the CEF and quadrupolar interaction model. Dashed lines are background elastic constants without magnetic interactions [79 L 2].

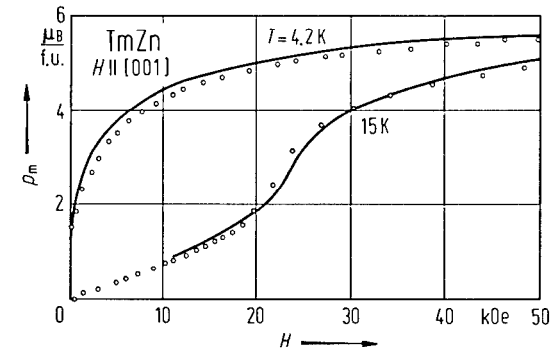

Fig. 69. TmZn. Magnetization curves corrected for demagnetization along [001] at 4.2 and 15 K. Lines are calculated considering, in particular, quadrupolar interactions [83 G 2].

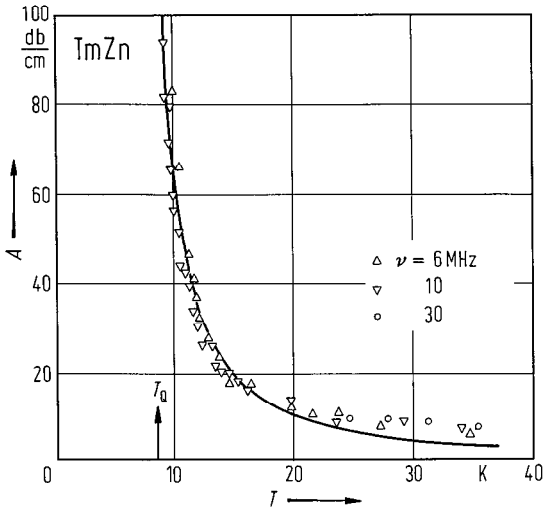

Fig. 71. TmZn. Attenuation coefficient A for the $\frac{1}{2}(c_{11}-c_{12})$ elastic mode at frequencies of 6 MHz, 10 MHz and 30 MHz. The solid line is a theoretical fit [79 L 1].

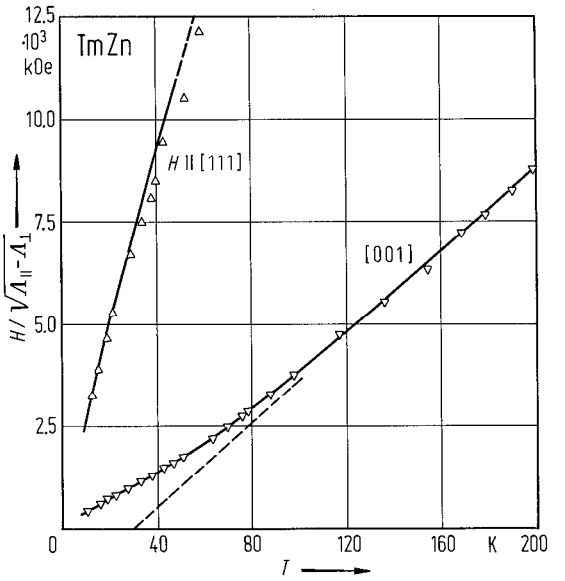

Fig. 72. TmZn. Reciprocal parastriction susceptibility $H/\sqrt{\Lambda_{\parallel}-\Lambda_{\perp}}$ vs. temperature for a magnetic field H along a [001] axis and a [111] axis. The changes of length, $\Lambda_{\parallel}$ and $\Lambda_{\perp}$, are measured parallel and perpendicular to H in the paramagnetic phase. Lines are calculated in presence of quadrupolar interactions [80 M 3].

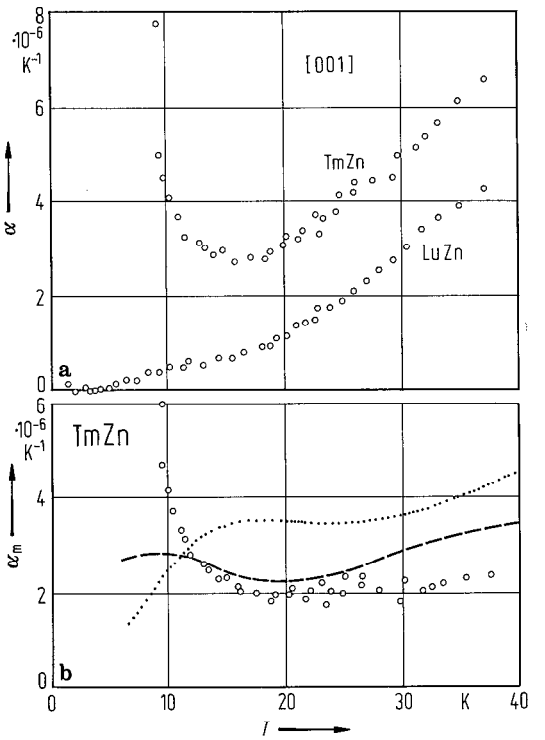

Fig. 73. TmZn, LuZn. (a) Linear thermal expansion coefficient α along the [001] axis vs. temperature. (b) Magnetic contribution to the linear thermal expansion coefficient, $\alpha_m = \alpha$ (TmZn) $-\alpha$ (LuZn), in TmZn. Lines are theoretical fits [84 M 1].

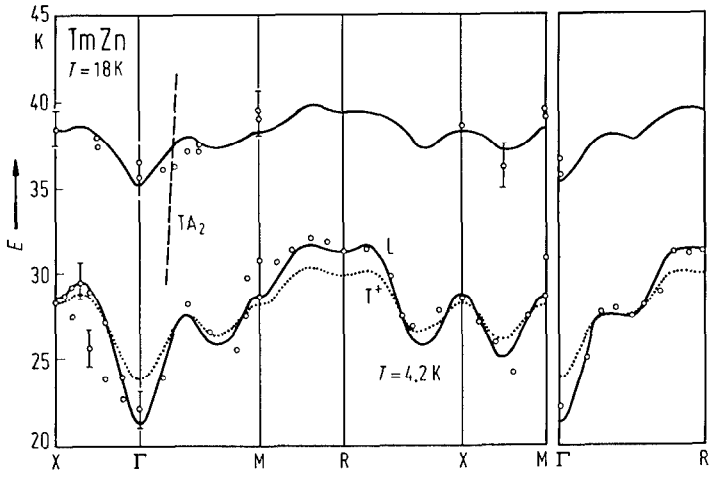

Fig. 74. TmZn. Dispersion curves of magnetic excitations at $T=18$ K in the paramagnetic phase and at $T=4.2$ K in the ordered one. Lines are calculated. L, T^+ and TA_2 correspond to magnetic longitudinal, magnetic transverse and acoustic phonon branches, respectively [80 M 2].

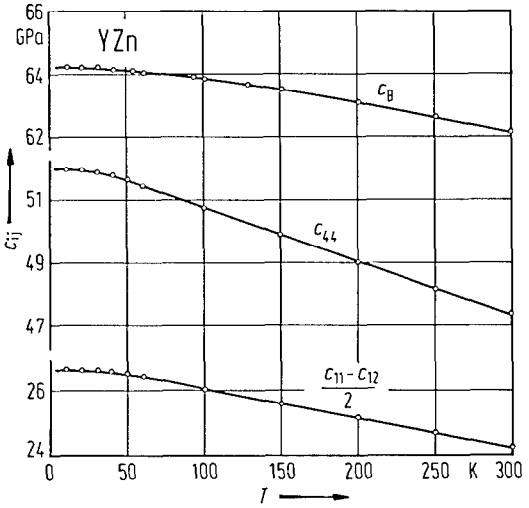

Fig. 75. YZn. Normal elastic modes, $\frac{1}{2}(c_{11}-c_{12})$, c_{44} and $c_B=\frac{1}{3}(c_{11}+2c_{12})$ vs. temperature [71 S 1].

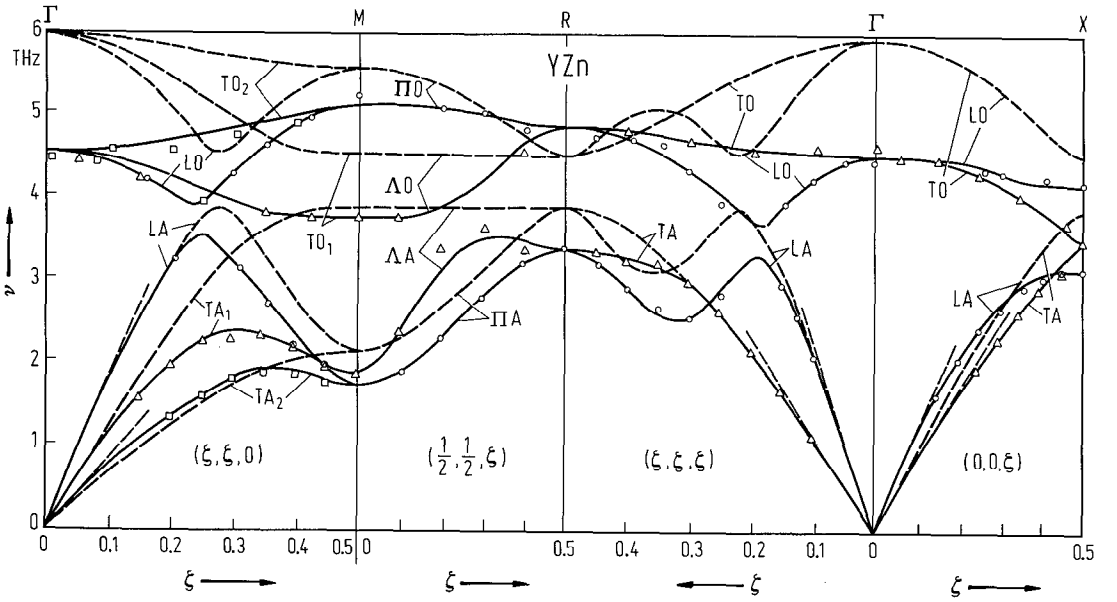

Fig. 76. YZn. Phonon distributions at room temperature along the principal symmetry directions. The solid lines represent dispersion curves fitted to the experimental points with a force-constant model including 6th-neighbour interactions. The dotted lines represent dispersion curves computed from a two-force-constant model involving only nearest-neighbour interactions with values for the force constants derived from single crystalline elastic constants. The dashed lines are limiting slopes at long-wavelength limits as indicated by measurements of ultrasonic wave velocities [72 P 2].

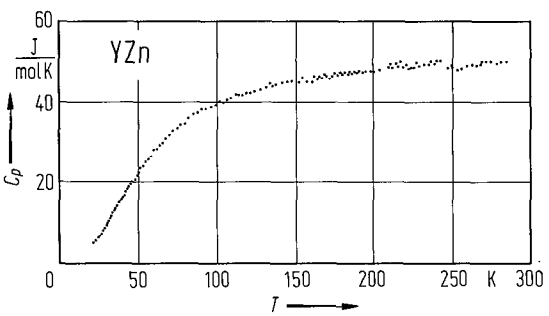

Fig. 77. YZn. Heat capacity C_p vs. temperature measured on a polycrystalline sample in increasing temperature [74 M 2].

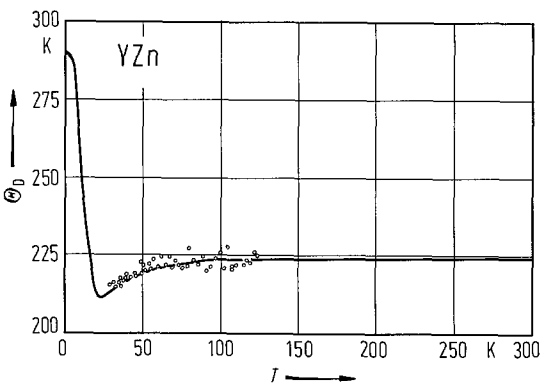

Fig. 78. YZn. Debye temperature Θ_D vs. temperature. The full line is deduced within a 6th-neighbour force-constant model from the phonon dispersion curves of Fig. 76. Dots are deduced from the specific heat of Fig. 77 within an Einstein model [75 M 3].

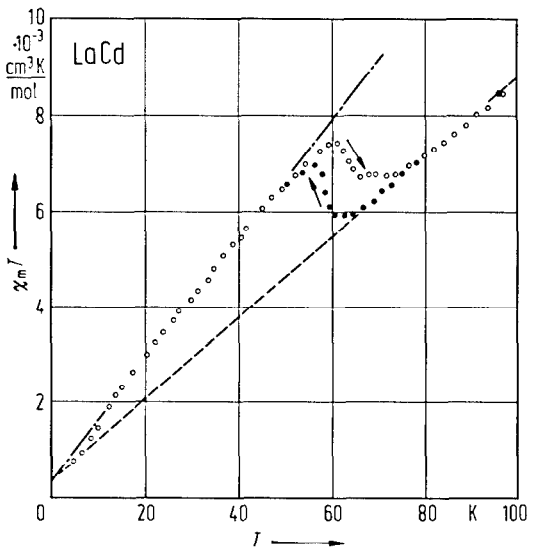

Fig. 79. LaCd. Temperature dependence of the product $\chi_m T$ for a monocrystalline sample. Arrows indicate the temperature drift [84 A 1].

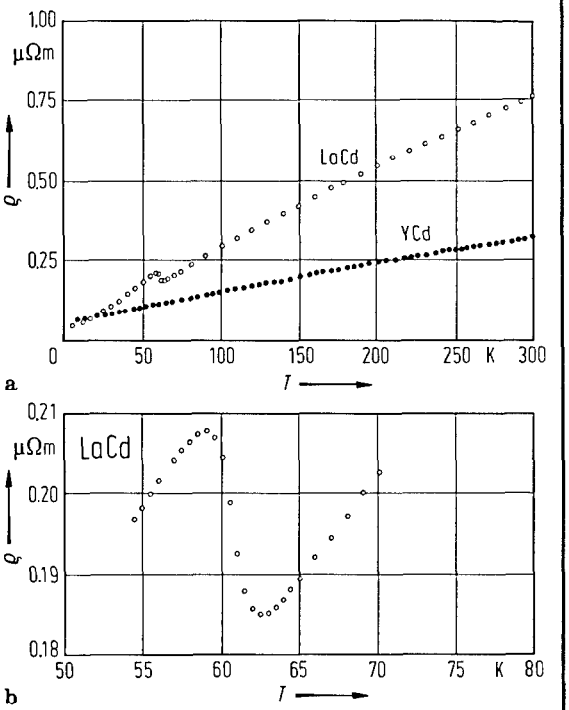

Fig. 80. LaCd, YCd. (a) Electrical resistivity ϱ vs. temperature. (b) gives the jump of ϱ at the structural instability [84 A 1].

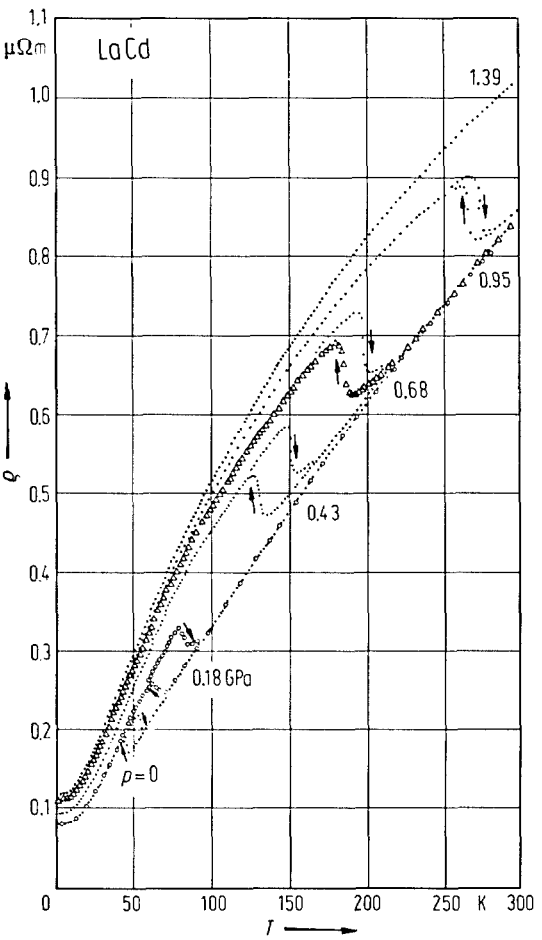

Fig. 81. LaCd. Isobaric electrical resistivity ϱ vs. temperature. For each curve, the pressure is indicated in GPa below the hysteretic behaviour at the structural phase transition temperature: the sharp jump in the electrical resistivity marks the cubic-to-tetragonal phase transition [81 P 1].

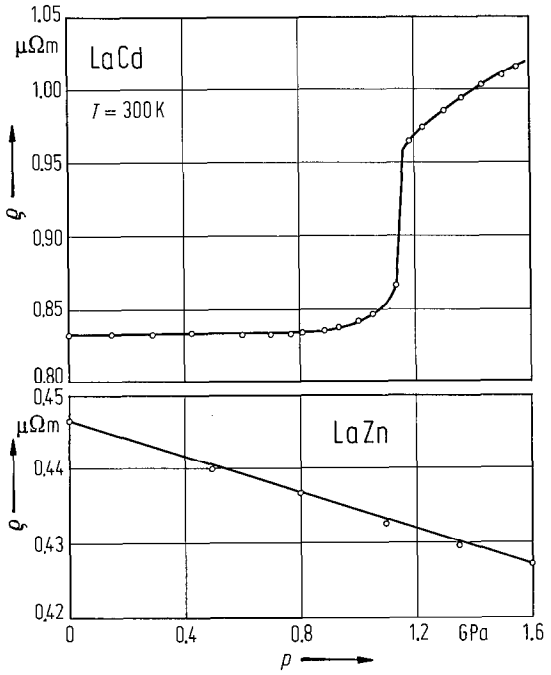

Fig. 82. LaCd, LaZn. Electric resistivity ϱ vs. hydrostatic pressure p at 300 K for increasing pressure (variations measured on polycrystalline samples) [81 P 1].

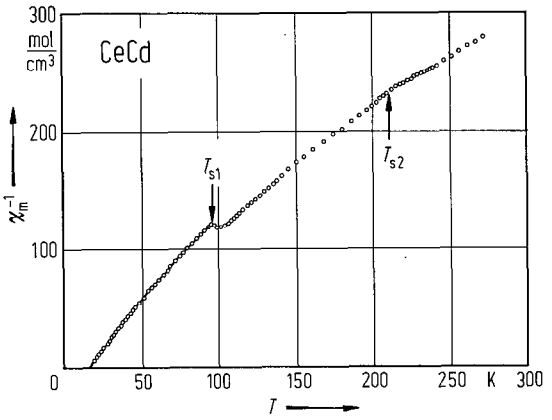

Fig. 83. CeCd. Reciprocal magnetic molar susceptibility χ_m^{-1} vs. temperature. T_{s1} and T_{s2} are the two structural phase transition temperatures [85 F 1].

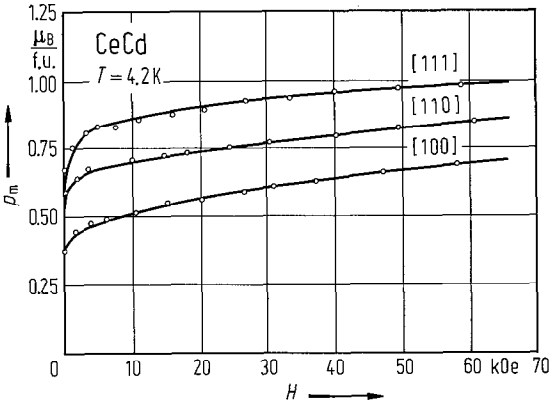

Fig. 85. CeCd. Magnetization processes corrected for demagnetization at 4.2 K along the three main crystallographic directions [85 F 1].

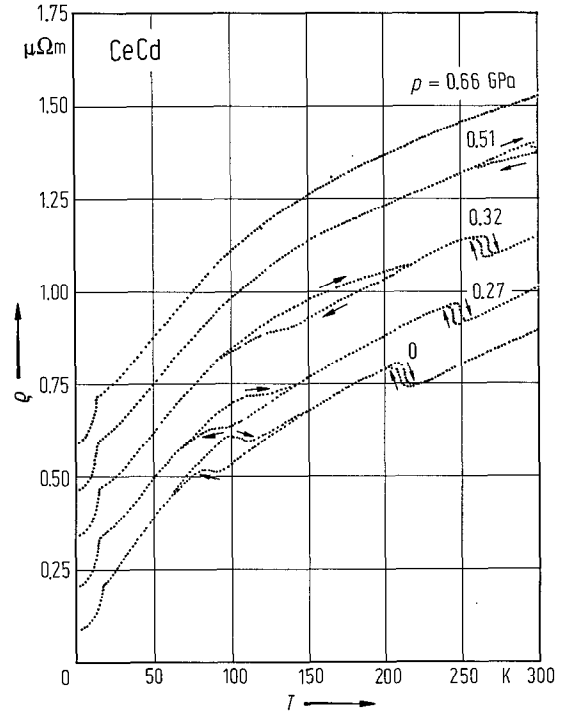

◀ Fig. 84. CeCd. Electrical resistivity ϱ vs. temperature at various pressures indicated at the ϱ-jump corresponding to the cubic-to-tetragonal phase transition. For clarity the curves are shifted in a vertical sense, but can be put on an absolute scale by substracting 0.5 μΩm for $p = 0.66$ GPa, 0.375 μΩm for $p = 0.51$ GPa, 0.25 μΩm for $p = 0.32$ GPa, and 0.125 μΩm for $p = 0.27$ GPa. Arrows indicate the temperature drift [83 K 1].

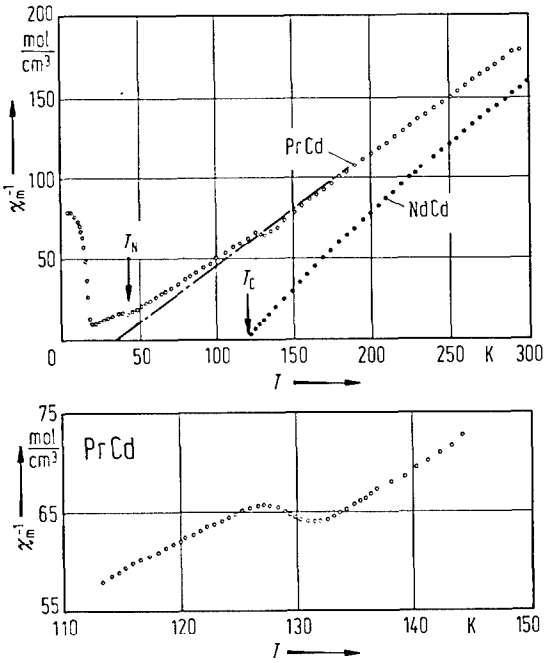

Fig. 86. PrCd, NdCd. Temperature variation of the reciprocal magnetic molar susceptibility χ_m^{-1} [84 A 1].

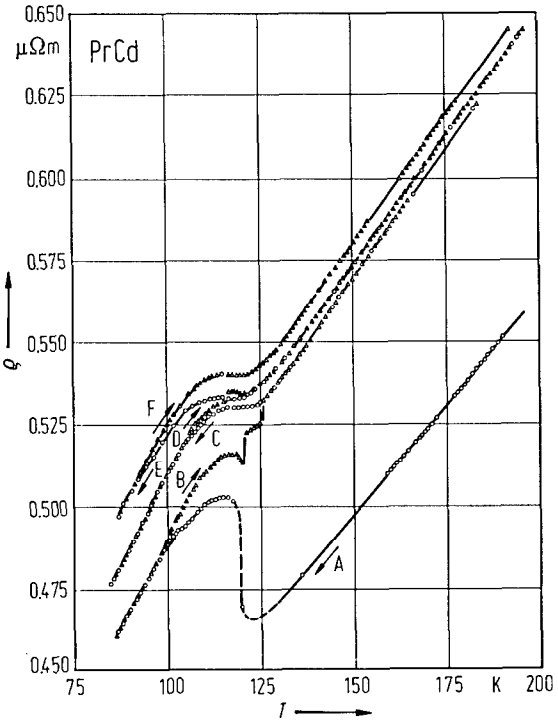

Fig. 87. PrCd. Hysteretic thermal behaviour of the electrical resistivity ϱ around the structural transition at 125 K for consecutive thermal cycle (A–F). Measurements on a single crystal [83 S 1].

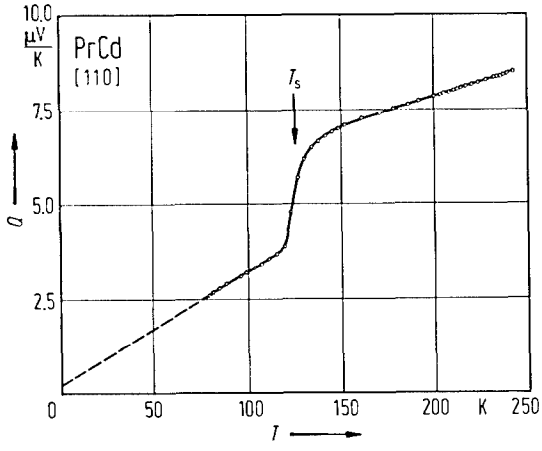

Fig. 88. PrCd. Thermoelectric power Q for increasing temperature near the structural transition, measured along the [110] direction [83 S 1].

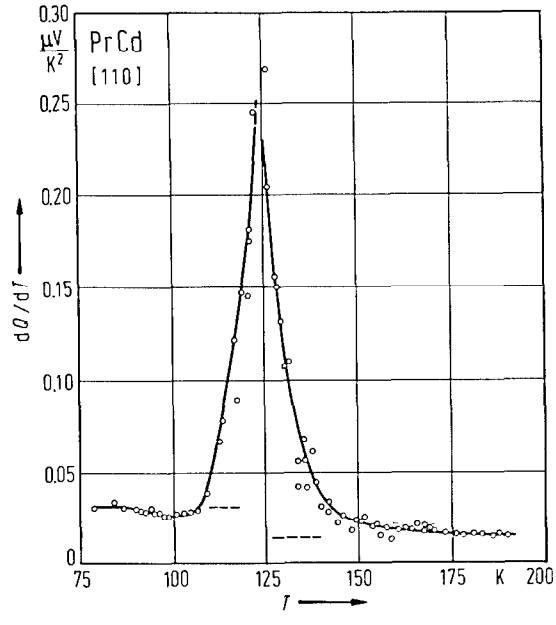

Fig. 89. PrCd. Temperature dependence of the derivative of the thermoelectric power dQ/dT along the [110] direction [83 S 1].

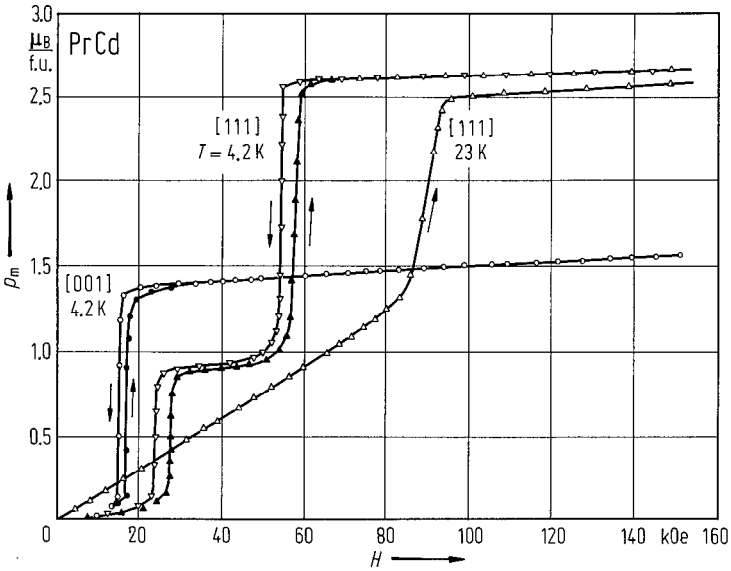

Fig. 90. PrCd. Isothermal magnetization curves along the threefold and fourfold axes at 4.2 K and 23 K, i.e. below and above the temperature of change for the magnetic structure, $T^* = 18$ K. Arrows indicate magnetic field drifts [84 A 1].

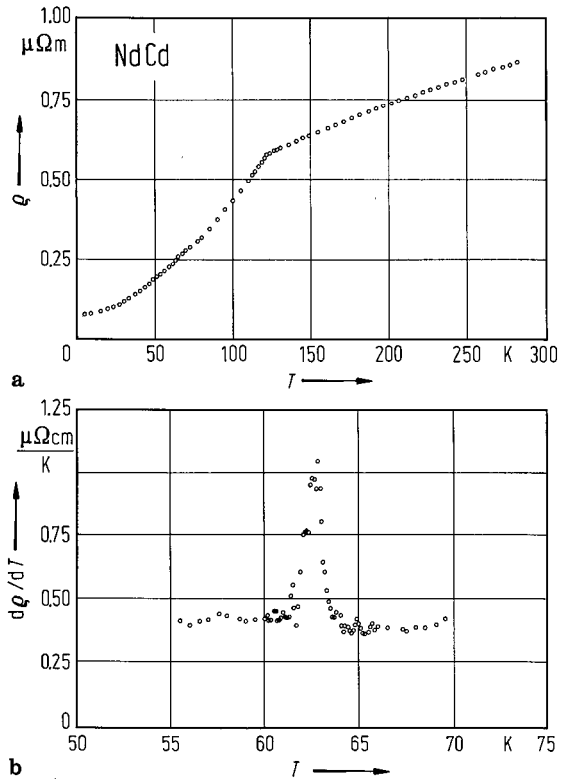

Fig. 91. NdCd. (a) Temperature dependence of the electrical resistivity ϱ for a single crystal. (b) gives the temperature derivative of ϱ as a function of temperature near the change of easy magnetization direction [84 A 1].

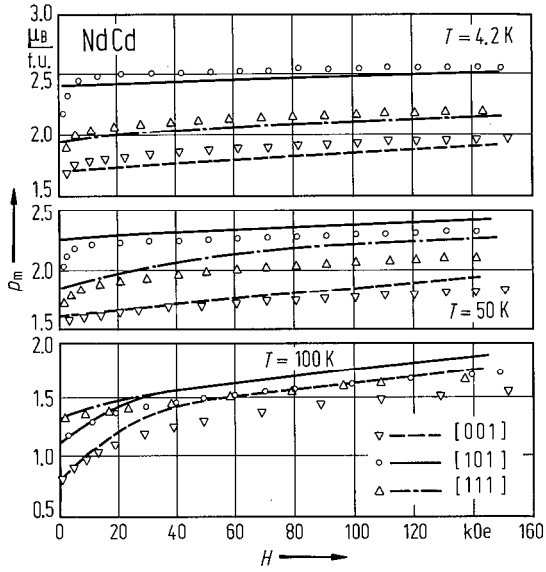

Fig. 92. NdCd. Magnetization processes corrected for demagnetization along the three main crystallographic directions at 4.2, 50 and 100 K. Lines are calculated behaviours within a CEF model [85 A 1].

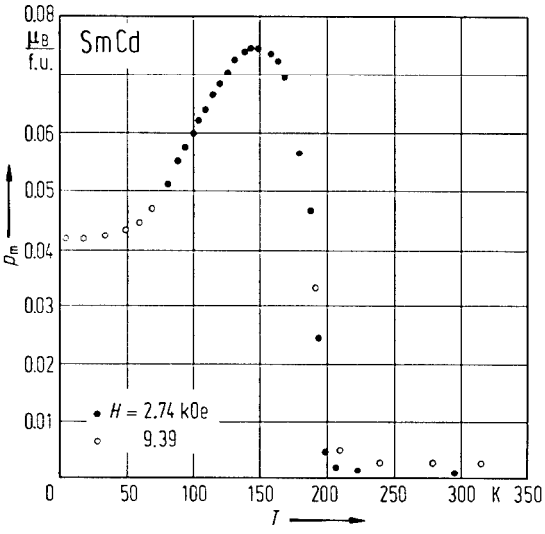

Fig. 93. SmCd. Magnetic moment p_m of a polycrystalline sample vs. temperature in applied magnetic fields of 2.74 kOe and 9.39 kOe [74 S 1].

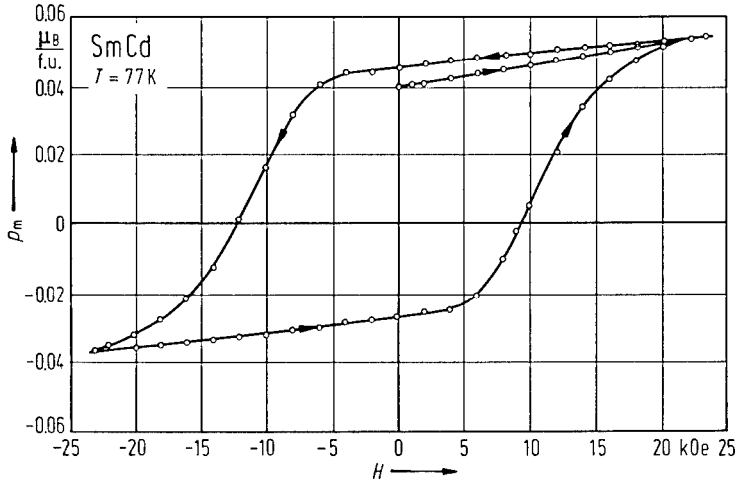

Fig. 94. SmCd. Hysteresis loop at 77 K. The polycrystalline specimen was cooled to this temperature in the remanent field of the magnet ($\approx$ 50 Oe) [74 S 1].

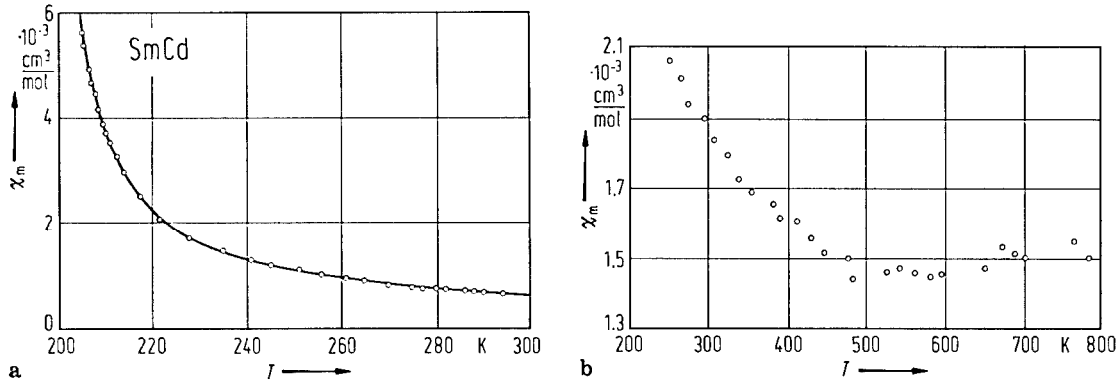

Fig. 95. SmCd. (a) Magnetic molar susceptibility χ_m vs. temperature for a polycrystalline sample. (b) shows the magnetic susceptibility above room temperature [74 S 1].

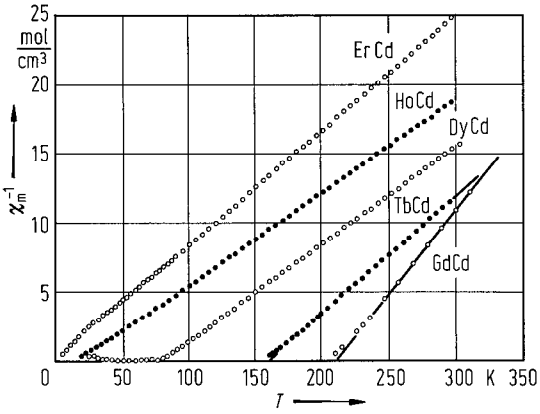

Fig. 96. RCd, R = Gd, Tb, Dy, Ho, Er. Temperature variation of the reciprocal magnetic molar susceptibility χ_m^{-1} [84 A 1].

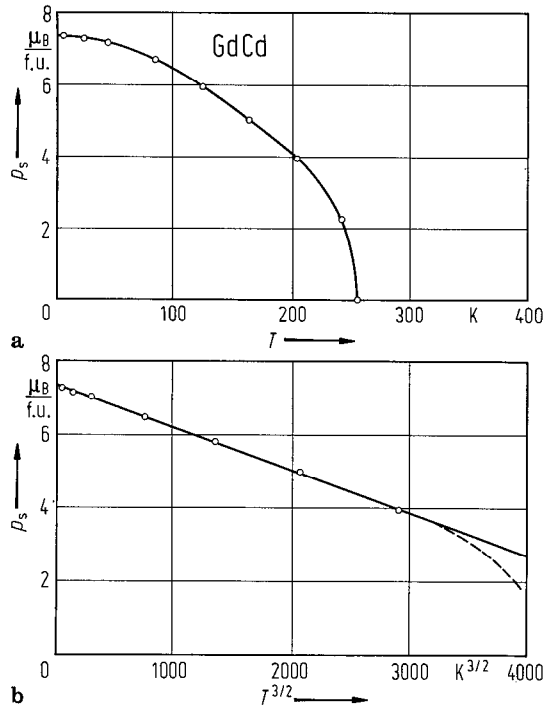

Fig. 97. GdCd. Spontaneous magnetic moment p_s vs. temperature (a) and vs. $T^{3/2}$ (b). Full curves are guide for the eye [80 S 2].

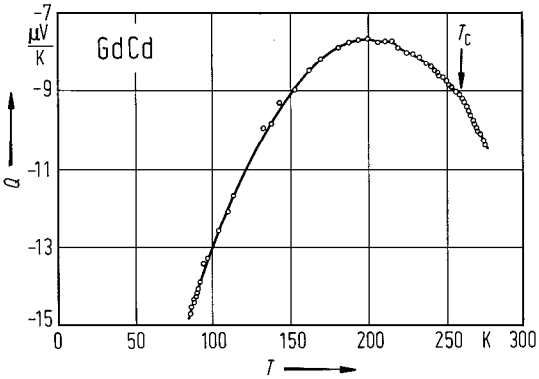

Fig. 98. GdCd. Thermoelectric power Q vs. temperature measured on a single crystal. Note the small anomaly at 210 K, corresponding to the weak structural phase transition occuring at this temperature (see Fig. 118) [80 S 2].

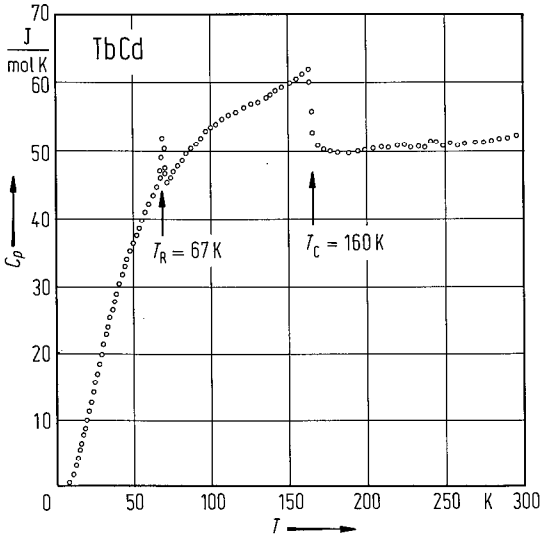

Fig. 99. TbCd. Specific heat C_p measured in increasing temperature on a polycrystalline sample [85 A 1].

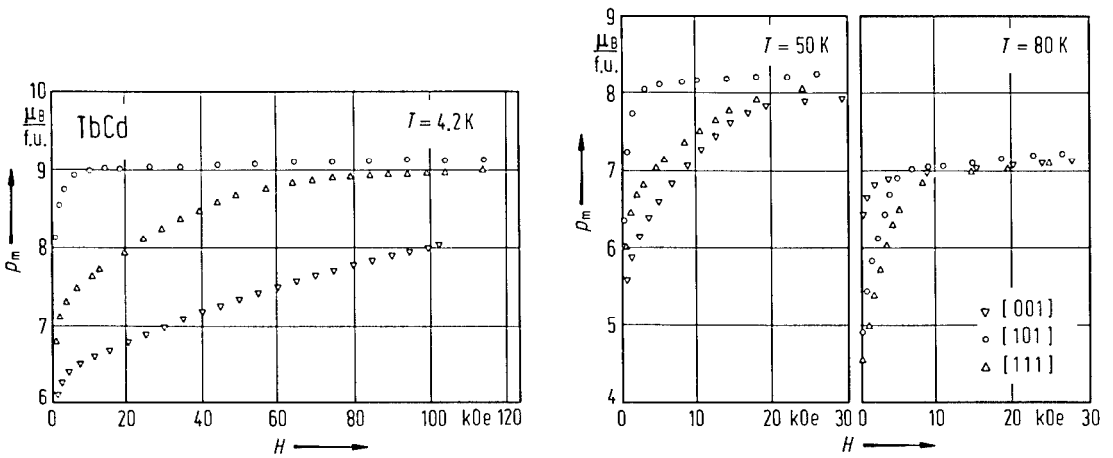

Fig. 100. TbCd. Magnetization processes, corrected for demagnetization along the three main crystallographic axes at 4.2 K, 50 K and 80 K. Note the change of easy magnetization axis between 50 and 80 K [85 A 1].

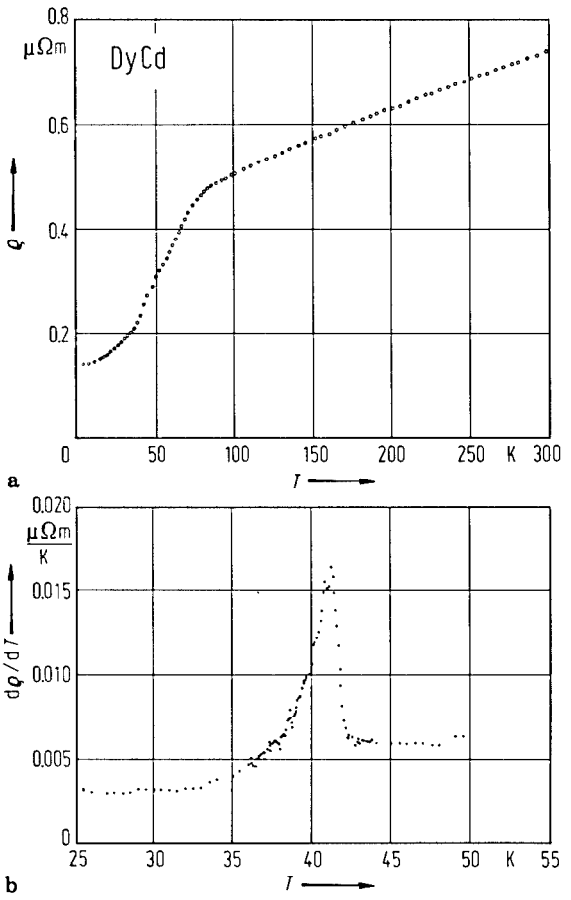

Fig. 101. DyCd. (a) Temperature variation of the electrical resistivity ϱ. (b) gives its temperature derivative close to the temperature of change for the magnetic structure, $T^* = 40$ K [84 A 1].

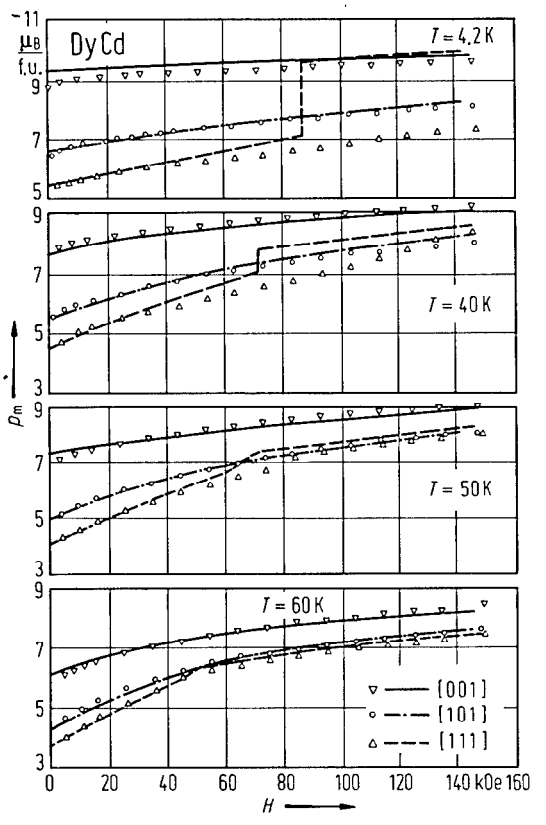

Fig. 102. DyCd. Magnetization processes corrected for demagnetization along the three main crystallographic axes at different temperatures. Curves are calculated in CEF model including quadrupolar interactions [85 A 1].

Fig. 103. DyCd. Magnetization hysteresis cycle at 4.2 K along [001] (full curve) and [111] (dashed curve) [85 A 1].

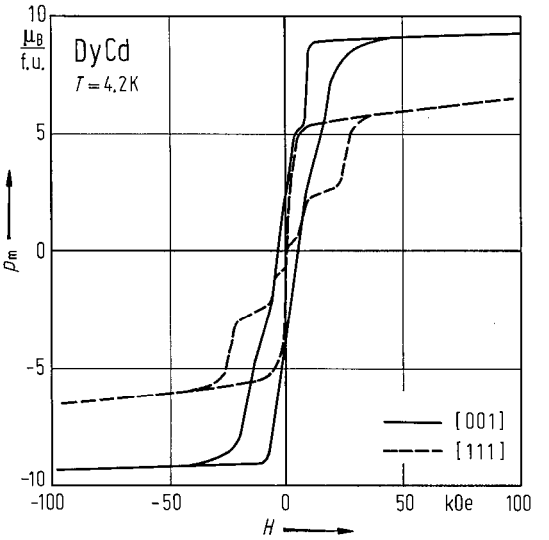

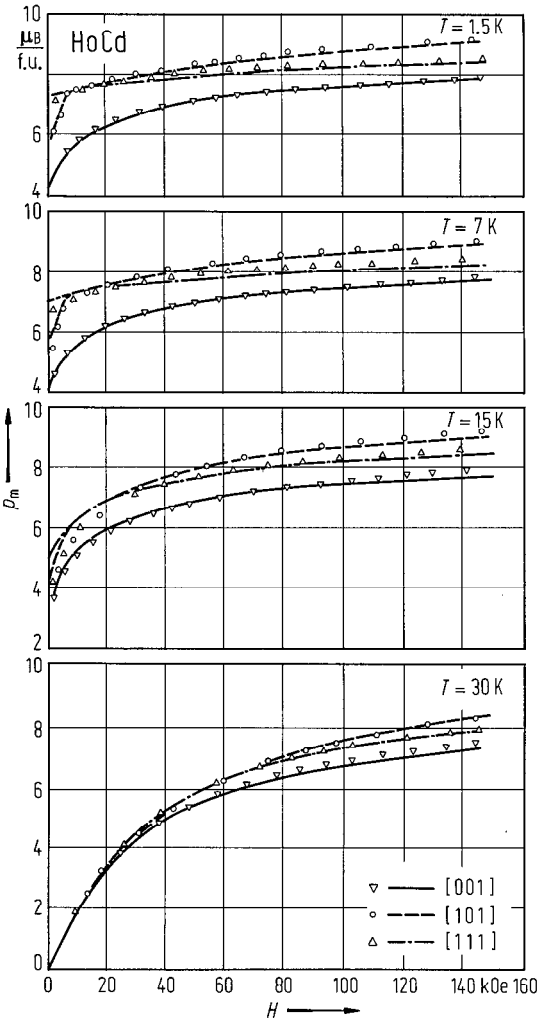

Fig. 104. HoCd. Magnetic processes corrected for demagnetization along the three principle axes at different temperatures. Curves are calculated variations [85 A 1].

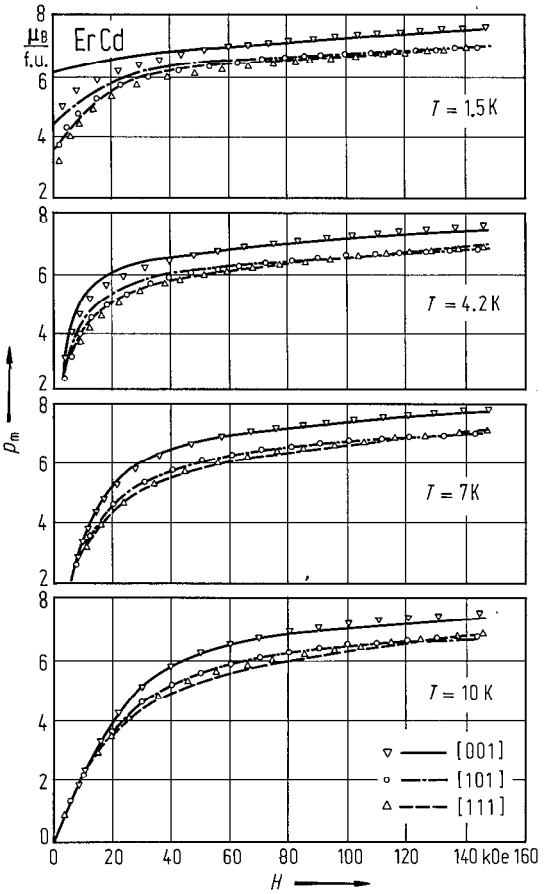

Fig. 105. ErCd. Magnetization processes corrected for demagnetization along the three principal axes at the temperatures indicated. Curves are calculated in CEF model [85 A 1].

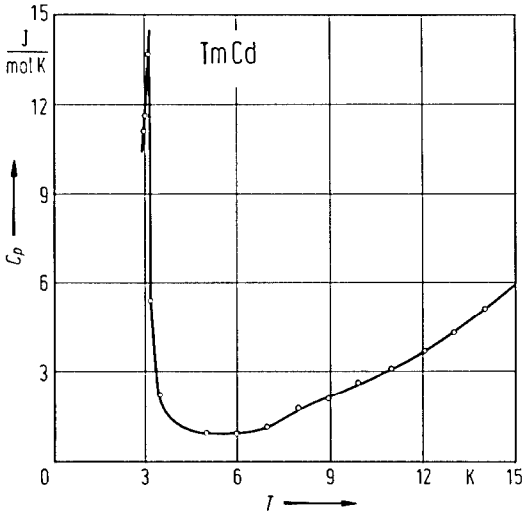

Fig. 106. TmCd. Specific heat C_p vs. temperature for a polycrystalline sample [73 L 1].

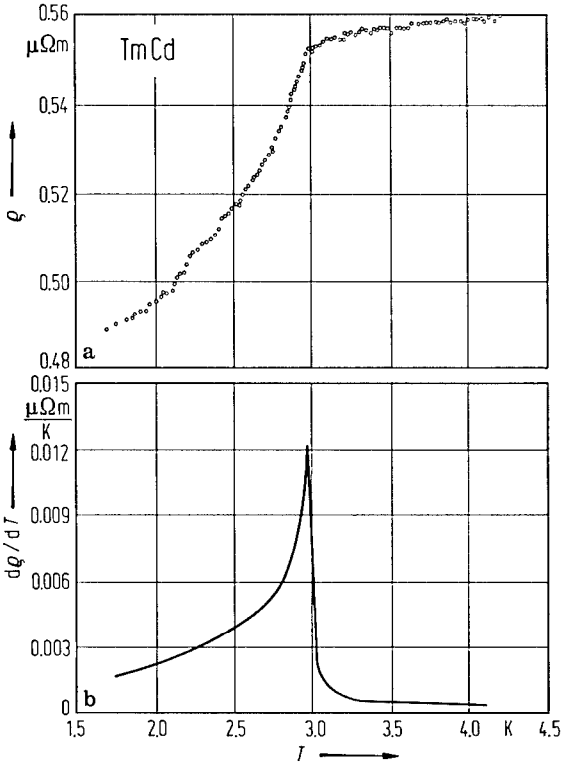

Fig. 107. TmCd. Temperature variation (a) of the electrical resistivity ϱ and (b) of its temperature derivative $d\varrho/dT$ in the range of the quadrupolar ordering (measurements in increasing temperature on a single crystal) [84 A 1].

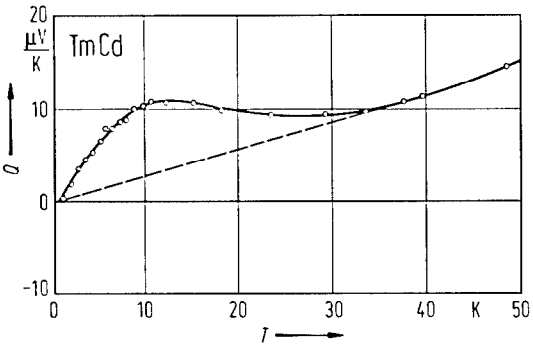

Fig. 108. TmCd. Thermoelectric power Q vs. temperature (measured on a polycrystalline sample) [75 S 1].

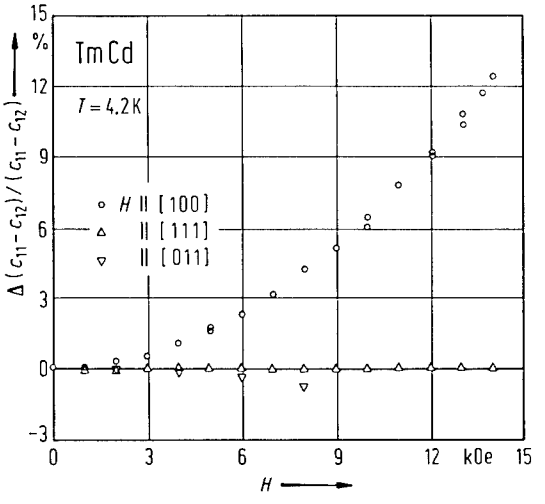

Fig. 109. TmCd. Magnetic field dependence of the shear elastic mode, $c_{11}-c_{12}$, normalized to the zero-field-value for the three main field directions at 4.2 K. The magnetic field is perpendicular to the ultrasonic propagation [0$\bar{1}$1] direction [73 L 1].

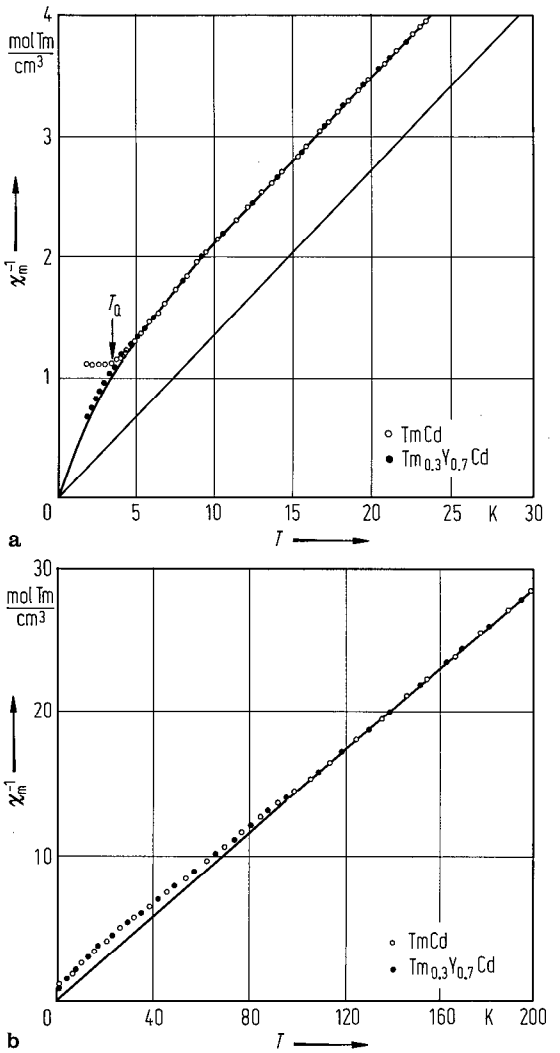

Fig. 110. TmCd, $Tm_{0.3}Y_{0.7}Cd$. Low (a) – and high (b) – temperature reciprocal magnetic molar susceptibility χ_m^{-1} vs. temperature. The straight lines are the extrapolations of the linear high-temperature behaviour. The full curves are calculated within a CEF model. The dilute compound does not exhibit a quadrupolar ordering temperature [79 A 1].

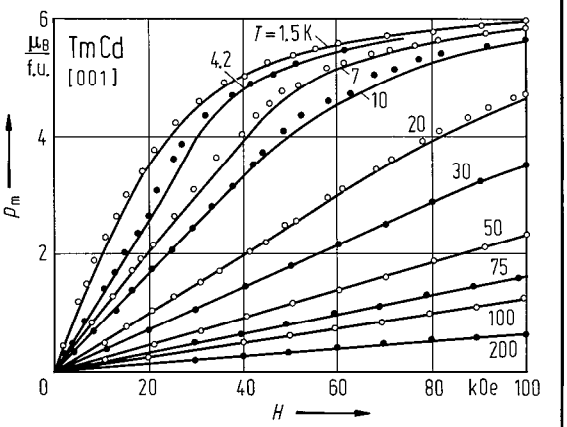

Fig. 111. TmCd. Experimental and calculated isothermal magnetization curves along [001] in both the tetragonal and cubic phases. Temperatures are indicated [79 A 1].

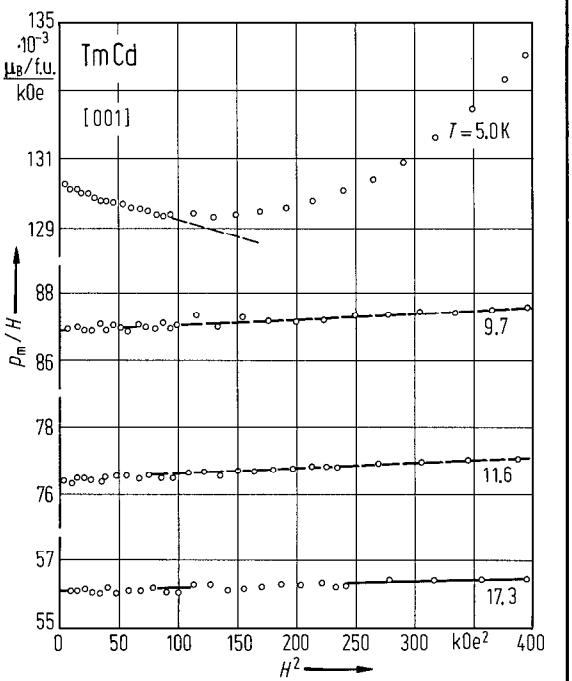

Fig. 112. TmCd. Plots of p_m/H vs. the square of the magnetic field, H^2, corrected for demagnetizing effects. H is applied along the [001] axis at the temperatures indicated [81 M 1].

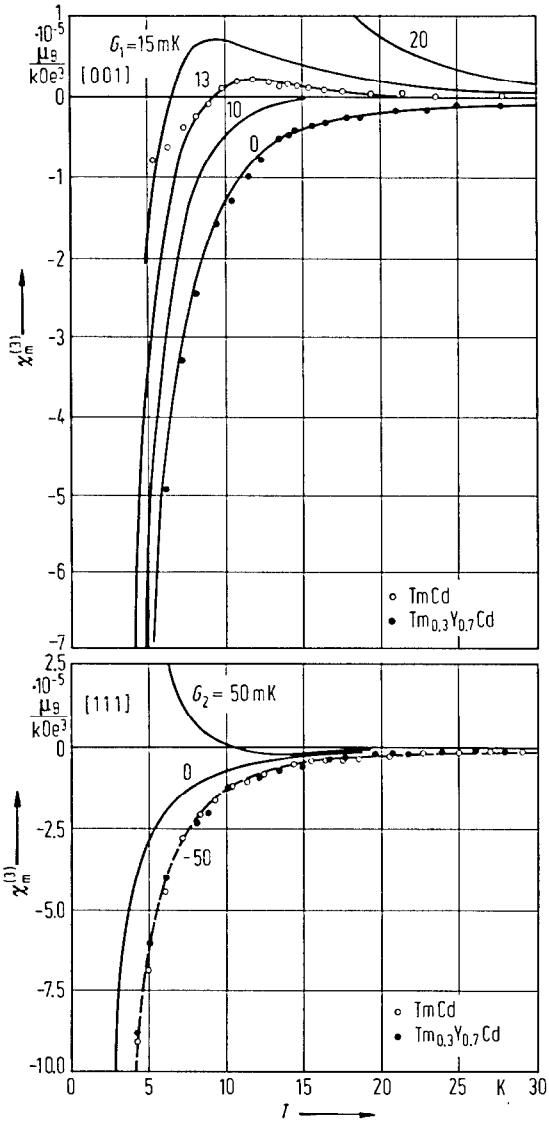

Fig. 113. TmCd, $Tm_{0.3}Y_{0.7}Cd$. Temperature dependence of the third-order magnetic susceptibility $\chi_m^{(3)}$, related to a 4f-site, along [001] and [111]. The lines are calculated taking into account quadrupolar interactions of both tetragonal and trigonal symmetries, characterized by the G_1 and G_2 values. For the trigonal symmetry the dilution does not modify the behaviour [81 M 1].

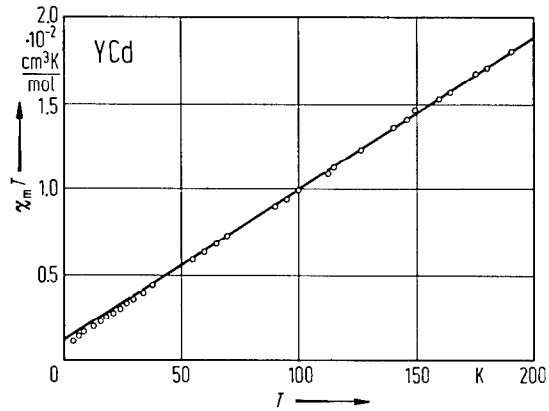

Fig. 114. YCd. Temperature variation of the product $\chi_m T$ for increasing temperature on a polycrystalline sample [84 A 1].

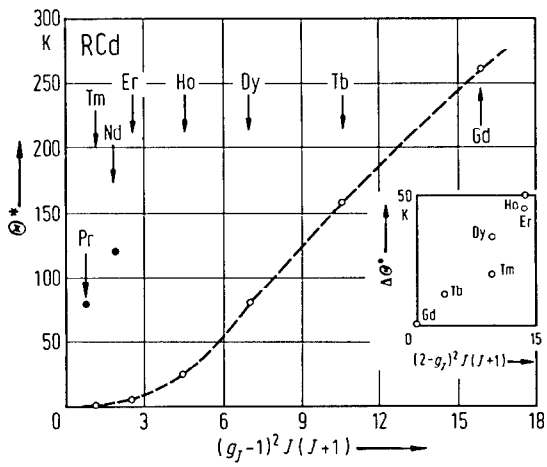

Fig. 115. RCd. Bilinear interaction coefficient Θ^* vs. the De Gennes factor $(g_J-1)^2 J(J+1)$. The inset gives the difference, $\Delta\Theta^*$, between the experimental Θ^* value and the De Gennes factor, as a function of the orbital coupling parameter $(2-g_J)^2 J(J+1)$ for the heavy RCd compounds [84 A 1]. Open circles: stable, solid circle: unstable compounds.

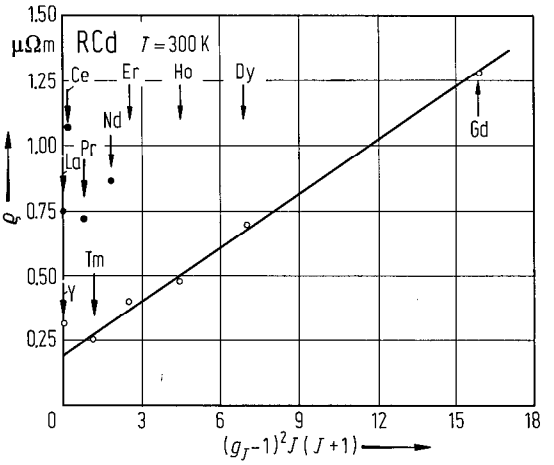

Fig. 116. RCd. Room-temperature electrical resistivity ϱ (open circles: stable compounds; solid circles: unstable ones) vs. the De Gennes factor, $(g_J-1)^2J(J+1)$ [84 A 1].

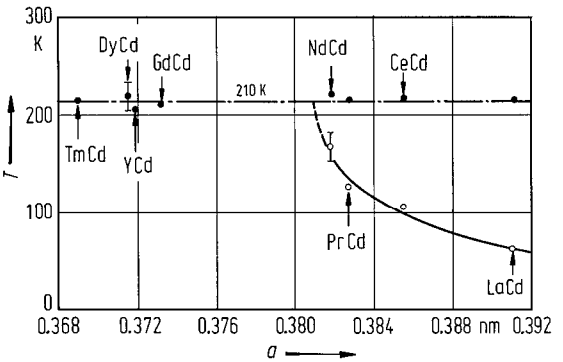

Fig. 118. RCd. Structural phase diagram as a function of the lattice parameter a. For $T>210$ K, the structure is cubic; for $T<210$ K, it remains very close to cubic for heavy RCd compounds (open circles). For light RCd compounds, the structure below 210 K is unknown [85 A 2].

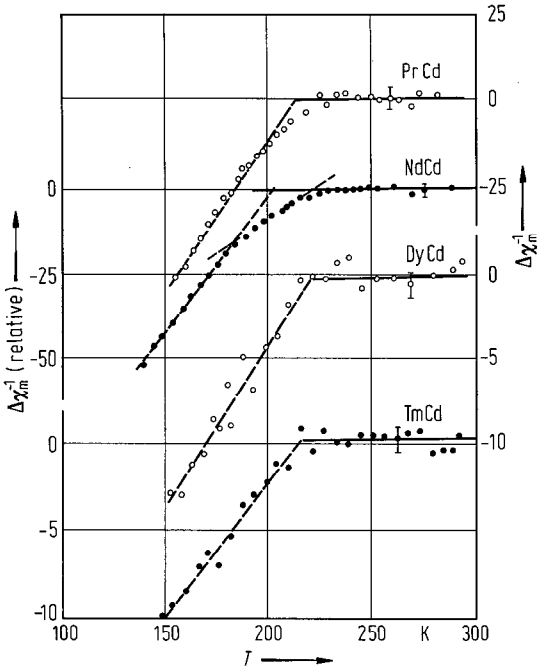

Fig. 117. RCd. Temperature variation of the shift from the high-temperature linear behaviour for the reciprocal magnetic susceptibility, $\Delta\chi_m^{-1}$ [85 A 2].

2.7.3 RX_2 compounds

Light RMg_2 compounds are cubic, heavy ones hexagonal. All of them have been studied only on polycrystalline materials; they are ferromagnetic except $SmMg_2$ and $EuMg_2$ which were found antiferromagnetic. Here again, the shortcoming of the RKKY model was shown by NMR studies [77 D 1] (Fig. 126). Large magnetic moment reductions were observed (Figs. 120, 121, 128). The existence of quadrupolar interactions was assumed in $PrMg_2$ for explaining the nature of the ferromagnetic transition [81 L 1].

RZn_2 crystallize in the orthorhombic $CeCu_2$-type structure. Their magnetism is characterized by commensurate or incommensurate antiferromagnetic structures. The Θ values are close to the Néel temperatures (Table 12). No single crystal has been grown in spite of the congruent melting point.

Very limited data are available in the literature about RCd_2 and RHg_2 compounds.

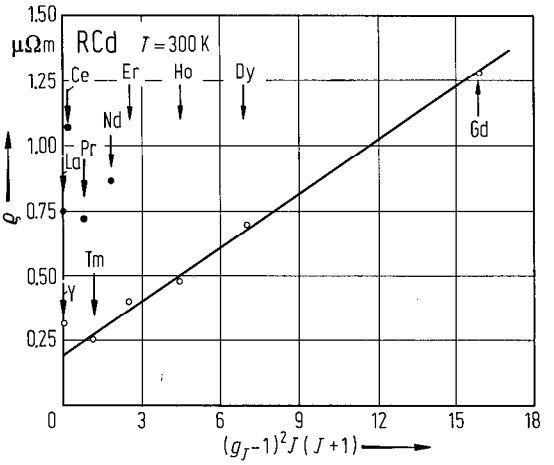

Fig. 116. RCd. Room-temperature electrical resistivity ϱ (open circles: stable compounds; solid circles: unstable ones) vs. the De Gennes factor, $(g_J-1)^2J(J+1)$ [84 A 1].

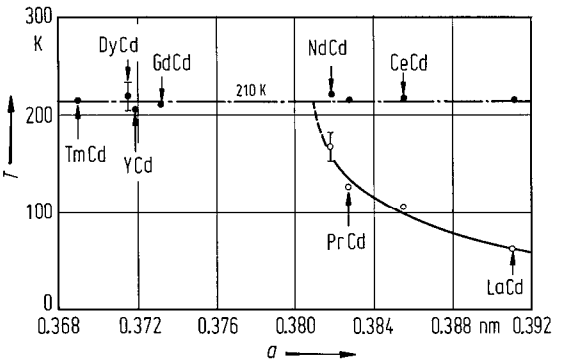

Fig. 118. RCd. Structural phase diagram as a function of the lattice parameter a. For $T>210$ K, the structure is cubic; for $T<210$ K, it remains very close to cubic for heavy RCd compounds (open circles). For light RCd compounds, the structure below 210 K is unknown [85 A 2].

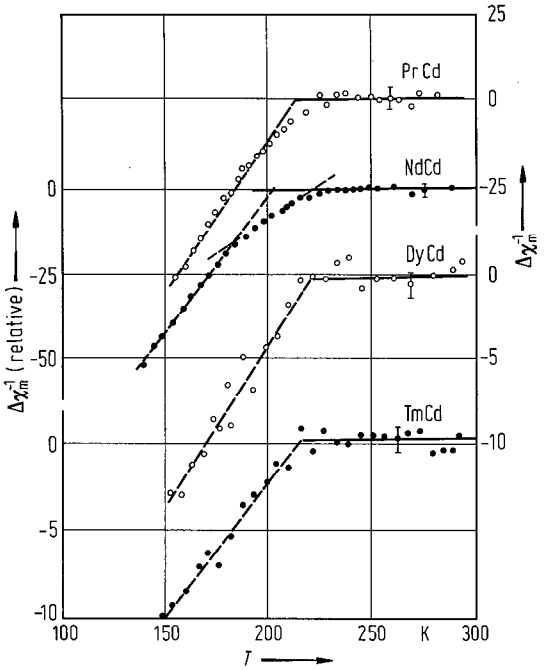

Fig. 117. RCd. Temperature variation of the shift from the high-temperature linear behaviour for the reciprocal magnetic susceptibility, $\Delta\chi_m^{-1}$ [85 A 2].

2.7.3 RX_2 compounds

Light RMg_2 compounds are cubic, heavy ones hexagonal. All of them have been studied only on polycrystalline materials; they are ferromagnetic except $SmMg_2$ and $EuMg_2$ which were found antiferromagnetic. Here again, the shortcoming of the RKKY model was shown by NMR studies [77 D 1] (Fig. 126). Large magnetic moment reductions were observed (Figs. 120, 121, 128). The existence of quadrupolar interactions was assumed in $PrMg_2$ for explaining the nature of the ferromagnetic transition [81 L 1].

RZn_2 crystallize in the orthorhombic $CeCu_2$-type structure. Their magnetism is characterized by commensurate or incommensurate antiferromagnetic structures. The Θ values are close to the Néel temperatures (Table 12). No single crystal has been grown in spite of the congruent melting point.

Very limited data are available in the literature about RCd_2 and RHg_2 compounds.

Table 11. RMg_2 compounds. Room-temperature lattice parameters a, c, magnetic properties in the paramagnetic phase (effective magnetic moment per rare earth ion, p_{eff}, paramagnetic Curie temperature, Θ) and in the ordered phase (magnetic ordering temperature, T_C or T_N, spin structure, easy magnetization direction, low-temperature spontaneous magnetic moment per rare earth ion, p_s), and CEF parameters. $A_4\langle r^4\rangle$, $A_6\langle r^6\rangle$.

	a	c	p_{eff}	Θ	T_C	T_N	Spin structure	Easy direction	p_s	$A_4\langle r^4\rangle$	$A_6\langle r^6\rangle$	Remarks	Figures
	nm		μ_B	K	K				μ_B	K			
$LaMg_2$	0.8801											χ (300 K) = 2.87 $\cdot 10^{-3}$ cm^3 mol^{-1}; Pauli paramagnet [78 B 1]	119
$CeMg_2$	0.8733		2.51	−19	3.6		F		0.5	> 0	0	[78 B 1]	119
$PrMg_2$	0.8688 [81 L 1]		3.34	7	9.6 [78 B 1]		F		2.0	58	−17 [81 L 1]		119–121
$NdMg_2$	0.8663 [81 L 1]		3.32	26 [78 B 1]	28.5		F		2.05	39	−12 [81 L 1]		122
$SmMg_2$	0.8629					26				> 0	0	no Curie-Weiss law [78 B 1]	123
$EuMg_2$	0.6344	1.0259	8.52	19		30						divalent [78 B 1]	124
$GdMg_2$	0.8576		8.90	100	81		F		7.23			[78 B 1]	125, 126
$TbMg_2$	0.6051	0.9807	10.11	83	88		F		5.69			[78 B 1]	
$DyMg_2$	0.6007	0.9745 [81 L 1]	10.82	56 [78 B 1]	80		F	$\perp c$	9.3 [81 L 1]				127
$HoMg_2$	0.6020	0.9764	10.74	23	27		F		6.05			[78 B 1]	
$ErMg_2$	0.5971	0.9680 [81 L 1]	9.86	7 [78 B 1]	18		F	$\parallel c$	7.60 [81 L 1]				128
$TmMg_2$	0.5968	0.9703	7.46	3	9		F		2.68			[78 B 1]	
$YbMg_2$	0.6224	1.0085										χ (300 K) = 1.12 $\cdot 10^{-3}$ cm^3 mol^{-1}; Pauli paramagnet [78 B 1]	
YMg_2	0.6038	0.9801										χ (300 K) = 1.78 $\cdot 10^{-3}$ cm^3 mol^{-1}; Pauli paramagnet [78 B 1]	

Table 12. RZn_2 compounds.

	a	b	c	p_{eff}	Θ	T_C	T_N	Magnetic structure	p_s	Easy axis	Remarks	Figures
	nm			μ_B	K	K			μ_B			
$LaZn_2$	0.4689	0.7638	0.7593 [67 F 1]								Pauli paramagnet [70 D 1] $\gamma = 8.34\,mJ\,K^{-2}\,mol^{-1}$ [74 D 1]	
$CeZn_2$	0.4635	0.7540	0.7501 [66 L 1]	2.25	24 [70 D 1]		7.5	AF	1.6	b [72 D 1]		129, 130
$PrZn_2$	0.4619	0.7474	0.7533 [67 F 1]	3.56	14 [70 D 1]							131
$NdZn_2$	0.4599	0.7409	0.7566 [67 F 1]	3.40	28 [70 D 1]		21	F + AFM	$p_F = 0.7$ $p_{AFM} = 1.7$	b [73 D 1]		131–133
$SmZn_2$	0.4552	0.7299	0.7590 [67 F 1]				45 [70 D 1]				no Curie-Weiss behaviour	129
$EuZn_2$	0.4728	0.7650	0.7655 [64 I 1]	8.22	27		30 [75 D 1]	AF			divalent; $p_{eff} = 7.1\,\mu_B$ [75 B 2]	134, 135
$GdZn_2$	0.4513	0.7214	0.7606 [67 F 1]	8.48	70	68		F	6.91 [70 D 1]			136
$TbZn_2$	0.4492	0.7142	0.7595 [67 F 1]	9.62	58 [70 D 1]		75	AFM ($T > 60$ K) AF ($T < 60$ K)	8.15	b [72 D 1]		136–139
$DyZn_2$	0.4477	0.7090	0.7600 [67 F 1]	10.45	31.5		35	AF [75 D 1]				134, 140
$HoZn_2$	0.4460	0.7042	0.7612 [67 F 1]	9.71	26 [70 D 1]		13.5 [75 D 2]	AFM	9.4	b [72 D 2]		136, 139
$ErZn_2$	0.4448	0.6984	0.7610 [67 F 1]	9.58	5.8	13		F			existence of magnetic satellites in powder neutron diffraction [75 D 1]	135, 141
$TmZn_2$	0.4433	0.6944	0.7604 [67 F 1]	6.48	11.5		5.2	AF [75 D 1]				140–142
$YbZn_2$	0.4573	0.7325	0.7569 [65 M 1]								no Curie-Weiss behaviour	[70 D 1]
$LuZn_2$	0.4416	0.6866	0.7600 [67 F 1]									
YZn_2	0.4504	0.7143	0.7664 [79 i]									

Table 13. RCd_2, RHg_2 compounds. Room-temperature lattice parameters a, b, c, magnetic characteristics (effective magnetic moment per rare-earth ion, p_{eff}, paramagnetic Curie temperature Θ, magneting ordering temperature T_N. low-temperature spontaneous magnetic moment per rare earth ion, p_s).

	a	b	c	p_{eff}	Θ	T_N	p_s	Ref.
	nm			μ_B	K	K	μ_B	
$CeCd_2$	0.5077		0.3447	2.18	− 75			63 O 1
$EuCd_2$	0.5057	0.7922	0.8500	7.82	34	36	7.1	77 B 1
$GdCd_2$	0.4941		0.3467	8.40	129			71 B 1
$YbCd_2$	0.5989		0.9597	divalent				71 P 1
$CeHg_2$	0.4942		0.3540	2.73	− 33			63 O 1
$EuHg_2$	0.4978		0.3710	8.00	29			68 I 1
$YbHg_2$	0.4896		0.3534	divalent				68 I 1

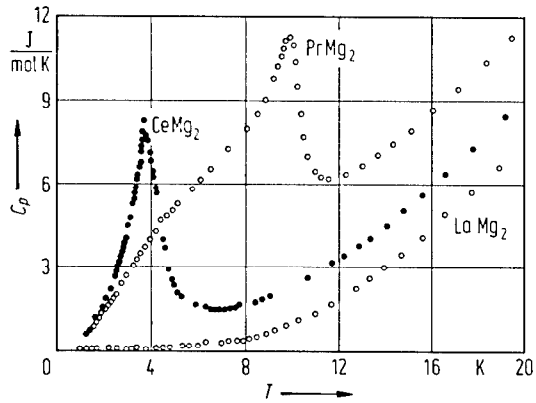

Fig. 119. RMg_2, R = La, Ce, Pr. Temperature variation of the molar heat capacity C_p for polycrystalline samples [78 B 1].

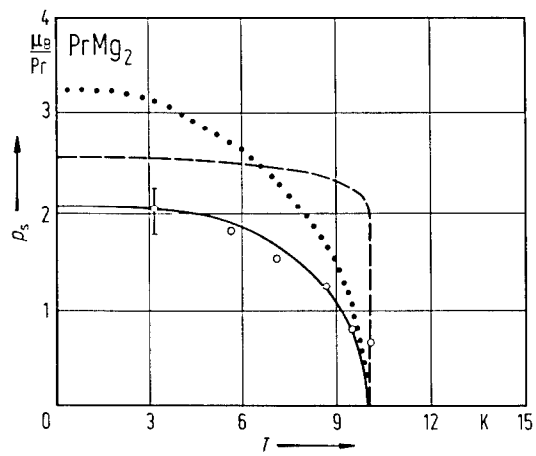

Fig. 120. $PrMg_2$. Spontaneous magnetic moment per Pr atom, p_s vs. temperature. The dotted line is the Brillouin curve for $J = 4$. The broken and full lines give the result of a mean-field calculation without and with quadrupolar interactions, respectively [81 L 1].

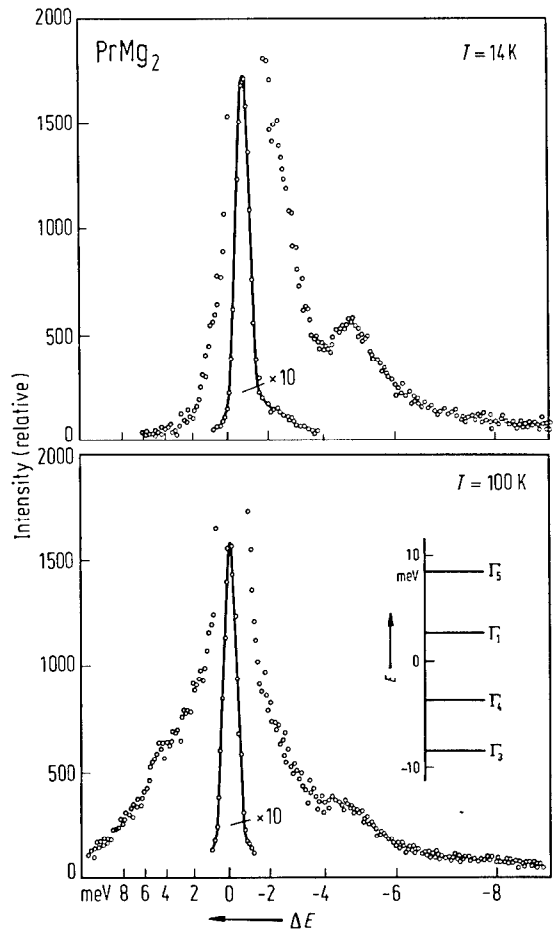

Fig. 121. $PrMg_2$. Inelastic neutron scattering intensity vs. the energy transfer ΔE from the incident neutron energy of 14 meV at the temperatures indicated. The inset shows the deduced crystal field level scheme of Pr [81 L 1].

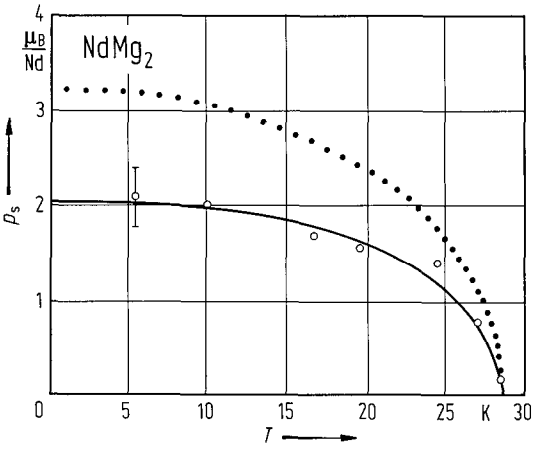

Fig. 122. $NdMg_2$. Spontaneous magnetic moment per Nd atom p_s vs. temperature. The dotted line is the Brillouin curve for $J=9/2$. The full line is calculated within a model including CEF and bilinear interactions [81 L 1].

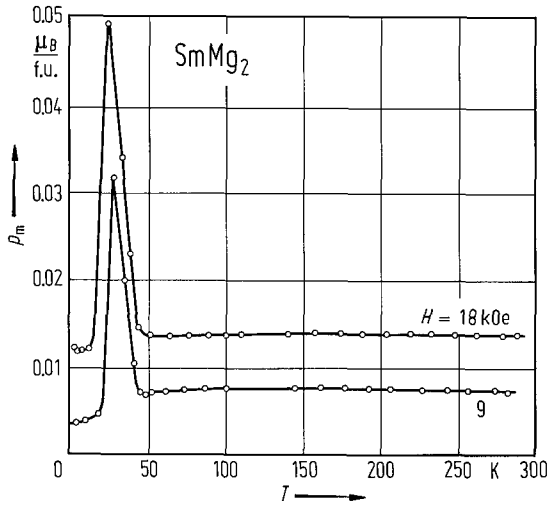

Fig. 123. $SmMg_2$. Magnetic moment p_m vs. temperature in applied magnetic fields of 9 kOe and 18 kOe [78 B 1].

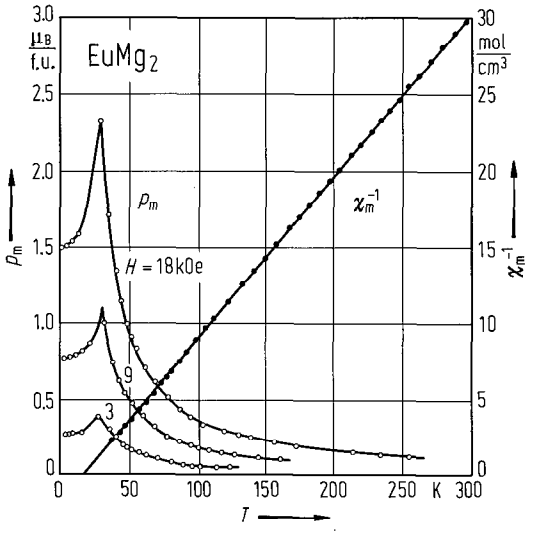

Fig. 124. $EuMg_2$. Temperature variation of the magnetic moment p_m, and of the reciprocal magnetic molar susceptibility χ_m^{-1}. The p_m vs. T curves refer to applied magnetic fields of 3, 9 and 18 kOe, respectively [78 B 1].

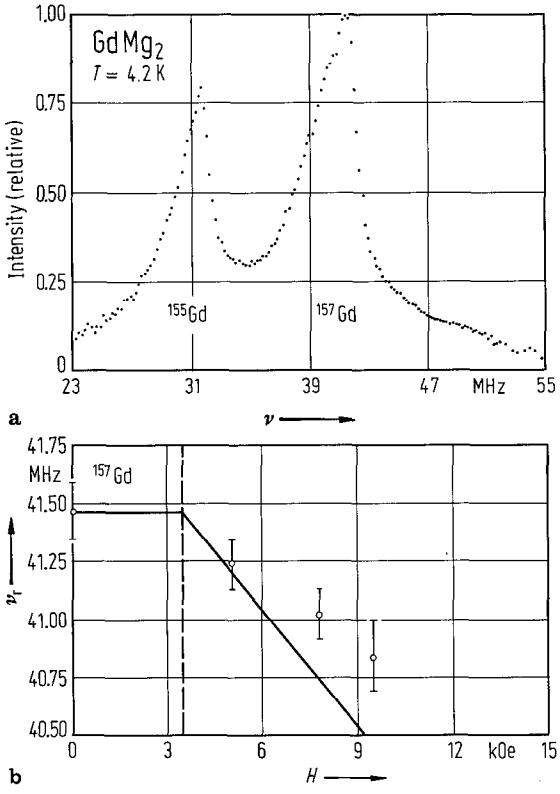

Fig. 125. $GdMg_2$. (a) Normalized intensity of the nuclear magnetic resonance spin-echo spectrum vs. the frequency ν at 4.2 K. (b) shows the magnetic field dependence of the ^{157}Gd resonance frequency ν_r [82 D 1].

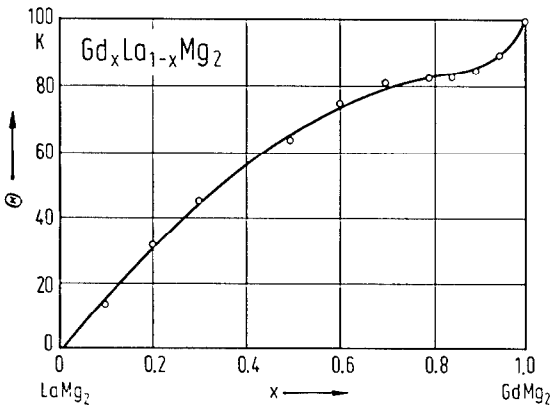

Fig. 126. $Gd_xLa_{1-x}Mg_2$. Paramagnetic Curie temperature Θ vs. Gd concentration for polycrystalline samples [82 D 1].

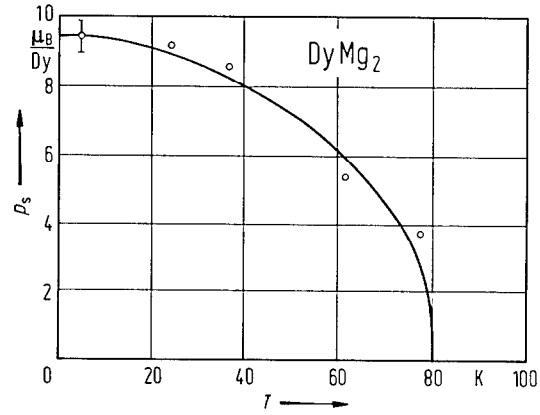

Fig. 127. $DyMg_2$. Spontaneous magnetic moment per Dy^{3+}, p_s vs. temperature. The full line is the Brillouin curve for $J = 15/2$ with an effective Landé factor $g_{eff} = 1.24$ [81 L 1].

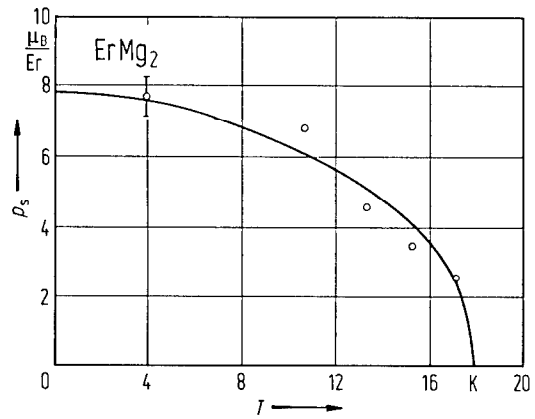

Fig. 128. $ErMg_2$. Spontaneous magnetic moment per Er^{3+} p_s vs. temperature. The full line represents the Brillouin curve for $J = 15/2$ with an effective Landé factor $g_{eff} = 1.04$ [81 L 1].

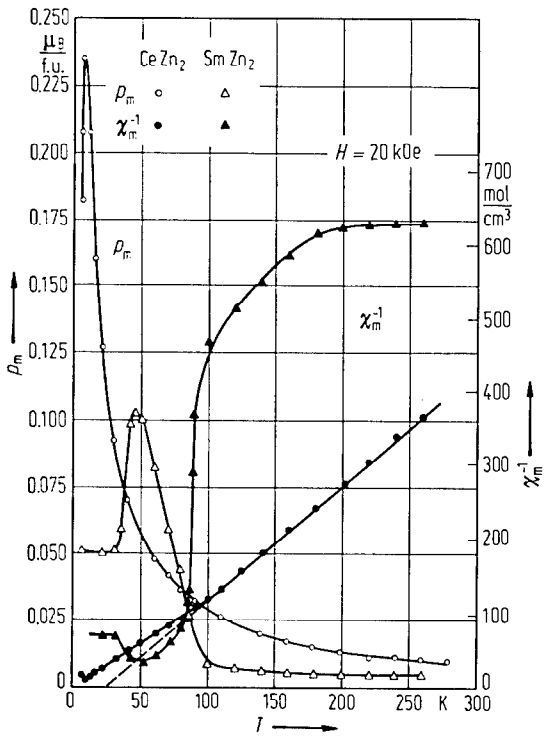

Fig. 129. $CeZn_2$, $SmZn_2$. Magnetic moment p_m and reciprocal magnetic molar susceptibility χ_m^{-1} vs. temperature (measurements in a 20 kOe-field on polycrystalline samples) [70 D 1].

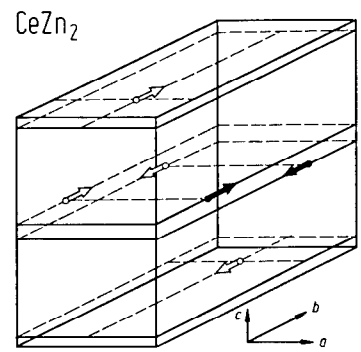

Fig. 130. $CeZn_2$. Magnetic unit cell. Circles represent the positions of the Ce atoms, the arrows the magnetic moment directions [72 D 1].

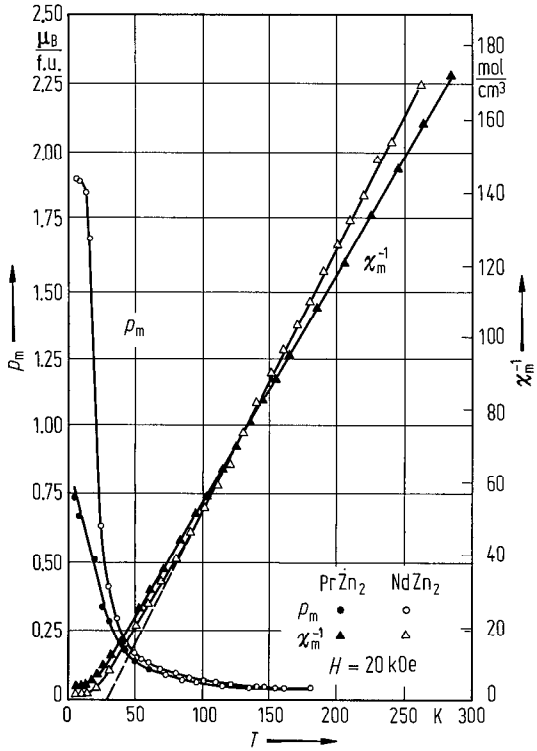

Fig. 131. $PrZn_2$, $NdZn_2$. Magnetic moment p_m, and reciprocal magnetic molar susceptibility χ_m^{-1} vs. temperature (measurements in a 20-kOe-field on polycrystalline samples) [70 D 1].

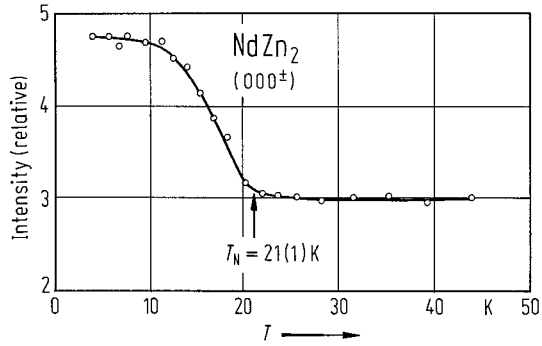

Fig. 132. $NdZn_2$. Temperature variation of the intensity of the $(000^{\pm})$ magnetic reflection of a powder neutron diffraction spectrum [73 D 1].

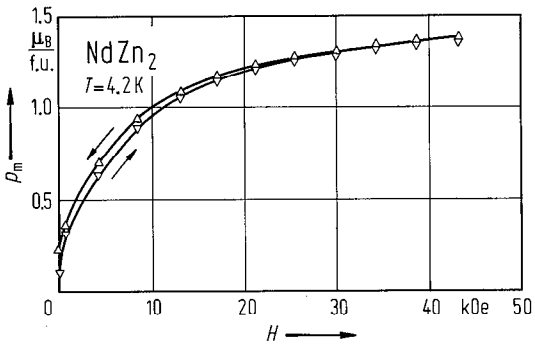

Fig. 133. $NdZn_2$. Magnetic moment p_m, vs. applied magnetic field H at 4.2 K for a powder sample frozen in oil to prevent grain rotation. Arrows indicate magnetic field drift [73 D 1].

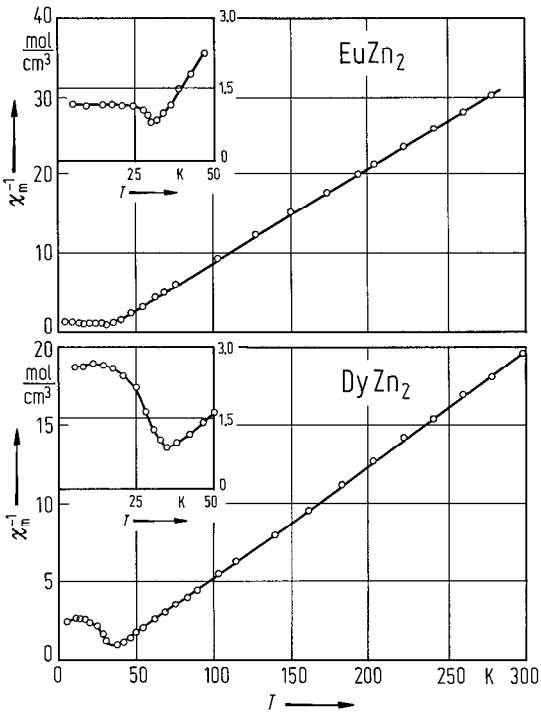

Fig. 134. $EuZn_2$, $DyZn_2$. Temperature variation of the reciprocal magnetic molar susceptibility χ_m^{-1}. The insets show the variation of χ_m^{-1} close to the Néel temperature [75 D 1].

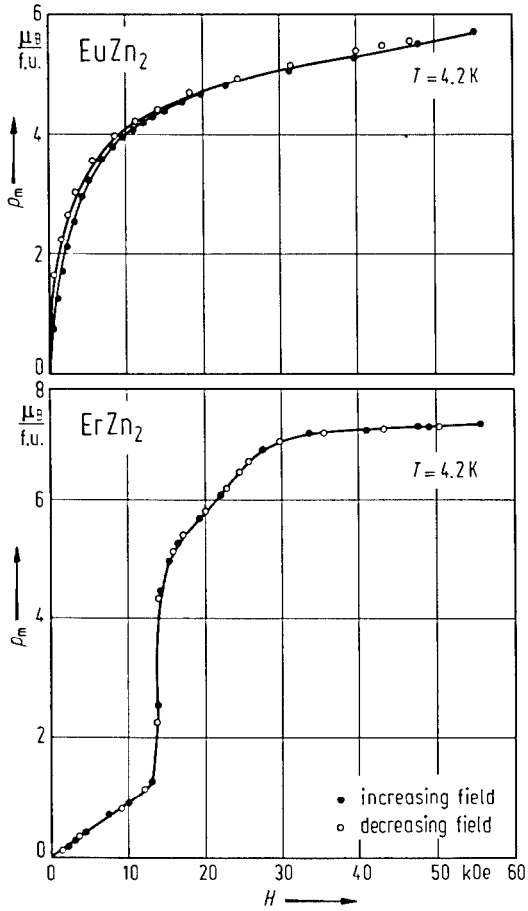

Fig. 135. $EuZn_2$, $ErZn_2$. Magnetic moment p_m, vs. magnetic field H at 4.2 K for polycrystalline samples [75 D 1].

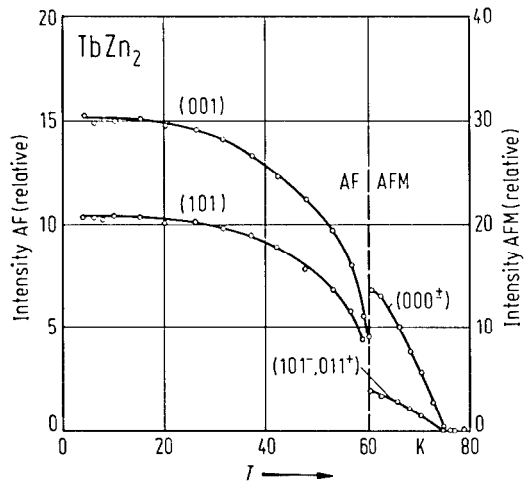

Fig. 137. $TbZn_2$. Temperature variation of the magnetic intensities of the powder neutron diffraction reflections (001) and (101) in the antiferromagnetic (AF) phase (below 60 K), and $(000^{\pm})$, (10^{-}) and (01^{+}) in the modulated (AFM) phase (above 60 K), respectively [72 D 1].

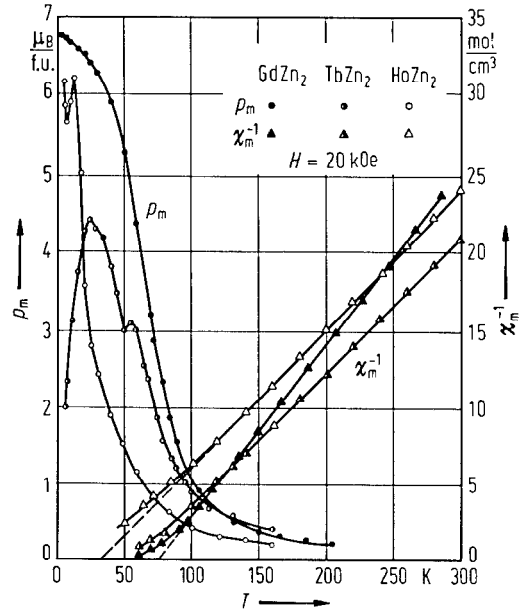

Fig. 136. RZn_2, R = Gd, Tb, Ho. Magnetic moment p_m, and reciprocal magnetic molar susceptibility χ_m^{-1}, vs. temperature (measurements in a 20 kOe magnetic field on polycrystalline samples) [70 D 1].

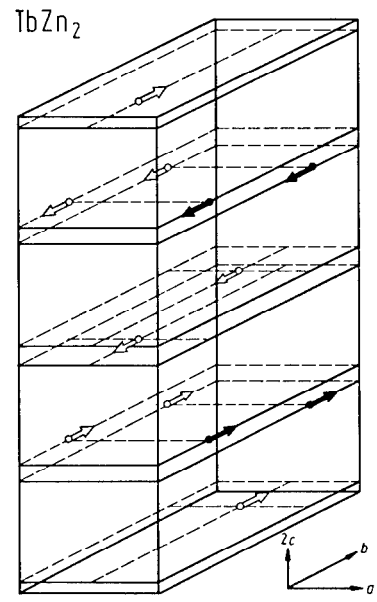

Fig. 138. $TbZn_2$. Magnetic unit cell for the low-temperature antiferromagnetic phase. Circles represent positions of the Tb atoms, arrows indicate magnetic moment directions [72 D 1].

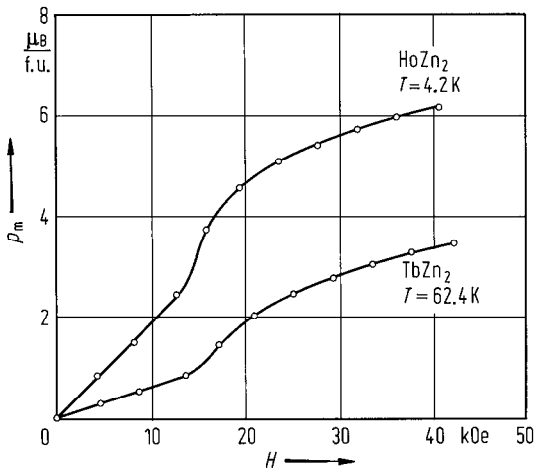

Fig. 139. $TbZn_2$, $HoZn_2$. Magnetic moment p_m vs. magnetic field H for polycrystalline samples. Temperatures are 4.2 K for $HoZn_2$ and 62.4 K for $TbZn_2$, respectively [73 D 2].

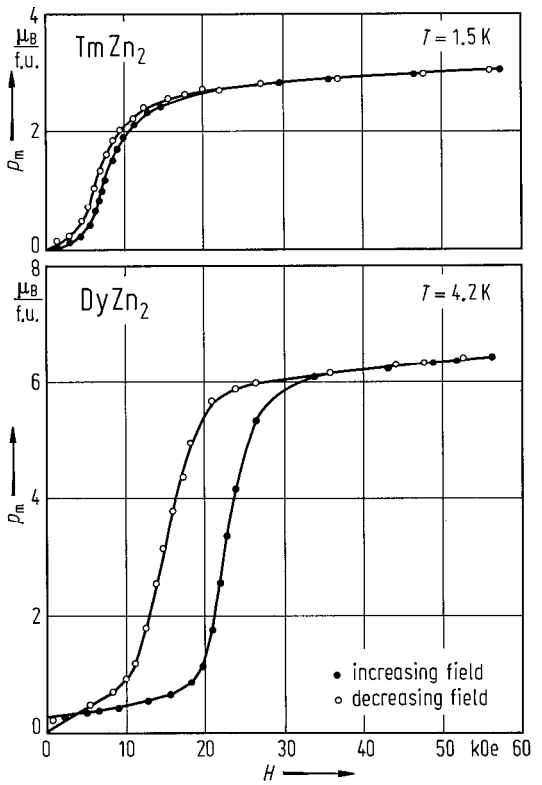

Fig. 140. $DyZn_2$, $TmZn_2$. Magnetic moment p_m vs. magnetic field H for polycrystalline samples. Temperatures are 4.2 K for $DyZn_2$ and 1.5 K for $TmZn_2$, respectively [75 D 1].

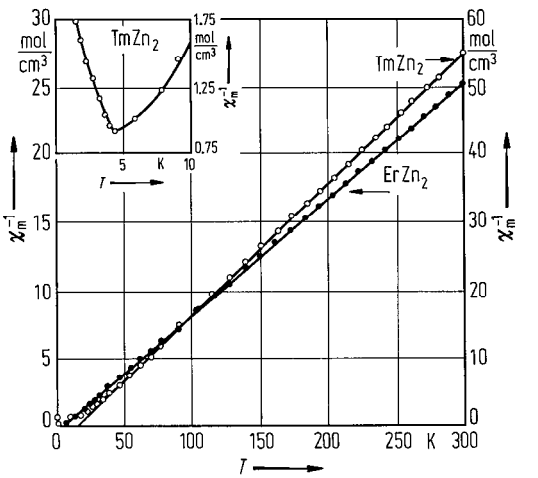

Fig. 141. $ErZn_2$, $TmZn_2$. Temperature dependence of the reciprocal magnetic molar susceptibility χ_m^{-1}. The inset shows the variation near the Néel temperature of $TmZn_2$ [75 D 1].

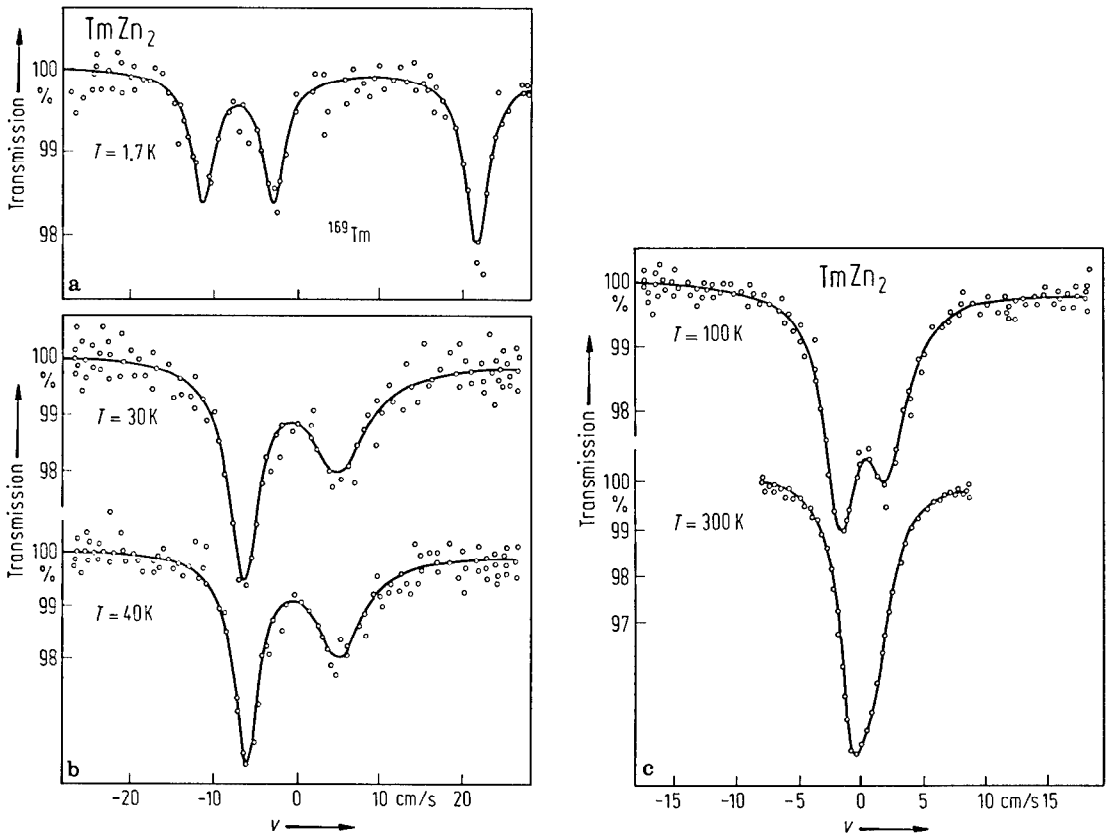

Fig. 142. $TmZn_2$. (a) ^{169}Tm Mössbauer spectrum below Néel point ($T = 1.7$ K). Due to the limited maximum velocity of the Mössbauer drive only the inner 3 lines of the complete six-line spectrum are shown. (b) and (c): ^{169}Tm Mössbauer spectra of $TmZn_2$ at various temperatures above the Néel point [80 R 1].

2.7.4 RX_3 compounds

The magnetic pair interactions and the CEF have been thoroughly studied for light RMg_3 compounds in spite of the lack of single crystals. Magnetic structures are antiferromagnetic with rather low Néel temperatures. $CeMg_3$ exhibits Kondo-like behaviour and $PrMg_3$ remains paramagnetic due to the nonmagnetic Γ_3 ground state. The fourth-order CEF parameter strongly decreases from $CeMg_3$ to $NdMg_3$. The last two compounds stable within this cubic structure, $GdMg_3$ and $TbMg_3$ exhibit magnetic properties strongly dependent on the stoichiometry: they are ferromagnetic but an excess of Mg seems to stabilize antiferromagnetism again as in light RMg_2 [78 B 2].

RZn_3 magnetic properties look like unstudied. Only paramagnetic data on Ce and Eu compounds with Cd and Hg have been obtained for this 1:3 stoichiometry in complement of crystallographic determinations.

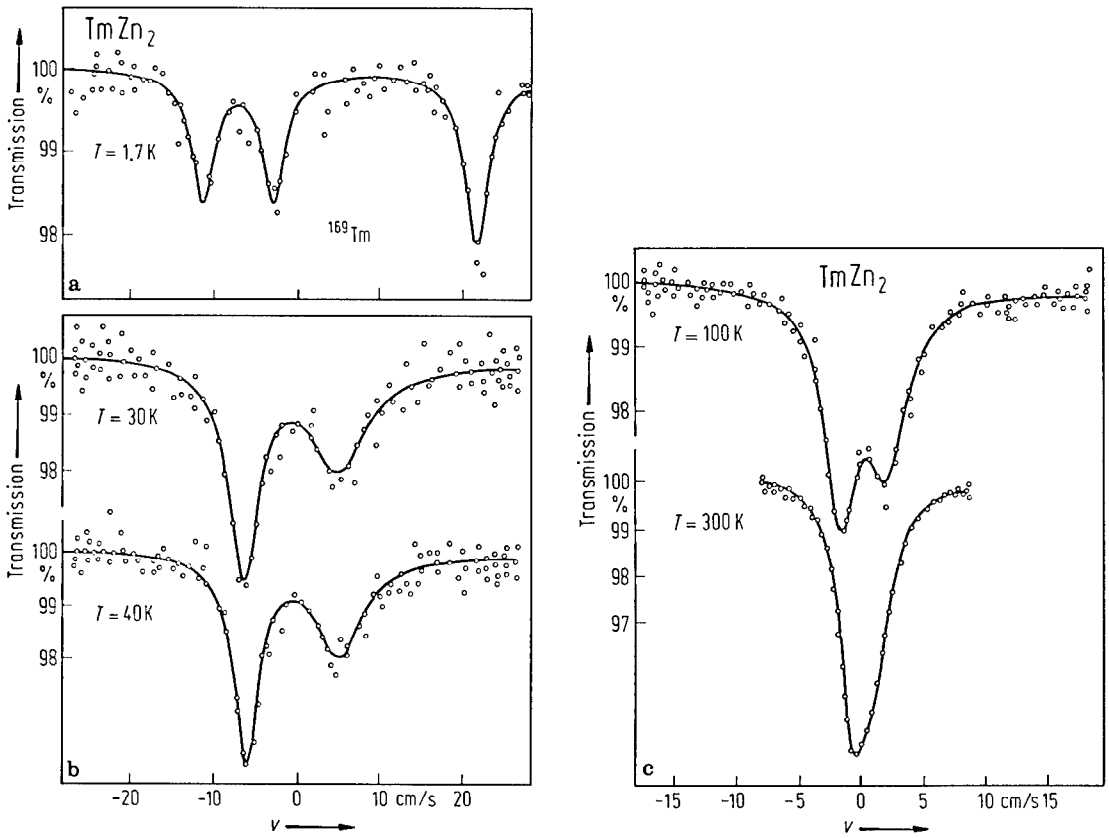

Fig. 142. $TmZn_2$. (a) ^{169}Tm Mössbauer spectrum below Néel point ($T = 1.7$ K). Due to the limited maximum velocity of the Mössbauer drive only the inner 3 lines of the complete six-line spectrum are shown. (b) and (c): ^{169}Tm Mössbauer spectra of $TmZn_2$ at various temperatures above the Néel point [80 R 1].

2.7.4 RX_3 compounds

The magnetic pair interactions and the CEF have been thoroughly studied for light RMg_3 compounds in spite of the lack of single crystals. Magnetic structures are antiferromagnetic with rather low Néel temperatures. $CeMg_3$ exhibits Kondo-like behaviour and $PrMg_3$ remains paramagnetic due to the nonmagnetic Γ_3 ground state. The fourth-order CEF parameter strongly decreases from $CeMg_3$ to $NdMg_3$. The last two compounds stable within this cubic structure, $GdMg_3$ and $TbMg_3$ exhibit magnetic properties strongly dependent on the stoichiometry: they are ferromagnetic but an excess of Mg seems to stabilize antiferromagnetism again as in light RMg_2 [78 B 2].

RZn_3 magnetic properties look like unstudied. Only paramagnetic data on Ce and Eu compounds with Cd and Hg have been obtained for this 1:3 stoichiometry in complement of crystallographic determinations.

Table 14. RMg_3 compounds. Room-temperature lattice parameter a, magnetic properties in the paramagnetic phase (effective magnetic moment per rare earth ion, p_{eff}, paramagnetic Curie temperature Θ) and in the ordered phase (magnetic ordering temperature, T_C or T_N, spin structure, low-temperature spontaneous magnetic moment per rare earth ion, p_s, easy magnetization direction).

	a nm	p_{eff}(HT)	p_{eff}(LT)	Θ(HT) K	T_C	T_N	Spin structure	p_s	Easy axis	Remarks	Figures
		μ_B			K			μ_B			
$LaMg_3$	0.7467 [76 B 2]									Pauli paramagnet $\gamma = 3.7\,mJ\,K^{-2}\,mol^{-1}$ [82 G 2]	143, 144
$CeMg_3$	0.7424 [76 B 2]	2.75	1.19	− 44 [81 G 1]		4.0	AF (type I)	0.59 [82 G 1]			143, 145–148
$PrMg_3$	0.7411 [76 B 2]	3.73		− 36 [81 G 1]							145, 149, 150
$NdMg_3$	0.7397 [76 B 2]	3.68	2.7	− 58 [81 G 1]		6.0	AF (type II)	1.30	[110] [82 G 1]		144, 148–151
$SmMg_3$	0.7360					6.5	AF			no Curie-Weiss behaviour [76 B 2]	
$GdMg_3$	0.7326	7.4		120	117		F			stoichiometric compound [76 B 2]	152
		8.81		−240		16	AF			6 at% Mg excess [78 B 2]	
$TbMg_3$	0.7296	9.44		15	108		F			stoichiometric compound [76 B 2]	152
	[76 B 2]	9.56		−110		20	AF (type II)	6.9	[111]	6 at% Mg excess [78 B 2]	

Table 15. RMg_3 compounds. Lea Leask and Wolf parameters W, x, CEF parameters $A_4\langle r^4\rangle$, $A_6\langle r^6\rangle$ and room-temperature electrical resistivity ϱ [81 G 1].

	W	x	$A_4\langle r^4\rangle$	$A_6\langle r^6\rangle$	ϱ (300 K)
	K		K		μΩ m
$LaMg_3$					0.48
$CeMg_3$	32.5 [1])	1 [1])	85.5 [1])	0 [1])	0.47
$PrMg_3$	− 3.71	0.64	52.1	−17.4	0.39
$NdMg_3$	2.51	−0.25	35.9	−19.7	0.34

[1]) [81 P 2].

Table 16. RCd_3, RHg_3 compounds. Room-temperature lattice parameters a, c, effective paramagnetic moment per rare earth ion, p_{eff}, and paramagnetic Curie temperature Θ.

	a	c	p_{eff}	Θ	Ref.
	nm		μ_B	K	
$CeCd_3$	0.7228 [1])		2.44	−29	63 O 1
$GdCd_3$	0.6621	0.4933	7.76	12	71 B 1
$CeHg_3$	0.6760	0.4941	2.93	−53	63 O 1
$EuHg_3$	0.6794	0.5074	7.63	−69	64 I 1

[1]) [73 B 2].

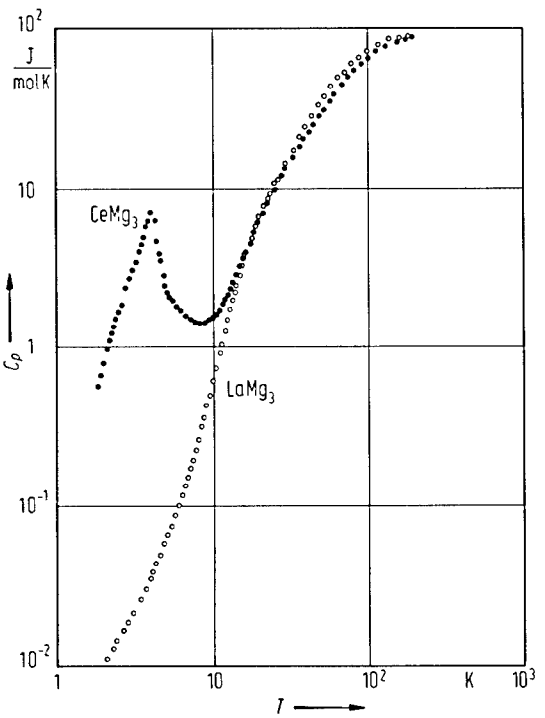

Fig. 143. $LaMg_3$, $CeMg_3$. Molar heat capacity C_p vs. temperature (logarithmic scales) measured on polycrystalline samples for increasing temperature [82 G 2].

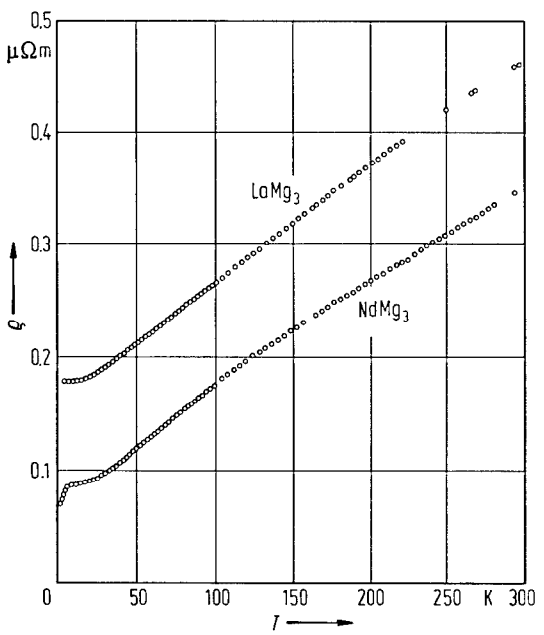

Fig. 144. $LaMg_3$, $NdMg_3$. Electrical resistivity ϱ vs. temperature (polycrystalline samples) [81 G 1].

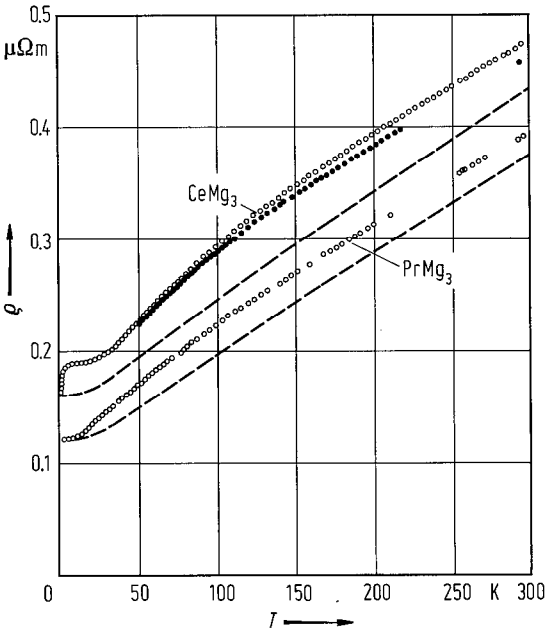

Fig. 145. $CeMg_3$, $PrMg_3$. Electrical resistivity ϱ vs. temperature for polycrystalline compounds (two samples for $CeMg_3$). The hatched lines correspond to the phonon contribution deduced from $LaMg_3$ (Fig. 144) [81 G 1].

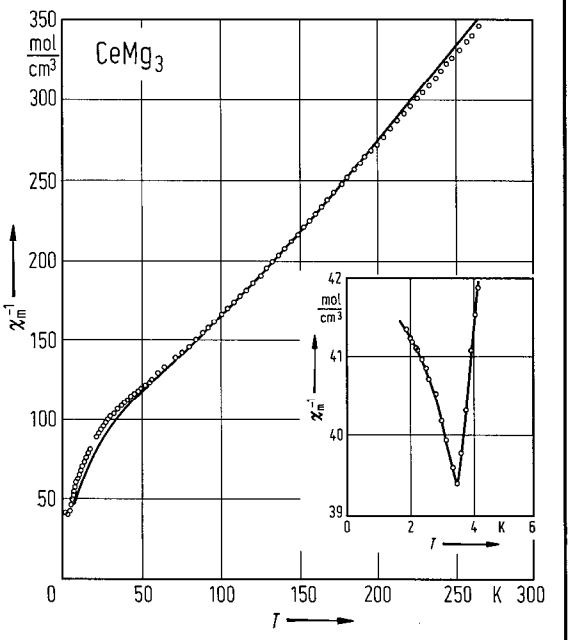

Fig. 146. $CeMg_3$. Reciprocal magnetic molar susceptibility χ_m^{-1} vs. temperature. The full line is calculated for a CEF splitting of 200 K (Γ_7 doublet as ground state). The inset shows the behaviour close to the Néel temperature [81 P 2].

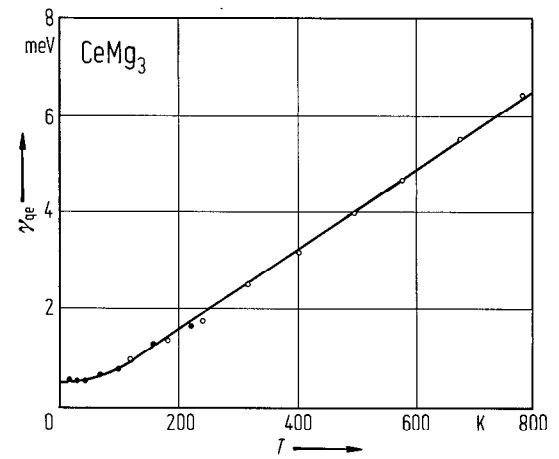

Fig. 147. $CeMg_3$. Temperature dependence of the linewidth, γ_{qe}, of the quasielastic contribution in inelastic neutron scattering spectra [82 G 2].

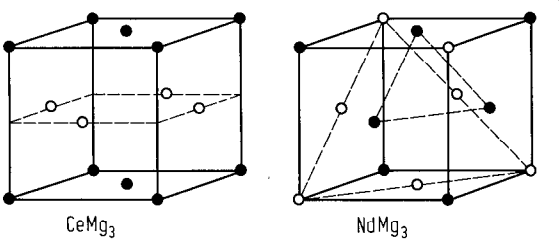

Fig. 148. $CeMg_3$, $NdMg_3$. Magnetic unit cell [82 G 1].

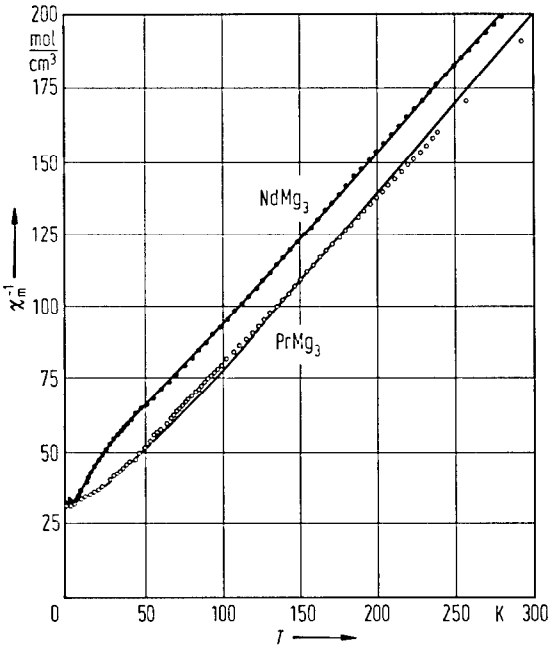

Fig. 149. $PrMg_3$, $NdMg_3$. Reciprocal magnetic molar susceptibility χ_m^{-1} vs. temperature for polycrystalline samples. Full lines are calculated considering CEF and bilinear interactions [81 G 1].

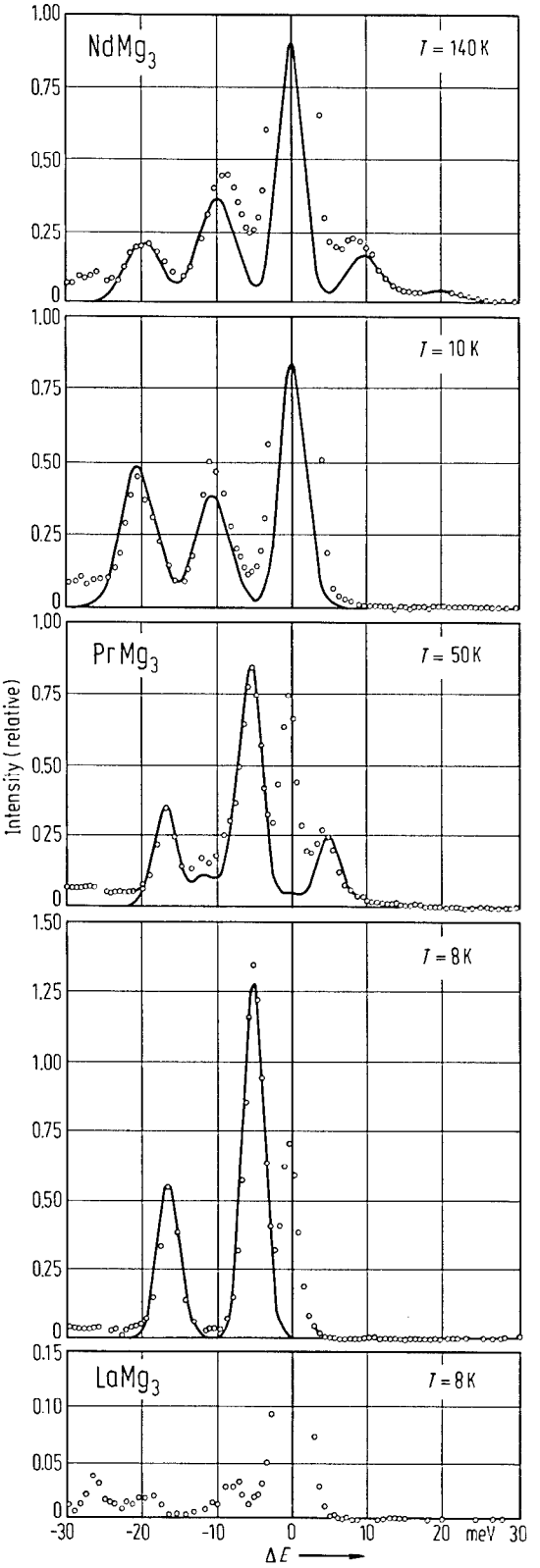

Fig. 150. $PrMg_3$, $NdMg_3$. Inelastic neutron scattering spectra in the paramagnetic phase at temperatures indicated. The incident neutron energy is 50.4 meV. ΔE is the neutron energy transfer from the incident neutron energy. The full lines are calculated within a CEF model. The $LaMg_3$ spectrum is used as a nonmagnetic background [81 G 1].

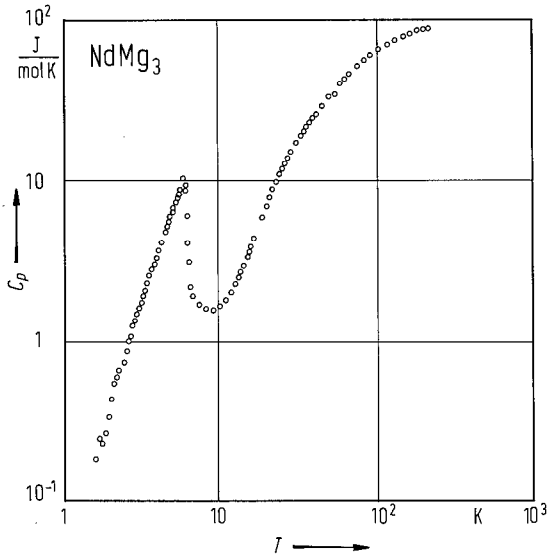

Fig. 151. $NdMg_3$. Molar heat capacity C_p vs. temperature in logarithmic scales (measurements in increasing temperature) [82 G 2].

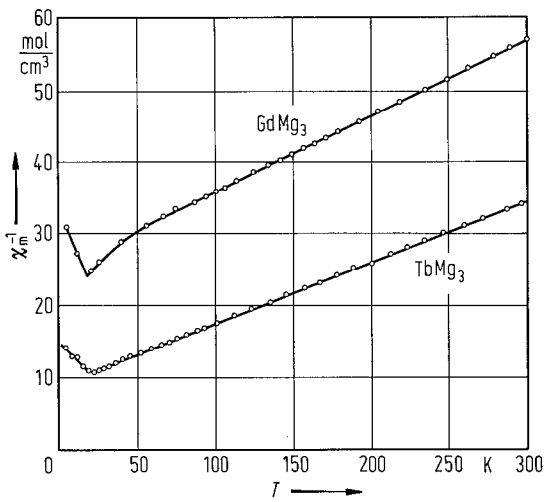

Fig. 152. $GdMg_3$, $TbMg_3$. Reciprocal magnetic molar susceptibility χ_m^{-1} vs. temperature for polycrystalline samples (6 at% Mg excess) [78 B 2].

2.7.5 X-rich compounds

For crystallographic and metallurgical reasons discussed in the introduction, compounds of this part have motivated only few magnetic studies. The RZn_{12} and R_2Zn_{17} series are antiferromagnetic with relatively low Néel temperatures. They exhibit clearly shortrange behaviours in the paramagnetic phase. Their antiferromagnetic structures are complicated, often described by two different propagation vectors in the reciprocal space.

Table 17. Mg-rich compounds. Room-temperature lattice parameters a, c, and magnetic characteristics (effective magnetic moment per rare earth ion, p_{eff}, paramagnetic Curie temperature Θ, magnetic ordering temperature, T_C or T_N, and low-temperature spontaneous magnetic moment per rare earth ion, p_s).

	a	c	Ref.	p_{eff}	Θ	T_C	T_N	p_s	Ref.
	nm			μ_B	K	K		μ_B	
Gd_5Mg_{24}				8.3	−119				79 b
Tb_5Mg_{24}	1.1283		60 K 1						
Dy_5Mg_{24}	1.1246		60 K 1	10.5	39				79 b
Ho_5Mg_{24}	1.1233		60 K 1						
Er_5Mg_{24}	1.1224		60 K 1	10.02	11	13		7.1	79 b
Tm_5Mg_{24}	1.1208		60 K 1	7.84	3	4		4.2	79 b
$EuMg_5$	1.0498	1.0830	79 D 1	8.23	4		7.8		79 D 1
Eu_2Mg_{17}	1.002	1.0328	79 D 1	8.66	− 20		7.9		79 D 1

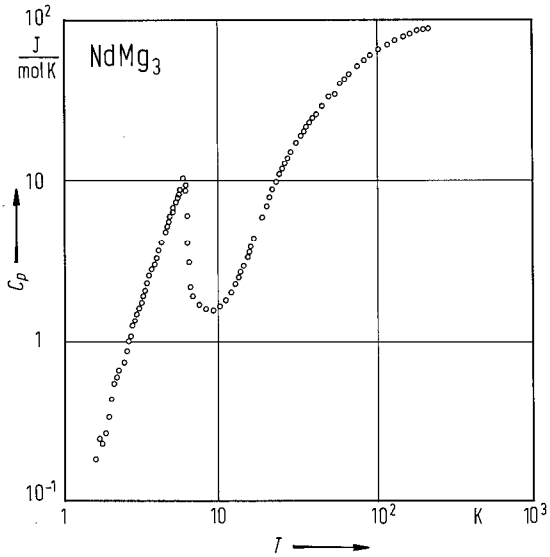

Fig. 151. $NdMg_3$. Molar heat capacity C_p vs. temperature in logarithmic scales (measurements in increasing temperature) [82 G 2].

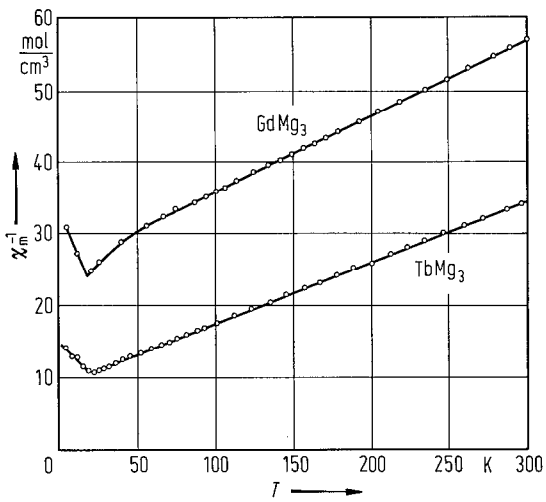

Fig. 152. $GdMg_3$, $TbMg_3$. Reciprocal magnetic molar susceptibility χ_m^{-1} vs. temperature for polycrystalline samples (6 at% Mg excess) [78 B 2].

2.7.5 X-rich compounds

For crystallographic and metallurgical reasons discussed in the introduction, compounds of this part have motivated only few magnetic studies. The RZn_{12} and R_2Zn_{17} series are antiferromagnetic with relatively low Néel temperatures. They exhibit clearly shortrange behaviours in the paramagnetic phase. Their antiferromagnetic structures are complicated, often described by two different propagation vectors in the reciprocal space.

Table 17. Mg-rich compounds. Room-temperature lattice parameters a, c, and magnetic characteristics (effective magnetic moment per rare earth ion, p_{eff}, paramagnetic Curie temperature Θ, magnetic ordering temperature, T_C or T_N, and low-temperature spontaneous magnetic moment per rare earth ion, p_s).

	a	c	Ref.	p_{eff}	Θ	T_C	T_N	p_s	Ref.
	nm			μ_B	K	K		μ_B	
Gd_5Mg_{24}				8.3	−119				79 b
Tb_5Mg_{24}	1.1283		60 K 1						
Dy_5Mg_{24}	1.1246		60 K 1	10.5	39				79 b
Ho_5Mg_{24}	1.1233		60 K 1						
Er_5Mg_{24}	1.1224		60 K 1	10.02	11	13		7.1	79 b
Tm_5Mg_{24}	1.1208		60 K 1	7.84	3	4		4.2	79 b
$EuMg_5$	1.0498	1.0830	79 D 1	8.23	4		7.8		79 D 1
Eu_2Mg_{17}	1.002	1.0328	79 D 1	8.66	− 20		7.9		79 D 1

Table 18. Zn-rich compounds. Room-temperature lattice parameters a, c, and magnetic characteristics (effective magnetic moment per rare earth ion p_{eff}, paramagnetic Curie temperature Θ, magnetic ordering temperature, T_C or T_N, magnetic structure, easy magnetization axis and low temperature spontaneous magnetic moment per rare earth ion, p_s).

	a	c	p_{eff}	Θ	T_C	T_N	Structure, propagation vector	Easy axis	p_s	Remarks	Figures
	nm		μ_B	K	K				μ_B		
$CeZn_5$	0.5416	0.4265 [65 M 1]	2.54	−44 [63 O 1]							
$EuZn_5$	0.5437	0.4312	7.99	−24		10				divalent [75 B 2]	153, 154
La_2Zn_{17}	0.9131	1.3334								[67 I 1]	
Ce_2Zn_{17}	0.9088	1.3290 [67 I 1]	2.64	0 [63 O 1]							
Pr_2Zn_{17}	0.9066	1.3274								[67 I 1]	
Nd_2Zn_{17}	0.9052	1.3236								[67 I 1]	
Sm_2Zn_{17}	0.9017	1.3211								[67 I 1]	
Gd_2Zn_{17}	0.8994	1.3169 [67 I 1]	7.84	−53 [74 S 2]		10					155, 156
Tb_2Zn_{17}	0.8977	1.3161 [67 I 1]	9.84	−17		28 [74 S 2]					155
Dy_2Zn_{17}	0.8967	1.3139 [67 I 1]	11.01	−14 [74 S 2]							157
Ho_2Zn_{17}	0.8956	1.3133 [67 I 1]	10.08	−11.5 [74 S 2]							155
Er_2Zn_{17}	0.8942	1.3118 [67 I 1]	9.63	− 4 [74 S 2]							157
Tm_2Zn_{17}	0.8937	1.3110 [67 I 1]	7.64	7 [74 S 2]							157
Yb_2Zn_{17}	0.9040	1.3216 [67 I 1]								divalent [74 S 2]	
Lu_2Zn_{17}	0.8920	1.3096								[67 I 1]	
$LaZn_{11}$	1.0686	0.6881								[67 I 1]	
$CeZn_{11}$	1.0662	0.6855 [63 O 1]	2.54	26 [63 O 1]							
$PrZn_{11}$	1.0626	0.6835								[67 I 1]	
$NdZn_{11}$	1.0608	0.6828								[67 I 1]	
$EuZn_{11}$	1.0719	0.6874								[67 I 1]	

$YbZn_{11}$	1.0637	0.6822 [67I1]								divalent [74S2]	
$SmZn_{12}$	0.8927	0.5215 [67I1]	0.74	−28		15	AF [74S2]				158
$GdZn_{12}$	0.8898	0.5210 [67I1]	8.07	−53		15.5	AF [78D2]				158–161
$TbZn_2$	0.8884	0.5200 [67I1]	9.74	−36		12.5	AF ($\frac{1}{2}\frac{1}{2}$0.29)	$\perp c$	7.5 [78D2]		158–160, 162
$DyZn_{12}$	0.8877	0.5198 [67I1]	10.74	−16.5		14.5	AF ($\frac{1}{2}\frac{1}{2}\frac{1}{2}$) ($\frac{1}{2}\frac{1}{2}$0.31)	$\perp c$	8.0 [78D2]		160
$HoZn_{12}$	0.8868	0.5195 [67I1]	10.76	−11.5		2.4	AF ($\frac{1}{2}\frac{1}{2}\frac{1}{4}$) ($\frac{1}{2}\frac{1}{2}\frac{1}{2}$)		7.5 [78D2]		160, 162
$ErZn_{12}$	0.8863	0.5193 [67I1]	9.35	− 5.5		2.8	AF ($\frac{1}{2}\frac{1}{2}\frac{1}{4}$)	$\parallel c$	7 [78D2]	ϱ (300 K) = 0.15 μΩ m [73S1]	160, 162–166
$TmZn_{12}$	0.8852	0.5190								[67I1]	
$LuZn_{12}$	0.8848	0.5186								[67I1]	
$EuZn_{13}$	1.2215		7.94	2	3.12					[75B2]	167

Table 19. Cd- and Hg-rich compounds. Room-temperature lattice parameters a, c and magnetic characteristics (effective magnetic moment per rare earth ion, p_{eff}, paramagnetic Curie temperature Θ).

	a	c	p_{eff}	Θ	Remarks	Ref.
	nm		μ_B	K		
$Gd_{11}Cd_{45}$	2.1603		7.46	− 6		71B1
$Gd_{13}Cd_{58}$	1.540	1.528	8.18	−52		71B1
$EuCd_6$	1.5950		7.80	−16	unknown magnetic ordering at 2.25 K	77B1
$GdCd_6$	1.5524		7.65	3		71B1
$YbCd_6$	1.5638				divalent	71P1
$CeCd_{11}$	0.9319		2.47	32		54I1, 63O1
$EuCd_{11}$	1.193	0.7682	7.87	− 2	unknown magnetic ordering at 2.75 K Fig. 168	77B1
Ce_5Hg_{21}	2.193		3.03	−55		67B1, 63O1
$EuHg_5$			7.79	10		64I1

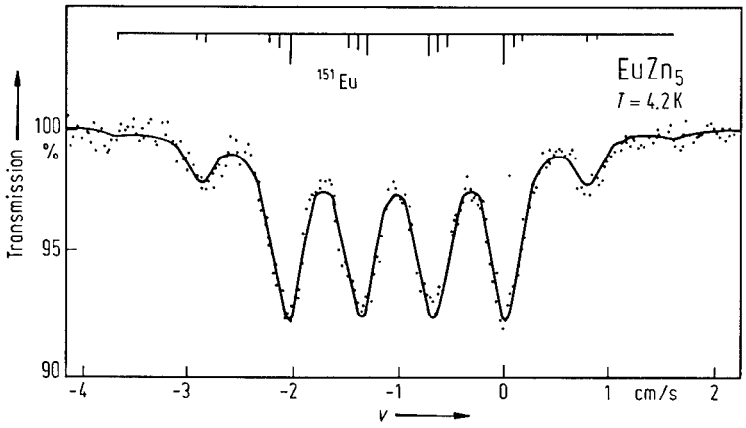

Fig. 153. $EuZn_5$. ^{151}Eu Mössbauer spectrum at 4.2 K. The full line is calculated with only magnetic bilinear interactions. The decomposition of the spectrum is given at the top of the figure [75 B 2].

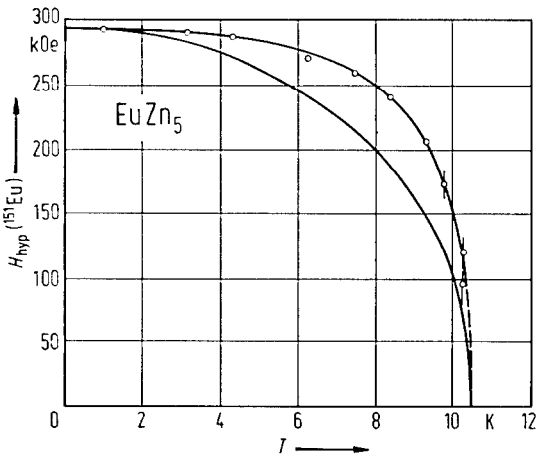

Fig. 154. $EuZn_5$. Effective hyperfine field on the ^{151}Eu nucleus, H_{hyp} vs. temperature. The lower curve represents the temperature dependence of the Brillouin function $B_{7/2}(T)$ for $J = 7/2$, the upper one is calculated [75 B 2].

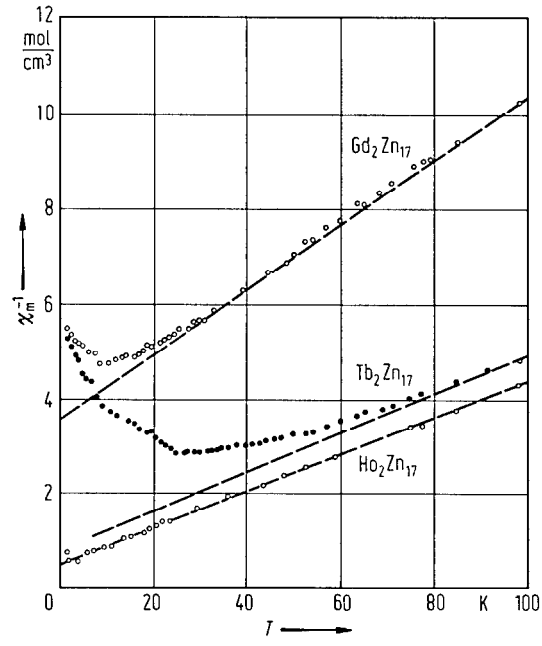

Fig. 155. R_2Zn_{17}, R = Gd, Tb, Ho. Reciprocal magnetic molar susceptibility χ_m^{-1} vs. temperature measured for polycrystalline samples. The broken lines are high-temperature asymptotes [74 S 2].

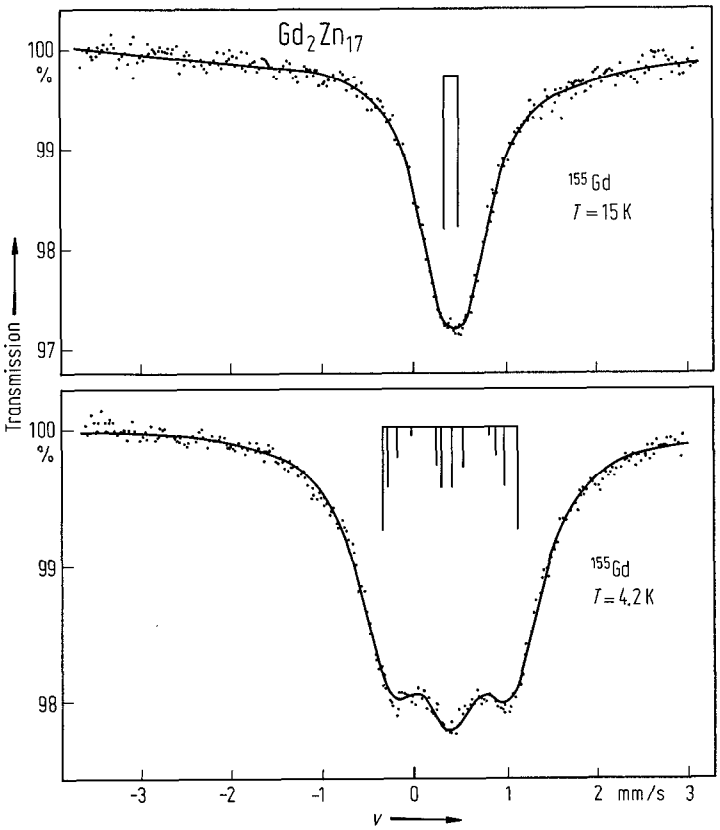

Fig. 156. Gd_2Zn_{17}. ^{155}Gd Mössbauer spectra at 4.2 (lower part) and 15 K (upper part). The full line is calculated. The decomposition of the spectra is given at the top of each figure [82 D 2].

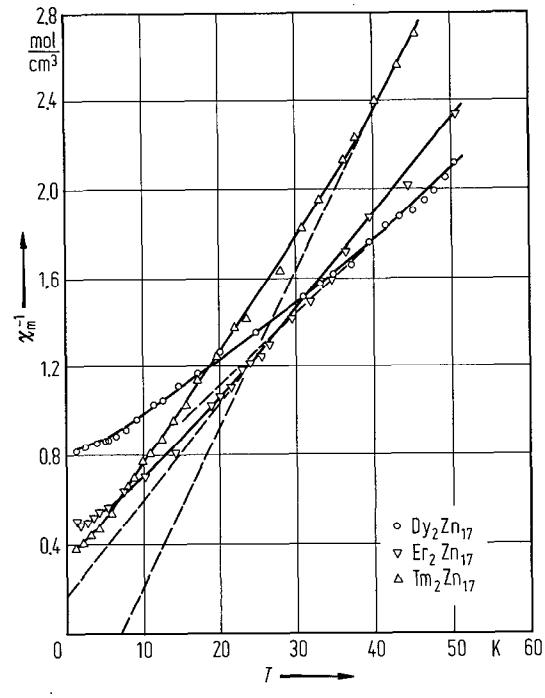

Fig. 157. R_2Zn_{17}, R = Dy, Er, Tm. Reciprocal magnetic molar susceptibility χ_m^{-1} vs. temperature for polycrystalline samples. Full lines are guides for the eye, broken ones high-temperature asymptotes [74 S 2].

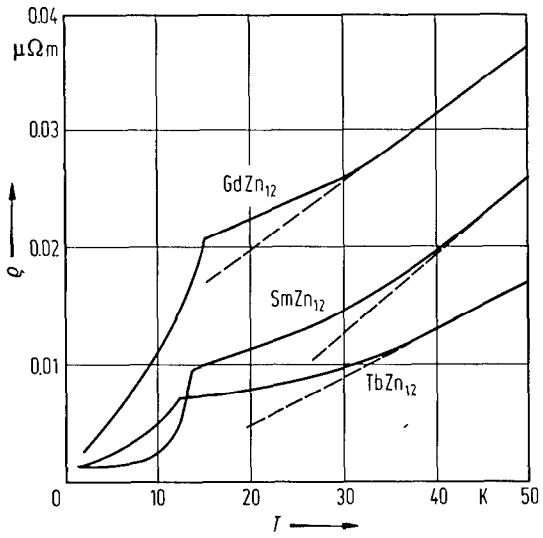

Fig. 158. RZn_{12}, R = Sm, Gd, Tb. Electrical resistivity ϱ vs. temperature in the low-temperature range. The broken lines are the high-temperature asymptotes (polycrystalline samples) [74 S 2].

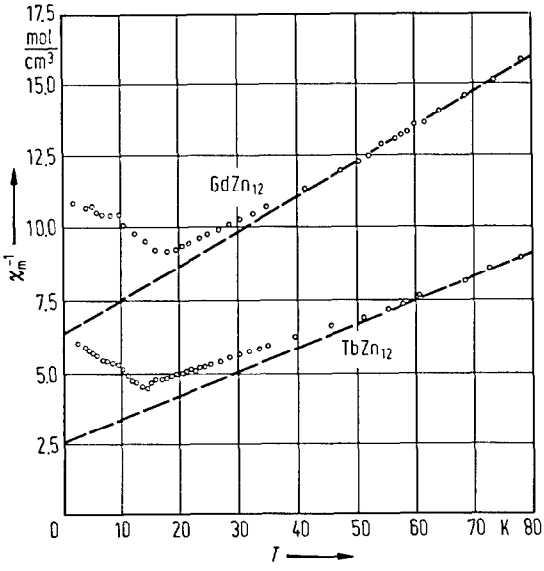

Fig. 159. $GdZn_{12}$, $TbZn_{12}$. Reciprocal magnetic molar susceptibility χ_m^{-1} vs. temperature for polycrystalline samples at low temperature [74 S 2].

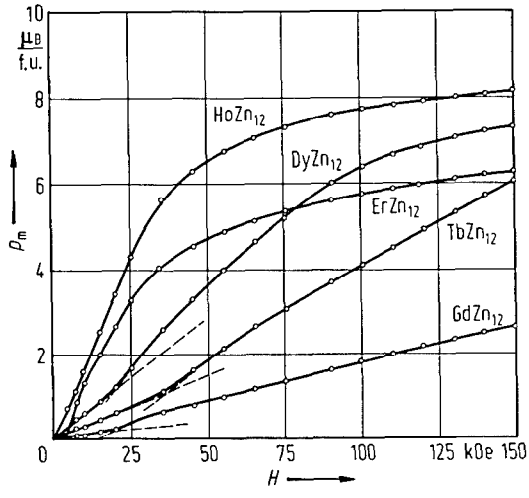

Fig. 160. RZn_{12}, R = Gd–Er. Magnetic moment p_m vs. applied magnetic field H at 1.5 K for polycrystalline samples (no demagnetization correction) [78 D 2].

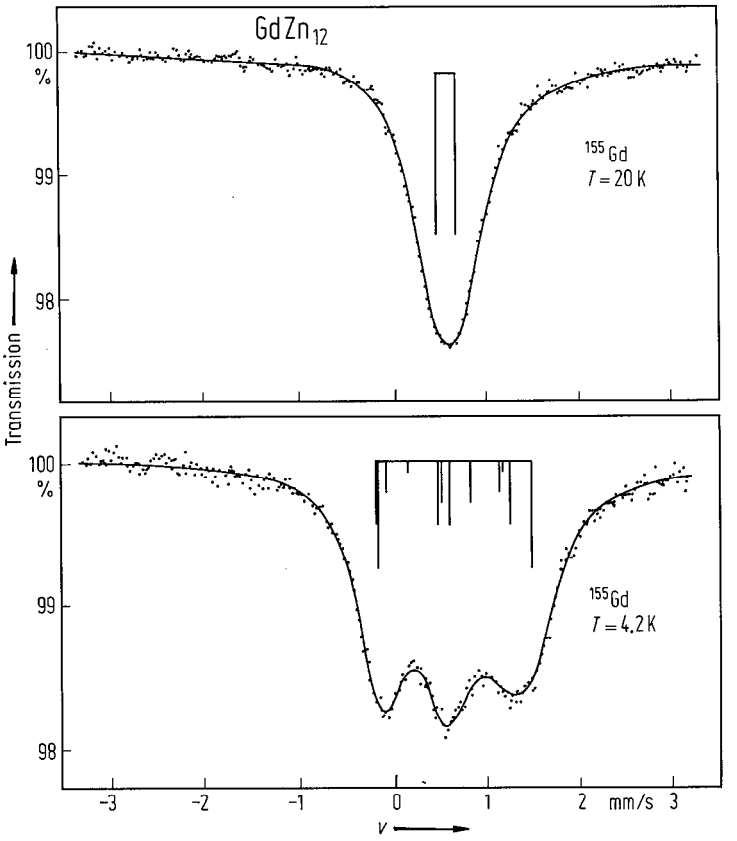

Fig. 161. $GdZn_{12}$. ^{155}Gd Mössbauer spectra at 20 K (upper part) and 4.2 K (lower part). The decomposition of the spectra is given at the top of the figures [82 D 2].

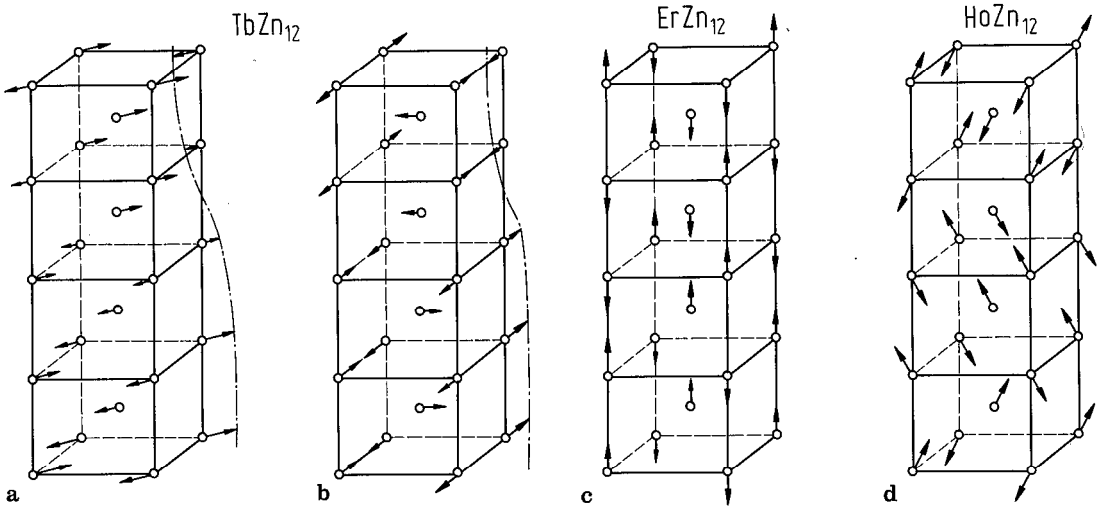

Fig. 162. RZn_{12}, R = Tb, Ho, Er. Magnetic structures with R atoms in [000] and $[\frac{1}{2}, \frac{1}{2}, \frac{1}{2}]$: (a) magnetic collinear structure of $TbZn_{12}$ obtained on the basis of a single propagation vector; (b) magnetic noncollinear structure of $TbZn_{12}$ obtained on the basis of two propagation vectors; (c) magnetic structure of $ErZn_{12}$; (d) magnetic structure of $HoZn_{12}$ [78 D 2].

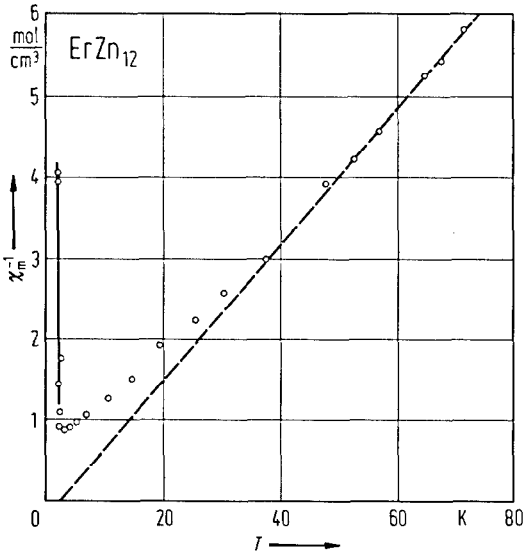

Fig. 163. $ErZn_{12}$. Reciprocal magnetic molar susceptibility χ_m^{-1} vs. temperature for a polycrystalline sample. The dotted line is the high-temperature asymptote, the full line a guide for the eye [73 S 2].

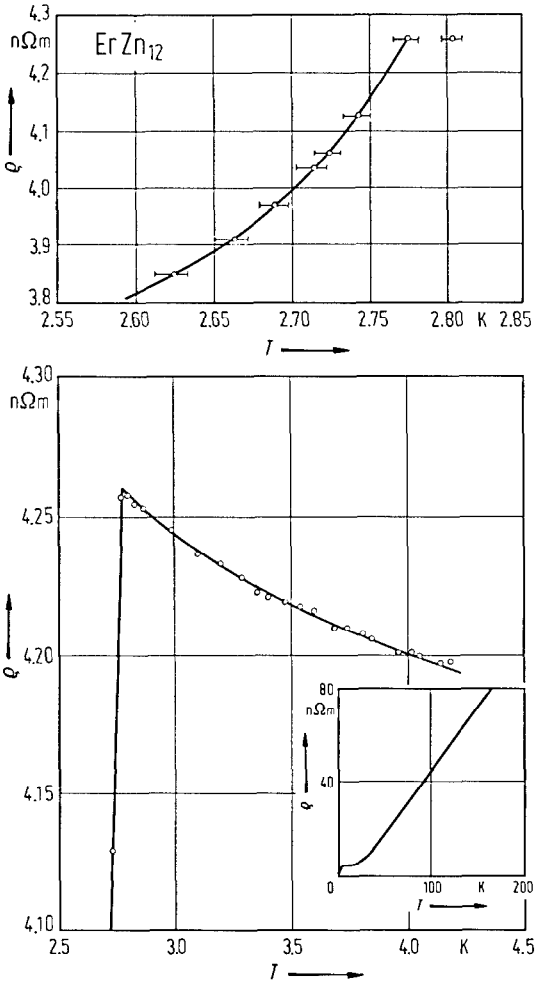

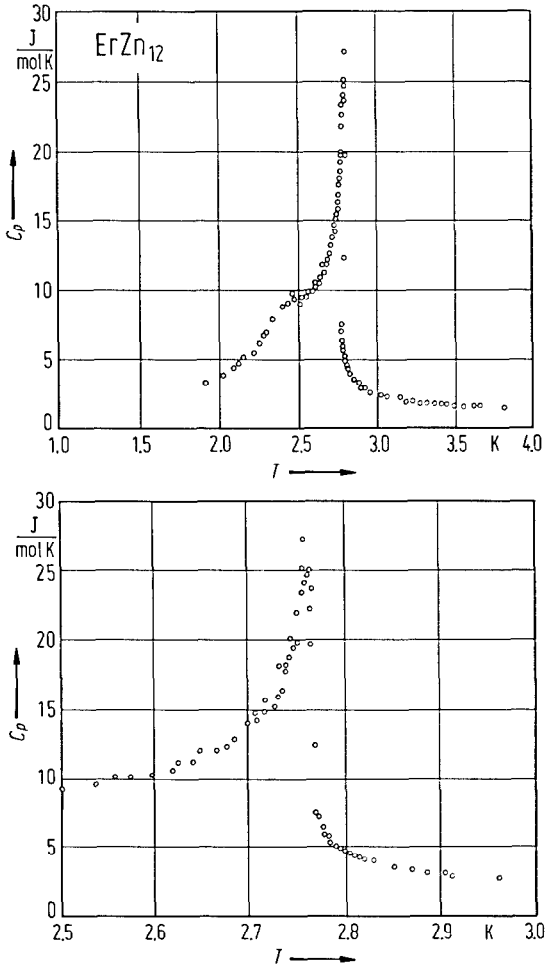

Fig. 164. $ErZn_{12}$. Molar heat capacity C_p vs. temperature for a polycrystalline sample at low temperature [73 S 2].

◀
Fig. 165. $ErZn_{12}$. Electrical resistivity ϱ vs. temperature for a polycrystalline sample. The inset gives the general feature up to 200 K [73 S 1].

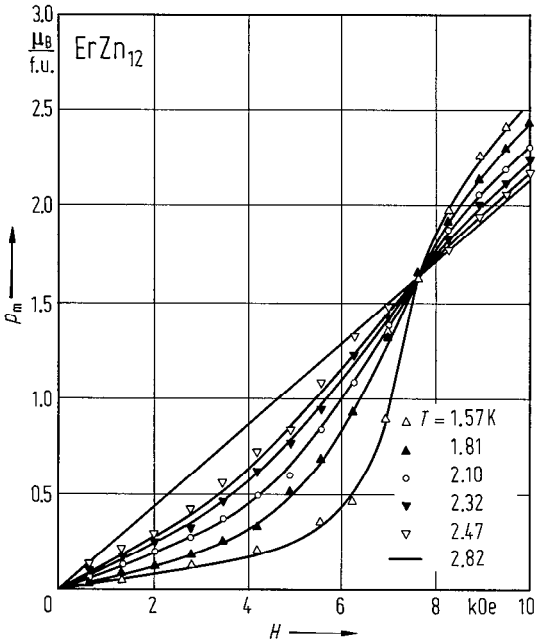

Fig. 166. $ErZn_{12}$. Magnetic moment p_m vs. applied magnetic field H (without demagnetization correction) for the temperatures indicated (polycrystalline sample). Lines are guides for the eye [73 S 2].

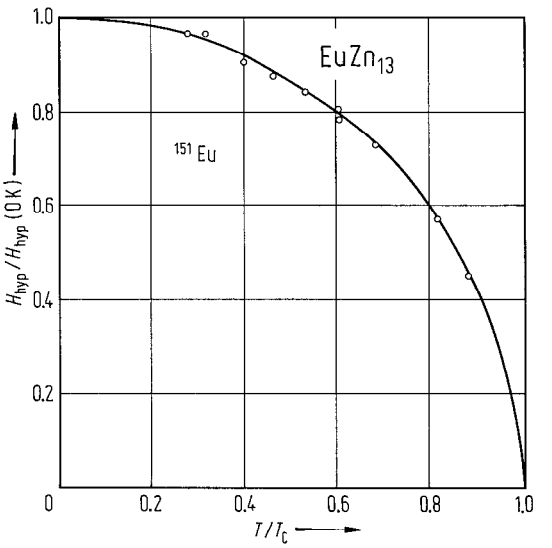

Fig. 167. $EuZn_{13}$. Reduced hyperfine field $H_{hyp}/H_{hyp}(0\,K)$ for ^{151}Eu vs. reduced temperature T/T_C with $H_{hyp}(0\,K) = 283(2)\,kOe$ and $T_C = 3.19(3)\,K$. The drawn line represents the temperature dependence calculated with the Brillouin function $B_{7/2}$ for $J = 7/2$ [75 B 2].

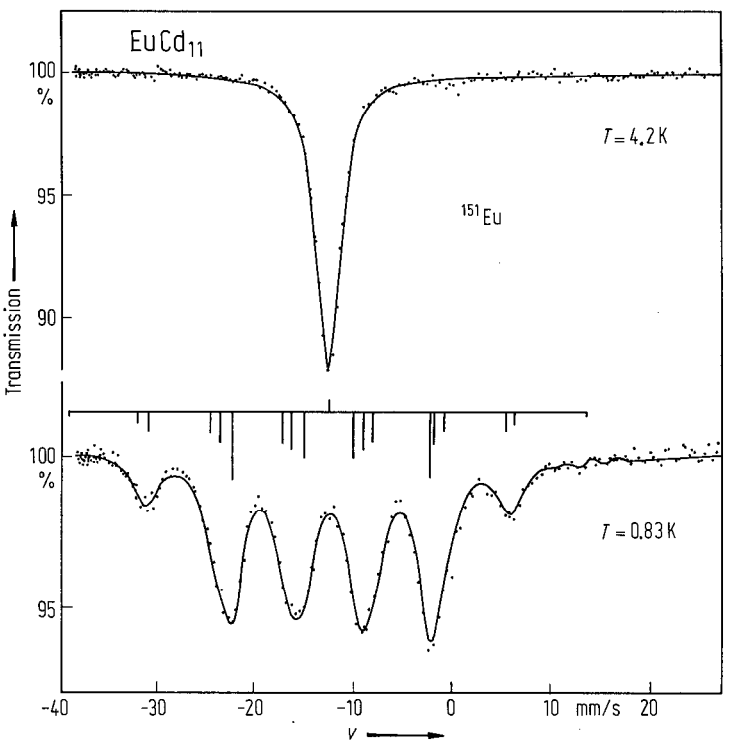

Fig. 168. $EuCd_{11}$. ^{151}Eu Mössbauer spectra at 4.2 K (upper part) and 0.83 K (lower part). The decomposition of the 0.83 K-spectrum is given at its top [77 B 1].

2.7.6 RBe_{13} compounds

The R–Be alloys reduce to only one full series, the RBe_{13} compounds. Its structure results from a CsCl-type arrangement of polyhedrons of 24 Be and 1 R at the centre (Fig. 169). As a consequence, mechanical properties are reminiscent of the Be ones. From a magnetic point of view, the fact that the rare earth is merged into a rather spherical surrounding may explain the relatively small CEF parameters (Table 21). One can note a change of sign for the fourth-order CEF parameter between light and heavy rare earth compounds. This reveals, here again, a significant electronic contribution to the CEF.

The resulting overall splitting is of the same order of magnitude as the bilinear interactions. The antiferromagnetic ordering is of helicoidal type at least for the heavy compounds; in relation with the strength of

Table 20. RBe_{13} compounds. Lattice parameters a at room temperature, magnetic characteristics (effective magnetic moment per rare earth ion, p_{eff}, paramagnetic Curie temperature Θ, Néel temperature T_N, spontaneous magnetic moment per rare earth ion, p_s, magnetic molar susceptibility χ_m), room-temperature electrical resistivity ϱ, and low-temperature Debye temperature Θ_D.

	a nm	p_{eff} μ_B	Θ K	T_N K	Spin structure	Spin direction	p_s μ_B
$LaBe_{13}$	1.0451 [75 B 3]						
$CeBe_{13}$	1.0372	2.65	−200				
$PrBe_{13}$	1.0369	3.58	− 8				
$NdBe_{13}$	1.0348	3.57	2.5	2.63 [75 B 3]			
$SmBe_{13}$	1.0304			8.8 [75 B 3]			
$EuBe_{13}$	1.0286						
$GdBe_{13}$	1.0273	7.94	25	25.7 [75 B 3]	IH	[001]	6.6 (3 K) [82 V 1]
$TbBe_{13}$	1.0247	9.71	14	15.3 [75 B 3]	CH: $T<8.5$ K IH: $T>8.5$ K	[001]	8.8 (4.2 K) [80 V 1]
$DyBe_{13}$	1.0233	10.47	13	9.3 [75 B 3]	CH	[001]	8.6 (4 K) [85 V 1]
$HoBe_{13}$	1.0219	10.57	6	5.45 [75 B 3]	IH: $T>4.5$ K CH: $T<4.5$ K	[001]	8.4 (1.4 K) [83 V 1]
$ErBe_{13}$	1.0203 [75 B 3]	9.53	6 [75 B 3]	2.37	CH	[001]	6.0 (0.5 K) [83 V 1]
$TmBe_{13}$	1.0189	7.55	1				
$YbBe_{13}$	1.0180 [75 B 3]	4.54	1	1.28 [79 H 1]			
$LuBe_{13}$	1.0170						
YBe_{13}	1.024						

the magnetocrystalline anisotropy in each compound, the helicoidal structure is either commensurate or not, either regular or not. In particular $TbBe_{13}$ exhibits at low temperature a lock-in of the magnetic propagation vector on a 1/3 commensurate value.

The Θ values, deduced from the magnetic susceptibility data, as well as the $J(q=0)$ exchange constant measured by EPR [76 B 4, 77 H 2], are positive and very close to the T_N values. $J(q=0)$ was shown to vary significantly across the series. All these features are, again, in disagreement with a simple RKKY approach.

A very large part of the literature on RBe_{13} is devoted to $CeBe_{13}$, which appears as an archetype of an intermediate valence compound. Ce dilution in a $LaBe_{13}$ matrix leads to conclude a continuous evolution towards a near-integer, but yet unstable Ce^{3+} valence with a Kondo-like behaviour $YbBe_{13}$ appears normal in spite of some unexplained features vanishing in presence of the magnetic ordering [83 V 2]. As an exception among Eu compounds, $EuBe_{13}$ is trivalent.

Note that the absence of any single crystal unfortunately limits studies in this series.

χ_m $cm^3\,mol^{-1}$	ϱ (300 K) $\mu\Omega m$	Θ_D (0 K) K	Other properties	Figures
$-25\cdot10^{-6}$ (300 K) [79 K 1]	0.17 [80 K 2]	865 [83 B 2]	$\gamma=7.8\,mJ\,K^{-2}\,mol^{-1}$ [83 B 2] α (300 K) $=10.3\cdot10^{-6}\,K^{-1}$ [81 P 3]	170, 172, 174–176, 179
$1.78\cdot10^{-3}$ (300 K) [79 K 1] $2.05\cdot10^{-3}$ (1.4 K) [83 B 2]	0.72 [80 K 2]	895 [83 B 2]	$\gamma=58.6\,mJ\,K^{-2}\,mol^{-1}$ [83 B 2] α (300 K) $=15.0\cdot10^{-6}\,K^{-1}$ [81 P 3]	170, 171, 173, 174, 176–181
0.047 (1 K) [75 B 3]	0.23 [82 B 1]	770 [80 K 2]	α (300 K) $=7.32\cdot10^{-6}\,K^{-1}$ [80 K 1]	173, 182–184
$6.47\cdot10^{-3}$ (1 K) [75 B 3]			trivalent; Van Vleck paramagnet ($J=0$)	
	0.34 [80 K 2]		magnetic propagation vector along [001]	170, 171, 176, 185–189
			magnetic propagation vector along [001]	170, 171, 189–194
			magnetic propagation vector along [001]	195–198
			magnetic propagation vector along [001]	199, 200
				199, 201–203
2.59 (1 K) [75 B 3]				204–206
$1.25\cdot10^{-3}$ (300 K) [75 B 3]			trivalent [79 H 1]	170, 171, 207, 208
$-125\cdot10^{-6}$ (300 K)		930 [75 B 3]	$\gamma=8.4\,mJ\,K^{-2}\,mol^{-1}$ [75 B 3] α (300 K) $=8\cdot10^{-6}\,K^{-1}$ [80 K 1]	170, 171, 173, 175, 177
		610	α (300 K) $=8\cdot10^{-6}\,K^{-1}$ [80 K 1]	173, 175

Table 21. RBe_{13} compounds. Lea Leask and Wolf parameters W, x, CEF parameters $A_4\langle r^4\rangle$, $A_6\langle r^6\rangle$ and overall CEF splitting Δ_{CEF}.

	W K	x	$A_4\langle r^4\rangle$ K	$A_6\langle r^6\rangle$ K	Δ_{CEF} K	Ref.
$PrBe_{13}$	2.1	−0.7	33	8.1	125	75 B 3
$NdBe_{13}$	−1.2	0.6	41	5.0	70	83 B 1
$SmBe_{13}$	5	1	33	–	30	83 B 1
$TbBe_{13}$	0.05	−0.8	− 5.4	−1.2	10	80 B 1
$ErBe_{13}$	0.094	−0.276	−10	2.4	38	80 V 2
$TmBe_{13}$	−0.134	0.35	− 4.8	2.06	30	75 B 3
$YbBe_{13}$	1.79	0.911	−15.4	0.96	51	85 W 1

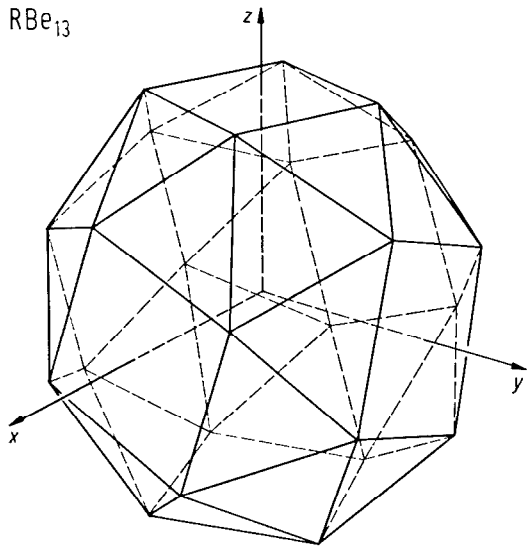

Fig. 169. RBe_{13}. The nearest-neighbour Be polyhedron: Be ions are located at the corners and the R ion at its centre [75 B 3].

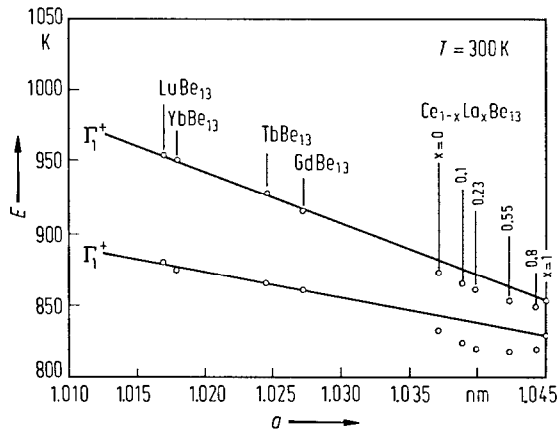

Fig. 170. RBe_{13}. Energies of the two Γ_1^+ symmetry optical phonons, E, vs. lattice parameter a at 300 K. Note the anomalous value for the $Ce_{1-x}La_xBe_{13}$ mixed-valent system [85 B 1].

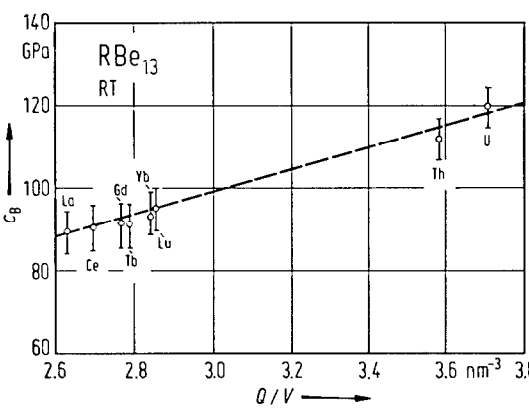

Fig. 171. RBe_{13}. Room-temperature bulk modulus c_B vs. the ratio Q/V between the valence Q and the unit cell volume V. The hatched line is the extrapolation to the actinide isomorphous compounds [85 M 1].

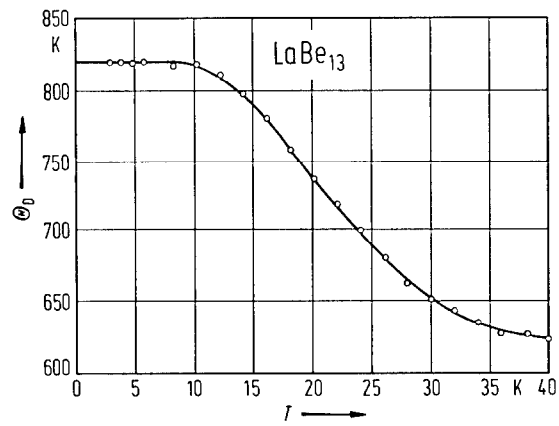

Fig. 172. $LaBe_{13}$. Debye temperature Θ_D vs. temperature from specific heat measurements on a polycrystalline sample [75 B 3].

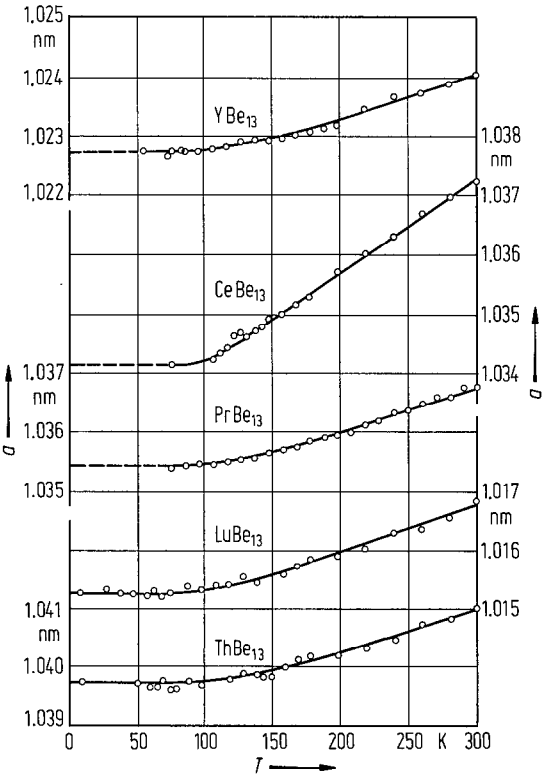

Fig. 173. RBe_{13}. Lattice parameter a vs. temperature [80 K 1].

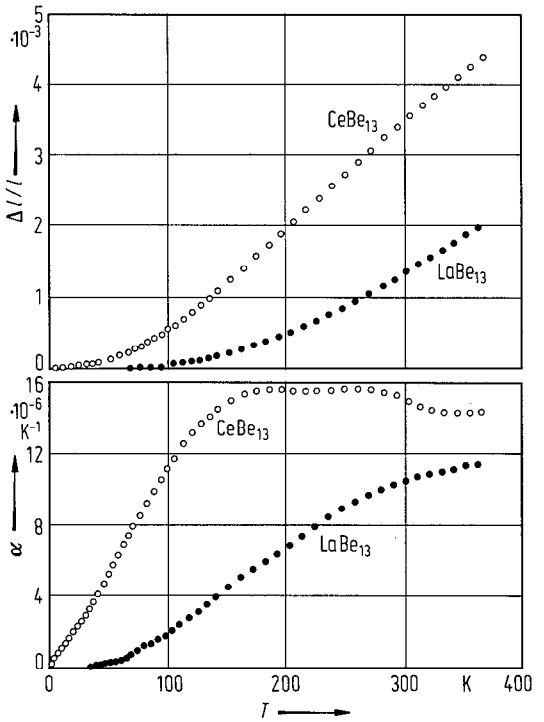

Fig. 174. $LaBe_{13}$, $CeBe_{13}$. Relative change of length $\Delta l/l$ and linear thermal expansion coefficient α vs. temperature, measured on polycrystalline samples [81 P 3].

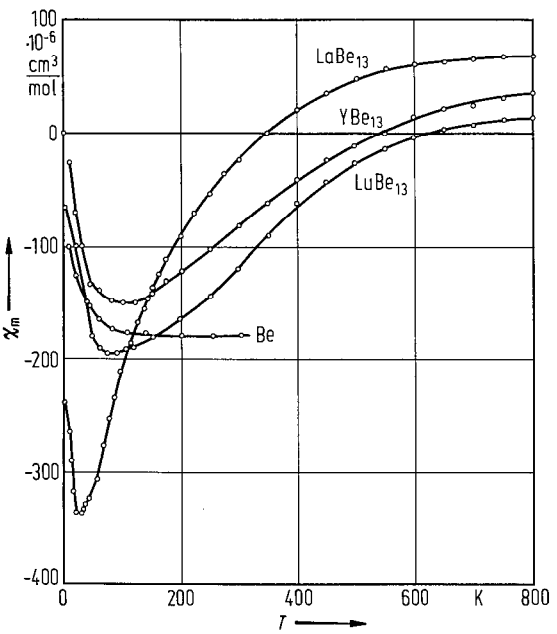

Fig. 175. RBe_{13}, R = La, Lu, Y. Magnetic molar susceptibility χ_m vs. temperature. The temperature variation for Be is also indicated in relation with impurity effects in the RBe_{13} polycrystalline samples [80 K 1].

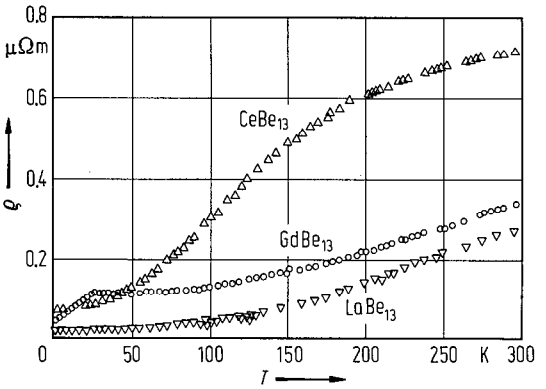

Fig. 176. RBe_{13}, R = La, Ce, Gd. Electrical resistivity ϱ vs. temperature for polycrystalline samples [80 K 2].

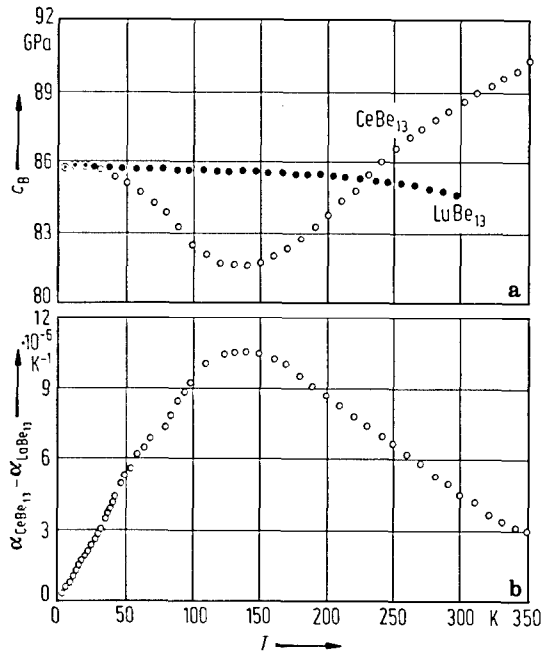

Fig. 177. $LuBe_{13}$, $CeBe_{13}$. (a) Bulk modulus c_B vs. temperature. (b) temperature variation of the difference between the thermal expansion coefficients in $CeBe_{13}$ and $LaBe_{13}$, $\alpha_{CeBe_{13}} - \alpha_{LaBe_{13}}$ [84 L 1].

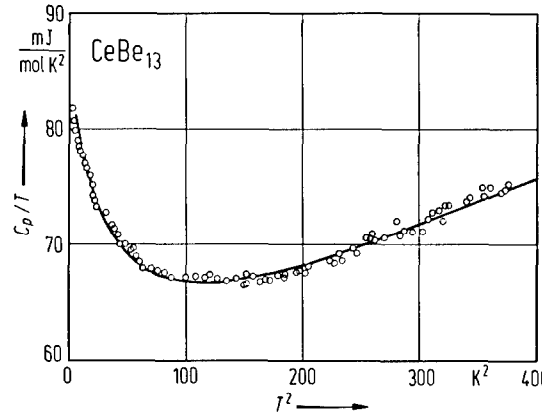

Fig. 178. $CeBe_{13}$. Ratio of the heat capacity and the temperature, C_p/T, vs. the square of the temperature, T^2. The solid line is a least-squares fit [83 B 2].

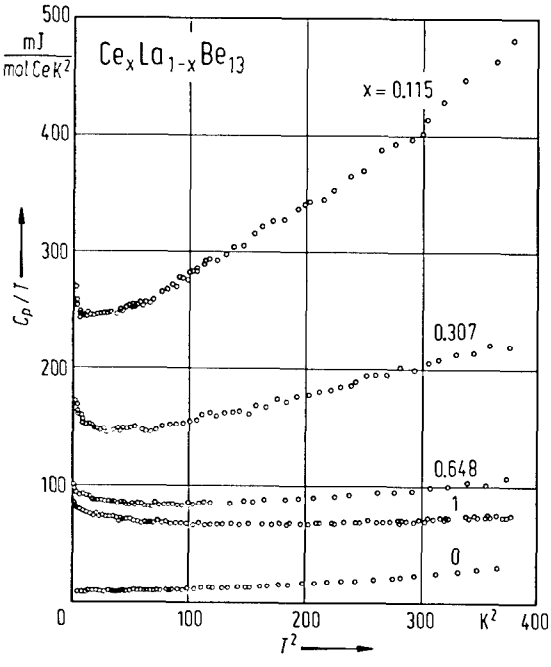

Fig. 179. $Ce_xLa_{1-x}Be_{13}$. Ratio of the heat capacity and the temperature, C_p/T, vs. the square of the temperature T^2 for the Ce concentration indicated [83 B 2].

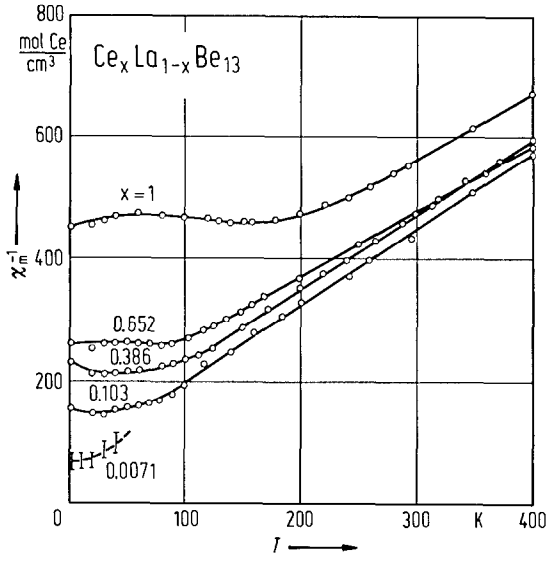

Fig. 180. $Ce_xLa_{1-x}Be_{13}$. Reciprocal magnetic molar susceptibility χ_m^{-1} vs. temperature for various Ce concentrations [79 K 1].

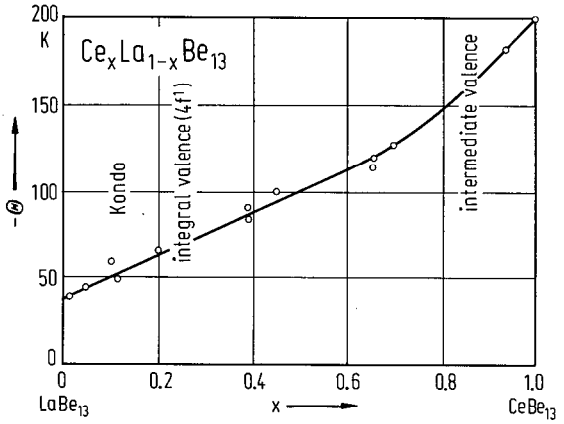

Fig. 181. $Ce_xLa_{1-x}Be_{13}$. Paramagnetic Curie temperature Θ vs. Ce concentration. The concentration range of the various regimes (intermediate valence, trivalent state and Kondo behaviour) are also indicated [81 K 1].

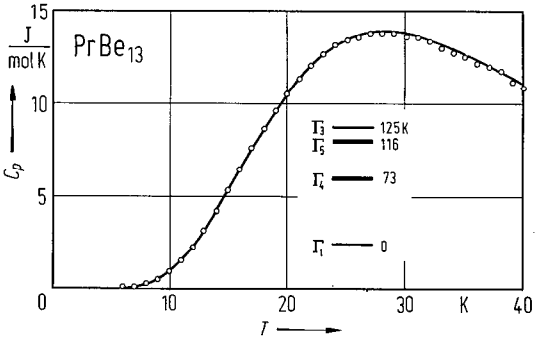

Fig. 182. $PrBe_{13}$. Molar heat capacity C_p vs. temperature for a polycrystalline sample. The full line is calculated in a CEF model for the level scheme indicated [75 B 3].

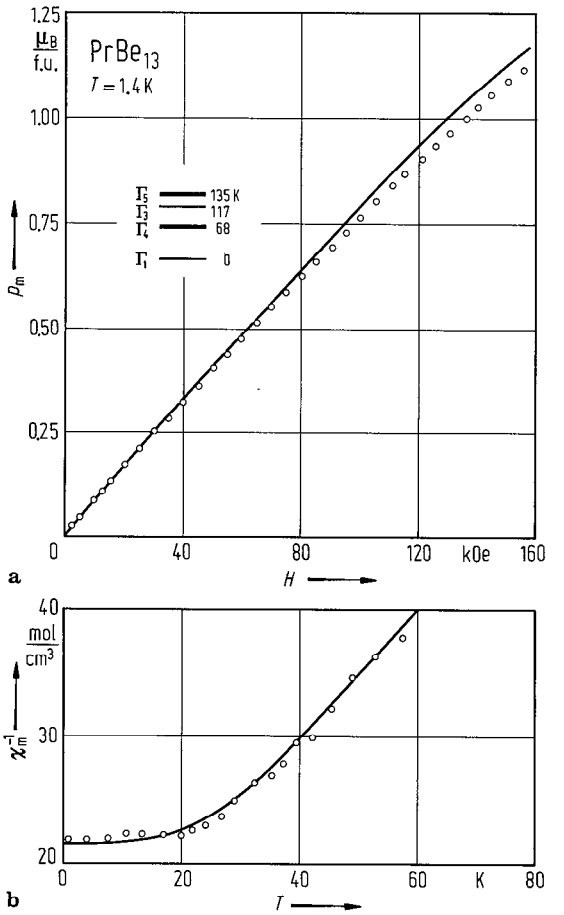

Fig. 183. $PrBe_{13}$. (a) Magnetic moment p_m vs. applied magnetic field H at 1.4 K. (b) gives the low-temperature variation of the reciprocal magnetic molar susceptibility χ_m^{-1} for a polycrystalline sample. The full lines are calculated considering bilinear exchange and CEF interactions [82 B 1].

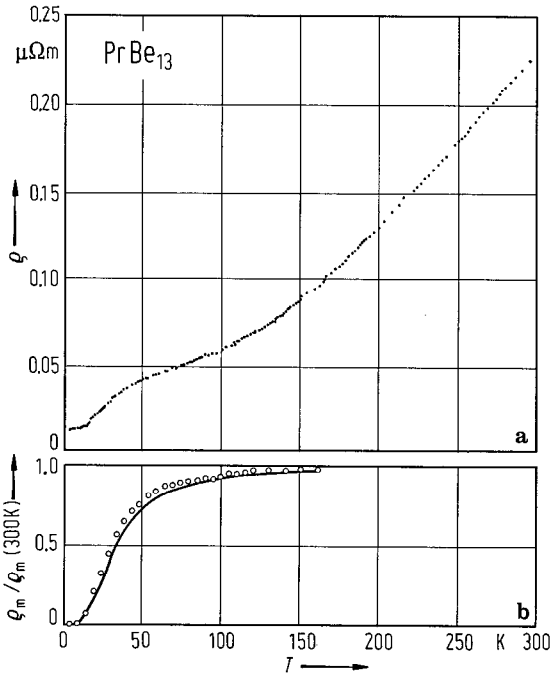

Fig. 184. $PrBe_{13}$. (a) Electrical resistivity ϱ vs. temperature for a polycrystalline sample. In (b) ϱ_m is the magnetic contribution to ϱ after subtraction of impurity and phonon contributions deduced from $LaBe_{13}$ study; ϱ_m is normalized to its room-temperature value and described in a CEF model using the same level scheme as in Fig. 183 [82 B 1].

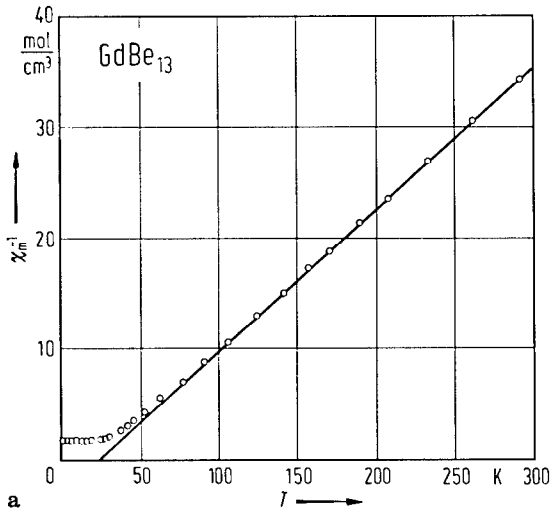

a

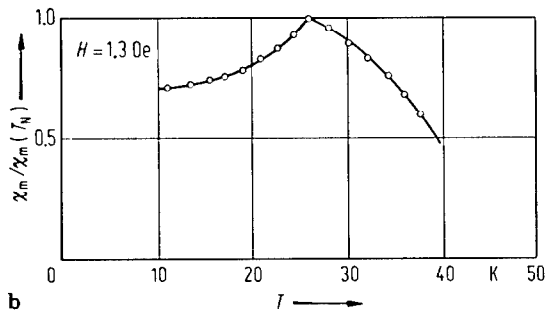

b

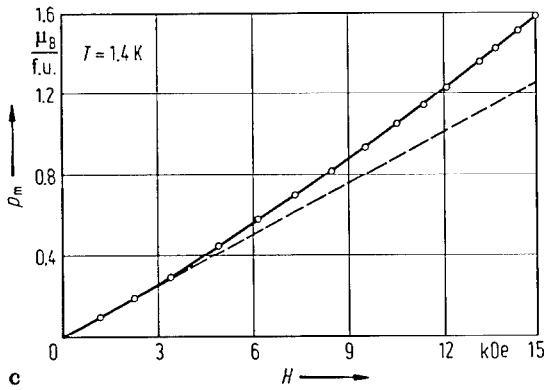

c

Fig. 185. $GdBe_{13}$. (a) Reciprocal magnetic molar susceptibility χ_m^{-1} vs. temperature for a polycrystalline sample. The full line is a guide for the eye. (b) gives the temperature variation of the magnetic molar susceptibility measured in 1.3 Oe and normalized at the value at $T_N = 25.7$ K. (c) gives the magnetization moment per Gd atom, p_m vs. the applied magnetic field H in the antiferromagnetic state at 1.4 K [75 B 3].

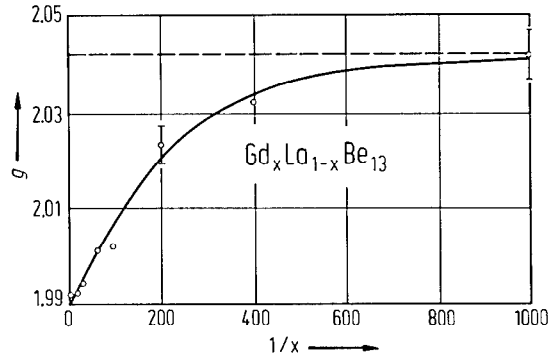

Fig. 186. $Gd_xLa_{1-x}Be_{13}$. Landé factor g vs. the reciprocal concentration, 1/x measured by electron spin resonance. The horizontal dashed line indicates the unbottlenecked limit [77 H 2].

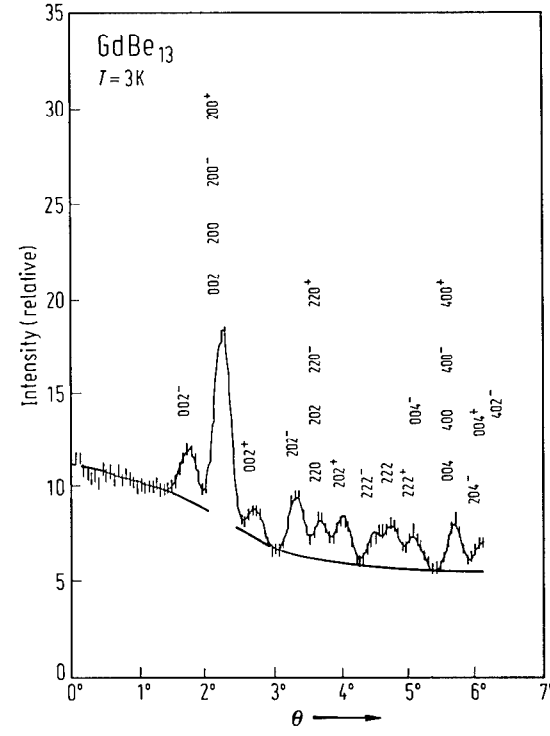

Fig. 187. $GdBe_{13}$. Powder neutron diffraction spectrum at 3 K for an incident neutron wavelength $\lambda = 0.504$ Å. Bars indicate uncertainties, full lines correspond to the background and to the refinement for the magnetic structure, respectively [82 V 1].

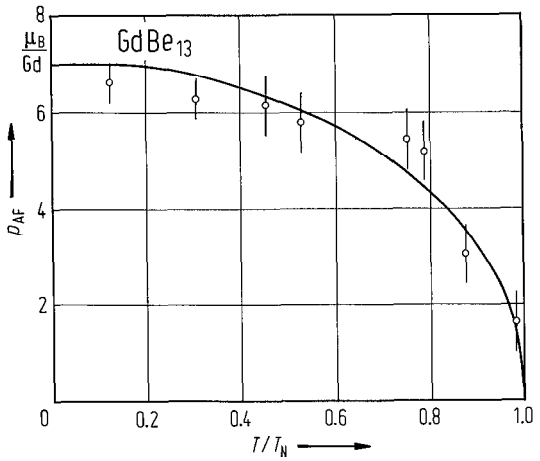

Fig. 188. $GdBe_{13}$. Antiferromagnetic moment per Gd site, p_{AF}, vs. reduced temperature T/T_N. The full curve is the Brillouin function B_J for $J=7/2$ [82 V 1].

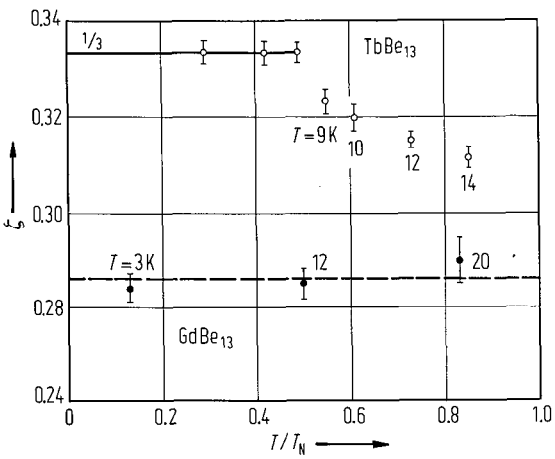

Fig. 189. $GdBe_{13}$, $TbBe_{13}$. Propagation vector of the helicoidal structure, $\tau=\zeta c^*$, vs. reduced temperature T/T_N [83 V 1].

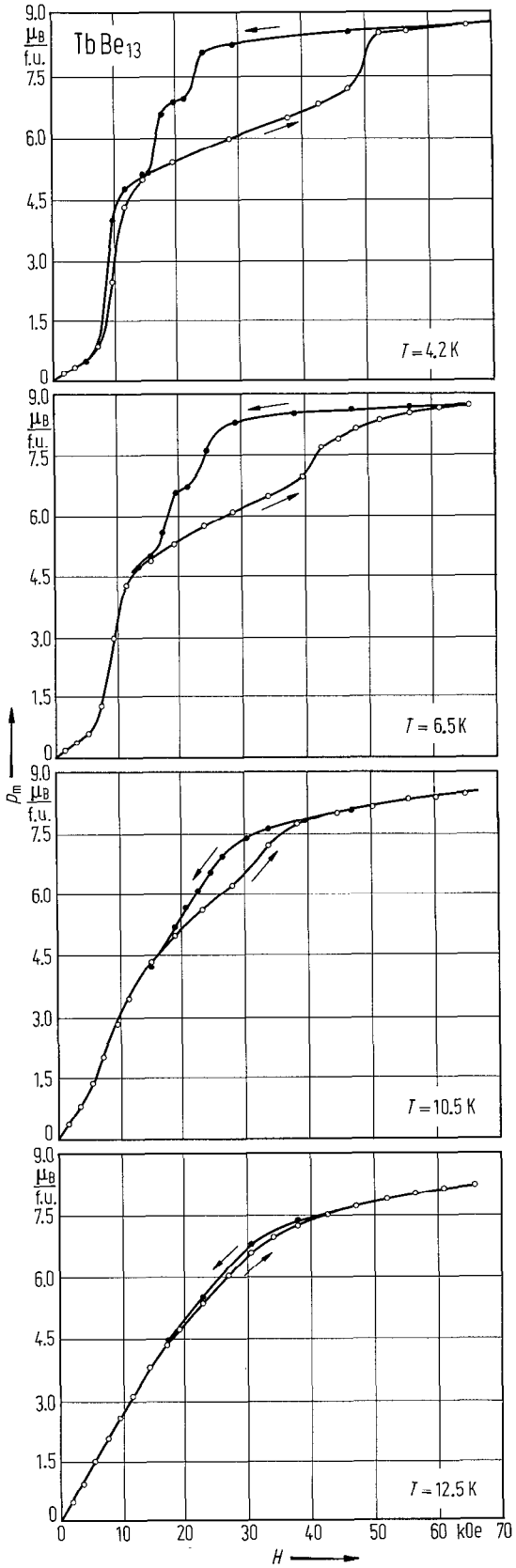

Fig. 190. $TbBe_{13}$. Magnetic moment p_m vs. applied magnetic field H for a polycrystalline sample at various temperatures. Arrows indicate field drift, lines are guides for the eye [81 C 1].

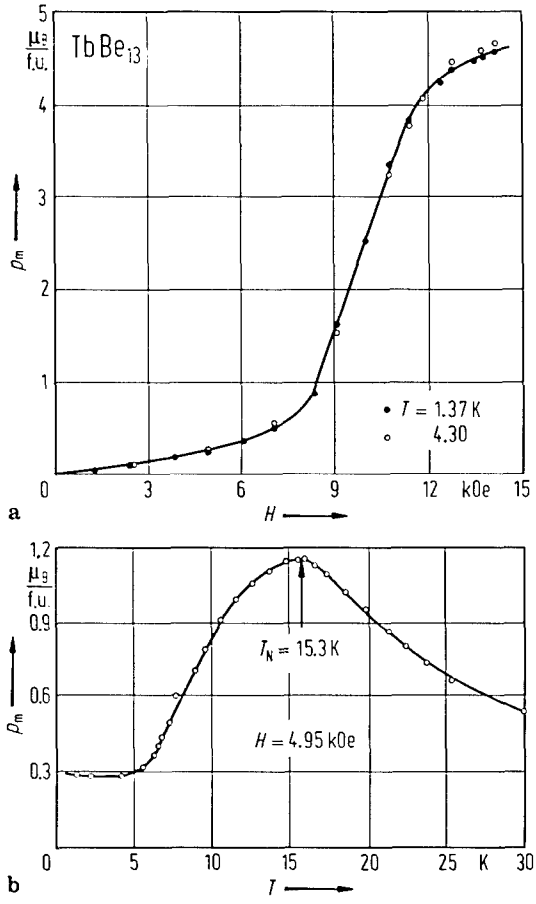

Fig. 191. $TbBe_{13}$. (a) Magnetic moment p_m vs. applied magnetic field H for a polycrystalline sample at 1.37 and 4.30 K. (b) shows the low-temperature behaviour of the magnetic moment p_m measured in a field of 4.95 kOe [75 B 3].

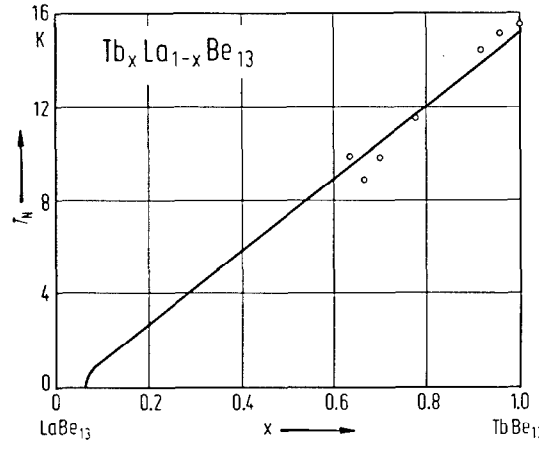

Fig. 194. $Tb_xLa_{1-x}Be_{13}$. Néel temperature T_N vs. Tb concentration x for polycrystalline samples. The full line is calculated in a CEF model assuming a bilinear exchange varying linearly with x; at low Tb concentration, the spin system is undercritical [80 C 1].

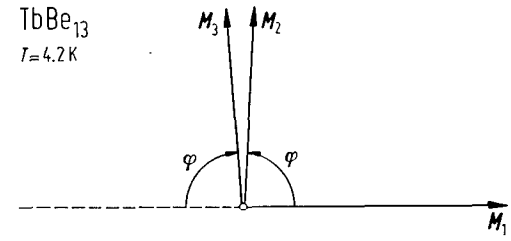

Fig. 192. $TbBe_{13}$. Helicoidal magnetic structure at 4.2 K, M_1 M_2 and M_3 are the magnetic moments for Tb sites in 3 successive (00 h) planes ($\varphi = 86.5°$) [80 V 1].

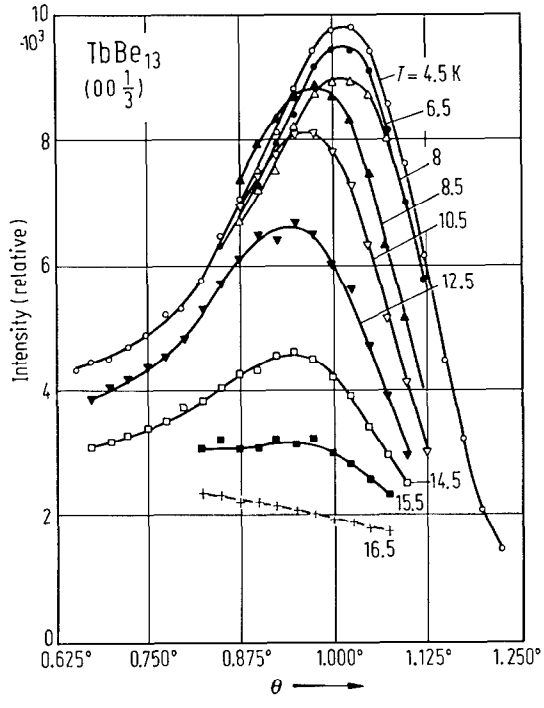

Fig. 193. $TbBe_{13}$. Angular dependence of intensity of the (0 0 1/3) magnetic reflection in powder neutron diffraction spectra at various temperature as indicated [80 V 1].

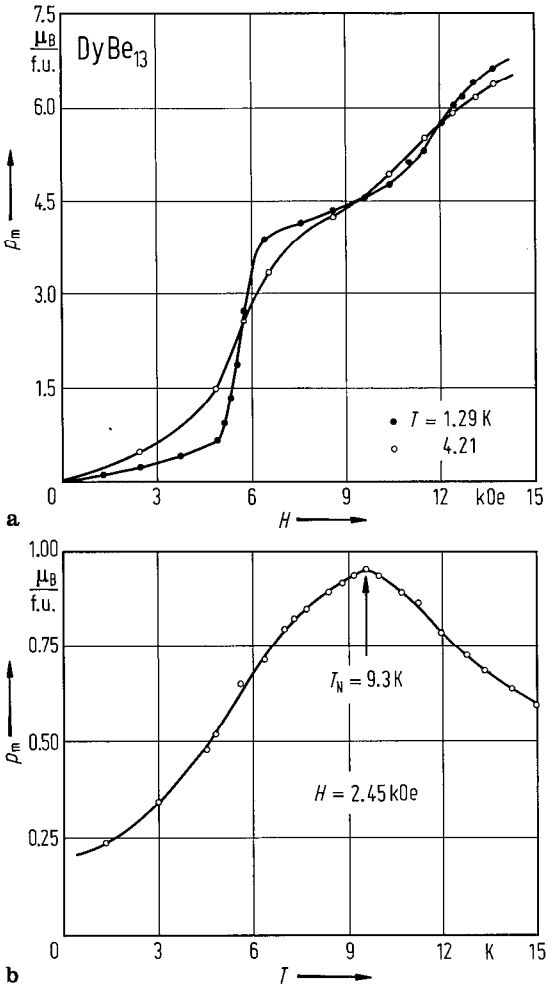

Fig. 195. $DyBe_{13}$. (a) Magnetic moment p_m vs. applied magnetic field H for a polycrystalline sample at 1.29 and 4.21 K. (b) gives the temperature variation of the magnetic moment p_m in 2.45 kOe [75 B 3].

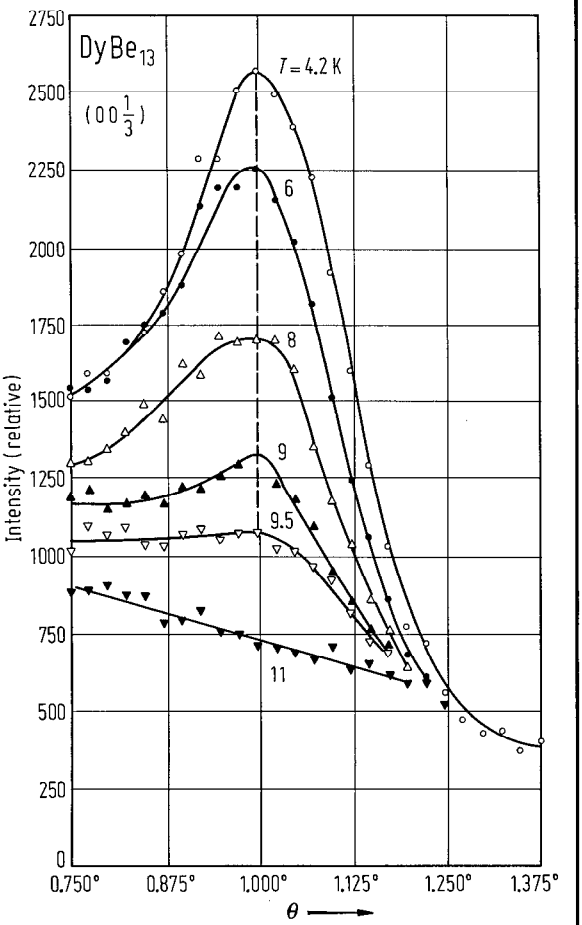

Fig. 196. $DyBe_{13}$. Angular dependence of the intensity of the (0 0 1/3) magnetic reflection in powder neutron diffraction spectra at various temperatures [85 V 1].

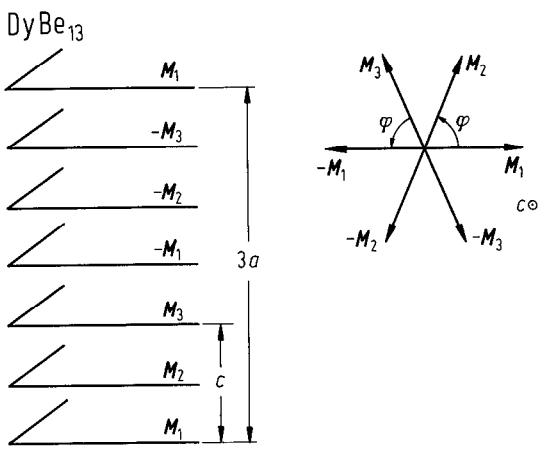

Fig. 197. $DyBe_{13}$. Commensurate helicoidal magnetic structure ($\varphi = 79°$ at 4.2 K) [85 V 1].

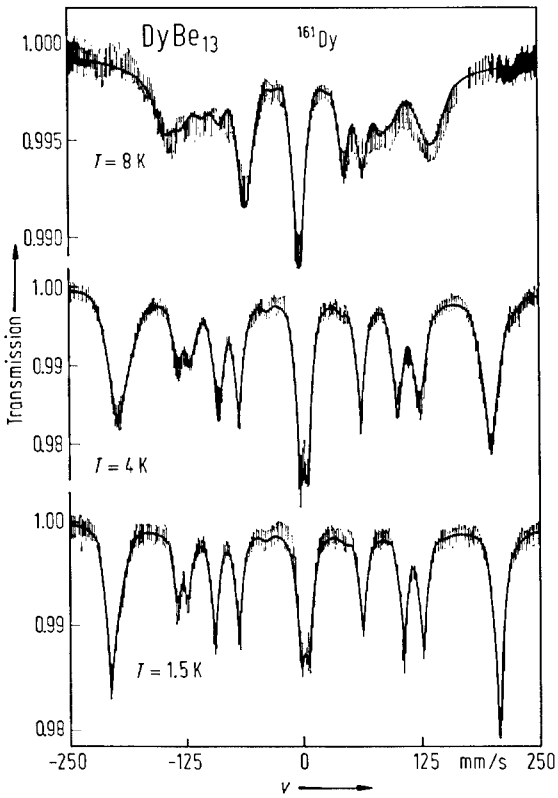

Fig. 198. $DyBe_{13}$. ^{161}Dy Mössbauer absorption spectra at 8, 4 and 1.5 K. Full lines are calculated in a relaxation model [85 V 1].

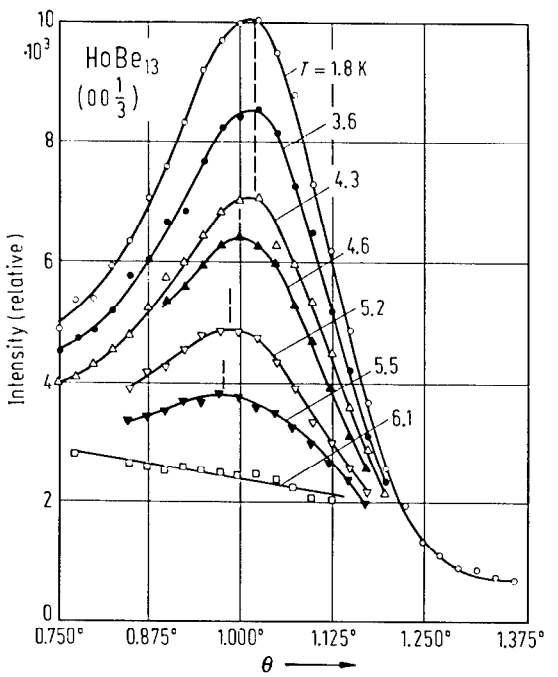

Fig. 200. $HoBe_{13}$. Angular dependence of the intensity of the (0 0 1/3) magnetic reflection in powder neutron diffraction spectra at temperatures indicated [83 V 1].

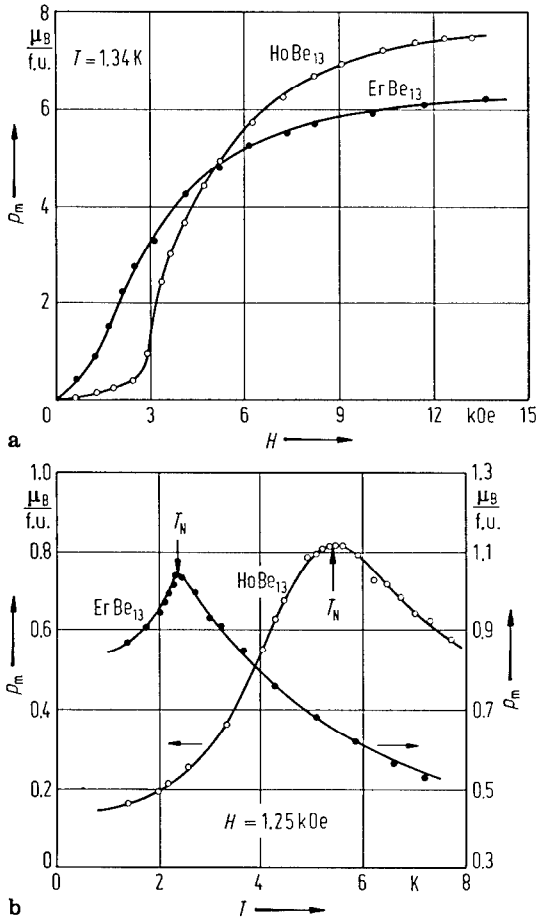

Fig. 199. $HoBe_{13}$, $ErBe_{13}$. (a) Magnetic moment p_m vs. applied magnetic field H at 1.34 K for polycrystalline samples. (b) shows the temperature dependence of the magnetic moment measured in 1.25 kOe [75 B 3].

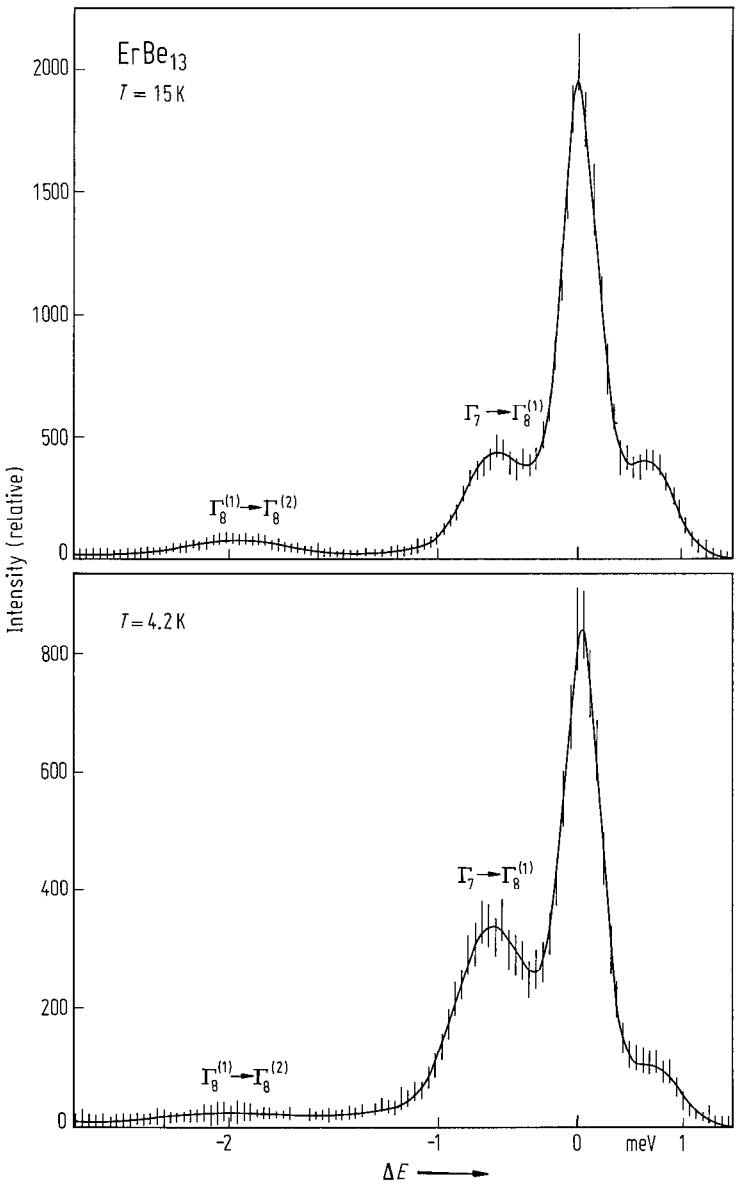

Fig. 201. $ErBe_{13}$. Inelastic neutron scattering intensity vs. the energy transfer ΔE from the neutron incident energy of 5.0 meV at 15 and 4.2 K. Bars indicate the intensity I and the $\pm 2\sqrt{I}$ uncertainties [80 V 2].

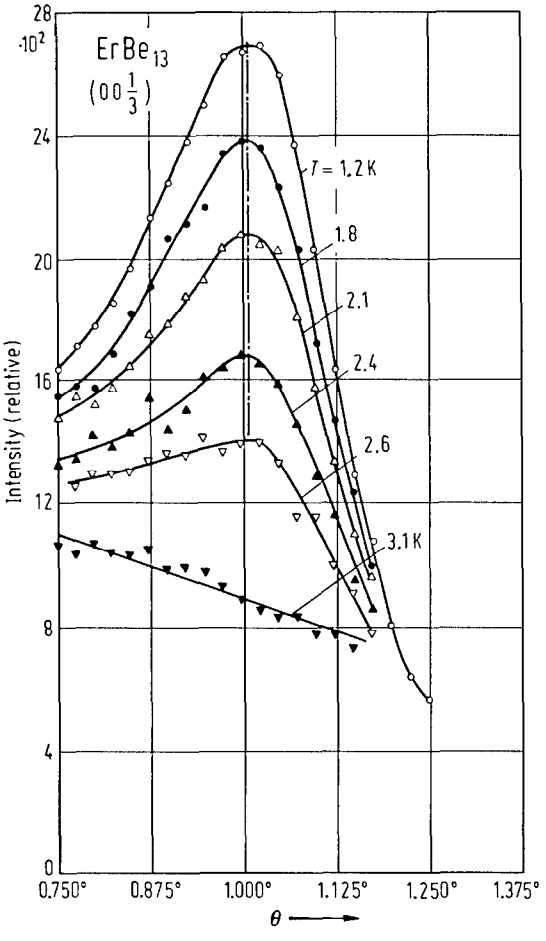

Fig. 202. $ErBe_{13}$. Angular dependence of the intensity of the (0 0 1/3) magnetic reflection in powder neutron diffraction spectra at temperatures indicated [83 V 1].

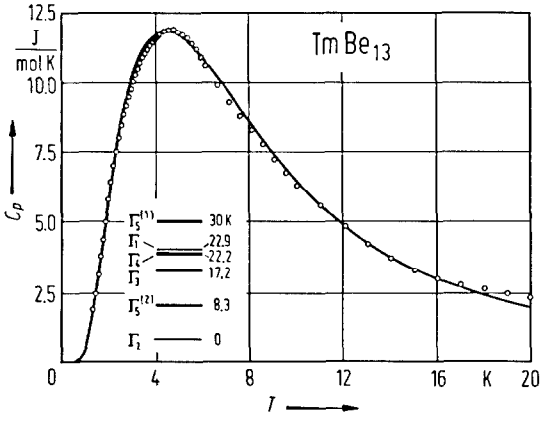

Fig. 205. $TmBe_{13}$. Molar heat capacity C_p vs. temperature. The full line is calculated in a CEF model for the level spacing indicated [75 B 3].

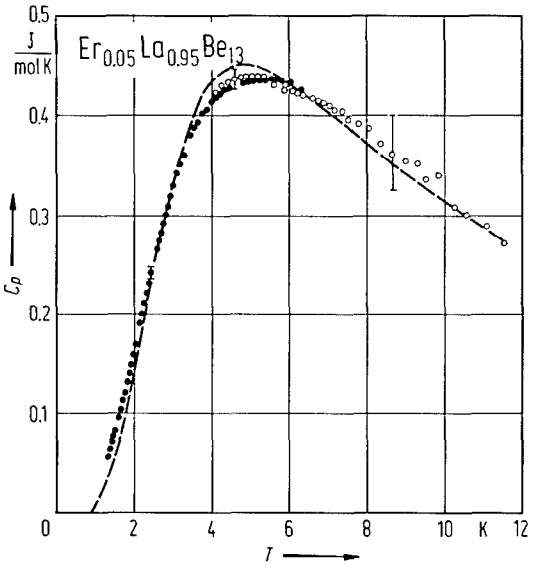

Fig. 203. $Er_{0.05}La_{0.95}Be_{13}$. Temperature dependence of the molar heat capacity C_p after subtraction of the lattice contribution deduced from the $LaBe_{13}$ study for polycrystalline samples in zero magnetic field. The hatched line is calculated in a CEF model [80 V 3].

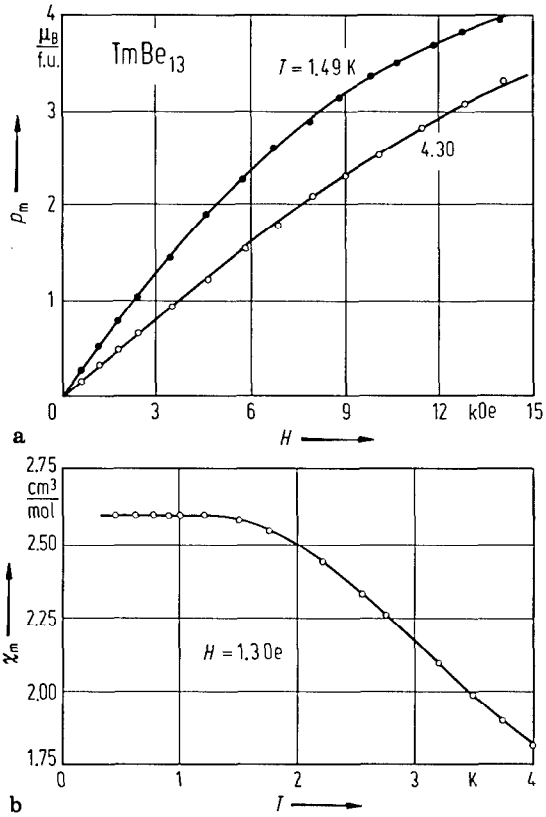

Fig. 204. $TmBe_{13}$. (a) Magnetic moment p_m vs. applied magnetic field H at 1.49 and 4.30 K for a polycrystalline sample. (b) shows the low temperature dependence of the magnetic molar susceptibility χ_m measured in 1.3 Oe [75 B 3].

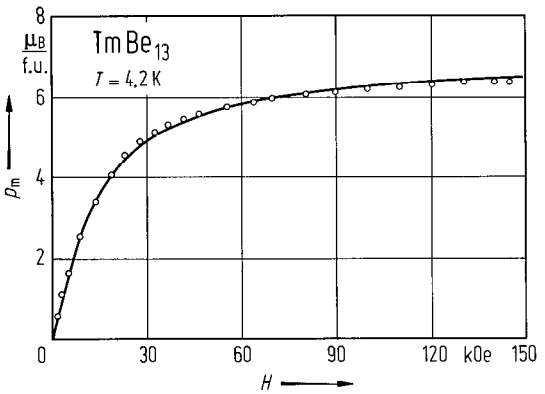

Fig. 206. $TmBe_{13}$. Magnetic moment p_m vs. applied magnetic field H at 4.2 K for a polycrystalline sample. The full line is calculated in a CEF model [81 C 2].

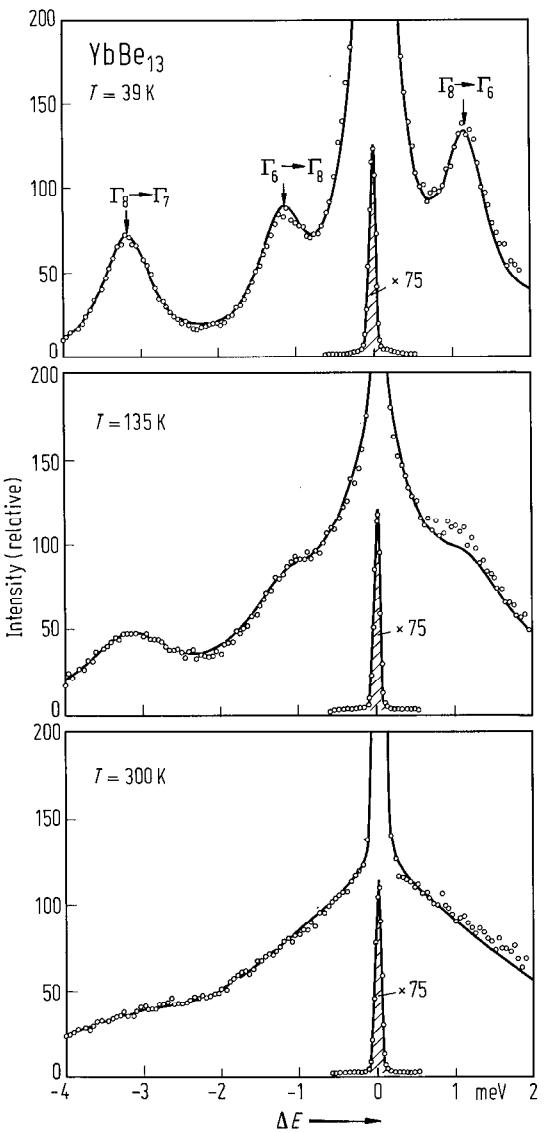

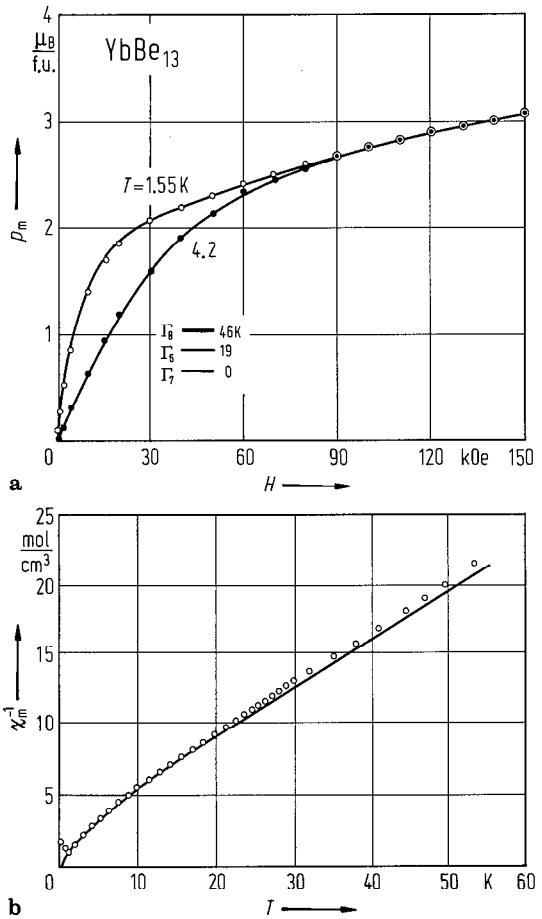

Fig. 207. $YbBe_{13}$. (a) Magnetic moment p_m vs. applied magnetic field H at 1.55 and 4.2 K for a polycrystalline sample. (b) gives the reciprocal magnetic molar susceptibility χ_m^{-1}. Full lines are calculated considering bilinear exchange and CEF interactions for the Yb level scheme indicated [79 H 1].

◀

Fig. 208. $YbBe_{13}$. Intensity of the inelastic neutron scattering vs. the energy transfer ΔE from the incident neutron energy of 3.1 meV at 39 K (upper part) 135 K (middle part) and 300 K (lower part). Solid lines are fits based on a CEF model. Shaded areas indicate elastic incoherent nuclear scattering [85 W 1].

2.7.7 Ternary compounds

Table 22. Si-based compounds. Structure type, space group, room-temperature lattice parameters a, c, room-temperature electrical resistivity ϱ and magnetic characteristics (paramagnetic Curie temperature Θ and effective magnetic moment per rare earth ion, p_{eff}).

	Structure type	Space group	a	c	ϱ (300 K)	Θ	p_{eff}	Figures	Ref.
			nm		μΩm	K	μ_B		
CeSiMg	α-$ThSi_2$	$P4_2/mmm$	0.7589	1.374				209	74 Z 1
$CeSi_2Mg_2$	$BaAl_4$	P4/mmm	0.4250	0.5765				209	71 Z 1
CeZnSi	AlB_2	P6/mmm	0.4223	0.4238	2.84	12	2.5	210–213	83 K 2
NdZnSi	AlB_2	P6/mmm	0.4167	0.4174	3.07	30	3.6	210–213	83 K 2
SmZnSi	AlB_2	P6/mmm	0.4167	0.4095	3.58			210–213	83 K 2
GdZnSi	AlB_2	P6/mmm	0.4163	0.4000	2.29	61	7.5	210–217	83 K 2, 84 K 3
TbZnSi	AlB_2	P6/mmm	0.4141	0.3962	4.96	38	9.3	210–213	83 K 2
HoZnSi	AlB_2	P6/mmm	0.4103	0.3941	5.28	50	10.2	210–213	83 K 2
YZnSi	AlB_2	P6/mmm	0.4135	0.3968				211	83 K 2

Table 23. RInZn, RTlZn, RInCd compounds. Room-temperature lattice parameters a, c of the $CaIn_2$-type hexagonal structure ($P6_3/mmc$ space groups). See Figs. 218–220.

	a	c	Ref.
	nm		
LaInZn	0.4796	0.7768	82 M 1
CeInZn	0.4787	0.7631	82 M 1
PrInZn	0.4786	0.7537	82 M 1
NdInZn	0.4719	0.7531	82 M 1
SmInZn	0.4697	0.7414	82 M 1
GdInZn	0.4676	0.7335	82 M 1
DyInZn	0.4649	0.7239	82 M 1
HoInZn	0.4636	0.7214	82 M 1
ErInZn	0.4616	0.7184	82 M 1
YbInZn	0.4725	0.7382	82 M 1
LaTlZn	0.4803	0.7796	83 M 1
CeTlZn	0.4783	0.7676	83 M 1
NdTlZn	0.4715	0.7561	83 M 1
SmTlZn	0.4680	0.7461	83 M 1
GdTlZn	0.4645	0.7396	83 M 1
DyTlZn	0.4611	0.7308	83 M 1
ErTlZn	0.4582	0.7247	83 M 1
LaInCd	0.4936	0.7652	81 R 2
CeInCd	0.4943	0.7809	81 R 2
PrInCd	0.4907	0.7609	81 R 2
NdInCd	0.4889	0.7572	81 R 2
SmInCd	0.4866	0.7469	81 R 2
GdInCd	0.4845	0.7398	81 R 2
DyInCd	0.4819	0.7318	81 R 2
HoInCd	0.4805	0.7301	81 R 2
ErInCd	0.4796	0.7253	81 R 2
YbInCd	0.4948	0.7302	81 R 2

Table 24. Miscellaneous ternary compounds. Structure type, space group and room-temperature lattice parameters *a*, *c*.

	Structure type	Space group	*a*	*c*	Fig.	Ref.
			nm			
$YMgAl_4$	$MgZn_2$	$P6_3/mmc$	0.533	0.857	221	80 Z 1
$Y_2Mg_3Zn_3$	$AlMnCu_2$	Fm3m	0.6848		222	82 P 1
$YMg_{12}Zn$	unknown				222	82 P 1
YMg_3Zn_6	unknown					82 P 1
$Nd_2Mg_2Zn_9$	unknown					74 D 2
$Nd_2Mg_6Zn_7$	unknown					74 D 2
Nd_4MgZn_5	unknown					74 D 2
$LaCo_{12}Zn$	$NaZn_{13}$	Fm3c	1.1404			83 C 1
$LaCo_{11}Zn_2$	$NaZn_{13}$	Fm3c	1.1467			83 C 1
$LaCo_{10}Zn_3$	$NaZn_{13}$	Fm3c	1.1524			83 C 1
$LaCo_9Zn_4$	$NaZn_{13}$	Fm3c	1.1650			83 C 1

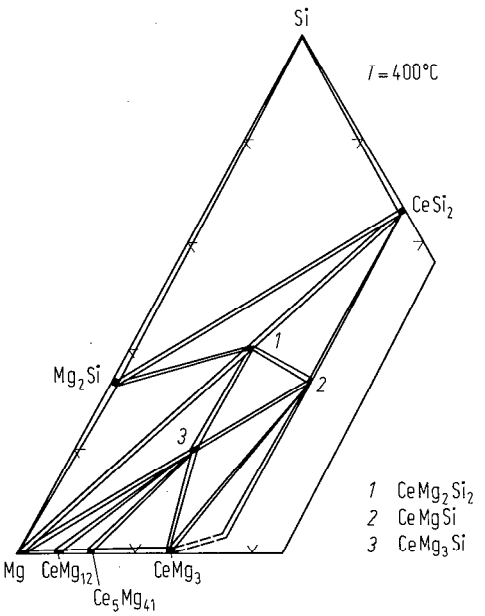

Fig. 209. CeMgSi system. Isothermal section at 400 °C of the partial phase diagram (0–33 at% Ce). $CeMg_2Si_2$, CeMgSi, $CeMg_3Si$ are three ternary defined compounds [84 r].

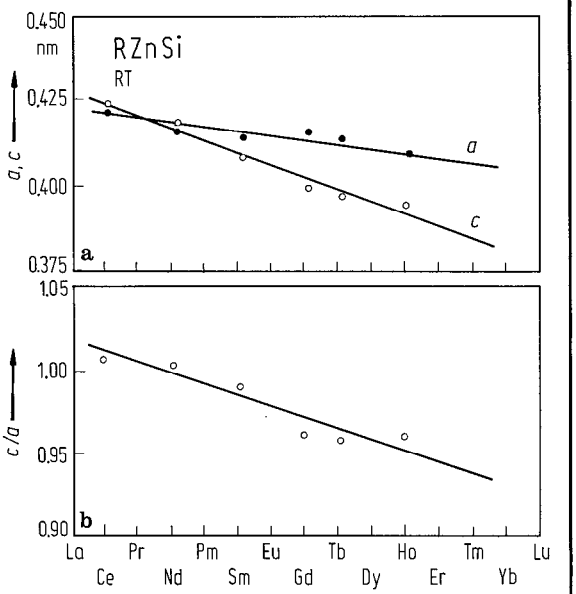

Fig. 210. RZnSi. (a) Lattice parameters *a*, *c* vs. rare earth atom at room temperature. (b) gives the variation of the ratio *c*/*a* for the AlB_2 structure [83 K 2].

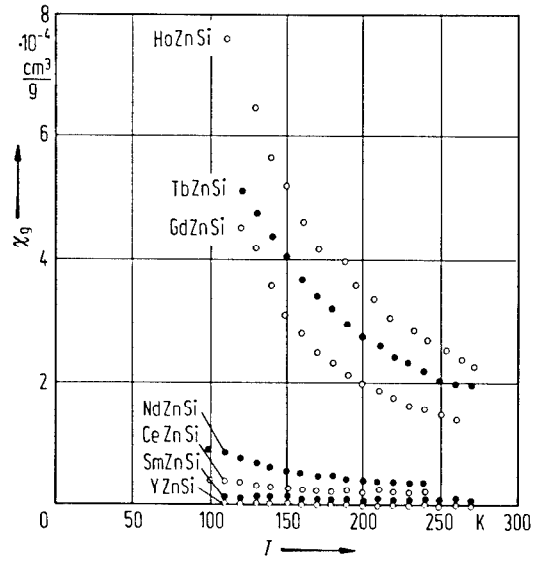

Fig. 211. RZnSi. Specific magnetic susceptibility χ_g vs. temperature between 100 and 280 K for polycrystalline samples [83 K 2].

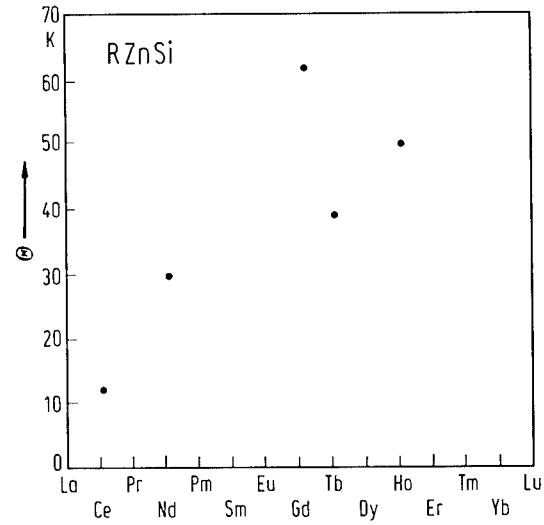

Fig. 212. Paramagnetic Curie temperature Θ as a function of the rare earth atom [83 K 2].

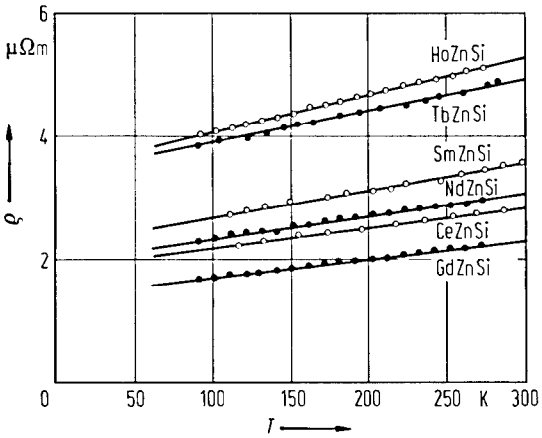

Fig. 213. RZnSi. Electrical resistivity ϱ vs. temperature at high temperature for polycrystalline samples [83 K 2].

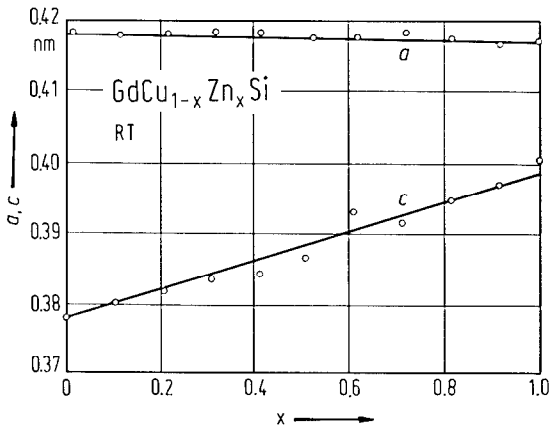

Fig. 214. $GdCu_{1-x}Zn_xSi$. Room-temperature lattice parameters a, c vs. Zn concentration [84 K 3].

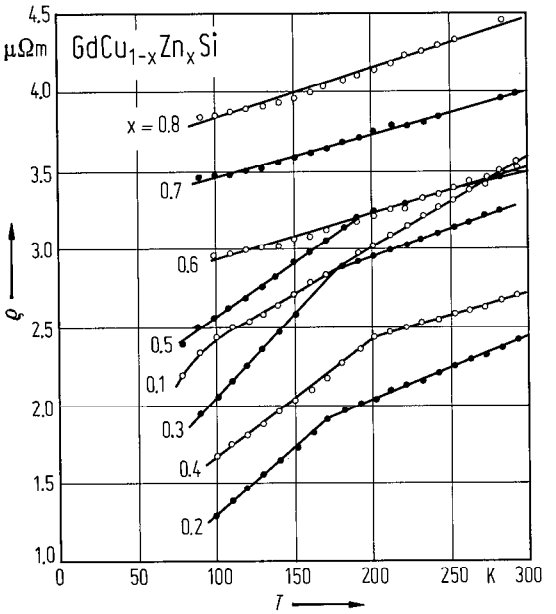

Fig. 215. $GdCu_{1-x}Zn_xSi$. Electrical resistivity ϱ vs. temperature for the Zn concentrations indicated. The anomaly indicates the ferromagnetic Curie temperature (polycrystalline samples) [84 K 3].

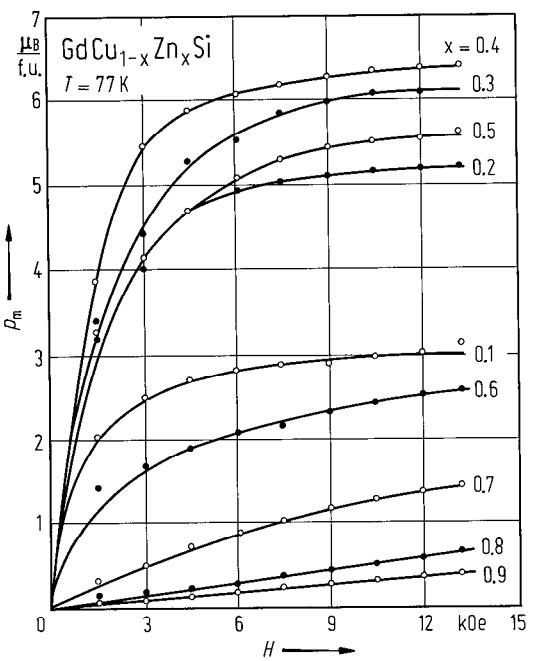

Fig. 216. $GdCu_{1-x}Zn_xSi$. Magnetic moment p_m vs. applied magnetic field H for the Zn concentrations indicated at 77 K (polycrystalline samples) [84 K 3].

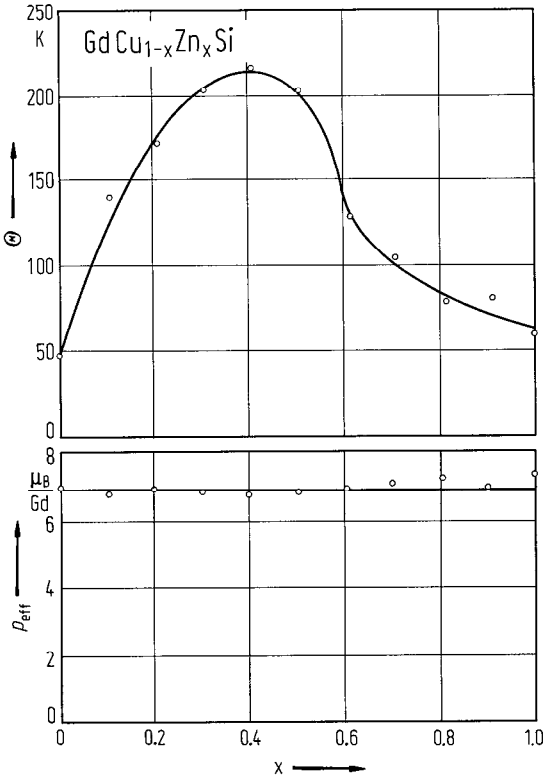

Fig. 217. $GdCu_{1-x}Zn_xSi$. Paramagnetic Curie temperature Θ and effective magnetic moment p_{eff} vs. Zn concentration for polycrystalline samples [84 K 3].

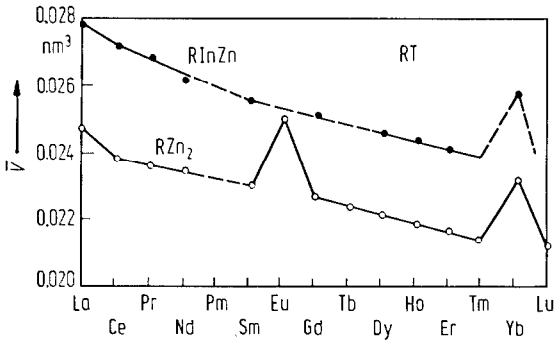

Fig. 218. RInZn, RZn_2. Room-temperature average atomic volumes, $\bar{V} = V_{cell}/6$, vs. the rare earth atom. Solid circles: RInZn $CaIn_2$-type; open circles: RZn_2–$CeCu_2$-type [82 M 1].

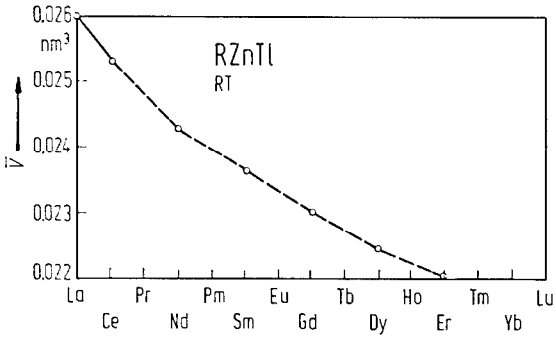

Fig. 219. RZnTl. Room-temperature average atomic volume, $\bar{V} = V_{cell}/6$, vs. the rare earth atom [83 M 1].

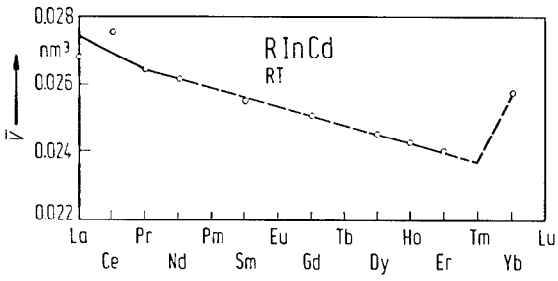

Fig. 220. RInCd. Room-temperature average atomic volume, $\bar{V} = V_{cell}/6$, vs. the rare earth atom [81 R 2].

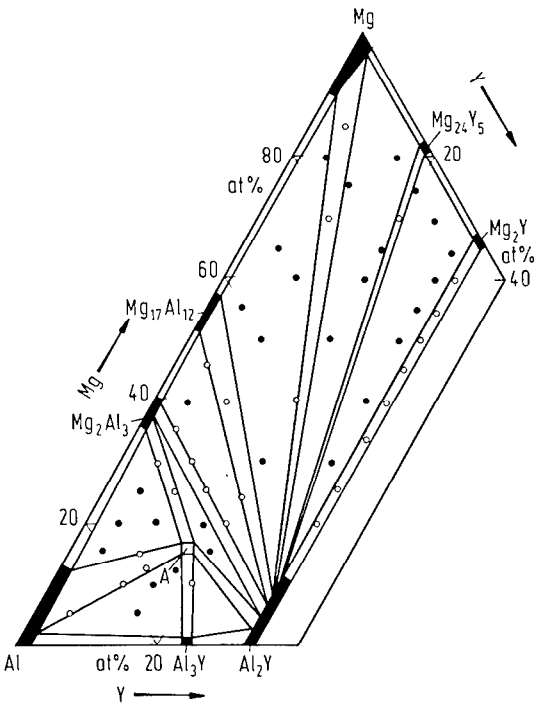

Fig. 221. YMgAl system. 400 °C isothermal section of the partial phase diagram. Symbols indicate the alloys prepared (open circles: two-phase, solid circles: three-phase). The ternary compound $A \equiv YMgAl_4$ has a hexagonal $MgZn_2$-type structure [80 Z 1].

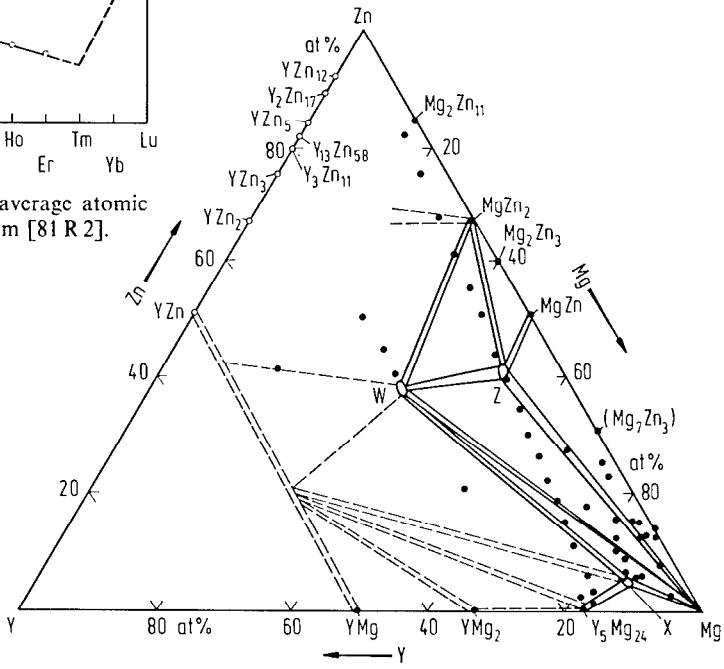

Fig. 222. YMgZn system. 300 °C isothermal section of the phase diagram. The ternary compound $W \equiv Y_2Mg_3Zn_3$ is cubic ($AlMnCu_2$ structure); $X \equiv YMg_{12}Zn$ and $Z \equiv YMg_3Zn_6$ have unknown structures [82 P 1].

2.7.8 References for 2.7

2.7.8.1 General references

58 h Hansen, M.: Constitution of Binary Alloys. New York: McGraw-Hill **1958**.

65 e Elliott, R.P.: Constitution of Binary Alloys, First Supplement. New York: McGraw-Hill **1965**.

67 p Pearson, W.B., in: Handbook of Lattice Spacings and Structures of Metals and Alloys. Oxford: Pergamon Press, Vol. 2 **1967**, p. 1.

69 s Shunk, F.A.: Constitution of Binary Alloys, Second Supplement. New York: McGraw-Hill **1969**.

72 p Pearson, W.B., in: The Crystal Chemistry and Physics of Metals and Alloys. New York: Wiley Interscience **1972**.

79 b Buschow, K.H.J.: Rep. Prog. Phys. **42** (1979) 1373.

79 f Fulde, P., in: Handbook on the Physics and Chemistry of Rare Earths, (Gschneider, Jr., K.A., Eyring, L., eds.), Amsterdam: North-Holland Publ. Co., Vol. 2, **1979**, p. 295.

79 i Iandelli, A., Palenzona, A., in: Handbook on the Physics and Chemistry of Rare Earths (Gschneider, Jr., K.A., Eyring, L., eds.), Amsterdam: North-Holland Publ. Co., Vol. 2 **1979**, p. 1.

79 k Kirchmayr, H.R., Poldy, C.A., in: Handbook on the Physics and Chemistry of Rare Earths (Gschneider, Jr., K.A., Eyring, L., eds.), Amsterdam: North-Holland Publ. Co., Vol. 2 **1979**, p. 55.

80 b Buschow, K.H.J., in: Ferromagnetic Materials (Wohlfarth, E.P., ed.), Amsterdam: North-Holland Publ. Co., Vol. 1 **1980**, p. 297.

80 l Lüthi, B., in: Dynamical Properties of Solids (Horton, G.K., Maradudin, A.A., eds.), Amsterdam: North-Holland Publ. Co., Vol. 3 **1980**, p. 245.

84 r Rögl, P., in: Handbook on the Physics and Chemistry of Rare Earths (Gschneider, Jr., K.A., Eyring, L., eds.), Amsterdam: North-Holland Publ. Co., Vol. 6 **1984**, p. 49.

85 v Villars, P., Calvert, L.D.: Pearson's Handbook of Crystallographic Data for Intermetallic Phases, Am. Soc. Metals, Metals Park, Oh. 44073, Vol. 1–3 **1985**.

2.7.8.2 Special references

51 I 1 Iandelli, A., Ferro, R.: Atti. Accad. Naz. Lincei, Cl. Sci. Fis. Mat. Nat. Rend. **8** (1951) 48.

54 I 1 Iandelli, A., Ferro, R.: Gazz. Chim. Ital. **84** (1954) 463.

54 R 1 Ruderman, M.A., Kittel, C.: Phys. Rev. **96** (1954) 99.

56 K 1 Kasuya, T.: Proc. Theor. Phys. (Kyoto) **16** (1956) 45.

57 Y 1 Yoshida, K.: Phys. Rev. **106** (1957) 893.

60 I 1 Iandelli, A.: Atti. Accad. Naz. Lincei, Cl. Sci. Fis. Mat. Nat. Rend. **29** (1960) 62.

60 K 1 Kripyakevich, P.I., Evdokimenko, V.I., Gladyshevskii, E.I.: Sov. Phys. Crystallogr. **9** (1960) 330.

61 G 1 Gchneider, Jr., K.A.: Rare Earth Alloys, Princeton, N.J.: Nostrand Company **1961**, p. 112–114.

62 D 1 De Gennes, P.G.: J. Phys. Radium **23** (1962) 510.

62 L 1 Lea, K.R., Leask, M.J.M., Wolf, W.P.: J. Phys. Chem. Solids **23** (1962) 1381.

62 R 1 Rocher, Y.A.: Philos. Mag. Suppl. **11** (1962) 233.

63 C 1 Chiotti, P., Mason, J.T., Gill, K.J.: Trans. Met. Soc. AIME **227** (1963) 910.

63 L 1 Laube, E., Nowotny, H.: Montash. Chem. **94** (1963) 853.

63 O 1 Olcese, G.: Atti Accad. Naz. Lincei, Cl. Sci. Fis. Mat. Nat. Rend. **35** (1963) 7.

64 C 1 Cable, J.W., Koehler, W.C., Wollan, E.O.: Phys. Rev. **136** (1964) A 240.

64 I 1 Iandelli, A., Palenzona, A.: Atti. Accad. Naz. Lincei, Cl. Sci. Fis. Mat. Nat. Rend. **37** (1964) 165.

64 M 1 Miller, A.E., Daane, A.H.: Trans. Met. Soc. AIME **230** (1964) 568.

64 M 2 McMasters, D.D., Gschneider, Jr., K.A.: Nucl. Metallurgy **10** (1964) 93.

65 C 1 Chiotti, P., Mason, J.T.: Trans. Met. Soc. AIME **233** (1965) 786.

65 I 1 Iandelli, A., Palenzona, A.: J. Less-Common Met. **9** (1965) 1.

65 M 1 Michel, D.J., Ryba, E.: Acta Crystallogr. **19** (1965) 687.

65 S 1 Smith, J.F., Bailey, D.M., Nowotny, D.B., Davison, J.E.: Acta Metall. **13** (1965) 889.

66 L 1 Lott, B.G., Chiotti, P.: Acta Crystallogr. **20** (1966) 733.

67 B 1 Berndt, A.F.: J. Less-Common Met. **13** (1967) 366.

67 F 1 Fornasini, M.L., Merlo, F.: Atti. Accad. Naz. Lincei, Cl. Sci. Fis. Mat. Nat. Rend. **43** (1967) 141.

67 I 1 Iandelli, A., Palenzona, A.: J. Less-Common Met. **12** (1967) 333.

67 J 1 Johnson, Q., Smith, G.S.: Acta Crystallogr. **23** (1967) 327.
67 V 1 Veleckis, E., Schablaske, R.V., Johnson, I., Feder, H.M.: Trans. Met. Soc. AIME **239** (1967) 58.
67 W 1 Wang, F.: Acta Crystallogr. **22** (1967) 579.
68 I 1 Iandelli, A., Palenzona, A.: J. Less-Common Met. **15** (1968) 273.
68 M 1 Michel, D.J., Ryba, E.: Acta Crystallogr. B **24** (1968) 1267.
69 R 1 Ryba, E., Kejrival, P.K., Elmendorf, R.: J. Less-Common Met. **18** (1969) 419.
70 B 1 Bruzzone, G., Fornasini, M.L., Merlo, F.: J. Less-Common Met. **22** (1970) 253.
70 D 1 Debray, D.K., Wallace, W.E., Ryba, E.: J. Less-Common Met. **22** (1970) 19.
70 J 1 Johnson, Q., Smith, G.S.: Acta Crystallogr. B **26** (1970) 434.
70 L 1 Levy, P.M.: Phys. Rev. B **2** (1970) 1429.
70 M 1 Mason, J.T., Chiotti, P.: Trans. Met. Soc. AIME **1** (1970) 2119.
70 M 2 Mühlpfordt, W.: Z. Anorg. Allg. Chem. **374** (1970) 174.
70 M 3 Mason, J.T., Sree Harsha, K.S., Chiotti, P.: Acta Crystallogr. B **26** (1970) 356.
71 B 1 Bruzzone, G., Fornasini, M.L., Merlo, F.: J. Less-Common Met. **25** (1971) 295.
71 F 1 Fornasini, M.L.: J. Less-Common Met. **25** (1971) 329.
71 L 1 Larson, A.C., Cromer, D.T.: Acta Crystallogr. B **27** (1971) 1875.
71 P 1 Palenzona, A.: J. Less-Common Met. **25** (1971) 367.
71 S 1 Schiltz, Jr., R.J., Prevender, T.S., Smith, J.F.: J. Appl. Phys. **42** (1971) 4680.
71 Z 1 Zmii, O.F., Gladyshevskij, E.I.: Sov. Phys. Crystallogr. **15** (1971) 817.
72 B 1 Buschow, K.H.J., Oppelt, A., Dormann, E.: Phys. Status Solidi (b) **50** (1972) 647.
72 D 1 Debray, D., Sougi, M., Meriel, P.: J. Chem. Phys. **56** (1972) 4325.
72 D 2 Debray, D., Sougi, M.: J. Chem. Phys. **57** (1972) 2156.
72 F 1 Fornasini, M.L., Merlo, F.: Acta Crystallogr. B **28** (1972) 3094.
72 P 1 Pahlman, J.E., Smith, J.F.: Metall. Trans. **3** (1972) 2423.
72 P 2 Prevender, T.S., Sinha, S.K., Smith, J.F.: Phys. Rev. B **6** (1972) 4438.
73 B 1 Bruzzone, G., Merlo, F.: J. Less-Common Met. **30** (1973) 303.
73 B 2 Bruzzone, G., Fornasini, M.L., Merlo, F.: J. Less-Common Met. **30** (1973) 361.
73 B 3 Buschow, K.H.J.: J. Less-Common Met. **33** (1973) 239.
73 D 1 Debray, D., Sougi, M.: J. Chem. Phys. **58** (1973) 1783.
73 D 2 Debray, D.: Phys. Status Solidi (a) **18** (1973) 227.
73 I 1 Ihrig, H., Vigren, D.T., Kübmer, J., Methfessel, S.: Phys. Rev. B **8** (1973) 4525.
73 J 1 Jan, J.P.: Phys. Rev. B **8** (1973) 3590.
73 L 1 Lüthi, B., Mullen, M.E., Andres, K., Bucher, E., Maita, J.P.: Phys. Rev. B **8** (1973) 2639.
73 M 1 Morin, P., Pierre, J.: Solid. State Commun. **13** (1973) 537.
73 M 2 Morin, P., Pierre, J.: Phys. Status Solidi (a) **17** (1973) 479.
73 S 1 Stewart, A.M.: Solid State Commun. **12** (1973) 455.
73 S 2 Stewart, A.M., Dunlop, J.B., Andreone, D., Costa, G.: J. Phys. Chem. Solids **34** (1973) 1939.
74 A 1 Aléonard, R., Morin, P., Pierre, J.: Colloques Internationaux du CNRS **242** (1974) 39.
74 B 1 Bruzzone, G., Fornasini, M.L., Merlo, F.: J. Less-Common Met. **35** (1974) 353.
74 B 2 Buschow, K.H.J.: J. Chem. Phys. **61** (1974) 4666.
74 B 3 Buschow, K.H.J., Oppelt, A.: J. Phys. F **4** (1974) 1246.
74 C 1 Chamard-Bois, R.: Thesis University of Grenoble (A.O. CNRS N° 9748) **1974** (unpublished).
74 D 1 Debray, D., Sakurai, J.: Phys. Rev. B **9** (1974) 2129.
74 D 2 Drits, M.E., Padezhnova, E.M., Miklina, N.V.: Izv. Akad. Nauk SSSR Met. **3** (1974) 225.
74 H 1 Hiraoka, T.: J. Phys. Soc. Jpn. **37** (1974) 1238.
74 M 1 Mason, J.T.: J. Less-Common Met. **37** (1974) 387.
74 M 2 Morin, P., Pierre, J., Chaussy, J.: Phys. Status Solidi (a) **24** (1974) 425.
74 M 3 Morin, P., Pierre, J., Rossat-Mignod, J., Knorr, K., Drexel, W.: Phys. Rev. B **9** (1974) 4932.
74 S 1 Stewart, A.M., Costa, G., Olcese, G.: Aust. J. Phys. **27** (1974) 383.
74 S 2 Stewart, A.M., Coles, B.R.: J. Phys. F **4** (1974) 458.
74 Z 1 Zmii, O.F., Gladyshevskij, E.I.: Visn. L'viv. Derzh. Univ., Ser. Khim. **15** (1974) 24.
75 A 1 Aléonard, R., Morin, P., Pierre, J., Schmitt, D.: Solid State Commun. **17** (1975) 599.
75 B 1 Buschow, K.H.J., De Jong, J.P., Zandbergen, H.W., Van Laar, B.: J. Appl. Phys. **46** (1975) 1352.
75 B 2 Buschow, K.H.J., Huiskamp, W.J., LeFever, H.Th., V. Steenwijk, F.J., Thiel, R.C.: J. Phys. F **5** (1975) 1625.
75 B 3 Bucher, E., Maita, J.P., Hull, G.W., Fulton, R.C., Cooper, A.S.: Phys. Rev. B **11** (1975) 440.
75 D 1 Debray, D., Wortmann, B.F., Methfessel, S.: Phys. Status. Solidi (a) **30** (1975) 713.
75 G 1 Goebel, U., Dormann, E., Buschow, K.H.J.: J. Phys. F **5** (1975) 2198.

75 M 1 Morin, P., Pierre, J.: Phys. Status. Solidi (a) **30** (1975) 549.
75 M 2 Morin, P., de Combarieu, A.: Solid State Commun. **17** (1975) 975.
75 M 3 Morin, P.: Thesis University of Grenoble (A.O. CNRS 9323) **1975** (unpublished).
75 S 1 Sierro, J., Bucher, E., Longinotti, L.D., Takayama, H., Fulde, P.: Solid State Commun. **17** (1975) 79.
76 A 1 Aléonard, R., Morin, P., Pierre, J., Schmitt, D.: J. Phys. F **6** (1976) 1361.
76 B 1 Bruzzone, G., Merlo, F.: J. Less-Common Met. **44** (1976) 259.
76 B 2 Buschow, K.H.J.: J. Less-Common Met. **44** (1976) 301.
76 B 3 Buschow, K.H.J., Schinkel, C.J.: Solid State Commun. **18** (1976) 609.
76 B 4 Bloch, J.M., Davidov, D., Felner, I., Shaltiel, D.: J. Phys. F **6** (1976) 1979.
76 D 1 Debray, D., Wortmann, B.F., Methfessel, S.: Phys. Rev. B **14** (1976) 4009.
76 E 1 Eckrich, K., Dormann, E., Oppelt, A., Buschow, K.H.J.: Z. Phys. B **23** (1976) 157.
76 M 1 Morin, P., Pierre, J., Schmitt, D., Drexel, W.: J. Phys. (Paris) **37** (1976) 611.
76 M 2 Morin, P., Waintal, A., Lüthi, B.: Phys. Rev. B **14** (1976) 2972.
76 M 3 Morin, P., Waintal, A., Lüthi, B., in: Proceedings of the 12th Rare Earth Research Conference, Vail, Colorado (Lundin, C.E., ed.), Denver: U.S. Bureau of Mines **1976**, p. 95.
76 M 4 Miedema, A., Boom, R., de Boer, F.: J. Less-Common Met. **46** (1976) 67.
76 S 1 Schäfer, W., Will, G., Buschow, K.H.J.: J. Phys. C **9** (1976) L 657.
77 B 1 Buschow, K.H.J., van Steenwijk, F.J.: Physica B **85** (1977) 122.
77 D 1 Dormann, E., Huck, M., Buschow, K.H.J.: J. Magn. Magn. Mater. **4** (1977) 47.
77 G 1 Goebel, U., Dormann, E., Buschow, K.H.J.: J. Magn. Magn. Mater. **6** (1977) 166.
77 H 1 Hasegawa, A., Yanase, A.: J. Phys. F **7** (1977) 1229.
77 H 2 Heinrich, G., Meyer, A.: Solid State Commun. **21** (1977) 21.
77 M 1 Morin, P., Rouchy, J., du Tremolet de Lacheisserie, E.: Phys. Rev. B **16** (1977) 3182.
77 S 1 Schäfer, W., Will, G., Buschow, K.H.J.: J. Magn. Magn. Mater. **4** (1977) 28.
77 S 2 Schmitt, D., Morin, P., Pierre, J.: Phys. Rev. B **15** (1977) 1698.
78 B 1 Buschow, K.H.J., Sherwood, R.C., Hsu, F.S.L., Knorr, K.: J. Appl. Phys. **49** (1978) 1510.
78 B 2 Buschow, K.H.J., Will, G., Bargouth, M.O.: J. Phys. C **11** (1978) 2405.
78 D 1 Drits, M.E., Rokhlin, L.L., Padezhnova, E.V., Guzzi, L.S.: Met. Sci. Heat Treat. **20** (1978) 771.
78 D 2 Déportes, J., Givord, D., Kebe, B.: Inst. Phys. Conf. Ser. **37** (1978) 278.
78 F 1 Fornasini, M.L., Chabot, B., Parthe, E.: Acta Crystallogr. B **34** (1978) 2093.
78 H 1 Hennion, B., Pierre, J.: J. Phys. F **8** (1978) 2617.
78 M 1 Morin, P., Pierre, J., Schmitt, D., Murani, A.: Solid State Commun. **25** (1978) 265.
78 M 2 Morin, P., Pierre, J., Schmitt, D., Givord, D.: Phys. Lett. A **65** (1978) 156.
78 M 3 Morin, P., Rouchy, J., Schmitt, D.: Phys. Rev. B **17** (1978) 3684.
78 M 4 Morin, P., Schmitt, D., du Trémolet de Lacheisserie, E.: Phys. Lett. A **69** (1978) 217.
78 M 5 Morin, P., Schmitt, D.: J. Phys. F **8** (1978) 951.
78 S 1 Schmitt, D., Morin, P., Pierre, J.: J. Magn. Magn. Mater. **8** (1978) 249.
79 A 1 Aléonard, R., Morin, P.: Phys. Rev. B **19** (1979) 3868.
79 D 1 De Graaf, H., Huiskamp, W.J., Thiel, R.C., LeFever, H.Th., Buschow, K.H.J.: Physica B **98** (1979) 60.
79 G 1 Givord, D., Morin, P., Schmitt, D.: Phys. Lett. A **73** (1979) 221.
79 H 1 Heinrich, G., Kappler, J.P., Meyer, A.: Phys. Lett. A **74** (1979) 121.
79 K 1 Kappler, J.P., Meyer, A.: J. Phys. F **9** (1979) 143.
79 L 1 Lueng, K.M., Huber, D.L., Lüthi, B.: J. Appl. Phys. **50** (1979) 1831.
79 L 2 Lüthi, B., Sommer, R., Morin, P.: J. Magn. Magn. Mater. **13** (1979) 198.
79 M 1 Merlo, F., Fornasini, M.L.: J. Less-Common Met. **64** (1979) 221.
79 P 1 Pierre, J., de Combarieu, A., Lagnier, R.: J. Phys. F **9** (1979) 1271.
79 S 1 Schmitt, D.: J. Phys. F **9** (1979) 1745.
80 B 1 Bouton, J.M., Clad, R., Herr, A., Mériel, P., Meyer, A., Vigneron, F.: J. Magn. Magn. Mater. **15–18** (1980) 49.
80 C 1 Clad, R., Bouton, J.M., Herr, A.: Phys. Status Solidi (b) **102** (1980) 357.
80 H 1 Hamaguchi, Y., Betsuyaku, H., Funuhashi, S.: J. Magn. Magn. Mater. **15–18** (1980) 377.
80 J 1 Jaussaud, C., Morin, P., Schmitt, D.: J. Magn. Magn. Mater. **22** (1980) 98.
80 K 1 Kappler, J.P., Krill, G., Ravet, M.F., Heinrich, G., Meyer, A.: J. Magn. Magn. Mater. **15–18** (1980) 965.
80 K 2 Krill, G., Kappler, J.P., Ravet, M.F., Amamou, A., Meyer, A.: J. Phys. F **10** (1980) 1031.
80 K 3 Knorr, K., Renker, B., Assmus, W., Lüthi, B., Takke, R., Lauter, H.J.: Z. Phys. B **39** (1980) 151.
80 M 1 Morin, P., Schmitt, D., du Trémolet du Lacheisserie, E.: Phys. Rev. B **21** (1980) 1742.
80 M 2 Morin, P., Schmitt, D., Vettier, C., Rossat-Mignod, J.: J. Phys. F **10** (1980) 1575.
80 M 3 Morin, P., Schmitt, D., du Trémolet de Lacheisserie, E.: J. Magn. Magn. Mater. **15–18** (1980) 601.

80 P 1 Pierre, J.: J. Magn. Magn. Mater. **15–18** (1980) 1233.
80 P 2 Pierre, J., Murani, A., in: Crystalline Electric Field and Structural Effects in f Electron Systems (Crow, J.E., Guertin, R.P., Mihalisin, T.W., eds.), New York: Plenum Press **1980**, p. 607.
80 R 1 Ruden, P., Micklitz, H.: J. Magn. Magn. Mater. **15–18** (1980) 993.
80 S 1 Sousa, J.B., Pinto, R.P., Amado, M.M., Moreira, J.M., Braga, M.E., Morin, P., Ausloos, M.: J. Phys. F **10** (1980) 1809.
80 S 2 Sousa, J.B., Pinto, R.P., Amado, M.M., Moreira, J.M., Braga, M.E., Morin, P., Aléonard, R., in: The Rare Earth in Modern Science and Technology (McCarthy, G.J., Rhyne, J.J., Silber, H.B., eds.), New York: Plenum Press, Vol. 2 **1980** p. 431.
80 S 3 Sousa, J.B., Amado, M.M., Pinto, R.P., Moreira, J.M., Braga, M.E., Ausloos, M., Leburton, J.P., Van Hay, J.C., Clippe, P., Vigneron, J.P., Morin, P.: J. Phys. F **10** (1980) 933.
80 V 1 Vigneron, F., Sougi, M., Mériel, P., Herr, A., Meyer, A.: J. Phys. (Paris) **41** (1980) 123.
80 V 2 Vigneron, F., Bonnet, M., Kahn, R., in: Crystalline Electric Field and Structural Effect in f Electron Systems (Crow, J.E., Guertin, R.P., Mihalisin, T.W., eds.), New York: Plenum Press **1980**, p. 513.
80 V 3 Van der Linden, H.W.M., Nieuwenhys, G.J., Dokter, H.D., Davidov, D., Felner, I.: J. Magn. Magn. Mater. **15–18** (1980) 42.
80 Z 1 Zarechnyuk, O.S., Drits, M.E., Rykhal', R.M., Kinzhibalo, V.V.: Russ. Metall. **5** (1980) 214.
81 C 1 Clad, R., Bouton, J.M.: J. Phys. F **11** (1981) 207.
81 C 2 Clad, R., Bouton, J.M., Herr, A.: C.R. Acad. Sci. Paris **292** (1981) 999.
81 G 1 Galera, R.M., Murani, A.P., Pierre, J.: J. Magn. Magn. Mater. **23** (1981) 317.
81 K 1 Kappler, J.P., Krill, G., Ravet, M.F., Besnus, M.J., Meyer, A., in: Valence Fluctuations in Solids (Falicov, L.M., Hanke, W., Maple, M.B., eds.), Amsterdam: North-Holland **1981**, p. 271.
81 L 1 Loidl, A., Knorr, K., Müllner, M., Buschow, K.H.J.: J. Appl. Phys. **52** (1981) 1433.
81 M 1 Morin, P., Schmitt, D.: Phys. Rev. B **23** (1981) 5936.
81 M 2 Morin, P., Schmitt, D., Vettier, C.: J. Phys. F **11** (1981) 1487.
81 P 1 Peukert, H., Schilling, J.S.: Z. Phys. B **41** (1981) 217.
81 P 2 Pierre, J., Murani, A.P., Galera, R.M.: J. Phys. F **11** (1981) 679.
81 P 3 Pott, R., Schefzyk, R., Boksch, W., Wohlleben, D., in: Valence Fluctuations in Solids (Falicov, L.M., Hanke, W., Maple, M.B., eds.), Amsterdam: North-Holland **1981**, p. 337.
81 R 1 Rouchy, J., Morin, P., du Trémolet de Lacheisserie, E.: J. Magn. Magn. Mater. **23** (1981) 59.
81 R 2 Rossi, D., Marazza, R., Mazzone, D., Ferro, R.: J. Less-Common Met. **78** (1981) P 1.
82 B 1 Besnus, M.J., Kappler, J.P., Lemius, B., Benakki, M., Meyer, A.: J. Appl. Phys. **53** (1982) 2158.
82 D 1 Dormann, E., de Graaf, H., Thiel, R.C., Buschow, K.H.J.: J. Magn. Magn. Mater. **30** (1982) 231.
82 D 2 de, Graaf H., Thiel, R.C., Buschow, K.H.J.: J. Phys. F **12** (1982) 2079.
82 G 1 Galera, R.M., Pierre, J., Pannetier, J.: J. Phys. F **12** (1982) 993.
82 G 2 Galera, R.M., Pierre, J., Murani, A.P., in: Valence instabilities (Wachter, P., Boppart, H., eds.), Amsterdam: North-Holland **1982**, p. 519.
82 M 1 Mazzone, D., Rossi, D., Marazza, R., Ferro, R.: J. Less-Common Met. **84** (1982) 301.
82 P 1 Padezhnova, E.M., Mel'nik, E.V., Miliyevskiy, R.A., Dabatkina, T.V., Kinzhibalo, V.V.: Russ. Metall. **4** (1982) 185.
82 V 1 Vigneron, F., Bonnet, M., Herr, A., Schweizer, J.: J. Phys. F **12** (1982) 223.
83 A 1 Adamyan, V.Y., Karagebakyan, G.G., Melikyan, M.A., Abovyan, E.S.: Phys. Met. Metallogr. USSR **55** (1983) 36.
83 B 1 Besnus, M.J., Panissod, P., Kappler, J.P., Heinrich, G., Meyer, A.: J. Magn. Magn. Mater. **31–34** (1983) 227.
83 B 2 Besnus, M.J., Kappler, J.P., Meyer, A.: Solid State Commun. **48** (1983) 835.
83 C 1 Contardi, V., Zanicchi, G., Marazza, R., Ferro, R.: J. Less-Common Met. **90** (1983) L 25.
83 G 1 Galera, R.M., Pierre, J., Voiron, J.: Solid State Commun. **46** (1983) 45.
83 G 2 Givord, D., Morin, P., Schmitt, D.: J. Magn. Magn. Mater. **40** (1983) 121.
83 K 1 Kadomatsu, H., Kurisu, M., Kitai, T., Okamoto, T., Fujiwara, H.: Phys. Lett. A **94** (1983) 178.
83 K 2 Kido, H., Hoshikawa, T., Shimada, M., Koizumi, M.: Phys. Status Solidi (a) **80** (1983) 601.
83 M 1 Mazzone, D., Rossi, D., Marazza, R., Ferro, R.: J. Less-Common Met. **90** (1983) L 35.
83 S 1 Sousa, J.B., Pinto, R.P., Braga, M.E., Aléonard, R., Morin, P., Schmitt, D.: J. Phys. F **13** (1983) 827.
83 V 1 Vigneron, F.: Thesis, University of Paris 6 **1983** (unpublished).
83 V 2 V. Eynatten, G., Wang, C., Dixon, N., Fritz, L., Hanna, S.: Z. Phys. B **51** (1983) 37.
84 A 1 Aléonard, R., Morin, P.: J. Magn. Magn. Mater. **42** (1984) 151.
84 K 1 Kropp, H., Dormann, E., Köbler, U., Assmus, W.: J. Phys. F **14** (1984) 2177.
84 K 2 Kitai, T., Fujii, H., Okamoto, T., Yashimoto, Y.: Solid State Commun. **52** (1984) 407.

84 K 3 Kido, H., Hoshikawa, T., Shimada, M., Koizumi, M.: Phys. Status Solidi (a) **83** (1984) 561.
84 L 1 Lanz, D., Schmidt, H., Ewert, S., Boksch, W., Pott, R., Wohlleben, D.: Solid State Commun. **52** (1984) 759.
84 M 1 Morin, P., Williamson, S.J.: Phys. Rev. B **29** (1984) 1425.
84 P 1 Pierre, J., Galera, R.M., Bouillot, J.: J. Magn. Magn. Mater. **42** (1984) 139.
85 A 1 Aléonard, R., Morin, P.: J. Magn. Magn. Mater. **50** (1985) 128.
85 A 2 Aléonard, R., Morin, P.: Solid State Commun. **56** (1985) 627.
85 B 1 Blumenröder, S., Zirngiebl, E., Güntherodt, G., Jayaraman, A., Batlogg, B., Meyer, A., Fisk, Z.: J. Magn. Magn. Mater. **47–48** (1985) 318.
85 F 1 Fujii, H., Kitai, T., Uwatoko, Y., Okamoto, T.: J. Magn. Magn. Mater. **52** (1985) 428.
85 G 1 Giraud, M., Morin, P., Schmitt, D.: J. Magn. Magn. Mater. **52** (1985) 41.
85 M 1 Mock, R., Hillebrands, B., Schmidt, H., Grüntherodt, G., Fizk, Z., Meyer, A.: J. Magn. Magn. Mater. **47–48** (1985) 312.
85 P 1 Pierre, J., Galera, R.M., Siaúd, E.: J. Phys. (Paris) **46** (1985) 621.
85 S 1 Schmitt, D., Levy, P.M.: J. Magn. Magn. Mater. **49** (1985) 15.
85 V 1 Vigneron, F., Bonnet, M., Chappert, J.: J. Phys. F **15** (1985) 181.
85 W 1 Walter, U., Fizk, Z., Holland-Moritz, E.: J. Magn. Magn. Mater. **47–48** (1985) 159.
86 G 1 Giraud, M., Morin, P., Rouchy, J., Schmitt, D.: J. Magn. Magn. Mater. **59** (1986) 255.
86 G 2 Giraud, M., Morin, P.: J. Magn. Magn. Mater. **58** (1986) 135.
86 M 1 Morin, P.: unpublished data, **1986**.

2.8 Compounds based on rare earth elements and B

2.8.1 Binary rare earth borides

The following types of binary rare earth borides have been reported [61 G 1]: RB_2, R_2B_5, RB_4, RB_6, and RB_{12}.

2.8.1.1 RB_2 compounds

The magnetic properties of the diboride compounds RB_2 were determined on polycrystalline material obtained by fusing stoichiometric proportions of the starting materials (rare earth elements 99.9% purity, B 99.99% purity) in an arc furnace. X-ray diffraction showed that the samples were single-phase in the cases of R = Tb, Dy, Ho and Er. The X-ray diagrams were indexed on the basis of the hexagonal AlB_2-type unit cell. The lattice constants are given in Table 1. They are in good agreement with data in literature. It proved impossible to prepare AlB_2-type compounds with rare earth elements lighter than R = Tb.

The magnetic properties of the diborides with R = Tb, Dy, Ho and Er are summarized in Table 1. Above the magnetic ordering temperature T_C the magnetic susceptibility displays Curie-Weiss behavior with effective magnetic moments p_{eff} close to the corresponding value of $g\mu_B\sqrt{J(J+1)}$. Except in the case of TbB_2 one observers considerable differences between T_C and the paramagnetic Curie temperature Θ derived from extrapolations of the χ^{-1} vs. T plots. This suggests that the magnetic ordering phenomena are more complicated than simple ferromagnetic ordering. This follows also from the shape of the magnetization vs. temperature curves of TbB_2 and DyB_2 (Fig. 1), which seem to involve two steps. Studies of the magnetic field dependence of the magnetization at 4.2 K suggest that relatively strong magneto-crystalline anisotropies are involved. For all the compounds investigated saturation was still not reached at 18 kOe, the ultimate field strength applied. This anisotropy is very probably induced by crystal fields. The magnetic moments p_m attained with 18 kOe are listed in Table 1; they fall appreciably below the corresponding values of $gJ\mu_B$ [77 B 1].

Table 1. RB_2. Room-temperature lattice constants and magnetic data for polycrystalline rare earth diborides (AlB_2(h)-type structure).

R	a	c	T_C	Θ	p_{eff}	p_m [1])	Ref.
	Å		K		μ_B/f.u.		
Tb	3.290	3.878	151	151	9.96	4.0	77 B 1
Dy	3.287	3.845	55	33	10.7	5.4	61 G 1, 77 B 1
Ho	3.281	3.813	15	25	10.2	7.5	77 B 1
Er	3.271	3.782	16	9	9.47	5.1	77 B 1

[1]) Measured at $T = 4.2$ K and $H = 18$ kOe.

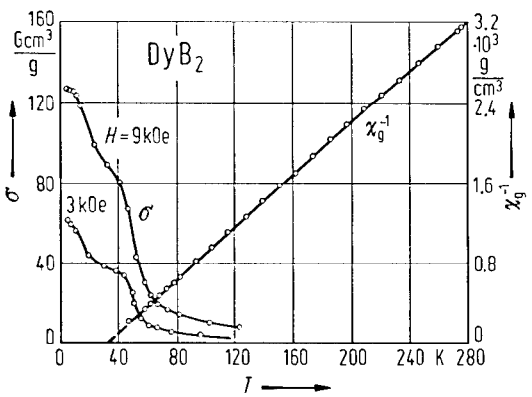

Fig. 1. DyB_2. Temperature dependence of magnetization and reciprocal magnetic susceptibility for polycrystalline sample [77 B 1].

2.8.1.2 R_2B_5 compounds

Table 2. R_2B_5. Magnetic data [77 B 2].

R	Θ	T_N
	K	
Pr	14	15.1
Nd	14	32.7
Sm		23.5
Gd		50

2.8.1.3 RB_4 compounds

There exists a wide discrepancy regarding the paramagnetic Curie temperatures reported in the various investigations which may be due to the large anisotropy in these compounds [81 G 1] which gives rise to different values of the magnetic susceptibility when measured parallel or perpendicular to the tetragonal *c* direction. The various investigations may refer to measurements involving a prevalence of crystallographic directions.

PrB_4 shows a ferromagnetic phase transition while for the other RB_4 compounds the transition is of the antiferromagnetic type.

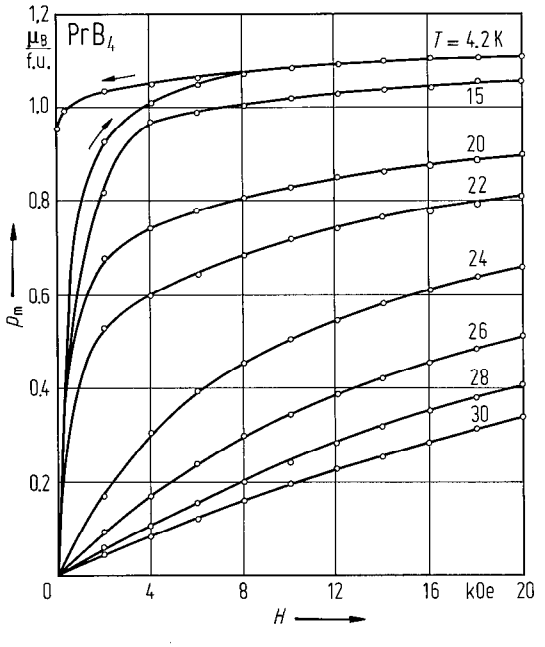

Fig. 2. PrB_4. Magnetization curves for polycrystalline sample [76 B 1].

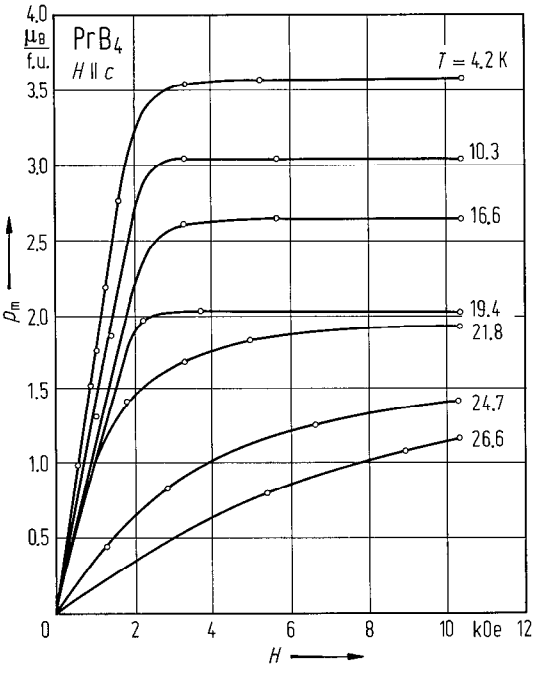

Fig. 3. PrB_4. Magnetization curves for the tetragonal *c* direction of a single crystal [76 B 1, 79 E 1].

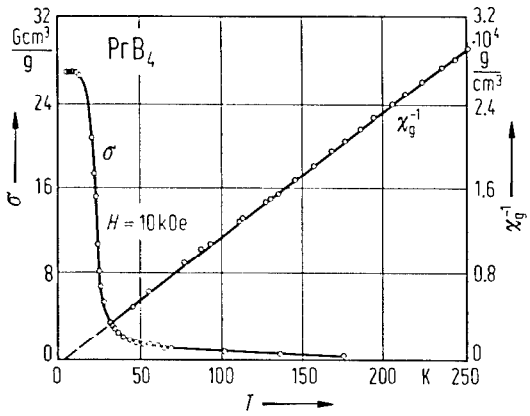

Fig. 4. PrB_4. Magnetization ($H = 10$ kOe) and reciprocal magnetic susceptibility as a function of temperature for polycrystalline sample [72 B 1, 77 B 1].

Magnetic susceptibility measurements [81 G 1] carried out on single crystals of TbB_4 along and perpendicular to the tetragonal c axis indicate a strong anisotropy favouring the ab plane, the magnetic moments being perpendicular to the c axis ($\Theta_{\parallel} = -48$ K, $\Theta_{\perp} = -18$ K), Fig. 5. At 4.2 K the variation in the magnetization as a function of magnetic field applied perpendicular to the c axis and for various directions in the ab plane [81 G 1] is explained by a spin-flipping effect and strongly suggests that the direction of antiferromagnetism is along the a or b axis, Fig. 6. Neutron diffraction experiments confirmed a colllinear antiferromagnetic arrangement of the moments along the a or the b axis. A magnetic moment $p_R = 7.7\ \mu_B$/Tb at 4.2 K was calculated from the measured intensities [81 G 1].

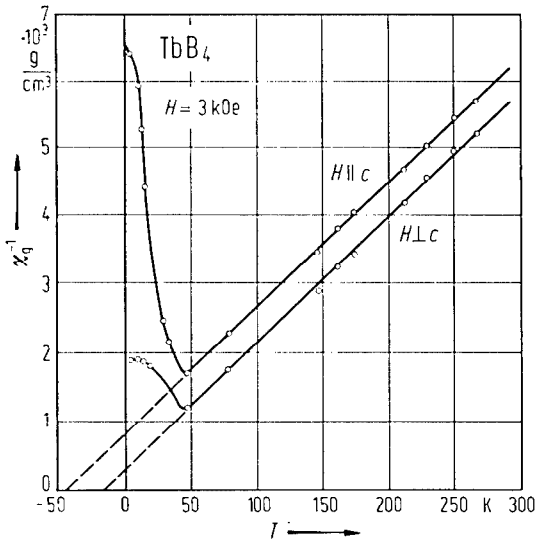

Fig. 5. TbB_4. Variation in the reciprocal magnetic susceptibilities, $\chi_{\parallel}^{-1}$ and $\chi_{\perp}^{-1}$, parallel and perpendicular to the tetragonal c axis of a single crystal as a function of temperature ($H = 3$ kOe) [81 G 1].

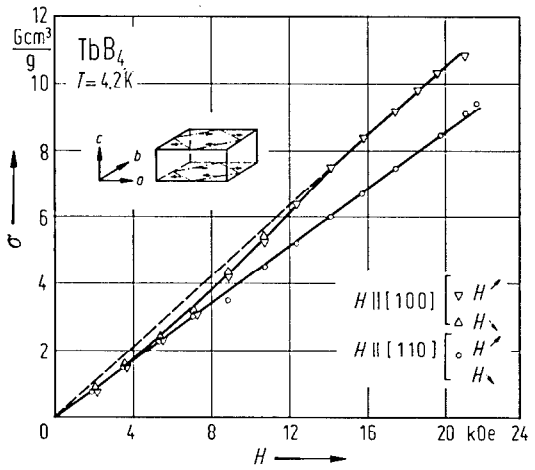

Fig. 6. TbB_4. Variation in the magnetization as a function of magnetic field applied perpendicular to the tetragonal c axis at 4.2 K for a single crystal [81 G 1].

As for ErB_4 and in contrast with those for TbB_4, the magnetic susceptibility measurements [81 G 1] performed on single crystals of HoB_4 indicate a strong anisotropy favouring the tetragonal c axis ($\Theta_{\parallel} = -9.8$ K and $\Theta_{\perp} = -13.4$ K), Fig. 7. $T_N \simeq 6$ K determined on HoB_4 single crystals [81 G 1] is lower than the value obtained from powder samples.

The variation in the magnetization as a function of magnetic field applied along the c axis at 2.25 K [81 G 1] shows that two metamagnetic transitions occur, Fig. 8. When the magnetic field is applied normal to the magnetic moments directed along the c axis [81 G 1], the variation in the magnetization as a function of magnetic field at low temperatures shows a transition between two antiferromagnetic phases, the high-field one having the higher magnetic susceptibility, Fig. 9.

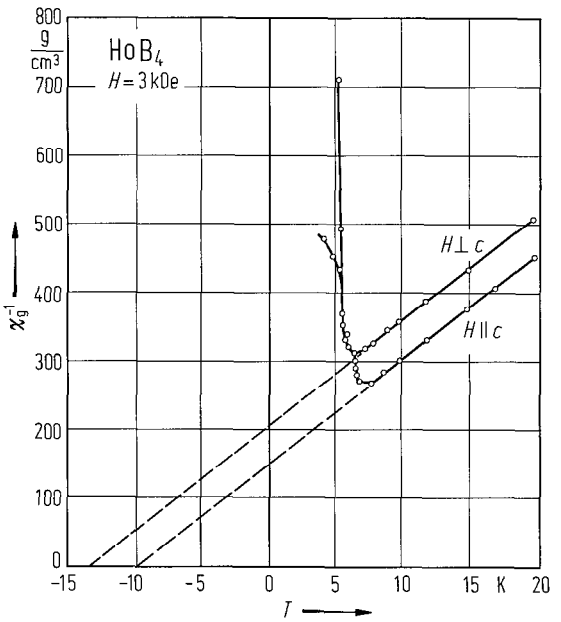

Fig. 7. HoB_4. Variation in the reciprocal magnetic susceptibilities, $\chi_{\parallel}^{-1}$ and $\chi_{\perp}^{-1}$, parallel and perpendicular to the tetragonal c axis of a single crystal as a function of temperature ($H=3$ kOe, $\Theta_{\parallel}=-9.8$ K, $\Theta_{\perp}=-13.4$ K) [81 G 1].

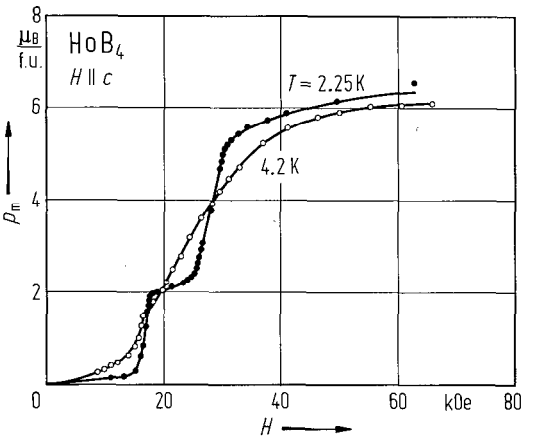

Fig. 8. HoB_4. Variation in the magnetization as a function of magnetic field applied along the tetragonal c axis at 2.25 K and at 4.2 K for a single crystal [81 G 1].

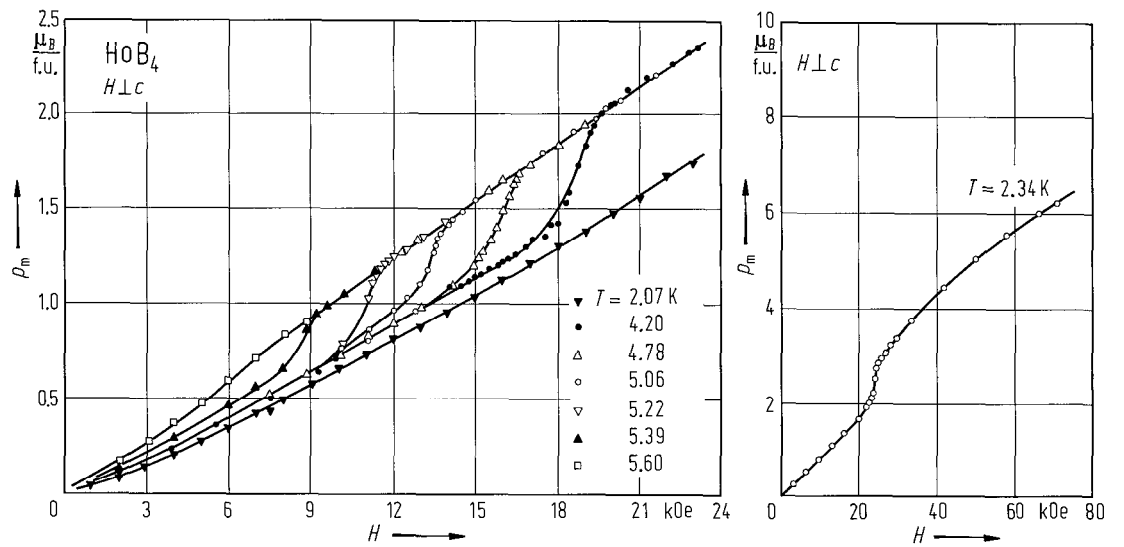

Fig. 9. HoB_4. Variation in the magnetization as a function of magnetic field applied normal to the tetragonal c axis at different temperatures for a single crystal [81 G 1].

Measurements performed on single crystals of ErB_4 [81 G 1] show strong anisotropy favouring the tetragonal c axis ($\Theta_{\parallel} = 13\,K$, $\Theta_{\perp} = -18\,K$).

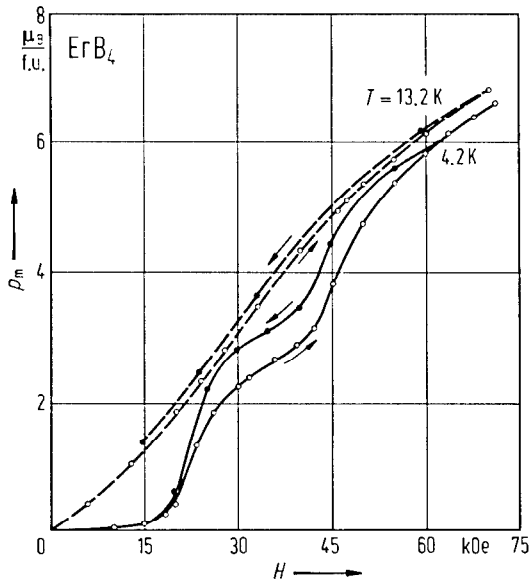

Fig. 10. ErB_4. Magnetization curves for a polycrystalline sample [76 B 1].

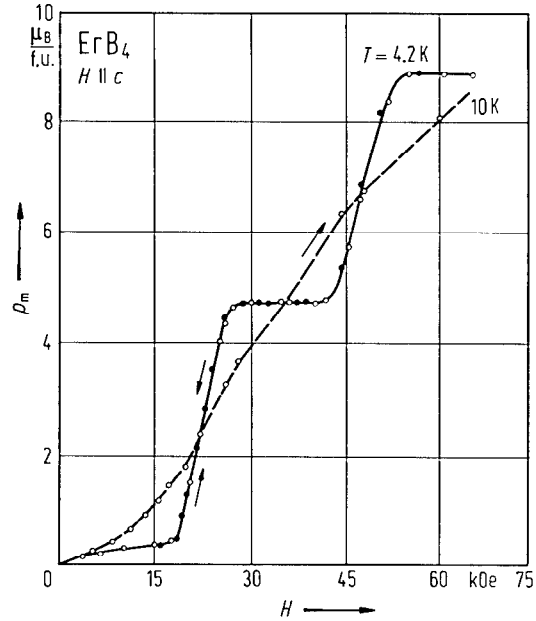

Fig. 11. ErB_4. Magnetization curves for the tetragonal c direction of a single crystal [76 B 1].

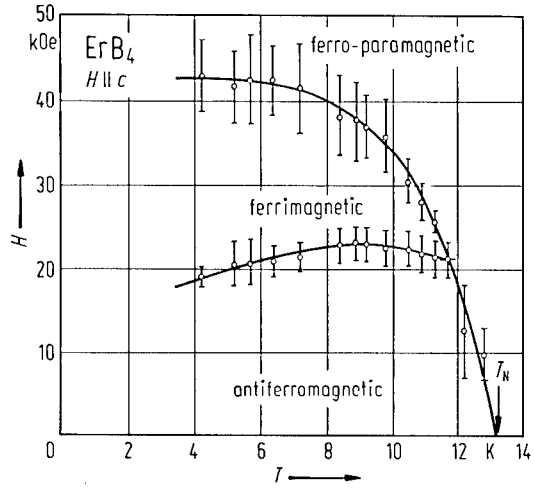

Fig. 12. ErB_4. $H-T$ phase diagram for a single crystal and the magnetic field along the tetragonal c axis. The three phases meet at $H = 26(1)\,kOe$ and $T = 11.4(2)\,K$ [79 P 1, 81 G 1].

Table 3. RB_4. Room-temperature lattice constants and magnetic data for polycrystalline rare earth tetraborides (UB_4(t)-type structure).

R	a	c	p_{eff}	Θ	p_s	T_N	Ref.
	Å		μ_B/f.u.	K	μ_B/f.u.	K	
Y	7.105	4.096	$\chi_m = -3.2 \cdot 10^{-5}$ cm^3 mol^{-1}				72 B 1
La	7.327	4.182	$\chi_m = -1.5 \cdot 10^{-5}$ cm^3 mol^{-1}				72 B 1
Ce	7.208	4.092	no CW behaviour				72 B 1, 77 B 1, 77 B 2
Pr	7.246	4.121	3.53, 3.15	5···27	1.54	24···25 [1])	72 B 1, 76 B 1, 77 B 1, 77 B 2
Nd	7.225	4.103	3.61	− 12		6.85···7	72 B 1, 77 B 1, 77 B 2
Sm	7.178	4.072	no CW behaviour			26···57	72 B 1, 76 B 1, 77 B 1, 77 B 2
Gd	7.145	4.050	7.81···8.07	− 66···−50		42···45.3	67 P 1, 71 F 2, 72 B 1, 76 B 1, 77 B 1, 77 B 2
Tb	7.122	4.032	9.30···9.72	− 43···−22		43···45	71 F 2, 72 B 1, 76 B 1, 77 B 1, 77 B 2
Dy	7.102	4.018	10.26···10.6	− 22···−11		20.7···23	67 P 1, 71 F 2, 72 B 1, 76 B 1, 76 S 1, 77 B 1, 77 B 2
Ho	7.086	4.009	10.4···10.8	− 21···−7		7···9	71 F 2, 72 B 1, 76 B 1, 77 B 1, 77 B 2
Er	7.070	3.996	9.52, 9.29	− 10···15		13···15	67 P 1, 71 F 2, 72 B 1, 76 B 1, 76 S 1, 77 B 1, 77 B 2
Tm	7.050	3.99	7.6···7.68	− 23···3		11.8	67 P 1, 77 B 2
Yb	7.059	3.992		−440		10	63 P 1, 77 B 2
Lu	6.997	3.938	$\chi_m = -4.6 \cdot 10^{-5}$ cm^3 mol^{-1}				

[1]) Curie temperature T_C.

2.8.1.4 RB_6 compounds

The absence of magnetic order and the peculiar temperature dependence of the magnetic susceptibility in SmB_6, Fig. 13, as well as the temperature-induced change from semiconductor to metal in this compound, have been discussed by various authors in terms of the phenomenology of intervalence compounds [69 M 1, 70 C 1, 71 M 1].

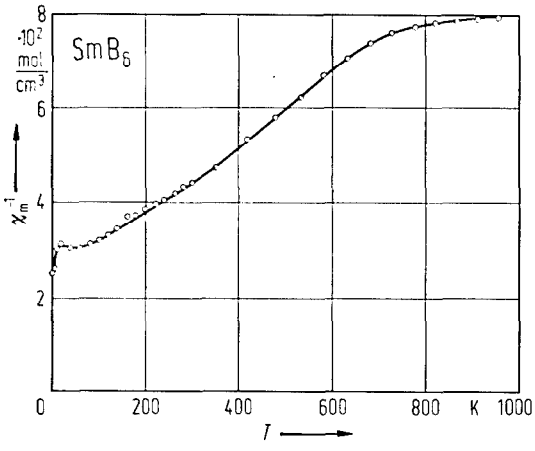

Fig. 13. SmB_6. Reciprocal magnetic molar susceptibility as a function of temperature for polycrystalline sample [69 M 1].

Deviant behaviour is shown by EuB_6 which commonly is found to be a ferromagnet whereas all the other magnetic RB_6 compounds are antiferromagnets. Explanations of the deviating ordering type have been made in terms of superexchange [68 G 1] and the Bloembergen-Rowland interaction [71 F 1, 71 W 1, 75 G 1]. Measurements on a EuB_6 single crystal indicate, however, that EuB_6, too, is antiferromagnetic [77 I 1].

The introduction of Eu vacancies decreases the carrier concentration and makes EuB_6 ferromagnetic. A comparison of the magnetic properties of a polycrystalline sample containing Eu defects with those of the EuB_6 single crystal is shown in Fig. 14.

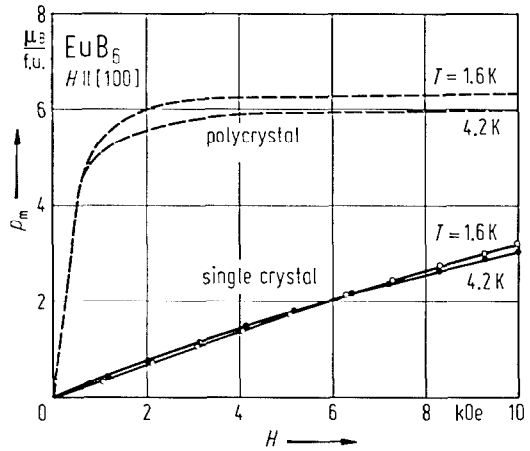

Fig. 14. EuB_6. Magnetization as a function of applied magnetic field. Circles: single crystal. Magnetic field is in the [100] direction. Dashed lines: polycrystal containing Eu defects [77 I 1].

Table 4. RB_6. Room-temperature lattice constants and magnetic data for rare earth hexaborides (CaB_6(c)-type structure).

R	a Å	p_{eff} μ_B/f.u.	Θ K	p_s μ_B/f.u.	T_N K	Ref.
Y	4.093					64 M 1
La	4.153	$\chi_m = -6.1 \cdot 10^{-5}$ cm^3 mol^{-1}				64 M 1, 70 E 1
Ce	4.134	2.49	− 76		3.0	64 M 1, 67 P 2, 68 M 1
Pr	4.123	3.56···3.59	− 68···−44		7	64 M 1, 68 G 1, 68 H 1, 68 M 1
Nd	4.116	3.54	− 42		8.45···8.6	64 M 1, 67 P 2, 68 H 1, 68 M 1
Sm	4.125	no CW behaviour				64 M 1, 67 P 2
Eu	4.174	8.1	8...9	8.5		64 M 1, 67 P 2, 68 G 1, 68 M 1, 71 H 1, 77 I 1
Gd	4.097	7.28···8.01	− 55···−60		13.5···18	61 C 1, 62 C 1, 64 M 1, 67 P 2, 68 M 1
Tb	4.094	9.43	− 35		23	64 M 1, 67 P 2, 68 M 1
Dy	4.13	10.63	− 21		21	64 M 1, 67 P 2, 68 M 1
Ho	4.12				9	64 M 1, 68 M 1
Yb	4.138		−161			64 M 1
Lu	4.11					64 M 1

2.8.1.5 RB_{12} compounds

LuB_{12} is reported to become superconducting below 0.48 K [68 M 1]. The compound YbB_{12} shows unusual electrical resistance behavior [69 F 1].

Table 5. RB_{12}. Room-temperature lattice constants and magnetic data for RB_{12} compounds (UB_{12}(c)-type structure).

R	a Å	p_{eff} μ_B/f.u.	Θ K	T_N K	Ref.
Dy	7.501	10.85	−23		61 L 1, 79 B 1
Ho	7.492			6.5	61 L 1, 68 M 1
Er	7.484			6.5	61 L 1, 68 M 1
Tm	7.476			4.2	61 L 1, 68 M 1
Lu	7.464				61 L 1

2.8.2 Ternary compounds

2.8.2.1 Compounds with RM_4B_4 stoichiometry (M = Ru, Rh, Os, Ir)

The degree of crystallographic order is an important parameter for the superconducting and magnetic interactions in $CeCo_4B_4$-type compounds. Experiments on pseudo-ternary rare earth compounds were used as a method for studying these interactions [79 K 2, 80 K 1, 80 K 2, 80 K 3, 81 K 1].

The $CeCo_4B_4$-type crystal structure of the RRh_4B_4 compounds contains Rh_4B_4 "clusters" consisting of interpenetrating Rh and B tetrahedra. The 4d electrons of Rh are relatively confined within the "clusters", producing sharp structure in the conduction electron density of states near the Fermi level. This could account for superconductivity with high values of the superconducting transition temperature T_s and the occurrence of itinerant electron ferromagnetism. Localization of the conduction electrons within the "clusters" isolates them from rare earth ions, leading to a decreased exchange interaction between the conduction-electron spins and the rare earth magnetic moments. This allows the compounds to retain their superconductivity and produces magnetic ordering at temperatures that are comparable to T_s. The T_s of several RRh_4B_4 compounds have been found to be sensitive to α-particle damage [79 R 2, 80 R 1, 81 D 2], a feature common to superconducting transition-metal cluster compounds. The other important ingredient for magnetic superconductors is the ordered rare earth sublattice which insures long-range magnetic order.

Table 6. RM_4B_4 (M = Ru, Rh, Os, Ir). Room-temperature lattice parameters and magnetic or superconducting data. TDP: temperature-dependent paramagnetism.

R	a	c	p_{eff}	Θ	T_C	T_N	T_s	Ref.
	Å		μ_B/f.u.	K				
				RRu_4B_4 ($LuRu_4B_4$-type)				
Sc	7.346	14.895					7.2	79 K 1, 80 K 1
Y	7.454	14.994					1.4	77 J 1, 79 K 1
Ce	7.470	15.085						77 J 1
Pr	7.505	15.066						77 J 1
Nd	7.502	15.053			1.62 [1]			77 J 1
Sm	7.482	15.049						77 J 1
Eu	7.477	15.035						77 J 1
Gd	7.470	15.009			4.55 [1]			77 J 1
Tb	7.456	14.995			4.30 [1]			77 J 1
Dy	7.453	14.983	10.22	13.3	2.65 [1]			77 J 1, 83 H 1
Ho	7.442	14.975			2.58 [1]			77 J 1
Er	7.438	14.972			2.16 [1]			77 J 1
Tm	7.429	14.965						77 J 1
Yb	7.427	14.962						77 J 1
Lu	7.419	14.955					2.0	77 J 1, 79 K 1
				RRh_4B_4 ($CeCo_4B_4$-type)				82 M 2
Y	5.308	7.403					11.3	77 M 1, 77 V 1
							10.8	79 W 1
Nd	5.333	7.468					5.3	77 M 1, 77 V 1
			3.58(5)	− 6.2(10)		0.89, 1.31		79 H 1
Sm	5.312	7.430					2.5	77 M 1, 77 V 1
			0.632	− 1.93		0.87	2.7	79 H 2
Gd	5.309	7.417			5.62			77 M 1, 77 V 1
			7.94	5.6	5.8			80 M 1, 81 A 1
Tb	5.303	7.404			7.08			77 M 1, 77 V 1
					7.4			80 M 1
Dy	5.302	7.395			12.03			77 M 1, 77 V 1
			10.55	19.3	10.7			80 M 1
Ho	5.293	7.379			6.56			77 M 1, 77 V 1
			10.6	6.5	6.7			80 M 1, 80 O 1
Er	5.292	7.374					8.5	77 M 1, 77 V 1
			9.62(15)	1(1)	0.93		8.7	77 F 1, 77 M 2, 78 O 1
Tm	5.287	7.359					9.8	77 M 1, 77 V 1
			7.51(3)	− 0.46(25)		0.4		81 H 1
Lu	5.294	7.359					11.7	77 M 1, 77 V 1
							11.5	79 W 1
				ROs_4B_4 ($NdCo_4B_4$-type)				79 R 1, 79 R 3
La	7.611	3.998	weak TDP					
Ce	7.538	4.005	weak TDP					
Pr	7.567	4.002	3.76	− 9				
Nd	7.552	4.003	3.88	− 6				
Sm	7.526	4.009	1.65 [2]					

(continued)

[1]) Given as unspecified magnetic phase transition temperature.
[2]) Room-temperature value.

Table 6 (continued).

R	a	c	p_{eff}	Θ	T_C	T_N	T_s	Ref.
	Å		μ_B/f.u.	K				
				RIr_4B_4 ($NdCo_4B_4$-type)				79 R 1, 79 R 3
Y	7.547	3.980	0					
La	7.672	3.974	weak TDP					
Ce	7.642	3.970	2.51	−16				
Pr	7.629	3.974	3.70	−18				
Nd	7.616	3.974	3.78	19				
Sm	7.590	3.976	1.75 [2])					
Gd	7.571	3.979	8.07	35				
Tb	7.557	3.979	9.89	6				
				RIr_4B_4 ($CeCo_4B_4$-type)				79 K 2
Ho							2.0	
Er	5.408	7.278					2.1	
Tm	5.404	7.281					1.6	

[2]) Room-temperature value.

The samples for $NdRh_4B_4$ were prepared off stoichiometry from RRh_4B_4 composition because the additional RhB stabilizes the $NdRh_4B_4$-phase.

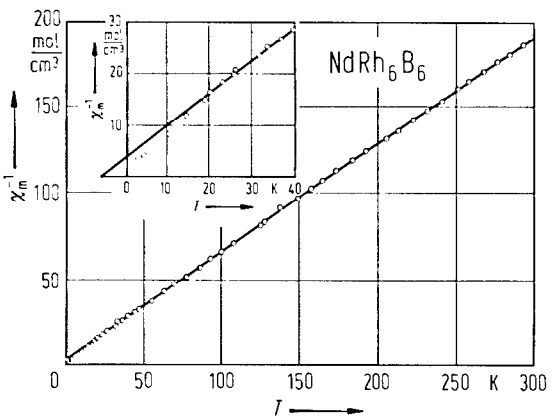

Fig. 15. $NdRh_6B_6$. Inverse magnetic molar susceptibility vs. temperature. The solid line represents a Curie-Weiss law with $p_{eff} = 3.58\,\mu_B$/Nd and $\Theta = -6.2(10)$ K [79 H 1].

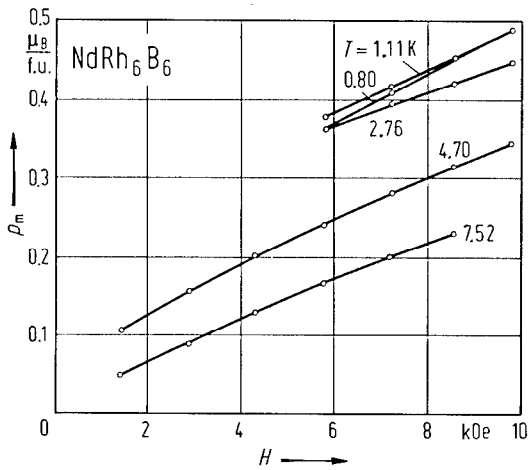

Fig. 16. $NdRh_6B_6$. Magnetization vs. applied magnetic field isotherms at various temperatures between 0.80 and 7.52 K [79 H 1].

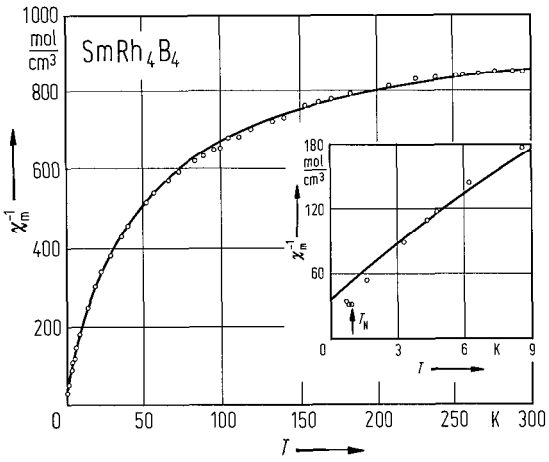

Fig. 17. $SmRh_4B_4$. Inverse magnetic molar susceptibility vs. temperature. The arrow represents the phase transition temperature defined by the λ-type anomaly observed at 0.87 K in the heat capacity data. The curve represents the sum of a Curie-Weiss law with $p_{eff} = 0.632\,\mu_B$/Sm and $\Theta = -1.93$ K and a temperature-independent Van Vleck term [79 H 2].

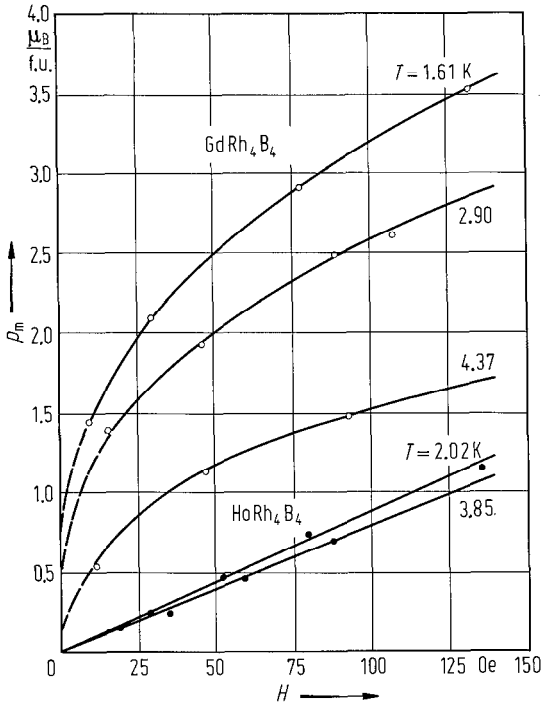

Fig. 18. $GdRh_4B_4$, $HoRh_4B_4$. Low-field magnetization curves corrected for demagnetization of $GdRh_4B_4$ (open circles) and $HoRh_4B_4$ (solid circles) at various temperatures below T_C [81 A 1].

The deviation of the data for the magnetic susceptibility of $DyRh_4B_4$ from Curie-Weiss behavior below $\simeq 50$ K apparently results from crystalline electric field splitting of the Hund's rule ground state of Dy^{3+}.

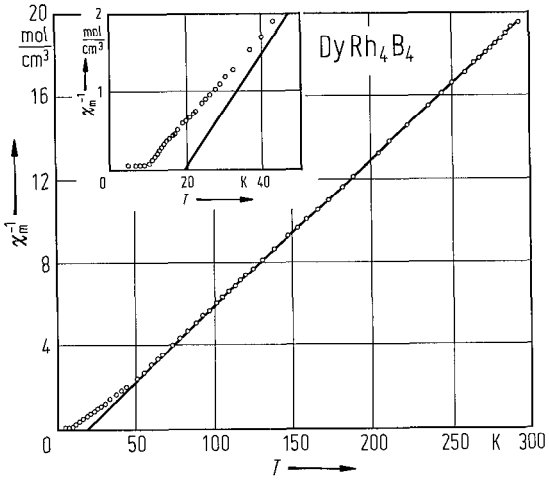

Fig. 19. $DyRh_4B_4$. Inverse magnetic molar susceptibility χ_m^{-1} vs. temperature. The solid line represents a Curie-Weiss fit to the high-temperature data with $p_{eff} = 10.55\,\mu_B$/Dy and $\Theta = 19.3$ K [80 M 1].

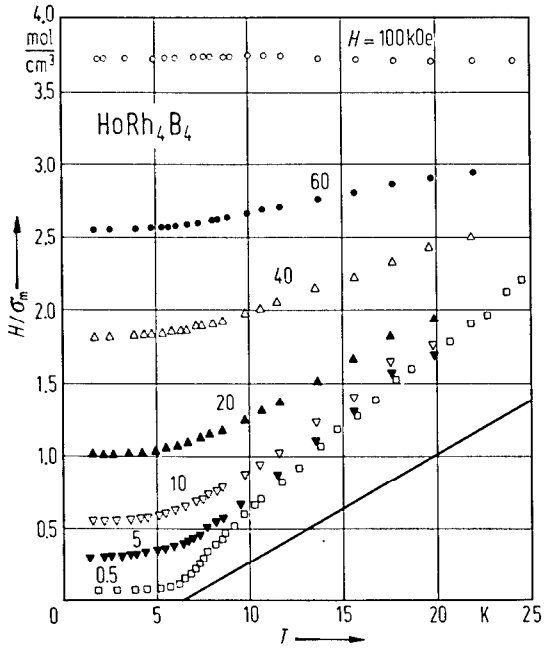

Fig. 20. $HoRh_4B_4$. H/σ_m in various applied magnetic fields between 1.5 and 25 K. The solid line is a Curie-Weiss fit to the high-temperature data with $p_{eff} = 10.25\ \mu_B$/Ho and $\Theta = 6.5$ K [80 O 1].

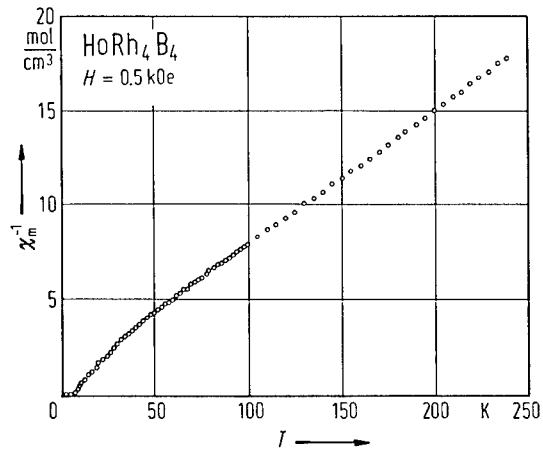

Fig. 21. $HoRh_4B_4$. Temperature dependence of the inverse low-field magnetic molar susceptibility χ_m^{-1} between 1.5 and 250 K. The applied magnetic field was 0.5 kOe [80 O 1].

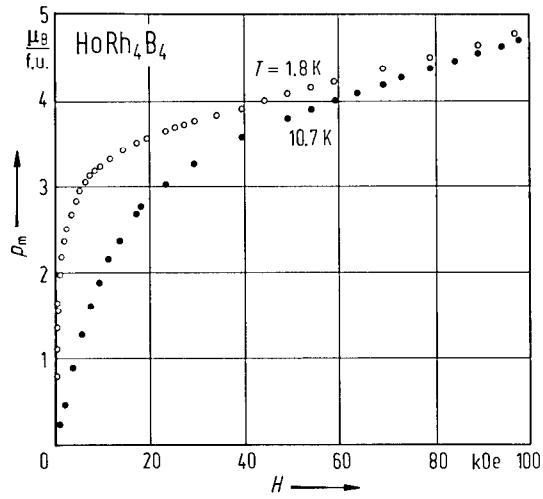

Fig. 22. $HoRh_4B_4$. Magnetization curves of polycrystalline sample above and below the Curie temperature [80 O 1].

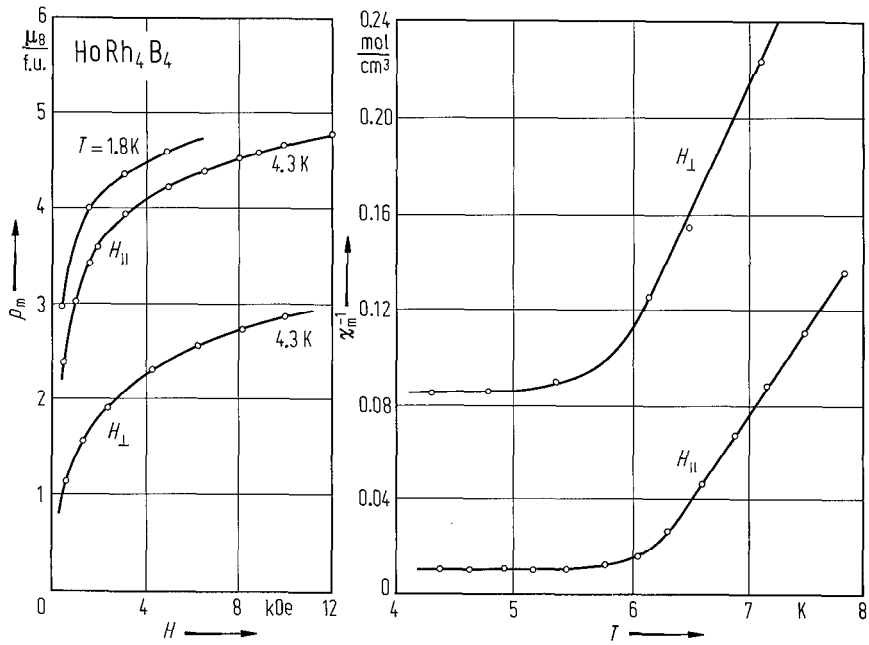

Fig. 23. $HoRh_4B_4$. Magnetization curves corrected for demagnetization and temperature variation of the inverse magnetic susceptibility as measured with the applied magnetic field parallel and perpendicular to the cooling direction of the sample in the arc furnace. $p_{eff} = 10.6\,\mu_B$/Ho [81 A 1].

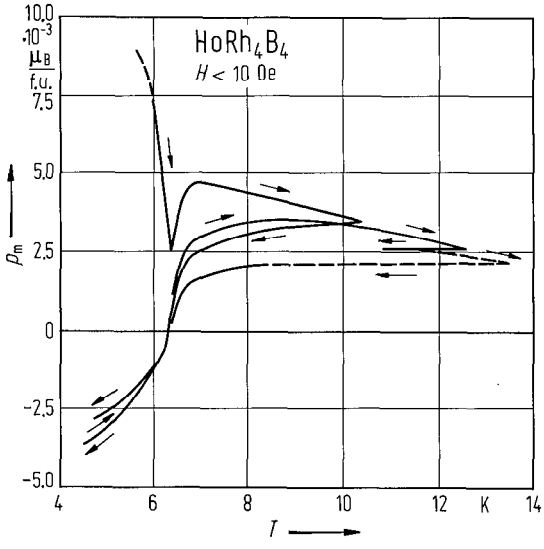

Fig. 24. $HoRh_4B_4$. Variation with temperature of the magnetization of a spherical sample in a small reverse field $H < 10$ Oe, after exposure to a magnetic field of 2.5 kOe at 4.2 K. The dashed curves indicate regions where no data were taken, and the arrows show how T was cycled, starting at 5.55 K [81 A 1].

The *a* direction spontaneous and saturation magnetic moments reported in [82 C 1] for $ErRh_4B_4$ are in excellent agreement with values measured by neutron scattering, 5.6 μ_B/Er [77 M 2], and Mössbauer effect, 8.3 μ_B/Er [80 S 2]. The spontaneous and saturation magnetic moments observed thus reconcile the basic discrepancy between magnetic moments deduced from neutron scattering and Mössbauer effect, respectively, and suggest that a neutron measurement of the saturation magnetic moment would agree with the Mössbauer result. However, the neutron measurement shows that the magnetic moment in zero magnetic field is constant [77 M 2] at 5.6 μ_B/Er for $T < 0.4$ K, implying that the spontaneous magnetic moment never equals the saturation magnetic moment, even at $T = 0$. The reason for this unusual behavior remains to be explained [82 C 1].

As an example of counterplay of superconductivity and magnetism Fig. 27 is included.

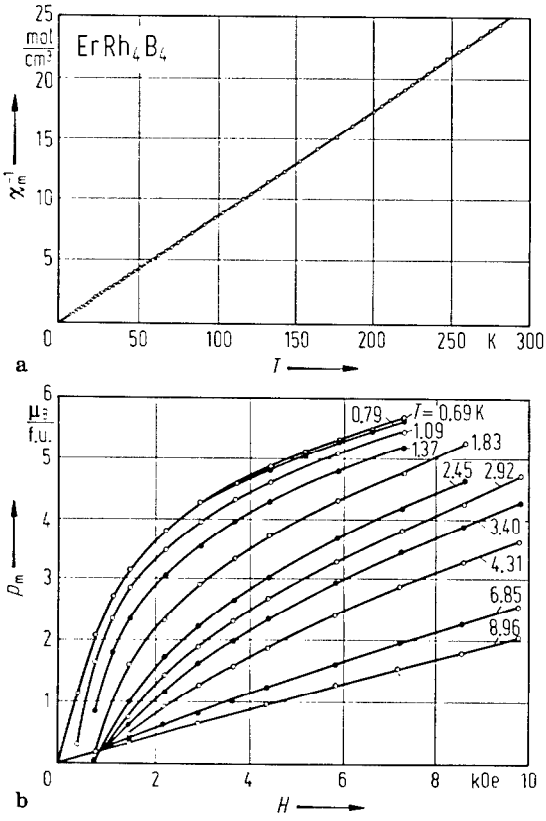

Fig. 25. $ErRh_4B_4$. (a) Inverse static low-field magnetic molar susceptibility χ_m^{-1} vs. temperature. The solid line represents a Curie-Weiss law with $p_{eff} = 9.62(15)\,\mu_B$/Er and $\Theta = 1(1)$ K. (b) Magnetization vs. applied magnetic field isotherms at temperatures between 0.69 and 8.96 K. Data were obtained with increasing magnetic field [77 F 1].

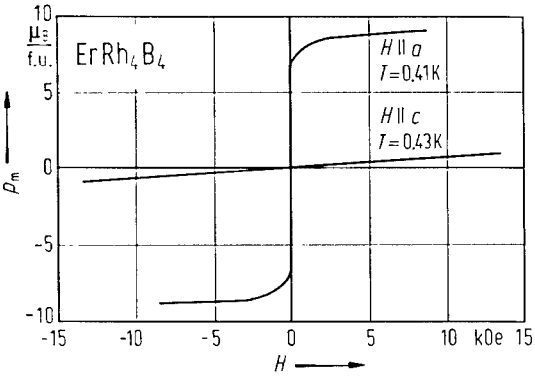

◀ Fig. 26. $ErRh_4B_4$. Magnetization for the *a* and *c* directions of a single crystal at 0.41 and 0.43 K, respectively [82 C 1].

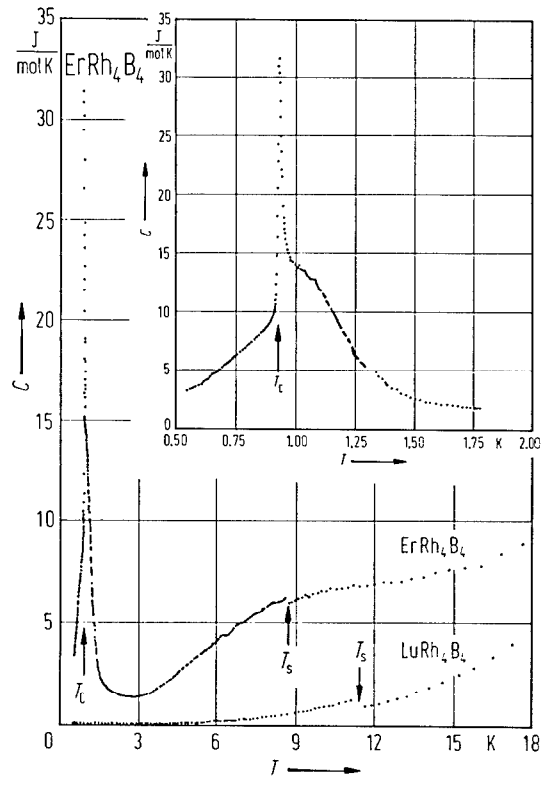

Fig. 27. $ErRh_4B_4$, $LuRh_4B_4$. Specific heat *C* vs. temperature. The inset shows a detailed plot of *C* vs. *T* for $ErRh_4B_4$ in the vicinity of the re-entrant phase transition temperature $T_C = 0.93$ K. Superconducting phase transition temperatures are $T_s = 8.7$ K for $ErRh_4B_4$ and 11.5 K for $LuRh_4B_4$ [82 M 2].

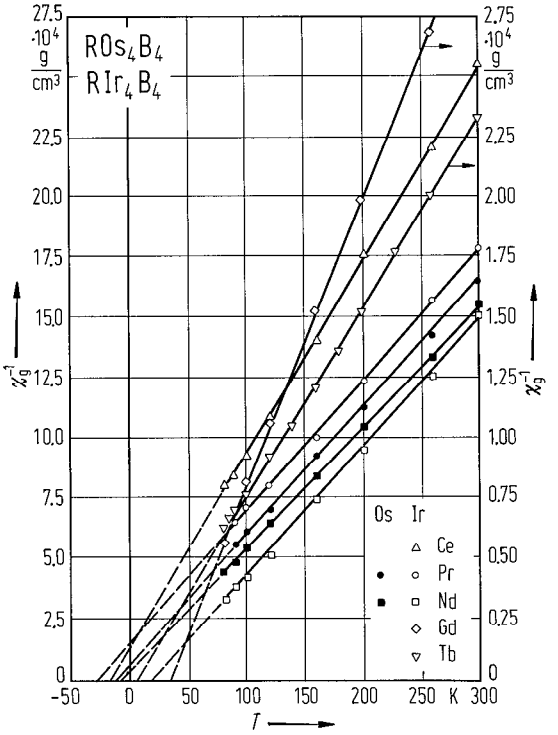

Fig. 28. ROs_4B_4, RIr_4B_4. Reciprocal magnetic susceptibility vs. temperature [79 R 3].

2.8.2.2 Compounds with RMB_2 stoichiometry (M = Ru, Os)

$LuRuB_2$ is a cluster compound of a kind qualitatively different from the superconducting RM_4B_4 compounds. In the latter materials, the transition-metal atoms M form clusters and the rare earth atoms R are isolated. In $LuRuB_2$ these roles of R and M atoms in the clustering behavior are reversed. The B_2 clusters are weakly bonded together to form chains in $LuRuB_2$, whereas they are isolated from each other in the RM_4B_4 compounds. The magnetic ordering temperatures T_m in compounds with $LuRuB_2$-type crystal structure are higher than values observed in the RRh_4B_4 compounds. These enhanced T_m values are probably due to shorter R–R interatomic distances and higher R concentration in $RRuB_2$ phases.

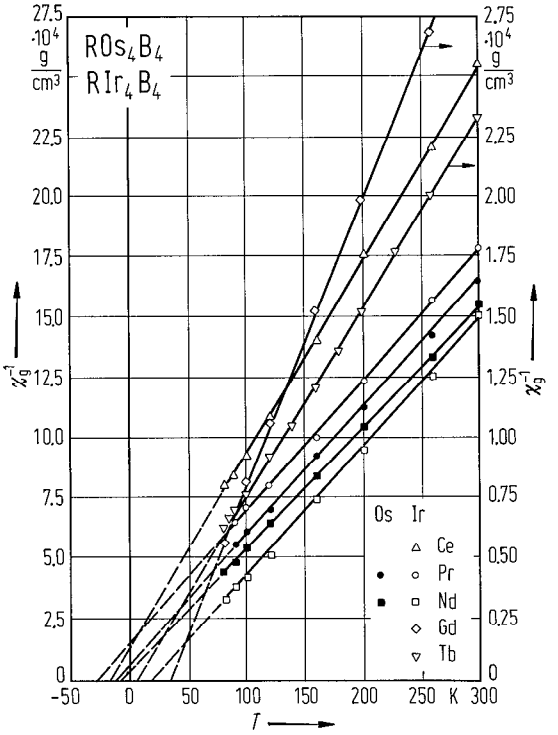

Fig. 28. ROs_4B_4, RIr_4B_4. Reciprocal magnetic susceptibility vs. temperature [79 R 3].

2.8.2.2 Compounds with RMB_2 stoichiometry (M = Ru, Os)

$LuRuB_2$ is a cluster compound of a kind qualitatively different from the superconducting RM_4B_4 compounds. In the latter materials, the transition-metal atoms M form clusters and the rare earth atoms R are isolated. In $LuRuB_2$ these roles of R and M atoms in the clustering behavior are reversed. The B_2 clusters are weakly bonded together to form chains in $LuRuB_2$, whereas they are isolated from each other in the RM_4B_4 compounds. The magnetic ordering temperatures T_m in compounds with $LuRuB_2$-type crystal structure are higher than values observed in the RRh_4B_4 compounds. These enhanced T_m values are probably due to shorter R–R interatomic distances and higher R concentration in $RRuB_2$ phases.

Table 7. RMB_2, M = Ru, Os. Room-temperature lattice parameters and magnetic or superconducting phase transition temperatures for ternary borides ($LuRuB_2$-type structure) [80 K 5, 80 S 1].

R	a	b	c	T_m	T_s
	Å			K	
			$RRuB_2$		
Y	5.918(6)	5.297(5)	6.377(7)		7.68···7.80
Tb	5.897(6)	5.311(5)	6.367(7)	45.6	
Dy	5.886(6)	5.300(5)	6.352(7)	21.9	
Ho	5.875(6)	5.287(5)	6.332(7)	15.5	
Er	5.868(6)	5.262(5)	6.323(7)	5.21	
Tm	5.831(6)	5.254(5)	6.299(7)	4.07	
Lu	5.809(6)	5.229(5)	6.284(7)		9.86···9.99
			$ROsB_2$		
Y	5.905(6)	5.299(5)	6.391(7)		1.60···2.22
Tb	5.885(6)	5.309(5)	6.392(7)	39.2	
Dy	5.869(6)	5.297(5)	6.369(7)	25.3	
Ho	5.850(6)	5.286(5)	6.355(7)	14.2	
Er	5.834(6)	5.274(5)	6.341(7)	3.80	
Tm	5.817(6)	5.258(5)	6.328(7)	2.26	
Lu	5.809(6)	5.231(5)	6.318(7)		2.14···2.66

2.8.2.3 Compounds with RM_3B_2 stoichiometry (M = Co, Ru, Rh, Ir)

In RM_3B_2 the R and M atoms both respectively form clusters and these clusters interpenetrate, whereas the B atoms are isolated from each other.

Table 8. RCo_3B_2. Room-temperature lattice parameters and magnetic data of ternary borides ($CeCo_3B_2$-type structure). p_s refers to $T = 4.2$ K.

R	a	c	p_{eff}	p_s	Θ	T_C	Ref.
	Å		μ_B/f.u.		K		
Y	5.033	3.038					69 K 1
	5.020	3.027					73 N 1
Ce	5.057	3.036					69 K 1
	5.058	3.040					73 N 1
Sm	5.101	2.991		0.12		40	77 O 1
	5.079	3.031					69 K 1, 73 N 1
Gd	5.059	3.019	7.7	6.9	75	58	77 O 1
	5.066	3.022					69 K 1, 73 N 1
Tb	5.048	3.005					69 K 1
	5.050	3.009					73 N 1
Dy	5.028	3.015					69 K 1
	5.031	3.021					73 N 1
Ho	5.026	3.029					69 K 1
	5.018	3.023					73 N 1
Er	5.003	3.024	10.2	4.8	10	20	77 O 1
	5.006	3.024					69 K 1, 73 N 1
Tm	4.991	3.019					69 K 1
	4.999	3.019					73 R 1
Yb	4.985	3.020					73 R 1
Lu	4.959	3.035					69 K 1

Table 7. RMB_2, M = Ru, Os. Room-temperature lattice parameters and magnetic or superconducting phase transition temperatures for ternary borides ($LuRuB_2$-type structure) [80 K 5, 80 S 1].

R	a	b	c	T_m	T_s
	Å			K	
			$RRuB_2$		
Y	5.918(6)	5.297(5)	6.377(7)		7.68···7.80
Tb	5.897(6)	5.311(5)	6.367(7)	45.6	
Dy	5.886(6)	5.300(5)	6.352(7)	21.9	
Ho	5.875(6)	5.287(5)	6.332(7)	15.5	
Er	5.868(6)	5.262(5)	6.323(7)	5.21	
Tm	5.831(6)	5.254(5)	6.299(7)	4.07	
Lu	5.809(6)	5.229(5)	6.284(7)		9.86···9.99
			$ROsB_2$		
Y	5.905(6)	5.299(5)	6.391(7)		1.60···2.22
Tb	5.885(6)	5.309(5)	6.392(7)	39.2	
Dy	5.869(6)	5.297(5)	6.369(7)	25.3	
Ho	5.850(6)	5.286(5)	6.355(7)	14.2	
Er	5.834(6)	5.274(5)	6.341(7)	3.80	
Tm	5.817(6)	5.258(5)	6.328(7)	2.26	
Lu	5.809(6)	5.231(5)	6.318(7)		2.14···2.66

2.8.2.3 Compounds with RM_3B_2 stoichiometry (M = Co, Ru, Rh, Ir)

In RM_3B_2 the R and M atoms both respectively form clusters and these clusters interpenetrate, whereas the B atoms are isolated from each other.

Table 8. RCo_3B_2. Room-temperature lattice parameters and magnetic data of ternary borides ($CeCo_3B_2$-type structure). p_s refers to $T = 4.2$ K.

R	a	c	p_{eff}	p_s	Θ	T_C	Ref.
	Å		μ_B/f.u.		K		
Y	5.033	3.038					69 K 1
	5.020	3.027					73 N 1
Ce	5.057	3.036					69 K 1
	5.058	3.040					73 N 1
Sm	5.101	2.991		0.12		40	77 O 1
	5.079	3.031					69 K 1, 73 N 1
Gd	5.059	3.019	7.7	6.9	75	58	77 O 1
	5.066	3.022					69 K 1, 73 N 1
Tb	5.048	3.005					69 K 1
	5.050	3.009					73 N 1
Dy	5.028	3.015					69 K 1
	5.031	3.021					73 N 1
Ho	5.026	3.029					69 K 1
	5.018	3.023					73 N 1
Er	5.003	3.024	10.2	4.8	10	20	77 O 1
	5.006	3.024					69 K 1, 73 N 1
Tm	4.991	3.019					69 K 1
	4.999	3.019					73 R 1
Yb	4.985	3.020					73 R 1
Lu	4.959	3.035					69 K 1

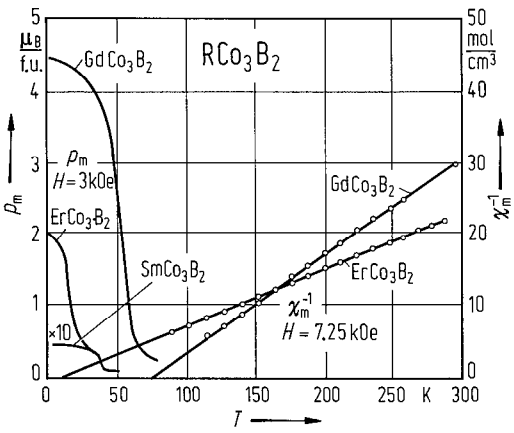

Fig. 29. RCo_3B_2, R = Sm, Gd, Er. Magnetization (applied magnetic field 3 kOe) and ivnerse magnetic molar susceptibility (applied magnetic field 7.25 kOe) vs. temperature. $SmCo_3B_2$ magnetic moments are multiplied by 10. For $GdCo_3B_2$ and $ErCo_3B_2$, the room-temperature impurity magnetizations were substrated from the measured values at all temperatures before calculating the inverse magnetic susceptibility. For $GdCo_3B_2$, the impurity contributed 14% and for $ErCo_3B_2$, 65% of the total magnetization at 295 K [77 O 1].

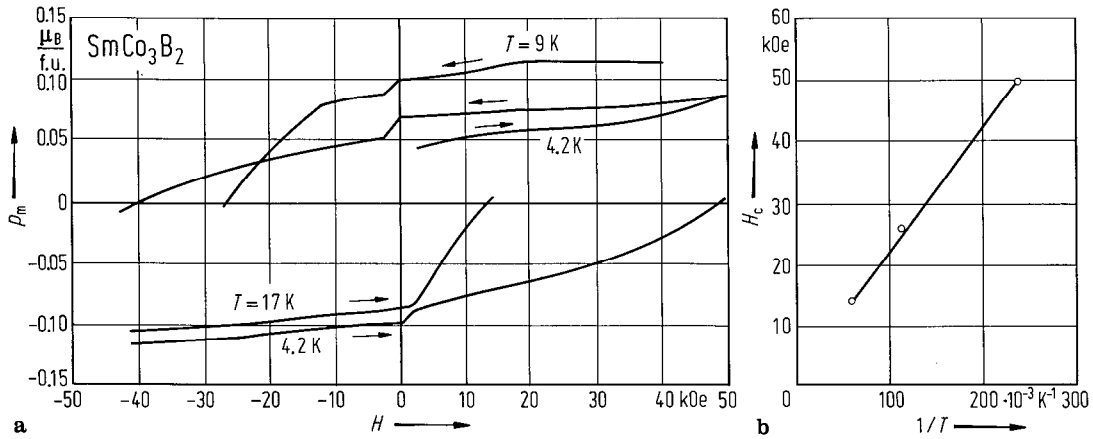

Fig. 30. $SmCo_3B_2$. (a) Demagnetization curves at different temperatures. Data were taken point-by-point, then smoothed. In each case, except for the 4.2 K data in the upper half, the sample was raised above the Curie temperature and cooled in a 50 kOe field in order to ensure saturation. (b) Inverse-temperature dependence of intrinsic coercive force [77 O 1].

Table 9. RRu_3B_2. Room-temperature lattice parameters and magnetic or superconducting data of ternary borides ($CeCo_3B_2$-type structure). Asterisk: no phase transition observed above 1.2 K.

R	a	c	p_{eff}	Θ	T_m	T_s	Ref.
	Å		μ_B/f.u.	K			
Y	5.471	3.027					80 H 1
	5.481	3.028			*	*	80 K 4
$La_{0.9}$	5.605	3.006			*	*	80 K 4
Ce	5.523	2.991	1.24 [2]				80 H 1
	5.527	2.991			*	*	80 K 4
Pr	5.532	3.015	3.70	51	5		80 H 1
	5.554	3.006			6.85	*	80 K 4
Nd	5.538	3.010	3.63	61	39		80 H 1
	5.554	3.010			33.2	*	80 K 4
Sm	5.514	3.010	1.70 [2]				80 H 1
	5.536	2.997			>45 [1]	*	80 K 4
Gd	5.493···5.505	3.015···3.024	8.04	65	10		80 H 1
	5.508	3.018				*	80 K 4
Tb	5.485	3.014	9.81	145	83		80 H 1
	5.495	3.010				*	80 K 4
Dy	5.474	3.016	10.78	105	50		80 H 1
	5.485	3.011			40.1	*	80 K 4
Ho	5.466	3.017	10.47	50	25		80 H 1
	5.474	3.017			16.1	*	80 K 4
Er	5.461	3.016	9.54	130	32		80 H 1
	5.467	3.017			27.3	*	80 K 4
Tm	5.454	3.010	7.69	185	27		80 H 1
	5.461	3.012			18.3	*	80 K 4
Yb	5.454	3.003	4.49	0			80 H 1
	5.464	3.006			*	*	80 K 4
Lu	5.439	3.016					80 H 1
	5.454	3.004			*	*	80 K 4

[1]) Given as unspecified transition temperature.
[2]) At 293 K.

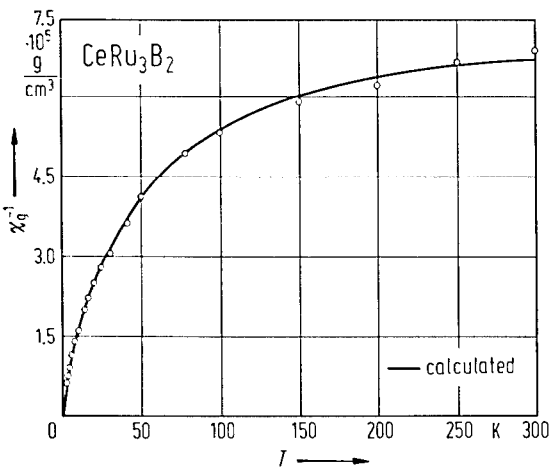

Fig. 31. $CeRu_3B_2$. Reciprocal magnetic susceptibility vs. temperature and calculated least-squares fit [80 H 1].

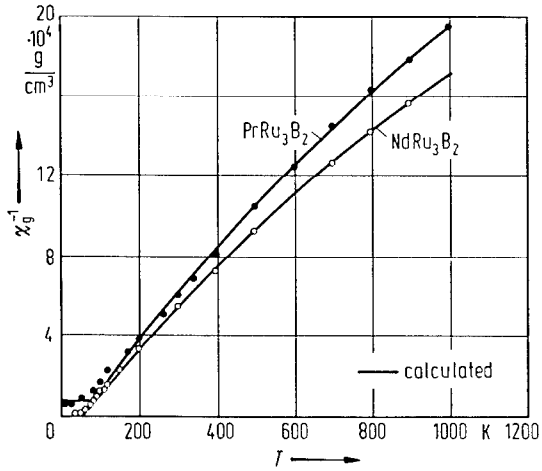

Fig. 32. $PrRu_3B_2$, $NdRu_3B_2$. Reciprocal magnetic susceptibility vs. temperature and calculated least-squares fit [80 H 1].

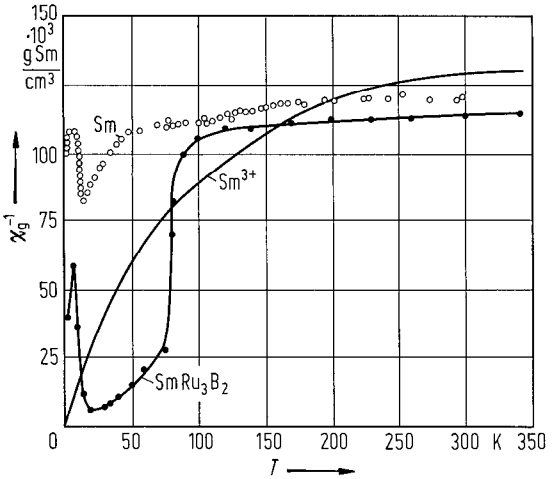

Fig. 33. $SmRu_3B_2$. Reciprocal magnetic susceptibility vs. temperature. For comparison the values obtained by Lock for Sm metal, as well as the theoretical values by Van Vleck for free Sm^{3+} are shown [80 H 1].

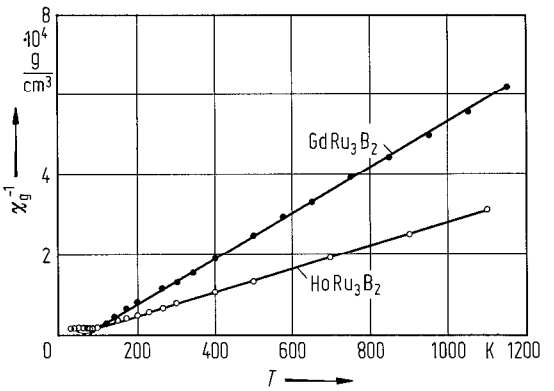

Fig. 34. $GdRu_3B_2$, $HoRu_3B_2$. Reciprocal magnetic susceptibility vs. temperature [80 H 1].

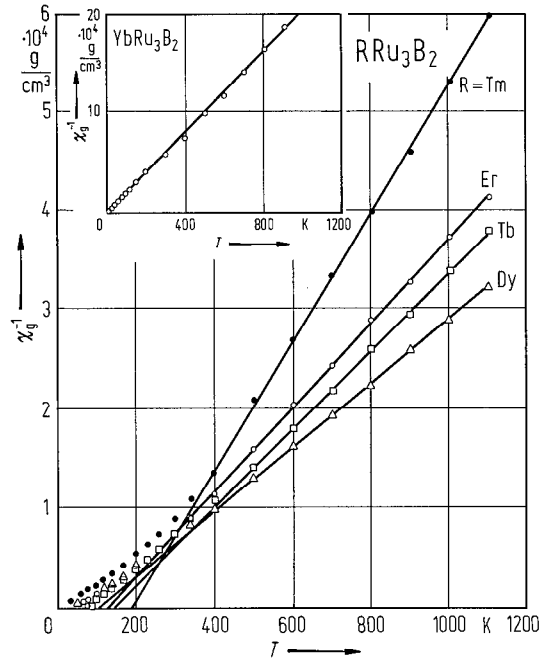

Fig. 35. RRu_3B_2, R = Tb, Dy, Er, Tm, Yb. Reciprocal magnetic susceptibility vs. temperature [80 H 1].

Table 10. RRh_3B_2. Room-temperature lattice parameters and magnetic or superconducting data of ternary borides ($CeCo_3B_2$-type structure). Asterisk: no phase transition observed above 1.2 K.

R	a	c	p_{eff}	p_m [1]	Θ	T_m	T_s	Ref.
	Å		μ_B/f.u.		K			
La	5.480	3.137					2.82···2.60	80 K 4
	5.483	3.141						83 M 1
Ce	5.474	3.085					*	80 K 4
	5.477	3.091	3.0 [2]	0.38	−373 [2]	115		81 D 1, 83 M 1
			1.01 [3]		119 [3]			84 Y 1
Pr	5.461	3.105				1.68	*	80 K 4
	5.461	3.108	3.74		2.1			83 M 1

(continued)

[1]) Measured at $T = 4.2$ K and $H = 20$ kOe.
[2]) High-temperature data.
[3]) Low-temperature data.

Table 10 (continued).

R	a	c	p_{eff}	p_m [1])	Θ	T_m	T_s	Ref.
	Å		μ_B/f.u.		K			
Nd	5.466	3.109				13.5	*	80 K 4
	5.445	3.122	3.70	2.16	28.3	31		83 M 1
			3.78		11	18.5		83 O 1
Sm	5.437	3.090					*	80 K 4
	5.433	3.109		0.046		89		83 M 1
Eu	5.601	2.906				41.7	*	80 K 4
	5.616	2.863	4.40	0.55	− 40.0	46		83 M 1
			4.40			40		82 M 1
Gd	5.404	3.115					*	80 K 4
	5.403	3.113	8.17	6.87	88.5	105		83 M 1

[1]) Measured at $T = 4.2$ K and $H = 20$ kOe.

Table 11. RM_3B_2, M = Rh, Ir. Room-temperature lattice parameters and magnetic ordering temperatures of ternary borides ($ErIr_3B_2$-type structure) [81 K 2]. Asterisk: no phase transition observed above 1.2 K.

R	a	b	c	T_m
	Å			K
		RRh_3B_3		
Y	5.377(6)	9.325(9)	3.102(4)	*
Tb	5.390(6)	9.335(9)	3.100(4)	45
Dy	5.379(6)	9.331(9)	3.093(4)	38.0
Ho	5.366(6)	9.307(9)	3.100(4)	24.2
Er	5.362(6)	9.288(9)	3.099(4)	20.4
Tm	5.357(6)	9.285(9)	3.091(4)	11.8
Yb	5.355(6)	9.280(9)	3.090(4)	*
Lu	5.353(6)	9.276(9)	3.089(4)	*
		RIr_3B_2		
Y	5.428(6)	9.406(9)	3.107(4)	*
Ce	5.502(6)	9.526(9)	3.090(4)	*
Nd	5.513(6)	9.540(9)	3.084(4)	4.72
Sm	5.492(6)	9.506(9)	3.076(4)	12.6
Gd	5.466(6)	9.473(9)	3.092(4)	29.8
Tb	5.459(6)	9.464(9)	3.084(4)	6.1
Dy	5.347(6)	9.393(9)	3.106(4)	17.7
Ho	5.420(6)	9.393(9)	3.107(4)	12.9
Er	5.409(6)	9.379(9)	3.101(4)	11.9
Tm	5.404(6)	9.371(9)	3.097(4)	5.69
Yb	5.401(6)	9.353(9)	3.099(4)	*
Lu	5.394(6)	9.354(9)	3.080(4)	*

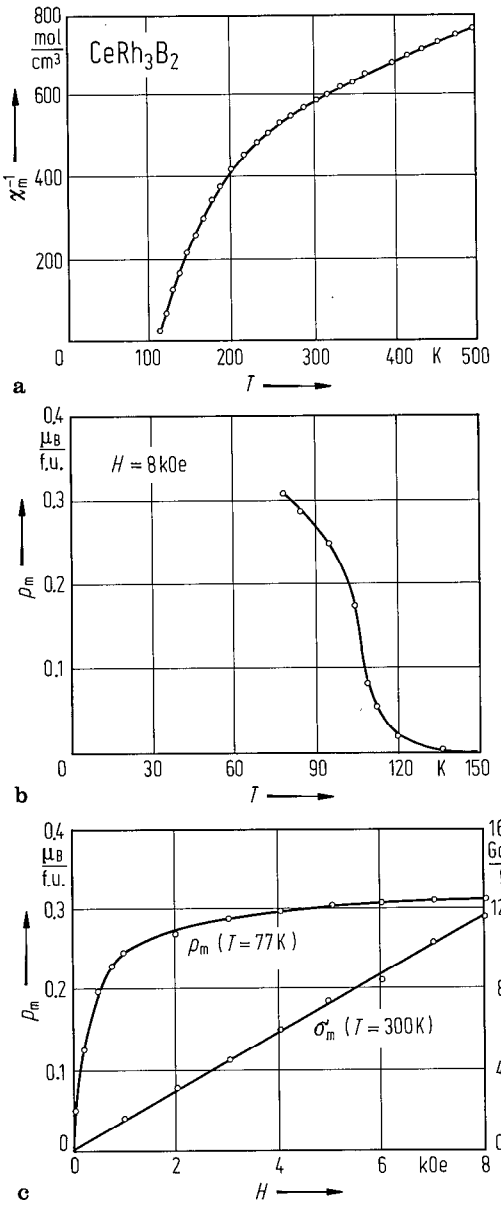

Fig. 36. $CeRh_3B_2$. (a) Temperature dependence of inverse magnetic molar susceptibility. (b) Magnetization in an applied magnetic field of 8 kOe near T_C. (c) Magnetization vs. applied magnetic field at 77 and 300 K [81 D 1].

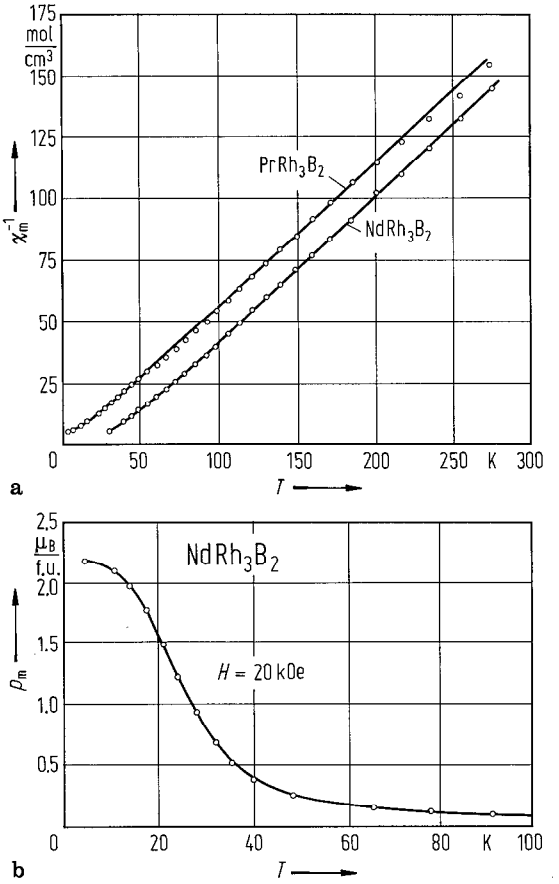

Fig. 37. $PrRh_3B_2$, $NdRh_3B_2$. (a) Inverse magnetic molar susceptibility vs. temperature. (b) Magnetization in 20 kOe applied magnetic field vs. temperature for $NdRh_3B_2$ near the Curie temperature [83 M 1].

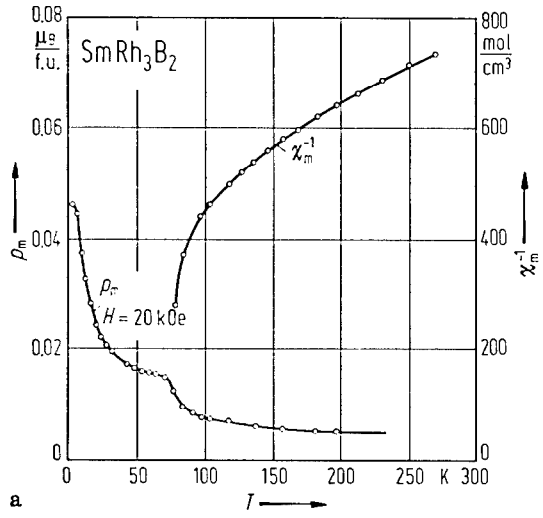

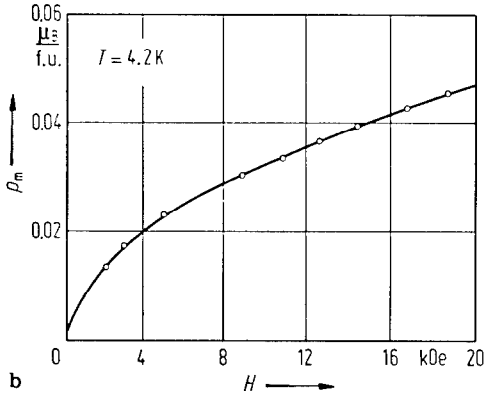

Fig. 38. $SmRh_3B_2$. (a) Magnetization in 20 kOe applied magnetic field and inverse magnetic molar susceptibility vs. temperature. (b) Magnetic field dependence of magnetization at 4.2 K [83 M 1].

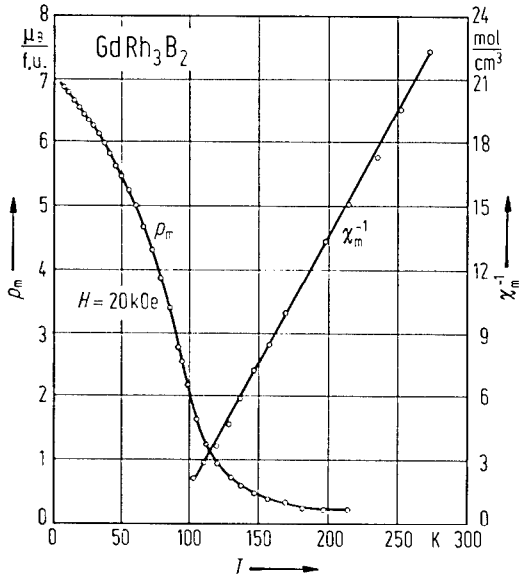

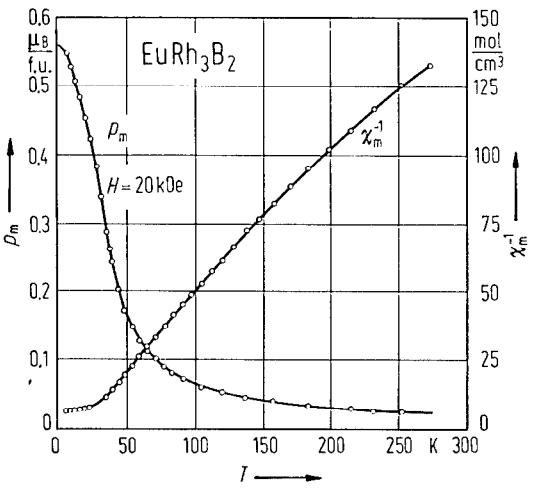

Fig. 39. $EuRh_3B_2$. Magnetization in 20 kOe applied magnetic field and inverse magnetic molar susceptibility vs. temperature [82 M 1].

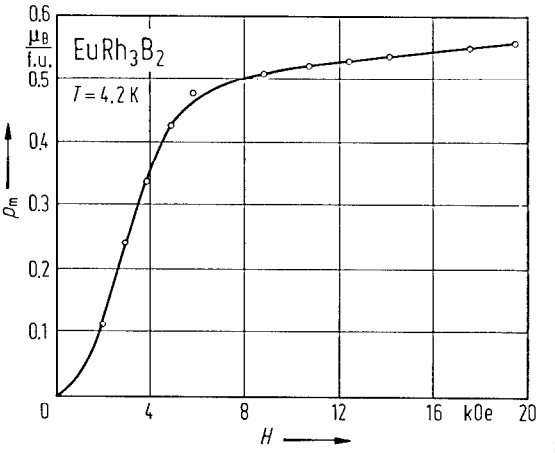

Fig. 40. $EuRh_3B_2$. Magnetization vs. applied magnetic field at 4.2 K [82 M 1].

◀

Fig. 41. $GdRh_3B_2$. Temperature dependence of magnetization in 20 kOe applied magnetic field and inverse magnetic molar susceptibility [83 M 1].

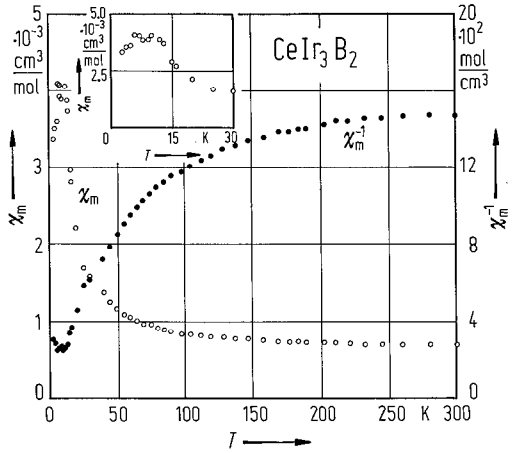

Fig. 42. $CeIr_3B_2$. Magnetic molar susceptibility χ_m and its inverse, χ_m^{-1}, vs. temperature for $3\,K \leqq T \leqq 300\,K$. Shown in the inset are the χ_m vs. T data for $T \leqq 30\,K$ [84 Y 1].

2.8.2.4 Compounds with $R_{0.57}Rh_{3.43}B_2$ stoichiometry

Table 12. $R_{0.57}Rh_{3.43}B_2$. Room-temperature lattice parameters and magnetic data [83 O 1].

R	a	c	Θ	T_C	p_{eff}	p_m [1]	p_m [2]
	Å		K		μ_B/f.u.	μ_B/f.u.	
Y	5.550	2.822	21	12···14	0.47	$3 \cdot 10^{-3}$	
La	5.621	2.844	20	12···14	0.21	$5 \cdot 10^{-3}$	
Nd	5.598	2.832	2	< 4.2	3.72		3.27
Sm	5.582	2.832		13	1.60 [3]	0.045	0.71
Gd	5.579	2.828	18	12	8.14	6.54	7
Tb	5.563	2.829	35	15	10.65	5.26	9
Dy	5.558	2.826	20	5	11.52	5.13	10
Ho	5.552	2.825	8	5	11.73	5.56	10
Er	5.542	2.822	13	7.5	10.13	4.88	9

[1]) Measured at $T = 4.2\,K$ and $H = 20\,kOe$.
[2]) Theoretical values.
[3]) Values of 300 K.

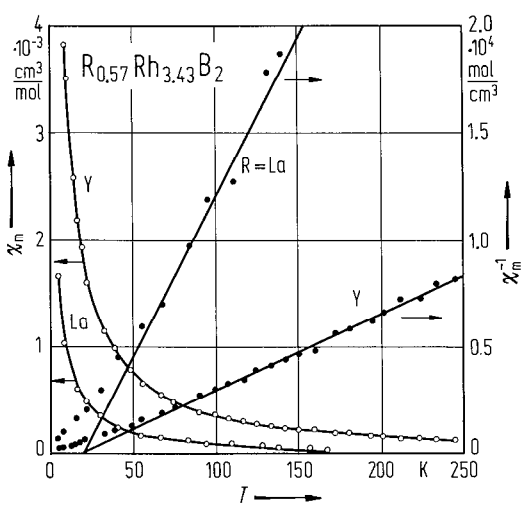

Fig. 43. $R_{0.57}Rh_{3.43}B_2$, R = Y, La. Magnetic molar susceptibility vs. temperature [83 O 1].

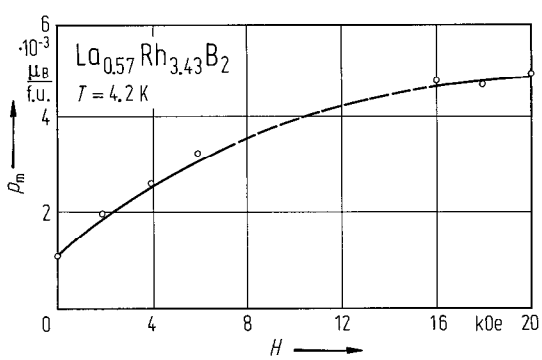

Fig. 44. $La_{0.57}Rh_{3.43}B_2$. Magnetization curves vs. magnetic field at 4.2 K [83 O 1].

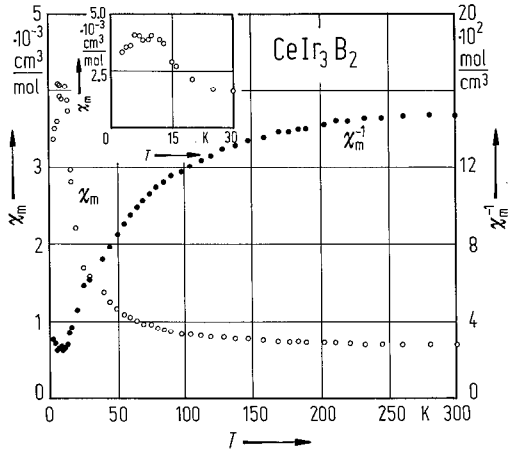

Fig. 42. $CeIr_3B_2$. Magnetic molar susceptibility χ_m and its inverse, χ_m^{-1}, vs. temperature for $3\,K \leqq T \leqq 300\,K$. Shown in the inset are the χ_m vs. T data for $T \leqq 30\,K$ [84 Y 1].

2.8.2.4 Compounds with $R_{0.57}Rh_{3.43}B_2$ stoichiometry

Table 12. $R_{0.57}Rh_{3.43}B_2$. Room-temperature lattice parameters and magnetic data [83 O 1].

R	a	c	Θ	T_C	p_{eff}	p_m [1]	p_m [2]
	Å		K		μ_B/f.u.	μ_B/f.u.	
Y	5.550	2.822	21	12···14	0.47	$3 \cdot 10^{-3}$	
La	5.621	2.844	20	12···14	0.21	$5 \cdot 10^{-3}$	
Nd	5.598	2.832	2	< 4.2	3.72		3.27
Sm	5.582	2.832		13	1.60 [3]	0.045	0.71
Gd	5.579	2.828	18	12	8.14	6.54	7
Tb	5.563	2.829	35	15	10.65	5.26	9
Dy	5.558	2.826	20	5	11.52	5.13	10
Ho	5.552	2.825	8	5	11.73	5.56	10
Er	5.542	2.822	13	7.5	10.13	4.88	9

[1]) Measured at $T = 4.2\,K$ and $H = 20\,kOe$.
[2]) Theoretical values.
[3]) Values of 300 K.

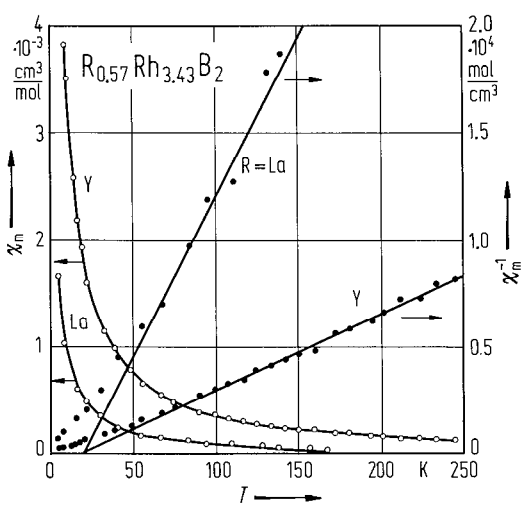

Fig. 43. $R_{0.57}Rh_{3.43}B_2$, R = Y, La. Magnetic molar susceptibility vs. temperature [83 O 1].

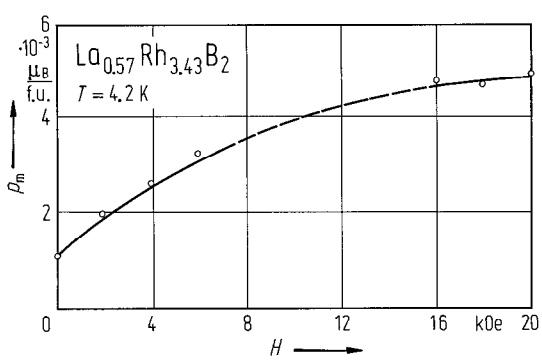

Fig. 44. $La_{0.57}Rh_{3.43}B_2$. Magnetization curves vs. magnetic field at 4.2 K [83 O 1].

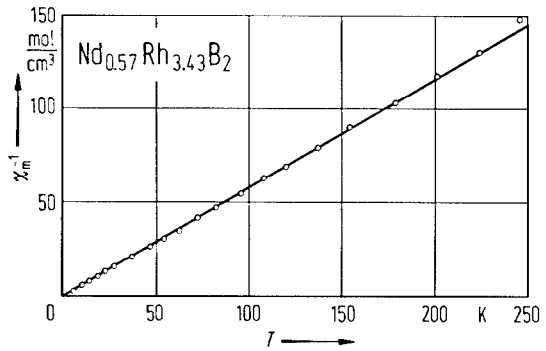

Fig. 45. $Nd_{0.57}Rh_{3.43}B_2$. Reciprocal magnetic molar susceptibility vs. temperature [83 O 1].

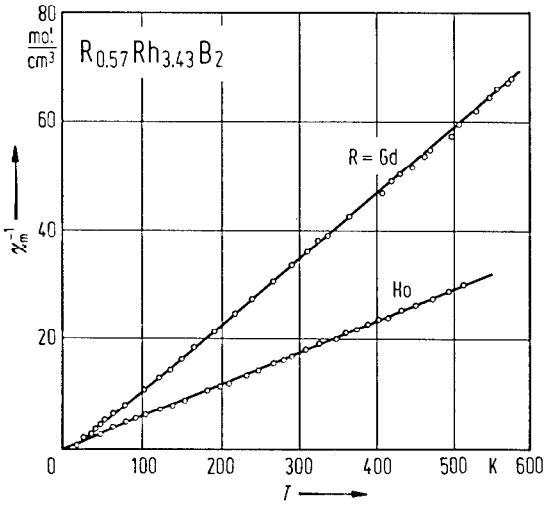

Fig. 47. $R_{0.57}Rh_{3.43}B_2$, R = Gd, Ho. Reciprocal magnetic molar susceptibility vs. temperature [83 O 1].

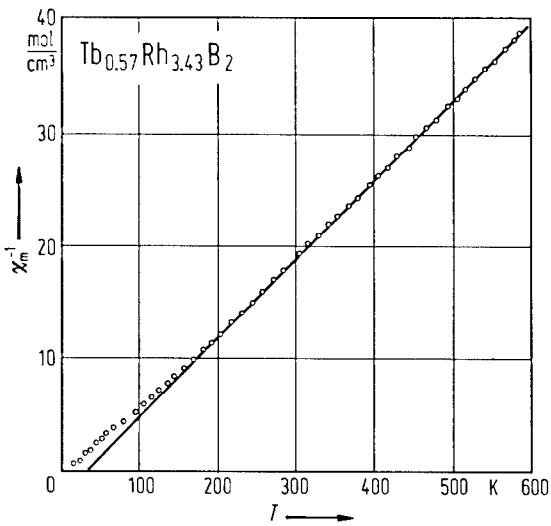

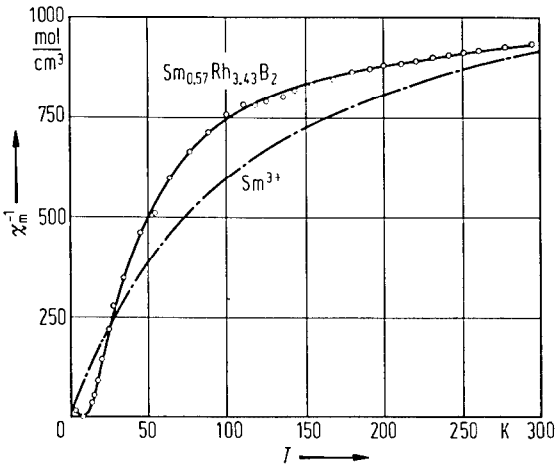

Fig. 46. $Sm_{0.57}Rh_{3.43}B_2$. Reciprocal magnetic molar susceptibility vs. temperature. The theoretical values by Van Vleck for free Sm^{3+} are also included [83 O 1].

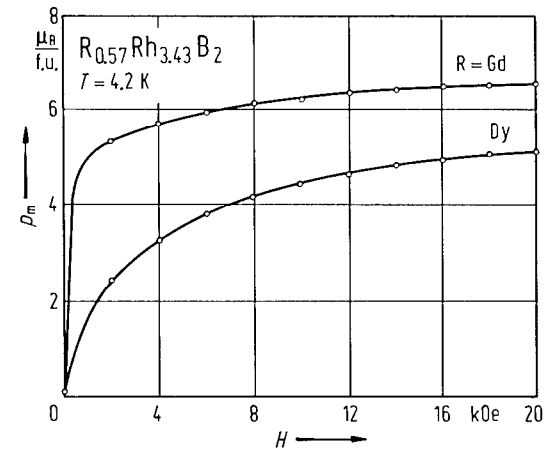

Fig. 48. $R_{0.57}Rh_{3.43}B_2$, R = Gd, Dy. Magnetization curves vs. magnetic field at 4.2 K [83 O 1].

◀
Fig. 49. $Tb_{0.57}Rh_{3.43}B_2$. Reciprocal magnetic molar susceptibility vs. temperature [83 O 1].

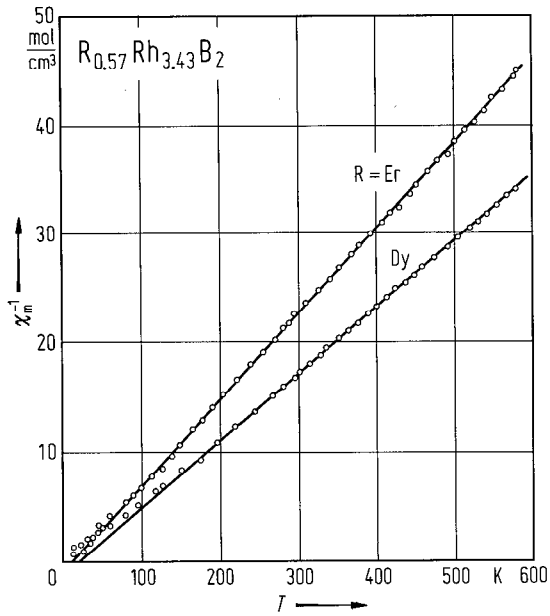

Fig. 50. $R_{0.57}Rh_{3.43}B_2$, R = Dy, Er. Reciprocal magnetic molar susceptibility vs. temperature [83 O 1].

2.8.2.5 Compounds with RRh_6B_4 stoichiometry

Table 13. RRh_6B_4. Room-temperature lattice parameters and magnetic data [85 P 1]. T_m: magnetic ordering temperature, T_{min}: lowest temperature reached in the experiment, V.V.: Van Vleck contribution to magnetic susceptibility is important. Samples were annealed, except for as-cast $LaRh_6B_4$ and $CeTh_6B_4$.

R	a	c	T_m	T_{min}	p_{eff}	Θ	χ_0
	Å		K		μ_B/f.u.	K	10^{-3} cm^3 mol^{-1}
Y	5.587(4)	8.469(7)		0.05			
La	5.647(1)	8.557(1)		0.05			
Ce	5.619(3)	8.555(5)		0.05	0.80	− 3.7	0.94
Pr	5.625(2)	8.528(5)		0.05	3.76	− 2.4	0.26
Nd	5.621(2)	8.518(4)	1.68	0.08	3.68	2.7	0.47
Sm	5.605(2)	8.507(5)		0.08	V.V.		
Eu	5.614(2)	8.505(5)		0.07	V.V.		
Gd	5.605(1)	8.510(3)	10.0	3	8.05	13.5	0.20
Tb	5.584(4)	8.499(7)	3.9	2	10.50	9.8	0.48
Dy	5.588(2)	8.480(4)	5.1	0.07	10.69	3.6	0.76
Ho	5.584(2)	8.496(3)	2.52	0.05	10.73	2.1	0.72
Er	5.581(2)	8.488(3)	0.35	0.08	9.57	3.3	0.42
Tm	5.562(2)	8.487(5)	0.61	0.05	8.00	− 1.3	0.30
Yb	5.558(1)	8.450(3)	0.14	0.05	4.35	− 9.9	0.35
Lu	5.540(2)	8.479(5)		0.05			

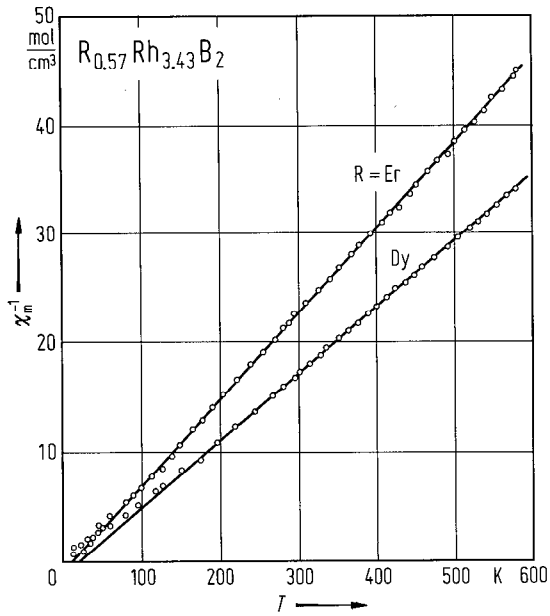

Fig. 50. $R_{0.57}Rh_{3.43}B_2$, R = Dy, Er. Reciprocal magnetic molar susceptibility vs. temperature [83 O 1].

2.8.2.5 Compounds with RRh_6B_4 stoichiometry

Table 13. RRh_6B_4. Room-temperature lattice parameters and magnetic data [85 P 1]. T_m: magnetic ordering temperature, T_{min}: lowest temperature reached in the experiment, V.V.: Van Vleck contribution to magnetic susceptibility is important. Samples were annealed, except for as-cast $LaRh_6B_4$ and $CeTh_6B_4$.

R	a	c	T_m	T_{min}	p_{eff}	Θ	χ_0
	Å		K		μ_B/f.u.	K	10^{-3} cm^3 mol^{-1}
Y	5.587(4)	8.469(7)		0.05			
La	5.647(1)	8.557(1)		0.05			
Ce	5.619(3)	8.555(5)		0.05	0.80	− 3.7	0.94
Pr	5.625(2)	8.528(5)		0.05	3.76	− 2.4	0.26
Nd	5.621(2)	8.518(4)	1.68	0.08	3.68	2.7	0.47
Sm	5.605(2)	8.507(5)		0.08	V.V.		
Eu	5.614(2)	8.505(5)		0.07	V.V.		
Gd	5.605(1)	8.510(3)	10.0	3	8.05	13.5	0.20
Tb	5.584(4)	8.499(7)	3.9	2	10.50	9.8	0.48
Dy	5.588(2)	8.480(4)	5.1	0.07	10.69	3.6	0.76
Ho	5.584(2)	8.496(3)	2.52	0.05	10.73	2.1	0.72
Er	5.581(2)	8.488(3)	0.35	0.08	9.57	3.3	0.42
Tm	5.562(2)	8.487(5)	0.61	0.05	8.00	− 1.3	0.30
Yb	5.558(1)	8.450(3)	0.14	0.05	4.35	− 9.9	0.35
Lu	5.540(2)	8.479(5)		0.05			

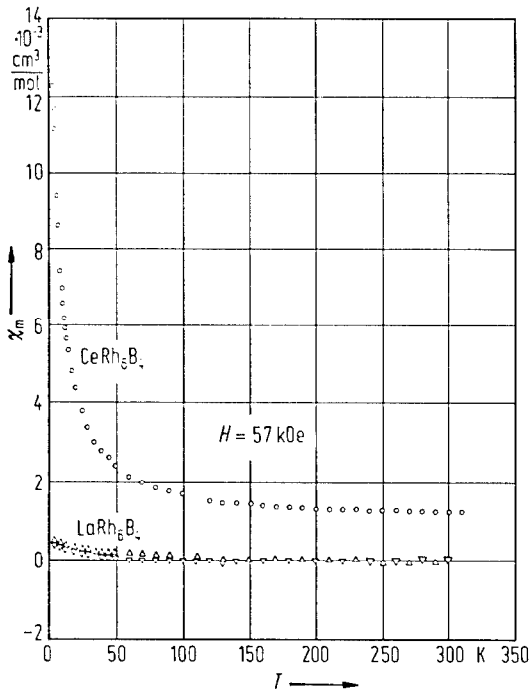

Fig. 51. $LaRh_6B_4$, $CeRh_6B_4$. Magnetic molar susceptibility at 57 kOe vs. temperature. Two $LaRh_6B_4$ samples were studied [80 K 2].

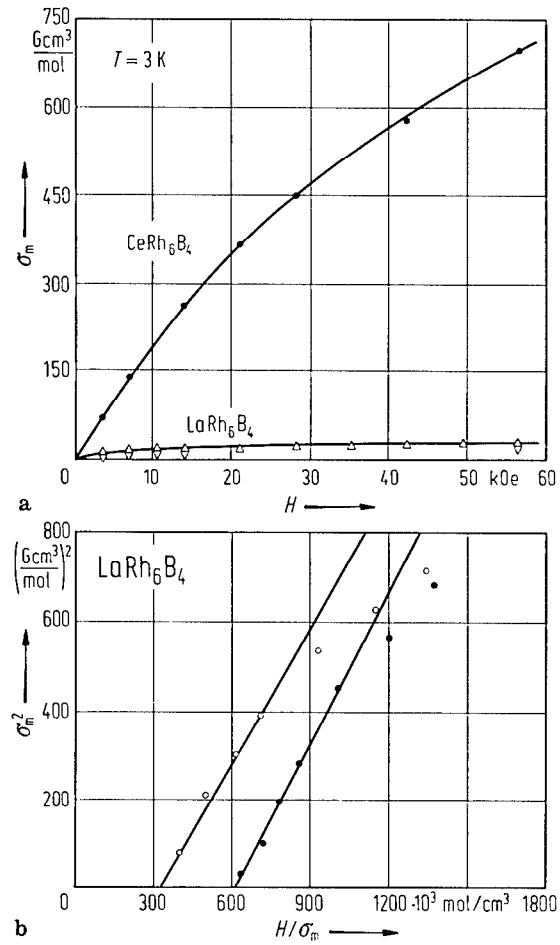

Fig. 52. $LaRh_6B_4$, $CeRh_6B_4$. (a) Magnetization at 3.0 K vs. magnetic field. Two $LaRh_6B_4$ samples were studied. (b) Arrott plot at 3.0 K for $LaRh_6B_4$ [83 S 1].

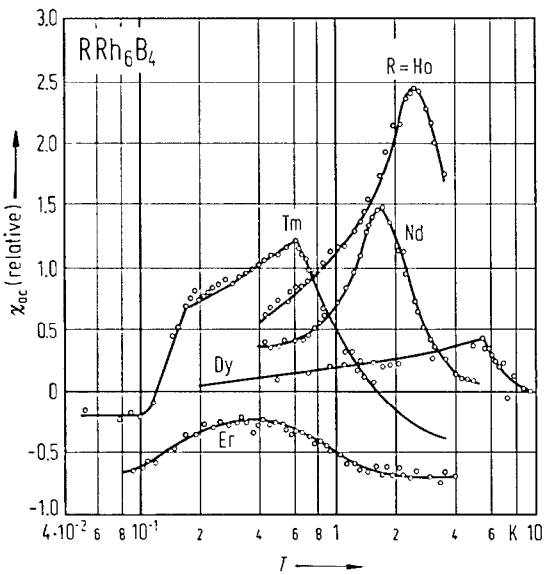

◀ Fig. 53. RRh_6B_4, R = Nd, Dy, Ho, Er, Tm. Low-field ac magnetic susceptibility vs. temperature for RRh_6B_4 with R = Er, Tm, Nd, Ho, and Dy, as indicated. Solid lines are guides to eye [85 P 1].

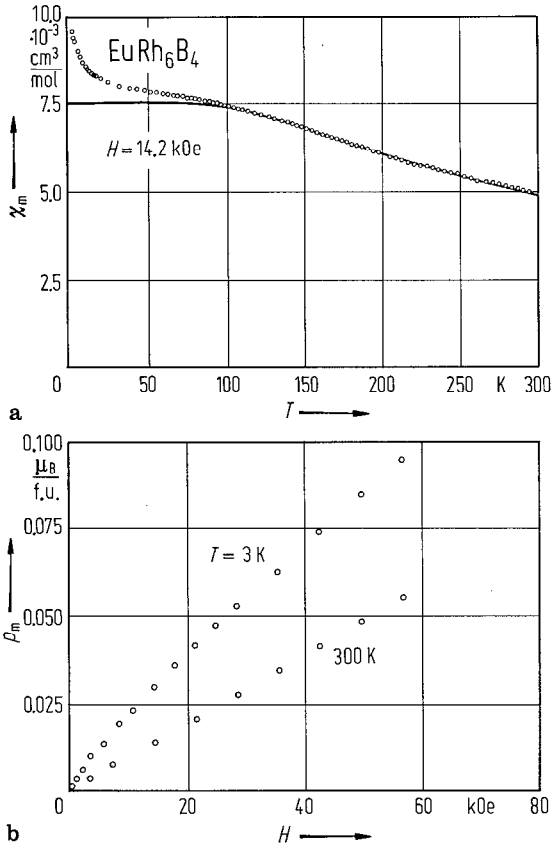

Fig. 54. $EuRh_6B_4$. (a) Magnetic susceptibility at 14.2 kOe vs. temperature. Solid line is calculated Van Vleck susceptibility. (b) Magnetization at 3 and 300 K vs. magnetic field [85 P 1].

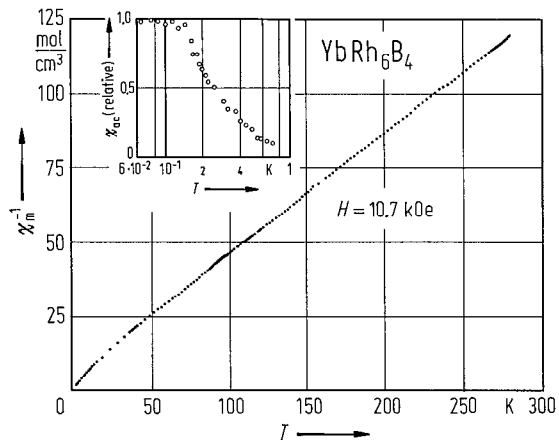

Fig. 55. $YbRh_6B_4$. Inverse magnetic molar susceptibility at 10.7 kOe vs. temperature. Inset shows low-field ac susceptibility vs. temperature [85 P 1].

2.8.2.6 Compounds with RMB_4 stoichiometry (M = Cr, Mn, Fe, Co, Ru, Os)

Table 15. R_2MB_6. Room-temperature lattice parameters and magnetic data of ternary borides (Y_2RB_6-type structure) [83 H 2].

	R	*a*	*b*	*c*	p_{eff}	Θ
		Å			μ_B/f.u.	K
$GdCrB_4$		5.953(3)	11.527(6)	3.494(2)	7.70	20
$GdMnB_4$		5.922(3)	11.466(6)	3.451(2)	7.5	90
$GdFeB_4$		5.918(3)	11.456(6)	3.457(2)	10.00	−46
$GdCoB_4$		5.924(3)	11.472(6)	3.453(2)	8.06	−12
$RRuB_4$	Y	5.954(3)	11.524(6)	3.559(2)	Pauli paramagnetism	
	Gd	5.973(3)	11.568(6)	3.570(2)	7.92	20
	Tb	5.958(3)	11.532(6)	3.551(2)	9.45	30
	Dy	5.948(3)	11.513(6)	3.541(2)	10.60	22
	Ho	5.933(3)	11.480(6)	3.533(2)	10.60	6
	Er	5.930(3)	11.481(6)	3.536(2)	9.60	14
	Tm	5.913(3)	11.440(6)	3.511(2)	7.92	14
	Yb	5.907(3)	11.429(6)	3.520(2)	≃ 4.4	−18
$ROsB_4$	Y	5.955(3)	11.527(6)	3.556(2)	Pauli paramagnetism	
	Gd	5.988(3)	11.587(6)	3.572(2)	7.85	17
	Tb	5.966(3)	11.553(6)	3.561(2)	9.95	20
	Dy	5.954(3)	11.527(6)	3.553(2)	10.60	10
	Ho	5.943(3)	11.495(6)	3.548(2)	10.60	8
	Er	5.928(3)	11.482(6)	3.539(2)	9.60	18
	Tm	5.919(3)	11.461(6)	3.532(2)	7.88	17
	Yb	5.911(3)	11.449(6)	3.535(2)	≃ 4.4	−26

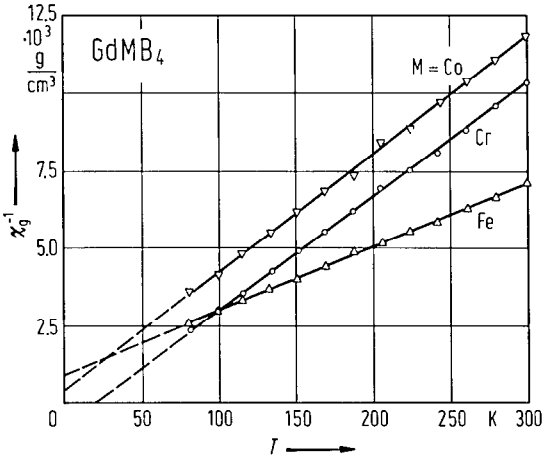

Fig. 56. $GdMB_4$, M = Cr, Fe, Co. Reciprocal magnetic susceptibility vs. temperature [78 S 1].

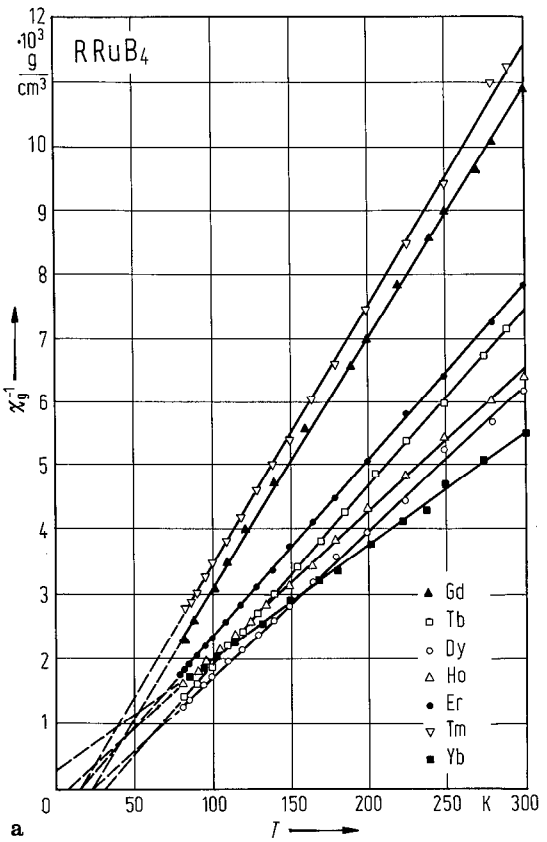

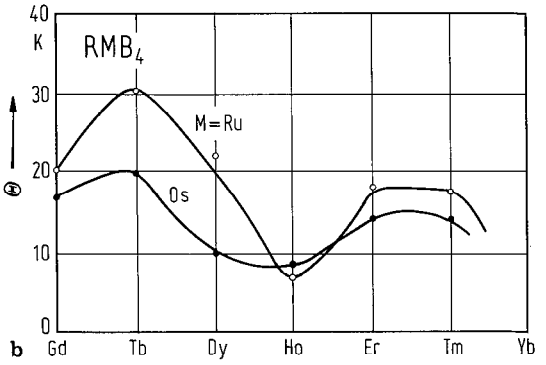

Fig. 57. RMB_4, M = Ru, Os. (a) Reciprocal magnetic susceptibility vs. temperature for $RRuB_4$. (b) Paramagnetic Curie temperature [78 S 1].

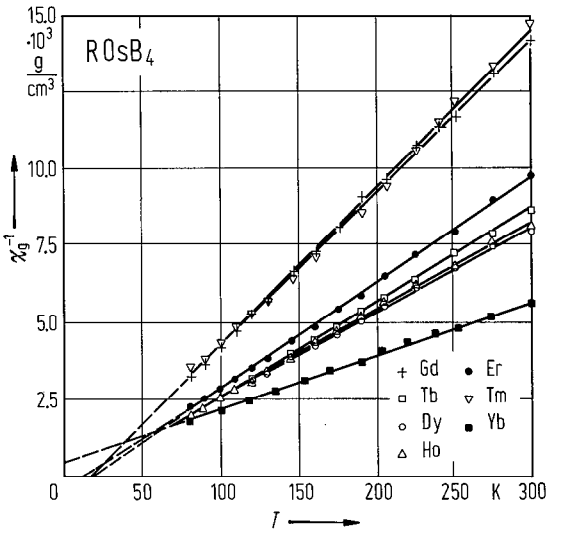

Fig. 58. $ROsB_4$. Reciprocal magnetic susceptibility vs. temperature [78 S 1].

2.8.2.7 Compounds with R_2MB_6 stoichiometry (M = Ru, Os)

Table 15. R_2MB_6. Room-temperature lattice parameters and magnetic data of ternary borides (Y_2RB_6-type structure) [83 H 2].

R	a	b	c	p_{eff}	Θ	T_C
	Å			μ_B/f.u.	K	
			R_2RuB_6			
Y	9.1498(16)	11.5139(32)	3.6501(2)	$\chi_m(300\,K) = 7.1 \cdot 10^{-4}\,cm^3\,mol^{-1}$		
Gd	9.2384(30)	11.5843(36)	3.6902(3)	8.0	55	46
Tb	9.1796(20)	11.5407(19)	3.6650(2)	9.6	50	38
Dy	9.1433(23)	11.5067(18)	3.6489(2)	10.5	28	29
Ho	9.1083(54)	11.4666(51)	3.6407(3)	10.5	14	14
Er	9.0822(31)	11.4439(56)	3.6266(4)	9.5	22	7.5
Tm	9.0605(28)	11.4203(31)	3.6091(3)	7.4	26	1
Yb	9.0371(67)	11.4129(58)	3.6011(8)			
Lu	9.0138(39)	11.3880(17)	3.5826(8)	$\chi_m(300\,K) = 3.6 \cdot 10^{-5}\,cm^3\,mol^{-1}$		
			R_2OsB_6			
Y	9.1592(10)	11.5311(25)	3.6473(2)			
Gd	9.2475(36)	11.5912(41)	3.6814(3)	7.9	22	34
Tb	9.1889(19)	11.5612(43)	3.6567(2)	9.7	36	27
Dy	9.1542(26)	11.5211(51)	3.6435(2)	10.6	30	16
Ho	9.1229(15)	11.4909(35)	3.6320(2)	10.6	12	13
Er	9.0973(21)	11.4644(21)	3.6169(3)	9.5	21	4.5
Tm	9.0677(29)	11.4336(36)	3.6037(3)	7.5	29	2
Yb	9.0504(53)	11.4224(48)	3.5939(6)			
Lu	9.0331(35)	11.4113(49)	3.5842(9)			

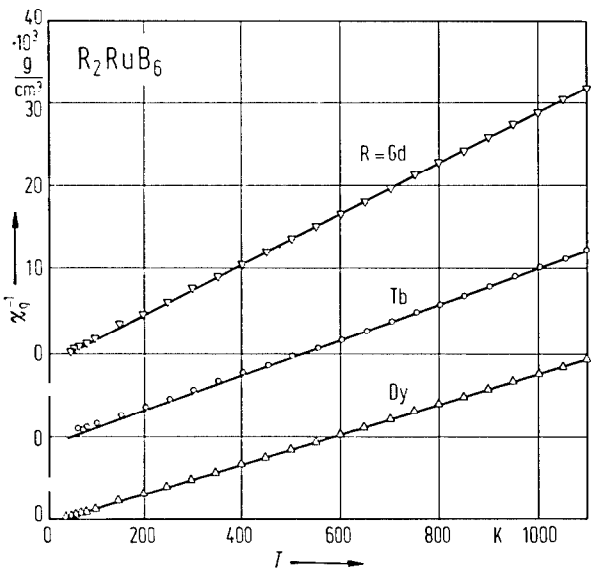

Fig. 59. R_2RuB_6, R = Gd, Tb, Dy. Reciprocal magnetic susceptibility and calculated least-squares fit [83 H 2].

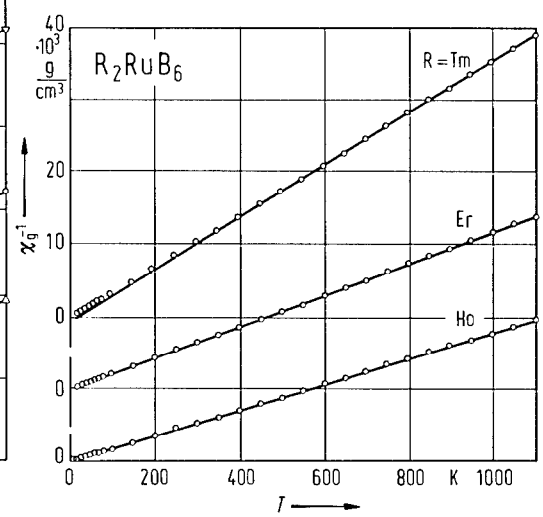

Fig. 60. R_2RuB_6, R = Ho, Er, Tm. Reciprocal magnetic susceptibility and calculated least-squares fit [83 H 2].

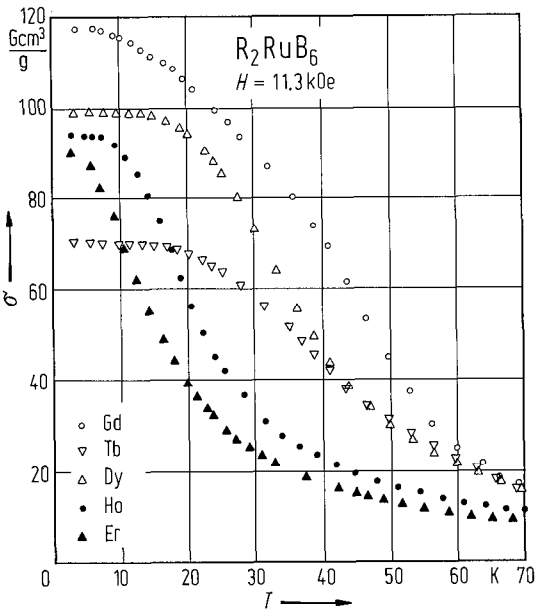

Fig. 61. R_2RuB_6, R = Gd, Tb, Dy, Ho, Er. Magnetization vs. temperature in a magnetic field of $H = 11.3$ kOe [83 H 2].

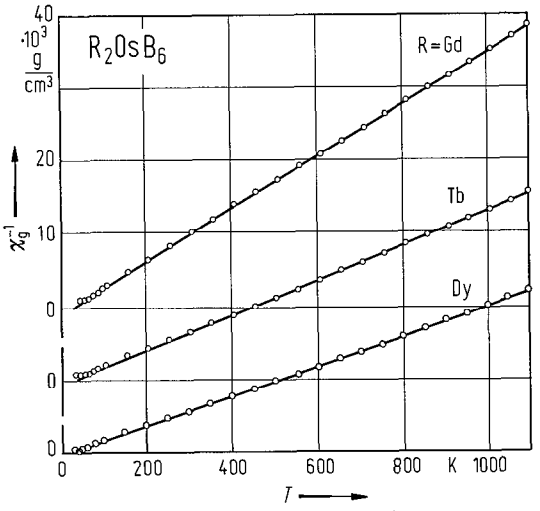

Fig. 62. R_2OsB_6, R = Gd, Tb, Dy. Reciprocal magnetic susceptibility and calculated least-squares fit [83 H 2].

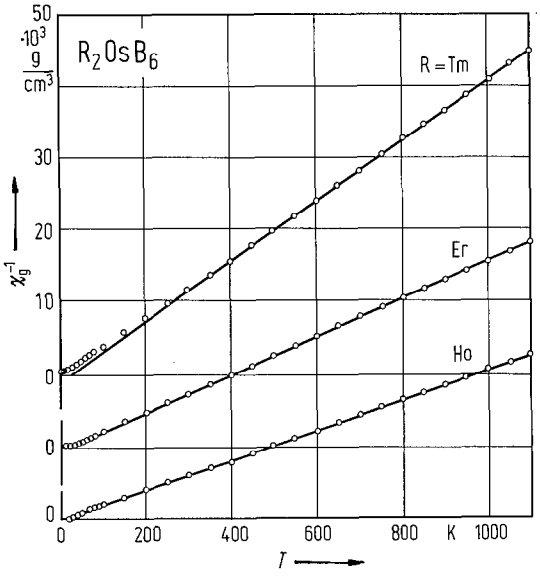

Fig. 63. R_2OsB_6, R = Ho, Er, Tm. Reciprocal magnetic susceptibility and calculated least-squares fit [83 H 2].

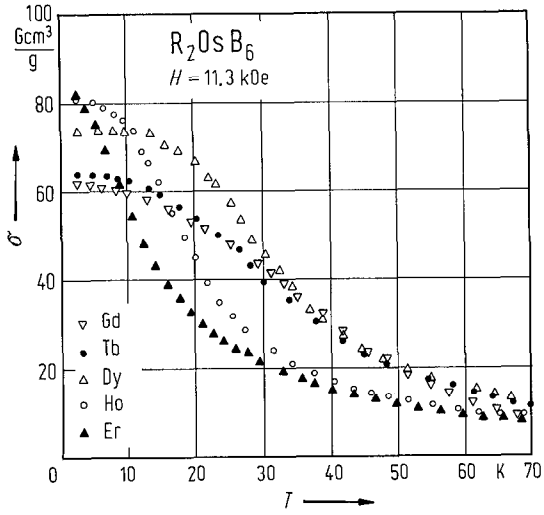

Fig. 64. R_2OsB_6, R = Gd, Tb, Dy, Ho, Er. Magnetization vs. temperature in a magnetic field of $H = 11.3$ kOe [83 H 2].

2.8.2.8 Compounds with RCo_4B stoichiometry (R = Y, Pr, Sm, Gd)

All RCo_4B (R = Y, Pr, Sm, Gd) compounds are ferromagnetic at room temperature, in contrast to RCo_3B_2 (R = Sm, Gd, Er) compounds which are ferromagnetic only below 60 K. X-ray analysis of RCo_4B powders aligned in a 10 kOe field at room temperature indicates that the easy axis of magnetization is the hexagonal *c* axis for YCo_4B, $SmCo_4B$, and $GdCo_4B$. The *b* axis, parallel to the [210] direction, is the easy direction in $PrCo_4B$.

$SmCo_4B$ was the only RCo_4B compound which exhibited significant coercivity at 4.2 K, but the *M* vs. *H* curve was quite asymmetric about the origin. A coercive field of 35 kOe was observed at 4.2 K after initial saturation at 85 kOe. Demagnetization following an 85 kOe reverse field yielded $H_c = 17$ kOe. Subsequent reversals in field direction with fields lower than 85 kOe resulted in diminishing H_c values. This behavior was observed in both aligned powder and bulk specimens of $SmCo_4B$.

YCo_4B shows a complex temperature dependence of the magnetic moment. The *c* axis is the easy direction of magnetization only above $T \simeq 160$ K. The *M* vs. *T* curve of $GdCo_4B$ displayed the features of a ferrimagnet with a compensation point at $T = 413$ K and Curie point at $T = 517$ K. $PrCo_4B$ and $SmCo_4B$ exhibited *M* vs. *T* behavior typical of simple ferromagnets with no unusual features [84 O 1].

Table 16. RCo_4B, R = Y, Pr, Sm, Gd. Room-temperature lattice parameters and magnetic data of ternary borides ($CeCo_4B$-type structure).

R	*a*	*c*	T_C	p_m [1]	H_A [2]	Ref.
	Å		K	μ_B/f.u.	kOe	
Y	5.021	6.895	383	5.8	20	84 O 1
Pr	5.112	6.875	459	6.8		84 O 1
Sm	5.081	6.861	510	3.8	906	84 O 1
			498			83 E 2
Gd	5.056	6.888	517	7.1	20	84 O 1
			321			83 E 2

[1]) Observed magnetic moment for aligned powders in 85 kOe at 4.2 K.
[2]) Extrapolated for 4.2 K.

2.8.2.9 Compounds of composition $R_2Co_7B_3$ and $R_3Co_{11}B_4$ (R = Sm, Gd)

Table 17. $R_2Co_7B_3$, $R_3Co_{11}B_4$, R = Sm, Gd. Magnetic parameters.

	p_s (77 K) μ_B/f.u.	T_C K	Ref.
$Sm_2Co_7B_3$	0.98	402	83 E 2
$Sm_3Co_{11}B_4$	1.69	448	83 E 2
	2.4	460	83 G 1
$Gd_2Co_7B_3$	0.81	287	83 E 2
$Gd_3Co_{11}B_4$	0.79	293	83 E 2

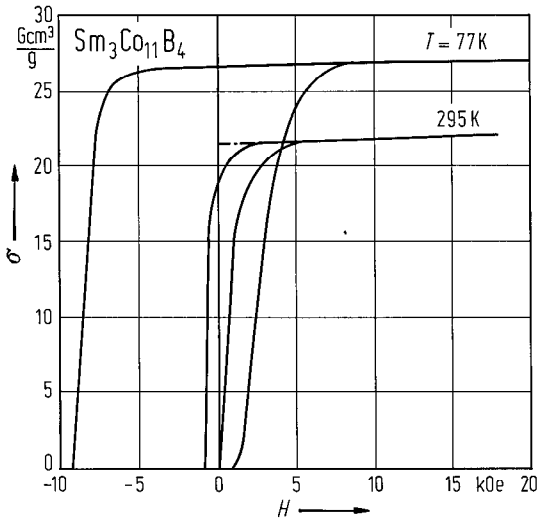

Fig. 65. $Sm_3Co_{11}B_4$. Magnetization vs. applied magnetic field at 295 and 77 K for bulk sample [83 G 1].

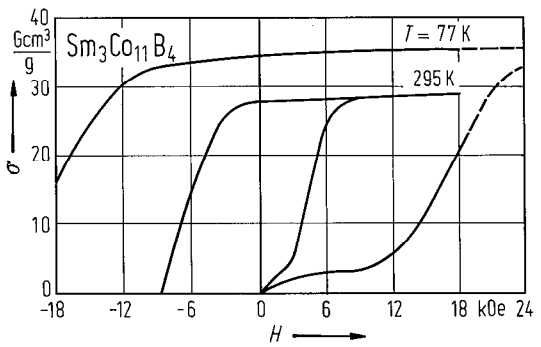

Fig. 66. $Sm_3Co_{11}B_4$. Magnetization vs. applied magnetic field at 295 and 77 K for oriented powders (<37 μm). σ stands for magnetization with aligned axis parallel to the magnetic field [83 G 1].

2.8.2.10 Compounds with $R_2M_{14}B$ stoichiometry (M = Fe, Co)

Compounds $R_2M_{14}B$ with the tetragonal $Nd_2Fe_{14}B$-type structure [84 B 1, 84 G 1, 84 H 1, 84 O 1, 84 S 1, 84 S 2] can exhibit large magnetic flux and high or variable crystal field magnetic anisotropy (of interest for applications) [84 G 2, 84 G 3, 84 O 1, 84 S 3, 84 S 4, 85 A 1, 85 B 3, 85 H 1, 85 K 1]. Representative data are shown in Tables 18–21 and Figs. 68–78. The structure contains slabs of Fe which are related to the σ-phase (e.g. σ-Fe,Cr) sandwiching a layer comprising Nd, Fe and B (σ_s = sandwich layer or σ_s compounds). This sandwich feature makes σ_s compounds anisotropy antitypes to $SmCo_5$ in the sense that rare earth representatives of positive second order Stevens factor S_2 (such as Sm) have nonaxial anisotropy due to the predominant interaction in the σ_s-layer [84 O 1]. The transition metal substructure has nonaxial anisotropy for M = Co and axial anisotropy for M = Fe.

Magnetization curves are shown in Figs. 69···72, while the temperature dependence of anisotropy field and anisotropy constants are depicted in Figs. 73, 74 and 70, 75, 76, respectively. The magnitude K of rare earth anisotropy contribution near 0 K roughly reflects the general formula $K = S_2 J(J-1/2) \langle r^2 \rangle n$, Fig. 77, where n is a normalization factor [86 A 2].

An unusual spin reorientation involving partial canting of the total magnetic moment from the c axis [84 G 2, 84 S 2] is observed for R = Nd and Ho (Figs. 71 and 75). This appears to have to do with competition of second- and fourth-order crystal field terms on R at lower temperatures [84 G 2, 84 G 3, 84 O 1, 84 S 3, 84 S 4, 85 K 1]. The relative influence [86 A 2] of second- and fourth-order terms for rare earths in σ_s-compounds is shown schematically in Fig. 78. One notices that Nd and Ho are most prone to this competition and were found to be the only candidates [86 A 2] to show this internally triggered spin reorientation (at $T_{sr} \simeq 150$ and 62 K, respectively). More conventional spin reorientations are also observed [86 A 2] on account of the different temperature dependence of anisotropy of the rare earth and transition metal substructure.

Mössbauer spectroscopy was used to determine the hyperfine fields (strength of magnetic moment) for the various Fe sites (Table 22), see [86 B 3]. The mid-plane sites of the σ-layer (most removed from σ_s) has the highest values. Larger atoms (e.g. Al) preferentially substitute for these sites [86 A 2].

Data [85 B 2] for the paramagnetic region are given in Fig. 67. For $Y_2Fe_{14}B$, $p_{eff} = 3.98\ \mu_B$/Fe and $\Theta = 562$ K [85 B 2]. For the ordered region, Figs. 68, 69 and 72 represent the temperature dependence of the saturation magnetization.

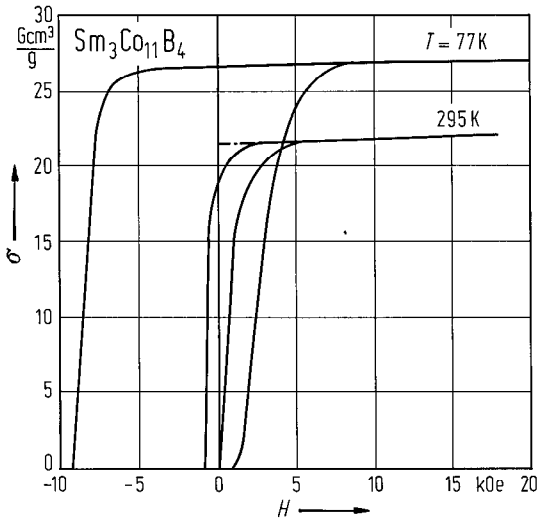

Fig. 65. $Sm_3Co_{11}B_4$. Magnetization vs. applied magnetic field at 295 and 77 K for bulk sample [83 G 1].

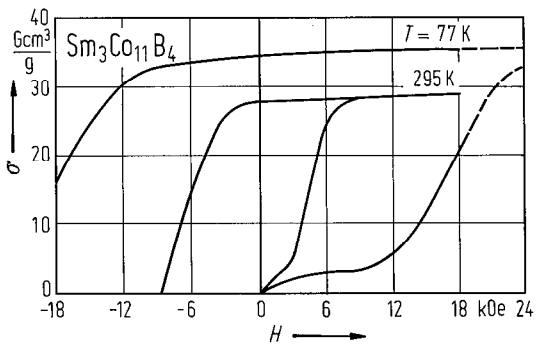

Fig. 66. $Sm_3Co_{11}B_4$. Magnetization vs. applied magnetic field at 295 and 77 K for oriented powders (<37 μm). σ stands for magnetization with aligned axis parallel to the magnetic field [83 G 1].

2.8.2.10 Compounds with $R_2M_{14}B$ stoichiometry (M = Fe, Co)

Compounds $R_2M_{14}B$ with the tetragonal $Nd_2Fe_{14}B$-type structure [84 B 1, 84 G 1, 84 H 1, 84 O 1, 84 S 1, 84 S 2] can exhibit large magnetic flux and high or variable crystal field magnetic anisotropy (of interest for applications) [84 G 2, 84 G 3, 84 O 1, 84 S 3, 84 S 4, 85 A 1, 85 B 3, 85 H 1, 85 K 1]. Representative data are shown in Tables 18–21 and Figs. 68–78. The structure contains slabs of Fe which are related to the σ-phase (e.g. σ-Fe,Cr) sandwiching a layer comprising Nd, Fe and B (σ_s = sandwich layer or σ_s compounds). This sandwich feature makes σ_s compounds anisotropy antitypes to $SmCo_5$ in the sense that rare earth representatives of positive second order Stevens factor S_2 (such as Sm) have nonaxial anisotropy due to the predominant interaction in the σ_s-layer [84 O 1]. The transition metal substructure has nonaxial anisotropy for M = Co and axial anisotropy for M = Fe.

Magnetization curves are shown in Figs. 69···72, while the temperature dependence of anisotropy field and anisotropy constants are depicted in Figs. 73, 74 and 70, 75, 76, respectively. The magnitude K of rare earth anisotropy contribution near 0 K roughly reflects the general formula $K = S_2 J(J-1/2) \langle r^2 \rangle n$, Fig. 77, where n is a normalization factor [86 A 2].

An unusual spin reorientation involving partial canting of the total magnetic moment from the c axis [84 G 2, 84 S 2] is observed for R = Nd and Ho (Figs. 71 and 75). This appears to have to do with competition of second- and fourth-order crystal field terms on R at lower temperatures [84 G 2, 84 G 3, 84 O 1, 84 S 3, 84 S 4, 85 K 1]. The relative influence [86 A 2] of second- and fourth-order terms for rare earths in σ_s-compounds is shown schematically in Fig. 78. One notices that Nd and Ho are most prone to this competition and were found to be the only candidates [86 A 2] to show this internally triggered spin reorientation (at $T_{sr} \simeq 150$ and 62 K, respectively). More conventional spin reorientations are also observed [86 A 2] on account of the different temperature dependence of anisotropy of the rare earth and transition metal substructure.

Mössbauer spectroscopy was used to determine the hyperfine fields (strength of magnetic moment) for the various Fe sites (Table 22), see [86 B 3]. The mid-plane sites of the σ-layer (most removed from σ_s) has the highest values. Larger atoms (e.g. Al) preferentially substitute for these sites [86 A 2].

Data [85 B 2] for the paramagnetic region are given in Fig. 67. For $Y_2Fe_{14}B$, $p_{eff} = 3.98\ \mu_B$/Fe and $\Theta = 562$ K [85 B 2]. For the ordered region, Figs. 68, 69 and 72 represent the temperature dependence of the saturation magnetization.

Partial substitution on transition metal sites according to $Nd_2Fe_{14-x}M_xB$ can increase (M = Co, Ni) or decrease (M = Cr, Mn, Al) T_C [86 A 1, 86 Y 1], Fig. 86.

The change of T_{sr} with partial rare earth substitution is shown in Fig. 98. For modifying the crystal field anisotropy in σ_s-compounds it is of interest to note that the more anisotropic R site (4g) is preferentially occupied by the larger atom (e.g. Nd over Dy) [86 A 1, 86 Y 1]. Relatively stable magnetization with temperature near 300 K can be obtained through rare earth sublattice compensation [86 A 2)], Fig. 99.

Table 18. $R_2Fe_{14}B$. Crystallographic and magnetic properties. a, c: room-temperature lattice constants, ϱ_X: X-ray density at room temperature, T_C: Curie temperature, σ: room-temperature magnetization measured at $\mu_0 H = 1.8$ T, $\mu_0 M$: magnetic induction at room-temperature, calculated by using σ and ϱ_X [84 S 3].

R	a	c	ϱ_X	T_C	σ	$\mu_0 M$
	Å		$g\,cm^{-3}$	K	$A\,m^2\,kg^{-1}$	T
Y	8.757	12.026	6.98	558	145	1.271
La	8.822	12.338	7.40	530	130	1.208
Ce	8.726	12.057	7.76	425	105	1.023
Pr	8.838	12.289	7.43	565	109	1.017
Nd	8.792	12.177	7.62	580	120	1.148
Sm	8.777	12.105	7.78	616	120	1.173
Gd	8.780	12.075	7.90	650	77	0.764
Tb	8.785	12.070	7.90	620	41	0.411
Dy	8.757	11.990	8.07	585	44	0.446
Ho	8.753	11.988	8.12	565	40	0.408
Er	8.734	11.942	8.21	550	96	0.997
Tm	8.728	11.928	8.26	540	114	1.183
Lu	8.712	11.883	8.41	535	95	1.004

Table 19. $R_2Fe_{14}B$. Saturation magnetization σ_s obtained at 4.2 K from measurements of the magnetization of aligned powder samples in magnetic fields up to $\mu_0 H = 14$ T. The quantities p_s, p_{Fe} and p_R represent the total saturation magnetic moment per formula unit, the Fe magnetic moment and the R magnetic moment, respectively. The nonzero values for p_R are derived from p_s by assuming $p_{Fe} = 2.2\,\mu_B$. The positive (negative) sign of p_R values indicates parallel (antiparallel) alignment of R and Fe magnetic moments. The values of $\mu_0 H_A$ represent the field strengths where the curves $\sigma_{\parallel}(H)$ and $\sigma_{\perp}(H)$ for magnetic fields parallel and perpendicular to the alignment field, respectively, intersect at 4.2 K. S_2 is the second-order Stevens factor [84 S 3].

R	σ_s $A\,m^2\,kg^{-1}$	p_s μ_B/f.u.	p_{Fe} μ_B	p_R μ_B	gJ	$\mu_0 H_A$ T	S_2
Y	117	30.7	2.20	0	0	3···4	0
La	160	30.6	2.19	0	0	3···3	0
Ce	157	30.2	2.14	0	0	5···6	0
Pr	168	32.3	(2.2)	+ 0.8	3.2	29	−
Nd	180	34.8	(2.2)	+ 2.0	3.3	32	−
Sm	160	31.3	(2.2)	+ 0.3	0.7	40	+
Gd	90	17.8	(2.2)	− 6.4	7.0	4···5	0
Tb	65	12.9	(2.2)	− 8.9	9.0		−
Dy	55	11.0	(2.2)	− 9.9	10.0	20	−
Ho	54	10.9	(2.2)	−10.0	10.0		−
Er	67	13.5	(2.2)	− 8.7	9.0	26	+
Tm	88	17.8	(2.2)	− 6.5	7.0	17	+
Lu	138	28.2	2.00	0	0	4···6	0

Table 20. $R_2Co_{14}B$. Curie temperature T_C obtained from dsc measurements and saturation magnetization σ_s obtained at 4.2 K from measurements of the magnetization of aligned powder samples in magnetic fields up to $\mu_0 H = 35$ T. The quantities p_s and p_{Co} represent the total saturation magnetic moment and the Co magnetic moment, respectively. The values of $\mu_0 H_A$ represent the field strengths where the curves $\sigma_{\parallel}(H)$ and $\sigma_{\perp}(H)$ for magnetic fields parallel and perpendicular to the alignment field, respectively, intersect at 4.2 K. The easy magnetization directions are given with respect to the tetragonal c axis; S_2 represents the second-order Stevens factor [85 B 3].

R	T_C K	σ_s $A\,m^2\,kg^{-1}$	p_s μ_B/f.u.	p_{Co} μ_B	$\mu_0 H_A$ T	Easy axis	S_2
Y	1015	107	19.42	1.39	6···7	$\perp c$	0
La	955	102	20.35	1.45	6···7	$\perp c$	0
Pr	995	124	24.82		75	$\parallel c$	−
Nd	1007	126	25.37		30	$\parallel c$	−
Sm	1029	(89)	18.10			$\perp c$	+
Gd	1050	(32)	6.90			$\perp c$	0
Tb	1035					$\parallel c$	−

Table 21. $R_2Fe_{14}B$. Anisotropy constant K_1 at 4.2 K and the second-order Stevens factor S_2 of the R^{3+} ions [85 H 1].

R	K_1 $10^6\,J\,m^{-3}$	S_2 10^{-3}
Y	0.77	0
Ce	1.65	−57.14
Pr	23.5	−21.01
Nd	−16	41.27
Sm	26	41.27
Gd	0.72	0
Tb	8.2	−10.10
Dy	3.8	− 6.349
Ho		− 2.222

Table 22. $Nd_2Fe_{14}B$, $Dy_2Fe_{14}B$. Comparison of ^{57}Fe hyperfine fields reported by various authors for the six Fe sites in $Nd_2Fe_{14}B$ and $Dy_2Fe_{14}B$. The number of nearest-neighbour Fe atoms corresponding to these sites is indicated by n_{Fe}. Values of the Fe magnetic moments obtained from the averaged hyperfine fields given for $Nd_2Fe_{14}B$ are also listed [86 B 1].

	Fe site	$8j_2$	$16k_2$	$16k_1$	$8j_1$	4e	4c
T [K]	n_{Fe}	12	10	9	9	9	8
		$Nd_2Fe_{14}B$ (B_{hyp} in T)					
25		40.0	35.7	33.7	32.5	32.7	31.1
77		37.5	34.0	32.0	31.5	29.1	36.0
80		34.7	34.7	32.5	30.0	36.5	38.0
300		34.4	30.7	28.6	28.8	25.2	26.5
300		34.3	30.6	28.9	28.0	28.3	26.1
300		34.3	(30.0)	(29.1)	26.2	30.0	29.2
300		34.6	30.7	28.7	26.4	26.3	31.2
		$Nd_2Fe_{14}B$ (p_{Fe} in μ_B)					
300		2.32	2.06	1.95	1.85	1.8	1.9
		$Dy_2Fe_{14}B$ (B_{hyp} in T)					
300		35.6	31.1	29.0	29.0	28.5	27.6
300		35.3	30.8	29.3	28.0	28.5	27.1
300		35.3	31.0	29.2			

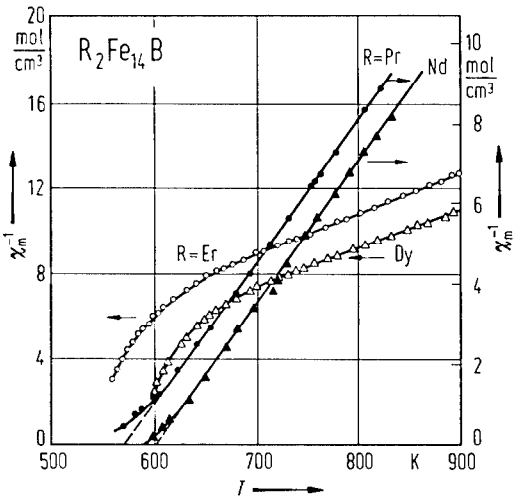

Fig. 67. $R_2Fe_{14}B$, R = Pr, Nd, Er, Dy. Reciprocal magnetic molar susceptibilities vs. temperature. Curie-Weiss-type behavior is observed for R = Pr and Nd, Néel-type behavior for R = Er and Dy [85 B 2].

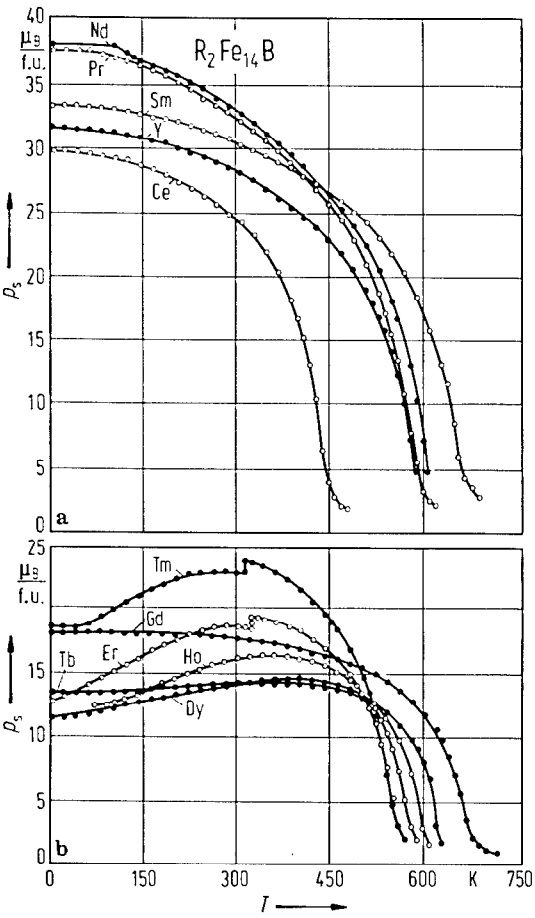

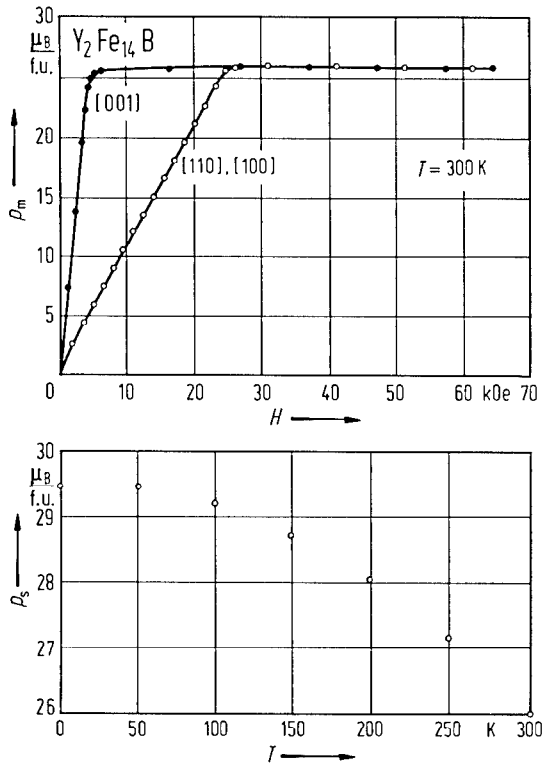

Fig. 69. $Y_2Fe_{14}B$. Magnetic field dependences of the magnetization at 300 K and temperature dependence of the spontaneous magnetization [84 G 2].

◀

Fig. 68. $R_2Fe_{14}B$. Temperature dependence of saturation magnetization measured on single crystals. (a) Light rare earth compounds and (b) heavy rare earth compounds [85 H 1].

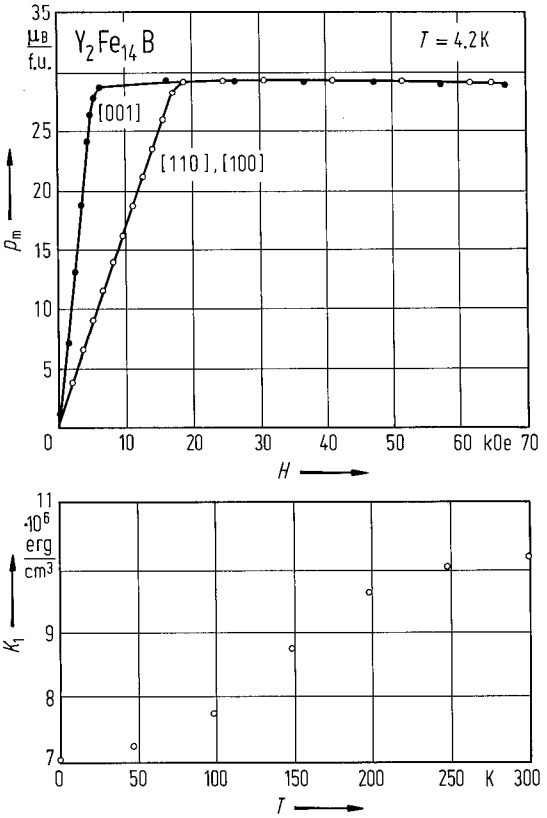

Fig. 70. $Y_2Fe_{14}B$. Magnetic field dependences of the magnetization at 4.2 K and temperature dependence of the anisotropy constant K_1 [84 G 2].

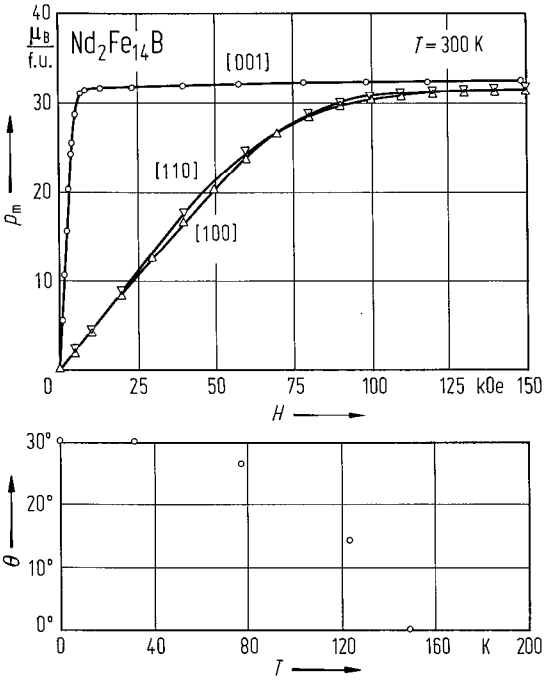

Fig. 71. $Nd_2Fe_{14}B$. Magnetic field dependences of the magnetization at 300 K and temperature dependence of the angle θ between the easy magnetization direction and the c axis [84 G 2].

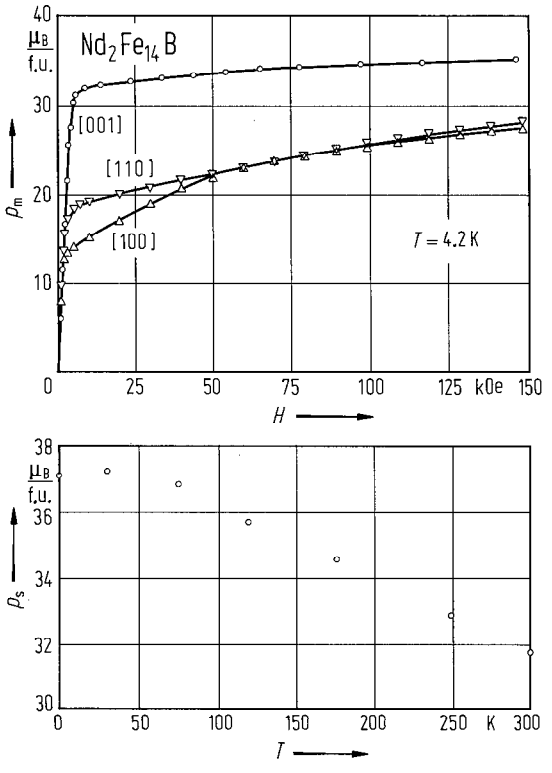

Fig. 72. $Nd_2Fe_{14}B$. Magnetic field dependences of the magnetization at 4.2 K and temperature dependence of the spontaneous magnetization [84 G 2].

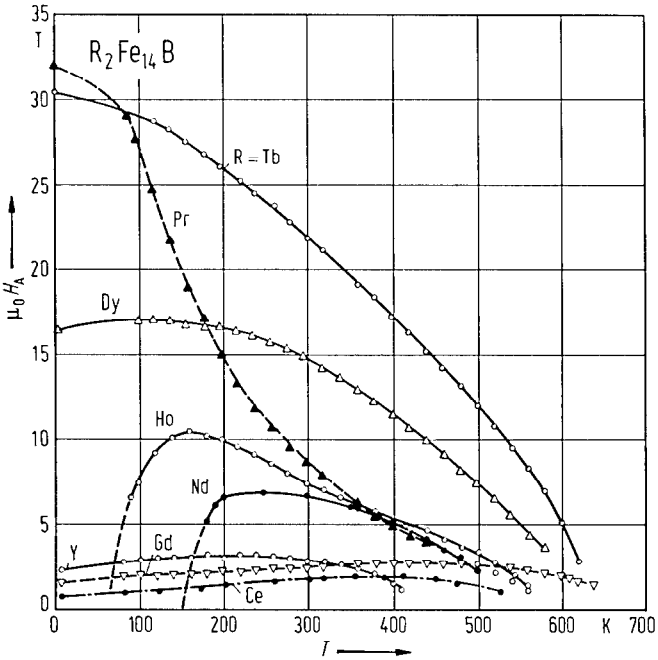

Fig. 73. $R_2Fe_{14}B$. Temperature dependence of anisotropy fields measured in an applied magnetic field of 800 kA/m [85 H 1].

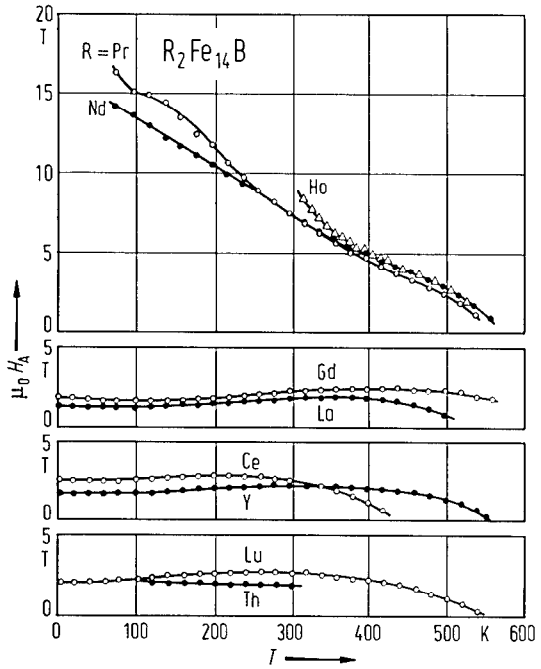

Fig. 74. $R_2Fe_{14}B$. Temperature dependence of the anisotropy field determined by means of the singular point detection (SPD) technique [86 G 1].

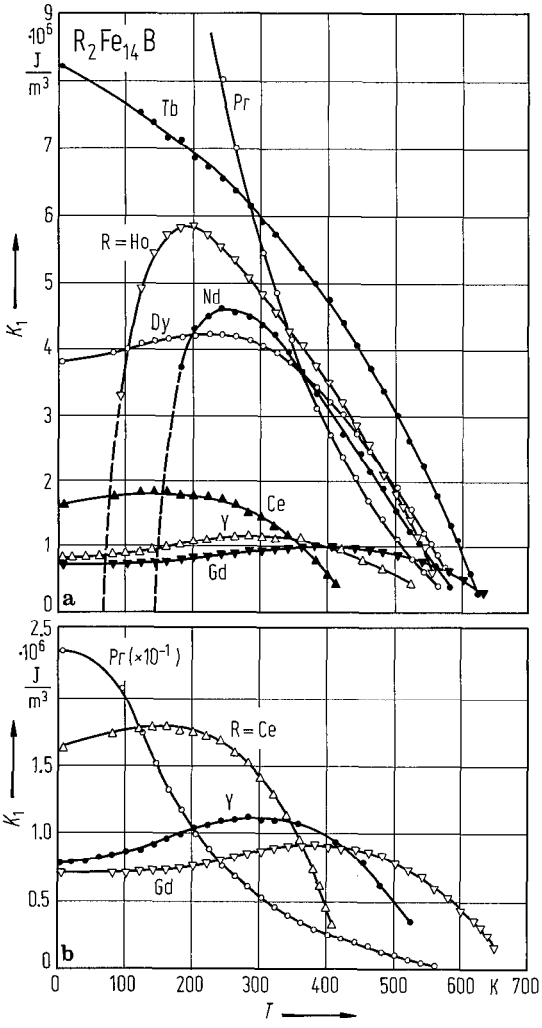

Fig. 75. $R_2Fe_{14}B$. Temperature dependence of the anisotropy constant K_1 for (a) R = Y, Ce, Pr, Nd, Gd, Tb, Dy, Ho and (b) R = Y, Ce, Pr, Gd [85 H 1].

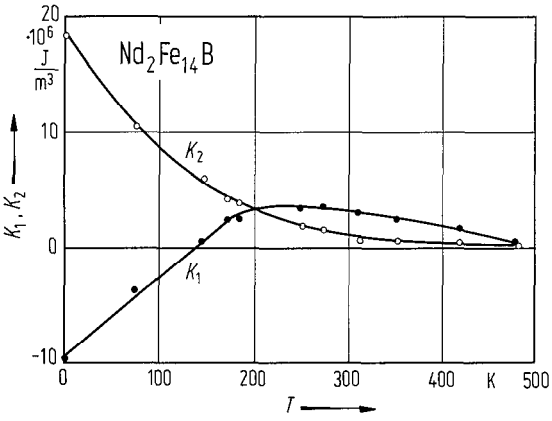

Fig. 76. $Nd_2Fe_{14}B$. Temperature dependence of the first- and second-order anisotropy constants K_1 and K_2 for a composition close to $Nd_2Fe_{14}B$ [85 Y 1].

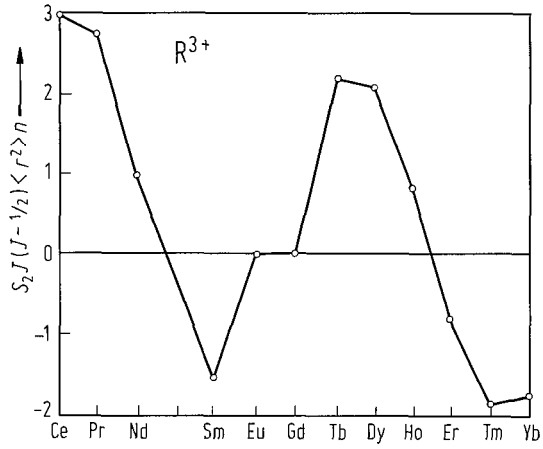

Fig. 77. R^{3+}. Anisotropy $S_2J(J-1/2)\langle r^2\rangle n$ for R^{3+} ions relative to Nd^{3+}. n is a normalization factor [86 A 2].

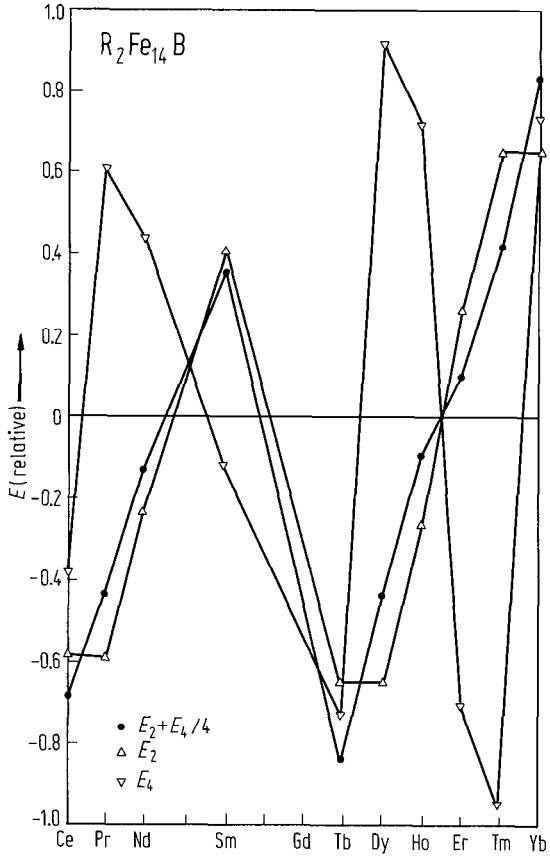

Fig. 78. $R_2Fe_{14}B$. Energies of crystal-field terms, $E_2 = S_2O_2^0(J)G_2^0$, $E_4 = S_4O_4^0(J)G_4^0/3$, and $E_2+E_4/4$. For both R = Nd and Ho, $E_2+E_4/4$ indicates susceptibility to a spin reorientation at cryogenic temperatures from axial to canted structure. Conversely, $Er_2Fe_{14}B$ should show a tendency from basal to canted [86 A 2].

2.8.2.11 Compounds with $R_2Fe_{14}BH_x$ stoichiometry

Compounds $R_2Fe_{14}B$ were found to take up H around ambient condition according to $R_2Fe_{14}BH_x$ [84 L 1, 84 O 2, 85 A 1, 85 D 1, 85 L 1, 85 S 1, 86 P 1]. The mode of uptake is above critical leading to solid-solution behavior rather than to specific hydride phases [86 P 1]. The general tendencies with increasing x are an increase in magnetic moment on Fe sites and an attendant increase in T_C. At the same time, however, rare earth – transition metal exchange is diminished and as a result the rare earth anisotropy contribution is less effective at elevated temperatures. Tables 23 and 24 list magnetic parameters. Typical magnetization curves are shown in Figs. 79···82, 84, 85. The variation in T_N with x is given in Fig. 83.

Table 23. $R_2Fe_{14}BH_x$. Curie temperature T_C of some of the compounds. The relative increase of T_C in the hydride compared to the virgin compound is denoted $\Delta T_C/T_C$ [85 L 1].

R	x	T_C K	$\Delta T_C/T_C$ %
Y	0	590	
	3.1	639	8.9
Ce	0	435	
	2.5	543	24.8
Nd	0	589	
	4.5	676	14.8
Dy	0	605	
	3.5	650	7.4
Er	0	560	
	3.3	627	12

Table 24. $Nd_2Fe_{14}BH_x$. Room-temperature lattice constants and magnetic parameters for aligned powder samples [84 O 2].

x	a	c	c/a	p_m [1])	T_C	H_A
	Å			μ_B/f.u.	K	kOe
0	8.792	1.2174	1.385	28.8	603	76 [1])
2.7	8.930	1.2360	1.384	31.8 [3])		20 [1])
						54 [2])

[1]) $T = 300$ K.
[2]) $T = 77$ K.
[3]) Formula unit was taken to be $Nd_2Fe_{14}B$.

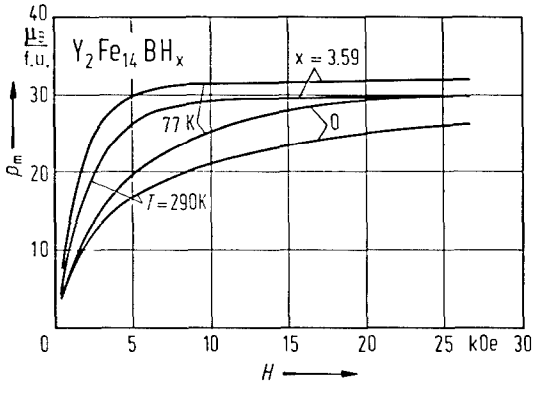

Fig. 79. $Y_2Fe_{14}BH_x$. Magnetic field dependence of magnetization at 77 and 290 K [85 L 1].

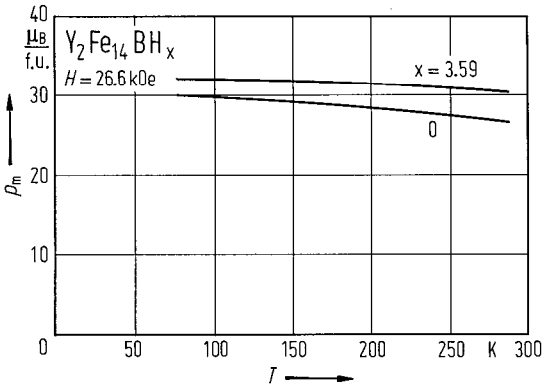

Fig. 80. $Y_2Fe_{14}BH_x$. Magnetization vs. temperature in an applied field of 26.6 kOe [85 L 1].

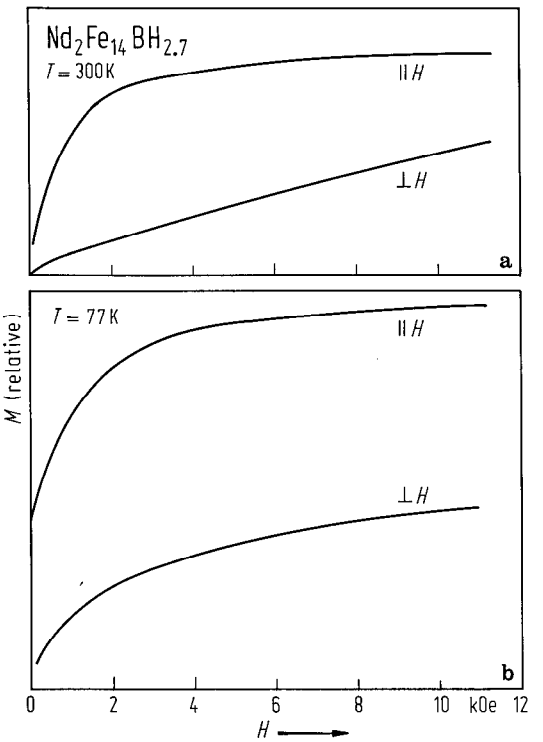

Fig. 81. $Nd_2Fe_{14}BH_{2.7}$. Magnetization vs. applied magnetic field at (a) 300 K and (b) 77 K for aligned powder sample oriented parallel and perpendicular to the field direction [84 O 2].

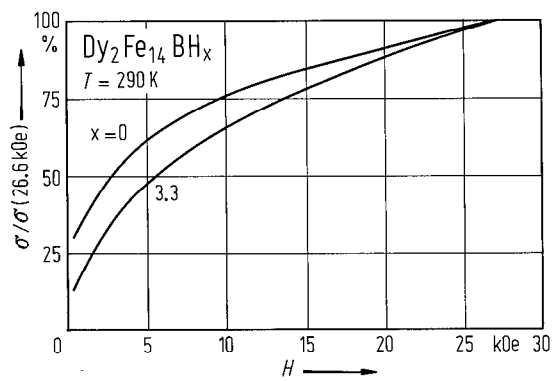

Fig. 82. $Dy_2Fe_{14}BH_x$. Relative magnetization vs. applied magnetic field up to 26.6 kOe at $T = 290$ K. The applied field is perpendicular to the samples (powders magnetically aligned, and fixed in epoxy resin) [85 L 1].

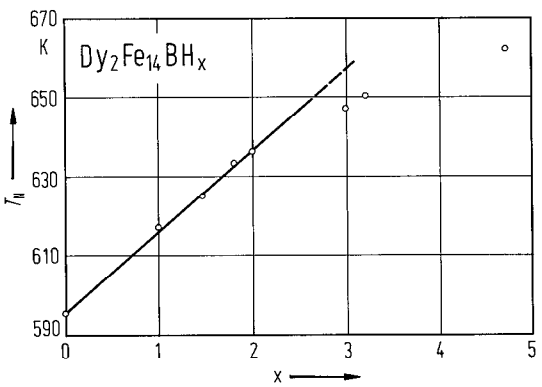

Fig. 83. $Dy_2Fe_{14}BH_x$. Variation of the Néel temperature T_N vs. hydrogen concentration [85 D 1].

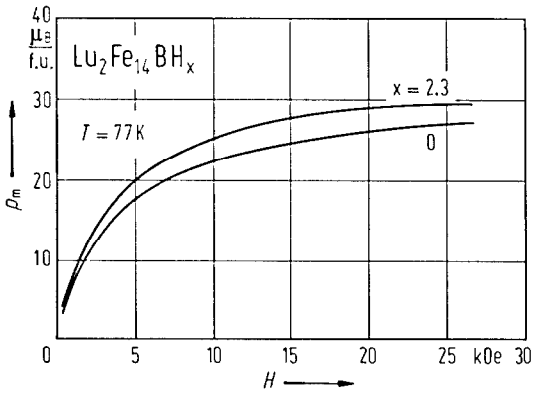

Fig. 84. $Lu_2Fe_{14}BH_x$. Magnetization vs. applied magnetic field at 77 K for fields up to 26.6 kOe [85 L 1].

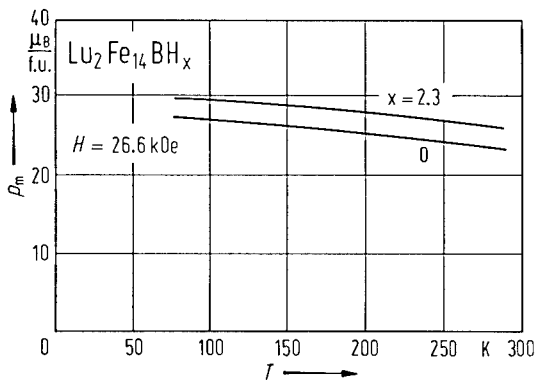

Fig. 85. $Lu_2Fe_{14}BH_x$. Magnetization vs. temperature in an applied field of 26.6 kOe [85 L 1].

2.8.2.12 Compounds with RCo_4BH_x stoichiometry

Several compounds of the type RCo_4B have been hydrided around ambient conditions forming several sucessive hydride phases RCo_4BH_x [85 S 1]. The magnetic properties of the α, β- and γ-hydrides of $SmCo_4B$ and the α-hydride of $PrCo_4B$ are summarized in Table 25. It is evident that both T_C and the magnetic moment decrease as the hydrogen content increases.

Table 25. RCo_4BH_x. Magnetic data [85 S 1].

R	x	T_C K	p_m [1] μ_B/f.u.
La [2]	0	431	
Pr	0	459	4.37
	1.0	219	3.67
Sm	0	510	3.34
	1.0	298	2.74
	2.5	181	1.98
	4.1	< 77	

[1]) Magnetic moment determined at 77 K in a 10 kOe applied magnetic field for samples aligned along the easy direction.

[2]) Multiphase material; p_m not calculated.

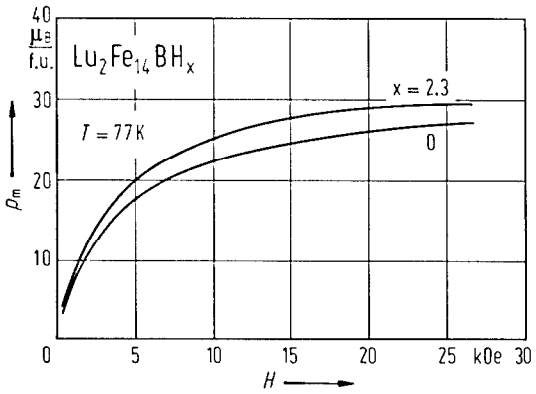

Fig. 84. $Lu_2Fe_{14}BH_x$. Magnetization vs. applied magnetic field at 77 K for fields up to 26.6 kOe [85 L 1].

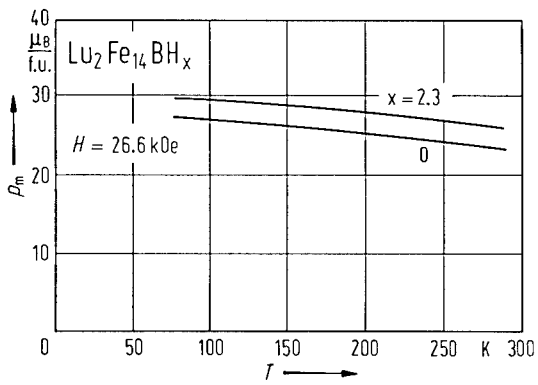

Fig. 85. $Lu_2Fe_{14}BH_x$. Magnetization vs. temperature in an applied field of 26.6 kOe [85 L 1].

2.8.2.12 Compounds with RCo_4BH_x stoichiometry

Several compounds of the type RCo_4B have been hydrided around ambient conditions forming several sucessive hydride phases RCo_4BH_x [85 S 1]. The magnetic properties of the α, β- and γ-hydrides of $SmCo_4B$ and the α-hydride of $PrCo_4B$ are summarized in Table 25. It is evident that both T_C and the magnetic moment decrease as the hydrogen content increases.

Table 25. RCo_4BH_x. Magnetic data [85 S 1].

R	x	T_C K	p_m [1] μ_B/f.u.
La [2]	0	431	
Pr	0	459	4.37
	1.0	219	3.67
Sm	0	510	3.34
	1.0	298	2.74
	2.5	181	1.98
	4.1	< 77	

[1]) Magnetic moment determined at 77 K in a 10 kOe applied magnetic field for samples aligned along the easy direction.

[2]) Multiphase material; p_m not calculated.

2.8.3 Pseudoternary compounds

2.8.3.1 Compounds with transition metal substitution

Magnetic data on $Nd_2Fe_{14-x}Co_xB$ are shown in Figs. 86···89. It was also indicated that the magnetic anisotropy in $La_2(Co_xFe_{1-x})_{14}B$ changes from axial to nonaxial at x = 0.86 [85 B 4].

Table 26. $Nd_2Fe_{13}CoB$, Sm–M–B. Room-temperature lattice constants and magnetic parameters of pseudoternary borides with transition metal substitution.

	x	Crystal structure	a	c	T_C	p_m [1]	H_A [2]	Ref.
			Å		K	μ_B/f.u.	kOe	
$Nd_2Fe_{13}CoB$		tetragonal	8.807	12.219	643	30 [3]	49 [3]	84 O 1
$SmFe_xCo_{4-x}B$	0.5				603	2.95		83 E 1
	1	$CeCo_4B$	5.118	6.860	721	4.5	439	84 O 1
					679	2.35		83 E 1
	1.5				718	3.20		83 E 1
	2	$CeCo_4B$	5.116	6.921	768	6.0	602	84 O 1
	2.5 [4]				603, 748, 855	≃ 5		83 E 1
$SmFe_2Ni_2B$		$CeCo_4B$	5.083	6.947	495	3.9	490	84 O 1
$SmFeNi_3B$		$CeCo_4B$	5.066	6.953	404	2.0	628	84 O 1
$SmCo_3NiB$		$CeCo_4B$	5.065	6.901	424	2.5	763	84 O 1
$Sm_3Fe_xCo_{11-x}B_4$	1				523	2.04		83 E 1
	2				545	2.26		83 E 1
	3				593	1.86		83 E 1
	4				635	2.55		83 E 1
	5				726	2.73		83 E 1
	6 [4]				726, 1016	≃ 4		83 E 1
$Sm_2Fe_xCo_{7-x}B_3$	1				519	1.27		83 E 1
	2				589	1.15		83 E 1
	3 [4]				553, 707	≃ 3		83 E 1

[1]) Observed magnetic moment per formula unit for aligned powders in 85 kOe at 4.2 K (10 kOe at 300 K for $Nd_2Fe_{13}CoB$).

[2]) Extrapolated for 4.2 K unless stated otherwise.

[3]) Extrapolated for 300 K.

[4]) Multiphase material.

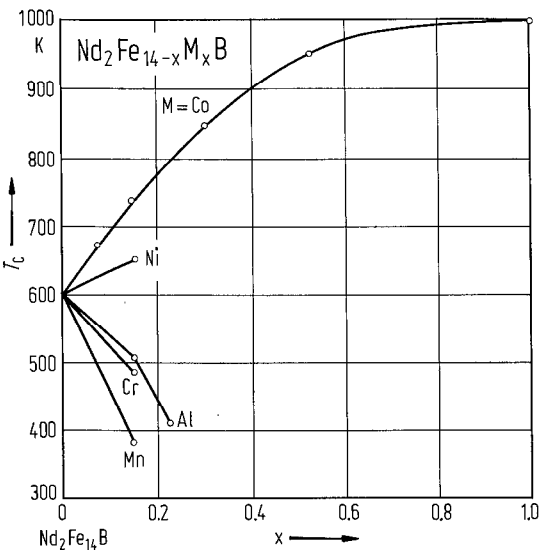

Fig. 86. $Nd_2Fe_{14-x}M_xB$, M = Cr, Mn, Co, Ni, Al. Variation of the Curie temperature T_C as a function of transition metal M concentration x [86 A 1, 86 Y 1].

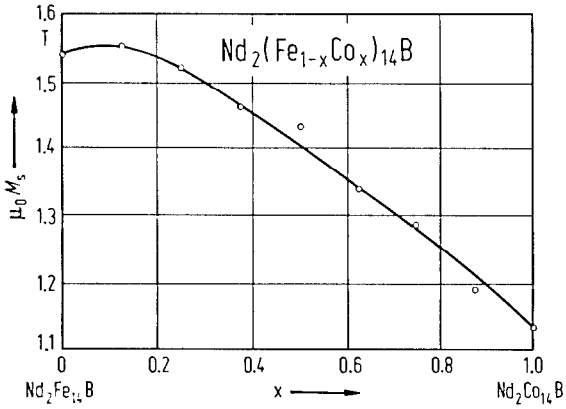

Fig. 87. $Nd_2(Fe_{1-x}Co_x)_{14}B$. Dependence of the saturation magnetization on the Co concentration [85 M 1].

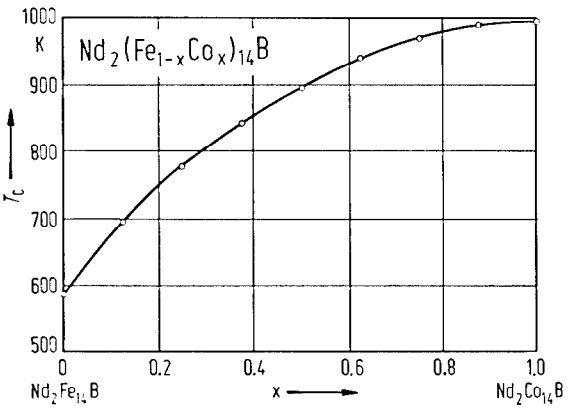

Fig. 88. $Nd_2Fe_{1-x}Co_x)_{14}B$. Dependence of the Curie temperature on the Co concentration [85 M 1].

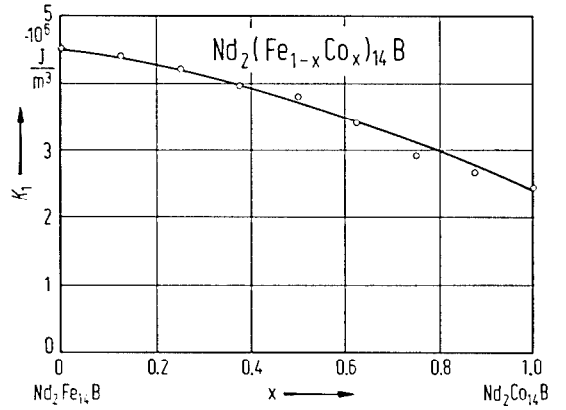

Fig. 89. $Nd_2(Fe_{1-x}Co_x)_{14}B$. Dependence of the first-order anisotropy constant on the Co concentration [85 M 1].

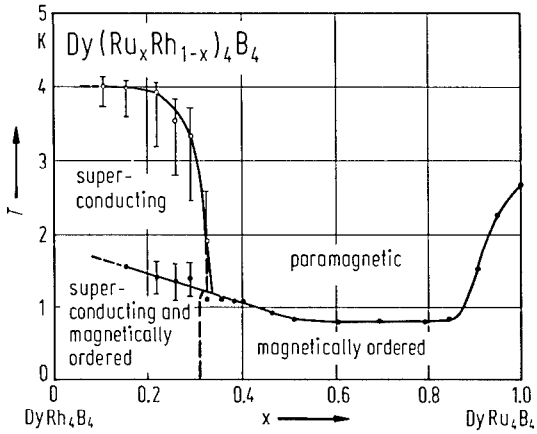

Fig. 90. $Dy(Ru_xRh_{1-x})_4B_4$. Low-temperature phase diagram determined from ac magnetic susceptibility and heat capacity measurements. Open circles represent paramagnetic-to-superconducting state transition temperatures, while solid circles are magnetic transition temperatures. Vertical bars represent temperatures at which superconducting transitions are 10% and 90% complete, and the dashed vertical bar for $x = 0.327$ indicates that the transition was less than 90% complete [83 H 1].

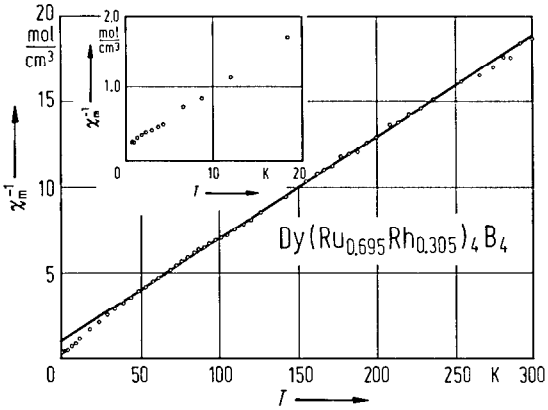

Fig. 91. $Dy(Ru_{0.695}Rh_{0.305})_4B_4$. Inverse magnetic molar susceptibility vs. temperature. The solid line represents a Curie-Weiss law with $p_{eff} = 11.5\ \mu_B$/f.u. and $\Theta = -16.0$ K [83 H 1].

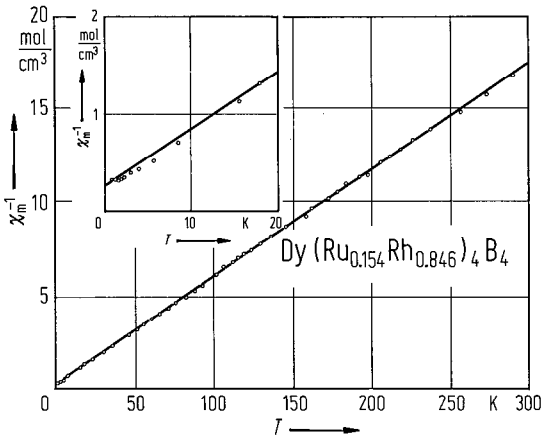

Fig. 92. $Dy(Ru_{0.154}Rh_{0.846})_4B_4$. Inverse magnetic molar susceptibility vs. temperature. The solid line represents a Curie-Weiss law with $p_{eff}=11.8\ \mu_B$/f.u. and $\Theta=-4.5$ K [83 H 1].

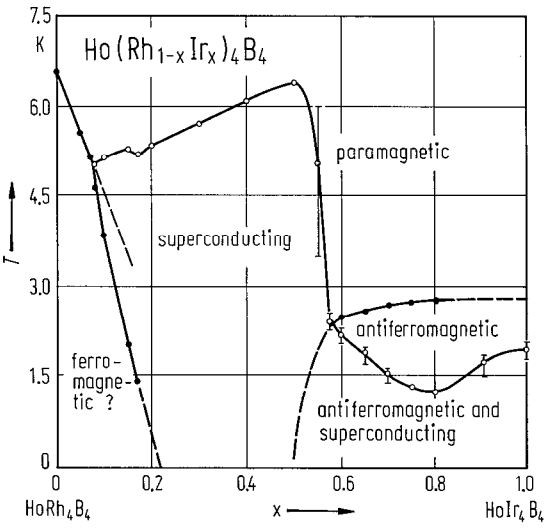

Fig. 94. $Ho(Rh_{1-x}Ir_x)_4B_4$. Low-temperature phase diagram determined from ac and static magnetic susceptibility measurements on arc-melted samples [80 K 3].

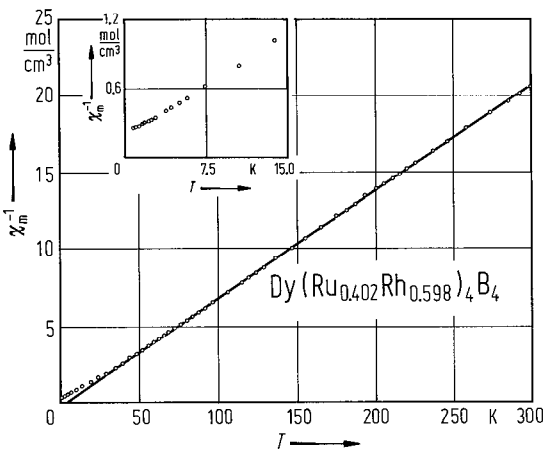

Fig. 93. $Dy(Ru_{0.402}Rh_{0.598})_4B_4$. Inverse magnetic molar susceptibility vs. temperature. The solid line represents a Curie-Weiss law with $p_{eff}=10.58\ \mu_B$/f.u. and $\Theta=4.3$ K [83 H 1].

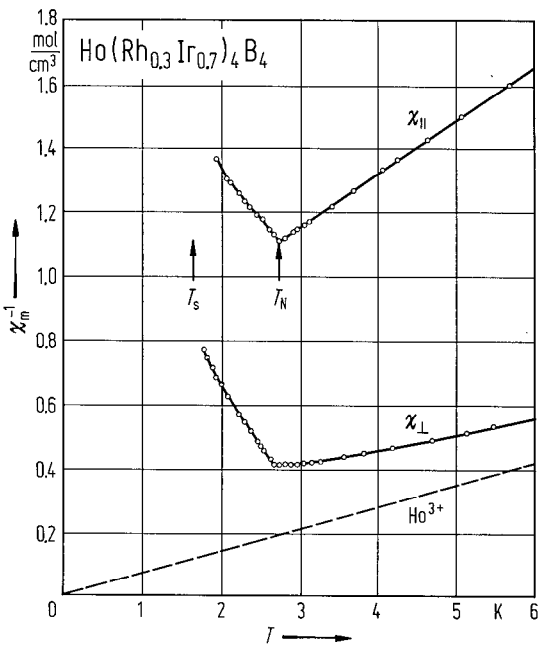

Fig. 95. $Ho(Rh_{0.3}Ir_{0.7})_4B_4$. Inverse magnetic molar susceptibility vs. temperature, measured in a magnetic field of 400 Oe for two directions approximately parallel and perpendicular to the cooling axis of the specimen in the arc furnace, and with demagnetization correction. Néel temperature $T_N=2.7$ K and superconducting transition temperature $T_s=1.6$ K. The inverse magnetic molar susceptibility of the Ho^{3+} free ions is shown by the dashed line [80 K 3].

Table 27. $ROs_{4-x}Ir_xB_4$. Room-temperature lattice constants and magnetic parameters of pseudoternary borides with transition metal substitution [82 H 1].

R	x	a	c	Θ	p_{eff}
		Å		K	μ_B/f.u.
Ce	2.48	7.6190(9)	3.9786(4)	0	2.14
	3	7.6304(10)	3.9780(7)	4.5	2.22
Pr	2	7.5991(12)	3.9835(5)	22	3.55
Sm	0	7.526(3)	4.009(2)		1.69 [1])
	1	7.5406(8)	3.9949(6)		1.87 [1])
	2	7.5538(6)	3.9860(4)		1.71 [1])
	3	7.5742(7)	3.9822(4)		1.62 [1])
	4	7.590(3)	3.976(2)		1.55 [1])
Eu	0	7.5262(9)	4.0159(6)	0.0	7.20
	4	7.6219(9)	3.9771(5)	2.5	7.84

[1]) Values at 295 K.

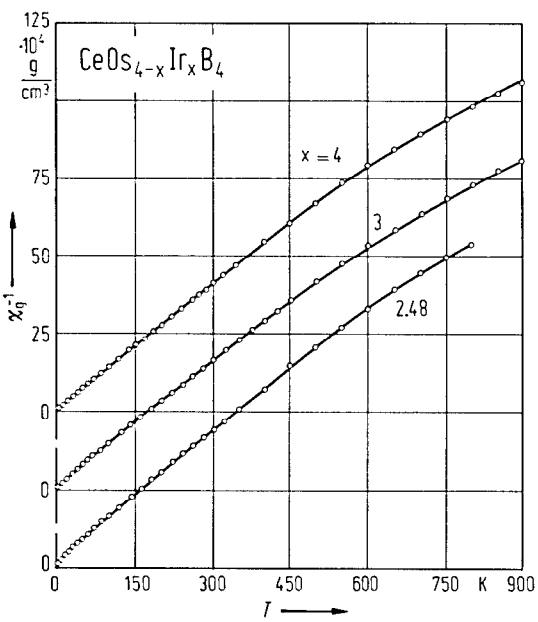

Fig. 96. $CeOs_{4-x}Ir_xB_4$. Reciprocal magnetic susceptibility vs. temperature for various compositions. Solid lines indicate least-squares fit [82 H 1].

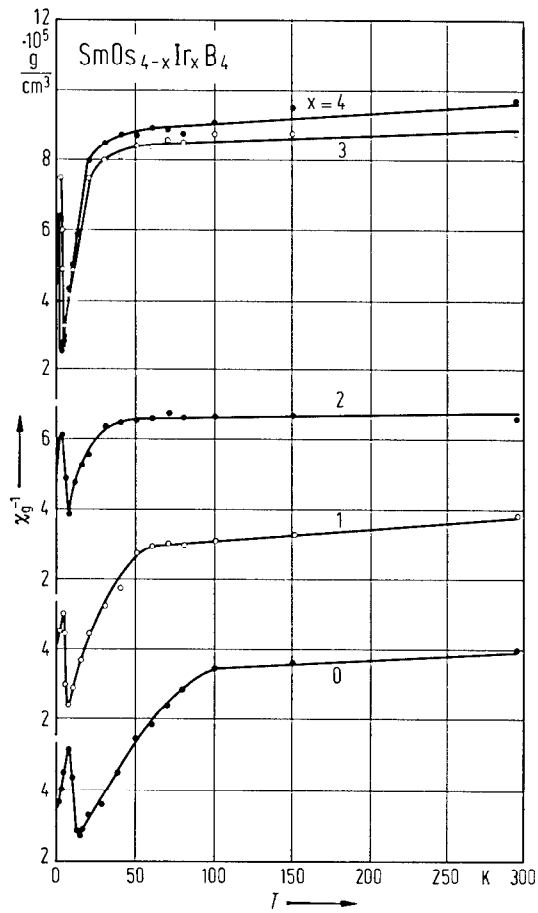

Fig. 97. $SmOs_{4-x}Ir_xB_4$. Reciprocal magnetic susceptibility vs. temperature for various compositions [82 H 1].

2.8.3.2 Compounds with rare earth metal substitution

Magnetic data on σ_s-compounds $(R_{1-x}R'_x)_2Fe_{14}B$ are represented in Figs. 98 and 99, see also subsect. 2.8.2.10.

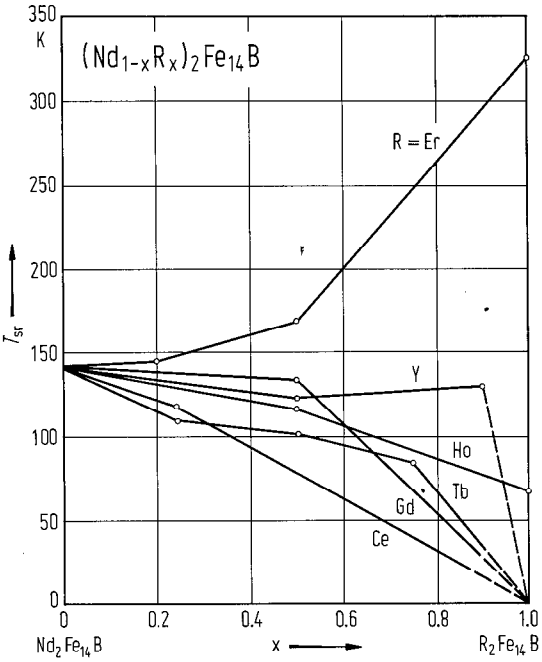

Fig. 98. $(Nd_{1-x}R_x)_2Fe_{14}B$, R = Y, Ce, Gd, Tb, Ho, Er. Spin reorientation temperature T_{sr} vs. R concentration. The lines are guides to the eye only [86 A 2].

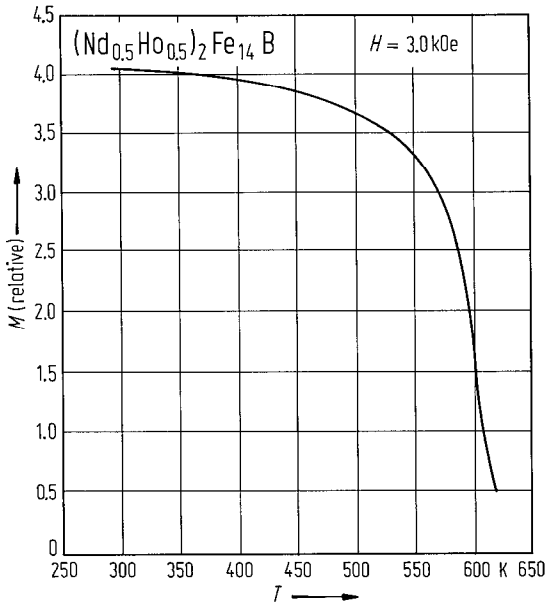

Fig. 99. $(Nd_{0.5}Ho_{0.5})_2Fe_{14}B$. Magnetization M vs. temperature in a magnetic field of 3.0 kOe [86 A 2].

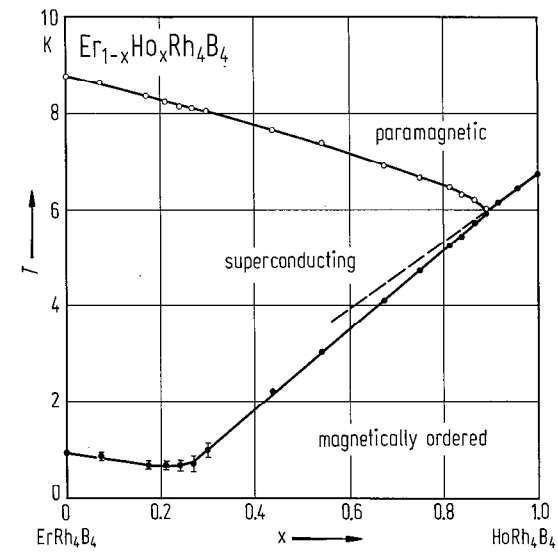

Fig. 100. $Er_{1-x}Ho_xRh_4B_4$. Low-temperature phase diagram determined from ac magnetic susceptibility measurements. The vertical bars on data points indicate the observed temperature hysteresis [77 J 2].

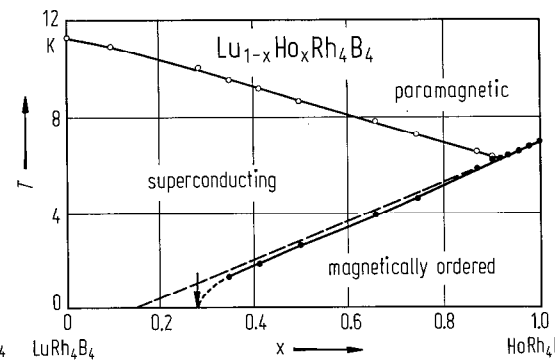

Fig. 101. $Lu_{1-x}Ho_xRh_4B_4$. Low-temperature phase diagram determined from ac magnetic susceptibility measurements on powdered samples [78 M 1].

2.8.4 References for 2.8

61 C 1 Coles, B.R., Griffith, D.: Proc. Phys. Soc. **77** (1961) 213.
61 G 1 Gschneidner, K.A.: Rare Earth Alloys, New York: Van Nostrand Co. **1961**.
61 L 1 LaPlaca, S., Binder, I., Post, B.: J. Inorg. Chem. Ukr. **18** (1961) 113.
62 C 1 Coles, B.R., Cole, T., Lambe, J., Laurance, N.: Proc. Phys. Soc. **79** (1962) 84.
63 P 1 Przybylska, M., Reddoch, A.H., Ritter, G.J.: J. Am. Chem. Soc. **85** (1963) 407.
64 M 1 McMasters, O.D., Gschneidner, K.A.: Nucl. Metallurgy **10** (1964) 93.
67 P 1 Paderno, Yu.B., Pokrzywnicki, S.: Phys. Status Solidi **24** (1967) K 11.
67 P 2 Paderno, Yu.B., Pokrzywnicki, S., Stalinski, B.: Phys. Status Solidi **24** (1967) K 73.
68 G 1 Geballe, T.H., Matthias, B.T., Andres, K., Maita, J.P., Cooper, A.S., Corenzwit, E.: Science **160** (1968) 1443.
68 H 1 Hacker, H., Liu, M.S.: Solid State Commun. **6** (1968) 379.
68 M 1 Matthias, B.T., Geballe, T.H., Andres, K., Corenzwit, E., Hull, G.W., Maita, J.P.: Science **159** (1968) 530.
69 F 1 Fisk, Z., Matthias, B.T., Corenzwit, E.: Proc. Nat. Acad. Sci. USA **64** (1969) 1151.
69 K 1 Kuz'ma, Yu.B., Krypyakevich, P.I., Bilonishko, N.S.: Dopov. Akad. Nauk Ukr. RSR Ser. A **10** (1969) 939.
69 M 1 Menth, A., Buehler, E., Geballe, T.H.: Phys. Rev. Lett. **22** (1969) 295.
70 C 1 Cohen, R.L., Eibschutz, M., West, K.W.: Phys. Rev. Lett. **24** (1970) 383.
70 E 1 Etourneau, J., Mercurio, J.P., Naslain, R., Hagenmuller, P.: J. Solid State Chem. **2** (1970) 333.
71 F 1 Fisk, Z.: Phys. Lett. A **34** (1971) 261.
71 F 2 Fisk, Z., Taylor, R.H., Coles, B.R.: J. Phys. C **4** (1971) L 292.
71 H 1 Hacker, H., Shimada, Y., Chung, K.S.: Phys. Status Solidi (a) **4** (1971) 459.
71 M 1 Maple, M.B., Wohlleben, D.: Phys. Rev. Lett. **27** (1971) 511.
71 W 1 Wood, V.E.: Phys. Lett. A **37** (1971) 357.
72 B 1 Buschow, K.H.J., Creijghton, J.H.N.: J. Chem. Phys. **57** (1972) 3910.
73 N 1 Niihara, K., Yajima, S.: Bull. Chem. Soc. Jpn. **46** (1973) 770.
73 R 1 Rogl, P.: Monatsh. Chem. **104** (1973) 1623.
75 G 1 Glaunsinger, W.S.: Phys. Status Solidi (b) **70** (1975) K 151.
75 S 1 Sales, B.C., Wohlleben, D.K.: Phys. Rev. Lett. **35** (1975) 1240.
76 B 1 Berrada, A., Mercurio, J.P., Chevalier, B., Etourneau, J., Hagenmuller, P., Lalanne, M., Gianduzzo, J.C., Georges, R.: Mater. Res. Bull. **11** (1976) 1519.
76 S 1 Schäfer, W., Will, G., Buschow, K.H.J.: J. Chem. Phys. **64** (1976) 1994.
77 B 1 Buschow, K.H.J.: Boron and Refractory Borides (Matkovich, V.I., ed.), Berlin: Springer **1977**, p. 494.
77 B 2 Bucher, E., Schmidt, P.H., Castellano, R.N., Dernier, P.: **1977** (unpublished).
77 F 1 Fertig, W.A., Johnston, D.C., DeLong, L.E., McCallum, R.W., Maple, M.B., Matthias, B.T.: Phys. Rev. Lett. **38** (1977) 987.
77 I 1 Isikawa, Y., Bajaj, M.M., Kasaya, M., Tanaka, T., Bannai, E.: Solid State Commun. **22** (1977) 573.
77 J 1 Johnston, D.C.: Solid State Commun. **24** (1977) 699.
77 J 2 Johnston, D.C., Fertig, W.A., Maple, M.B., Matthias, B.T.: Solid State Commun. **26** (1977) 141.
77 M 1 Matthias, B.T., Corenzwit, E., Vandenberg, J.M., Barz, H.E.: Proc. Nat. Acad. Sci. USA **74** (1977) 1334.
77 M 2 Moncton, D.E., McWhan, D.B., Eckert, J., Shirane, G., Thomlinson, W.: Phys. Rev. Lett. **39** (1977) 1164.
77 O 1 Oesterreicher, H., Parker, F.T., Misroch, M.: Appl. Phys. **12** (1977) 287.
77 V 1 Vandenberg, J.M., Matthias, B.T.: Proc. Nat. Acad. Sci. USA **74** (1977) 1336.
78 M 1 Maple, M.B., Hamaker, H.C., Johnston, D.C., MacKay, H.B., Woolf, L.D.: J. Less-Common Met. **62** (1978) 251.
78 O 1 Oh, H.R., Fertig, W.A., Johnston, I.C., Maple, M.B., Matthias, B.T.: J. Low Temp. Phys. **33** (1978) 159.
78 R 1 Rogl, P.: Mater. Res. Bull. **13** (1978) 519.
78 S 1 Sobczak, R., Rogl, P.: J. Solid State Chem. **27** (1978) 343.
79 B 1 Buschow, K.H.J.: Rep. Prog. Phys. **42** (1979) 1373.
79 E 1 Etourneau, J., Mercurio, J.P., Berrada, A., Hagenmuller, P., Georges, R., Bourezg, R., Gianduzzo, J.C.: J. Less-Common. Met. **67** (1979) 531.
79 H 1 Hamaker, H.C., Woolf, L.D., MacKay, H.B., Fisk, Z., Maple, M.B.: Solid State Commun. **31** (1979) 139.
79 H 2 Hamaker, H.C., Woolf, L.D., MacKay, H.B., Fisk, Z., Maple, M.B.: Solid State Commun. **32** (1979) 289.

79 K 1 Ku, H.C., Johnston, D.C., Matthias, B.T., Barz, H., Burri, G., Rinderer, L.: Mater. Res. Bull. **14** (1979) 1591.

79 K 2 Ku, H.C., Matthias, B.T., Barz, H.: Solid State Commun. **32** (1979) 937.

79 P 1 Pfeiffer, F., Schäfer, W., Will, G., Etourneau, J., Georges, R.: J. Magn. Magn. Mater. **14** (1979) 306.

79 R 1 Rogl, P.: Monatsh. Chem **110** (1979) 235.

79 R 2 Rowell, J.M., Dynes, R.C., Schmidt, P.H.: Solid State Commun. **30** (1979) 191.

79 R 3 Rupp, B., Rogl, P., Sobczak, R.: Mater. Res. Bull. **14** (1979) 1301.

79 W 1 Woolf, L.D., Johnston, D.C., MacKay, H.B., McCallum, R.W., Maple, M.B.: J. Low. Temp. Phys. **35** (1979) 651.

80 H 1 Hiebl, K., Rogl, P., Uhl, E., Sienko, M.J.: Inorg. Chem. **19** (1980) 3316.

80 K 1 Ku, H.C.: Superconductivity, Magnetism and Structural Study of Some New Ternary Transition Metal Borides, Ph.D. Dissertation, San Diego. CA: Univ. of Calif., **1980**.

80 K 2 Ku, H.C., Acker, F.: Solid State Commun. **35** (1980) 937.

80 K 3 Ku, H.C., Acker, F., Matthias, B.T.: Phys. Lett. A **76** (1980) 399.

80 K 4 Ku, H.C., Meisner, G.P., Acker, F., Johnston, C.C.: Solid State Commun. **35** (1980) 91.

80 K 5 Ku, H.C., Shelton, R.N.: Mater. Res. Bull. **15** (1980) 1441.

80 M 1 MacKay, H.B., Woolf, L.D., Maple, M.B., Johnston, D.C.: J. Low Temp. Phys. **41** (1980) 639.

80 M 2 Maple, M.B., Hamaker, H.C., Woolf, L.D., MacKay, H.B., Fisk, Z., Odoni, W., Ott, H.R., in: Crystalline Electric Field and Structural Effects in f-Electrons Systems (Crow, J.E., Guertin, R.P., Mihalian, T.W., eds.), New York: Plenum Press **1980**, p. 533.

80 O 1 Ott, H.R., Woolf, L.D., Maple, M.B., Johnston, D.C.: J. Low. Temp. Phys. **39** (1980) 383.

80 R 1 Rowell, J.M., Dynes, R.C., Schmidt, P.H., in: Superconductivity in d- and f-Band Metals, New York: Academic Press **1980**, p. 409.

80 S 1 Shelton, R.N., Ku, H.C.: Mater. Res. Bull. **15** (1980) 1445.

80 S 2 Shenoy, G.K., Dunlap, B.D., Fradin, F.Y., Sinha, S.K., Potzel, W., Pröbst, F., Kalvius, G.M.: Phys. Rev. B **21** (1980) 3886.

81 A 1 Acker, F., Ku, H.C.: J. Low Temp. Phys. **42** (1981) 449.

81 D 1 Dhar, S.K., Malik, S.K., Vijayaraghavan, R.: J. Phys. C **14** (1981) L 321.

81 D 2 Dynes, R.C., Rowell, J.M., Schmidt, P.H., in: Ternary Superconductors, New York: Elsevier North Holland **1981**, p. 169.

81 G 1 Gianduzzo, J.C., Georges, R., Chevalier, B., Etourneau, J., Hagenmuller, P., Will, G., Schäfer, W.: J. Less-Common Met. **82** (1981) 29.

81 H 1 Hamaker, H.C., MacKay, H.B., Woolf, L.D., Maple, M.B., Odoni, W., Ott, H.R.: Phys. Lett. A **81** (1981) 91.

81 K 1 Ku, H.C., Barz, H., in: Ternary Superconductors, New York: Elsevier North Holland **1981**, p. 209.

81 K 2 Ku, H.C., Meisner, G.P.: J. Less-Common Met. **78** (1981) 99.

82 C 1 Crabtree, G.W., Behroozi, F., Campbell, S.A., Hinks, D.G.: Phys. Rev. Lett. **49** (1982) 1342.

82 H 1 Hiebl, K., Rogl, P., Sienko, M.J.: Inorg. Chem. **21** (1982) 1128.

82 M 1 Malik, S.K., Vijayaraghavan, R., Boltich, E.B., Wallace, W.E., Dhar, S.K.: Solid State Commun. **43** (1982) 461.

82 M 2 Maple, M.B., Hamaker, H.C., Woolf, L.D., in: Superconductivity in Ternary Compounds II, Superconductivity and Magnetism. Topics in Current Physics (Maple, M.B., Fischer, Ø., eds.), Berlin, Heidelberg, New York: Springer **1982**, p. 99.

83 E 1 ElMasry, N.A., Stadelmaier, H.H.: Z. Metallkd. **74** (1983) 86.

83 E 2 ElMasry, N.A., Stadelmaier, H.H., Shahwan, C.J., Jordan, L.T.: Z. Metallkd. **74** (1983) 33.

83 G 1 Gupta, H.O., Malik, S.K., Wallace, W.E.: J. Magn. Magn. Mater. **40** (1983) 32.

83 H 1 Hamaker, H.C., Maple, M.B.: J. Low Temp. Phys. **51** (1983) 633.

83 H 2 Hiebl, K., Rogl, P., Nowotny, H.: J. Solid State Chem. **54** (1983) 414.

83 M 1 Malik, S.K., Vijaraghavan, R., Wallace, W.E., Dhar, S.K.: J. Magn. Magn. Mater. **37** (1983) 303.

83 O 1 Ohtani, R., Chevalier, B., Lejay, P., Etourneau, J., Vlasse, M., Hagenmuller, P.: J. Appl. Phys. **54** (1983) 5928.

83 S 1 Schilling, J.S., Shelton, R.N., Klavins, P., Shaheen, S.A.: Phys. Rev. B **28** (1983) 6548.

84 B 1 Boller, H., Oesterreicher, H.: J. Less-Common Met. **103** (1984) 65.

84 G 1 Givord, D., Li, H.S., Moreau, J.M.: Solid State Commun. **50** (1984) 497.

84 G 2 Givord, D., Li, H.S., Perrier de la Bathie, R.: Solid State Commun. **51** (1984) 857.

84 G 3 Grossinger, R., Orbitsch, P., Sun, X.K., Eibler, R., Kirchmayr, H.R., Sassik, H.: Mat. Lett. **2** (1984) 539.

84 H 1 Herbst, J.F., Croat, J.J., Pinkerton, F.E., Yelon, W.B.: Phys. Rev. B **29** (1984) 4176.

84 L 1 L'Heritier, P., Chaudouet, P., Madar, R., Roualt, A., Senateur, J.P., Fruchart, R.: C.R. Acad. Sci. Paris **299** II, (1984) 849.
84 O 1 Oesterreicher, H., Spada, F., Abache, C.: Mater. Res. Bull. **19** (1984) 1069.
84 O 2 Oesterreicher, K., Oesterreicher, H.: Phys. Status Solidi (a) **85** (1984) K 61.
84 S 1 Sagawa, M., Fujimura, S., Togawa, N., Yamamoto, H., Matsura, Y.: J. Appl. Phys. **55** (1984) 2083.
84 S 2 Shoemaker, C.B., Shoemaker, D.P., Fruchart, F.: Acta Crystallogr. C **40** (1984) 1665.
84 S 3 Sinnema, S., Radwanski, R.J., Franse, J.J.M., de Mooij, D.B., Buschow, K.H.: J. Magn. Magn. Mater. **44** (1984) 333.
84 S 4 Spada, F., Abache, H.C., Oesterreicher, H.: J. Less-Common Met. **99** (1984) L 21.
84 Y 1 Yang, K.N., Torikachvili, M.S., Maple, M.B., Ku, H.C.: J. Low Temp. Phys. **56** (1984) 601.
85 A 1 Abache, H.C., Oesterreicher, H.: J. Appl. Phys. **57** (1985) 4112.
85 B 1 Boltich, E.B., Wallace, W.E.: Solid State Commun. **55** (1985) 529.
85 B 2 Burzo, E., Oswald, E., Huang, M.Q., Boltich, E., Wallace, W.E.: J. Appl. Phys. **57** (1985) 4109.
85 B 3 Buschow, K.H.J., de Mooij, D.B., Sinnema, S., Radwanski, R.J., Franse, J.J.M.: J. Magn. Magn. Mater. **51** (1985) 211.
85 B 4 Buschow, K.H.J., de Vries, J.W.C., Thiel, R.C.: Physica B **132** (1985) 13.
85 D 1 Dalmas de Réotier, P., Fruchart, D.: Wolfers, P., Vuilliet, P., Yaovans, A., Fruchart, R., L'Héretier, P.: J. Phys. (Paris) C **6** (1985) 249.
85 H 1 Hirosawa, S., Matsuura, Y., Yamamoto, H., Fujimura, S., Sagawa, M., Yamanchi, H.: Jpn. J. Appl. Phys. **24** (1985) L 803.
85 K 1 Koon, N.C., Das, B.N., Rubinstein, M., Tyson, J.: J. Appl. Phys. **57** (1985) 4091.
85 L 1 L'Héritier, P., Fruchart, R.: J. Phys. (Paris) C **6** (1985) 319.
85 M 1 Matsuura, Y., Hirosawa, S., Yamamoto, H., Fujimura, S., Sagawa, M.: Appl. Phys. Lett. **46** (1985) 308.
85 O 1 Oesterreicher, H.: Phys. Status Solidi (b) **131** (1985) K 123.
85 P 1 Pontkees, F., Schilling, J.S., Klavins, P., Athreya, K.S., Shelton, R.N.: Solid State Commun. **53** (1985) 943.
85 S 1 Spada, F., Oesterreicher, H.: J. Less-Common Met. **107** (1985) 301.
85 Y 1 Yang, F.M., Zhao, X.C., Zhao, R.W., Yu, Z.H., Zhang, S.G.: Proc. 4th Int. Symp. on Magnetic Anisotropy (Struat, K., ed.), Dayton: University Press **1985**, p. 529.
86 A 1 Abache, H.C., Oesterreicher, H.: J. Appl. Phys. **60** (1986) 1114.
86 A 2 Abache, H.C., Oesterreicher, H.: J. Appl. Phys. **60** (1986) 3671.
86 B 1 Buschow, K.H.J.: Mat. Sci. Repts. **1** (1986) 1.
86 G 1 Grossinger, R., Sun, X.K., Eibler, R., Buschow, K.H.J., Kirchmayr, H.R.: J. Magn. Magn. Mater. **58** (1986) 55.
86 P 1 Pollard, R., Oesterreicher, H.: IEEE Trans. Magn. MAG **22** (1986) 735.
86 Y 1 Yelon, W.B., Foley, B., Abache, C., Oesterreicher, H.: J. Appl. Phys. **60** (1986) 2982.

2.9 Compounds of rare earth elements and Al, Ga, In or Tl

2.9.1 Introduction

The tables and figures presented in this section contain magnetic data on metallic or pseudometallic compounds of rare earth elements which contain besides the rare earth elements at least one group 3B element Al, Ga, In, Tl, excluding B. They may contain also as a third element another metallic element of the periodic system, excluding the group 1B elements Cu, Ag, Au, the group 2A elements Be, Mg, the group 2B elements Zn, Cd, Hg, and the group 3B element B. For rare earth compounds of the latter elements see the preceding sects. 2.6, 2.7 and 2.8.

The survey of the compounds in subsect. 2.9.2 is divided into three tables. Binary and pseudobinary compounds of the rare earth elements and the group 3B elements mentioned above are listed in Table 1. Ternary compounds which contain at least one rare earth element, one group 3B element, and, as a third element, another metallic element of the periodic system (with the exception of those mentioned above) are listed in Table 2 for nonstoichiometric compounds and in Table 3 for stoichiometric compounds.

The compounds listed in the tables are designated by their chemical formula. The compounds are arranged in the order as their elements appear in the periodic system as far as rare earth and group 3B elements are concerned. For the other elements the alphabetical order is adopted. Thus the rare earth elements are listed in the following order

Sc, Y, La, Ce, Pr, Nd, Pm, Sm, Eu, Gd, Tb, Dy, Ho, Er, Tm, Yb, Lu

and the group 3B elements in the order

Al, Ga, In, Tl.

Moreover, the compounds are listed in the tables according to the decreasing atomic ratio of the rare earth elements to the group 3B elements. Consequently, the rare-earth-rich compounds are given in the beginning of each table. The figures presented in subsect. 2.9.3 are arranged similarly.

The tables provide information on paramagnetic Curie temperature Θ, ferromagnetic Curie temperature T_C, Néel temperature T_N, magnetic susceptibility χ, effective paramagnetic moment p_{eff}, saturation or spontaneous magnetic moment p_s, remanent magnetic moment p_r, and coercive field H_c. The column "Remarks" may provide further data.

The observed effective paramagnetic moments as well as the saturation magnetic moments depend on the crystal electric field (CEF) splitting, which depends on the electron configuration and on the symmetry of the particular element. This splitting is characterized by the CEF Hamiltonian which can be expressed in different ways, in terms of the CEF overall-splitting, CEF parameters B_n (64 h 1), or in the case of cubic symmetry by the so-called Lea Leask and Wolf parameters W and x [6211]. All these parameters are used in this compilation.

2.9.2 Survey of compounds and properties

Table 1. Binary and pseudobinary compounds of rare earth elements with the group 3B elements Al, Ga, In, Tl. p_s, p_r and H_c refer to 4.2 K, unless stated otherwise. R: rare earth element, M: group 3B element.

	Θ K	T_C K	T_N K	χ	p_{eff} μ_B/R	p_s μ_B/R	p_r μ_B/R	H_c kOe	Remarks	Ref.
R_3M										
Sc_3In		5.5							weak intinerant-electron ferromagnet	84 I 1
$Sc_{1-x}In_x$	Fig. 1				Fig. 2				$\sigma(x)$ at 1.4 K and 4 kOe: Fig. 3	61 M 1
$La_3Al_{0.3}In_{0.7}$				Fig. 4						78 D 1
La_3In				Fig. 5						78 D 1
$La_3Ga_{0.3}In_{0.7}$										78 D 1
$La_3In_{0.5}Tl_{0.5}$				Fig. 4						78 D 1
La_3Tl				Fig. 5						78 D 1
$(La_{1-x}Pr_x)_3Tl$		Fig. 6				Fig. 8			$p_{Pr}(H)$ for x = 0.95 and 1 at 1.1 K: Fig. 7	72 A 1
				0.051 ···0.117					for x < 0.3 superconductor; χ_m at 1.42 K in cm^3/mol Pr for x = 0.05···0.65	72 B 1
Ce_3Al	− 24				2.52					68 M 1
Ce_3Ga	− 56				2.64					63 C 1
Ce_3In	− 33				2.68					63 C 1
Pr_3Al	2	16			3.62	1.16				68 M 1
Pr_3In	22	56.5			3.37	1.4			$p_{Pr}(H)$ at 4.2 K: Figs. 9, 11; $\sigma_m(T)$ at 1.23 kOe: Fig. 10; $\sigma_m(T,H)$: Fig. 11	73 S 1 74 S 1
Pr_3Tl		11.3							induced-moment ferromagnet; $p_{Pr}(H)$ at 1.1 K: Fig. 7	72 A 1
Nd_3In	10	114			3.4	0.37				73 H 2
Gd_3In	196	113			8.8	5.2				73 H 2
									$\sigma_m(H)$ at 4.2 K: Fig. 12	74 H 1
Dy_3In	113	138			10.4	5.8				73 H 2
									$\sigma_m(H)$ at 4.2 K: Fig. 12	74 H 1
Er_3In	31	51			9.6	5.2				73 H 2
									$\sigma_m(H)$ at 4.2 K: Fig. 12	74 H 1

R_2M									
Y_2In									weak temperature-independent magnetization 79 G 1
									p_s and p_r per Pr atom 80 P 1
$(La_{1-x}Pr_x)_2In$									
x = 0.50							0.14	1	
0.625						1.3	0.9	2	
0.80						1.7	1.4	3	
0.90						1.7	1.4	17	
0.95						1.5	1.1	14	
Ce_2In	− 1				2.62				63 C 1
Ce_2Tl	− 33				2.65				63 C 1
Pr_2Al	− 4				3.64		≦0.2		78 S 2
Pr_2In						1.8	1.5	8	hysteresis loop at 4.2 K: Fig. 13 80 P 1
Nd_2Al	27	36			3.60	3.27	2.23		78 S 2
Nd_2In	97			Fig. 14	3.2				$\sigma(H)$ at 4.2 K: Fig. 14 79 G 1
Sm_2Al	− 85		150		0.68	0.11	0		78 S 2
Sm_2In	97			Fig. 15					$\sigma(H)$ at 4.2 and 150 K: Fig. 15 79 G 1
Gd_2Al	150				8.02				75 B 1
	170		44		7.77		≦0.08		78 S 2
									$p_{Gd}(H, T)$: Fig. 16 77 O 1
Gd_2In	212			Fig. 17	9.6				$\sigma(H)$ at 4.2 K: Fig. 18 79 G 1
									$p_{Gd}(T, H)$: Fig. 19 84 M 1
Tb_2Al	86		52	Fig. 20	9.68		2.15		$\sigma(T, H)$, $\chi_g^{-1}(T)$: Fig. 20 78 S 2
Tb_2In	170			Fig. 17	10.4				$\sigma(H)$ at 4.2 K: Fig. 18 79 G 1
Dy_2Al	34		37	Fig. 21	10.67		1.95		$\sigma(T, H)$, $\chi_g^{-1}(T)$: Fig. 21 78 S 2
Dy_2In	114			Fig. 17	10.6				$\sigma(H)$ at 4.2 K: Fig. 18 79 G 1
Ho_2Al	5		11		11.0		<0.01		78 S 2
Ho_2In	83			Fig. 22	11.7				$\sigma(H)$ at 4.2 and 64 K: Fig. 23 79 G 1
Er_2Al	0		6		10.10		<0.01		78 S 2
Er_2In	42			Fig. 22	9.8				$\sigma(H)$ at 4.2 K: Fig. 23 79 G 1
Tm_2Al	5				7.90		<0.01		78 S 2
Tm_2In	6			Fig. 22	7.6				$\sigma(H)$ at 4.2 K: Fig. 23 79 G 1

continued

Table 1 (cont.)

	Θ K	T_C K	T_N K	χ	p_{eff} μ_B/R	p_s μ_B/R	p_r μ_B/R	H_c kOe	Remarks	Ref.
R_5M_3										
Sc_5Ga_3				Figs. 24, 25						81 S 1
Y_5In_3									temperature-independent magnetic susceptibility	83 S 3
Gd_5Ga_3	25		80		8.5				small amount of elemental Gd present	76 B 1
Gd_5In_3			78	Fig. 26		6.08			p_s at 18 kOe; $\sigma(H)$ at 4.5 and 245 K: Fig. 26	83 S 5
Tb_5In_3	166		52			6.08			p_s at 18 kOe	83 S 5
Dy_5In_3	118		42			6.66			p_s at 18 kOe	83 S 5
Ho_5In_3		< 4.2				0.36			p_s at 18 kOe	83 S 5
Er_5In_3	10	< 4.2				0.56			p_s at 18 kOe	83 S 5
Tm_5In_3	6	< 4.2				0.48			p_s at 18 kOe	83 S 5
R_3M_2										
$(Y_{1-x}Gd_x)_3Al_2$	Fig. 27									75 B 1
Ce_3Ga_2	− 40				2.74					63 C 1
Gd_3Al_2	280	275			8.17	7.25				66 S 1
	270	287			7.9					75 B 1
Gd_3Ga_2	− 31		55	Fig. 28	8.23				impurity of elemental Gd detected	76 B 1
	− 23		53		8.51					76 H 1
Tb_3Al_2	125	203			9.6				$p_{Tb}(H, T)$: Fig. 29	68 B 2
Dy_3Al_2	31	76			10.8					68 B 2
				Fig. 30	11.2	5.9			$\sigma(H, T)$ for single crystal: Fig. 30; p_s along c axis	69 B 1
Ho_3Al_2	10	33			10.9					68 B 2
Er_3Al_2	− 3		9		9.6					68 B 2
Tm_3Al_2	− 10		3		7.8				$T < T_N$: metamagnetic	68 B 2
RM										
CeAl	− 3				2.538					72 N 1
	4		9		2.34					68 B 2

CeGa	− 21				2.73			63 C 1
CeIn	6				2.63			63 C 1
CeTl	− 22				2.58			63 C 1
PrAl	11		20		3.58			68 B 2
PrGa	18	32		Fig. 31	3.66	2.0	single crystal: $\Theta_a = 28$ K, $\Theta_b = 8$ K, $\Theta_c = 4.6$ K; $\sigma(H, T)$: Fig. 31	77 S 1
NdAl	− 4		29		3.53			68 B 2
							$p_{Nd}(H)$ at 4.2 K: Fig. 32	70 B 1
NdGa	30	44		Fig. 33	3.68	2.7	single crystal: $\Theta_a = 41$ K, $\Theta_b = 34$ K, $\Theta_c = 43$ K; $\sigma(H, T)$: Fig. 33	77 S 1
SmGa		108		Fig. 34		0.4	single crystal; hysteresis loop along the easy direction b axis and $\sigma(T)$ at 10 kOe along a and c axes: Fig. 34	77 S 1
EuTl	4				7.77			65 I 1
GdAl	260				5.69			66 S 1
	64		42	Fig. 35	8.15			68 B 2
	64		42				$p_{Gd}(H)$ at 4.2 K: Fig. 32	70 B 1
	85		42		8.52			75 B 1
GdGa	199	183			8.7	7.2		77 S 1
	210	200		Fig. 36	8.23	6.5	$\sigma(T)$ at 12 kOe: Fig. 36	76 B 1
GdIn	18			Fig. 37				76 L 2
	− 66		28		8.1		$\sigma_s = 0.07$ G cm^3 g^{-1} at 4.2 K	66 S 2
GdTl	− 30		< 200		8.2		cubic phase of CsCl-type structure;	83 S 4
	− 36		204		8.1		tetragonal phase	
TbAl	10		72		10.0			68 B 2
				Fig. 38			$p_{Tb}(H)$ at 4.2 K: Fig. 32	70 B 1
	24				10.11			68 V 1
TbGa	161	158		Fig. 39	9.4	9.2	single crystal: $\Theta_a = 134$ K, $\Theta_b = 134$ K, $\Theta_c = 175$ K; $\sigma(H, T)$ along a, b and c axes: Fig. 39	77 S 1
							$p_{Tb}(H)$ at 4.2 K and 77 K: Fig. 40	71 B 1
TbIn	16		145	Fig. 37				76 L 2

continued

Table 1 (cont.)

	Θ K	T_C K	T_N K	χ	p_{eff} μ_B/R	p_s μ_B/R	p_r μ_B/R	H_c kOe	Remarks	Ref.
DyAl	25		20	Fig. 35	10.6				below T_N metamagnetic	68 B 2
	25		20						$p_{Dy}(H)$ at 4.2 K: Fig. 32	70 B 1
	17				11.15					68 V 1
DyGa	119	116		Fig. 41	10.1	9.8			single crystal: $\Theta_a = 94$ K, $\Theta_b = 68$ K, $\Theta_c = 133$ K; $\sigma(H, T)$ along *a*, *b*, and *c* axes: Fig. 41	77 S 1
DyIn	10		120	Fig. 37						76 L 2
HoAl	17	26			10.7	6.2			p_s at 70 kOe;	68 B 2
	17	26							$p_{Ho}(H)$ at 4.2 K: Fig. 32	70 B 1
	22				11.25					68 V 1
HoGa	53	63		Fig. 42	10.3	10.0			single crystal: $\Theta_a = 53$ K, $\Theta_b = 22$ K, $\Theta_c = 68$ K; $\sigma(H, T)$ along *a*, *b*, and *c* axes: Fig. 42	77 S 1
HoIn	8		42	Fig. 37						76 L 2
ErAl	23		13		9.65				below T_N metamagnetic	68 B 2
	23		10	Fig. 38					$p_{Er}(H)$ at 4.2 K: Fig. 32	70 B 1
ErGa	26		32	Fig. 43	9.8	8.2			single crystal: $\Theta_a = 35$ K, $\Theta_b = 35$ K, $\Theta_c = 12$ K; $\sigma(H, T)$ along *a*, *b*, and *c* axes: Fig. 43	77 S 1
TmAl	− 2		10		7.70				below T_N metamagnetic	68 B 2
	− 2		11	Fig. 38					$p_{Tm}(H)$ at 4.2 K: Fig. 32	70 B 1
TmGa	10	15			7.72	4.42				72 B 1
R_2M_3										
Ce_2In_3	− 8				2.73					63 C 1
RM_2										
$ScAl_2$				Fig. 45						85 I 1
$Sc_{1-x}Eu_xAl_2$				Fig. 44						80 F 1
$Sc_{1-x}Gd_xAl_2$				Fig. 44						80 F 1

$Sc_{1-x}Yb_xAl_2$			Fig. 45			homogeneous alloys; lattice constant follows Vegard's law; χ far from Curie-Weiss law; Yb in a mixed valence state dependent on T and x	85 I 1
YAl_2			103			χ_m in 10^{-6} cm^3mol^{-1}	62 W 1
			Fig. 53				85 I 1
$Y_{1-x}Ce_xAl_2$			Fig. 46			exists for $0 \leqq x \leqq 1$; lattice constant follows Vegard's law; χ follows Curie-Weiss law; Ce close to the trivalent state; p_{eff} per Ce atom	85 I 1
x = 0.6	− 55			2.50			
0.8	− 36			2.51			
$Y_{1-x}Pr_xAl_2$						p_s per formula unit, p_{eff} per Pr atom	69 M 1
x = 0.05	− 5			3.58		corrected for YAl_2	
0.1	− 9	13		3.68	0.83	corrected for YAl_2	
0.2	3	15		3.70	1.44		
0.4	10	20		3.70	1.83		
0.6	17	25		3.60	2.09		
0.8	22	32		3.53	2.36		
$Y_{1-x}Eu_xAl_2$			Fig. 47			exists for $0 \leqq x \leqq 1$, homogeneity achieved by annealing; lattice constant does not follow Vegard's law; χ follows Curie-Weiss law; Eu close to the divalent state; p_{eff} per Eu atom	85 I 1
x = 0.2	− 7			7.68			
0.5	5			7.81			
0.8	11			7.97			
$Y_{1-x}Gd_xAl_2$	Fig. 48					exists for $0 \leqq x \leqq 1$	67 B 1
	Fig. 49	Fig. 49				lattice constant follows Vegard's law	82 H 1
$Y_{1-x}Tb_xAl_2$	Fig. 50	Fig. 50					67 B 1

continued

Table 1 (cont.)

	Θ K	T_C K	T_N K	χ	p_{eff} μ_B/R	p_s μ_B/R	p_r μ_B/R	H_c kOe	Remarks	Ref.
$Y_{1-x}Dy_xAl_2$		Fig. 52								78 B 2
$Y_{1-x}Er_xAl_2$	Fig. 50	Fig. 50								67 B 1
									$p_{Er}(T, x)$ from neutron diffraction: Fig. 51	72 W 1
									magnetic phase diagram: Fig. 51	79 B 3
$Y_{1-x}Yb_xAl_2$				Fig. 53					homogeneous alloys for $0 \leqq x \leqq 1$; lattice constant follows Vegard's law; χ far from Curie-Weiss law; Yb in a mixed-valent state dependent on T and x	85 I 1
$LaAl_2$				60					χ_m in 10^{-6} cm^3 mol^{-1}	79 B 1
				Fig. 59					$\varrho(T)$: Fig. 72	69 V 1, 85 I 1
$La_{1-x}Ce_xAl_2$									$p_{Ce}(H, x)$ at 1.4 and 4.2 K: Fig. 55	81 A 1
$La_{1-x}Pr_xAl_2$		Fig. 56				Fig. 57			p_{eff} and p_s per Pr atom corrected for $LaAl_2$	79 T 1, 69 M 1
x = 0.05	− 11	5			3.72	1.73				
0.2	− 8	8			3.64	2.34				
0.4	3	13			3.59	2.47				
0.6	11	19			3.50	2.59				
0.8	18	30			3.55	2.50				
$La_{1-x}Eu_xAl_2$									p_{eff} and p_s per Eu atom	68 M 2
x = 0.1	− 1	11			7.80	5.7			p_s at 0 K	
0.2	− 4	6			7.85	5.5			p_s at 0 K	
0.4	− 6	< 4			7.85					
0.6	− 6				8.10				not ordered at 4 K	
0.8	− 3		14		7.95					
$La_{1-x}Gd_xAl_2$	Fig. 58	Fig. 58							$T_{tr}(x)$: Fig. 58	84 C 1
		Fig. 49							lattice constant follows Vegard's law	82 H 1
$La_{1-x}Yb_xAl_2$				Fig. 59					homogeneous alloys; lattice constant does not follow Vegard's law;	85 I 1

							χ far from Curie-Weiss law; Yb in a mixed-valent state dependent on T and x
$CeAl_2$	− 33				2.54		68 S 1
			4		2.53		Ce in trivalent state 70 V 1
	− 7				2.64		72 N 1
						0.7	p_s at 1.7 K and 50 kOe; 75 B 4
							$p_{Ce}(H)$ for single crystal at 1.7 K: Fig. 60
				Fig. 60			antiferromagnetic structure sinusoidally modulated suggested 77 B 1
			3.86				T_N from single crystal heat capacity 85 S 1
$Ce_{1-x}Pr_xAl_2$				Fig. 61			$p_m(H, T, x)$: Fig. 61 79 B 2
							$p_m(T, x)$ at 19 kOe: Fig. 62; T_C measured in 19 kOe 68 S 1
x = 0.2	− 17	11			2.72	0.95	
0.4	0	17			2.92	1.34	
0.6	23	11			3.16	1.75	
0.8	32	28			3.28	2.15	
$Ce_{1-x}Nd_xAl_2$							$p_m(T, x)$ at 19 kOe: Fig. 63; T_C measured in 19 kOe 68 S 1
x = 0.2	− 14	12			2.74	0.78	
0.4	4	27			2.97	1.17	
0.6	23	39			3.21	1.56	
0.8	59	44			3.34	1.90	
$Ce_{1-x}Eu_xAl_2$							68 S 1
x = 0.2	− 18				4.34		
0.4	− 41				5.36		
0.6	− 7				6.32		
0.8	− 6		23		7.21		
$Ce_{1-x}Gd_xAl_2$	Fig. 64	Fig. 64				Fig. 66	single crystal and polycrystal; $p_m(H, x)$ at 4.2 K: Fig. 65 85 I 2
$Ce_{1-x}Lu_xAl_2$				Fig. 67			for $0 \leqq x \leqq 1$ complete solubility; lattice constant does not follow Vegard's law 85 I 1
x = 0.2	− 33				2.54		p_{eff} per Ce atom

continued

Table 1 (cont.)

	Θ K	T_C K	T_N K	χ	p_{eff} μ_B/R	p_s μ_B/R	p_r μ_B/R	H_c kOe	Remarks	Ref.
$CeGa_2$	12.5		4.1	Fig. 69	2.51				$p_{Ce}(H)$ at 4.2 K: Fig. 70	78 T 1
$PrAl_2$	30	37			3.46	2.60			T_C measured in 19 kOe	68 S 1
	32			Fig. 71	3.5	2.94				68 N 1
		31							T_C from electrical resistivity: Fig. 72	69 V 1
						Fig. 73				74 P 1
		33				2.85			$p_{Pr}(H)$ at 4.2 K: Fig. 74	82 E 1
$Pr_{1-x}Nd_xAl_2$									T_C measured in 19 kOe	68 S 1
x = 0.2	36	48			3.48	2.42				
0.4	40	55			3.47	2.48				
0.6	51	64			3.52	2.34				
0.8	65	69			3.49	2.33				
$Pr_{1-x}Dy_xAl_2$									$p_m(T, x)$ at 19 kOe: Fig. 75; T_C measured in 19 kOe	68 S 1
x = 0.2	26				5.58	0.50				
0.4	22	56			7.16	2.19				
0.6	46	62			8.52	4.45				
0.8	60	65			9.52	7.18				
$Pr_{1-x}Ho_xAl_2$									T_C measured in 19 kOe	68 S 1
x = 0.1	12	39			4.68	1.80				
0.25	5				6.20	0				
0.5	15	40			7.98	3.39				
0.75	24	40			9.31	6.28				
$PrGa_2$	9		11		3.6					71 B 2
	10.6		7.3	Fig. 69	3.50				$p_{Pr}(H)$ at 4.2 K: Fig. 70	78 T 1
$NdAl_2$	61	65			3.1					66 N 1
	70	76			3.59	2.27				68 S 1
		76							T_C from electrical resistivity: Fig. 72	69 V 1
		65				2.47				74 C 2
		65				2.42			$p_{Nd}(H)$ at 4.2 K: Fig. 76	82 E 1
	61	79			3.1	2.5			p_s and T_C from neutron diffraction	83 M 1

$Nd_{1-x}Ho_xAl_2$							$p_m(T,x)$ at 19 kOe: Fig. 77; T_C measured in 19 kOe 68 S 1
x = 0.1	23				4.71	1.20	
0.25	0				6.25	0.65	
0.5	12	51			7.83	3.51	
0.75	33	48			9.25	6.65	
$NdAl_{2-x}Ga_x$							p_s, T_C and T_N from neutron diffraction 83 M 1
x = 0.25	73.4		4.8		3.46	1.5	$MgCu_2$ structure type
0.75	− 1.0		6.0		3.51	2.06	AlB_2 structure type
1.0	− 0.3		2.5		3.54	0.9	AlB_2 structure type
1.5	3.4	71.4			3.61	2.32	AlB_2 structure type
$NdGa_2$	12.4		9.2	Fig. 69	3.63		78 T 1
	10		14		3.7		71 B 2
$SmAl_2$		120		Fig. 78			$p_{Sm}(T)$ at 21 kOe and hysteresis loop at 2 K: Fig. 78 73 D 1
$EuAl_2$	0		15	Fig. 79	7.84… 8.05	0.79… 1.21	p_s at 20 kOe for different samples; $\sigma(H)$ at 4.2 K: Fig. 80 68 M 2
$EuGa_2$	6				8.04		64 I 1
$EuIn_2$	8				7.79		64 I 1
$EuTl_2$	− 10				7.78		64 I 1
$GdAl_2$	171.5	171			7.88	6.90	66 S 1
	168	182			7.94	7.10	T_C measured in 19 kOe 68 S 1
	171	180			7.94	7.0	T_C measured in ≅ 1 kOe, p_s at 30 kOe 67 B 1
	171	168		Fig. 81	7.85	7.0	$\sigma(T,H)$: Fig. 82 72 H 1
		173					T_C from electrical resistivity: Fig. 83; 69 V 1
							$p_{Gd}(H,T)$: Fig. 84 77 B 2
	169				7.92		82 H 1
	169	170				7.2	p_s at 0 K 81 L 1
$Gd_{1-x}Tb_xAl_2$	Fig. 85	Fig. 85			Fig. 85		T_C from electrical resistivity 82 C 1
x = 0.2	160	168			8.36	7.40	T_C measured in 19 kOe 68 S 1
0.4	146	142			8.69	7.56	
0.6	133	130			9.06	7.85	
0.8	120	126			9.45	8.22	

continued

Table 1 (cont.)

	Θ K	T_C K	T_N K	χ	p_{eff} μ_B/R	p_s μ_B/R	p_r μ_B/R	H_c kOe	Remarks	Ref.
$Gd_{1-x}Dy_xAl_2$	Fig. 86	Fig. 86			Fig. 86				T_C from electrical resistivity	82 C 1
$Gd_{1-x}Ho_xAl_2$	Fig. 87	Fig. 87							T_C from electrical resistivity	82 C 1
									T_C measured in 19 kOe	68 S 1
x = 0.2	142	145			8.45	7.56				
0.4	114	114			8.99	8.10				
0.6	90	87			9.62	8.48				
0.8	65	63			10.0	8.75				
$Gd_{1-x}Er_xAl_2$	Fig. 88	Fig. 88			Fig. 88				T_C from electrical resistivity	82 C 1
$Gd_{1-x}Yb_xAl_2$									$\chi^{-1}(T)$ corresponds to $J = 7/2$ of Gd and to $J = 0$ for divalent Yb	75 B 1
$Gd_{1-x}Lu_xAl_2$	Fig. 49	Fig. 49			Fig. 89				lattice constant follows Vegard's law;	82 H 1
									T_C from electrical resistivity	85 C 3
$Gd(Al_{1-x}In_x)_2$										
x = 0.1	163				7.96					
0.2	150				7.91					
0.3	122				7.74					
$GdGa_2$	− 17.4		2.1	Fig. 69	7.92					78 T 1
				Fig. 28						76 B 1
$TbAl_2$	110	121			9.81	8.60			T_C measured in 19 kOe	68 S 1
	108	114			9.82	8.1			p_s at 30 kOe	67 B 1
		111							T_C from electrical resistivity: Fig. 83	69 V 1
						9.2			from neutron diffraction at 4.2 K	72 M 1
									single crystal,	74 B 1
									$\sigma(H)$, $p_{Tb}(H)$ at 4.2 K: Fig. 90; $\sigma_s(T)$: Fig. 91	
$Tb_{1-x}Dy_xAl_2$									$p_m(T)$ at 19 kOe: Fig. 92; T_C measured in 19 kOe	68 S 1
x = 0.2	96	109			9.96	8.52				
0.4	88	99			10.3	8.78				
0.6	84	94			10.2	9.07				
0.8	75	80			10.6	9.10				

								79 G 2
$TbAl_{2-x}Ga_x$								
x = 1.0			47.0			6.7		a second magnetic phase transition at 23 K
1.5			19.3					
								71 B 2
$TbGa_2$	−	20	18		9.8			
		25.6	14.8	Fig. 69	9.29			$p_{Tb}(H)$ at 4.2 K: Fig. 70
					9.6			$\chi^{-1}(T)$ along *a* [100], *b*[120] and *c* directions are linear for $T > 60$ K; $\Theta_c = -98$ K, $\Theta_b = -17$ K, $\Theta_a = -11$ K; $p_{Tb}(H)$ at 4.2 K along *a*, *b* and *c* axes: Fig. 93
								78 T 1
								77 A 1
$DyAl_2$		68	62		9.7			T_C measured in 19 kOe
		64	70		10.7	9.62		$p_m(T)$ at 19 kOe: Fig. 75
			62					T_C from electrical resistivity: Fig. 83
								66 N 1
								68 S 1
								69 V 1
					9.24		0.60	
								72 O 1
								single crystal, $p_{Dy}(H)$ at 4.2 K: Fig. 94
								82 K 1
$Dy_{1-x}Ho_xAl_2$								
x = 0.2		60	66		10.5	9.51		T_C measured in 19 kOe
0.4		48	61		10.7	9.43		
0.6		39	54		10.6	9.29		$p_m(T)$ at 19 kOe: Fig. 92
0.8		32	47		10.6	9.20		
								68 S 1
$Dy_{1-x}Er_xAl_2$								
x = 0.2		55	61		10.4	8.75		T_C measured in 19 kOe
0.4		43	49		10.3	8.32		
0.6		33	39		10.0	7.92		$p_m(T)$ at 19 kOe: Fig. 92
0.8		24	31		9.79	7.63		
								68 S 1
$DyGa_2$	−	6	15		10.7			
		1.8	6.4	Fig. 69	10.72			
								71 B 2
								78 T 1

continued

Table 1 (cont.)

	Θ K	T_C K	T_N K	χ	p_{eff} μ_B/R	p_s μ_B/R	p_r μ_B/R	H_c kOe	Remarks	Ref.
$HoAl_2$	30	42			10.7	9.16			T_C measured in 19 kOe	68 S 1
		29							T_C from electrical resistivity: Fig. 83	69 V 1
						8.13			p_s from neutron diffraction	72 M 1
	36	33				9.18				75 B 3
		31.5				9.05			single crystal, $p_{Ho}(H)$ at 4.2 K along [100], [110] and [111] directions: Fig. 95; easy direction changes at 20 K from [110] to [100]	83 S 2
$HoAl_{2-x}Ga_x$ x = 1			30			8.2			second magnetic phase transition at 17.8 K	76 G 2
$HoGa_2$	− 2		10		10.7					71 B 2
	13.1		8	Fig. 96	10.10				$p_{Ho}(H)$ at 4.2 K: Fig. 70;	78 T 1
				Fig. 69		8.81			single crystal, p_s along [100] at 80 kOe; $p_{Ho}(H)$ at 4.2 K: Fig. 97	
$ErAl_2$	16	14.5			9.56	7.6			T_C measured in ≅ 1 kOe, p_s at 30 kOe	67 B 1
	14	24			9.46	7.05			T_C measured in 19 kOe	68 S 1
	14			Fig. 98	9.2	8.3			p_s from neutron diffraction	68 N 1
		12							T_C from electrical resistivity: Fig. 83	69 V 1
		13.5				8.8			from neutron diffraction, p_s at 0 K	72 W 1, 72 W 2
									single crystal, $p_{Er}(H)$ at 4.2 K: Fig. 99	76 P 1
$ErAl_{2-x}Ga_x$									p_s, T_C and T_N from neutron diffraction	83 M 1
x = 0.25	9.9	14.0			9.24	4.83			$MgCu_2$ structure type	
1.0	− 10.3		2.8		9.19	4.9			AlB_2 structure type	
1.5	− 7.1		2.5		9.37	3.8			AlB_2 structure type	

$ErGa_2$	1.7		7.5	Fig. 69 Fig. 100	9.41		78 T 1 single crystal, 82 D 2 $p_{Er}(H)$ along c axis at 1.5, 5 and 8 K: Fig. 101, $p_{Er}(H)$ along a, b, and c axes at 1.5 K: Fig. 102
$TmAl_2$		7				4.8	p_s at 1.4 K 62 W 1
$YbAl_2$				Fig. 103 1.75			$\sigma(H)$ at 4.2 K: Fig. 104 73 K 1 χ_g at 0 K in 10^{-6} cm^3 g^{-1} deduced after correction for Yb_2O_3 73 H 1 Pauli paramagnetism 75 B 1
$Yb_{1-x}Lu_xAl_2$				Fig. 105			homogeneous alloys; 85 I 1 lattice constant does not follow Vegard's law; χ far from Curie-Weiss law; Yb in a mixed-valent state strongly dependent on x and T
$YbGa_2$				− 30			χ_m at 0 K in 10^{-6} cm^3 mol^{-1}, 77 K 1 no Curie-Weiss behaviour; χ slightly temperature-dependent
$YbIn_2$				− 70			χ_m at 0 K in 10^{-6} cm^3 mol^{-1}, 77 K 1 no Curie-Weiss behaviour; χ temperature-independent
$LuAl_2$				75 Fig. 105			χ_m in 10^{-6} cm^3 mol^{-1} 79 B 1 85 I 1
RM_3							
$Y_{1-x}Pr_xAl_3$							χ_m in 10^{-3} cm^3 mol^{-1} 69 M 1
x = 0.2	− 14			52.3	3.64		χ_m at 4.2 K
				5.20			χ_m at 300 K
0.4	− 9			60.5	3.67		χ_m at 4.2 K
				5.35			χ_m at 300 K
0.6	− 12			62.0	3.70		χ_m at 4.2 K
				5.48			χ_m at 300 K
0.8	− 10			62.1	3.64		χ_m at 4.2 K
				5.41			χ_m at 300 K
YIn_3				290			χ_m in 10^{-6} cm^3 mol^{-1}, 70 H 1 Pauli paramagnetism

continued

Table 1 (cont.)

	Θ K	T_C K	T_N K	χ	p_{eff} μ_B/R	p_s μ_B/R	p_r μ_B/R	H_c kOe	Remarks	Ref.
$Y_{1-x}Ce_xIn_3$				Fig. 107					$p_{Ce}(H,x)$ at 4.2 K: Fig. 107	82 D 1
$LaAl_3$				80					χ_m in 10^{-6} cm^3 mol^{-1}	67 V 1
$La_{1-x}Pr_xAl_3$									χ_m in 10^{-3} cm^3 mol^{-1}	69 M 1
x = 0.2	– 6			85.9	3.66				χ_m at 4.2 K	
				5.45					χ_m at 300 K	
0.4	– 6			83.9	3.61				χ_m at 4.2 K	
				5.30					χ_m at 300 K	
0.6	– 6			74.4	3.67				χ_m at 4.2 K	
				5.34					χ_m at 300 K	
0.8	– 6			74.1	3.65				χ_m at 4.2 K	
				5.40					χ_m at 300 K	
$LaIn_3$				270					χ_m in 10^{-6} cm^3 mol^{-1}; Pauli paramagnetism	70 H 1
$La_{1-x}Ce_xIn_3$			Fig. 107	Fig. 107					$p_{Ce}(H,x)$ at 4.2 K: Fig. 107	80 E 2
										82 D 1
$La_{0.75}Nd_{0.25}In_3$				Fig. 108						76 L 1
$CeAl_3$	– 46			Fig. 109	2.63					66 B 1
	– 25				2.525					72 N 1
				Fig. 110					$p_{Ce}(H)$ at 1.4 and 4.2 K: Fig. 110	85 D 1
$Ce_{1-x}Gd_xAl_3$				Fig. 111					$\sigma(H)$ for x = 0.05 and 0.20 at 2.01 K: Fig. 112	84 E 1
$CeIn_3$	– 46		11	Fig. 113	2.54					69 B 2
			10			0.48			p_s at 1.8 K and 46.5 kOe	83 B 1
$CeTl_3$	– 9		3.85	Fig. 116	2.47				$p_{Ce}(H)$ at 1.3 and 4.2 K: Fig. 117	80 E 1
$PrAl_3$	– 7			71	3.67				χ_m in 10^{-3} cm^3 mol^{-1}	69 M 1
	– 14			Fig. 118						66 B 1
$PrIn_3$	– 10				3.58					69 B 2
	– 9			Fig. 119	3.72					76 L 1
$PrTl_3$					3.67					79 B 1
$NdAl_3$	5			Fig. 118	4.11					66 B 1

$NdIn_3$	− 17	7	Fig. 120	3.62		69 B 2, 79 S 1
	− 12	6.8	Fig. 108	3.78		76 L 1
		5.9			T_N from heat capacity, in ordered state two first-order transitions at 4.61 K and 5.13 K with change of magnetic structure; magnetic field applied in [001] direction induces two magnetic transitions: Fig. 121; $p_{Nd}(H)$ at 1.45 K: Fig. 122	86 C 2, 85 C 1
$SmAl_3$			Fig. 109		no Curie-Weiss behaviour	66 B 1
			Fig. 123			67 D 1
$SmIn_3$		16	Fig. 124			69 B 1
$EuIn_3$		10			T_N measured at 6.5 kOe; $\sigma_m(T)$ at 40 and 70 kOe and magnetic phase diagram: Fig. 126; $\sigma_m(H)$ at 4.2 K: Fig. 125	74 S 1
		4.5			T_N measured at 70 kOe	
$EuTl_3$		6.5			T_N measured at 6.5 kOe	74 S 1
		5.5			T_N measured at 70 kOe	
					$\sigma_m(H)$ at 4.2 K: Fig. 125	
$GdAl_3$	− 89	17	Fig. 127	8.29		66 B 1
$GdIn_3$	− 85	45	Fig. 113	8.02		69 B 2
		45.5			T_N measured at 6.5 kOe;	74 S 1
		48			T_N measured at 70 kOe	
		46				84 A 1
			Fig. 113		single crystal,	79 S 1
					$p_m(H)$ at 4.2 K: Fig. 125	
$GdTl_3$		13			T_N measured at 6.5 kOe;	74 S 1
		12			T_N measured at 70 kOe	
					$\sigma_m(H)$ at 4.2 K: Fig. 125	79 S 1
$TbAl_3$	− 64	21	Fig. 129	10.0		66 B 1
$TbIn_3$	− 62	36	Fig. 120	10.05		69 B 2
					$p_{Tb}(H)$ at 4.2 K: Fig. 130	73 L 1
				7.2	neutron diffraction indicates [110]; antiferromagnetic ordering; p_{Tb} along c axis	74 C 1

continued

Table 1 (cont.)

	Θ K	T_C K	T_N K	χ	p_{eff} μ_B/R	p_s μ_B/R	p_r μ_B/R	H_c kOe	Remarks	Ref.
$DyAl_3$	− 51		23	Fig. 129	10.85					66 B 1
$DyIn_3$	− 35		23	Fig. 120						69 B 2
			24			8.8			from neutron diffraction	69 A 1
									$p_{Dy}(H)$ at 4.2 K: Fig. 130	73 L 1
				Fig. 120					single crystal,	79 S 1
									$p_{Dy}(H)$ at 4.2 K: Fig. 130	
$DyTl_3$	− 20				11.29					70 O 1
$HoAl_3$	− 26		9	Fig. 129	10.89					66 B 1
$HoIn_3$	− 18		11	Fig. 120	10.65					69 B 2
									$p_{Ho}(H)$ at 4.2 K: Fig. 130	73 L 1
			7.92						from $C_p(T)$ on single crystal: Fig. 132	86 C 1
$HoTl_3$			7.5			8.5			from neutron diffraction; p_s at 4.7 K; modulated magnetic structure	81 K 1
$ErAl_3$	6		21		9.87					66 B 1
				Fig. 133						68 B 1
			5.1						from neutron diffraction;	72 W 2
						3.5			at 4.2 K;	
						4.4			at 2.2 K;	
						5.1			extrapolated to 0 K	
									$p_{Er}(H)$ along c axis at 2.1 and 4.2 K: Fig. 134	73 W 1
$ErIn_3$	− 10		6	Fig. 113	9.75					69 B 2
			4.86						from $C_p(T)$ on single crystal: Fig. 135	86 C 1
$ErTl_3$			6						neutron diffraction indicates modulated magnetic structure	81 K 1
$TmAl_3$	− 19			Fig. 136	7.88					68 B 1
$TmGa_3$									$p_{Tm}(H, T)$ and magnetic phase diagram: Fig. 137; magnetic and structural transitions deduced from $C(T)$: Fig. 138	85 C 2

$TmIn_3$	– 6			7.6				69 B 2
$YbAl_3$			Fig. 139					75 S 1
$YbIn_3$			Fig. 124					69 B 2
			Fig. 103				$\sigma(H)$ at 4.2 K: Fig. 104	73 K 1
			Fig. 140				$\sigma_m(H)$ at 4.2 K: Fig. 141	74 S 1
								74 S 2
$YbTl_3$							$\sigma_m(H)$ at 4.2 K: Fig. 141	74 S 1
								74 S 2
R_3M_{11}								
La_3Al_{11}			–480				χ_m in 10^{-6} cm^3 mol^{-1}	69 V 2
Ce_3Al_{11}	– 25			2.53			χ follows Curie-Weiss law for $T > 100$ K	70 V 2
	– 25	9		2.2				78 C 1
	– 24.6	6.2		2.3			$\sigma(T)$ at 1 kOe and phase diagram: Fig. 142, ferromagnetic for 3 K < T < 6 K	80 C 2
Pr_3Al_{11}	0			3.50				69 V 2
Nd_3Al_{11}	– 9			3.62				69 V 2
RM_4								
$CeAl_4$	– 20			2.505				72 N 1
$PrAl_4$	4	12.3		3.52		0.67		68 M 1
$EuAl_4$	14	6	Fig. 143	8.02	6.7		p_s at 80 kOe; $\sigma(T)$ at 14.24 kOe: Fig. 143; $p_{Eu}(H)$ at 4.2 K: Fig. 144	67 W 1
	12	13	Fig. 145	7.79			Eu divalent; $T_N(H)$: Fig. 145	68 M 2
	14			7.75				69 V 2
$GdAl_4$	152	163		7.94	6.9			77 O 2
$TbAl_4$							no single phase, $TbAl_3$ and Al present; no sign of magnetic ordering for $T > 4.2$ K	77 O 2
R_2M_{17}								
Gd_2Al_{17}	– 68			7.96				79 P 1
			490				χ_g in 10^{-6} cm^3 g^{-1}	85 C 3

Table 2. Nonstoichiometric ternary compounds of rare earth elements and the group 3B elements Al, Ga, In, Tl with other metallic elements of the periodic system, excluding the group 1B elements Cu, Ag, Au, the group 2 elements Be, Mg, Zn, Cd, Hg, and the group 3B element B. p_s, p_r and H_c refer to 4.2 K, unless stated otherwise. R: rare earth element, M: group 3B element.

	Θ K	T_C K	T_N K	χ	p_{eff} μ_B/f.u.	p_s μ_B/f.u.	p_r μ_B/f.u.	H_c kOe	Remarks	Ref.
R/M=5/3										
$Sc_{5-x}Hf_xGa_3$				Fig. 25						81 S 1
$Sc_{5-x}Zr_xGa_3$				Figs. 24, 25						81 S 1
R/M=3/2										
$(Gd_xTh_{1-x})_3Al_2$	Fig. 27									75 B 1
R/M=1/1										
$Y_{1-x}Gd_xInPd$	Fig. 173									75 B 2
$Y_{1-x}Th_xInPd$				Fig. 174						75 B 2
$Gd_xTh_{1-x}InPd$	Fig. 173									75 B 2
R/M=1/2										
$Sc(Al_xFe_{1-x})_2$		Fig. 148							$\sigma(x)$ at 4.2 K and 20 kOe, and composition dependence of structure type: Fig. 148	76 S 1
$Y(Al_xCo_{1-x})_2$	Fig. 146	Fig. 146							$\sigma(H,x)$ at 4.2 K: Fig. 147; weakly itinerant ferromagnet for $x \cong 0.15$	85 Y 1
$Y(Al_xFe_{1-x})_2$									$\chi_{HF}(x)$ at 4.2 K: Fig. 149 $x=0.5$: Table 3	78 B 1
	Fig. 150	Fig. 150			Fig. 151				$T_M(x)$ and $T_A(x)$: Fig. 150	84 R 1
$Y_{1-x}Th_xAl_2$				Fig. 54						70 V 1
$Ce_{1-x}Th_xAl_2$			Fig. 68						for $x \leqq 0.4$	80 C 1
$Pr_{1-x}Ca_xAl_2$									p_{eff} per Pr atom, p_s at 4 K and 20 kOe	80 R 1
$x=0.1$	37	34			2.84	1.7				
0.3	18	23			2.87	1.4				
0.5	12	17			3.46	1.0				
0.7	− 6	24			3.50	0.2				
0.9	− 2				3.46	0.1				
$Gd(Al_xCo_{1-x})_2$		Fig. 152			Fig. 152				$x=0.5$: cf. Table 3	79 K 1
						Fig. 153				81 B 1

$Gd(Al_xFe_{1-x})_2$		Fig. 154		Fig. 154	$\sigma(H,x)$ at 4.2 K: Fig. 155; $p_{Fe}(x)$ at 4.2 K: Fig. 156 x = 0.5: cf. Table 3	79 B 4
$Gd(Al_xMn_{1-x})_2$						78 S 1 83 S 1
x = 0.2			8.52			
0.4			8.30			
0.5			8.10	2.50	cf. Table 3	
0.7		108	8.20	6.17		
0.8		116	8.10	6.62		
0.9		166	7.00	7.00		
0.95	176	174	7.93			
0.975	180	173	7.90			
0.99	178	171	7.92			
1	170	168	7.92			
$Gd(Al_xNi_{1-x})_2$					for x < 0.8 not single phase; for x = 0.5 cf. Table 3	85 K 1
x = 0.8	80	60	7.92			
0.814		70				
0.875		158				
0.888	130	160	7.8			
0.902	159	165	7.85			
0.916		165				
0.929	159	170	7.8			
0.946	170	175	7.76			
0.954	173	175				
0.960	169	175	7.7			
0.965	170	175	7.75			
0.973		175				
1	170	171	7.9			
$Gd(Al_xPd_{1-x})_2$					for x < 0.7 not single phase	85 C 3
x = 0.70	95		8.03			
0.75	92		8.10			
0.80	108		8.06			
0.85	115		8.02			
0.90	144		7.95			
0.95	165		7.87			
1	171		7.91			

continued

Table 2 (cont.)

	Θ K	T_C K	T_N K	χ	p_{eff} μ_B/f.u.	p_s μ_B/f.u.	p_r μ_B/f.u.	H_c kOe	Remarks	Ref.
$Gd(Al_xSn_{1-x})_2$									for $x<0.8$ not single phase	85 C 3
$x=0.80$	80				7.83					
0.90	125				7.87					
0.93	138				7.80					
0.95	140				7.97					
1	171				7.91					
$Gd_xTh_{1-x}Al_2$	Fig. 48								for $x>0.35$ cubic Laves phase	67 B 1
	Fig. 58	Fig. 58								84 C 1
$Gd_xU_{1-x}Al_2$	Fig. 58	Fig. 58								84 C 1
$Gd_{1-x}Ca_xAl_2$									p_s at 4 K and 20 kOe	80 R 1
$x=0.1$		162				5.45				
0.2		152				5.32				
0.3		145				4.43				
0.4		150				3.56				
0.5		132				3.36				
$\geqq 0.8$									paramagnetic	
$Tb(Al_xCo_{1-x})_2$									samples annealed at 1273 K for 100 h; very dispersed data, strongly dependent on heat-treatment;	73 O 3
$x=0.10$						5.80	1.58		$MgCu_2$ structure type	
0.17						5.90	1.90		$MgCu_2$ structure tpye	
0.32		51				7.75			$MgZn_2$ structure type; T_C measured in 20 kOe	
0.36						6.96	2.38		$MgZn_2$ structure type	
0.47		81				6.41	2.55		$MgZn_2$ structure type; T_C measured in 20 kOe	
0.50						6.62	2.52		$MgCu_2$ structure type	
0.66		54				6.09			$MgCu_2$ structure type; T_C measured in 13.5 kOe	
0.70		47				6.89	2.84		$MgCu_2$ structure type T_C measured in 13.5 kOe	
0.74						7.10	2.65		$MgCu_2$ structure type	
0.76						7.08	2.90		$MgCu_2$ structure type	

0.81				7.04		$MgCu_2$ structure type
0.85				7.17	1.85	$MgCu_2$ structure type
0.88				7.61	1.85	$MgCu_2$ structure type
1.0				8.38		$MgCu_2$ structure type
$Tb(Al_xFe_{1-x})_2$		Fig. 157				for $0.34 \leqq x \leqq 0.5$ $MgZn_2$ structure type, for other alloys $MgCu_2$ structure: Fig. 157; cf. Table 3 for $x = 0.5$ 76 O 1
				Fig. 157		$p_r(x)$ at 1.6 K: Fig. 157 73 O 3
$Dy(Al_xCo_{1-x})_2$						for large Co concentration first-order phase transition 80 S 1
$x = 0.05$			187	11.15		$MgCu_2$ structure type
0.1			199	11.30		$MgCu_2$ structure type
0.15	210		206	11.23		$MgCu_2$ structure type
0.2	187		177	11.18		$MgCu_2$ structure type
0.4			118	11.05		$MgZn_2$ structure type
0.5	36			10.9	6.65	$MgZn_2$ structure type; cf. Table 3
0.8	55			9.33		$MgCu_2$ structure type
0.9	72			9.70		$MgCu_2$ structure type
$Dy(Al_xFe_{1-x})_2$						short-range magnetic order (Fe magnetic clusters) for $T_C < T < T_{cl}$ T_{cl}: magnetic clusters disappear for $T > T_{cl}$ p_{cl}: average magnetic moment of the Fe clusters for $T_C < T < T_{cl}$ 85 K 2
$x = 0$		635		11.90		$MgCu_2$ structure type; $T_{cl} = 660$ K 85 K 2
0.075					6.37 4.92	72 O 1
0.10		505		11.40		$MgCu_2$ structure type; $T_{cl} = 590$ K; $p_{cl} = 2500\ \mu_B$ 85 K 2
0.15					7.12 5.10	72 O 1
0.20		364.5		10.40		$MgCu_2$ structure type; $T_{cl} = 480$ K; $p_{cl} = 2300\ \mu_B$ 85 K 1
0.30		217.5		9.60		$MgCu_2$ structure type; $T_{cl} = 380$ K; $p_{cl} = 2100\ \mu_B$ 85 K 1
					7.81 5.26	72 O 1

continued

Table 2 (cont.)

	Θ K	T_C K	T_N K	χ	p_{eff} μ_B/f.u.	p_s μ_B/f.u.	p_r μ_B/f.u.	H_c kOe	Remarks	Ref.
$Dy(Al_xFe_{1-x})_2$ (cont.)										
x = 0.40		163			9.50				$MgZn_2$ structure type; T_{cl} = 380 K; p_{cl} = 960 μ_B	85 K 2
0.45						7.41	4.53			72 O 1
0.50		144.5			9.60				$MgZn_2$ structure type; T_{cl} = 400 K, p_{cl} = 40 μ_B; cf. Table 3	85 K 2
0.52						6.96	4.06			72 O 1
0.75						6.51	3.35			72 O 1
0.80		58			9.75				$MgCu_2$ structure type; T_{cl} = 80 K, p_{cl} = 16 μ_B	85 K 2
0.90						7.50	2.62			72 O 1
1		60			9.75				$MgCu_2$ structure type; T_{cl} = 80 K	85 K 2
						9.24	0.6			72 O 1
$Ho(Al_xCo_{1-x})_2$									T_C measured in 20 kOe	73 O 3
x = 0		90				7.85			$MgCu_2$ structure type	
0.50						8.32			$MgZn_2$ structure type; cf. Table 3	
0.73		34				7.12	0.30		$MgZn_2$ structure type	
0.85		35				8.56	0.35		$MgCu_2$ structure type	
0.92		38				9.60	0.18		$MgCu_2$ structure type	
1.0						8.64	0.10		$MgCu_2$ structure type	
$Ho(Al_xFe_{1-x})_2$									$p_m(H)$ at 4.2 K: Fig. 158 p_s at 65 kOe	85 S 2
x = 0.70		58				7.95			$H_{hyp}(^{57}Fe) = 0$ for $T \geqq 58$ K;	
0.75		46				7.80			$H_{hyp}(^{57}Fe) = 0$ for $T \geqq 48$ K; $p_s(Ho) = 6.1\ \mu_B$, $p_s(Fe) = 1.2\ \mu_B$ from neutron scattering	
0.80		36				7.90			$H_{hyp}(^{57}Fe) = 0$ for $T \geqq 33$ K;	
0.90		39				8.5			$H_{hyp}(^{57}Fe) = 0$ for $T \geqq 38$ K; $p_s(Ho) = 7.3\ \mu_B$ from neutron scattering	
1		37				8.85			$p_s(Ho) = 8.7\ \mu_B$ from neutron scattering	

$Er(Al_xCo_{1-x})_2$							magnetic behaviour strongly dependent on heat-treatment	81 K 2
x = 0.10		115.5					$MgCu_2$ structure type	
0.30		60					$MgZn_2$ structure type	
0.70	14			9.0			$MgZn_2$ structure type	
0.75	14			9.2			$MgZn_2$ structure type	
0.90	24			9.4			$MgCu_2$ structure type	
1	40			9.0				
$Er(Al_xFe_{1-x})_2$							T_C for $x \geqq 0.5$ measured in 5.587 kOe; p_s at 42 kOe	71 O 1
x = 0.1		> 297			5.45		$MgCu_2$ structure type	
0.2					6.41		$MgCu_2$ structure type	
0.3					5.47		$MgCu_2$ structure type	
0.4					6.07		$MgZn_2$ structure type	
0.5		56			6.32		$MgZn_2$ structure type; cf. Table 3	
0.63		43			5.46		$MgZn_2$ structure type	
0.66					6.42		two-phase	
0.7		24			6.92		$MgCu_2$ structure type	
0.84					6.40		$MgCu_2$ structure type	
0.9		16			5.32		$MgCu_2$ structure type	
0.94		16			6.80		$MgCu_2$ structure type	
1		25			7.45		$MgCu_2$ structure type	
$Yb_{1-x}Ca_xAl_2$			Fig. 106				homogeneous alloys; lattice constant does not follow Vegard's law; χ far from Curie-Weiss law; Yb in a mixed-valent state dependent on T and x	85 I 1
R/M = 1/3								
$CeIn_xSn_{3-x}$			Fig. 114 Fig. 115				$p_{Ce}(H, T, x)$: Fig. 115	80 D 1
$Gd(Al_xCo_{1-x})_3$		Fig. 159		Fig. 159	Fig. 159			82 B 3
$Gd(Al_xFe_{1-x})_3$		Fig. 160		Fig. 160	Fig. 160		$p_m(H, x)$ at 4.2 K: Fig. 161	82 B 2
$Gd(In_xSn_{1-x})_3$			Fig. 128					84 A 1
$Tb(Al_xFe_{1-x})_3$								76 O 1, 73 O 4
x = 0		651			2.62	1.24	$PuNi_3$ structure type	

continued

Table 2 (cont.)

	Θ K	T_C K	T_N K	χ	p_{eff} μ_B/f.u.	p_s μ_B/f.u.	p_r μ_B/f.u.	H_c kOe	Remarks	Ref.
$Tb(Al_xFe_{1-x})_3$ (cont.)										
x = 0.07		712				3.44	1.86		$PuNi_3$ structure type	
0.2		453				5.04	2.89			
0.33		355				5.48	3.4		$CeNi_3$ structure type	
$Tb(In_xSn_{1-x})_3$	Fig. 131		Fig. 131			8.5			p_s from neutron diffraction for x = 0.4	73 L 1
$Dy(Al_xFe_{1-x})_3$										77 O 5
x = 0.07						5.08		7.1		
0.13						5.08		9.4		
0.20						5.64		10.1		
0.23						5.96		10.2		
0.27						5.12		9.3		
0.30						5.52		10.6		
0.33								11		
0.40						8.24		9.4		
R/M = 6/23										
$Dy_6(Al_xFe_{1-x})_{23}$										77 O 5
x = 0.06						22.6		1		
0.13						24.1		3		
0.19						25.6		5		
0.25						26.1		5.4		
R/M = 2/17										
$Y_2Al_xFe_{17-x}$										76 M 1
x = 7.65						9.14		2		
9.52						7.66		2		
$Y_2Al_xNi_{17-x}$				Fig. 162					$\sigma_m(T,x)$: Fig. 163	83 C 1
$Sm_2Al_xFe_{17-x}$									homogeneous compounds for $3.74 \leqq x \leqq 9.52$ when annealed 1073 K; Sm in 6(C_1) position, Fe and Al statistically distributed on 6(C_2), 9(d), 18(f) and 18(h) sites	76 M 1
x = 3.74						25.6		0		
5.78		395				20.0		0.4		

7.65	197		14.3		7	
8.00	144		6.54		13.5	
9.52	129		6.06		15	
$Gd_2Al_xFe_{17-x}$						76 M 1
x = 9.52			3.76		2.6	
$Gd_2Al_xNi_{17-x}$		Fig. 164				79 P 1
	Fig. 165					82 P 1
					$\sigma_m(T,x)$ at 9.5 kOe; Figs. 166, 167	
$Tb_2Al_xFe_{17-x}$						76 O 1,
x = 0.95	431		14.10	6.56	Th_2Ni_{17} structure type	73 O 4
1.90	455		13.26	6.02	Th_2Ni_{17} structure type	
2.86	482		9.90	6.02	Th_2Ni_{17} structure type	
3.81	515				Th_2Zn_{17} structure type	
5.71	317				Th_2Zn_{17} structure type	
8.52	305		0.75	0.02		
$Dy_2Al_xFe_{17-x}$					$T_C(x)$: Fig. 168;	85 R 1
					$\sigma(T,x)$ at 10 kOe: Fig. 169;	84 P 2
					$\sigma(H,x)$ at 4.2 K: Fig. 170	
					p_s(Fe) calculated assuming p_s(Dy) = 10 μ_B independent of Al concentration	
x = 0			16.35		0.5	77 O 5
0.95			15.80		2.6	77 O 5
1.02	416		13.40	9.38	p_{eff}(Fe) = 4.2 μ_B, p_s(Fe) = 2.1 μ_B	84 P 2
1.90			10.96		3.7	77 O 5
2.04	448		10.67	9.10	p_{eff}(Fe) = 4.3 μ_B, p_s(Fe) = 2.0 μ_B	84 P 2
2.86			9.91		4.9	77 O 5
3.06	460		7.4	5.75	p_{eff}(Fe) = 4.3 μ_B, p_s(Fe) = 1.9 μ_B	84 P 2
3.81			6.70		1.8	77 O 5
3.91	451		3.94	1.45	p_{eff}(Fe) = 3.9 μ_B, p_s(Fe) = 1.8 μ_B	84 P 2
4.93	389		4.76	1.40	p_{eff}(Fe) = 3.9 μ_B, p_s(Fe) = 1.2 μ_B	84 P 2
5.71			3.19		0.5	77 O 5
5.95	326		6.31	3.21	p_{eff}(Fe) = 3.6 μ_B, p_s(Fe) = 1.2 μ_B	84 P 2
6.97	259		7.10	4.38	p_{eff}(Fe) = 3.6 μ_B, p_s(Fe) = 1.3 μ_B	84 P 2
8.52			3.00		62.5	77 O 5
$Dy_2Al_xNi_{17-x}$		Fig. 171			$\sigma_m(T)$: Fig. 172	83 C 1
R/M = 1/13						
$La(Al_xFe_{1-x})_{13}$					magnetic phase diagram: Fig. 214	84 P 1
					$p_{Fe}(H)$ at 4.2 K for x = 0.123: Fig. 215	84 P 3

Table 3. Stoichiometric ternary compounds of rare earth elements and the group 3B elements Al, Ga, In, Tl with other metallic elements of the periodic system, excluding the group 1B elements Cu, Ag, Au, the group 2 elements Be, Mg, In, Cd, Hg, and the group 3B element B. p_s, p_r and H_c refer to 4.2 K, unless stated otherwise. R: rare earth element, M: group 3B element.

	Θ K	T_C K	T_N K	χ	p_{eff} μ_B/f.u.	p_s μ_B/f.u.	p_r μ_B/f.u.	H_c kOe	Remarks	Ref.
R/M=3/1										
$La_3In_{0.8}Sn_{0.2}$				Fig. 4						78 D 1
$La_3Tl_{0.8}Pb_{0.2}$				Fig. 4						78 D 1
R/M=2/1										
Y_2AlNi_2									Pauli paramagnet	82 R 1
Y_2GaNi_2									Pauli paramagnet	82 R 1
$La_2Al_{0.75}Ni_{2.25}$									Pauli paramagnet	82 R 1
$Ce_2Al_{0.85}Ni_{2.15}$									Pauli paramagnet; tetravalent Ce suggested	82 R 1
$Ce_2Ga_{0.85}Ni_{2.15}$									Pauli paramagnet; tetravelent Ce suggested	82 R 1
Pr_2AlNi_2	41				3.45					82 R 1
Pr_2GaNi_2	10				3.31					82 R 1
Nd_2AlNi_2	25				3.51					82 R 1
Nd_2GaNi_2	0				3.90					82 R 1
Sm_2AlNi_2									no Curie-Weiss behaviour	82 R 1
Sm_2GaNi_2									no Curie-Weiss behaviour	82 R 1
Gd_2AlNi_2	− 20				9.07					82 R 1
Gd_2GaNi_2	3				9.81					82 R 1
Tb_2AlNi_2	− 2				10.84					82 R 1
Tb_2GaNi_2	14				10.81					82 R 1
Dy_2AlNi_2	− 11				12.04					82 R 1
Dy_2GaNi_2	− 3				11.96					82 R 1
Ho_2AlNi_2	− 7				11.24					82 R 1
Ho_2GaNi_2	− 1				11.53					82 R 1
Er_2AlNi_2	23				9.94					82 R 1
Er_2GaNi_2	19				9.68					82 R 1
Tm_2AlNi_2	24				8.59					82 R 1
Tm_2GaNi_2	25				8.36					82 R 1
Yb_2AlNi_2									Pauli paramagnet; divalent Yb suggested	82 R 1
Yb_2GaNi_2									Pauli paramagnet; divalent Yb suggested	82 R 1

Lu_2AlNi_2								Pauli paramagnet	82 R 1
Lu_2GaNi_2								Pauli paramagnet	
R/M=1/1									
YAlFe		38			0.10		2	cf. Table 2	77 O 4
YGaCo	− 91			1.66				$p_{eff}(Co)=1.66\,\mu_B$	83 R 1
CeAlNi								no magnetic ordering	73 O 2
CeGaCo	59.4			1.59				$p_{eff}(Co)=1.59\,\mu_B$	83 R 1
PrAlCo		14			1.65	0.45	1		77 O 3
PrGaCo	− 60.3			4.21				$p_{eff}(Co)=2.22\,\mu_B$	83 R 1
PrAlNi	− 10			3.73					65 O 1
NdAlCo		22			1.76	0.42	1		77 O 3
NdAlNi	5	17		3.84	1.64				73 O 2
NdGaCo	− 24.8			4.23				$p_{eff}(Co)=2.19\,\mu_B$	83 R 1
GdAlCo		112			7.18	0	0	cf. Table 2	77 O 2
GdAlFe		260			5.81		16	cf. Table 2	77 O 4
GdAlMn		202		8.52				cf. Table 2	78 S 1
GdAlNi	53	61		8.90	6.36	1.6		cf. Table 2	65 O 1
	70	70							75 B 2
	56	66		8.5		0			73 O 2
GdInNi	80	83							75 B 2
GdInPd	103	102							75 B 2
TbAlFe		185			6.44			cf. Table 2	71 O 2
DyAlCo		47			6.65	1.42	4	cf. Table 2	77 O 3
DyAlFe		125			7.12		12	cf. Table 2	77 O 4
DyAlNi	30	47		11.0	7.82	1.6			65 O 1
	30	39		11.1	7.38	0.2		p_s at 1.6 K	73 O 2
HoAlCo		33			8.32	0.81	3	cf. Table 2	77 O 3
HoAlFe		92			8.11		8	cf. Table 2	77 O 4
HoAlNi	12	27		10.6	7.85	1.6			65 O 1
	11	25		10.8	8.86	0		p_s at 1.6 K	73 O 2
ErAlCo		22			7.40	0.53	1	cf. Table 2	77 O 3
ErAlFe		56			6.32		7	cf. Table 2	77 O 4
TmAlCo		14			4.12	0.2	0.5		77 O 3
TmAlFe		38			2.93		6		77 O 4
TmAlNi	− 11	12	4.2	7.8	4.72	0		p_s at 1.6 K	73 O 2
						1.6			65 O 1
LuAlCo					0				77 O 3
LuAlFe		39			0.1	0.1			77 O 4

continued

Table 3 (cont.)

	Θ K	T_C K	T_N K	χ	p_{eff} μ_B/f.u.	p_s μ_B/f.u.	p_r μ_B/f.u.	H_c kOe	Remarks	Ref.
R/M=1/2										
YAl_2Ni									Pauli paramagnet	82 R 2
$GdAl_2Ni$	43				8.04					82 R 2
$TbAl_2Ni$	39				10.82					82 R 2
$DyAl_2Ni$	25				11.75					82 R 2
$HoAl_2Ni$	7				11.53					82 R 2
$ErAl_2Ni$	4				10.32					82 R 2
$TmAl_2Ni$	18				8.09					82 R 2
$TmGa_2Ni$	−263			Fig. 175	6.87					81 Y 1
$YbAl_2Ni$									Pauli paramagnet; divalent Yb suggested	82 R 2
$LuAl_2Ni$									Pauli paramagnet	82 R 2
R/M=1/4										
$TmGa_4Ni$	−256			Fig. 175	7.46					81 Y 1
R/M=2/11										
$Gd_2Al_{11}Co_6$	81			470	11.84				χ_0 in $10^{-6}\,cm^3\,mol^{-1}$;	78 P 1
									$p_{eff}(Co)=3.04\,\mu_B$ obtained by subtracting $\chi-\chi_0$ of $Gd_2Cu_6Al_{11}$ from that of $Gd_2Co_6Al_{11}$	85 C 3
R/M=1/6										
YAl_6Fe_6	327	345			11.6				$p_{eff}(Fe)=4.7\,\mu_B$ from high-T behaviour ($p_{eff}(Fe)=3.0\,\mu_B$ from intermediate-T behaviour);	81 F 2
									$p_m(T)$ at 15 kOe: Fig. 177;	
									$p_m(H)$ at 4.2 and 240 K: Fig. 178;	
									T_C derived from Mössbauer effect: Fig. 176;	
									relative population of Fe ions in 8(f), 8(j) and 8(i) sites 67, 17 and 16%, respectively; Fig. 179	
YAl_6Mn_6	− 44				3.5				$p_{eff}(Mn)=1.4\,\mu_B$	81 F 1
$EuAl_6Fe_6$		135							Eu in a mixed-valent state suggested	81 F 2

$GdAl_6Cr_6$	158	170			5.5	p_s at 18 kOe; $\sigma_m(T)$ at 10 kOe and $p_m(H)$ at 4.1 K: Fig. 180	81 F 1
$GdAl_6Fe_6$	328	345		11.3		$p_{eff}(Fe) = 3.3\,\mu_B$ calculated using $p_{eff}(Gd) = 7.94\,\mu_B$; $p_m(T)$ experimental, at 15 kOe: Fig. 177, and theoretical: Fig. 181; T_C derived from Mössbauer effect: Fig. 182; relative population of Fe ions in 8(f), 8(j) and 8(i) sites 60, 26 and 14%, respectively; Fig. 179	81 F 2, 81 F 1
$GdAl_6Mn_6$	− 9	15			1.1	p_s at 18 kOe	81 F 1
						$\sigma_m(T)$ at 15 kOe: Fig. 183	81 F 1
$GdAl_6Rh_6$	47	30			4.5	p_s at 18 kOe	81 F 1
$TbAl_6Fe_6$	328	335		12.3		$p_{eff}(Fe) = 3.1\,\mu_B$ calculated using $p_{eff}(Tb) = 9.72\,\mu_B$; $p_m(T)$ at 15 kOe: Fig. 177; T_C derived from Mössbauer effect: Fig. 182; hysteresis at 122 K: Fig. 184; relative population of Fe ions in 8(f), 8(j) and 8(i) sites 60, 30 and 10%, respectively: Fig. 179	81 F 2
$TbAl_6Mn_6$	− 26	8			0.3	p_s at 18 kOe	81 F 1
$DyAl_6Cr_6$	− 5	20			1.9	p_s at 18 kOe; $\sigma_m(T)$ at 10 kOe and $p_m(H)$ at 4.1 K: Fig. 180; CEF effect suggested	81 F 1
$DyAl_6Fe_6$	320	325	Fig. 185	12.5		$p_{eff}(Fe) = 3.0\,\mu_B$ calculated using $p_{eff}(Dy) = 10.63\,\mu_B$; large hysteresis at temperatures below $\sigma(T)$ maximum; $p_m(H)$ at 4.2 and 250 K: Fig. 178; $p_m(T)$ at 17.5 kOe: Fig. 186; relative population of Fe ions in 8(f), 8(j) and 8(i) sites 63, 32 and 5%, respectively: Fig. 179	81 F 2

continued

Table 3 (cont.)

	Θ K	T_C K	T_N K	χ	p_{eff} μ_B/f.u.	p_s μ_B/f.u.	p_r μ_B/f.u.	H_c kOe	Remarks	Ref.
$DyAl_6Mn_6$	− 7	6				2.1			p_s at 18 kOe; $\sigma_m(T)$ at 10 kOe: Fig. 183	81 F 1
$HoAl_6Fe_6$	311	310			12.5				$p_{eff}(Fe) = 2.7\,\mu_B$ calculated using $p_{eff}(Ho) = 10.60\,\mu_B$; T_C derived from Mössbauer effect: Fig. 182; large hysteresis; $p_m(T)$, experimental, at 17.5 kOe: Fig. 186, and theoretical: Fig. 181; relative population of Fe ions in 8(f), 8(j) and 8(i) sites 61, 35 and 3%, respectively: Fig. 179	81 F 2
$ErAl_6Cr_6$	− 1	15			10.4				$p_{eff}(Cr) = 1.6\,\mu_B$ calculated using $p_{eff}(Er) = 9.59\,\mu_B$; $p_m(H)$ at 4.1 K: Fig. 180; CEF effects suggested	81 F 1
$ErAl_6Fe_6$	328	320			12.3				$p_{eff}(Fe) = 3.1\,\mu_B$ calculated using $p_{eff}(Er) = 9.59\,\mu_B$; large hysteresis at temperature below the $\sigma(T)$ maximum; $p_m(H)$ at 4.2 and 215 K: Fig. 178; $p_m(T)$ at 15 kOe: Fig. 186; relative population of the Fe atoms in 8(f), 8(j) and 8(i) sites 66, 30 and 1%, respectively: Fig. 179	81 F 2
$ErAl_6Mn_6$	− 4	2.6			9.6				$p_{eff}(Mn) = 1.4\,\mu_B$ calculated using $p_{eff}(Er) = 9.59\,\mu_B$; CEF effect suggested	81 F 1
$TmAl_6Fe_6$	345	320 Fig. 176			10.7				$p_{eff}(Fe) = 3.1\,\mu_B$ calculated using $p_{eff}(Tm) = 7.57\,\mu_B$; large hysteresis at temperature below the $\sigma(T)$ maximum;	81 F 2

							$p_m(T)$ at 17.5 kOe: Fig. 186; relative population of Fe ions in 8(f), 8(j) and 8(i) sites 62, 30 and 7%, respectively: Fig. 179	
$TmAl_6Mn_6$	– 18	2		8.1	1.9		p_s at 18 kOe; $p_{eff}(Mn) = 1.2\,\mu_B$ calculated using $p_{eff}(Tm) = 7.57\,\mu_B$	81 F 1
$YbAl_6Fe_6$		210					$p_m(T)$ at 15 kOe: Fig. 177; Yb in mixed-valent state suggested; sample contained $YbAl_2$; relative population of Fe ions in 8(f), 8(j) and 8(i) sites 61, 31 and 9%, respectively: Fig. 179	81 F 1
$YbAl_6Mn_6$	– 23			5.4			$p_{eff}(Mn) = 1.2\,\mu_B$ calculated using $p_{eff}(Yb) = 4.54\,\mu_B$	81 F 1
$LuAl_6Cr_6$							diamagnetic	81 F 1
R/M = 1/7								
YAl_7Fe_5	230	215		9.9	5.8	2	$H_{hyp}(^{57}Fe)$ vanishes for $T \geqq 165$ K; $p_{eff}(Fe) = 4.4\,\mu_B$ calculated using $p_{eff}(Y) = 0$; p_s at 50 kOe; hysteresis: Fig. 199; relative population of Fe ions in 8(f), 8(j) and 8(i) sites 53, 40 and 7%, respectively: Fig. 179	83 F 1
$SmAl_7Fe_5$	265	220		8.8	5.1	13.6	$p_{eff}(Fe) = 3.9\,\mu_B$ calculated using $p_{eff}(Sm) = 0.84\,\mu_B$ p_s at 50 kOe; $p_m(T)$ at 30 Oe: Fig. 187; hysteresis, time-dependent phenomena: Fig. 188; relative population of Fe ions in 8(f), 8(j) and 8(i) sites 63, 34 and 3%, respectively: Fig. 179	83 F 1

continued

Table 3 (cont.)

	Θ K	T_C K	T_N K	χ	p_{eff} μ_B/f.u.	p_s μ_B/f.u.	p_r μ_B/f.u.	H_c kOe	Remarks	Ref.
$GdAl_7Fe_5$	241	268			11.6	0.4		0.4	$H_{hyp}(^{57}Fe)$ vanishes for $T \geqq 260$ K $p_{eff}(Fe) = 3.8\,\mu_B$ calculated using $p_{eff}(Gd) = 7.94\,\mu_B$; p_s at 18 kOe; $p_m(T, H)$: Fig. 189; relative population of Fe ions in 8(f), 8(j) and 8(i) sites 53, 44 and 3%, respectively: Fig. 179	83 F 1
$TbAl_7Fe_5$	174	248			11.2	0.6		6.3	$H_{hyp}(^{57}Fe)$ vanishes for $T \geqq 240$ K; $p_{eff}(Fe) = 2.5\,\mu_B$ calculated using $p_{eff}(Tb) = 9.72\,\mu_B$; p_s at 50 kOe; $p_m(T)$ at 100 Oe: Fig. 190; hysteresis: Fig. 191; relative population of Fe ions in 8(f), 8(j) and 8(i) sites 56, 39 and 5% respectively: Fig. 179	83 F 1
$DyAl_7Fe_5$	177	227			13.1	1.8		24.3	$H_{hyp}(^{57}Fe)$ vanishes for $T \geqq 225$ K; $p_{eff}(Fe) = 3.4\,\mu_B$ calculated using $p_{eff}(Dy) = 10.63\,\mu_B$; p_s at 50 kOe; $p_m(T)$: Fig. 192; hysteresis: Fig. 193; relative population of Fe ions in 8(f), 8(j) and 8(i) sites 53, 39 and 8%, respectively: Fig. 179	83 F 1
$HoAl_7Fe_5$	186	227			13.1	2.3		9.5	$H_{hyp}(^{57}Fe)$ vanishes for $T \geqq 210$ K; $p_{eff}(Fe) = 3.5\,\mu_B$ calculated using $p_{eff}(Ho) = 10.60\,\mu_B$; p_s at 50 kOe; $p_m(T)$: Fig. 194;	83 F 1

							hysteresis: Fig. 195; relative population of Fe ions in 8(f), 8(j) and 8(i) sites 58, 38 and 4%, respectively: Fig. 179	
$ErAl_7Fe_5$	192	218		12.5	1.7	18.5	$H_{hyp}(^{57}Fe)$ vanishes for $T \geqq 215$ K; $p_{eff}(Fe) = 3.6\,\mu_B$ calculated using $p_{eff}(Er) = 9.59\,\mu_B$; p_s at 50 kOe; $p_m(T)$: Fig. 196; hysteresis: Fig. 197; relative population of Fe ions in 8(f), 8(j) and 8(i) sites 52, 41 and 7%, respectively: Fig. 179	83 F 1
$TmAl_7Fe_5$	109				0.5		p_s at 18 kOe; contains an appreciable amount of a second phase	83 F 1
$YbAl_7Fe_5$	224	207		8.8	3.6	2	$H_{hyp}(^{57}Fe)$ vanishes for $T \geqq 180$ K; $p_{eff}(Fe) = 3.5\,\mu_B$ calculated using $p_{eff}(Yb) = 4.54\,\mu_B$; p_s at 50 kOe; $p_m(T)$ at 30 Oe and 15 kOe; Fig. 198; hysteresis: Fig. 199; relative population of Fe ions in 8(f), 8(j) and 8(i) sites 52, 38 and 10%, respectively: Fig. 179	83 F 1
$LuAl_7Fe_5$	224	212		9.5	5.4	2	$H_{hyp}(^{57}Fe)$ vanishes for $T \geqq 165$ K; $p_{eff}(Fe) = 4.2\,\mu_B$ calculated using $p_{eff}(Lu) = 0$; p_s at 50 kOe; $p_m(T)$ at 30 Oe and 18 kOe; Fig. 198; hysteresis: Fig. 199; relative population of Fe ions in 8(f), 8(j) and 8(i) sites 62, 36 and 2%, respectively: Fig. 179	83 F 1

continued

Table 3 (cont.)

	Θ K	T_C K	T_N K	χ	p_{eff} μ_B/f.u.	p_s μ_B/f.u.	p_r μ_B/f.u.	H_c kOe	Remarks	Ref.
R/M = 1/8										
YAl_8Cr_4									Cr nonmagnetic	79 F 1
YAl_8Fe_4	− 16				9.2	0.28			$p_{eff}(Fe) = 4.6\,\mu_B$ calculated using $p_{eff}(Y) = 0$;	78 F 1
									p_s at 16 kOe;	
									$\sigma(T)$ at 5 kOe: Fig. 200	
									about 80% of Fe atoms in 8(f) sites: Fig. 179	83 F 1
YAl_8Mn_4				Fig. 201						78 B 3
	5				1.6				$p_{eff}(Mn) = 0.8\,\mu_B$ calculated using $p_{eff}(Y) = 0$	79 F 1
$LaAl_8Cr_4$									Cr nonmagnetic	79 F 1
$LaAl_8Fe_4$	− 68				8.8	0.36			$p_{eff}(Fe) = 4.4\,\mu_B$ calculated using $p_{eff}(La) = 0$;	78 F 1
									p_s at 16 kOe;	
									$\sigma(T)$ at 10 kOe: Fig. 200	
									about 80% of Fe atoms in 8(f) sites: Fig. 179	83 F 1
$LaAl_8Mn_4$									contained additional phase	79 F 1
$CeAl_8Cr_4$									tetravalent Ce suggested; Cr nonmagnetic	79 F 1
$CeAl_8Fe_4$	23				8.3	0.26			$p_{eff}(Fe) = 4.2\,\mu_B$ calculated using $p_{eff}(Ce) = 0$;	78 F 1
									tetravalent Ce suggested;	
									$\sigma(T)$ at 8 kOe: Fig. 200	
				Fig. 202						78 B 3
									about 80% of Fe atoms in 8(f) sites: Fig. 179	
$CeAl_8Mn_4$	8				1.8				$p_{eff}(Mn) = 0.9\,\mu_B$ calculated using $p_{eff}(Ce) = 0$;	79 F 1
									tetravalent Ce suggested	
$PrAl_8Cr_4$	− 16		6		4.2	0.38			$p_{eff}(Cr) = 0.16\,\mu_B$ (induced) calculated using $p_{eff}(Pr) = 3.58\,\mu_B$;	79 F 1
									p_s at 17 kOe	

$PrAl_8Fe_4$	35	12		9.2	1.06	$p_{eff}(Fe) = 4.2\,\mu_B$ calculated using $p_{eff}(Pr) = 3.58\,\mu_B$; p_s at 16 kOe; $\sigma(T)$ at 10 kOe: Fig. 203	78 F 1
						about 80% of Fe atoms in 8(f) sites: Fig. 179	83 F 1
$PrAl_8Mn_4$	− 1	11		4.8	0.38	$p_{eff}(Mn) = 1.6\,\mu_B$ calculated using $p_{eff}(Pr) = 3.58\,\mu_B$ $\sigma(T)$ at 5 kOe and $p_m(H)$ at 4.1 and 13 K: Fig. 204	79 F 1
$NdAl_8Cr_4$	− 11			4.1		$p_{eff}(Cr) = 0.12\,\mu_B$ (induced) calculated using $p_{eff}(Nd) = 3.62\,\mu_B$	79 F 1
$NdAl_8Fe_4$	44	19		9.5	0.18	$p_{eff}(Fe) = 4.4\,\mu_B$ calculated using $p_{eff}(Nd) = 3.62\,\mu_B$; p_s at 16 kOe; $\sigma(T)$ at 5 kOe: Fig. 203	78 F 1
			Fig. 205			$\sigma(T,H)$: Fig. 205	78 B 1
						about 80% of Fe atoms in 8(f) sites: Fig. 179	83 F 1
$NdAl_8Mn_4$	− 8	7		4.9	6.48	$p_{eff}(Mn) = 1.7\,\mu_B$ calculated using $p_{eff}(Nd) = 3.62\,\mu_B$; p_s at 17 kOe	79 F 1
$SmAl_8Cr_4$	− 24	19		3.3	0.03	$p_{eff}(Cr) = 0.61\,\mu_B$ (induced) calculated using $p_{eff}(Sm) = 0.86\,\mu_B$; p_s at 17 kOe; $\sigma(T)$ at 5 kOe: Fig. 206	79 F 1
$SmAl_8Fe_4$	68			8.1	0.46	$p_{eff}(Fe) = 4.0\,\mu_B$ calculated using $p_{eff}(Sm) = 0.86\,\mu_B$; p_s at 16 kOe; $\sigma(T)$ at 5 kOe: Fig. 207	78 F 1
						about 80% of Fe atoms in 8(f) sites: Fig. 179	83 F 1
$SmAl_8Mn_4$	− 18	12		2.9	0.14	$p_{eff}(Mn) = 1.4\,\mu_B$ calculated using $p_{eff}(Sm) = 0.86\,\mu_B$; p_s at 17 kOe; $\sigma(T)$ at 10 kOe: Fig. 204	79 F 1

continued

Table 3 (cont.)

	Θ K	T_C K	T_N K	χ	p_{eff} μ_B/f.u.	p_s μ_B/f.u.	p_r μ_B/f.u.	H_c kOe	Remarks	Ref.
$EuAl_8Fe_4$	−148				9.5	0.27			$p_{eff}(Fe)=4.5\,\mu_B$ calculated using $p_{eff}(Eu)=3.52\,\mu_B$;	78 F 1
									p_s at 16 kOe;	
									Eu in a mixed-valent state;	
									$\sigma(T)$ at 2 kOe: Fig. 200	
									about 80% of Fe atoms in 8(f) sites: Fig. 179	83 F 1
$EuAl_8Mn_4$			20	Fig. 208		0.46			p_s at 17 kOe;	79 F 1
									Eu in a mixed-valent state;	
									$\sigma(T)$ at 2 kOe and $p_m(H)$ at 4.1 K: Fig. 204	
$GdAl_8Cr_4$	− 9		8		8.5	1.5			$p_{eff}(Cr)=0.15\,\mu_B$ (induced) calculated using $p_{eff}(Gd)=7.94\,\mu_B$	79 F 1
									p_s at 17 kOe;	
									$\sigma(T)$ at 5 kOe: Fig. 209	
$GdAl_8Fe_4$	−151	11		Fig. 210	12.0	2.40			$p_{eff}(Fe)=4.5\,\mu_B$ calculated using $p_{eff}(Gd)=7.94\,\mu_B$;	78 F 1
									p_s at 16 kOe;	
									$\sigma(T,H)$: Fig. 210	78 B 1
									about 80% of Fe atoms in 8(f) sites: Fig. 179	83 F 1
$GdAl_8Mn_4$				Fig. 201						78 B 3
	4		28		8.6	3.1			$p_{eff}(Mn)=1.6\,\mu_B$ calculated using $p_{eff}(Gd)=7.94\,\mu_B$;	76 F 1
									p_s at 17 kOe;	
									$\sigma(T)$ at 10 kOe: Fig. 211	
$TbAl_8Cr_4$	− 5		12		9.72	3.3			$p_{eff}(Cr)=0.08\,\mu_B$ (induced) calculated using $p_{eff}(Tb)=9.72\,\mu_B$;	79 F 1
									p_s at 17 kOe;	
									$\sigma(T)$ at 10 kOe and $p_m(H)$ at 4.1 and 13 K: Fig. 209	
$TbAl_8Fe_4$	− 105	20			13.1	2.10			$p_{eff}(Fe)=4.4\,\mu_B$ calculated using $p_{eff}(Tb)=9.72\,\mu_B$;	78 F 1

						p_s at 17 kOe; $\sigma(T)$ at 40 Oe and 10 kOe: Fig. 203	
						about 80% of Fe atoms in 8(f) sites: Fig. 179	83 F 1
$TbAl_8Mn_4$	7		21	10.3	4.3	$p_{eff}(Mn) = 1.7\,\mu_B$ calculated using $p_{eff}(Tb) = 9.72\,\mu_B$; p_s at 17 kOe	79 F 1
$DyAl_8Cr_4$	– 5		16	11.1	4.2	$p_{eff}(Cr) = 0.12\,\mu_B$ (induced) calculated using $p_{eff}(Dy) = 10.63\,\mu_B$; p_s at 17 kOe; $\sigma(T)$ at 5 kOe: Fig. 209	79 F 1
$DyAl_8Fe_4$	– 80	25		13.4	2.30	$p_{eff}(Fe) = 4.2\,\mu_B$ calculated using $p_{eff}(Dy) = 10.6\,\mu_B$; p_s at 16 kOe; $\sigma(T)$ at 5 kOe: Fig. 203	78 F 1
			Fig. 212			$\sigma(T, H)$: Fig. 212	78 B 3
						about 80% of Fe atoms in 8(f) sites: Fig. 179	83 F 1
						neutron diffraction revealed magnetic transition at 25 K attributed to a conical spiral structure of Fe atoms, there was no indication of rare earth sublattice ordering at 1.8 K	83 S 3
$DyAl_8Mn_4$	– 26		19	11.3	4.0	$p_{eff}(Mn) = 1.9\,\mu_B$ calculated using $p_{eff}(Dy) = 10.63\,\mu_B$; p_s at 16 kOe; $\sigma(T)$ at 5 kOe and $p_m(H)$ at 4.1 and 20 K: Fig. 211	79 F 1
$HoAl_8Cr_4$	– 5		8	10.5	4.1	p_s at 17 kOe	79 F 1
$HoAl_8Fe_4$	– 66	22		13.8	1.65	$p_{eff}(Fe) = 4.4\,\mu_B$ calculated using $p_{eff}(Ho) = 10.6\,\mu_B$; p_s at 16 kOe	78 F 1
						about 80% of Fe atoms in 8(f) sites: Fig. 179	83 F 1

continued

Table 3 (cont.)

	Θ K	T_C K	T_N K	χ	p_{eff} μ_B/f.u.	p_s μ_B/f.u.	p_r μ_B/f.u.	H_c kOe	Remarks	Ref.
$HoAl_8Fe_4$ (cont.)									neutron diffraction revealed magnetic transition at 25 K attributed to a conical spiral structure of Fe atoms, there was no indication of rare earth sublattice ordering at 4.2 K	83 S 3
$HoAl_8Mn_4$	– 2		14		11.2	4.8			$p_{eff}(Mn) = 1.5\,\mu_B$ calculated using $p_{eff}(Ho) = 10.6\,\mu_B$; p_s at 17 kOe	79 F 1
$ErAl_8Cr_4$	– 4		14		9.59	3.8			$p_{eff}(Cr) = 0.08\,\mu_B$ (induced) calculated using $p_{eff}(Er) = 9.59\,\mu_B$ p_s at 17 kOe	79 F 1
$ErAl_8Fe_4$	– 38	25			12.8	2.80			$p_{eff}(Fe) = 4.3\,\mu_B$ calculated using $p_{eff}(Er) = 9.56\,\mu_B$; p_s at 16 kOe; $\sigma(T)$ at 2.5 kOe: Fig. 207	78 F 1
									intensity vs. T of (110) neutron diffraction: Fig. 213	77 B 3
									about 80% of Fe atoms in 8(f) sites: Fig. 179	83 F 1
$ErAl_8Mn_4$	– 2		15		9.8	4.1			$p_{eff}(Mn) = 1.0\,\mu_B$ calculated using $p_{eff}(Er) = 9.59\,\mu_B$; p_s at 17 kOe	79 F 1
$TmAl_8Cr_4$	– 11		11		7.57	2.4			$p_{eff}(Cr) = 0.07\,\mu_B$ (induced) calculated using $p_{eff}(Tm) = 7.57\,\mu_B$ p_s at 17 kOe	79 F 1
$TmAl_8Fe_4$	7	20			11.4	2.0			$p_{eff}(Fe) = 4.3\,\mu_B$ calculated using $p_{eff}(Tm) = 7.6\,\mu_B$; p_s at 16 kOe	78 F 1
									about 80% of Fe atoms in 8(f) sites: Fig. 179	83 F 1

$TmAl_8Mn_4$	5		13		8.1	3.7	$p_{eff}(Mn) = 1.5\,\mu_B$ calculated using $p_{eff}(Tm) = 7.57\,\mu_B$; p_s at 17 kOe	79 F 1
$YbAl_8Cr_4$	7				1.46		$p_{eff}(Cr) = 0.1\,\mu_B$ (induced) Yb in a mixed-valent state suggested	79 F 1
$YbAl_8Fe_4$	62	8			10.3	2.80	$p_{eff}(Fe) = 4.6\,\mu_B$ calculated using $p_{eff}(Yb) = 4.54\,\mu_B$; p_s at 16 kOe; trivalent Yb suggested; $\sigma(T)$ at 2.5 kOe: Fig. 207	78 F 1
							about 80% of Fe atoms in 8(f) sites: Fig. 179	83 F 1
$YbAl_8Mn_4$							contained additional phase; divalent Yb suggested	79 F 1
$LuAl_8Cr_4$							$\sigma(T)$ at 5 kOe: Fig. 206	79 F 1
$LuAl_8Fe_4$				Fig. 202				78 B 3
	79				8.7	0.6	$p_{eff}(Fe) = 4.3\,\mu_B$ calculated using $p_{eff}(Lu) = 0$; p_s at 16 kOe	78 F 1
							about 80% of Fe atoms in 8(f) sites: Fig. 179	83 F 1
$LuAl_8Mn_4$	10				1.8		$p_{eff}(Mn) = 0.9\,\mu_B$ calculated using $p_{eff}(Lu) = 0$; $\sigma(T)$ at 10 kOe: Fig. 204	79 F 1

2.9.3 Figures

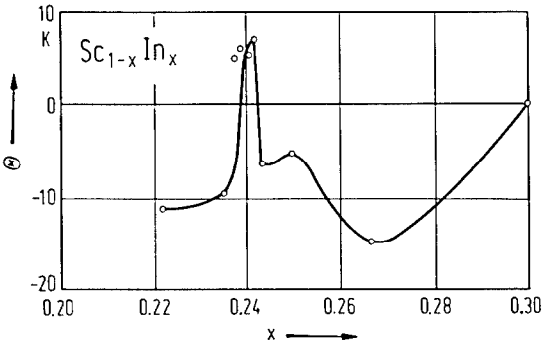

Fig. 1. $Sc_{1-x}In_x$. Composition dependence of Θ [61 M 1].

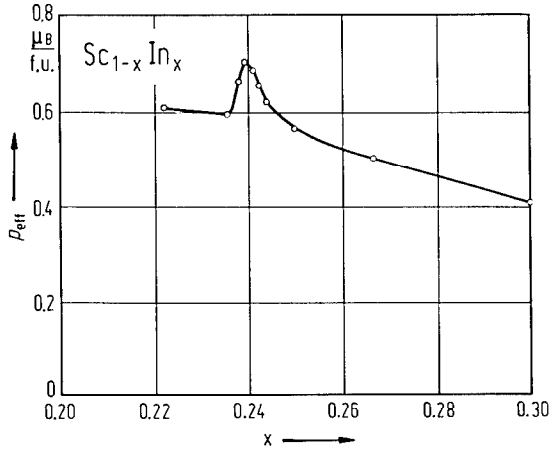

Fig. 2. $Sc_{1-x}In_x$. Composition dependence of p_{eff} [61 M 1].

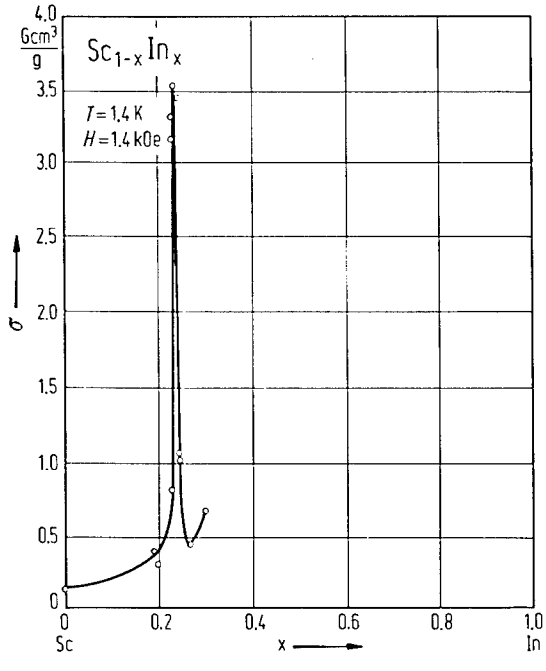

Fig. 3. $Sc_{1-x}In_x$. Composition dependence of σ at 1.4 K and 1.4 kOe [61 M 1].

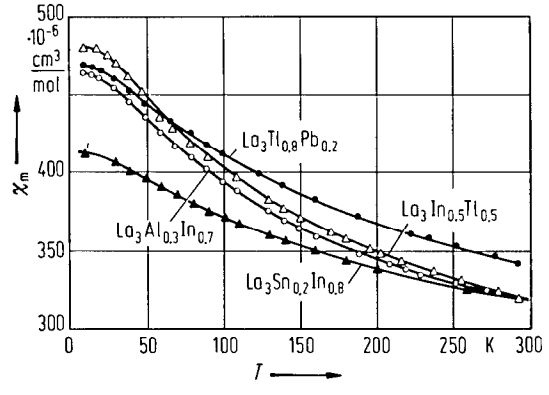

Fig. 4. $La_3M_{1-x}M'_x$, M, $M'=Al$, In, Tl, Sn, Pb. Temperature dependence of χ_m after subtraction of a $C/(T-\Theta)$ term ($\Theta=-7$ K) for impurities [78 D 1].

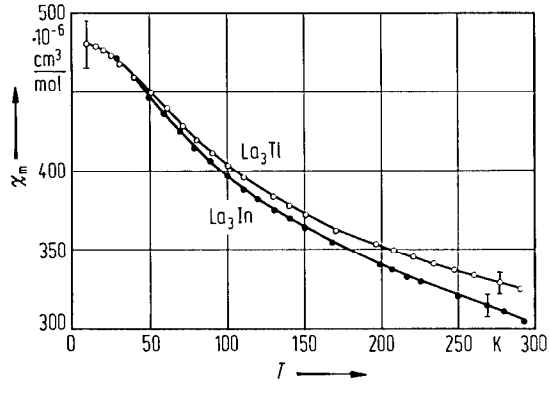

Fig. 5. La_3In, La_3Tl. Temperature dependence of χ_m after subtraction of a $C_i/(T-\Theta)$ term ($\Theta=-7$ K) for impurities [78 D 1].

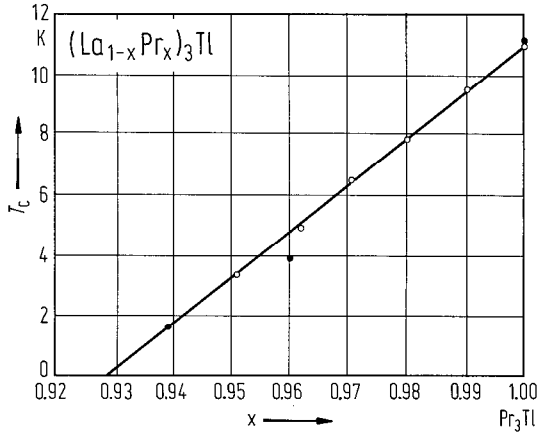

Fig. 6. $(La_{1-x}Pr_x)_3Tl$. Composition dependence of T_C. Solid circles [72 A 1], open circles [72 B 2].

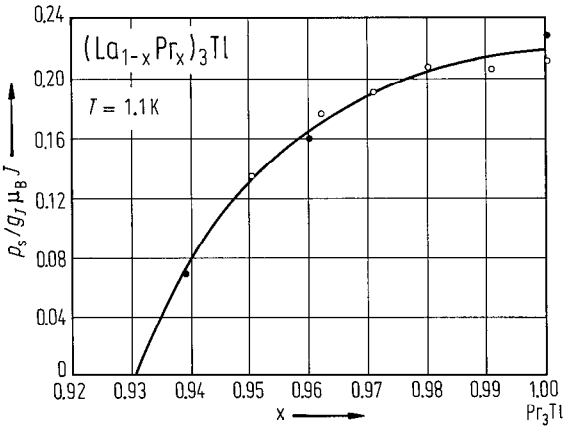

Fig. 8. $(La_{1-x}Pr_x)_3Tl$. Composition dependence of the spontaneous magnetic moment per Pr atom, p_s, at 1.1 K. Solid circles [72 A 1], open circles [72 B 2]. $g_J J = 3.2$.

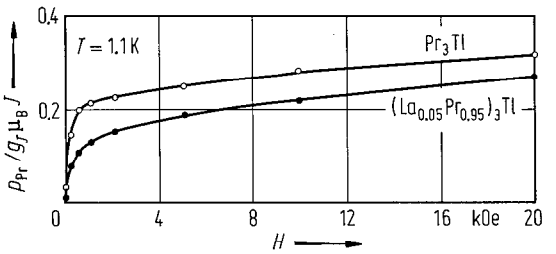

Fig. 7. $(La_{1-x}Pr_x)_3Tl$. Magnetic field dependence of the magnetic moment per Pr atom, p_{Pr}, at 1.1 K for x = 1 and x = 0.95 [72 A 1]. $g_J J = 3.2$.

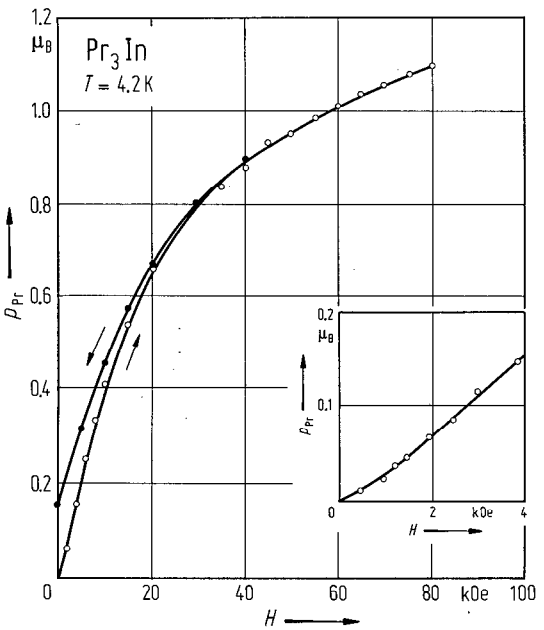

Fig. 9. Pr_3In. Magnetic field dependence of the magnetic moment per Pr atom, p_{Pr}, at 4.2 K [73 S 1].

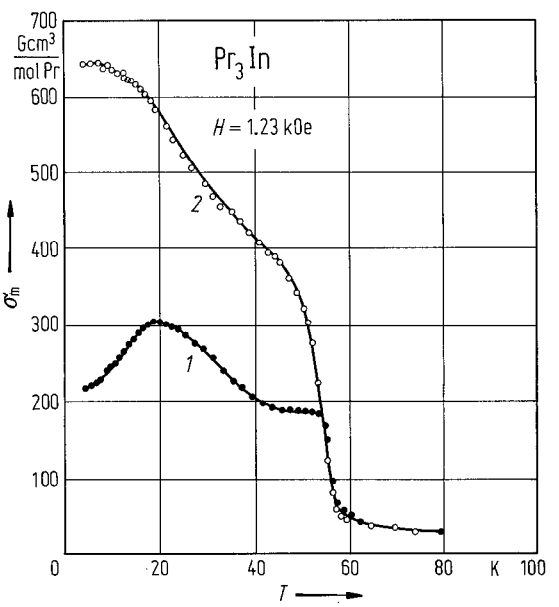

Fig. 10. Pr_3In. Temperature dependence of σ_m at 1.23 kOe after zero field cooling (1) and after cooling in the field [73 S 1].

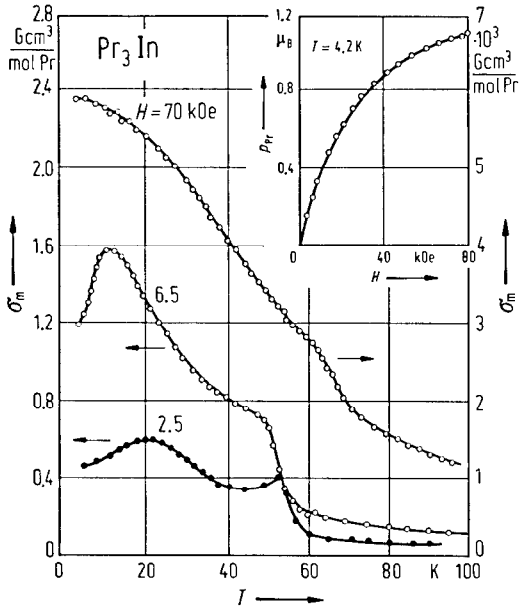

Fig. 11. Pr_3In. Temperature dependence of σ_m and magnetic field dependence of the magnetic moment per Pr atom, p_{Pr}, at 4.2 K [74 S 1].

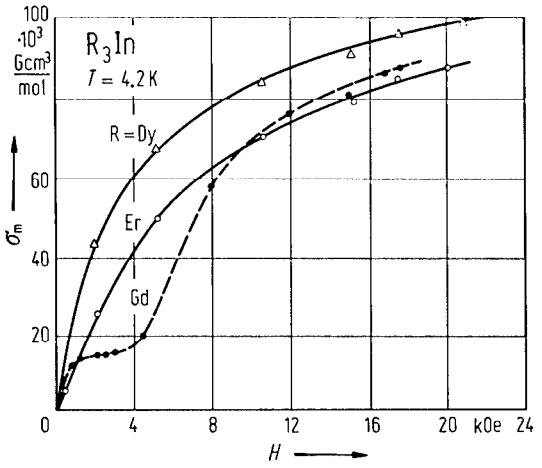

Fig. 12. R_3In, R = Gd, Dy, Er. Magnetic field dependence of σ_m at 4.2 K [74 H 1].

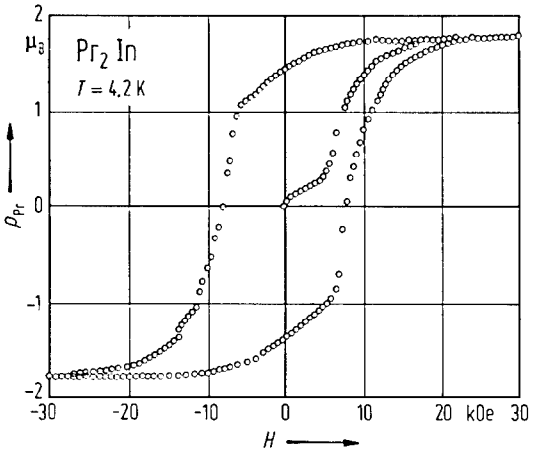

Fig. 13. Pr_2In. Hysteresis loop at 4.2 K. Sample annealed for 14 days at 1000 K [80 P 1].

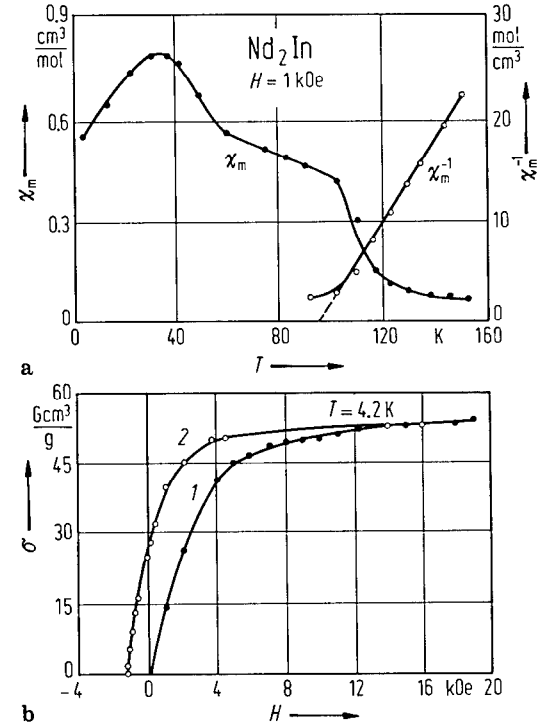

Fig. 14. Nd_2In. (a) Temperature dependence of χ_m and χ_m^{-1} at 1 kOe. (b) Magnetic field dependence of σ at 4.2 K, curve (*1*) after cooling in zero field, and (*2*) after cooling in the field [79 G 1].

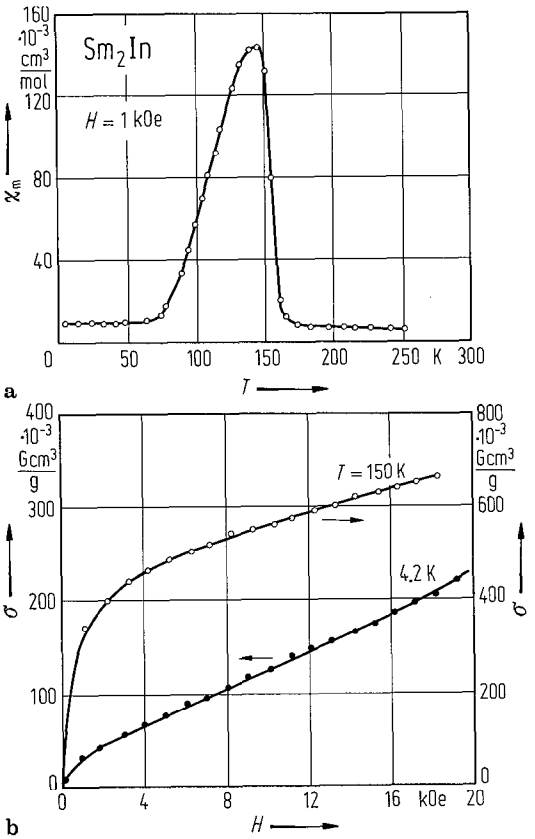

Fig. 15. Sm_2In. (a) Temperature dependence of χ_m at 1 kOe and (b) magnetic field dependence of σ at 4.2 and 150 K [79 G 1].

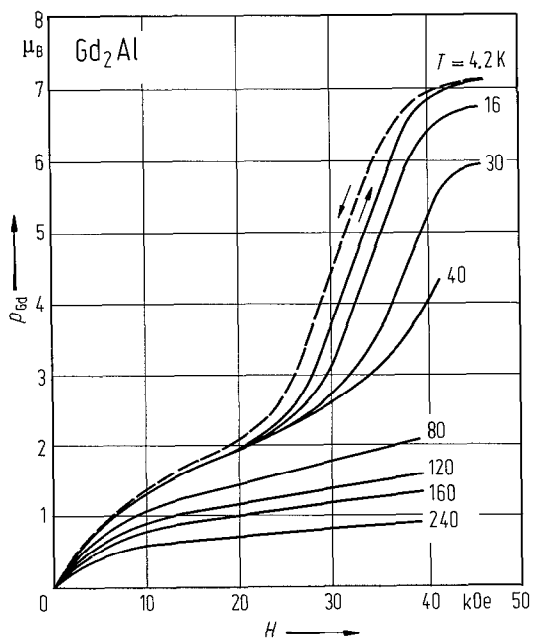

Fig. 16. Gd_2Al. Magnetic field dependence of magnetic moment per Gd atom, p_{Gd}, at various temperatures [77 O 1].

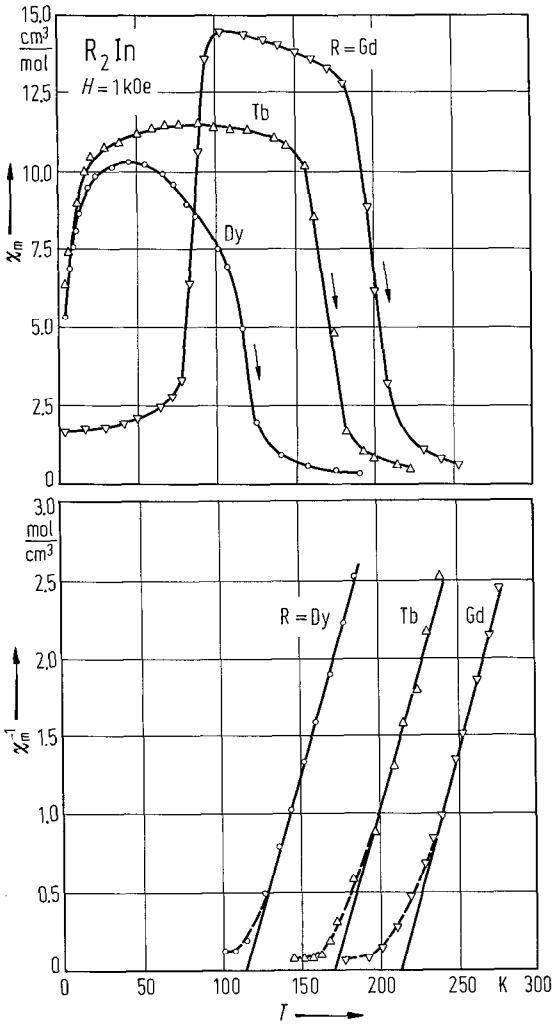

Fig. 17. R_2In, R = Gd, Tb, Dy. Temperature dependence of χ_m and χ_m^{-1} at 1 kOe [79 G 1].

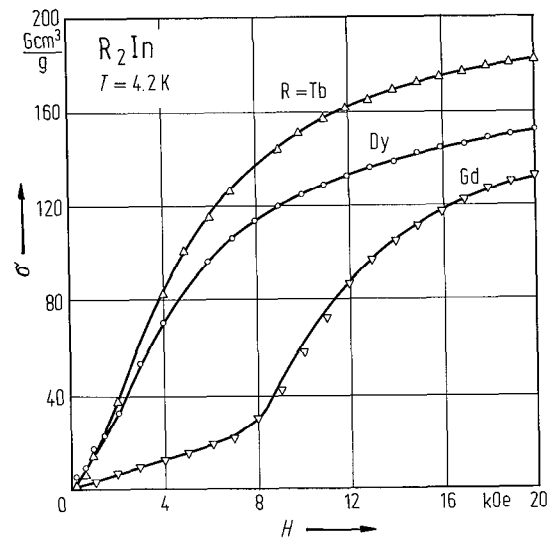

Fig. 18. R_2In, R = Gd, Tb, Dy. Magnetic field dependence of σ at 4.2 K [79 G 1].

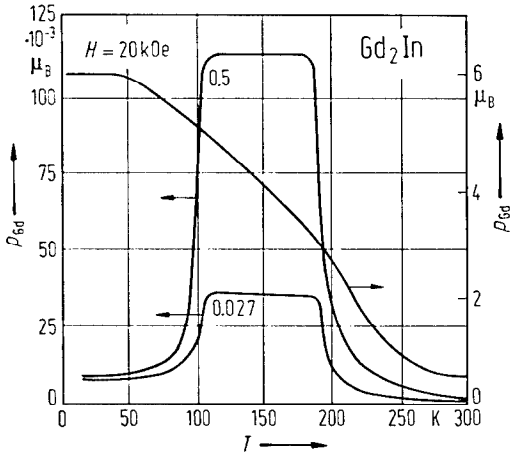

Fig. 19. Gd_2In. Temperature dependence of magnetic moment per Gd atom, p_{Gd}, in magnetic fields of 0.027, 0.5 and 20 kOe [84 M 1].

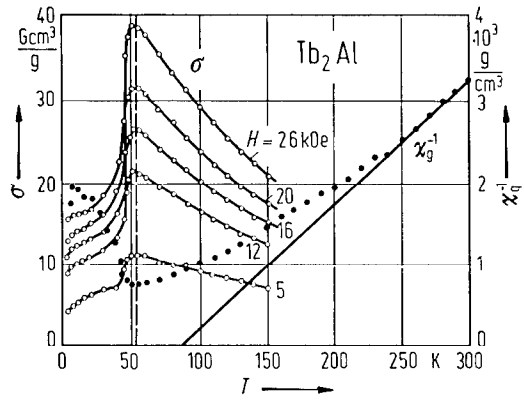

Fig. 20. Tb_2Al. Temperature dependence of σ and χ_g^{-1} [78 S 2].

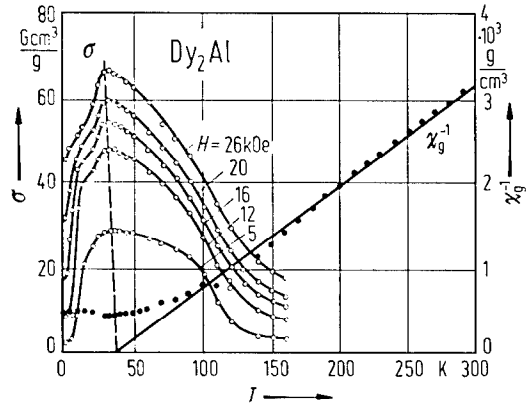

Fig. 21. Dy_2Al. Temperature dependence of σ and χ_g^{-1} [78 S 2].

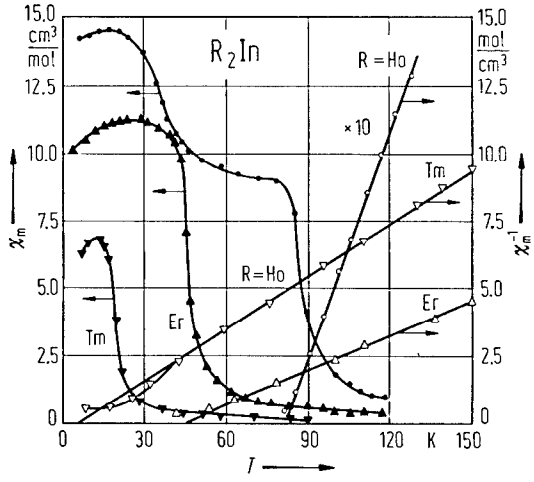

Fig. 22. R_2In, R = Ho, Er, Tm. Temperature dependence of χ_m and χ_m^{-1} [79 G 1].

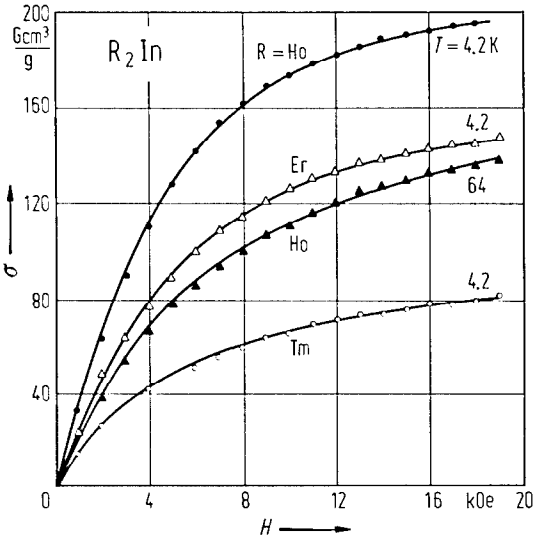

Fig. 23. R_2In, R = Ho, Er, Tm. Magnetic field dependence of σ at 4.2 K and 64 K (R = Ho) [79 G 1].

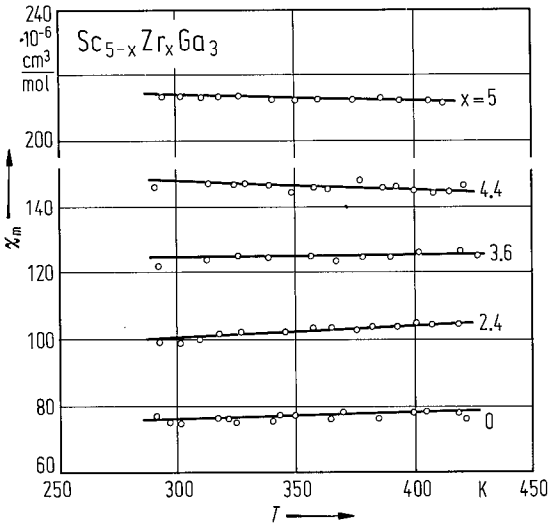

Fig. 24. $Sc_{5-x}Zr_xGa_3$. Temperature dependence of χ_m for various compositions [81 S 1].

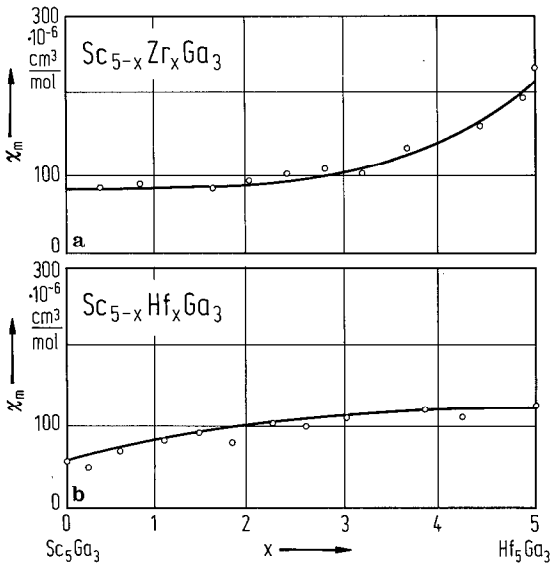

Fig. 25. $Sc_{5-x}M_xGa_3$, M = Zr, Hf. Composition dependence of χ_m [81 S 1].

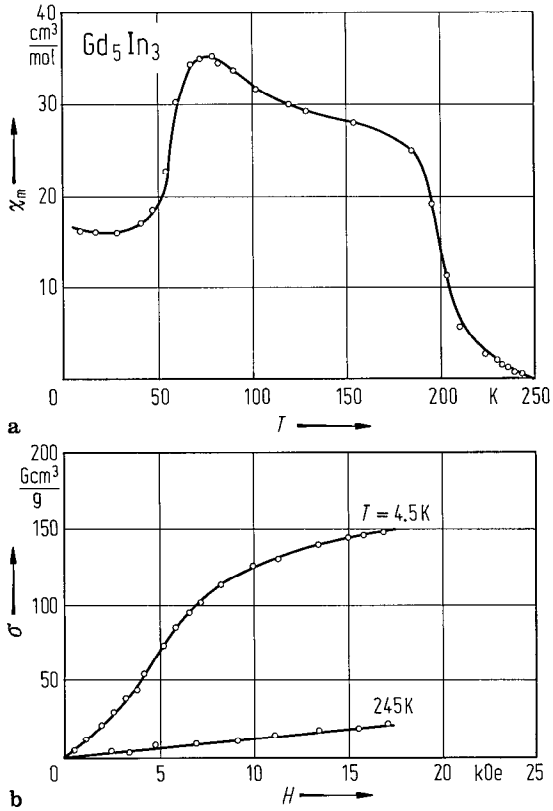

Fig. 26. Gd_5In_3. Temperature dependence of (a) χ_m and (b) magnetic field dependence of σ [83 S 5].

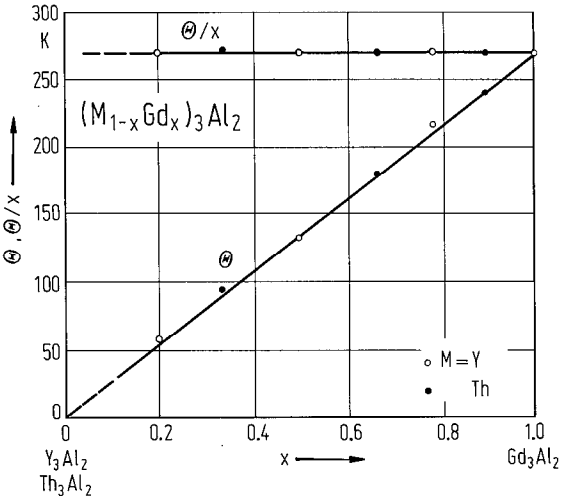

Fig. 27. $(M_{1-x}Gd_x)_3Al_2$, M = Y, Th. Composition dependence of Θ and the effective paramagnetic Curie temperature Θ/x [75 B 1].

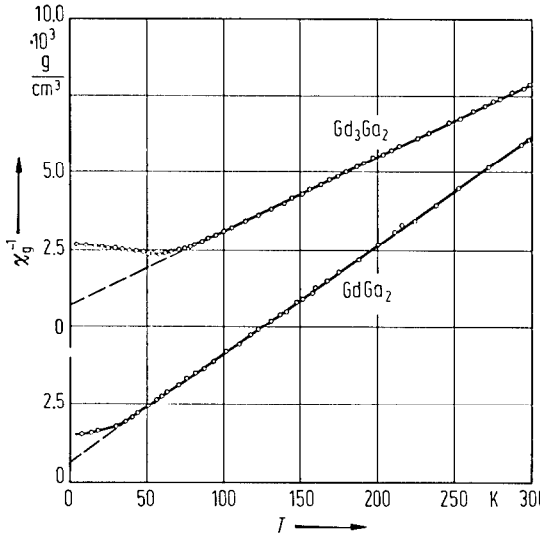

Fig. 28. Gd_3Ga_2, $GdGa_2$. Temperature dependence of χ_g^{-1} [76 B 1].

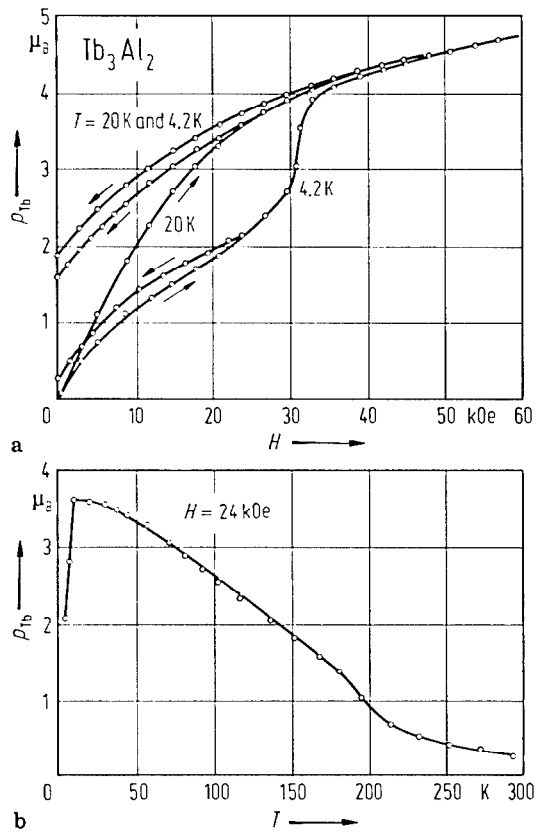

Fig. 29. Tb_3Al_2. (a) Magnetic moment per Tb atom, p_{Tb}, vs. magnetic field at 4.2 K and 20 K and (b) temperature variation of magnetization at 24 kOe. From 10 K to the Curie point a ferromagnetic behaviour is observed, below 10 K the magnetization decreases rapidly if measured in fields lower than 30 kOe. In higher fields the magnetization is practically the same as it is at 20 K [68 B 2].

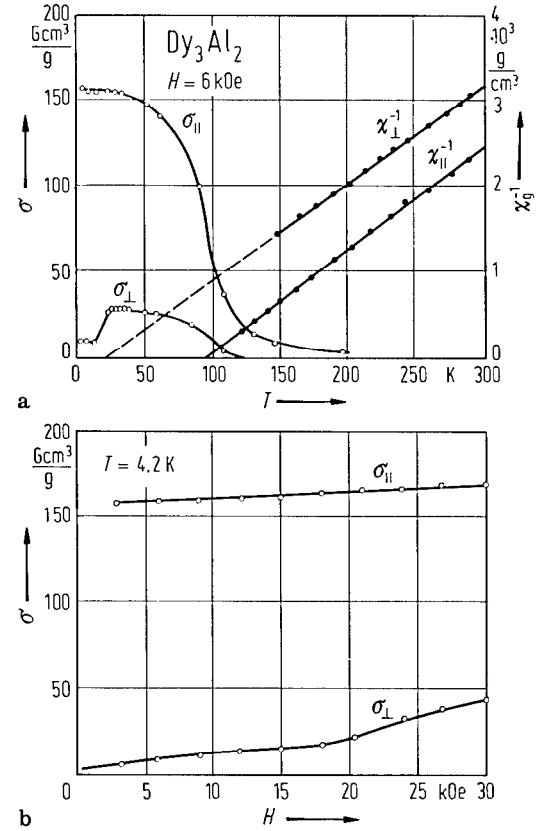

Fig. 30. Dy_3Al_2. (a) Magnetization $\sigma_\parallel, \sigma_\perp$ and reciprocal magnetic susceptibility $\chi_\parallel^{-1}$, $\chi_\perp^{-1}$ vs. temperature for a magnetic field of 6 kOe applied parallel and perpendicular to the c direction of pseudo single crystal. (b) Magnetic field dependence of σ at 4.2 K [69 B 1].

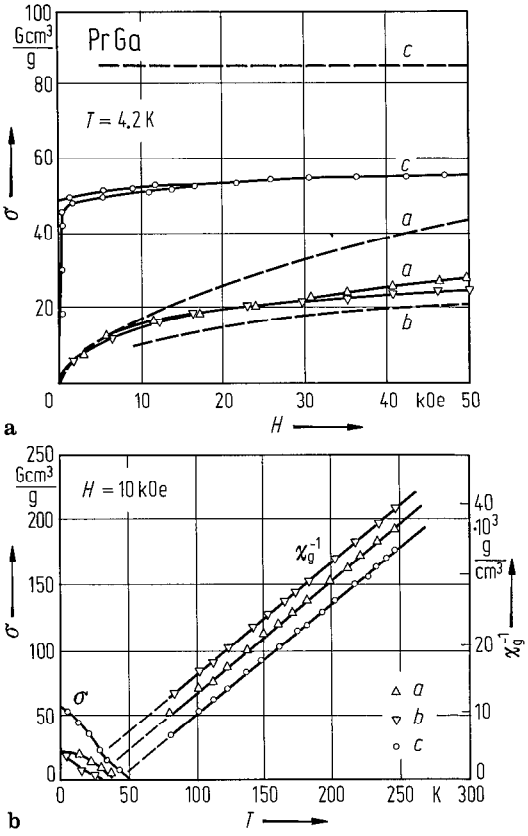

Fig. 31. PrGa. (a) Magnetic field dependence of σ at 4.2 K and (b) temperature dependence of σ at 10 kOe and χ_g^{-1} along *a*, *b*, and *c* axes of a single crystal. Dashed lines are calculated including CEF Hamiltonian [77 S 1].

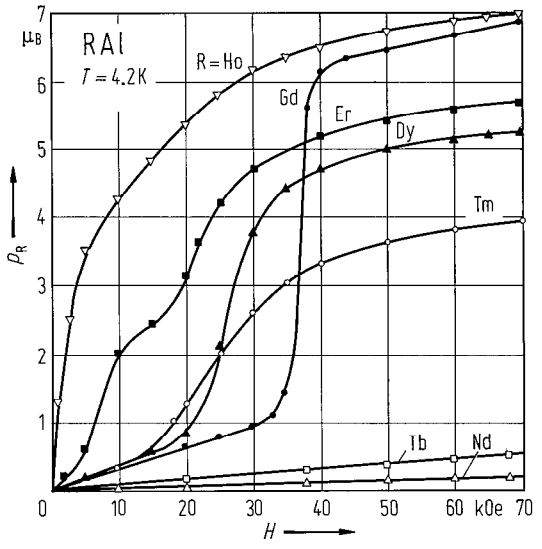

Fig. 32. RAl, R = Nd, Gd, Tb, Dy, Ho, Er, Tm. Magnetic field dependence of p_R at 4.2 K [70 B 1].

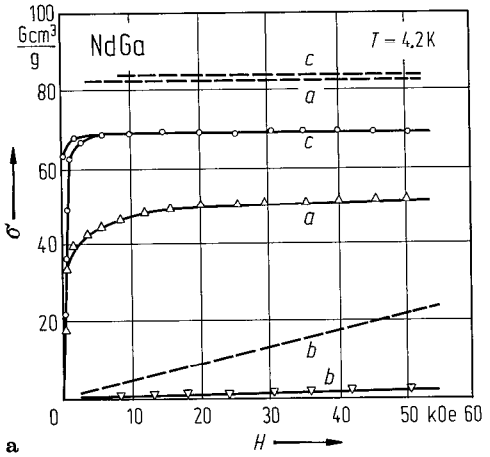

Fig. 33. NdGa. (a) Magnetic field dependence of σ at 4.2 K and (b) temperature dependence of σ and χ_g^{-1} along *a*, *b*, and *c* axes of a single crystal. Dashed lines are calculated including CEF Hamiltonian [77 S 1].

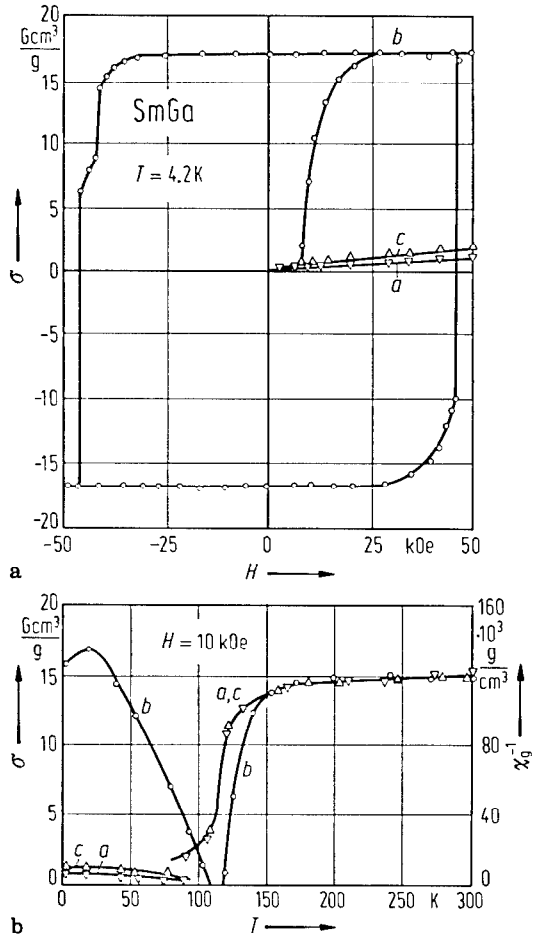

Fig. 34. SmGa. (a) Hysteresis loop of single crystal at 4.2 K along easy direction of magnetization, *b* axis, and magnetization σ along the *a* and *c* axes. (b) Temperature dependence of σ and χ_g^{-1} at 10 kOe [77 S 1].

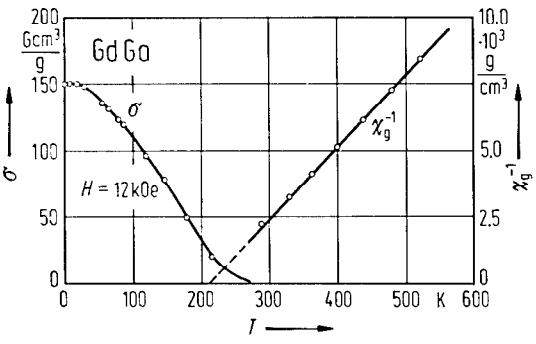

Fig. 36. GdGa. Temperature dependence of σ and χ_g^{-1}. The curve σ was recorded with a magnetic field of 12 kOe [76 B 1].

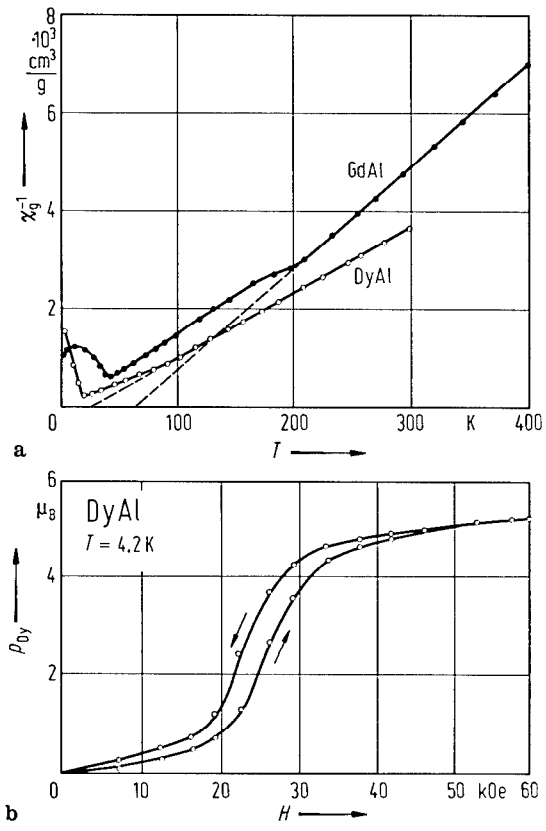

Fig. 35. GdAl, DyAl. (a) Temperature dependence of χ_g^{-1}. (b) Magnetization behaviour of DyAl at 4.2 K [68 B 2].

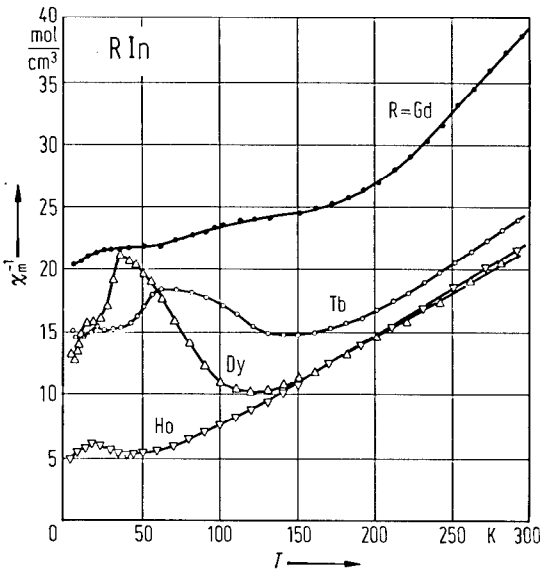

Fig. 37. RIn, R = Gd, Tb, Dy, Ho. Temperature dependence of χ_m^{-1} [76 L 2].

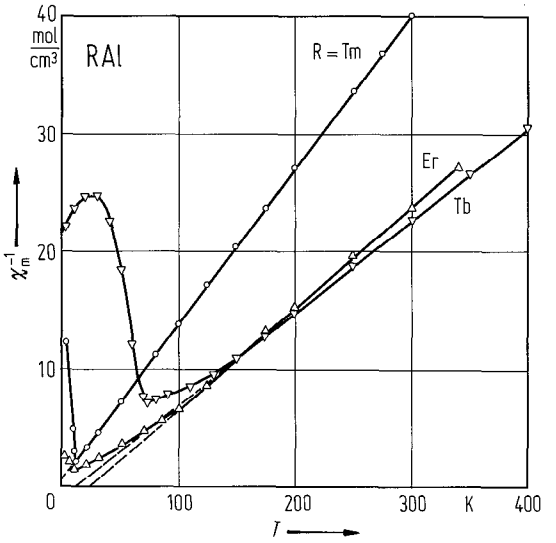

Fig. 38. RAl, R = Tb, Er, Tm. Temperature dependence of χ_m^{-1} [70 B 1].

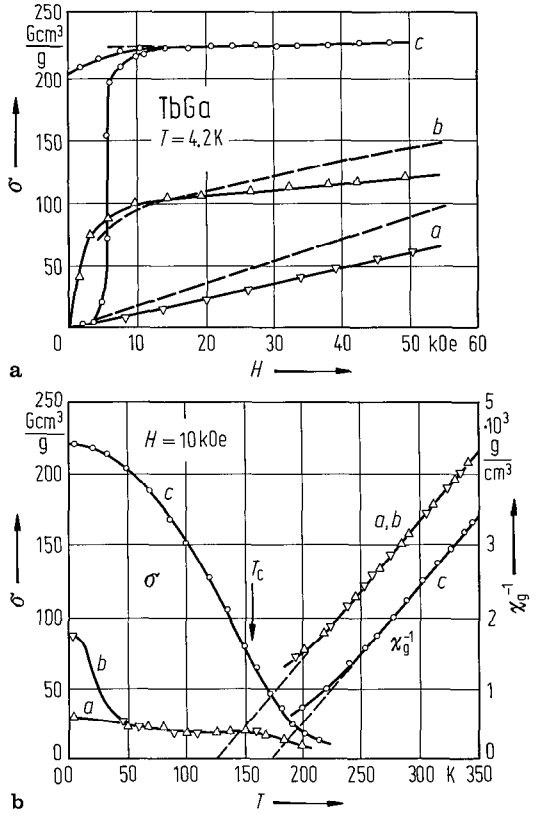

Fig. 39. TbGa. (a) Magnetic field dependence of σ at 4.2 K and (b) temperature dependence of σ and χ_g^{-1} at 10 kOe along the *a*, *b*, and *c* axes of a single crystal. The dashed lines are calculated including CEF Hamiltonian [77 S 1].

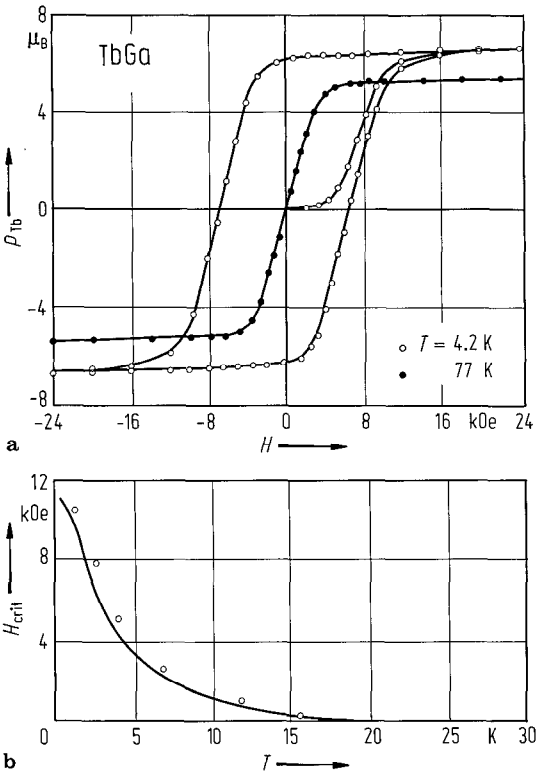

Fig. 40. TbGa. (a) Magnetic isotherms at 4.2 K and 77 K. (b) Shows the temperature dependence of the critical field H_{crit} below which wall propagation is impeded [71 B 1].

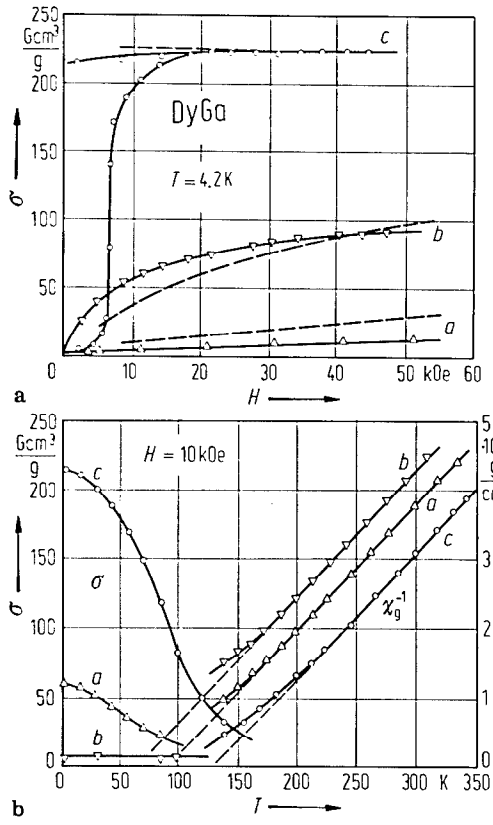

Fig. 41. DyGa. (a) Magnetic field dependence of σ at 4.2 K. (b) Temperature dependence of σ at 10 kOe and χ_g^{-1} along the *a*, *b*, and *c* axes of a single crystal. The dashed lines are calculated including CEF Hamiltonian [77 S 1].

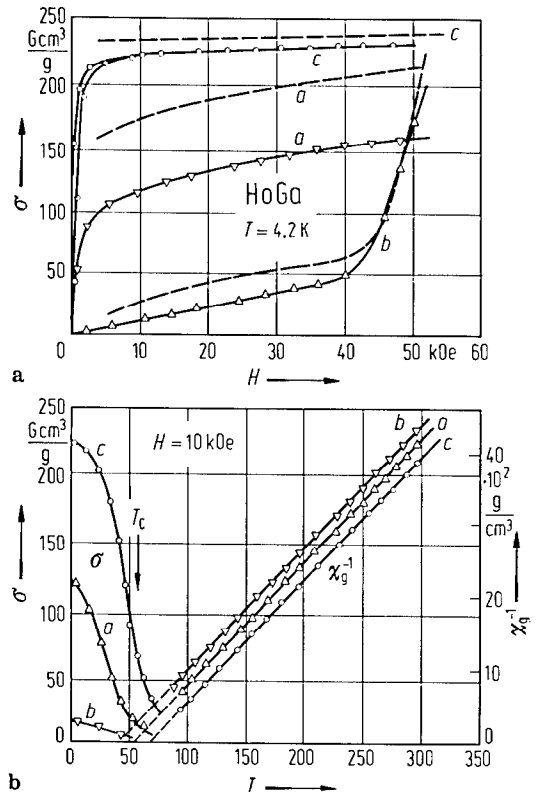

Fig. 42. HoGa. (a) Magnetic field dependence of σ at 4.2 K. (b) Temperature dependence of σ at 10 kOe and χ_g^{-1} along the *a*, *b* and *c* axes of a single crystal. The dashed lines are calculated including CEF Hamiltonian [77 S 1].

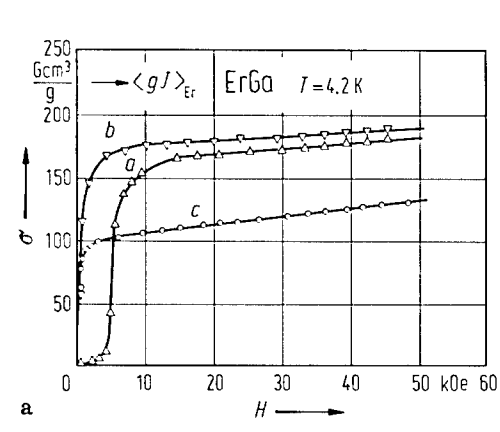

Fig. 43. ErGa. (a) Magnetic field dependence of σ at 4.2 K. (b) Temperature dependence of σ at 10 kOe and χ_g^{-1} along the *a*, *b*, and *c* axes of a single crystal. The dashed lines are calculated including CEF Hamiltonian [77 S 1].

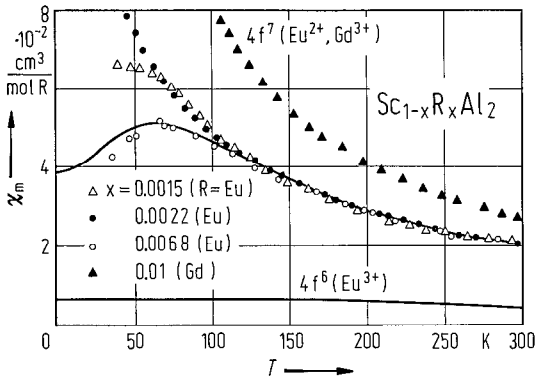

Fig. 44. $Sc_{1-x}R_xAl_2$, R = Eu, Gd. Temperature dependence of the magnetic susceptibility for dilute Eu and Gd impurities in $ScAl_2$. The data of the x = 0.0068 Eu sample are corrected for the contribution of residual $EuAl_2$ detected in the Mössbauer spectra [80 F 1].

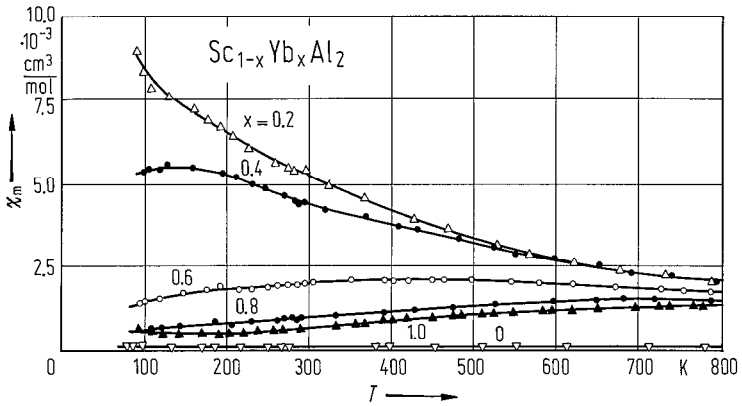

Fig. 45. $Sc_{1-x}Yb_xAl_2$. Temperature dependence of χ_m for various compositions corrected for the $ScAl_2$ contribution [85 I 1].

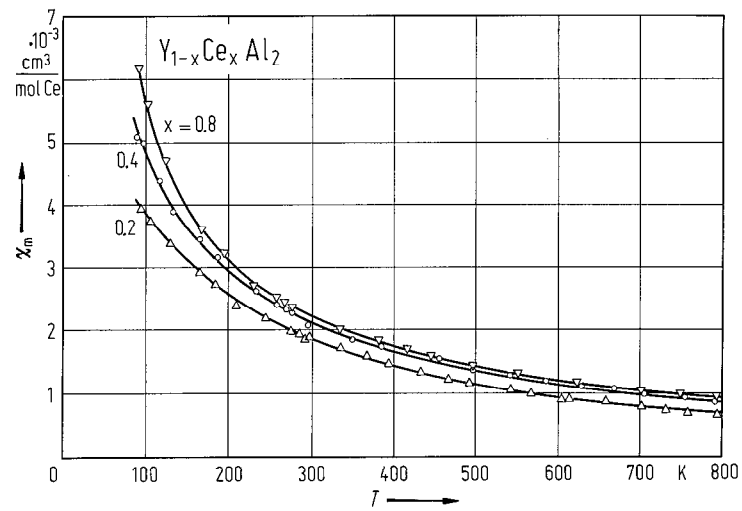

Fig. 46. $Y_{1-x}Ce_xAl_2$. Temperature dependence of χ_m for various compositions corrected for the contribution of YAl_2 [85 I 1].

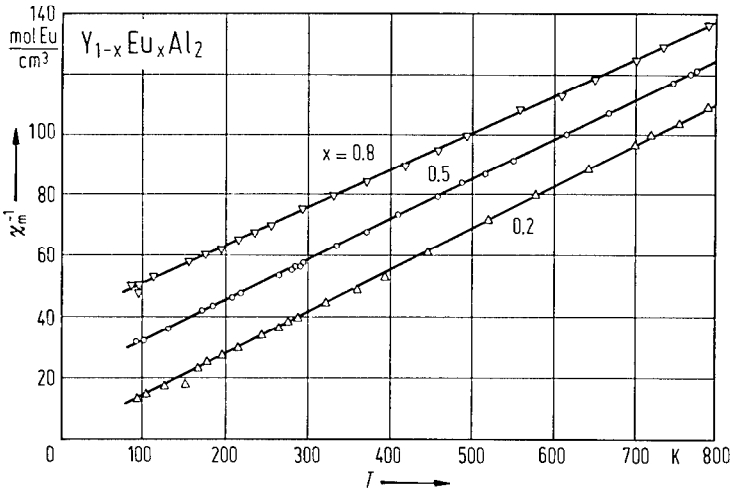

Fig. 47. $Y_{1-x}Eu_xAl_2$. Temperature dependence of χ_m^{-1} for various compositions. For clarity, the ordinates are shifted, see Table 1 for Θ values [85I1].

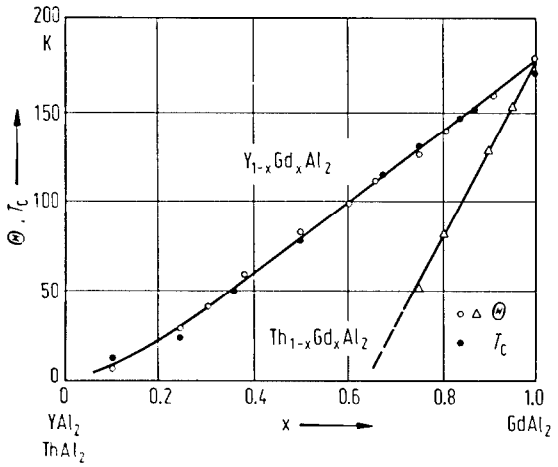

Fig. 48. $Th_{1-x}Gd_xAl_2$, $Y_{1-x}Gd_xAl_2$. Composition dependence of Θ and T_C [67B1].

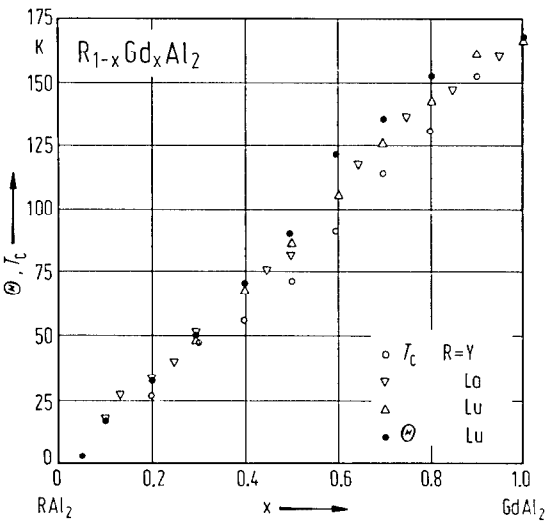

Fig. 49. $R_{1-x}Gd_xAl_2$, R = Y, La, Lu. Composition dependence of T_C and Θ. The values for T_C were obtained from the cusps in the electrical resistivity curves [82H1].

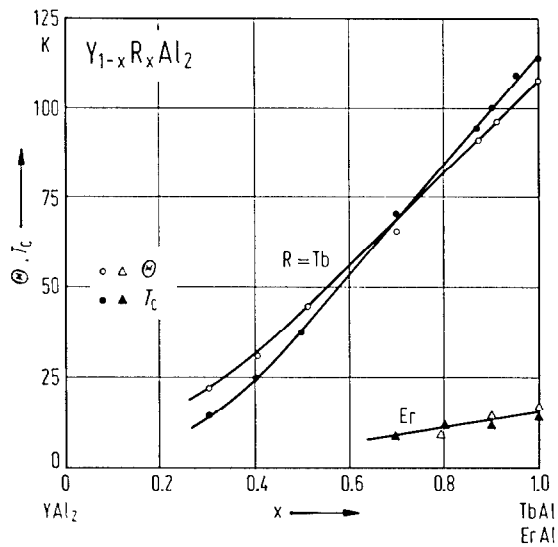

Fig. 50. $Y_{1-x}R_xAl_2$, R = Tb, Er. Composition dependence of T_C and Θ [67B1].

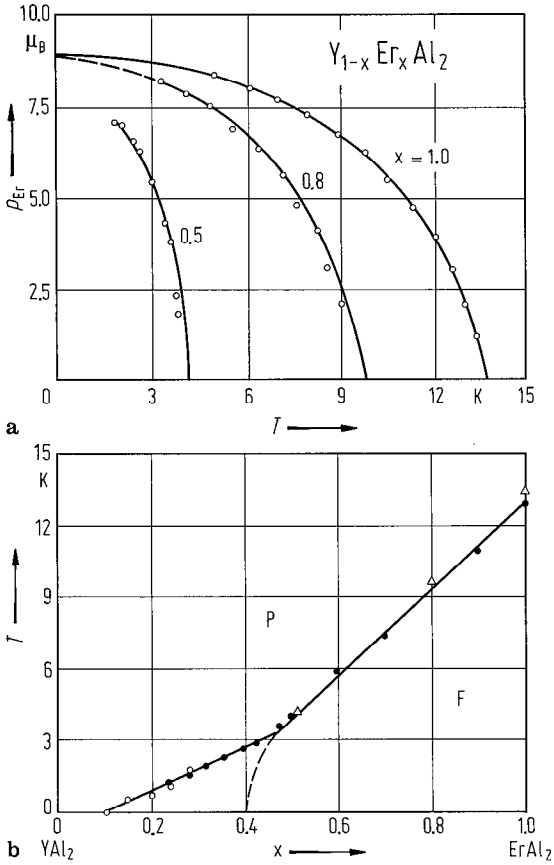

Fig. 51. $Y_{1-x}Er_xAl_2$. (a) Temperature dependence of the Er magnetic moment, p_{Er}, obtained from neutron diffraction [72 W 1]. (b) Magnetic phase diagram. Solid circles indicate the cusp temperature T_f, open circles the Curie-Weiss temperature Θ. Open triangles the magnetic ordering temperature T_C determined by neutron diffraction [79 B 3].

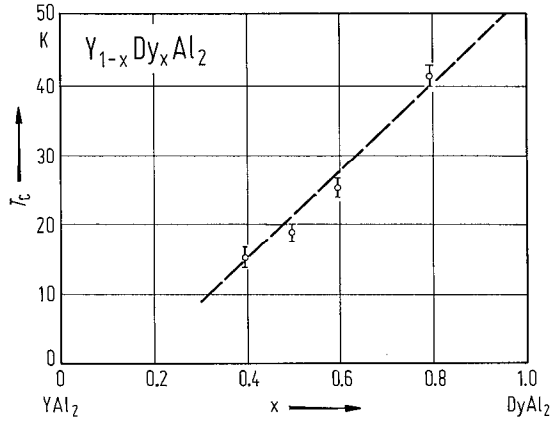

Fig. 52. $Y_{1-x}Dy_xAl_2$. Composition dependence of T_C [78 B 2].

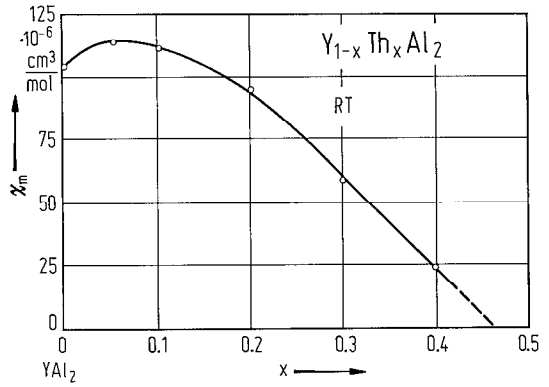

Fig. 54. $Y_{1-x}Th_xAl_2$. Composition dependence of χ_m at room temperature [70 V 1].

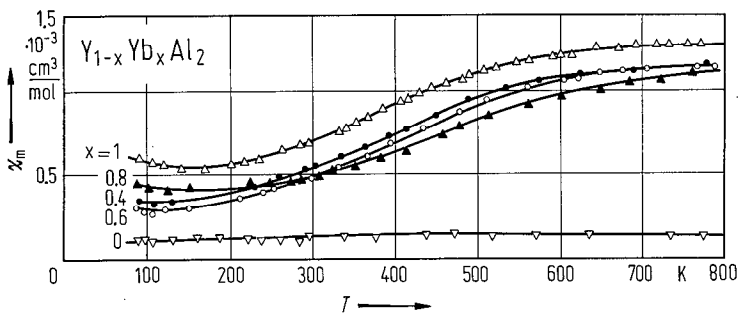

Fig. 53. $Y_{1-x}Yb_xAl_2$. Temperature dependence of χ_m for different compositions [85 I 1].

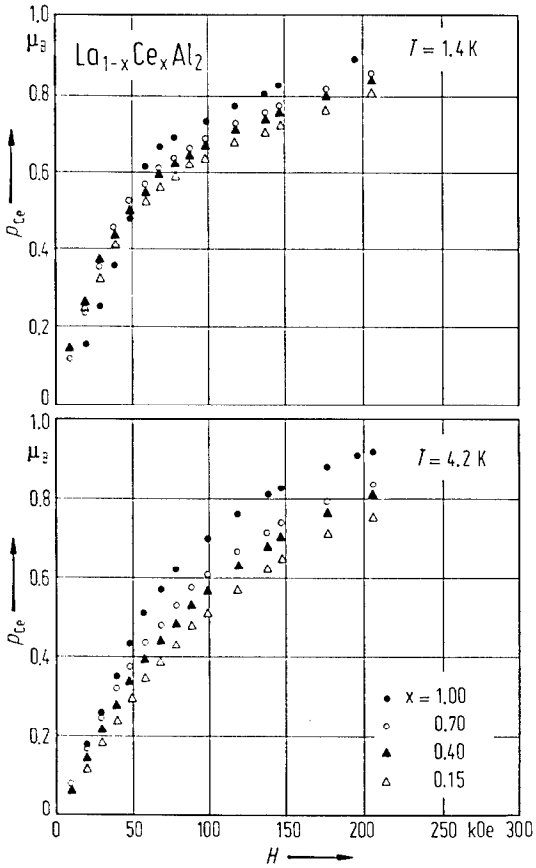

Fig. 55. $La_{1-x}Ce_xAl_2$. Magnetic moment per Ce atom, p_{Ce}, vs. magnetic field for different compositions at 1.4 K and 4.2 K [81 A 1].

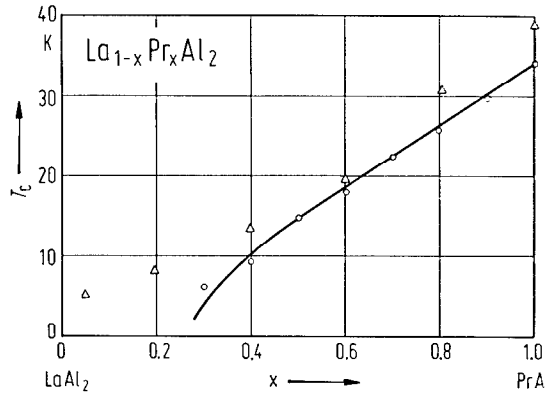

Fig. 56. $La_{1-x}Pr_xAl_2$. Concentration dependence of T_C. The line indicates the calculated curve based on the combined effect of CEF and molecular field for CEF parameters $x = 0.81$ and $W = 0.53$ meV [79 T 1] (circles); triangles after [69 M 1].

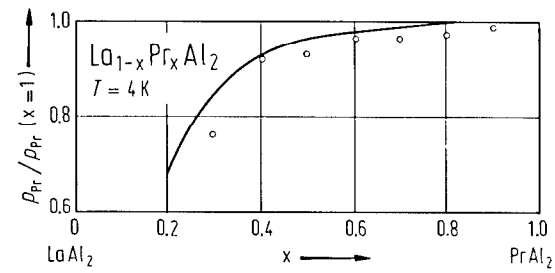

Fig. 57. $La_{1-x}Pr_xAl_2$. Composition dependence of the normalized magnetic moment per Pr atom, p_{Pr}, at 4 K. The solid line indicates the calculated curve using the CEF parameters $x = 0.81$ and $W = 0.53$ meV [79 T 1].

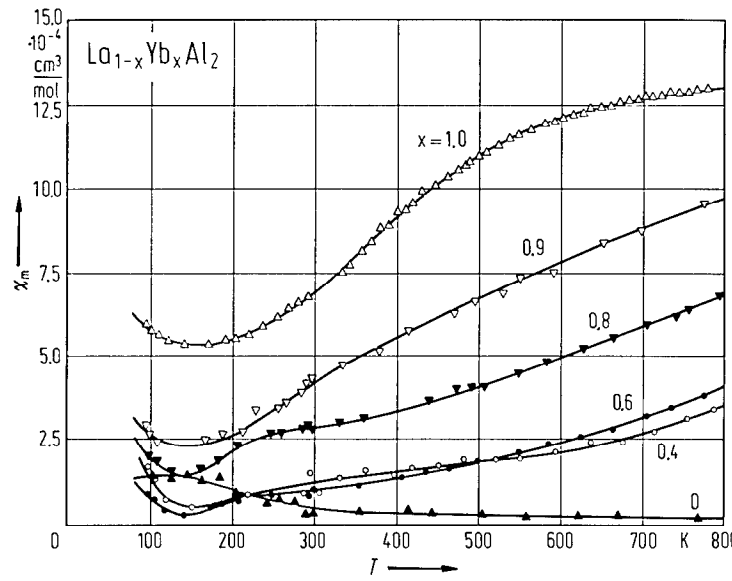

Fig. 59. $La_{1-x}Yb_xAl_2$. Temperature dependence of χ_m for different compositions, corrected for the $LaAl_2$ contribution [85 I 1].

For Fig. 58, see next page.

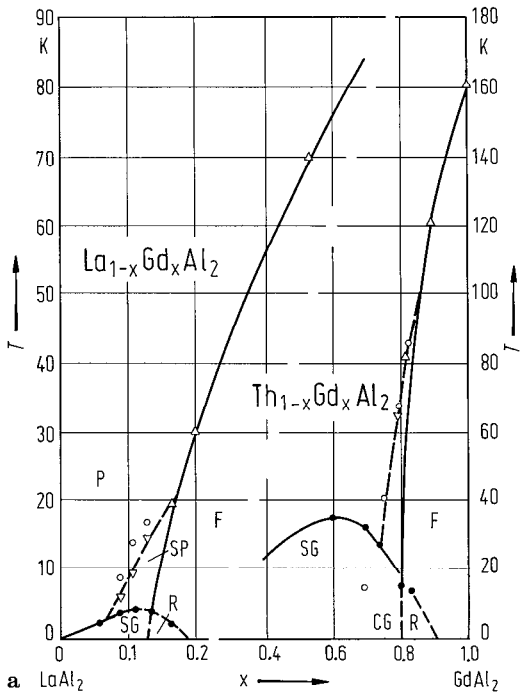

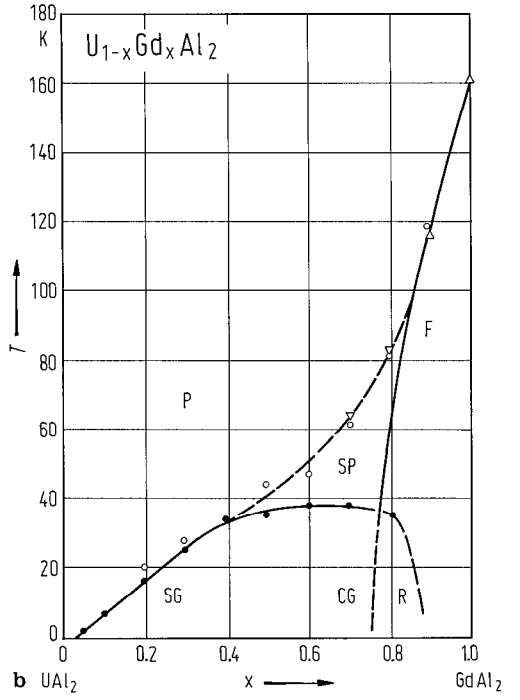

Fig. 58. $M_{1-x}Gd_xAl_2$, (a) M = La, Th, (b) M = U. Composition dependence of the magnetic transition temperatures. Triangles upward: Curie temperature T_C; triangles downward: quasi Curie temperature of alloys showing superparamagnetic (SP) behaviour, taken as temperatures where $|d\sigma/dT|$ has a maximum value; open circles: paramagnetic Curie temperature Θ; solid circles: spin glass (SG), cluster glass (CG), or re-entrant glass (R) freezing temperatures T_f [84 C 1].

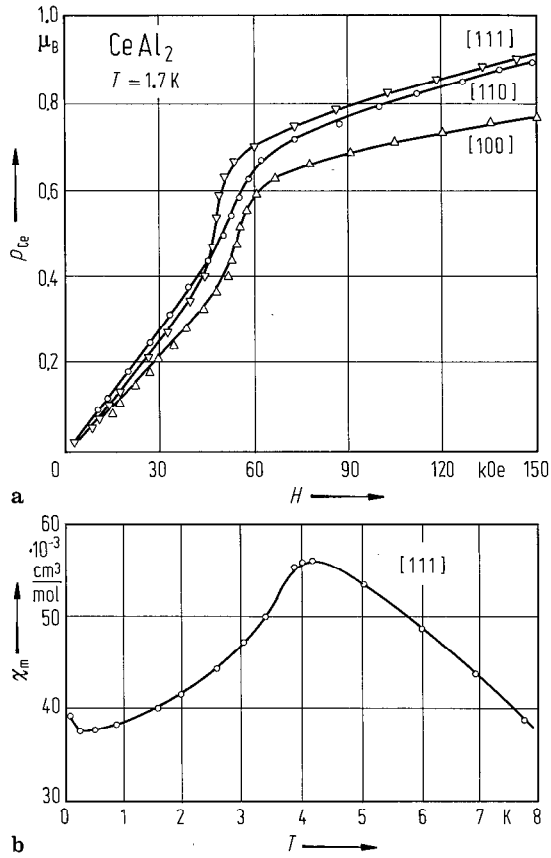

Fig. 60. $CeAl_2$. (a) Magnetic field dependence of the magnetic moment per Ce atom, p_{Ce}, along the three principal directions at 1.7 K and (b) thermal variation of the initial magnetic susceptibility measured parallel to [111] [77 B 1, 75 B 4].

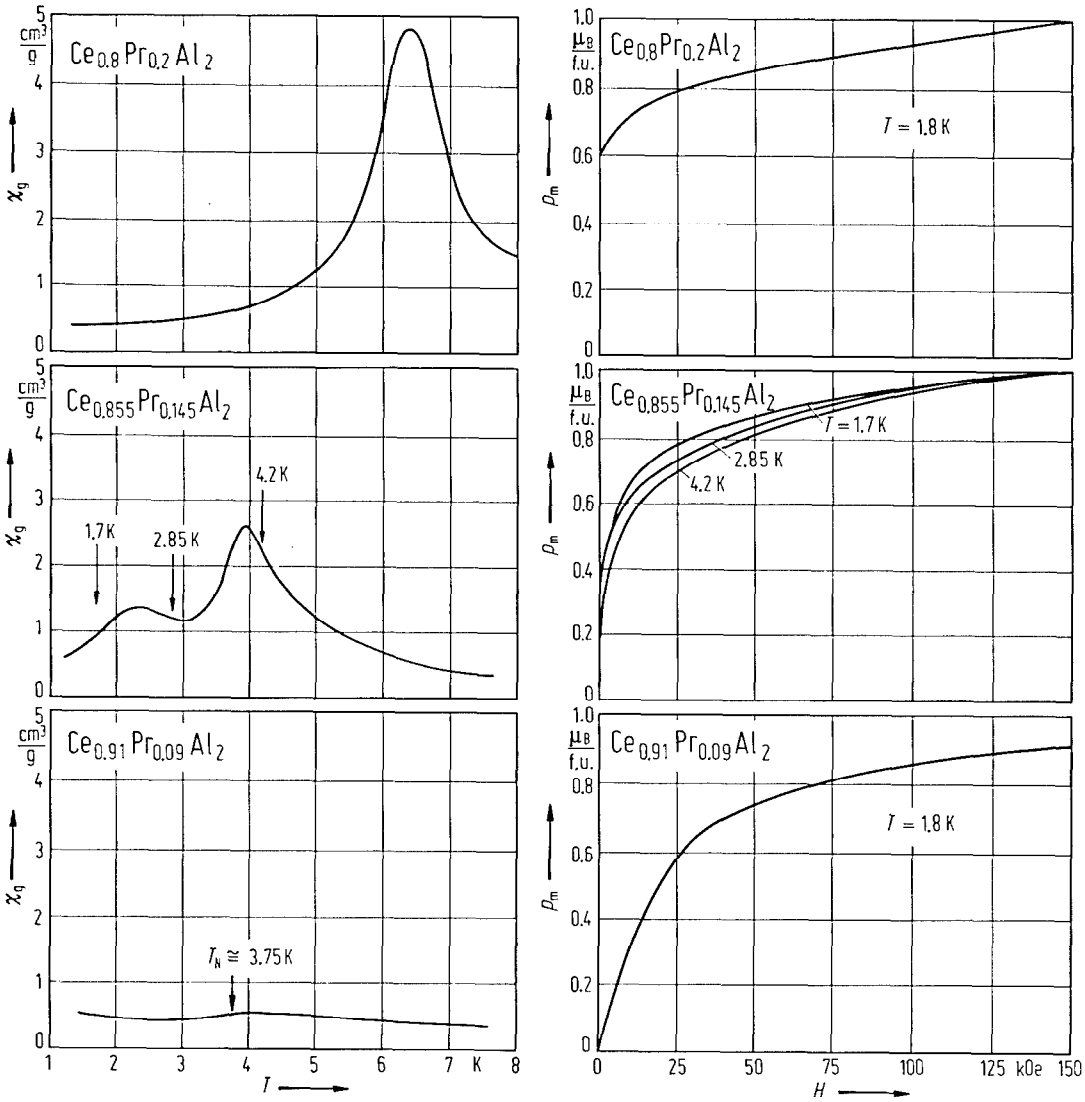

Fig. 61. $Ce_{1-x}Pr_xAl_2$. Thermal variation of χ_g. The right-hand figures show the magnetic moment per formula unit, p_m, as a function of the magnetic field [79 B 2].

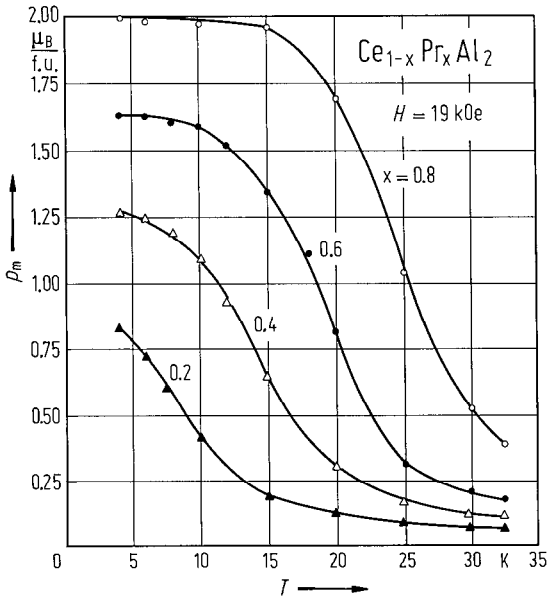

Fig. 62. $Ce_{1-x}Pr_xAl_2$. Temperature dependence of the magnetic moment per formula unit, p_m, at 19 kOe for various compositions [68 S 1].

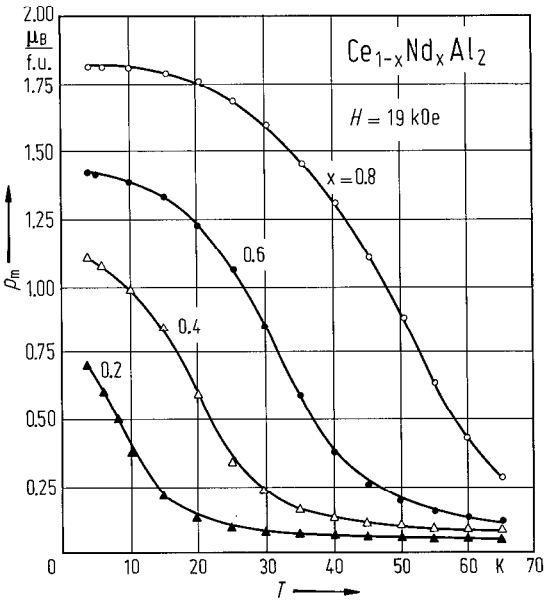

Fig. 63. $Ce_{1-x}Nd_xAl_2$. Temperature dependence of the magnetic moment per formula unit, p_m, at 19 kOe for various compositions [68 S 1].

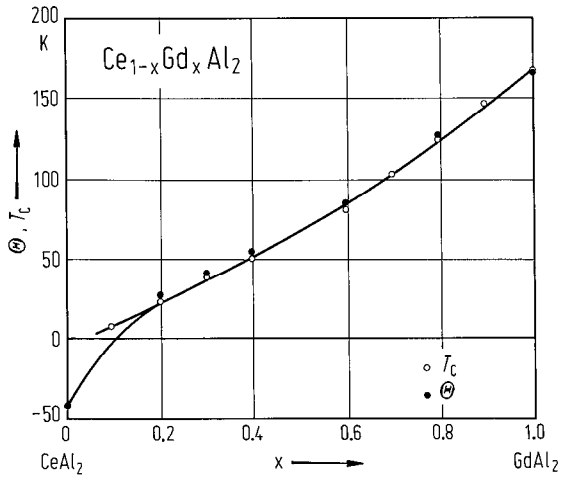

Fig. 64. $Ce_{1-x}Gd_xAl_2$. Composition dependence of Θ and T_C [85 I 2].

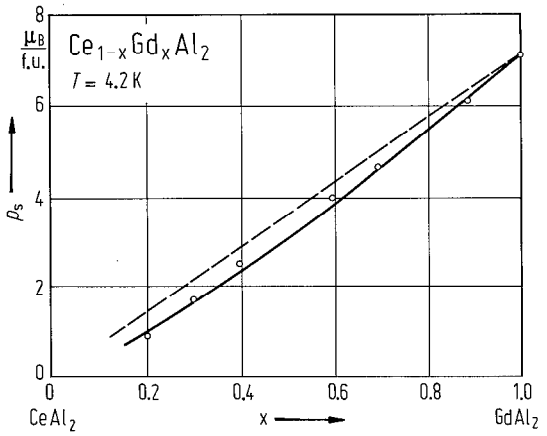

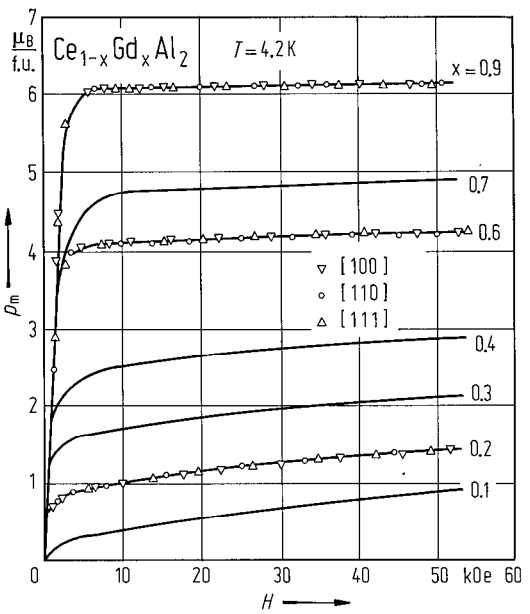

Fig. 65. $Ce_{1-x}Gd_xAl_2$. Magnetic field dependence of the magnetic moment per formula unit, p_m, at 4.2 K for single crystals with x = 0.2, 0.6 and 0.9 and polycrystalline samples with x = 0.1, 0.3, 0.4 and 0.7 [85 I 2].

◀ Fig. 66. $Ce_{1-x}Gd_xAl_2$. Composition dependence of the spontaneous magnetic moment at 4.2 K. The broken line represents the magnetization provided the Ce atom carries no magnetic moment. The solid curve represents the calculated magnetization for CEF parameter B_4 = 0.28 K [85 I 2].

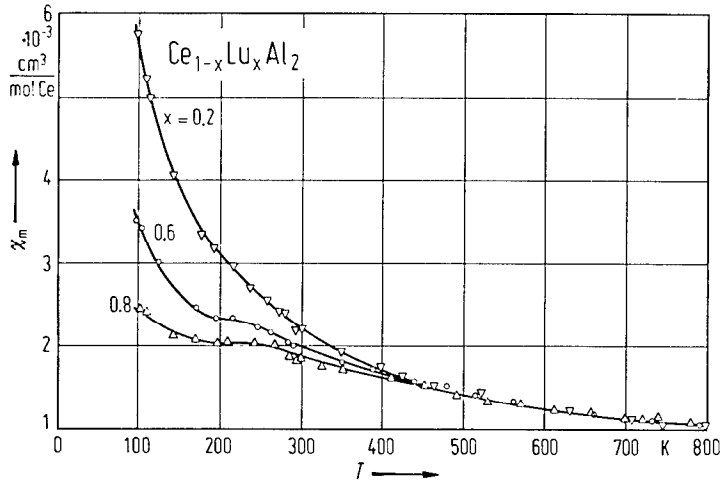

Fig. 67. $Ce_{1-x}Lu_xAl_2$. Temperature dependence of χ_m for different compositions, corrected for $LuAl_2$ contribution [85 I 1].

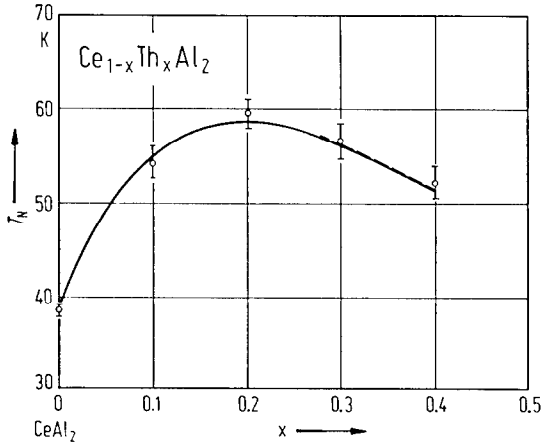

Fig. 68. $Ce_{1-x}Th_xAl_2$. Concentration dependence of T_N [80 C 1].

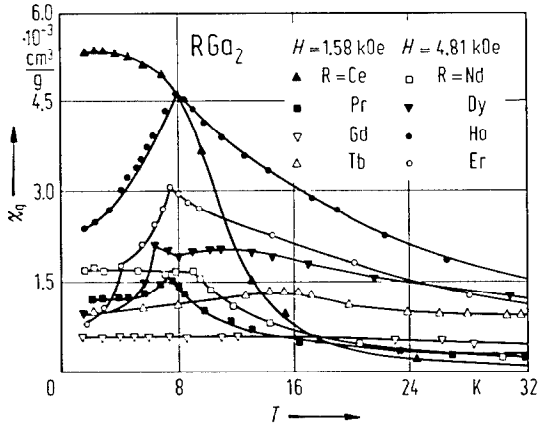

Fig. 69. RGa_2. Temperature dependence of χ_g for 1.58 kOe (R = Ce, Pr, Gd, Tb) and 4.81 kOe (R = Nd, Dy, Ho, Er) [78 T 1].

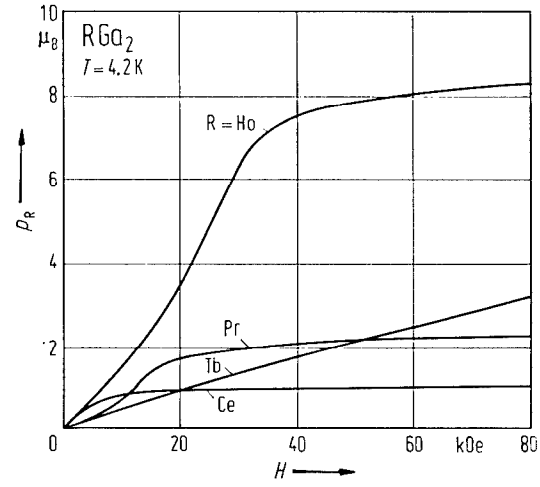

Fig. 70. RGa_2, R = Ce, Pr, Tb, Ho. Magnetic field dependence of the magnetic moment per R atom, p_R, for polycrystalline sample at 4.2 K [78 T 1].

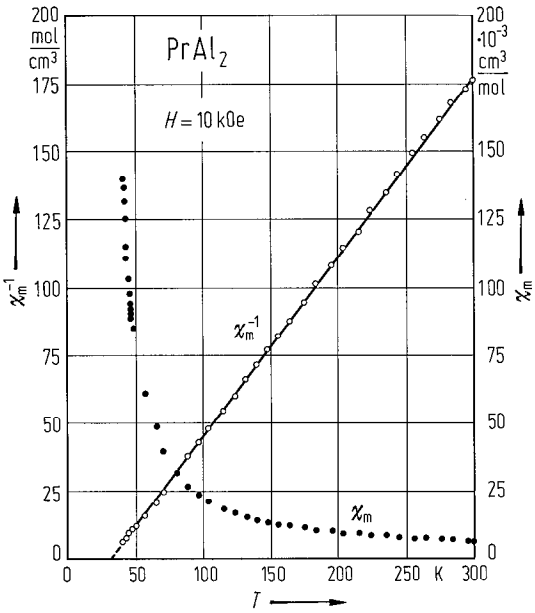

Fig. 71. $PrAl_2$. Temperature dependence of χ_m and χ_m^{-1} at 10 kOe [68 N 1].

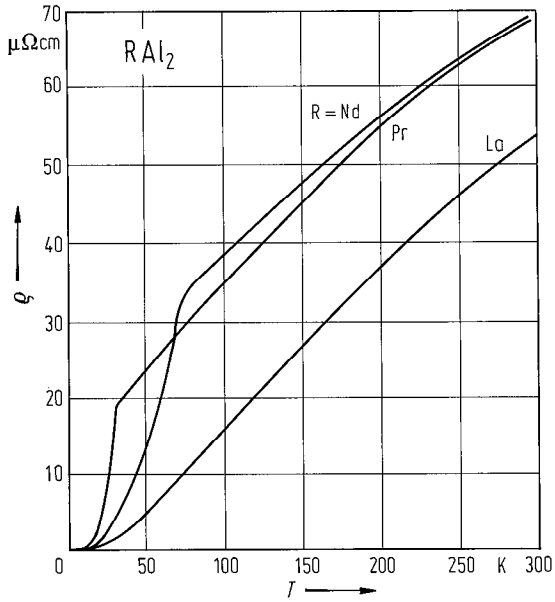

Fig. 72. RAl_2, R = La, Pr, Nd. Temperature dependence of the electrical resistivity. The residual resistivity has been subtracted from the measured values. The transition from the ferromagnetic to the paramagnetic region (T_C) is accompanied by a change in the temperature dependence of ϱ [69 V 1].

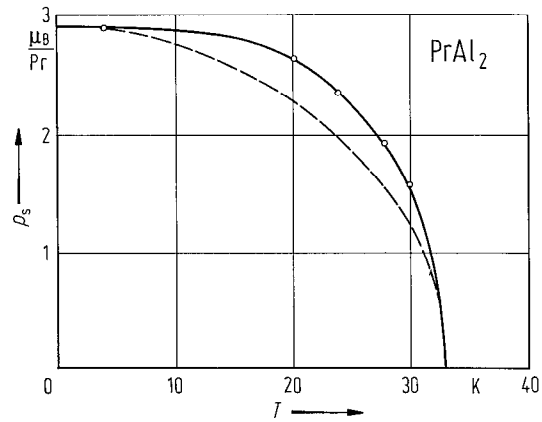

Fig. 73. $PrAl_2$. Experimental points and theoretical curves for the temperature dependence of the spontaneous magnetic moment. The broken line is the Brillouin curve for $J=1$, $T_C=33$ K and a zero-temperature magnetic moment of 2.88 μ_B. The full line is the theoretical curve using the CEF parameters $B_4=-44\cdot10^{-4}$ meV, $B_6=-88\cdot10^{-6}$ meV and $T_C=33$ K [74 P 1].

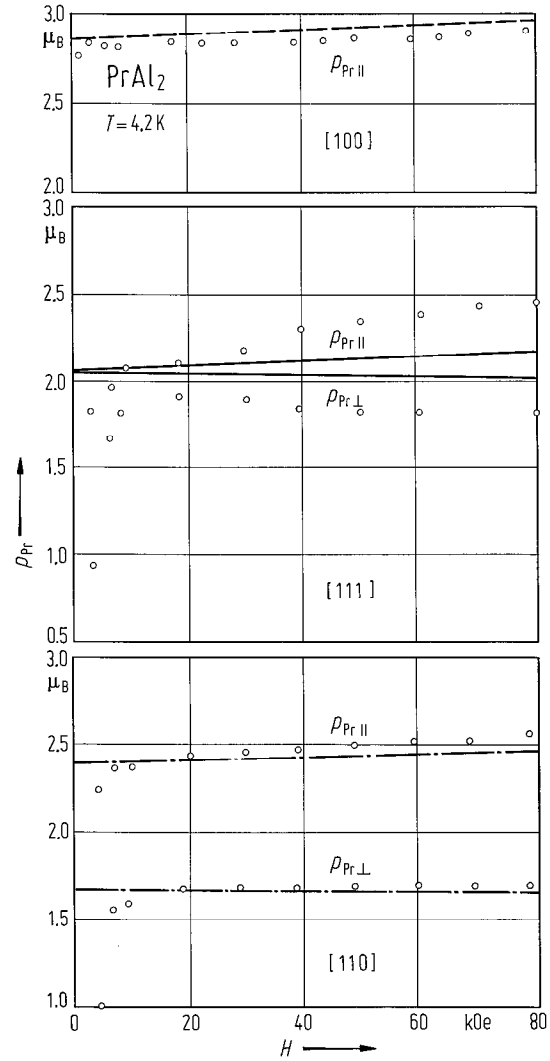

Fig. 74. $PrAl_2$. Magnetic field dependence of p_{Pr}. Magnetic field applied in the three main symmetry directions at 4.2 K. $p_{Pr\parallel}$ and $p_{Pr\perp}$ are the components parallel and perpendicular to the applied field, respectively. The lines are the theoretical curves for CEF parameters $B_4=-44\cdot10^{-4}$ meV, $B_6=-88\cdot10^{-6}$ meV and $T_C=33$ K [82 E 1].

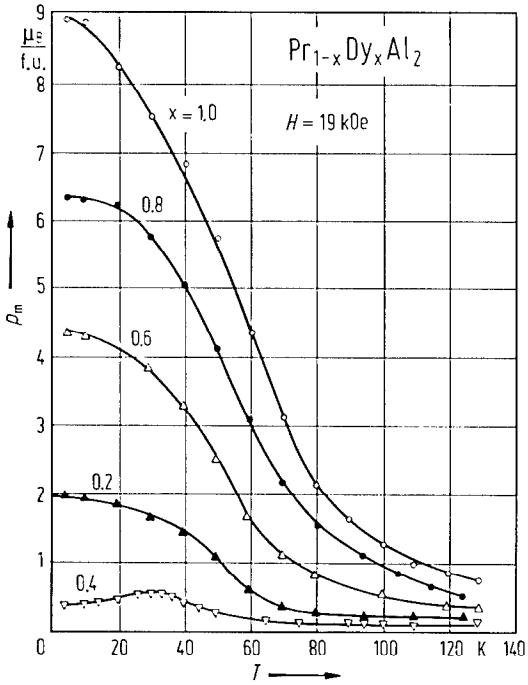

Fig. 75. $Pr_{1-x}Dy_xAl_2$. Temperature dependence of p_m at 19 kOe for different compositions [68 S 1].

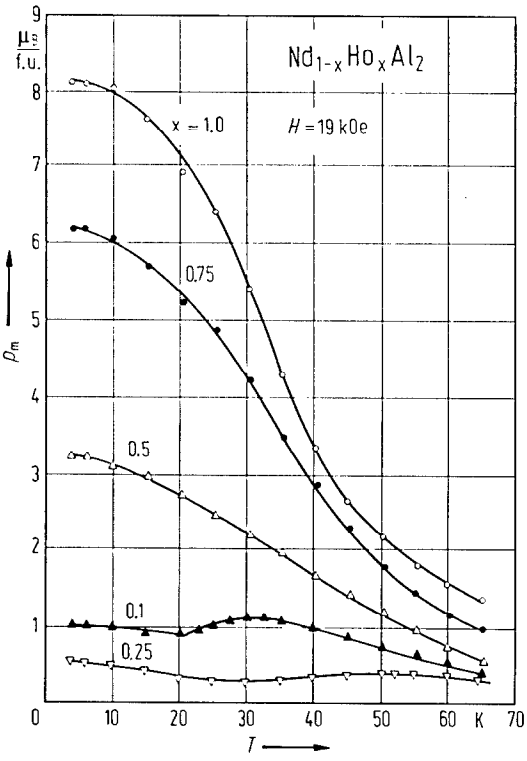

Fig. 77. $Nd_{1-x}Ho_xAl_2$. Temperature dependence of p_m at 19 kOe for different compositions [68 S 1].

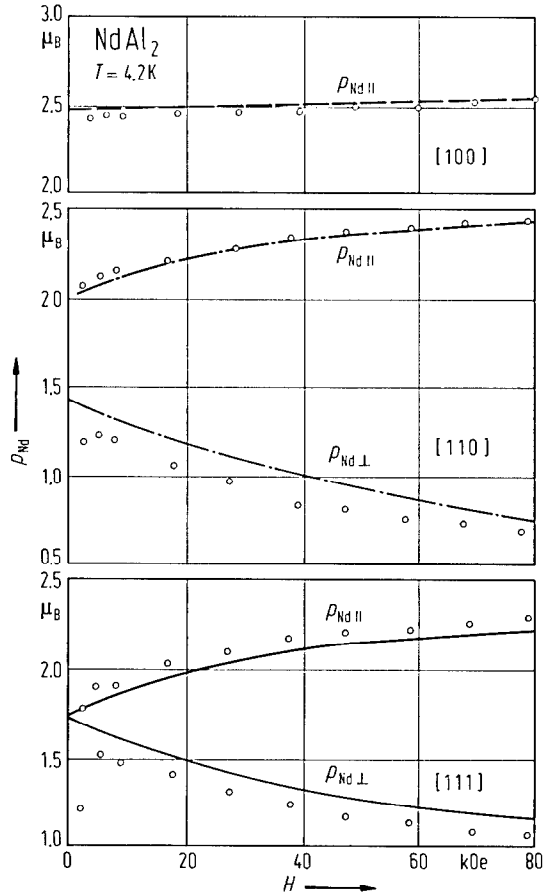

Fig. 76. $NdAl_2$. Magnetic field dependence of p_{Nd} of single crystal for magnetic fields parallel to [100] and near to [110] and [111] directions at 4.2 K. $p_{Nd\parallel}$ and $p_{Nd\perp}$ are the components parallel and perpendicular to the applied field, respectively. The lines are the theoretical curves for CEF parameters $B_4 = -12 \cdot 10^{-4}$ meV, $B_6 = 50 \cdot 10^{-6}$ meV, $T_C = 65$ K [82 E 1].

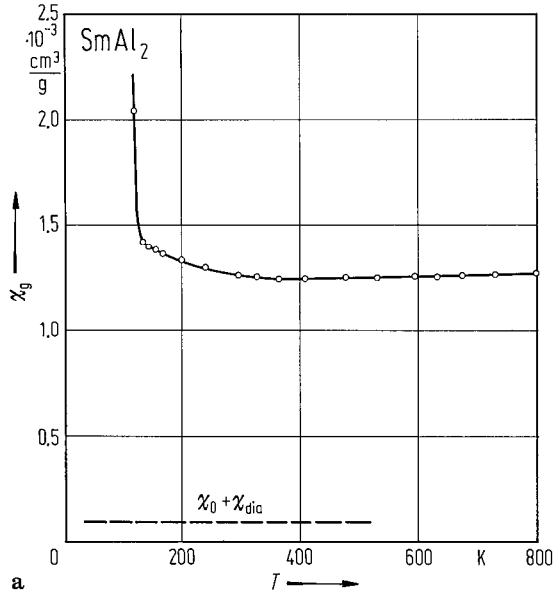

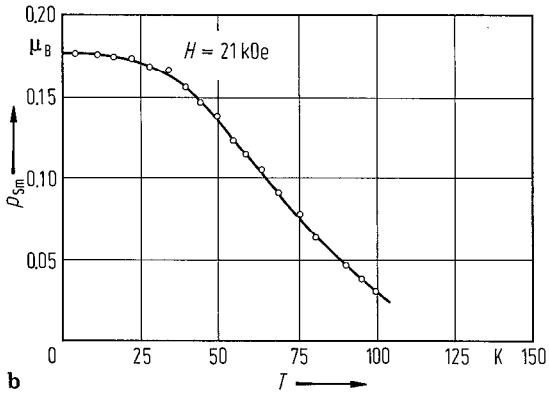

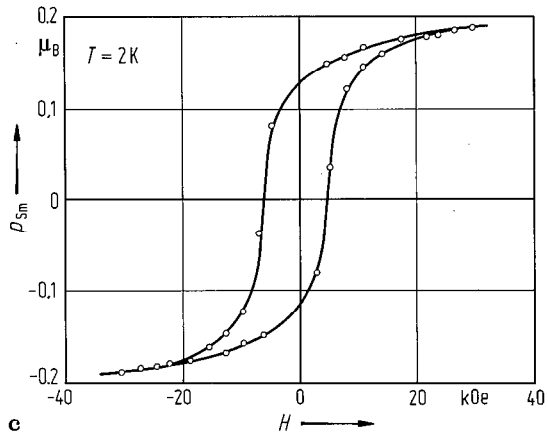

Fig. 78. $SmAl_2$. Temperature dependence of (a) χ_g and (b) p_{Sm} at 21 kOe. (c) Hysteresis loop at 2 K [73 D 1].

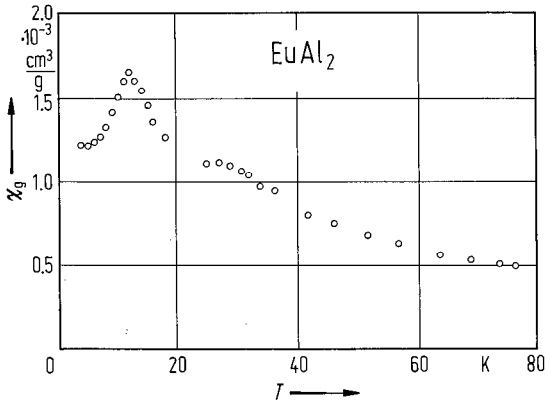

Fig. 79. $EuAl_2$. Temperature dependence of χ_g [68 M 2].

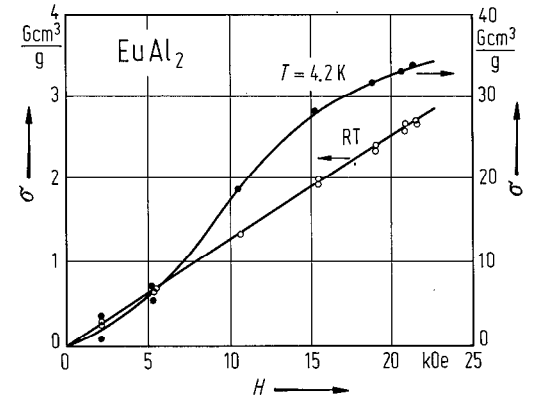

Fig. 80. $EuAl_2$. Magnetic field dependence of σ at 4.2 K and at room temperature [68 M 2].

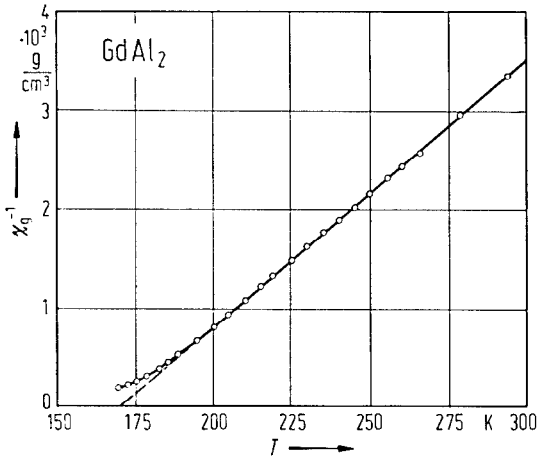

Fig. 81. $GdAl_2$. Temperature dependence of χ_g^{-1} [72 H 1].

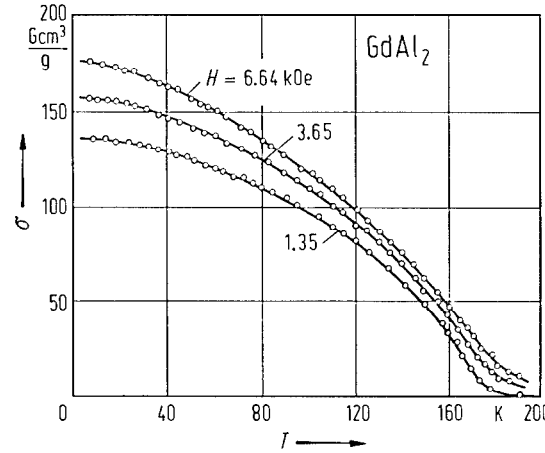

Fig. 82. $GdAl_2$. Temperature dependence of σ for various magnetic fields [72 H 1].

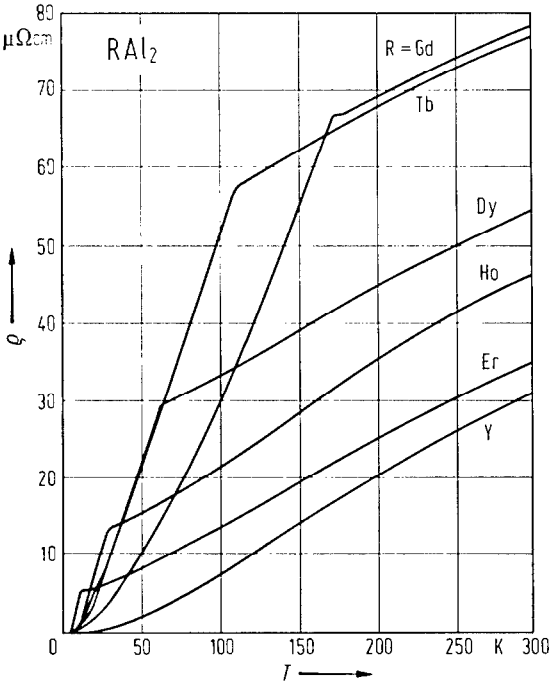

Fig. 83. RAl_2, R = Gd, Tb, Dy, Ho, Er, Y. Temperature dependence of the electrical resistivity. The residual resistivity has been subtracted from the measured values. The transition from the ferromagnetic to the paramagnetic region (T_C) is accompanied by a change in the temperature dependence of ϱ [69 V 1].

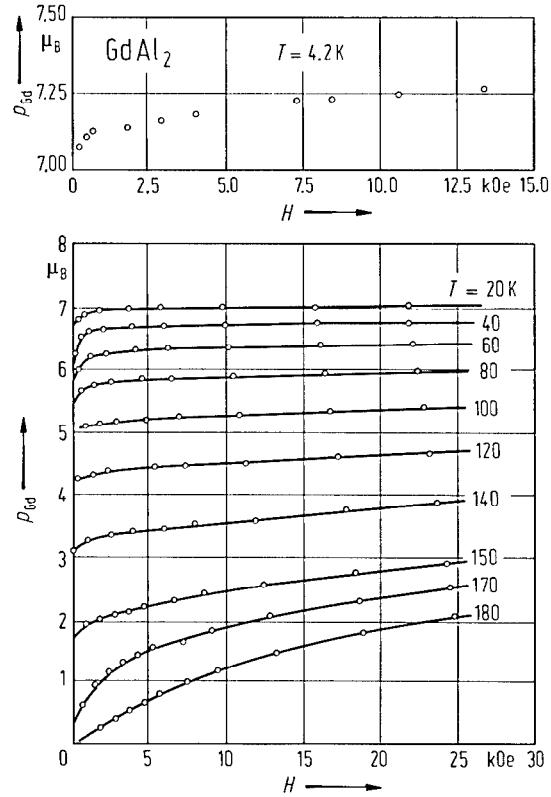

Fig. 84. $GdAl_2$. Magnetic field dependence of p_{Gd} for the magnetic field along [110] direction at various temperatures [77 B 2].

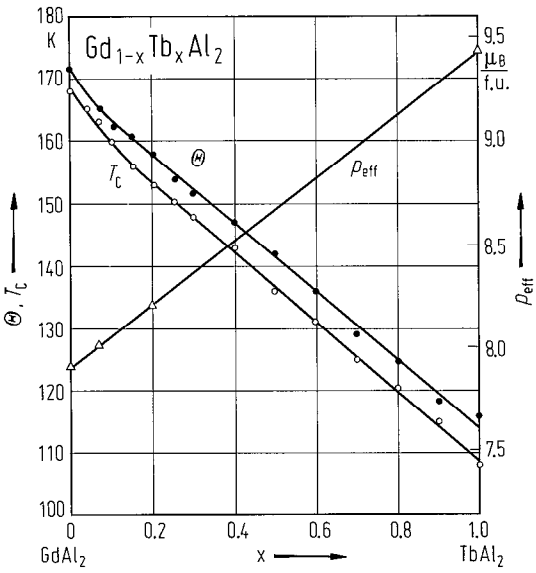

Fig. 85. $Gd_{1-x}Tb_xAl_2$. Composition dependence of Θ, T_C (from electrical resistivity measurements), and p_{eff} [82 C 1].

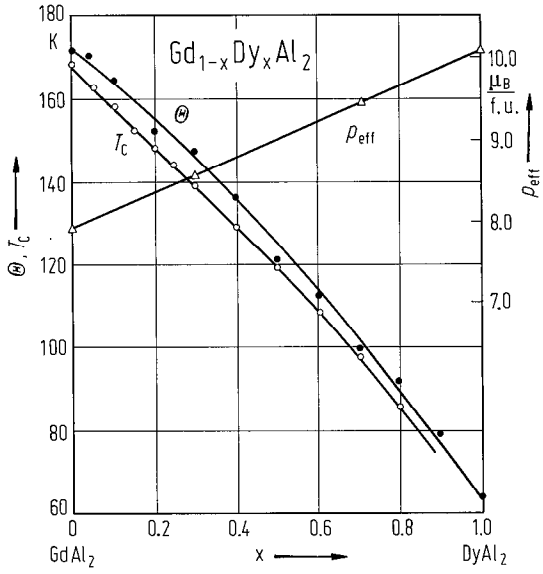

Fig. 86. $Gd_{1-x}Dy_xAl_2$. Composition dependence of Θ, T_C (from electrical resistivity measurements), and p_{eff} [82 C 1].

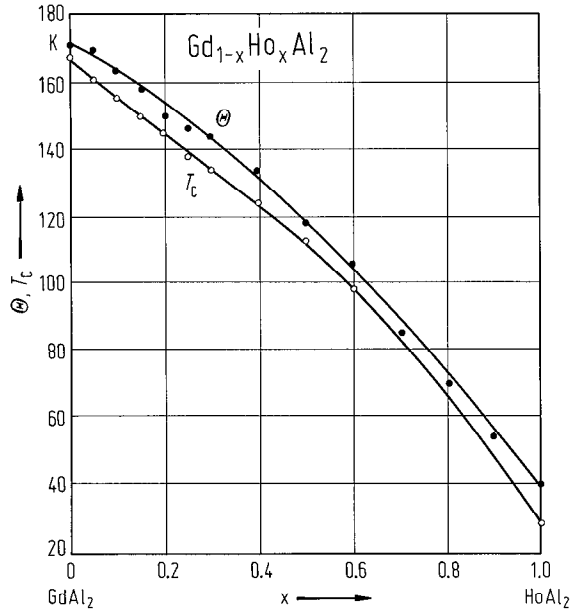

Fig. 87. $Gd_{1-x}Ho_xAl_2$. Composition dependence of Θ, T_C (from electrical resistivity measurements) [82 C 1].

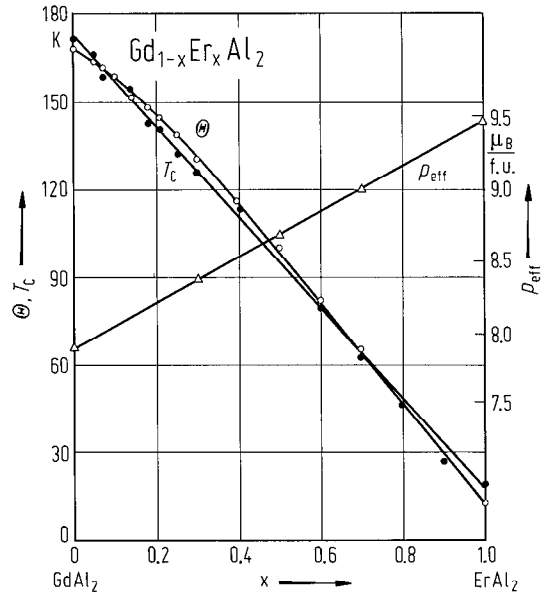

Fig. 88. $Gd_{1-x}Er_xAl_2$. Composition dependence of Θ, T_C (from electrical resistivity measurements), and p_{eff} [82 C 1].

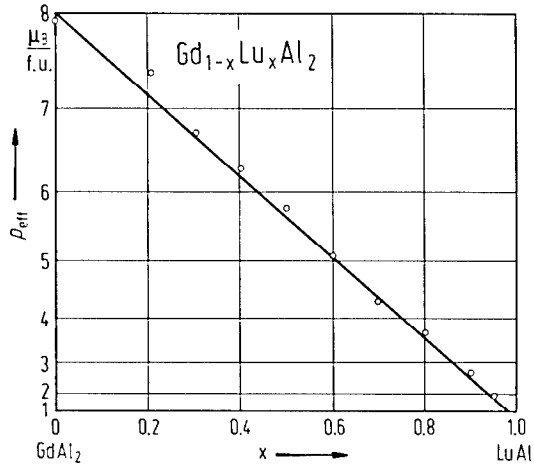

Fig. 89. $Gd_{1-x}Lu_xAl_2$. Composition dependence of p_{eff} [82 H 1].

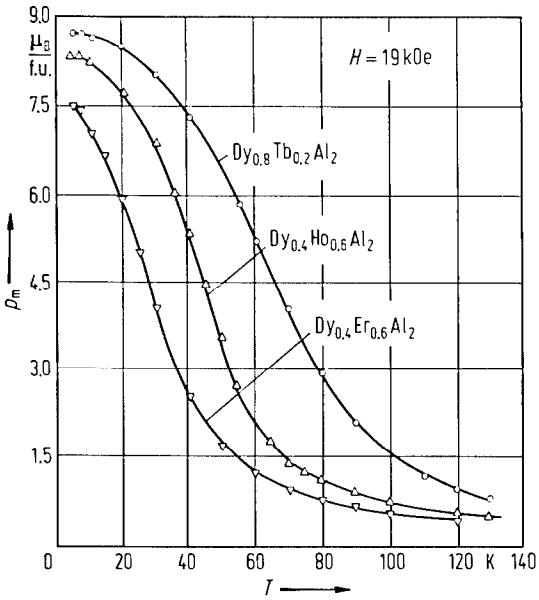

Fig. 92. $Dy_{1-x}R_xAl_2$, R = Tb, Ho, Er. Temperature dependence of p_m [68 S 1].

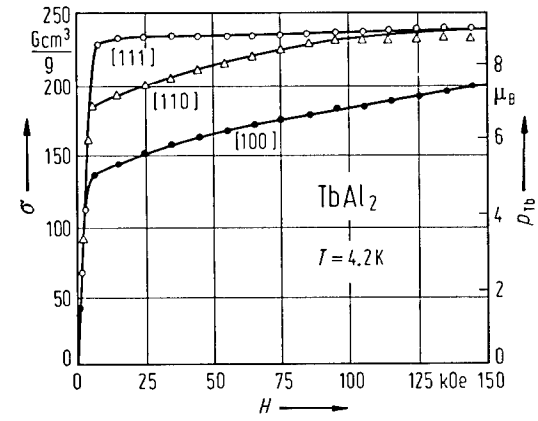

Fig. 90. $TbAl_2$. Magnetic field dependence of σ and p_{Tb} for the field applied along the [111], [110] and [100] directions at 4.2 K [74 B 1].

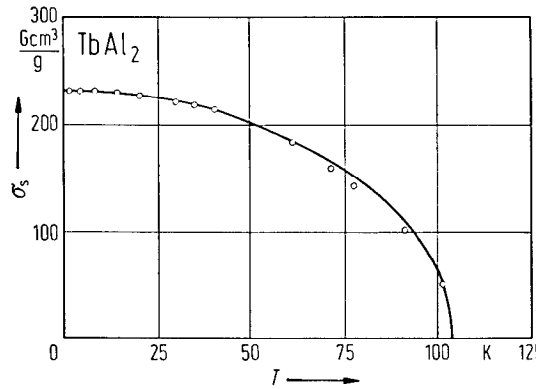

Fig. 91. $TbAl_2$. Temperature dependence of the spontaneous magnetization σ_s. The solid line represents the Brillouin law [74 B 1].

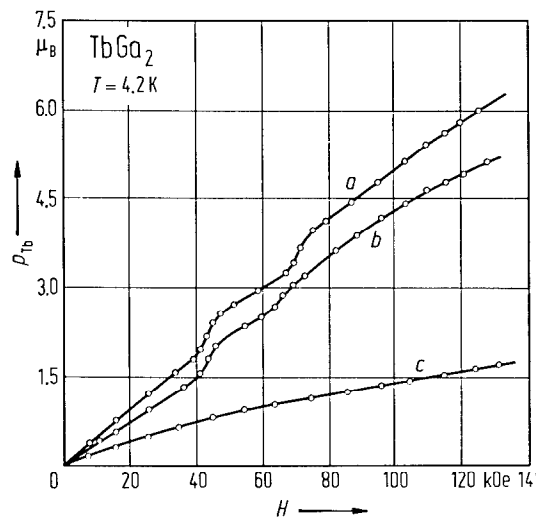

Fig. 93. $TbGa_2$. Magnetic field dependence of p_{Tb} at 4.2 K for fields applied parallel to the three main symmetry directions *a*, *b* and *c* [77 A 1].

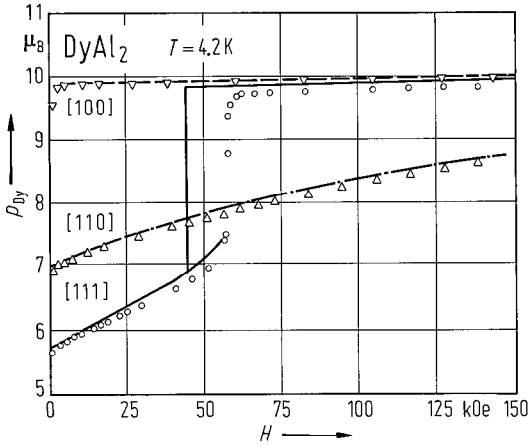

Fig. 94. $DyAl_2$. Magnetic field dependence of p_{Dy} at 4.2 K for the field applied parallel to the three main symmetry directions [100], [110] and [111], respectively. The lines represents theoretical calculations with CEF parameters $B_4 = -0.50 \cdot 10^{-4}$ meV, $B_6 = -0.51 \cdot 10^{-6}$ meV and $T_C = 62$ K [82 K 1].

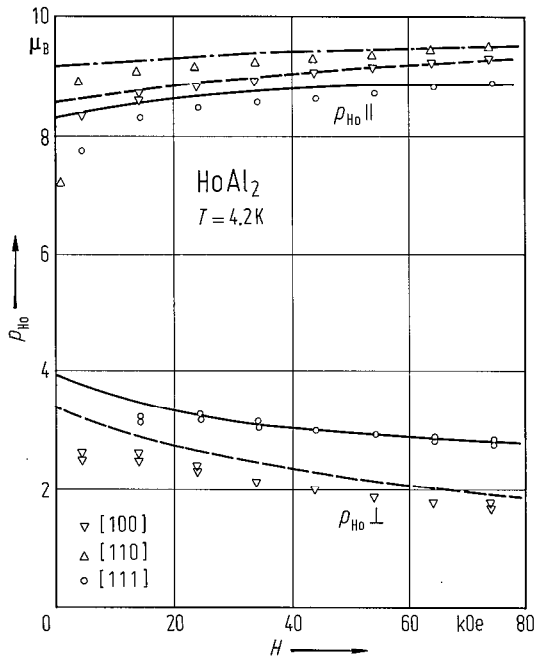

Fig. 95. $HoAl_2$. Magnetic field dependence of p_{Ho} at 4.2 K parallel and perpendicular to the magnetic field applied parallel to directions near [100], [110] and [111], respectively. The lines represent theoretical calculations with CEF parameters $B_4 = -0.85 \cdot 10^{-4}$ meV, $B_6 = 0.71 \cdot 10^{-6}$ meV and $T_C = 31.5$ K [83 S 2].

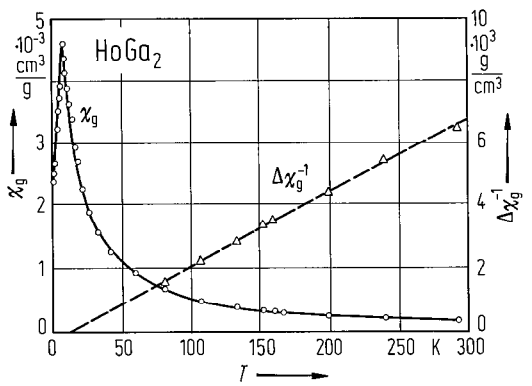

Fig. 96. Curie-Weiss fit for polycrystalline $HoGa_2$. $\Delta\chi(T) = \chi(T) - \chi_0$. Curie constant $C_g = 4.19 \cdot 10^{-2}$ cm³ K/g, $p_{eff} = 10.10\,\mu_B$/f.u., $\Theta = 13$ K [78 T 1].

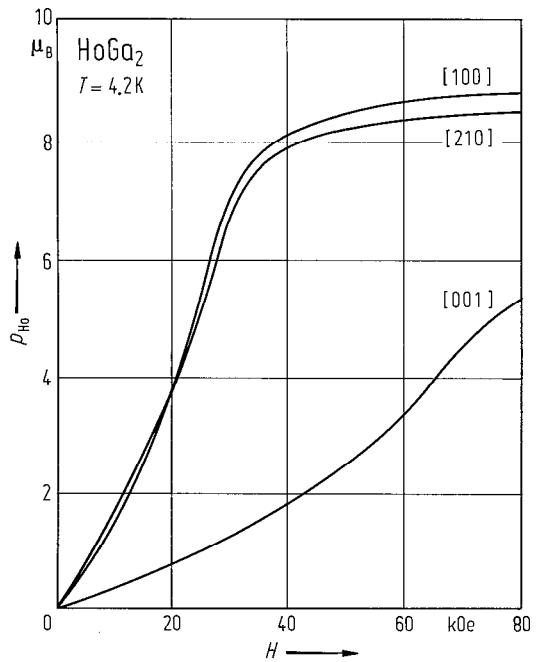

Fig. 97. $HoGa_2$. Magnetic field dependence of p_{Ho} along [100], [210] and [001] directions of a single crystal at 4.2 K [78 T 1].

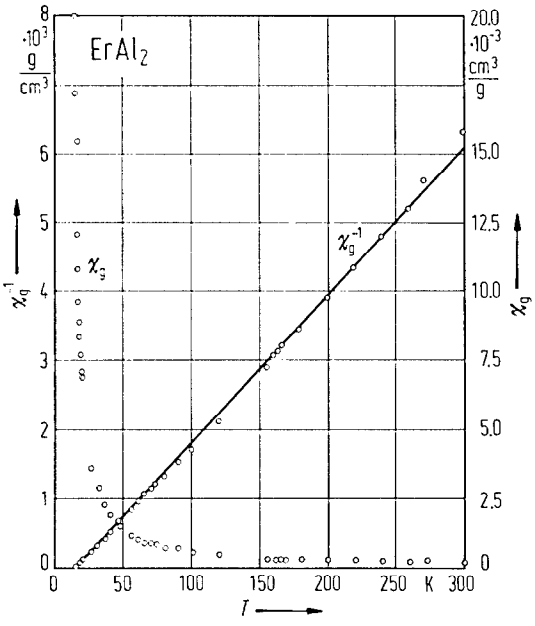

Fig. 98. $ErAl_2$. Temperature dependence of χ_g and χ_g^{-1} [68 N 1].

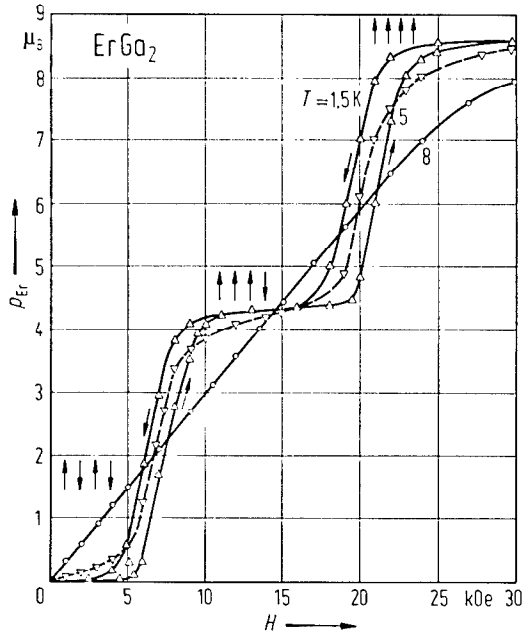

Fig. 101. $ErGa_2$. Single crystal magnetization vs. applied magnetic field along the c axis at 1.5, 5 and 8 K [82 D 2].

Fig. 102. $ErGa_2$. Single crystal magnetization vs. applied magnetic field at 1.5 K along the a, b and c axes of the orthohexagonal lattice. Dashed lines are the experimental variations, full lines are the calculated ones [82 D 2].

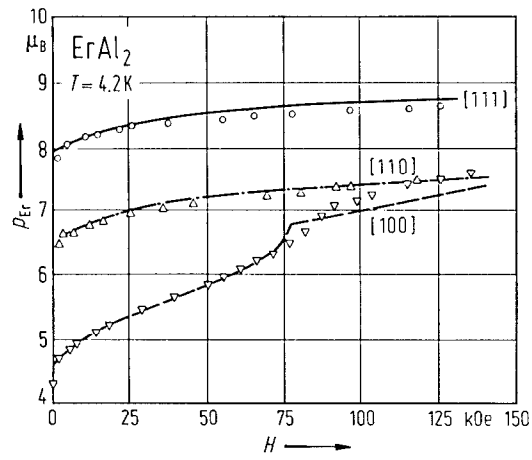

Fig. 99. $ErAl_2$. Magnetic field dependence of p_{Er} in the main symmetry directions at 4.2 K. The theoretical curves are calculated using the total Hamiltonian including the CEF parameters for $B_4 = 1.1 \cdot 10^{-4}$ meV, $B_6 = -1.35 \cdot 10^{-6}$ meV, $T_C = 14$ K [76 P 1].

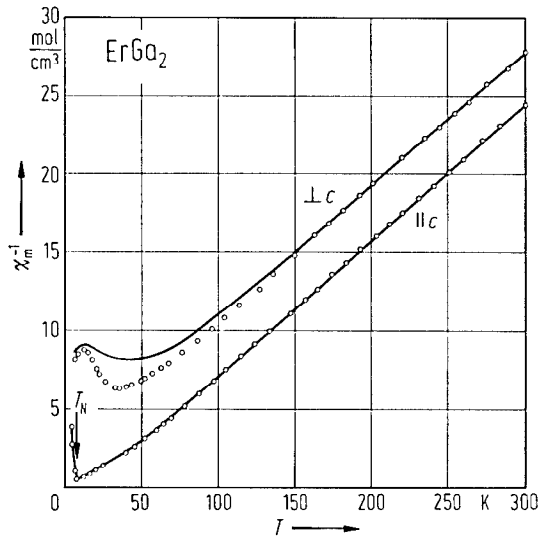

Fig. 100. $ErGa_2$. Single crystal reciprocal magnetic susceptibility vs. temperature for magnetic fields perpendicular and parallel to the c axis, respectively [82 D 2].

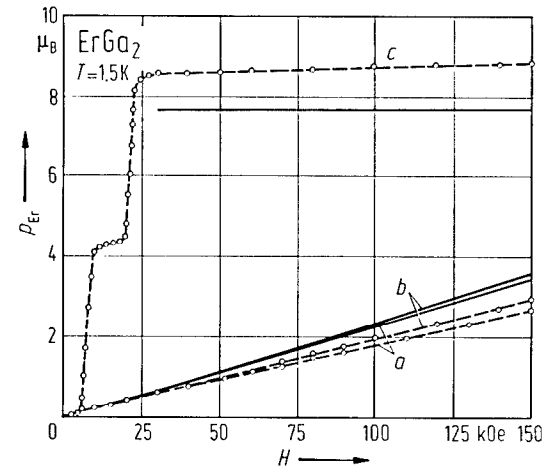

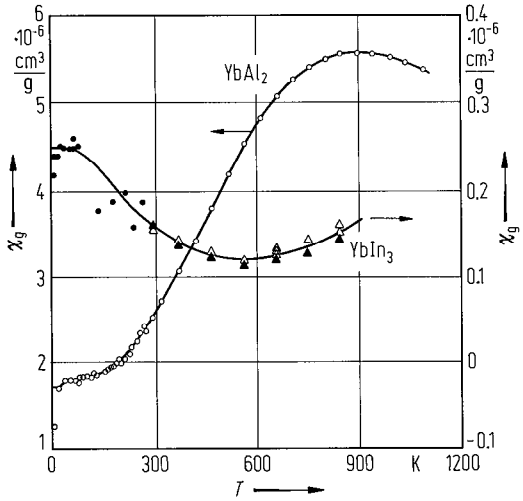

Fig. 103. $YbAl_2$, $YbIn_3$. Temperature dependence of χ_g after correction for Yb_2O_3. Different symbols for $YbIn_3$ indicate results of various authors [73 K 1].

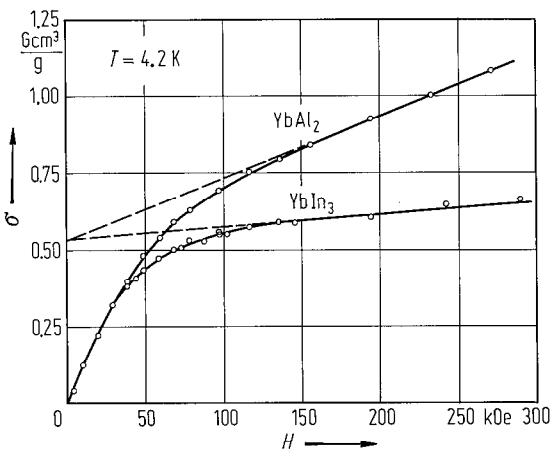

Fig. 104. $YbAl_2$, $YbIn_3$. Magnetic field dependence of σ at 4.2 K [73 K 1].

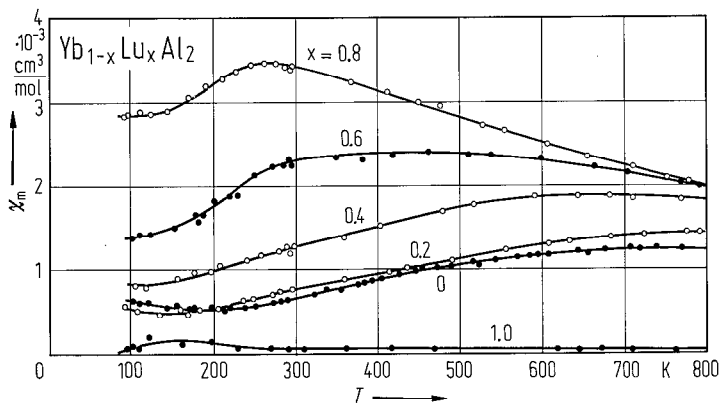

Fig. 105. $Yb_{1-x}Lu_xAl_2$. Temperature dependence of χ_m corrected for the $LuAl_2$ contribution [85 I 1].

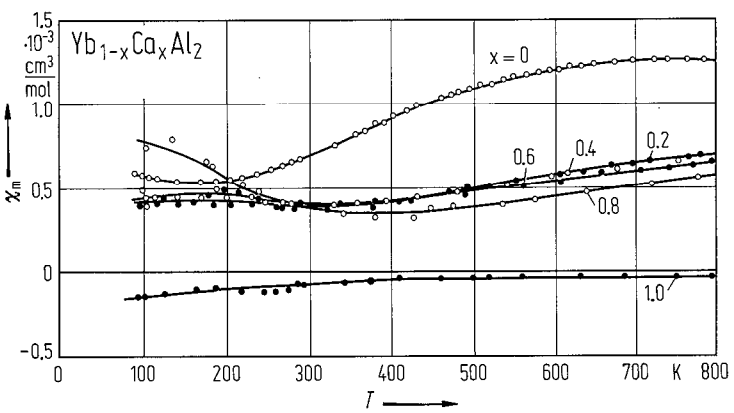

Fig. 106. $Yb_{1-x}Ca_xAl_2$. Temperature dependence of χ_m corrected for the $CaAl_2$ contribution [85 I 1].

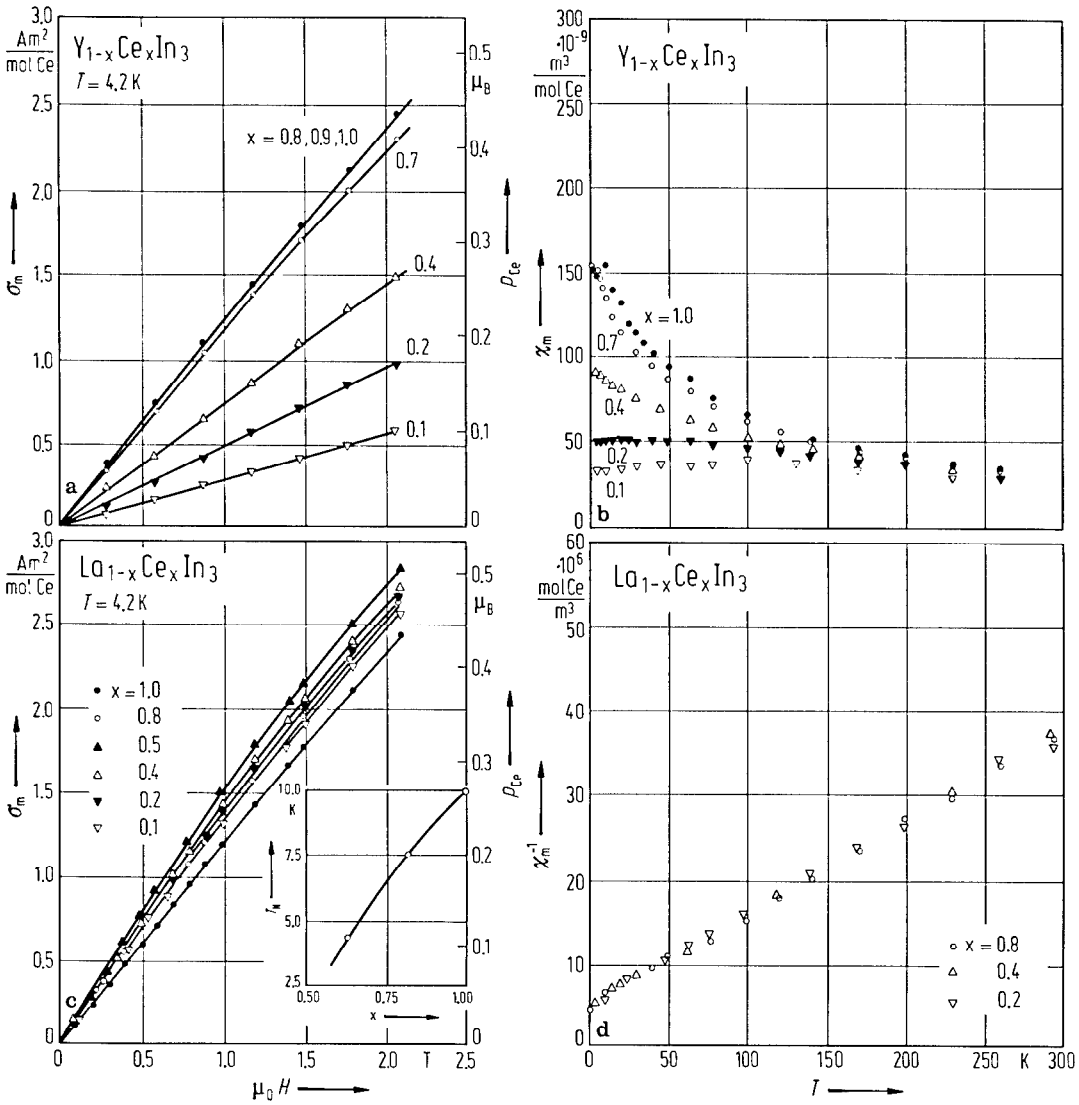

Fig. 107. $R_{1-x}Ce_xIn_3$, R = Y, La [82 D 1]. (a) $Y_{1-x}Ce_xIn_3$. Magnetic field dependence of σ_m at 4.2 K, with corresponding $Y_{1-x}La_xIn_3$ matrix magnetization subtracted. (b) $Y_{1-x}Ce_xIn_3$. Temperature dependence of χ_m corrected for low-temperature impurity contribution and the magnetic susceptibility of corresponding $Y_{1-x}La_xIn_3$ matrix. (c) $La_{1-x}Ce_xIn_3$. Magnetic field dependence of σ_m at 4.2 K, with corresponding $LaIn_3$ magnetization subtracted. (In the insert Ce concentration dependence of T_N [80 E 2].) (d) $La_{1-x}Ce_xIn_3$. Temperature dependence of χ_m^{-1} with corresponding $LaIn_3$ susceptibility subtracted.

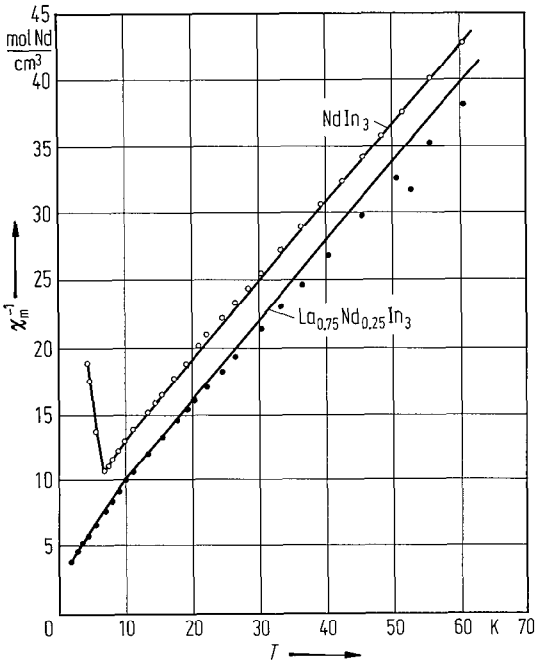

Fig. 108. $NdIn_3$, $La_{0.75}Nd_{0.25}In_3$. Temperature dependence of χ_m^{-1}. The lines represents theoretical calculations with CEF parameters $W=0.91$ K and $x=0.3$ [76 L 1].

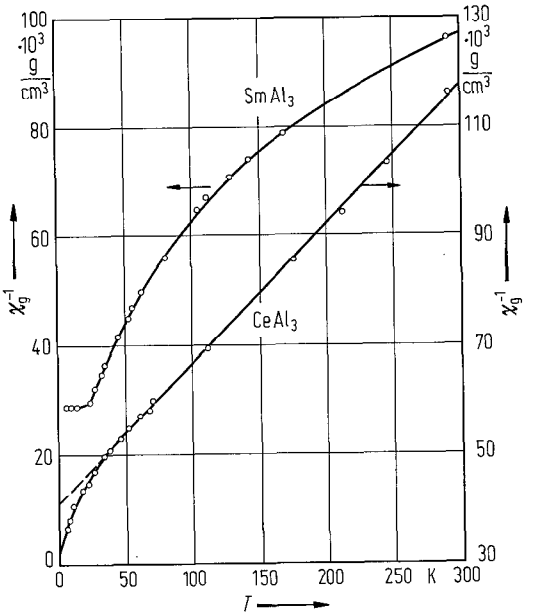

Fig. 109. $SmAl_3$, $CeAl_3$. Temperature dependence of χ_g^{-1} [66 B 1].

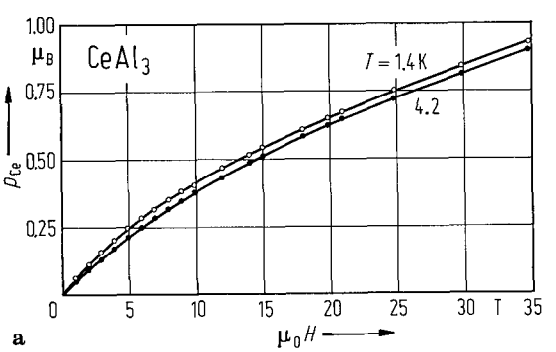

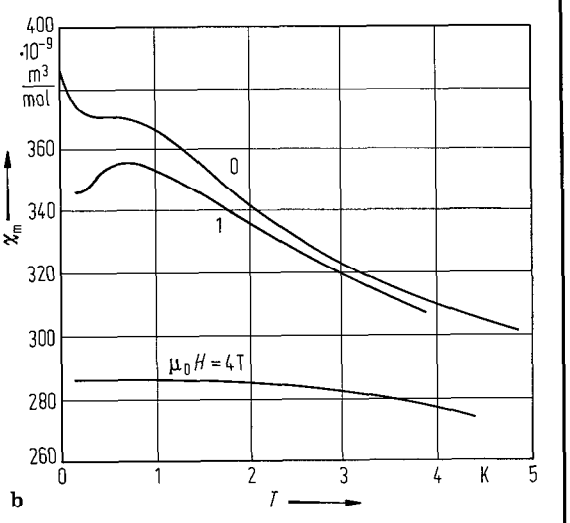

Fig. 110. $CeAl_3$. (a) Magnetic field dependence of the dc magnetization at 1.4 K and 4.2 K. (b) Shows low-temperature ac magnetic susceptibility data [85 D 1].

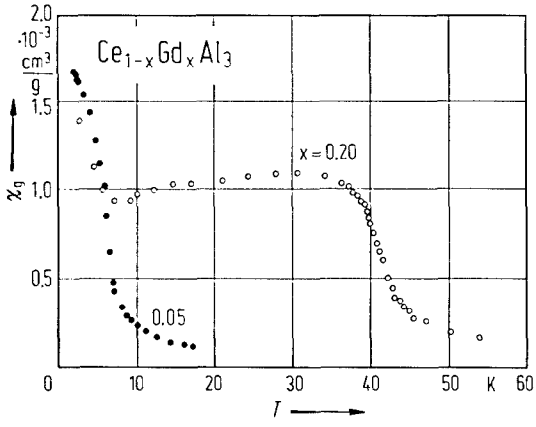

Fig. 111. $Ce_{1-x}Gd_xAl_3$. Temperature dependence of χ_g [84 E 1].

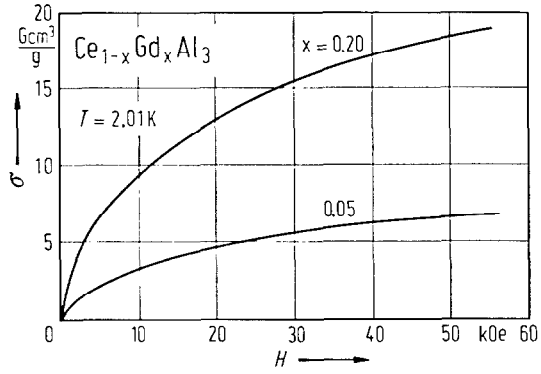

Fig. 112. $Ce_{1-x}Gd_xAl_3$. Magnetic field dependence of σ at 2.01 K [84 E 1].

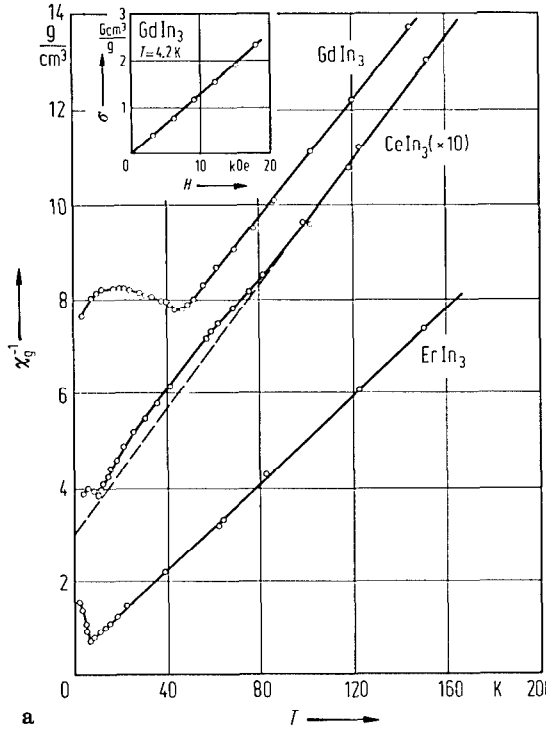

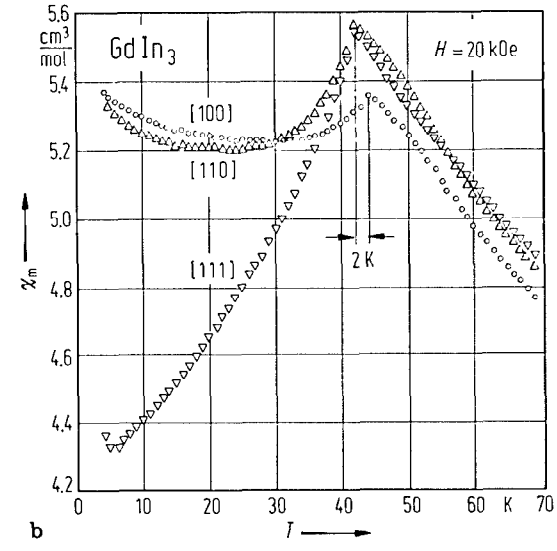

Fig. 113. RIn_3, R = Ce, Gd, Er. (a) Temperature dependence of χ_g^{-1} (insert: magnetization curve for $GdIn_3$ at 4.2 K) [69 B 2]. (b) Temperature dependence of χ_m for a single crystal of $GdIn_3$ at 20 kOe [79 S 1].

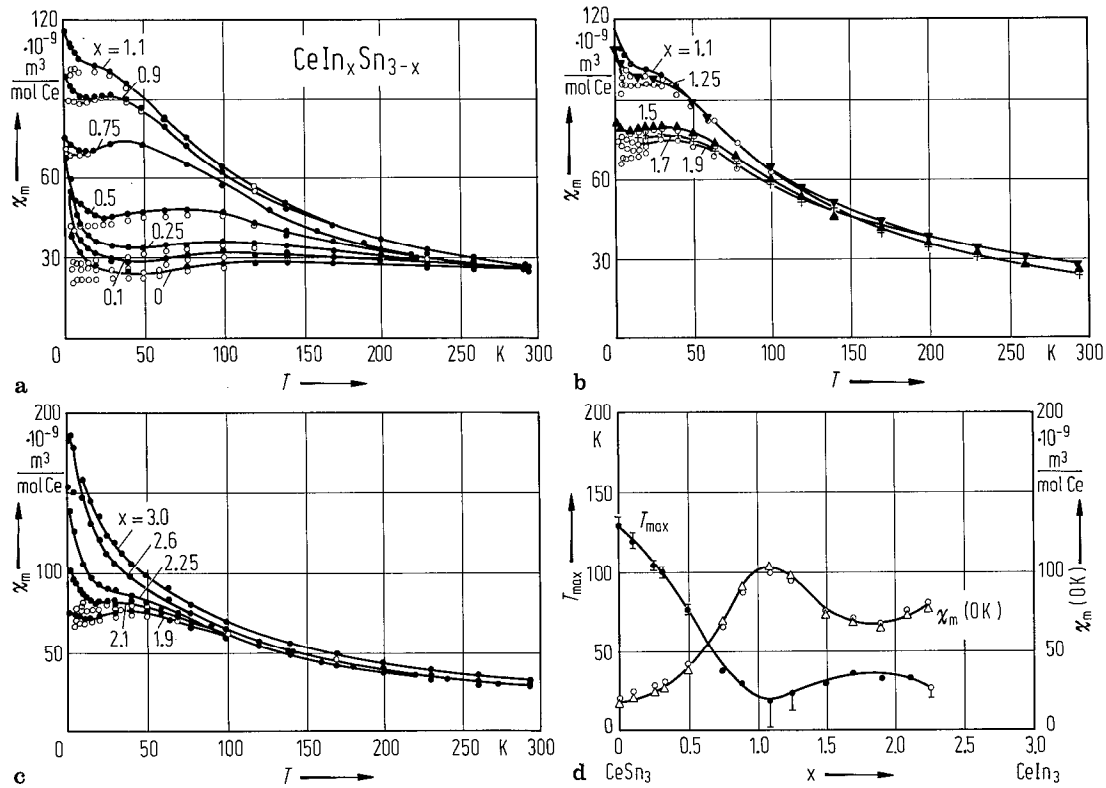

Fig. 114. CeIn$_x$Sn$_{3-x}$. Magnetic susceptibility χ_m vs. temperature (a–c) and composition dependence of the position of the susceptibility maximum and the corrected low-temperature susceptibility (d). Full symbols refer to as-measured data, open symbols to data corrected for the contribution of paramagnetic "Ce^{3+} impurities". The open triangles (d) give data corrected also for a matrix contribution amounting to χ (LaIn$_x$Sn$_{3-x}$); the error bars (d) give the uncertainity of the T_{max} determination [80 D 1].

For Fig. 115, see next page.

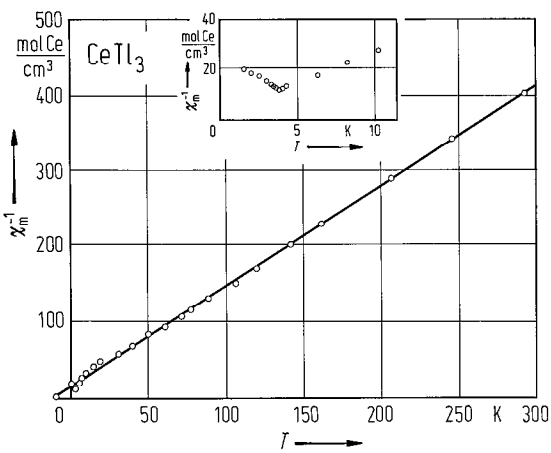

Fig. 116. CeTl$_3$. Temperature dependence of χ_m^{-1}. The data are corrected for a conduction electron contribution taken equal to χ (LaTl$_3$), and Van Vleck susceptibility due to the higher $J = 7/2$ multiplet, adding up to $\chi_{corr} = 0.13 \cdot 10^{-3}$ cm^3/mol Ce [80 E 1].

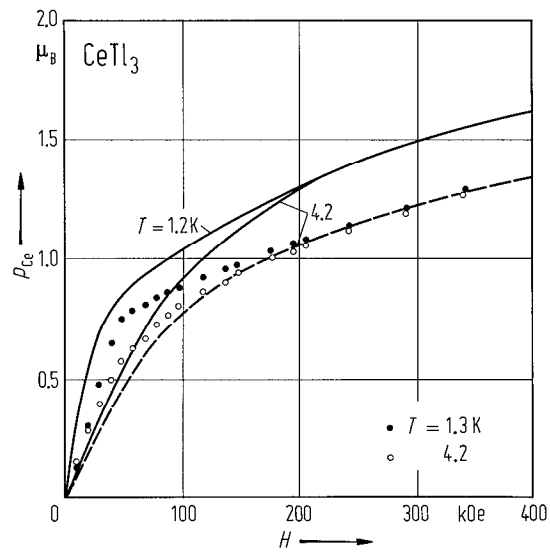

Fig. 117. CeTl$_3$. Magnetic field dependence of p_{Ce} at 1.3 K and 4.2 K. The solid and dashed lines are calculated with a CEF splitting of 60 and 110 K, respectively, averaged over the three principal axes [80 E 1].

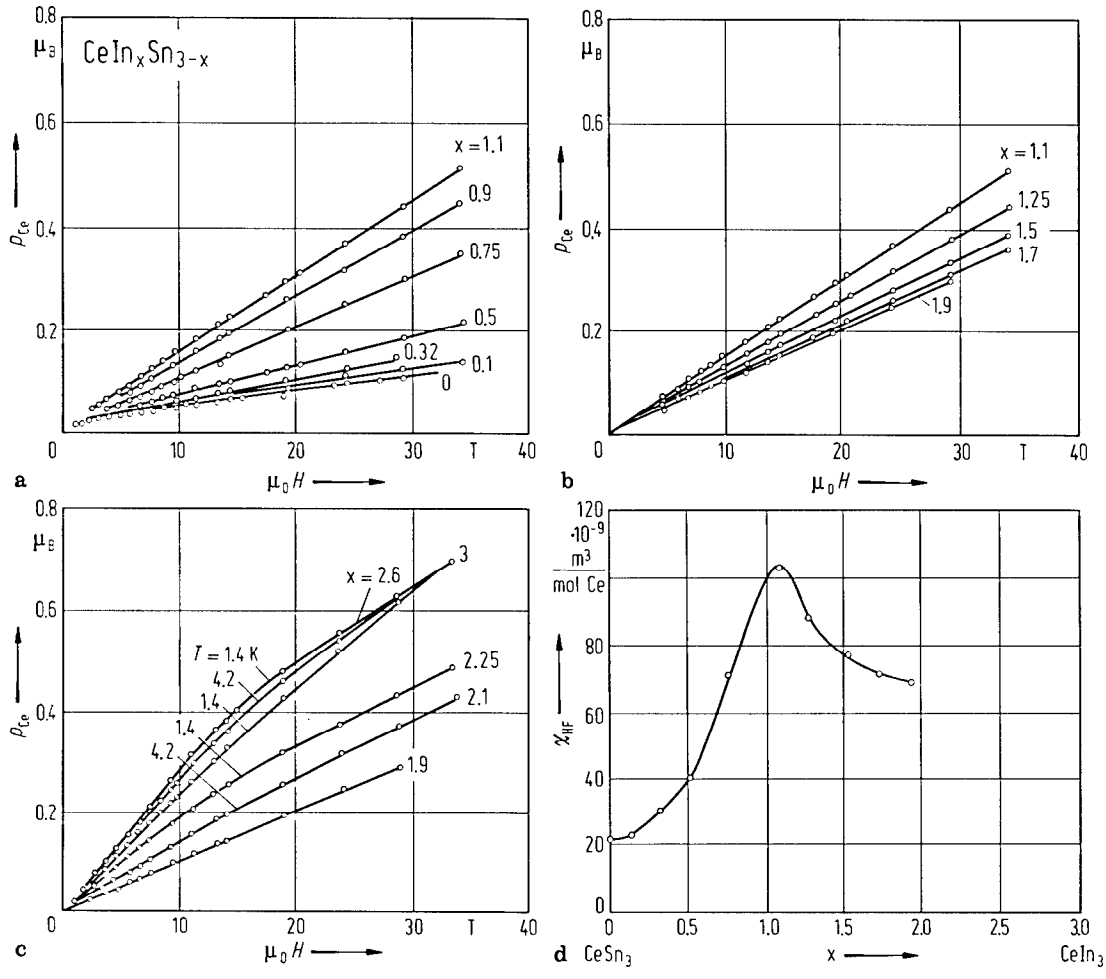

Fig. 115. CeIn$_x$Sn$_{3-x}$. (a–c) High-field magnetization below 4.2 K vs. magnetic field for various compositions. (d) Composition dependence of the magnetic susceptibility in high fields $\mu_0 H > 10$ T. Where no temperature is given the magnetization curves are independent of temperature for $\mu_0 H > 10$ T [80 D 1].

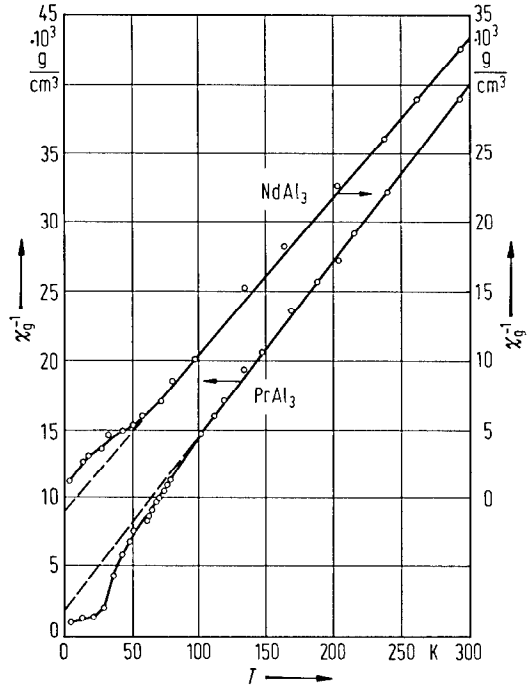

Fig. 118. PrAl$_3$, NdAl$_3$. Temperature dependence of χ_g^{-1} [66 B 1].

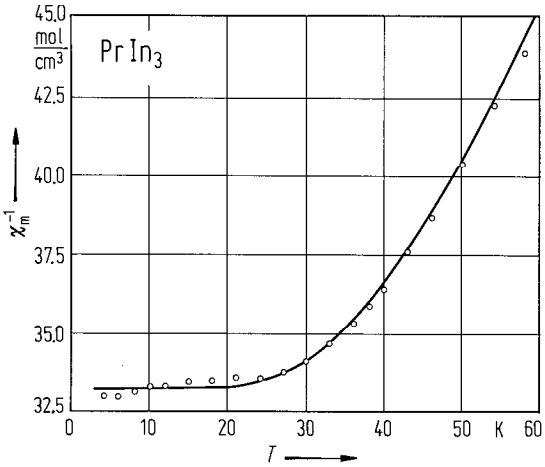

Fig. 119. $PrIn_3$. Temperature dependence of χ_m^{-1}. The line represents theoretical calculations with CEF parameters $W = 2.36$ K and $x = -0.6$ [76 L 1].

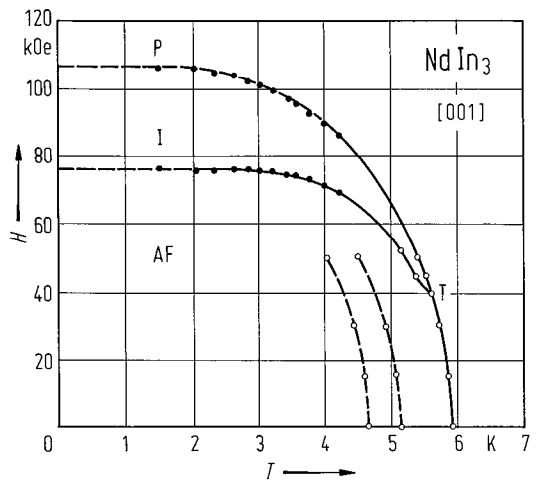

Fig. 121. $NdIn_3$. Phase diagram for magnetic field in the [001] direction. The solid curves denote the second-order phase transition and the dashed curves the first-order phase transition; I: intermediate phase and T: triple point [85 C 1].

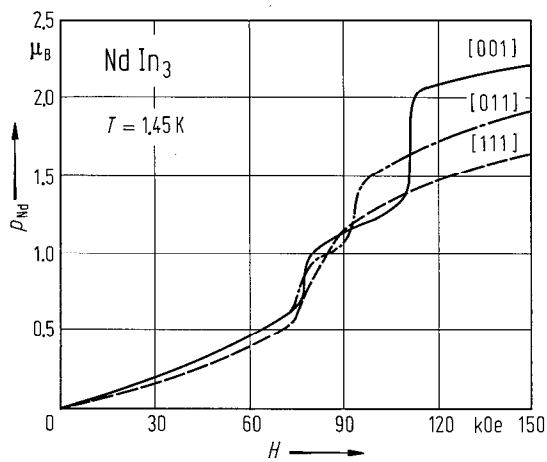

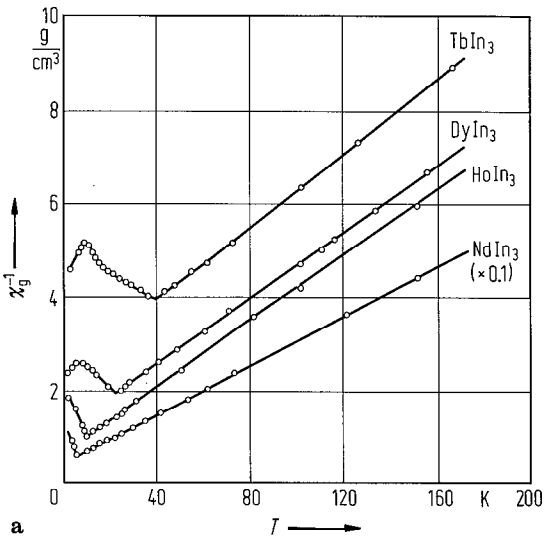

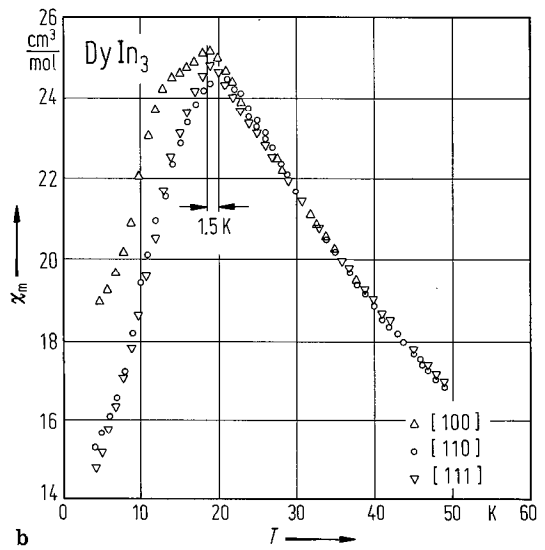

Fig. 120. RIn_3, R = Nd, Tb, Dy, Ho. Temperature dependence of χ_g^{-1} [69 B 2], and of χ_m for single crystal of $DyIn_3$ at 20 kOe [79 S 1].

◀
Fig. 122. $NdIn_3$. Magnetic field dependence of p_{Nd} along principal crystallographic axes at 1.45 K [85 C 1].

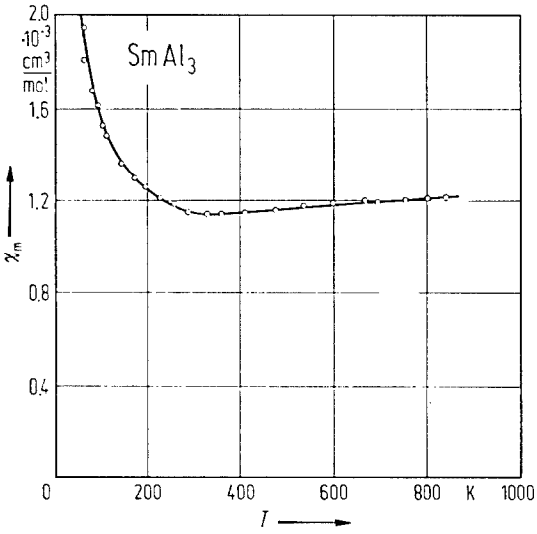

Fig. 123. $SmAl_3$. Temperature dependence of χ_m [67 D 1].

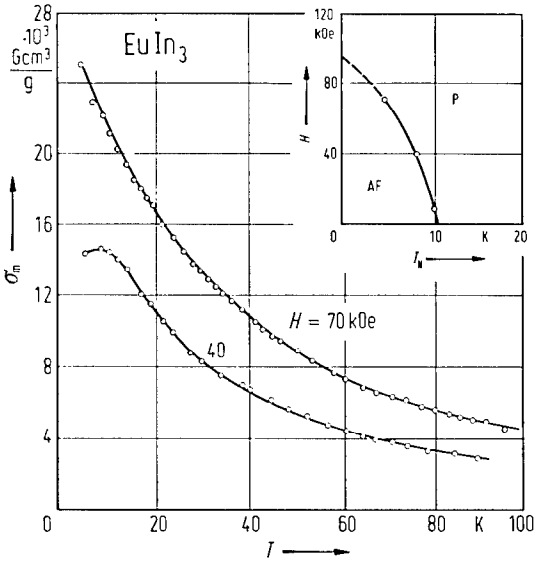

Fig. 126. $EuIn_3$. Temperature dependence of σ_m and phase diagram [74 S 1].

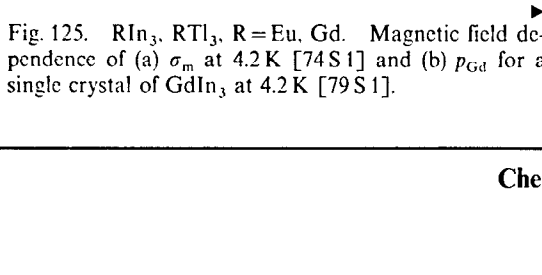

Fig. 124. $YbIn_3$, $SmIn_3$. Temperature dependence of χ_g^{-1} [69 B 2].

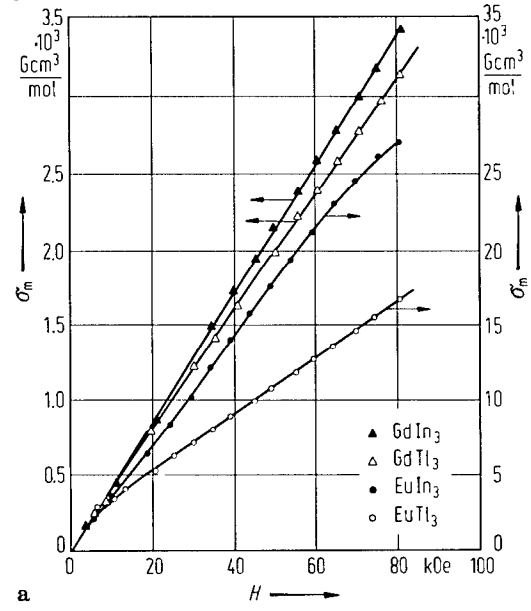

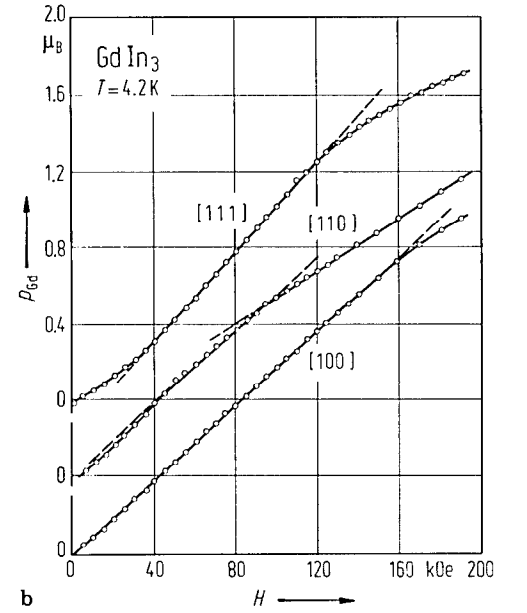

Fig. 125. RIn_3, RTl_3, R = Eu, Gd. Magnetic field dependence of (a) σ_m at 4.2 K [74 S 1] and (b) p_{Gd} for a single crystal of $GdIn_3$ at 4.2 K [79 S 1].

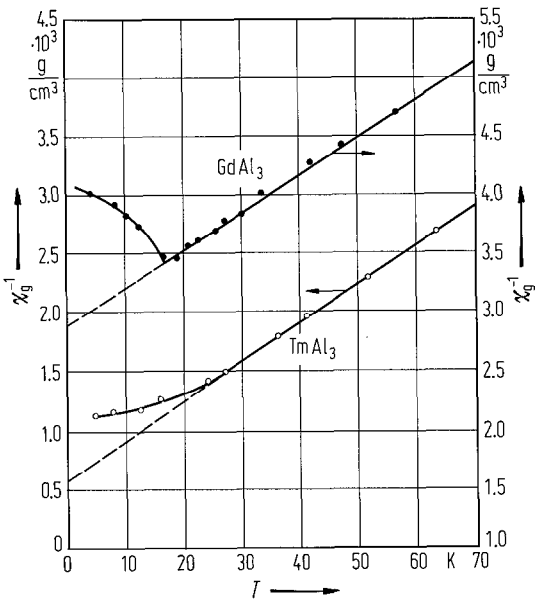

Fig. 127. $GdAl_3$, $TmAl_3$. Temperature dependence of χ_g^{-1} [66 B 1].

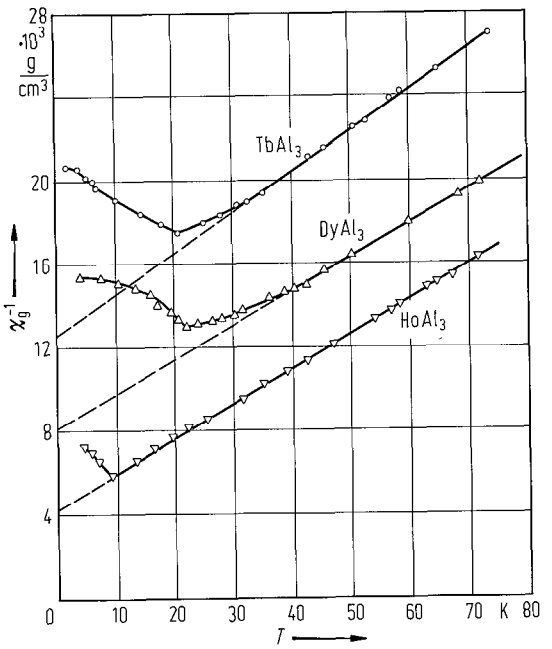

Fig. 129. RAl_3, R = Tb, Dy, Ho. Temperature dependence of χ_g^{-1} [66 B 1].

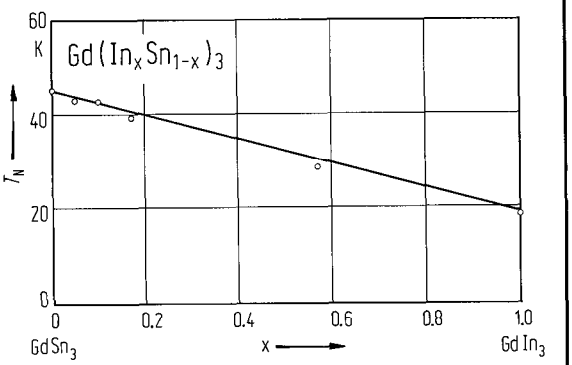

Fig. 128. $Gd(In_xSn_{1-x})_3$. Concentration dependence of T_N [84 A 1].

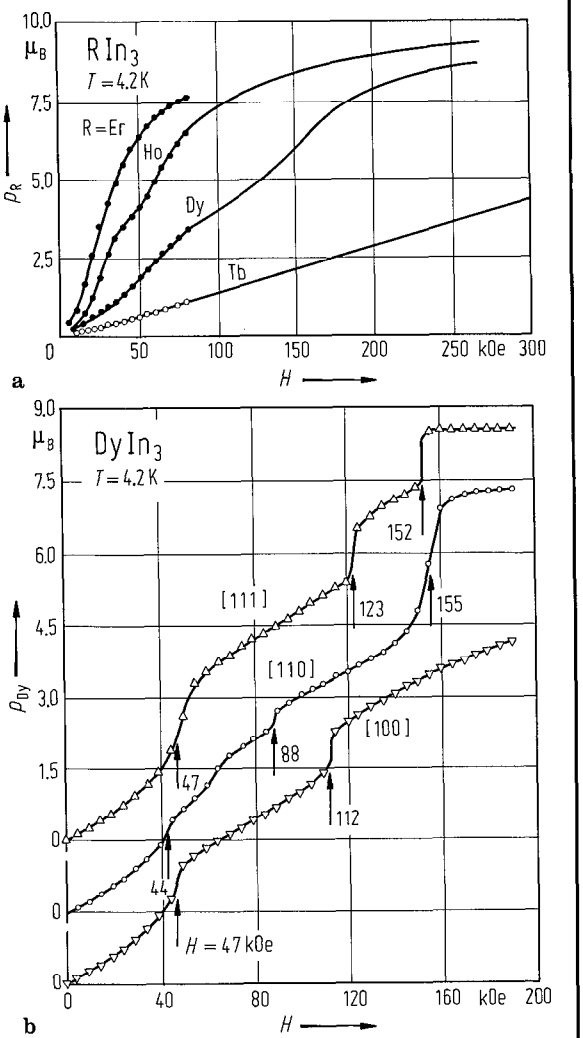

Fig. 130. RIn_3, R = Tb, Dy, Ho, Er. Magnetic field dependence of (a) p_R at 4.2 K [73 L 1] and (b) for a single crystal of $DyIn_3$ at 4.2 K [79 S 1].

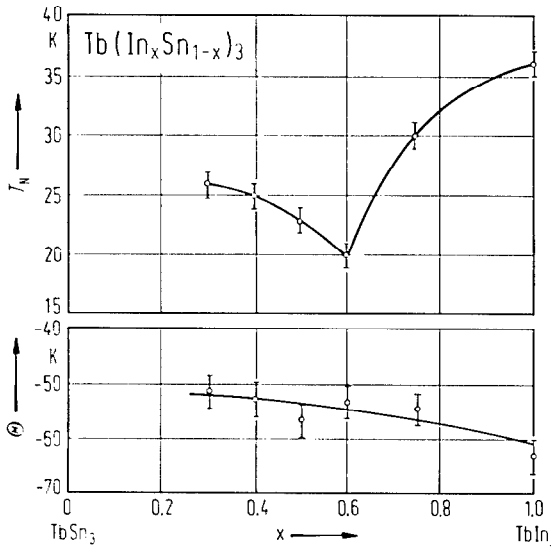

Fig. 131. $Tb(In_xSn_{1-x})_3$. Concentration dependence of T_N and Θ [73 L 1].

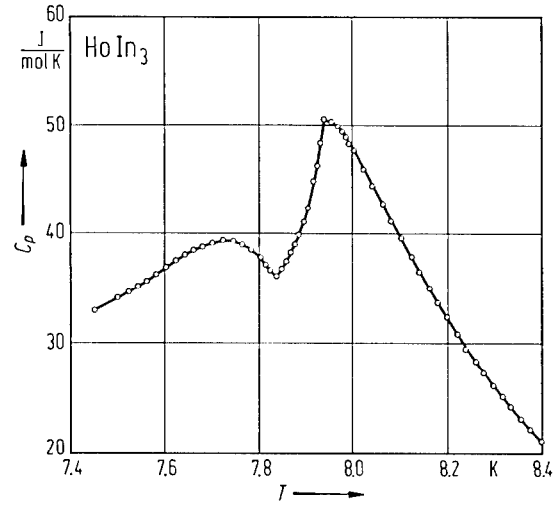

Fig. 132. $HoIn_3$. Temperature dependence of heat capacity C_p in the vicinity of T_N [86 C 1].

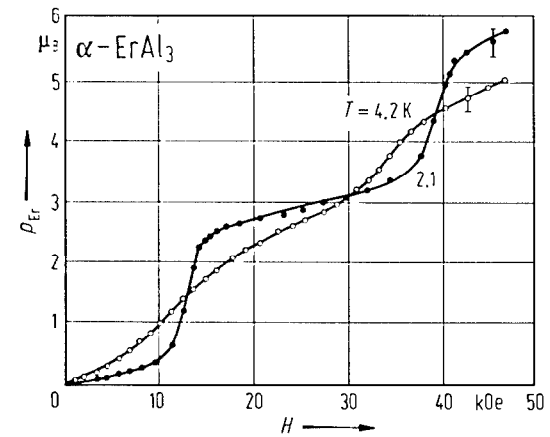

Fig. 134. $ErAl_3$. Magnetic field dependence of p_{Er} at 2.1 K and 4.2 K along the c axis of a single crystal of α-$ErAl_3$ [73 W 1].

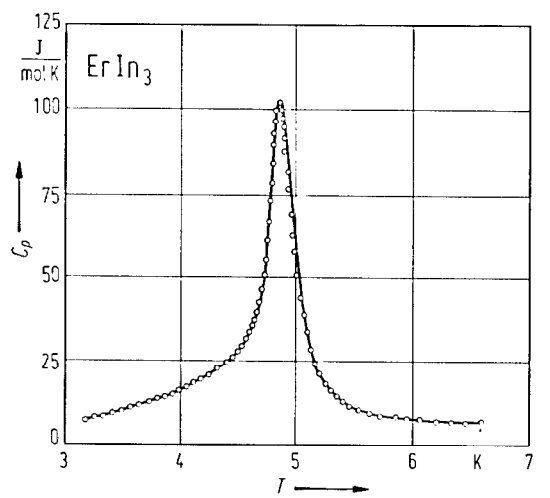

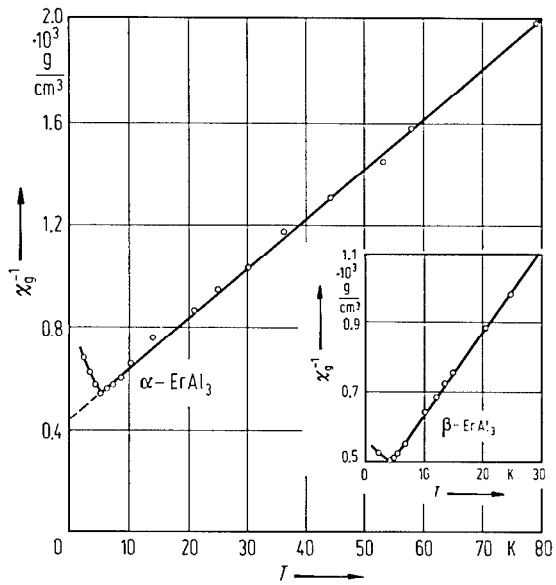

Fig. 133. $ErAl_3$. Temperature dependence of χ_g^{-1} for α-$ErAl_3$ and β-$ErAl_3$ [68 B 1].

◀

Fig. 135. $ErIn_3$. Temperature dependence of the heat capacity C_p in the vicinity of T_N [86 C 1].

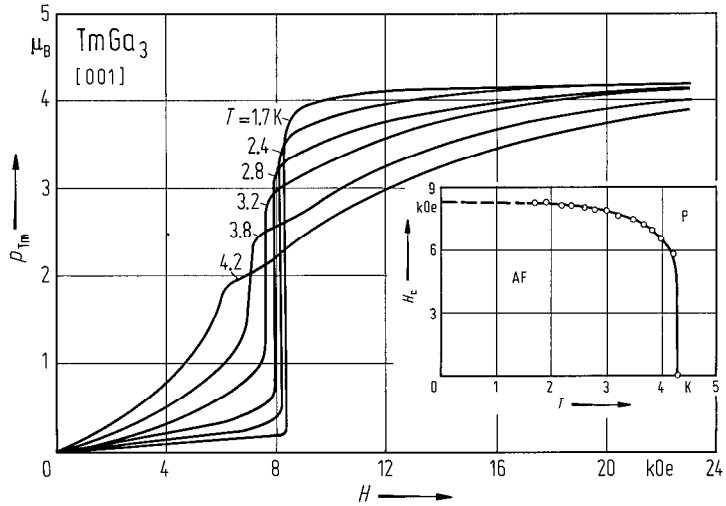

Fig. 137. $TmGa_3$. Magnetic field dependence of p_{Tm} for the magnetic field in the [001] direction at several temperatures. The insert shows the magnetic phase diagram in this direction [85 C 2].

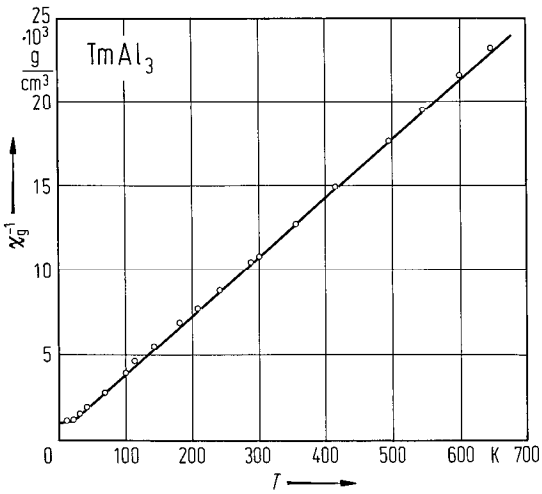

Fig. 136. $TmAl_3$. Temperature dependence of χ_g^{-1}. The line represents the theoretical value for an overall CEF splitting of $350\,cm^{-1}$ [68 B 1].

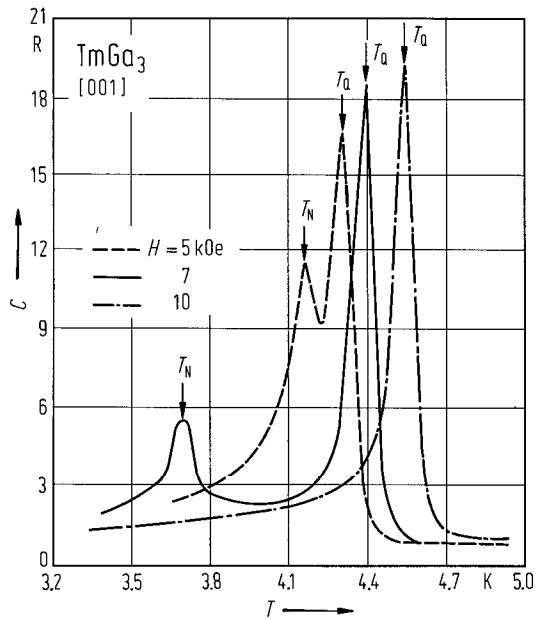

Fig. 138. $TmGa_3$. Influence of the magnetic field applied parallel to the [001] direction on the magnetic (T_N) and structural (T_Q) phase transitions. C: molar heat capacity [85 C 2]. $1\,R \triangleq 8.314\,J\,mol^{-1}\,K^{-1}$.

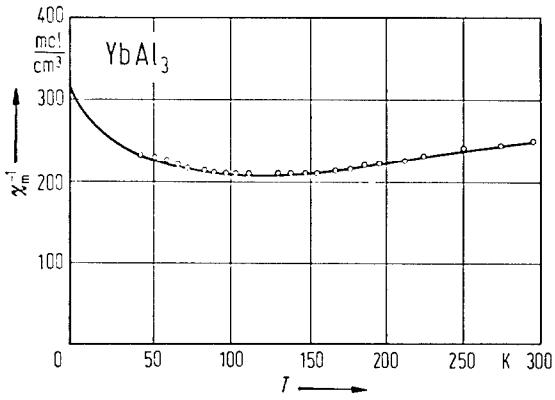

Fig. 139. $YbAl_3$. Temperature dependence of χ_m^{-1}. Yb is in a mixed-valence state. The data have been corrected for Yb_2O_3 magnetic contaminant. Solid line shown is the best fit obtained with the equations

$$\chi_m = N_A p_{eff}^2 v(T)/3k_B(T - T_{sf})$$

and

$$v^{-1}(T) = 1 + \exp[-E_{ex}/k_B(T - T_{sf})]/8$$

for $T_{sf} = 160(10)$ K and $E_{ex}/k_B = -560(25)$ K. $v(T)$ is the fractional occupation of the state corresponding to Yb^{3+} with $p_{eff} = 4.54\,\mu_B$ [75 S 1].

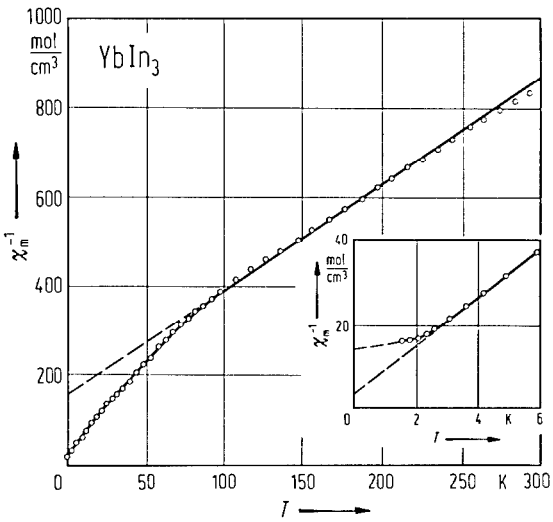

Fig. 140. $YbIn_3$. Temperature dependence of χ_m^{-1}, χ_m corrected for the diamagnetism of ionic cores [74 S 2].

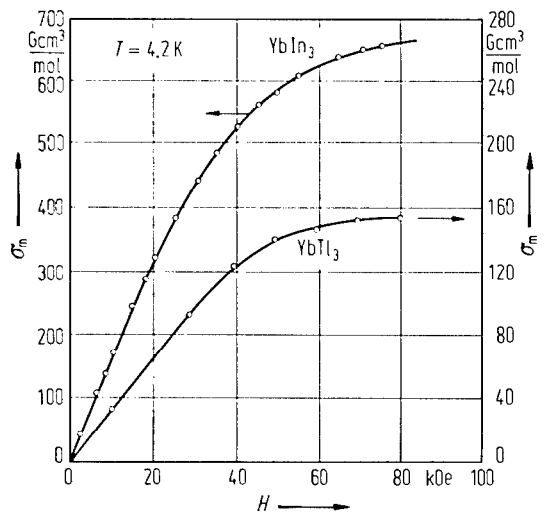

Fig. 141. $YbIn_3$, $YbTl_3$. Magnetic field dependence of σ_m at 4.2 K [74 S 1].

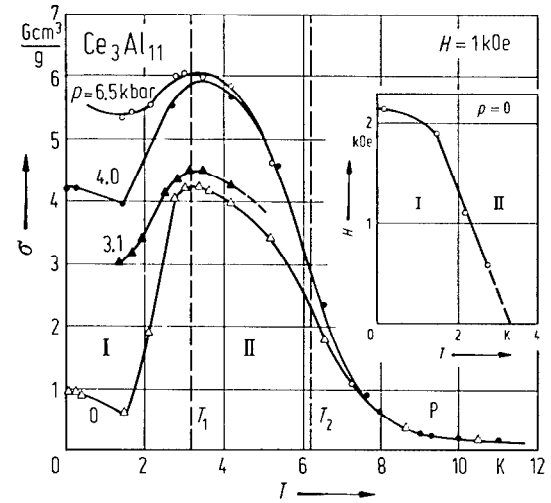

Fig. 142. Ce_3Al_{11}. Magnetization σ in 1 kOe at different pressures vs. temperature. Two ordering temperatures $T_1 = 3.2$ K and $T_2 = 6.2$ K are indicated by vertical lines. The insert shows the thermal variation of the phase transition magnetic field for $p = 0$ kbar. I, II and P indicate the ordered phases I and II and the paramagnetic phase, respectively [80 C 2].

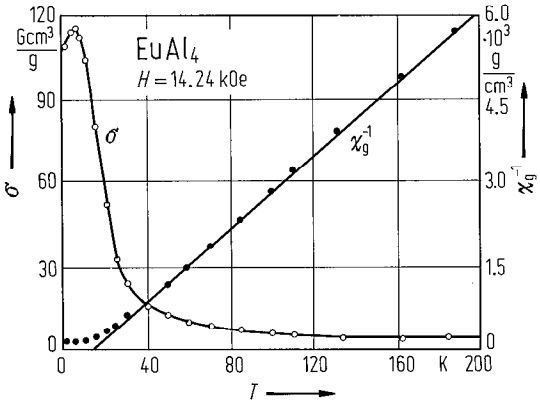

Fig. 143. $EuAl_4$. Temperature dependence of χ_g^{-1} and the magnetization σ at 14.24 kOe [67 W 1].

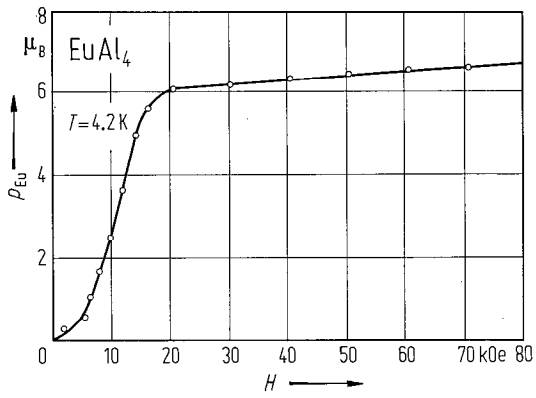

Fig. 144. $EuAl_4$. Magnetic field dependence of p_{Eu} at 4.2 K [67 W 1].

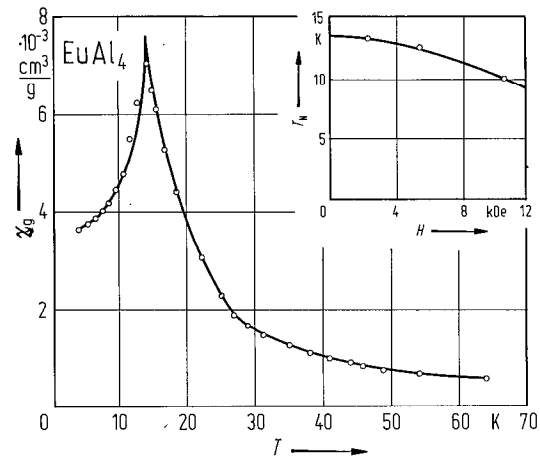

Fig. 145. $EuAl_4$. Temperature dependence of χ_g, and T_N vs. magnetic field (insert) [68 M 2].

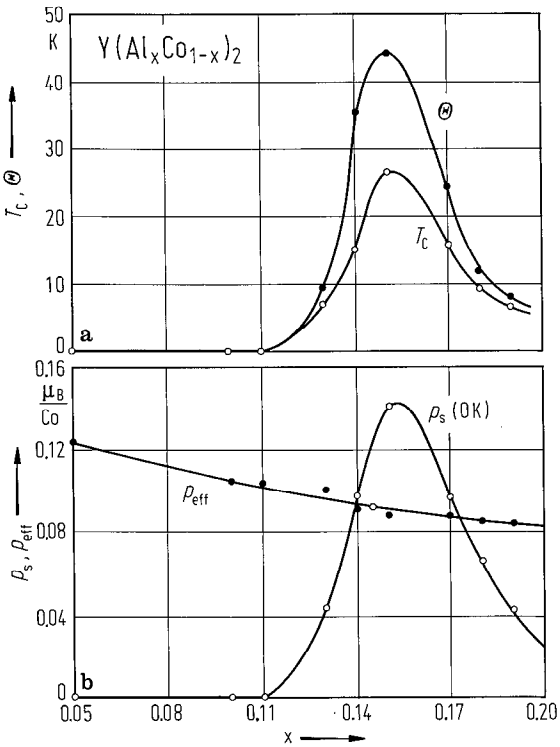

Fig. 146. $Y(Al_xCo_{1-x})_2$. Composition dependence of (a) T_C and Θ, and of (b) the effective paramagnetic moment p_{eff} and of the spontaneous magnetic moment p_s at 0 K [85 Y 1].

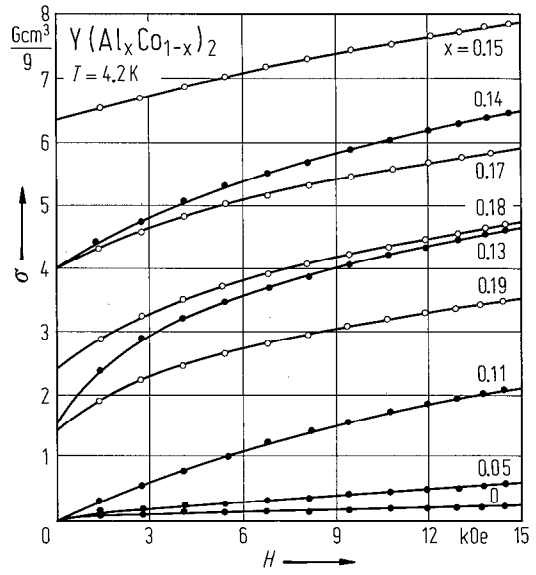

Fig. 147. $Y(Al_xCo_{1-x})_2$. Magnetic field dependence of σ at 4.2 K for $0 \leq x \leq 0.19$ [85 Y 1].

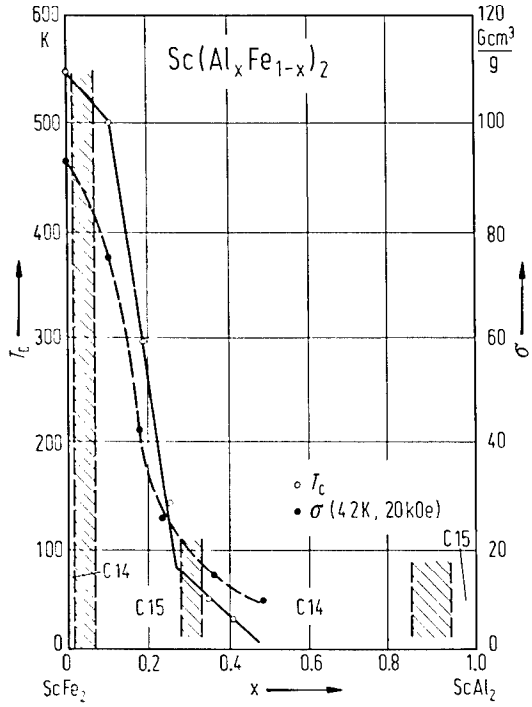

Fig. 148. $Sc(Al_xFe_{1-x})_2$. Composition dependence of the crystal structure (C14, C15), T_C, and σ at 4.2 K and 20 kOe [76 S 1].

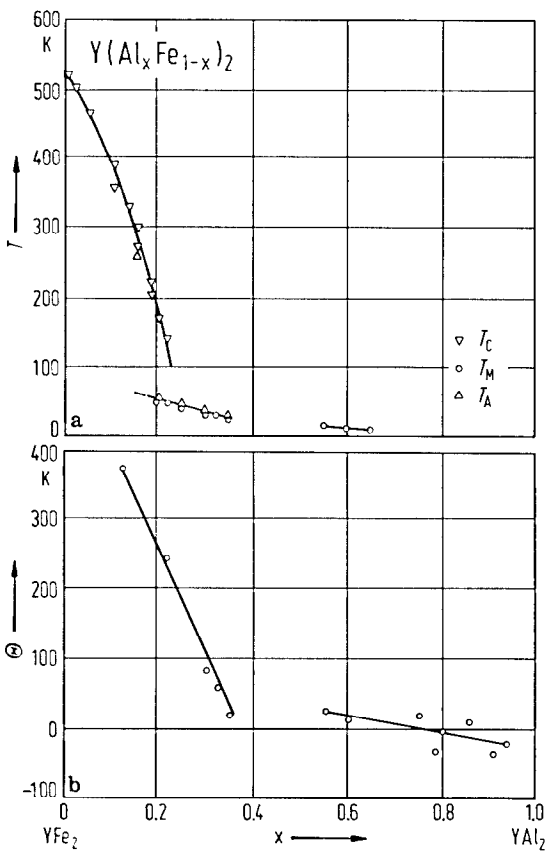

Fig. 150. $Y(Al_xFe_{1-x})_2$. (a) Composition dependence of T_C, freezing temperature T_M and temperature T_A for vanishing magnetic hyperfine splitting (from Mössbauer experiment on ^{57}Fe). (b) Composition dependence of the paramagnetic Curie temperature Θ [84 R 1].

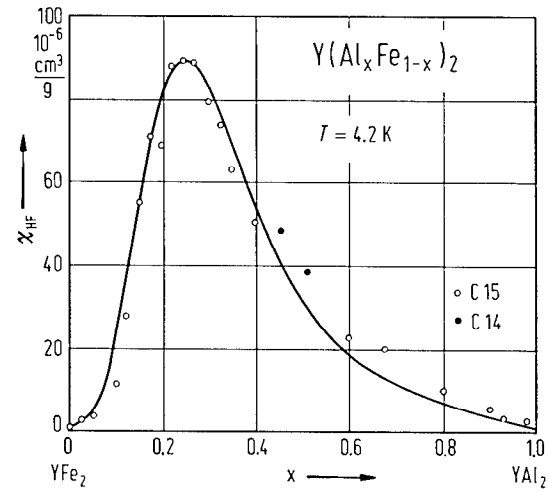

Fig. 149. $Y(Al_xFe_{1-x})_2$. Composition dependence of the magnetic high-field susceptibility at 4.2 K for C15 (open circles) and C14 (solid circles) crystal structures. The theoretical curve is calculated for a local environment model in which the Fe atoms carry a magnetic moment if surrounded by $n \geqq n_0 = 15$ Fe neighbours [78 B 1].

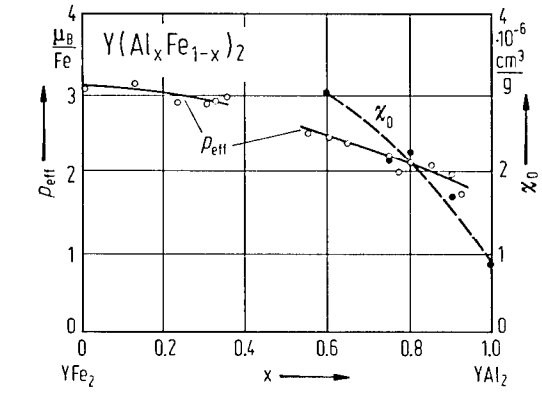

Fig. 151. $Y(Al_xFe_{1-x})_2$. Composition dependence of the mean effective Fe magnetic moment, p_{eff}, and of the temperature-independent contribution χ_0 to the magnetic susceptibility [84 R 1].

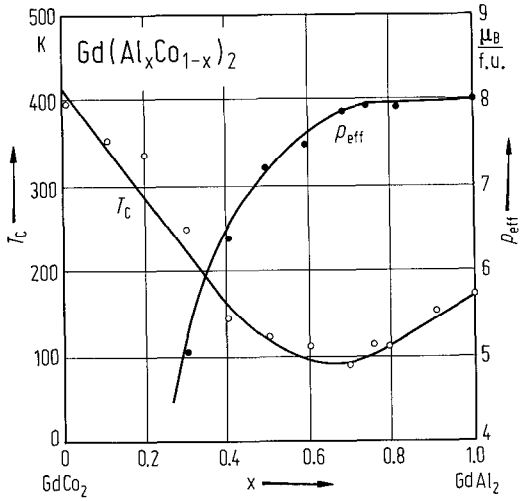

Fig. 152. $Gd(Al_xCo_{1-x})_2$. Composition dependence of p_{eff} and T_C [79 K 1].

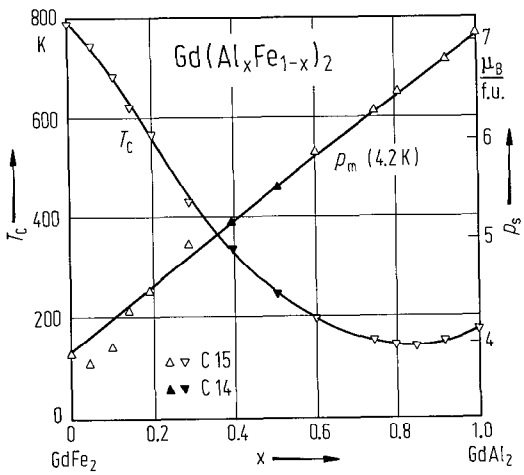

Fig. 154. $Gd(Al_xFe_{1-x})_2$. Composition dependence of T_C and of the saturation magnetic moment p_s at 4.2 K. Open and full symbols are for C15 and C14 structure type, respectively [79 B 4].

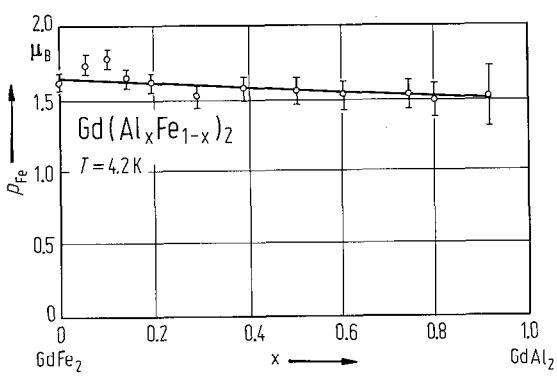

Fig. 156. $Gd(Al_xFe_{1-x})_2$. Concentration dependence of the mean Fe magnetic moment, p_{Fe}, at 4.2 K [79 B 4].

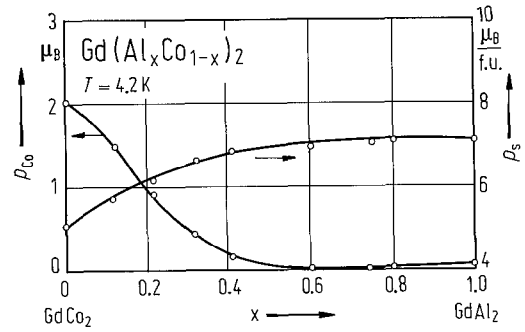

Fig. 153. $Gd(Al_xCo_{1-x})_2$. Composition dependence of the saturation magnetic moment p_s and the Co magnetic moment p_{Co} at 4.2 K [81 B 1]. In deriving p_{Co} a Gd magnetic moment of 7 μ_B was assumed.

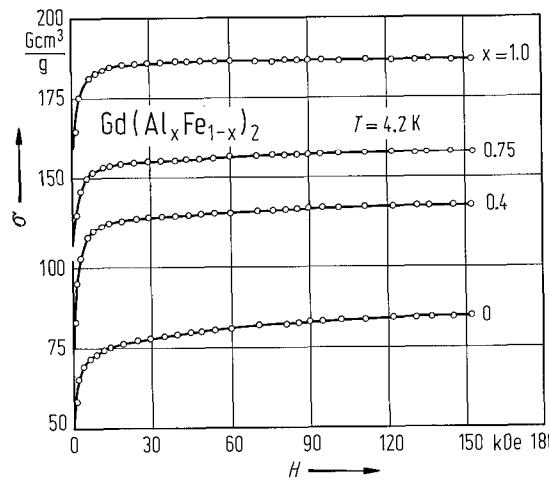

Fig. 155. $Gd(Al_xFe_{1-x})_2$. Magnetic field dependence of σ at 4.2 K [79 B 4].

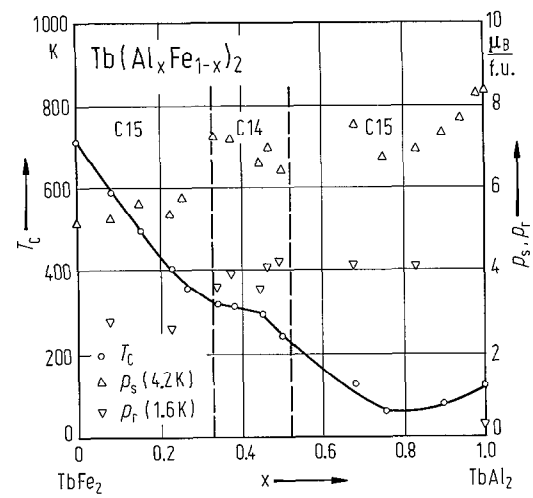

Fig. 157. $Tb(Al_xFe_{1-x})_2$. Composition dependence of T_C, the saturation magnetic moment p_s at 4.2 K, and the remanent magnetic moment p_r at 1.6 K. C15 and C14 indicate the crystal structure [76 O 1].

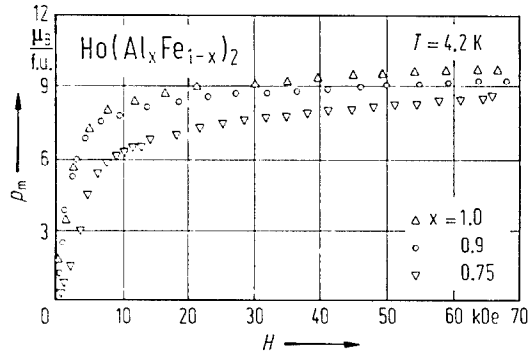

Fig. 158. $Ho(Al_xFe_{1-x})_2$. Magnetic field dependence of p_m at 4.2 K [85 S 2].

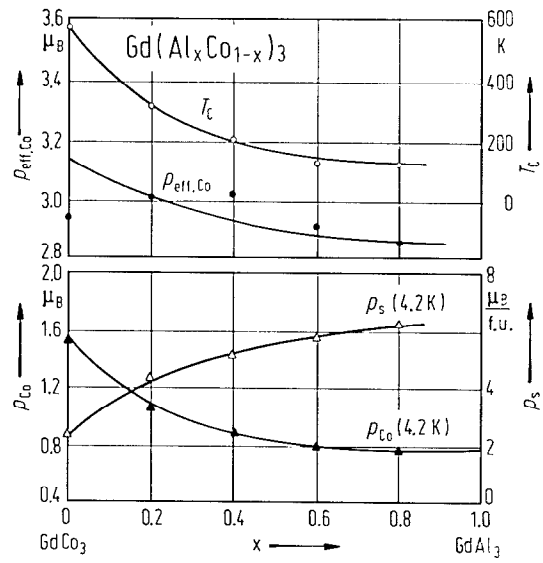

Fig. 159. $Gd(Al_xCo_{1-x})_3$. Composition dependence of the Curie temperature T_C, the saturation magnetization p_s and the mean Co magnetic moment p_{Co} at 4.2 K, and the Co effective magnetic moment $p_{eff,Co}$ [82 B 3]. In deriving p_{Co} a Gd magnetic moment of 7 μ_B was assumed.

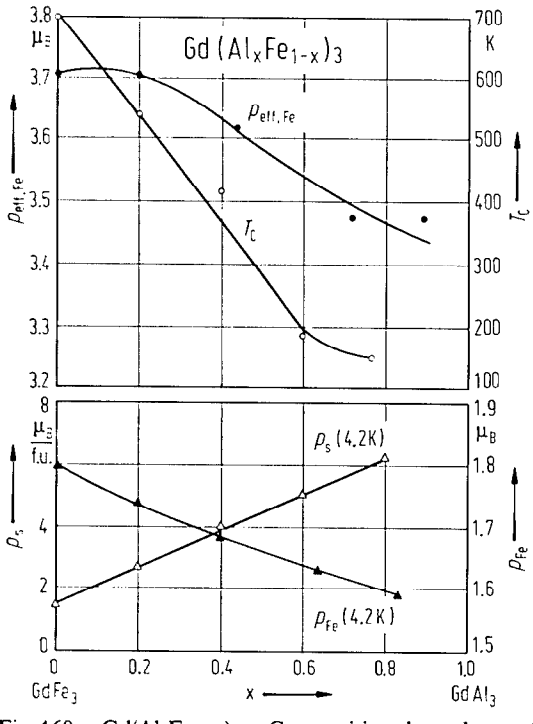

Fig. 160. $Gd(Al_xFe_{1-x})_3$. Composition dependence of the Curie temperature T_C, the saturation magnetic moment p_s and the mean Fe magnetic moment p_{Fe} at 4.2 K, and the effective Fe magnetic moment $p_{eff,Fe}$ [82 B 2]. In deriving p_{Fe} a Gd magnetic moment of 7 μ_B was assumed.

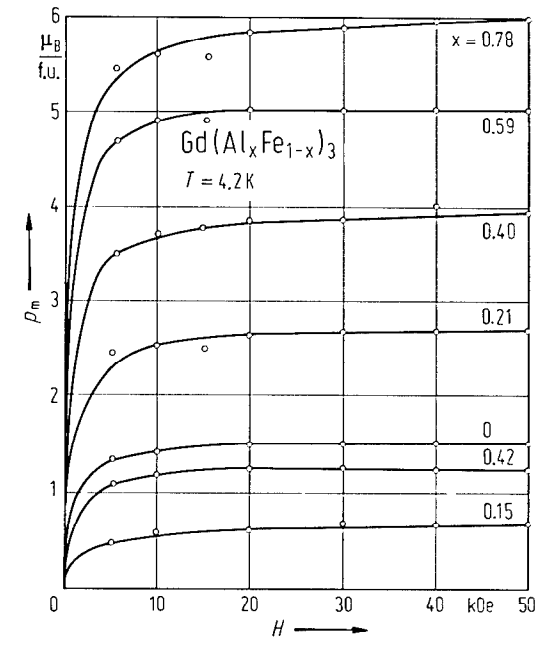

Fig. 161. $Gd(Al_xFe_{1-x})_3$. Magnetic field dependence of p_m at 4.2 K [82 B 2].

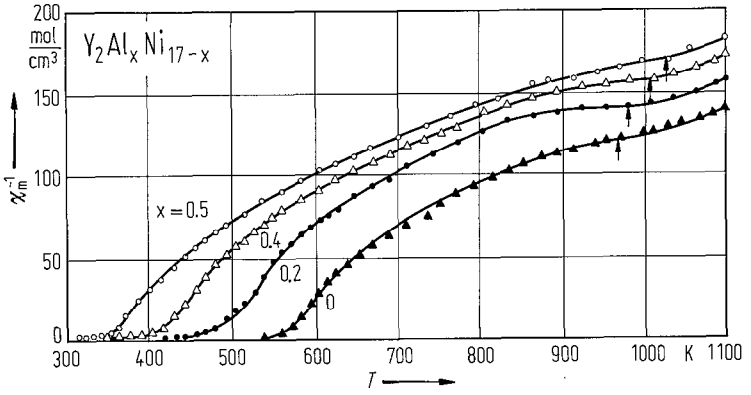

Fig. 162. $Y_2Al_xNi_{17-x}$. Temperature dependence of χ_m^{-1} for different compositions. The arrows indicate the Néel temperatures [83 C 1].

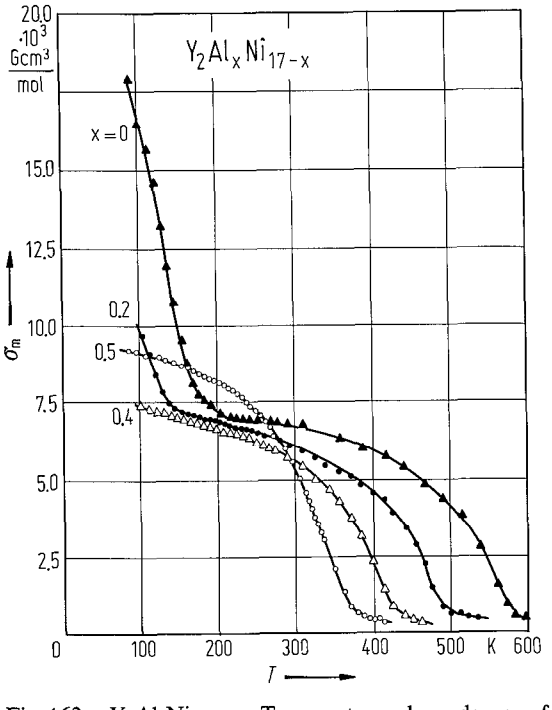

Fig. 163. $Y_2Al_xNi_{17-x}$. Temperature dependence of σ_m for different compositions [83 C 1].

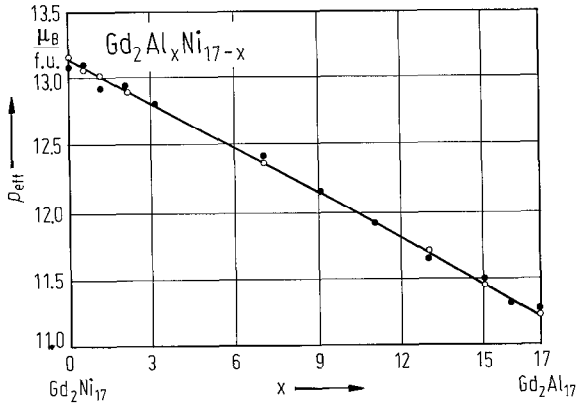

Fig. 164. $Gd_2Al_xNi_{17-x}$. Composition dependence of the effective magnetic moment per formula unit, p_{eff}. Solid circles: experimental values, open circles: values calculated for $p_{eff,Gd} = 7.94\,\mu_B$ and $p_{eff,Ni} = 1.64\,\mu_B$ [79 P 1].

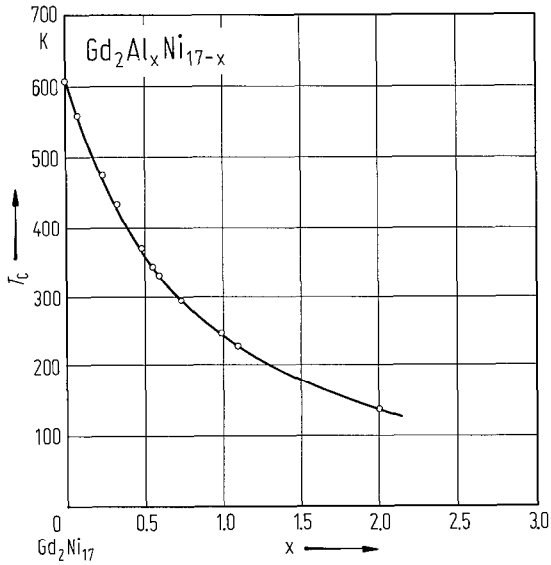

Fig. 165. $Gd_2Al_xNi_{17-x}$. Composition dependence of T_C [82 P 1].

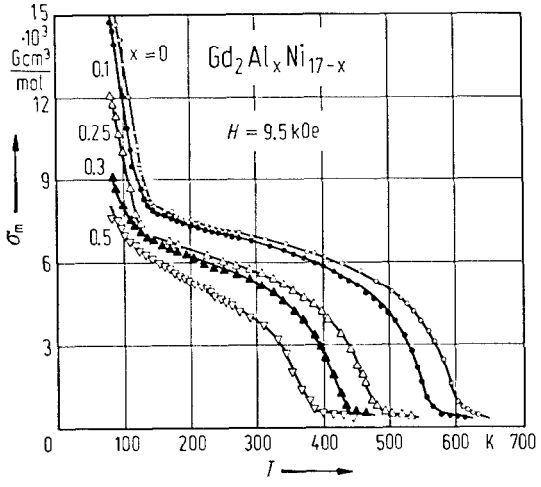

Fig. 166. $Gd_2Al_xNi_{17-x}$. Temperature dependence of σ_m at 9.5 kOe for different compositions [82 P 1].

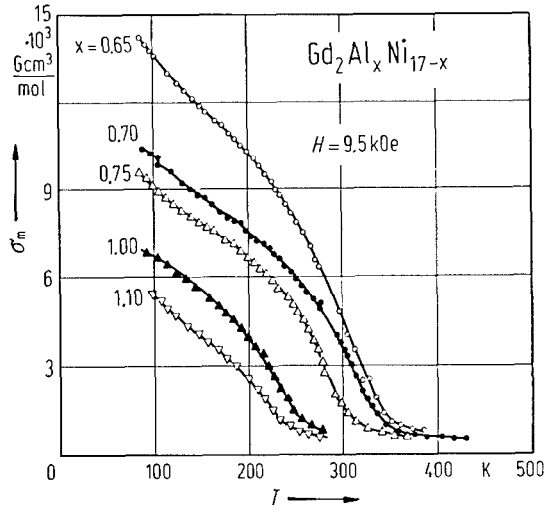

Fig. 167. $Gd_2Al_xNi_{17-x}$. Temperature dependence of σ_m at 9.5 kOe for different compositions [82 P 1].

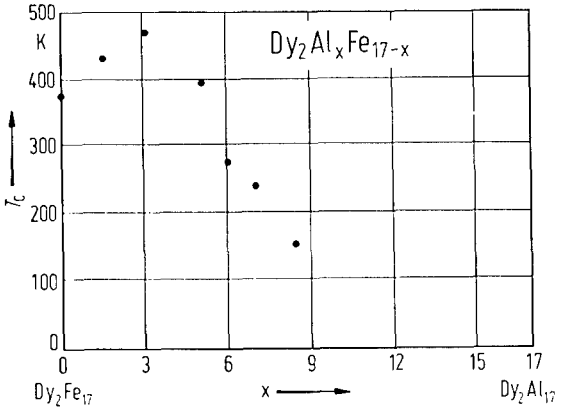

Fig. 168. $Dy_2Al_xFe_{17-x}$. Composition dependence of T_C [85 R 1].

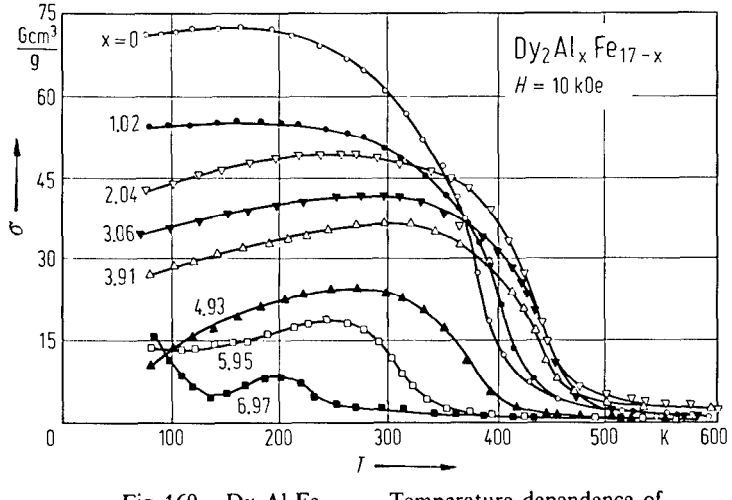

Fig. 169. $Dy_2Al_xFe_{17-x}$. Temperature dependence of σ at 10 kOe for different compositions [84 P 2].

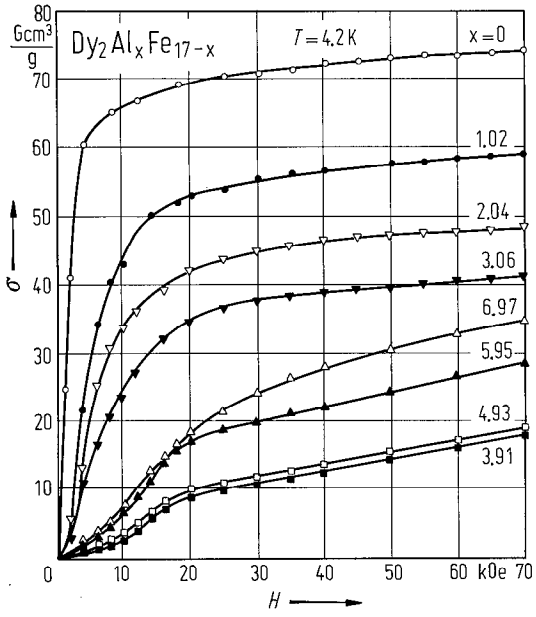

Fig. 170. $Dy_2Al_xFe_{17-x}$. Magnetic field dependence of σ at 4.2 K for different compositions [84 P 2].

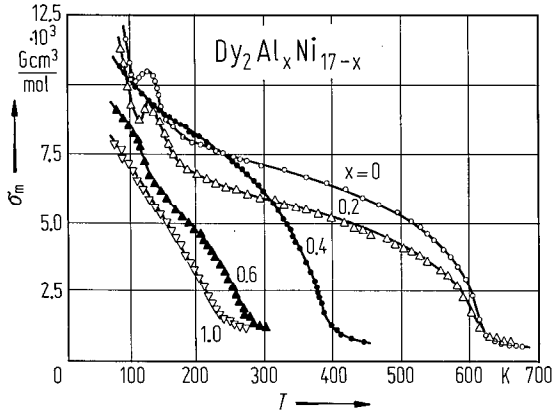

Fig. 172. $Dy_2Al_xNi_{17-x}$. Temperature dependence of σ_m for different compositions [83 C 1].

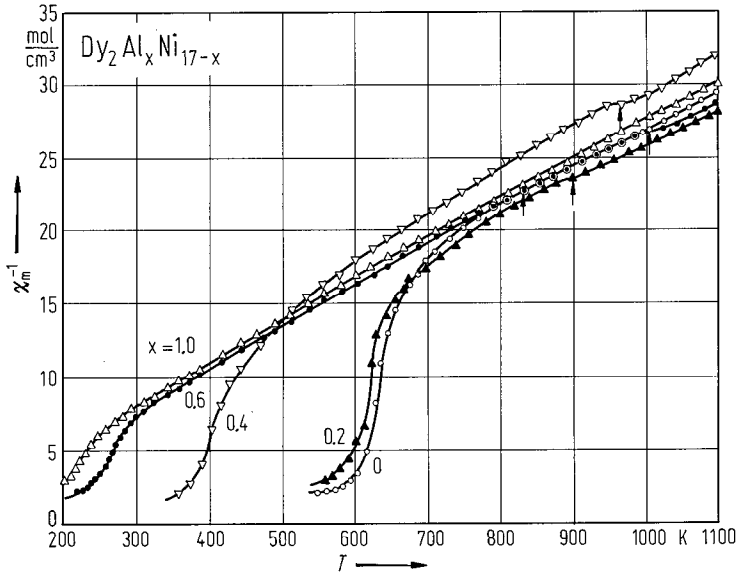

Fig. 171. $Dy_2Al_xNi_{17-x}$. Temperature dependence of χ_m^{-1} for different compositions. The arrows indicate the Néel temperatures [83 C 1].

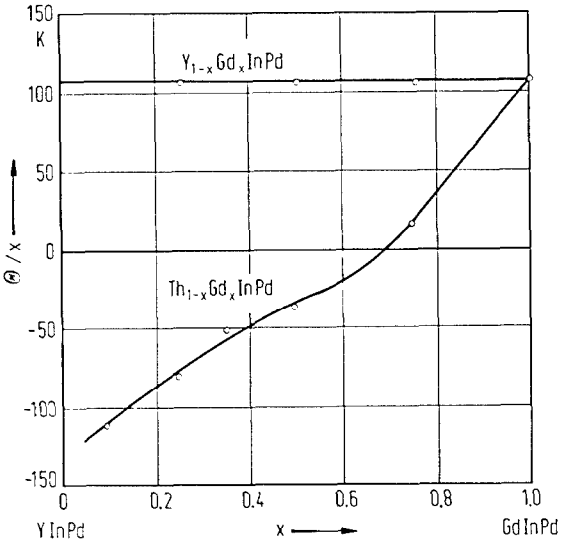

Fig. 173. $M_{1-x}Gd_xInPd$, M = Y, Th. Composition dependence of Θ/x [75 B 2].

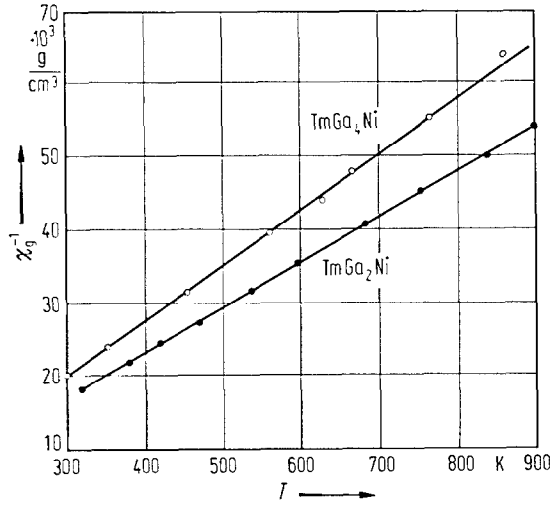

Fig. 175. $TmGa_2Ni$, $TmGa_4Ni$. Temperature dependence of χ_g^{-1} [81 Y 1].

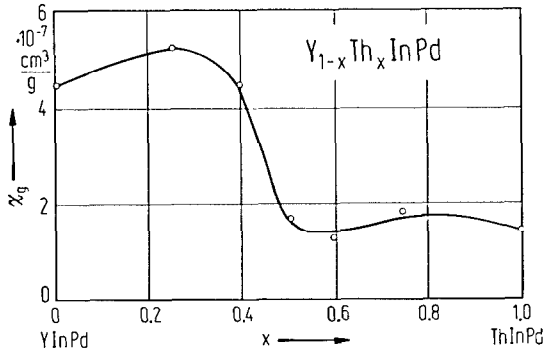

Fig. 174. $Y_{1-x}Th_xInPd$. Composition dependence of χ_g at room temperature [75 B 2].

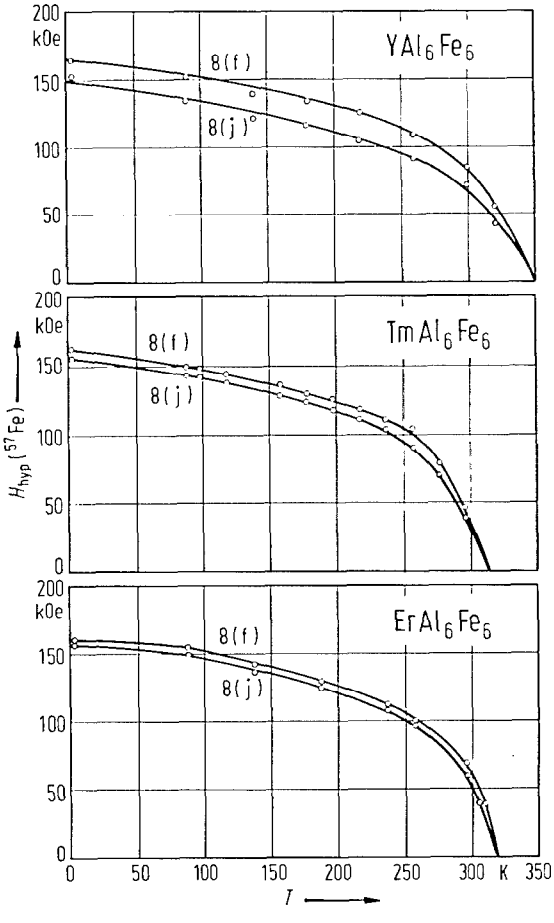

Fig. 176. RAl_6Fe_6, R = Er, Tm, Y. Temperature dependence of hyperfine fields H_{hyp} for ^{57}Fe on 8(f) and 8(j) sites (cf. Fig. 179) [81 F 2]. See Fig. 182 for R = Gd, Tb and Ho.

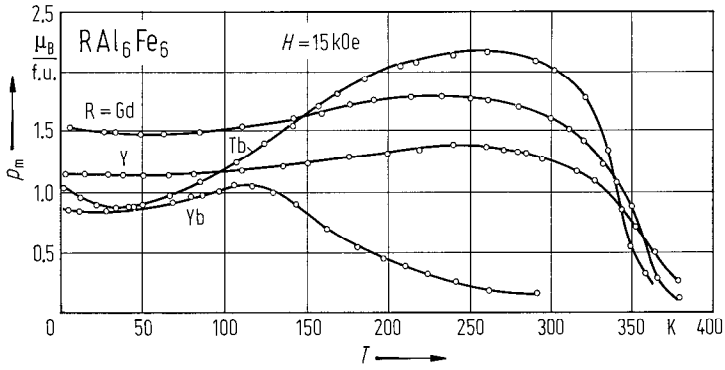

Fig. 177. RAl_6Fe_6, R = Yb, Y, Gd, Tb. Temperature dependence of p_m at 15 kOe [81 F 2].

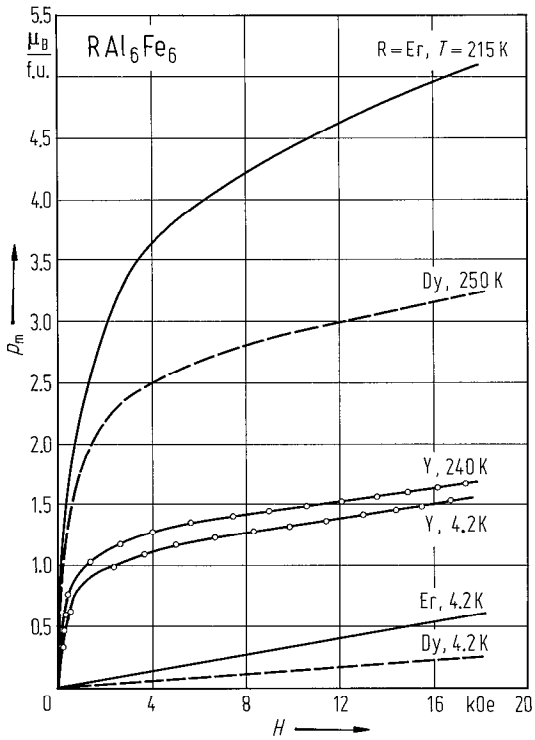

Fig. 178. RAl_6Fe_6, R = Dy, Er, Y. Magnetic field dependence of p_m [81 F 2].

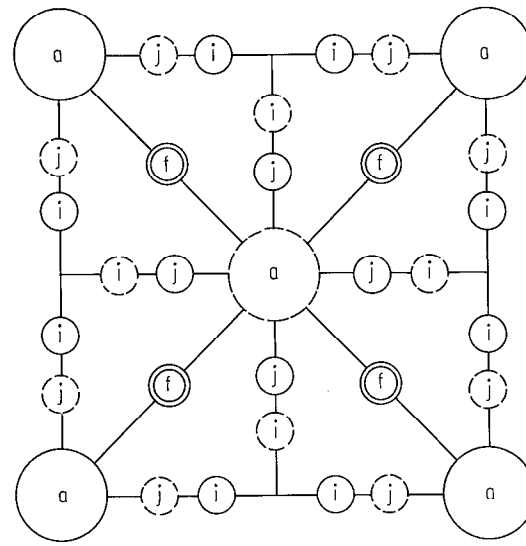

Fig. 179. $ThMn_{12}$-type structure of I4/mmm space group. Th atoms on the 2(a) sites and Mn atoms on the sites 8(j) and 8(i) lie in the planes $z = 0$ (full lines) or $z = 1/2$ (dashed lines). Mn atoms on the site 8(f) lie in $z = 1/4$ and $z = 3/4$ [77 D 1]. In the case of RAl_xT_{12-x} compounds where R is a rare earth and T is a transition metal atom the unit cell contains two formula units. The R ions occupy the 2(a) sites, the 8(f) and 8(i) sites are the majority T and Al sites, respectively. The Fe atom on the 8(i) site is nonmagnetic. The Fe atom on the 8(f) site shows an antiferromagnetic intrasublattice exchange with the ferromagnetic component, while the Fe atom on the 8(j) site shows a ferromagnetic intrasublattice exchange [78 B 3, 78 F 1, 79 F 1, 81 F 2, 83 F 1]. In the case of RAl_8Fe_4, the Fe ions occupy in majority the 8(f) site, but about 20% of the Fe ions occupy the 8(j) and 8(i) sites. In the case of RAl_6Fe_6, the Fe ions occupy the 8(f), 8(j) and 8(i) sites in about 58, 36 and 6%, respectively. The situation in the RAl_7Fe_5 compounds is very similar [83 F 1]. The R–R exchange was suggested to be ferromagnetic [78 B 3, 81 F 2, 83 F 1]. But no indication of R sublattice ordering was observed from neutron diffraction for $ErAl_8Fe_4$ and $DyAl_8Fe_4$ at 4.2 K [83 S 3]. The Curie temperature was taken from the $\chi^{-1}(T)$ data in the manner indicated in Fig. 185.

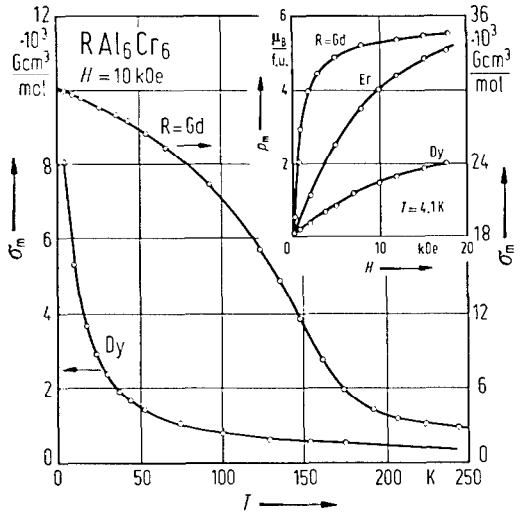

Fig. 180. RAl_6Cr_6, R = Gd, Dy, Er. Temperature dependence of σ_m at 10 kOe for R = Gd and Dy. Inset: magnetic field dependence of p_m at 4.1 K [81 F 1].

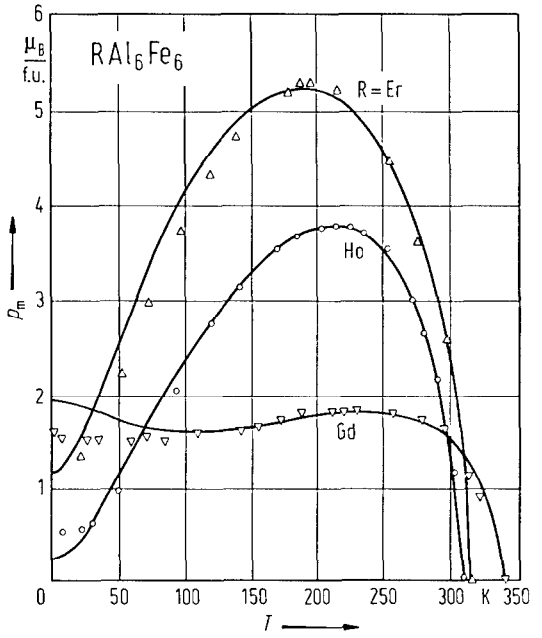

Fig. 181. RAl_6Fe_6, R = Gd, Ho, Er. Theoretical magnetization p_m curves calculated from the molecular field model by the approximate formula

$$g_J\mu_B J H_m(T) = A_{RR}(g_J-1)^2 J^2 \sigma_R(T) + A_{RFe}(g_J-1) J S_{Fe}\sigma_{Fe}(T),$$

where σ_R and σ_{Fe} are normalized sublattice magnetizations. The experimental points were obtained from the experimental curves at high magnetic fields. The points at high temperatures ($T > 0.9\,T_C$) were taken from low-field measurements ($H \to 0$). The theoretical curves (solid curves) were renormalized by a factor RN < 1 which represents the degree of saturation. RN = 0.9, 0.85 and 0.55 for R = Er, Ho and Gd, respectively [81 F 2].

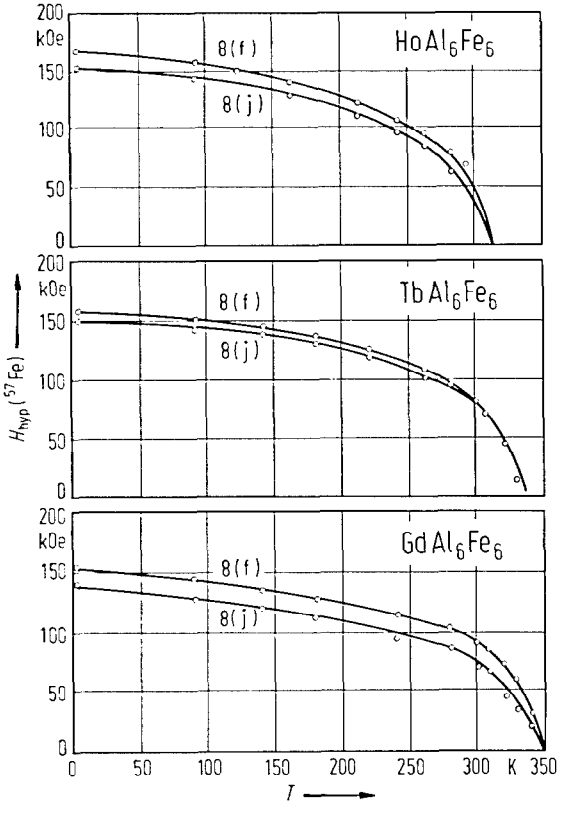

Fig. 182. RAl_6Fe_6, R = Gd, Tb, Ho. Temperature dependence of hyperfine fields H_{hyp} for ^{57}Fe on the 8(f) and 8(j) sites (see Fig. 179) [81 F 2]. For R = Er, Tm and Y, see Fig. 176.

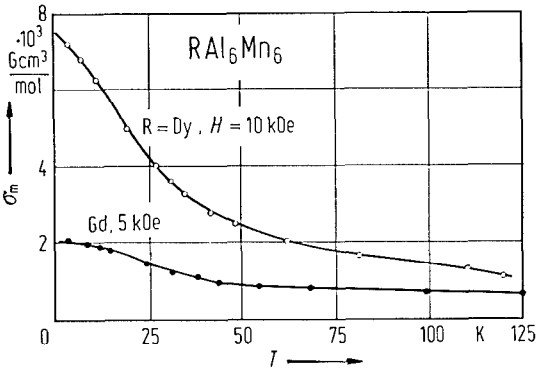

Fig. 183. RAl_6Mn_6, R = Gd, Dy. Temperature dependence of σ_m at 5 kOe (Gd) and 10 kOe (Dy) [81 F 1].

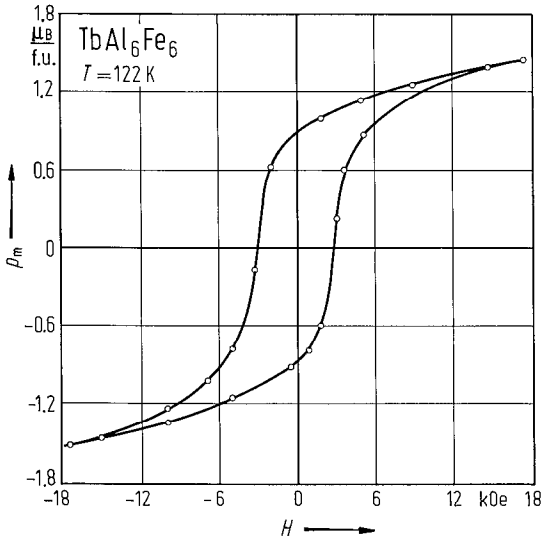

Fig. 184. $TbAl_6Fe_6$. Hysteresis curve at 122 K [81 F 2].

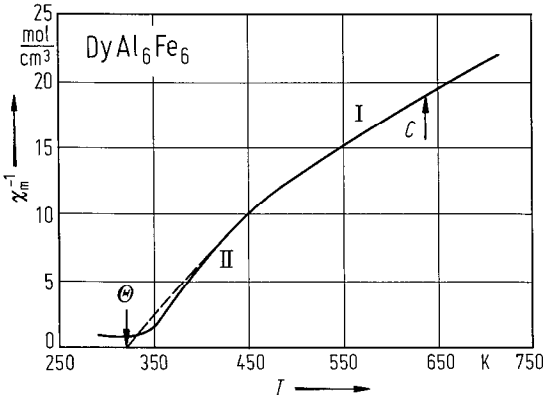

Fig. 185. $DyAl_6Fe_6$. Temperature dependence of χ_m^{-1}. The Curie constant C is taken from the χ_m^{-1} slope in range I and the paramagnetic Curie temperature Θ is the intercept of χ_m^{-1} extrapolation and temperature axis in range II [81 F 2].

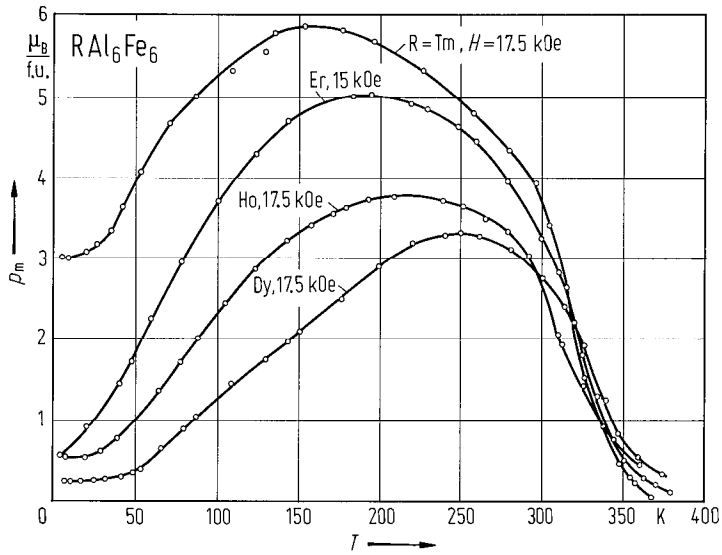

Fig. 186. RAl_6Fe_6, R = Dy, Ho, Er, Tm. Temperature dependence of p_m for 15 kOe (Er) and 17.5 kOe (Dy, Ho, Tm) [81 F 2].

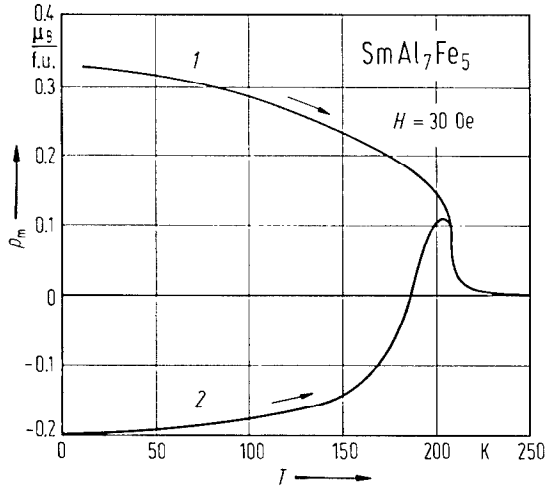

Fig. 187. $SmAl_7Fe_5$. Temperature dependence of p_m at various speeds of the cooling process; slow cooling (*1*) and fast cooling (*2*) [83 F 1].

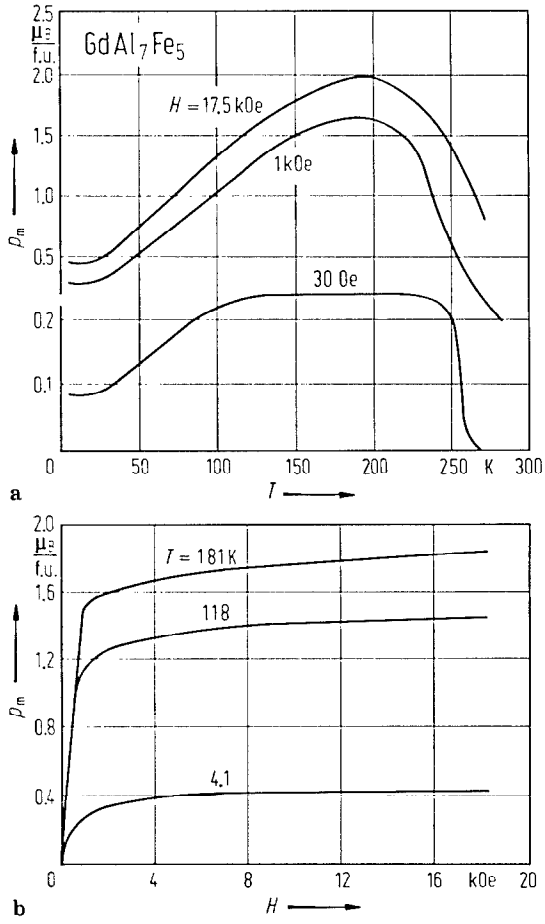

Fig. 189. $GdAl_7Fe_5$. (a) Temperature dependence of p_m for 30 Oe, 1 kOe and 17.5 kOe. (b) Magnetic field dependence of p_m for 4.1, 118 and 181 K [83 F 1].

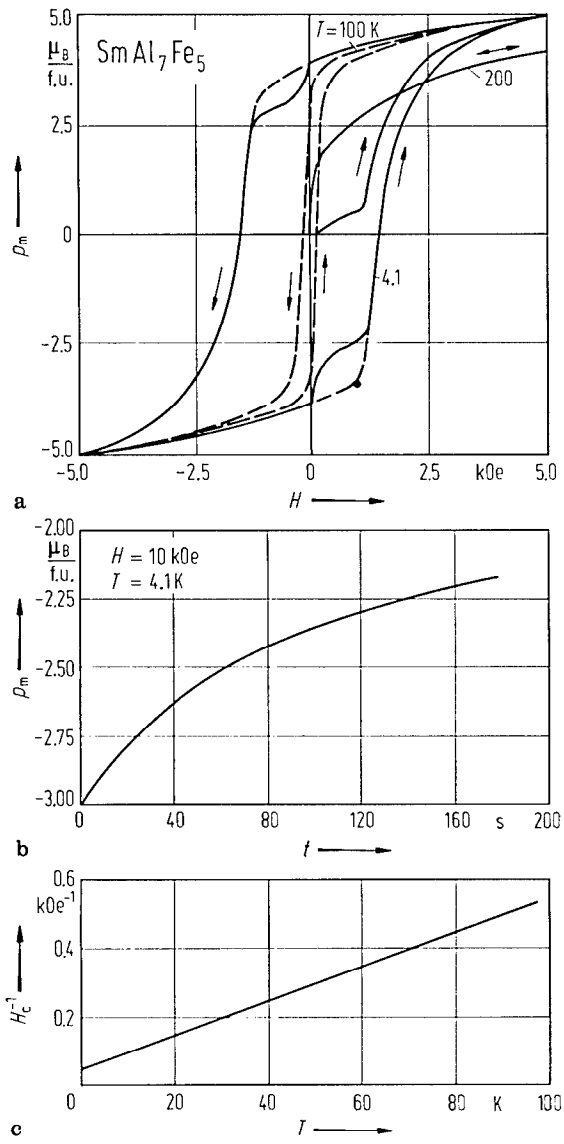

Fig. 188. $SmAl_7Fe_5$. (a) Hysteresis curves. The dashed line in the 4.1 K curve refers to measurements in which the magnetic field was changed rapidly. The solid circle shows the initial condition for the time-dependent phenomenon depicted in (b). (b) Time dependence of the magnetic moment after switching on the magnetic field from 0 to 10 kOe at the bottom point of the hysteresis curve. (c) Temperature dependence of the coercive field [83 F 1].

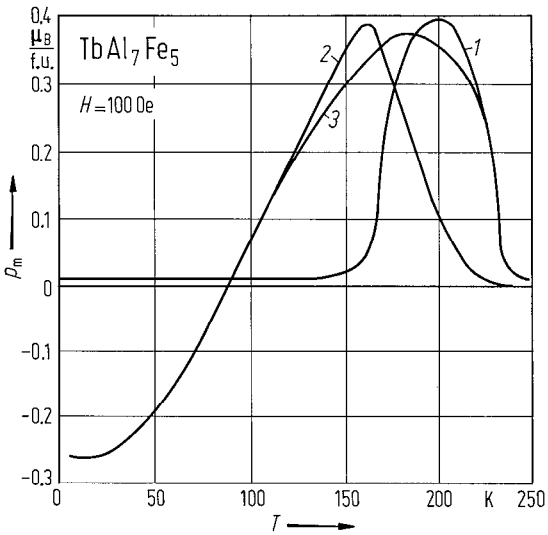

Fig. 190. $TbAl_7Fe_5$. Temperature dependence of the magnetization in 100 Oe for sample cooled to 4.1 K in zero magnetic field (*1*) and 100 Oe for increasing (*2*) and decreasing (*3*) temperature [83 F 1].

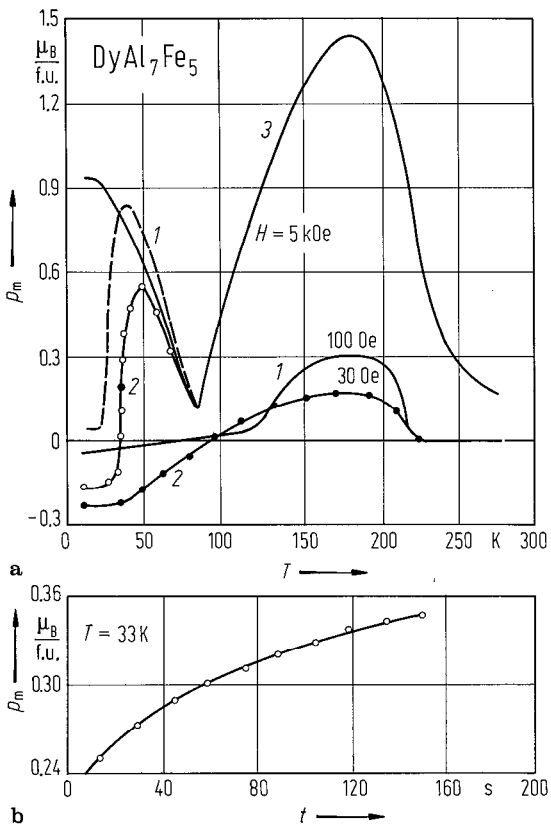

Fig. 192. $DyAl_7Fe_5$. (a) Temperature dependence of p_m. Sample cooled to 4.1 K in ≅1 Oe (*1*), 30 Oe (*2*), and 5 kOe (*3*). Time dependence of p_m at 33 K (solid circle of curve *2*) is shown in (b) [83 F 1].

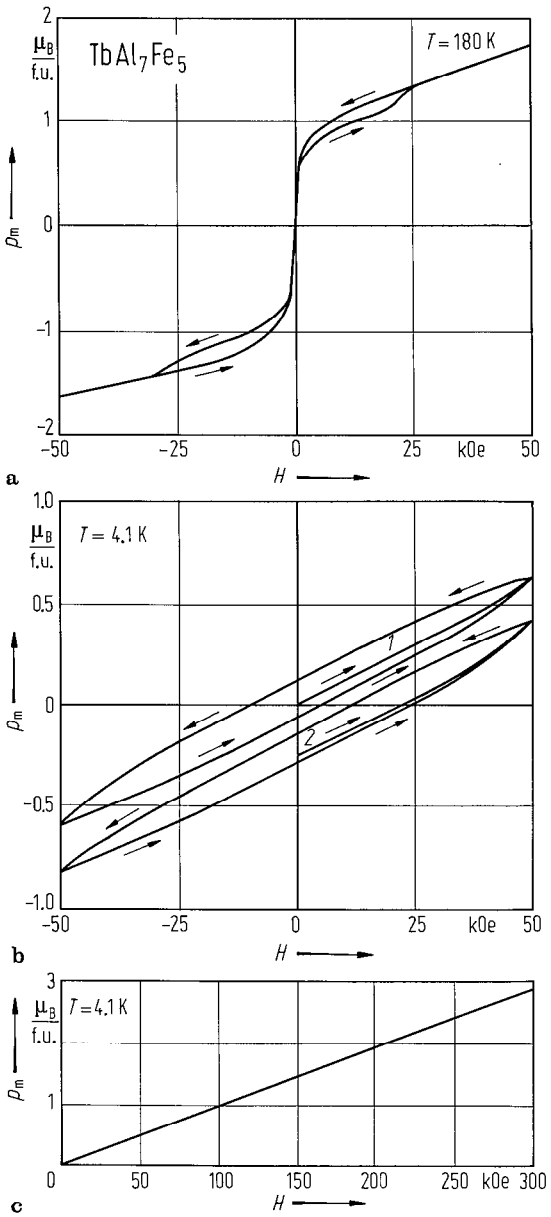

Fig. 191. $TbAl_7Fe_5$. (a) Hysteresis curve at 180 K. (b) Hysteresis curves at 4.1 K for sample cooled to 4.1 K in zero magnetic field (*1*) and in 100 Oe (*2*), respectively. (c) Linear magnetization p_m at 4.1 K up to 300 kOe [83 F 1].

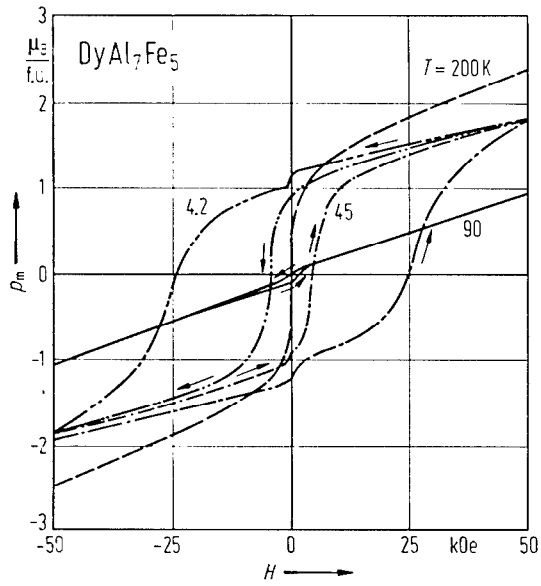

Fig. 193. $DyAl_7Fe_5$. Hysteresis curves at different temperatures [83 F 1].

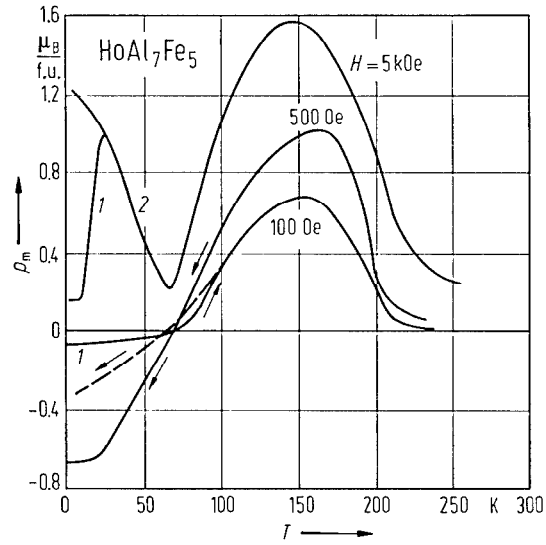

Fig. 194. $HoAl_7Fe_5$. Temperature dependence of p_m. Sample cooled to 4.1 K in 30 Oe (*1*) and 5 kOe (*2*) [83 F 1].

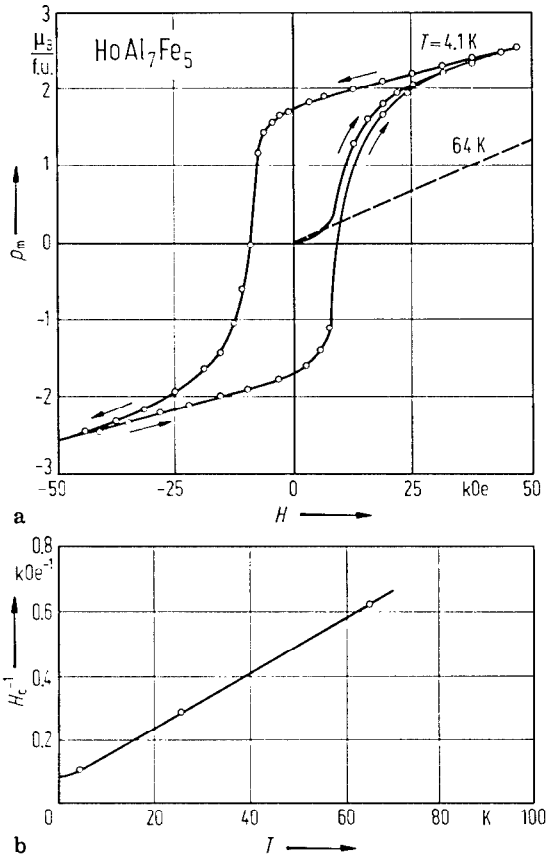

Fig. 195. $HoAl_7Fe_5$. (a) Hysteresis curves at 4.1 K and 64 K. (b) Temperature dependence of the coercive field H_c [83 F 1].

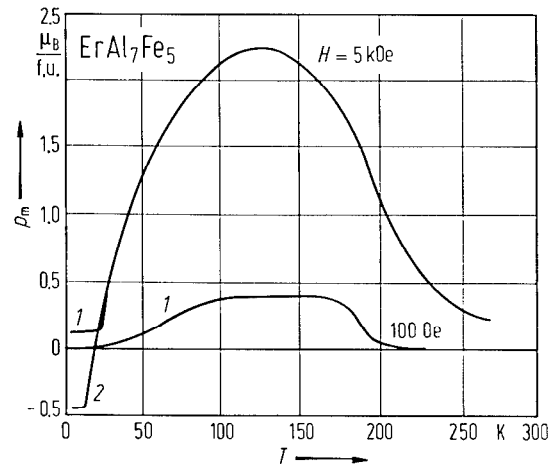

Fig. 196. $ErAl_7Fe_5$. Temperature dependence of p_m. The curves were obtained when sample was cooled to 4.1 K in zero magnetic field (*1*) and in 5 kOe (*2*), respectively [83 F 1].

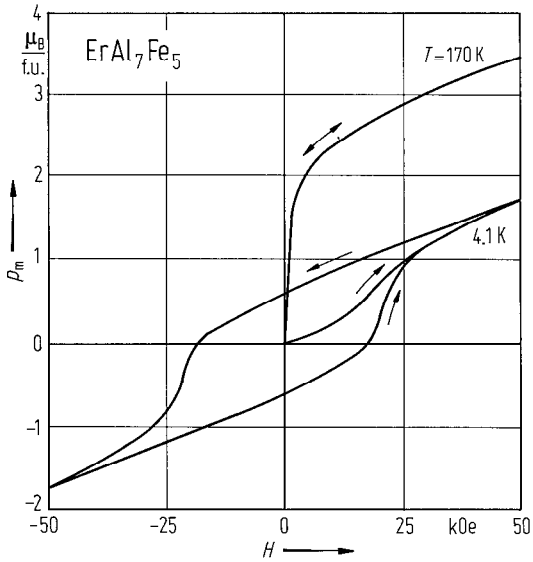

Fig. 197. $ErAl_7Fe_5$. Hysteresis curves at 4.1 K and 170 K [83 F 1].

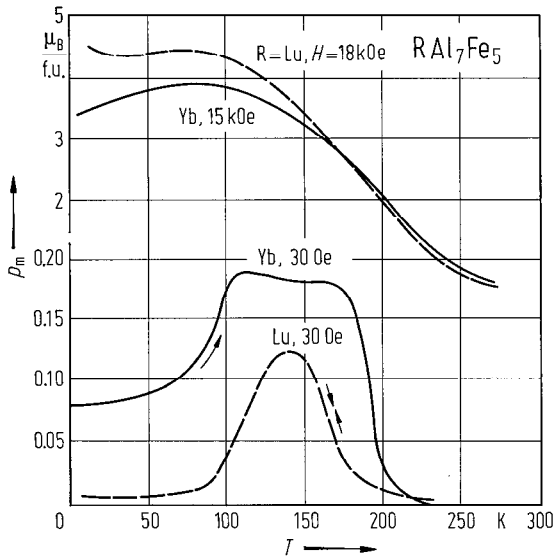

Fig. 198. RAl_7Fe_5, R = Yb, Lu. Temperature dependence of p_m for 30 Oe (Yb, Lu), 15 kOe (Yb) and 18 kOe (Lu) [83 F 1].

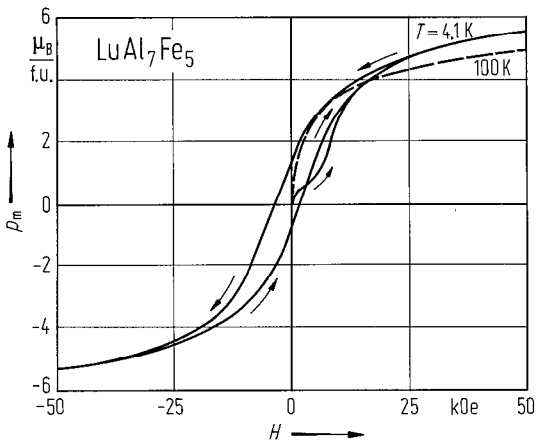

Fig. 199. $LuAl_7Fe_5$. Hysteresis curves. Almost identical curves were obtained for YAl_7Fe_5 and $YbAl_7Fe_5$ [83 F 1].

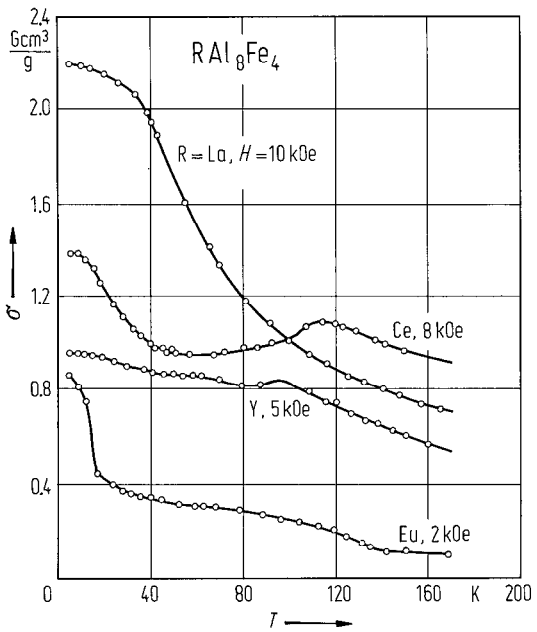

Fig. 200. RAl_8Fe_4, R = La, Ce, Eu, Y. Temperature dependence of σ at 2 kOe (Eu), 5 kOe (Y), 8 kOe (Ce) and 10 kOe (La) [78 F 1].

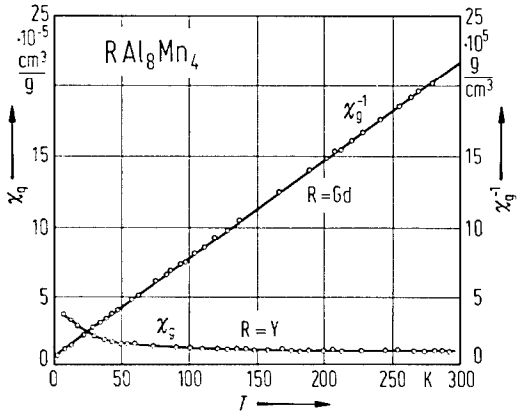

Fig. 201. RAl_8Mn_4, R = Gd, Y. Temperature dependence of χ_g (Y) and χ_g^{-1} (Gd) [78 B 3].

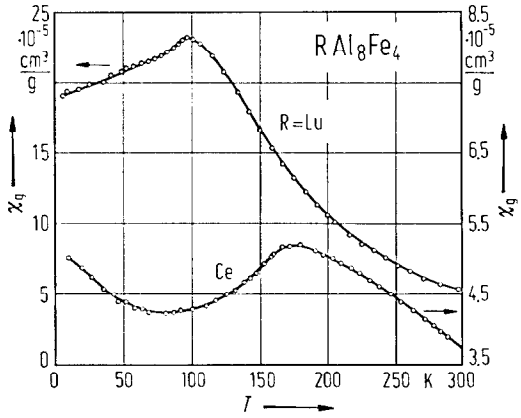

Fig. 202. RAl_8Fe_4, R = Ce, Lu. Temperature dependence of χ_g [78 B 3].

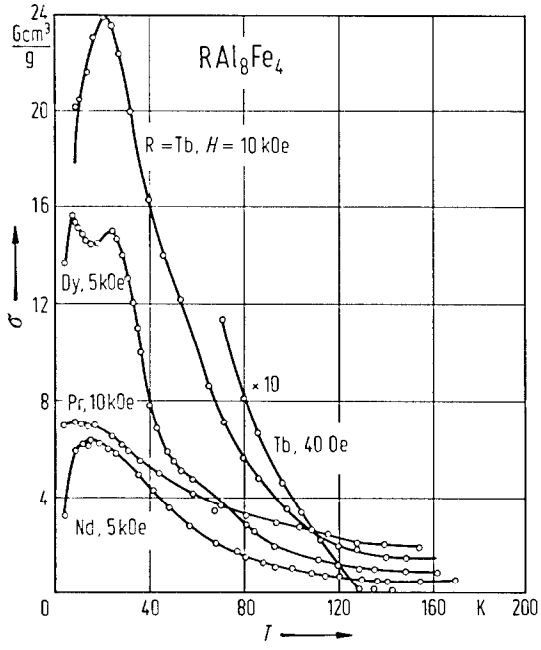

Fig. 203. RAl_8Fe_4, R = Pr, Nd, Tb, Dy. Temperature dependence of σ for 40 Oe (Tb), 5 kOe (Nd, Dy) and 10 kOe (Pr, Tb) [78 F 1].

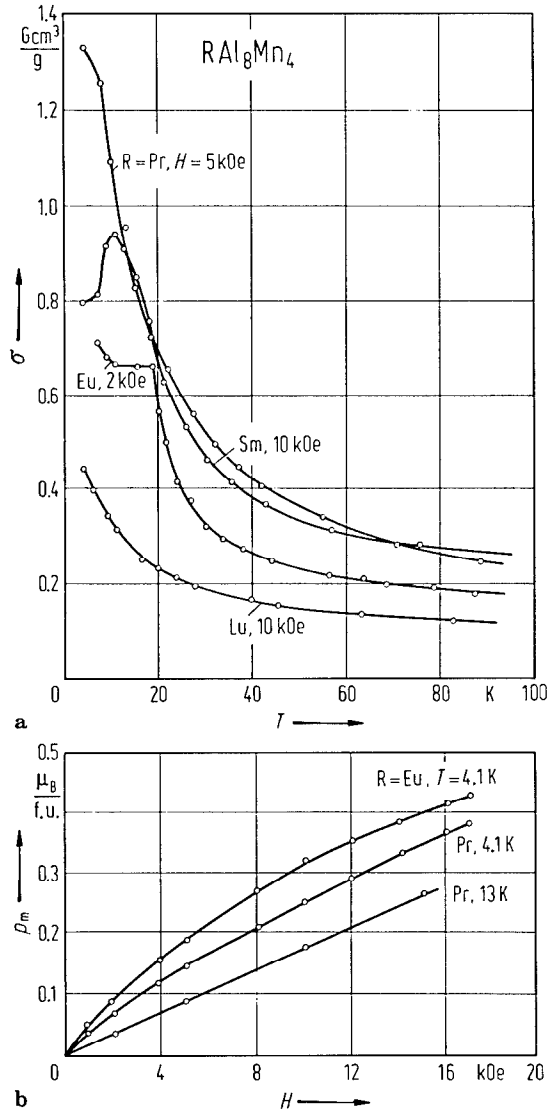

Fig. 204. RAl_8Mn_4, R = Pr, Sm, Eu, Lu. (a) Temperature dependence of σ for 2 kOe (Eu), 5 kOe (Pr) and 10 kOe (Sm, Lu), and (b) magnetic field dependence of p_m for 4.1 K (Pr, Eu) and 13 K (Pr) [79 F 1].

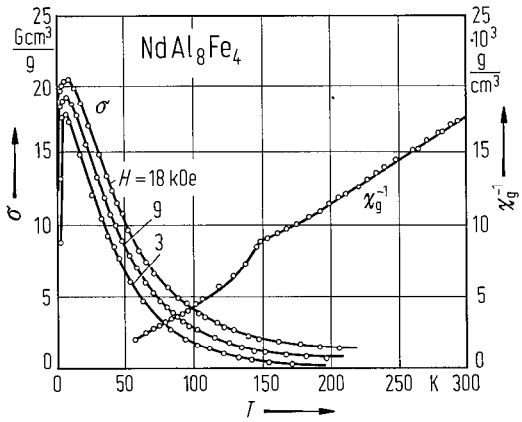

Fig. 205. $NdAl_8Fe_4$. Temperature dependence of σ for 3, 9 and 18 kOe, and χ_g^{-1} [78 B 3]. See also Fig. 203.

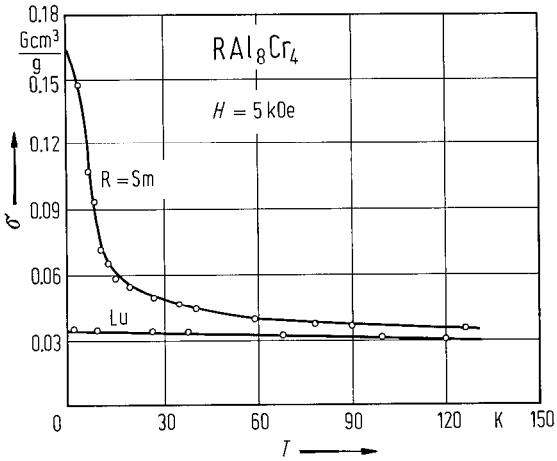

Fig. 206. RAl_8Cr_4, R = Sm, Lu. Temperature dependence of σ at 5 kOe [79 F 1].

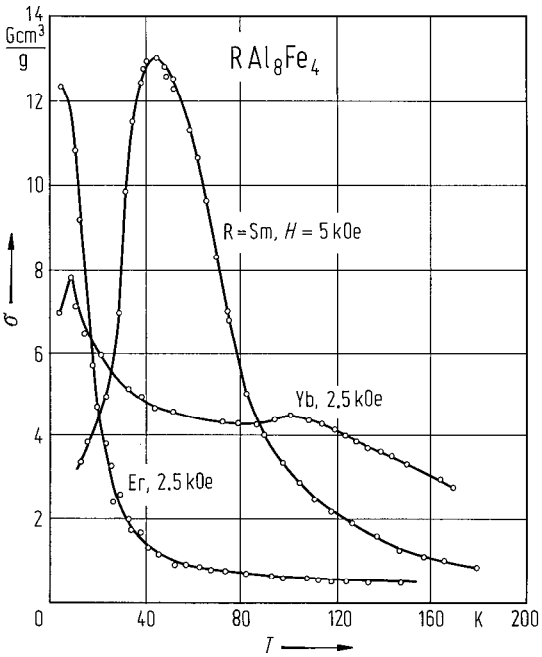

Fig. 207. RAl_8Fe_4, R = Sm, Er, Yb. Temperature dependence of σ for 2.5 kOe (Er, Yb) and 5 kOe (Sm) [78 F 1].

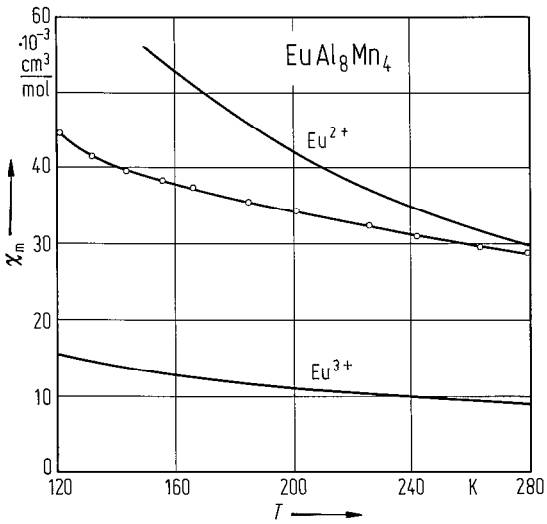

Fig. 208. $EuAl_8Mn_4$. Magnetic molar susceptibility χ_m and theoretical $Eu^{3+}Al_8Mn_4$ and $Eu^{2+}Al_8Mn_4$ curves. For calculation of the Mn contribution to the susceptibility a value of $p_{eff} = 1.5\,\mu_B$/Mn and $\Theta = 6$ K was assumed [79 F 1].

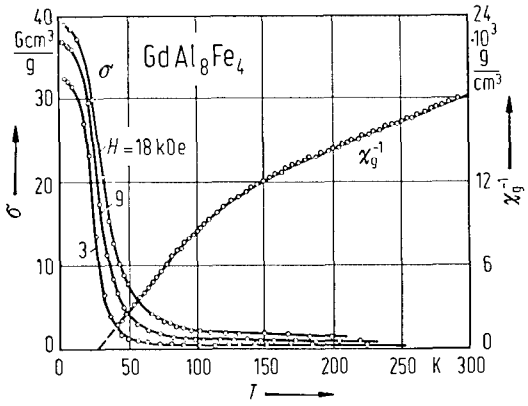

Fig. 210. $GdAl_8Fe_4$. Temperature dependence of σ at 3, 9 and 18 kOe, and χ_g^{-1} [78 B 3].

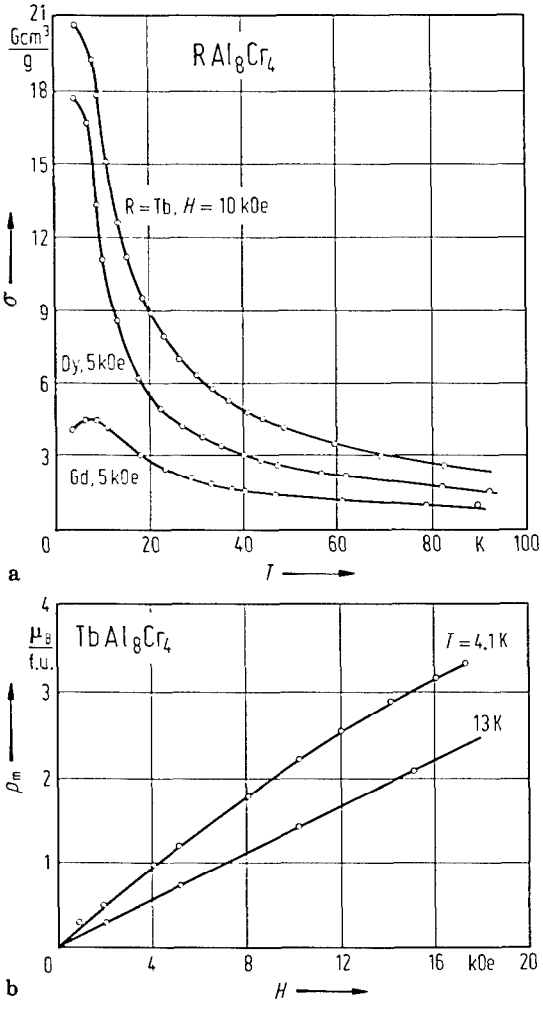

Fig. 209. RAl_8Cr_4, R = Gd, Tb, Dy. (a) Temperature dependence of σ for 5 kOe (Gd, Dy) and 10 kOe (Tb), and (b) magnetic field dependence of p_m for 4.1 K and 13 K (Tb) [79 F 1].

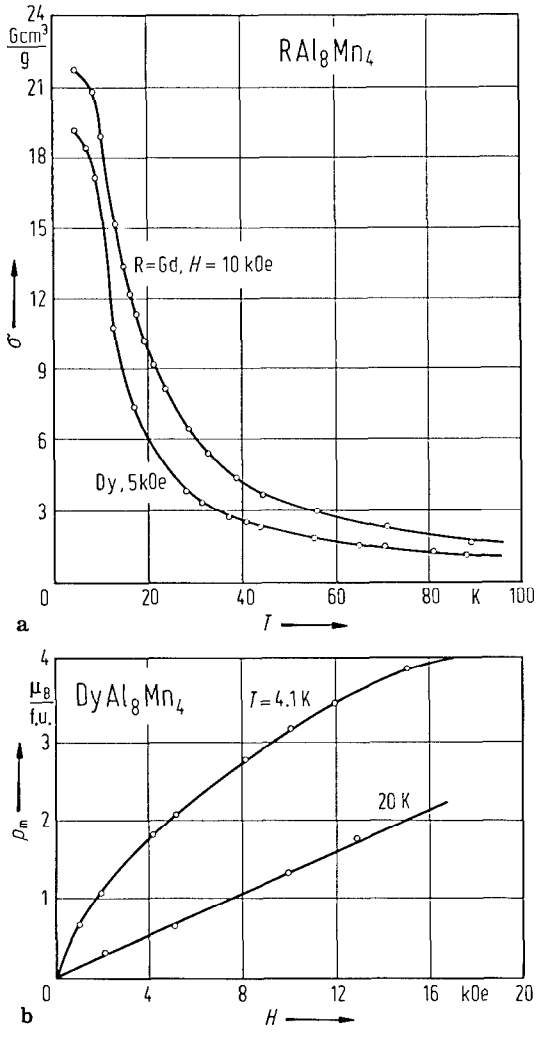

Fig. 211. RAl_8Mn_4, R = Gd, Dy. (a) Temperature dependence of σ at 5 kOe (Dy) and 10 kOe (Gd), and (b) magnetic field dependence of p_m at 20 K and 4.1 K (Dy) [79 F 1].

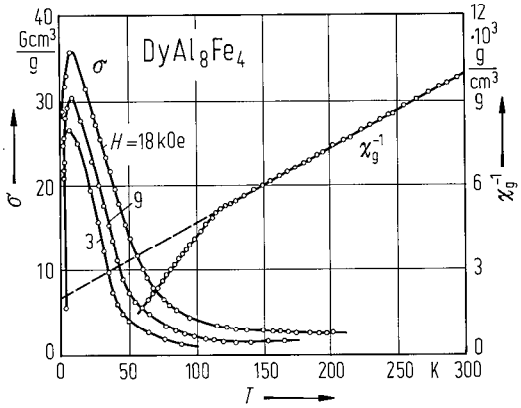

Fig. 212. $DyAl_8Fe_4$. Temperature dependence of σ in magnetic fields of 3, 9 and 18 kOe, and temperature dependence of χ_g^{-1} [78 B 3].

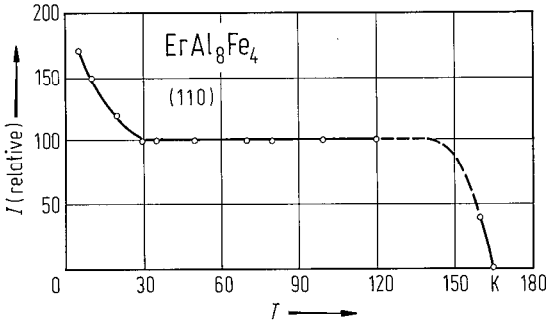

Fig. 213. $ErAl_8Fe_4$. Neutron diffraction intensity I of the (110) reflection vs. temperature. Ordering of the Fe magnetic moments at 165 K and the Er magnetic moments at 30 K suggested [77 B 3], but see also [83 S 3].

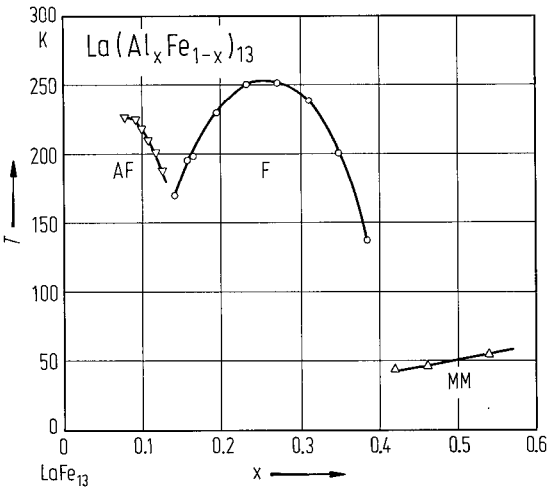

Fig. 214. $La(Al_xFe_{1-x})_{13}$. Magnetic phase diagram. Three magnetic regions are indicated: (i) The mictomagnetic regime (MM). In this regime the magnetic susceptibility has a distinct mictomagnetic cusp at about 50 K and large positive Θ. (ii) The soft ferromagnetic (F) regime. In this regime the saturation magnetic moment increases linearly with x, in the range $0.14 \leqq x \leqq 0.16$ hysteresis is observed. (iii) The antiferromagnetic (AF) regime. Above T_N hysteresis has been observed in the region $0.08 \leqq x \leqq 0.1$ [84 P 1].

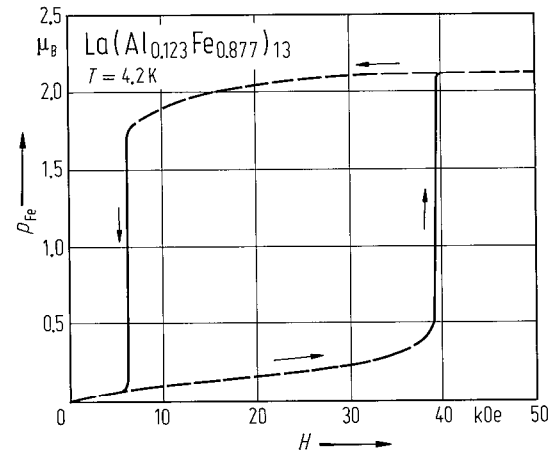

Fig. 215. $La(Al_{0.123}Fe_{0.877})_{13}$. Magnetization curve at 4.2 K [84 P 3].

2.9.4 References for 2.9

General references

621 1 Lea, K.R., Leask, M.J.M., Wolf, P.W.: The Raising of Angular Momentum Degeneracy of f-Electron Terms by Cubic Crystal Fields. J. Phys. Chem. Solids **23** (1962) 1381.

64 h 1 Hutchings, M.T.: Point-Charge Calculations of Energy Levels of Magnetic Ions in Crystalline Electric Fields. Solid State Physics, Advances in Research and Applications (Seitz, F., Turnbull, D., eds.), New York, London: Academic Press, Vol. 16, **1964**, p. 227.

71 t 1 Taylor, K.N.R.: Intermetallic Rare-Earth Compounds. Adv. Phys. **20** (1971) 551.

72 t 1 Taylor, K.N.R., Darby, M.J.: Physics of Rare Earth Solids, London: Chapman and Hall, Ltd. **1972**.

73 w 1 Wallace, W.E.: Rare Earth Intermetallics. New York, London: Acad. Press. Inc. **1973**.

79 b 1 Buschow, K.H.J.: Intermetallic Compounds of Rare-Earth and Non-magnetic Metals. Rep. Prog. Phys. **42** (1979) 1373.

79 i 1 Iandelli, A., Palenzona, A.: Crystal Chemistry of Intermetallic Compounds. Handbook on the Physics and Chemistry of Rare Earths (Gschneidner jr., K.A., Eyring, L., eds.), Amsterdam: North-Holland Publ. Co., Vol. 2, **1979**, p. 1.

79 k 1 Kirchmayr, H.R., Poldy, C.A.: Magnetic Properties of Intermetallic Compounds of Rare Earth Metals. Handbook on the Physics and Chemistry of Rare Earths (Gschneidner jr., K.A., Eyring, L., eds.), Amsterdam: North Holland Publ. Co., Vol. 2, **1979**, p. 55.

80 b 1 Buschow, K.H.J.: Rare Earth Compounds in Ferromagnetic Materials. A Handbook on the Properties of Magnetically Ordered Substances (Wohlfarth, E.P., ed.), Amsterdam: North-Holland Publ. Co., Vol. 1, **1980**, p. 297.

Special references

61 M 1 Matthias, B.T., Clogston, A.M., Williams, E., Corenzwit, E., Sherwood, R.C.: Phys. Rev. Lett. **7** (1961) 7.

62 W 1 Williams, H.J., Wernick, H.J., Nesbitt, E.A., Sherwood, R.C.: J. Phys. Soc. Jpn. **17**, Suppl. B-1 (1962) 91.

63 C 1 Colombo, L., Olcese, G.L.: Atti. Accad. Naz. Lincei, Rend. Cl. Sci. Fis. Mat. Nat. **35** (1963) 12.

64 I 1 Iandelli, A.: Z. Anorg. Allg. Chem. **330** (1964) 221.

65 H 1 Harris, J.R., Raynor, G.V.: J. Less-Common Met. **9** (1965) 7.

65 I 1 Iandelli, A., Palenzona, A.: J. Less-Common Met. **9** (1965) 1.

65 O 1 Oesterreicher, H., Wallace, W.E.: J. Less-Common Met. **13** (1965) 91.

66 B 1 Buschow, K.H.J., Fast, J.F.: Z. Phys. Chem. N. F. **50** (1966) 1.

66 N 1 Nereson, N., Olson, C., Arnold, G.: J. Appl. Phys. **37** (1966) 4575.

66 S 1 Staliński, B., Pokrzywnicki, S.: Phys. Status Solidi **14** (1966) K 157.

66 S 2 Sekizawa, K., Yasukochi, K.: J. Phys. Soc. Jpn. **21** (1966) 684.

67 B 1 Buschow, K.H.J., Fast, J.F., van Diepen, A.M., de Wijn, H.W.: Phys. Status Solidi **24** (1967) 715.

67 D 1 de Wijn, H.W., van Diepen, A.M., Buschow, K.H.J.: Phys. Rev. **161** (1967) 253.

67 V 1 van Diepen, A.M., de Wijn, H.W., Buschow, K.H.J.: J. Chem. Phys. **46** (1967) 3489.

67 W 1 Wernick, J.H., Williams, H.J., Gossard, A.C.: J. Phys. Chem. Solids **28** (1967) 271.

68 B 1 Buschow, K.H.J.: Z. Phys. Chem. N. F. **59** (1968) 21.

68 B 2 Barbara, B., Bécle, C., Lemaire, R., Panthenet, R.: J. Appl. Phys. **39** (1968) 1084.

68 M 1 Mader, K.H., Wallace, W.E.: J. Less-Common Met. **16** (1968) 85.

68 M 2 Mader, K.H., Wallace, W.E.: J. Chem. Phys. **49** (1968) 1521.

68 N 1 Nereson, N., Olson, C., Arnold, G.: J. Appl. Phys. **39** (1968) 4605.

68 S 1 Swift, W.M., Wallace, W.E.: J. Phys. Chem. Solids **29** (1968) 2053.

68 V 1 van Diepen, A.M., de Wijn, H.W., Buschow, K.H.J.: Phys. Status Solidi **29** (1968) 189.

69 A 1 Arnold, G., Nereson, N.: J. Chem. Phys. **51** (1969) 1495.

69 B 1 Buschow, K.H.J.: Phys. Lett. A **29** (1969) 12.

69 B 2 Buschow, K.H.J., de Wijn, H.W., van Diepen, A.M.: J. Chem. Phys. **50** (1969) 137.

69 M 1 Mader, K.H., Segal, E., Wallace, W.E.: J. Phys. Chem. Solids **30** (1969) 1.

69 V 1 van Daal, H.J., Buschow, K.H.J.: Solid State Commun. **7** (1969) 217.

69 V 2 van Diepen, A.M., Buschow, K.H.J., de Wijn, H.W.: J. Chem. Phys. **51** (1969) 5259.

70 B 1 Bécle, C., Lemaire, R., Paccard, D.: J. Appl. Phys. **41** (1970) 855.

70 H 1 Havinga, E.E., Damsma, H., van Maaren, M.M.: J. Phys. Chem. Solids **31** (1970) 2653.

70 O 1 Olson, C.E., Arnold, G.P., Nereson, N.G.: Proc. 8th Rare Earth Research Conf., Reno, Nevada, US Bureau of Mines, Reno, Nevada **1970**, 63.
70 V 1 van Daal, H.J., Buschow, K.H.J.: Phys. Status Solidi (a) **3** (1970) 853.
70 V 2 van Daal, H.J., Buschow, K.H.J.: Phys. Lett. A **31**, (1970) 103.
71 B 1 Barbara, B., Bécle, C., Nguyen, V.N., Siaud, E.: Proc. Conf. Rare Earth and Actinides, digest no. 3, pp. 219 (The Institute of Physics, London 1971).
71 B 2 Barbara, B., Bécle, C., Siaud, E.: J. Phys. (Paris) **32** (1971) C 1–1126.
71 O 1 Oesterreicher, H.: J. Appl. Phys. **42** (1971) 5137.
71 O 2 Oesterreicher, H.: Phys. Status Solidi (a) **7** (1971) K 55.
72 A 1 Andres, K., Bucher, E., Darack, S., Maita, J.P.: Phys. Rev. B **6** (1972) 2716.
72 B 1 Barbara, B., Nguyen, V.N., Siaud, E.: C.R. Acad. Sci., Ser. B **274** (1972) 1053.
72 B 2 Bucher, E., Maita, J.P., Cooper, A.S.: Phys. Rev. B **6** (1972) 2709.
72 H 1 Hacker, H., Gupta, R., Shepard, M.L.: Phys. Status Solidi (a) **9** (1972) 601.
72 M 1 Milhouse, A.H., Purwins, H.G., Walker, E.: Solid State Commun. **11** (1972) 707.
72 N 1 Niculescu, V., Pop, I., Rosenberg, M.: Phys. Status Solidi (b) **53** (1972) 701.
72 O 1 Oesterreicher, H., Pitts, R.: J. Appl. Phys. **43** (1972) 5174.
72 W 1 Will, G., Bargouth, M.O.: Z. Naturforsch. A **27** (1972) 1581.
72 W 2 Will, G., Bargouth, M.O.: Int. J. Magn. **3** (1972) 87.
73 D 1 de Wijn, H.W., van Diepen, A.M., Buschow, K.H.J.: Phys. Rev. B **7** (1973) 524.
73 H 1 Havinga, E.E., Buschow, K.H.J., van Daal, H.J.: Solid State Commun. **13** (1973) 621.
73 H 2 Hutchens, R.D., Wallace, W.E., Craig, R.S., Rao, V.U.S.: Rare Earth Intermetallics, New York: Academic Press **1973**.
73 K 1 Klaasse, J.C.P., Sterkenburg, J.W.E., Bleyendaal, A.H.M., de Boer, F.R.: Solid State Commun. **12** (1973) 561.
73 L 1 Lethuillier, P., Pierre, J., Fillion, G., Barbara, B.: Phys. Status Solidi (a) **15** (1973) 613.
73 O 1 Oesterreicher, H.: J. Appl. Phys. **44** (1973) 2350.
73 O 2 Oesterreicher, H.: J. Less-Common Met. **30** (1973) 225.
73 O 3 Oesterreicher, H.: J. Phys. Chem. Solids **34** (1973) 1267.
73 O 4 Oesterreicher, H., Pitts, R.: J. Appl. Phys. **44** (1973) 5570.
73 S 1 Staliński, B., Czopnik, A., Iliew, N., Mydlarz, T.: Phys. Status Solidi (a) **19** (1973) K 161.
73 W 1 Weber, K.: Proc. 5th Int. Conf. Mössbauer Spectrometry Bratislava **1973**, after Kirchmayr, H. et al. in Handbook on the Physics and Chemistry of Rare Earths (Gschneidner jr., K.A., Eyring, L., eds.), Amsterdam: North-Holland Publ. Co. **1979**.
74 B 1 Barbara, B., Rossignol, M.F., Purwins, H.G., Walker, E.: Phys. Status Solidi (a) **22** (1974) 553.
74 C 1 Crangle, J.: Phys. Lett. A **48** (1974) 370.
74 C 2 Cock, G.J., Roeland, L.W., Purwins, H.G., Walker, E., Furrer, A.: Solid State Commun. **15** (1974) 845.
74 H 1 Hutchens, R.D., Wallace, W.E., Nereson, N.: J. Solid State Chem. **9** (1974) 152.
74 P 1 Purwins, H.G., Walker, E., Barbara, B., Rossignol, M.F., Bak, P.: J. Phys. C **7** (1974) 3573.
74 S 1 Staliński, B.: AIP Conf. Proc. **18** (1974) 490.
74 S 2 Staliński, B., Czopnik, A., Iliew, N., Mydlarz, T.: Proc. ICM-73 TOM V, Moscow: Nauka **1974**, 349.
75 B 1 Buschow, K.H.J.: J. Less-Common Met. **43** (1975) 55.
75 B 2 Buschow, K.H.J.: J. Less-Common Met. **39** (1975) 185.
75 B 3 Barbara, B., Rossignol, M.F., Boucherle, J.X.: Phys. Lett. A **55** (1975) 321.
75 B 4 Barbara, B., Rossignol, M.F., Purwins, H.G., Walker, E.: Solid State Commun. **17** (1975) 1525.
75 S 1 Sales, B.C., Wohlleben, D.K.: Phys. Rev. Lett. **35** (1975) 1240.
76 B 1 Buschow, K.H.J., van den Hoogenhof, W.W.: J. Less-Common Met. **45** (1976) 309.
76 H 1 Hacker, H., Gupta, R.M.: J. Less-Common Met. **45** (1976) 331.
76 L 1 Lethuillier, P., Chaussy, J.: J. Phys. (Paris) **37** (1976) 123.
76 L 2 Lethuillier, P., Percheron-Guegan, A.: J. Less-Common Met. **46** (1976) 85.
76 M 1 McNeely, D., Oesterreicher, H.: J. Less-Common Met. **44** (1976) 183.
76 O 1 Oesterreicher, H.: J. Less-Common Met. **46** (1976) 127.
76 P 1 Purwins, H.G., Walker, E., Barbara, B., Rossignol, M.F., Furrer, A.: J. Phys. C **9** (1976) 1025.
76 S 1 Sankar, S.G., Wallace, W.E.: Magn. Lett. **1** (1976) 3.
77 A 1 Asmat, H., Gignoux, D., Lemaire, R.: Physica B **86–88** (1977) 185.
77 B 1 Barbara, B., Boucherle, J.X., Buevoz, J.L., Rossignol, M.F., Schweizer, J.: Solid State Commun. **24** (1977) 481.
77 B 2 Barbara, B., Rossignol, M.F., Purwins, H.G., Walker, E. in: Crystal Field Effects in Metals and Alloys (Furrer, A., ed.), N.Y.: Plenum **1977**, p. 148.

77 B 3 Bargouth, M.O., Will, G., Buschow, K.H.J.: J. Magn. Magn. Mater. **6** (1977) 129.
77 D 1 Deportes, J., Givord, D., Lemaire, R., Nagai, H.: Physica B **86–88** (1977) 69.
77 K 1 Klaasse, J.C.P., Mattens, W.C.M., de Boer, F.R., de Châtel, P.F.: Physics B **86–88** (1977) 234.
77 O 1 Oesterreicher, H.: Phys. Status Solidi (a) **39** (1977) K 91.
77 O 2 Oesterreicher, H.: J. Less-Common Met. **55** (1977) 135.
77 O 3 Oesterreicher, H.: J. Less-Common Met. **55** (1977) 199.
77 O 4 Oesterreicher, H.: Phys. Status Solidi (a) **40** (1977) K 139.
77 O 5 Oesterreicher, H., McNeely, D.: J. Less-Common Met. **53** (1977) 245.
77 S 1 Shohata, N.: J. Phys. Soc. Jpn. **42** (1977) 1873.
78 B 1 Besnus, M.J., Bauer, P., Génin, J.M.: J. Phys. F **8** (1978) 191.
78 B 2 Bowden, G.J., Day, R.K.: J. Phys. F **8** (1978) 533.
78 B 3 Buschow, K.H.J., van der Kraan, A.M.: J. Phys. F **8** (1978) 921.
78 C 1 Chouteau, G., Floquet, J., Keradac, J.P., Palleau, J., Peyrard, J., Tournier, R.: J. Phys. (Paris) **39** (1978) L-461.
78 D 1 Descouts, P., Perrin, B., Dupanloup, A., Treyvaud, A.: J. Phys. Chem. Solids **39** (1978) 161.
78 F 1 Felner, I., Nowik, I.: J. Phys. Chem. Solids **39** (1978) 951.
78 P 1 Pop, I., Coldea, M., Wallace, W.E.: J. Solid State Chem. **26** (1978) 115.
78 S 1 Ślebarski, A.: J. Less-Common Met. **59** (1978) 1.
78 S 2 Sill, L.R., Biggers, R.R.: J. Appl. Phys. **49** (1978) 1500.
78 T 1 Tsai, T.H., Gerber, J.A., Weymouth, J.W., Sellmyer, D.J.: J. Appl. Phys. **49** (1978) 1507.
79 B 1 Buschow, K.H.J.: Rep. Prog. Phys. **42** (1979) 1373.
79 B 2 Barbara, B., Boucherle, J.X., Buevoz, J.L., Rossignol, M.F., Schweizer, J.: J. Magn. Magn. Mater. **14** (1979) 221.
79 B 3 Bruss, F., Baberschke, K., Loewenhaupt, M., Scheuer, H.: Solid State Commun. **32** (1979) 135.
79 B 4 Besnus, M.J., Herr, A., Fischer, G.: J. Phys. F **9** (1979) 745.
79 F 1 Felner, I., Nowik, I.: J. Phys. Chem. Solids **40** (1979) 1035.
79 G 1 Gamari-Seale, H., Anagnostopoulos, T., Yakinthos, J.K.: J. Appl. Phys. **50** (1979) 434.
79 G 2 Girgs, K., Fischer, P.: J. Phys. (Paris) **40** (1979) C 5-159.
79 K 1 Kaczmarska, K., Kwapulińska, E., Chełkowski, A.: Acta Phys. Pol. A **55** (1979) 69.
79 P 1 Pop, I., Dihoiu, N., Coldea, M.: Philos. Mag. B **39** (1979) 245.
79 S 1 Staliński, B., Czopnik, A., Iliew, N.: J. Phys. (Paris) **40** (1979) C 5-149.
79 T 1 Tanigawa, S., Tsuchida, T., Nakamura, Y.: J. Phys. Soc. Jpn. **46** (1979) 1488.
80 C 1 Croft, M., Levine, H.H.: Phys. Rev. B **22** (1980) 4366.
80 C 2 Chouteau, G., Palleau, G.: J. Magn. Magn. Mater. **15–18** (1980) 311.
80 D 1 Dijkman, W.H., de Boer, F.R., de Châtel, P.F., Aarts, J.: J. Magn. Magn. Mater. **15–18** (1980) 970.
80 E 1 Elenbaas, R.A., Schinkel, C.J., Storm van Leeuwen, S., van Deudekom, C.J.M.: J. Magn. Magn. Mater. **15–18** (1980) 1218.
80 E 2 Elenbaas, R.A., Schinkel, C.J., van Dendekom, C.J.M.: J. Magn. Magn. Mater. **15–18** (1980) 979.
80 F 1 Franz, W., Steglich, F., Zell, W., Wohlleben, D., Pobell, F.: Phys. Rev. Lett. **45** (1980) 64.
80 P 1 Parviainen, S., Penttilä, S.: Phys. Status Solidi (a) **60** (1980) K 119.
80 R 1 Rivillo, T., Wallace, W.E.: J. Solid State Chem. **33** (1980) 309.
80 S 1 Ślebarski, A.: J. Less-Common Met. **72** (1980) 231.
81 A 1 Aarts, J., de Boer, F.R., Horn, S., Steglich, F.: Physica B **107** (1981) 381.
81 B 1 Burzo, E.: J. Less-Common Met. **77** (1981) 251.
81 F 1 Felner, I., Seh, M., Nowik, I.: J. Phys. Chem. Solids **42** (1981) 1091.
81 F 2 Felner, I., Seh, M., Rakavy, M., Nowik, I.: J. Phys. Chem. Solids **42** (1981) 369.
81 K 1 Knorr, K., Loidl, A., Stühn, B., Buévoz, J.L.: Z. Phys. B **41** (1981) 315.
81 K 2 Konopka, D., Zarek, W.: J. Less-Common Met. **81** (1981) 5.
81 L 1 Lee, E.W., Montenegro, J.F.D.: J. Magn. Magn. Mater. **22** (1981) 282.
81 S 1 Suprunenko, P.A., Belyavina, N.N., Markiv, V.Ya., Shevchenko, I.P.: Ukr. Fiz. Zh. USSR **26** (1981) 1169.
81 Y 1 Yarmolyuk, Ya.P., Grin, Yu.N.: Izv. Akad. Nauk SSSR, Met. **1981** (No. 5), p. 228.
82 B 1 Bara, J.J., Pędziwiatr, A.T., Zarek, W., Konopka, D., Gacek, U.: J. Magn. Magn. Mater. **27** (1982) 159.
82 B 2 Burzo, E., Seitabla, D.: J. Phys. F **12** (1982) 2675.
82 B 3 Burzo, E., Seitabla, D., Chipara, M.: Phys. Status Solidi (b) **113** (1982) 87.
82 C 1 Chełkowski, A., Talik, E., Wnętrzak, G.: J. Phys. F **13** (1982) 483.
82 D 1 Dijkman, W.H., de Groot, W.H., de Boer, F.R., de Châtel, P.F.: Proc. Int. Conf. on Valence Instabilities, Zürich, April 13 16, 1982, North Holland Publ. **1982**, 547.

82 D 2 Doukouré, M., Gignoux, D.: J. Magn. Magn. Mater. **30** (1982) 111.
82 E 1 Eyers, A., Alke, A., Leson, A., Kohake, D., Purwins, H.G.: J. Phys. C **15** (1982) 2459.
82 H 1 Heimann, J., Kaczmarska, K., Kwapulińska, E., Ślebarski, A., Chełkowski, A.: J. Magn. Magn. Mater. **27** (1982) 187.
82 K 1 Kohake, D., Leson, A., Purwins, H.G., Furrer, A.: Solid State Commun. **43** (1982) 965.
82 P 1 Pop, J., Dihoiu, N., Coldea, M.: J. Phys. Chem. Solids **43** (1982) 125.
82 R 1 Romaka, V.A., Grin, Yu.N., Yarmolyuk, Ya.P., Zarechnyuk, O.S., Scolozdra, R.V.: Fiz. Met. Metalloved. **54** (1982) 691.
82 R 2 Romaka, V.A., Zarechnyuk, O.S., Rykhal, R.M., Yarmolyuk, Ya.P., Skolozdra, R.V.: Fiz. Met. Metalloved. **54** (1982) 410.
83 B 1 Boucherle, J.X., Flouquet, J., Lassailly, Y., Palleau, J., Schweizer, J.: J. Magn. Magn. Mater. **31–34** (1983) 409.
83 C 1 Coldea, M., Pop, I., Dihoiu, N.: J. Magn. Magn. Mater. **31–34** (1983) 204.
83 C 2 Chełkowski, A., Talik, E., Wnętrzak, G., Jelonek, M.: J. Magn. Magn. Mater. **40** (1983) 17.
83 F 1 Felner, I., Nowik, I., Seh, M.: J. Magn. Magn. Mater. **38** (1983) 172.
83 M 1 Martin, O.E., Girgis, K., Fischer, P.: J. Magn. Magn. Mater. **37** (1983) 231.
83 R 1 Romaka, V.A., Sichevich, O.M., Gladyshevskiy, R.Ye., Yarmolyuk, Ya.P., Grin, Yu.N.: Fiz. Met. Metalloved. **56** (1983) 479.
83 S 1 Ślebarski, A., Kaczmarska, K., Kwapulińska, E.: J. Magn. Magn. Mater. **38** (1983) 51.
83 S 2 Schelp, W., Leson, A., Drewes, W., Purwins, H.G., Grimm, H.: Z. Phys. B **51** (1983) 41.
83 S 3 Schäfer, W., Will, G.: J. Less-Common Met. **94** (1983) 205.
83 S 4 Sekizawa, K., Watanabe, T., Yasukochi, K.: J. Magn. Magn. Mater. **31–34** (1983) 181.
83 S 5 Semitelou, I.P., Yakinthos, J.K.: J. Phys. Chem. Solids **44** (1983) 31.
84 A 1 Abou-Aly, A.I., Harrus, A., Schultz, C., Crow, J.E., Mihalisin, T.: J. Magn. Magn. Mater. **42** (1984) 100.
84 C 1 Coles, B.R., Ping, J.Y., Bennett, M.H.: Philos. Mag. B **50** (1984) 1.
84 E 1 Edelstein, A.S., Koon, N.C.: J. Appl. Phys. **55** (1984) 1984.
84 I 1 Ikeda, K., Gschneidner jr., K.A., Kobayashi, N., Noto, K.: J. Magn. Magn. Mater. **42** (1984) 1.
84 M 1 McAlister, S.P.: J. Phys. F **14** (1984) 2167.
84 P 1 Palstra, T.T.M., Nieuwenhuys, G.I., Mydosh, J.A., Buschow, K.H.J.: J. Appl. Phys. **55** (1984) 2367.
84 P 2 Płusa, D., Pfranger, R., Wysłocki, B.: J. Less-Common Met. **99** (1984) 87.
84 P 3 Plastra, T.T.M., Werij, H.G.C., Nieuwenhuys, G.I., Mydosh, J.A., de Boer, F.R., Buschow, K.H.J.: J. Phys. F **14** (1984) 1961.
84 R 1 Reissner, M., Steiner, W., Kappler, J.P., Bauer, P., Besnus, M.J.: J. Phys. F **14** (1984) 1249.
85 C 1 Czopnik, A., Iliew, N., Staliński, B., Bazan, C., Mädge, H., Pott, R.: Physica B **130** (1985) 259.
85 C 2 Czopnik, A., Iliew, N., Staliński, B., Mädge, H., Bazan, C., Pott, R.: Physica B **130** (1985) 262.
85 C 3 Chełkowski, A., Wnętrzak, G.: J. Less-Common Met. **111** (1985) 157.
85 D 1 de Boer, F.R., Klaasse, J., Aarts, J., Bredl, C.D., Lieke, W., Rauchschwalbe, U., Steglich, F., Felten, R., Umhofer, U., Weber, G.: J. Magn. Magn. Mater. **47–48** (1985) 60.
85 I 1 Iandelli, A., Olcese, G.L.: J. Less-Common Met. **111** (1985) 145.
85 I 2 Iwata, N., Fujii, H., Okamoto, T.: J. Magn. Magn. Mater. **46** (1985) 312.
85 K 1 Kaczmarska, K., Kwapulińska, E., Ślebarski, A., Zipper, E., Chełkowski, A.: J. Magn. Magn. Mater. **50** (1985) 101.
85 K 2 Kasprzyk, A., Zarek, W., Ślebarski, A.: J. Less-Common Met. **105** (1985) 231.
85 R 1 Radwański, R.J.: J. Phys. F **15** (1985) 459.
85 S 1 Schefzyk, W., Lieke, W., Steglich, F.: Solid State Commun. **54** (1985) 525.
85 S 2 Steiner, W., Reissner, M., Schäfer, W., Will, G.: Physica B **130** (1985) 426.
85 Y 1 Yoshimura, K., Nakamura, Y.: Solid State Commun. **56** (1985) 767.
86 C 1 Czopnik, A., Mädge, H., Staliński, B: Phys. Status Solidi (a) **94** (1986) K 13.
86 C 2 Czopnik, A., Mädge, H., Pott, R., Staliński, B.: Phys. Status Solidi (a), in press.

2.10 Compounds of rare earth elements and C, Si, Ge, Sn or Pb

2.10.1 Introduction

The tables and figures presented in this section contain data on the magnetic properties of metallic or pseudo-metallic compounds of rare earth elements which contain besides the rare earth element at least one group 4B element C, Si, Ge, Sn, Pb. They may contain also as a third element another element of the periodic system, excluding the group 1B elements Cu, Ag, Au, the group 2 elements Be, Mg, Zn, Cd, Hg, and the group 3B elements B, Al, Ga, In, Tl, whose rare earth compounds are dealt with in the preceding sections.

The survey of the compounds in subsect. 2.10.2 is divided into two tables. Table 1 is devoted to binary and pseudobinary compounds of rare earth and group 4B elements while Table 2 is devoted to ternary compounds which contain besides the rare earth element at least one group 4B element and as a third element another metallic element of the periodic system (with the exception of those elements mentioned above).

The compounds listed in the tables are designated by their chemical formula. The compounds are arranged in the order as their elements appear in the periodic system as far as rare earth and group 4B elements are concerned. For the other elements the alphabetical order is adopted.

Thus the rare earth elements are listed in the following order

Sc, Y, La, Ce, Pr, Nd, Pm, Sm, Eu, Gd, Tb, Dy, Ho, Er, Tm, Yb, Lu

and the group 4B elements in the order

C, Si, Ge, Sn, Pb.

The compounds are listed in the tables according to the decreasing atomic ratio of the rare earth elements to the group 4B elements. Consequently, the rare-earth-rich compounds are given in the beginning of each table. The figures presented in subsect. 2.10.3 are arranged similarly.

The tables provide information on paramagnetic Curie temperature Θ, ferromagnetic Curie temperature T_C, Néel temperature T_N, magnetic susceptibility χ, effective paramagnetic moment p_{eff}, and saturation or spontaneous magnetic moment p_s. Further data are given in the column "Remarks".

The observed effective paramagnetic moments as well as the saturation moments depend on the crystal electric field (CEF) splitting, which depends on the electron configuration and on the symmetry of the particular components. This splitting is characterized by the CEF Hamiltonian which can be expressed in different ways, in terms of the CEF parameters B_n [64 h 1], the CEF overall-splitting or in the case of cubic symmetry by the so-called Lea Leask and Wolf parameters W and x [6211]. All this parameters are used in this compilation.

2.10.2 Survey of compounds and properties

Table 1. Binary and pseudobinary compounds of rare earth elements with the group 4B elements C, Si, Ge, Sn, Pn. p_s refers to 4.2 K unless stated otherwise. R: rare earth element, M: group 4B element.

	Θ K	T_C K	T_N K	χ	p_{eff} μ_B/R	p_s μ_B/R	Remarks	Ref.
R_2M								
Tb_2C						7.6	from neutron diffraction	81 A 2
		266				8.6	from neutron diffraction: Tb moment along c axis	69 A 1
Dy_2C		168				6.8	from neutron diffraction	81 A 2
Ho_2C		100				7.16	from neutron diffraction	81 A 3
R_5M_3								
Ce_5Ge_3	−50	<4.2			2.66		$\sigma(T)$: Fig. 1	67 B 1
Pr_5Ge_3	10		12		3.80		$\sigma(T)$: Fig. 1	67 B 1
Nd_5Si_3	94.5	107.2		Fig. 2	3.29		ordering of the Nd ions in the 6g and 4d sites are suggested to be ferromagnetic and antiferromagnetic, respectively	69 N 1
	53.7			Fig. 3	3.67		$\sigma(T)$: Fig. 5	76 G 1
$Nd_{5-x}Dy_xSi_3$	Fig. 4			Fig. 3	Fig. 4		$\sigma(T)$: Fig. 5	76 G 1
$Nd_5Si_{1.5}Ge_{1.5}$	76.5	76.5		Fig. 2				69 N 1
Nd_5Ge_3	20	45		Fig. 6	3.73	1.92	$\sigma(T)$: Fig. 7, p_s at 80 kOe, H_c = 15 kOe at 4.2 K is observed, ordering of Nd ions in the 6g and 4d sites are suggested to be ferromagnetic and antiferromagnetic, respectively	67 B 1
	58.4	58.4		Fig. 2	3.32			69 N 1
	45							76 G 1
Gd_5Si_3	97		62	Fig. 8	8.34		$\sigma(T)$: Fig. 9, $\sigma(H)$: Fig. 10, $p_m(H)$ at 4.2 K: Fig. 11, orders helimagnetically, hexagonal structure	76 G 1

continued

Table 1 (continued)

	Θ K	T_C K	T_N K	χ	p_{eff} μ_B/R	p_s μ_B/R	Remarks	Ref.
$Gd_5Si_{3-x}Ge_x$				Fig. 12			ordering of Gd ions in the 6g	69 N 1
x = 0	205.2	280			7.48		and 4d sites are suggested to	
1	176.8	220			7.51		be ferromagnetic and anti-	
1.5	191.8	217			7.55		ferromagnetic, respectively	
2	151.1	151.1			8.25			
3	54.8				8.24			
Gd_5Ge_3	70		48		8.42		$\sigma(T)$: Fig. 1	67 B 1
	80							76 G 1
			70				$\sigma(T)$: Fig. 13, from electrical resistivity $T_N = 68$ K: Fig. 14, from linear thermal expansion $T_N = 68$ K	80 B 1
Tb_5Ge_3	93		85		9.98		$\sigma(T)$: Fig. 1	67 B 1
			79				$\sigma(T)$: Fig. 13, from electrical resistivity $T_N = 76$ K: Fig. 14, from linear thermal expansion $T_N = 75$ K	80 B 1
	93		85			8.9	from neutron diffraction: incommensurate magnetic transition in the range 75···50 K, the Tb moment alignment at 75 and 50 K collinear and ferromagnetic within each chemical cell, changing the direction of magnetization with temperature from collinear antiferromagnetic to a spiral along the hexagonal axis, at 4.2 K flat spiral with a helical angle of 166.14°: Fig. 15, p_s for both Tb positions	82 S 1
Dy_5Si_3	99.7	107.0		Fig. 16	10.36		ordering of the Dy ions in the 6g and 4d sites are suggested to be ferromagnetic and anti- ferromagnetic, respectively	69 N 1

	90			Fig. 3	10.47		$\sigma(T)$: Fig. 5	76 G 1
Dy_5Ge_3	45		40	Fig. 6	10.47		$\sigma(T)$: Fig. 1	67 B 1
	39.9			Fig. 16	10.30		ordering of the Dy ions in the 6g and 4d sites are suggested to be ferromagnetic and antiferromagnetic, respectively	69 N 1
	40							76 G 1
							from electrical resistivity $T_N = 40$ K: Fig. 14, from linear thermal expansion $T_N = 38$ K	80 B 1
Ho_5Ge_3	10		10		11.10		$\sigma(T)$: Fig. 1	67 B 1,
							from electrical resistivity $T_N = 10$ K: Fig. 14	80 B 1
$ErC_{0.6}$		90				2.5	from neutron diffraction: large CEF effects, Ho moment parallel to [100] axis	81 A 4
Er_5Ge_3	35		31		9.48		$\sigma(T)$: Fig. 17, $\sigma(H)$ at 4.2 K: Fig. 18	67 B 1
							from electrical resistivity $T_N = 31$ K: Fig. 14, from linear thermal expansion $T_N = 30$ K	80 B 1
R_5M_4								
Nd_5Ge_4		52					$p_{Nd}(H)$ at 4.2 K: Fig. 19; from neutron diffraction: three Nd sites with ordered Nd moments 2.6, 3.1 and 2.4 μ_B, respectively, plane of easy magnetization (010)	81 S 3
Gd_5Si_4	349	336			8.10	7.22	p_s at 25 kOe, σ at 4.2 K and 25 kOe: Fig. 24	67 H 1
	347	330		Fig. 20	7.9		$\sigma(T)$: Fig. 21	80 S 3
		330					T_C from heat capacity: Fig. 22	85 S 3
$Gd_5Si_{4-x}Ge_x$	Fig. 23	Fig. 23	Fig. 23				$\sigma(x)$ at 4.2 K and 25 kOe: Fig. 24 $\sigma(T)$: Fig. 25, Fig. 26	67 H 1
Gd_5Ge_4	94		15	Fig. 27	8.10	2.02	p_s at 25 kOe, $\sigma(H)$ and $\sigma(T)$: Fig. 27, magnetization $\sigma(T)$ at 10 and 20 kOe: Fig. 28	67 H 1
			47					

continued

Table 1 (continued)

	Θ K	T_C K	T_N K	χ	p_{eff} μ_B/R	p_s μ_B/R	Remarks	Ref.
Tb_5Si_4	216	225		Fig. 29	9.52	6.43	p_s at 25 kOe, $\sigma(T)$ and $\sigma(H)$: Fig. 29	67 H 1
		217					T_C from electrical resistivity: Fig. 30	85 S 3
Tb_5Ge_4	80		30		9.59	2.04	p_s at 25 kOe	67 H 1
Dy_5Si_4	133	140			10.31	7.07	p_s at 25 kOe	67 H 1
Dy_5Ge_4	43		40		10.72	1.98	p_s at 25 kOe, $\sigma(T)$ and $\sigma(H)$: Fig. 31	67 H 1
Ho_5Si_4	69	76			11.02	7.45	p_s at 25 kOe	67 H 1
Ho_5Ge_4	16		21		10.69	6.00	p_s at 25 kOe	67 H 1,
	16		21				at 18 K modulation wavevector $k=0$, magnetic moments at three Ho positions (8a, 8d, 4c) are 6.9, 5.2, 5.8 μ_B, respectively, below 18 K a second order phase transition occurs with $k=(\frac{1}{2},0,0)$, and Ho magnetic moments 1.3, -0.3, 0 μ_B, respectively	79 S 3
Er_5Si_4	20	25			9.86	6.13	p_s at 25 kOe	67 H 1
Er_5Ge_4	10		7		9.72	5.08	p_s at 25 kOe	67 H 1
$R_{11}M_{10}$								
$Ho_{11}Ge_{8.75}Si_{1.25}$			27	Fig. 32			from neutron diffraction: below T_N and up to 5.8 K modulation wavevector $k=0$, four Ho symmetry positions with $p_{Ho}=3.3$, 0.6, 5.5 and 7.9 μ_B, respectively	80 S 2
RM								
YGe							Pauli paramagnet	66 B 1
LaGe							Pauli paramagnet	66 B 1
$La_{0.1}Pr_{0.9}Ge$		33					$\sigma(T)$ at $H=240$ kA m^{-1}: Fig. 33	85 S 2
CeGe	≈ 0		10	Fig. 34	2.50		Ce trivalent	66 B 1
$PrSi_xGe_{1-x}$							$\sigma(T)$ at $H=240$ kA m^{-1}: Fig. 33, for x = 0.05 and 0.1 $T_C=37$ K	85 S 2

PrGe	30	39			3.69	1.73	$\sigma(T)$ at 6 kOe: Fig. 35	66 B 1
		42				3.2	for CrB structure from neutron diffraction	85 S 2
		36.5				2.9	for FeB structure from neutron diffraction from neutron diffraction: collinear ferromagnetic structure, Pr moment parallel to the c axis and b axis for CrB and FeB structure types, respectively	
NdGe	18	28			3.74	1.64	$\sigma(T)$: Fig. 35	66 B 1
						2.38	from neutron diffraction: Nd moment parallel to c axis	85 S 2
SmGe			40	Fig. 36			no Curie-Weiss behaviour	66 B 1
GdSi	5		50	Fig. 37	8.23		$\sigma(T)$ and $\sigma(H)$: Fig. 38	76 G 1
GdGe	−13		62	Fig. 36	8.21			66 B 1
TbSi			57	Fig. 39				70 N 1
$TbSi_{0.8}Ge_{0.2}$	17		56		9.85	8.8	from neutron diffraction, $p_{Tb}(H)$ at 4.2 K: Fig. 40	71 N 1
			55				from neutron diffraction: pure sinusoidal modulation along [100] direction, wavevector $k=(k_x, 0, 1/2)$ incommensurate with lattice and temperature-dependent down to 43.5 K, at which temperature magnetic transition to commensurate phase with $k=(1/2, 0, 1/2)$ takes place: Fig. 41	84 N 1
TbGe	−5		48	Fig. 36	9.76			66 B 1
DyGe	~0		36	Fig. 36	10.60			66 B 1
HoSi	2		25		10.64	6.5	p_s at 1.9 K and 80 kOe, $p_{Ho}(H)$ at 4.2 K: Fig. 40, from neutron diffraction: $p_{Ho}=7.0\,\mu_B$	71 N 1
HoGe	−5		18	Fig. 34	10.77		$\sigma(T)$: Fig. 42 and $\sigma(H)$ at 4.2 K: Fig. 43, in high magnetic field induced magnetic transitions observed: Fig. 43	66 B 1

continued

Table 1 (continued)

	Θ K	T_C K	T_N K	χ	p_{eff} μ_B/R	p_s μ_B/R	Remarks	Ref.
ErSi	−5		10		9.38	7.2	$p_{Er}(H)$ at 4.2 K: Fig. 40, p_s at 100 kOe	71 N 1
						6.25	from neutron diffraction	
			11.5				from neutron diffraction: pure sinusoidal modulation of Er moments along [100] direction, wavevector $k=(k_x, 0, 1/2)$ incommensurate with lattice, temperature-dependent down to 7.25 K, at which temperature transition to commensurate phase with $k=(1/2, 0, 1/2)$ takes place: Fig. 44	84 N 1
ErGe	−15		7	Fig. 34	10.0			66 B 1
	−7		6	Fig. 45	9.70	6.87	from neutron diffraction: p_s amplitude of Er moments, $T_N=6.5$ K, incommensurate magnetic structure along c axis with wavevector $k_z=0.446c^*$ and phase difference from cell to cell along c axis 167.76°: Fig. 46, magnetic moment polarized along b axis	85 S 1
TmSi	10		10		7.45	6.0	$p_{Tm}(H)$ at 4.2 K: Fig. 40, p_s at 100 kOe	71 N 1
						5.0	from neutron diffraction	
R_2M_3								
Pr_2C_3			8			1.3	AF Pr moment alignment is not influenced by an applied field of up to 21 kOe	78 A 1
Nd_2C_3			24			3.0	AF Nd moment alignment is not influenced by an applied field of up to 21 kOe	78 A 1
Tb_2C_3			36				from neutron diffraction	69 A 1

Dy_2C_3			22			9.5	AF Dy moment alignment is not influenced by an applied field of up to 21 kOe	78 A 1
R_3M_5								
Ce_3Ge_5	2	7.2			2.40	≅0.7	p_s spontaneous moment at 1.5 K	86 L 1
$GdGe_{1.67}$	−26		22		7.8			66 S 1
$DyGe_{1.62}$	13		6.5	Fig. 47	10.6		high-temperature phase (C_c)	66 S 1
	−8		23		10.5		low-temperature phase (C32)	
$DyGe_{1.67}$	10		12	Fig. 47	10.5			66 S 1
Er_3Si_5				Fig. 48			electrical resistance vs. T: Fig. 49	83 W 1
Tm_3Si_5				Fig. 48			electrical resistance vs. T: Fig. 50	83 W 1
Yb_3Si_5				Fig. 51			Yb in a mixed valence state	79 I 1
$YbSi_{1.8}$				Fig. 51			Yb in a mixed valence state	79 I 1
RM_2								
$Y_xDy_{1-x}C_2$				Fig. 52			T_F low-temperature minimum of $\chi(T)$ curve: Fig. 52 and Fig. 53	79 S 2
				Fig. 53				
x = 0	−89		61		10.20		T_F = 50 K	
0.13	−81		56		10.63		T_F = 41 K	
0.20	−71		48		9.94			
0.56	−40		29		7.35			
0.83	−16		8		4.42			
1.0							Pauli paramagnet	
$La_xCe_{1-x}C_2$							magnetic susceptibility obeys	81 S 2
x = 0	12		30		2.40		Curie-Weiss law in the range 100···300 K	
0.15	11		21		2.00		with p_{eff} in agreement with Ce	
0.36	9		16		1.85		trivalent	
0.50	6		8		1.65			
0.72	0		< 3		1.28			
1							superconductor below 1.6 K	81 S 1
$La_xCe_{1-x}Si_2$				Fig. 54				83 Y 2
$La_xCe_{1-x}Ge_2$	Fig. 56	Fig. 57		Fig. 55	Fig. 56		Kondo temperature vs. x: Fig. 57, specific heat vs. T for different x: Fig. 58	85 M 2
CeC_2	−61				2.19			59 V 1
			33			1.74	from neutron diffraction: Ce moment parallel to c axis	67 A 1
				Fig. 59				80 S 1
	12		30		2.40		$\varrho(T)$: Fig. 60	81 S 1

continued

Table 1 (continued)

	Θ K	T_C K	T_N K	χ	p_{eff} μ_B/R	p_s μ_B/R	Remarks	Ref.
$Ce_xDy_{1-x}C_2$				Fig. 61			T_F low-temperature minimum of $\chi(T)$ curve	80 S 1
x = 0	−89		61		10.20		T_F = 50 K	
0.28	−59		30		9.13			
0.39	−49		24		8.40		T_F = 11 K	
0.52	−39		28		6.91		T_F = 7 K	
0.80	−13		29		5.03		T_F = 6 K	
1.0	12		30		2.40		T_F = 13 K	
$CeSi_{2-x}$							$p_{Ce}(H)$ at 4.2 K: Fig. 62	82 Y 2,
x = 0				4.2			χ_m at T = 0 K in 10^{-3} $cm^3 mol^{-1}$	82 Y 3
0.10				7.0				
0.15				40				
0.20		9.0						
0.30		10.9						
$CeSi_{2-x}Ge_x$				Fig. 63			p_s spontaneous moment at 1.5 K from low-field data	86 L 1
x = 0	−286				2.87		$ThSi_2$ structure type	
0.2	−153				2.66		$ThSi_2$ structure type	
0.4	−86				2.52		$ThSi_2$ structure type	
0.5	−74				2.56		$ThSi_2$ structure type	
0.6	−60	4.3			2.50	0.13	$ThSi_2$ structure type	
0.8	−34	8.1			2.46	0.19	$ThSi_2$ structure type	
1.0	−16	9.5			2.44	0.29	$GdSi_2$ structure type	
1.4	−6	9.4			2.42	0.36	$GdSi_2$ structure type	
1.6	0	9.3			2.42	0.40	$GdSi_2$ structure type	
2	−3	6.8			2.53	0.70	$GdSi_2$ structure type	
$CeSi_{2-x}Ga_x$				Fig. 64			on alloying induced discontinuous change in volume accompanies drastic change in magnetism related to the 4f state of Ce	84 M 4
$CeGe_2$		≅4.5						58 M 1
							$p_{Ce}(H)$ at 4.2 K: Fig. 62	82 Y 2
							$p_{Ce}(H)$ and hysteresis loop at 4.2 K: Fig. 65	85 M 2

PrC_2			15			1.14	from neutron diffraction: Pr moment parallel to c axis	67 A 1
	0	7		Fig. 66	3.31		$\sigma(T)$ and $\sigma(H)$: Fig. 66, $\varrho(T)$: Fig. 67, T_C determined by extrapolating $T_C(H)$ to $H=0$	81 S 1
$Pr_{0.50}Dy_{0.50}C_2$	−28				7.92			81 S 2
$PrGe_2$		19						58 M 1
	22	19			3.6			66 S 1
NdC_2			29			2.95	from neutron diffraction: Nd moment parallel to c axis	67 A 1
	−10		24	Fig. 68	3.29		$\varrho(T)$: Fig. 67	81 S 1
$Nd_{0.54}Dy_{0.46}C_2$	−8		40		7.46			81 S 2
$NdGe_2$		3.6						58 M 1
	7	3.6			3.7			66 S 1
SmC_2			21	Fig. 69			no Curie-Weiss behaviour, $\varrho(T)$: Fig. 67	81 S 1
$Sm_{0.50}Dy_{0.50}C_2$	−46		27		8.09			81 S 2
$EuSi_2$				Fig. 70	8.0			83 E 1
GdC_2	−53		42	Fig. 71	7.67		another magnetic phase transition observed at 19 K: Fig. 71, $\sigma(H)$: Fig. 71	79 S 1
	−53		42		7.68		from electrical resistivity $T_N=43$ K: Fig. 72	81 S 2
$Gd_xDy_{1-x}C_2$				Fig. 73			T_{N1} and T_{N2} temperatures of two cusps of the $\chi(T)$ curves: Fig. 73, T_F low-temperature minimum of $\chi(T)$ curve, susceptibility follows Curie-Weiss law	79 S 1
$x=0.20$	−75				10.47		$T_{N1}=57$ K, $T_{N2}=25$ K, $T_F=17$ K	
0.42	−65				9.53		$T_{N1}=53$ K, $T_{N2}=31$ K, $T_F=20$ K	
0.51	−57				9.55		$T_{N1}=50$ K, $T_{N2}=33$ K, $T_F=25$ K	
0.62	−57				9.29		$T_{N1}=48$ K, $T_{N2}=36$ K, $T_F=20$ K	
0.82	−56				8.67		$T_{N1}=46$ K, $T_{N2}=38$ K, $T_F=20$ K	
$Gd_{0.51}Dy_{0.49}C_2$	−57		50		9.55			81 S 2
			33					
$GdSi_2$	Fig. 76		Fig. 76	Fig. 74	Fig. 76			66 S 2
	−47			Fig. 75	7.81			66 Y 1

continued

Table 1 (continued)

	Θ K	T_C K	T_N K	χ	p_{eff} μ_B/R	p_s μ_B/R	Remarks	Ref.
$GdGe_2$	−54		28	Fig. 77	8.1			66 S 1
TbC_2			66				from neutron diffraction: antiferromagnetic elliptic-helical Tb spin alignment propagating along a axis with the repetition quadrupole of the atomic spacing: Fig. 79, the root-mean-square ordered moment 5.1 μ_B/Tb in $b-c$ plane, below 40 K the above structure is modulated with maximum possible additional moment of 0.54 μ_B/Tb at 2 K, below ≅33 K another complex magnetic structure coexists	67 A 1
	−150		67 20	Fig. 78	10.88		T_N attributed to the coexistence of the type I(67 K) and type II(20 K) spin alignment, from electrical resistivity T_N = 67 and 18 K: Fig. 72	81 S 2
$Tb_{0.50}Dy_{0.50}C_2$	−121		68		10.91			81 S 2
$TbSi_2$	Fig. 76	Fig. 76		Fig. 74	Fig. 76			66 S 2
$TbGe_2$	−48		42	Fig. 77	9.9			66 S 1
DyC_2			59			11.8	from neutron diffraction: below T_N static moment wave along a axis polarized in c axis direction, p_s amplitude of Dy moments	68 A 1
	−89		61	Fig. 80	10.20		second magnetic phase transition observed at 50 K: Fig. 80	79 S 1
			60				from electrical resistivity T_N = 60 K: Fig. 72	81 S 2
$Dy_{0.50}Ho_{0.50}C_2$	−46		43		10.98			81 S 2
$Dy_{0.5}Er_{0.5}C_2$	−19		30		9.82			81 S 2

$DySi_2$	Fig. 76	Fig. 76		Fig. 74	Fig. 76		66 S 2
$DyGe_2$	−26		28	Fig. 77	10.9		66 S 1
$DyGe_2$	−26		28	Fig. 77	10.9		66 S 1
				Fig. 47			
HoC_2			26			from neutron diffraction: antiferromagnetic, elliptic-helical Ho spin alignment propagating along *a* axis with the repetition quadrupole of the atomic spacing: Fig. 79, the root-mean-square ordered moment 6.9 μ_B/Ho in $b-c$ plane, below 16 K the above structure is modulated with the maximum additional moment of 1.65 μ_B/Ho at 2 K	67 A 1
	−36		25	Fig. 78	10.75	from electrical resistivity $T_N = 24$ K: Fig. 72	81 S 2
$HoSi_2$	Fig. 76		Fig. 76		Fig. 76		66 S 2
$HoGe_2$	−4		11	Fig. 77	10.7		66 S 1
ErC_2			19		9.5	from neutron diffraction	72 A 1
	−17		8	Fig. 78	9.43	from electrical resistivity $T_N = 8$ K: Fig. 72	81 S 2
$ErSi_2$	Fig. 76				Fig. 76		66 S 2
$ErGe_2$	20				9.4		66 S 1
TmC_2					7.2	from neutron diffraction	70 A 1
RM_3							
$LaSn_3$	−267			Fig. 81	1.0	no magnetically ordered state observed by neutron diffraction, Mössbauer and NMR experiments, superconductor at 6.5 K	71 W 1
				Fig. 82			80 D 1
				Fig. 83			81 C 2
				Fig. 84			83 S 3

continued

Table 1 (continued)

	Θ K	T_C K	T_N K	χ	p_{eff} μ_B/R	p_s μ_B/R	Remarks	Ref.
$La_xCe_{1-x}Sn_3$				Fig. 85	Fig. 88		$\sigma(H)$ at 4.2 K: Fig. 89	80 D 1
				Fig. 86				
				Fig. 87				
$La_xPr_{1-x}Sn_3$				Fig. 90				75 M 1
				Fig. 91				
x = 0	−5.2		8.5	Fig. 92				76 L 2
0.3	−4		6.1					
0.6	−3.1		3.1					
				Fig. 93			singlet ground-state system in which the Kondo effect arises from excited CEF levels suggested	77 B 2
$La(Sn_{1-x}Pb_x)_3$				Fig. 94			superconductor	70 H 1
$LaPb_3$				Fig. 95				83 C 1
				Fig. 96				86 D 1
$CeSn_3$				Fig. 97	2.8			65 T 1
	203			Fig. 98	2.78		susceptibility at 7 kbar and 30 kOe	77 B 1
				Fig. 99				79 B 1
				Fig. 100			bulk susceptibility vs. T and localized susceptibility from neutron diffraction	79 S 6, 79 S 5
				Fig. 82			$\sigma(H)$ at 4.2 K: Fig. 108	80 D 1
				Fig. 101				
				Fig. 102			$\sigma_m(H)$: Fig. 109	80 S 4
				Fig. 84				83 S 3
				Fig. 103				
				Fig. 105			single crystal, pressure dependence of susceptibility: Fig. 104	84 T 1
				Fig. 106			single crystal	85 G 3, 85 G 2
				Fig. 107			$p_{Ce}(H)$: Fig. 110, no intrinsic increase of the high-field susceptibility at low temperatures established: Fig. 107	86 V 1

$CePb_3$	−36		Fig. 97	2.74			65 T 1
	Fig. 111						73 L 2
	−17		Fig. 112	2.54			76 L 1
	33		Fig. 113	2.32			83 C 1
	−25	1.25	Fig. 114	2.50		$\sigma_m(H)$: Fig. 115, for the second region of Curie-Weiss behaviour (Fig. 114c) ($1\,K < T < 4\,K$) $p_{eff} = 1.6\,\mu_B$/Ce and $\Theta_1 = -7.5\,K$, the smaller part of $\Theta(\Theta_1 = -7.5\,K)$ and the larger part $\Theta - \Theta_1 = -17.5\,K$ are suggested to be attributed to the quadrupole interaction and to the 4f instability, respectively	86 D 1
		Fig. 114					
		1.1				heavy-fermion ferromagnet and magnetic field induced superconductor in fields $>150\,kOe$, phase diagram: Fig. 116	86 L 2
		1.16				from neutron diffraction: Ce moment modulation in the cubic (001) plane, moment alignment along [001] axis parallel to antiferromagnetic direction	86 V 2
$Ce(Pb_{1-x}In_x)_3$		Fig. 117					86 L 2
$PrSn_3$		8.6	Fig. 118	3.55		from electrical resistivity also the same T_N	70 C 1
			Fig. 119				
			Fig. 119			$\sigma(T)$ at different pressures Fig. 121	79 D 1
		8.6				from neutron diffraction	80 G 1
	−8	8.6	Fig. 120	3.42			65 T 1
	−8	8.6			2.65	$p_{Pr}(H)$ at 4.2 K: Fig. 122, p_s from neutron diffraction, Pr moment along tetragonal axis, modulation vector $k = (0.5, 0, 0)$	73 L 1

continued

Table 1 (continued)

	Θ K	T_C K	T_N K	χ	p_{eff} μ_B/R	p_s μ_B/R	Remarks	Ref.
$PrPb_3$	−8			Fig. 123	3.63			73 L 2
	Fig. 111							
	−8		0.35	Fig. 124	3.58			76 L 1
							from neutron diffraction: magnetic ordering observed	80 G 1
	−9			Fig. 125			Van Vleck paramagnet, quadrupolar ordering at 0.35 K suggested	82 M 1
$NdSn_3$	−22		4.7	Fig. 120	3.6			65 T 1
	−22		4.7			1.5	p_s from neutron diffraction, Nd moment perpendicular to the tetragonal axis, magnetic structure modulation vector $k=(0.5, 0, 0)$	73 L 1
			4.6	Fig. 126			$p_{Nd}(H)$ at 1.35 K: Fig. 127	75 L 1
				Fig. 119			$\sigma(T)$: Fig. 128, $\sigma(T)$ at different pressures: Fig. 121	79 D 1
$NdPb_3$	−22		2.7	Fig. 123	3.61			73 L 2
	Fig. 111		Fig. 111					
			2.6	Fig. 126			$p_{Nd}(H)$ at 1.35 K: Fig. 127	75 L 1
$SmSn_3$			12	Fig. 129			no Curie-Weiss behaviour	65 T 1
			10.3				from electrical resistivity: Fig. 130	75 S 2
$SmPb_3$			6	Fig. 123				73 L 2
			Fig. 111					
$EuSn_3$			36.4				from electrical resistivity: Fig. 130	75 S 2
$EuPb_3$	−66			20.900	7.81		χ_m in 10^{-6} cm^3 mol^{-1} at 298 K	66 P 1
$GdSn_3$	−73			Fig. 129	8.0			65 T 1
			32.3				from electrical resistivity: Fig. 130	75 S 2
$GdPb_3$	Fig. 111		Fig. 111					73 L 2
$TbPb_3$	−55		15	Fig. 131	9.21		$p_{Tb}(H)$: Fig. 132	73 L 2
	Fig. 111		Fig. 111					
$DyPb_3$	−29		11	Fig. 131	10.20		$p_{Dy}(H)$: Fig. 132	73 L 2
	Fig. 111		Fig. 111					

$HoPb_3$	−17	3.7	Fig. 131	10.0		$p_{Ho}(H)$: Fig. 132	73 L 2
	Fig. 111	Fig. 111					
		3.7				T_N from neutron diffraction	80 G 1
		7.0			8.3	p_s amplitude of Ho moments at 3.3 K, magnetic moment vs. T: Fig. 133; from neutron diffraction: Ho moments sinusoidally modulated, longitudinal static spin waves with a propagation vector $k=(0, 0.2, 0.5)$	81 K 1
$ErPb_3$		5				from neutron diffraction	80 G 1
		4.5			8.3	p_s amplitude of Er moments at 3.2 K, magnetic moment vs. T: Fig. 133; from neutron diffraction: Er moments sinusoidally modulated, longitudinal static spin waves with a propagation vector $k=(0, 0.2, 0.5)$	81 K 1
$YbSn_3$	−3.6		Fig. 134	0.59		$\sigma_m(H)$: Fig. 135	74 S 1
$YbPb_3$			Fig. 136				74 S 1
RM_6							
EuC_6			Fig. 137			$M(T)$: Fig. 137 and $M(H)$: Fig. 138	81 S 6

Table 2. Ternary compounds of rare earth elements and group 4B elements C, Si, Ge, Sn, Pb with other metallic elements of the periodic system, excluding the elements dealt with in preceding sections. p_s refers to 4.2 K unless stated otherwise. R: rare earth element, M: group 4B element.

	Θ K	T_C K	T_N K	χ	p_{eff} μ_B/R	p_s μ_B/R	Remarks	Ref.
R/M = 1/0.05								
$CePd_3Si_x$				Fig. 139				84 M 1
x = 0.05	−50				2.24			
0.1	−21				2.40			
0.2	−11				2.44			
0.3	−15				2.66			
$EuPd_3Si_x$				Fig. 140			for x = 0.2 and 0.25, Eu in $EuPd_3$ trivalent, the addition of Si to $EuPd_3$ induced valence fluctuation	83 D 1, 84 M 1
R/M = 6/1								
Tb_6Ni_2Sn	42				9.98			84 S 1
Dy_6Ni_2Sn	24			Fig. 141	10.67			84 S 1
Tm_6Ni_2Sn	3			Fig. 141	7.64			84 S 1
R/M = 1/1								
YRh_2Si						$4.06 \cdot 10^{-3}$	saturation magnetization at 1.5 K, $p_m(H)$ at 1.5 K: Fig. 142, $p_m(T)$ at 8 kOe: Fig. 142	85 P 1
YCoSn				1.71 Fig. 143			χ_g in 10^{-6} cm^3 g^{-1}, Pauli paramagnet	82 S 2
YNiSn				0.36			χ_g in 10^{-6} cm^3 g^{-1}, Pauli paramagnet	84 S 3
$CePd_2Si$	−11	2.3			2.49	1.1	p_s at 1.7 K and 80 kOe, spontaneous magnetization at 1.7 K, 0.7 μ_B/Ce atom, $p_m(H)$ and $\sigma(T)$: Fig. 144, $\varrho(T)$: Fig. 145, Kondo system suggested	86 B 2
$CePd_2Ge$							ordering temperature < 1.1 K	83 J 1
CeNiSn	−57			Fig. 146	2.86		below 120 K no Curie-Weiss behaviour, Ce mixed valent	84 S 3

$PrPd_2Ge$							ordering temperature <1.1 K	83 J 1
PrNiSn	17				3.56			84 S 3
$NdPd_2Ge$							ordering temperature 1.7 K	83 J 1
NdNiSn	−15				3.50			84 S 3
$SmPd_2Ge$							ordering temperature <1.1 K	83 J 1
SmNiSn				Fig. 146			no Curie-Weiss behaviour	84 S 3
$EuPd_2Ge$							ordering temperature 6.5 K	83 J 1
GdCoSi	131	250					$\sigma(T)$: Fig. 147	82 K 1
GdMnSi	220	320					$\sigma(T)$: Fig. 147	82 K 1
$GdPd_2Si$	14		13.5	Fig. 148	8.06	6.98	p_s at 1.5 K and 77 kOe, $p_m(H)$ at 1.5 K: Fig. 149, in low field metamagnetic phase transition observed: Fig. 149	84 G 1
GdRhSi	94	100			7.95		$p_m(H)$: Fig. 150	82 C 1
				Fig. 151			$p_s(T)$: Fig. 151, complex magnetic structure suggested	83 C 3
GdTiSi	10.4			Fig. 152	7.07			84 K 1
$GdPd_2Ge$			7.2					83 J 1
GdNiSn	0				8.12			84 S 3
GdPtSn			30		7.99			85 D 2
$TbPd_2Si$	16		21	Fig. 148	9.90	5.64	p_s at 1.5 K and 77 kOe, $p_m(H)$ at 1.5 and 14 K: Fig. 149, in low field metamagnetic phase transition observed: Fig. 149, at 8.5 K transition between two antiferromagnetic phases	84 G 1
TbRhSi	48	55		Fig. 153	9.92		$p_m(H)$: Fig. 154, hysteresis loop at 4.2 K: Fig. 155	82 C 1
							complex magnetic structure at low temperature suggested	83 C 3
			13			8.1	from neutron diffraction, magnetic structure at 4.2 K doubled flat spiral with propagation vector $k=(0.025, 0.056, 0.745)$: Fig. 156, phase difference between spirals 68°, spiral axis parallel to c axis	85 B 1
$TbPd_2Ge$		9.7					probably ferromagnetic	83 J 1
TbCoSn	30			Fig. 143	9.77			82 S 2
TbNiSn	−2				9.83			84 S 3

continued

Table 2 (continued)

	Θ K	T_C K	T_N K	χ	p_{eff} μ_B/R	p_s μ_B/R	Remarks	Ref.
$DyPd_2Si$	6	9		Fig. 148	10.61	7.38	p_s at 1.5 K and 77 kOe, $p_m(H)$ at 1.5 K: Fig. 157	84 G 1
DyRhSi	11.5	25		Fig. 158	10.31		$p_m(H)$: Fig. 159	82 C 1
							complex magnetic structure suggested	83 C 3
DyZnSi	$\cong 4$			Fig. 160	$\cong 4$		magnetization at 77 K and 13 kOe: $\cong 4$ G cm^3 g^{-1}	85 K 1
$DyPd_2Ge$			8.1					83 J 1
DyCoSn	27			Fig. 143	10.43			82 S 2
DyNiSn	0				10.4			84 S 3
$HoPd_2Si$	2	3.5		Fig. 148	10.53	7.68	p_s at 1.5 K and 77 kOe, $p_m(H)$ at 1.5 K: Fig. 157	84 G 1
HoRhSi	10.5		8	Fig. 161	10.71		$p_m(H)$ at 4.2 K: Fig. 162, meta-magnetic phase transition with increasing magnetic field: Fig. 162	82 C 1, 83 C 3
			11			8.7	from neutron diffraction, magnetic structure at 4.2 K doubled flat spiral collinear with two directions of magnetic moment with propagation vector $k=(0.5, 0, 0.5)$: Fig. 163, magnetic moments of Ho ions 1 and 2, and 3 and 4 coupled ferromagnetically inside the chemical unit cell but anti-ferromagnetically in the magnetic one, the components of the first and second pairs are: $p_{s1}^x = 1.7\,\mu_B$, $p_{s1}^y = 8.5\,\mu_B$, $p_{s2}^x = 8.6\,\mu_B$, $p_{s2}^y = 0.5\,\mu_B$, $p_{s1} = p_{s2} = 8.7\,\mu_B$	85 B 1

$HoPd_2Ge$		3.6					probably ferromagnetic	83 J 1
HoCoSn	9			Fig. 143	10.47			82 S 2
HoNiSn	0				10.4			84 S 3
$ErPd_2Si$	1	2.8		Fig. 148	9.48	6.62	p_s at 1.5 K and 77 kOe, $p_m(H)$ at 1.5 K: Fig. 157	84 G 1
ErRhSi	−3		7.5	Fig. 164	9.54		$p_m(H)$ at 4.2 K: Fig. 162, phase transition with H suggested	82 C 1, 83 C 3
			12			6.6	from neutron diffraction, magnetic structure at 4.2 K doubled flat spiral with propagation vector $k=(0, 0.4, 0)$, phase difference between spirals 39°, spiral makes angle 119° with c axis and −2° with a axis: Fig. 165	85 B 1
$ErPd_2Ge$		3						83 J 1
ErCoSn	11			Fig. 143	9.42			82 S 2
ErNiSn	5				9.54			84 S 3
$TmPd_2Ge$							ordering temperature 1.2 K	83 J 1
TmCoSn	5			Fig. 143	7.57			82 S 2
TmNiSn	8			Fig. 146	7.58			84 S 3
YbNiSn	−65			Fig. 146	4.57			84 S 3
$YbNi_2Sn$	−38			Fig. 166	4.33		Yb trivalent	83 S 5
$YbPd_2Sn$				Fig. 167	Fig. 167		superconductor at 2.46 K, magnetic transition at 0.23 K, coexistence of magnetically ordered state and superconductivity, CEF parameters $W=-12$ K and $x=-0.65$, Yb^{3+} ground state Γ_7	85 K 2
LuCoSn	31			Fig. 143	0.79			82 S 2
LuNiSn				0.43			χ_g in 10^{-6} cm^3 g^{-1}, Pauli paramagnet	84 S 3
				Fig. 146				
$LuNi_2Sn$				0.47			χ_g in 10^{-6} cm^3 g^{-1} at 293 K, Pauli paramagnet	83 S 5
				Fig. 166				
$LuNi_4Sn$				0.93			χ_g in 10^{-6} cm^3 g^{-1} at 293 K, Pauli paramagnet	83 S 5
				Fig. 166				

continued

Table 2 (continued)

	Θ K	T_C K	T_N K	χ	p_{eff} μ_B/R	p_s μ_B/R	Remarks	Ref.
R/M=3/4								
$LaFe_{0.67}Ge_{1.33}$				Fig. 168			σ(T) at 5 kOe: Fig. 168	73 F 1
$NdNi_{0.67}Si_{1.33}$	12	23			3.68	1.0	p_s spontaneous magnetization	73 F 1
$NdFe_{0.67}Ge_{1.33}$	14	24		Fig. 168	3.72	0.6	σ(T) at 5 kOe: Fig. 168 p_s spontaneous magnetization	73 F 1
$SmFe_{0.67}Ge_{1.33}$	33		26	Fig. 169			Curie constant 0.0737 cm^3 K mol^{-1}, Fe nonmagnetic, σ(T) at 15.3 kOe: Fig. 169	72 F 1
R/M=2/3								
Y_2RhSi_3							diamagnetic at room temperature	84 C 1
La_2RhSi_3							diamagnetic at room temperature	84 C 1
Ce_2RhSi_3	−83		6	Fig. 170	2.40			84 C 1
Nd_2RhSi_3	7	15		Fig. 170	3.76		$p_m(H)$: Fig. 171, CEF effects	84 C 1
Gd_2RhSi_3				Fig. 172			orders antiferromagnetically	83 C 3
	2		14		7.61		$p_m(H)$ at 4.2 K: Fig. 173	84 C 1
Tb_2RhSi_3				Fig. 172				83 C 3
	6		11		9.7		$p_m(H)$ at 4.2 K: Fig. 173	84 C 1
Dy_2RhSi_3				Fig. 172			orders antiferromagnetically	83 C 3
	−7				10.67		$p_m(H)$ at 4.2 K: Fig. 173	84 C 1
Ho_2RhSi_3							orders antiferromagnetically	83 C 3
	1			Fig. 170	10.66		$p_m(H)$ at 4.2 K: Fig. 173	84 C 1
Er_2RhSi_3							orders antiferromagnetically	83 C 3
	6			Fig. 170	9.36		$p_m(H)$ at 4.2 K: Fig. 173	84 C 1
R/M=1/1.6								
$CeCo_{0.4}Si_{1.6}$	−9						Curie constant 2.98 cm^3 K mol^{-1}	73 F 1
$NdNi_{0.4}Si_{1.6}$	0			Fig. 174			Curie constant 2.98 cm^3 K mol^{-1}, σ(T) at 10 and 15 kOe: Fig. 174	73 F 1
$SmFe_{0.4}Si_{1.6}$	0						Curie constant 4.10 cm^3 K mol^{-1}	73 F 1
$GdCo_{0.4}Si_{1.6}$	0						Curie constant 9.99 cm^3 K mol^{-1}, above 4.2 K paramagnetic	72 F 1
$GdFe_{0.4}Si_{1.6}$	−30						Curie constant 10.18 cm^3 K mol^{-1}	72 F 1

R/M=1/2						
$YCoSi_2$				Fig. 175		82 P 1
YFe_2Si_2		790				$\sigma(T)$ Fig. 178, $p_s=0.3\,\mu_B$/Fe, crystal structure: Fig. 176 — 76 S 1
	100		275	Fig. 177	0.8	crystal structure: Fig. 176 — 80 S 5
$Y_{0.74}Ho_{0.26}Fe_2Si_2$	−100		250	Fig. 177		$p_{eff}=13.4\,\mu_B$/f.u., $p_{eff}(Fe)=3.4\,\mu_B$ calculated for $p_{eff}(Ho)=10.6\,\mu_B$, ordering temperature of Ho sublattice 40 K, crystal structure: Fig. 176 — 80 S 5
YMn_2Si_2	385		460 Fig. 179		3.5	from neutron diffraction: $p_{Mn}=2.4\,\mu_B$ at 80 K, crystal structure: Fig. 176 — 81 S 7, 81 S 4
$Y_xLa_{1-x}Mn_2Si_2$				Fig. 180 Fig. 181 Fig. 182		hysteresis at different T: Fig. 183 — 83 C 2 for x=0.2 complex magnetic behaviour, $\sigma(T)$ at 8 kOe: Fig. 184, $\sigma(H)$: Fig. 185, crystal structure: Fig. 176 — 83 S 1
x=0	310	310			4.3	
0.1	310	300			4.0	
0.2	310				4.2	
0.3	320		328		4.3	
0.4	360		355		4.3	
0.6			430			
0.8			478			
1.0			516			
$Y_2Mo_3Si_4$				1.04		χ_g in $10^{-6}\,cm^3\,g^{-1}$, Pauli paramagnet — 84 B 1
YOs_2Si_2				120		χ_m in $10^{-6}\,cm^3\,mol^{-1}$ at 300 K, crystal structure: Fig. 176 — 83 H 2
YPt_2Si_2				12		χ_m in $10^{-6}\,cm^3\,mol^{-1}$ at 300 K, crystal structure: Fig. 176 — 85 H 2
YRh_2Si_2						superconductor at 3.11 K, no magnetic ordering observed — 83 C 3
	−8			Fig. 186	0.2	peak in susceptibility at 5 K, superconductor at 3.1 K, crystal structure: Fig. 176 — 83 F 1, 84 F 1

continued

Table 2 (continued)

	Θ K	T_C K	T_N K	χ	p_{eff} μ_B/R	p_s μ_B/R	Remarks	Ref.
YRh_3Si_2				−107.095			χ_m in 10^{-6} cm^3 mol^{-1} at 300 K	81 C 1
YRu_2Si_2				200			χ_m in 10^{-6} cm^3 mol^{-1}, Pauli paramagnet, crystal structure: Fig. 176	83 H 1
$Y_{0.2}Ce_{0.8}Ru_2Si_2$	−178			Fig. 187			$p_{Ce}(H)$ at 1.3 and 4.2 K: Fig. 188, crystal structure: Fig. 176	85 B 2
YCo_2Ge_2				Fig. 189			Pauli paramagnet, crystal structure: Fig. 176	73 M 1
YMn_2Ge_2	385		395 Fig. 179		3.8		from neutron diffraction: $p_{Mn} = 2.95\,\mu_B$ at 80 K, crystal structure: Fig. 176	81 S 7, 81 S 4
	420		445				Mn–Mn intralayer interaction ferromagnetic and dominant compared to the interlayer one	86 F 1
$Y_xLa_{1-x}Mn_2Ge_2$			Fig. 192				$\sigma(H)$ at 4.2 K: Fig. 190, $\sigma(T)$ at 1 kOe: Fig. 191, magnetic phase diagram: Figs. 191 and 192, crystal structure: Fig. 176	86 F 1
YRh_2Ge_2							no itinerant electron magnetism and superconductivity observed down to 1.4 K, crystal structure: Fig. 176	85 F 3
$LaCo_2Si_2$							Pauli paramagnet, crystal structure: Fig. 176	82 K 2
$LaFe_2Si_2$		668					$\sigma(T)$: Fig. 193, $p_s(T)$: Fig. 194, crystal structure: Fig. 176	75 F 1
							Pauli paramagnet	83 U 1
$LaMn_2Si_2$		303 Fig. 179			4.8	3.08	crystal structure: Fig. 176	81 S 7
	310	310			4.3		$\sigma_m(T)$: Fig. 184, crystal structure: Fig. 176	83 S 1

$La_xCe_{1-x}Mn_2Si_2$			Fig. 195 Fig. 196			$\sigma(T)$: Fig. 196, for $x<0.5$ antiferromagnetic, for $x=0.6$ the sample undergoes transition AF–F as the temperature rises, for $x>0.7$ ferromagnetic; from neutron diffraction: collinear magnetic structure, type of magnetic ordering depends on Mn–Mn interatomic distances in the basal plane, Mn moment parallel to *c* axis; crystal structure: Fig. 176	82 S 4
x=0	330		379	4.2			
0.15	286		348	4.2			
0.25	288		333	4.0			
0.4	290		315	4.1			
0.5	303		260	3.9			
0.6	311			4.0			
0.7	300	302		4.4	1.62	p_s per Mn atom at 80 K	
0.8	302	298		4.4	1.54	p_s per Mn atom at 80 K	
0.9	312	312		4.3	1.61	p_s per Mn atom at 80 K	
1.0	309	311		4.3	1.33	p_s per Mn atom at 80 K	
		303			1.54	p_s per Mn atom at 4.2 K	
$LaNi_{11}Si_2$			2.5			χ_g in $10^{-7}\,m^3\,kg^{-1}$, Pauli paramagnet	83 P 1
$LaOs_2Si_2$			80			χ_m in $10^{-6}\,cm^3\,mol^{-1}$ at 300 K, crystal structure: Fig. 176	83 H 2
$LaPd_2Si_2$			Fig. 186			$\sigma_m(T)$ at 10 kOe: Fig. 197	83 F 1, 84 F 1
$LaPt_2Si_2$			40			χ_m in $10^{-6}\,cm^3\,mol^{-1}$ at 300 K, crystal structure: Fig. 176	85 H 2

continued

Table 2 (continued)

	Θ K	T_C K	T_N K	χ	p_{eff} μ_B/R	p_s μ_B/R	Remarks	Ref.
$LaRh_2Si_2$							superconductor at 3.90 K, no magnetic ordering observed, crystal structure: Fig. 176	83 C 3
	−41			Fig. 186	2.0		superconductor at 3.8 K, itinerant electron magnetism, hysteresis and $\sigma_m(H)$: Fig. 198, orders magnetically at 7 K, crystal structure: Fig. 176	83 F 1
							σ_m vs. orientation of the sample relative to H at 4.1 K: Fig. 186	84 F 1
$LaRh_3Si_2$				−49.876			χ_m in 10^{-6} cm^3 mol^{-1} at 300 K	81 C 1
$LaRu_2Si_2$				Fig. 199				83 G 2
				200			χ_m in 10^{-6} cm^3 mol^{-1}, Pauli paramagnet, crystal structure: Fig. 176	83 H 1
	−10						enhanced paramagnet, $\sigma_m(T)$ and $\sigma_m(H)$: Fig. 197, superconductor at 3.5 K	84 F 1
$La_{0.2}Ce_{0.8}Ru_2Si_2$	−5			Fig. 187			$p_{Ce}(H)$ at 1.3 and 4.2 K: Fig. 188, crystal structure: Fig. 176	85 B 2
$LaCo_2Ge_2$				Fig. 189			Pauli paramagnet, crystal structure: Fig. 176	73 M 1
$LaMn_2Ge_2$		306				3.0	p_s at 20 kOe, $\sigma(T)$: Figs. 201 and 202, $p_m(H)$: Fig 204, crystal structure: Fig. 176	75 N 1
		306			4.7	3.0	crystal structure: Fig. 176	81 S 7
	270	310		Fig. 200	4.9	3.10	$p_m(T)$ at 7 kOe: Fig. 203, $p_m(H)$ at 4.2 K: Fig. 205, crystal structure: Fig. 176	85 S 4
		Fig. 192						85 F 4
$LaRh_2Ge_2$							no itinerant electron magnetism and superconductivity down to 1.4 K, crystal structure: Fig. 176	85 F 3

$LaRu_2Ge_2$			8.6		χ_m in 10^{-3} cm^3 mol^{-1} at 4.1 K, susceptibility almost temperature-independent, no superconductivity down to 1.8 K, crystal structure: Fig. 176	85 F 3
$LaNi_2Sn_2$			3.8		χ_g in 10^{-9} m^3 kg^{-1} at 300 K, susceptibility nearly temperature-independent, at 873 K monoclinic, crystal structure: Fig. 176	81 S 5
$CeCoSi_2$			Fig. 175		Ce tetravalent, Pauli paramagnet	82 P 1
$CeFe_2Si_2$					weak paramagnetic, Ce tetravalent suggested	83 U 1
$CeFeMnSi_2$					$\sigma(H)$ at 4.2 K: Fig. 206	79 S 4
$CeIrSi_2$					itinerant magnetism associated with the 5d bands of Ir suggested	83 C 3
$CeIr_2Si_2$			Fig. 207		Ce in an intermediate valence state, crystal structure: Fig. 176	86 B 3
$CeMn_2Si_2$	330	379	Fig. 208	4.2	from neutron diffraction: $p_{Mn}=2.30\,\mu_B$ at 78 K, magnetic structure: Fig. 209, Ce tetravalent at 78 K suggested, crystal structure: Fig. 176	78 S 1
		379 Fig. 179		5.1		81 S 7
$CeMn_2(Si_xGe_{1-x})_2$		Fig. 211	Fig. 210		magnetic phase diagram: Fig. 211, $\sigma(T)$: Fig. 210	79 S 4
$CeOs_2Si_2$	−5		Fig. 212	0.98	Ce mixed valent, crystal structure: Fig. 176	83 H 2
$CeOs_xRu_{2-x}Si_2$			Fig. 213		Ce in a mixed valence state dependent on x and T: Fig. 214	84 H 1
x=0	−11			2.27		
0.25	−50			2.24		
0.50	−94			2.23		
1.0	−150			2.20		
1.40	−280			2.20		
1.45	−370			2.05		
1.75	−480			2.01		
2.0	−580			1.53		

continued

Table 2 (continued)

	Θ K	T_C K	T_N K	χ	p_{eff} μ_B/R	p_s μ_B/R	Remarks	Ref.
$CePd_2Si_2$			10			0.62	from neutron diffraction: p_s at 5 K, magnetic structure: Fig. 215, crystal structure: Fig. 176	84 G 2
			Fig. 216				T_N vs. pressure from electrical resistivity: Fig. 216, Kondo system with $T_K > T_N$, Kondo spin compensation suppresses T_N rapidly with pressure, crystal structure: Fig. 176	86 T 1
	−57		10.5		2.55			86 P 1
$CePt_2Si_2$	−70				2.6	0.15	p_s saturation magnetization at 1.5 K, $p_s = 0.1\ \mu_B$/Ce at 1.5 K and 60 kOe, Curie-Weiss law obeyed from about 200 to 600 K, Ce trivalent at room temperature, crystal structure: Fig. 176	85 D 1
				Fig. 217	2.24		spin fluctuation temperature −30 K, Ce mixed valent, crystal structure: Fig. 176	85 H 2
	−86		6		2.42			86 P 1
$CeRh_2Si_2$				Fig. 218			Ce trivalent	83 C 3
	−81				2.9		Ce trivalent suggested, peaks in susceptibility at 5 and 36 K	83 F 1, 84 F 1
	−72		37	Fig. 219	2.9		small susceptibility peak at 5.2 K observed due to the magnetism of Rh 4d band suggested	83 G 1
			39			1.28	from neutron diffraction: p_s at 32 K, another second order magnetic transition at 27 K to a complex commensurate structure with modulated moment, magnetic structure at 10 K: Fig. 220	84 G 2

	−61		36		2.56		magnetic structure: Fig. 215, crystal structure: Fig. 176	84 Q 1
			36			1.50	from neutron diffraction: T_N, p_s at 10 K, orders antiferromagnetically with wavevector $k=(0.5, 0.5, 0)$, magnetic moment parallel to c axis	85 C 1
	−163		37		2.43			86 P 1
			Fig. 216				T_N vs. pressure from electrical resistivity: Fig. 216, Kondo system with $T_K > T_N$, Kondo spin compensation suppresses T_N rapidly with pressure	86 T 1
$CeRu_2Si_2$	−54			Fig. 199	2.38		low-temperature magnetic properties similar to those of heavy-fermion superconductor $CeCu_2Si_2$ suggested, ground state nonmagnetic, Kondo-type spin fluctuation, Ce mixed valent, no superconductivity down to 0.04 K	83 G 2
	0.5			Fig. 221	2.12		about 85% of Ce trivalent suggested	83 H 1
	−18		10		2.46		Ce trivalent, crystal structure: Fig. 176	84 F 1
	−20			Fig. 187			$p_{Ce}(H)$ at 1.3 and 4.2 K: Fig. 188	85 B 2
	2.8			Fig. 222	2.53		nonmagnetic Kondo lattice compound with $T_K = 12$ K, huge magnetic anisotropy	85 K 3
	−170			Fig. 223 Fig. 224 Fig. 225 Fig. 226	2.39		at low temperatures $p_{eff} = 1.44\,\mu_B$/Ce	85 T 1
$CeRu_3Si_2$							below 1 K type II superconductor	84 R 1
$CeCo_2Ge_2$	−151.9			Fig. 189	2.74		crystal structure: Fig. 176	73 M 1
$CeFe_2Ge_2$		605					$\sigma(T)$: Fig. 227, crystal structure: Fig. 176	75 F 1

continued

Table 2 (continued)

	Θ K	T_C K	T_N K	χ	p_{eff} μ_B/R	p_s μ_B/R	Remarks	Ref.
$CeMn_2Ge_2$		316				3.10	p_s at 20 kOe, $\sigma(T)$: Figs. 201 and 202, $p_m(H)$ at 4.2 K: Fig. 228	75 N 1
		322 Fig. 179 Fig. 192			3.9	3.0	crystal structure: Fig. 176	81 S 7 85 F 4
$CePt_2Ge_2$	−20			Fig. 229	2.5		Ce trivalent at room temperature suggested, crystal structure: Fig. 176	85 D 1
$CeRh_2Ge_2$	−3		15		2.70		$\sigma_m(T)$ and $\sigma_m(H)$ at 4.2 K: Fig. 230, T_N: Ce sublattice ordering temperature, second peak in magnetization at 3 K due to Rh sublattice ordering suggested, crystal structure: Fig. 176	85 F 3
$CeRu_2Ge_2$	−70	11			2.30	0.67	p_s at 17 kOe, Ru conduction electrons only contribute enhanced itinerant paramagnetism, $\sigma_m(T)$ and $p_m(H)$ at 4.1 K: Fig. 231, complicated magnetic structure with large ferromagnetic component suggested, crystal structure: Fig. 176	85 F 3
$CeNi_2Sn_2$				Fig. 232	2.14		crystal structure: Fig. 176, at 873 K monoclinic	81 S 5
$PrCo_2Si_2$	−15		30		3.7	0.5	p_s at 50 kOe, $\sigma(T)$: Fig. 233, $\sigma(H)$ at 4.2 K: Fig. 234, jump in susceptibility at 12 K,	82 K 2
			30			3.19	from neutron diffraction: T_N=49 K, p_s; at about 10 K magnetic phase transition suggested, Co nonmagnetic, Pr moment along c axis, collinear antiferromagnetic order of + − + − type: Fig. 215; crystal structure: Fig. 176	83 L 1

			31			3.19	from neutron diffraction: magnetic space group P_I4/mnc is body-anticentered, modulation vector $k=(0.5, 0.5, 0.5)$ referring to P_I cell, magnetic structure: Fig. 215	84 Y 1
$PrFe_2Si_2$		693					$\sigma(T)$: Fig. 193, $p_s(T)$: Fig. 194, crystal structure: Fig. 176	75 F 1
$PrMn_2Si_2$			348 Fig. 179		5.1		crystal structure: Fig. 176	81 S 7
	290			Fig. 235			from neutron diffraction: $p_{Mn}=2.45\,\mu_B$ at 4.2 K, $p_m(H)$: Fig. 235	81 S 4
$PrNi_2Si_2$			18	Fig. 236 Fig. 237	3.67	2.43	$\varrho(T)$: Fig. 238, p_s at 1.5 K and 150 kOe along c axis, $p_m(H)$: Fig. 237, $\Theta_a=-57$ K, $\Theta_c=33$ K, crystal structure: Fig. 176, from neutron diffraction: p_s, magnetic modulation vector $k=(0, 0, 0.870)$, magnetic moment direction of Pr^{3+} [001], maximum moment 2.6 μ_B at 5.5 K, Ni nonmagnetic	86 B 1
$PrOs_2Si_2$	53	12.6		Fig. 239	3.53		crystal structure: Fig. 176	83 H 2
$PrPt_2Si_2$	7			Fig. 240	3.46		paramagnetic down to 1.8 K, crystal structure: Fig. 176	85 H 2
$PrRu_2Si_2$	46.8	17.8		Fig. 241	3.49		crystal structure: Fig. 176	83 H 1
			18.1			3.18	from neutron diffraction: at low temperatures ferromagnetic ordering observed along c axis	84 S 4
		17.8				3.25	from neutron diffraction: p_s, $T_C=18$ K, Pr moments at 4.2 K arranged along c axis	85 L 1

continued

Table 2 (continued)

	Θ K	T_C K	T_N K	χ	p_{eff} μ_B/R	p_s μ_B/R	Remarks	Ref.
$PrCo_2Ge_2$	−8.7		13.28	Fig. 189	2.87			73 M 1
			≅27			3.7	from neutron diffraction: p_s amplitude of Pr moment, Co nonmagnetic, sinusoidal magnetic structure with period of 13.94 Å along c axis, magnetic structure: Fig. 245; crystal structure: Fig. 176	79 P 1
	−9		28	Fig. 242	2.9	3.98	from neutron diffraction: p_s, amplitude of Pr moment, Co nonmagnetic, below 28 K antiferromagnetic with sinusoidal magnetic structure, modulation vector $k=(0,0,0.73)$ along c axis	80 S 6
			Fig. 179					81 S 4
	−9		28.5		2.9	0.55	p_s at 50 kOe, jump in susceptibility at 18 K, $\sigma(T)$: Fig. 243, $\sigma(H)$: Fig. 244	82 K 2
$PrFe_2Ge_2$			Fig. 179					81 S 4
	10		13		3.5	3.22	p_s saturation magnetic moment, $\sigma(T)$ and $\sigma(H)$: Fig. 246, from neutron diffraction: $T_N=9$ K, amplitude of Pr magnetic moment, $p_{Pr}=3.6\,\mu_B$, a sinusoidal magnetic structure along c axis with modulation vector $k=(0, 0, 0.515)$, Pr magnetic moment parallel to c axis: Fig. 215, Fe nonmagnetic, crystal structure: Fig. 176	83 L 4
			14			3.44	ferromagnetic layers perpendicular to c axis coupled antiferromagnetically with the sequence $+--+$ and $k=(0, 0, 0.5)$	83 S 7

$PrMn_2Ge_2$		334				3.90	p_s at 4.2 K and 20 kOe, $\sigma(T)$: Figs. 201 and 202, $p_m(H)$ at 4.2 K: Fig. 228	75 N 1
		334				3.9	crystal structure: Fig. 176	81 S 7
		Fig. 179						
		Fig. 192						85 F 4
		329				5.9	$p_m(H)$ at 4.2 K: Fig. 247, $p_s(T)$ along [001] and $p_m(T)$ at 9.3 kOe along [100] axis: Fig. 248	86 I 1
$PrRh_2Ge_2$	14		47		3.90		$\sigma_m(T)$: Fig. 230, T_N: Pr sublattice ordering temperature, second peak in magnetization at 4 K due to ordering of the Rh sublattice, crystal structure: Fig. 176	85 F 3
$PrRu_2Ge_2$	27	18			3.85	1.82	p_s at 17 kOe, $\sigma_m(T)$ and $p_m(H)$ at 4.1 K: Fig. 231, Ru conduction electrons only contribute enhanced itinerant paramagnetism, complicated magnetic structure with large ferromagnetic component suggested, crystal structure: Fig. 176	85 F 3
$PrNi_2Sn_2$				Fig. 232	3.59		crystal structure: Fig. 176, at 873 K monoclinic	81 S 5
$NdCoSi_2$	−28		2.5	Fig. 249	3.0			82 P 1
				Fig. 250				
$NdCo_2Si_2$			26		3.39		from neutron diffraction: p_s at 4.2 K, Co nonmagnetic, collinear antiferromagnetic ordering of $+-+-$ type, with magnetic moment parallel to c axis: Fig. 215, crystal structure: Fig. 176	83 L 1

continued

Table 2 (continued)

	Θ K	T_C K	T_N K	χ	p_{eff} μ_B/R	p_s μ_B/R	Remarks	Ref.
$Nd(Cr_xMn_{1-x})_2Si_2$							$\sigma(T)$ in low H: Fig. 251, and at 21 kOe: Fig. 252, $\sigma(H)$: Fig. 253, crystal structure: Fig. 176	79 O 1
x = 0			380			5.14		
0.1			325			5.0		
0.2			260			4.08		
0.3			200			3.04		
0.4						2.41		
0.6						2.27	paramagnetic down to 4.2 K	
$NdFe_2Si_2$			15.6			3.1	from neutron diffraction: T_N, p_s, magnetic structure: Fig. 215, weak ferromagnetic moment below 1.5 K; crystal structure: Fig. 176	73 P 1
							$\sigma(T)$: Fig. 254	74 B 1
		713					$\sigma(T)$: Fig. 255, $\sigma(H)$: Fig. 256, $p_s(T)$: Fig. 194	75 F 1
			Fig. 179					81 S 4
			Fig. 257				Fe nonmagnetic, Nd-produced hyperfine magnetic field in half of the Fe sites: Fig. 215, crystal structure: Fig. 176	83 N 3, 83 U 1
$NdIrSi_2$							itinerant magnetism associated with the 5d bands of Ir suggested	83 C 3
$NdMn_2Si_2$			380			5.14		79 O 1
			365		5.1		crystal structure: Fig. 176;	81 S 7
			Fig. 179				from neutron diffraction: ferromagnetic layers of Mn ions piled up along c axis coupled antiferromagnetically: Fig. 209	
	290			Fig. 235			from neutron diffraction: $p_{Mn} = 2.57\ \mu_B$, $\sigma(T)$ and $p_m(H)$: Fig. 235	81 S 4

$NdOs_2Si_2$	19	2.9		Fig. 239	3.56		crystal structure: Fig. 176	83 H 2
$NdPt_2Si_2$	−4.5			Fig. 240	3.55		paramagnetic down to 1.8 K, crystal structure: Fig. 176	85 H 2
$NdRh_2Si_2$				Fig. 218			$p_m(H)$ at 4.2 K: Fig. 258	83 C 3
	−4		56		4.7		other peak in magnetization at 8 K due to the itinerant electron ordering of the Rh sublattice suggested, crystal structure: Fig. 176	83 F 1, 84 F 1
	7		53	Fig. 259	3.59	3.25	$\sigma(T)$ and $\sigma(H)$: Fig. 259	84 S 6, 85 L 1
			56			3.25	from neutron diffraction: $T_N = 55$ K, no magnetic moment on Rh, simple collinear antiferromagnetic structure, the same as below	
	27		57		3.78	3.24	from neutron diffraction: T_N, p_s at 2.75 K, collinear antiferromagnetic structure of wavevector $k=(0, 0, 1)$ corresponding to a $+-+-$ sequence of ferromagnetic (001) planes, magnetic moment parallel to c axis, Fig. 215	85 C 1
$NdRh_3Si_2$	2			Fig. 260	3.92	2.12	p_s at 4.2 K, anisotropic, see Fig. 269, p_{eff} higher than the Nd^{3+} free-ion value, itinerant magnetism associated with 4d bands of Rh suggested, orders ferromagnetically	81 C 1, 83 C 3
$NdRu_2Si_2$	29.9	17.4		Fig. 241	3.54			83 H 1
	−6		26		3.56		$p_m(T)$ and $p_m(H)$: Fig. 261, exhibits time-dependent magnetization	84 F 1
		17.4				3.25	from neutron diffraction: magnetic moment along c axis, $T_N = 18$ K	84 L 2, 85 L 1

continued

Table 2 (continued)

	Θ K	T_C K	T_N K	χ	p_{eff} μ_B/R	p_s μ_B/R	Remarks	Ref.
$NdRu_2Si_2$ (cont.)	29	15	23.5		3.64	3.27	$p_m(T)$: Fig. 262; from neutron diffraction: p_s, $T_N = 24$ K, incommensurate sine wave for $24\,K > T > 15.5\,K$, square wave for $15.5\,K > T > 10\,K$, ferro + square wave for $10\,K > T > 2.8\,K$ with $k = (0.13, 0.13, 0)$, magnetic moment parallel to c axis, magnetic structure Fig. 263, crystal structure: Fig. 176	83 C 1
$NdRu_{3.5}Si_2$							magnetic ordering temperature 17.95 K	80 B 2
$NdCo_2Ge_2$	−32.5		28	Fig. 189	3.34			73 M 1
	−5.5		26.5		4.09	0.4	p_s at 50 kOe, jump in susceptibility at 10 K, $\sigma(T)$ at different magnetic fields: Fig. 264	82 K 2
			26			3.39	T_N from neutron diffraction	83 L 1
	−5.5		26.5		4.1	3.24	magnetization $\sigma(H)$ at 4.2 K: Fig. 265, crystal structure: Fig. 176; from neutron diffraction: $T_N = 30$ K, collinear antiferromagnetic order of + − + − type, Nd magnetic moment parallel to c axis, Co nonmagnetic, magnetic structure: Fig. 215	83 L 4
$NdFe_2Ge_2$		665	13				$\sigma(T)$: Fig. 227, weak ferromagnetic ordering below T_C, Nd sublattice undergoes a spin-flop transition which at 4.2 K is at 11 kOe, Fe sublattice diamagnetic	75 F 1
								81 S 4

Fig. 179

			13			3.38	from neutron diffraction: T_N, p_s, Nd moment parallel to c aixs, Fe nonmagnetic, ferromagnetic layers perpendicular to c axis coupled antiferromagnetically with sequence $+--+$: Fig. 215; crystal structure: Fig. 176	83 S 7
$NdMn_2Ge_2$		334				6.0	p_s at 20 kOe, $\sigma(T)$: Figs. 201 and 202, $p_m(H)$ at 4.2 K: Fig. 204	75 N 1
		334			6.0		crystal structure: Fig. 176	81 S 7
		Fig. 179						
		Fig. 192						85 F 4
$NdRh_2Ge_2$	0		46		3.82		phase transition of the Rh sublattice not observed down to 2 K, $\sigma_m(T)$ at 1 kOe and $\sigma_m(H)$ at 4.1 K: Fig. 230, crystal structure: Fig. 176	85 F 3
$NdRu_2Ge_2$	44	7			3.44	1.66	p_s at 17 kOe, two magnetic transitions, $p_m(T)$ at 1 kOe and $p_m(H)$ at 4.1 K: Fig. 266, crystal structure: Fig. 176	85 F 3
		21						
$NdNi_2Sn_2$				Fig. 232	3.73		crystal structure: Fig. 176	81 S 5
$SmCoSi_2$			4.0	Fig. 249				82 P 1
				Fig. 250				
$SmFe_2Si_2$		723					$\sigma(T)$: Fig. 193, $p_s(T)$: Fig. 194, crystal structure: Fig. 176	75 F 1
$SmMn_2Si_2$			398	Fig. 267	3.3		crystal structure: Fig. 176	81 S 7
			Fig. 179					
$SmOs_2Si_2$	12		5	Fig. 212	0.47		crystal structure: Fig. 176	83 H 2
$SmPt_2Si_2$	0			Fig. 217	0.70		paramagnetic down to 1.8 K, crystal structure: Fig. 176	85 H 2
$SmRh_2Si_2$							orders antiferromagnetically peaks in magnetization at 8 and 46 K, due to the itinerant electron ordering of the Rh sublattice and antiferromagnetic ordering of the Sm sublattice, respectively, suggested crystal structure: Fig. 176	83 C 3, 83 F 1, 84 F 1

continued

Table 2 (continued)

	Θ K	T_C K	T_N K	χ	p_{eff} μ_B/R	p_s μ_B/R	Remarks	Ref.
$SmRh_3Si_2$		34		Fig. 268	1.63	0.15	hysteresis loops at different temperatures: Fig. 269	81 C 1
							orders ferromagnetically, anisotropic	83 C 3
$SmRu_2Si_2$	14.4		7	Fig. 221	0.54		crystal structure: Fig. 176	83 H 1
$SmRu_3Si_2$							magnetic ordering temperature over 25 K, polyphase	80 B 2
$SmCo_2Ge_2$	−43.8			Fig. 189	1.12		crystal structure: Fig. 176	73 M 1
$SmMn_2Ge_2$		350			3.0	3.4	crystal structure: Fig. 176	81 S 7
		Fig. 179						
		Fig. 192	Fig. 272				$p_s(T)$: Fig. 270, $p_m(H)$ at different temperatures: Fig. 271, magnetic phase diagram: Fig. 272, magnetic structure: Fig. 273,	85 F 4
		Fig. 272					crystal structure: Fig. 176	
$SmRh_2Ge_2$			7				Sm sublattice ordering temperature, T_N, second peak in magnetization at 3.5 K corresponds to the Rh sublattice ordering,	85 F 3
							crystal structure: Fig. 176	
$SmRu_2Ge_2$		10				0.23	p_s at 17 kOe, complicated magnetic structure with large ferromagnetic component suggested, $\sigma_m(T)$ at 1 kOe and $p_m(H)$ at 4.1 K: Fig. 231,	85 F 3
							crystal structure: Fig. 176	
$SmNi_2Sn_2$				3.0			χ_g in $10^{-8}\,m^3\,kg^{-1}$ and in the temperature range $225 < T < 300$ K practically temperature-independent,	81 S 5
							crystal structure: Fig. 176	

$EuCo_2SiGe$	26	46			$\sigma(T)$ at 10 and 15 kOe: Fig. 274, Curie constant 5.8 $cm^3 K mol^{-1}$, 26% of Eu trivalent, crystal structure: Fig. 176	78 F 1
$EuPd_2Si_2$	60		Fig. 275		$\Theta = 72, 90, 100, 120$ K at 3, 4, 5, 7 kbar, respectively, thermally induced valence transition becomes more gradual on application of pressure, crystal structure: Fig. 176	84 S 5
			Fig. 276			85 N 1
$EuPd_2Si_{1.95}Ge_{0.05}$	−22	22		7.50	easy axis of magnetization in the basal plane, crystal structure: Fig. 176	85 F 1
$EuPd_{2-x}Rh_xSi_2$			Fig. 277		Eu mixed valent with valency dependent on local chemical environment, magnetic phase transition of the Eu^{2+} present in all samples always above 4.1 K, for $x < 2$ transition is antiferromagnetic, crystal structure: Fig. 176	85 F 2
					valence phase transition temperature T_v: Fig. 277, above T_v Curie-Weiss behaviour, crystal structure: Fig. 176	85 F 1
x = 0		≅ 10			$T_v = 200$ K	
0.25	−18	8		7.81	$T_v = 106$ K	
0.5	−5	13		7.62	$T_v = 55$ K	
1	−4	13		7.53	$T_v = 42$ K	
$EuPd_{2-x}Ru_xSi_2$					Eu in mixed valent state, for x = 2 Eu trivalent, for $x < 1$ at 85 K Eu divalent suggested, crystal structure: Fig. 176	85 F 1
x = 0.25	−18	12		7.30		
1.0	−4	≅ 26		8.60		
1.5	47	12		9.1		
		≅ 70				
2	−63	78		3.95		

continued

Table 2 (continued)

	Θ K	T_C K	T_N K	χ	p_{eff} μ_B/R	p_s μ_B/R	Remarks	Ref.
$EuRh_2Si_2$	22				7.2		Eu divalent suggested, peak in susceptibility at 25 K	83 F 1, 84 F 1
							$p_m(T)$ and $p_m(H)$: Fig. 278, crystal structure: Fig. 176	84 F 1
$EuRu_2Si_2$	−63		78		3.95		$p_m(T)$ and $p_m(H)$: Fig. 279, Eu trivalent, sample contains 6% Eu^{2+}, crystal structure: Fig. 176	84 F 1
$EuRu_3Si_2$							magnetic ordering temperature over 25 K, polyphase	80 B 2
$EuCo_2Ge_2$	−19		23			1.3	$\sigma(T)$ at 10 kOe: Fig. 280, p_s at 15 kOe, Curie constant 17.9 cm^3 K mol^{-1}, p_{eff}(Co) = 6.0 μ_B, crystal structure: Fig. 176	78 F 1
$EuMn_2Ge_2$	52	330	9		6.9		below 9 K ferrimagnetic structure suggested, $\sigma(T)$ and $\sigma(H)$: Fig. 281	78 F 1
			Fig. 179 330			4.4	additional magnetic phase transition at 9 K observed, crystal structure: Fig. 176	81 S 7
$EuNi_2Ge_2$	−8		30			0.6	$\sigma(T)$ at 10 kOe: Fig. 280, p_s at 15 kOe, Curie constant 7.7 cm^3 K mol^{-1}, Ni non-magnetic, crystal structure: Fig. 176	78 F 1
$EuRh_2Ge_2$	13		14		7.94		Eu divalent, $p_m(T)$ and $p_m(H)$ at 4.1 K: Fig. 282, crystal structure: Fig. 176	85 F 3
$EuRu_2Ge_2$		62					T_C from Mössbauer effect	85 F 2
	62	62			7.53	5.0	Eu divalent, p_s at 17 kOe, $p_m(T)$ at 10 kOe and $p_m(H)$ at 4.1 K: Fig. 283, crystal structure: Fig. 176	85 F 3
$GdCoSi_2$	−8		7.5	Fig. 249 Fig. 250	7.5			82 P 1

$GdCo_2Si_2$			46.4					80 N 1
	−55		44	Fig. 284	9.9			80 Y 2
	−40		43	Fig. 285	8.35	1.0	p_s at 50 kOe, $\sigma(H)$ at 4.2 K: Fig. 286, crystal structure: Fig. 176	82 K 2
$GdFe_2Si_2$							$\sigma(T)$: Fig. 254	74 B 1
		738					$\sigma(T)$: Fig. 255, $\sigma(H)$: Fig. 256	75 F 1
			9.0					80 N 1
			Fig. 257				Fe nonmagnetic	83 N 3
			10.0				magnetic structure: Fig. 215, Gd produced hyperfine magnetic field in half of the Fe sites: Fig. 215, crystal structure: Fig. 176	83 U 1
$GdIr_2Si_2$	35				10.3		crystal structure: Fig. 176	82 S 3
							itinerant magnetism associated with the 5d bands of Ir suggested, crystal structure: Fig. 176	83 C 3
	−8		77		8.42	1.6	p_s at 50 kOe	84 Z 1
$GdMn_2Si_2$			453		8.4	4.37	p_{eff} from high-temperature susceptibility, low-temperature susceptibility gives $p_{eff} = 7.7\,\mu_B$/Gd, additional magnetic phase transition at 65 K, crystal structure: Fig. 176	81 S 7
			Fig. 179					
$GdNi_2Si_2$			11.6					80 N 1
	−6		15.5	Fig. 287	8.0		crystal structure: Fig. 176	80 Y 1
$GdOs_2Si_2$	27		26	Fig. 288	8.12		crystal structure: Fig. 176	83 H 2
$GdPd_2Si_2$			17.7					80 N 1
	−39				8.7		crystal structure: Fig. 176	82 S 3
	2		13	Fig. 289	8.8		$\sigma(H)$ at 4.2 K: Fig. 291	82 Y 1
				Fig. 290				
	10				8.77	3.4	p_s at 50 kOe, no magnetic ordering observed down to 4.2 K	84 Z 1
$GdPt_2Si_2$			7.2					80 N 1
	−7		10	Fig. 292	8.13		crystal structure: Fig. 176	85 H 2

continued

Table 2 (continued)

	Θ K	T_C K	T_N K	χ	p_{eff} μ_B/R	p_s μ_B/R	Remarks	Ref.
$GdRh_2Si_2$	31				6.9		crystal structure: Fig. 176	82 S 3
							orders antiferromagnetically, p_{eff} higher than the Gd^{3+} free-ion value, itinerant magnetism associated with 4d bands of Rh suggested	83 C 3
	25				5.6		peaks in magnetization at 16 and 132 K due to the itinerant electrons of the Rh sublattice and antiferromagnetic ordering of the Gd sublattice, respectively suggested	83 F 1, 84 F 1
				Fig. 293				84 F 1
	−7		101		7.89	1.1	p_s at 50 kOe	84 Z 1
			90	Fig. 294			pressure dependence	86 S 2
			Fig. 294	Fig. 295			of ac susceptibility and T_N: Fig. 294, T_N = 99 K at 10 kOe	
$GdRh_3Si_2$	36	31		Fig. 296	7.91	6.65		81 C 1
							anisotropic (see for instance	83 C 3
$GdRu_2Si_2$	12				7.9		Fig. 269)	78 B 1
	12				7.9		crystal structure: Fig. 176	82 S 3
	54.7		31	Fig. 297	8.02			83 H 1
			Fig. 297					
	40		45		8.20		$p_m(T)$ and $p_m(H)$ at 4.1 K: Fig. 298	84 F 1
	57	49.3		Fig. 299	7.51	5.8	T_C at 10 kOe, from neutron diffraction: T_C = 58 K, T_t = 33.5 K corresponds to AF⇌F phase transition at 10 kOe, at 20 kOe, T_t = 17.7 K, $\sigma(T)$ at 10 and 20 kOe: Fig. 299, $\sigma(H)$ at 4.2 K: Fig. 300	84 S 4, 84 Z 1
							nonlinearity of magnetization observed at 11.7 kOe, jump in susceptibility at 33.5 K	84 Z 1

$GdRu_3Si_2$							magnetic ordering temperature over 25 K, polyphase	80 B 2
$GdCo_2Ge_2$	−39.5		40	Fig. 301 Fig. 302	6.96			73 M 1
	−40		40				Curie constant 6.2 $cm^3 K mol^{-1}$, crystal structure: Fig. 176	78 F 1
$GdFe_2Ge_2$	−42		11				Curie constant 8.2 $cm^3 K mol^{-1}$, contained an additional phase, crystal structure: Fig. 176	78 F 1
		683						75 F 1
$GdMn_2Ge_2$		97	365	Fig. 303		3.00	p_s at 120 kOe, $\sigma(T)$: Figs. 202, 304 and 305, $p_m(H)$ at 4.2 K: Fig. 204, $\varrho(T)$: Fig. 308	75 N 1
		96	365				ferrimagnetic transition temperature T_C suggested, crystal structure: Fig. 176	78 F 1
			365 Fig. 179			3.6	additional phase transition 97 K observed	81 S 7
		95 Fig. 306 Fig. 309	365 Fig. 306 Fig. 309	Fig. 306			single crystal, $\sigma(T)$ along c axis, at 7.2 kOe: Fig. 306 and $p_m(H)$ at 4.2 K: Fig. 307, susceptibility above 600 K follows Curie-Weiss law, in the range 365 K < T < 480 K weak ferromagnet: Figs. 306 and 309	83 S 4
			Fig. 192					85 F 4
$GdNi_2Ge_2$	−19		22				$\sigma(T)$ at 15 kOe: Fig. 310 Curie constant 8.6 $cm^3 K mol^{-1}$, crystal structure: Fig. 176	78 F 1
$GdRh_2Ge_2$	20		90		7.60		Gd sublattice ordering temperature, T_N, second peak in magnetization at 7 K corresponds to the Rh sublattice ordering, $\sigma_m(T)$ and $\sigma_m(H)$ at 4.1 K: Fig. 311, crystal structure: Fig. 176	85 F 3

continued

Table 2 (continued)

	Θ K	T_C K	T_N K	χ	p_{eff} μ_B/R	p_s μ_B/R	Remarks	Ref.
$GdRu_2Ge_2$	39		32		8.20	5.4	p_s at 17 kOe, $\sigma_m(T)$ and $p_m(H)$ at 4.1 K: Fig. 312, undergoes a spin-flop transition at relatively low field, crystal structure: Fig. 176	85 F 3
$TbCoSi_2$	−18		18.5	Fig. 249 Fig. 250	9.8			82 P 1
$TbCo_2Si_2$	−18	8		Fig. 313	9.4			80 Y 2
	−73		45	Fig. 314	10.2	0.85	p_s at 50 kOe, $\sigma(H)$: Fig. 314	82 K 2
			45			8.9	from neutron diffraction: Co nonmagnetic, Tb moment along c axis, collinear antiferromagnetic order of $+-+-$ type: Fig. 215, crystal structure: Fig. 176	83 L 1
	20		30	Fig. 315	10.2	8.8	magnetic structure: Fig. 215, Co nonmagnetic suggested, p_s from neutron diffraction	83 N 1
			46			9.12	from neutron diffraction: magnetic space group P_I4/mnc is body-anticentered, wavevector $k=(0.5, 0.5, 0.5)$ referring to P_I cell	84 Y 1
			46			9.2	from neutron diffraction: p_{Tb} at 4.2 K, Tb moment along c axis, magnetic wavevector $k=(0, 0, 1)$, ferromagnetic (001) planes couple antiferromagnetically	85 P 2
$TbFe_2Si_2$		820	5.5	Fig. 316		6.9	p_s at 120 kOe, ordering temperature T_N of Tb sublattice $p_m(H)$ at 4.2 K: Fig. 317, $\sigma(T)$: Figs. 318 and 319	76 S 1
			Fig. 257				Fe nonmagnetic	83 N 3

			10.5				from neutron diffraction: unsolved incommensurate magnetic structure, Fe non-magnetic, crystal structure: Fig. 176	85 P 2
$TbIr_2Si_2$			72			8.1	from neutron diffraction: simple collinear antiferromagnet of $+-+-$ type with moments localized on Tb only, aligned along tetragonal axis: Fig. 215	83 S 6
	42		80	Fig. 320	9.95		low-temperature modification, consists of ferromagnetic layers perpendicular to c axis, $ThCr_2Si_2$ structure type	84 H 2
	13		13	Fig. 321	9.78		high-temperature modification $CaBe_2Ge_2$ structure type: Fig. 176	
	−21		75		10.4	1.27	p_s at 50 kOe, nonlinearity of magnetization observed at 12 kOe, jump in susceptibility at 13 K	84 Z 1
$TbMn_2Si_2$			501 Fig. 179	Fig. 322	9.3	5.6	$\sigma(T)$: Fig. 322, $\sigma(H)$: Fig. 324, p_{eff} for high-temperature modification, for low-temperature modification $p_{eff} = 9.8\,\mu_B$/Tb	81 S 7
	200		550			7.0	single crystal, $p_m(H)$ at 4.2 K: Fig. 325, $p_m(T)$ along c axis at 9.3 kOe: Fig. 323; magnetic structures: at $53\,K < T < 65\,K$ coexistence of ferromagnetic Tb sublattice and antiferromagnetic Mn sublattice observed, canted ferromagnetic structure at $T < 53$ K, and collinear Mn antiferromagnetic structure at $65\,K < T < 550\,K$: Fig. 326, crystal structure: Fig. 176	86 S 1

continued

Table 2 (continued)

	Θ K	T_C K	T_N K	χ	p_{eff} μ_B/R	p_s μ_B/R	Remarks	Ref.
$Tb_2Mo_3Si_4$	31			Fig. 327	9.66			84 B 1
$TbNi_2Si_2$	9		14	Fig. 328	10.2			80 Y 1
	−5		10	Fig. 315	10.1	8.8	from neutron diffraction: p_s, magnetic structure: Fig. 215, Ni nonmagnetic suggested, crystal structure: Fig. 176	83 N 1
$TbOs_2Si_2$	100		42	Fig. 329	9.64		crystal structure: Fig. 176	83 H 2
			42			12.5	from neutron diffraction: p_s amplitude of Tb moments, T_N=48 K, helicoidal magnetic structure with modulation vector k=(0, 0.312, 0), static linear transverse spin wave along b axis, Tb along c axis	84 L 1, 85 K 4
	20		41	Fig. 330	10.5	5.4	p_s at 50 kOe, $\sigma(T)$: Fig. 330, $\sigma(H)$: Fig. 331, at 4.2 K and critical field of 10 kOe becomes ferromagnetic, magnetic structure: Fig. 332	85 K 4
$TbPd_2Si_2$	−1		20	Fig. 289 Fig. 290	9.8		$\sigma(H)$: Figs. 291 and 333	82 Y 1
			15				from neutron diffraction: T_N, incommensurate Tb moment alignment of a modulated transverse wave type with a wavevector k=(0.602, 0, 0.148), magnetic structure: Fig. 334, crystal structure: Fig. 176	86 S 3
$TbPt_2Si_2$	58.5		6.5	Fig. 335	9.55		crystal structure: Fig. 176	85 H 2
$TbRh_2Si_2$							orders antiferromagnetically, p_{eff} higher than the Tb^{3+} free-ion value, itinerant magnetism associated with 4d bands of Rh suggested	83 C 3

	−26			Fig. 293	8.4		peaks in magnetization at 12 and 92 K due to the itinerant electrons of the Rh sublattice and Tb sublattice ordering, respectively, suggested: Fig. 293, crystal structure: Fig. 176	83 F 1, 84 F 1
			98			8.92	from neutron diffraction: simple collinear antiferromagnet of $+-+-$ type with moment along c axis localized on Tb only: Fig. 215,	83 S 6, 84 L 2, 85 L 1
	43		94	Fig. 336	10.0		$\sigma(T)$ at 18 kOe applied along and perpendicular to c axis: Fig. 339, magnetic structure: Fig. 215	84 Q 1
			92			8.5	p_s at 15 K and T_N from neutron diffraction	85 C 1
	−11		88		10.1	0.37	p_s at 50 kOe	84 Z 1
			94	Fig. 338			single crystal, $\Theta_c = 50$ K,	85 C 2
				Fig. 337			$p_{eff,c} = 10.3\,\mu_B$/R; $\Theta_a = -70$ K, $p_{eff,a} = 10.5\,\mu_B$/R as measured from $\chi_m^{-1}(T)$	
			92	Fig. 295			pressure dependence of ac susceptibility and T_N: Fig. 294, at 10 kOe, $T_N = 94$ K	86 S 2
				Fig. 294				
$TbRh_3Si_2$	55	37		Fig. 296	9.82	6.25	anisotropic (see for instance Fig. 261)	81 C 1, 83 C 3
$TbRu_2Si_2$	100		55	Fig. 297	9.65			83 H 1
			Fig. 297					
			55			12.4	p_s amplitude of Tb moments, from neutron diffraction: helicoidal magnetic structure with modulation vector $k = (0, 0.233, 0)$, static linear transverse spin wave along b axis, magnetic moment along c axis, root-mean-square moment and amplitude of Tb moments at 4.2 K are 8.77 and 12.4 μ_B, respectively	84 L 2, 84 S 4, 85 L 1, 87 L 1

continued

Table 2 (continued)

	Θ K	T_C K	T_N K	χ	p_{eff} μ_B/R	p_s μ_B/R	Remarks	Ref.
$TbRu_2Si_2$ (cont.)	10		53	Fig. 340	11.02	5.06	$\sigma(T)$ at 10 kOe: Fig. 340, $\sigma(H)$ at 4.2 K: Fig. 300, magnetic structure: Fig. 342	84 S 4, 84 Z 1
	106		55		10.45	9.82	from neutron diffraction: p_s at 3.1 K assuming complete squaring of Tb moments, at high temperatures below T_N, Tb moments parallel to c axis sinusoidally modulated with $k=(0.232, 0, 0)$, at temperatures below 3.1 K square-wave modulation: Fig. 341, at high temperatures $CaBe_2Ge_2$ structure type, crystal structure: Fig. 176	85 C 1
$TbRu_{3.5}Si_2$							magnetic ordering temperature above 25 K	80 B 2
$TbCo_2Ge_2$	−43.9		30	Fig. 302	9.27			73 M 1
	−22		32		10.3	0.7	p_s at 50 kOe, $\sigma(T)$: Fig. 343, $\sigma(H)$: Fig. 244 crystal structure: Fig. 176	82 K 2
$TbFe_2Ge_2$			7.5				from neutron diffraction: unsolved incommensurate magnetic structure	85 P 2
$TbMn_2Ge_2$		33				6.02	p_s at 20 kOe, $\sigma(T)$: Figs. 304 and 344, $p_m(H)$: Fig. 228	75 N 1
			413 Fig. 179		8.3	6.0	p_{eff} high-temperature value, at low temperatures p_{eff} $=9.6\,\mu_B$/f.u., additional magnetic phase transition at 33 K observed, crystal structure: Fig. 176	81 S 7
							single crystal, $p_m(H)$ at 4.2 K: Fig. 345	83 S 4

		110	413 26	9.1	p_s total Tb moment: ferromagnetic component 7.6 μ_B, antiferromagnetic component 5.5 μ_B, $p_{Mn}=2.3\,\mu_B$ at 4.2 K, magnetic structure: Fig. 346, between 4.2 K and T_N (413 K) Mn orders antiferromagnetically along c axis with sequence $+-+-$, below T_C (110 K) Tb moments order ferromagnetically along tetragonal c axis at 26 K Tb magnetic sublattice transforms into an antiferromagnetic one with monoclinic unit cell, magnetic moments have two components: a ferromagnetic one parallel to the tetragonal c axis and an antiferromagnetic one parallel to the [120] direction of the monoclinic unit cell, Tb moments up to 26 K sustain a helicoidal type of magnetic ordering apart from the antiferromagnetic order of Mn moments of $+-+-$ type stable up to T_N	84 L 3
			Fig. 192			85 F 4
$TbNi_2Ge_2$			16 9		two phase transition temperatures; from neutron diffraction: unsolved incommensurate magnetic structure; crystal structure: Fig. 176	85 P 2
$TbRh_2Ge_2$	−12		77	10.3	Tb sublattice ordering temperature T_N, second peak in magnetization at 8 K corresponds to the Rh sublattice ordering, $\sigma_m(T)$ at 1 kOe and $\sigma_m(H)$ at 4.1 K: Fig. 311, crystal structure: Fig. 176	85 F 3

continued

Table 2 (continued)

	Θ K	T_C K	T_N K	χ	p_{eff} μ_B/R	p_s μ_B/R	Remarks	Ref.
$TbRu_2Ge_2$	1		30		10.9	4.9	p_s at 50 kOe, nonlinearity of magnetization observed at 11 kOe and 21 kOe, crystal structure: Fig. 176	84 Z 1
	−3		30		12.10	2.0	p_s at 17 kOe, $\sigma_m(T)$ at 5 kOe and $p_m(H)$ at 4.1 K: Fig. 312, undergoes a spin-flop transition at relatively low field, crystal structure: Fig. 176	85 F 3
			32			9.06	from neutron diffraction: below T_N sinusoidally modulated incommensurate magnetic structure with $k=(0.2331, 0, 0)$ which becomes square-modulated at 4 K with Tb magnetic moment p_s along c axis: Fig. 341, crystal structure: Fig. 176	86 Y 1
$DyCoSi_2$	8		10.5	Fig. 249 Fig. 250	10.7			82 P 1
$DyCo_2Si_2$			19					79 G 1
	−35		21	Fig. 284	13.2			80 Y 2
	−27		19.5		10.5	4.5	p_s at 50 kOe, $\sigma(T)$: Fig. 347, $\sigma(H)$ at 4 K: Fig. 348, crystal structure: Fig. 176	82 K 2
			21			9.4	from neutron diffraction: p_s, T_N, magnetic moment localized on Dy only and is parallel to c axis: Fig. 215	83 L 3
			21			9.5	from neutron diffraction: p_s along c axis, magnetic structure: Fig. 215	83 P 2

$DyFe_2Si_2$		753					$\sigma(T)$: Fig. 193, $\sigma(H)$: Fig. 256	75 F 1
							paramagnet down to 4.2 K	79 G 1
	−95		310	Fig. 177	12.4		$p_{eff}(Fe) = 4.5\,\mu_B$ calculated for $p_{eff}(Dy) = 10.63\,\mu_B$, ordering temperature of Dy sublattice 30 K	80 S 5
			Fig. 257				Fe nonmagnetic crystal structure: Fig. 176	83 N 3
$Dy_{0.74}Ho_{0.26}Fe_2Si_2$	−95		310		12.2		$p_{eff}(Fe) = 4.3\,\mu_B$ calculated for $p_{eff}(R) = g_J[J(J+1)]^{1/2}\,\mu_B$ ordering temperature of R sublattice 30 K, crystal structure: Fig. 176	80 S 5
$DyIr_2Si_2$	−2				10.0	6.2	p_s at 50 kOe, no magnetic ordering observed down to 4.2 K, crystal structure: Fig. 176	84 Z 1
$DyMn_2Si_2$			473	Fig. 322	11.0	6.5	p_{eff} at high temperature, at low temperature $p_{eff} = 10.1\,\mu_B$/R, additional magnetic phase transition at 55 K observed, $\sigma(T)$: Fig. 322, $\sigma(H)$: Fig. 324, crystal structure: Fig. 176	81 S 7
$Dy_2Mo_3Si_4$	28			Fig. 327	10.52			84 B 1
$DyNi_2Si_2$							paramagnet down to 4.2 K	79 G 1
	−4		7	Fig. 287	10.7		crystal structure: Fig. 176	80 Y 1
$DyOs_2Si_2$	101		23	Fig. 329	10.35		crystal structure: Fig. 176	83 H 2
$DyPd_2Si_2$	−25				6.8		crystal structure: Fig. 176	82 S 3
	−4			Fig. 289 Fig. 349	10.8		$\sigma(H)$ at 4.2 K: Fig. 291	82 Y 1
	−4				9.9	5.4	p_s at 50 kOe, no magnetic ordering observed down to 4.2 K, crystal structure: Fig. 176	84 Z 1
$DyPt_2Si_2$	37	<3		Fig. 335	10.59		crystal structure: Fig. 176	85 H 2

continued

Table 2 (continued)

	Θ K	T_C K	T_N K	χ	p_{eff} μ_B/R	p_s μ_B/R	Remarks	Ref.
$DyRh_2Si_2$	−50				6.8		itinerant magnetism associated with the 4d bands of Rh suggested	82 S 3, 83 C 3
	7			Fig. 293	10.6		at 4.2 K undergoes a spin-flop transition at 36 kOe, peaks in susceptibility at 15 and 55 K due to the itinerant electrons of the Rh sublattice and antiferromagnetic ordering of the Dy sublattice, respectively suggested, crystal structure: Fig. 176	83 F 1, 84 F 1
	−1		55		11.4	3.4	p_s at 50 kOe, nonlinearity of magnetization at 37 kOe	84 Z 1
			52			9.9	from neutron diffraction: p_s along c axis, below 52 K type I antiferromagnetic structure: Fig. 215, below 15 K the Dy moment at angle of 19° from the c axis suggested ($p_{Dy}^{\parallel} \cong 9.4\,\mu_B$, $p_{Dy}^{\perp} \cong 3.2\,\mu_B$)	84 M 2
$DyRh_3Si_2$	36	29		Fig. 350	10.81	5.55	anisotropic (see for instance Fig. 269 and Fig. 296)	81 C 1, 83 C 3
$DyRu_2Si_2$	−18				6.3			78 B 1
	100		25 Fig. 351	Fig. 351	10.59			83 H 1
	−18				6.3			82 S 3
	7		29		10.98		$p_m(T)$ and $p_m(H)$: Fig. 298, crystal structure: Fig. 176	84 F 1
	12		25	Fig. 352	11.4	6.1	$\sigma(H)$ at 4.2 K: Fig. 300, $\sigma(T)$ at 10 kOe: Fig. 352; from neutron diffraction:	84 S 4, 87 L 1

							$T_N = 29$ K, static Dy moment wave propagating along b axis with $k = (0, 0.222, 0)$ and polarized along c axis: Fig. 342	
			25			13.2	from neutron diffraction: p_s amplitude of Dy moments, $T_N = 29$ K, helicoidal magnetic structure with modulation vector $k = (0, 0.222, 0)$, static linear transverse spin wave along b axis with Dy moment along c axis,	84 L 2, 85 L 1, 87 L 1
$DyRu_{3.5}Si_2$							magnetic ordering temperature 14.95 K	80 B 2
$DyCo_2Ge_2$	−4.7		14.5	Fig. 302	10.17			73 M 1
			16			9.5	from neutron diffraction: p_s along c axis, wavevector $k = (0, 0, 1)$, ferromagnetic (001) planes coupled antiferromagnetically: Fig. 215, crystal structure: Fig. 176	85 P 2
$DyMn_2Ge_2$		47				3.5	p_s at 20 kOe, $\sigma(T)$: Figs. 304 and 344, $p_m(H)$: Fig. 228	75 N 1
		57						
			383		9.9	3.5	p_{eff} at high temperatures, at low temperature $p_{eff} = 9.8\ \mu_B$/Dy, additional magnetic phase transition at 47 K observed, $p_m(H)$ at 293 K: Fig. 353, crystal structure: Fig. 176	81 S 7
			Fig. 179					
			Fig. 192					85 F 4
$DyRh_2Ge_2$	−3		44		10.68		Dy sublattice ordering temperature, T_N, second peak in magnetization at 9 K corresponds to the Rh sublattice ordering, $\sigma_m(T)$ at 2 kOe and $\sigma_m(H)$ at 4.1 K: Fig. 311, crystal structure: Fig. 176	85 F 3

continued

Table 2 (continued)

	Θ K	T_C K	T_N K	χ	p_{eff} μ_B/R	p_s μ_B/R	Remarks	Ref.
$DyRu_2Ge_2$	−8		22		10.50	2.8	p_s at 17 kOe, $\sigma_m(T)$ at 2 kOe and $p_m(H)$ at 4.1 K: Fig. 312, undergoes a spin-flop transition at relatively low field, crystal structure: Fig. 176	85 F 3
$HoCoSi_2$	−6		6.3	Fig. 249 Fig. 250	10.6			82 P 1
$HoCo_2Si_2$	−47		295	Fig. 177			$p_{eff}=11.5\,\mu_B$/f.u., $p_{eff}(Co)=3.2\,\mu_B$ calculated for $p_{eff}(Ho)=10.6\,\mu_B$, ordering temperature of Ho sublattice 77 K, crystal structure: Fig. 176	80 S 5
	−8	15		Fig. 313	10.7			80 Y 2
	−10		11.2		10.5	6.1	p_s at 50 kOe, $\sigma(H)$ at 4 K: Fig. 346, $\sigma(T)$: Fig. 354	82 K 2
			11.2			10.4	from neutron diffraction: $T_N=10$ K, Co nonmagnetic, Ho moment along c axis, collinear antiferromagnetic order of $+-+-$ type	83 L 1
	4		13	Fig. 315	10.6	8.1	from neutron diffraction: p_s, Co nonmagnetic, magnetic structure: Fig. 215	83 N 1
			12			9.85	from neutron diffraction: collinear antiferromagnet, Ho moment parallel to the c axis	83 S 2
			10.2				from neutron diffraction: Ho moment along c axis, wavevector $k=(0, 0, 1)$, ferromagnetic (001) planes coupled antiferromagnetically	85 P 2
$HoFeCoSi_2$	−70		280	Fig. 177			$p_{eff}=11.7\,\mu_B$/f.u., $p_{eff}(3d)=3.6\,\mu_B$ calculated for $p_{eff}(Ho)=10.6\,\mu_B$, ordering temperature of Ho sublattice 58 K, crystal structure: Fig. 176	80 S 5

$HoFe_{1.5}Co_{0.5}Si_2$	−70		280				$p_{eff}=11.7\,\mu_B$/f.u., $p_{eff}(3d)=3.7\,\mu_B$, calculated for $p_{eff}(Ho)=10.6\,\mu_B$, ordering temperature of Ho sublattice 55 K, crystal structure: Fig. 176	80 S 5
$HoFe_2Si_2$		820				8.5	p_s at 120 kOe, $\sigma(T)$: Figs. 355 and 356	76 S 1
	−100		300	Fig. 177			$p_{eff}=11.9\,\mu_B$/f.u., $p_{eff}(Fe)=3.8\,\mu_B$ calculated for $p_{eff}(Ho)=10.6\,\mu_B$, ordering temperature of Ho sublattice 34 K crystal structure: Fig. 176	80 S 5
			Fig. 257				Fe nonmagnetic	83 N 3
			2				from neutron diffraction: below T_N incommensurate moment alignment of a modulated transverse wave type with a wavevector $k=(0, 0.328, 0.152)$, angle between moment and the c axis 15°: Fig. 334	85 L 3
$HoIr_2Si_2$	2				11.1	7.73	p_s at 50 kOe, no magnetic ordering observed down to 4.2 K, crystal structure: Fig. 176	84 Z 1
$HoMn_2Si_2$			453 Fig. 279		10.5	6.65	p_{eff} at high temperature, at low temperature $p_{eff}=10.2\,\mu_B$/Ho, crystal structure: Fig. 176	81 S 7
$Ho_2Mo_3Si_4$	8			Fig. 327	10.24			84 B 1
$HoNi_2Si_2$	−6			Fig. 357	10.9		ordering temperature <4.2 K	80 Y 1
			3.1 4.2				from neutron diffraction: unsolved incommensurate magnetic structure, two transition temperatures, crystal structure: Fig. 176	85 P 2

continued

Table 2 (continued)

	Θ K	T_C K	T_N K	χ	p_{eff} μ_B/R	p_s μ_B/R	Remarks	Ref.
$HoOs_2Si_2$	30	8.5		Fig. 358	10.61			83 H 2
			8.5			14.0	from neutron diffraction: p_s amplitude of Ho moments, $T_N = 17$ K, helicoidal magnetic structure with modulation vector $k = (0, 0.295, 0)$, static linear transverse spin wave along b axis, Ho moment along c axis,	84 L 1, 87 L 1
	6.5		19	Fig. 330	10.9	6.83	p_s at 50 kOe, $\sigma(T)$: Fig. 330, $\sigma(H)$: Fig. 331, at 4.2 K and 2 kOe becomes ferromagnetic; from neutron diffraction:	85 K 4
			17			14	p_s amplitude of Ho moments, helicoidal magnetic structure with propagation vector $k = (0, 0.298, 0)$, static linear transverse spin wave propagating along b axis, magnetic moment along c axis: Fig. 332, crystal structure: Fig. 176	
$HoPd_2Si_2$	0				10.0		crystal structure: Fig. 176	82 S 3
	−5			Fig. 289 Fig. 290	10.5		$\sigma(H)$ at 4.2 K: Figs. 291 and 333	82 Y 1
	0		5.6		9.8	6.35	p_s at 50 kOe	84 Z 1
			21				from neutron diffraction: incommensurate Ho moment alignment, a helicoidal magnetic structure with modulation vector $k = (0.58, 0, 0.15)$ represented by a static linear transverse spin wave, maximum Ho moment 10.9 μ_B, angle between Ho^{3+} moment and c axis 63°: Fig. 359	85 L 2

$HoPt_2Si_2$	0			Fig. 360	10.0		$\sigma(H)$ at 4.2 K: Fig. 360, paramagnetic down to 2 K, $CaBe_2Ge_2$ structure type: Fig. 176, absence of long-range magnetic ordering down to 2 K	84 L 4
	11	<3		Fig. 361	10.56		crystal structure: Fig. 176	85 H 2
$HoRh_2Si_2$	−10				9.7		crystal structure: Fig. 176	82 S 3
			27			8.8	from neutron diffraction: Ho moment p_s with components $p^a_{Ho}=4.1\ \mu_B$, $p^c_{Ho}=7.8\ \mu_B$, at 4.2 K simple collinear antiferromagnet of + − + − type, Ho moments form an angle of 28° with c axis: Fig. 215	83 S 6, 84 L 2, 85 L 1
							orders antiferromagnetically, $p_m(H)$ at 4.2 K: Fig. 258, p_{eff} higher than the Ho^{3+} free-ion value, itinerant magnetism associated with the 4d bands of Rh suggested	83 C 3
	3				9.3		peaks in susceptibility at 14 and 27 K due to the itinerant electrons of the Rh sublattice and antiferromagnetic ordering of the Ho sublattice suggested: Fig. 293	83 F 1, 84 F 1
	8		27		10.2	5.5	p_s at 50 kOe, nonlinearity of magnetization observed at 15 and 43.2 kOe, jump in susceptibility at 11.8 K	84 Z 1
$HoRh_3Si_2$	18	10		Fig. 350	10.61	7.60		81 C 1
							anisotropic (see for instance, Fig. 269)	83 C 3
$HoRu_2Si_2$	−12				9.9			78 B 1, 82 S 3
	47	6.4		Fig. 351	10.60		crystal structure: Fig. 176	83 H 1

continued

Table 2 (continued)

	Θ K	T_C K	T_N K	χ	p_{eff} μ_B/R	p_s μ_B/R	Remarks	Ref.
$HoRu_2Si_2$ (cont.)			19			13.1	from neutron diffraction: below $T_N = 19$ K the Ho spin alignment forms a linear transverse spin wave mode, static moment wave along b axis with wave vector $k = (0, 0.2, 0)$ polarized along c axis, root-mean-square moment and amplitude of Ho moments at 4.2 K are 9.25 and 13.1 μ_B, respectively, magnetic structure: Fig. 362, from magnetic measurement $T_N = 6.4$ K	83 S 6, 84 L 2, 85 L 1, 87 L 1
				Fig. 363			$\sigma(T)$ at 2.59 and 10 kOe: Fig. 363, $\sigma(H)$ at 4.2 K: Fig. 300	84 S 4
	11.6		17		11.1	6.8	p_s at 50 kOe, nonlinearity of magnetization observed at 4.5 kOe	84 Z 1
$HoRu_{3.5}Si_2$							magnetic ordering temperature 14.17 K	80 B 2
$HoCo_2Ge_2$	6.0		8	Fig. 302	10.38		$\sigma(H)$ at 4.2 K: Fig. 364	73 M 1
	−10		8	Fig. 242	10.0	8.64	from neutron diffraction: p_s, ferromagnetic layers perpendicular to c axis coupled antiferromagnetically to adjacent layers, Ho moment along c axis: Fig. 215	80 S 6
	−10		8	Fig. 365	10.0	6.2	p_s at 50 kOe, $\sigma(H)$ at 4.2 K: Fig. 365, crystal structure: Fig. 176	82 K 2
$HoMn_2Ge_2$		37				5.50	p_s at 20 kOe, $\sigma(T)$: Fig. 304 and 344, $p_m(H)$: Fig. 228	75 N 1
			403 Fig. 179		8.4	5.5	p_{eff} at high temperature, at low temperature $p_{eff} = 8.5\ \mu_B$/f.u.,	81 S 7

						additional magnetic phase transition at 37 K observed, crystal structure: Fig. 176	
			Fig. 192				
$HoNi_2Ge_2$			6			≅8	from neutron diffraction: Ho moment p_s at 2.1 K, incommensurate magnetic spiral structure with Ho moment perpendicular to c axis and wavevector $k=(0, 0, 0.76)$, crystal structure: Fig. 176	85 P 2
$HoRh_2Ge_2$	−27		40		10.80		Ho sublattice ordering temperature T_N, second peak in magnetization at 5 K corresponds to the Rh sublattice ordering, crystal structure: Fig. 176	85 F 3
$HoRu_2Ge_2$	−64		3		11.13	1.4	p_s at 1.8 and 17 kOe, undergoes a spin-flop transition at relatively low field, crystal structure: Fig. 176	85 F 3
$ErCoSi_2$	−17		4.5	Fig. 249 Fig. 250	9.6			82 P 1
$ErCo_2Si_2$	−9		6	Fig. 284	10.4		$\sigma(H)$ at 4.2 K: Fig. 284	80 Y 2
						6.75	from neutron diffraction: p_s, collinear antiferromagnet with Er magnetic moments making an angle of 56.2° with c axis, crystal structure: Fig. 176	83 Y 1
$ErFe_2Si_2$		825				7.7	p_s at 120 kOe, $\sigma(T)$: Figs. 355 and 366	76 S 1
			Fig. 257				Fe nonmagnetic	83 N 3
			2.6				magnetic structure: Fig. 215, Er produced hyperfine magnetic field in half of the Fe sites, crystal structure: Fig. 176	83 U 1
			2.6			7.4	from neutron diffraction: collinear antiferromangetic structure of + − − + type: Fig. 215, p_s at 1.8 K	83 L 2

continued

Table 2 (continued)

	Θ K	T_C K	T_N K	χ	p_{eff} μ_B/R	p_s μ_B/R	Remarks	Ref.
$ErIr_2Si_2$	−27				6.8		crystal structure: Fig. 176	82 S 3
	7				8.64	4.84	p_s at 50 kOe, no magnetic ordering observed down to 4.2 K	84 Z 1
$ErMn_2Si_2$			508 Fig. 179	Fig. 322	10.2	4.22	p_{eff} at high temperature, at low temperature $p_{eff}=10.0\,\mu_B$/f.u., additional magnetic phase transition at 34 K observed $\sigma(T)$: Fig. 322, $\sigma(H)$: Fig. 324, crystal structure: Fig. 176	81 S 7
		34				4.2	p_s at 50 kOe, from neutron diffraction: at 77 K and room temperature Mn moment parallel to c axis, at 4.2 K Er sublattice orders ferromagnetically with $p_{Er}=8.9\,\mu_B$ at 1.8 K, $p_{Mn}\cong 2\,\mu_B$, and $T_C=10$ K, magnetic structure: Fig. 209	83 L 2
$Er_2Mo_3Si_4$	4			Fig. 327	9.77			84 B 1
$ErNi_2Si_2$	1.4			Fig. 367	9.4		no magnetic ordering down to 4.2 K, crystal structure: Fig. 176	80 Y 1
$ErOs_2Si_2$	30	5.1		Fig. 358	9.70		crystal structure: Fig. 176	83 H 2
	−16			Fig. 330	9.6	5.13 11.65	p_s at 50 kOe, from neutron diffraction: p_s amplitude of Er moments at 1.8 K, helicoidal magnetic structure with magnetic wave-vector $k=(0, 0.295, 0)$, static longitudinal spin wave along b axis: Fig. 332, $\sigma(H)$ at 4.2 K: Fig. 331	84 L 1, 85 K 4, 87 L 1

$ErPd_2Si_2$	−20				7.3		crystal structure: Fig. 176	82 S 3
	−3			Fig. 289 Fig. 349	9.5		$\sigma(H)$ at 4.2 K: Fig. 291	82 Y 1
	0				9.66	5.47	p_s at 50 kOe, no magnetic ordering down to 4.2 K, crystal structure: Fig. 176	84 Z 1
$ErPt_2Si_2$	26	<3		Fig. 361	9.57		crystal structure: Fig. 176	85 H 2
$ErRh_2Si_2$	−27				7.9			82 S 3
							orders antiferromagnetically, $p_m(H)$ at 4.2 K: Fig. 258, p_{eff} in good agreement with the Er^{3+} free-ion value	83 C 3
	8				7.6		peaks in susceptibility at 13 and 103 K crystal structure: Fig. 176	83 F 1, 84 F 1
			13			7.74	from neutron diffraction: p_s, $T_N = 18$ K, collinear antiferromagnetic ordering of AFI type, magnetic moment perpendicular to c axis: Fig. 215	84 L 2, 84 S 6, 85 L 1
	−2		12.8		9.45			84 S 6, 84 Z 1
				Fig. 368			$\sigma(T)$ and $\sigma(H)$ at 4.2 K: Fig. 368	84 S 6
						4.8	nonlinearity of magnetization observed at 12 kOe	84 Z 1
$ErRh_3Si_2$	41	24		Fig. 369	9.20	7.49	anisotropic (see for instance Fig. 269 and Fig. 296)	81 C 1 83 C 3
$ErRu_2Si_2$	−33				6.7			78 B 1, 82 S 3
	39.6	4.5		Fig. 370	9.66			83 H 1
	−4		8		10.0		crystal structure: Fig. 176	84 F 1
			4.2			9.3	from neutron diffraction: p_s amplitude of Er moments at 1.8 K, helicoidal structure with magnetic wavevector $k = (0, 0.20, 0)$, static longitudinal spin wave along b axis, root-mean-square Er moment 6.6 μ_B, magnetic structure: Fig. 342	84 L 2, 84 S 4, 85 L 1, 87 L 1

continued

Table 2 (continued)

	Θ K	T_C K	T_N K	χ	p_{eff} μ_B/R	p_s μ_B/R	Remarks	Ref.
$ErRu_2Si_2$ (cont.)			4.5					84 L 2, 85 L 1
	2		5		9.48	6.0		84 S 4, 84 Z 1
				Fig. 371			$\sigma(H)$ at 4.2 K: Fig. 300, $\sigma(T)$ at 0.9 kOe: Fig. 371	84 S 4
							nonlinearity of magnetization at 2.5 kOe	84 Z 1
$ErRu_3Si_2$							magnetic ordering temperature 16.19 K, polyphase	80 B 2
$ErCo_2Ge_2$	8.7			Fig. 372	7.60			73 M 1
			6			8.7	from neutron diffraction: $T_N = 11$ K	83 L 1
	−8.0		4.2		8.7	7.3	from neutron diffraction: p_s, T_N, collinear antiferromagnetic order of + − + − type, Er magnetic moment perpendicular to c axis: Fig. 215, Co non-magnetic	83 L 4
			4.2				from neutron diffraction: Er moment perpendicular to the c axis, modulation vector $k = (0, 0, 1)$, ferromagnetic (001) planes coupled antiferro-magnetically: Fig. 215; crystal structure: Fig. 176	85 P 2
$ErMn_2Ge_2$		38				6.0	p_s at 20 kOe, $\sigma(T)$: Figs. 202 and 304, $p_m(H)$: Fig. 228	75 N 1
			390 Fig. 179		9.0	6.0	p_{eff} at high temperatures, at low temperatures $p_{eff} = 8.8\ \mu_B$/Er, additional magnetic phase transition at 38 K observed	81 S 7
		8.5				7.7	from neutron diffraction: magnetic structure: Fig. 209,	83 L 2

						$p_{Mn} \cong 2\,\mu_B$, at 77 K and room temperature Mn moment parallel to c axis, at 4.2 K Er sublattice orders ferromagnetically with $p_s = 7.7\,\mu_B$/Er perpendicular to c axis and $T_C = 8.5$ K, crystal structure: Fig. 176	85 F 4
			Fig. 192				
$ErRu_2Ge_2$	−1				9.65	paramagnetic down to 1.8 K, crystal structure: Fig. 176	85 F 3
$TmCoSi_2$	−76		2.5	Fig. 249 Fig. 250	7.8		82 P 1
$TmCo_2Si_2$	−8				6.9	3.2	p_s at 50 kOe, crystal structure: Fig. 176	82 K 2
			3			6.2	from neutron diffraction: p_s, collinear antiferromagnet of $+-+-$ type, magnetic moment localized on Tm only and is normal to the c axis: Fig. 215	83 L 3
$TmMn_2Si_2$			498 Fig. 179		3.7		crystal structure: Fig. 176	81 S 7
$Tm_2Mo_3Si_4$	1			Fig. 327	7.30			84 B 1
$TmNi_2Si_2$	8			Fig. 357	7.6		ordering temperature < 4.2 K, crystal structure: Fig. 176	80 Y 1
$TmOs_2Si_2$	64	1		Fig. 288	7.34		crystal structure: Fig. 176	83 H 2
$TmPt_2Si_2$	65	<3		Fig. 292	7.32		crystal structure: Fig. 176	85 H 2
$TmRu_2Si_2$	65.7	$\cong 1$		Fig. 370	7.38		crystal structure: Fig. 176	83 H 1
$TmRu_{3.5}Si_2$							magnetic ordering temperature 7.50 K	80 B 2
$TmCo_2Ge_2$	−0.8			Fig. 372	5.89		crystal structure: Fig. 176	73 M 1
$TmMn_2Ge_2$			458 Fig. 179	Fig. 267	6.2		p_{eff} at high temperature, at low temperature $p_{eff} = 8.2\,\mu_B$/Tm, crystal structure: Fig. 176	81 S 7
$TmRu_2Ge_2$	−6				7.10		crystal structure: Fig. 176	85 F 3

continued

Table 2 (continued)

	Θ K	T_C K	T_N K	χ	p_{eff} μ_B/R	p_s μ_B/R	Remarks	Ref.
$YbMn_2Si_2$			513 Fig. 179	Fig. 267	4.6		crystal structure: Fig. 176	81 S 7
$YbOs_2Si_2$	−21			Fig. 358	4.38		sample was inhomogeneous, crystal structure: Fig. 176	83 H 2
$YbPt_2Si_2$	−180				3.5		contained small amounts of secondary phase, crystal structure: Fig. 176	85 H 2
$YbRu_2Si_2$	−18			Fig. 370	3.54		alloy used was inhomogeneous, crystal structure: Fig. 176	83 H 1
$YbCo_2Ge_2$							Pauli paramagnet, crystal structure: Fig. 176	73 M 1
$YbMn_2Ge_2$			338 Fig. 179	Fig. 267	5.8		crystal structure: Fig. 176	81 S 7
$YbNi_2Ge_2$				Fig. 373			Yb in a mixed-valent state, crystal structure: Fig. 176	77 O 1
$LuCo_2Si_2$							Pauli paramagnet, crystal structure: Fig. 176	82 K 2
$LuMn_2Si_2$			464 Fig. 179		4.2		crystal structure: Fig. 176	81 S 7
$LuOs_2Si_2$				120			χ_m in 10^{-6} cm^3 mol^{-1} at 300 K, crystal structure: Fig. 176	83 H 2
$LuPt_2Si_2$				20			χ_m in 10^{-6} cm^3 mol^{-1}, crystal structure: Fig. 176	85 H 2
$LuRh_2Si_2$	−28			Fig. 186	0.7		peak in susceptibility at 17 K, no superconductivity down to 1.4 K, crystal structure: Fig. 176	83 F 1, 84 F 1
$LuRu_2Si_2$				80			Pauli paramagnet, χ_m in 10^{-6} cm^3 mol^{-1}	83 H 1
							enhanced paramagnet, superconductor at 2.4 K, crystal structure: Fig. 176	84 F 1
$LuCo_2Ge_2$				Fig. 372			Pauli paramanget, crystal structure: Fig. 176	73 M 1
$LuMn_2Ge_2$			453 Fig. 179		3.8		crystal structure: Fig. 176	81 S 7

R/M=2/5						
$Sc_2Fe_3Si_5$					$p_{Fe}<0.03\,\mu_B$, at 4.2 K, superconductor at 4.6 K	80 C 1
$Y_2Co_3Si_5$			Fig. 374		Pauli paramagnet	85 G 1
$Y_2Rh_3Si_5$			502		χ_m in $10^{-6}\,cm^3\,mol^{-1}$ at 300 K, Pauli paramagnet, superconductor at 4.4 K	82 C 2
$La_2Rh_3Si_5$			388		χ_m in $10^{-6}\,cm^3\,mol^{-1}$ at 300 K, Pauli paramagnet, superconductor at 2.7 K	82 C 2
$Ce_2Rh_3Si_5$					p_{eff} higher than the Ce^{3+} free-ion value, itinerant magnetism associated with 4d bands of Rh suggested	83 C 3
$Nd_2Rh_3Si_5$	−3		Fig. 375	3.85	at low temperature antiferromagnetic p_{eff} higher than the Nd^{3+} free-ion value, itinerant magnetism associated with 4d band of Rh suggested	82 C 2, 83 C 3
$Sm_2Fe_3Si_5$					magnetic transition temperatures from heat capacity $T_m=5.05$, 6.19, 7.35, 8.96 K: Fig. 376	83 V 1
$Sm_2Rh_3Si_5$			Fig. 377			82 C 2
$Gd_2Co_3Si_5$	−17.4		Fig. 374	7.89		85 G 1
$Gd_2Fe_3Si_5$	−15.4	Fig. 378	Fig. 379	7.8	Θ_c parallel to tetragonal axis (see caption to Fig. 380), Mössbauer effect studies indicate an effective moment smaller than $7\cdot10^{-3}\,\mu_B$/Fe in an applied field of 50 kOe at 4.2 K	81 B 1
	−23		Fig. 381	8.1	at 10 K paramagnetic, at 4.2 K magnetically ordered	83 N 2
					magnetic transition temperature from heat capacity $T_m=8.40$ K: Fig. 376	83 V 1

continued

Table 2 (continued)

	Θ K	T_C K	T_N K	χ	p_{eff} μ_B/R	p_s μ_B/R	Remarks	Ref.
$Gd_2Rh_3Si_5$	−26			Fig. 382	8.18		at low temperature antiferromagnetic, itinerant magnetism associated with 4d bands of Rh suggested	82 C 2, 83 C 3
$Tb_2Co_3Si_5$	8.8			Fig. 374	9.73			85 G 1
$Tb_2Fe_3Si_5$	1.8		Fig. 378	Fig. 379 Fig. 380 Fib. 383	9.6		Θ_c parallel to tetragonal axis (see caption to Fig. 380), Mössbauer effect studies indicate $p_{eff} < 7 \cdot 10^{-3}$ μ_B/Fe at 50 kOe and 4.2 K	81 B 1
			10.3		9.6	8.7	from neutron diffraction: p_s at 4.9 K	82 M 2
							magnetic transition temperatures from heat capacity $T_m = 7.06$ and 10.02 K: Fig. 376	83 V 1
$Tb_2Ir_3Si_5$	4		11	Fig. 321	10.72			84 H 2
$Tb_2Rh_3Si_5$	−8		~8.5	Fig. 384	10.04			82 C 2
							itinerant magnetism associated with 4d bands of Rh suggested	83 C 3
$Dy_2Co_3Si_5$	8.7			Fig. 374	11.01			85 G 1
$Dy_2Fe_3Si_5$	−11.4		Fig. 378	Fig. 379	10.4		Θ_c parallel to tetragonal axis (see caption to Fig. 380)	81 B 1
							magnetic transition temperature from heat capacity $T_m = 4.2$ K: Fig. 376	83 V 1
$Dy_2Rh_3Si_5$	−1		Fig. 385		11		at low temperature antiferromagnetic, itinerant magnetism associated with 4d band of Rh suggested	82 C 2, 83 C 3
$Ho_2Co_3Si_5$	−5.8			Fig. 374	10.7			85 G 1

$Ho_2Fe_3Si_5$	0.3	Fig. 378	Fig. 379	10.4		Θ_c parallel to tetragonal axis (see caption to Fig. 380) 81 B 1 magnetic transition temperature from heat capacity $T_m = 2.82$ K: Fig. 376 83 V 1
$Ho_2Rh_3Si_5$	−1		Fig. 386	10.61		at low temperature antiferromagnetic 82 C 2, 83 C 3, 85 G 1
$Er_2Co_3Si_5$	3.1		Fig. 374	9.64		
$Er_2Fe_3Si_5$	−8.0	Fig. 378	Fig. 379 Fig. 383	9.7		Θ_c parallel to the tetragonal axis (see caption to Fig. 380) 81 B 1
					8.0	Er moment p_s from Mössbauer effect study; 83 S 3 magnetic transition temperatures from heat capacity $T_m = 2.352$, 2.381, 2.401 and 2.79 K: Fig. 376 83 V 1
$Er_2Rh_3Si_5$	−3		Fig. 386	9.72		at low temperature antiferromagnetic 82 C 2, 83 C 3, 85 G 1
$Tm_2Co_3Si_5$	−4.1		Fig. 374	7.66		
$Tm_2Fe_3Si_5$						magnetic transition temperature from heat capacity $T_m = 1.06$ K: Fig. 376 83 V 1
		1.15 Fig. 387	Fig. 387		6.5 Fig. 387	from neutron diffraction: 85 M 1 noncollinear antiferromagnetic structure, Tm moments along the [110] direction at 0.35 K,
			Fig. 388			low-temperature phase diagram: Fig. 389 ac susceptibility at different pressure: Fig. 388 85 V 1
$Yb_2Fe_3Si_5$						magnetic transition temperature from heat capacity $T_m = 1.70$ K: Fig. 376 83 V 1
$Lu_2Co_3Si_5$			Fig. 374			Pauli paramagnet 85 G 1
$YFeSi_3$			Fig. 390			Pauli paramagnet 78 G 1
$CeCoSi_3$			Fig. 391 Fig. 392			Ce in mixed-valent state suggested, below 1.4 K superconductor 85 H 1

continued

Table 2 (continued)

	Θ K	T_C K	T_N K	χ	p_{eff} μ_B/R	p_s μ_B/R	Remarks	Ref.
$CeIrSi_3$	−113			Fig. 391	2.59		Ce trivalent suggested	85 H 1
	−10			Fig. 392	1.38		from Curie-Weiss behaviour at low temperatures	
$CeOsSi_3$	−3			Fig. 391	1.03		Ce in mixed-valent state suggested, p_{eff} from Curie-Weiss behaviour at low temperatures	85 H 1
$CeRhSi_3$	−106			Fig. 391	2.62		Ce trivalent	85 H 1
	−7			Fig. 392	1.33		from Curie-Weiss behaviour at low temperatures	
$CeRuSi_3$				Fig. 391			Ce in mixed-valent state suggested	85 H 1
$GdFeSi_3$	35			Fig. 390	7.79			78 G 1
$TbFeSi_3$	47			Fig. 390	9.36			78 G 1
$DyFeSi_3$	82			Fig. 390	9.72			78 G 1
$HoFeSi_3$	49			Fig. 390	10.18			78 G 1
$ErFeSi_3$	65			Fig. 390	9.10			78 G 1
$LuFeSi_3$				Fig. 390			Pauli paramagnet	78 G 1
R/M = 1/3.6								
$ErRh_{1.1}Sn_{3.6}$	0.17	0.46		Fig. 393	8.66		$\sigma_m(T)$: Fig. 393, superconductor at 1.36 K, below T_C superconductivity disappears, p_{eff} for ground-state doublet	81 A 1
	−2			Fig. 394	9.62		single crystal, in low-temperature range 1.7 to 4.2 K for $H \rightarrow 0$: $\Theta = 0.2$ K, $\sigma(H)$ at 4.2 K: Fig. 395	86 R 1
$Er_{4.75}Rh_6Sn_{18.25}$				Fig. 396			$\chi_{ac}(T)$ at low temperatures: Fig. 396, superconductor at 0.68 K	84 M 3
R/M = 1/4								
$LuRh_{1.2}Sn_{4.0}$				$\cong 1$			χ_g in 10^{-6} cm^3 g^{-1}	86 R 1

$GdRh_{1.07}Sn_{4.21}$	−28.8		11.6	Fig. 397	7.96		$\sigma(H)$ at 4.2 K: Fig. 398, coexistence of Gd ion antiferromagnetism and itinerant electron ferromagnetism of Rh atoms suggested	86 R 2
R/M=2/9								
$Y_2Fe_4Si_9$				0.53 Fig. 399	0		no Curie-Weiss behaviour, χ_g in $10^{-6}\,cm^3\,g^{-1}$ at room temperature	78 G 1
$Gd_2Fe_4Si_9$	102			Fig. 399	7.25			78 G 1
$Tb_2Fe_4Si_9$	167			Fig. 399	7.91			78 G 1
$Dy_2Fe_4Si_9$	2			Fig. 399	9.26			78 G 1
$Ho_2Fe_4Si_9$	−41			Fig. 399	9.05			78 G 1
$Er_2Fe_4Si_9$	−31			Fig. 399	8.09			78 G 1
$Tm_2Fe_4Si_9$	−47			Fig. 399	6.55			78 G 1
$Yb_2Fe_4Si_9$	−65			Fig. 399	3.59			78 G 1
$Lu_2Fe_4Si_9$				0.77 Fig. 399			no Curie-Weiss behaviour, χ_g in $10^{-6}\,cm^3\,g^{-1}$ at room temperature	78 G 1
R/M=1/6								
YCo_6Sn_6				1.62			χ_g in $10^{-6}\,cm^3\,g^{-1}$, for $78\,K < T < 293\,K$ susceptibility temperature-independent, Pauli paramagnet	84 S 2
$TbCo_6Sn_6$	−15				9.59			84 S 2
$DyCo_6Sn_6$	2			Fig. 400	10.66			84 S 2
$HoCo_6Sn_6$	−3			Fig. 400	10.59			84 S 2
$ErCo_6Sn_6$	3			Fig. 400	9.59			84 S 2
$TmCo_6Sn_6$	20				7.51			84 S 2
$LuCo_6Sn_6$				Fig. 400			Pauli paramagnet, χ_g at 78 and 293 K, $2.11 \cdot 10^{-6}$ and $1.44 \cdot 10^{-6}\,cm^3\,g^{-1}$, respectively	84 S 2
R/M=1/13								
$La(Co_xSi_{1-x})_{13}$						Fig. 401		83 P 1
$La(Fe_xSi_{1-x})_{13}$		Fig. 402		Fig. 403 Fig. 404		Fig. 402	$\sigma(T)$ at 3 kOe: Fig. 405	83 P 1

2.10.3 Figures

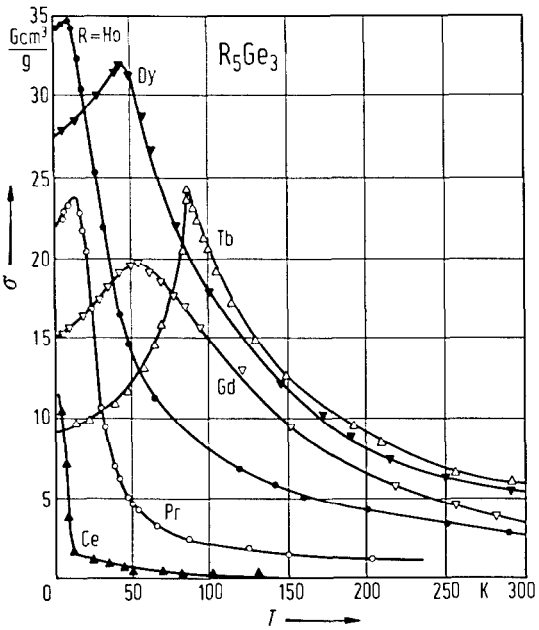

Fig. 1. R_5Ge_3, R = Ce, Pr, Gd, Tb, Dy, Ho. Temperature dependence of σ at 9 kOe for R = Ce and Ho compounds and at 18 kOe for the rest [67 B 1].

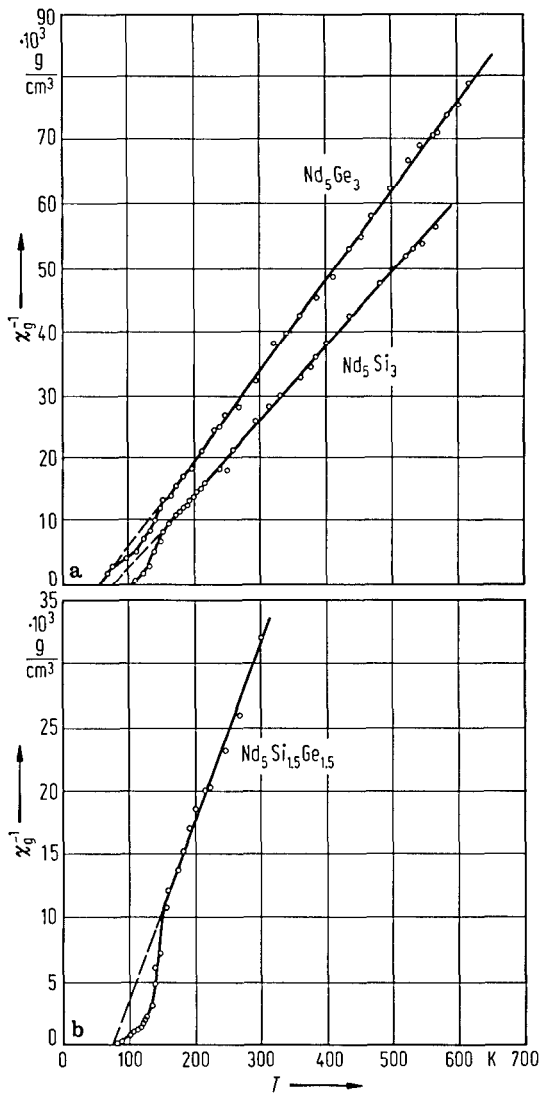

Fig. 2. Nd_5M_3, (a) M = Si, Ge, (b) M = $Si_{1.5}Ge_{1.5}$. Temperature dependence of χ_g^{-1} [69 N 1].

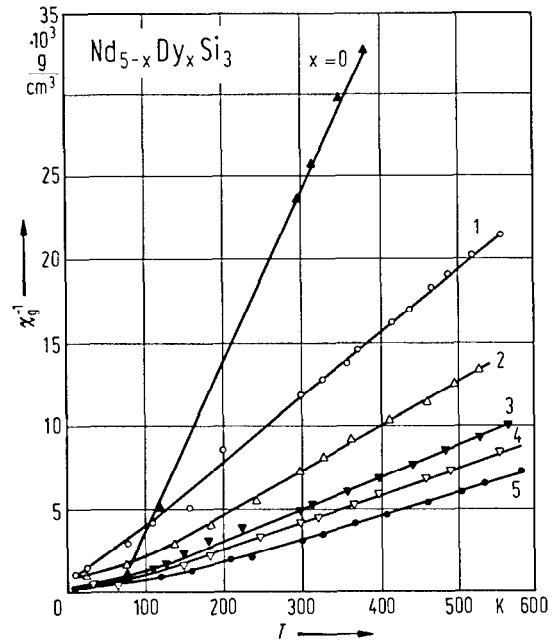

Fig. 3. $Nd_{5-x}Dy_xSi_3$. Temperature dependence of χ_g^{-1} for various compositions [76 G 1].

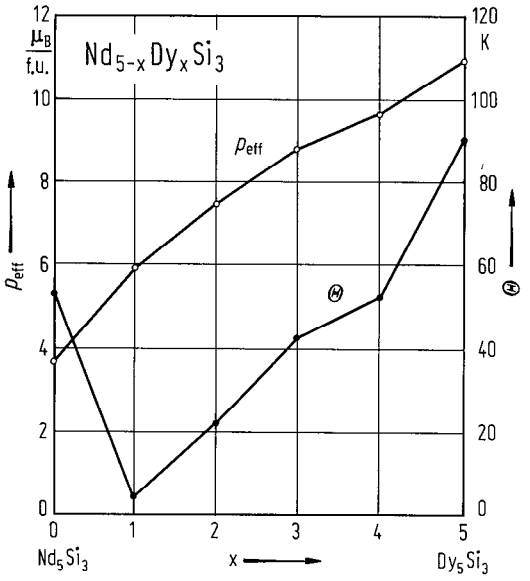

Fig. 4. $Nd_{5-x}Dy_xSi_3$. Composition dependence of Θ and p_{eff} [76 G 1].

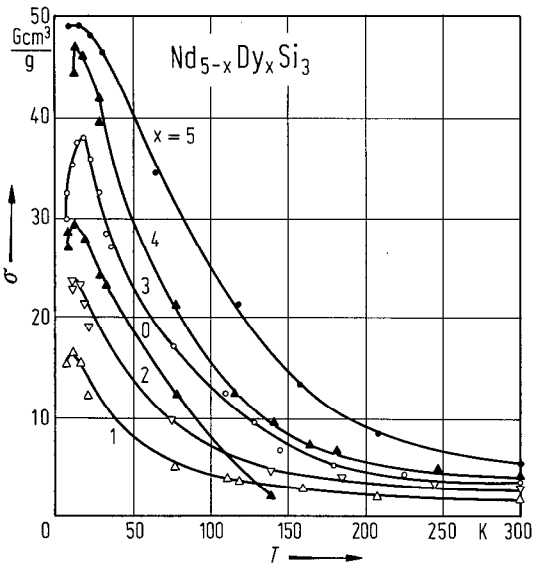

Fig. 5. $Nd_{5-x}Dy_xSi_3$. Temperature dependence of σ for various compositions [76 G 1].

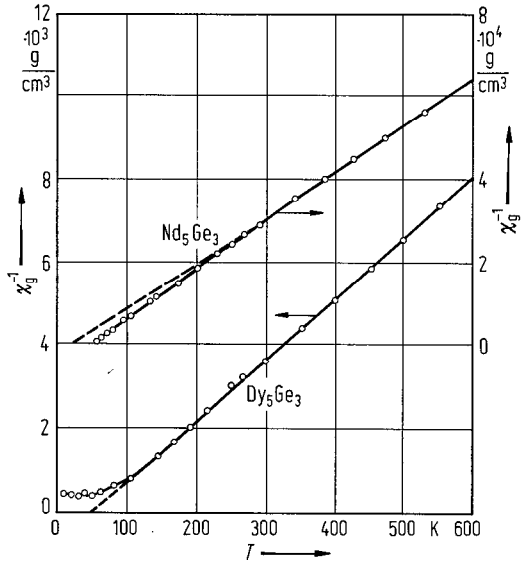

Fig. 6. Nd_5Ge_3, Dy_5Ge_3. Temperature dependence of χ_g^{-1} [67 B 1].

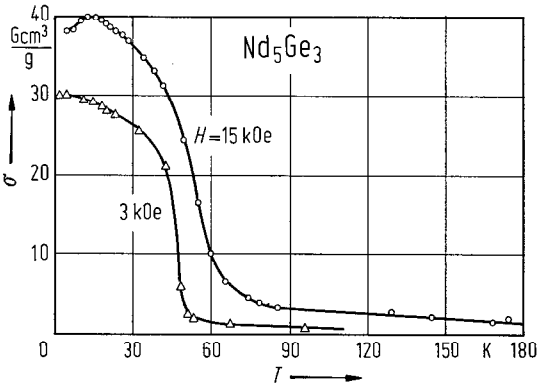

Fig. 7. Nd_5Ge_3. Temperature dependence of σ at 3 and 15 kOe [67 B 1].

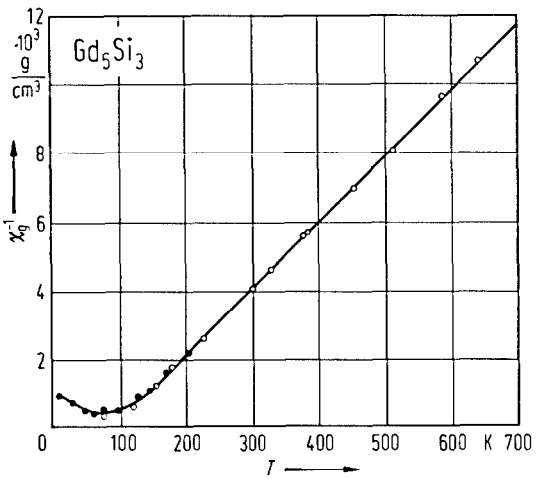

Fig. 8. Gd_5Si_3. Temperature dependence of χ_g^{-1}. Open circles: vibrating-sample magnetometer, solid circles: Faraday balance [76 G 1].

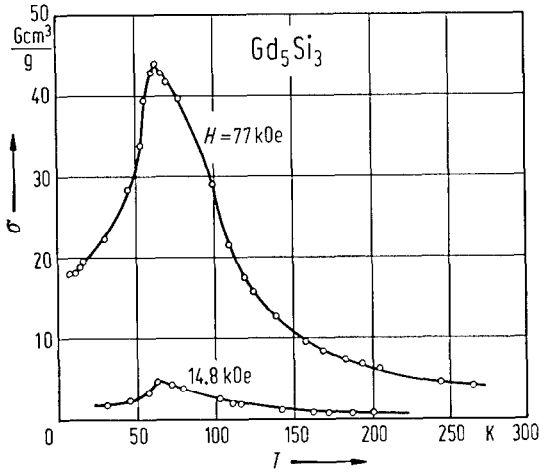

Fig. 9. Gd_5Si_3. Temperature dependence of σ at 14.8 and 77 kOe [76 G 1].

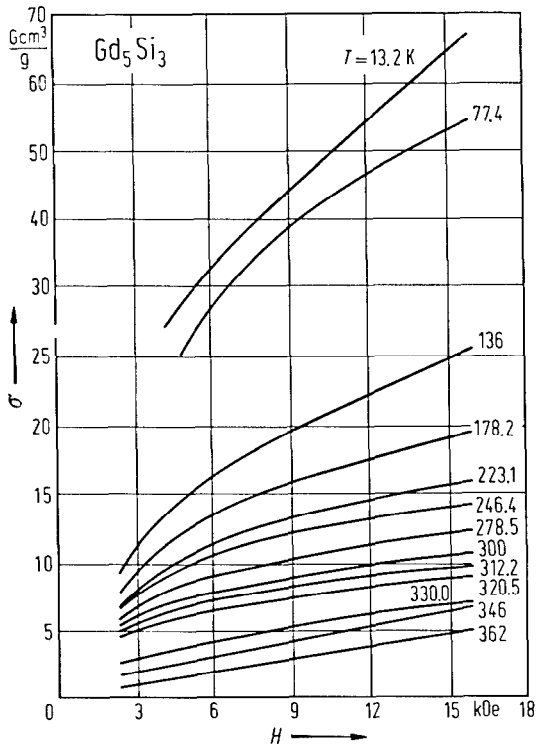

Fig. 10. Gd_5Si_3. Magnetic field dependence of σ at different temperatures [76 G 1].

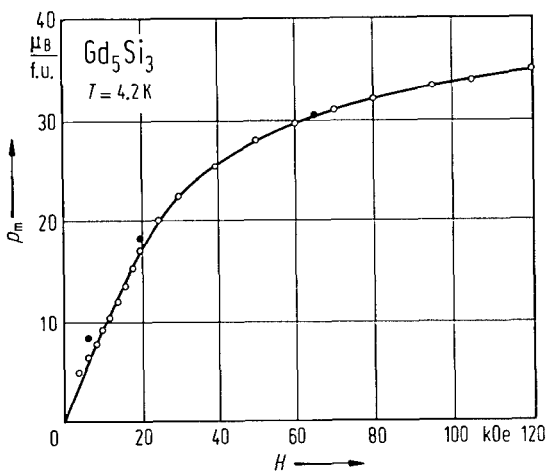

Fig. 11. Gd_5Si_3. Magnetic field dependence of p_m at 4.2 K. Open and solid circles denote data obtained with increasing and decreasing field, respectively [76 G 1].

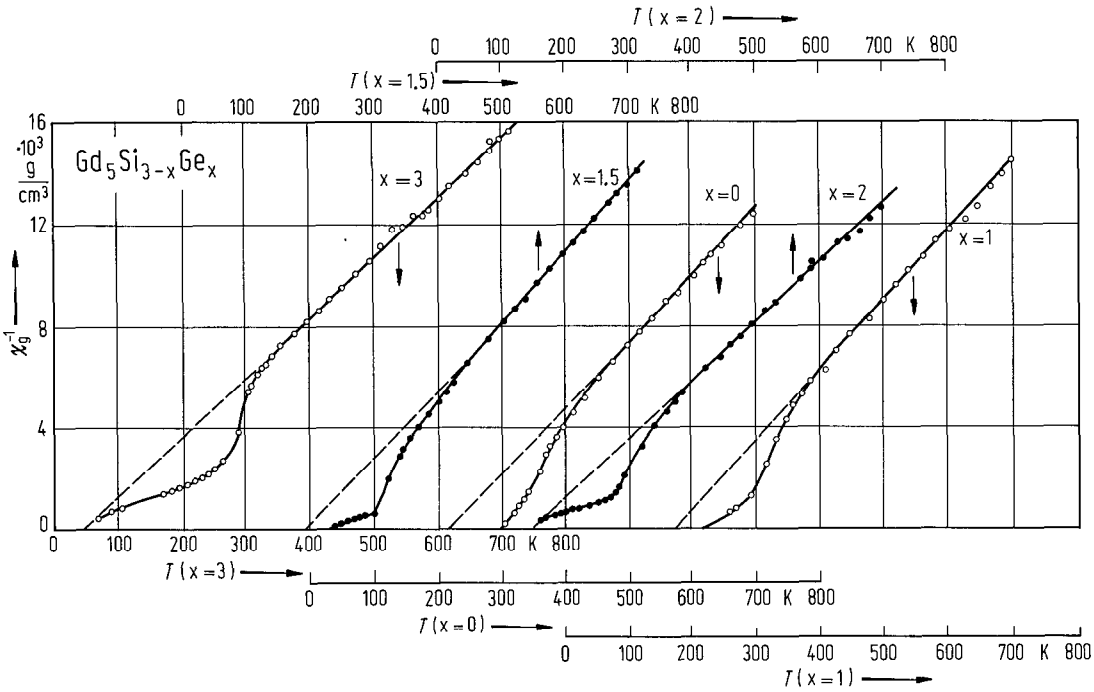

Fig. 12. $Gd_5Si_{3-x}Ge_x$. Temperature dependence of χ_g^{-1} [69 N 1].

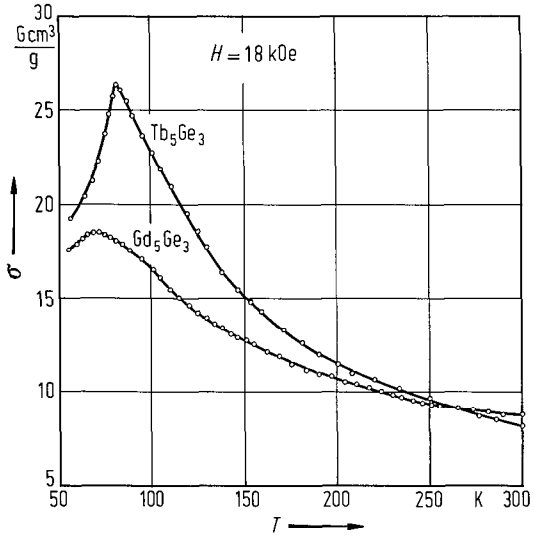

Fig. 13. Gd_5Ge_3, Tb_5Ge_3. Temperature dependence of σ at 18 kOe [80 B 1].

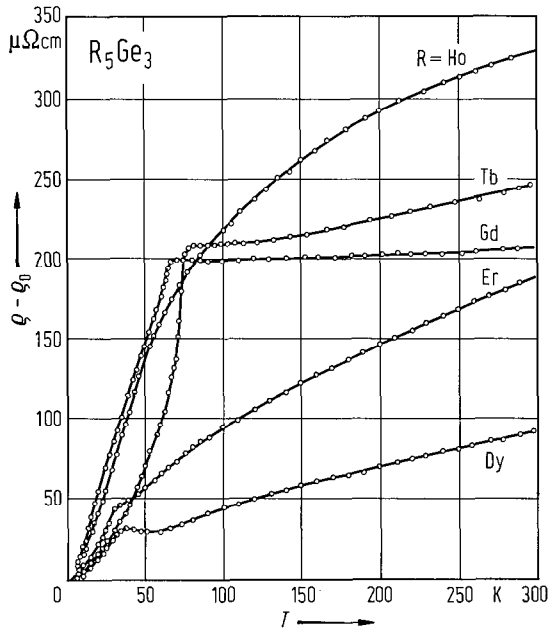

Fig. 14. R_5Ge_3, R = Gd, Tb, Dy, Ho, Er. Temperature dependence of the electrical resistivity $\varrho - \varrho_0$. The phase transition temperatures are accompanied by a cusp in the temperature dependence of ϱ [80 B 1].

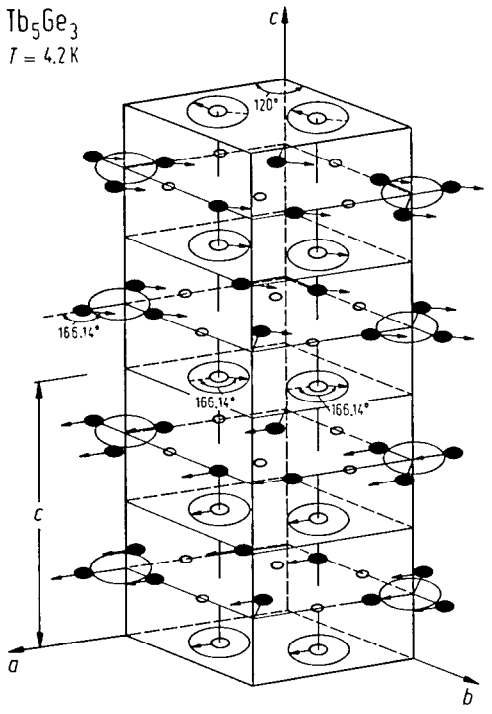

Fig. 15. Tb_5Ge_3. Magnetic spiral structure at 4.2 K showing two crystallographic unit cells. Solid and open circles with arrows correspond to Tb at 6(g) and 4(d) positions, respectively. The open circles (without arrows) correspond to the Ge 6(g) position. The spiral angle of 166.14° is between the magnetic moments of second nearest Tb neighbours [82 S 1].

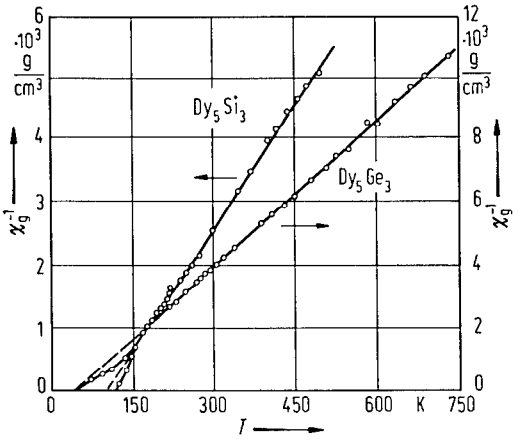

Fig. 16. Dy_5Si_3, Dy_5Ge_3. Temperature dependence of χ_g^{-1} [69 N 1].

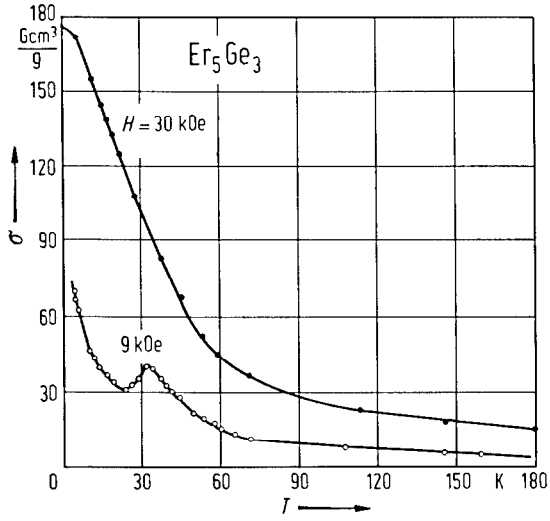

Fig. 17. Er_5Ge_3. Temperature dependence of σ at 9 and 30 kOe [67 B 1].

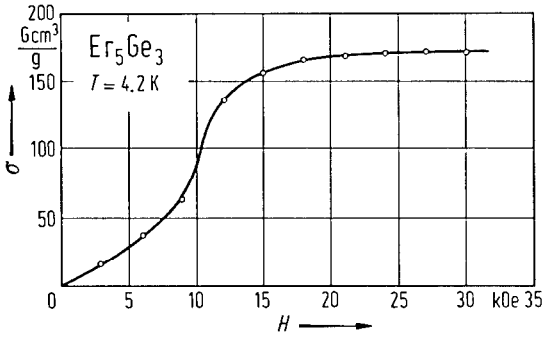

Fig. 18. Er_5Ge_3. Magnetic field dependence of σ at 4.2 K [67 B 1].

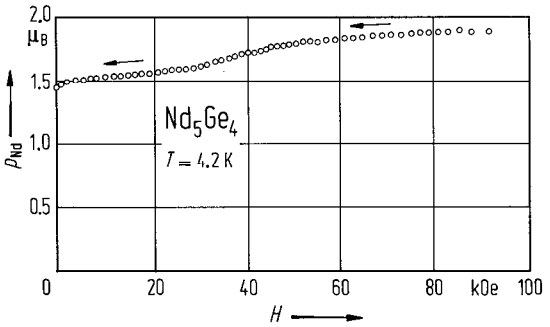

Fig. 19. Nd_5Ge_4. Magnetic field dependence of the magnetic moment per Nd atom at 4.2 K. A field of 95 kOe had been applied on cooling the powder sample through the Curie point down to 4 K [81 S 3].

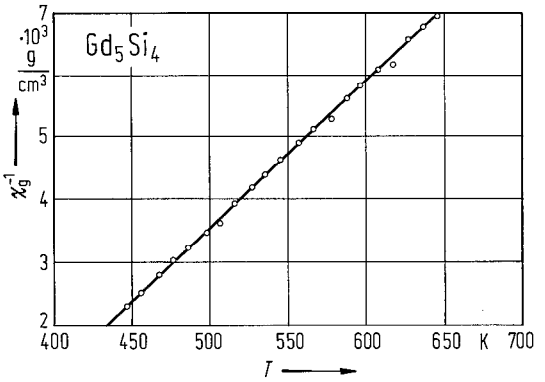

Fig. 20. Gd_5Si_4. Temperature dependence of χ_g^{-1} [80 S 3].

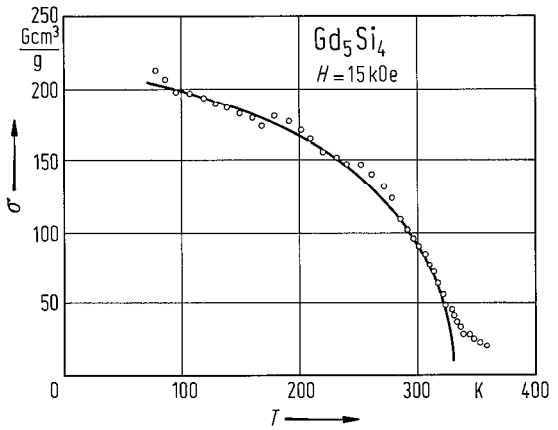

Fig. 21. Gd_5Si_4. Temperature dependence of σ at 15 kOe [80 S 3].

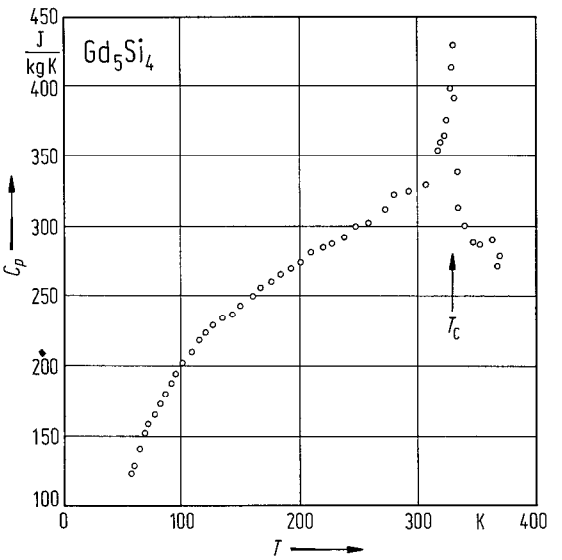

Fig. 22. Gd_5Si_4. Temperature dependence of the heat capacity C_p [85 S 3].

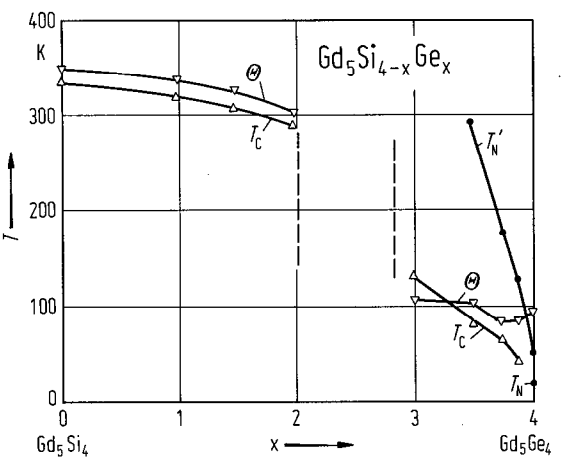

Fig. 23. $Gd_5Si_{4-x}Ge_x$. Composition dependence of Θ, T_C, and Néel temperatures T_N and T_N' [67 H 1].

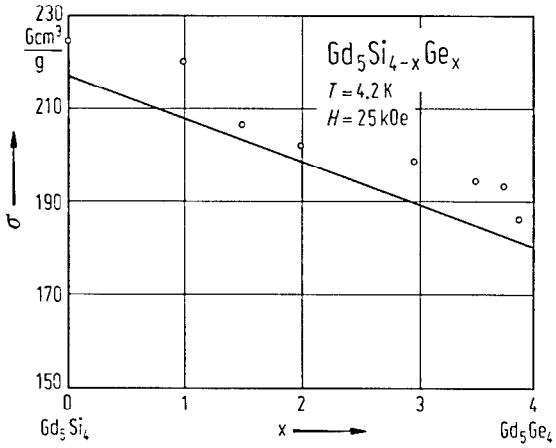

Fig. 24. $Gd_5Si_{4-x}Ge_x$. Composition dependence of σ at 4.2 K and 25 kOe. The solid line is theoretical [67 H 1].

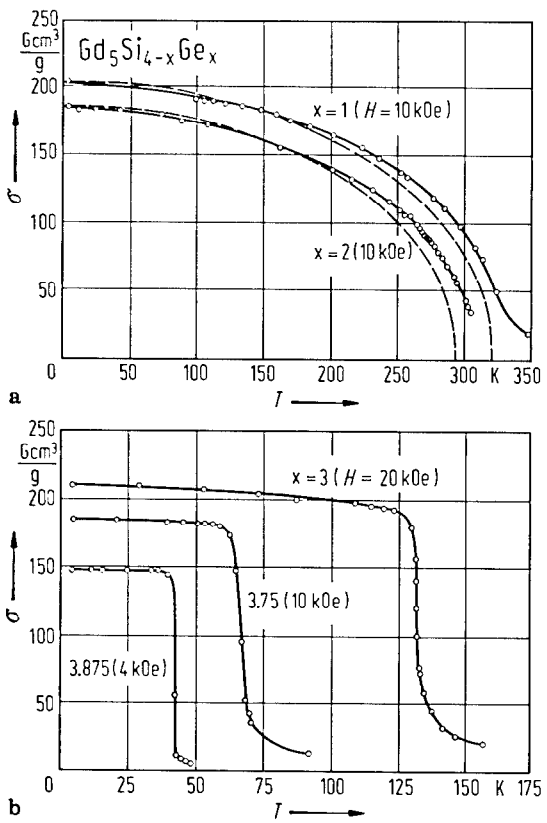

Fig. 25. $Gd_5Si_{4-x}Ge_x$. Temperature dependence of σ for (a) x = 1 and x = 2 at 10 kOe. Dashed curves are Brillouin functions for $J = 7/2$. (b) x = 3 at 20 kOe, x = 3.75 at 10 kOe and x = 3.875 at 4 kOe [67 H 1].

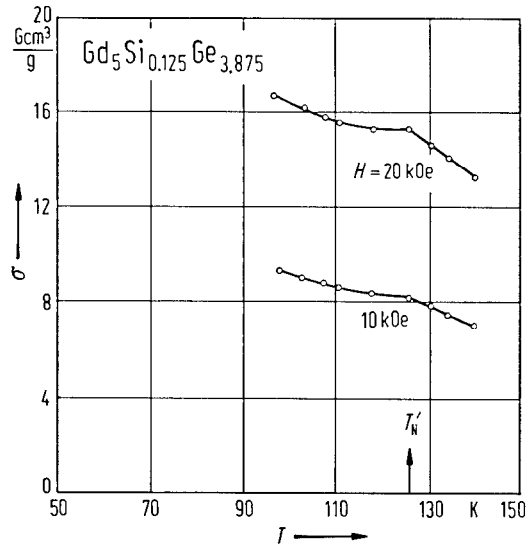

Fig. 26. $Gd_5Si_{0.125}Ge_{3.875}$. Temperature dependence of σ at 10 and 20 kOe in the temperature range where a small peak at T_N' is observed [67 H 1].

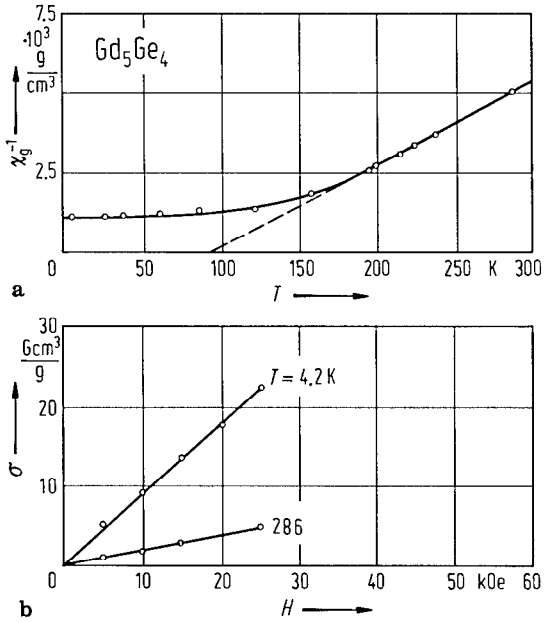

Fig. 27. Gd_5Ge_4. (a) Temperature dependence of χ_g^{-1}. $\Theta = 94$ K. (b) Magnetic field dependence of σ at 4.2 and 286 K [67 H 1].

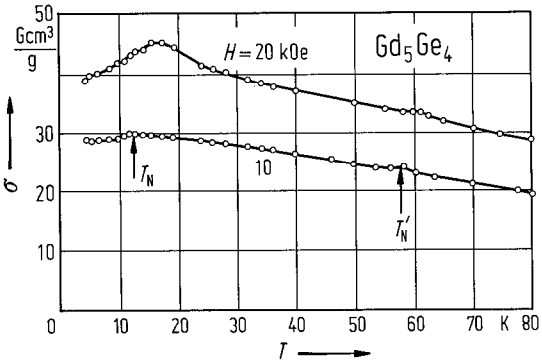

Fig. 28. Gd_5Ge_4. Temperature dependence of σ. Two Néel temperatures T_N and T_N' are observed [67 H 1].

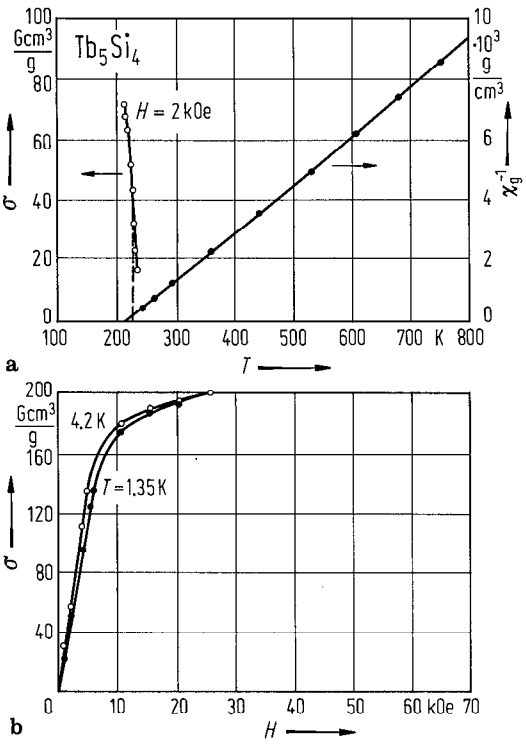

Fig. 29. Tb_5Si_4. (a) Temperature dependence of σ at 2 kOe and χ_g^{-1}. The dashed line represents the extrapolation of the $\sigma(T)$ data used in a σ^2 vs. H/σ plot to derive T_C. (b) Magnetic field dependence of σ at 1.35 and 4.2 K [67 H 1].

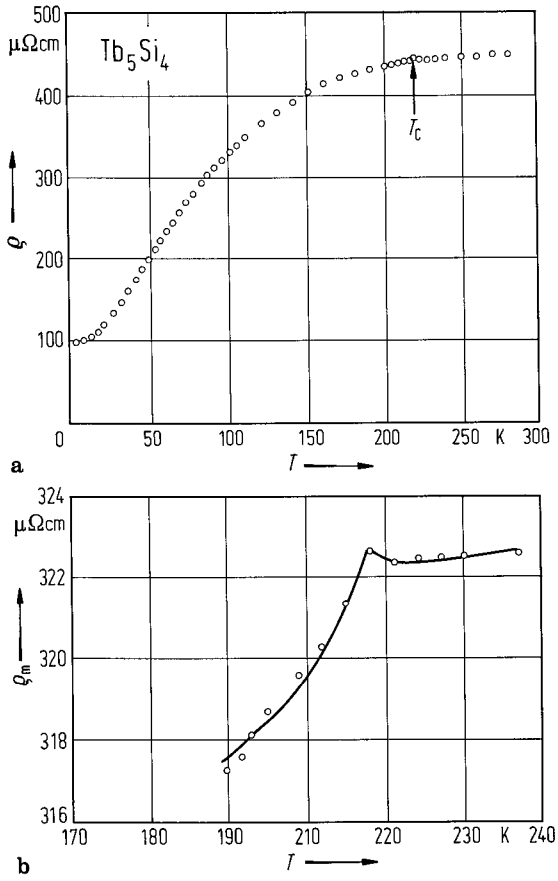

Fig. 30. Tb_5Si_4. (a) Temperature dependence of the electrical resistivity ϱ. (b) The magnetic ordering temperature is given by the cusp in the magnetic contribution to the electrical resistivity curve, ϱ_m [85 S 3].

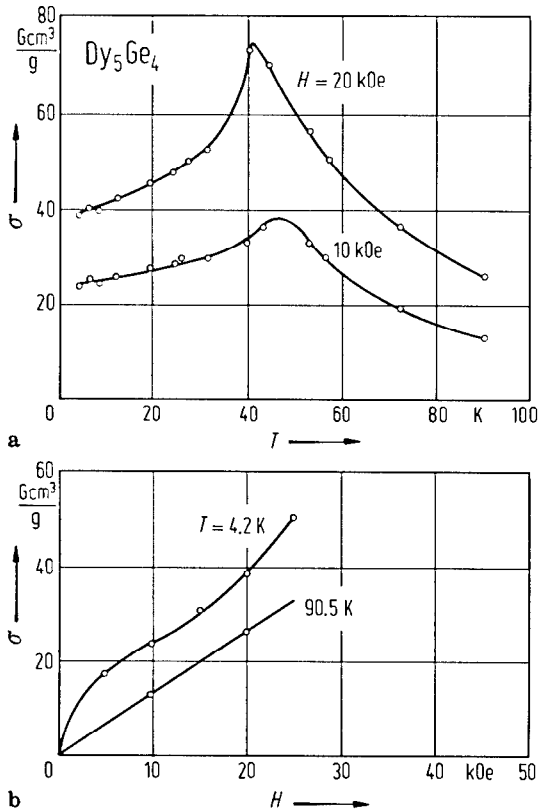

Fig. 31. Dy_5Ge_4. Temperature dependence of σ at 10 and 20 kOe, and magnetic field dependence of σ at 4.2 and 90.5 K [67 H 1].

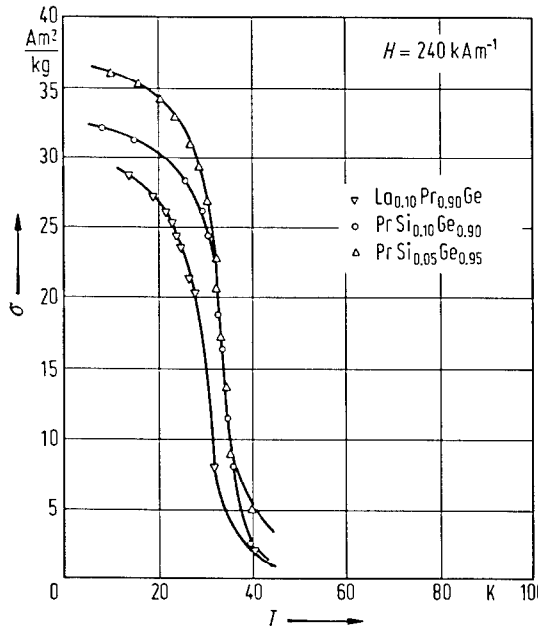

Fig. 33. $La_{0.10}Pr_{0.90}Ge$, $PrSi_{0.10}Ge_{0.90}$, $PrSi_{0.05}Ge_{0.95}$. Temperature dependence of σ at 240 kA/m [85 S 2].

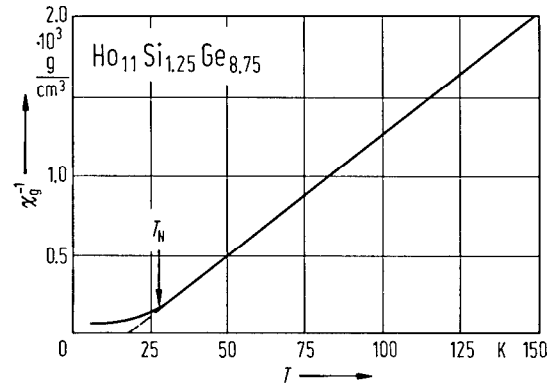

Fig. 32. $Ho_{11}Si_{1.25}Ge_{8.75}$. Temperature dependence of χ_g^{-1} [80 S 2].

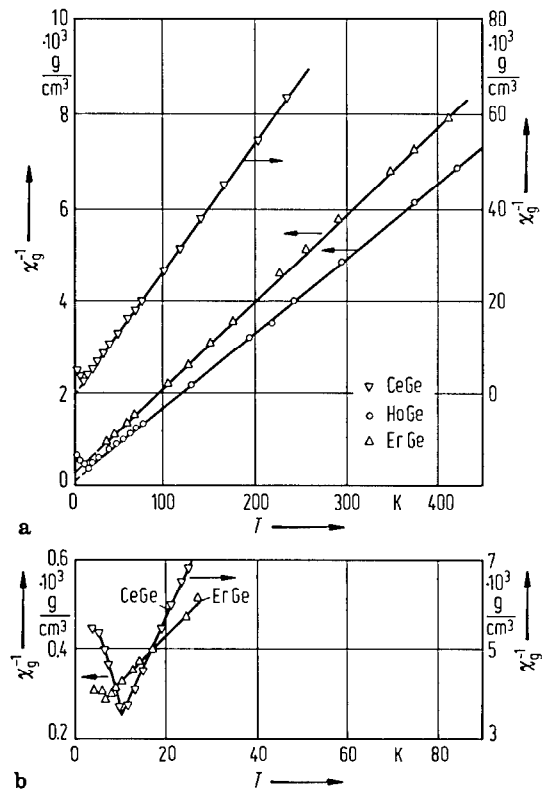

Fig. 34. RGe, R = Ce, Ho, Er. (a) Temperature dependence of χ_g^{-1}. (b) Low-temperature part for CeGe and ErGe [66 B 1].

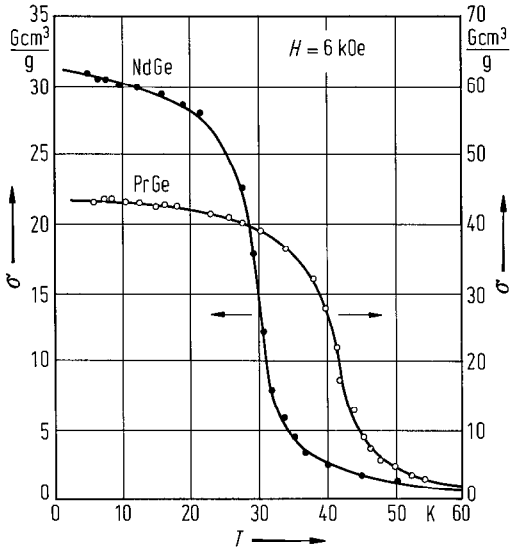

Fig. 35. PrGe, NdGe. Temperature dependence of σ at 6 kOe [66 B 1].

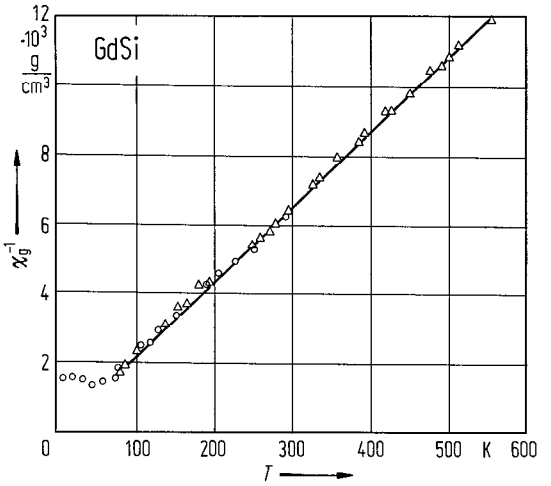

Fig. 37. GdSi. Temperature dependence of χ_g^{-1}. Circles: vibrating-sample magnetometer, triangles: Faraday balance [76 G 1].

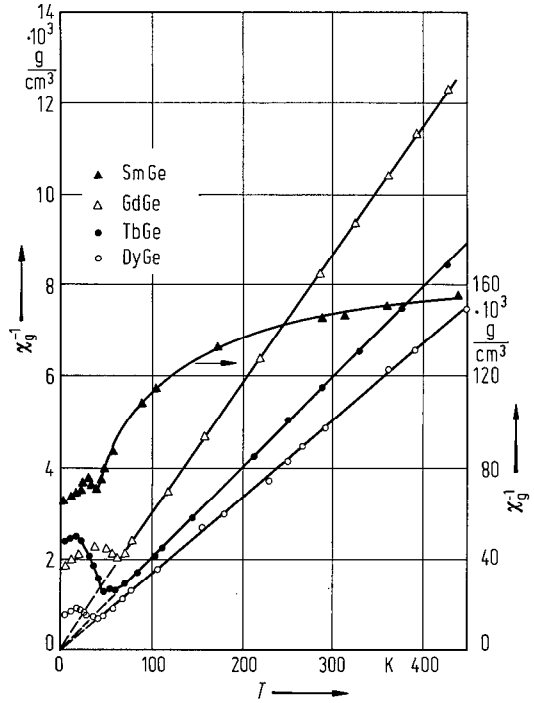

Fig. 36. RGe, R = Sm, Gd, Tb, Dy. Temperature dependence of χ_g^{-1} [66 B 1].

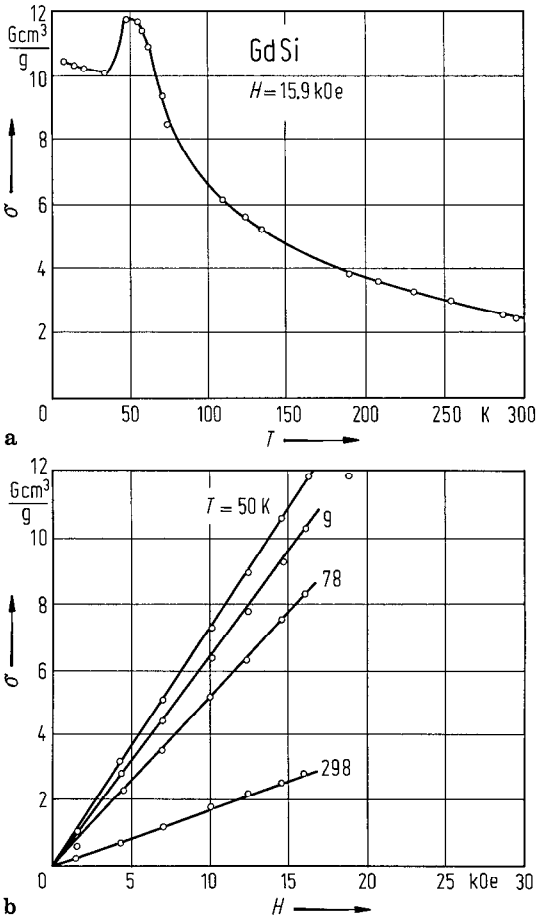

Fig. 38. GdSi. (a) Temperature dependence of σ at 15.9 kOe. (b) Magnetic field dependence of σ at various temperatures [76 G 1].

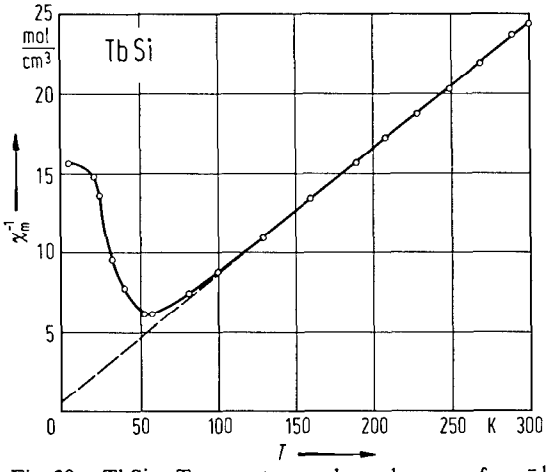

Fig. 39. TbSi. Temperature dependence of χ_m^{-1} [70 N 1].

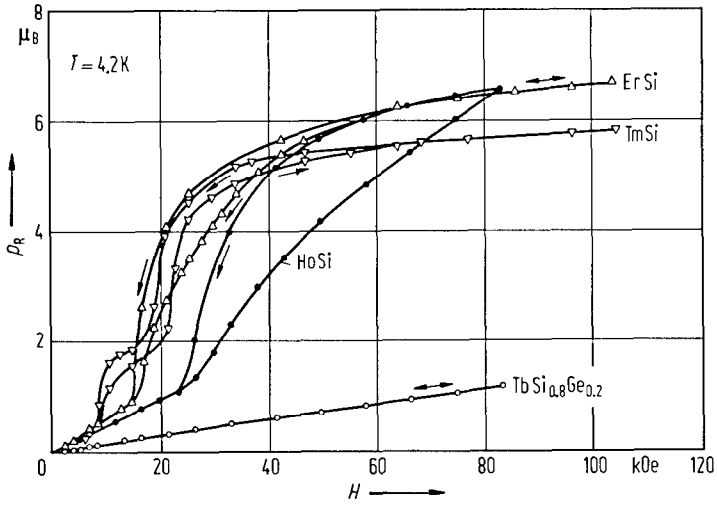

Fig. 40. RSi, R = Ho, Er, Tm; $TbSi_{0.8}Ge_{0.2}$. Magnetic field dependence of the magnetic moment per rare earth atom at 4.2 K [71 N 1].

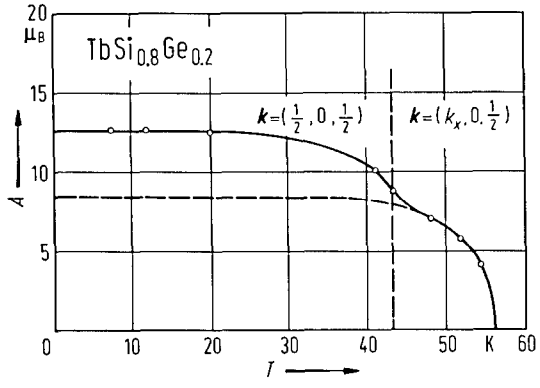

Fig. 41. $TbSi_{0.8}Ge_{0.2}$. Temperature dependence of the magnetic amplitude A of the sinusoidal modulation of the Tb magnetic moments in the ordered state. Modulation wavevectors k are indicated. Dashed line represents the Brillouin law [84 N 1].

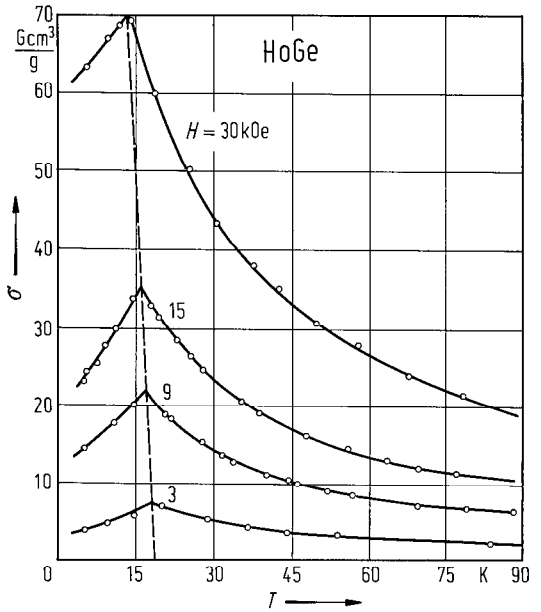

Fig. 42. HoGe. Temperature dependence of σ at various magnetic fields [66 B 1].

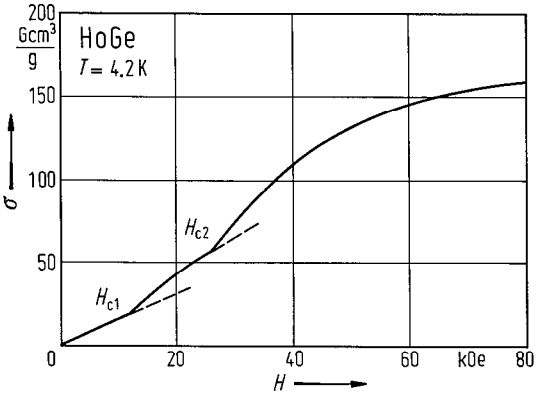

Fig. 43. HoGe. Magnetic field dependence of σ at 4.2 K. H_{c1} and H_{c2} are two magnetic critical fields, above H_{c2} the ordering is ferromagnetic [66 B 1].

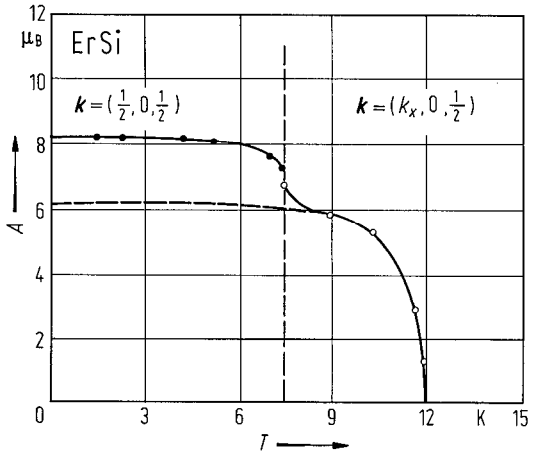

Fig. 44. ErSi. Temperature dependence of the magnetic amplitude A of the sinusoidal modulation of the Er magnetic moments in the ordered state. Modulation wavevectors k are indicated. Dashed line represents the Brillouin law [84 N 1].

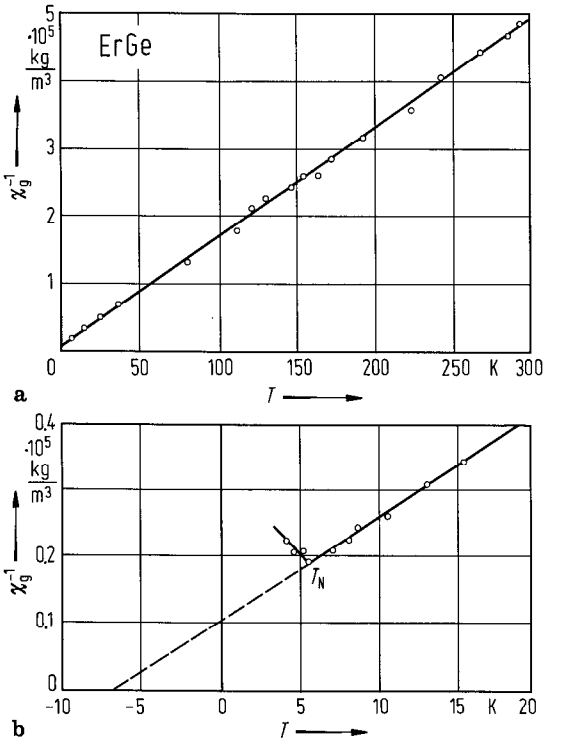

Fig. 45. ErGe. (a) Temperature dependence of χ_g^{-1}. (b) Shows the low temperature behaviour using enlarged scales [85 S 1].

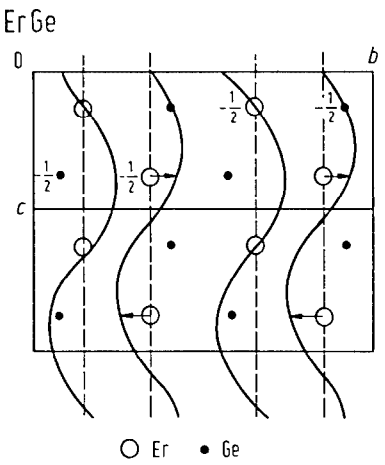

Fig. 46. ErGe. Magnetic structure at 4.2 K. The wavevector $k_z = 0.466 \cdot 2\pi/c$ corresponds to a phase difference of 167.76° from unit cell to unit cell along the c axis [85 S 1].

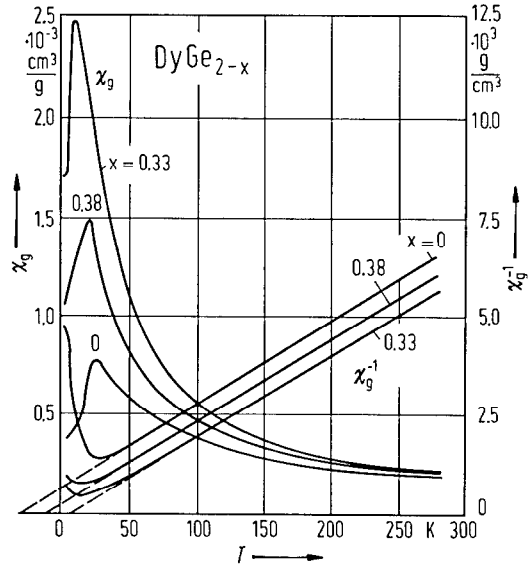

Fig. 47. $DyGe_{2-x}$. Temperature dependence of χ_g and χ_g^{-1} [66 S 1].

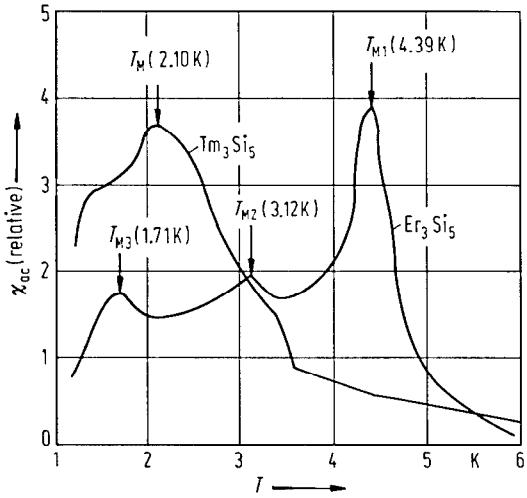

Fig. 48. Er_3Si_5, Tm_3Si_5. Temperature dependence of the magnetic ac susceptibility. Magnetic ordering temperatures are indicated by arrows [83 W 1].

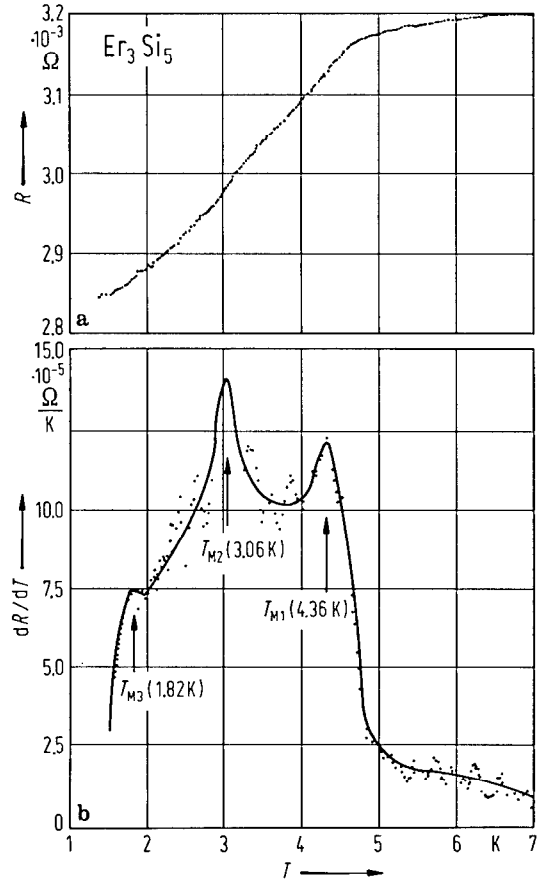

Fig. 49. Er_3Si_5. Temperature dependence of low-temperature resistance (a) and temperature derivate of the resistance (b). The transition temperature is accompanied by a cusp in the temperature dependence of R [83 W 1].

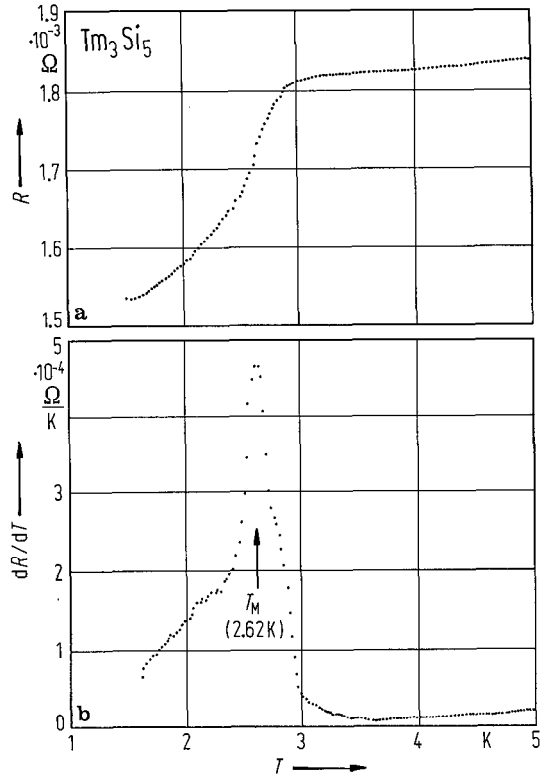

Fig. 50. Tm_3Si_5. Temperature dependence of low-temperature resistance (a) and temperature derivative of the resistance (b). The transition temperature is accompanied by a cusp in the temperature dependence of R [83 W 1].

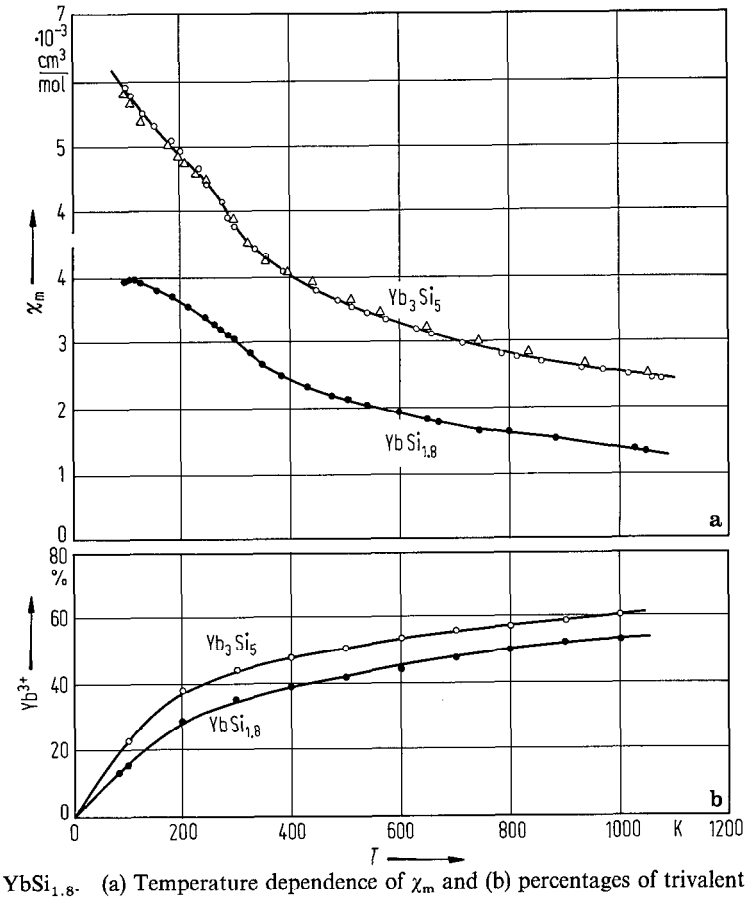

Fig. 51. Yb_3Si_5, $YbSi_{1.8}$. (a) Temperature dependence of χ_m and (b) percentages of trivalent Yb atoms [79I1].

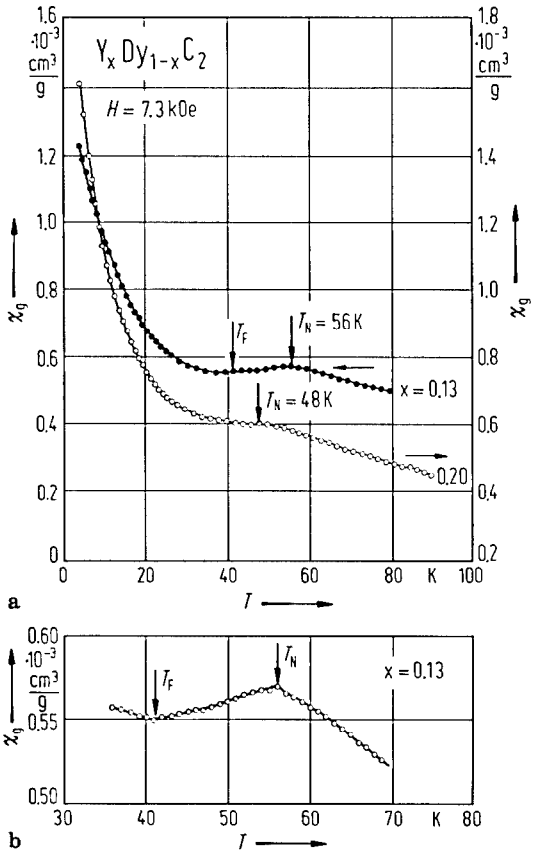

Fig. 52. $Y_xDy_{1-x}C_2$. (a) Temperature dependence of χ_g at 7.3 kOe for x = 0.13 and 0.20. (b) shows the data for x = 0.13 near the Néel point. Low-temperature minimum of the magnetic susceptibility at T_F [79 S 2].

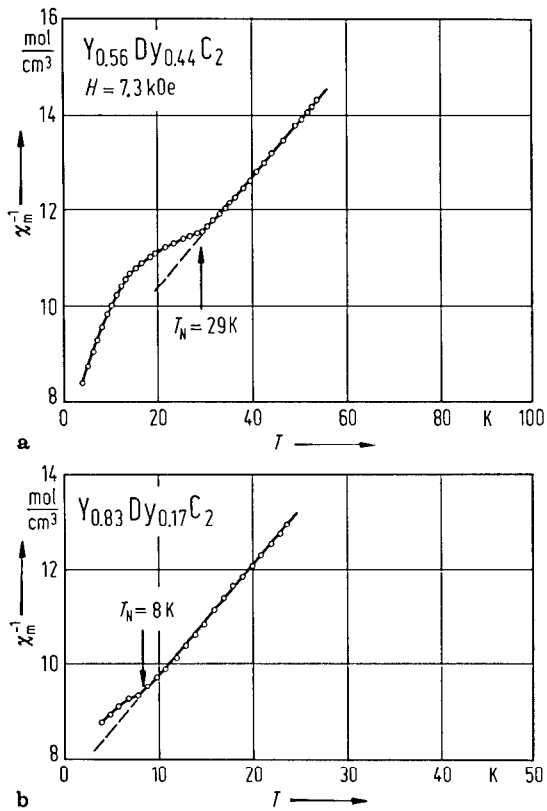

Fig. 53. $Y_xDy_{1-x}C_2$. Temperature dependence of χ_m^{-1} at 7.3 kOe for (a) x = 0.56 and (b) x = 0.83 [79 S 2].

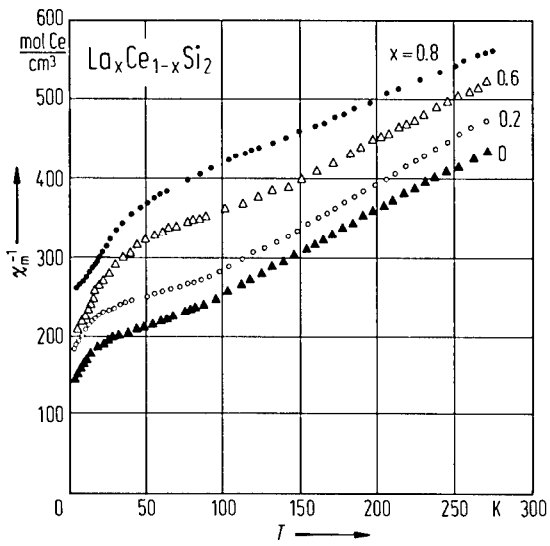

Fig. 54. $La_xCe_{1-x}Si_2$. Temperature dependence of χ_m^{-1} for various compositions [83 Y 2].

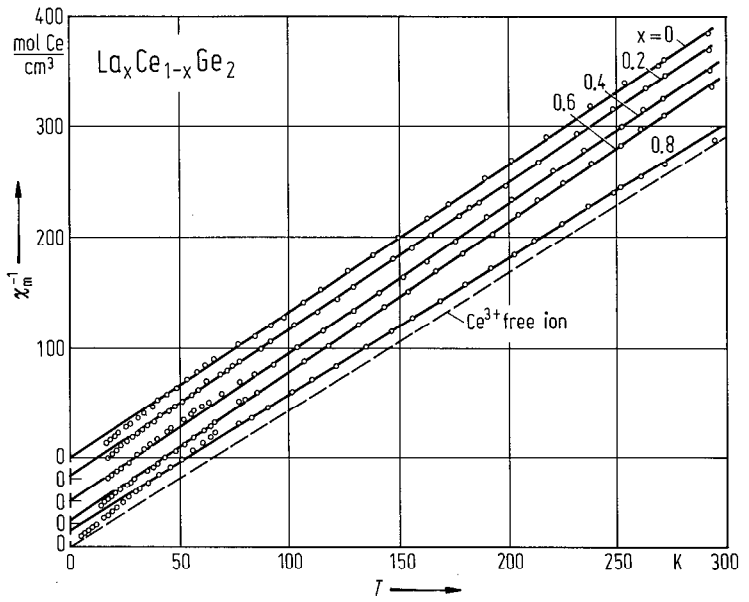

Fig. 55. $La_xCe_{1-x}Ge_2$. Temperature dependence of χ_m^{-1} after $LaGe_2$ matrix correction. The ordinate is successively shifted [85 M 2].

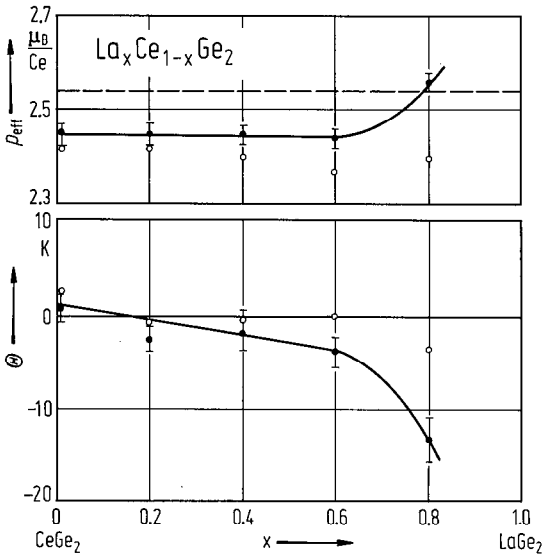

Fig. 56. $La_xCe_{1-x}Ge_2$. Composition dependence of Θ and p_{eff}. Solid circles: after $LaGe_2$ matrix correction, open circles: without matrix correction. The dashed line represents $p_{eff} = 2.54\,\mu_B$ for free Ce^{3+} ions [85 M 2].

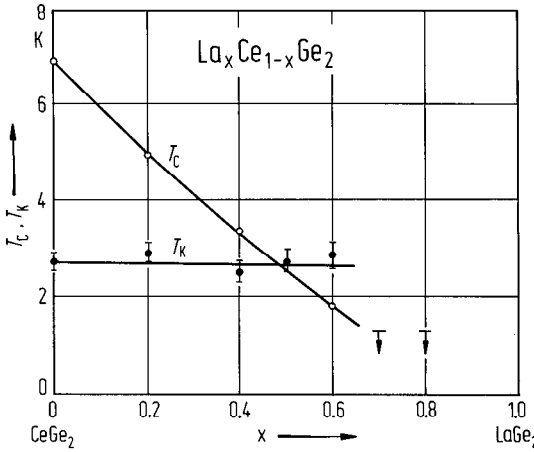

Fig. 57. $La_xCe_{1-x}Ge_2$. Composition dependence of T_C and the Kondo temperature T_K [85 M 2].

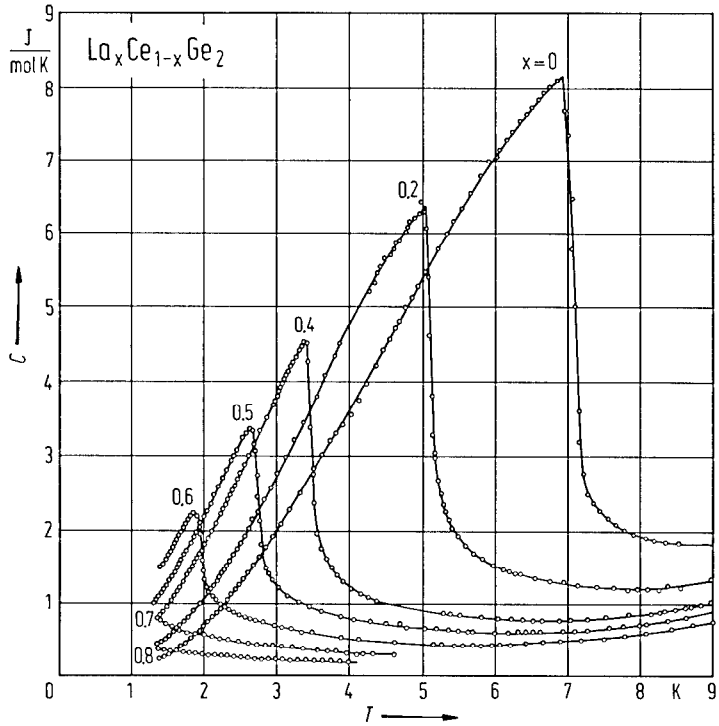

Fig. 58. $La_xCe_{1-x}Ge_2$. Temperature dependence of specific heat for different compositions [85 M 2].

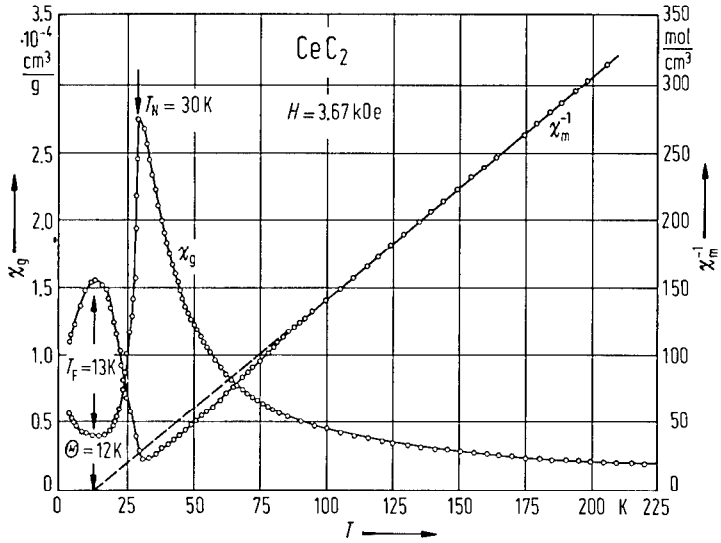

Fig. 59. CeC_2. Temperature dependence of χ_g and χ_m^{-1} at 3.67 kOe. Low-temperature minimum of the magnetic susceptibility at T_F [80 S 1].

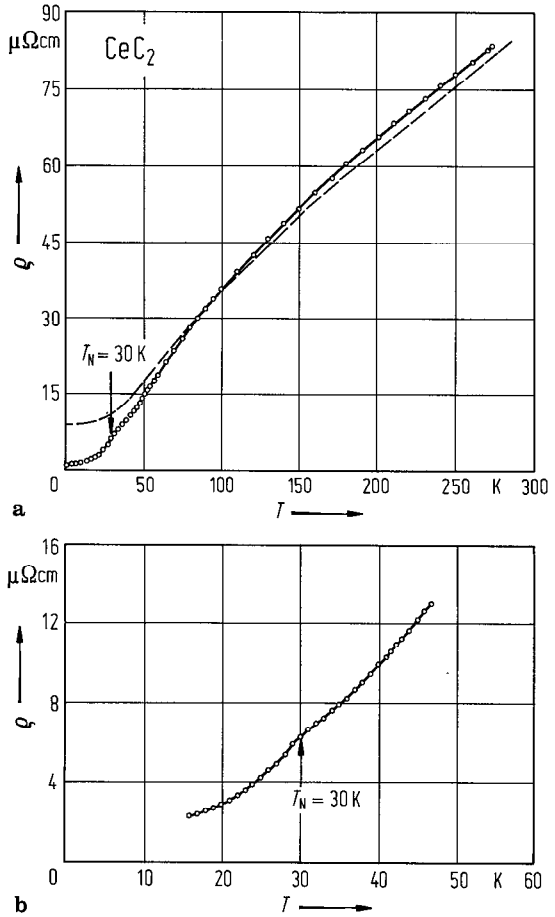

Fig. 60. CeC_2. (a) Temperature dependence of the electrical resistivity. (b) Resistivity near T_N. Dashed line is theoretical [81 S 1].

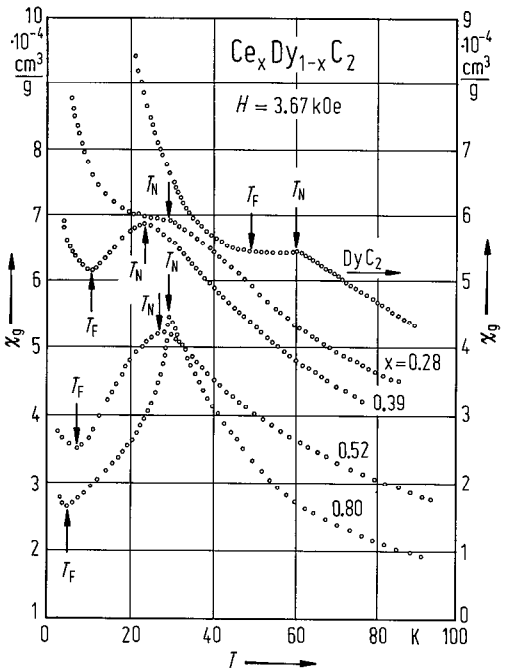

Fig. 61. $Ce_xDy_{1-x}C_2$. Temperature dependence of χ_g at 3.67 kOe. For DyC_2 right-hand scale, left-hand scale for the rest. Low-temperature minimum of the magnetic susceptibility at T_F [80 S 1].

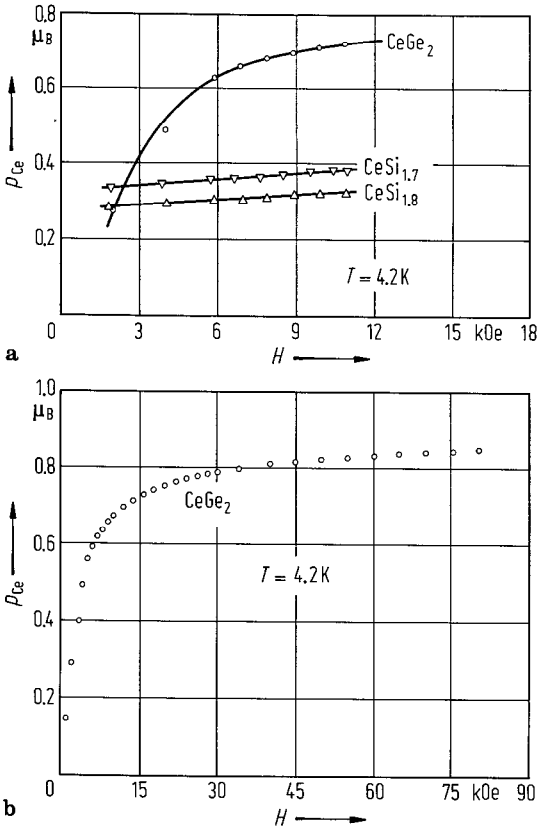

Fig. 62. $CeGe_2$, $CeSi_{2-x}$. Magnetic field dependence of the magnetic moment per Ce atom at 4.2 K for magnetic fields up to (a) 11 kOe and (b) 80 kOe ($CeGe_2$) [82 Y 2].

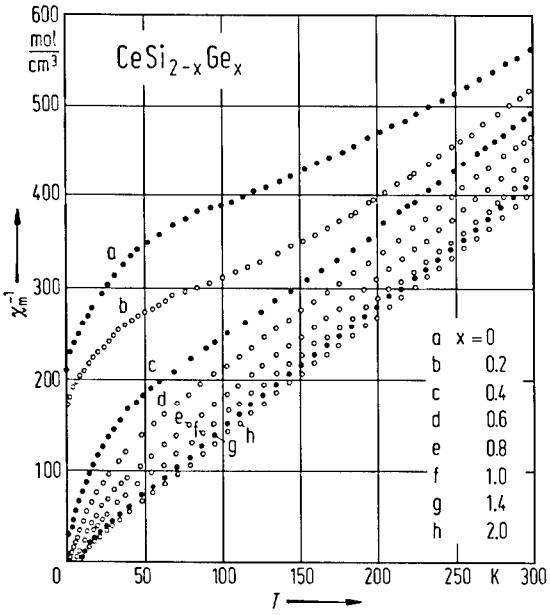

Fig. 63. $CeSi_{2-x}Ge_x$. Temperature dependence of χ_m^{-1} for various compositions [86 L 1].

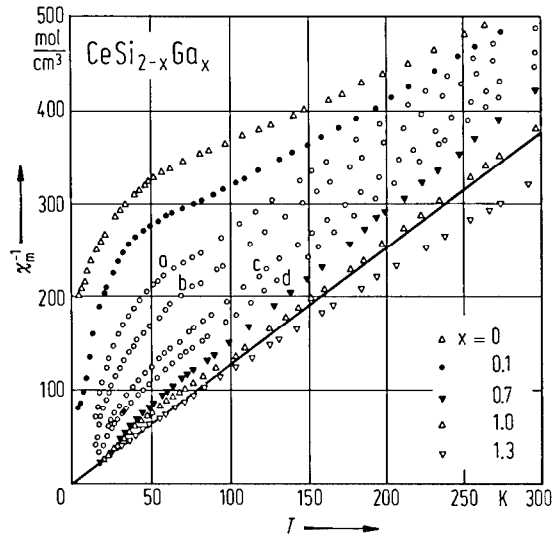

Fig. 64. $CeSi_{2-x}Ga_x$. Temperature dependence of χ_m^{-1} for different compositions. For $x < 0.2$ no magnetic ordering is observed, for $0.2 \leqq x \leqq 0.5$ one observes isostructural two-phase region (a–d), and for $0.5 < x < 1.3$ ferromagnetic ordering around 10 K is observed [84 M 4].

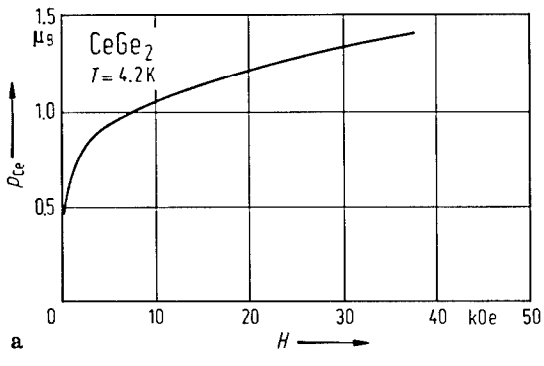

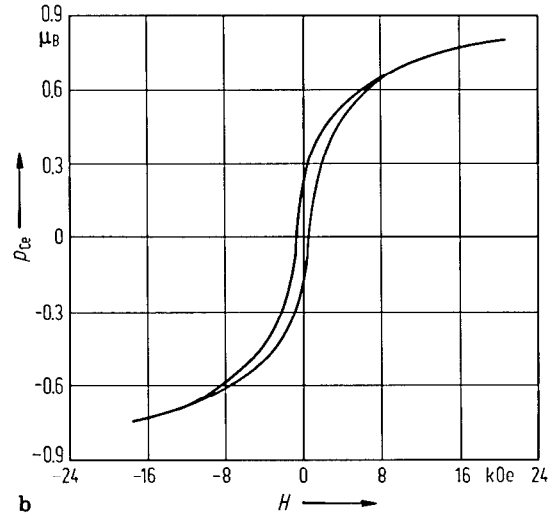

Fig. 65. $CeGe_2$. (a) Magnetic field dependence of the magnetic moment per Ce atom and (b) hysteresis loop at 4.2 K [85 M 2].

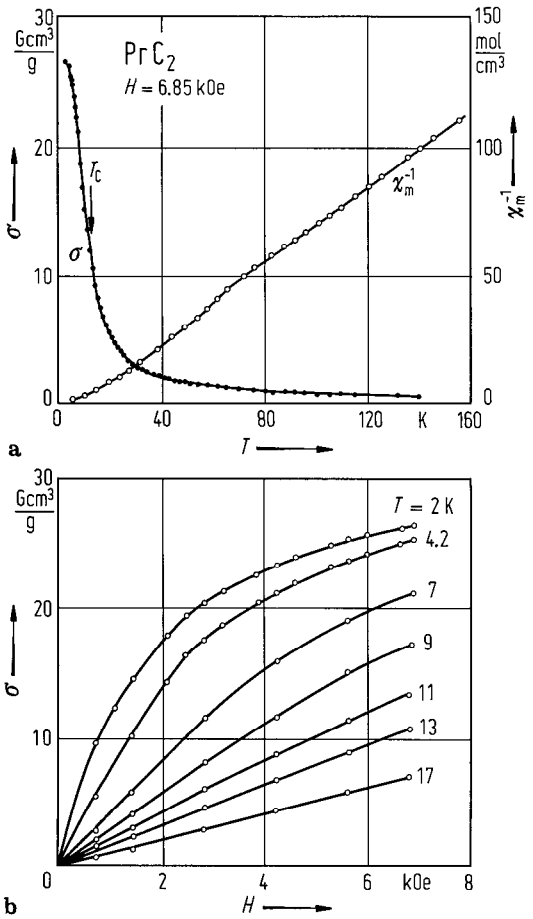

Fig. 66. PrC_2. (a) Temperature dependence of χ_m^{-1} and σ at 6.85 kOe. (b) Magnetic field dependence of σ for different temperatures [81 S 1].

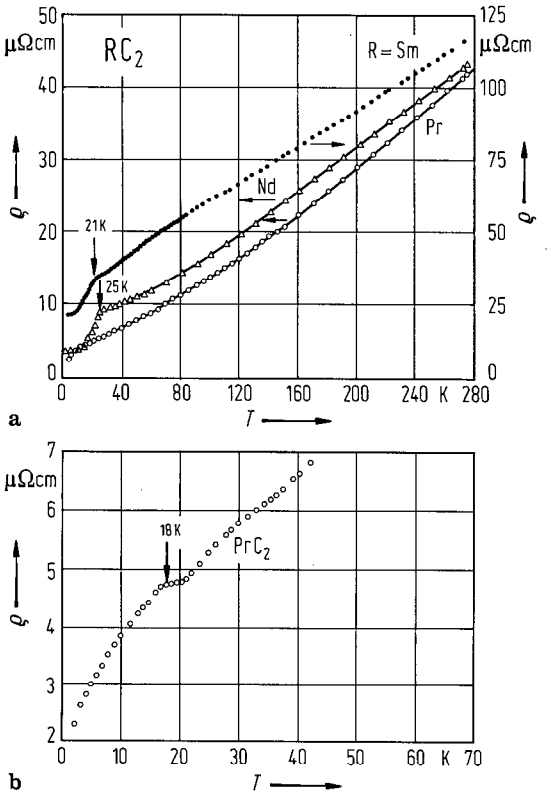

Fig. 67. RC_2, R = Pr, Nd, Sm. (a) Temperature dependence of the electrical resistivity. (b) Low-temperature electrical resistivity of PrC_2 [81 S 1].

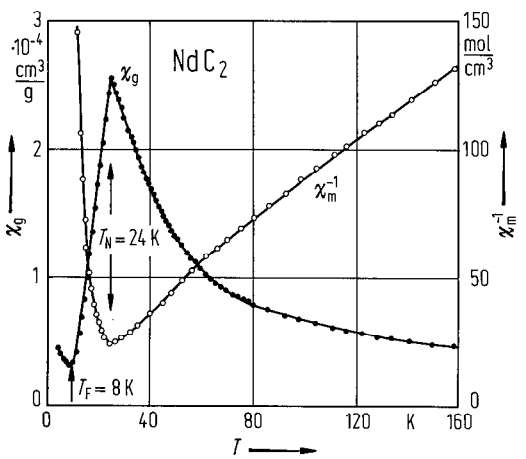

Fig. 68. NdC_2. Temperature dependence of χ_g and χ_m^{-1}. Low-temperature minimum of the magnetic susceptibility at T_F [81 S 1].

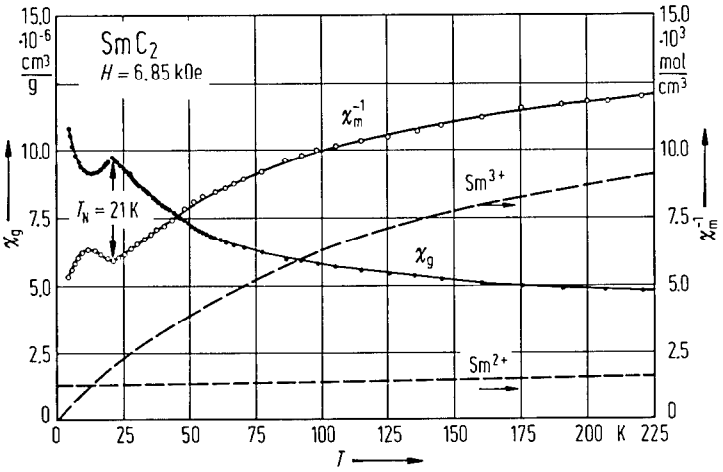

Fig. 69. SmC_2. Temperature dependence of χ_g and χ_m^{-1} at 6.85 kOe. Van Vleck theoretical values for Sm^{3+} and Sm^{+2} are shown by dashed lines [81 S 1].

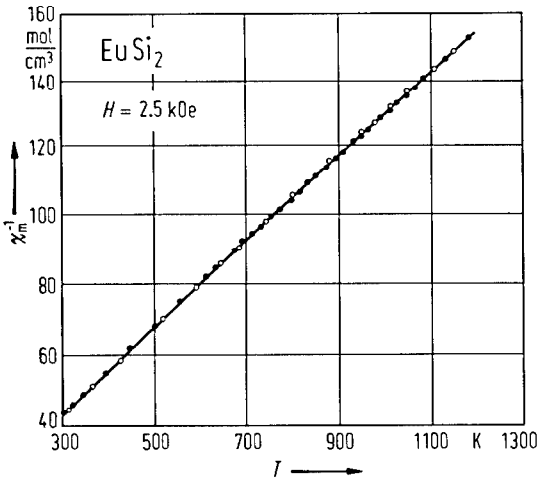

Fig. 70. $EuSi_2$. Temperature dependence of χ_m^{-1} at 2.5 kOe for increasing (solid circles) and decreasing (open circles) temperature [83 E 1].

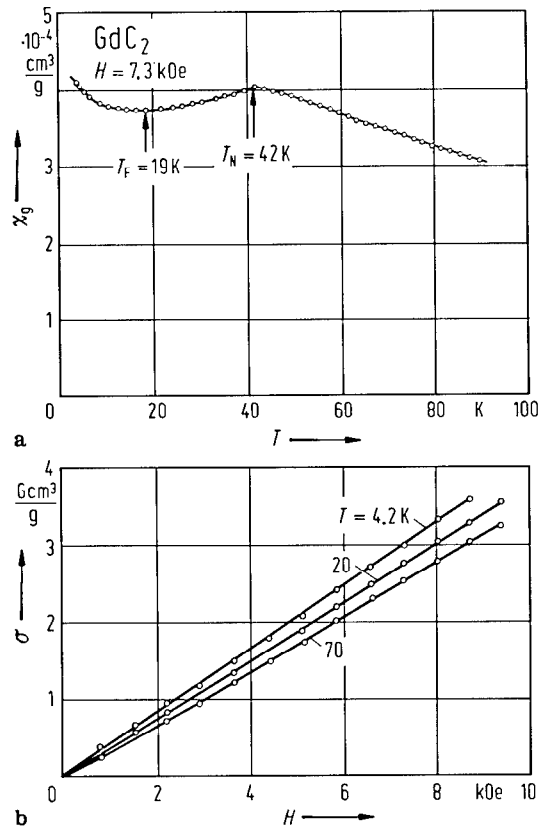

Fig. 71. GdC_2. (a) Temperature dependence of χ_g at 7.3 kOe and (b) magnetic field dependence of σ at different temperatures. Another magnetic phase transition is observed at T_F [79 S 1].

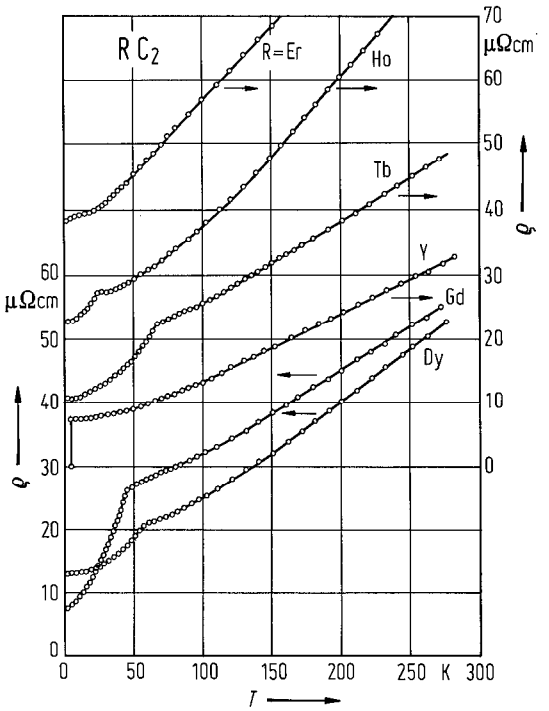

Fig. 72. RC_2, R = Y, Gd, Tb, Dy, Ho, Er. Temperature dependence of electrical resistivity. The magnetic phase transition is accompanied by a cusp in temperature dependence of ϱ [81 S 2].

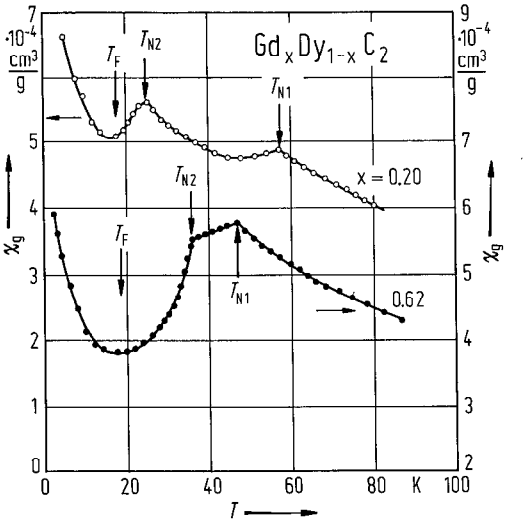

Fig. 73. $Gd_xDy_{1-x}C_2$. Temperature dependence of χ_g. T_{N1} and T_{N2} are two antiferromagnetic phase transition temperatures. The magnetic phase transition observed at T_F occurs at nearly the same temperature as that of GdC_2 (19 K), cf. Fig. 71 [79 S 1].

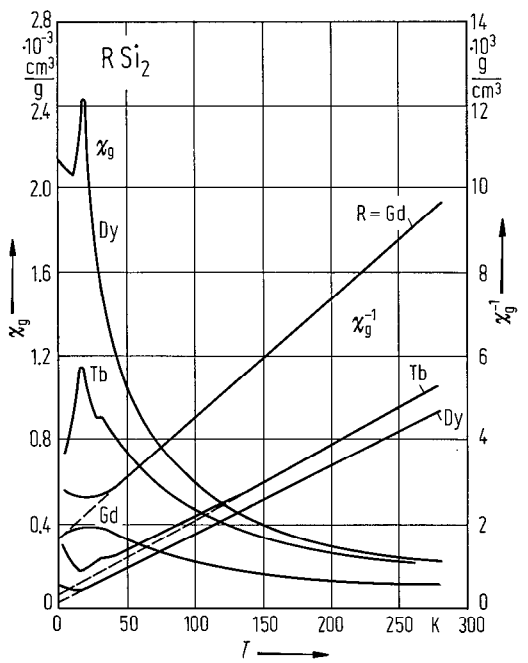

Fig. 74. RSi_2, R = Gd, Tb, Dy. Temperature dependence of χ_g and χ_g^{-1} [66 S 2].

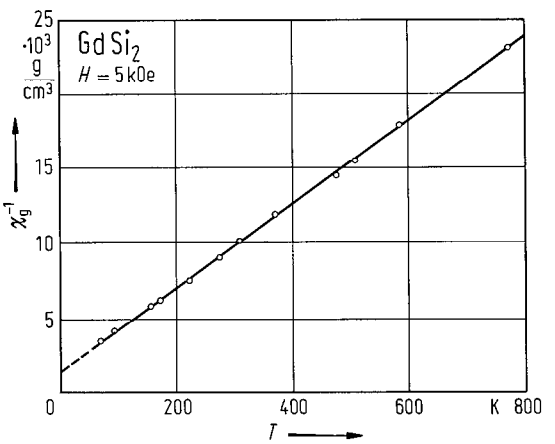

Fig. 75. $GdSi_2$. Temperature dependence of χ_g^{-1} at 5 kOe [66 Y 1].

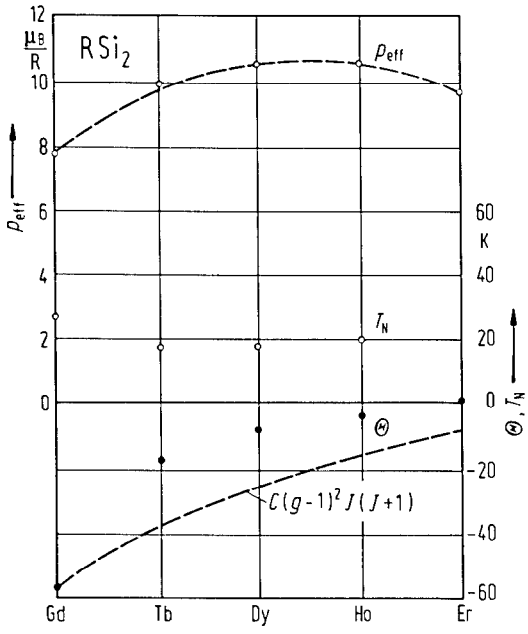

Fig. 76. RSi_2, R = Gd, Tb, Dy, Ho, Er. Néel temperature T_N, paramagnetic Curie temperature Θ, and effective paramagnetic moment p_{eff}. Dashed lines are theoretical [66 S 2].

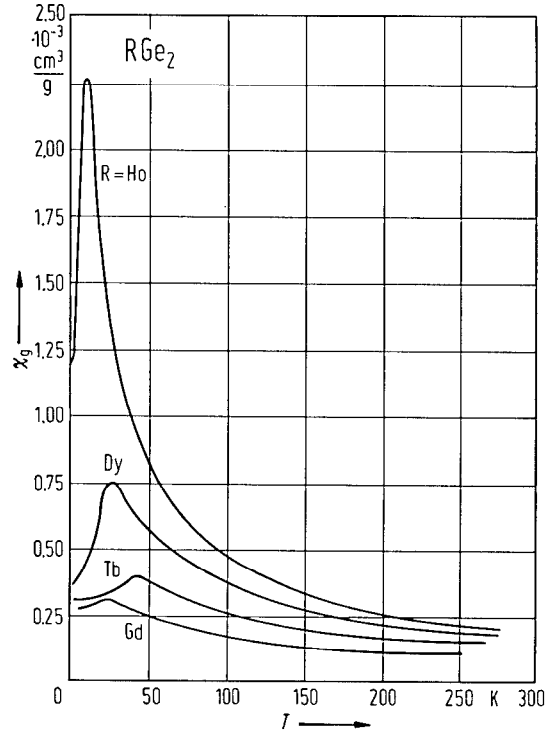

Fig. 77. RGe_2, R = Gd, Tb, Dy, Ho. Temperature dependence of χ_g [66 S 1].

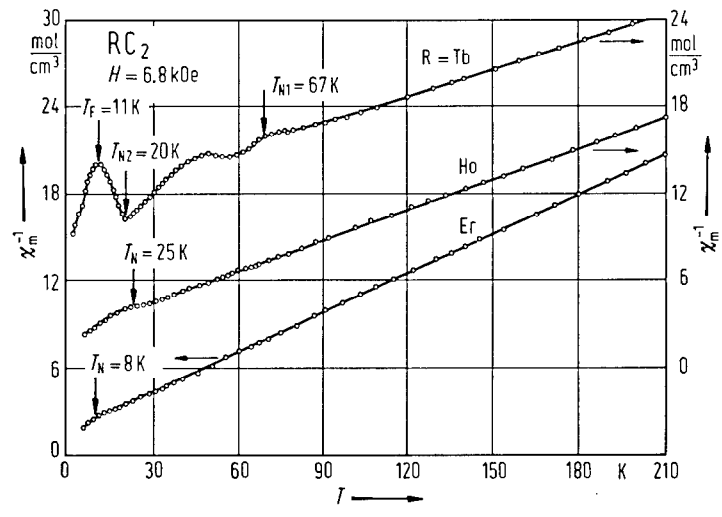

Fig. 78. RC_2, R = Tb, Ho, Er. Temperature dependence of χ_m^{-1} at 6.8 kOe. Low-temperature minimum of the magnetic susceptibility at T_F [81 S 2].

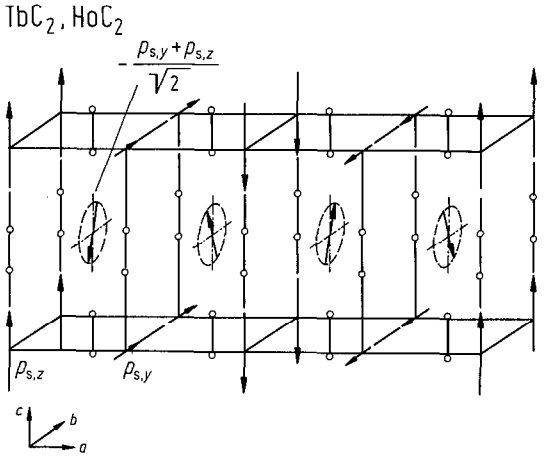

Fig. 79. TbC_2, HoC_2. Schematic representation of the higher temperature antiferromagnetic structure. The small circles represent the C_2 molecules and the magnetic moment vectors are placed at the metal-atom positions [67 A 1].

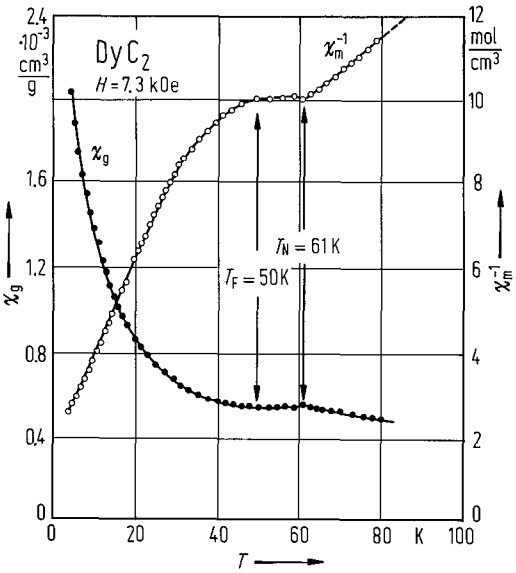

Fig. 80. DyC_2. Temperature dependence of χ_m^{-1} and χ_g at 7.3 kOe. Another magnetic phase transition is observed at T_F [79 S 1].

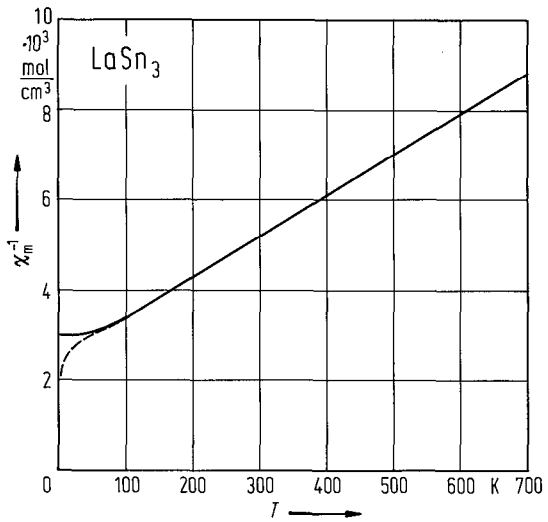

Fig. 81. $LaSn_3$. Temperature dependence of χ_m^{-1}. Dashed line: corrected only for the diamagnetic core contribution. Solid line corrected for paramagnetic impurity contributions as well [71 W 1].

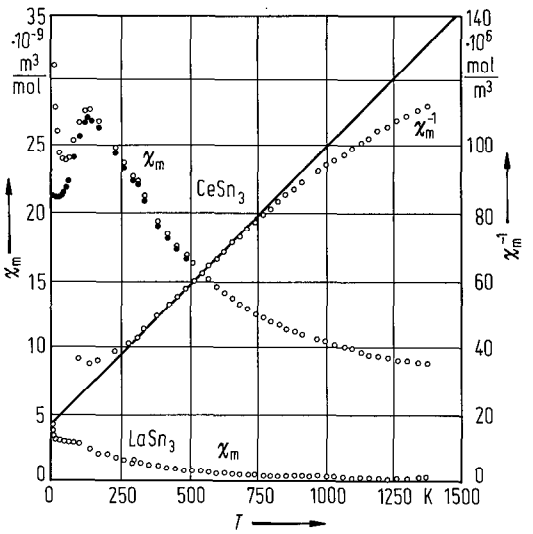

Fig. 82. $LaSn_3$, $CeSn_3$. Temperature dependence of χ_m and χ_m^{-1}. Open circles: as measured, solid circles: impurity-corrected [80 D 1].

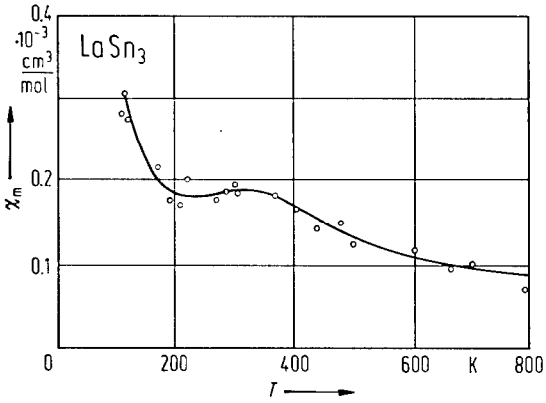

Fig. 83. $LaSn_3$. Temperature dependence of χ_m [81 C 2].

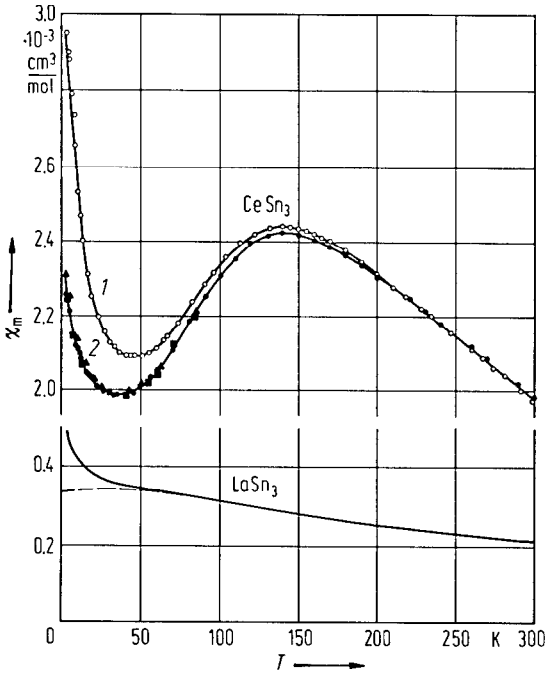

Fig. 84. $LaSn_3$, $CeSn_3$. Temperature dependence of χ_m. Curve *1* polycrystalline $CeSn_3$, thirty pieces (open circles); curve *2* single-crystalline (solid circles) and polycrystalline $CeSn_3$, five pieces (triangles), thirty pieces (squares). Dashed line for $LaSn_3$ has impurity Curie tail subtracted [83 S 3].

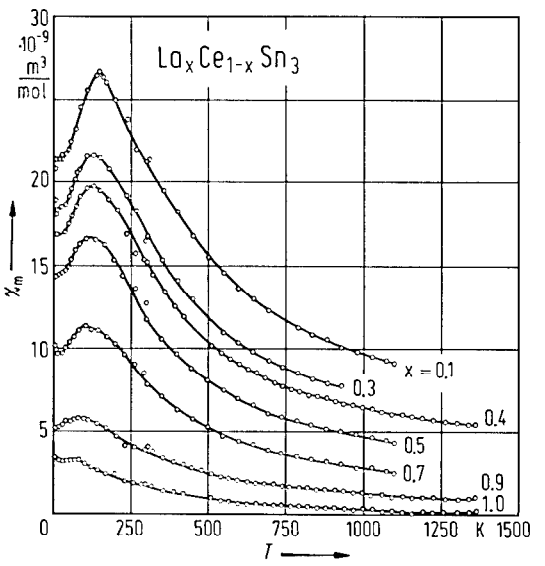

Fig. 85. $La_xCe_{1-x}Sn_3$. Temperature dependence of χ_m corrected for low-temperature impurity contribution [80 D 1].

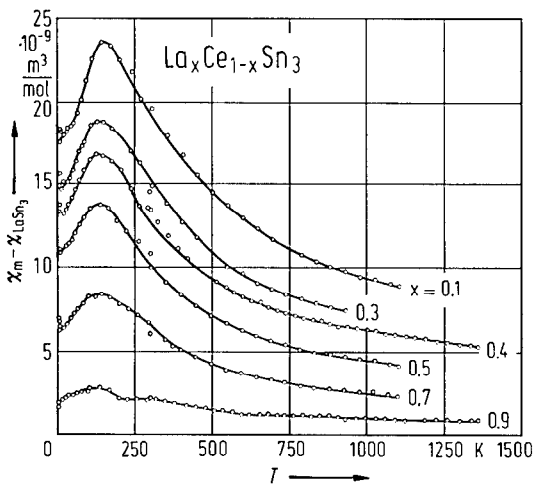

Fig. 86. $La_xCe_{1-x}Sn_3$. Temperature dependence of $\chi_m - \chi_{LaSn_3}$. The magnetic susceptibility curves have been corrected for a low-temperature impurity contribution, and the temperature-dependent magnetic susceptibility of $LaSn_3$ has been subtracted [80 D 1].

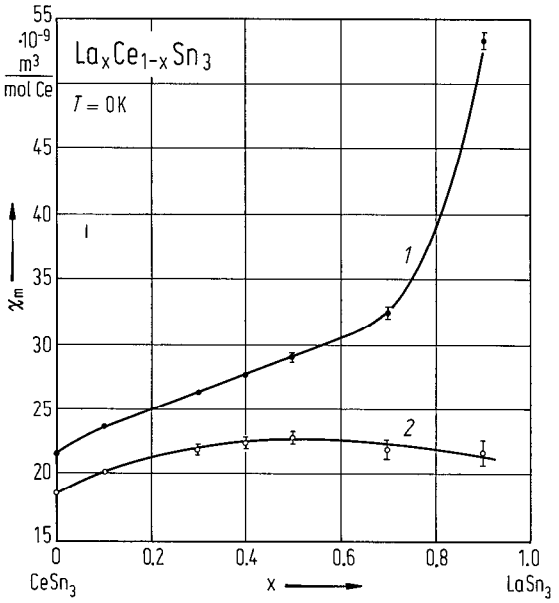

Fig. 87. $La_xCe_{1-x}Sn_3$. Composition dependence of the magnetic susceptibility at 0 K. Solid circles: impurity corrected, open circles: impurity corrected and $LaSn_3$-matrix subtracted [80 D 1].

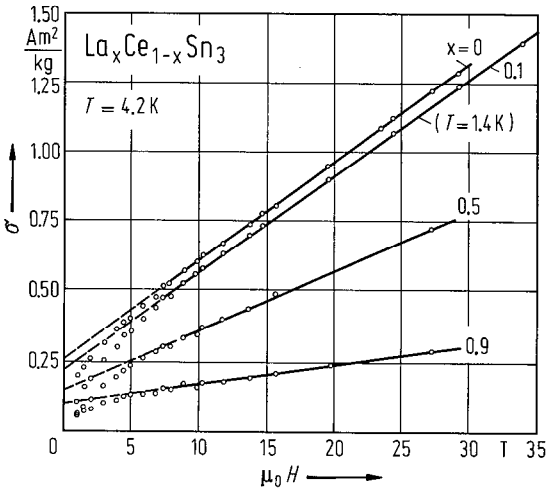

Fig. 89. $La_xCe_{1-x}Sn_3$. Magnetic field dependence of σ at 4.2 K. For x = 0.1 the temperature is 1.4 K [80 D 1].

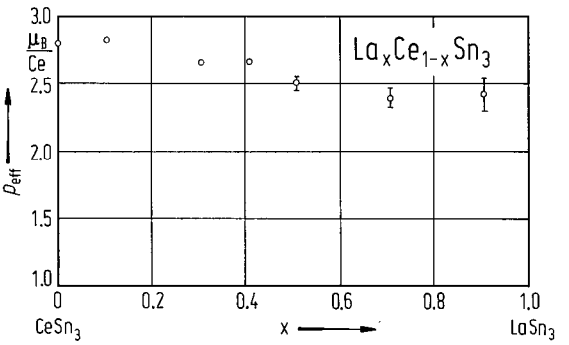

Fig. 88. $La_xCe_{1-x}Sn_3$. Composition dependence of p_{eff} deduced from the impurity-corrected magnetic susceptibility after subtraction of the $LaSn_3$ magnetic susceptibility [80 D 1].

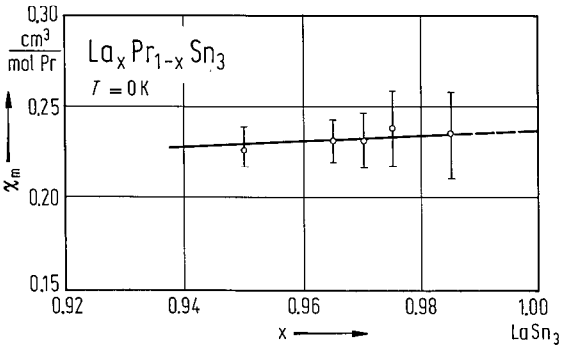

Fig. 90. $La_xPr_{1-x}Sn_3$. Composition dependence of the magnetic susceptibility at 0 K [75 M 1].

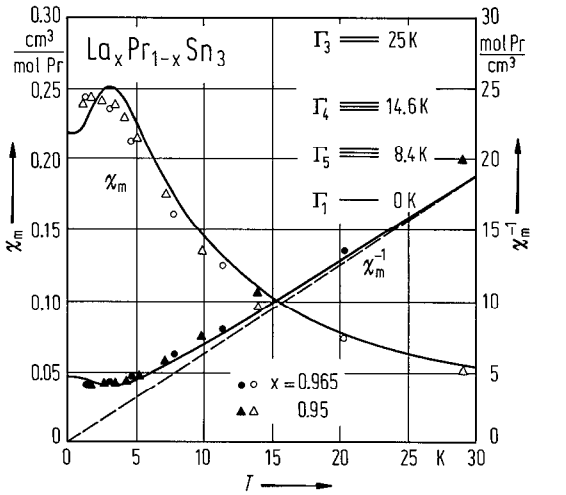

Fig. 91. $La_xPr_{1-x}Sn_3$. Temperature dependence of χ_m and χ_m^{-1} for x = 0.965 and 0.95. The solid curves are derived from the Pr^{3+} energy level scheme (insert) [75 M 1].

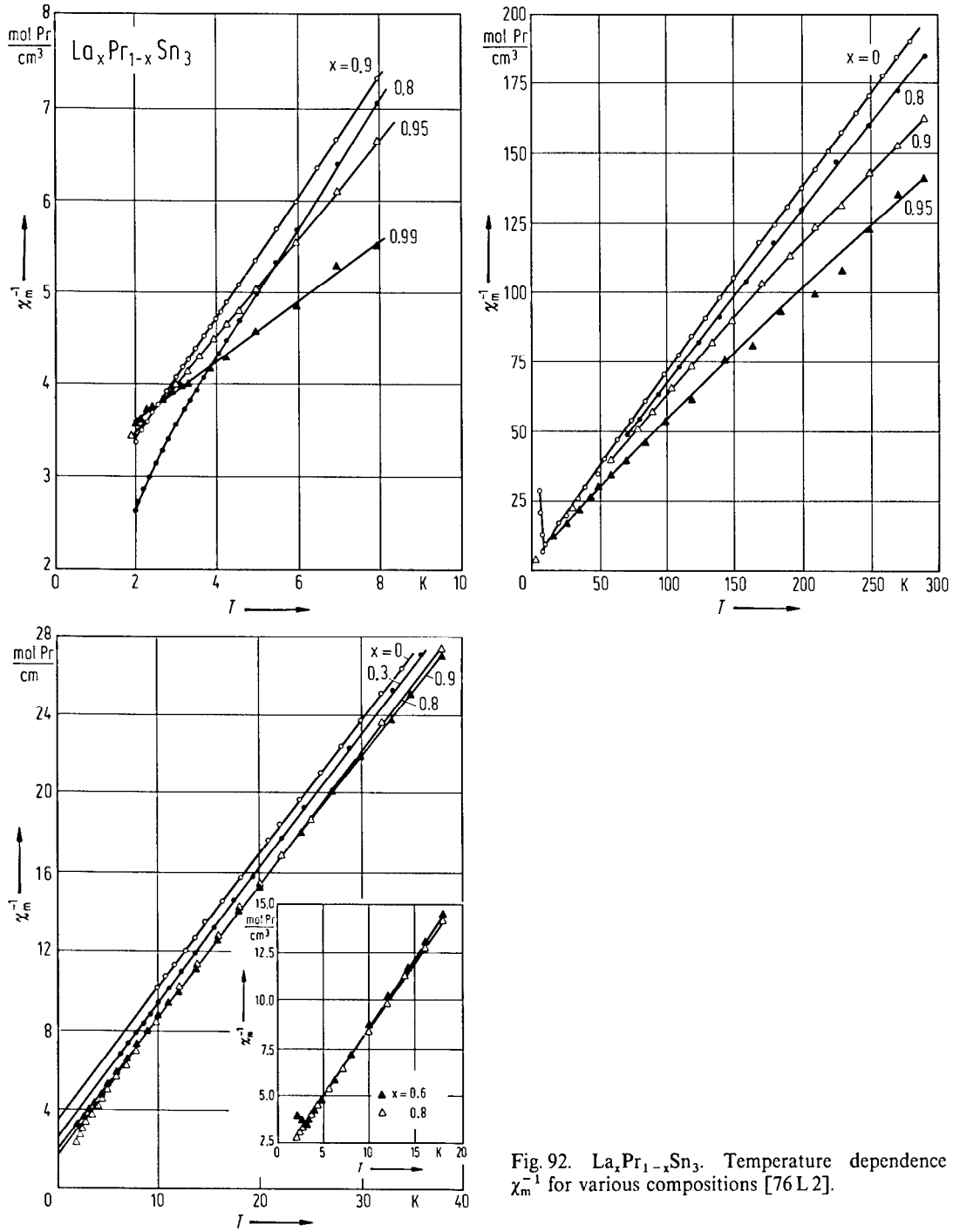

Fig. 92. $La_xPr_{1-x}Sn_3$. Temperature dependence of χ_m^{-1} for various compositions [76 L 2].

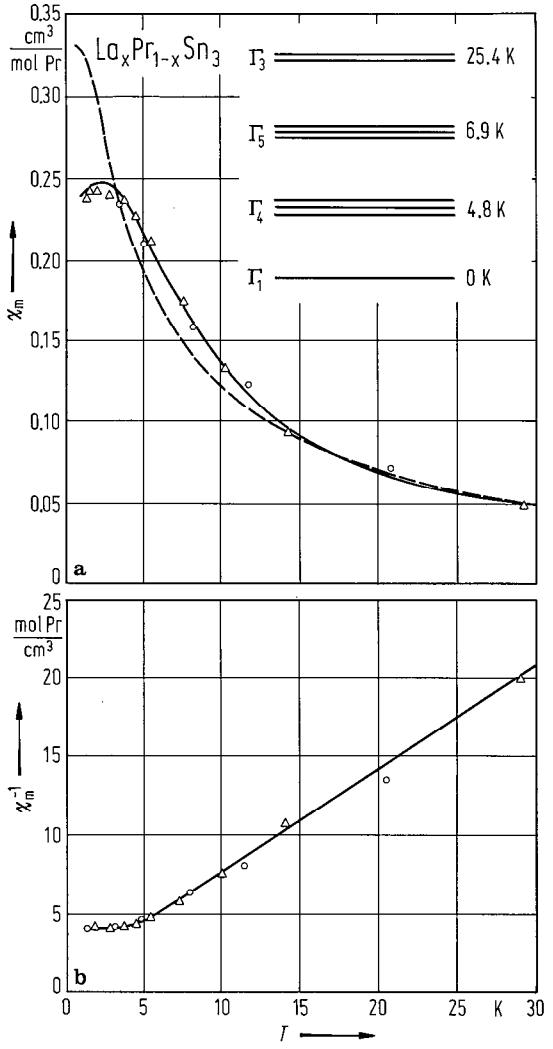

Fig. 93. $La_xPr_{1-x}Sn_3$. Temperature dependence of (a) χ_m and (b) χ_m^{-1} [75 M 1]. The full lines refer to the CEF energy level scheme of Pr^{3+} as is depicted and $|n(E_F)\Gamma| = 0.095$, $\Theta = -2.4$ K and $D = 250$ K. The dashed line shows the contribution of only CEF, i.e. for $|n(E_F)\Gamma| = 0$. $|n(E_F)\Gamma|$ is the s–f exchange parameter, D is the bandwidth [77 B 2].

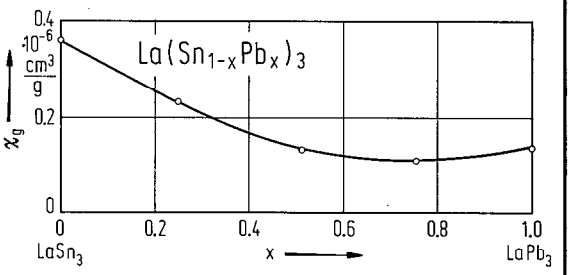

Fig. 94. $La(Sn_{1-x}Pb_x)_3$. Composition dependence of χ_g [70 H 1].

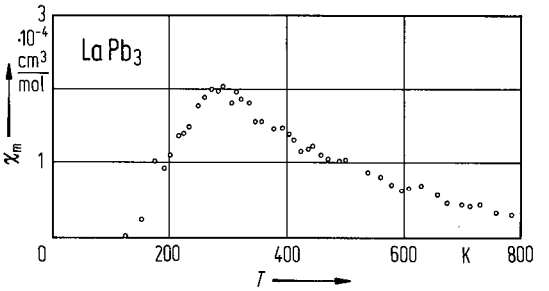

Fig. 95. $LaPb_3$. Temperature dependence of χ_m [83 C 1].

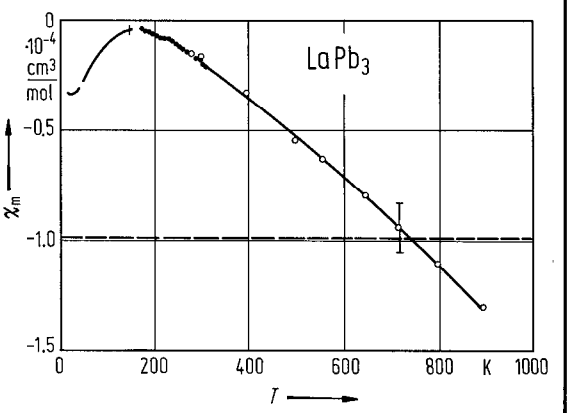

Fig. 96. $LaPb_3$. Temperature dependence of χ_m corrected for a temperature-independent ferromagnetic impurity magnetization. Dashed line: theoretical diamagnetic core contribution [86 D 1].

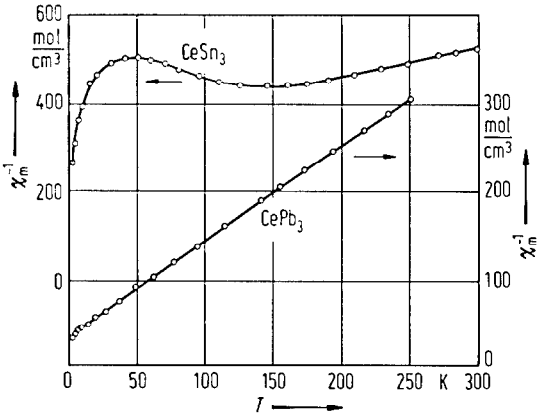

Fig. 97. $CeSn_3$, $CePb_3$. Temperature dependence of χ_m^{-1} [65 T 1].

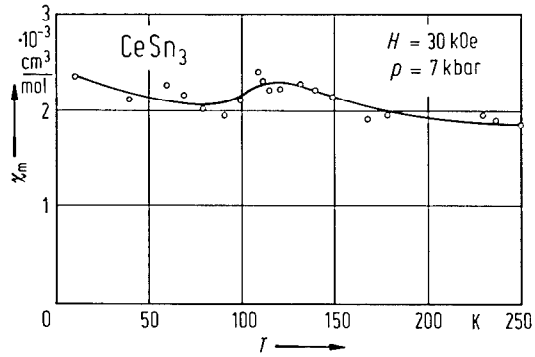

Fig. 98. $CeSn_3$. Temperature dependence of χ_m at 7 kbar and 30 kOe [77 B 1].

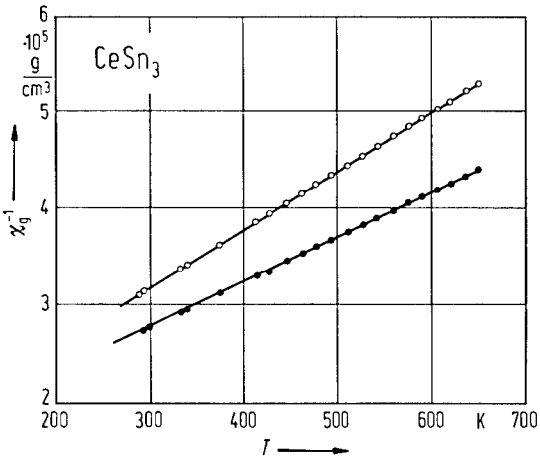

Fig. 99. $CeSn_3$. Temperature dependence of χ_g^{-1} (solid circles). The open circles are obtained after correction for the Pauli paramagnetic contribution determined on $LaSn_3$ [79 B 1].

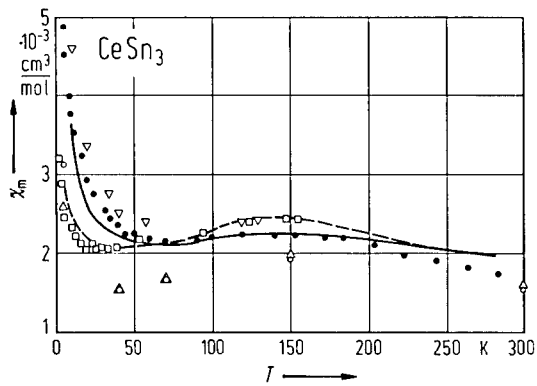

Fig. 100. $CeSn_3$. Temperature dependence of χ_m measured by various authors. The local magnetic susceptibility obtained in neutron scattering measurements is depicted by triangles and open circles for the 4 mm and 2 mm thick crystals, respectively [79 S 5].

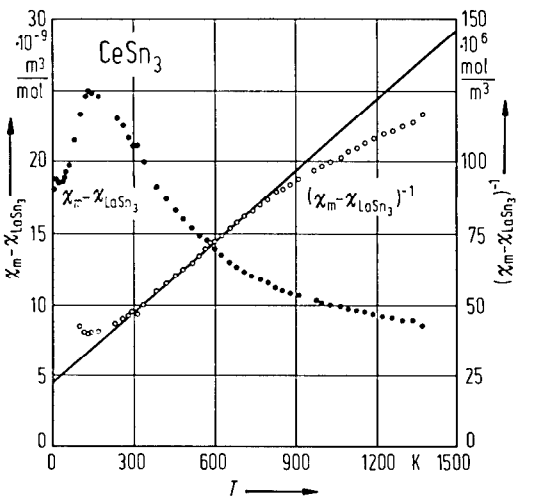

Fig. 101. $CeSn_3$. Temperature dependence of $\chi_m - \chi_{LaSn_3}$ and $(\chi_m - \chi_{LaSn_3})^{-1}$. The magnetic susceptibility is impurity-corrected and the temperature-dependent magnetic susceptibility of $LaSn_3$ is subtracted [80 D 1].

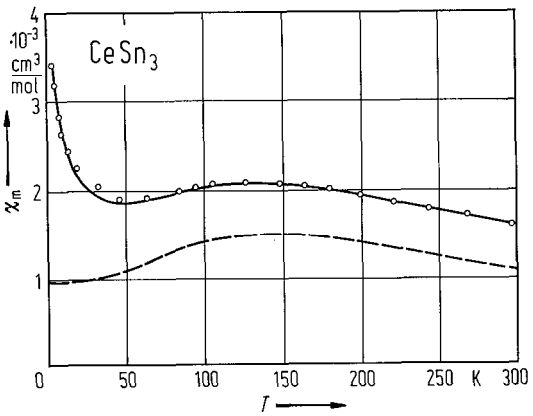

Fig. 102. $CeSn_3$. Temperature dependence of χ_m and theoretical fit (full curve) $\chi_m(T)=\frac{C_i}{T-\Theta}+\chi_{Ce}(T)+\chi_0$. $C_i=0.018\,K\,cm^3\,mol^{-1}$ and $\Theta=-3.3\,K$ due to magnetic impurities. The temperature-independent contribution is $\chi_0=0.5\cdot10^{-3}\,cm^3\,mol^{-1}$. $\chi_{Ce}(T)=C_m\frac{S^2}{1-n}\left[-\frac{\partial}{\partial E}\left(\frac{n}{S}\right)\right]$ where $S=1-\frac{5}{6}n$ and the Curie constant $C_m=\frac{N_A g^2\mu_B^2 J(J+1)}{3k_B}=0.805\,cm^3\,K\,mol^{-1}$ for $g=6/7$ and $J=5/2$. n and E denote occupation number and (normalized) energy of the f-level, respectively. The dashed line represents $\chi_{Ce}(T)$ at ambient pressure [80 S 4].

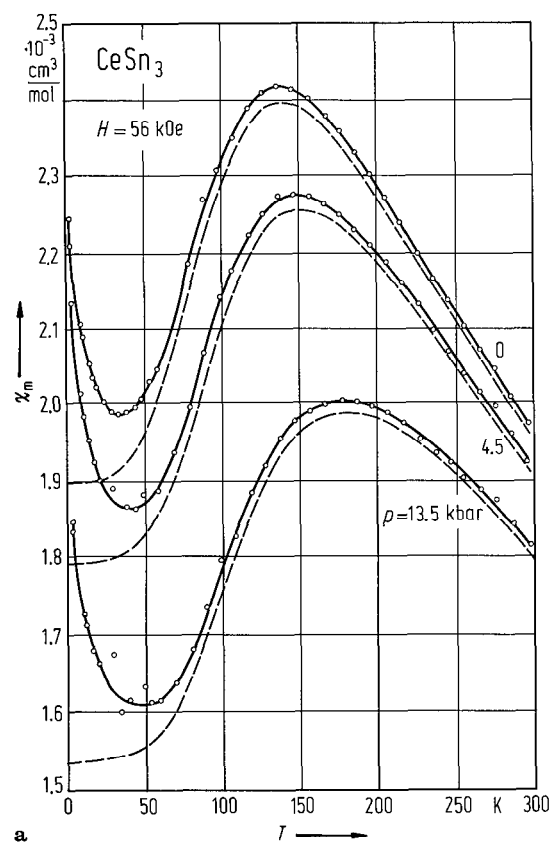

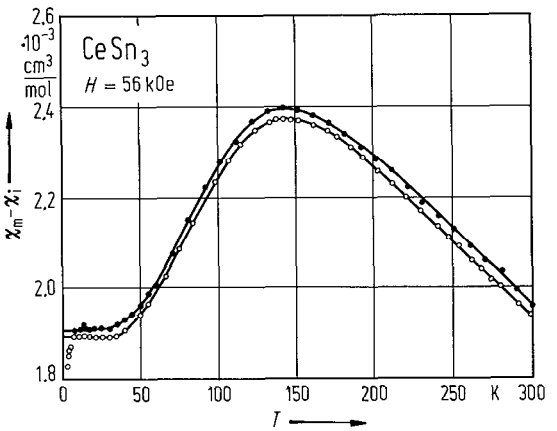

Fig. 103. $CeSn_3$. Single and polycrystal. Temperature dependence of χ_m at 56 kOe after subtraction of a Curie-Weiss magnetic impurity susceptibility χ_i. Solid circles: single crystal, $\chi_i=\frac{0.0026}{T+3.2\,K}\frac{cm^3\,K}{mol}$; open circles: polycrystal, $\chi_i=\frac{0.0079}{T+3.2\,K}\frac{cm^3\,K}{mol}$ [83 S 3].

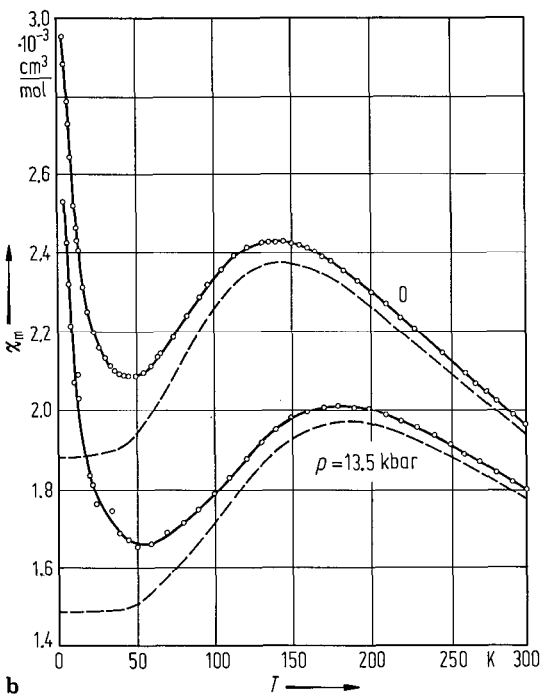

Fig. 104. $CeSn_3$. Temperature dependence of χ_m at 56 kOe for (a) a single crystal and (b) a polycrystal at different pressures. Pressures given are at room temperature; approximately 2.5 kbar is lost upon cooling. Dashed lines: after subtraction of a pressure-independent Curie-Weiss term χ_i (see caption to Fig. 103) from the measured data [83 S 3].

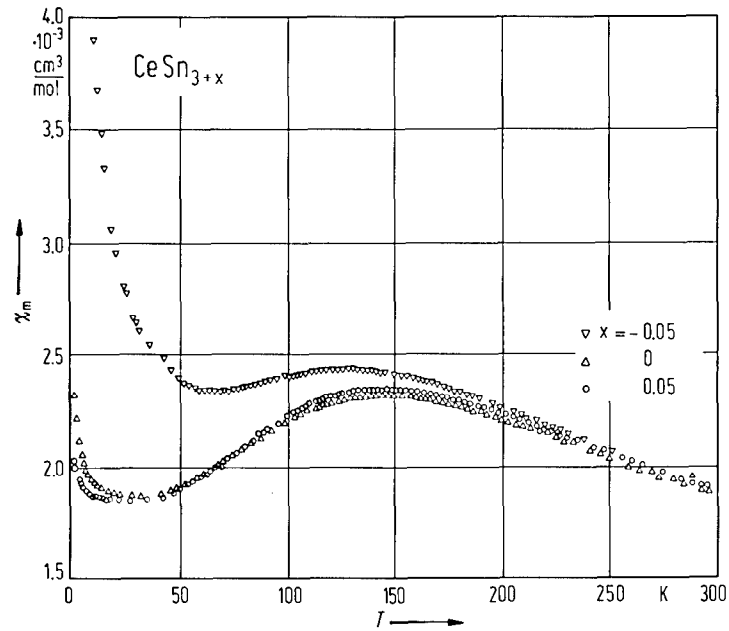

Fig. 106. $CeSn_{3+x}$. Temperature dependence of χ_m for different samples [85 G 3, 85 G 2].

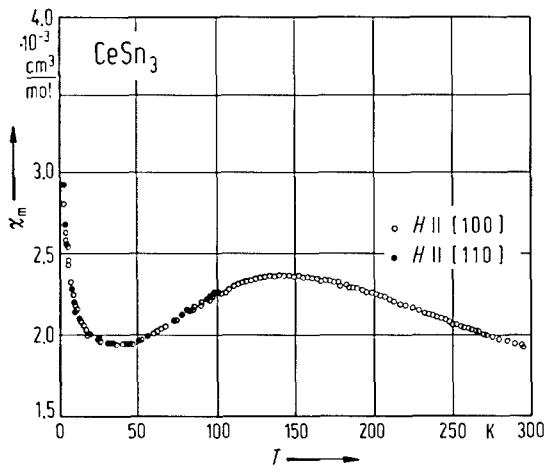

Fig. 105. $CeSn_3$. Temperature dependence of χ_m for a single crystal after correction for the contribution due to the magnetic impurities [84 T 1].

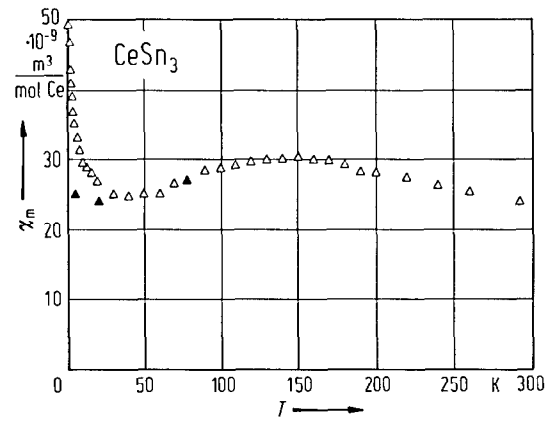

Fig. 107. $CeSn_3$. Temperature dependence of χ_m. The solid symbols correspond to the intrinsic susceptibility values derived from high-field magnetization measurements [86 V 1].

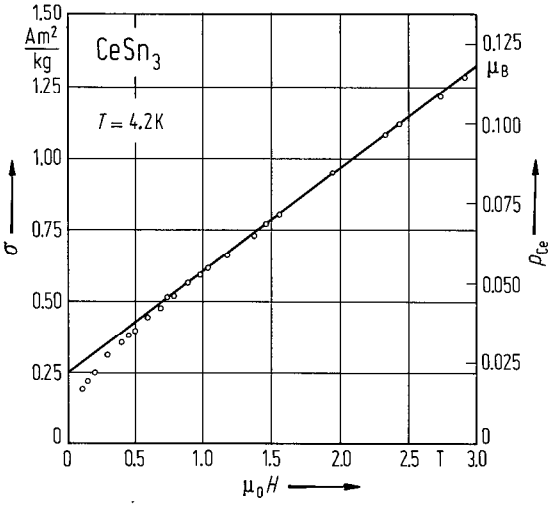

Fig. 108. $CeSn_3$. Magnetic field dependence of the magnetic moment per unit mass and per Ce atom at 4.2 K [80 D 1].

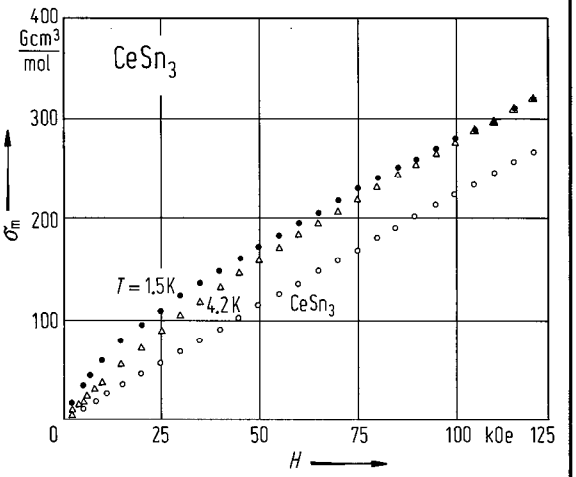

Fig. 109. $CeSn_3$. Magnetic field dependence of σ_m at 1.5 K (solid circles) and 4.2 K (triangles). The open circles denote the $CeSn_3$ low-temperature magnetization after subtraction of the contribution due to magnetic impurities [80 S 4].

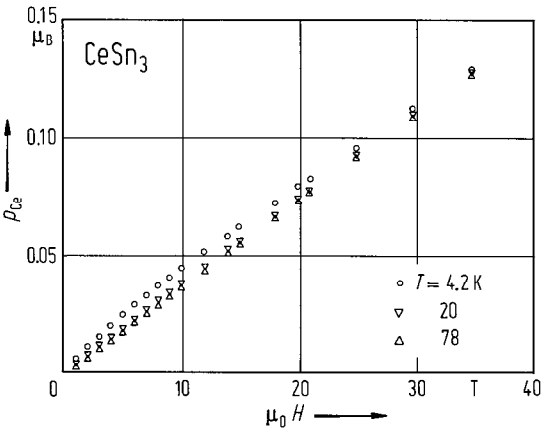

Fig. 110. $CeSn_3$. Magnetic field dependence of the magnetic moment per Ce atom at 4.2, 20 and 78 K [86 V 1].

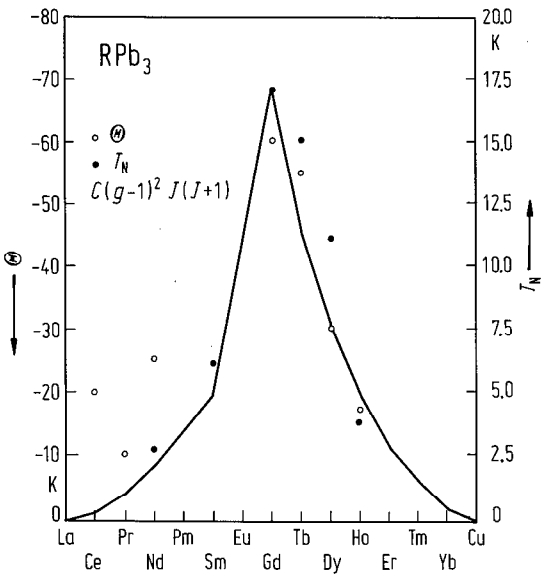

Fig. 111. RPb_3. Paramagnetic Curie temperature and Néel temperature. The solid line is theoretical [73 L 2].

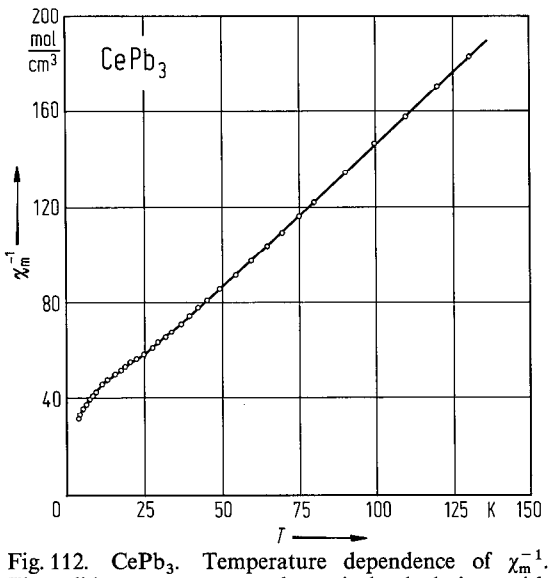

Fig. 112. $CePb_3$. Temperature dependence of χ_m^{-1}. The solid curve represents theoretical calculations with CEF parameters $W = 11$ K and $x = 1.0$ [76 L 1].

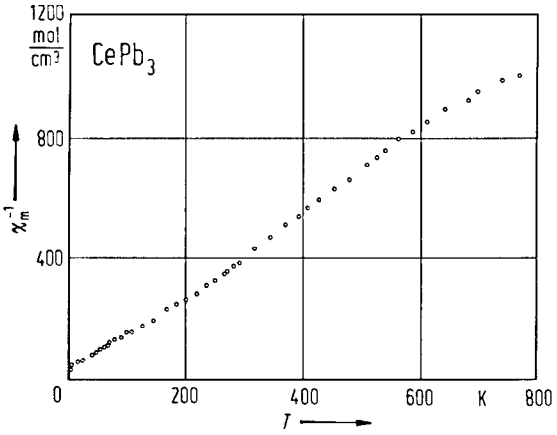

Fig. 113. $CePb_3$. Temperature dependence of χ_m^{-1} [83 C 1].

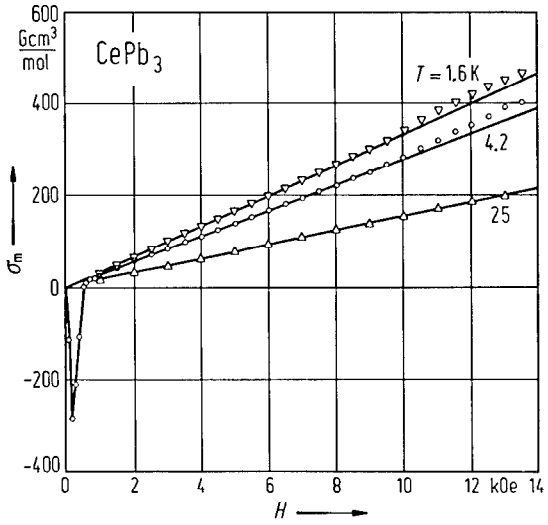

Fig. 115. $CePb_3$. Magnetic field dependence of σ_m at 1.6, 4.2 and 25 K. The superconducting magnetization ($H < 1$ kOe) shown for 4.2 K is due to free-Pb contamination of the sample [86 D 1].

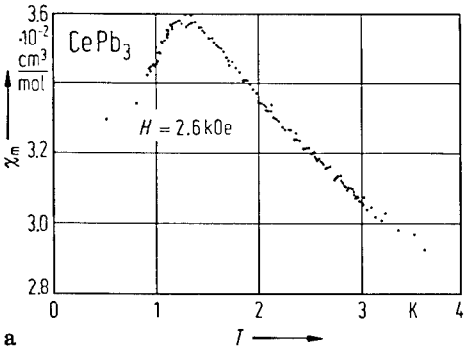

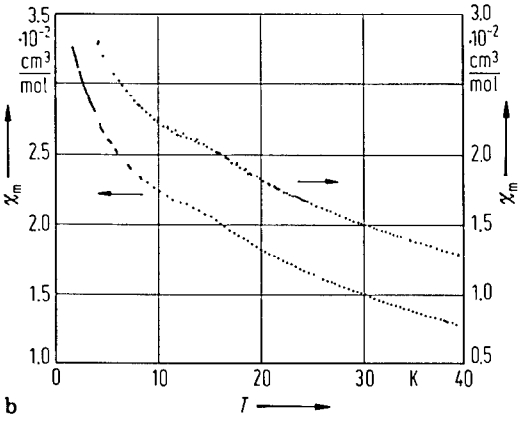

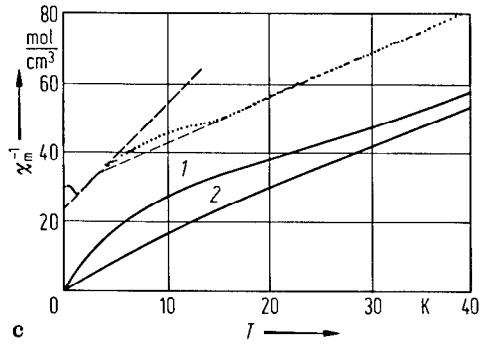

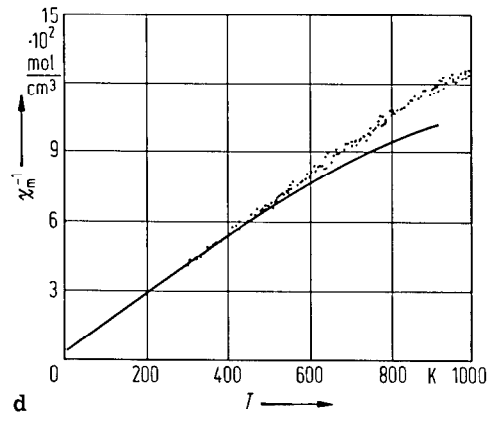

Fig. 114. $CePb_3$. (a) Low-temperature dependence of χ_m at 2.6 kOe. (b) Temperature dependence of χ_m below 40 K for two samples. (c) Temperature dependence of χ_m^{-1} below 40 K. The dashed lines represent two Curie-Weiss slopes; curve *1*: CEF calculation with Γ_7 ground state, Γ_8 excited state, $\Delta E = 70$ K; curve *2*: CEF calculation with Γ_8 ground state, Γ_7 excited state, $\Delta E = 60$ K. (d) Temperature dependence of χ_m^{-1} as measured (dots) and with $LaPb_3$ background correction (solid line) [86 D 1].

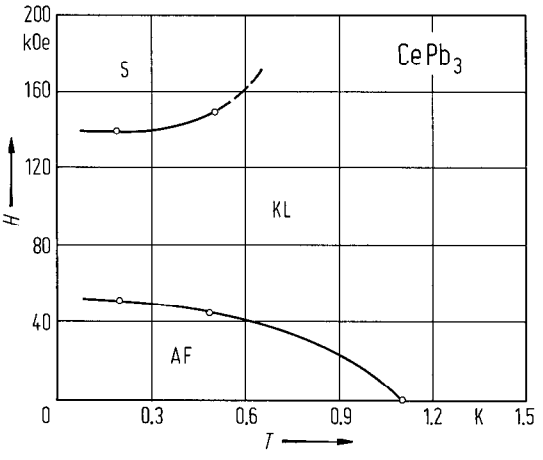

Fig. 116. $CePb_3$. Phase diagram. AF: antiferromagnetic, S: superconducting, KL: Kondo lattice [86 L 2].

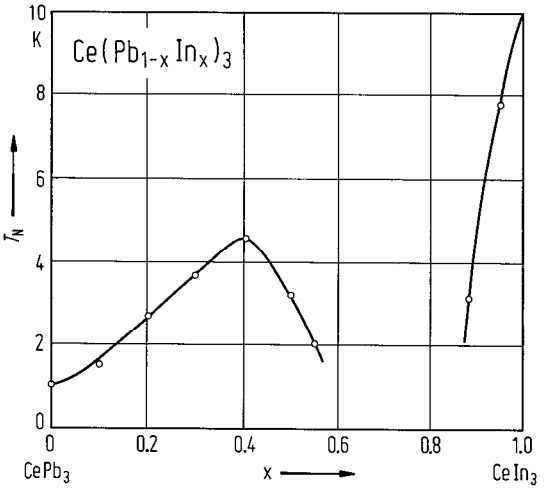

Fig. 117. $Ce(Pb_{1-x}In_x)_3$. Composition dependence of T_N [86 L 2].

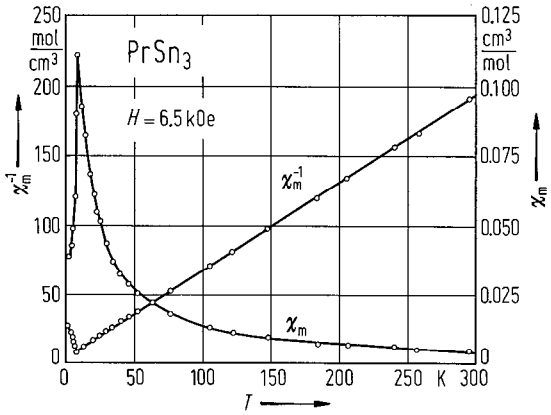

Fig. 118. $PrSn_3$. Temperature dependence of χ_m and χ_m^{-1} at 6.5 kOe [70 C 1].

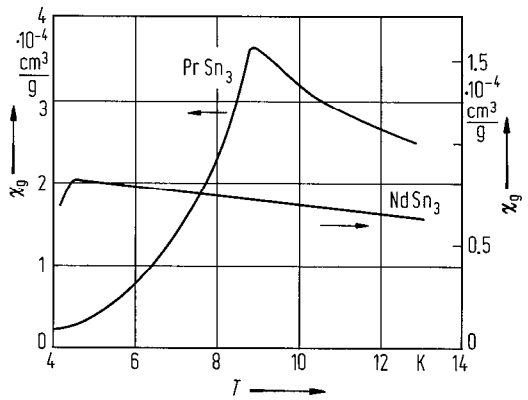

Fig. 119. $PrSn_3$, $NdSn_3$. Temperature dependence of χ_g [79 D 1].

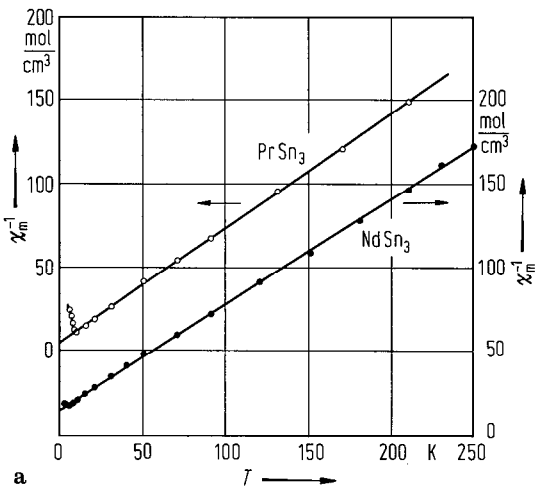

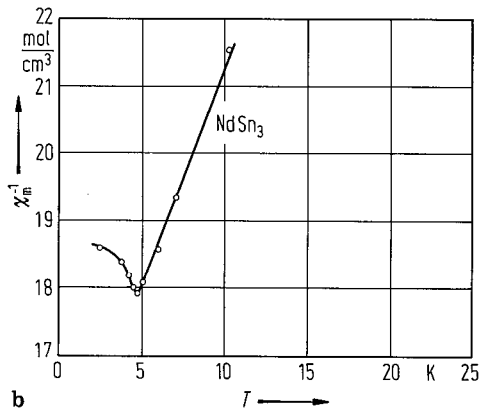

Fig. 120. $PrSn_3$, $NdSn_3$. (a) Temperature dependence of χ_m^{-1}. (b) gives low-temperature data for $NdSn_3$ [65 T 1].

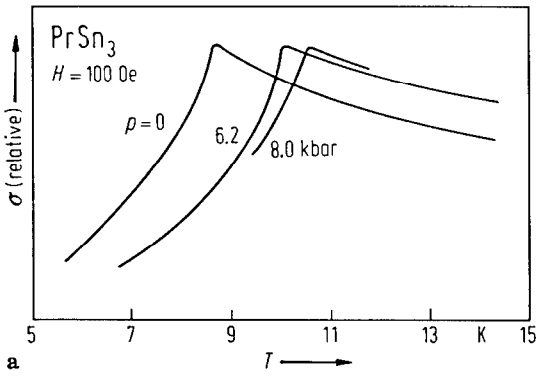

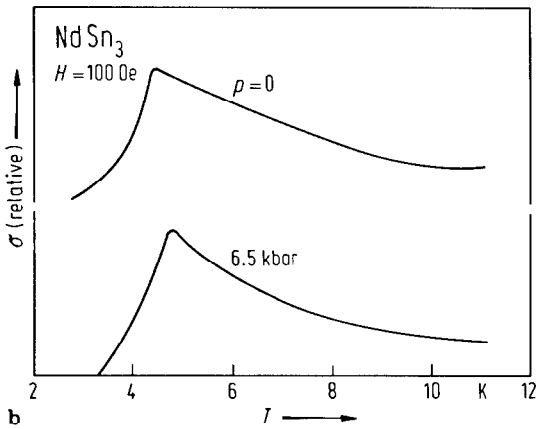

Fig. 121. $PrSn_3$ (a), $NdSn_3$ (b). Temperature dependence of σ (arbitrary units) at different pressures. The measuring field $H = 100$ Oe [79 D 1].

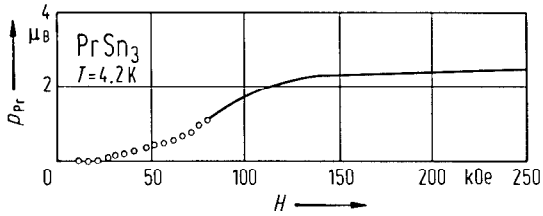

Fig. 122. $PrSn_3$. Magnetic field dependence of the magnetic moment per Pr atom at 4.2 K [73 L 1].

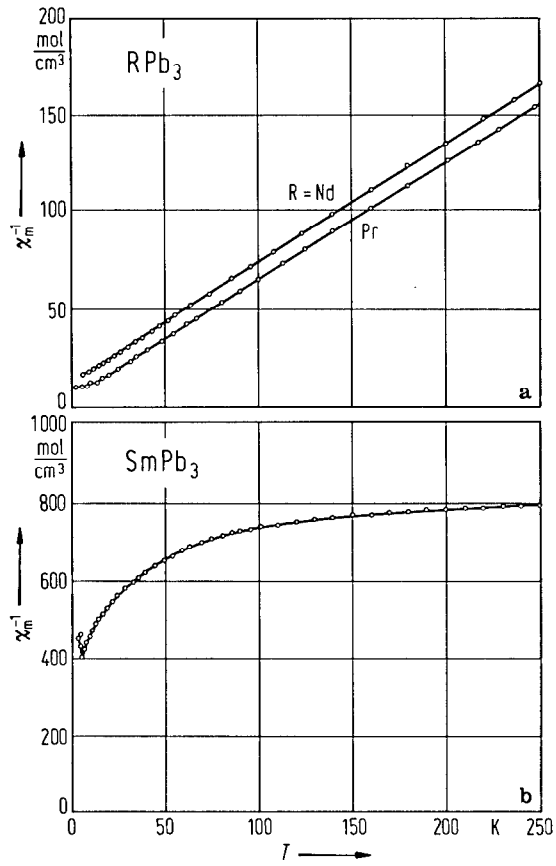

Fig. 123. RPb_3, (a) R = Pr, Nd, (b) R = Sm. Temperature dependence of χ_m^{-1} [73 L 2].

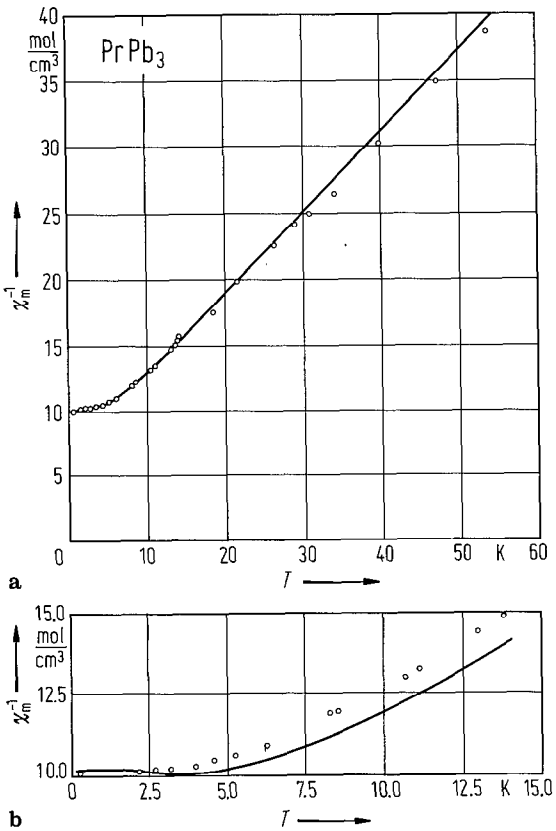

Fig. 124. $PrPb_3$. (a) Temperature dependence of χ_m^{-1}. The solid curve represents theoretical calculations with CEF parameters $W=-0.65$ and $x=0.6$. (b) is an expanded scale of the low-temperature data with solid curve for CEF parameters $W=-1$ K and $x=-0.635$ [76 L 1].

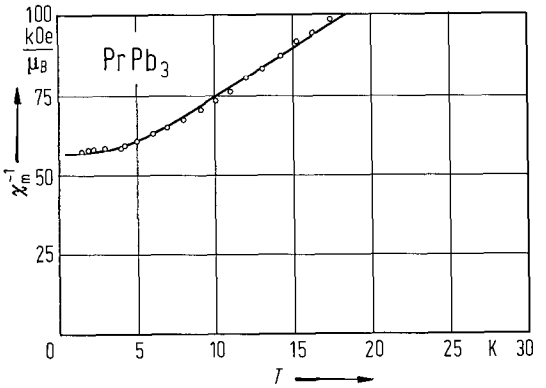

Fig. 125. $PrPb_3$. Temperature dependence of χ_m^{-1}. The full line is calculated with CEF parameters $W=-0.65$ K and $x=0.6$ and $\Theta=-9$ K [82 M 1].

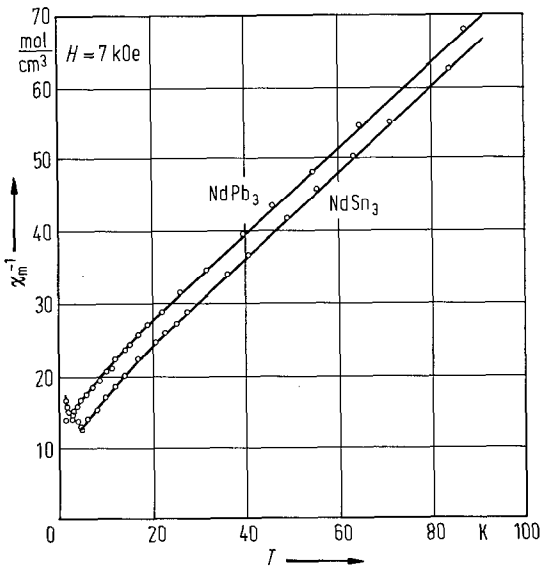

Fig. 126. $NdPb_3$, $NdSn_3$. Temperature dependence of χ_m^{-1} at 7 kOe. Continuous curves are calculated for, respectively, $W=1.26$; $x=0.13$ and $W=1.43$; $x=0.24$ [75 L 1].

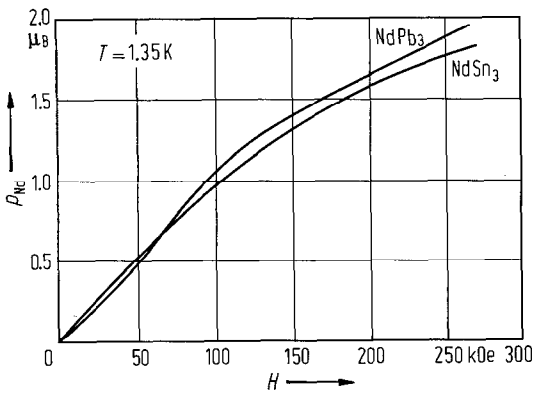

Fig. 127. $NdSn_3$, $NdPb_3$. Magnetic field dependence of the magnetic moment per Nd atom at 1.35 K [75 L 1].

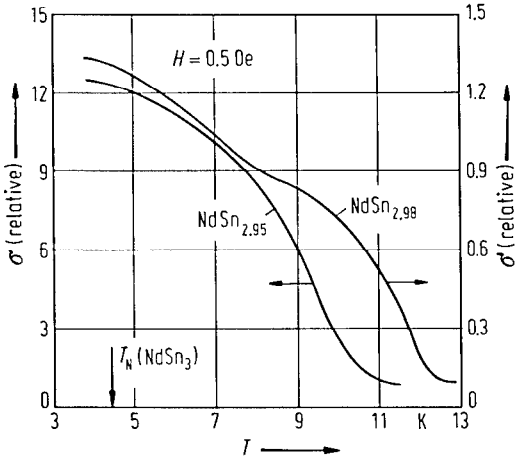

Fig. 128. $NdSn_{2.95}$, $NdSn_{2.98}$. Temperature dependence of σ (arbitrary units) at 0.5 Oe (earth's field). The arrow marks T_N for $NdSn_3$ [79 D 1].

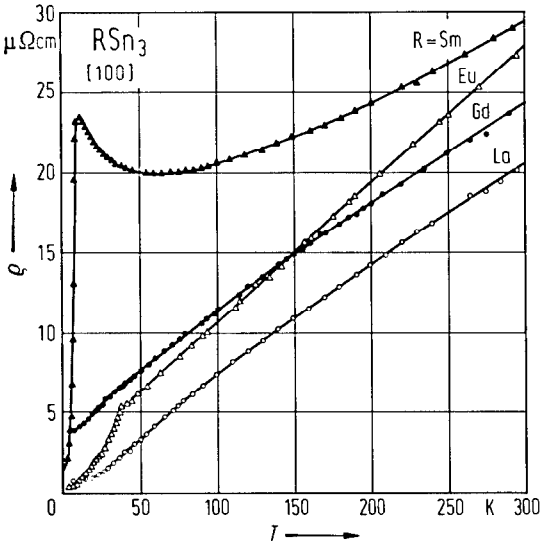

Fig. 130. RSn_3, R = La, Sm, Eu, Gd. Temperature dependence of electrical resistivity ϱ along the [100] axis of single crystals. The phase transition temperature is accompanied by a cusp in the ϱ vs. T plot [75 S 2].

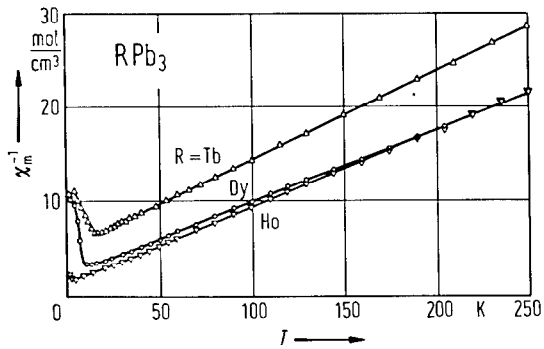

Fig. 131. RPb_3, R = Tb, Dy, Ho. Temperature dependence of χ_m^{-1} [73 L 2].

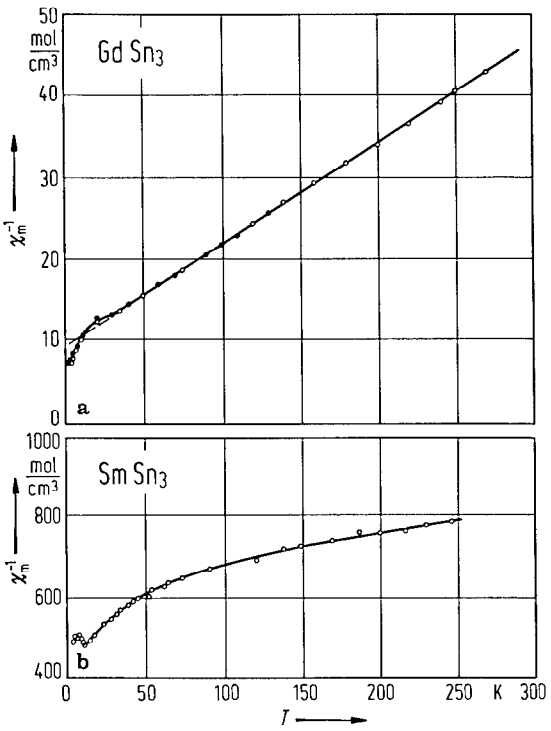

Fig. 129. $SmSn_3$, $GdSn_3$. Temperature dependence of χ_m^{-1} for (a) two samples of $GdSn_3$ and (b) $SmSn_3$ [65 T 1].

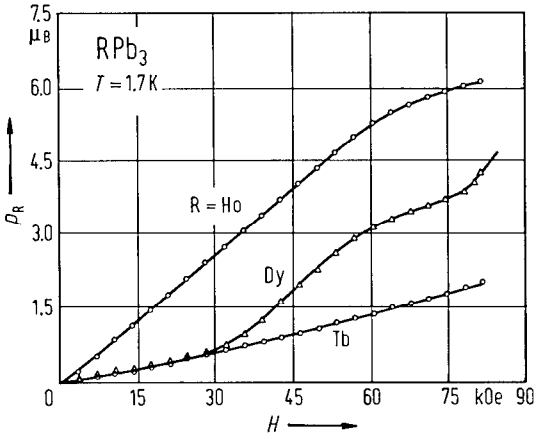

Fig. 132. RPb_3, R = Tb, Dy, Ho. Magnetic field dependence of the magnetic moment per rare earth atom at 1.7 K [73 L 2].

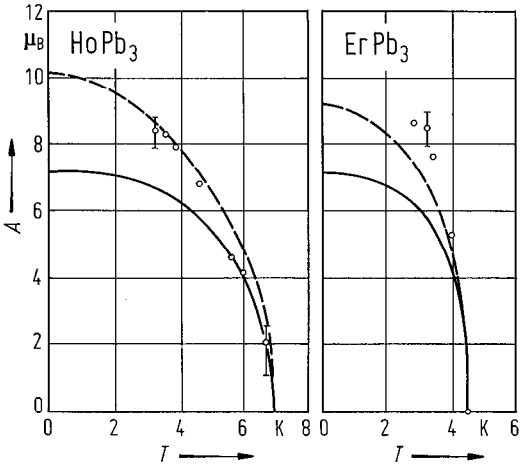

Fig. 133. $HoPb_3$, $ErPb_3$. Temperature dependence of the amplitude A of the sinusoidally modulated rare earth magnetic moments. The dashed lines give the Brillouin type magnetization for the free-ion case. The solid lines are the result of a mean-field calculation based on CEF schemes with parameters $W=-0.32$ K, $x=0.33$ and $W=0.13$ K, $x=0.079$ [80G1] for $ErPb_3$ and $HoPb_3$, respectively [81K1].

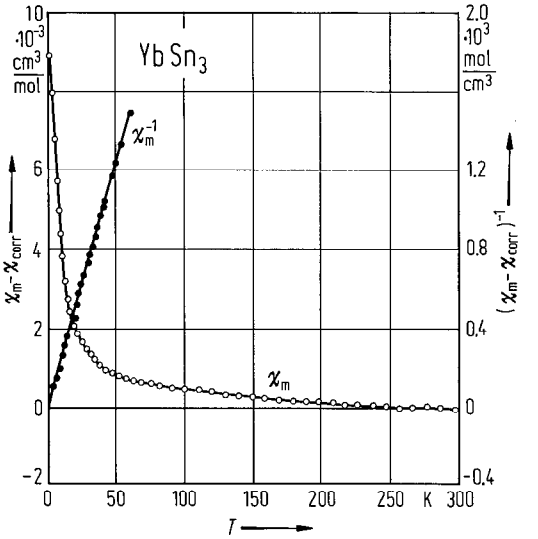

Fig. 134. $YbSn_3$. Temperature dependence of χ_m and χ_m^{-1}, corrected for diamagnetism of ionic cores (equal to $-96\cdot10^{-6}$ cm^3 mol^{-1}) [74S1].

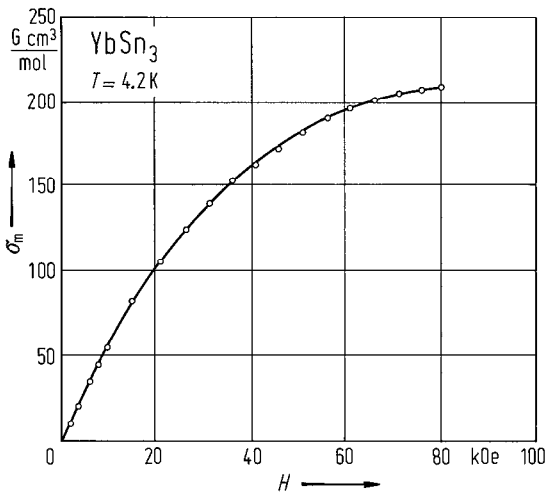

Fig. 135. $YbSn_3$. Magnetic field dependence of σ_m at 4.2 K [74S1].

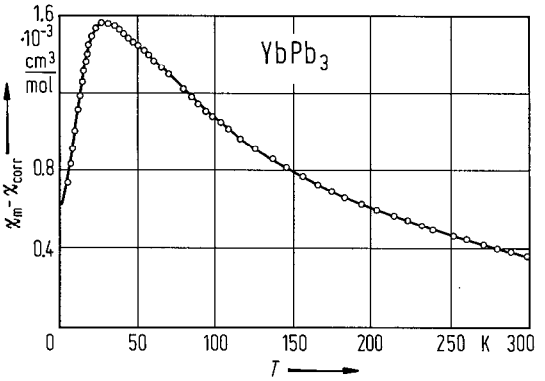

Fig. 136. $YbPb_3$. Temperature dependence of χ_m, corrected for diamagnetism of ionic cores (equal to $-125\cdot10^{-6}$ cm^3 mol^{-1}) [74S1].

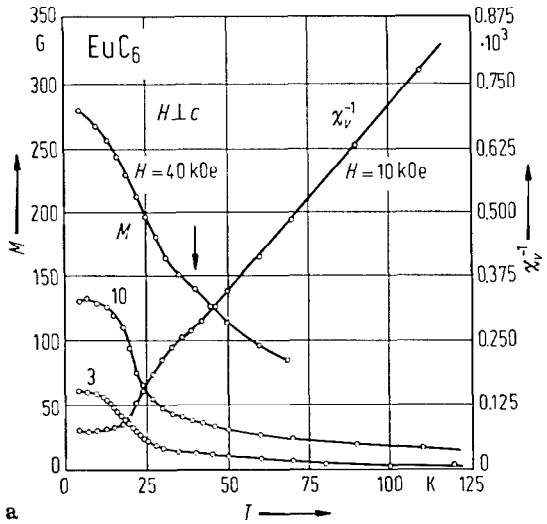

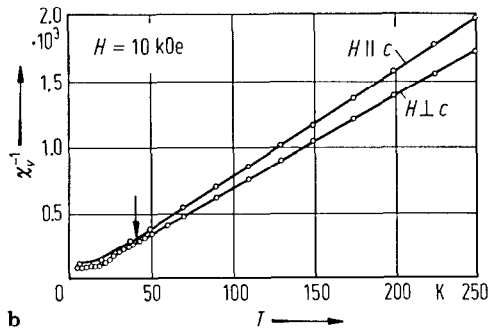

Fig. 137. EuC_6. (a) Temperature dependence of χ_V^{-1} (in cgs-units) at 10 kOe and of M at different magnetic fields perpendicular to the c axis. (b) Temperature dependence of χ_V^{-1} at 10 kOe parallel and perpendicular to the c axis. The arrows indicate the magnetic transition temperatures [81 S 6].

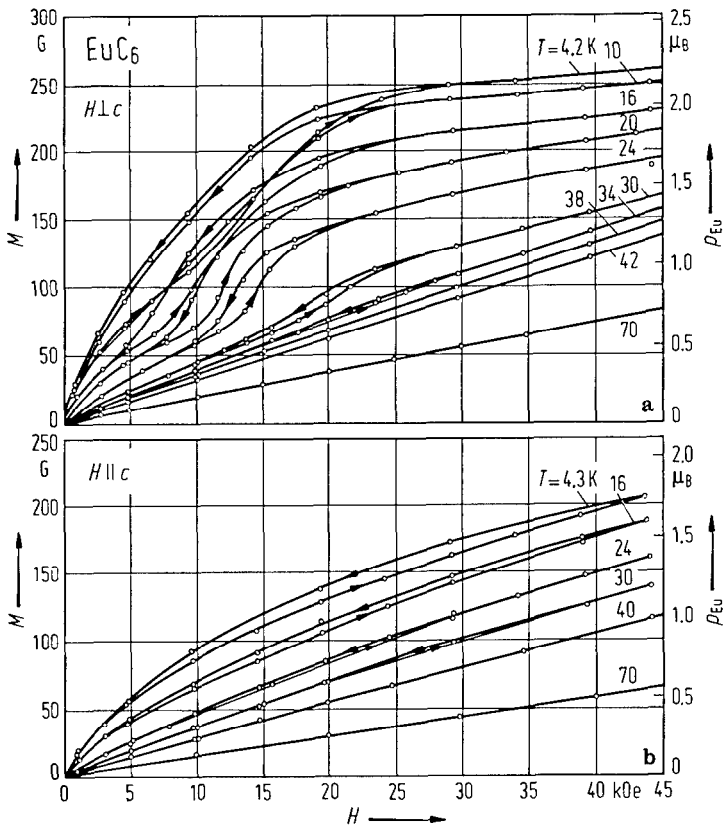

Fig. 138. EuC_6. Magnetic field dependence of the magnetization and the magnetic moment per Eu atom perpendicular (a) and parallel (b) to the c axis at different temperatures. The data are obtained for increasing and decreasing magnetic fields [81 S 6].

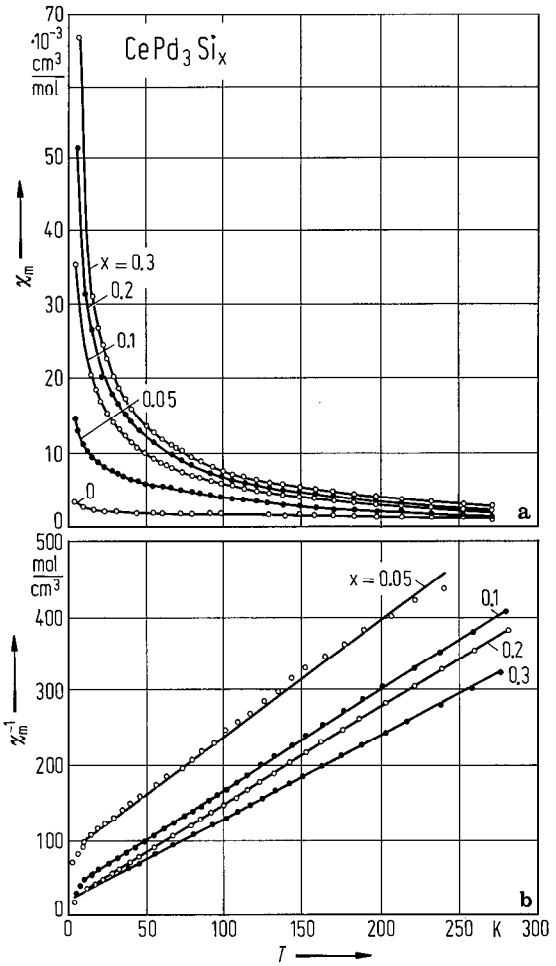

Fig. 139. $CePd_3Si_x$. Temperature dependence of (a) χ_m and (b) χ_m^{-1} for various compositions [84 M 1].

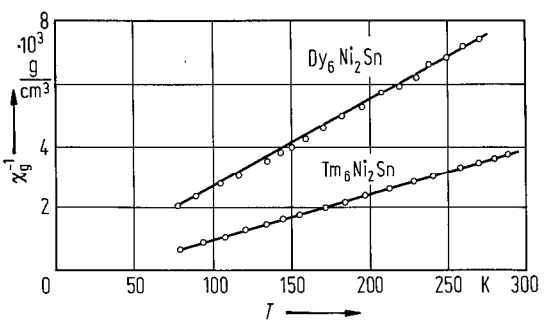

Fig. 141. Dy_6Ni_2Sn, Tm_6Ni_2Sn. Temperature dependence of χ_g^{-1} [84 S 1].

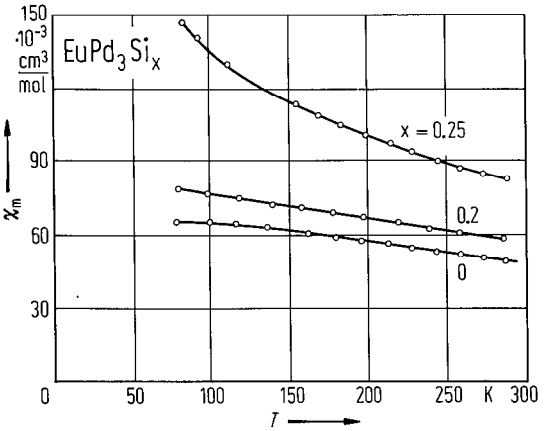

Fig. 140. $EuPd_3Si_x$. Temperature dependence of χ_m [83 D 1].

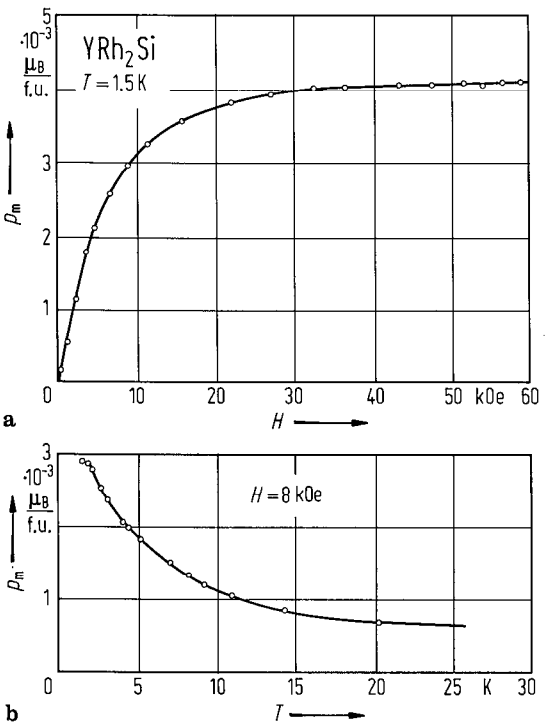

Fig. 142. YRh_2Si. Magnetic field dependence of (a) p_m at 1.5 K and temperature dependence of (b) p_m at 8 kOe [85 P 1].

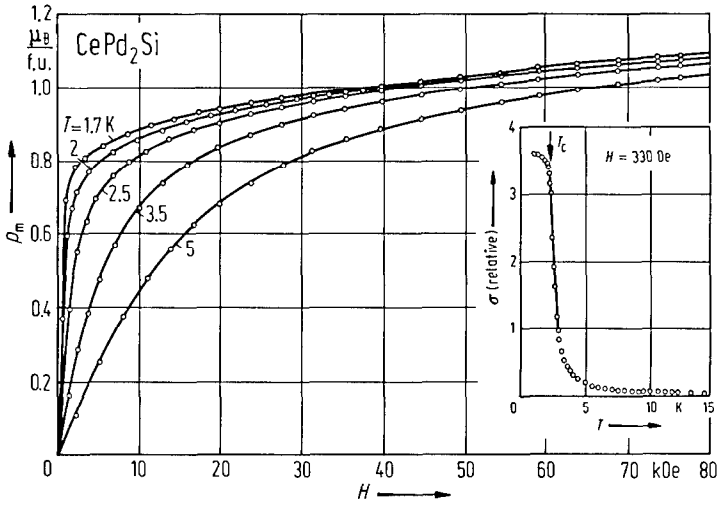

Fig. 144. $CePd_2Si$. Magnetic field dependence of p_m and temperature dependence of σ at 330 Oe (in the insert) [86 B 2].

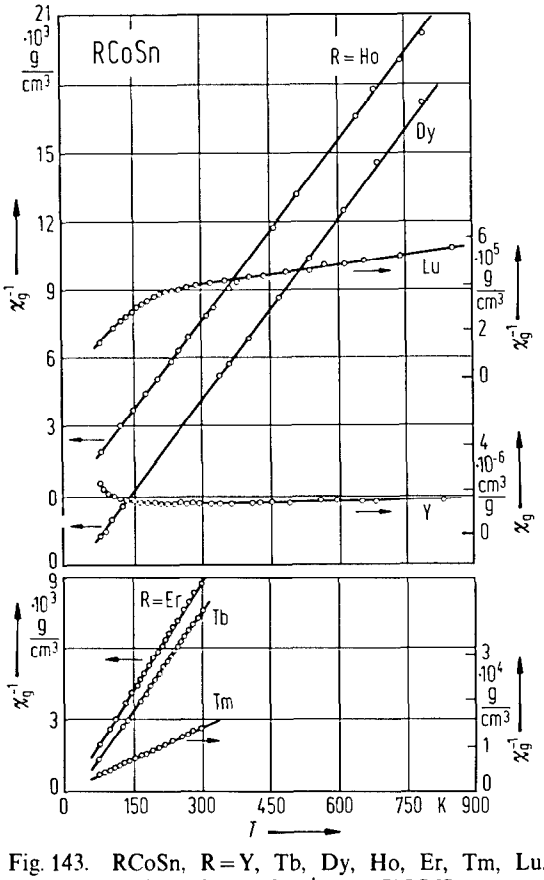

Fig. 143. RCoSn, R = Y, Tb, Dy, Ho, Er, Tm, Lu. Temperature dependence of χ_g^{-1} or χ_g [85 S 2].

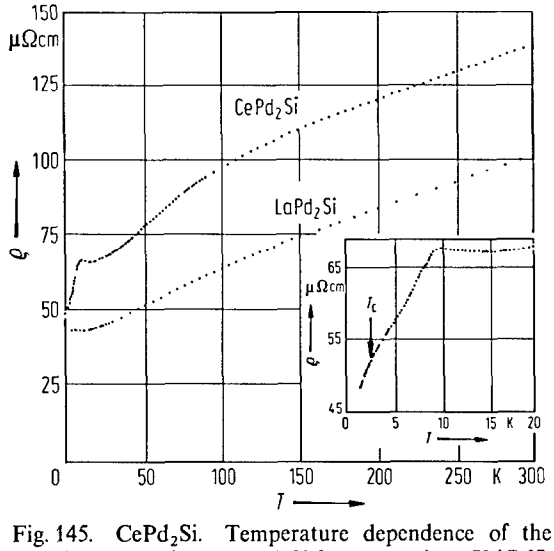

Fig. 145. $CePd_2Si$. Temperature dependence of the electrical resistivity ϱ. $LaPd_2Si$ for comparison [86 B 2].

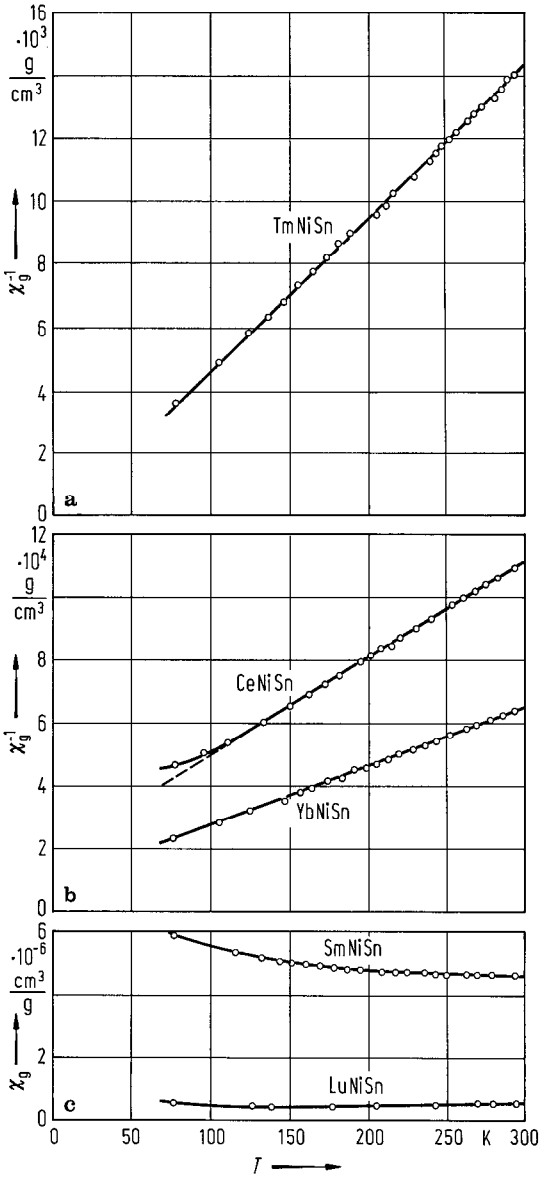

Fig. 146. RNiSn, R = Ce, Sm, Tm, Yb, Lu. Temperature dependence of χ_g^{-1} or χ_g [84 S 1].

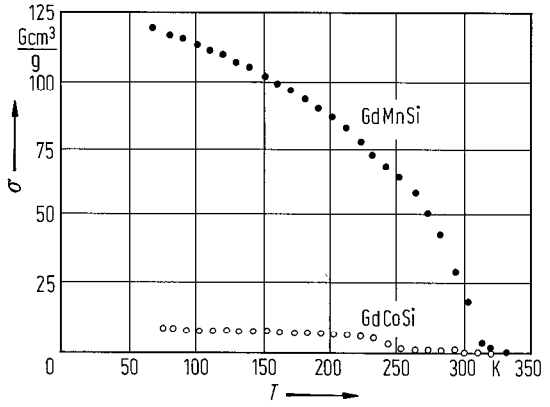

Fig. 147. GdCoSi, GdMnSi. Temperature dependence of σ [82 K 1].

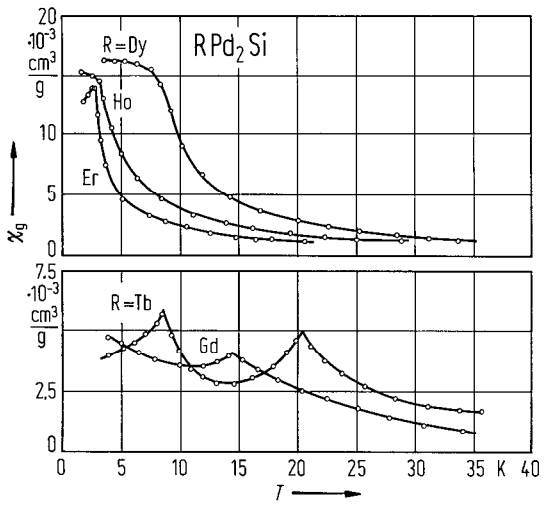

Fig. 148. RPd_2Si, R = Gd, Tb, Dy, Ho, Er. Temperature dependence of χ_g [84 G 1].

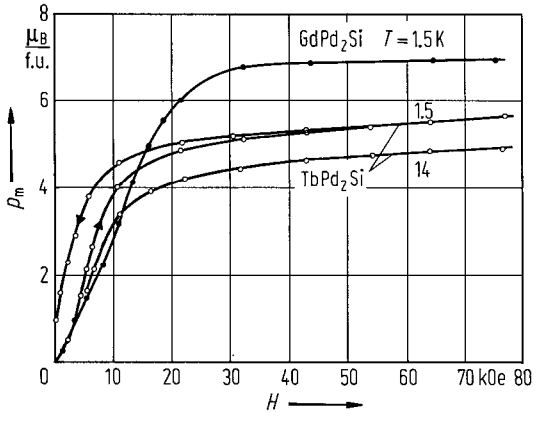

Fig. 149. $GdPd_2Si$, $TbPd_2Si$. Magnetic field dependence of p_m at 1.5 and 14 K [84 G 1].

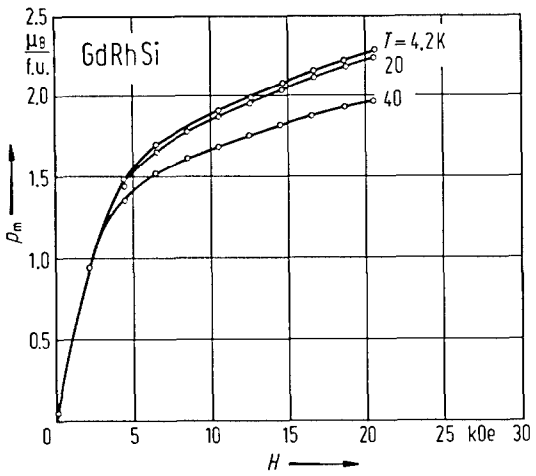

Fig. 150. GdRhSi. Magnetic field dependence of p_m at different temperatures [82 C 1].

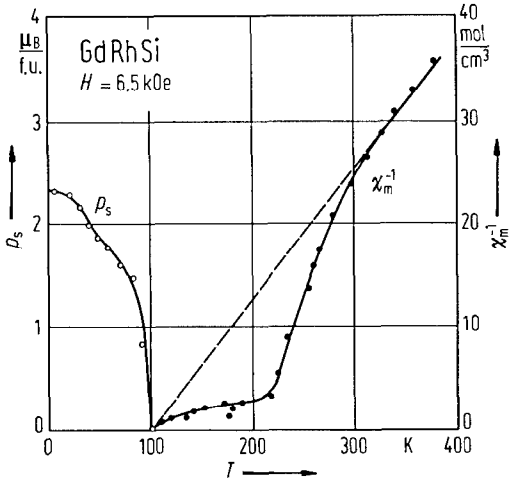

Fig. 151. GdRhSi. Temperature dependence of χ_m^{-1} at 6.5 kOe and spontaneous magnetization p_s [83 C 3].

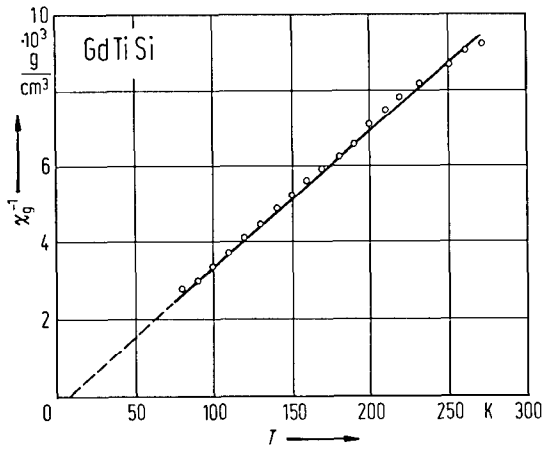

Fig. 152. GdTiSi. Temperature dependence of χ_g^{-1} [84 K 1].

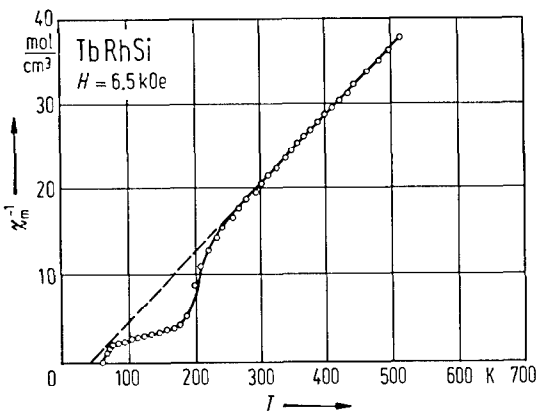

Fig. 153. TbRhSi. Temperature dependence of χ_m^{-1} at 6.5 kOe [82 C 1].

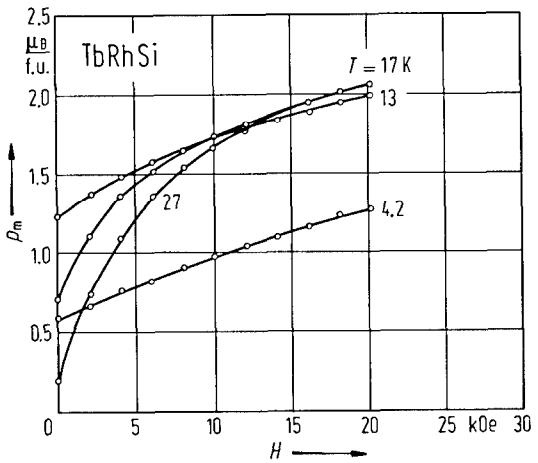

Fig. 154. TbRhSi. Magnetic field dependence of p_m at different temperatures [82 C 1].

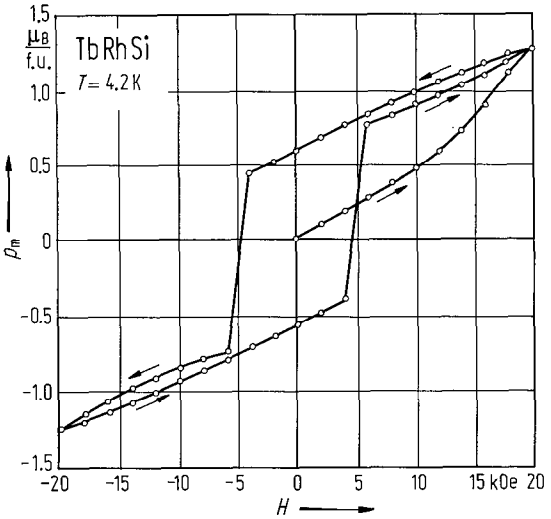

Fig. 155. TbRhSi. Hysteresis loop at 4.2 K [82 C 1].

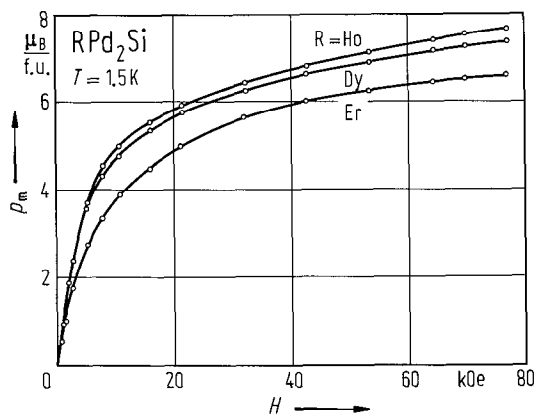

Fig. 157. RPd_2Si, R = Dy, Ho, Er. Magnetic field dependence of p_m at 1.5 K [84 G 1].

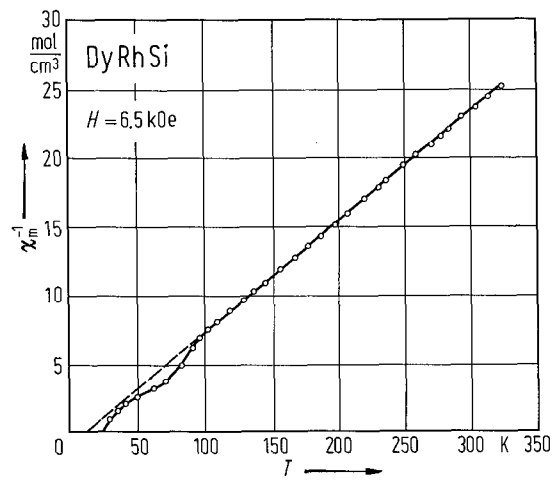

Fig. 158. DyRhSi. Temperature dependence of χ_m^{-1} at 6.5 kOe [82 C 1].

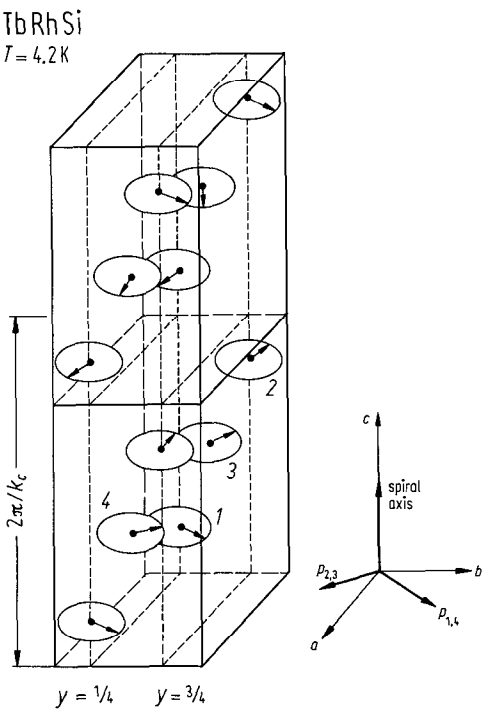

Fig. 156. TbRhSi. Magnetic structure at 4.2 K. The Tb magnetic moments p_1 and p_4 located at positions (*1*) $x, \frac{1}{4}, z$ and (*4*) $\frac{1}{2}+x, \frac{1}{4}, \frac{1}{2}-z$, respectively, form the first spiral, and p_2 and p_3 located at positions (*2*) $\bar{x}, \frac{3}{4}, \bar{z}$ and (*3*) $\frac{1}{2}-x, \frac{3}{4}, \frac{1}{2}+z$, respectively, form the second one [85 B 1].

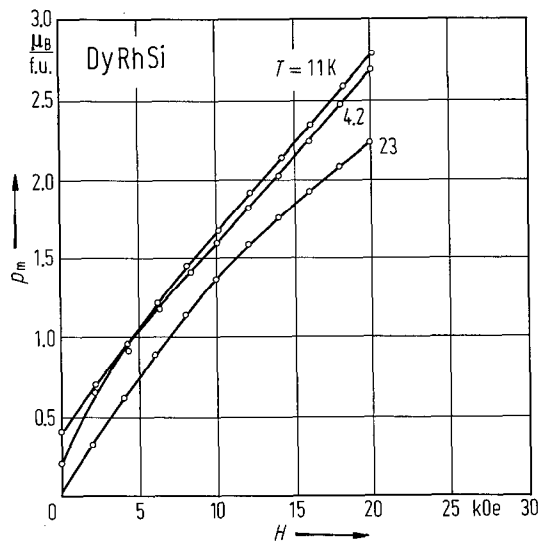

Fig. 159. DyRhSi. Magnetic field dependence of p_m at different temperatures [82 C 1].

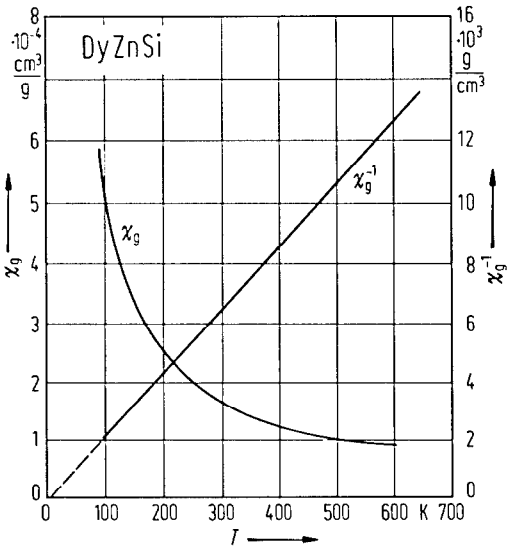

Fig. 160. DyZnSi. Temperature dependence of χ_g and χ_g^{-1} [85 K 1].

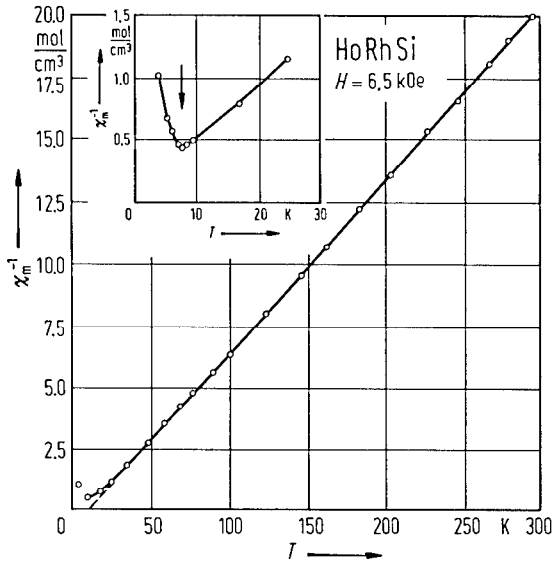

Fig. 161. HoRhSi. Temperature dependence of χ_m^{-1} at 6.5 kOe [82 C 1].

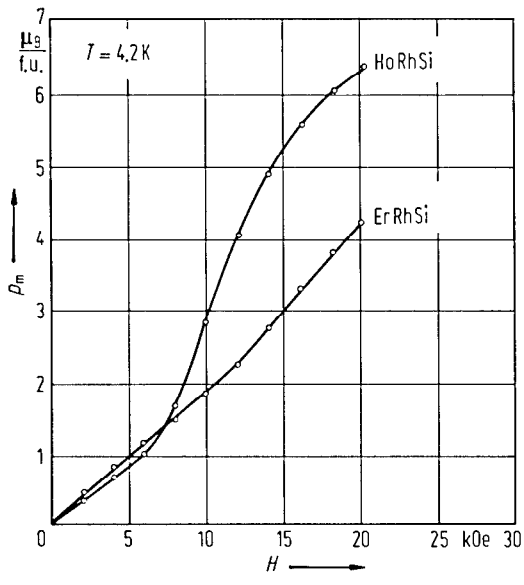

Fig. 162. HoRhSi, ErRhSi. Magnetic field dependence of p_m at 4.2 K [82 C 1].

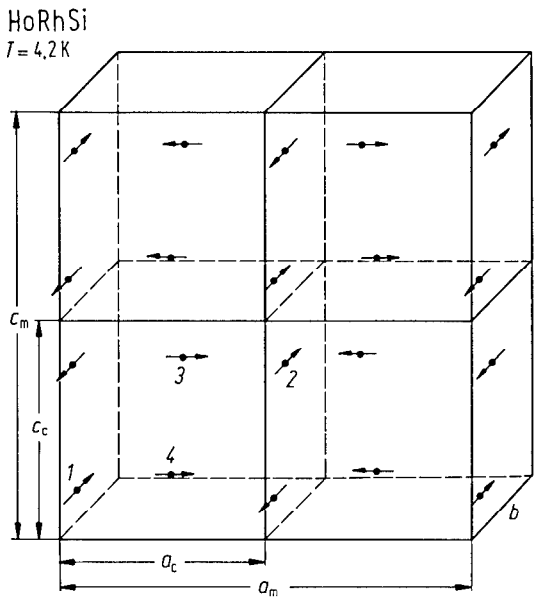

Fig. 163. HoRhSi. Magnetic structure at 4.2 K. Crystallographic (c) and magnetic (m) unit cells are depicted [85 B 1].

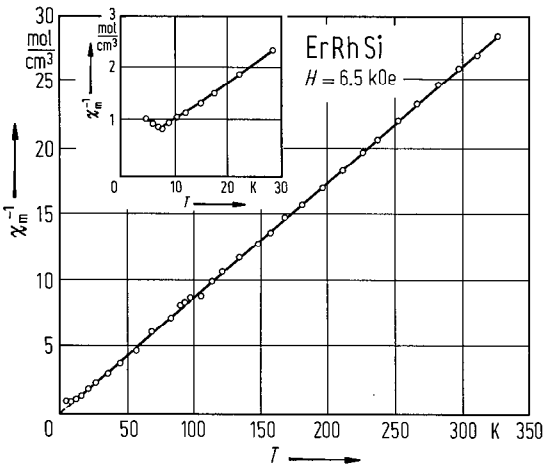

Fig. 164. ErRhSi. Temperature dependence of χ_m^{-1} at 6.5 kOe [82 C 1].

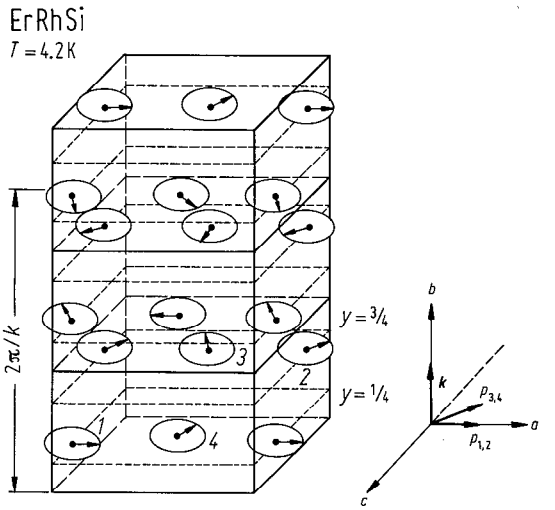

Fig. 165. ErRhSi. Magnetic structure at 4.2 K. The Er magnetic moments p_1 and p_2 constitute the first spiral, while p_3 and p_4 form the second one. The modulation vector $\boldsymbol{k}$ is along the b axis. For location of rare earth positions (*1*···*4*), see caption to Fig. 156 [85 B 1].

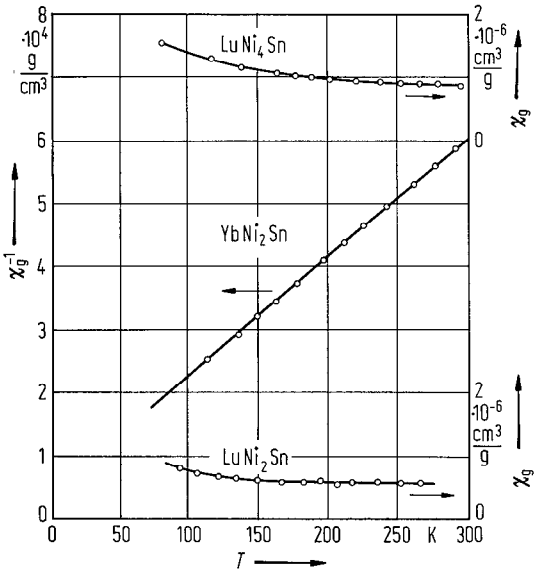

Fig. 166. $LuNi_4Sn$, $YbNi_2Sn$, $LuNi_2Sn$. Temperature dependence of χ_g or χ_g^{-1} [83 S 5].

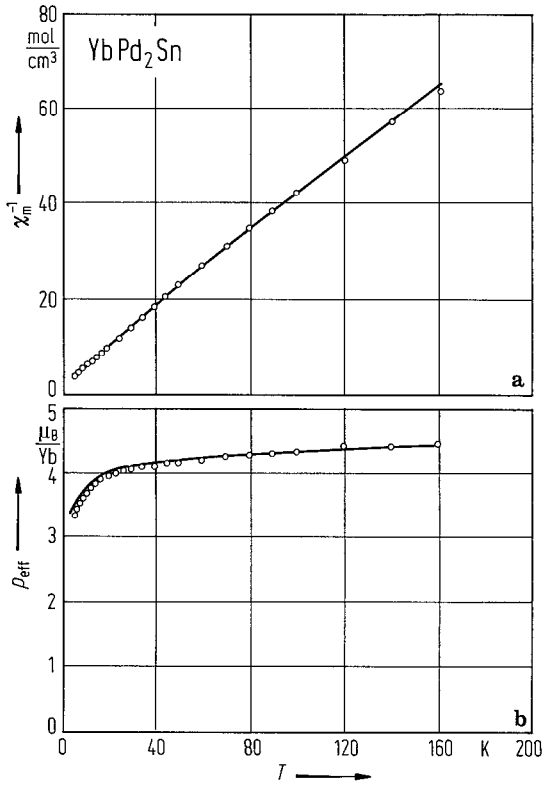

Fig. 167. $YbPd_2Sn$. Temperature dependence of (a) χ_m^{-1} and (b) p_{eff}. The solid line includes CEF splitting and exchange effects in the mean-field approximation for CEF parameters $W = -12$ K, $x = -0.65$ and $T_m = 0.36$, $\lambda = -0.3307$ mol cm^{-3}, where λ is the exchange coupling parameter and T_m is the magnetic ordering temperature [85 K 2].

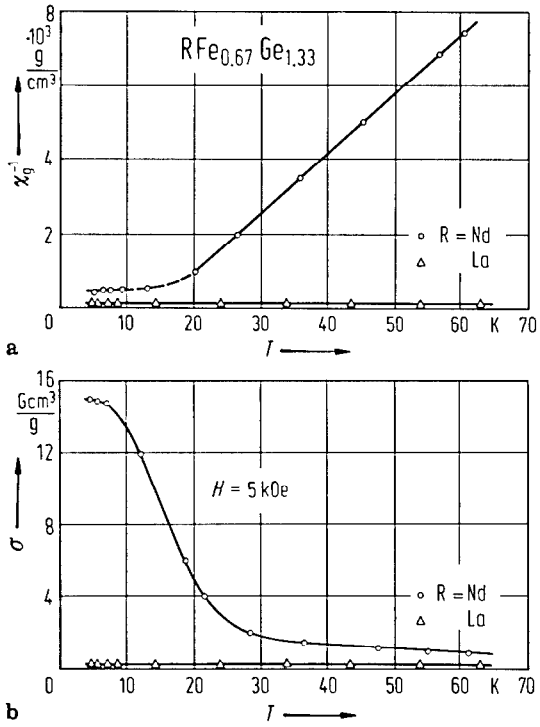

Fig. 168. $RFe_{0.67}Ge_{1.33}$, R = La, Nd. Temperature dependence of (a) χ_g^{-1} and (b) σ at 5 kOe [73 F 1].

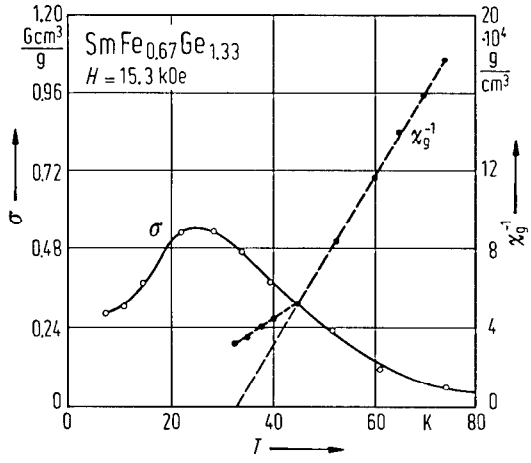

Fig. 169. $SmFe_{0.67}Ge_{1.33}$. Temperature dependence of χ_g^{-1} and σ at 15.3 kOe [72 F 1].

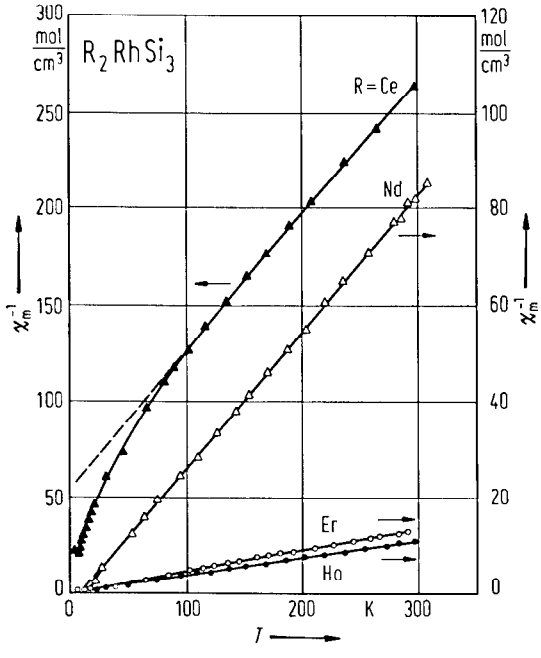

Fig. 170. R_2RhSi_3, R = Ce, Nd, Ho, Er. Temperature dependence of χ_m^{-1} [84 C 1].

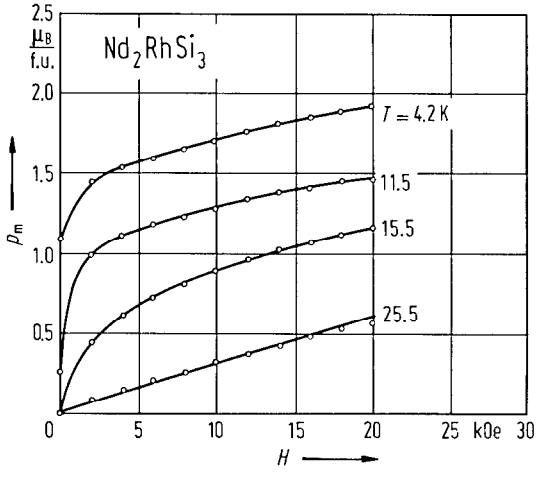

Fig. 171. Nd_2RhSi_3. Magnetic field dependence of p_m at different temperatures [84 C 1].

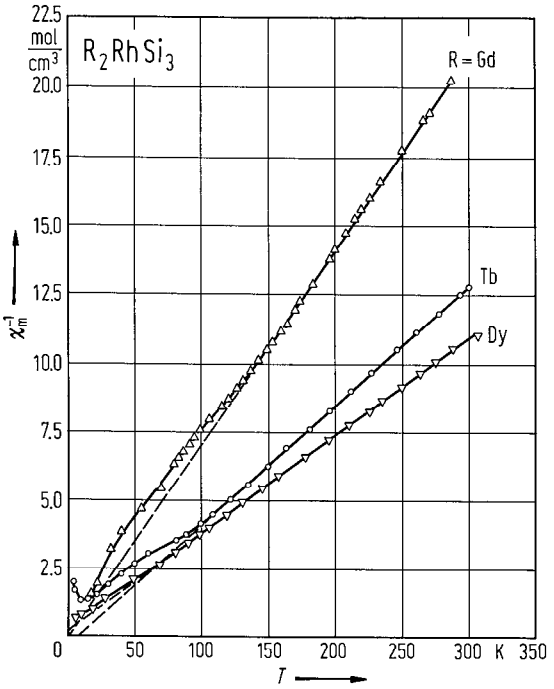

Fig. 172. R_2RhSi_3, R = Gd, Tb, Dy. Temperature dependence of χ_m^{-1} [83 C 1].

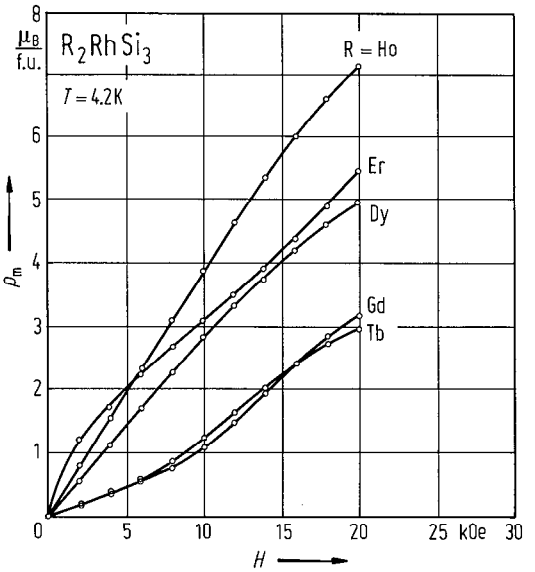

Fig. 173. R_2RhSi_3, R = Gd, Tb, Dy, Ho, Er. Magnetic field dependence of p_m at 4.2 K [84 C 1].

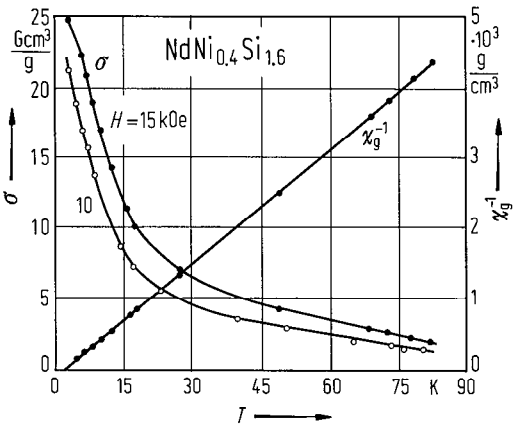

Fig. 174. $NdNi_{0.4}Si_{1.6}$. Temperature dependence of χ_g^{-1} and σ at 10 and 15 kOe [73 F 1].

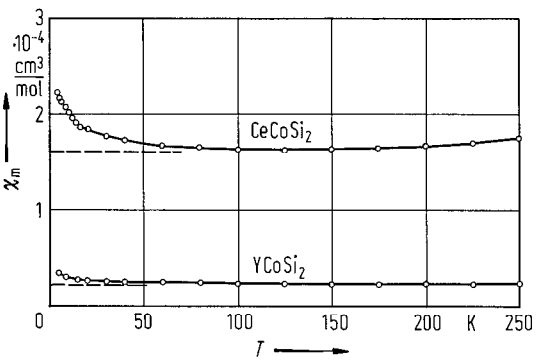

Fig. 175. $YCoSi_2$, $CeCoSi_2$. Temperature dependence of χ_m, corrected for ferromagnetic impurities (dashed line) [82 P 1].

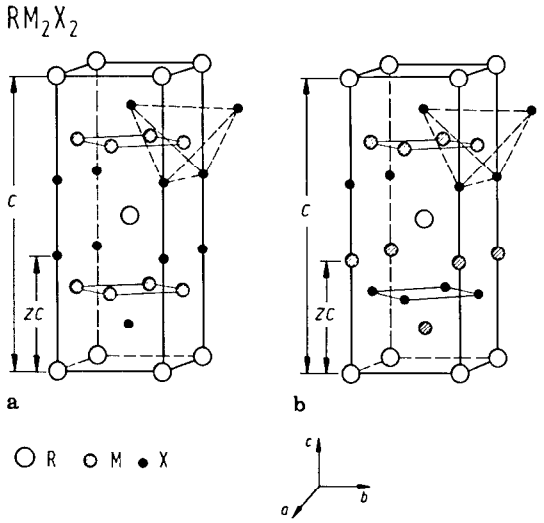

Fig. 176. RM_2X_2, R = rare earth, M = transition metal, X = Si, Ge, Sn. Crystal structure. The compounds crystallize in majority in the $ThCr_2Si_2$ structure type with I4/mmm space group (a). The R atoms form a square network with the R–R separation $\simeq 4$ Å. The M atoms form also a square network with M–M separation $\simeq 2.8$ Å. The X atoms form a tetrahedron around M atoms. The unit cell contains two formula units. The atomis positions are the following: R in 2a sites [0, 0, 0], $[\frac{1}{2}, \frac{1}{2}, \frac{1}{2}]$; M in 4d sites $[0, \frac{1}{2}, \frac{1}{4}]$, $[\frac{1}{2}, 0, \frac{1}{4}]$, $[0, \frac{1}{2}, \frac{3}{4}]$, $[\frac{1}{2}, 0, \frac{3}{4}]$; X in 4e sites $[0, 0, z]$, $[0, 0, \bar{z}]$, $[\frac{1}{2}, \frac{1}{2}, \frac{1}{2}+z]$, $[\frac{1}{2}, \frac{1}{2}, \frac{1}{2}-z]$, where $z \cong \frac{3}{8} = 0.375$. Some of these compounds are suggested to crystallize in the $CaBe_2Ge_2$ structure type with the P4/nmm space group (b) (YIr_2Si_2) [85 H 1], $TbIr_2Si_2$ [84 H 2] at high temperatures; $CePt_2Si_2$, $CePt_2Ge_2$ [85 D 1] and $HoPt_2Si_2$ [84 L 4] are suggested to crystallize only in this structure). Above 500 K, $CePt_2Si_2$ structure type with P4/mm space group was suggested for RPt_2Si_2 compounds [85 H 2] (but see also remark above [84 L 4]). A mixing between M and X atoms in the 4d and 4e sites was suggested in RRu_2Si_2 [85 C 1]. $CeNi_2Sn_2$ was found to be monoclinic at 873 K [81 S 5].

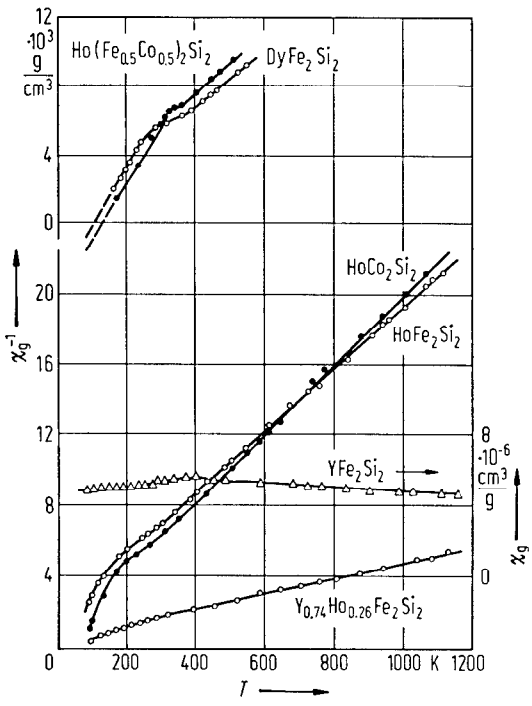

Fig. 177. RM_2Si_2, R = Y, Dy, Ho, $Y_{0.74}Ho_{0.26}$, M = Fe, Co, $Fe_{0.5}Co_{0.5}$. Temperature dependence of χ_g or χ_g^{-1} [80 S 5].

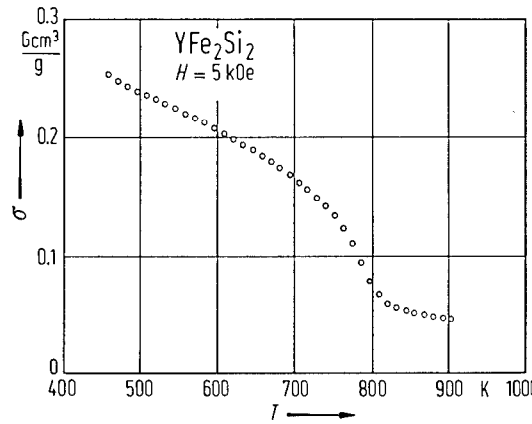

Fig. 178. YFe_2Si_2. Temperature dependence of σ at 5 kOe [76 S 1].

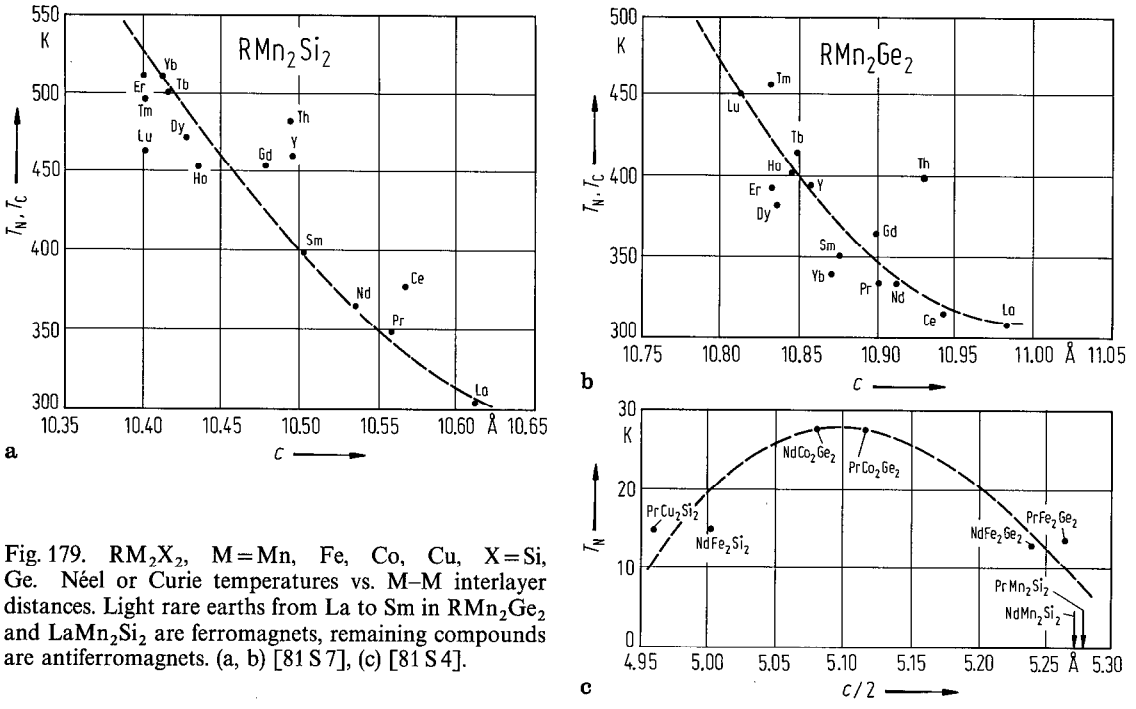

Fig. 179. RM_2X_2, M = Mn, Fe, Co, Cu, X = Si, Ge. Néel or Curie temperatures vs. M–M interlayer distances. Light rare earths from La to Sm in RMn_2Ge_2 and $LaMn_2Si_2$ are ferromagnets, remaining compounds are antiferromagnets. (a, b) [81 S 7], (c) [81 S 4].

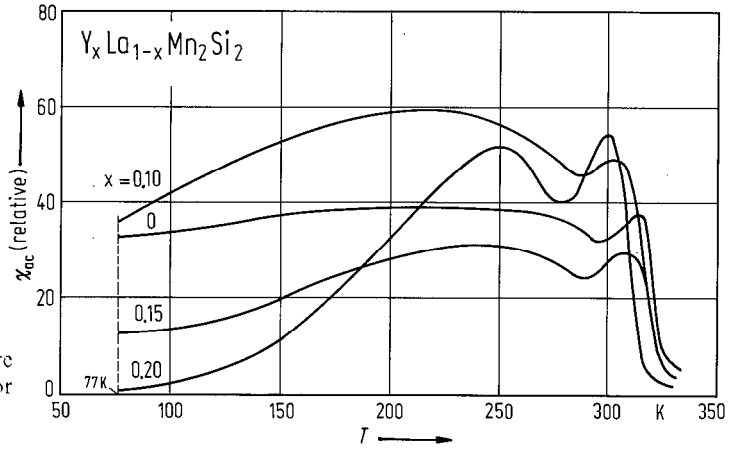

Fig. 180. $Y_xLa_{1-x}Mn_2Si_2$. Temperature dependence of χ_{ac} (in arbitrary units) for various compositions [83 C 2].

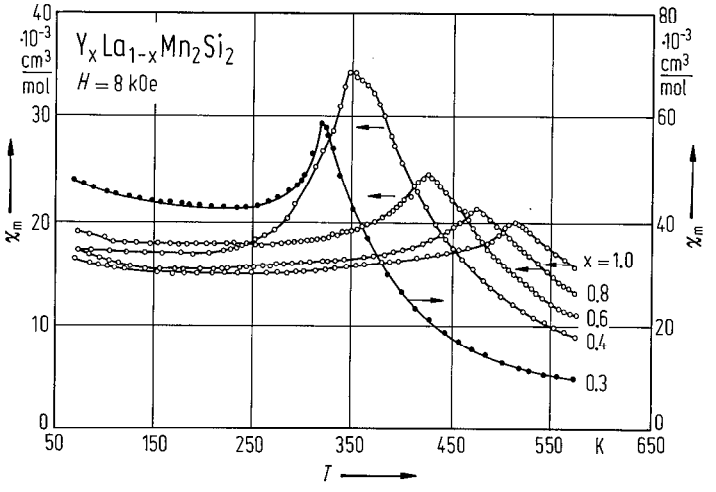

Fig. 181. $Y_xLa_{1-x}Mn_2Si_2$. Temperature dependence of χ_m at 8 kOe for various compositions [83 S 1].

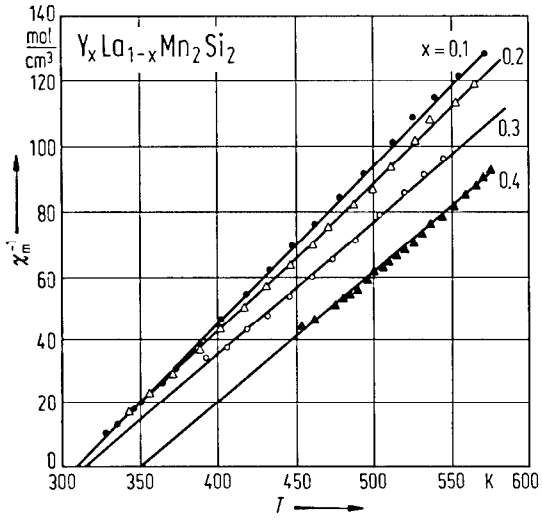

Fig. 182. $Y_xLa_{1-x}Mn_2Si_2$. Temperature dependence of χ_m^{-1} for various compositions [83 S 1].

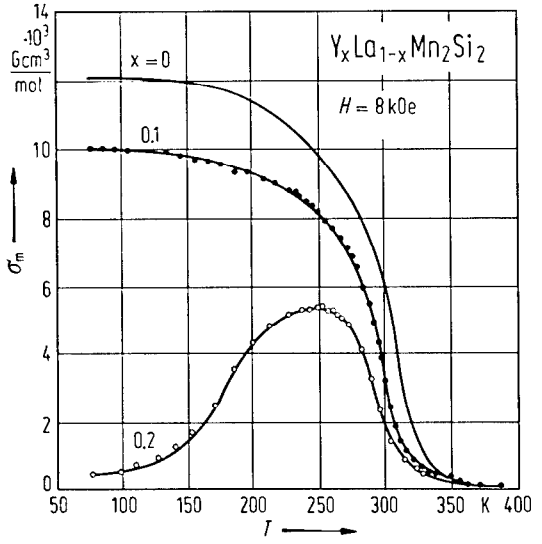

Fig. 184. $Y_xLa_{1-x}Mn_2Si_2$. Temperature dependence of σ_m at 8 kOe for various compositions [83 S 1].

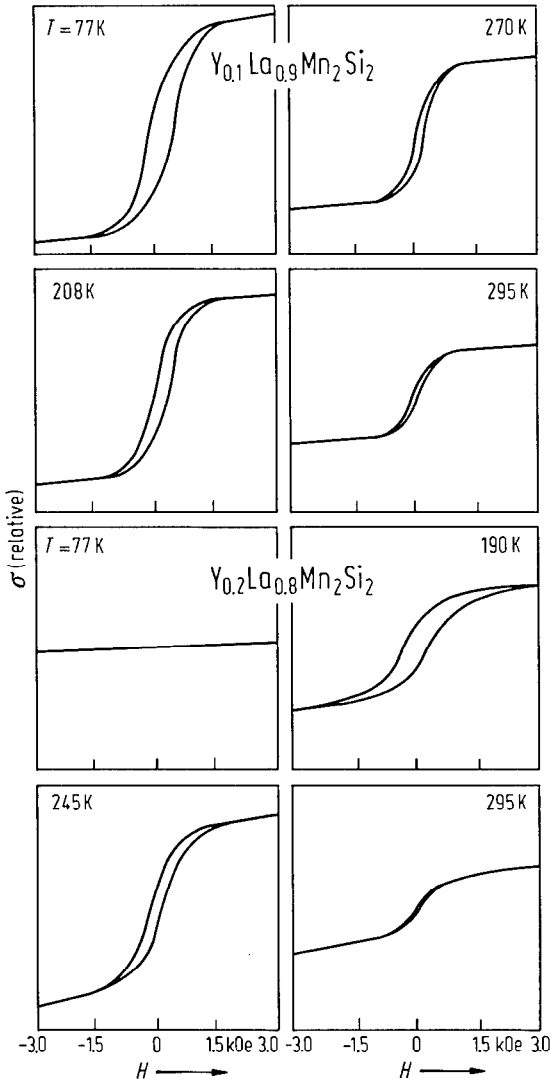

Fig. 183. $Y_xLa_{1-x}Mn_2Si_2$. Hysteresis loops at different temperatures for x = 0.1 and 0.2. H_{max} = 3 kOe. The relative scale for σ is the same for all temperatures [83 C 2].

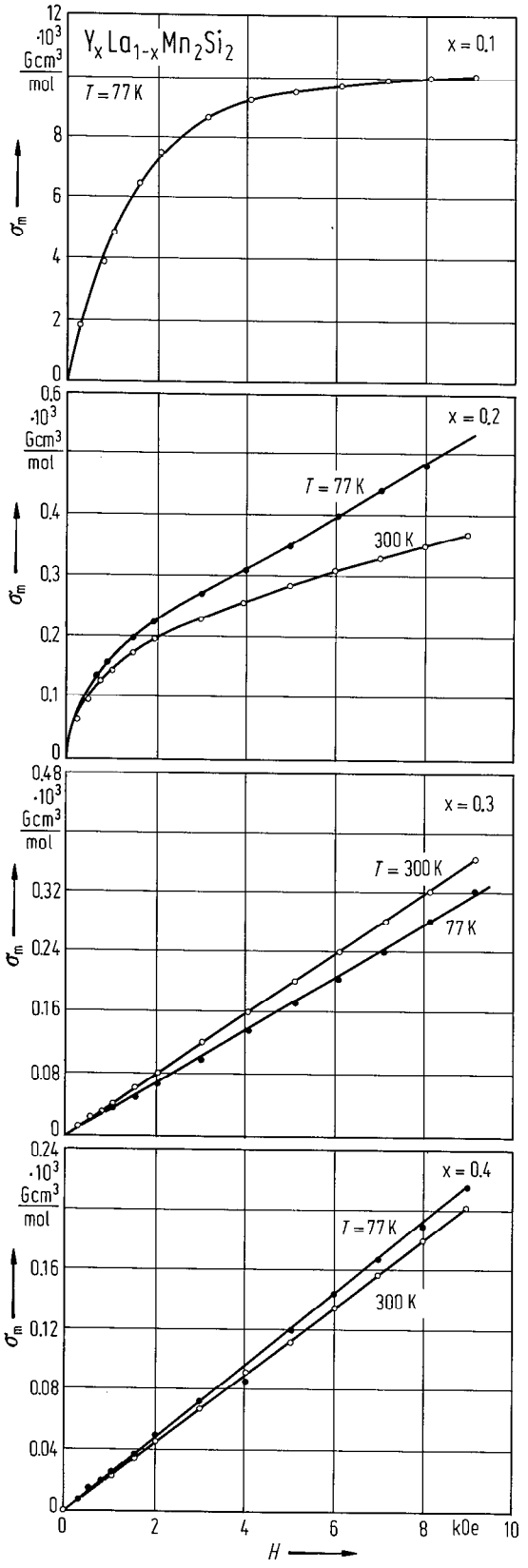

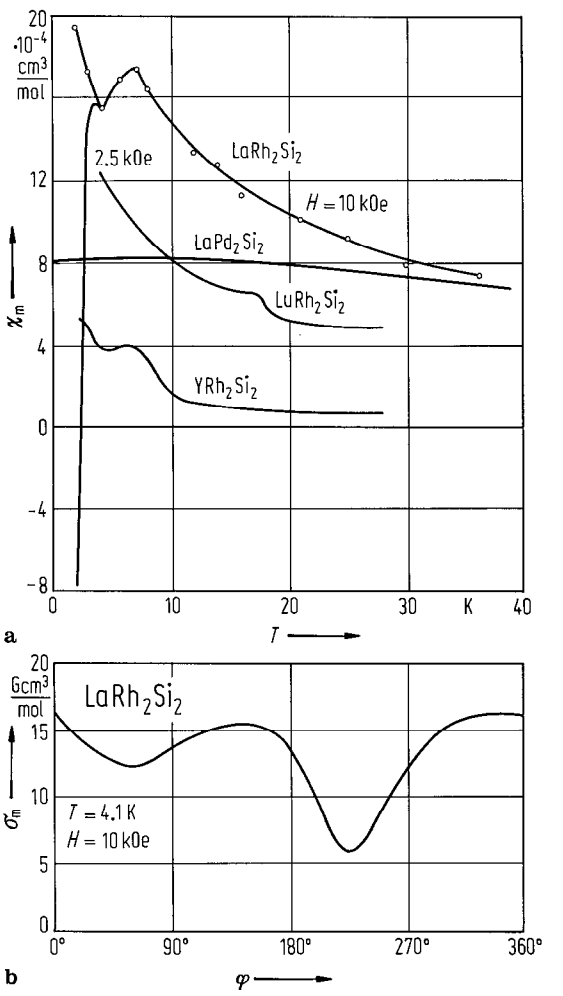

Fig. 186. RRh_2Si_2, R = Y, La, Lu; $LaPd_2Si_2$. (a) Temperature dependence of χ_m at 2.5 and 10 kOe. (b) Magnetization of $LaRh_2Si_2$ at 4.1 K as a function of the orientation φ of the sample relative to an applied magnetic field of 10 kOe [83 F 1, 84 F 1].

Fig. 185. $Y_xLa_{1-x}Mn_2Si_2$. Magnetic field dependence of σ_m at 77 and 300 K for various compositions [83 S 1].

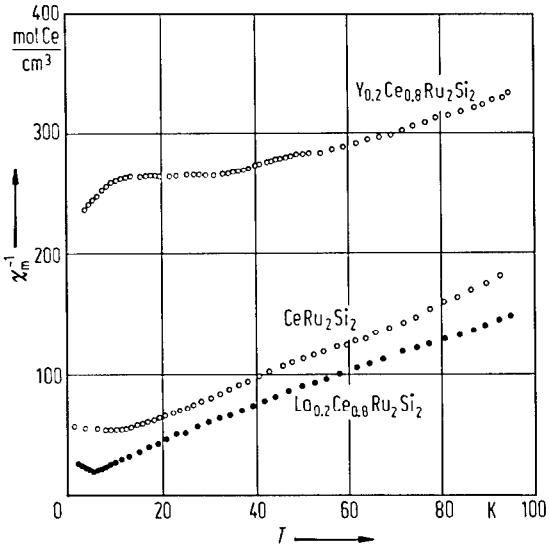

Fig. 187. $R_{1-x}Ce_xRu_2Si_2$, R = Y, La. Temperature dependence of χ_m^{-1} [85 B 2].

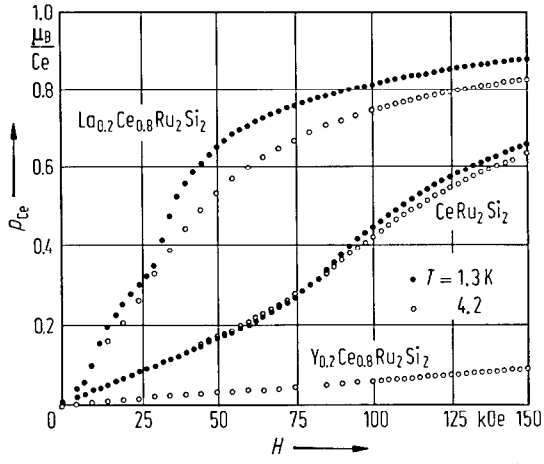

Fig. 188. $R_{1-x}Ce_xRu_2Si_2$, R = Y, La. Magnetic field dependence of the magnetic moment per Ce atom at 1.3 and 4.2 K [85 B 2].

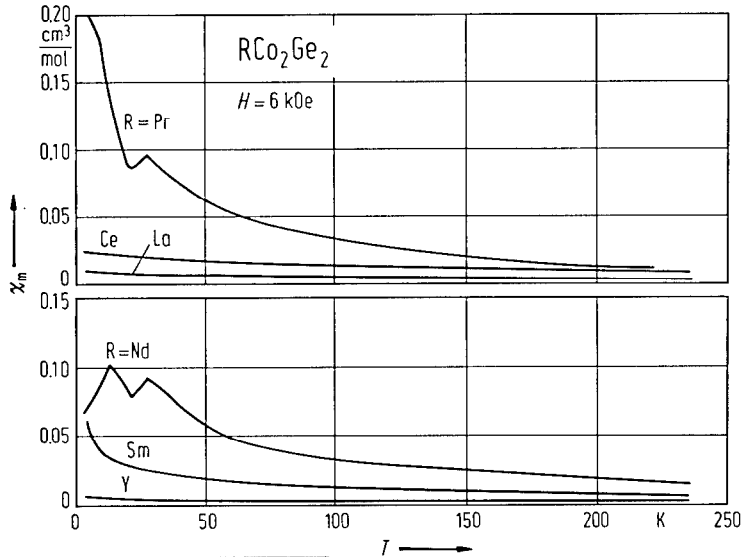

Fig. 189. RCo_2Ge_2, R = Y, La, Ce, Pr, Nd, Sm. Temperature dependence of χ_m at 6 kOe [73 M 1].

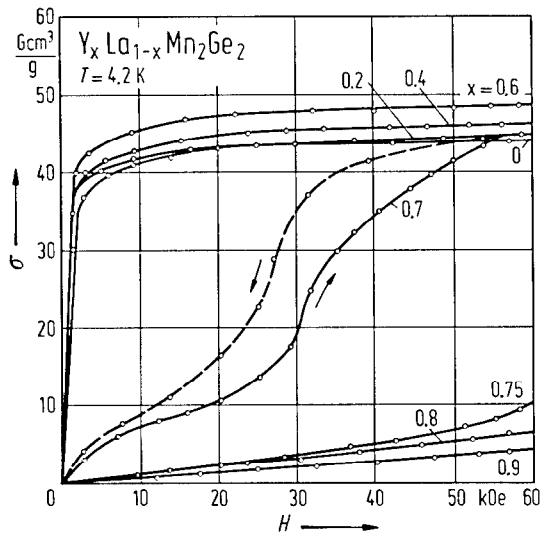

Fig. 190. $Y_xLa_{1-x}Mn_2Ge_2$. Magnetic field dependence of σ at 4.2 K [86 F 1].

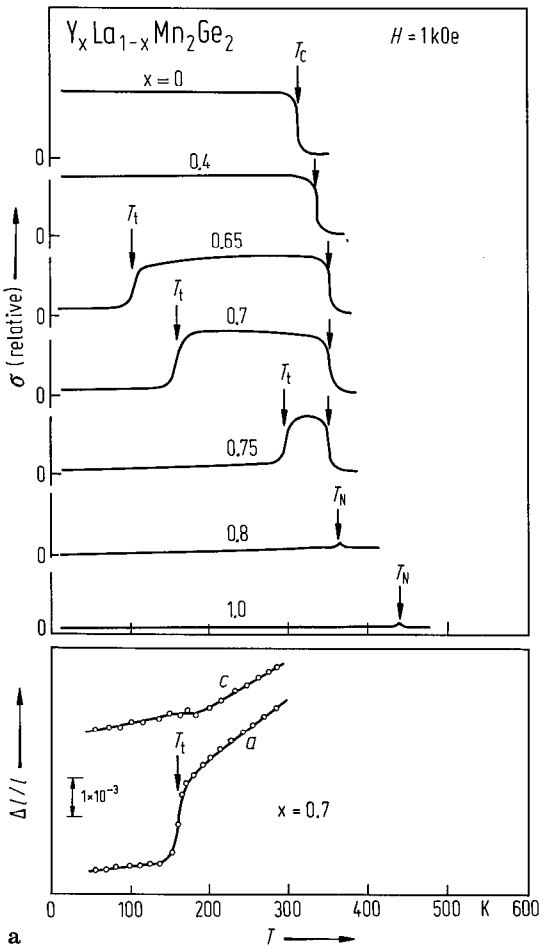

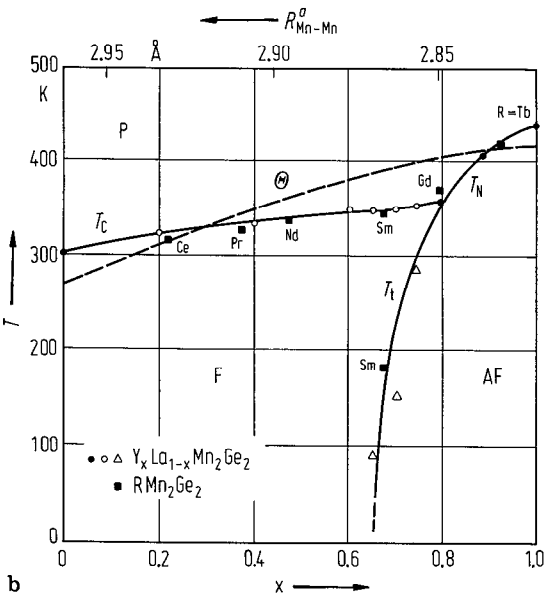

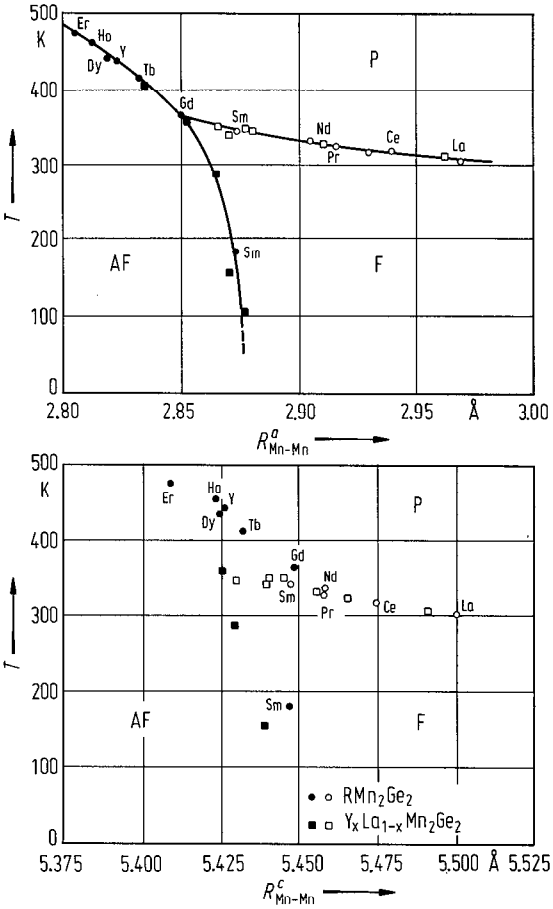

Fig. 192. RMn_2Ge_2, $Y_xLa_{1-x}Mn_2Ge_2$. Magnetic phase diagram as a function of the intralayer (R^a) and interlayer (R^c) Mn–Mn distances. Solid symbols: T_N and F⇌AF transition temperature, open symbols: T_C. Squares are for pseudoternaries $Y_xLa_{1-x}Mn_2Ge_2$ [85 F 4].

Fig. 191. $Y_xLa_{1-x}Mn_2Ge_2$, RMn_2Ge_2. (a) Temperature dependence of σ at 1 kOe. At T_t the lattice parameter a changes rapidly (b) Magnetic phase diagram as a function of composition and/or intralayer distances R^a_{Mn-Mn}. Squares are the data for RMn_2Ge_2 [86 F 1].

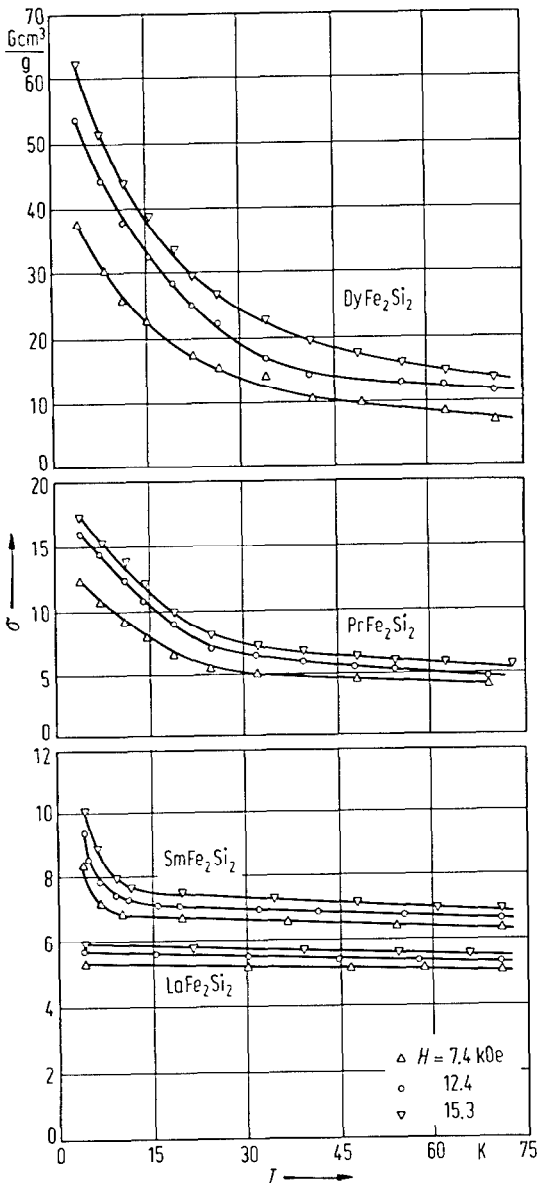

Fig. 193. RFe_2Si_2, R = La, Pr, Sm, Dy. Temperature dependence of σ at 7.4, 12.4 and 15.3 kOe [75 F 1].

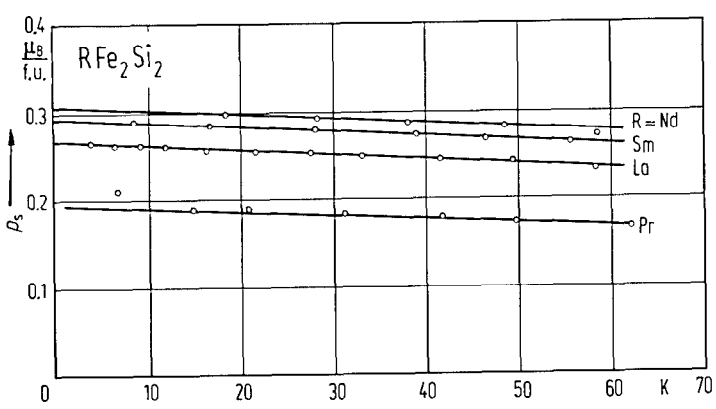

Fig. 194. RFe_2Si_2, R = La, Pr, Nd, Sm. Temperature dependence of the spontaneous magnetic moment [75 F 1].

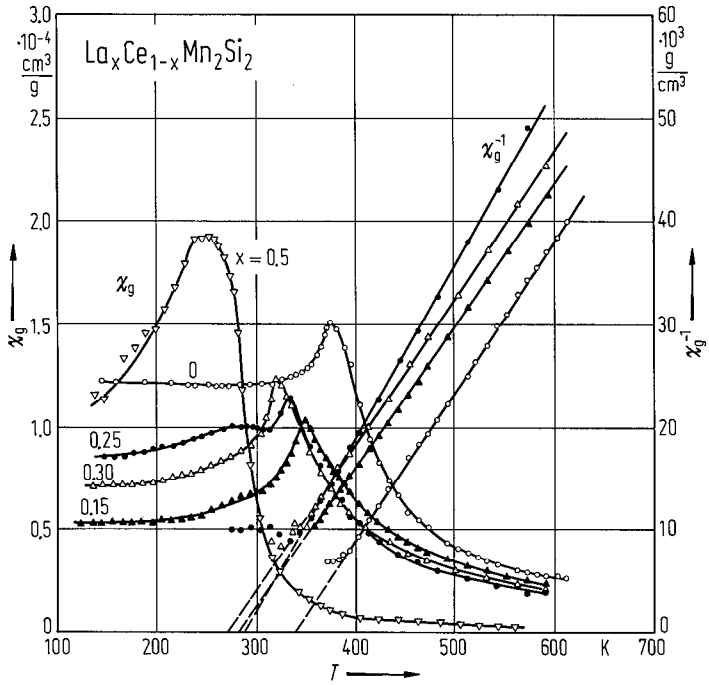

Fig. 195. $La_xCe_{1-x}Mn_2Si_2$. Temperature dependence of χ_g^{-1} and χ_g [82 S 4].

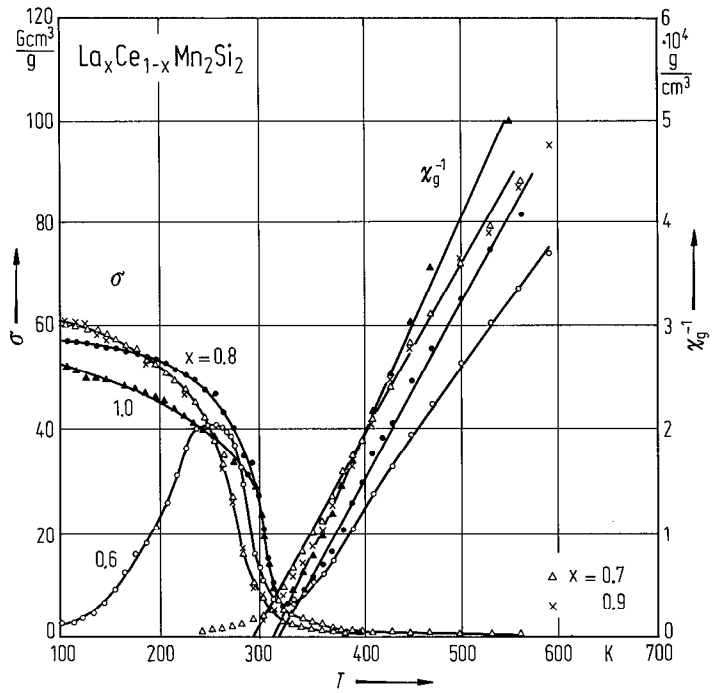

Fig. 196. $La_xCe_{1-x}Mn_2Si_2$. Temperature dependence of χ_g^{-1} and σ [82 S 4].

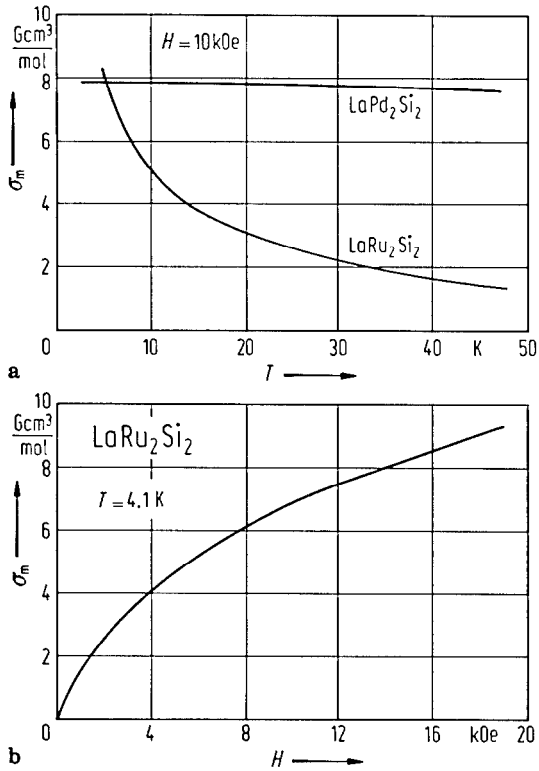

Fig. 197. $LaRu_2Si_2$, $LaPd_2Si_2$. (a) Temperature dependence of σ_m at 10 kOe. (b) Magnetic field dependence of σ_m at 4.1 K for $LaRu_2Si_2$ [84 F 1].

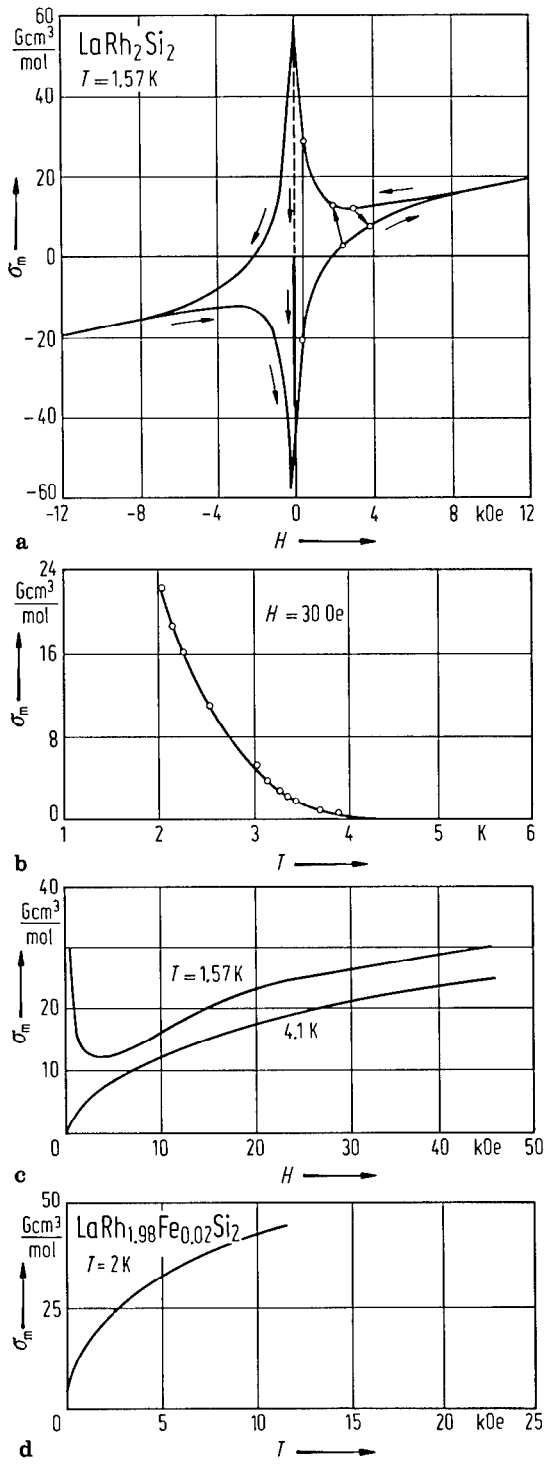

Fig. 198. $LaRh_2Si_2$. (a) Hysteresis curve at 1.57 K. The dashed line is for a sample cooled in a magnetic field of 30 Oe. Jumps between branches due to field reversal within several Oe are indicated by arrows. (b) Temperature dependence of σ_m at 30 Oe. (c) Magnetic field dependence of σ_m at 1.57 and 4.1 K. (d) Magnetic field dependence of σ_m at 2.0 K for $LaRh_{1.98}Fe_{0.02}Si_2$ [83 F 1].

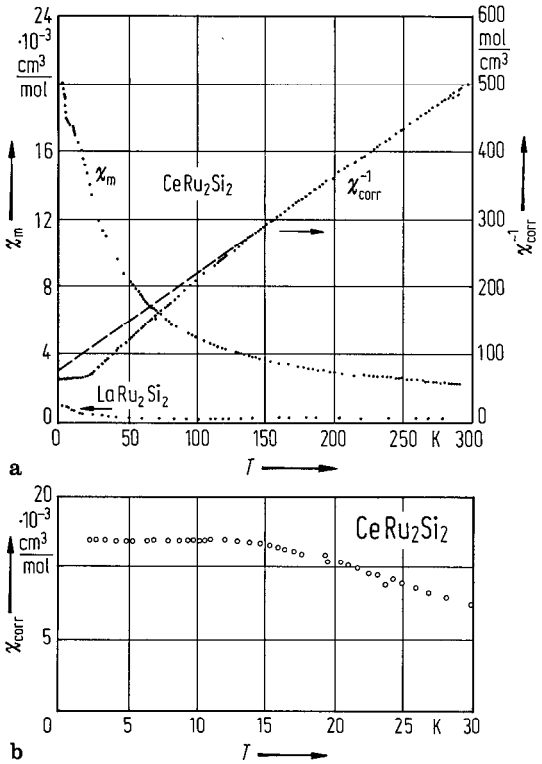

Fig. 199. $LaRu_2Si_2$, $CeRu_2Si_2$. (a) Temperature dependence of χ_m and reciprocal magnetic molar susceptibility χ^{-1}_{corr} for $CeRu_2Si_2$ after correcting for impurity contribution and subtracting the magnetic susceptibility of $LaRu_2Si_2$. Dashed line is the Curie-Weiss fit to the corrected high-temperature data. (b) Temperature dependence of χ_{corr} for $CeRu_2Si_2$ [83 G 2].

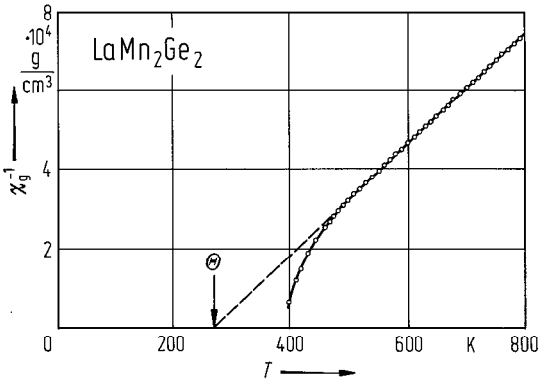

Fig. 200. $LaMn_2Ge_2$. Temperature dependence of χ_g^{-1} [85 S 4].

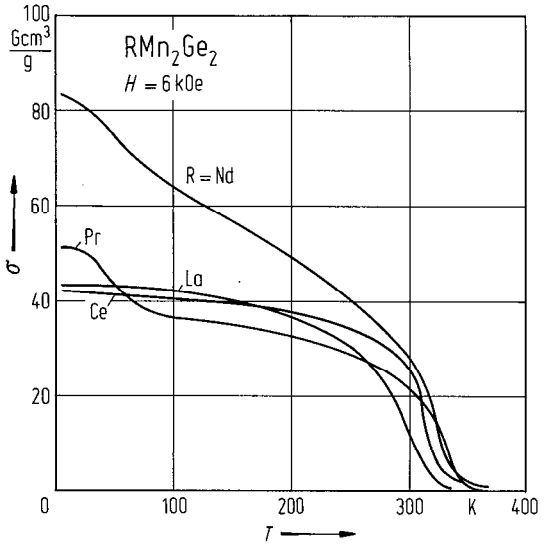

Fig. 201. RMn_2Ge_2, R = La, Ce, Pr, Nd. Temperature dependence of σ at 6 kOe [75 N 1].

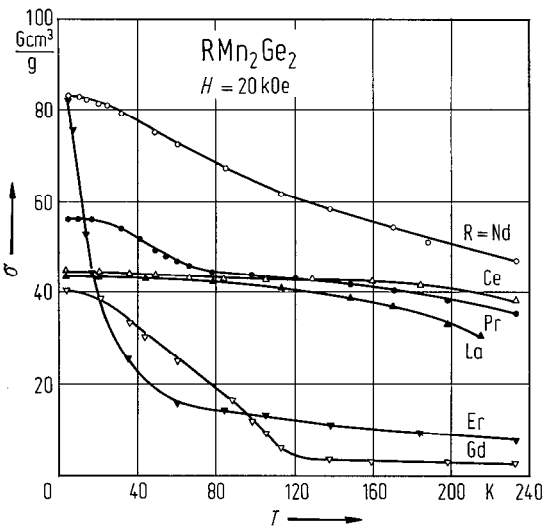

Fig. 202. RMn_2Ge_2, R = La, Ce, Pr, Nd, Gd, Er. Temperature dependence of σ at 20 kOe [75 N 1].

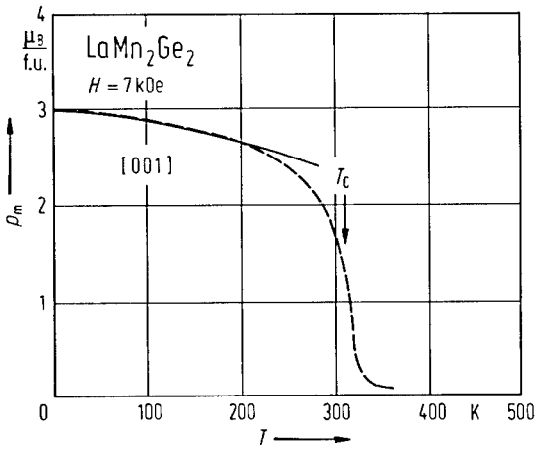

Fig. 203. $LaMn_2Ge_2$. Temperature dependence of p_m along the [001] axis at 7 kOe. Broken line represents the experimental values and solid line obeys the $T^{3/2}$ law: $p_m(T) = p_m(0\,K)\,(1-0.22(T/T_C)^{3/2})$ [85 S 4].

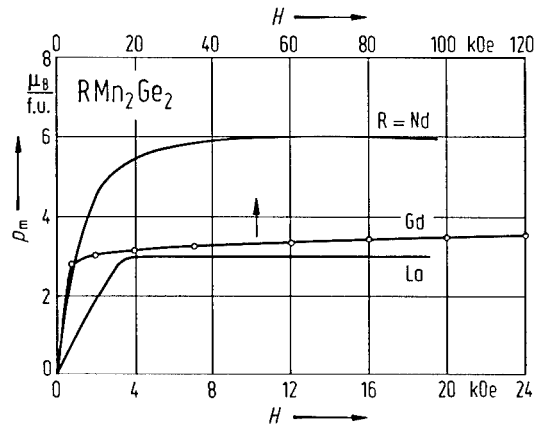

Fig. 204. RMn_2Ge_2, R = La, Nd, Gd. Magnetic field dependence of p_m at 4.2 K [75 N 1].

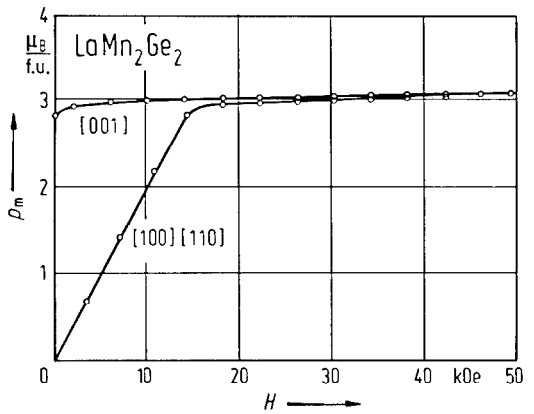

Fig. 205. $LaMn_2Ge_2$. Magnetic field dependence of p_m for a single crystal at 4.2 K along [001], [100] and [110] axes [85 S 4].

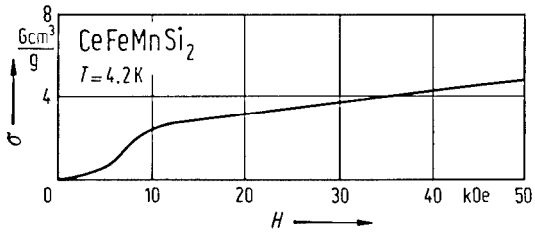

Fig. 206. $CeFeMnSi_2$. Magnetic field dependence of σ at 4.2 K [79 S 4].

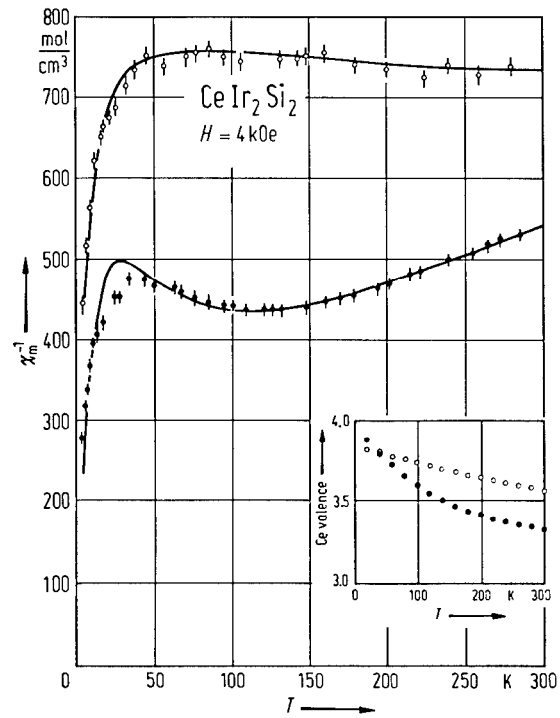

Fig. 207. $CeIr_2Si_2$. Temperature dependence of χ_m^{-1} for the two modifications melted (open circles) and annealed (solid circles) at 4 kOe; solid line is the theoretical fit taking into account the fractional valence of Ce according to [75 S 1]. For explanation, see caption to Fig. 214 [86 B 3].

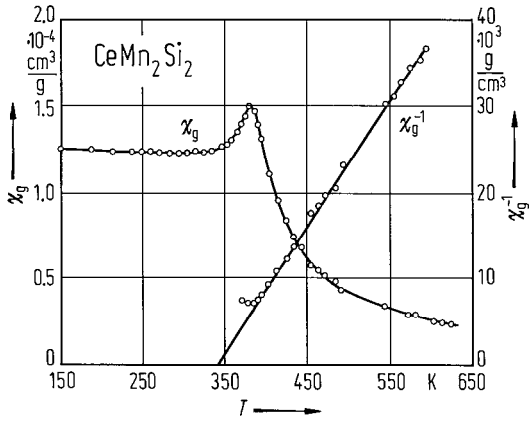

Fig. 208. $CeMn_2Si_2$. Temperature dependence of χ_g and χ_g^{-1} [78 S 1].

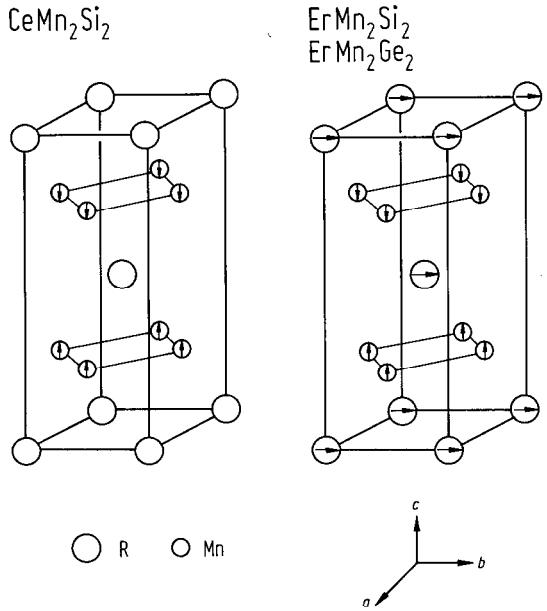

Fig. 209. $CeMn_2Si_2$, $ErMn_2Si_2$, $ErMn_2Ge_2$. Magnetic structure: R = Ce [78 S 1], R = Er [84 L 4].

For Fig. 210, see next page.

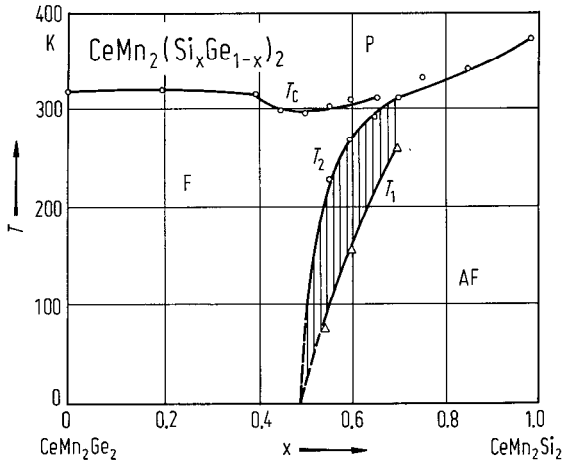

Fig. 211. $CeMn_2(Si_xGe_{1-x})_2$. Magnetic phase diagram. The samples undergo a transition from the antiferromagnetic (AF) to ferromagnetic state (F) through a transitional state as the temperature rises. The transition temperatures T_1, T_2 and T_C correspond to the transition from AF to the transitional state, from the transitional state to F, and from F to the paramagnetic state, respectively [79 S 4].

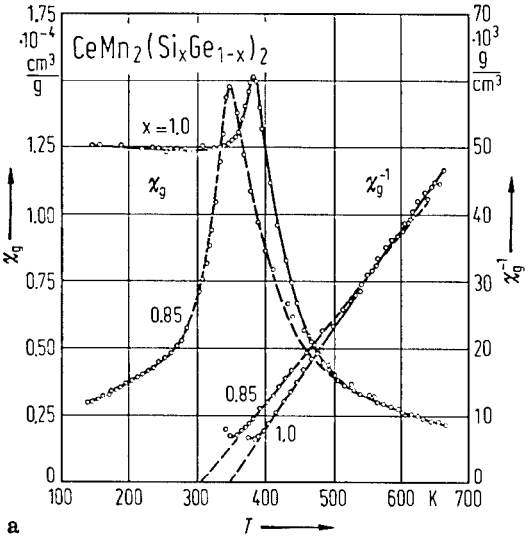

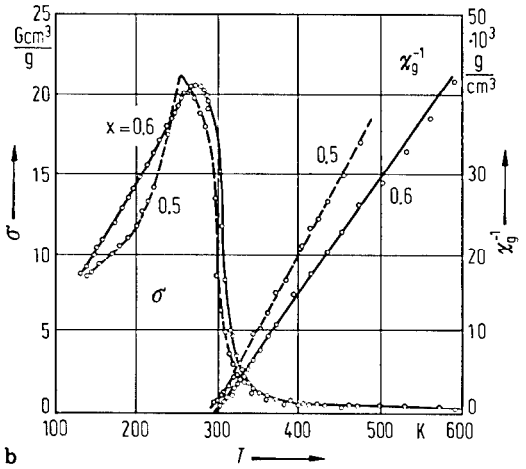

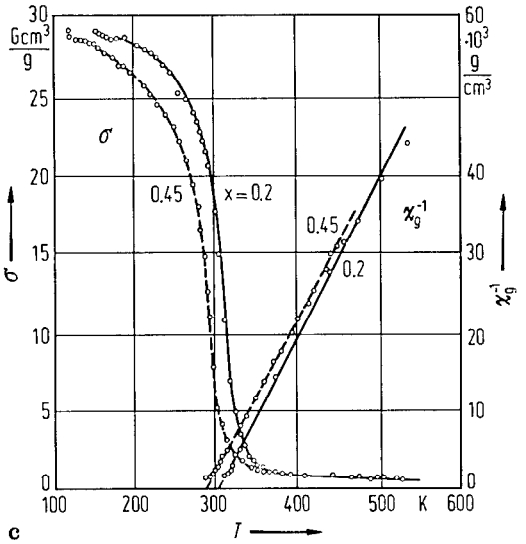

Fig. 210. $CeMn_2(Si_xGe_{1-x})_2$. (a) Temperature dependence of χ_g and χ_g^{-1} for $x = 1$ and 0.85, and temperature dependence of σ and χ_g^{-1} for (b) $x = 0.5$ and 0.6, and (c) $x = 0.45$ and 0.2 [79 S 4].

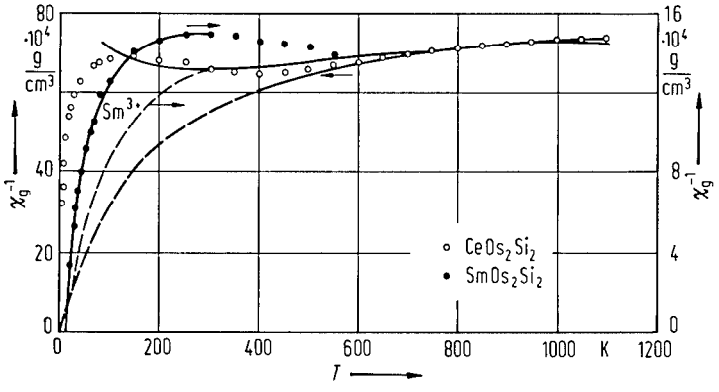

Fig. 212. $CeOs_2Si_2$, $SmOs_2Si_2$. Temperature dependence of χ_g^{-1}, calculated least-squares fits (solid lines) and theoretical (Van Vleck) curve for Sm^{3+} (dashed line). The broken line is the low-temperature extrapolation of a fit to the high-temperature data of $CeOs_2Si_2$ [83 H 2].

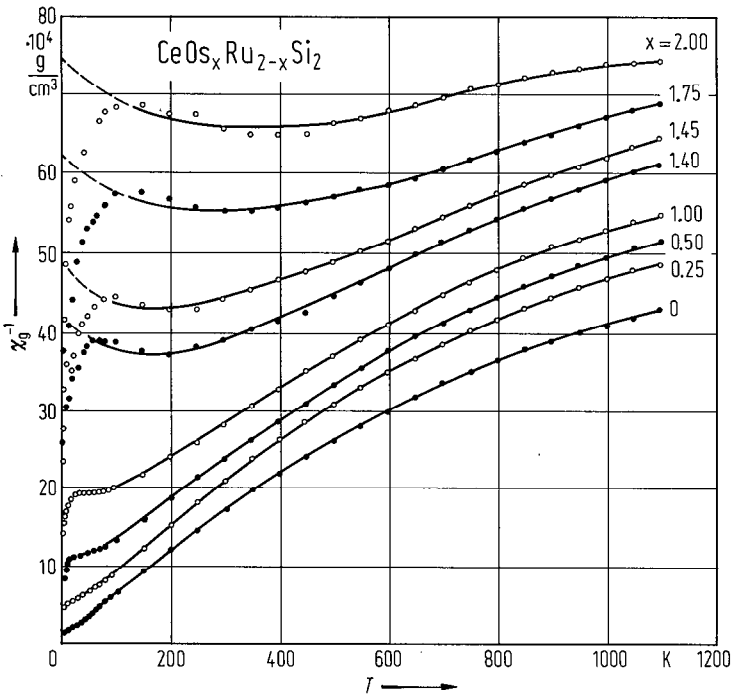

Fig. 213. $CeOs_xRu_{2-x}Si_2$. Temperature dependence of χ_g^{-1} and calculated least-squares fits (solid lines) for various compositions [84 H 2].

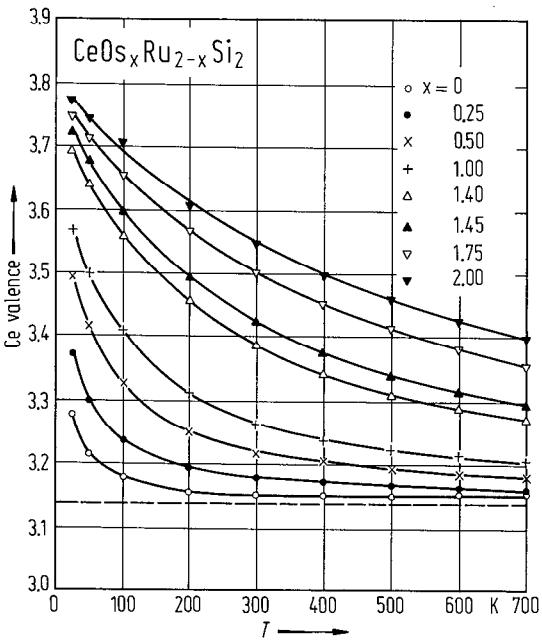

Fig. 214. $CeOs_xRu_{2-x}Si_2$. Temperature dependence of the fractional valence of Ce obtained by equation $\chi_m = N_A(p_{n-1}^2 v(T) + p_n^2 [1 - v(T)])/3k_B(T - T_{sf}) + nC_m/T + \chi_0$, where $v(T) = (2J_{n-1}+1)/[(2J_{n-1}+1)+(2J_n+1) \exp[-E_{ex}/k_B(T-T_{sf})]]$ according to [75 S 1]. p_n and $2J_n+1$ denote, respectively, the effective magnetic moment and degeneracy of the state containing n 4f electrons. $E_{ex} = E(Ce^{3+}) - E(Ce^{4+})$ is the energy gap between the Ce^{3+} and Ce^{4+} states, $v(T)$ is the probability of occupation of the $J_{n-1} = 0(Ce^{4+})$ state, T_{sf} is the spin-fluctuation temperature, $C_m = 0.807\,cm^3\,K\,mol^{-1}$ is the molar Curie constant for free $(J = 5/2)$ Ce^{3+} ions ($p_{eff} = 2.54\,\mu_B$/Ce, n is the fraction of stable Ce^{3+} ions and χ_0 is the temperature-independent magnetic susceptibility) [84 H 1].

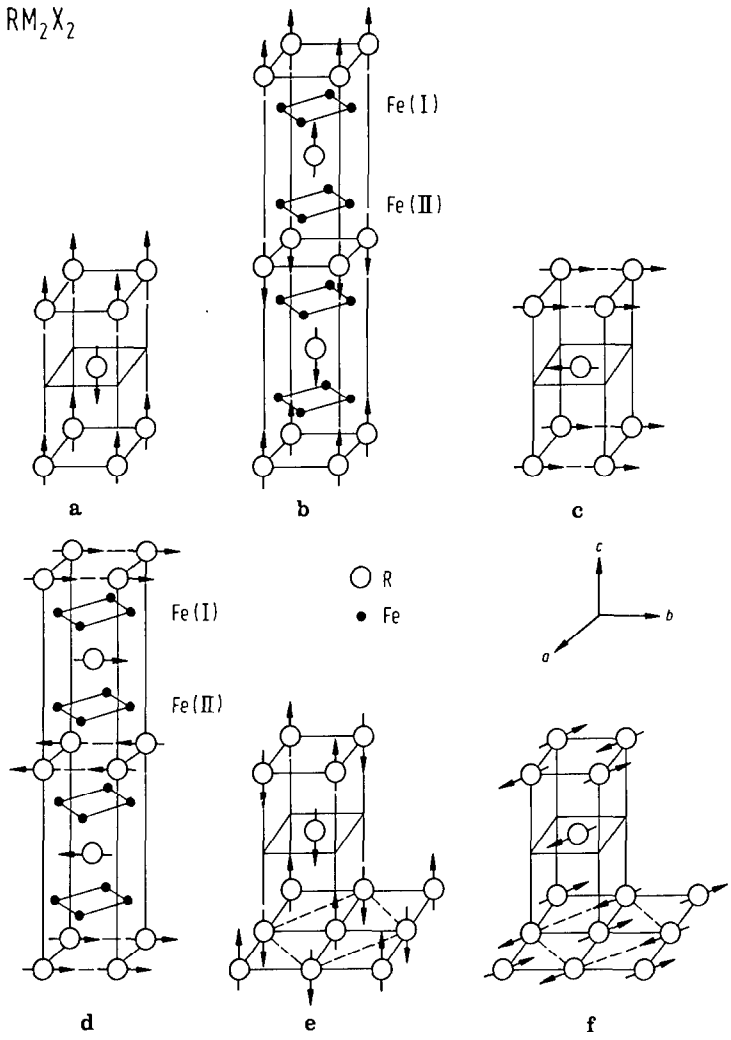

Fig. 215. RM_2X_2, M = transition metal, X = Si, Ge. Commensurate magnetic structure of the R sublattice for compounds with M and X nonmagnetic. The following types of magnetic structure were observed: (a) and (c): collinear antiferromagnetic structure. The structure consists of a stacking of ferromagnetic (001) planes with $+ - + -$ sequence along the c axis. The R magnetic moments are parallel (a) or perpendicular (c) to the c axis. The wavevector $\boldsymbol{k} = (0, 0, 1)$. This type of magnetic ordering was found in (a) $PrCo_2Si_2$ [83 L 1], $NdCo_2Si_2$ [83 L 4, 83 L 1], $NdRh_2Si_2$ [84 Q 1, 85 C 1], $NdCo_2Ge_2$ [83 L 4, 83 L 1], $TbCo_2Si_2$ [83 L 1, 85 P 2, 86 P 2], $TbIr_2Si_2$ [83 S 6, 84 H 2], $TbRh_2Si_2$ [83 S 6, 84 Q 1, 85 C 1], $DyCo_2Si_2$ [83 L 3], $DyRh_2Si_2$ [84 M 2], $DyCo_2Ge_2$ [85 P 2, 86 P 2], $HoCo_2Si_2$ [83 L 1, 83 S 2, 83 N 1, 85 P 2], $HoCo_2Ge_2$ [80 S 6], and (c) $ErCo_2Si_2$ [83 L 1, 85 P 2], $ErRh_2Si_2$ [85 L 1], $ErCo_2Ge_2$ [83 L 4], $TmCo_2Si_2$ [83 L 3]. (b) and (d): (M = Fe) collinear antiferromagnetic structure. The structure consists of a stacking of ferromagnetic (001) planes with $+ - - +$ sequence along the c axis. The R magnetic moments are parallel (b) or perpendicular (d) to the c axis. R produces a hyperfine magnetic field at the Fe(I) sites and no field at the Fe(II) sites. The magnetic unit cell consists of the chemical one doubled along c axis. The wavevector $\boldsymbol{k} = (0, 0, \frac{1}{2})$ [83 U 1]. This type of magnetic ordering was found in (b) $PrFe_2Ge_2$ [83 S 7], $NdFe_2Si_2$ [83 U 1], $NdFe_2Ge_2$ [83 L 4], and (d) $GdFe_2Si_2$ [83 U 1], $ErFe_2Si_2$ [83 U 1, 83 L 2]. (e) and (f): (X = Si) simple antiferromagnetic ordering within (001) planes with a $+ - + -$ stacking sequence along a [110] direction. The R magnetic moments are parallel (e) or perpendicular (f) to the c axis. The wavevector $\boldsymbol{k} = (\frac{1}{2}, \frac{1}{2}, 0)$ [83 N 1, 84 Q 1]. This type of magnetic ordering was found in (e) $CeRh_2Si_2$ [84 Q 1, 85 C 1], $TbNi_2Si_2$ [83 N 1]; and (f) $CePd_2Si_2$ [84 G 2].

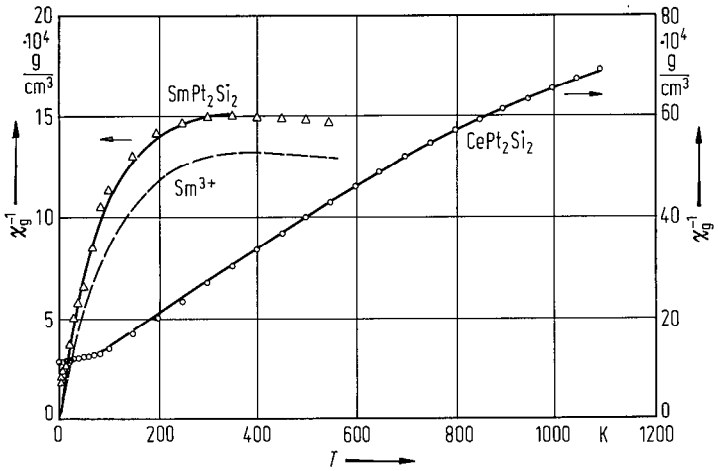

Fig. 217. $CePt_2Si_2$, $SmPt_2Si_2$. Temperature dependence of χ_g^{-1} and calculated least-squares fit (solid line). Dashed line is theoretical for free Sm^{3+} ion model (Van Vleck) [85 H 2].

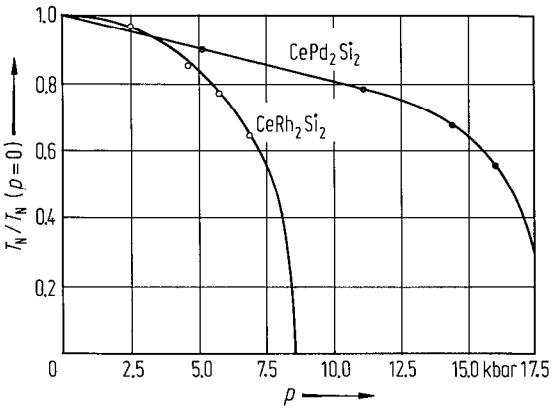

Fig. 216. $CePd_2Si_2$, $CeRh_2Si_2$. Pressure dependence of T_N normalized to its value at $p=0$, obtained from electrical resistance measurements under hydrostatic pressure. In this series $T_N(p=0)=10$ and 32 K for Pd and Rh compounds, respectively. An electrical resistance signal for T_N was not detected in Rh compound above 7 kbar [86 T 1].

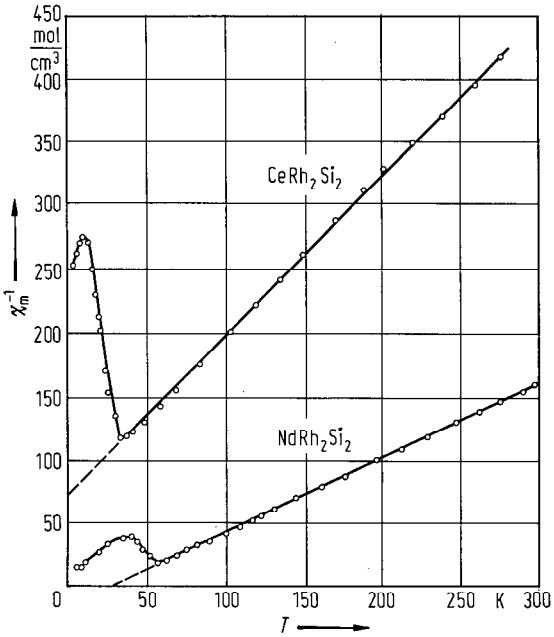

Fig. 218. $CeRh_2Si_2$, $NdRh_2Si_2$. Temperature dependence of χ_m^{-1} [83 C 3].

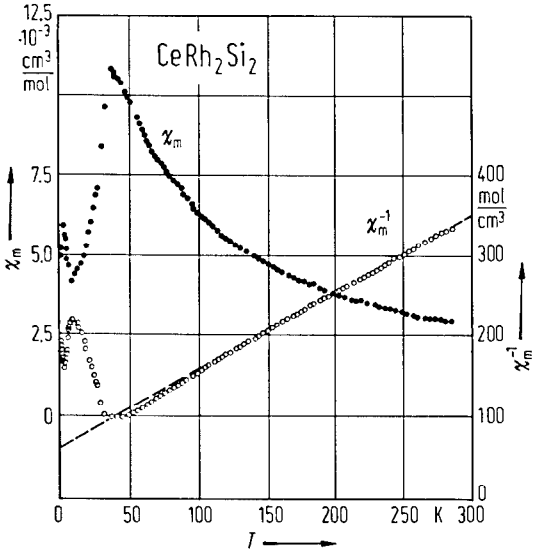

Fig. 219. $CeRh_2Si_2$. Temperature dependence of χ_m and χ_m^{-1} [83 G 1]. Very similar curves were obtained by [84 Q 1, 86 S 3].

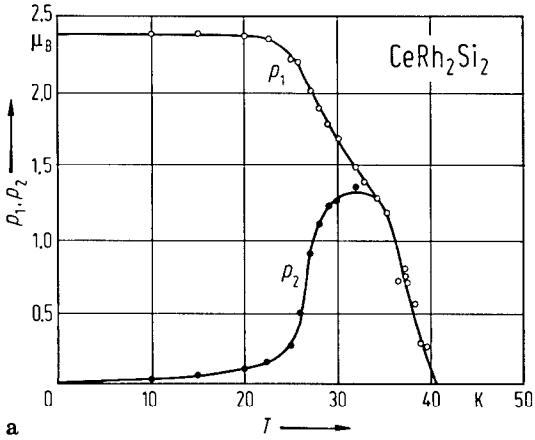

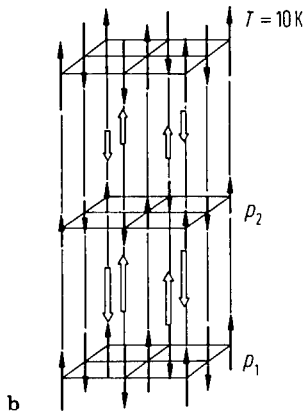

Fig. 220. $CeRh_2Si_2$. Neutron diffraction study. (a) Temperature dependence of two Ce magnetic moments determined from the peak intensities of the (1/2, 1/2, 0) and (1/2, 1/2, 1/2) neutron diffraction peaks assuming the possible modulated structure at 10 K shown in (b). The large arrows represent magnetic moments of 2.39 μ_B and the smaller ones of 0.16 μ_B. See also Fig. 215e [84 G 2].

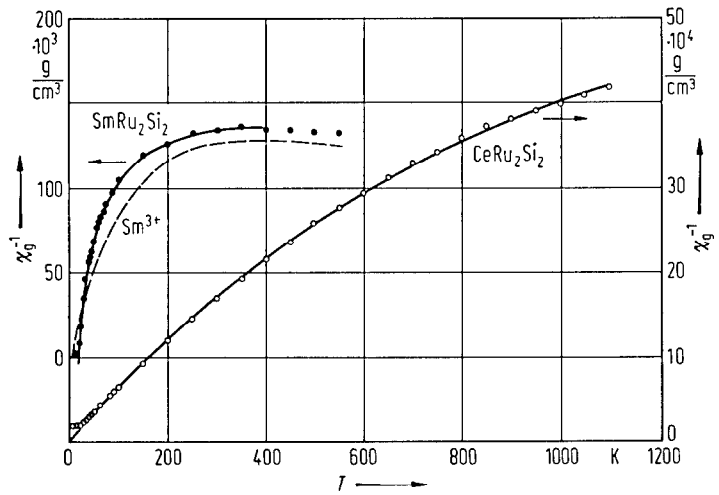

Fig. 221. $CeRu_2Si_2$, $SmRu_2Si_2$. Temperature dependence of χ_g^{-1} and calculated least-squares fit (solid line). Dashed line is theoretical for free Sm^{3+} (Van Vleck) [83 H 1].

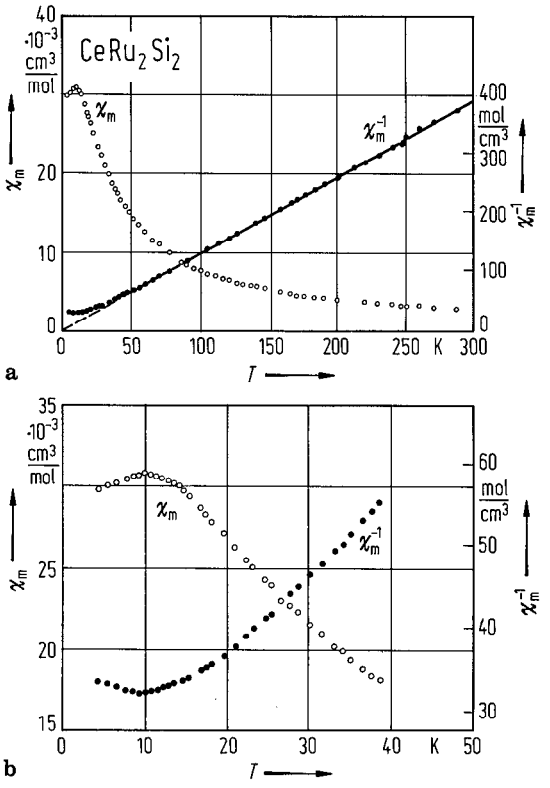

Fig. 222. $CeRu_2Si_2$. Temperature dependence of χ_m and χ_m^{-1} [85 K 3].

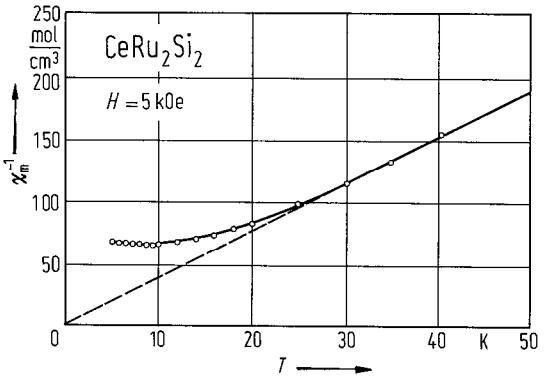

Fig. 223. $CeRu_2Si_2$. Temperature dependence of χ_m^{-1} at 5 kOe [85 T 1].

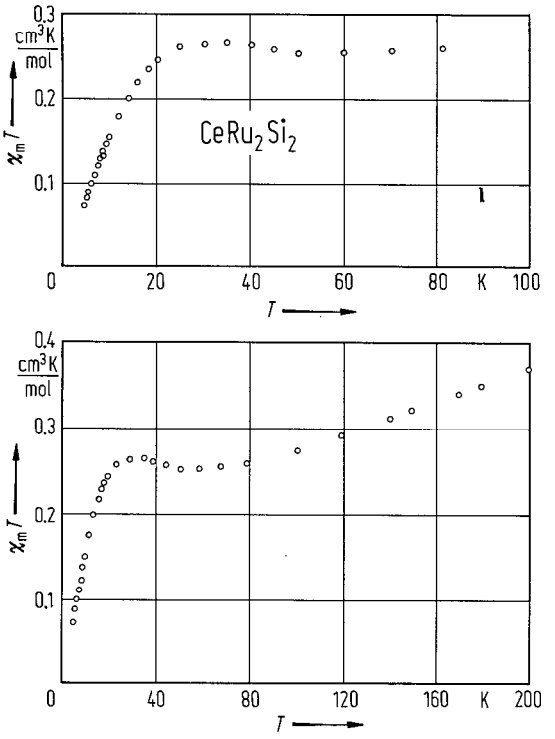

Fig. 224. $CeRu_2Si_2$. Temperature dependence of $\chi_m T$ [85 T 1].

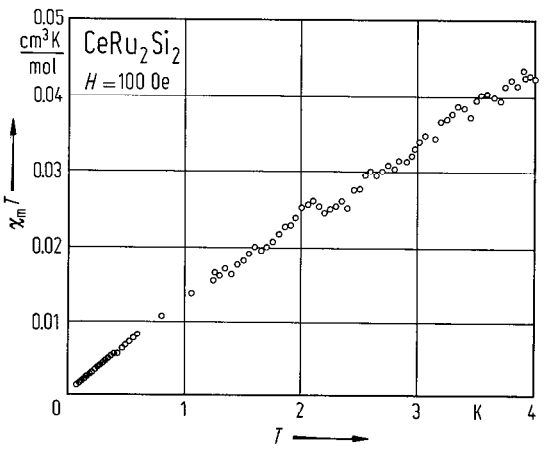

Fig. 225. $CeRu_2Si_2$. Low-temperature dependence of $\chi_m T$ at 100 Oe [85 T 1].

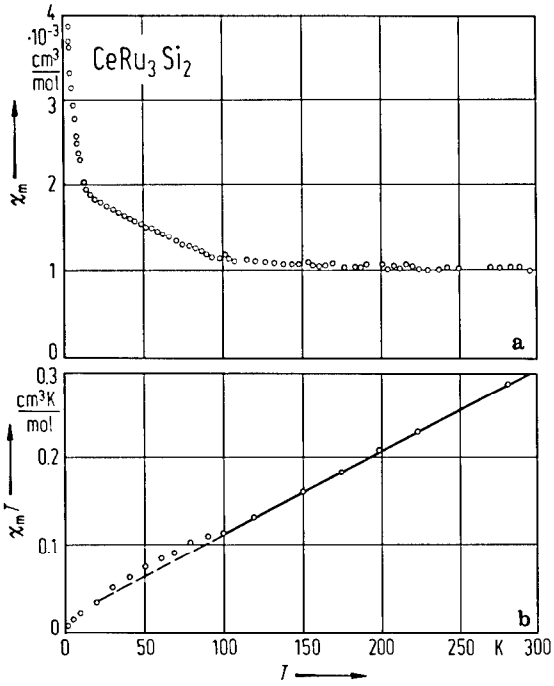

Fig. 226. $CeRu_3Si_2$. Temperature dependence of (a) χ_m and (b) $\chi_m T$ [84 R 1].

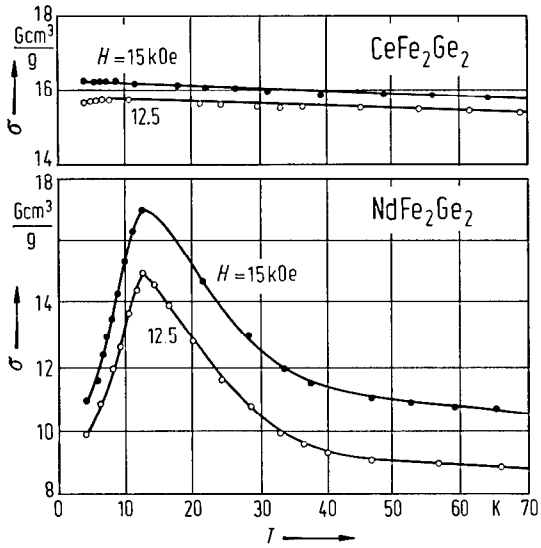

Fig. 227. $CeFe_2Ge_2$, $NdFe_2Ge_2$. Temperature dependence of σ at 12.5 and 15 kOe [75 F 1].

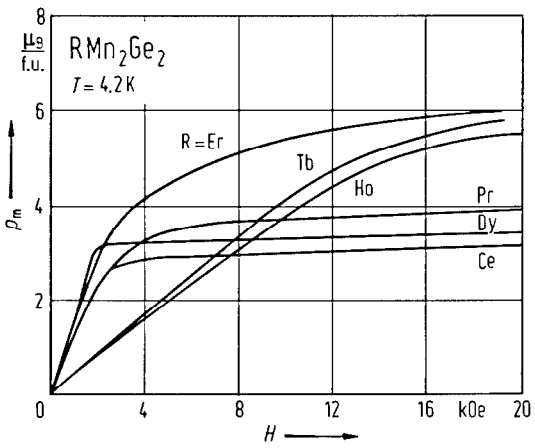

Fig. 228. RMn_2Ge_2, R = Ce, Pr, Tb, Dy, Ho, Er. Magnetic field dependence of p_m at 4.2 K [75 N 1].

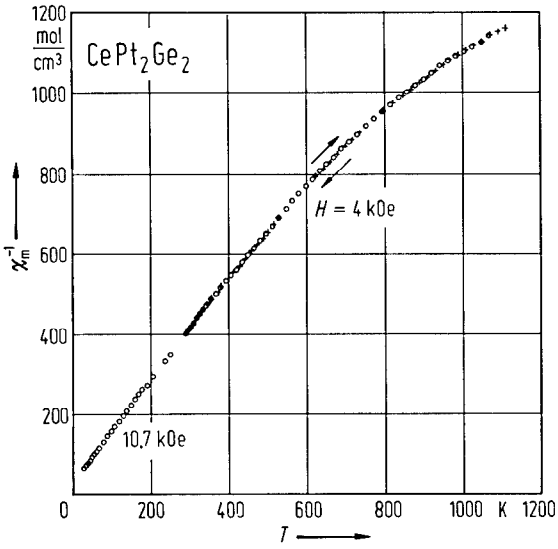

Fig. 229. $CePt_2Ge_2$. Temperature dependence of χ_m^{-1} at 4 and 10.7 kOe [85 D 1].

Fig. 231. RRu_2Ge_2, R = Ce, Pr, Sm. (a) Temperature dependence of σ_m and (b) magnetic field dependence of p_m at 4.1 K [85 F 3].

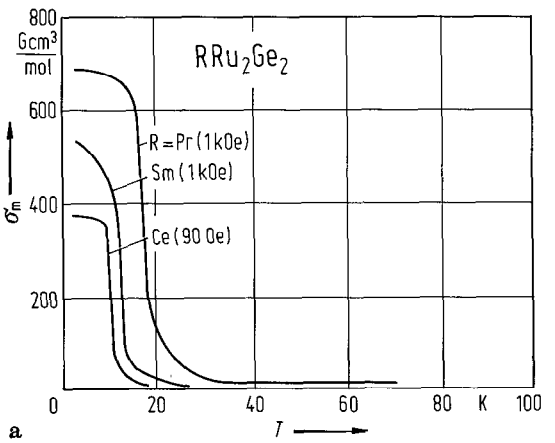

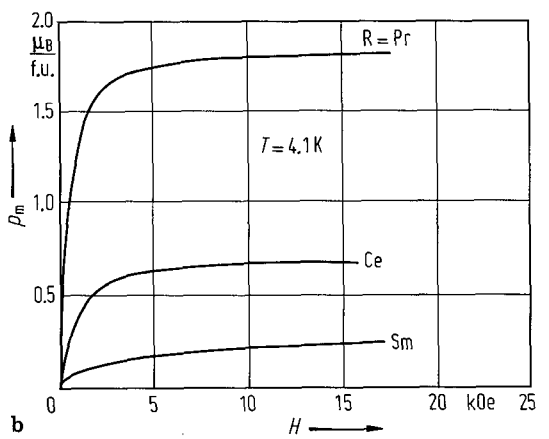

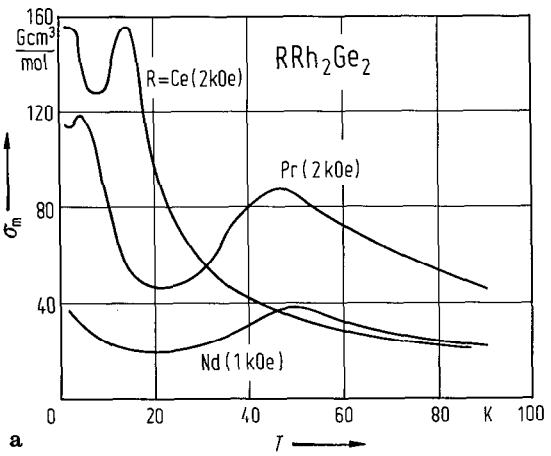

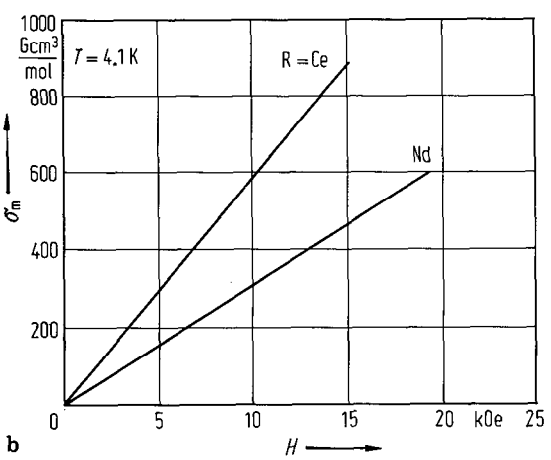

Fig. 230. RRh_2Ge, R = Ce, Pr, Nd. (a) Temperature dependence of σ_m and (b) magnetic field dependence of σ_m at 4.1 K [85 F 3].

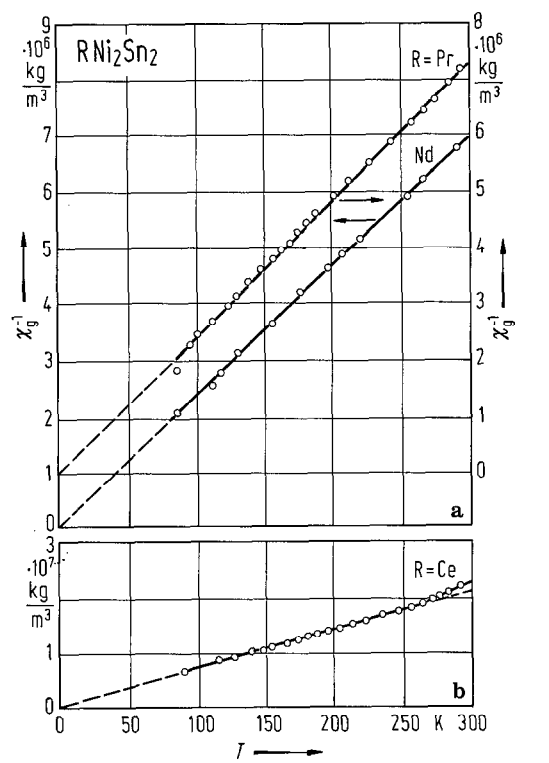

Fig. 232. RNi_2Sn_2, R = Ce, Nd, Pr. Temperature dependence of χ_g^{-1} for (a) R = Pr, Nd and (b) R = Ce [81 S 5].

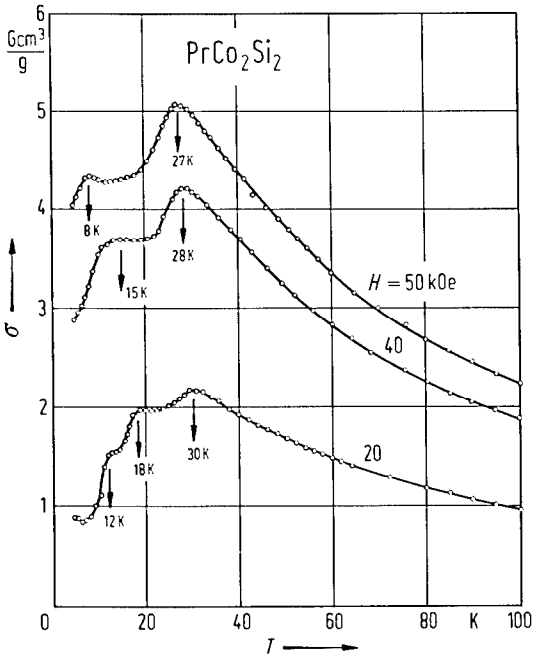

Fig. 233. $PrCo_2Si_2$. Temperature dependence of σ at 20, 40 and 50 kOe [82 K 2].

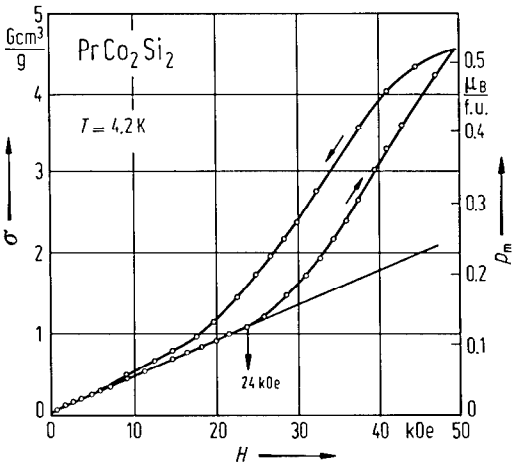

Fig. 234. $PrCo_2Si_2$. Magnetic field dependence of σ and p_m at 4.2 K [82 K 2].

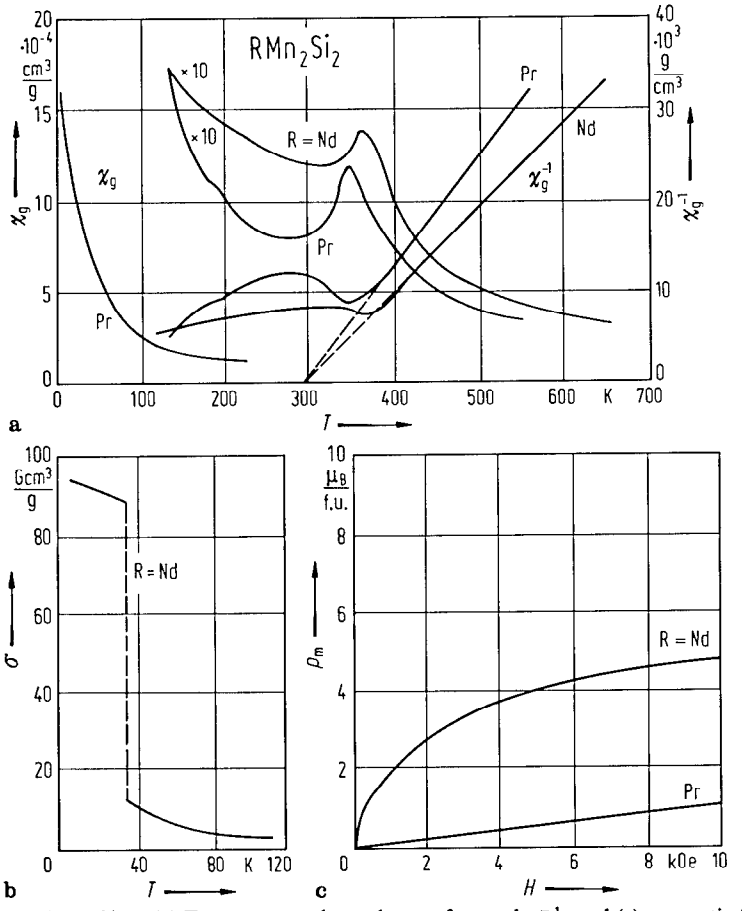

Fig. 235. $PrMn_2Si_2$, $NdMn_2Si_2$. (a) Temperature dependence of χ_g and χ_g^{-1}, and (c) magnetic field dependence of p_m. (b) shows temperature dependence of σ for R = Nd [81 S 4].

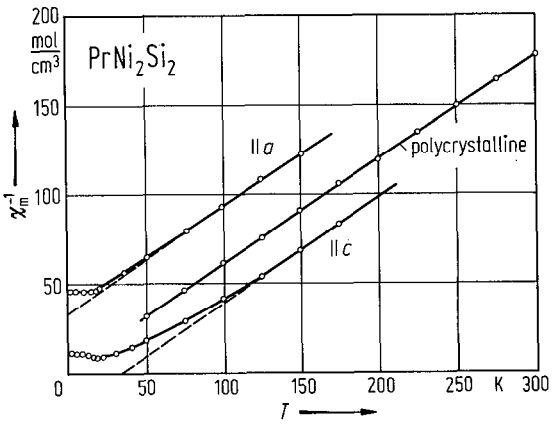

Fig. 236. $PrNi_2Si_2$. Temperature dependence of χ_m^{-1} for a polycrystalline sample, and along the a and c axes of a single crystal [86 B 1].

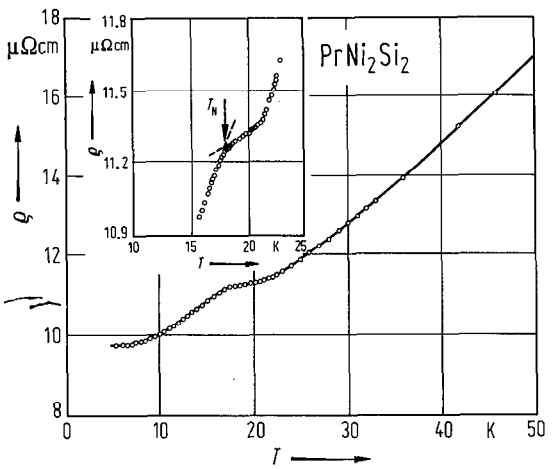

Fig. 238. $PrNi_2Si_2$. Temperature dependence of the electrical resistivity ϱ [86 B 1].

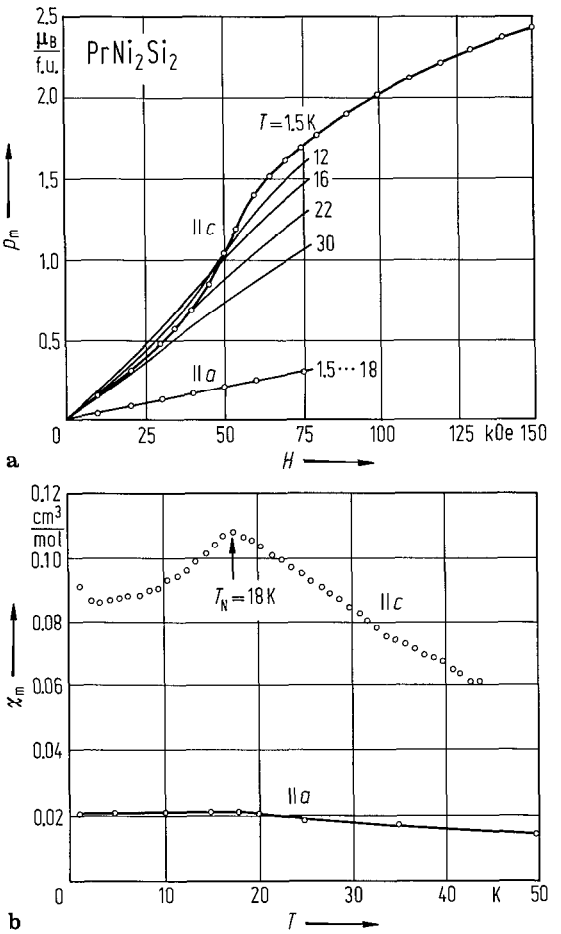

Fig. 237. $PrNi_2Si_2$. (a) Magnetic field dependence of p_m at different temperatures and (b) temperature dependence of χ_m along the a and c axes of a single crystal [86 B 1].

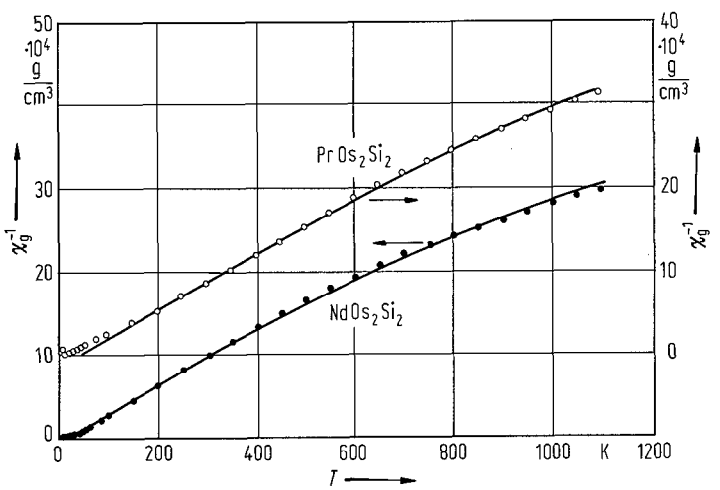

Fig. 239. $PrOs_2Si_2$, $NdOs_2Si_2$. Temperature dependence of χ_g^{-1} and calculated least-squares fit (solid line) [83 H 2].

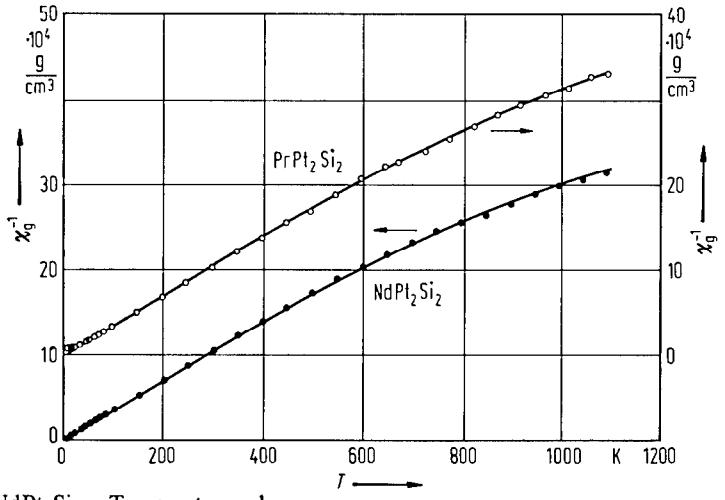

Fig. 240. $PrPt_2Si_2$, $NdPt_2Si_2$. Temperature dependence of χ_g^{-1} and calculated least-squares fit (solid line) [85 H 2].

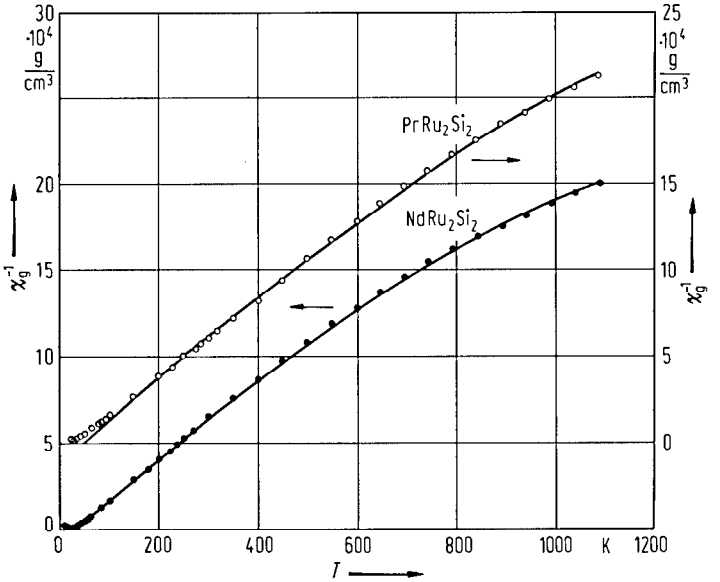

Fig. 241. $PrRu_2Si_2$, $NdRu_2Si_2$. Temperature dependence of χ_g^{-1} and calculated least-squares fit [83 H 1].

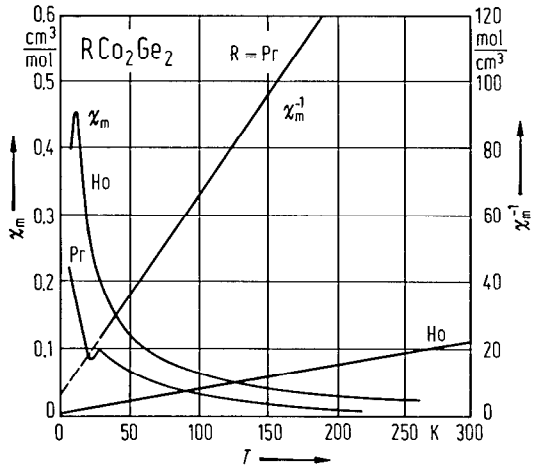

Fig. 242. $PrCo_2Ge_2$, $HoCo_2Ge_2$. Temperature dependence of χ_m and χ_m^{-1} [80 S 6].

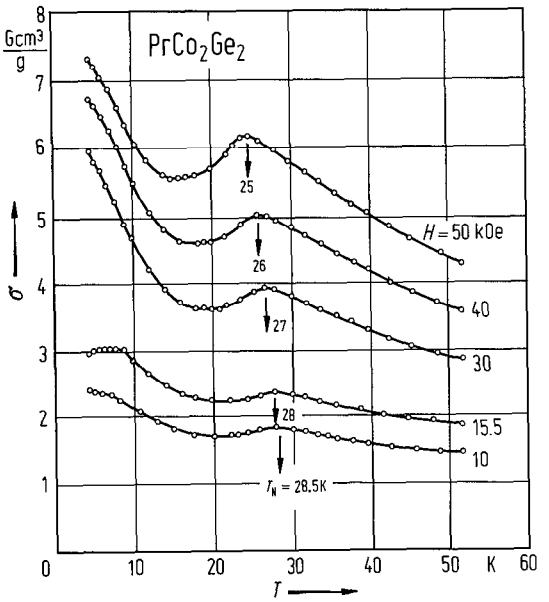

Fig. 243. $PrCo_2Ge_2$. Temperature dependence of σ at various magnetic fields [82 K 2].

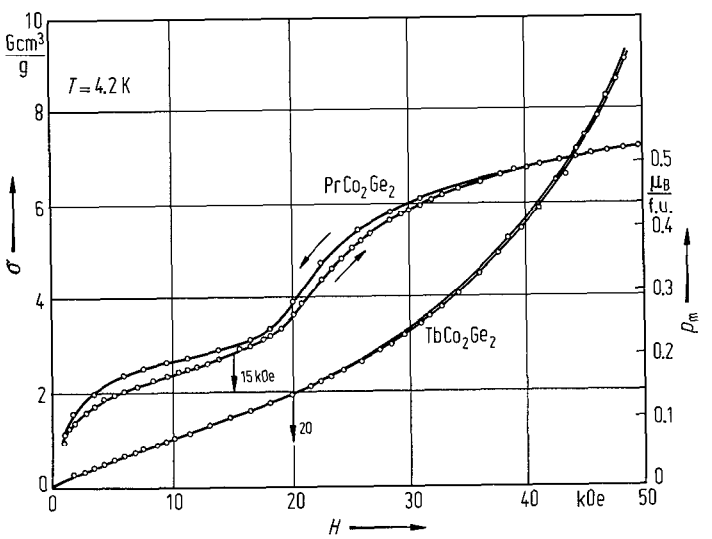

Fig. 244. $PrCo_2Ge_2$, $TbCo_2Ge_2$. Magnetic field dependence of σ and p_m at 4.2 K [82 K 2].

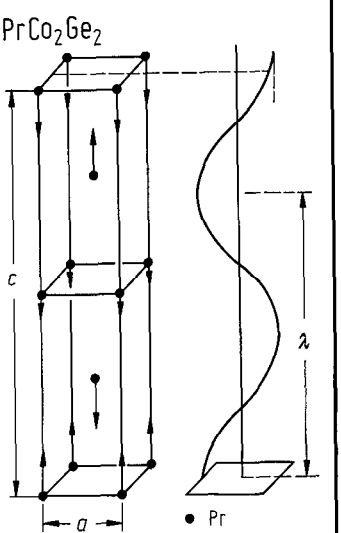

Fig. 245. $PrCo_2Ge_2$. Magnetic structure. Two crystallographic unit cells and the modulation period λ of the Pr magnetic moments are shown [79 P 1].

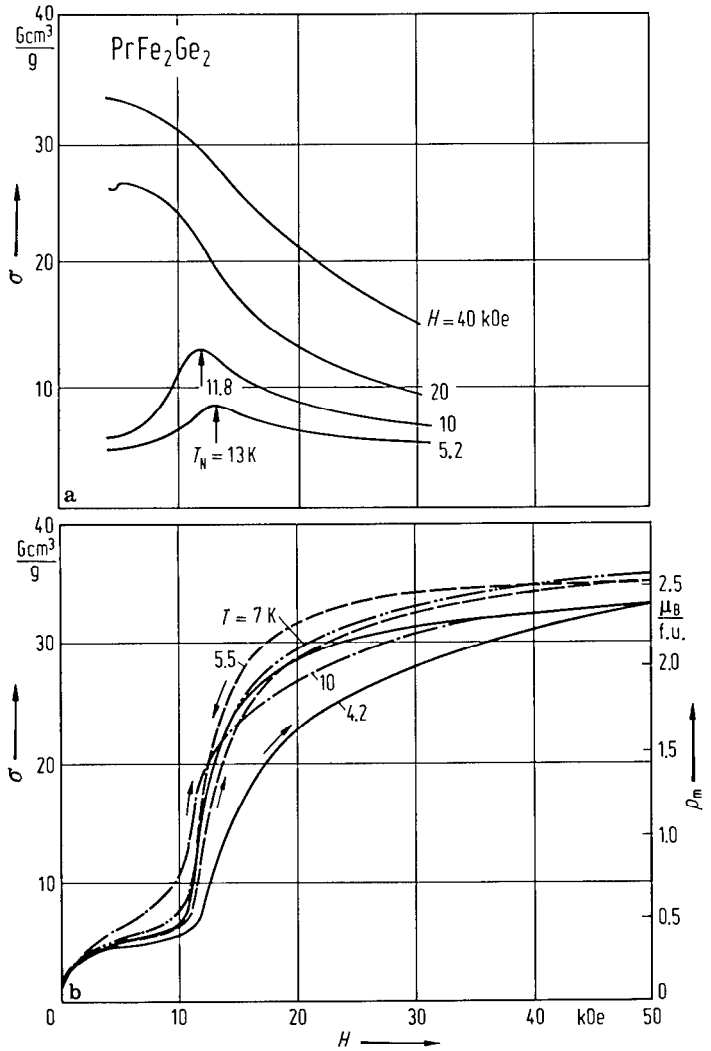

Fig. 246. $PrFe_2Ge_2$. (a) Temperature dependence of σ at different magnetic fields and (b) magnetic field dependence of σ and p_m at different temperatures [83 L 4].

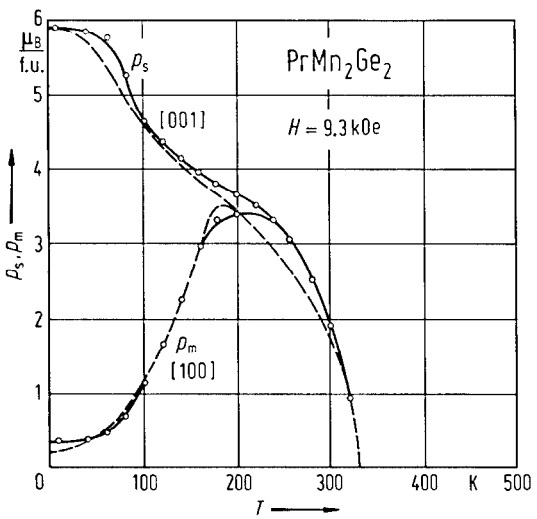

For Fig. 247, see next page.

Fig. 248. $PrMn_2Ge_2$. Temperature dependence of spontaneous magnetization p_s along the easy axis [001] and magnetization p_m at 9.3 kOe along the hard [100] axis. The broken line calculated with CEF parameters $B_2^0 = -0.7$ K, $B_4^0 = -0.02$ K and exchange parameters $J^{Pr} = \sum_j J_{ij}^{PrPr} = 33.6$ K, $J^{PrMn} = \sum_i J_{ik}^{PrMn} = -74.0$ K and $J^{Mn} = \sum_k J_{kl}^{MnMn} = 480$ K [86 I 1].

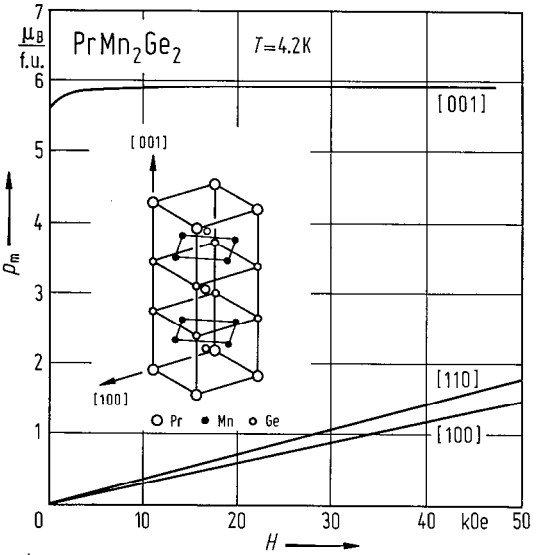

Fig. 247. $PrMn_2Ge_2$. Magnetic field dependence of p_m at 4.2 K along different crystal axes of a single crystal [86I1].

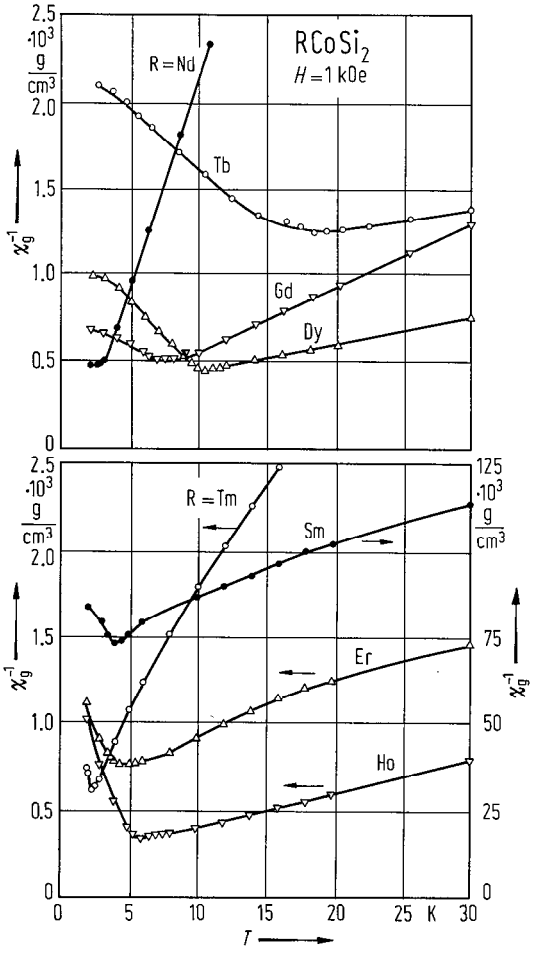

Fig. 249. $RCoSi_2$. Temperature dependence of χ_g^{-1} at 1 kOe (as measured) [82 P 1].

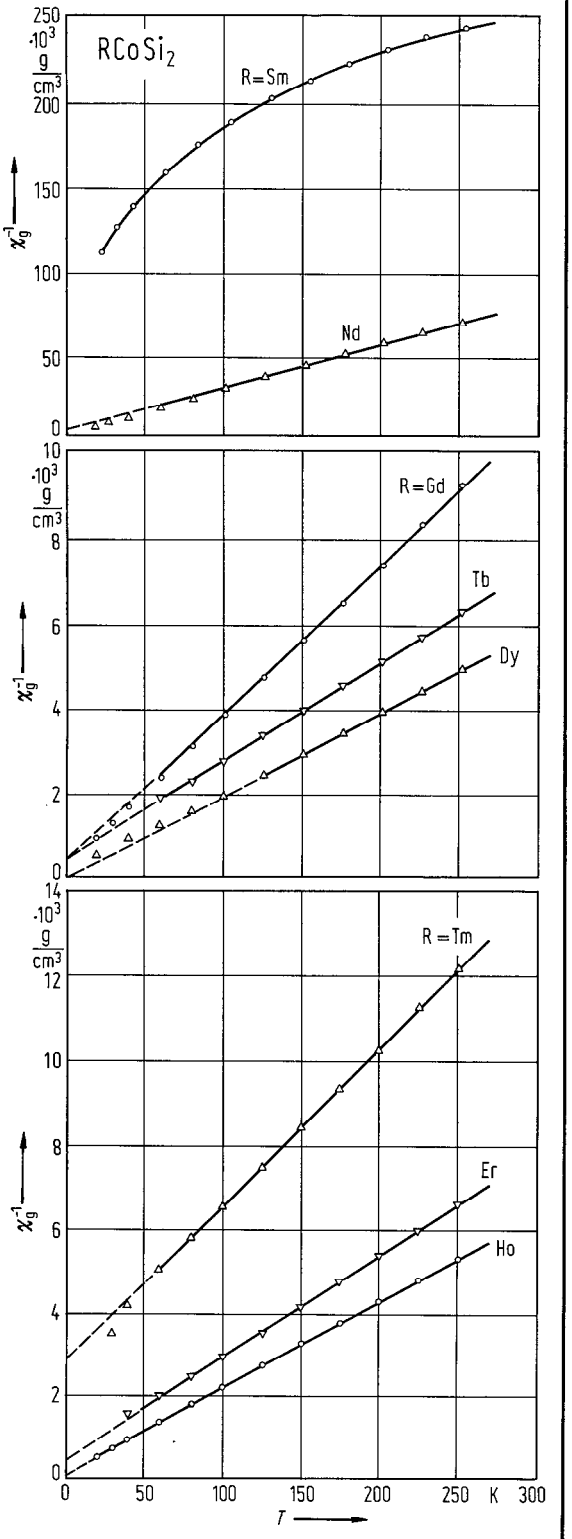

Fig. 250. $RCoSi_2$. Temperature dependence of χ_g^{-1} corrected for the magnetic field dependence of the magnetic susceptibility and for the small temperature-independent contribution of the Co–Si framework [82 P 1].

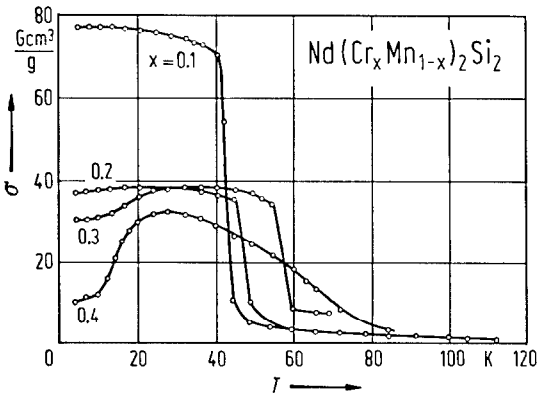

Fig. 251. $Nd(Cr_xMn_{1-x})_2Si_2$. Temperature dependence of σ in low applied magnetic fields for different compositions [79 O 1].

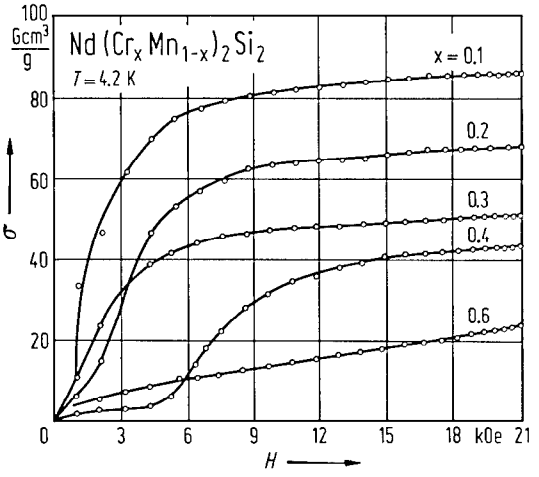

Fig. 253. $Nd(Cr_xMn_{1-x})_2Si_2$. Magnetic field dependence of σ at 4.2 K for different compositions [79 O 1].

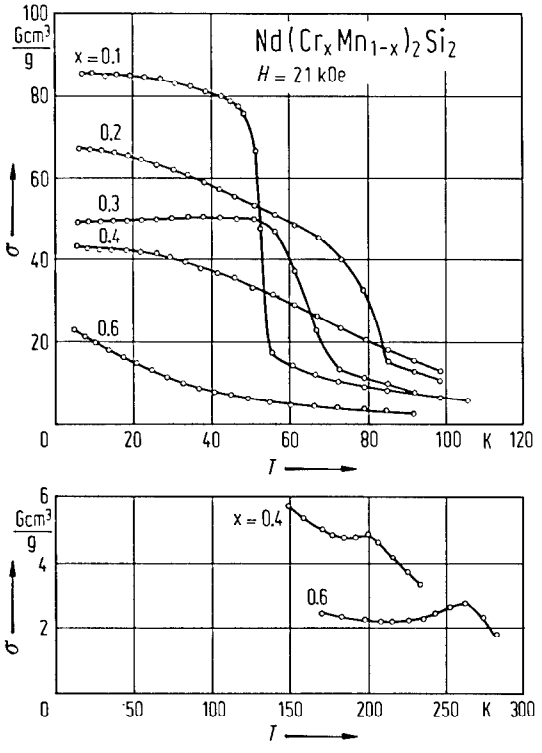

Fig. 252. $Nd(Cr_xMn_{1-x})_2Si_2$. Temperature dependence of σ at 21 kOe for different compositions [79 O 1].

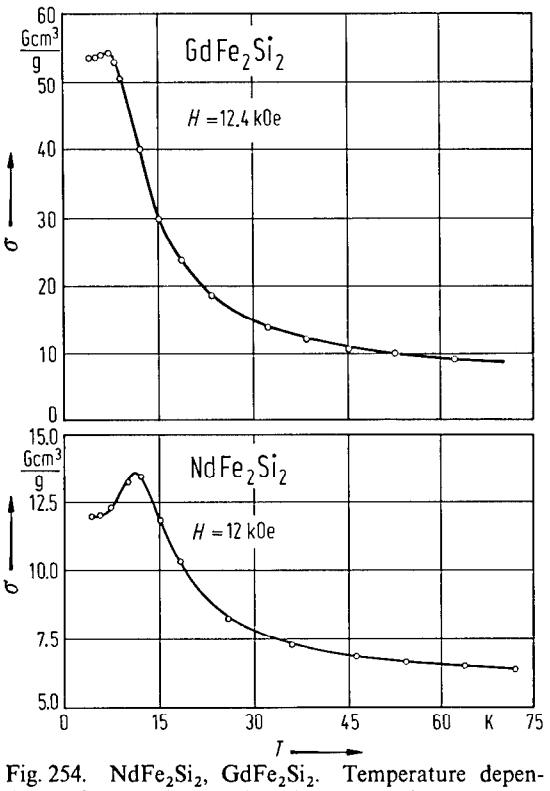

Fig. 254. $NdFe_2Si_2$, $GdFe_2Si_2$. Temperature dependence of σ at 12 kOe (Nd) and 12.4 kOe (Gd) [74 B 1].

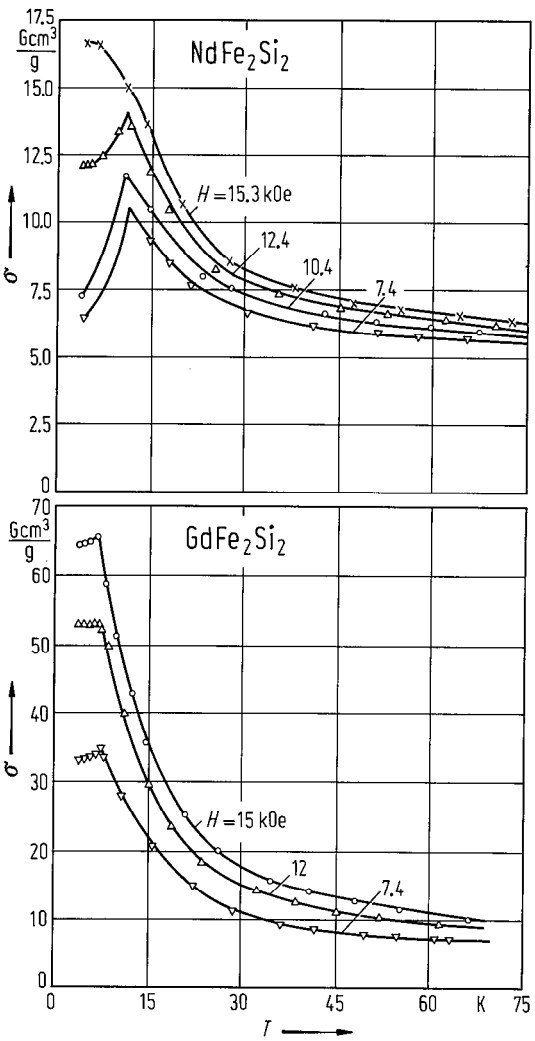

Fig. 255. $NdFe_2Si_2$, $GdFe_2Si_2$. Temperature dependence of σ at different magnetic fields [75 F 1].

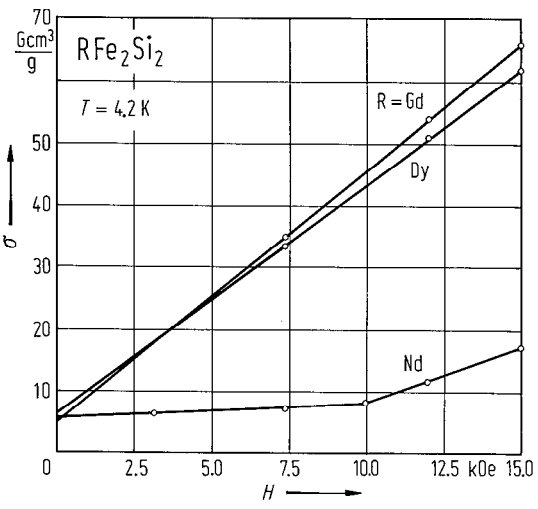

Fig. 256. RFe_2Si_2, R = Nd, Gd, Dy. Magnetic field dependence of σ at 4.2 K [75 F 1].

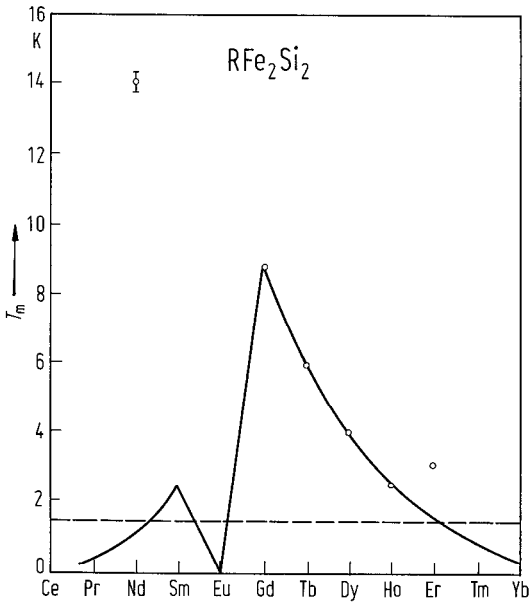

Fig. 257. RFe_2Si_2. Magnetic transition temperatures T_m measured by ac susceptibility. Solid line is the Gennes rule trend [83 N 3].

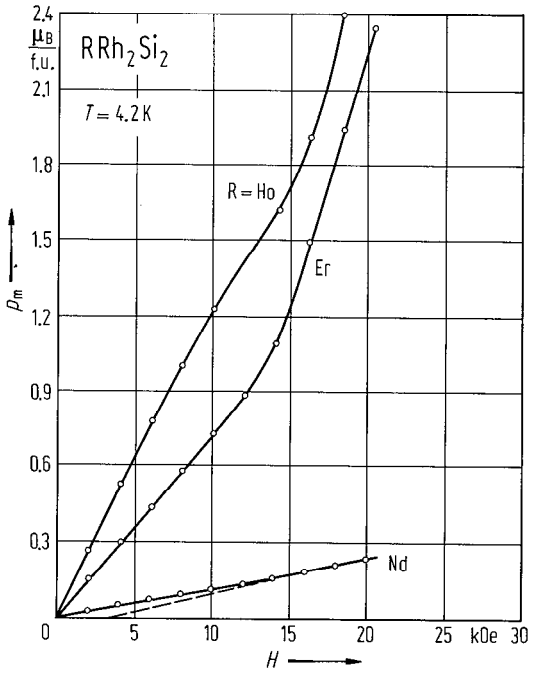

Fig. 258. RRh_2Si_2, R = Nd, Ho, Er. Magnetic field dependence of p_m at 4.2 K [83 C 3].

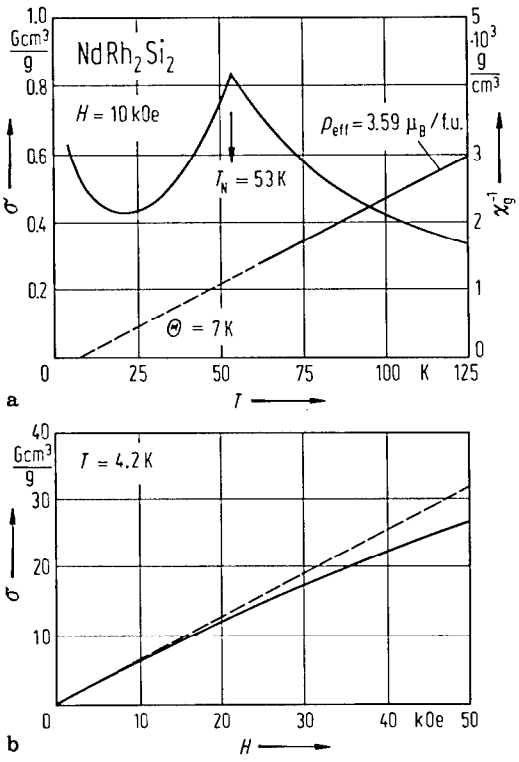

Fig. 259. $NdRh_2Si_2$. (a) Temperature dependence of χ_g^{-1} and σ at 10 kOe and (b) magnetic field dependence of σ at 4.2 K [84 S 6].

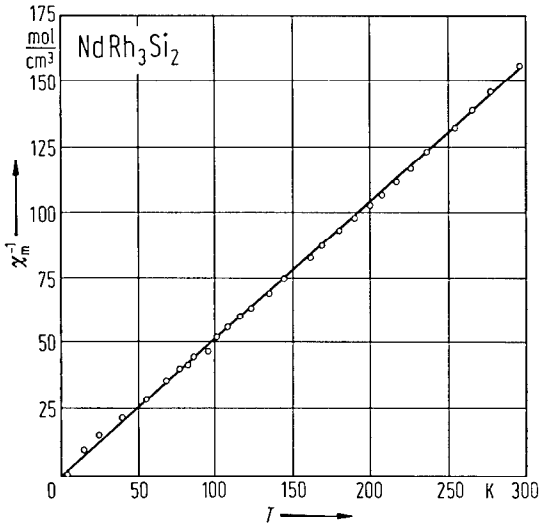

Fig. 260. $NdRh_3Si_2$. Temperature dependence of χ_m^{-1} [81 C 1].

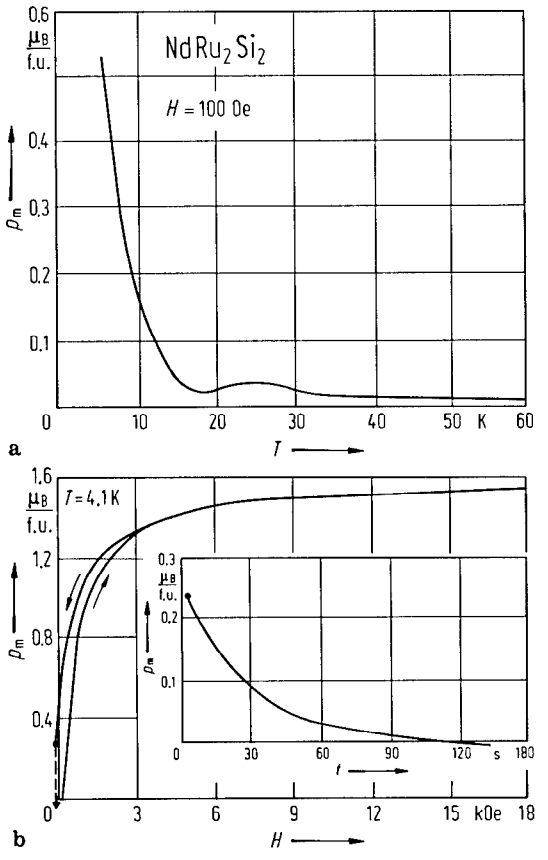

Fig. 261. $NdRu_2Si_2$. (a) Temperature dependence of p_m at 100 Oe. (b) Magnetic field dependence of p_m at 4.1 K and time dependence of p_m in −30 Oe at 4.1 K (solid circle in the magnetization curve) [84 F 1].

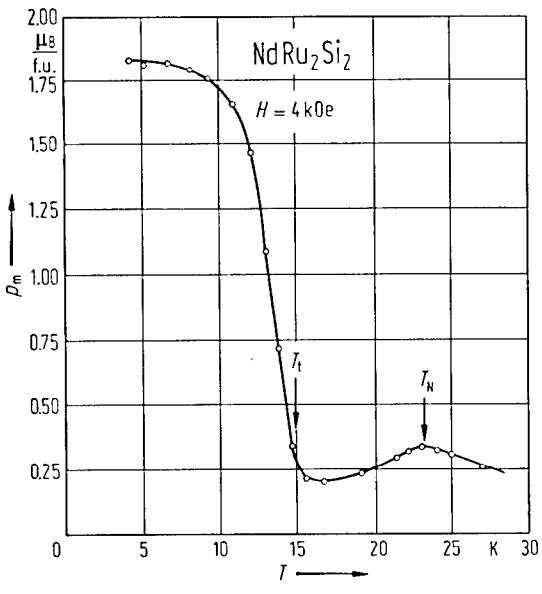

Fig. 262. $NdRu_2Si_2$. Temperature dependence of p_m at 4 kOe [85 C 1].

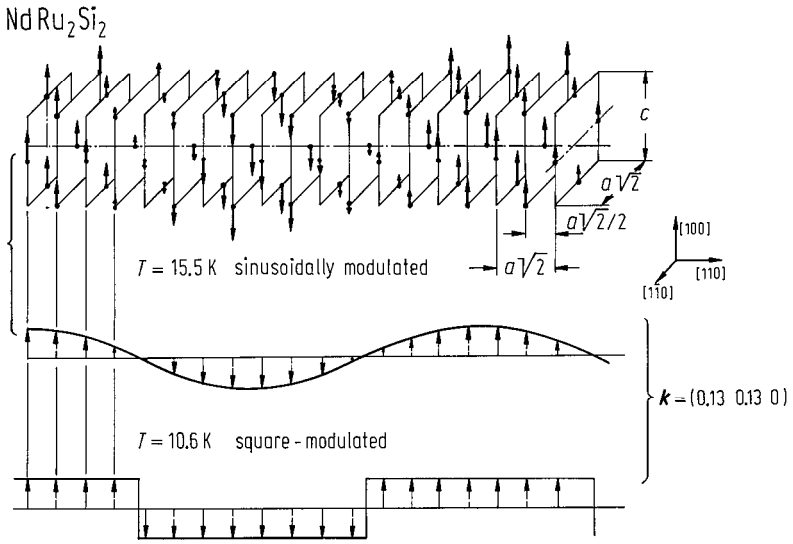

Fig. 263. $NdRu_2Si_2$. Schematic representation of the Nd magnetic moment alignement for sinusoidally modulated and square-modulated phases [85 C 1].

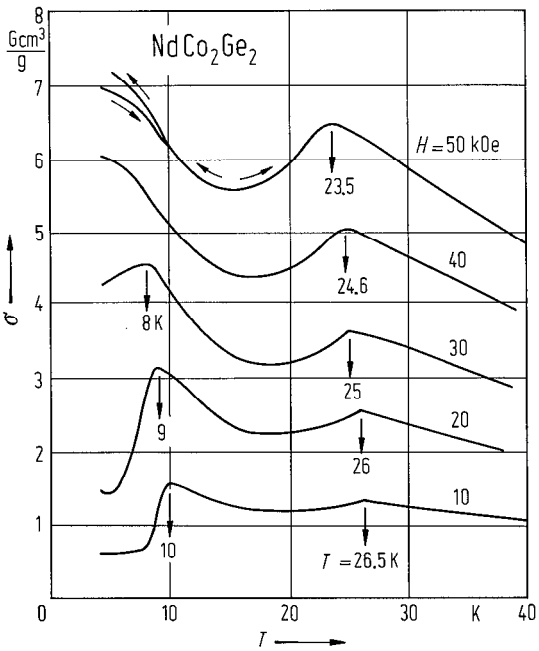

Fig. 264. $NdCo_2Ge_2$. Temperature dependence of σ at various magnetic fields [82 K 2, 83 L 4].

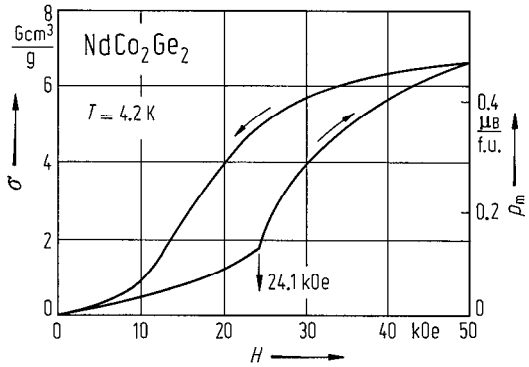

Fig. 265. $NdCo_2Ge_2$. Magnetic field dependence of σ and p_m at 4.2 K [82 K 2, 83 L 4].

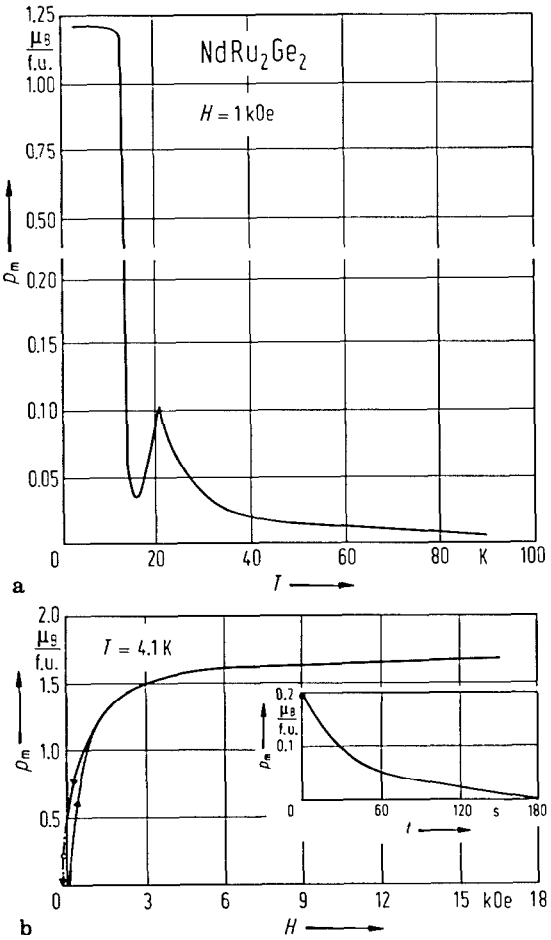

Fig. 266. $NdRu_2Ge_2$. (a) Temperature dependence of p_m at 1 kOe. (b) Magnetic field dependence of p_m at 4.1 K and time dependence of magnetization at 4.1 K (cf. Fig. 261) [85 F 3].

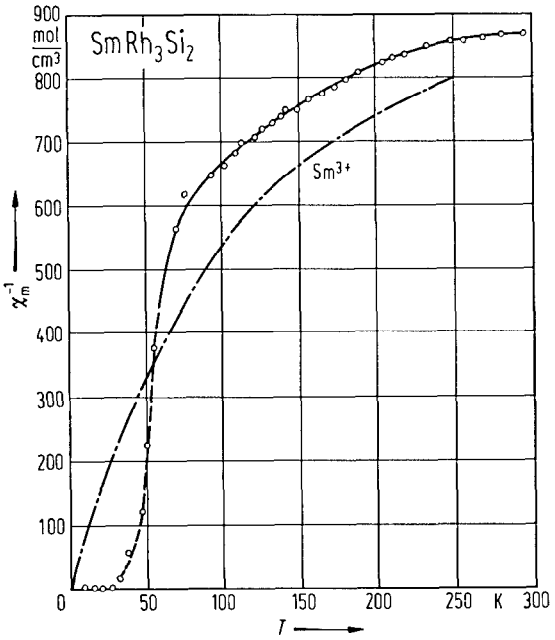

Fig. 268. $SmRh_3Si_2$. Temperature dependence of χ_m^{-1}. Dashed-dotted line: theoretical for Sm^{3+} free ion (Van Vleck) [81 C 1].

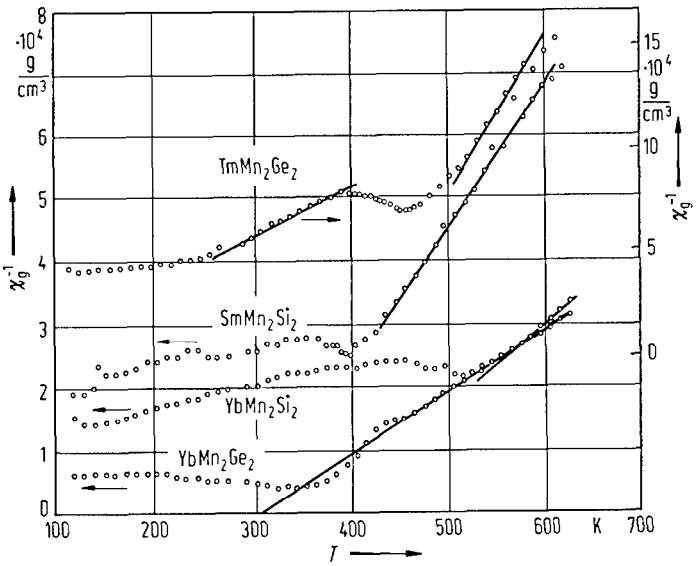

Fig. 267. RMn_2M_2, R = Sm, Tm, Yb, M = Si, Ge. Temperature dependence of χ_g^{-1} [81 S 7].

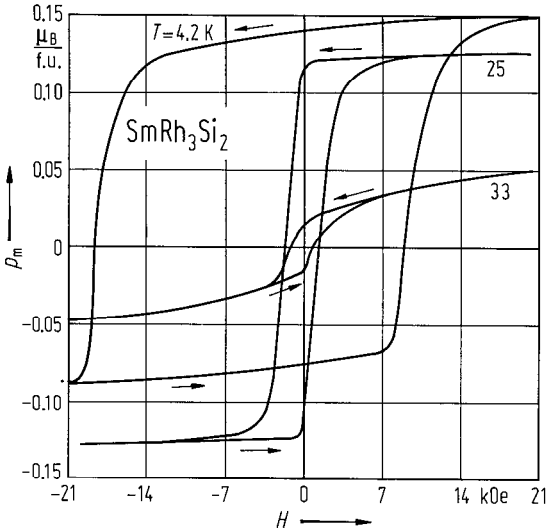

Fig. 269. $SmRh_3Si_2$. Hysteresis loops at different temperatures [81 C 1, 83 C 3].

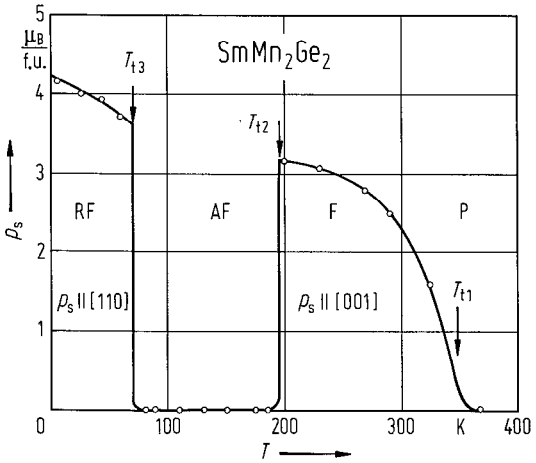

Fig. 270. $SmMn_2Ge_2$. Temperature dependence of the spontaneous magnetization of a single crystal. T_{t1}, T_{t2} and T_{t3} are the P⇌F, F⇌AF and AF⇌RF (re-entrant ferromagnetic) phase transition temperatures, respectively [85 F 4].

Fig. 271. $SmMn_2Ge_2$. Magnetic field dependence of p_m along the principal axes of the tetragonal lattice at various temperatures [85 F 4].

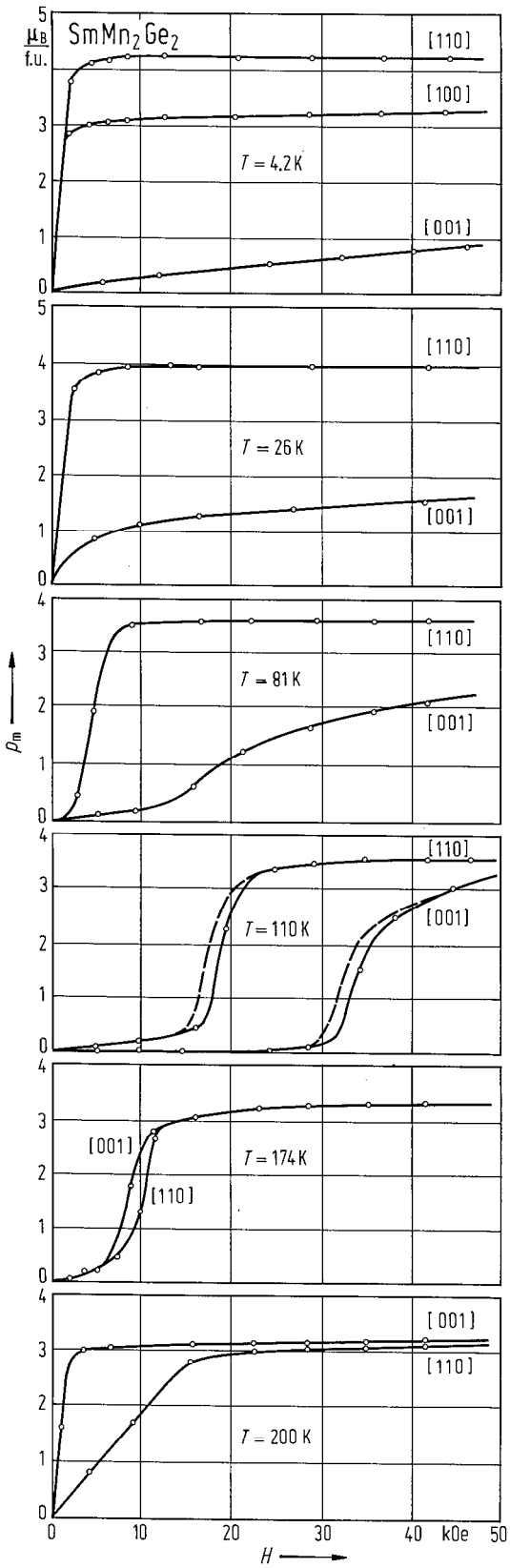

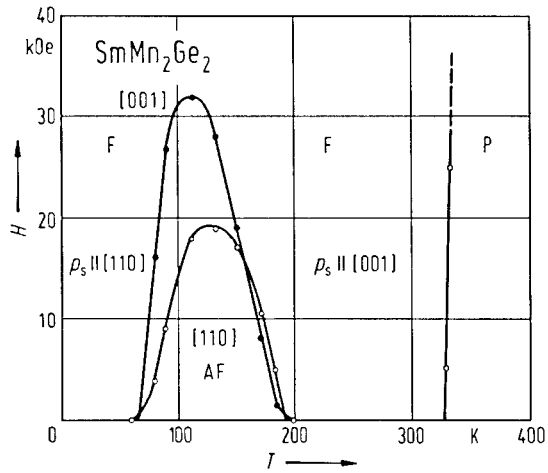

Fig. 272. $SmMn_2Ge_2$. Magnetic phase diagram. The critical magnetic fields along the [110] and [001], directions are indicated by open and solid circles, respectively. The easy magnetization directions in the ferromagnetic phases are shown as well [85 F 4].

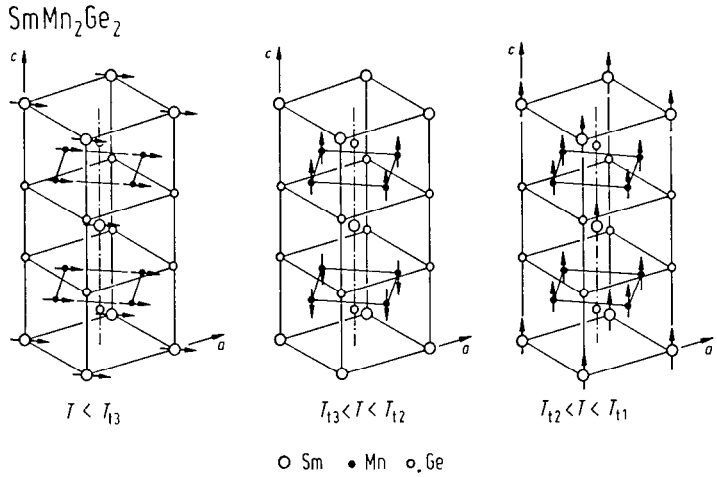

Fig. 273. $SmMn_2Ge_2$. Magnetic structure deduced from the magnetization measurements on single crystal (see Fig. 270 for transition temperatures T_t) [85 F 4].

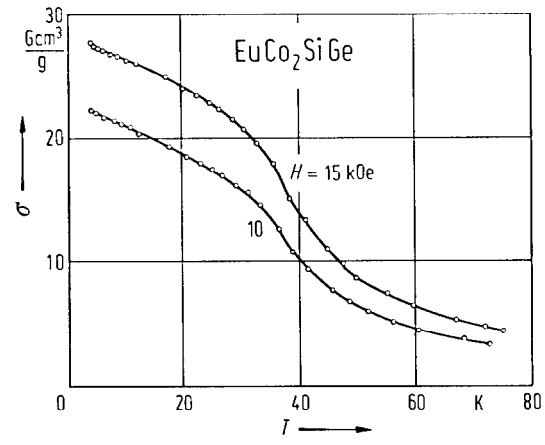

Fig. 274. $EuCo_2SiGe$. Temperature dependence of σ at 10 and 15 kOe, respectively [78 F 1].

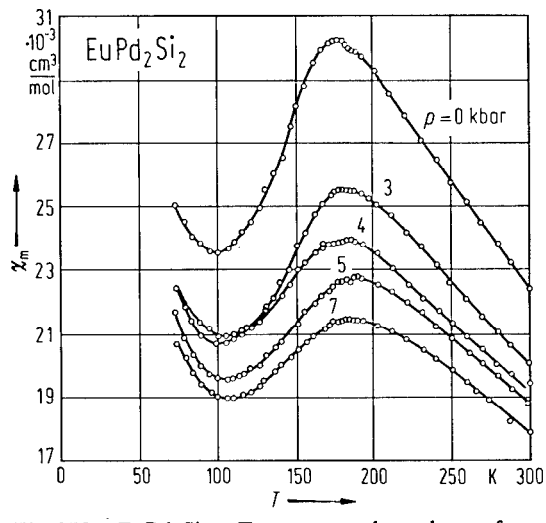

Fig. 275. $EuPd_2Si_2$. Temperature dependence of χ_m at different pressures [84 S 5].

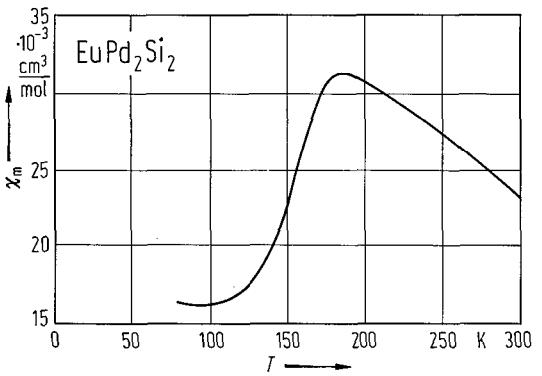

Fig. 276. $EuPd_2Si_2$. Temperature dependence of χ_m [85 N 1].

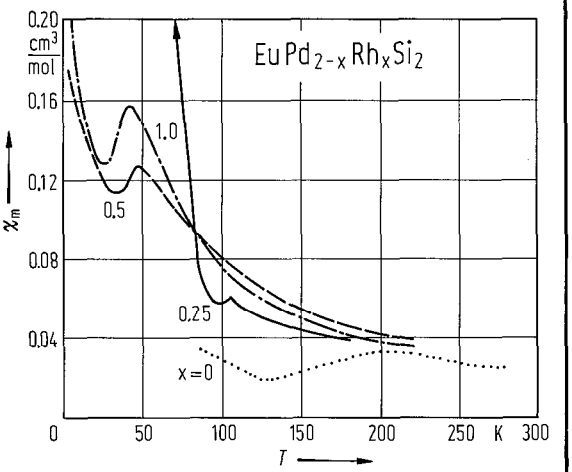

Fig. 277. $EuPd_{2-x}Rh_xSi_2$. Temperature dependence of χ_m for different compositions [85 F 2, 85 F 1].

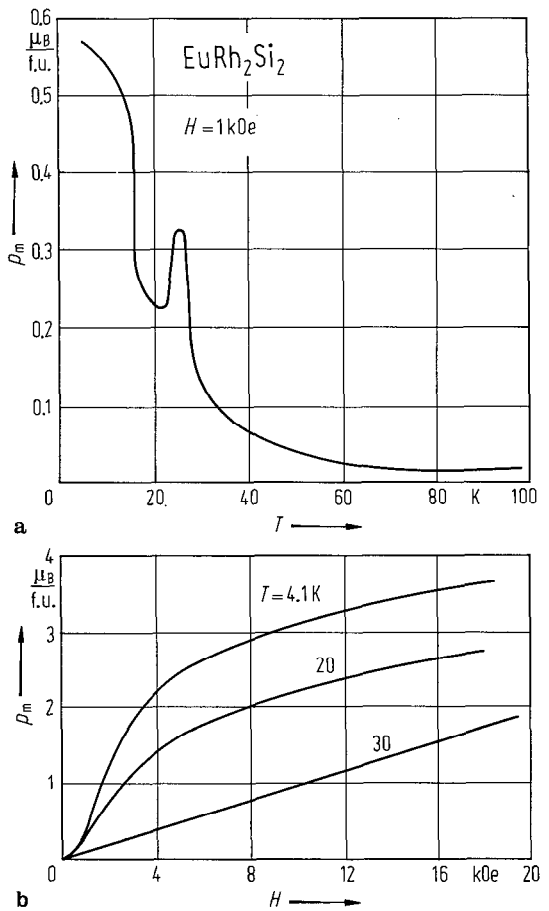

Fig. 278. $EuRh_2Si_2$. (a) Temperature dependence of p_m at 1 kOe and (b) magnetic field dependence of p_m at various temperatures [84 F 1].

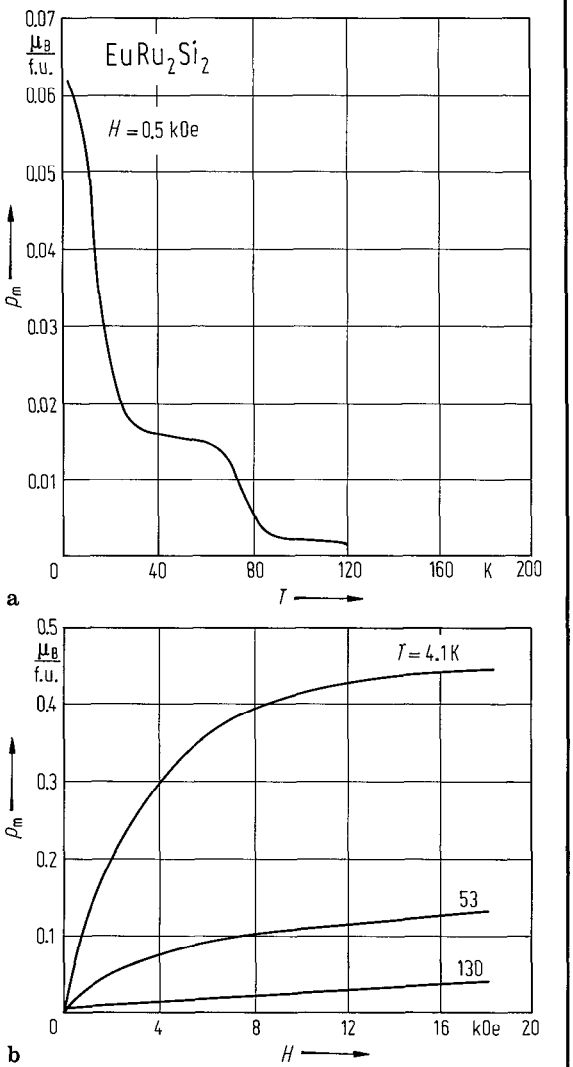

Fig. 279. $EuRu_2Si_2$. (a) Temperature dependence of p_m at 0.5 kOe and (b) magnetic field dependence of p_m at various temperatures [84 F 1].

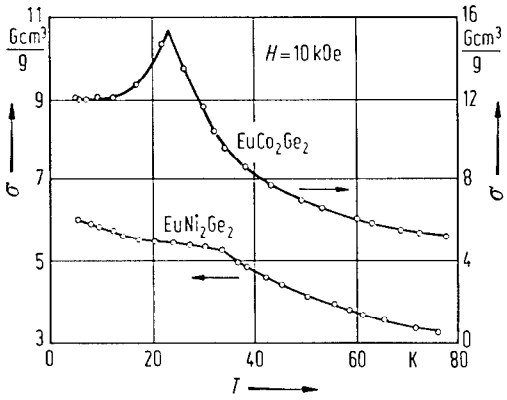

Fig. 280. $EuCo_2Ge_2$, $EuNi_2Ge_2$. Temperature dependence of σ at 10 kOe [78 F 1].

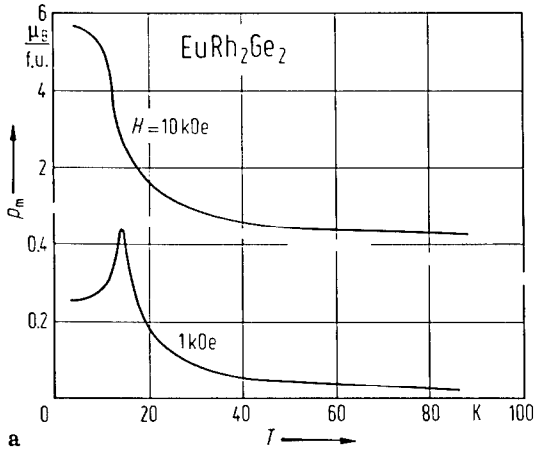

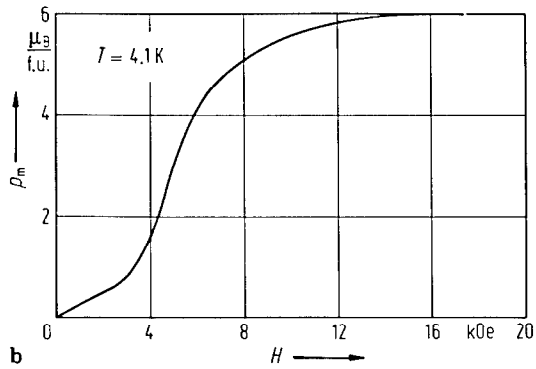

Fig. 282. $EuRh_2Ge_2$. (a) Temperature dependence of p_m at 1 and 10 kOe and (b) magnetic field dependence of p_m at 4.1 K [85 F 3].

Fig. 283. $EuRu_2Ge_2$. (a) Temperature dependence of p_m at 10 kOe and (b) magnetic field dependence of p_m at 4.1 K [85 F 3].

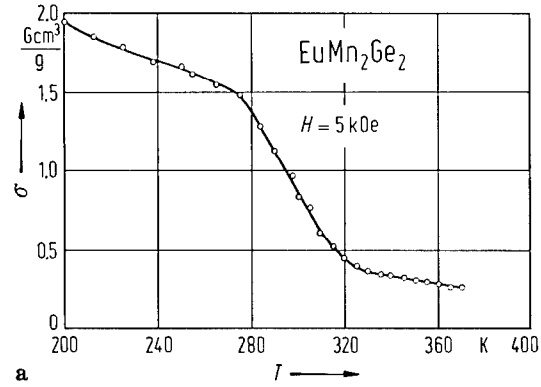

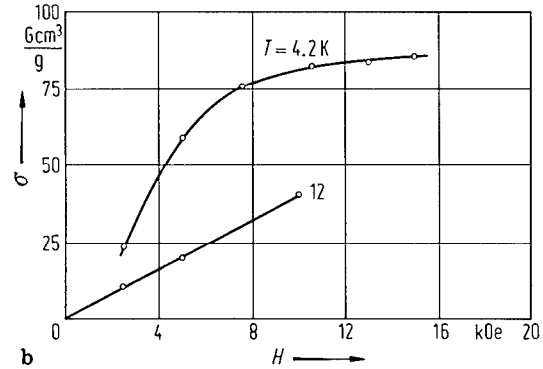

Fig. 281. $EuMn_2Ge_2$. (a) Temperature dependence of σ at 5 kOe and (b) magnetic field dependence of σ at 4.2 and 12 K [78 F 1].

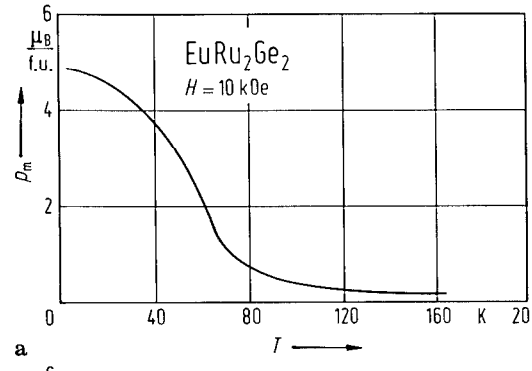

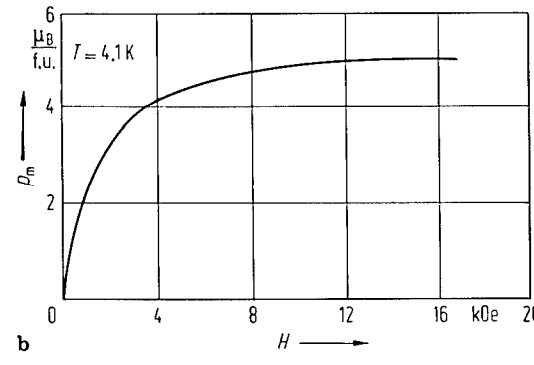

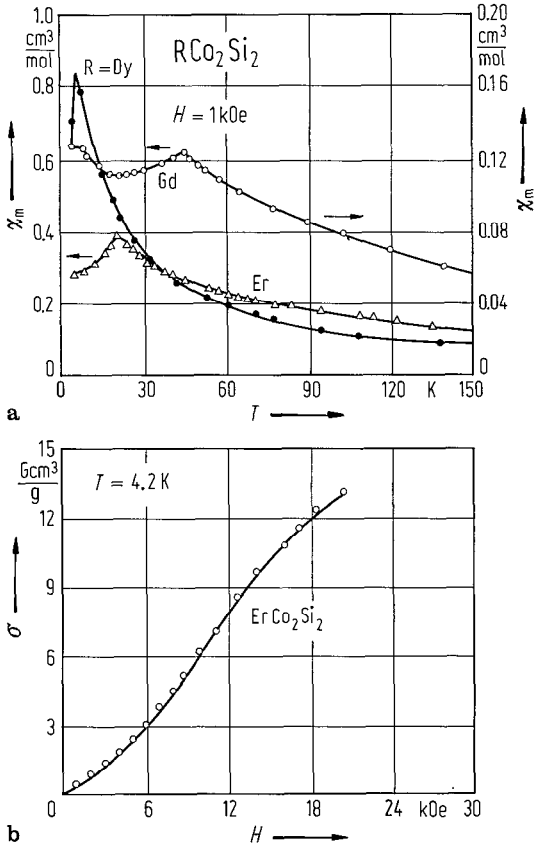

Fig. 284. RCo_2Si_2, R = Gd, Dy, Er. (a) Temperature dependence of χ_m at 1 kOe and (b) magnetic field dependence of σ at 4.2 K for $ErCo_2Si_2$ [80 Y 2].

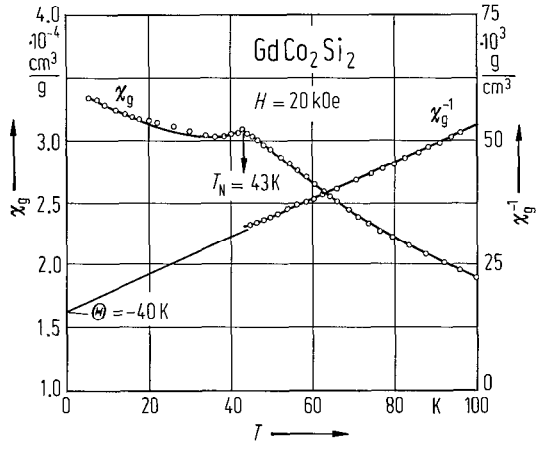

Fig. 285. $GdCo_2Si_2$. Temperature dependence of χ_g and χ_g^{-1} at 20 kOe [82 K 2].

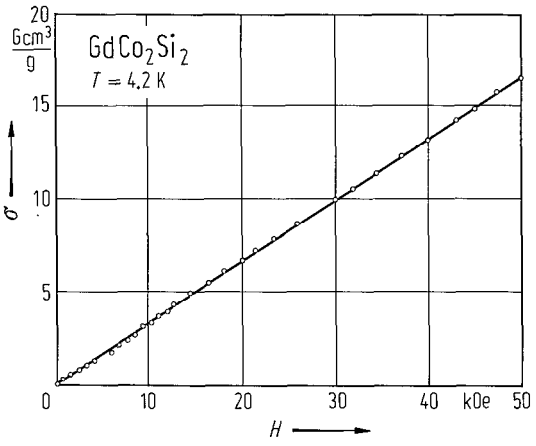

Fig. 286. $GdCo_2Si_2$. Magnetic field dependence of σ at 4.2 K [82 K 2].

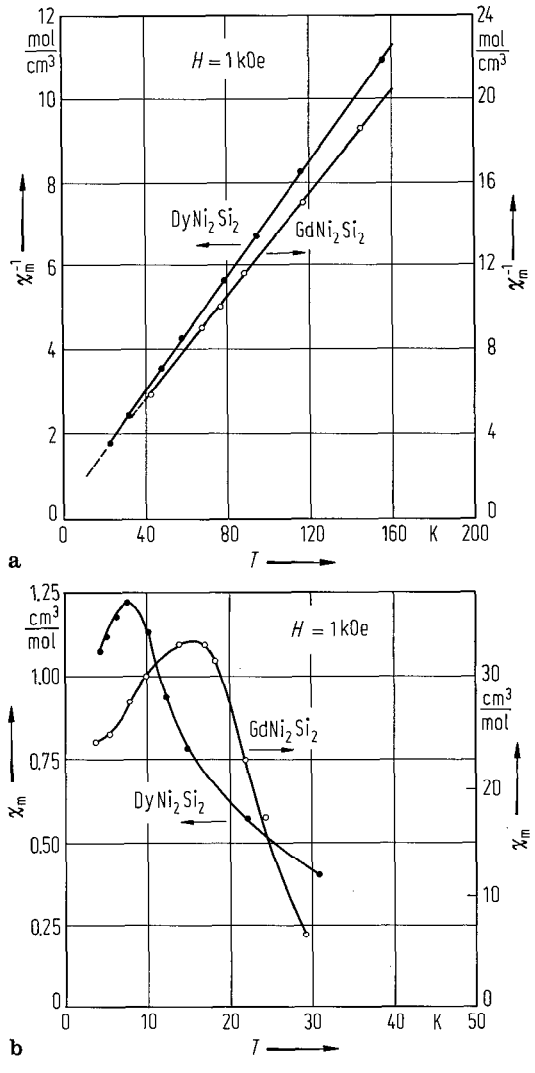

Fig. 287. $GdNi_2Si_2$, $DyNi_2Si_2$. Temperature dependence of (a) χ_m^{-1} and (b) χ_m at 1 kOe [80 Y 1].

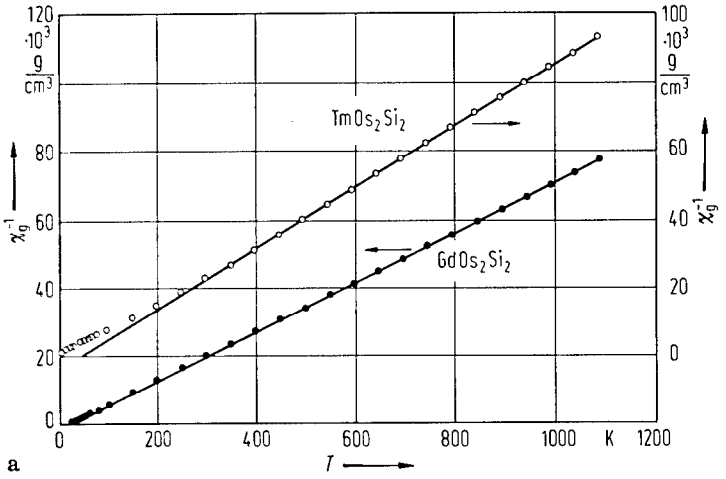

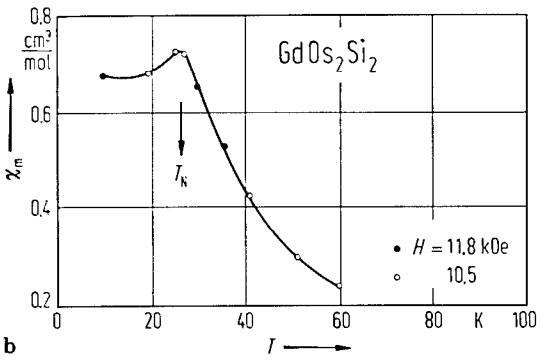

Fig. 288. $GdOs_2Si_2$, $TmOs_2Si_2$. (a) Temperature dependence of χ_g^{-1} and calculated least-squares fit (solid line). (b) Temperature dependence of χ_m at 10.5 and 11.8 kOe showing antiferromagnetic ordering for $GdOs_2Si_2$ [83 H 2].

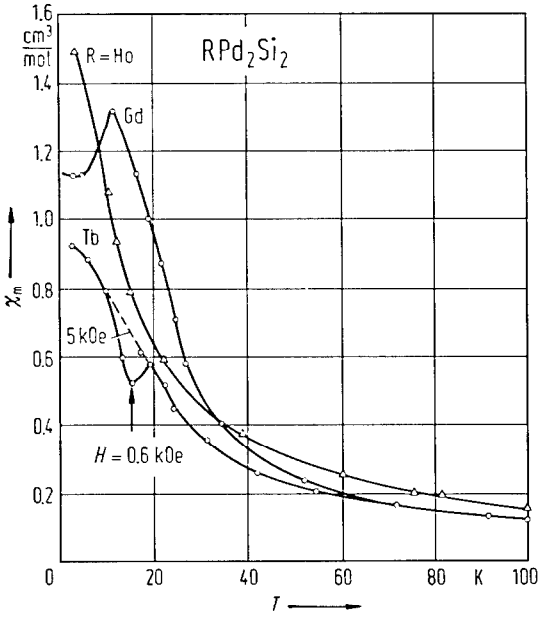

Fig. 290. RPd_2Si_2, R = Gd, Tb, Ho. Temperature dependence of χ_m. R = Gd, Ho: initial magnetic susceptibility, R = Tb: χ_m at 0.6 and 5 kOe [82 Y 1].

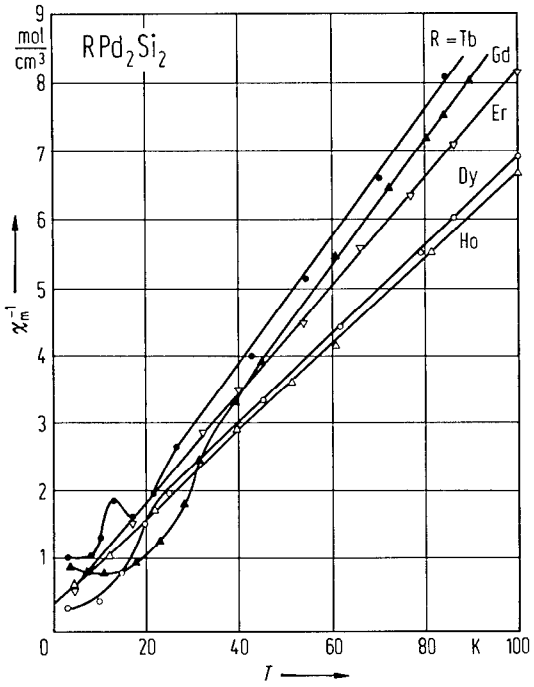

Fig. 289. RPd_2Si_2, R = Gd, Tb, Dy, Ho, Er. Temperature dependence of χ_m^{-1} [82 Y 2].

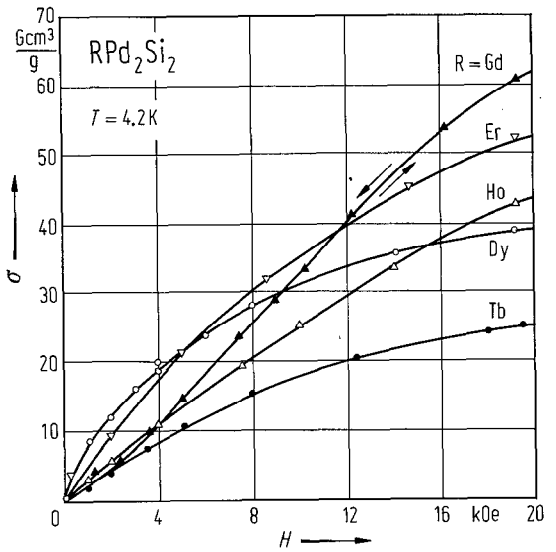

Fig. 291. RPd_2Si_2, R = Gd, Tb, Dy, Ho, Er. Magnetic field dependence of σ at 4.2 K [82 Y 2].

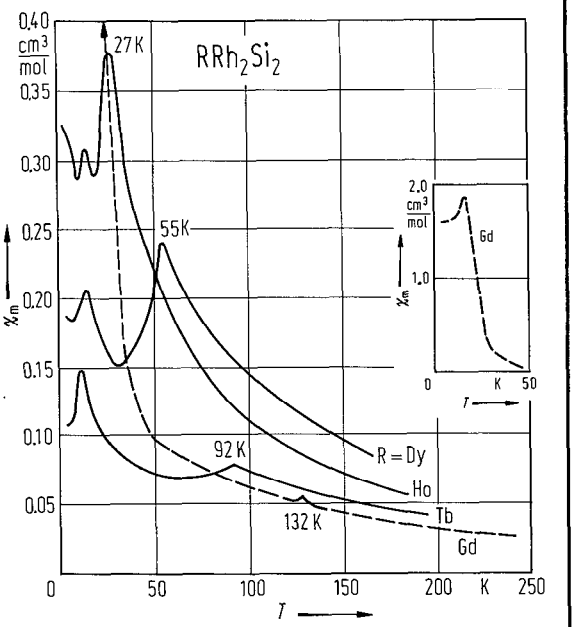

Fig. 293. RRh_2Si_2, R = Gd, Tb, Dy, Ho. Temperature dependence of χ_m [84 F 1].

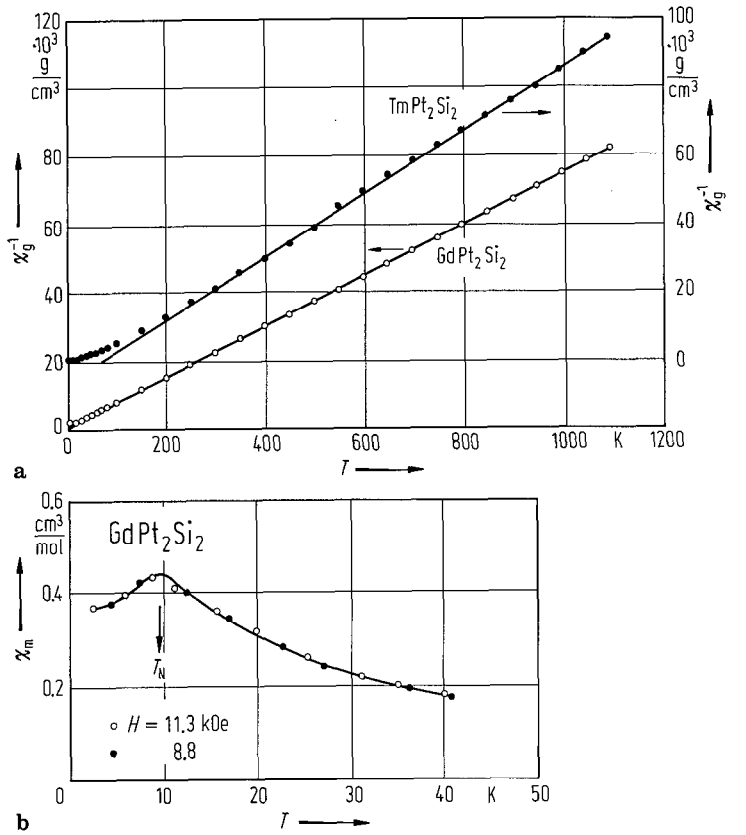

Fig. 292. $GdPt_2Si_2$, $TmPt_2Si_2$. (a) Temperature dependence of χ_g^{-1} and calculated least-square fit (solid line). (b) Temperature dependence of χ_m at 8.8 and 11.3 kOe showing antiferromagnetic ordering of $GdPt_2Si_2$ [85 H 2].

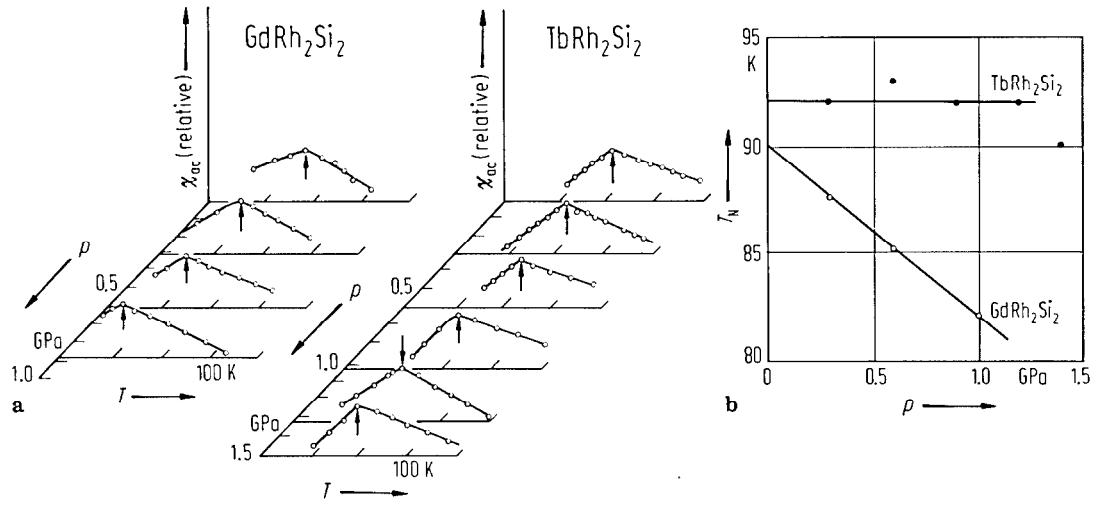

Fig. 294. $GdRh_2Si_2$, $TbRh_2Si_2$. (a) Temperature dependence of magnetic ac susceptibility at different pressures and (b) pressure dependence of T_N [86 S 2].

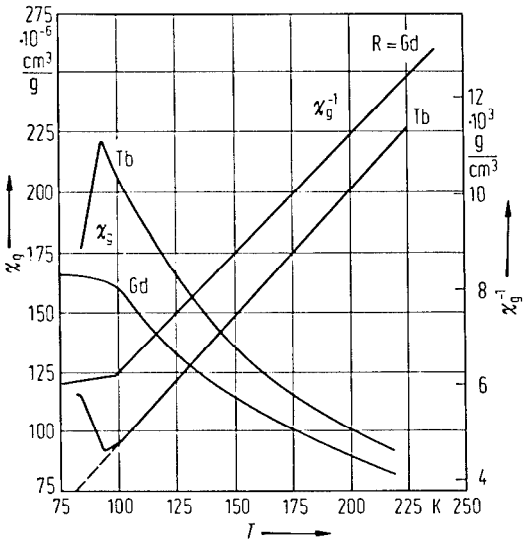

Fig. 295. RRh_2Si_2. Temperature dependence of χ_g and χ_g^{-1} [86 S 2].

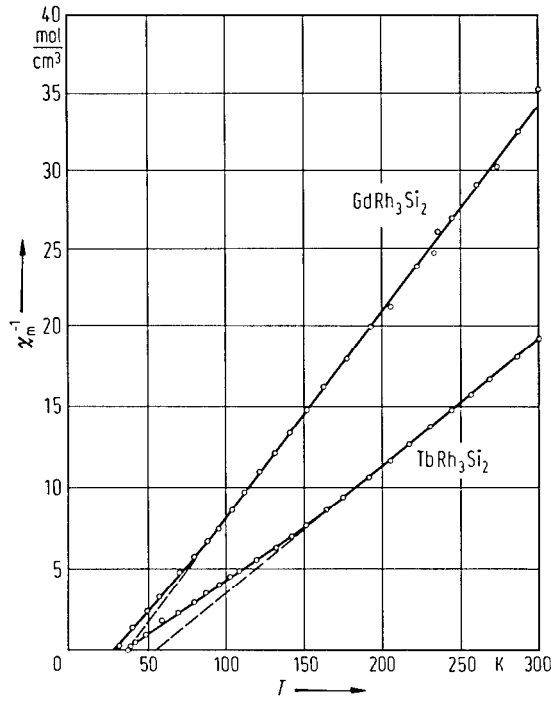

Fig. 296. $GdRh_3Si_2$, $TbRh_3Si_2$. Temperature dependence of χ_m^{-1} [81 C 1, 83 C 3].

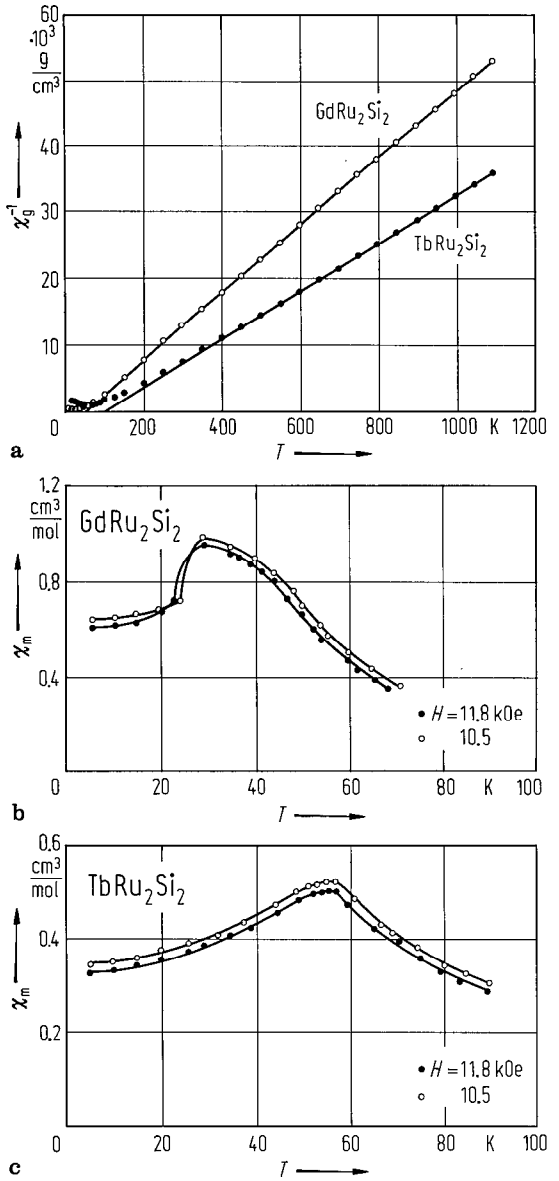

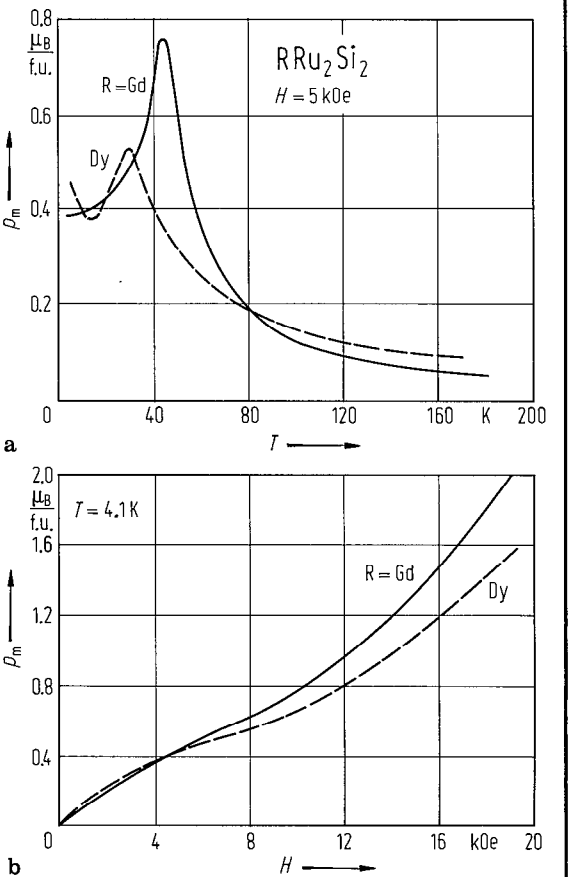

Fig. 298. $GdRu_2Si_2$, $DyRu_2Si_2$. (a) Temperature dependence of p_m at 5 kOe and (b) magnetic field dependence of p_m at 4.1 K [84 F 1].

Fig. 297. $GdRu_2Si_2$, $TbRu_2Si_2$. (a) Temperature dependence of χ_g^{-1} and calculated least-squares fit. Temperature dependence of χ_m at 10.5 and 11.8 kOe showing antiferromagnetic ordering for (b) $GdRu_2Si_2$ and (c) $TbRu_2Si_2$ [83 H 1].

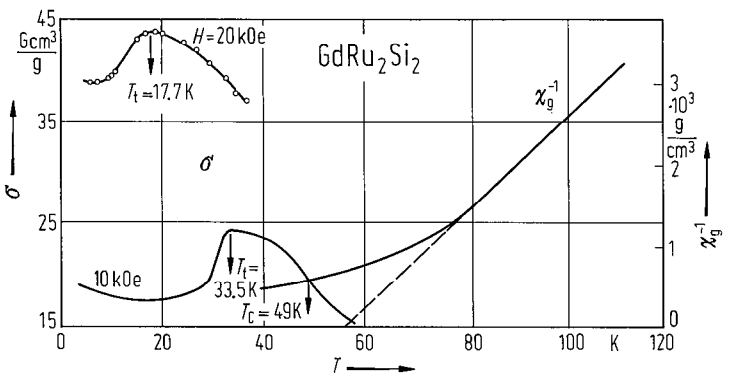

Fig. 299. $GdRu_2Si_2$. Temperature dependence of χ_g^{-1} and σ at 10 and 20 kOe [84 S 4].

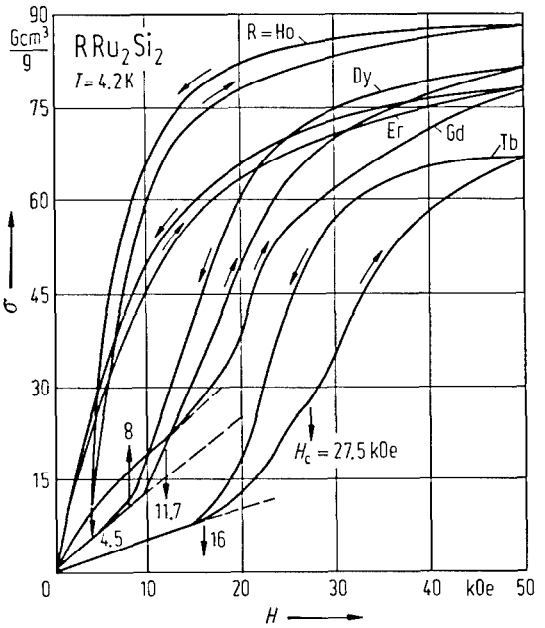

Fig. 300. RRu_2Si_2, R = Gd, Tb, Dy, Ho, Er. Magnetic field dependence of σ at 4.2 K [84 S 4].

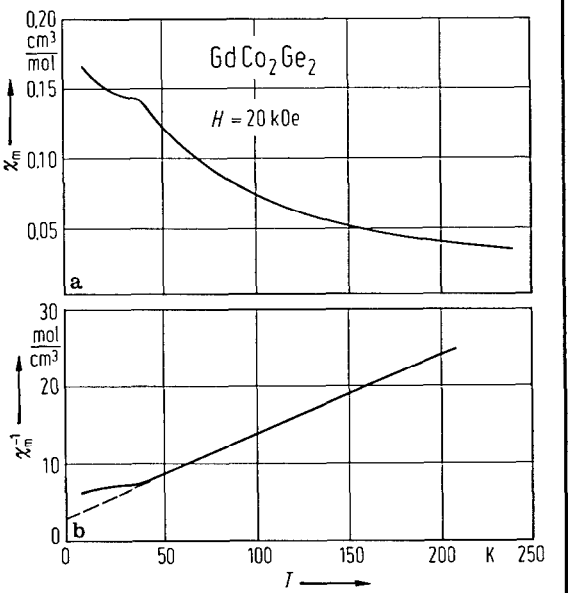

Fig. 301. $GdCo_2Ge_2$. Temperature dependence of (a) χ_m and (b) χ_m^{-1} at 20 kOe [73 M 1].

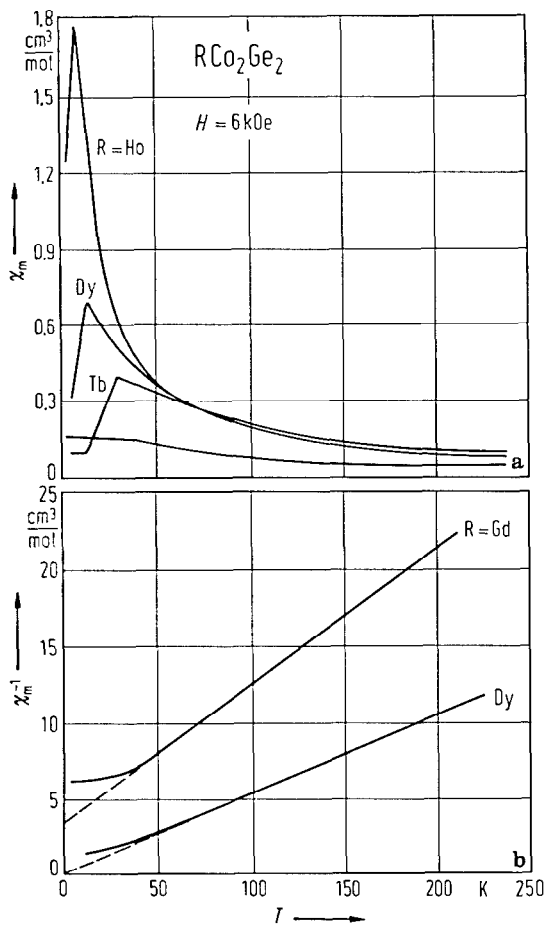

Fig. 302. RCo_2Ge_2, R = Gd, Tb, Dy, Ho. Temperature dependence of (a) χ_m and (b) χ_m^{-1} at 6 kOe [73 M 1].

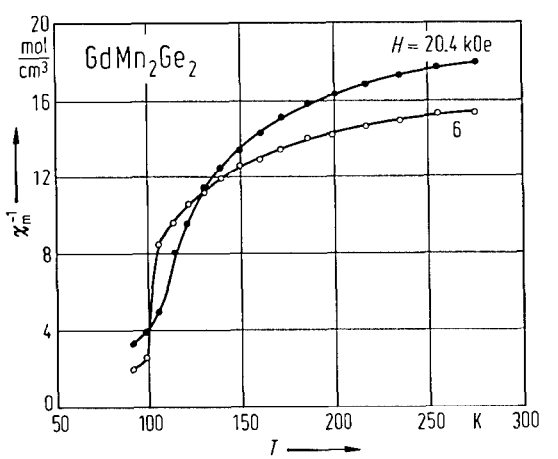

Fig. 303. $GdMn_2Ge_2$. Temperature dependence of χ_m^{-1} at 6 and 20.4 kOe [75 N 1].

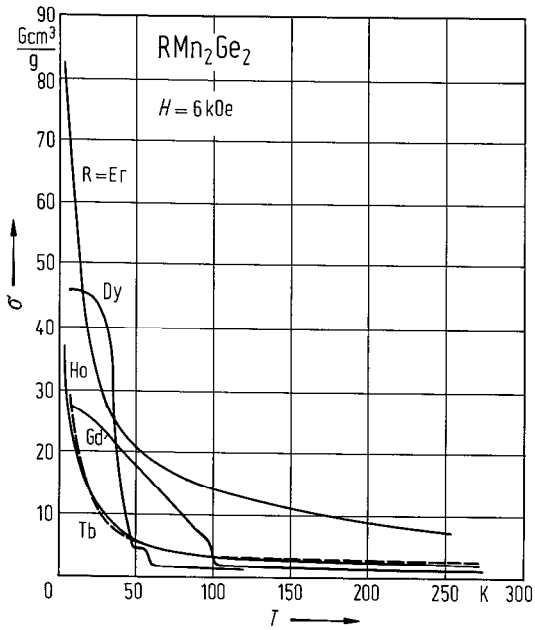

Fig. 304. RMn_2Ge_2, R = Gd, Tb, Dy, Ho, Er. Temperature dependence of σ at 6 kOe [75 N 1].

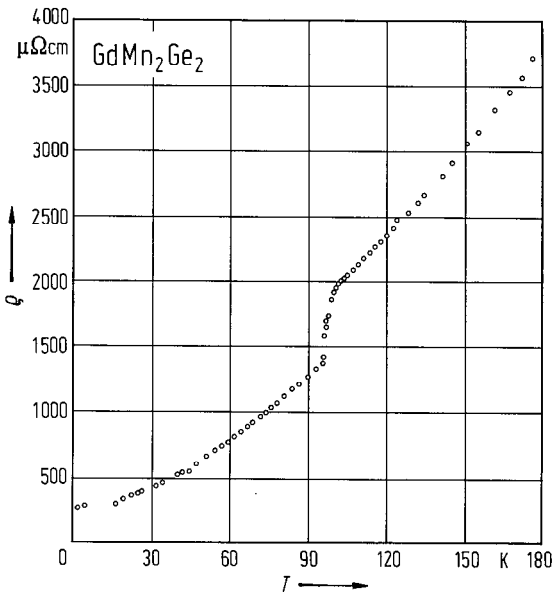

Fig. 308. $GdMn_2Ge_2$. Temperature dependence of electrical resistivity. The magnetic phase transition is accompanied by a change in the temperature dependence of ϱ [75 N 1].

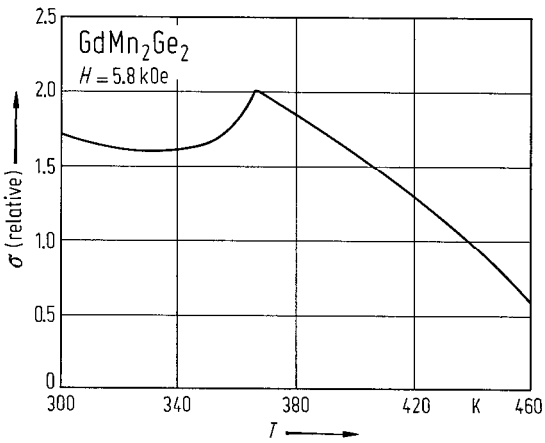

Fig. 305. $GdMn_2Ge_2$. Temperature dependence of σ (in arbitrary units) at 5.8 kOe [75 N 1].

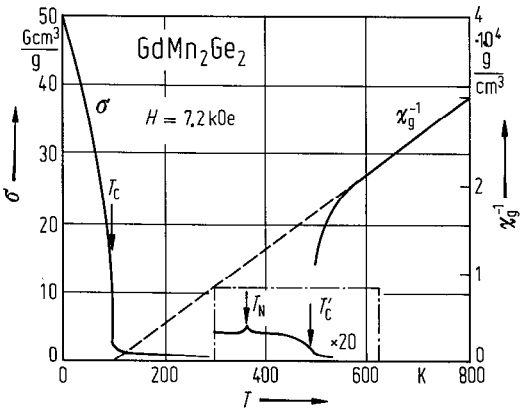

Fig. 306. $GdMn_2Ge_2$. Temperature dependence of σ at 7.2 kOe along the c axis and temperature dependence of χ_g^{-1} [83 S 4].

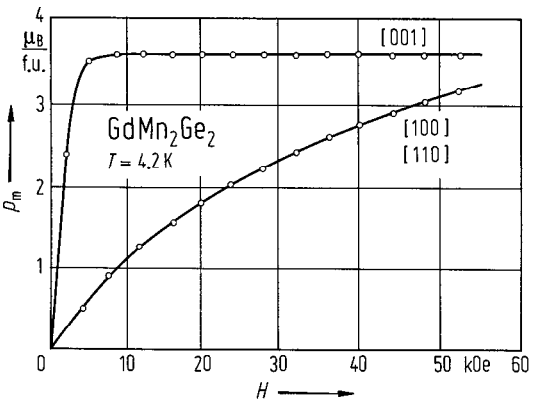

Fig. 307. $GdMn_2Ge_2$. Magnetic field dependence of p_m at 4.2 K along the principal axes [001], [100] and [110] of a single crystal [83 S 4].

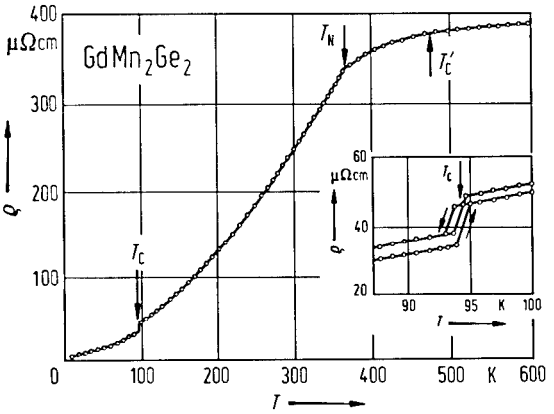

Fig. 309. $GdMn_2Ge_2$. Temperature dependence of the electrical resistivity. The magnetic phase transition temperatures T_C and T_N are accompanied by a change in the temperature dependence of ϱ (see Fig. 308) [83 S 4].

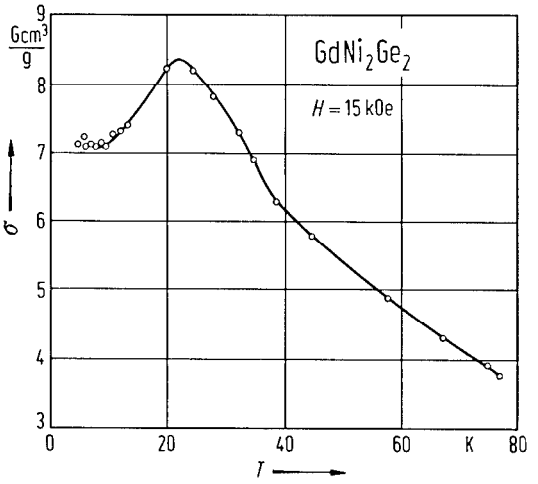

Fig. 310. $GdNi_2Ge_2$. Temperature dependence of σ at 15 kOe [78 F 1].

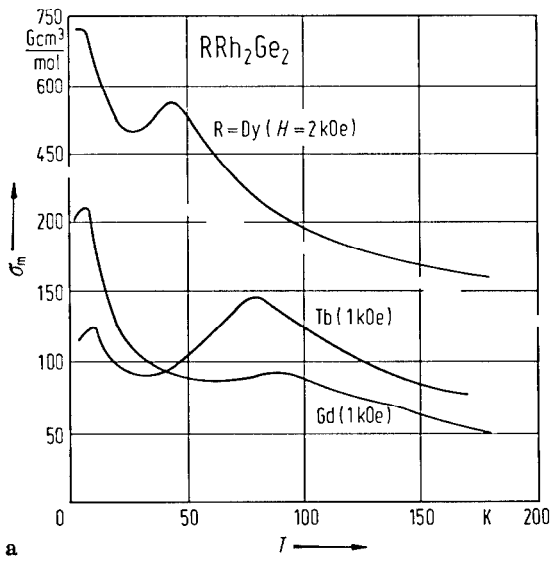

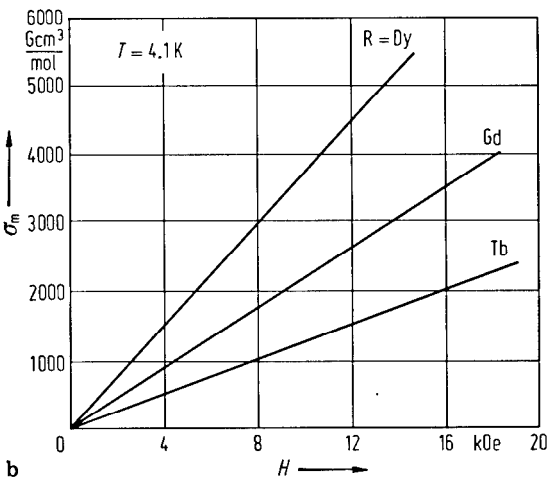

Fig. 311. RRh_2Ge_2, R = Gd, Tb, Dy. (a) Temperature dependence of σ_m at different magnetic fields and (b) magnetic field dependence of σ_m at 4.1 K [85 F 3].

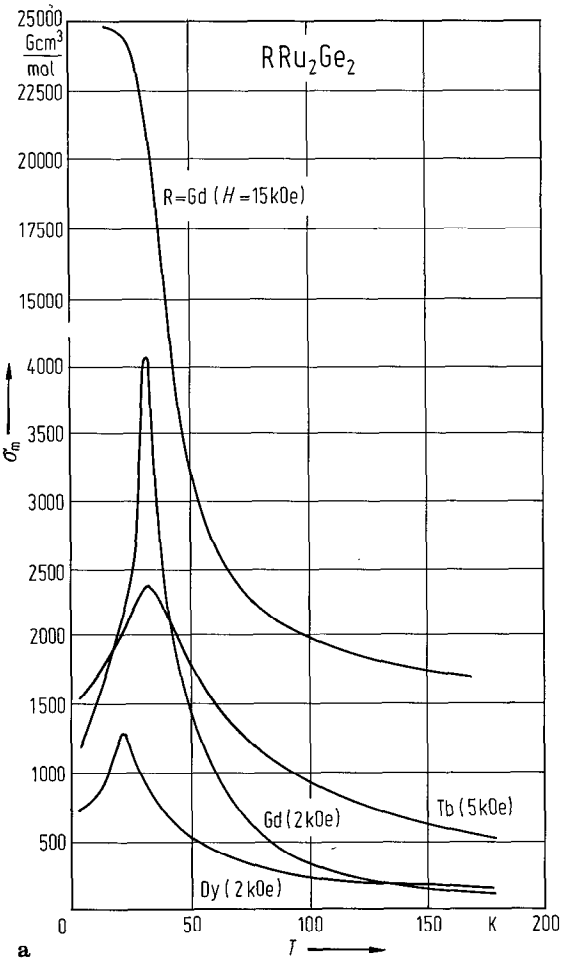

Fig. 312. RRu_2Ge_2, R = Gd, Tb, Dy. (a) Temperature dependence of σ_m at different magnetic fields and (b) magnetic field dependence of p_m at 4.1 K [85 F 3].

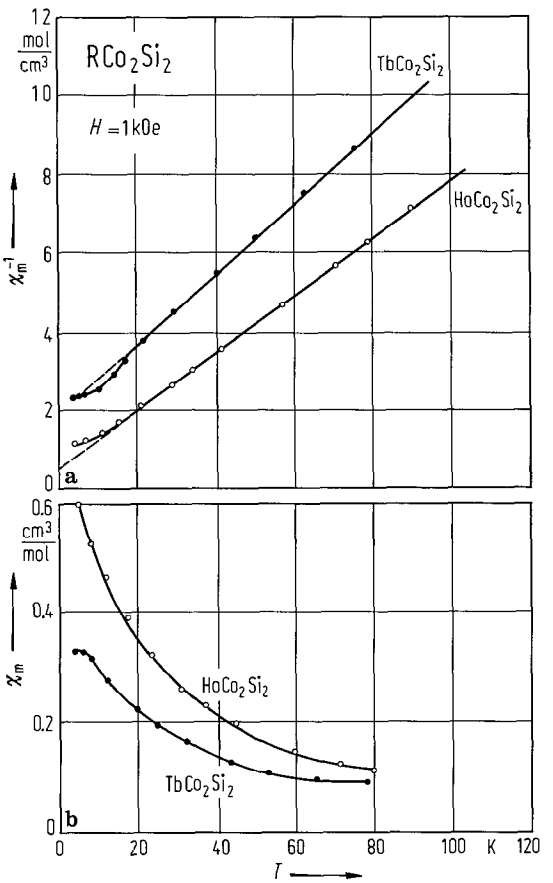

Fig. 313. $TbCo_2Si_2$, $HoCo_2Si_2$. Temperature dependence of (a) χ_m^{-1} at 1 kOe and (b) χ_m [80 Y 2].

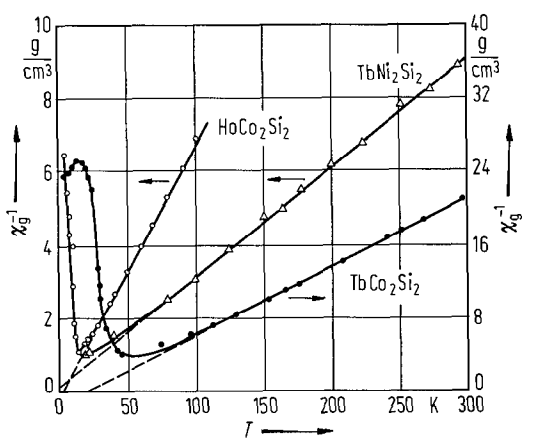

Fig. 315. $TbCo_2Si_2$, $TbNi_2Si_2$, $HoCo_2Si_2$. Temperature dependence of χ_g^{-1} [83 N 1].

For Fig. 314, see next page.

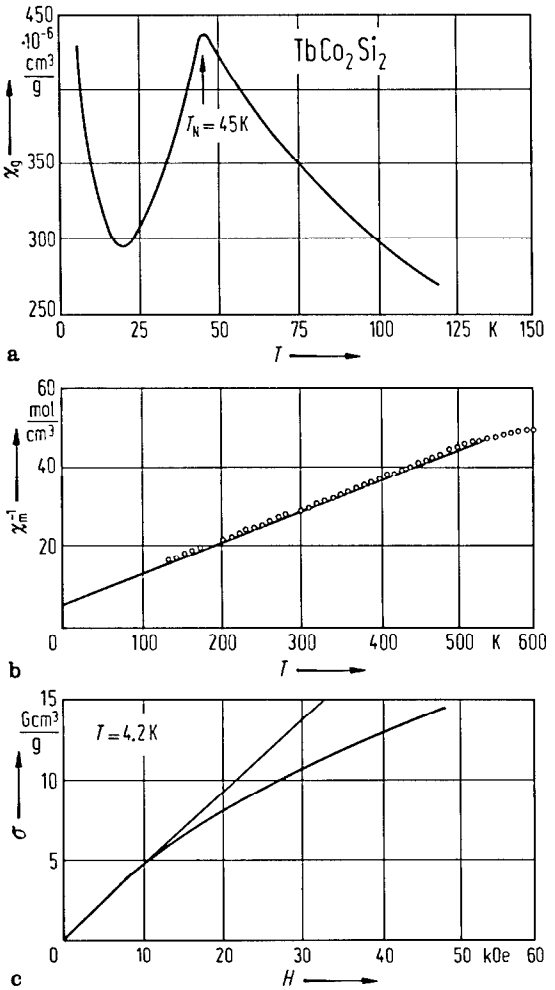

Fig. 314. $TbCo_2Si_2$. Temperature dependence of (a) χ_g, (b) $\chi_m^{-1}(\Theta = -73\,K)$, (c) magnetic field dependence of σ at 4.2 K [82 K 2].

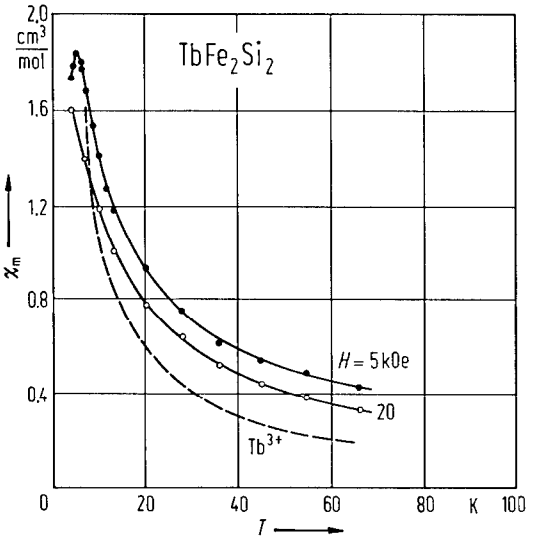

Fig. 316. $TbFe_2Si_2$. Temperature dependence of χ_m at 5 and 20 kOe and for free Tb^{3+} ions [76 S 1].

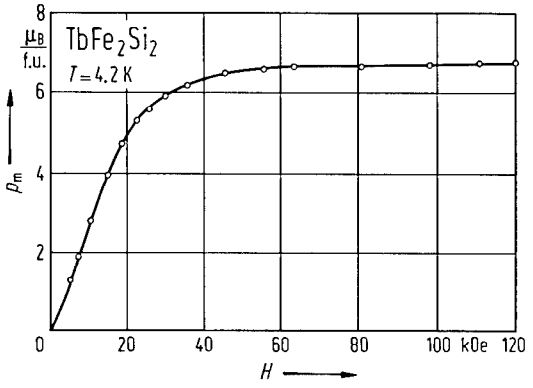

Fig. 317. $TbFe_2Si_2$. Magnetic field dependence of p_m at 4.2 K [76 S 1].

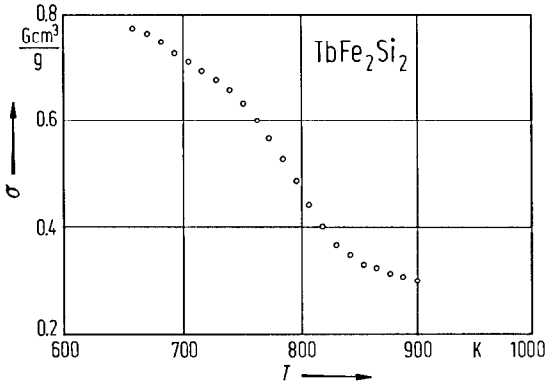

Fig. 318. $TbFe_2Si_2$. Temperature dependence of σ at high temperatures [76 S 1].

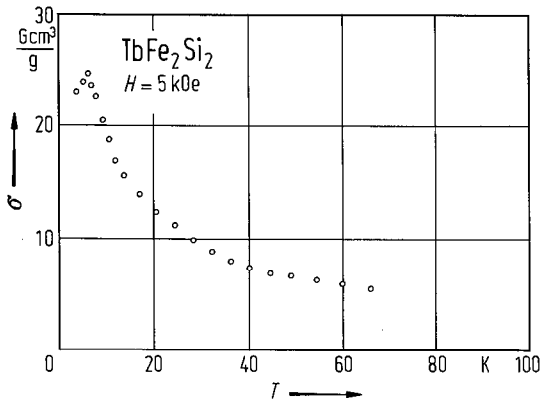

Fig. 319. $TbFe_2Si_2$. Low-temperature dependence of σ at 5 kOe [76 S 1].

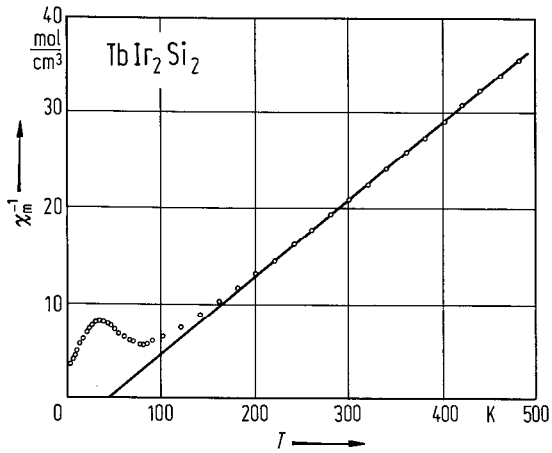

Fig. 320. $TbIr_2Si_2$, (low-temperature modification). Temperature dependence of χ_m^{-1}. Sample annealed for 8 days at 1173 K [84 H 2].

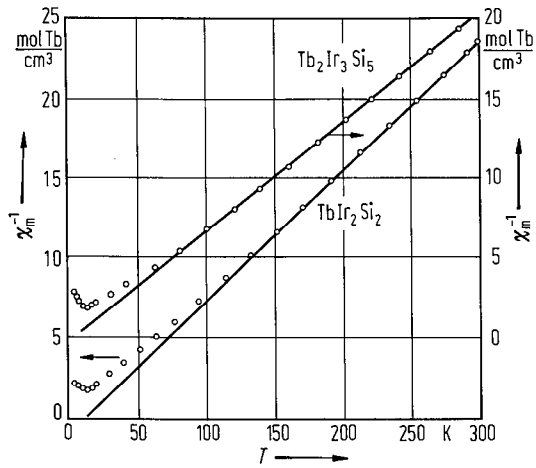

Fig. 321. $TbIr_2Si_2$ (high-temperature modification) $Tb_2Ir_3Si_5$. Temperature dependence of χ_m^{-1} for $Tb_2Ir_3Si_5$ and the high-temperature modification of $TbIr_2Si_2$ obtained by quenching after melting [84 H 2].

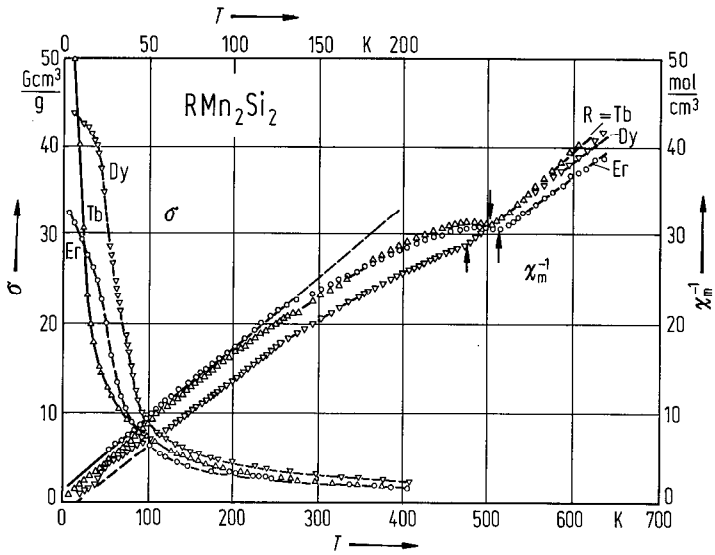

Fig. 322. RMn_2Si_2, R = Tb, Dy, Er. Temperature dependence of χ_m^{-1} and σ [81 S 7].

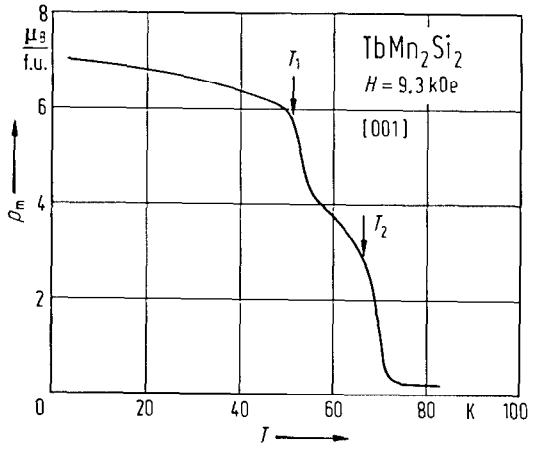

Fig. 323. $TbMn_2Si_2$. Temperature dependence of p_m at 9.3 kOe along the easy axis of magnetization, [001] of a single crystal; at $T_N = 550$ K a cusp is observed [86 S 1].

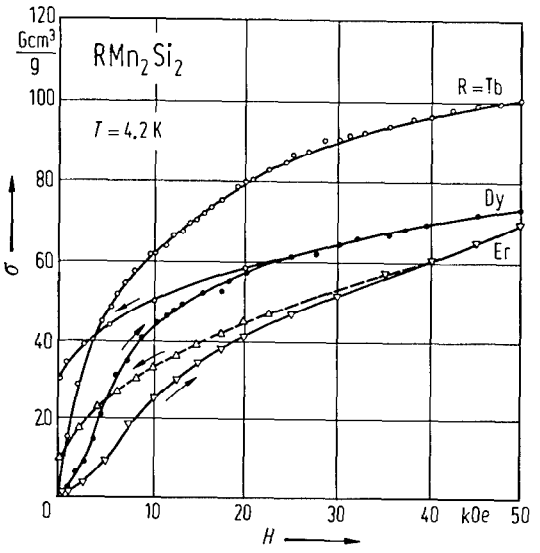

Fig. 324. RMn_2Si_2, R = Tb, Dy, Er. Magnetic field dependence of σ at 4.2 K [81 S 7].

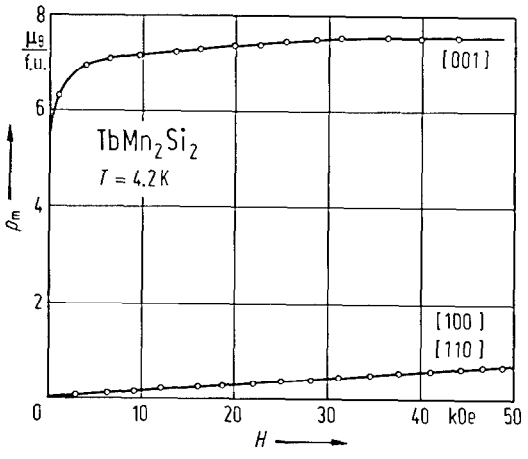

Fig. 325. $TbMn_2Si_2$. Magnetic field dependence of p_m at 4.2 K in [001], [100] and [110] directions of a single crystal [86 S 1].

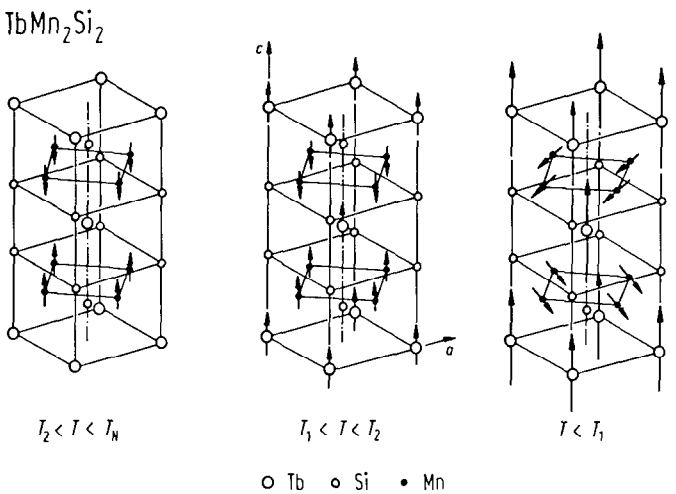

Fig. 326. $TbMn_2Si_2$. Magnetic structure at different ranges of temperature (see Fig. 323) [86 S 1].

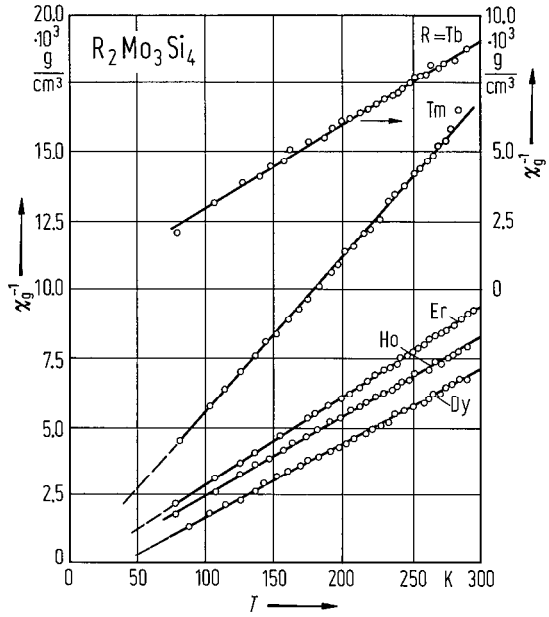

Fig. 327. $R_2Mo_3Si_4$, R=Tb, Dy, Ho, Er, Tm. Temperature dependence of χ_g^{-1} [84 B 1].

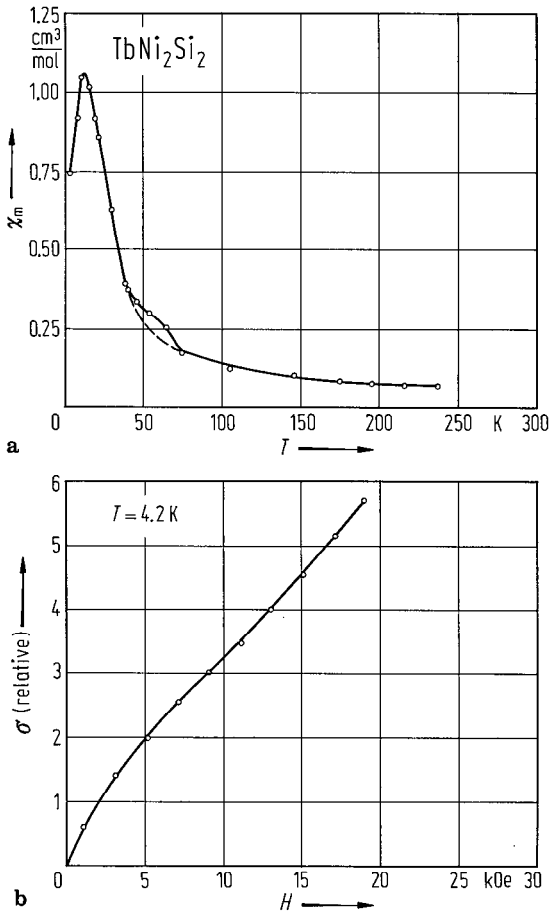

Fig. 328. $TbNi_2Si_2$. (a) Temperature dependence of χ_m and (b) magnetic field dependence of σ at 4.2 K [80 Y 1].

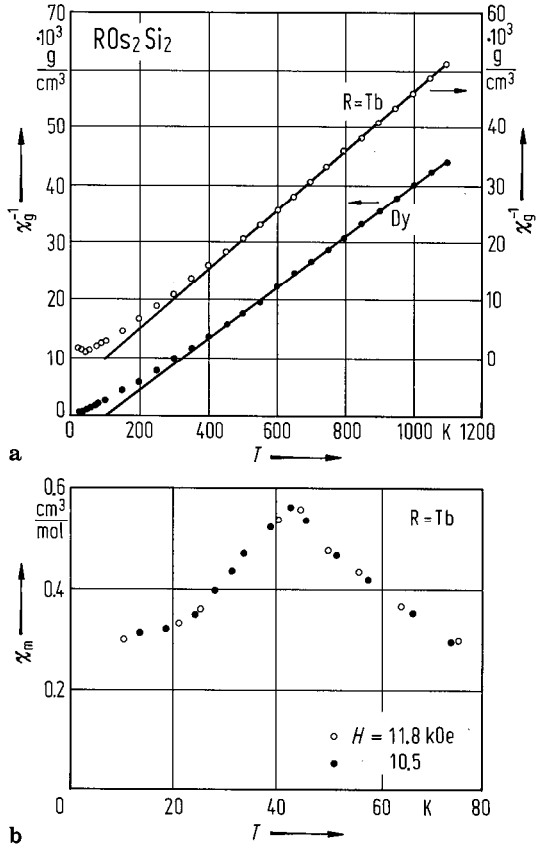

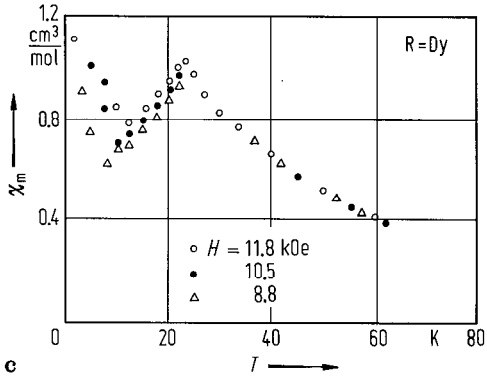

Fig. 329. $TbOs_2Si_2$, $DyOs_2Si_2$. (a) Temperature dependence of χ_g^{-1} and calculated least-squares fit (solid line). Temperature dependence of χ_m at various magnetic fields showing antiferromagnetic ordering for (b) $TbOsSi_2$ and (c) $DyOs_2Si_2$ [83 H 2].

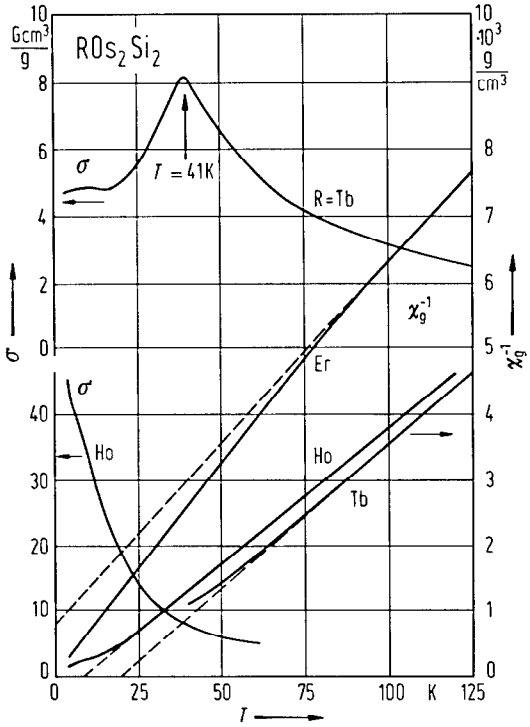

Fig. 330. ROs_2Si_2, R = Tb, Ho, Er. Temperature dependence of χ_g^{-1} and σ [85 K 4].

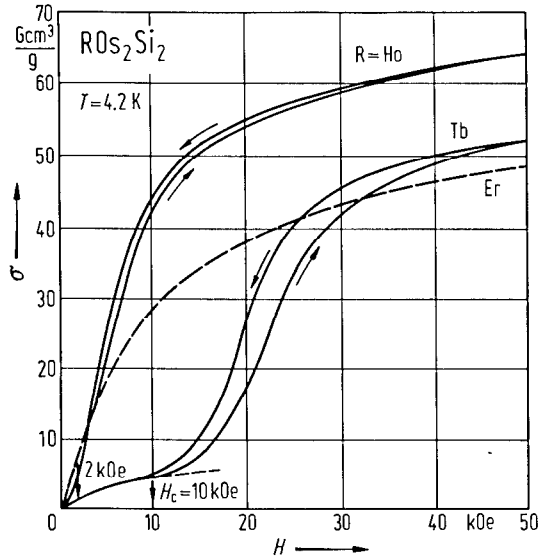

Fig. 331. ROs_2Si_2, R = Tb, Ho, Er. Magnetic field dependence of σ at 4.2 K [85 K 4].

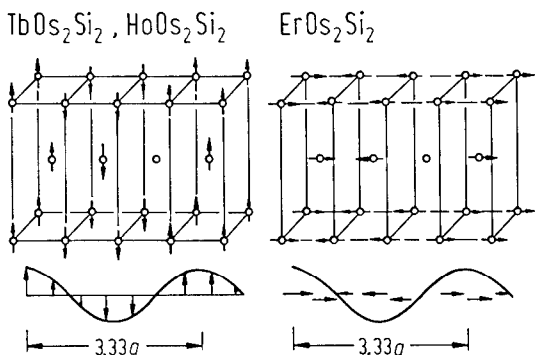

Fig. 332. ROs_2Si_2, R = Tb, Ho, Er. Magnetic structure [85 K 4].

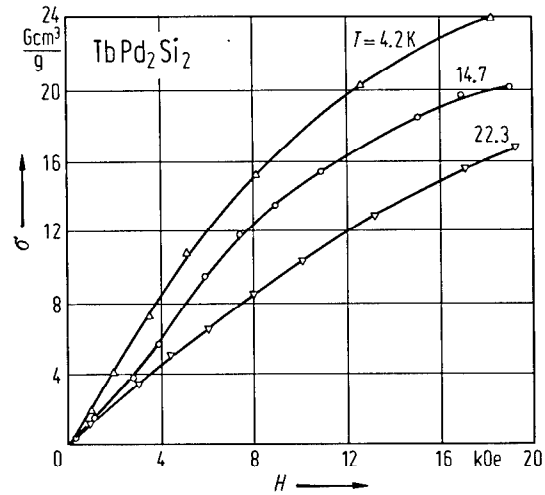

Fig. 333. $TbPd_2Si_2$. Magnetic field dependence of σ at different temperatures [82 Y 1].

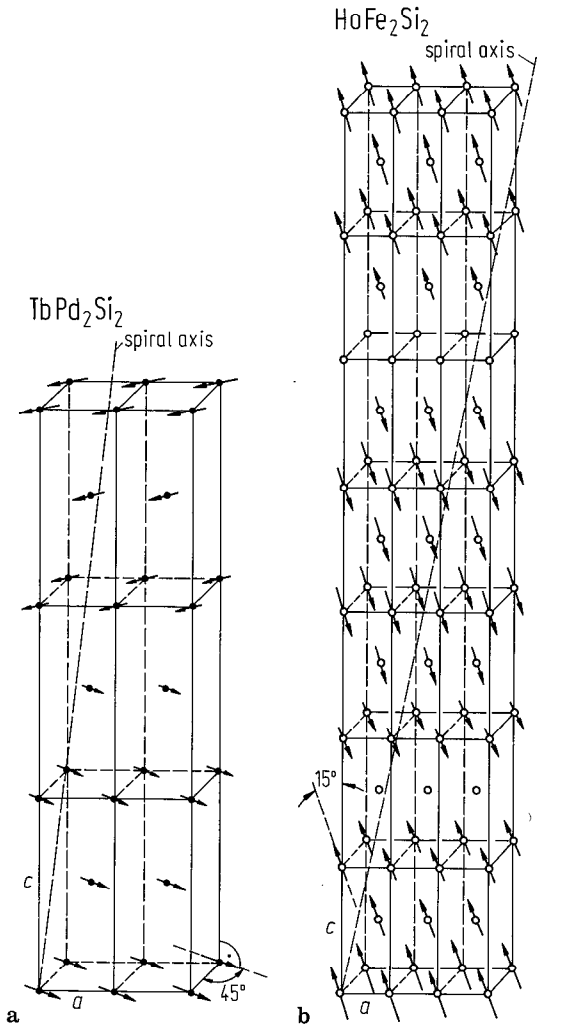

Fig. 334. $TbPd_2Si_2$, $HoFe_2Si_2$. Magnetic structure; (a) [86 S 3], (b) [85 L 3].

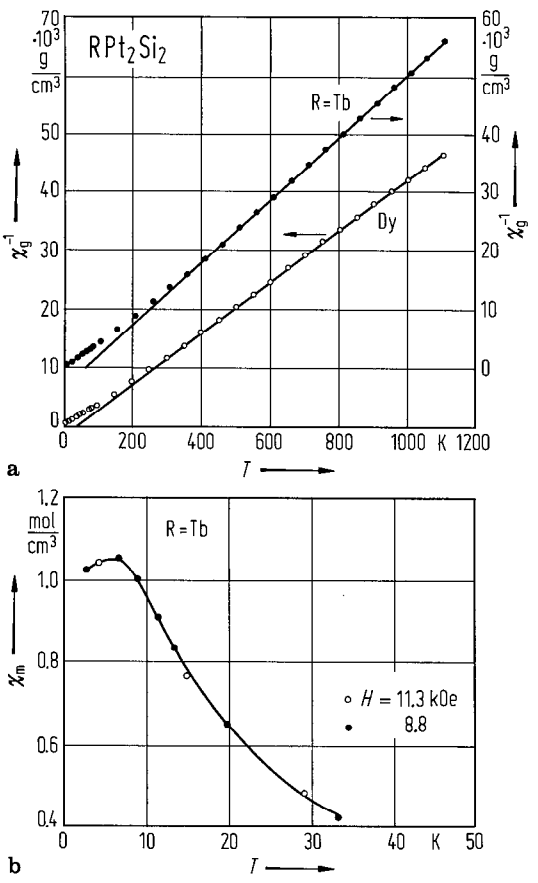

Fig. 335. $TbPt_2Si_2$, $DyPt_2Si_2$. (a) Temperature dependence of χ_g^{-1} and calculated least-squares fit (solid line). (b) Temperature dependence of χ_m at 8.8 and 11.3 kOe and antiferromagnetic ordering of $TbPt_2Si_2$ [85 H 2].

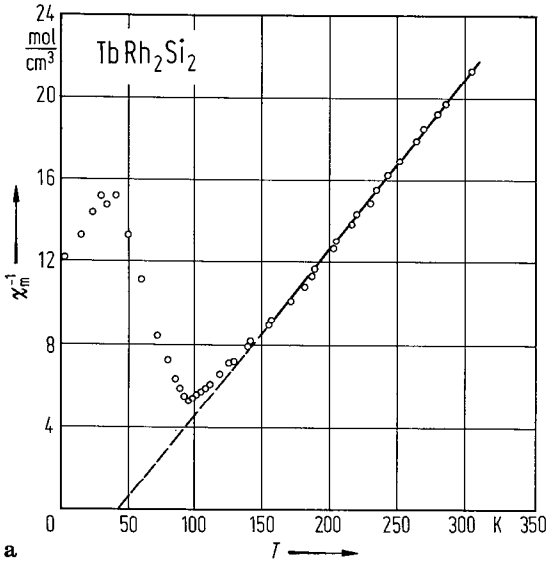

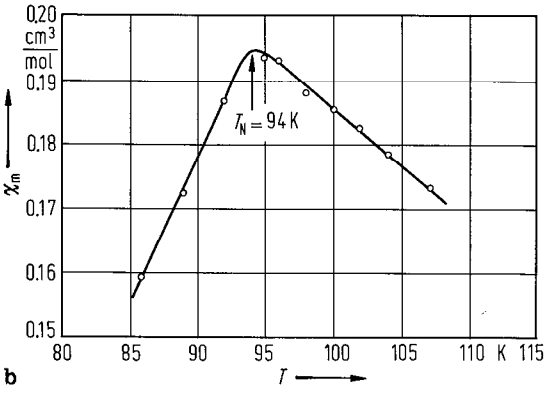

Fig. 336. $TbRh_2Si_2$. Temperature dependence of (a) χ_m^{-1} and (b) χ_m near T_N [84 Q 1].

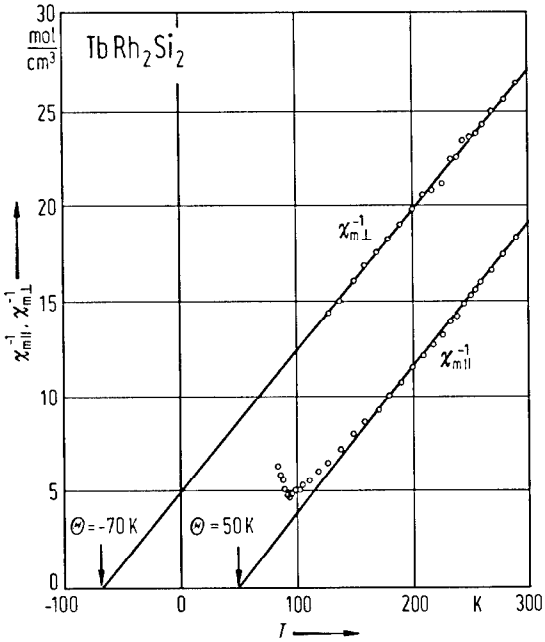

Fig. 337. $TbRh_2Si_2$. Single crystal. Temperature dependence of $\chi_{m\parallel}^{-1}$ and $\chi_{m\perp}^{-1}$ for directions parallel and perpendicular to the c axis, respectively [85 C 2].

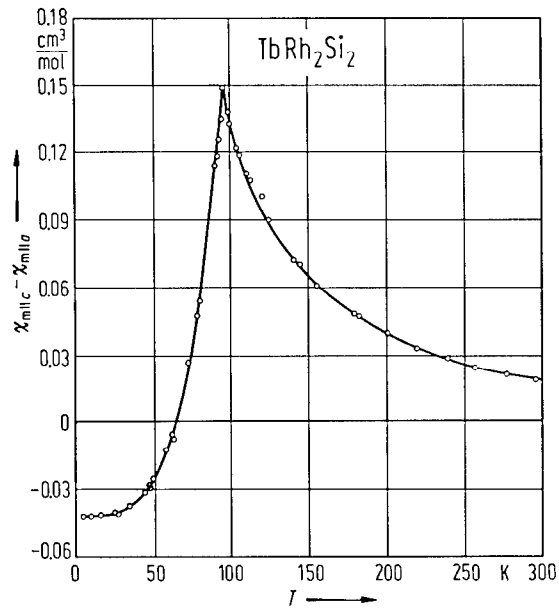

Fig. 338. $TbRh_2Si_2$. Temperature dependence of the differential magnetic susceptibility $\chi_{m\parallel c} - \chi_{m\parallel a}$ vs. temperature [85 C 2].

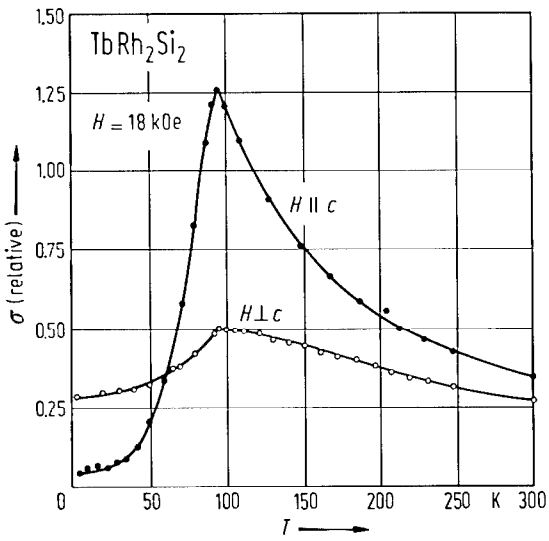

Fig. 339. $TbRh_2Si_2$. Temperature dependence of σ at 18 kOe perpendicular and parallel to the c axis [84 Q 1].

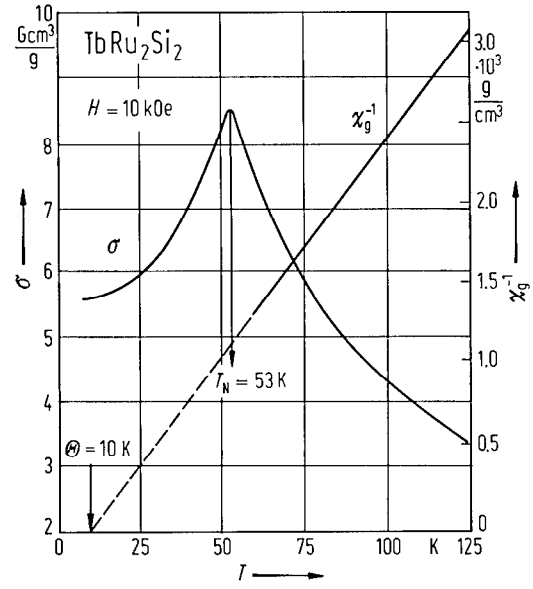

Fig. 340. $TbRu_2Si_2$. Temperature dependence of χ_g^{-1} and σ at 10 kOe [84 S 4].

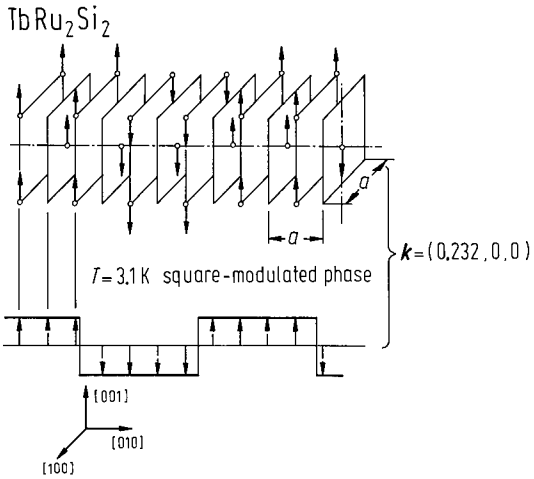

Fig. 341. $TbRu_2Si_2$. Schematic representation of magnetic moment alignment for the square-modulated phase of $TbRu_2Si_2$ [85 C 1]. For $TbRu_2Ge_2$, see [86 Y 1].

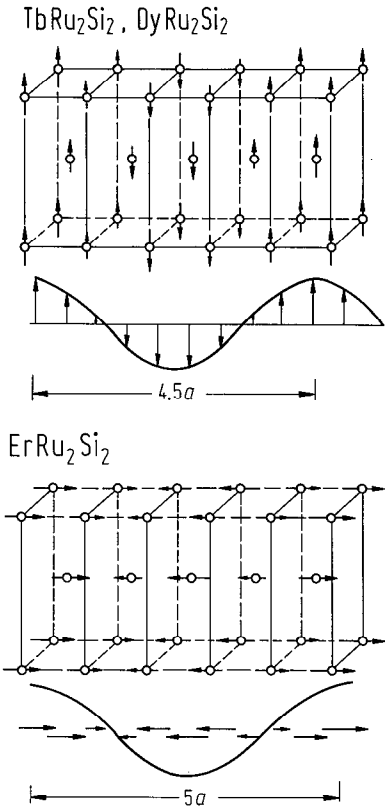

Fig. 342. RRu_2Si_2, R = Tb, Dy, Ho. Magnetic structure at 4.2 K [84 S 4].

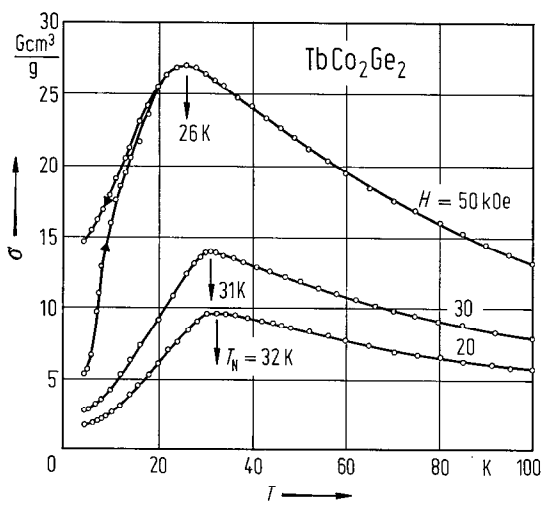

Fig. 343. $TbCo_2Ge_2$. Temperature dependence of σ at various magnetic fields [82 K 2].

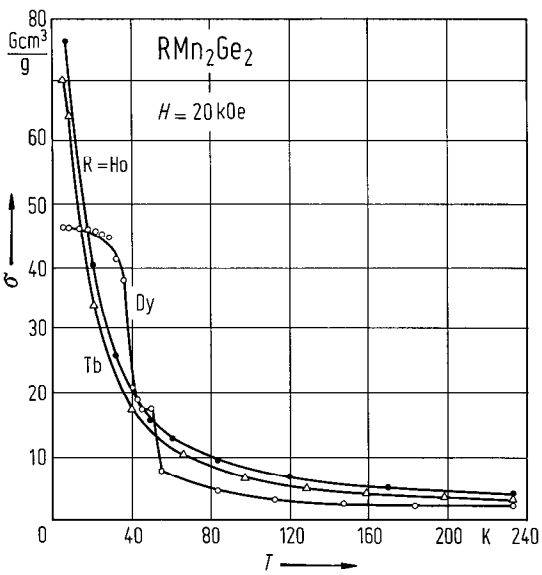

Fig. 344. RMn_2Ge_2, R = Tb, Dy, Ho. Temperature dependence of σ at 20 kOe [75 N 1].

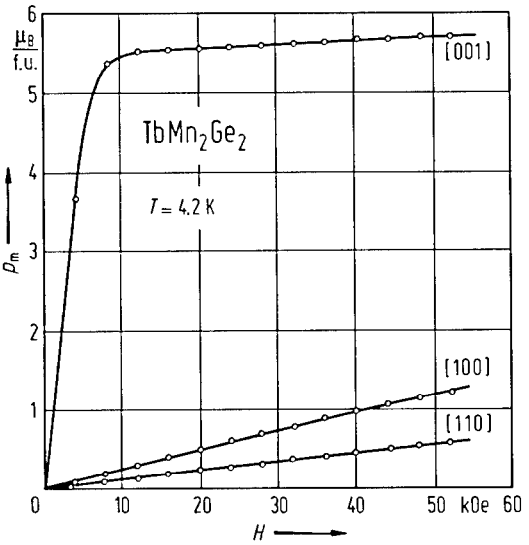

Fig. 345. $TbMn_2Ge_2$. Magnetic field dependence of p_m at 4.2 K along the principal axes [001], [100] and [110] of a single crystal [83 S 4].

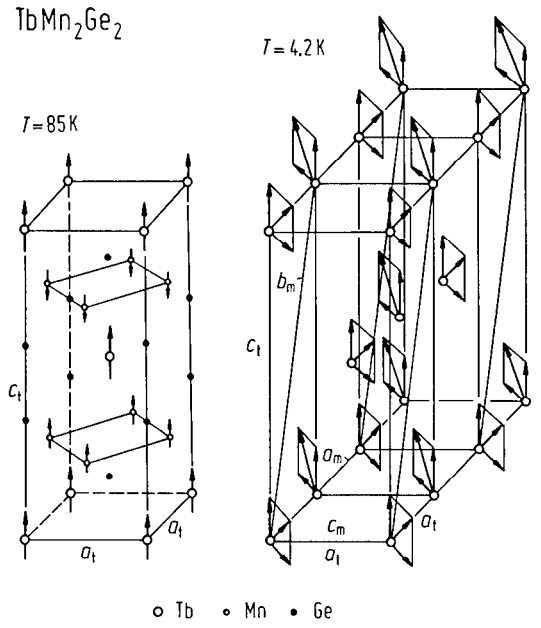

Fig. 346. $TbMn_2Ge_2$. Magnetic structure: tetragonal unit cell (a_t, c_t) with Tb and Mn sublattices at 85 K, and monoclinic unit cell (a_m, b_m, c_m) with Tb sublattices at 4.2 K [84 L 3].

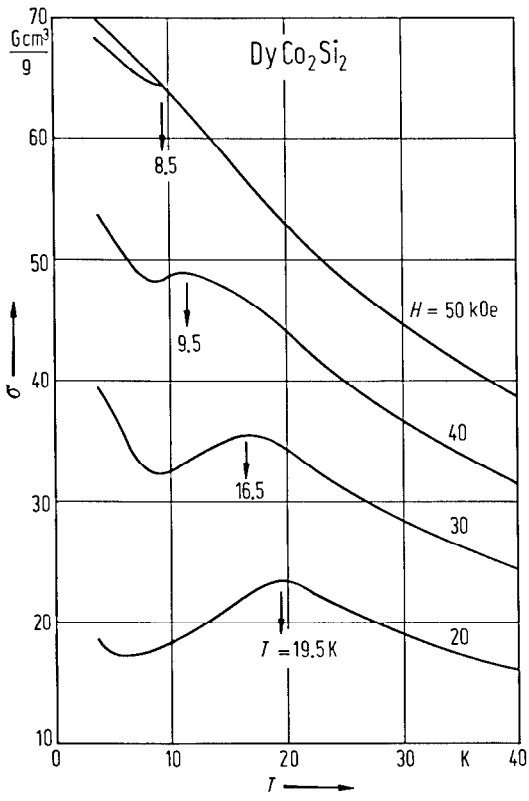

Fig. 347. $DyCo_2Si_2$. Temperature dependence of σ at various magnetic fields [82 K 2].

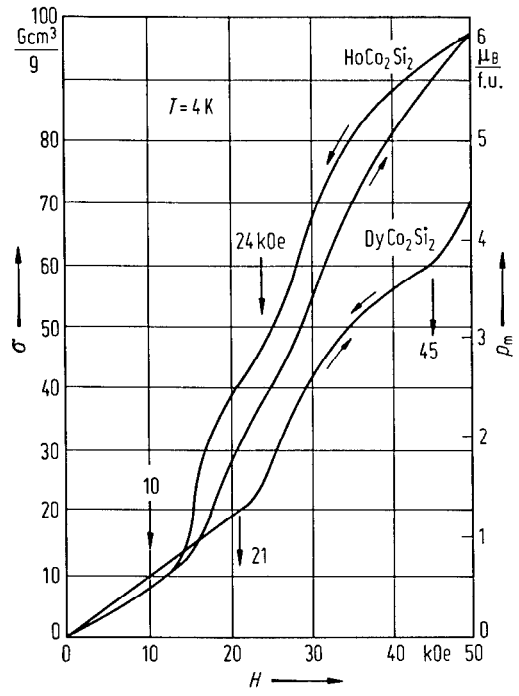

Fig. 348. $DyCo_2Si_2$, $HoCo_2Si_2$. Magnetic field dependence of σ and p_m at 4 K [82 K 2].

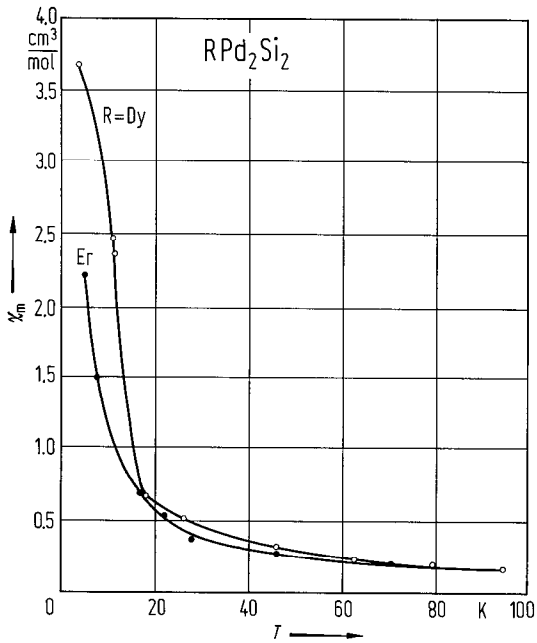

Fig. 349. $DyPd_2Si_2$, $ErPd_2Si_2$. Temperature dependence of χ_m [82 Y 1].

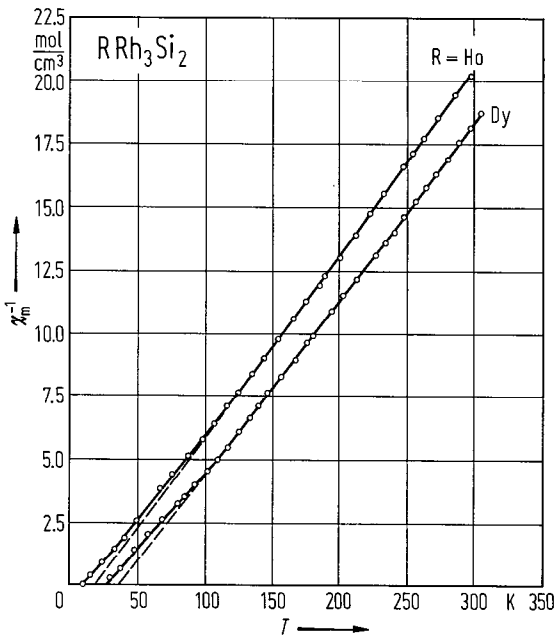

Fig. 350. $DyRh_3Si_2$, $HoRh_3Si_2$. Temperature dependence of χ_m^{-1} [81 C 1].

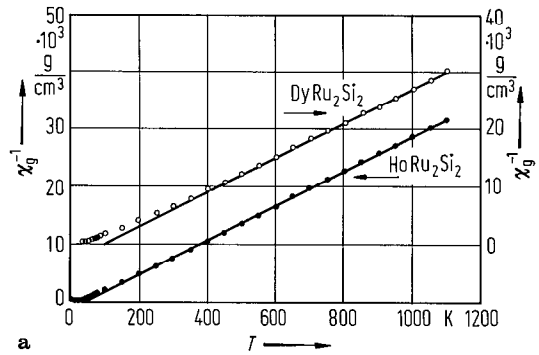

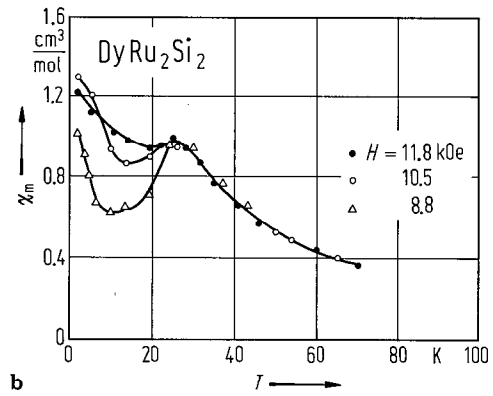

Fig. 351. $DyRu_2Si_2$, $HoRu_2Si_2$. (a) Temperature dependence of χ_g^{-1} and calculated least-squares fit. (b) Temperature dependence of χ_m at various magnetic fields showing antiferromagnetic ordering of $DyRu_2Si_2$ [83 H 1].

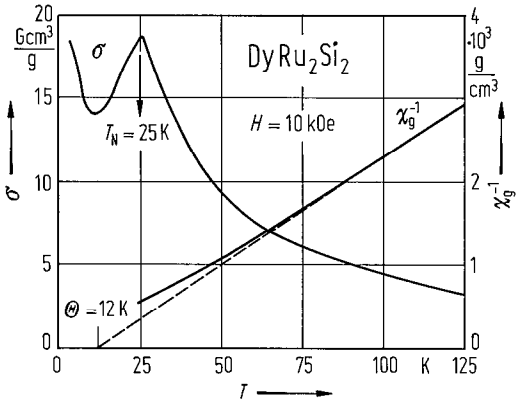

Fig. 352. $DyRu_2Si_2$. Temperature dependence of χ_g^{-1} and σ at 10 kOe [84 S 4].

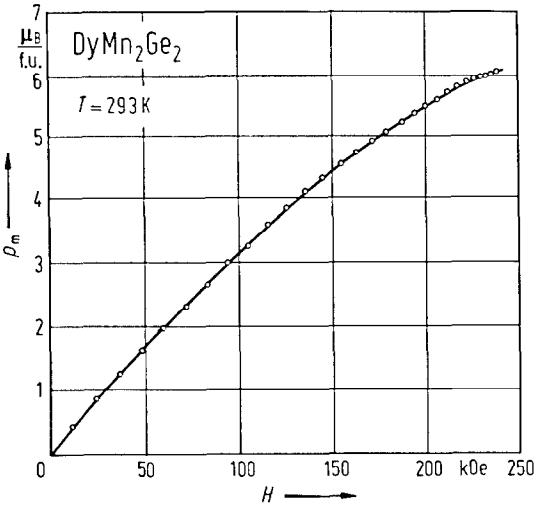

Fig. 353. $DyMn_2Ge_2$. Magnetic field dependence of p_m at 293 K [81 S 7].

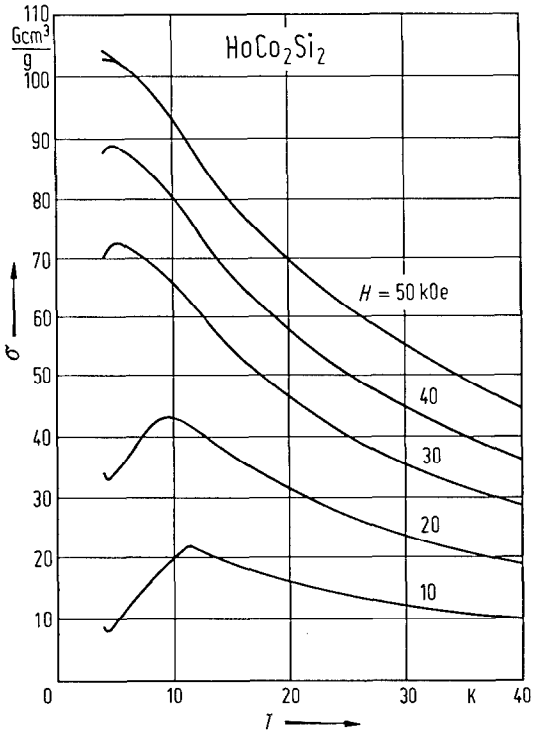

Fig. 354. $HoCo_2Si_2$. Temperature dependence of σ at various magnetic fields [82 K 2].

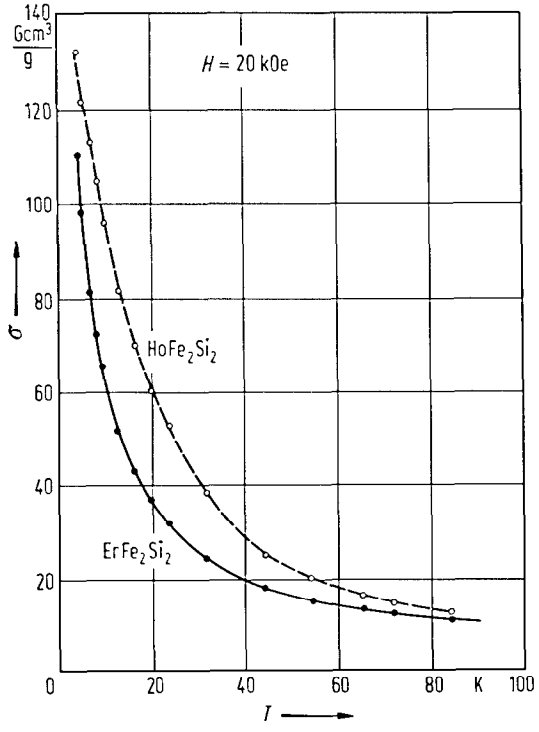

Fig. 355. $HoFe_2Si_2$, $ErFe_2Si_2$. Low-temperature dependence of σ at 20 kOe [76 S 1].

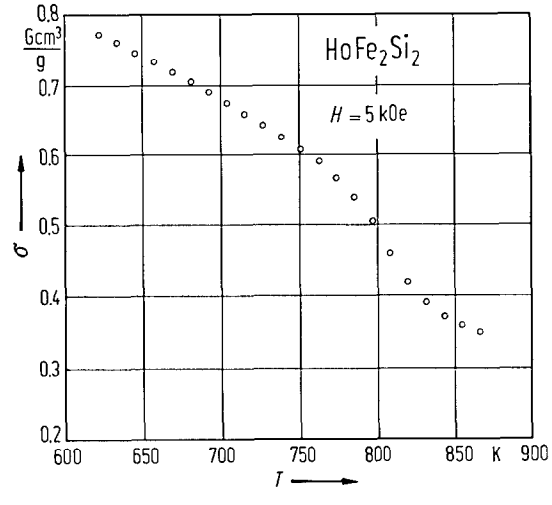

Fig. 356. $HoFe_2Si_2$. High-temperature dependence of σ at 5 kOe [76 S 1].

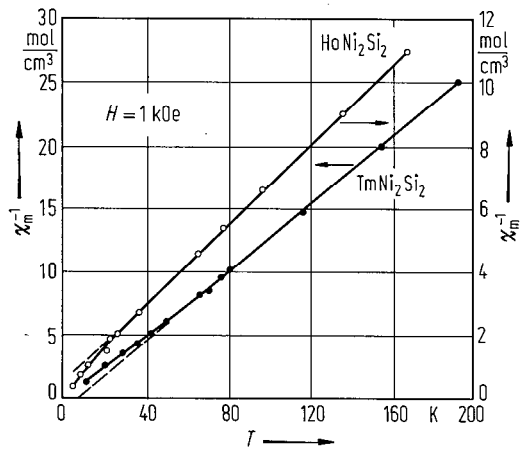

Fig. 357. $HoNi_2Si_2$, $TmNi_2Si_2$. Temperature dependence of χ_m^{-1} at 1 kOe [80 Y 1].

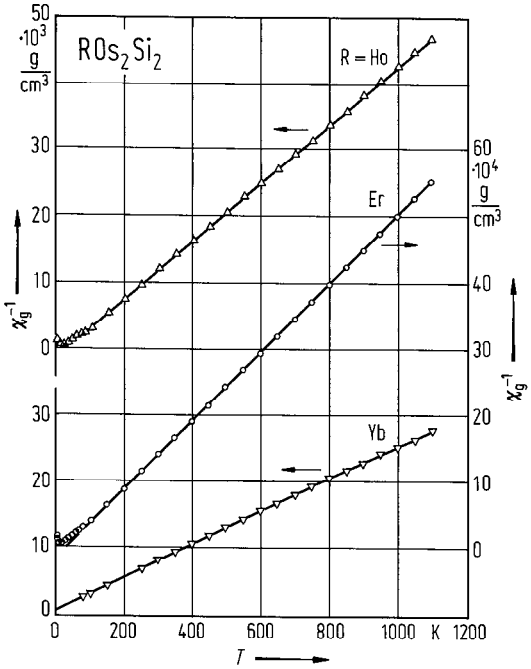

Fig. 358. ROs_2Si_2, R = Ho, Er, Yb. Temperature dependence of χ_g^{-1} and calculated least-squares fit (solid line) [83 H 2].

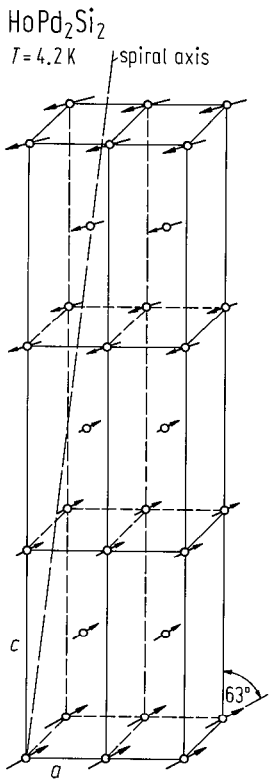

Fig. 359. $HoPd_2Si_2$. Magnetic structure at 4.2 K [85 L 2].

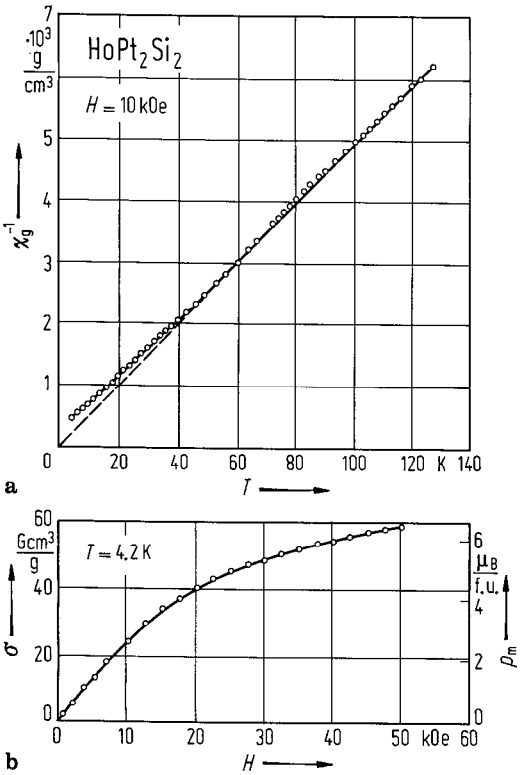

Fig. 360. $HoPt_2Si_2$. (a) Temperature dependence of χ_g^{-1} at 10 kOe and (b) magnetic field dependence of σ and p_m at 4.2 K [84 L 4].

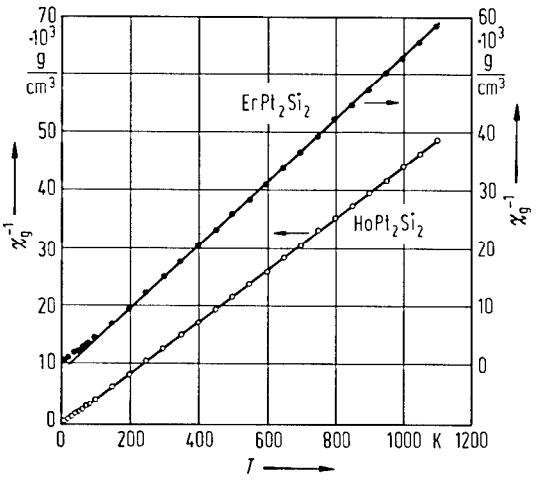

Fig. 361. $HoPt_2Si_2$, $ErPt_2Si_2$. Temperature dependence of χ_g^{-1} and calculated least-squares fit (solid line) [85 H 2].

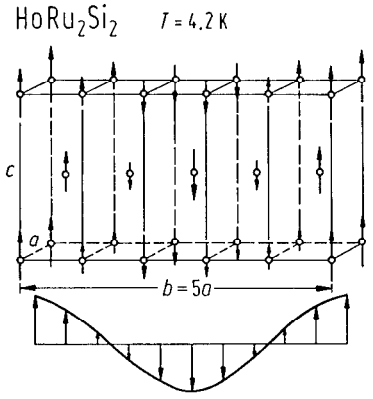

Fig. 362. $HoRu_2Si_2$. Schematic representation of the magnetic spin alignment at 4.2 K [83 S 6].

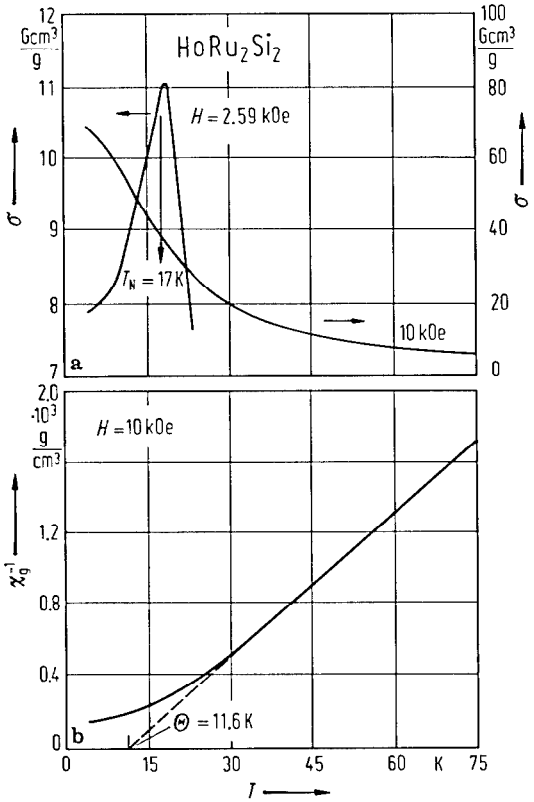

Fig. 363. $HoRu_2Si_2$. Temperature dependence of (a) σ at 2.59 and 10 kOe and (b) χ_g^{-1} at 10 kOe [84 S 4].

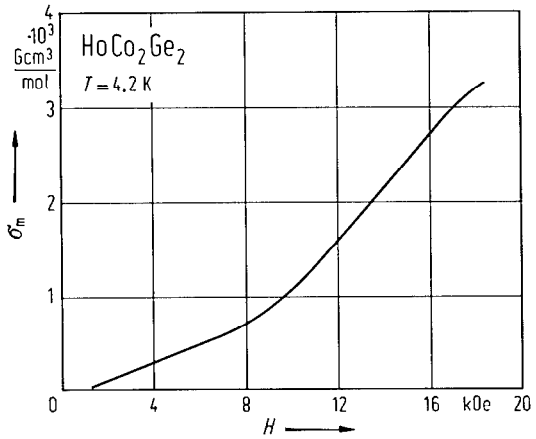

Fig. 364. $HoCo_2Ge_2$. Magnetic field dependence of σ_m at 4.2 K [73 M 1].

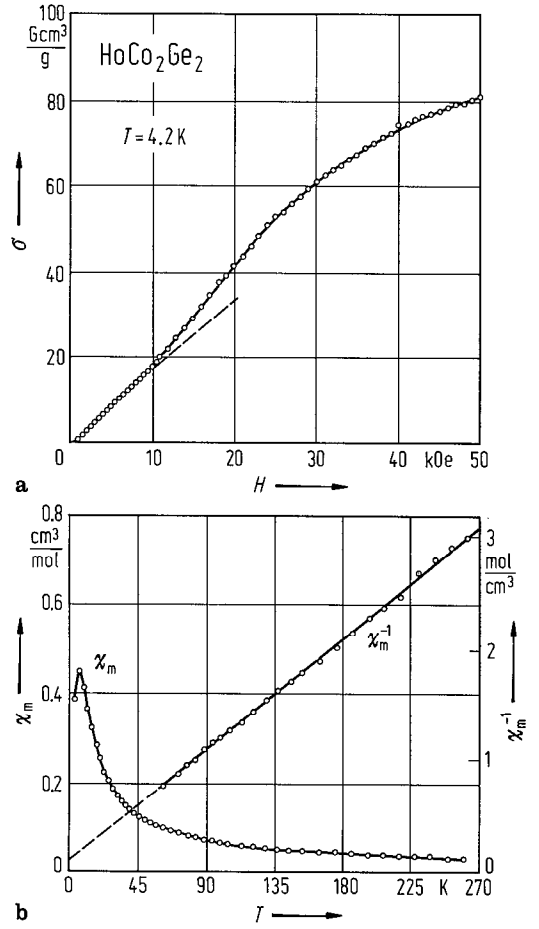

Fig. 365. $HoCo_2Ge_2$. (a) Magnetic field dependence of σ at 4.2 K and (b) temperature dependence of χ_m and χ_m^{-1} [82 K 2].

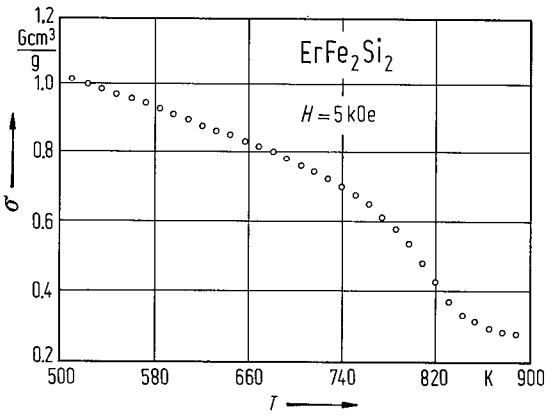

Fig. 366. $ErFe_2Si_2$. High-temperature dependence of σ at 5 kOe [76 S 1].

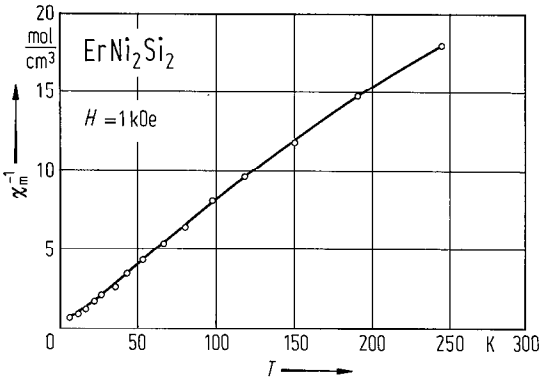

Fig. 367. $ErNi_2Si_2$. Temperature dependence of χ_m^{-1} at 1 kOe [80 Y 1].

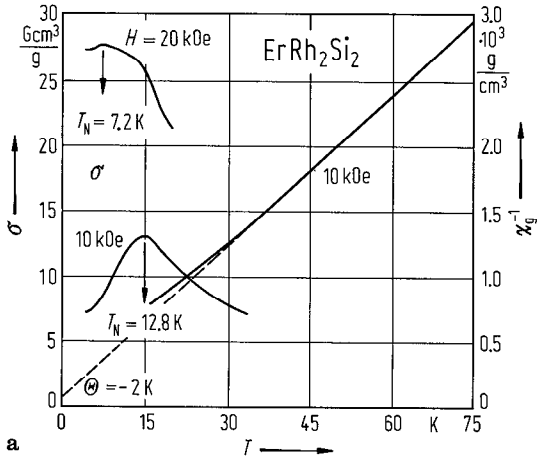

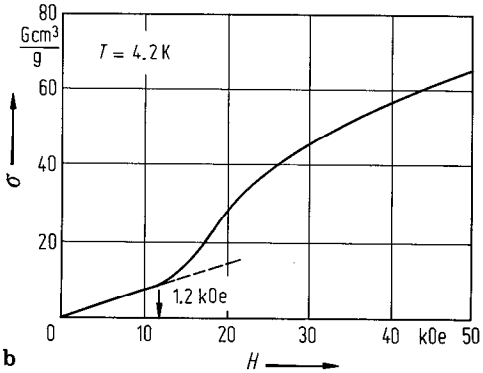

Fig. 368. $ErRh_2Si_2$. (a) Temperature dependence of χ_g^{-1} and σ at 10 and 20 kOe. (b) Magnetic field dependence of σ at 4.2 K [84 S 6].

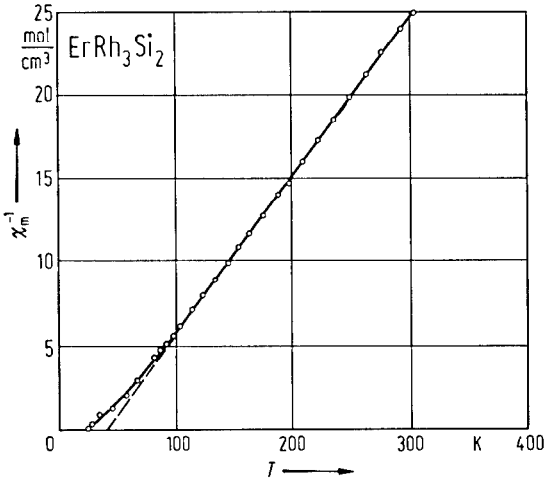

Fig. 369. $ErRh_3Si_2$. Temperature dependence of χ_m^{-1} [81 C 1].

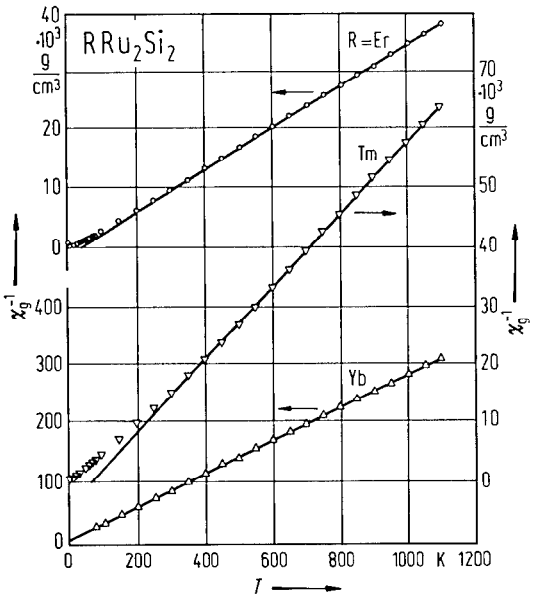

Fig. 370. RRu_2Si_2, R = Er, Tm, Yb. Temperature dependence of χ_g^{-1} and calculated least-squares fit [83 H 1].

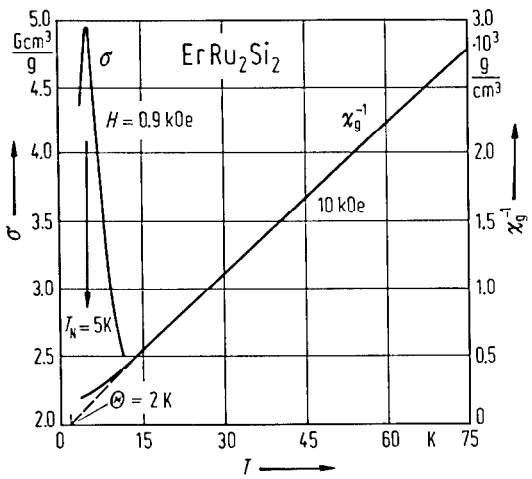

Fig. 371. $ErRu_2Si_2$. Temperature dependence of χ_g^{-1} at 10 kOe and σ at 0.9 kOe [84 S 4].

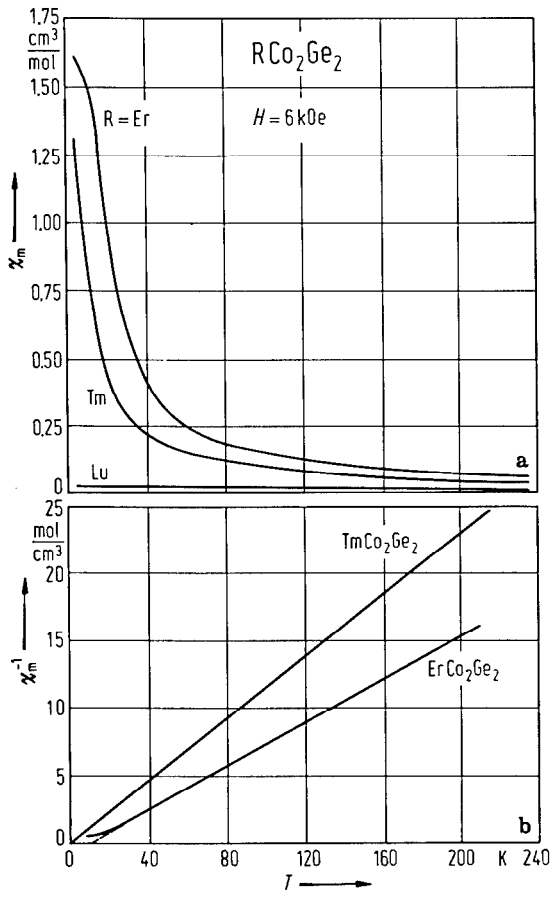

Fig. 372. RCo_2Ge_2, R = Er, Tm, Lu. Temperature dependence of (a) χ_m and (b) χ_m^{-1} at 6 kOe [73 M 1].

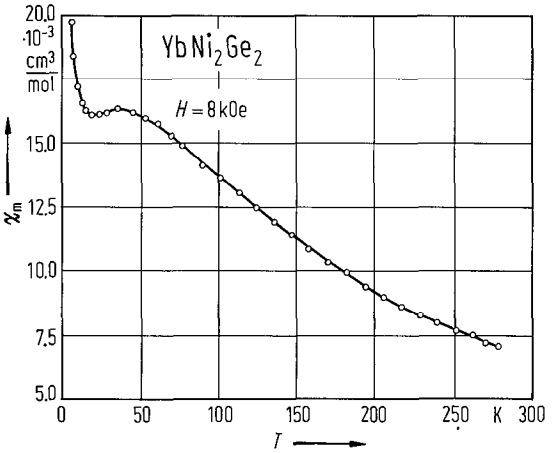

Fig. 373. $YbNi_2Ge_2$. Temperature dependence of χ_m at 8 kOe and calculated least-squares fit with Yb^{2+} ground state ($J=0$) and Yb^{3+} first excited state ($J=7/2$). For details, see caption to Fig. 214 [77 O 1].

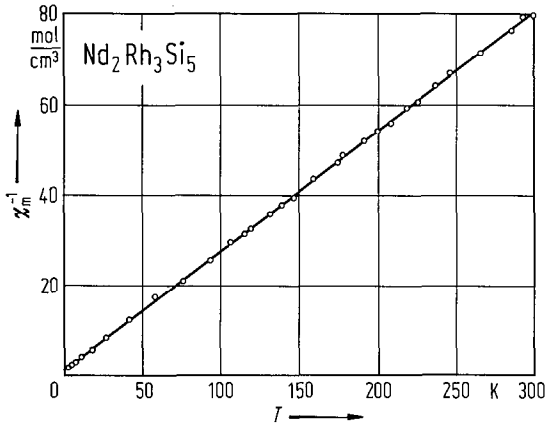

Fig. 375. $Nd_2Rh_3Si_5$. Temperature dependence of χ_m^{-1} [82 C 2].

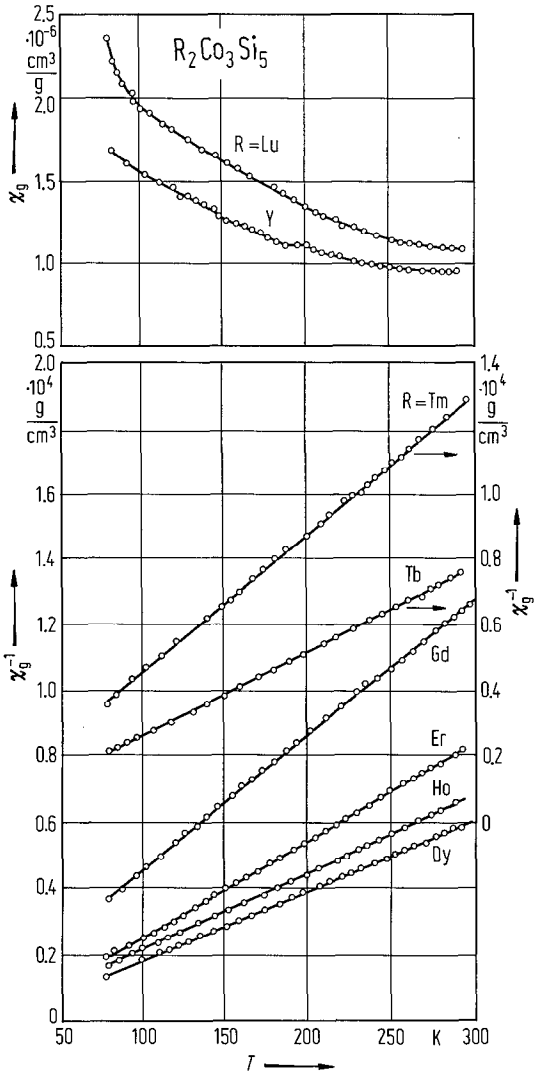

Fig. 374. $R_2Co_3Si_5$, R = Y, Gd, Tb, Dy, Ho, Er, Tm, Lu. Temperature dependence of χ_g and χ_g^{-1} [85 G 1].

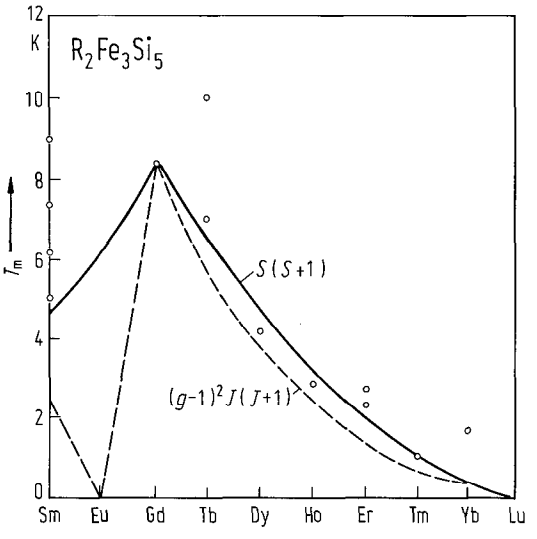

Fig. 376. $R_2Fe_3Si_5$, R = Sm, Gd, Tb, Dy, Ho, Er, Tm, Yb. Magnetic phase transition temperature T_m. The solid line indicates ordering temperatures expected if the effective magnetic moment on R varies as S and the dashed line indicates the ordering temperatures if the effective magnetic moment varies as J [83 V 1].

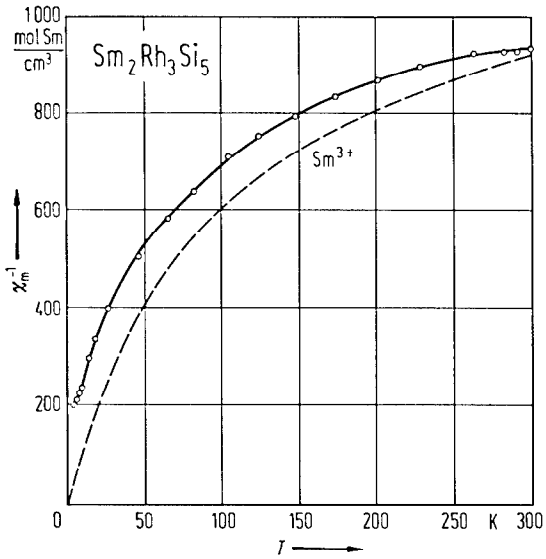

Fig. 377. $Sm_2Rh_3Si_5$. Temperature dependence of χ_m^{-1} experimental and for free Sm^{3+} ion (Van Vleck) [82 C 2].

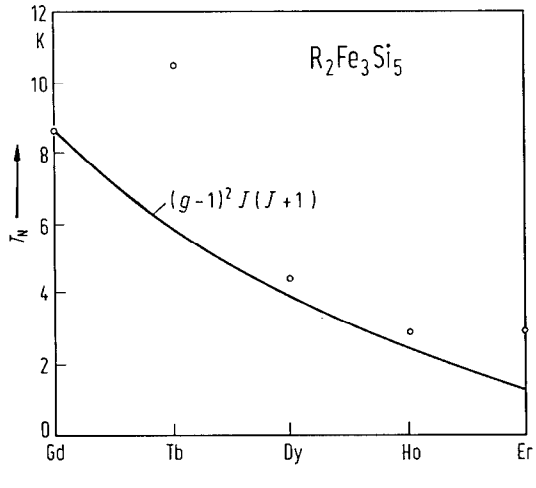

Fig. 378. $R_2Fe_3Si_5$, R = Gd, Tb, Dy, Ho, Er. Néel temperatures and the de Gennes curve scaled to Gd [81 B 1].

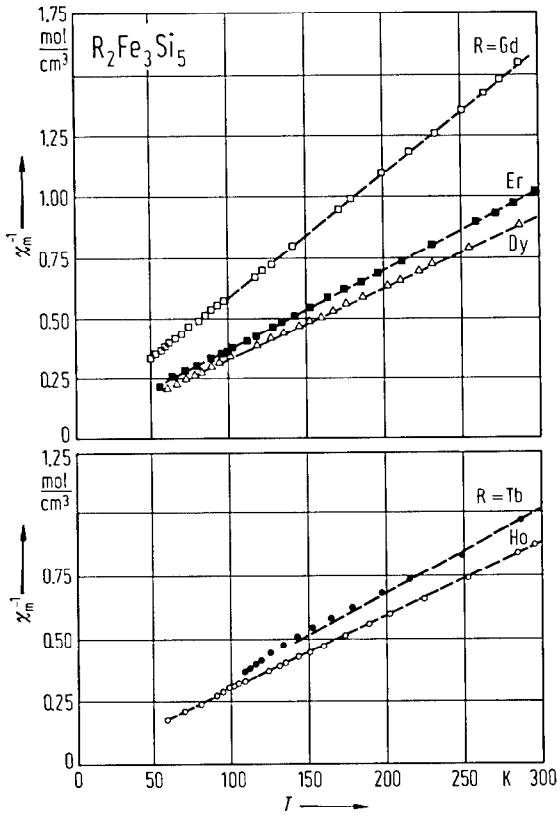

Fig. 379. $R_2Fe_3Si_5$, R = Gd, Er, Dy, Ho, Tb. Temperature dependence of χ_m^{-1} measured with the field parallel to the sample growth direction [81 B 1].

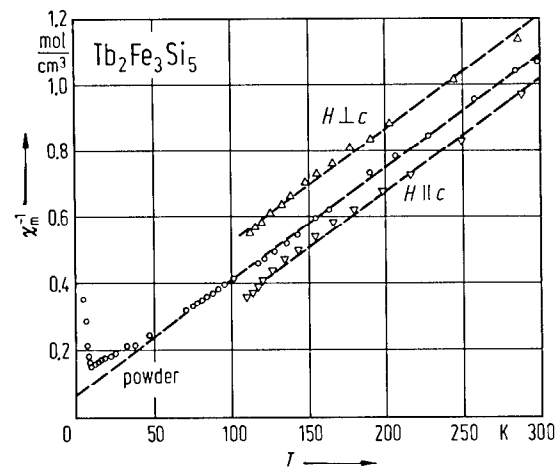

Fig. 380. $Tb_2Fe_3Si_5$. Temperature dependence of χ_m^{-1} for powder sample and parallel and perpendicular to the tetragonal [001] axis for a polycrystalline sample which showed directed [001] crystalline growth nucleating at the surface in contact with the Cu electrode of the arc furnace [81 B 1].

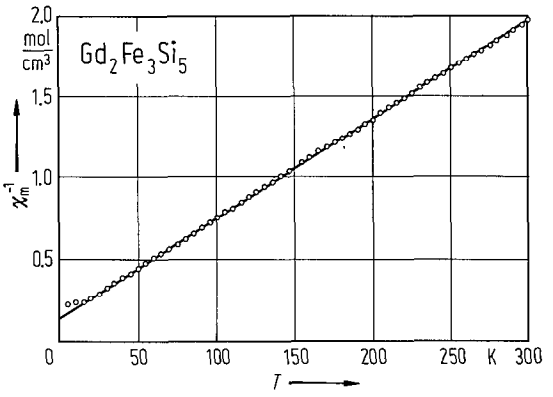

Fig. 381. $Gd_2Fe_3Si_5$. Temperature dependence of χ_m^{-1} for powdered sample [83 N 2].

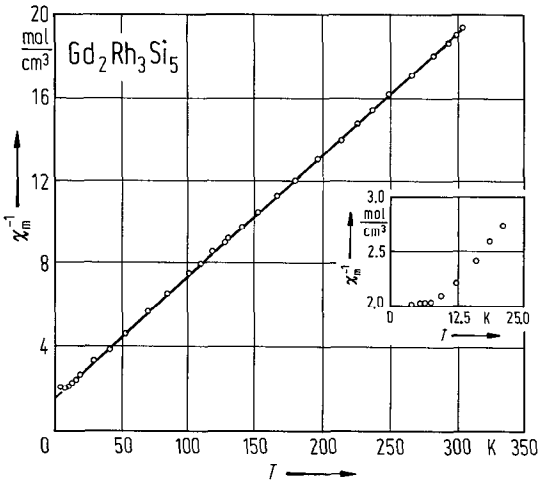

Fig. 382. $Gd_2Rh_3Si_5$. Temperature dependence of χ_m^{-1} [82 C 2].

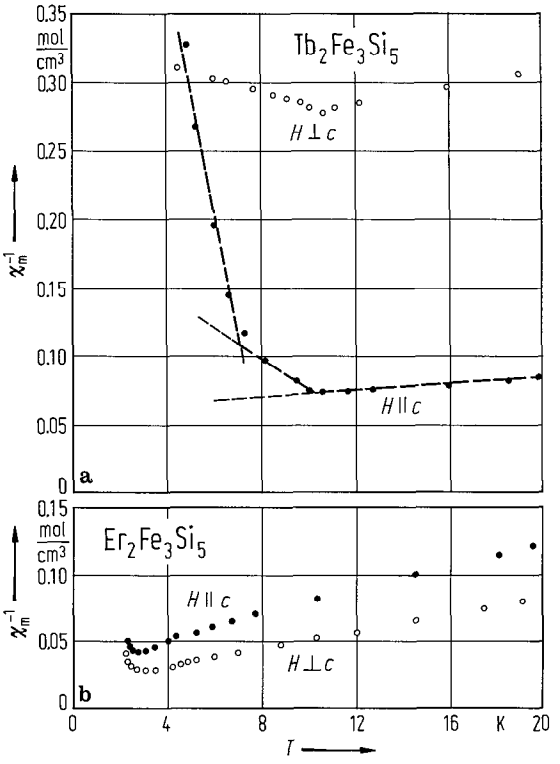

Fig. 383. $Tb_2Fe_3Si_5$, $Er_2Fe_3Si_5$. Low-temperature dependence of χ_m^{-1} for polycrystalline samples (see caption to Fig. 380) [81 B 1].

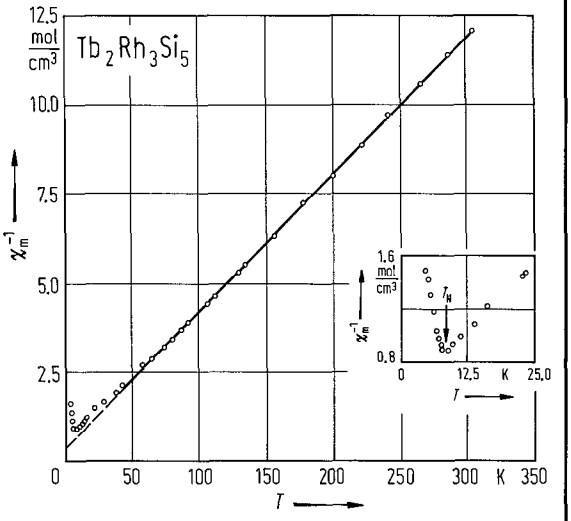

Fig. 384. $Tb_2Rh_3Si_5$. Temperature dependence of χ_m^{-1} [82 C 2].

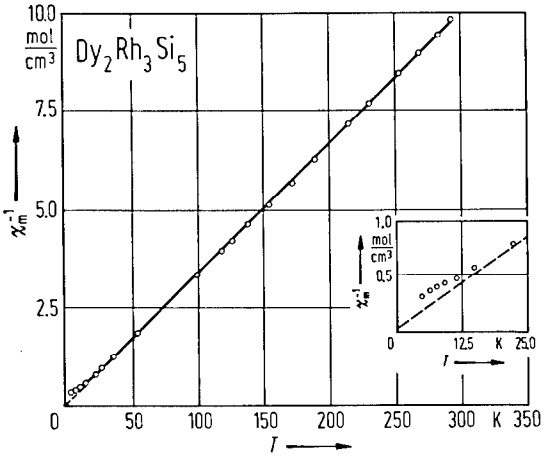

Fig. 385. $Dy_2Rh_3Si_5$. Temperature dependence of χ_m^{-1} [82 C 2].

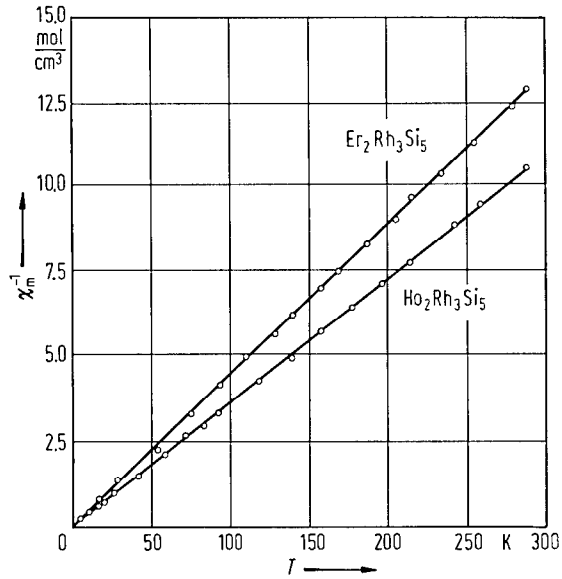

Fig. 386. $Ho_2Rh_3Si_5$, $Er_2Rh_3Si_5$. Temperature dependence of χ_m^{-1} [82 C 2].

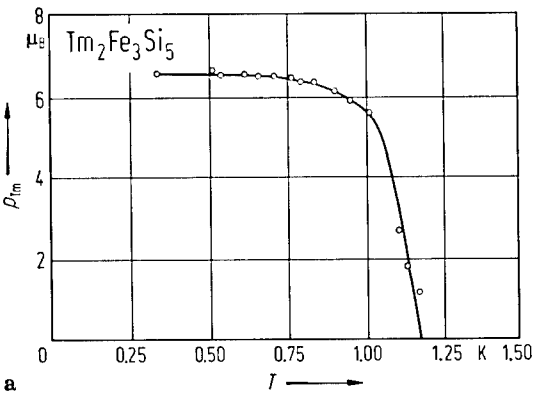

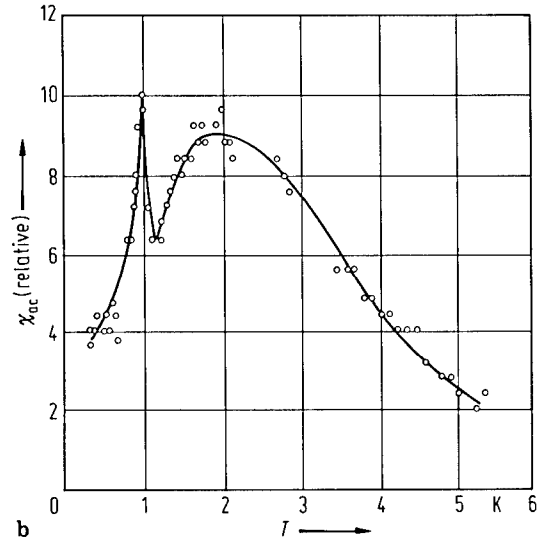

Fig. 387. $Tm_2Fe_3Si_5$. (a) Neutron diffraction study. Temperature dependence of the Tm magnetic moment calculated from the relative intensity of the (100) neutron diffraction peak. The Tm magnetic moment was normalized to the value of 6.5 μ_B found at 0.35 K. (b) Temperature dependence of χ_{ac} [85 M 1].

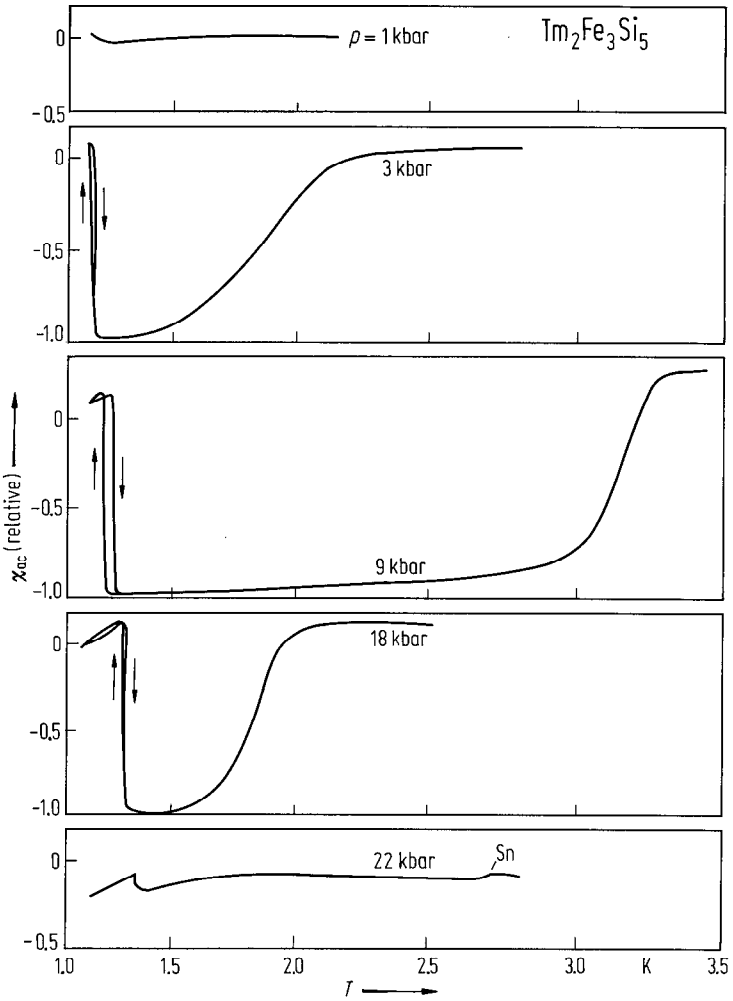

Fig. 388. $Tm_2Fe_3Si_5$. Low-temperature dependence of χ_{ac} at different pressures. The superconducting transition of a superconducting (Sn) manometer is indicated at 22 kbar [85 V 1].

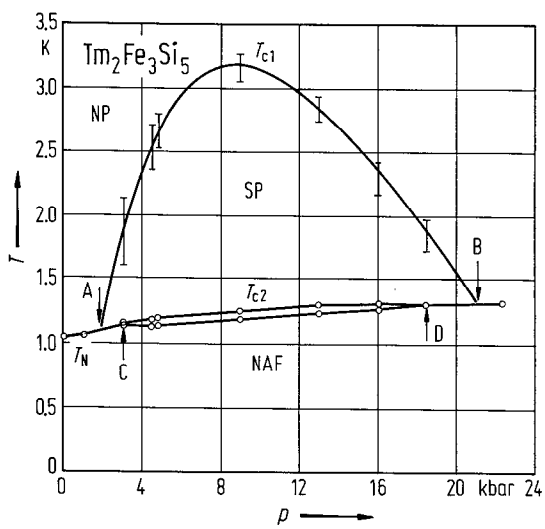

Fig. 389. $Tm_2Fe_3Si_5$. Low-temperature phase diagram. Phase transition temperatures are T_{c1}: normal paramagnetic (NP)$\rightleftharpoons$superconducting paramagnetic (SP), T_{c2}: SP$\rightleftharpoons$normal antiferromagnetic (NAF), and T_N: NP$\rightleftharpoons$NAF. A and B are multicritical points. Between C and D thermal hysteresis of about 50 mK is observed [85 V 1].

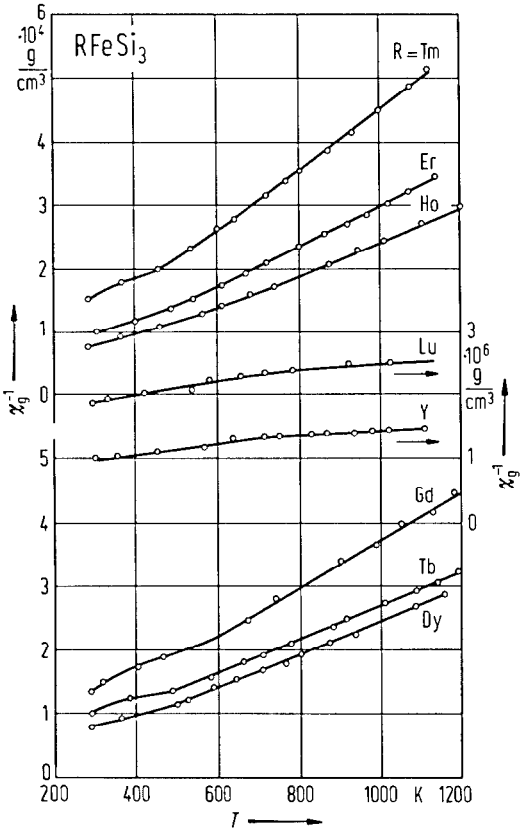

Fig. 390. $RFeSi_3$, R = Y, Gd, Tb, Dy, Ho, Er, Tm, Lu. Temperature dependence of χ_g^{-1} [78 G 1].

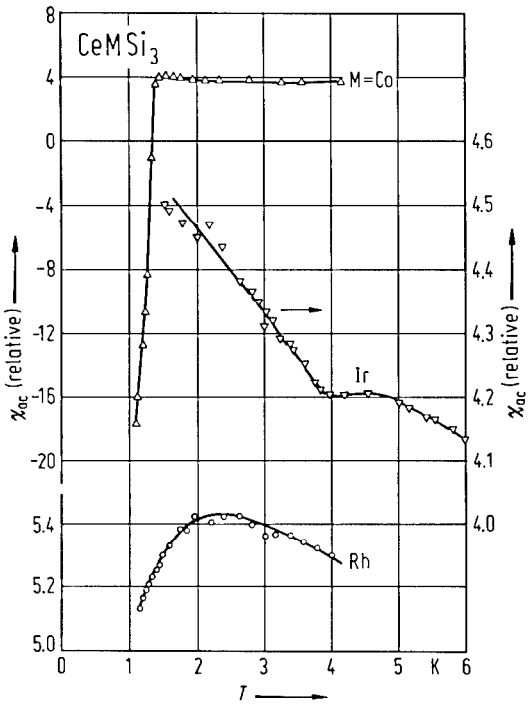

Fig. 392. $CeMSi_3$, M = Co, Ir, Rh. Low-temperature dependence of χ_{ac}. $CeCoSi_3$ shows superconductivity at 1.4 K [85 H 1].

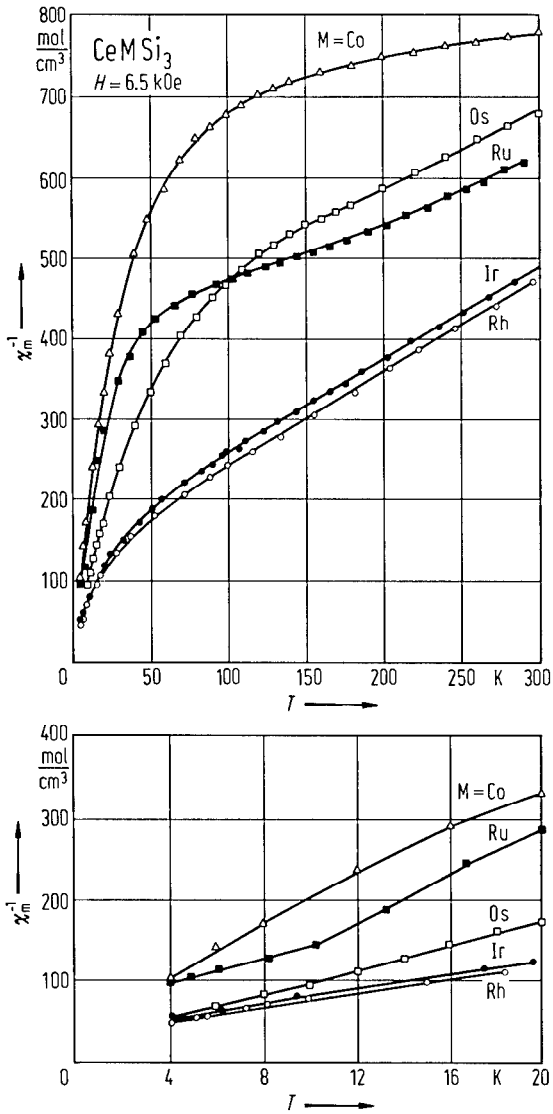

Fig. 391. $CeMSi_3$, M = Co, Ir, Os, Rh, Ru. Temperature dependence of χ_m^{-1} at 6.5 kOe [85 H 1].

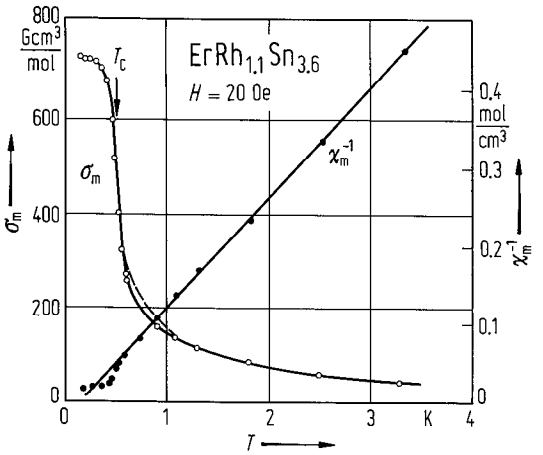

Fig. 393. $ErRh_{1.1}Sn_{3.6}$. Temperature dependence of χ_m^{-1} and σ_m at 20 Oe [81 A 1].

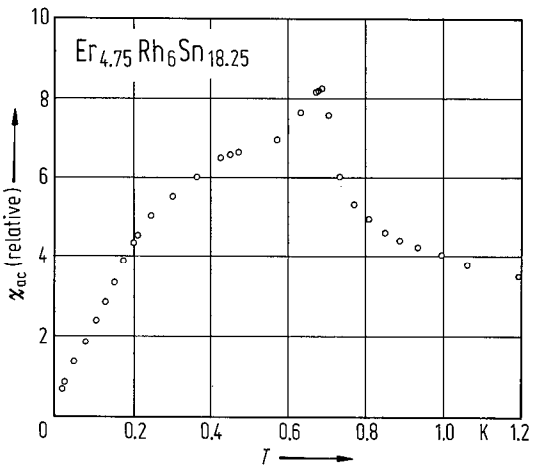

Fig. 396. $Er_{4.75}Rh_6Sn_{18.25}$. Single crystal. Low temperature dependence of χ_{ac} for a single crystal [84 M 3].

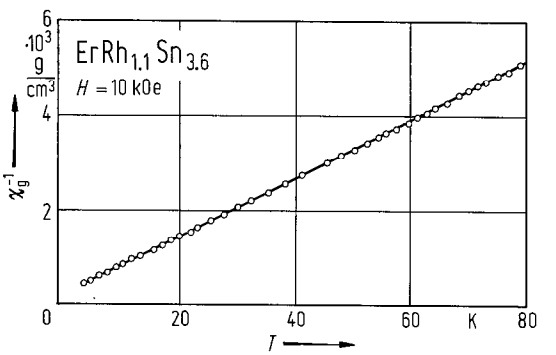

Fig. 394. $ErRh_{1.1}Sn_{3.6}$. Temperature dependence of χ_g^{-1} at 10 kOe [86 R 1].

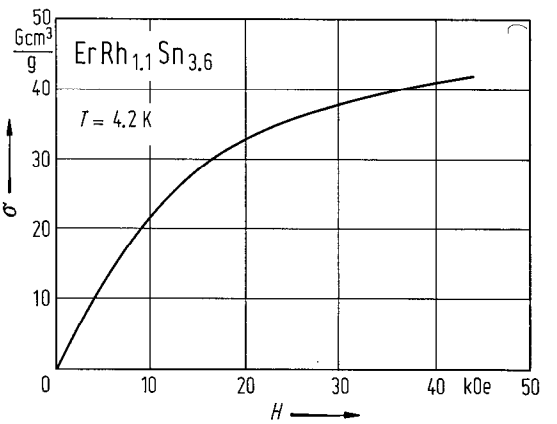

Fig. 395. $ErRh_{1.1}Sn_{3.6}$. Magnetic field dependence of σ at 4.2 K [86 R 1].

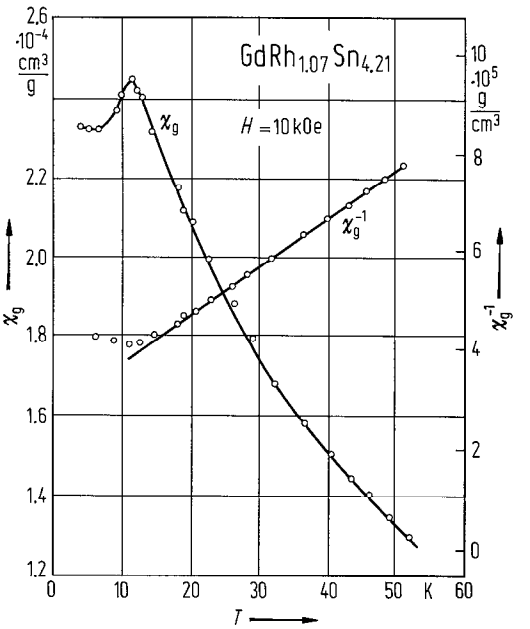

Fig. 397. $GdRh_{1.07}Sn_{4.21}$. Single crystal. Temperature dependence of χ_g and χ_g^{-1} at 10 kOe [86 R 2].

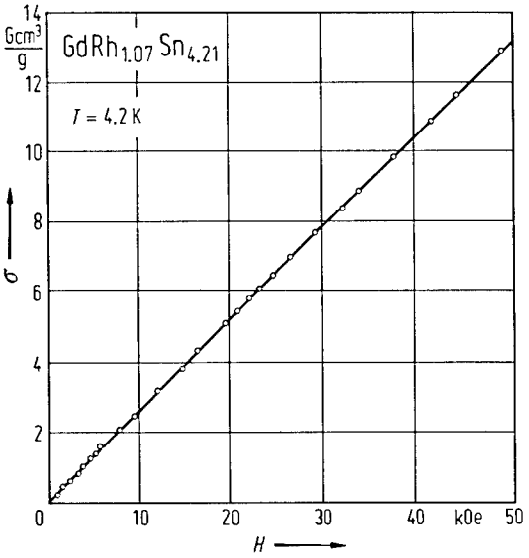

Fig. 398. $GdRh_{1.07}Sn_{4.21}$. Magnetic field dependence of σ at 4.2 K for a single crystal [86 R 2].

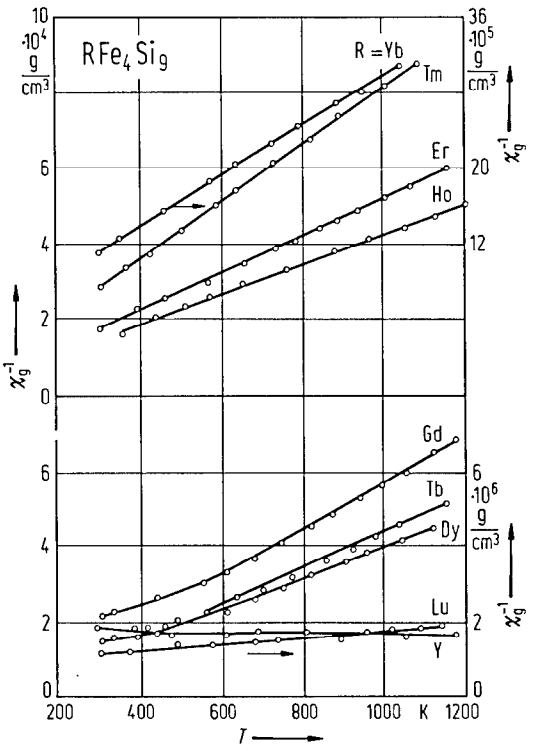

Fig. 399. RFe_4Si_9, R = Y, Gd, Tb, Dy, Ho, Er, Tm, Yb, Lu. Temperature dependence of χ_g^{-1} [78 G 1].

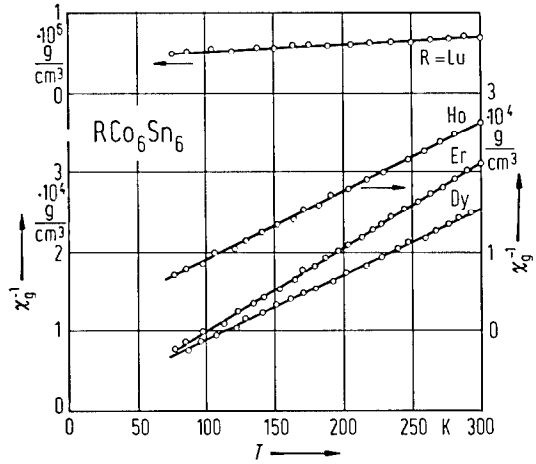

Fig. 400. RCo_6Sn_6, R = Dy, Ho, Er, Lu. Temperature dependence of χ_g^{-1} [84 S 2].

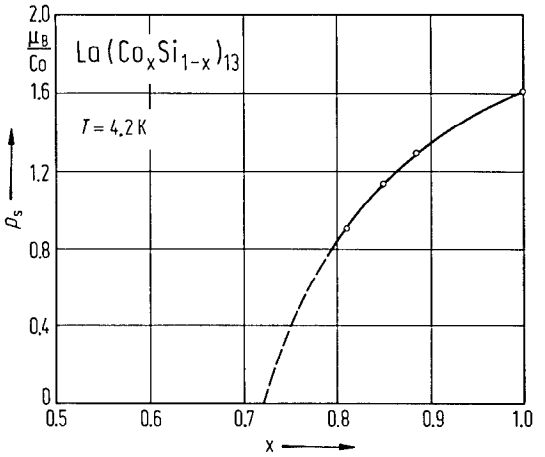

Fig. 401. $La(Co_xSi_{1-x})_{13}$. Composition dependence of the saturation magnetic moment p_s at 4.2 K [83 P 1].

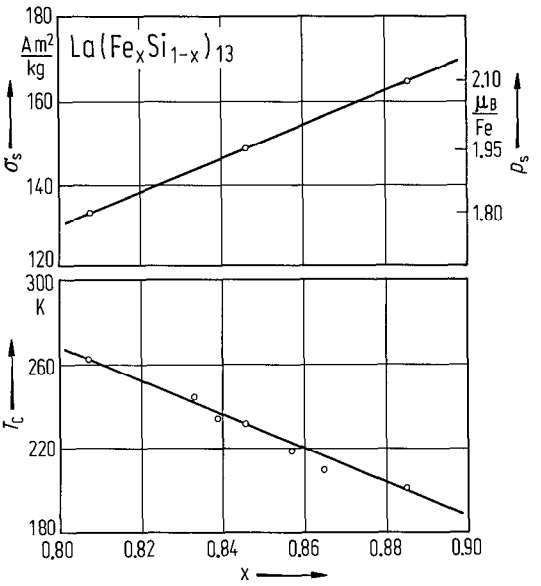

Fig. 402. $La(Fc_xSi_{1-x})_{13}$. Composition dependence of T_C and saturation magnetic moments p_s and σ_s [83 P 1].

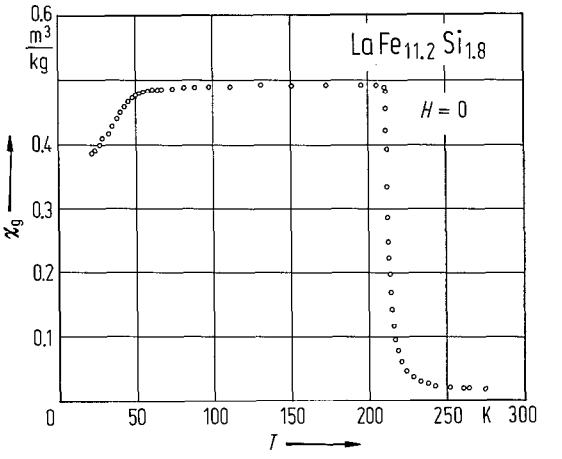

Fig. 403. $LaFe_{11.2}Si_{1.8}$. Temperature dependence of the zero-field magnetic susceptibility χ_g [83 P 1].

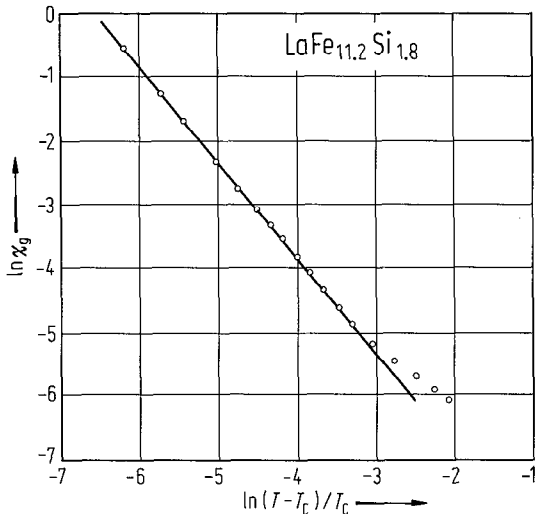

Fig. 404. $LaFe_{11.2}Si_{1.8}$. Zero-field magnetic susceptibility [$m^3\,kg^{-1}$] vs. $(T-T_C)/T_C$ on a logarithmic scale. The slope of the straight line corresponds to $\gamma=1.38$ ($\chi \propto (T-T_C)^{-\gamma}$) for the isotropic Heisenberg model [83 P 1].

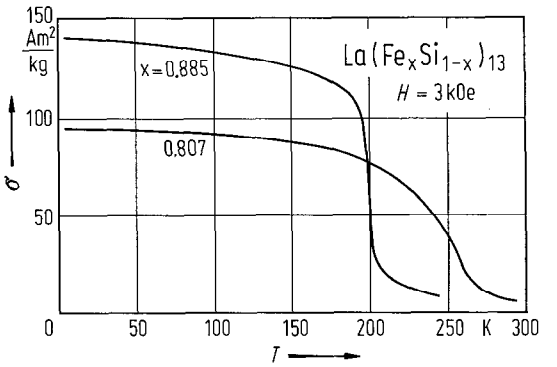

Fig. 405. $La(Fe_xSi_{1-x})_{13}$. Temperature dependence of σ at 3 kOe for x = 0.885 and 0.807 [83 P 1].

2.10.4 References for 2.10

General references

62 l 1 Lea, K.R., Leask, M.J.M., Wolf, P.W.: The Raising of Angular Momentum Degeneracy of f-Electron Terms by Cubic Crystal Fields. J. Phys. Chem. Solids **23** (1962) 1381.

64 h 1 Hutchings, M.T.: Point-Charge Calculations of Energy Levels of Magnetic Ions in Crystalline Electric Fields. Solid State Physics, Advances in Research and Applications (Seitz, F., Turnbull, D., eds.), New York, London: Academic Press, Vol. 16, **1964**, p. 227.

71 t 1 Taylor, K.N.R.: Intermeatllic Rare-Earth Compounds. Adv. Phys. **20** (1971) 551.

72 t 1 Taylor, K.N.R., Darby, M.I.: Physics of Rare Earth Solids, Chapman and Hall Ltd. London **1972**.

73 w 1 Wallace, W.E.: Rare Earth Intermetallics. New York, London: Acad. Press Inc. **1973**.

79 b 1 Buschow, K.H.J.: Intermetallic Compounds of Rare-Earth and Non-magnetic Metals. Rep. Progr. Phys. **42** (1979) 1373.

79 i 1 Iandelli, A., Palenzona, A.: Crystal Chemistry of Intermetallic Compounds. Handbook on the Physics and Chemistry of Rare Earths (Gschneidner jr., K.A., Eyring, L., eds.), Amsterdam: North-Holland Publ. Co. Vol. 2, **1979**, p. 1.

79 k 1 Kirchmayr, H.R., Poldy, C.A.: Magnetic Properties of Intermetallic Compounds of Rare Earth Metals. Handbook on the Physics and Chemistry of Rare Earths (Gschneidner jr., K.A., Eyring, L., eds.), Amsterdam: North-Holland Publ. Co. Vol. 2, **1979**, p. 55.

80 b 1 Buschow, K.H.J.: Rare Earth Compounds in Ferromagnetic Materials. A Handbook on the Properties of Magnetically Ordered Substances, (Wohlfarth, E.P., ed.), Amsterdam: North-Holland Publ. Co., Vol. 1, **1980**, p. 297.

Special references

58 M 1 Matthias, B.T., Corenzwit, E., Zachariasen, W.H.: Phys. Rev. **112** (1958) 89.

59 V 1 Vickery, R.C., Sedlacek, R., Ruben, A.: J. Chem. Soc. **104** (1959) 503.

65 T 1 Tsuchida, T., Wallace, W.E.: J. Chem. Phys. **43** (1965) 3811.

66 B 1 Buschow, K.H.J., Fast, J.F.: Phys. Status Solidi **16** (1966) 467.

66 P 1 Palenzona, A.: J. Less-Common Met. **10** (1966) 290.

66 S 1 Sekizawa, K.: J. Phys. Soc. Jpn. **21** (1966) 1137.

66 S 2 Sekizawa, K., Yasukochi, K.: J. Phys. Soc. Jpn. **21** (1966) 274.

66 Y 1 Yaguchi, K.: J. Phys. Soc. Jpn. **21** (1966) 405.

67 A 1 Atoji, M.: J. Chem. Phys. **46** (1967) 1891.

67 B 1 Buschow, K.H.J., Fast, J.F.: Phys. Status Solidi **21** (1967) 593.

67 H 1 Holtzberg, F., Gambino, R.J., McGuire, T.R.: J. Phys. Chem. Solids **28** (1967) 2283.

68 A 1 Atoji, M.: J. Chem. Phys. **48** (1968) 3384.

69 A 1 Atoji, M.: J. Chem. Phys. **51** (1969) 3872.

69 N 1 Narasimhan, K.S.V.L., Steinfink, H., Ganapathy, E.V.: J. Appl. Phys. **40** (1969) 51.

70 A 1 Atoji, M.: J. Chem. Phys. **52** (1970) 6431.

70 C 1 Czopnik, A., Kletowski, Z., Staliński, B.: Phys. Status Solidi (a) **3** (1970) K 263.

70 H 1 Havinga, E.E., Damsma, H., van Maaren, M.H.: J. Phys. Chem. Solids **31** (1970) 2653.

70 N 1 Nguyen van Nhung, Laforest, J., Sivardiere, J.: Solid State Commun. **8** (1970) 23.

71 N 1 Nguyen van Nhung, Barlet, A., Laforest, J.: J. Phys. (Paris) **32** (1971) C 1-1133.

71 W 1 Welsh, L.B., Toxen, A.M., Gambino, R.J.: Phys. Rev. B **4** (1971) 2921.

72 A 1 Atoji, M.: J. Chem. Phys. **57** (1972) 2410.

72 F 1 Felner, I., Mayer, I., Grill, A., Schieber, M.: Solid State Commun. **11** (1972) 1231.

73 F 1 Felner, I., Schieber, M.: Solid State Commun. **13** (1973) 457.

73 L 1 Lethuillier, P., Pierre, J., Fillion, G., Barbara, B.: Phys. Status Solidi (a) **15** (1973) 613.

73 L 2 Lethuillier, P., Quezel-Ambrunaz, G., Percheron, A.: Solid State Commun. **12** (1973) 105.

73 M 1 McCall, W.M., Narasimhan, K.S.V.L.,, Butera, R.A.: J. Appl. Phys. **44** (1973) 4724.

73 P 1 Pinto, H., Shaked, H.: Phys. Rev. B **7** (1973) 3261.

74 B 1 Bauminger, E.R., Felner, I., Froindlich, D., Grill, A., Lebenbaum, D., Mayer, I., Nowik, I., Ofer, S., Schieber, M.: Proc. Int. Conf. Magn. ICM-73 Publ. House "Nauka" Moscov Vol. V (1974) 56.

74 S 1 Staliński, B., Czopnik, A., Iliew, N., Mydlarz, T.: Proc. Int. Conf. Magn. ICM-73 Publ. House "Nauka" Moscov Vol. V (1974) 349.

75 F 1 Felner, I., Mayer, I., Grill A., Schieber, M.: Solid State Commun. **16** (1975) 1005.
75 L 1 Lethuillier, P., Pierre, J., Knorr, K., Drexel, W.: J. Phys. (Paris) **36** (1975) 329.
75 M 1 McCallum, R.W., Fertig, W.A., Luengo, C.A., Maple, M.B., Bucher, E., Maita, J.P., Sweedler, A.R., Mattix, L., Fulde, P., Keller, J.: Phys. Rev. Lett. **34** (1975) 1620.
75 N 1 Narasimhan, K.S.V.L., Rao, V.U.S., Bergner, R.L., Wallace, W.E.: J. Appl. Phys. **46** (1975) 4957.
75 S 1 Sales, B.C., Wohlleben, D.K.: Phys. Rev. Lett. **35** (1975) 1240.
75 S 2 Staliński, B., Kletowski, Z., Henkie, Z.: Bull. Acad. Pol. Sci. Ser. Sci. Chim. **XXIII** (1975) 827.
76 G 1 Ganapathy, E.V., Kugimiya, K., Steinfink, H., Tchernev, D.I.: J. Less-Common Met. **44** (1976) 245.
76 L 1 Lethuillier, P., Chaussy, J.: J. Phys. (Paris) **37** (1976) 123.
76 L 2 Lethuillier, P., Chaussy, J.: Phys. Rev. B **13** (1976) 3132.
76 S 1 Sankar, S.G., Malik, S.K., Rao, V.U.S., Obermyer, R.: AIP Conf. Proc. **34** (1976) 236.
77 B 1 Beille, J., Bloch, D., Voiron, J., Parisot, G.: Physica **86–88** (1977) 231.
77 B 2 Borchi, E., de Gennaro, S., Pelosi, G., Rettori, A.: J. Magn. Magn. Mater. **5** (1977) 325.
77 O 1 Oesterreicher, H., Parker, F.T.: Phys. Rev. B **16** (1977) 5009.
78 A 1 Atoji, M.: J. Solid State Chem. **26** (1978) 51.
78 B 1 Ballestracci, M.R., Astier, G.: C.R. Acad. Sci. (Paris) Ser. B **286** (1978) 109.
78 F 1 Felner, I., Nowik, I.: J. Phys. Chem. Solids **39** (1978) 767.
78 G 1 Gladyshevskij, E.I., Bodak, O.I., Jarovets, V.I., Gorolenko, Yu.K., Skolozdra, R.V.: Ukr. Fiz. Zh. (USSR) **23** (1978) 77.
78 S 1 Siek, S., Szytuła, A., Leciejewicz, J.: Phys. Status Solidi (a) **46** (1978) K 101.
79 B 1 Buschow, K.H.J., Goebel, U., Dormann, E.: Phys. Status Solidi (b) **93** (1979) 607.
79 D 1 DeLong, L.E., Guertin, R.P., Foner, S.: Solid State Commun. **32** (1979) 833.
79 G 1 Görlich, E.A., Hrynkiewicz, A.Z., Latka, K., Kmieć, R., Szytuła, A., Tomala, K.: J. Phys. (Paris) **40** (1979) C 2–656.
79 I 1 Iandelli, A., Palenzona, A., Olcese, G.L.: J. Less-Common Met. **64** (1979) 213.
79 O 1 Obermyer, R., Sankar, S.G., Rao, V.U.S.: J. Appl. Phys. **50** (1979) 2312.
79 P 1 Pinto, H., Melamud, M., Gurewitz, E.: Acta Crystallogr. A **40** (1979) 533.
79 S 1 Sakai, T., Adachi, G.-y., Shiokawa, J.: J. Appl. Phys. **50** (1979) 3592.
79 S 2 Sakai, T., Adachi, G.-y., Shiokawa, J.: Mater. Res. Bull. **14** (1979) 791.
79 S 3 Schobinger-Papamantellos, P., Niggli, A.: J. Phys. (Paris) **40** (1979) C 5–156.
79 S 4 Siek, S., Szytuła, A.: J. Phys. (Paris) **40** (1979) C 5–162.
79 S 5 Stassis, C., Loong, C.-K., Harmon, B.N., Liu, S.H., Moon, R.M.: J. Appl. Phys. **50** (1979) 7567.
79 S 6 Stassis, C., Loong, C.-K., McMasters, O.D., Moon, R.M.: J. Appl. Phys. **50** (1979) 2091.
80 B 1 Barmin, S.M., Emelyanov, D.A., Krentsis, R.P., Geld, P.V.: Fiz. Tverd. Tela (SSSR) **22** (1980) 1224 (Sov. Phys. Solid State **22** (1980) 714).
80 B 2 Barz, H.: Mater. Res. Bull. **15** (1980) 1489.
80 C 1 Cashion, J.D., Shenoy, G.K., Niarchos, D., Viccaro, P.J., Falco, Ch.M.: Phys. Lett. A **79** (1980) 454.
80 D 1 Dijkman, W.H., de Boer, F.R., de Chatel, P.F.: Physica B **98** (1980) 271.
80 G 1 Gross, W., Knorr, K., Murani, A.P., Buschow, K.H.J.: Z. Phys. B **37** (1980) 123.
80 N 1 Nowik, I., Felner, I., Seh, M.: J. Magn. Magn. Mater. **15–18** (1980) 1215.
80 S 1 Sakai, T., Adachi, G.-y., Shiokawa, J.: Mater. Res. Bull. **15** (1980) 1001.
80 S 2 Schobinger-Papamantellos, P.: The Rare Earth in Modern Science and Technology Vol. 2 (McCarthy, G.J., Rlyne, J.I., Silber, H.B., eds.), Plenum Publ. Comp. **2** (1980) 409.
80 S 3 Serdyuk, Y.V., Krentsis, R.P., Geld, P.V., Batalin, V.G.: Fiz. Tverd. Tela (USSR) **22** (1980) 2149.
80 S 4 Sereni, J.G.: J. Phys. F **10** (1980) 2831.
80 S 5 Skolozdra, R.V., Gorelenko, Yu.K., Bodak, O.I., Yarovets, V.I.: Ukr. Fiz. Zh. (USSR) **25** (1980) 1683.
80 S 6 Szytuła, A., Leciejewicz, J., Bińczycka, H.: Phys. Status Solidi (a) **58** (1980) 67.
80 Y 1 Yakinthos, J.K., Ikonomou, P.F.: Solid State Commun. **34** (1980) 777.
80 Y 2 Yakinthos, J.K., Routsi, Ch., Ikonomou, P.F.: J. Less-Common Met. **72** (1980) 205.
81 A 1 Andres, K., Remeika, J.P., Espinosa, G.P., Cooper, A.S.: Phys. Rev. B **23** (1981) 1179.
81 A 2 Atoji, M.: J. Chem. Phys. **75** (1981) 1434.
81 A 3 Atoji, M.: J. Chem. Phys. **74** (1981) 1893.
81 A 4 Atoji, M.: J. Chem. Phys. **74** (1981) 1898.
81 B 1 Braun, H.F., Segre, C.U., Acker, F., Rosenberg, M., Dey, S., Deppe, P.: J. Magn. Magn. Mater. **25** (1981) 117.
81 C 1 Chevalier, B., Cole, A., Lejay, P., Etourneau, J.: Mater. Res. Bull. **16** (1981) 1067.
81 C 2 Costa, G.A., Canepa, F., Olcese, G.L.: Solid State Commun. **40** (1981) 169.
81 K 1 Knorr, K., Loidl, A., Stuhn, B., Buevoz, J.L.: Z. Phys. B **41** (1981) 315.

81 S 1 Sakai, T., Adachi, G.-y., Yoshida, T., Shiokawa, J.: J. Chem. Phys. **75** (1981) 3027.
81 S 2 Sakai, T., Adachi, G.-y., Yoshida, T., Shiokawa, J.: J. Less-Common Met. **81** (1981) 91.
81 S 3 Schobinger-Papamantellos, P., Niggli, A.: J. Phys. Chem. Solids **42** (1981) 583.
81 S 4 Siek, S., Szytuła, A., Leciejewicz, J.: Solid State Commun. **39** (1981) 863.
81 S 5 Skolozdra, R.V., Mandzyk, V.M., Gorelenko, Yu.K., Tkachuk, V.D.: Fiz. Met. Metalloved. (SSSR) **52** (1981) 966.
81 S 6 Suematsu, H., Ohmatsu, K., Yoshizaki, R.: Solid State Commun. **38** (1981) 1103.
81 S 7 Szytuła, A., Szott, I.: Solid State Commun. **40** (1981) 199.
82 C 1 Chevalier, B., Cole, A., Lejay, P., Vlasse, M., Etourneau, J., Hagenmuller, P., Georges, R.: Mater. Res. Bull. **17** (1982) 251.
82 C 2 Chevalier, B., Lejay, P., Etourneau, J., Vlasse, M., Hagenmuller, P.: Mater. Res. Bull. **17** (1982) 1211.
82 K 1 Kido, H., Shimada, M., Koizumi, M.: Phys. Status Solidi (a) **70** (1982) K 23.
82 K 2 Kolenda, M., Szytuła, A., Zygmunt, A.: Proc. Int. Conf. on Crystal Field and Structural Effects in f-electron Systems, Wrocław 1981 (Guertin, R.P., Suski, W., Zolnierek, Z., eds.), Plenum, New York **1982**, p. 309.
82 M 1 Marin, P., Schmitt, D., du Tremolet de Lacheisserie, E.: J. Magn. Magn. Mater. **30** (1982) 257.
82 M 2 Moodenbaugh, A.R., Cox, D.E., Braun, H.F.: Phys. Rev. B **25** (1982) 4702.
82 P 1 Pelizzone, M., Braun, H.F., Muller, J.: J. Magn. Magn. Mater. **30** (1982) 33.
82 S 1 Schobinger-Papamantellos, P.: J. Magn. Magn. Mater. **28** (1982) 97.
82 S 2 Skolozdra, R.V., Koretskaya, O.E., Gorelenko, Yu.K.: Ukr. Fiz. Zh. (USSR) **27** (1982) 263.
82 S 3 Slaski, M., Szytuła, A.: J. Less-Common Met. **87** (1982) L 1.
82 S 4 Szytuła, A., Siek, S.: J. Magn. Magn. Mater. **27** (1982) 49.
82 Y 1 Yakinthos, J.K., Gamari-Seale, H.: Z. Phys. B **48** (1982) 251.
82 Y 2 Yashima, H., Mori, H., Satoh, T., Kohn, K.: Solid State Commun. **43** (1982) 193.
82 Y 3 Yashima, H., Sato, N., Mori, H., Satoh, T.: Solid State Commun. **43** (1982) 595.
83 C 1 Canepa, F., Costa, G.A., Olcese, G.L.: Solid State Commun. **45** (1983) 725.
83 C 2 Chaughule, R.S., Radhakrishnamurty, C., Sampathkumaran, E.V., Malik, S.K., Vijayaraghavan, R.: Mater. Res. Bull. **18** (1983) 817.
83 C 3 Chevalier, B., Lejay, P., Etourneau, J., Hagenmuller, P.: Mater. Res. Bull. **18** (1983) 315.
83 D 1 Dhar, S.K., Nagarjan, R., Malik, S.K., Rambabu, D., Vijayaraghavan, R.: J. Magn. Magn. Mater. **31–34** (1983) 393.
83 E 1 Evres, J., Oehlinger, G., Weiss, A., Hulliger, F.: J. Less-Common Met. **90** (1983) L 19.
83 F 1 Felner, I., Nowik, I.: Solid State Commun. **47** (1983) 831.
83 G 1 Godart, C., Gupta, L.C., Ravet-Krill, M.F.: J. Less-Common Met. **94** (1983) 187.
83 G 2 Gupta, L.C., MacLaughlin, D.E., Tien, Ch., Godart, C., Edwards, M.A., Parks, R.D.: Phys. Rev. B **28** (1983) 3673.
83 H 1 Hiebl, K., Horvath, C., Rogl, P., Sienko, M.J.: J. Magn. Magn. Mater. **37** (1983) 287.
83 H 2 Hiebl, K., Horvath, C., Rogl, P., Sienko, M.J.: Solid State Commun. **48** (1983) 211.
83 J 1 Jorda, J.L., Ishikawa, M., Hovestreydt, E.: J. Less-Common Met. **92** (1983) 155.
83 L 1 Leciejewicz, J., Kolenda, M., Szytuła, A.: Solid State Commun. **45** (1983) 145.
83 L 2 Leciejewicz, J., Siek, S., Szytuła, A.: J. Magn. Magn. Mater. **40** (1983) 265.
83 L 3 Lieciejewicz, J., Szytuła, A.: Solid State Commun. **48** (1983) 55.
83 L 4 Leciejewicz, J., Szytuła, A., Zygmunt, A.: Solid State Commun. **45** (1983) 149.
83 N 1 Nguyen van Nhung, Tcheou, F., Rossat-Mignod, J., Ballestracci, R.: Solid State Commun. **45** (1983) 209.
83 N 2 Noakes, D.R., Shenoy, G.K., Niarchos, D., Umarji, A.M., Aldred, A.T.: Phys. Rev. B **27** (1983) 4317.
83 N 3 Noakes, D.R., Umarji, A.M., Shenoy, G.K.: J. Magn. Magn. Mater. **39** (1983) 309.
83 P 1 Palstra, T.T.M., Mydosh, J.A., Nieuwenhuys, G.J., van der Kraan, A.M., Buschow, K.H.J.: J. Magn. Magn. Mater. **36** (1983) 290.
83 P 2 Pinto, H., Melamud, M., Gal, J., Shaked, H., Kalvius, G.M.: Phys. Rev. B **27** (1983) 1861.
83 S 1 Sampathkumaran, E.V., Chaughule, R.S., Gopalakrishnan, K.V., Malik, S.K., Vijayaraghavan, R.: J. Less-Common Met. **92** (1983) 35.
83 S 2 Schobinger-Papamantellos, P., Routsi, Ch., Yakinthos, J.K.: J. Phys. Chem. Solids **44** (1983) 875.
83 S 3 Shaheen, S.A., Schilling, J.S., Liu, S.H., McMasters, O.D.: Phys. Rev. B **27** (1983) 4325.
83 S 4 Shigeoka, T., Fujii, H., Fujiwara, H., Yagasaki, K., Okamoto, T.: J. Magn. Magn. Mater. **31–34** (1983) 209.
83 S 5 Skolozdra, R.V., Komarovskaya, L.P.: Ukr. Fiz. Zh. (USSR) **28** (1983) 1093.
83 S 6 Slaski, M., Leciejewicz, J., Szytuła, A.: J. Magn. Magn. Mater. **39** (1983) 268.

83 S 7 Szytuła, A., Bażela, W., Leciejewicz, J.: Solid State Commun. **48** (1983) 1053.
83 U 1 Umarji, A.M., Noakes, D.R., Viccaro, P.J., Shenoy, G.K., Aldred, A.T., Niarchos, D.: J. Magn. Magn. Mater. **36** (1983) 61.
83 V 1 Vining, C.B., Shelton, R.N.: Phys. Rev. B **28** (1983) 2732.
83 W 1 Woolf, L.D.: Solid State Commun. **47** (1983) 519.
83 Y 1 Yakinthos, J.K., Routsi, Ch., Schobinger-Papamantellos, P.: J. Magn. Magn. Mater. **30** (1983) 355.
83 Y 2 Yashima, H., Mori, H., Sato, N., Satoh, T., Kohn, K.: J. Magn. Magn. Mater. **31–34** (1983) 411.
84 B 1 Bodak, O.I., Gorelenko, Yu.K., Yarovets, V.I., Skolozdra, R.V.: Ivz. Acad. Nauk (SSSR) Neorg. Mat. **20** (1984) 853.
84 C 1 Chevalier, B., Lejay, P., Etourneau, J., Hagenmuller, P.: Solid State Commun. **49** (1984) 753.
84 F 1 Felner, I., Nowik, I.: J. Phys. Chem. Solids **45** (1984) 419.
84 G 1 Gignoux, D., Gomez-Sal, J.C., Paccard, D.: Solid State Commun. **49** (1984) 75.
84 G 2 Grier, B.H., Lawrance, J.M., Murgai, V., Parks, R.D.: Phys. Rev. B **29** (1984) 2664.
84 H 1 Hiebl, K., Horvath, C., Rogl. P., Sienko, M.J.: Z. Phys. B **56** (1984) 201.
84 H 2 Hirjak, M., Chevalier, B., Etourneau, J., Hagenmuller, P.: Mater. Res. Bull. **19** (1984) 727.
84 K 1 Kido, H., Hoshikawa, T., Koizumi, M., Shimada, M.: J. Less-Common Met. **99** (1984) 151.
84 L 1 Leciejewicz, J., Kolenda, M., Szytuła, A.: 2nd Int. Conf. Phys. Magn. Mat. Jadwisin, Poland, September **1984**, p. 248.
84 L 2 Leciejewicz, J., Ptasiewicz-Bak, H., Szytuła, A., Slaski, M.: Acta Magnetica, Suppl. **84** (1984) 175.
84 L 3 Leciejewicz, J., Szytuła, A.: Solid State Commun. **49** (1984) 361.
84 L 4 Leciejewicz, J., Szytuła, A., Slaski, M., Zygmunt, A.: Solid State Commun. **52** (1984) 475.
84 M 1 Malik, S.K., Dhar, S.K., Vijayaraghavan, R.: Pramana (India) **22** (1984) 329.
84 M 2 Melamud, M., Pinto, H., Felner, I., Shaked, H.: J. Appl. Phys. **55** (1984) 2034.
84 M 3 Miraglia, S., Hodeau, J.L., Marezio, M., Ott, H.R., Remeika, J.P.: Solid State Commun. **52** (1984) 135.
84 M 4 Mori, H., Sato, N., Satoh, T.: Solid State Commun. **49** (1984) 955.
84 N 1 Nguyen van Nhung, Tcheou, F., Rossat-Mignod, J.: J. Phys. (Paris) **45** (1984) 163.
84 Q 1 Quezel, S., Rossat-Mignod, J., Chevalier, B., Lejay, P., Etourneau, J.: Solid State Commun. **49** (1984) 685.
84 R 1 Rauchschwalbe, U., Lieke, W., Steglich, F., Godart, C., Gupta, L.C., Parks, R.D.: Phys. Rev. B **30** (1984) 444.
84 S 1 Sichevich, O.M., Komarovska, L.P., Grin, Yu.N., Yarmolyuk, Ya.P., Skolozdra, R.V.: Ukr. Fiz. Zh. (USSR) **29** (1984) 1342.
84 S 2 Skolozdra, R.V., Koretska, O.E.: Ukr. Fiz. Zh. (USSR) **29** (1984) 877.
84 S 3 Skolozdra, R.V., Koretskaya, O.E., Gorelenko, Yu.K.: Izv. Akad. Nauk SSSR Neorg. Mater. **20** (1984) 604.
84 S 4 Slaski, M., Szytuła, A., Leciejewicz, J., Zygmunt, A.: J. Magn. Magn. Mater. **46** (1984) 114.
84 S 5 Srinivasan, R., Usha, S., Sampathkumaran, E.V., Vijayaraghavan, R.: J. Phys. F **14** (1984) L 33.
84 S 6 Szytuła, A., Slaski, M., Ptasiewicz-Bak, H., Leciejewicz, J., Zygmunt, A.: Solid State Commun. **52** (1984) 395.
84 T 1 Tsang, T.-W.E., Gschneidner jr., K.A., McMasters, O.D., Stierman, R.J., Dhar, S.K.: Phys. Rev. B **29** (1984) 4185.
84 Y 1 Yakinthos, J.K., Routsi, Ch., Schobinger-Papamantellos, P.: J. Phys. Chem. Solids **45** (1984) 689.
84 Z 1 Zygmunt, A., Szytuła, A.: Acta Magnetica, Suppl. **84** (1984) 193.
85 B 1 Bażela, W., Leciejewicz, J., Szytuła, A.: Acta Phys. Pol. A **68** (1985) 575.
85 B 2 Besnus, M.J., Kappler, J.P., Lehmann, P., Meyer, A.: Solid State Commun. **55** (1985) 779.
85 C 1 Chevalier, B., Etourneau, J., Hagenmuller, P., Quezel, S., Rossat-Mignod, J.: J. Less-Common Met. **111** (1985) 161.
85 C 2 Chevalier, B., Etourneau, J., Greedan, J.E., Coey, J.M.D., Maaroufi, A.: J. Less-Common Met. **111** (1985) 171.
85 D 1 Dommann, A., Hulliger, F., Ott, H.R., Gramlich, V.: J. Less-Common Met. **110** (1985) 331.
85 D 2 de Vries, J.W.C., Thiel, R.C., Buschow, K.H.J.: J. Less-Common Met. **111** (1985) 313.
85 F 1 Felner, I., Nowik, I.: Acta Phys. Pol. A **68** (1985) 97.
85 F 2 Felner, I., Nowik, I.: J. Magn. Magn. Mater. **47–48** (1985) 420.
85 F 3 Felner, I., Nowik, I.: J. Phys. Chem. Solids **46** (1985) 681.
85 F 4 Fujii, H., Okamoto, T., Shigeoka, T., Iwata, N.: Solid State Commun. **53** (1985) 715.
85 G 1 Gorelenko, Yu.K., Skolozdra, R.V., Dutchak, Ya.I., Yarovets, V.J., Shcherba, I.D., Bodak, O.I.: Ukr. Fiz. Zh. (USSR) **30** (1985) 301.
85 G 2 Gschneidner, jr., K.A.: J. Magn. Magn. Mater. **47–48** (1985) 57.

85 G 3 Gschneidner, jr., Ka.A., Dhar, S.K., Stierman, R.J., Tsang, T.-W.E., McMasters, O.D.: J. Magn. Magn. Mater. **47–48** (1985) 51.
85 H 1 Haen, P., Lejay, P., Chevalier, B., Lloret, B., Etourneau, J., Sera, M.: J. Less-Common Met. **110** (1985) 321.
85 H 2 Hiebl, K., Rogl, P.: J. Magn. Magn. Mater. **50** (1985) 39.
85 H 3 Hirjak, M., Lejay, P., Chevalier, B., Etourneau, J., Hagenmuller, P.: J. Less-Common Met. **105** (1985) 139.
85 K 1 Kido, H., Hoshikawa, T., Shimada, M., Koizumi, M.: Phys. Status Solidi (a) **90** (1985) 307.
85 K 2 Kierstead, H.A., Dunlap, B.D., Malik, S.K., Umarji, A.M., Shenoy, G.K.: Phys. Rev. B **32** (1985) 135.
85 K 3 Kitaoka, Y., Arimoto, H., Kohori, Y., Asayama, K.: J. Phys. Soc. Jpn. **54** (1985) 3236.
85 K 4 Kolenda, M., Szytuła, A., Leciejewicz, J., Zygmunt, A.: J. Magn. Magn. Mater. **49** (1985) 250.
85 L 1 Leciejewicz, J., Ptasiewicz-Bak, H., Szytuła, A., Slaski, M.: Physica B **130** (1985) 382.
85 L 2 Leciejewicz, J., Szytuła, A.: J. Magn. Magn. Mater. **49** (1985) 177.
85 L 3 Leciejewicz, J., Szytuła, A.: Solid State Commun. **56** (1985) 1051.
85 M 1 Moodenbaugh, A.R., Cox, D.E., Vining, C.B.: Phys. Rev. B **32** (1985) 3103.
85 M 2 Mori, H., Yashima, H., Sato, N.: J. Low Temp. Phys. **58** (1985) 513.
85 N 1 Nowik, I., Sampathkumaran, E.V., Kaindl, G.: Solid State Commun. **55** (1985) 721.
85 P 1 Paccard, L., Paccard, D., Moreau, J.M., Gomez-Sal, J.C., Fremy, M.A.: J. Less-Common Met. **110** (1985) 315.
85 P 2 Pinto, H., Melamud, M., Kuznietz, M., Shaked, H.: Phys. Rev. B **31** (1985) 508.
85 S 1 Schobinger-Papamantellos, P., Buschow, K.H.J.: J. Less-Common Met. **111** (1985) 117.
85 S 2 Schobinger-Papamantellos, P., Buschow, K.H.J.: J. Less-Common Met. **111** (1985) 125.
85 S 3 Serdyuk, U., Krentsis, R.P., Geld, P.V.: J. Less-Common Met. **111** (1985) 347.
85 S 4 Shigeoka, T., Iwata, N., Fujii, H., Okamoto, T.: J. Magn. Magn. Mater. **53** (1985) 83.
85 T 1 Tholence, J.L., Haen, P., Jaccard, D., Lejay, P., Floquet, J., Braun, H.: J. Appl. Phys. **57** (1985) 3172.
85 V 1 Vining, C.B., Shelton, R.N.: Solid State Commun. **54** (1985) 53.
86 B 1 Barandiaran, J.M., Gignoux, D., Schmitt, D., Gomez-Sal, J.C.: Solid State Commun. **57** (1986) 941.
86 B 2 Barandiaran, J.M., Gignoux, D., Schmitt, D., Gomez-Sal, J.C.: Solid State Commun. **59** (1986) 223.
86 B 3 Buffat, B., Chevalier, B., Tuilier, M.H., Lloret, B., Etourneau, J.: Solid State Commun. **59** (1986) 17.
86 D 1 Durkop, D., Braun, E., Politt, B., Schmidt, H., Roden, B., Wohlleben, D.: Z. Phys. B **63** (1986) 55.
86 F 1 Fujii, H., Isoda, M., Okamoto, T., Shigeoka, T., Iwata, N.: J. Magn. Magn. Mater. **54–57** (1986) 1345.
86 I 1 Iwata, N., Ikeda, T., Shigeoka, T., Fujii, H., Okamoto, T.: J. Magn. Magn. Mater. **54–57** (1986) 481.
86 L 1 Lahiouel, R., Galera, R.M., Pierre, J., Siaud, E.: Solid State Commun. **58** (1986) 815.
86 L 2 Lin, C.L., Crow, J.E., Mihalisin, T., Brooks, J., Stewart, G., Abou-Aly, A.I.: J. Magn. Magn. Mater. **54–57** (1986) 379.
86 P 1 Palstra, T.T.M., Menovsky, A.A., Neuwenhuys, G.J., Mydosh, J.A.: J. Magn. Magn. Mater. **54–57** (1986) 435.
86 P 2 Pearson, W.B.: Phys. Rev. B **33** (1986) 3545.
86 R 1 Rojek, A., Sułkowski, C.: Phys. Status Solidi (b) **134** (1986) K 133.
86 R 2 Rojek, A., Sułkowski, C., Zygmunt, A., Kozłowski, G.: Phys. Status Solidi (b) **134** (1986) 125.
86 S 1 Shigeoka, T., Iwata, N., Fujii, H., Okamoto, T.: J. Magn. Magn. Mater. **54–57** (1986) 1343.
86 S 2 Szytuła, A., Budkowski, A., Slaski, M., Zach, R.: Solid State Commun. **57** (1986) 813.
86 S 3 Szytuła, A., Leciejewicz, J., Slaski, M.: Solid State Commun. **58** (1986) 683.
86 T 1 Thompson, J.D., Parks, R.D., Borges, H.: J. Magn. Magn. Mater. **54–57** (1986) 377.
86 V 1 Veenhuizen, P.A., van Kalkeren, G., Klaasse, J.C.P., Menovsky, A., Moleman, A.C., de Boer, F.R.: J. Magn. Magn. Mater. **54–57** (1986) 425.
86 V 2 Vettier, C., Morin, P., Flouquet, J.: Phys. Rev. Lett. **56** (1986) 1980.
86 Y 1 Yakinthos, J.K., Roudaut, E.: J. Phys. (Paris) **47** (1986) 1239.
87 L 1 Leciejewicz, J., Szytuła, A.: J. Magn. Magn. Mater. **63–64** (1987) 190.